

Vasundhara Mahajan
Anandita Chowdhury
Narayana Prasad Padhy
Fernando Lezama *Editors*

Sustainable Technology and Advanced Computing in Electrical Engineering

Proceedings of ICSTACE 2021

Lecture Notes in Electrical Engineering

Volume 939

Series Editors

Leopoldo Angrisani, Department of Electrical and Information Technologies Engineering, University of Napoli Federico II, Naples, Italy

Marco Arteaga, Departament de Control y Robótica, Universidad Nacional Autónoma de México, Coyoacán, Mexico

Bijaya Ketan Panigrahi, Electrical Engineering, Indian Institute of Technology Delhi, New Delhi, Delhi, India

Samarjit Chakraborty, Fakultät für Elektrotechnik und Informationstechnik, TU München, Munich, Germany

Jiming Chen, Zhejiang University, Hangzhou, Zhejiang, China

Shanben Chen, Materials Science and Engineering, Shanghai Jiao Tong University, Shanghai, China

Tan Kay Chen, Department of Electrical and Computer Engineering, National University of Singapore, Singapore, Singapore

Rüdiger Dillmann, Humanoids and Intelligent Systems Laboratory, Karlsruhe Institute for Technology, Karlsruhe, Germany

Haibin Duan, Beijing University of Aeronautics and Astronautics, Beijing, China

Gianluigi Ferrari, Università di Parma, Parma, Italy

Manuel Ferre, Centre for Automation and Robotics CAR (UPM-CSIC), Universidad Politécnica de Madrid, Madrid, Spain

Sandra Hirche, Department of Electrical Engineering and Information Science, Technische Universität München, Munich, Germany

Faryar Jabbari, Department of Mechanical and Aerospace Engineering, University of California, Irvine, CA, USA

Limin Jia, State Key Laboratory of Rail Traffic Control and Safety, Beijing Jiaotong University, Beijing, China

Janusz Kacprzyk, Systems Research Institute, Polish Academy of Sciences, Warsaw, Poland

Alaa Khamis, German University in Egypt El Tagamoa El Khames, New Cairo City, Egypt

Torsten Kroeger, Stanford University, Stanford, CA, USA

Yong Li, Hunan University, Changsha, Hunan, China

Qilian Liang, Department of Electrical Engineering, University of Texas at Arlington, Arlington, TX, USA

Ferran Martín, Departament d'Enginyeria Electrònica, Universitat Autònoma de Barcelona, Bellaterra, Barcelona, Spain

Tan Cher Ming, College of Engineering, Nanyang Technological University, Singapore, Singapore

Wolfgang Minker, Institute of Information Technology, University of Ulm, Ulm, Germany

Pradeep Misra, Department of Electrical Engineering, Wright State University, Dayton, OH, USA

Sebastian Möller, Quality and Usability Laboratory, TU Berlin, Berlin, Germany

Subhas Mukhopadhyay, School of Engineering & Advanced Technology, Massey University, Palmerston North, Manawatu-Wanganui, New Zealand

Cun-Zheng Ning, Electrical Engineering, Arizona State University, Tempe, AZ, USA

Toyooki Nishida, Graduate School of Informatics, Kyoto University, Kyoto, Japan

Luca Oneto, Department of Informatics, Bioengineering, Robotics, University of Genova, Genova, Genova, Italy

Federica Pascucci, Dipartimento di Ingegneria, Università degli Studi "Roma Tre", Rome, Italy

Yong Qin, State Key Laboratory of Rail Traffic Control and Safety, Beijing Jiaotong University, Beijing, China

Gan Woon Seng, School of Electrical & Electronic Engineering, Nanyang Technological University, Singapore, Singapore

Joachim Speidel, Institute of Telecommunications, Universität Stuttgart, Stuttgart, Germany

Germano Veiga, Campus da FEUP, INESC Porto, Porto, Portugal

Haitao Wu, Academy of Opto-electronics, Chinese Academy of Sciences, Beijing, China

Walter Zamboni, DIEM - Università degli studi di Salerno, Fisciano, Salerno, Italy

Junjie James Zhang, Charlotte, NC, USA

The book series *Lecture Notes in Electrical Engineering* (LNEE) publishes the latest developments in Electrical Engineering—quickly, informally and in high quality. While original research reported in proceedings and monographs has traditionally formed the core of LNEE, we also encourage authors to submit books devoted to supporting student education and professional training in the various fields and applications areas of electrical engineering. The series cover classical and emerging topics concerning:

- Communication Engineering, Information Theory and Networks
- Electronics Engineering and Microelectronics
- Signal, Image and Speech Processing
- Wireless and Mobile Communication
- Circuits and Systems
- Energy Systems, Power Electronics and Electrical Machines
- Electro-optical Engineering
- Instrumentation Engineering
- Avionics Engineering
- Control Systems
- Internet-of-Things and Cybersecurity
- Biomedical Devices, MEMS and NEMS

For general information about this book series, comments or suggestions, please contact leontina.dicecco@springer.com.

To submit a proposal or request further information, please contact the Publishing Editor in your country:

China

Jasmine Dou, Editor (jasmine.dou@springer.com)

India, Japan, Rest of Asia

Swati Meherishi, Editorial Director (Swati.Meherishi@springer.com)

Southeast Asia, Australia, New Zealand

Ramesh Nath Premnath, Editor (ramesh.premnath@springernature.com)

USA, Canada:

Michael Luby, Senior Editor (michael.luby@springer.com)

All other Countries:

Leontina Di Cecco, Senior Editor (leontina.dicecco@springer.com)

**** This series is indexed by EI Compendex and Scopus databases. ****


Vasundhara Mahajan · Anandita Chowdhury ·
Narayana Prasad Padhy · Fernando Lezama
Editors

Sustainable Technology and Advanced Computing in Electrical Engineering

Proceedings of ICSTACE 2021

 Springer

Editors

Vasundhara Mahajan 
Department of Electrical Engineering
Sardar Vallabhbhai National Institute
of Technology
Surat, Gujarat, India

Anandita Chowdhury
Department of Electrical Engineering
Sardar Vallabhbhai National Institute
of Technology
Surat, Gujarat, India

Narayana Prasad Padhy
Department of Electrical Engineering
Indian Institute of Technology Roorkee
Roorkee, Uttarakhand, India

Fernando Lezama
GECAD-Research Group
Polytechnic Institute of Porto
Porto, Portugal

ISSN 1876-1100

ISSN 1876-1119 (electronic)

Lecture Notes in Electrical Engineering

ISBN 978-981-19-4363-8

ISBN 978-981-19-4364-5 (eBook)

<https://doi.org/10.1007/978-981-19-4364-5>

© The Editor(s) (if applicable) and The Author(s), under exclusive license to Springer Nature Singapore Pte Ltd. 2022

This work is subject to copyright. All rights are solely and exclusively licensed by the Publisher, whether the whole or part of the material is concerned, specifically the rights of translation, reprinting, reuse of illustrations, recitation, broadcasting, reproduction on microfilms or in any other physical way, and transmission or information storage and retrieval, electronic adaptation, computer software, or by similar or dissimilar methodology now known or hereafter developed.

The use of general descriptive names, registered names, trademarks, service marks, etc. in this publication does not imply, even in the absence of a specific statement, that such names are exempt from the relevant protective laws and regulations and therefore free for general use.

The publisher, the authors, and the editors are safe to assume that the advice and information in this book are believed to be true and accurate at the date of publication. Neither the publisher nor the authors or the editors give a warranty, expressed or implied, with respect to the material contained herein or for any errors or omissions that may have been made. The publisher remains neutral with regard to jurisdictional claims in published maps and institutional affiliations.

This Springer imprint is published by the registered company Springer Nature Singapore Pte Ltd.

The registered company address is: 152 Beach Road, #21-01/04 Gateway East, Singapore 189721, Singapore

ICSTACE 2021 Committee members

International Advisory Board

Dr. Siqi Bu, Associate Professor, Departmental Leader of EngD Program, Department of Electrical Engineering, The Hong Kong Polytechnic University, Hung Hom, Kowloon, Hong Kong

Dr. Fernando Lezama, GECAD—Research Group on Intelligent Engineering and Computing for Advanced Innovation and Development, Institute of Engineering, Polytechnic of Porto (ISEP/IPP), Portugal

Dr. João Soares, GECAD—Research Group on Intelligent Engineering and Computing for Advanced Innovation and Development, Institute of Engineering, Polytechnic of Porto (ISEP/IPP), Portugal

Dr. Bruno Canizes, GECAD—Research Group on Intelligent Engineering and Computing for Advanced Innovation and Development, Institute of Engineering, Polytechnic of Porto (ISEP/IPP), Portugal

Dr. Zita Vale, Professor, Department of Electrical Engineering, Institute of Engineering, Polytechnic of Porto (ISEP), 4200-072, Porto, Portugal

Dr. Ruben Romero, UNESP, Ilha Solteira, São Paulo, Brazil

Dr. Francisco Gonzalez-Longatt, Professor, Electrical Power Engineering, Department of Electrical Engineering, IT and Cybernetics, University of Southeast Norway

Dr. Vladimiro Miranda, INESC TEC—INESC Technology and Science, Portugal—Associate Director, International Affairs, President of INESC P&D Brasil, São Paulo, Brazil, Full Professor, Faculty of Engineering of the University of Porto, Portugal

Dr. Amin Mohammadpour Shotorbani, Faculty of Applied Science, School of Engineering, The University of British Columbia, Okanagan Campus, Canada

Dr. Tarlochan S. Sidhu, Professor, Faculty of Engineering and Applied Science, Ontario Tech University, Canada

Dr. Sanjeevikumar Padmanaban, CTiF Global Capsule, Department of Business Development and Technology, Aarhus University, Herning, Denmark

Dr. Subham Sahoo, Assistant Professor, Department of Energy Technology, and The Faculty of Engineering and Science, Aalborg University, Denmark

Dr. Kwang Y. Lee, Professor and Chair, Department of Electrical and Computer Engineering, Baylor University

Dr. Santiago Torres, Assistant Professor, Department of Electrical, Electronics and Telecommunications Engineering, University of Cuenca, Ecuador

Mr. Vamsi Krishna Adhikamsetty, Leonardo S.p.A. (Italy), USA

Dr. Reshmi Mitra, Assistant Professor, Computer Science, Southeast Missouri State University, USA

Dr. Fushuan Wen, Professor in Energy Systems, Tallinn University of Technology (TalTech), Estonia, Yusheng Xue Education Foundation Distinguished Professor, Hangzhou Dianzi University, China (part time)

Dr. Hemanshu Pota, Associate Professor, Engineering and Information Technology, The University of New South Wales Australia

Dr. Jai Govind Singh, Associate Professor and Head, Department of Energy, Environment and Climate Change, School of Environment, Resources and Development, Asian Institute of Technology, Thailand

Dr. Vandana Sakhre, Assistant Professor, Department of Chemical Engineering, School of Engineering and IT, Manipal Academy of Higher Education (MAHE), Dubai, UAE

Dr. Ravishankar Dudhe, Associate Professor, Ph.D. coordinator, School of Engineering and IT, Manipal Academy of Higher Education (MAHE), Dubai, UAE

Dr. Ramesh C. Bansal, Professor, Electrical Engineering Department, College of Engineering, University of Sharjah, Sharjah

Dr. Shamsul Jamel Elias, Computer Science Department, Universiti Teknologi MARA (UiTM), Cawangan Kedah, Malaysia

Dr. Dao Zhou, Associate Professor, Department of Energy Technology, Aalborg University, Denmark

Dr. Ariya Sangwongwanich, Postdoc Fellow, Department of Energy Technology, Aalborg University, Denmark

Dr. Saeed Peyghami, Assistant Professor, The Faculty of Engineering and Science, Aalborg University, Denmark

Dr. Bhekisipho Twala, Professor, Artificial Intelligence and Data Science, Department of Electrical and Mining Engineering, University of South Africa

Dr. Monjur Mourshed, Professor, School of Engineering, Cardiff University Cardiff, UK

Dr. Marcin Paprzycki, Associate Professor, Systems Research Institute, Polish Academy of Sciences, Poland

National Advisory Board

Dr. S. N. Singh, Professor, Department of Electrical Engineering, IIT Kanpur, Vice-chancellor, MMMUT, Gorakhpur

Dr. Hariom Gupta, Director, Jaypee Institute of engineering and Technology, Noida, Delhi

Dr. Narayana Prasad Padhy, Professor, Department of Electrical Engineering, IIT Roorkee

Dr. Pramod Agarwal, Professor, Department of Electrical Engineering, IIT Roorkee

Dr. G. N. Pillai, Professor and Head, Department of Electrical Engineering, IIT Roorkee

Dr. E. Fernandez Associate Professor, Department of Electrical Engineering, IIT Roorkee

Dr. Dheeraj Khatod, Associate Professor, Department of Electrical Engineering, IIT Roorkee

Dr. Bhawana Verma, Associate Professor, Chemical Engineering, IIT BHU, Varanasi

Dr. R. Raghvan, Associate Professor, Department of Electrical Engineering, IIT Gandhinagar, Gujarat

Dr. Bhim Singh, Professor, Department of Electrical Engineering, IIT Delhi

Dr. Abhijit R. Abhyankar, NTPC Chair Professor, Department of Electrical Engineering, IIT Delhi

Dr. Dipankar Debnath, Assistant Professor, Department of Electrical Engineering, IIT Kharagpur

Dr. Nishchal K. Verma, Professor, Department of Electrical Engineering, IIT Kanpur

Dr. Anil Sao, Associate Professor, School of Computing and Electrical Engineering, IIT Mandi

Dr. Bharat Singh Rajpurohit, Associate Professor, School of Computing and Electrical Engineering, IIT Mandi

Dr. Trapti Jain, Associate Professor, Department of Electrical Engineering, IIT Indore

Dr. Prabhat Kumar Upadhyay, Associate Professor, Department of Electrical Engineering, IIT Indore

Dr. Amod C. Umarikar, Associate Professor, Department of Electrical Engineering, IIT Indore

Dr. Bidyadhar Subdhi, Professor, Department of Electrical Engineering, IIT Goa

Dr. Nagesh Prabhu, Professor and Head, NMAM Karnataka

Dr. Seshan Srirangarajan, Assistant Professor, Department of Electrical Engineering, IIT Delhi

Dr. Prashant Agnihotri, Assistant Professor, Department of Electrical Engineering and Computer Science, IIT Bhilai, GEC Campus Sejbahar Raipur, Chhattisgarh

Dr. Sukanya Parui, Assistant Professor, Department of Electrical Engineering, IEST Shibpur, West Bengal

Dr. H. M. Suryavanshi, Professor, Department of Electrical Engineering, VNIT Nagpur

Dr. Subhrata Gupta, Professor, Department of Electrical Engineering, NIT Raipur

Dr. Shailendra Kumar, Professor, Department of Electrical Engineering, MANIT Bhopal

Dr. Ashwini Kumar, Professor, Department of Electrical Engineering, NIT Kurukshetra

Dr. Saurabh Mani Tripathi, Assistant Professor, Department of Electrical Engineering, KNIT Sultanpur, Uttar Pradesh

Dr. P. N. Tekwani, Professor, Department of Electrical Engineering, Nirma University, Ahmedabad

Dr. Santosh Vora, Professor and Head, Department of Electrical Engineering, Nirma University, Ahmedabad.

Dr. Deep Kiran, Assistant Professor, Department of Electrical Engineering, IIT Roorkee

Dr. Dipankar Deb, Professor, Electrical Engineering, Institute of Infrastructure, Technology, Research and Management (IITRAM), Ahmedabad, Gujarat

Dr. Srinivasan Krishnaswamy, Assistant professor, Department of Electronics and Electrical Engineering, IIT Guwahati

Dr. Sisir Kumar Nayak, Assistant professor, Department of Electronics and Electrical Engineering, IIT Guwahati

Dr. Deepak Reddy, Assistant Professor, Department of Electrical Engineering, NIT Warangal

Dr. Sailaja Kumari M., Professor and Head, Department of Electrical Engineering, NIT Warangal

Dr. Mahesh Bunde, Principal and Director, Poornima College of Engineering Jaipur, Rajasthan, India

Dr. Sachin Untawale, Director and Professor Department of Mechanical Engineering, G. H. Rasoni College of Engineering, Nagpur

Dr. Vivek Kapur, Director, G. H. Rasoni Institute of Engineering and Technology, Nagpur

Dr. Varsha Varwandkar, Director, Career Psychologist, Educational Consultant, My Aglakadam Academy of Guidance and Counselling Pvt. Ltd., Raipur

Dr. S. D. Varwandkar, Former Director, VJTI, Mumbai

Dr. Debasis Das, Assistant Professor, Department of Computer Science and Engineering, Indian Institute of Technology (IIT), Jodhpur

Dr. Premlata Jena, Associate Professor, Department of Electrical Engineering, IIT Roorkee, Roorkee

Dr. Pratima Meshram, Principal Scientist, Metal Extraction and Recycling Division, CSIR-National Metallurgical Laboratory, Jamshedpur, Jharkhand

Technical Program Committee

Dr. Fushuan Wen, Professor in Energy Systems, Tallinn University of Technology (TalTech), Estonia, Yusheng Xue Education Foundation Distinguished Professor, Hangzhou Dianzi University, China

Dr. Hemanshu Pota, Associate Professor, Engineering and Information Technology, The University of New South Wales Australia

Dr. Jai Govind Singh, Associate Professor and Head, Department of Energy, Environment and Climate Change, School of Environment, Resources and Development, Asian Institute of Technology, Thailand

Dr. Bhekisipho Twala, Professor, Artificial Intelligence and Data Science, Department of Electrical and Mining Engineering, University of South Africa

Dr. Reza Abrishambaf, Associate Professor at Miami University, Hamilton Ohio, USA

Dr. Hassan Haes Alhelou, School of Electrical and Electronic Engineering, University College Dublin, Dublin, Ireland.

Dr. Hafiz Ahmed, Senior Lecturer (Associate Professor) in Nuclear Control and Instrumentation, Nuclear Futures Institute, Bangor University, Dean St., Bangor, Gwynedd, LL57 1UT, UK

Dr. Ariya Sangwongwanich, Postdoc Fellow, Department of Energy Technology, Aalborg University, Denmark

Dr. Saeed Peyghami, Assistant Professor, The Faculty of Engineering and Science, Aalborg University, Denmark

Dr. Dmitri Vinnikov, Research Professor, Power Electronics Research Group, Tallinn University of Technology, Tallinn, Estonia

Dr. Ahmed Al Durra, Professor, Power System and Power Electronics, Khalifa University of Science and Technology, Abu Dhabi, UAE

Dr. Prashant Bedekar, Professor, Department of Electrical Engineering, GEC Amravati

Dr. Sanjay Dambhare, Professor, Department of Electrical Engineering, COEP Pune

Dr. Sunanda Ghanagaonkar, Professor, Department of Electrical Engineering, COEP Pune

Dr. Anjali Dharme, Professor, Department of Electrical Engineering, COEP Pune

Dr. V. N. Pandey, Professor, Department of Electrical Engineering, COEP Pune

Dr. Subham Sahoo, Assistant Professor, Department of Energy Technology and The Faculty of Engineering and Science, Aalborg University, Denmark

Dr. Rezkallah Miloud, Senior Researcher, Ecole de Technologie Superieure (ETS), Montral, Canada

Dr. Nidhi Singh Pal, Assistant Professor and Head, School of Engineering, Gautam Buddha University (GBU), Noida

Dr. Josep Pou, Professor, School of Electrical and Electronic Engineering, NTU Singapore

Dr. Hiren Gami, Assistant Professor, Dept. of Engineering Technology, Miami University, Middletown

Dr. Akshay Jain, VP of Telecommunications Engineering, Neutron Technologies, S.L

Ms. Shivani Abrol, Professor, Department of Electrical Engineering, Centennial College, Canada

Dr. Janardhana Rao Kotturu, Research Fellow at Rolls-Royce, NTU Corporate Laboratory, Singapore.

Dr. Krishna Murari, Department of Electrical Engineering, Postdoctoral Research Associate, University of NC at Charlotte, USA

Dr. Sanjeev Pannala, Department of Electrical Engineering, Postdoctoral Research Associate, Washington State University, USA

Dr. Zeljko V. Despotovic, Full Research Professor, Department of Robotics and Mechatronics, Mihajlo Pupin Institute, Belgrade, Serbia

Dr. Rohit Bhakar, Associate Professor, Department of Electrical Engineering, MNIT Jaipur

Dr. Prerna Jain, Associate Professor, Department of Electrical Engineering, MNIT Jaipur

Dr. Kusum Verma, Associate Professor, Department of Electrical Engineering, MNIT Jaipur

Dr. Parul Mathuria, Assistant Professor, Centre for Energy and Environment, MNIT Jaipur

Dr. Omhari Gupta, Assistant Professor, Department of Electrical Engineering, NIT Jamshedpur

Dr. Pradyumn Chaturvedi, Assistant Professor, Department of Electrical Engineering, VNIT Nagpur

Dr. Makrand Lokhande, Assistant Professor, Department of Electrical Engineering, VNIT Nagpur

Dr. Varsha Singh, Assistant Professor, Department of Electrical Engineering, NIT Raipur

Dr. S. Ghosh, Associate Professor, Department of Electrical Engineering, NIT Raipur

Dr. Ebha Koley, Assistant Professor, Department of Electrical Engineering, NIT Raipur

Dr. Ramnarayan Patel, Associate Professor, Department of Electrical Engineering, NIT Raipur

Dr. Lalit Sahu, Assistant Professor, Department of Electrical Engineering, NIT Raipur

Dr. D. Sreenivasarao, Assistant Professor, Department of Electrical Engineering, NIT Warangal

Dr. Giribabu Dyanamina, Assistant Professor, Department of Electrical Engineering, MANIT Bhopal

Dr. Deepti Singh, Assistant Professor, School of Applied Sciences, Gautam Buddha University (GBU), Noida

Dr. Damanjeet Kaur, Associate Professor, Department of Electrical Engineering, Punjab University

Dr. Anand Kumar Tiwari, Assistant Professor, Chemical Engineering, DDU Nadidad

Dr. Satish Sharma, Associate Professor, Department of Electrical Engineering, MNIT Jaipur

Dr. Vivek Shrivastava, Associate Professor, Department of Electrical Engineering, NIT Delhi

Dr. Sachin Kumar Jain, Assistant Professor, Electronics and Communications Engineering, IIITDM Jabalpur, Madhya Pradesh

Dr. Ritula Thakur, Associate Professor, Department of Electrical Engineering, National Institute of Technical Teachers Training and Research, Sector 26, Chandigarh

Dr. C. Sharmeela, Assistant Professor, Department of Electrical and Electronics Engineering, College of Engineering, Guindy, Anna University, Chennai

Dr. Anupama Huddar, Head, Department of Electrical Engineering, Bhilai Institute of Technology, Durg, Chhattisgarh

Dr. Supriya Tripathi, Professor, Department of Electrical Engineering, Bhilai Institute of Technology, Durg, Chhattisgarh

Dr. Nagendra Tripathi, Professor, Department of Electrical Engineering, Bhilai Institute of Technology, Durg, Chhattisgarh

Dr. Ajat Shatru Arora, Department of Electrical and Instrumentation Engineering, Sant Longowal Institute of Engineering and Technology, Sangrur

Dr. Dilbag Singh, Department of Instrumentation and control and Electrical Engineering, Dr. B. R. Ambedkar National Institute of Technology, Jalandhar

Dr. Chandra Prakash, Assistant Professor, Department of Electrical Engineering, NIT Delhi

Dr. Abhilash Kumar Gupta, Assistant Professor, Department of Electrical Engineering, GLA University, Mathura

Dr. Supriya Jaiswal, Assistant Professor, Department of Electrical Engineering, NIT Hamirpur, Himachal Pradesh

Dr. Shashank Vyas, Manager—Innovation (Energy Storage), SB Energy (SoftBank Group), Central Delhi

Dr. Sujil A., Assistant Professor, Department of Electrical Engineering, RIT, Rajaramnagar

Dr. Deepak Sonje, Associate Professor, Department of Electrical Engineering, RH Sapat College of Engineering and Management, Nasik

Dr. Leena G., Professor, Department of Electrical Engineering, Manav Rachna University

Dr. Nilesh V. Shah, Associate Professor, Department of Electrical Engineering, SCET Surat

Dr. Indu Maheshwari, Director National Power Training Institute (NPTI), Delhi

Dr. Srinivasan Krishnaswamy, Assistant professor, Department of Electronics and Electrical Engineering, IIT Guwahati

Dr. Sisir Kumar Nayak, Assistant professor, Department of Electronics and Electrical Engineering, IIT Guwahati

Dr. Deepak Reddy, Assistant Professor, Department of Electrical Engineering, NIT Warangal

Dr. Saurabh Mani Tripathi, Assistant Professor, Department of Electrical Engineering, KNIT Sultanpur, Uttar Pradesh

Dr. Sheshan Srirangarajan, Assistant Professor, Department of Electrical Engineering, IIT Delhi

Dr. Prashant Agnihotri, Assistant Professor, Department of Electrical Engineering and Computer Science, IIT Bhilai, GEC Campus Sejbahar Raipur, Chhattisgarh

Dr. Sukanya Parui, Assistant Professor, Department of Electrical Engineering, IEST Shibpur, West Bengal

Dr. Debasis Das, Assistant Professor, Department of Computer Science and Engineering, IIT Jodhpur

Dr. Santosh Vora, Professor and Head, Department of Electrical Engineering, Nirma University, Ahmedabad

Dr. Maria Thomas, Assistant Professor, Department of Electrical Engineering, IIT BHU

Dr. Lillie Dewan, Professor, Department of Electrical Engineering, NIT Kurukshetra

Dr. Jyoti Ohri, Professor, Department of Electrical Engineering, NIT Kurukshetra

Dr. Chayan Bhawal, Assistant Professor, Department of Electronics and Electrical Engineering, IIT Guwahati

Dr. Chetan K. Lad, Assistance Professor and Incharge Head, Department of Electrical Engineering, C. K. Pithawala College of Engineering and Technology, Surat, Gujarat

Dr. Bhavin Shah, Associate Professor, Department of Electrical Engineering, L. D. College of Engineering, Ahmedabad

Dr. Bhargav Vyas, Associate Professor, Department of Electrical Engineering, L. E. College, Morbi, Gujarat

Dr. Ravi Eswar K.M., Assistant Professor, Department of Electrical and Electronics Engineering, Faculty of Engineering and Technology, SRM Institute of science and Technology, Kattankulathur Campus

Dr. Hareesh Myneni, Assistant Professor, Department of Electrical Engineering, NIT Srinagar

Dr. S Kayalvizhi, Assistant Professor, Department of Electrical Engineering, NIT Trichy

Dr. Venu Sonti, Assistant Professor, Department of Electrical Engineering, NIT Raipur, Chhattisgarh

Dr. T. Vinay Kumar, Assistant Professor, Department of Electrical Engineering, NIT Warangal

Dr. Rajesh Kumar, Professor, Department of Electrical Engineering, MNIT Jaipur

Dr. Nitin Gupta, Assistant Professor, Department of Electrical Engineering, MNIT Jaipur

Dr. Rajesh Kumar Nema, Professor, Department of Electrical Engineering, NIT Bhopal

Dr. Sreeraj E. S., Assistant Professor, Department of Electrical and Electronics, NIT Goa

Dr. Vikas Singh Bhadoria, Associate Professor and Associate Head Placement and Training, Electrical and Electronics Engineering, ABES Engineering College, Ghaziabad Campus, Uttar Pradesh

Dr. Jayaram N., Assistant Professor, Department of Electrical Engineering, NIT Andhra Pradesh

Dr. Anurag Sharma, Assistant Professor, School of Electrical and Electronic Engineering, Newcastle University, Singapore Campus

Dr. Suryasnata Tripathy, Assistant Professor, Department of Electronics and Communication Engineering, Indian Institute of Information Technology (IIIT), Surat, Gujarat

Dr. Anirban Roy, Assistant Professor, Department of Electronics and Communication Engineering, Indian Institute of Information Technology (IIIT), Surat, Gujarat

Dr. Darshan Medhane, Assistant Professor, Department of Computer Science and Engineering, Indian Institute of Information Technology (IIIT), Pune

Dr. Mahdi Saadatmand, Researcher, Power System Secure Operation Research Center, Amirkabir University of Technology, Tehran, Iran

Dr. Hicham Gouabi, Researcher, Control Analysis and Optimization of Electro Energetic Systems (CAOSEE) research laboratory, Tahri Mohammed University, Bechar, Algeria

Ms. Miao Lin Pay, M.Sc. B.Eng., Researcher, Institute for Future Transport and Cities, Coventry University, Coventry, UK

Dr. Md. Samar Ahmad, Research Scientist, Rolls-Royce Corporate Lab@NTU, Nanyang Technological University, Singapore

Dr. Trilochan Penthia, Postdoctoral Fellow, College of Electrical Engineering, Zhejiang University, China.

Dr. Hocine Abdelhak Azzeddine, Faculty of Sciences and Technology, LSTE Laboratory Mustapha Stambouli University of Mascara, Algeria

Dr. Chaouch Djamel Eddine, Professor, Faculty of Sciences and Technology, LSTE Laboratory, Mustapha Stambouli University of Mascara, Algeria

SVNIT Committee Members

Dr. R. A. Christian, Professor, CED, SVNIT

Dr. J. Banerjee, Professor, MED, SVNIT

Dr. Arun Kumar Jana, Associate Professor, ChED, SVNIT

Dr. Rasika Dhavse, Associate Professor, ECED, SVNIT

Dr. Kirti Inamdar, Assistant Professor, ECED, SVNIT

Dr. Dipti Rana, Assistant Professor, COED, SVNIT

Dr. Rupa G. Mehta, Associate Professor, COED, SVNIT

Dr. Udai Rao, Assistant Professor, COED, SVNIT

Dr. Bhavesh Gohil, Assistant Professor, COED, SVNIT

Dr. Shriniwas Arkatkar, Associate Professor, CED SVNIT

Dr. Namrata Jariwala, Assistant Professor, CED SVNIT

Dr. P. V. Bhale, Associate Professor, MED, SVNIT

Dr. Manish K. Rathore, Assistant Professor, MED SVNIT

Dr. Premlata Kumari, Associate Professor, ACD, SVNIT

Electrical Department Committee Members

Dr. Varsha Shah, Professor, EED, SVNIT

Dr. Ashish K. Panchal, Associate Professor, EED, SVNIT

Dr. M. A. Mulla, Associate Professor, EED, SVNIT

Dr. Sabharaj Arya, Associate Professor, EED, SVNIT

Dr. Hiren G. Patel, Associate Professor, EED, SVNIT
Ms. Chandani P. Gor, Assistant Professor, EED, SVNIT
Dr. Mahesh Aeidapu, Assistant Professor, EED, SVNIT
Dr. Sanjay Tolani, Assistant Professor, EED, SVNIT
Dr. Rahul Radhakrishnan, Assistant Professor, EED, SVNIT
Dr. Kunisetti V. Praveen Kumar, Assistant Professor, EED, SVNIT
Dr. Gangireddy Sushnigdha, Assistant Professor, EED, SVNIT
Dr. J. Venkataramanaiah, Assistant Professor, EED, SVNIT
Dr. Suresh Lakhimsetty, Assistant Professor, EED, SVNIT
Dr. Akansha Shukla, Assistant Professor, EED, SVNIT
Dr. Sukanta Haldar, Assistant Professor, EED, SVNIT

Preface

The event is a perfect occasion to celebrate the *National Education Day*, November 11, the Birth Anniversary of Maulana Abdul Kalam Azad, great freedom fighter, eminent educationist and first Union Minister of Education. The day is also seen as an occasion to remember Azad's contribution in laying the foundations of the education system in an independent India and evaluating and improving the country's current performance in the field.

The event is the part of the SVNIT Diamond Jubilee Celebrations. In line with our service to the humanity, the conference aims to provide a global platform to the researchers for sharing and showcasing their discoveries/findings/innovations. This conference involves the areas related to sustainable development. In this conference, the academicians and industry experts will address new challenges and share solutions at the interface of technology, information, and complex systems and discuss future research directions. Sustainable development is very much essential in the contemporary scenario due to increasing environmental concerns, demand for energy, global warming and end of life safe disposal of products.

The conference is aligned with sustainable development goal 7 of "Affordable and Clean Energy." This ensures access to inexpensive, trustworthy, sustainable and modern facilities for all. During the conference, the sustainable aspect and technological progress related to different engineering branches, renewable, green technology and smart cities will be explored.

The main focus is electrical engineering. However, the sustainable advancement in other engineering branches is also accommodated for a broader perspective. The conference has received overwhelming response from researchers across the globe. During the event, there will be 11 keynote sessions on the vital and relevant topics related to sustainability by various experts from various institutes from India and abroad. In addition, there will be around 100 paper presentations in 17 sessions by the participants and researchers from India and abroad.

We are thankful to the SVNIT administration for permitting us for this thoughtful conference and providing us the necessary infrastructure and facilities. So, lets join hands and explore the horizons for the betterment of the society.

Surat, India
Surat, India
Roorkee, India
Porto, Portugal

Vasundhara Mahajan
Anandita Chowdhury
Narayana Prasad Padhy
Fernando Lezama

Details of Keynote Speakers

1. **Prof. Mohammad Shahidehpour, IEEE Fellow, Robert W. Galvin Centre for Electricity Innovation, Illinois Institute of Technology, Chicago, IL 60616, USA.**
Topic of keynote: “Energy Hubs for Co-optimization of Interdependent Infrastructures in an Urban Community”
2. **Dr. Kalyan K. Sen, Co-Founder/Chief Technology Officer of Sen Engineering Solutions, Inc.**
Topic of keynote: “Power Flow Control Solutions for a Modern Grid using SMART Power Flow Controllers”
3. **Prof. Fushuan Wen, Professor in Energy Systems at Tallinn University of Technology.**
Topic of keynote: “Flexible ramping products for maintaining power system operation security in renewable generation-rich power systems”
4. **Prof. Narayana Prasad Padhy, Professor and Chair Professor, Department of Electrical Engineering, IIT Roorkee, Uttarakhand.**
Topic of keynote: “Smart Grid Future and Challenges”
5. **Dr. Fernando Lezama, GECAD–Research Group on Intelligent Engineering and Computing for Advanced Innovation and Development, Institute of Engineering, Polytechnic of Porto (ISEP/IPP), 4200-072 Porto, Portugal.**
Topic of keynote: “Computational intelligence applications in smart grid optimization”
6. **Prof. Francisco Gonzalez-Longatt, Professor, Electrical Power Engineering, Department of Electrical Engineering, IT and Cybernetics, University of Southeast Norway.**
Topic of keynote: “Tool for analyzing power converter dominated systems: Co-simulation, digital real-time simulation and more...”
7. **Prof. Nandini Gupta, Professor, EED, IIT Kanpur.**
Topic of keynote: “Nano-dielectrics as novel insulating materials for power apparatus and systems”

8. **Dr. Marcin Paprzycki, Associate Professor, Systems Research Institute, Polish Academy of Sciences, Poland.**
Topic of keynote: "Introduction to federated learning"
9. **Prof. Abhijit R. Abhyankar, NTPC Chair Professor of Electrical Engineering Department at Indian Institute of Technology Delhi, New Delhi, India.**
Topic of keynote: "DSO conceptualization for future distribution systems"
10. **Dr. Maria Ganza, Associate Professor, Faculty of Mathematics and Informatics, Warsaw University of Technology, Warsaw, Poland.**
Topic of keynote: "Introduction to reinforcement learning"
11. **Mr. Kartikesh Kumar Jha, Application Engineer in ARK Infosolutions Pvt. Ltd. (elite channel partner of Ansys).**
Topic of keynote: "Design and Development of Electric Vehicles using Ansys"

Contents

Analysis of Effect of Rotor Slot Shape on Torque Ripple in Induction Motor Using FEM	1
A. E. Aishwarya and B. A. Sridhara	
Comparative Analysis of Tensile Strength for Scrap Electrical Wire-Reinforced Concrete	11
Abhishek Kumar Gupta, Km. Shalini Kumari, and Sawan Kumar Gupta	
IoT and Cloud Network Based Water Quality Monitoring System Using IFTTT Framework	23
Abhishek Kumar, Sanjay Kumar Suman, L. Bhagyalakshmi, and Anil Kumar Sahu	
Advanced Power Flow Management System for Electric Vehicle Charging Station	33
Abhishek Pratap Singh and Yogendra Kumar	
Analysis of Graphene Field-Effect Transistor (GFET) as a Sensor	45
Arpitkumar Chaudhari, Abhishek Bhowmik, Jay Patel, Achal Parikh, and Rutu Parekh	
Optimal Location and Size of Multi-distributed Generation with Minimization of Network Losses	61
Akhilesh Kumar Barnwal, Shailendra Singh, and M. K. Verma	
Bi-q MSZSI Topology for Grid-Tied Inverter Under Ideal Grid Conditions	73
Anish Tiwari and Anandita Chowdhury	
ASIC Implementation of a 16-Bit Brent–Kung Adder at 45 nm Technology Node	83
Anmol Saxena, Vyom Saraf, and Rutu Parekh	

Autonomous Vehicles: A Detailed Bird Eye View	107
Ansh Jain and N. Gupta	
Imperceptible Digital Image Watermarking Based on Discrete Wavelet Transform and Schur Decomposition	119
Anurag Tiwari and V. K. Srivastava	
Analysis of Effective Area Radius and Its Dependency on Soil Nature in Grounding System	129
Aravelli S. L. K. Gopalamma and R. Srinu Naik	
Attack and Defense Methodology Against the Share Intents in Android	141
B. N. Arunakumari, P. Shrivathsa, and G. Vinodkumar	
Comparative Study of Traffic Light and Sign Detection Techniques	153
Aryan Jain, Swarup Totloor, Tanisha Agarwal, M. N. Pavan Kumar, and M. L. J. Shruthi	
A New Fuzzy Cascaded Controller for Hybrid Power System with Integration of FACTS Device	165
Ashiwani Kumar and Ravi Shankar	
MATLAB GUI-Based Partial Discharge Localization in Power Transformers Using UHF Acoustic Method	177
Avinash S. Welankiwar and Sagar Kudkelwar	
A Study and Investigation of Structural Parameters of Vertically Aligned Carbon Nanotube Arrays as a Thermal Interface Material	189
Ayush Nirwal, Rushabh Agrawal, Ragini Meena, Aayush Raval, Akash Parmar, and Rutu Parekh	
Review on Reliability Assessment in Power System	205
Bansi R. Kanzariya, Trisha Parekh, Kartavi Patel, Mithilesh G. Solanki, Neeraj Kumar Singh, Atul Kumar Yadav, Mahshooq Abdul Majeed, Lalit Tak, and Vasundhara Mahajan	
Synchronization of Optimized Traffic Signals Designed by Webster Method Along Six Intersections of Raipur City from Sharda Chowk to Telibandha Chowk	223
Bhavesk Kumar Kashyap, Harshit Mishra, Shubham Tiwary, Abhishek Bisen, Mayank Verma, Anurag Wahane, and Alok Kumar Jain	

Comparison Between Incremental Conductance MPPT of Two-Phase Interleaved Boost Converter and Boost Converter Using MATLAB Simulink 235
 Boga Jyothi, Sudheer Vinnakoti, Madisa V. G. Varaprasad, and S. Leela Tejaswini Kavya

A Novel Converter for Bidirectional Power Flow in Hybrid Electric Vehicle Systems Using ANN Controller 245
 C. H. Mohan Murali Krishna, R. S. Ravi Sankar, Madisa V. G. Varaprasad, and K. K. Deepika

Multiple Optimal Solutions for Optimal PMU Placement Using Graph Theory 267
 Chejarla Madhu Kishore Devara and Matam Sailaja Kumari

LVRT Performance Enhancement of Multi-machine Power System with High Penetration of Wind Energy Sources Considering Fault Current Limiters 277
 Chintan R. Mehta and Santosh C. Vora

Comparative Analysis of Electromagnetic Forces on Two Different Structures of Sen Transformer 295
 Dhruva Patel and Anandita Chowdhury

Eunoia: A Website for Self-CBT and Psychotherapy 311
 Dhruv Rastogi, Shubhangi Thakur, and Leena Singh

Performance Evaluation of Basic, Modified, and Advanced DC-DC Boost Converters Used with PV System 325
 Dilip Yadav and Nidhi Singh

Energy and SLA-Aware VM Placement Policy for VM Consolidation Process in Cloud Data Centers 351
 Dipak Dabhi and Devendra Thakor

Analysis and Prevention of Denial of Service Attacks in Smart Grid Using IoT 367
 Harsh Kakadiya, Janavi Popat, Neeraj Kumar Singh, Lalit Tak, Mahshooq Abdul Majeed, Soumya Mudgal, and Vasundhara Mahajan

Convolutional Neural Network-Based Contemporaneous Human Facial Expression Identification 379
 B. K. Harsha, M. L. J. Shruthi, and G. Indumathi

Photovoltaic Maximum Power Point Tracking Using Artificial Neural Network and PI Controller 393
 Hocine Abdelhak Azzeddine, Djamel-eddine Chaouch, Mourad Hebali, Ahmed Labaoui, Youcef Islam Djilani Kobibi, and Benaoumeur Ibari

Performance Analysis of DGFET, MESFET, and SOI on Varying Device Intrinsic Input Parameters	405
Isha Desai, Jhanvi Shroff, and Rutu Parekh	
Distraction of Experienced Drivers at a Construction Site Using Eye Tracker	423
Kamini Gupta, Piyush Miglani, Purva Dua, Amit Agarwal, and Neelima Chakrabarty	
Detailed Economic Analysis of Solar Rooftop Photovoltaic System: Case Study of Institutional Building	441
Kritika Kohli, Saurabh Kumar Rajput, and Sulochana Wadhvani	
Multi-agent System for Energy Management of Renewable Energy in Domestic Cooking	453
M. Lakshmi Swarupa, G. Divya, and V. Ch. S. N. Lavanya	
Hourly Load Forecasting Using Sequence-to-Sequence LSTM-Based Deep Machine Learning Model	469
Mahshooq Abdul Majeed, Soumya Mudgal, Lalit Tak, Janavi Papat, Harsh Kakadiya, Neeraj Kumar Singh, and Vasundhara Mahajan	
Symmetrical Pulse Width Modulation Technique for Harmonic Elimination in PWM AC Voltage Regulator Using Random Search Method	479
M. S. Patil and A. S. Koshti	
Design of Three-Phase, 400 Hz Power Supply Using Three-Level T-Type Topology	493
Gayatri Kher, M. T. Shah, and Vinod Patel	
An Overview of Recently Developed Liquefaction Mitigation Methods	515
Md Asad Ahmad and Yamin Wasti	
Review on Cybersecurity and Major Cyberthreats of Smart Meters	527
Mithilesh G. Solanki, Kartavi S. Patel, Bansi R. Kanzariya, Trisha H. Parekh, Neeraj Kumar Singh, Atul Kumar Yadav, Mahshooq Abdul Majeed, Lalit Tak, and Vasundhara Mahajan	
A Brief Review of Different Estimation Methods of SOC for Li-ion Battery	543
Mona Rani and Supriya Jaiswal	
Various Machine Learning Techniques to Diagnose Alzheimer’s Disease—A Systematic Review	557
Narmada Kari, Sanjay Kumar Singh, and S. Velliangiri	

Technical Aspect of Water Resource Management of Aligarh District	569
Nazish Mohammad, Mahfooz Alam, and Mubeen Beg	
Flood Modelling and Simulation Using iRIC Model for Dhom Dam on Krishna River	581
Shaikh Neha Anjum Nisar and Aditya P. Nilawar	
A Review on Performance and Reliability Aspects of Photovoltaic Modules	589
Neha Kumari, Sanjay Kumar Singh, and Sanjay Kumar	
A Game-Theoretic Approach for Enabling Peer-to-Peer Sharing of Rooftop Solar Energy	603
Nilesh Hadiya, Shashank Vyas, Falti Teotia, and Rohit Bhakar	
Recent Technological Advances in Solar Photovoltaic System and Its Applications in Building Integrated Photovoltaic System	625
Noorul Islam, Aslam Nat, and Rashid Ahmed Khan	
Performative Analysis on Ion-Sensitive Field-Effect Transistor by Varying Intrinsic Parameter	637
Keval Thakrar, Parth Katrodiya, Dhruvam Panchal, Hitarth Bharad, Jaimin Vaghela, Sai Deepak, and Ritu Parekh	
Alignment Format for Semantic Translation	651
Paweł Szmęja, Wiesław Pawłowski, Maria Ganzha, Marcin Paprzycki, and Katarzyna Wasielewska-Michniewska	
Topical Classification of Food Safety Publications with a Knowledge Base	673
Piotr Sowinski, Katarzyna Wasielewska-Michniewska, Maria Ganzha, and Marcin Paprzycki	
Comparative Study of Different Types of Slab Structures	695
Pranav Mene and Aditya P. Nilawar	
Model Order Reduction of MIMO Linear System Using Grey Wolf Optimization	705
Pranay Bhadauria and Nidhi Singh	
Smart Wheelchair for Specially Abled People	717
Prashant Verma and Kirti Pal	
Integration of Plugged-in Electric Vehicles for Load Frequency Control in Two-Area System	727
Pratik Sanjay Kadge and Rajesh Joseph Abraham	
Investigation on the Occurrence of Ferroresonance with the Variation of Degree of Transformer Core Saturation	747
Rajat Shubhra Pal and Madhab Roy	

Application of Modified Artificial Bee Colony Algorithm for Optimization of Reactive Power	757
Rohini Mahadik, A. R. Thorat, and Iranna Korachagaon	
Levy Flight-Based Crow Search Algorithm for Optimum Protection Coordination in Combined Overhead/Cable Distribution System	771
Sagar Kudkelwar and Bam Bahadur Sinha	
Optimization of Graphene Oxide Layer Thickness of ZnO-Based Hybrid Solar Cell Using SCAPS 1D: A Comparative Study on ZnO/GO and ZnO/SiO₂ Hybrid Cells	785
Sakshi Tyagi, Pawan Kumar Singh, and Arun Kumar Tiwari	
An Algorithm for Estimation of Reference Current for a Shunt Active Power Filter with Active Compensation of DC Offset	801
Sangeeta L. Mahaddalkar and Vinayak N. Shet	
Optimal Design of Controllers for Brix Regulation in Sugar Industry	813
Sanjay Kumar Singh, Nitish Katal, Sanjay Kumar, and Neha Kumari	
DNN Machine Translation for Indian Languages	823
Shashi Pal Singh, Ajai Kumar, Lenali Singh, and Tanya Angra	
Cyber Security for Smart Grid: Vulnerabilities, Attacks, and Solution	835
Shreyash More, Suraj Hajari, Mahshooq Abdul Majeed, Neeraj Kumar Singh, and Vasundhara Mahajan	
Descriptive and Comparative Analysis of YouTube Trending Videos	859
Janki Chandiwala, Sarvesh Agrawal, and Shrushti Agarwal	
Phase Frequency Detector Using CNTFET	877
Shubham Tomar and Rutu Parekh	
RTL to GDSII: Fully Digital Indirect Time of Flight SoC	889
Het Suthar, Shubham Tomar, and Rutu Parekh	
MOODY: A Natural Language Processing-Based Chatbot for Mental Health Care	899
Shubhangi Thakur, Dhruv Rastogi, and Leena Singh	
Predictive Shift of Vehicles by Recent Market Trends	909
Rajgor Siddhi Bharatkumar, Shubh Patel, Shambhavi Chakrabarti, and Siddharth Joshi	
Energy Management of Grid Connected Renewable Sources with Energy Storage Unit for an EV Charging Station	925
Sohankumar Prajapati and Sanjay R. Vyas	

Design and Techno-Economic Analysis of Electric Vehicle Charging Station for a Railway Metro Station Parking Area 937
 Sumit Kumar Verma, Sombir Kundu, and Sukhbir Singh

IoT-Assisted Framework for Efficient Healthcare Monitoring and Alert Unit for a Patient 955
 Suneeta S. Raykar and Vinayak N. Shet

Comprehensive Survey on Recent Trends in Optimization Methods and Different Facts Controllers-Based Power Quality Improvement System 971
 A. V. Sunil Kumar, Prakash, Shivakumara R. S. Aradhya, and G. Swetha

Speed Control of Brushless DC Motor by Using Particle Swarm Optimization Algorithm 987
 Suraj R. Kamde and Meghraj S. Morey

A New Approach to Analysis of Disturbances in Generation-Deficit Regions Interfaced with a Large Grid 1007
 Suresh Varwandkar and Vijay L. Sonavane

Human Activity Recognition Using 1-Dimensional CNN and Comparison with LSTM 1017
 Suryakant Kumar Kashyap, Parikshit Narendra Mahalle, and Gitanjali Rahul Shinde

Optimal VA Loading of UPQC Using Rao-1 Algorithm 1031
 Swati Gade and Rahul Agrawal

Effective Stabilization of the Retaining Wall with Inclusion of Geo-Cell: A Review and Critique of Research 1047
 Sweta Soni

Swarm Intelligence-Based Tuning of Hybrid Controller for Control of Neutron Density in Nonlinear Pressurized Water Reactor 1063
 Swetha R. Kumar and D. Jayaprasanth

False Data Injection Attack Detection Using Machine Learning in Smart Grid: Approaches, Datasets, and Comparative Study 1081
 Tania Gupta, Richa Bhatia, and Richa Sharma

A Protection Approach for Power System Fault Categorization 1091
 Tarachand Yadav, Shoyab Ali, and Gaurav Kapoor

Analysis and Simulation of Various Parameters of Mixed CNT Bundle for Interconnect Applications	1099
Tirth Patel, Nishtha Diwanji, Michika Gayari, Himadri Patel, Kinjal Patel, and Rutu Parekh	
Reliability Evaluation in Physical Power Systems and Communication Network for Protection Failures	1117
Trisha Parekh, Bansi R. Kanzariya, Kartavi Patel, Mithilesh G. Solanki, Neeraj Kumar Singh, Atul Kumar Yadav, Mahshooq Abdul Majeed, Lalit Tak, and Vasundhara Mahajan	
Metallographic Image Analysis for Quality Assurance of Metals: A Review	1135
Tushar Shirsat and Vinayak Bairagi	
‘Smart Construction Safety Helmet’: a Construction Safety Tool Embedded with Health Monitoring and Salary Deduction Function	1149
Vikas Suresh and Raju Narwade	
Analysis of Quadratic Boost Converter with PV and BESS Using SMC	1169
Vinay Kumar Naguboina and Satish Kumar Gudey	
Thickness Control of Anti-Reflection Coatings Using TiO₂/SiO₂ Multilayer Films for Silicon Solar Cells	1185
M. Vishwas	
Implementation of Optocoupler Test Fixture in Incoming Quality Control	1193
S. G. Yashaswini and Rashmi	
Energy Resource Planning for a Rural Microgrid: A Sensitivity Analysis	1203
Yuvraj Praveen Soni and E. Fernandez	
Optimized Renewable Energy Resource Planning for a Rural Microgrid with Linear and Nonlinear Algorithms	1211
Yuvraj Praveen Soni, E. Fernandez, Md. Mustafa Kamal, and Imtiaz Ashraf	

About the Editors

Vasundhara Mahajan is an associate professor in the Department of Electrical Engineering, Sardar Vallabhbhai National Institute of Technology, India. She obtained her doctoral (Ph.D.) in 2014 and master's degree (M.Tech.) in 2005 from IIT Roorkee and graduated in electrical engineering from NIT Raipur (formerly GEC) in 1999. She worked as a lecturer at Christian College of Engineering and Technology, Bhilai, Chhattisgarh, from September 2000 to October 2007. Then joined Sardar Vallabhbhai National Institute of Technology (SVNIT), Surat, Gujarat. Since October 2007, she is at SVNIT. Dr. Mahajan has 20+ years of teaching and research experience. She has published around 70 papers in international/national journals and conferences. She has guided many Ph.D., M.Tech., and B.Tech. projects. Under her guidance, two students have completed their doctoral program in 2020. Presently, she is guiding three doctoral candidates. Her research areas are power system reliability, cybersecurity, restructuring/deregulation, energy market, congestion management, power quality improvement, active power filters, FACTS, artificial intelligence, and machine/deep learning.

Anandita Chowdhury is a professor of Electrical Engineering in Sardar Vallabhbhai National Institute of Technology, Surat, Gujarat, India. She did her Bachelors and Masters degree from Bengal Engineering College, currently Indian Institute of Engineering, Science and Technology, Shibpur, West Bengal, and Ph.D. from Indian Institute of Technology, Kharagpur. Anandita is a passionate teacher, she has more than twenty five years of teaching experience. Apart from teaching she has guided significant number of Ph.D. and M.Tech theses. Her areas of research interest are Electrical Machines, Drives, Power system and Renewable Energy. She has appreciable number of publications in reputed journals and conferences. Anandita has organized several workshop and short term training programme on recent trends and development in Electrical Engineering for teachers and students. She is reviewer of many reputed international journals.

Narayana Prasad Padhy is a professor in the Department of Electrical Engineering at the Indian Institute of Technology, Roorkee, India. He completed his Ph.D. from Anna University, Chennai, India. Prof. Padhy has over decades of academic and research experience. He is currently guiding 27 out of 42 research scholars. Most of the scholars have settled down as faculties in various reputed universities worldwide and working as Post-Doc in the USA. He has 194 papers, 04 textbooks, and 3 Indian patents published to his credit. He is aggressively involved in the Mission Innovation Activities, which includes 22 international countries, participated in the international discussion forums and smart grid conclaves. He also heads the responsibilities of the Mission Innovation Resource Center (MIRC) at IIT Roorkee. His areas of specialization are power system engineering and AC-DC smart grid.

Fernando Lezama received a Ph.D. in ICTs, in 2014 and an M.Sc. in Electronic Engineering-Telecommunications, in 2011, from the Monterrey Institute of Technology and Higher Education (ITESM). He also has a Bachelor in Electronic Engineering from the Minatitlan Technological Institute (ITM), in 2008. Since August 2017, Dr. Lezama is a researcher at GECAD—Polytechnic of Porto, where he contributes to the application of CI in the energy domain under the scope of diverse projects such as SIMOCE (ANI | P2020 17690), COLORS (FCT P2020 28967), MAS-Society (FCT P2020 28954), and H2020 DOMINOES (GA 771066). Dr. Lezama has published over 60 articles in prestigious journals and conferences, and over the last five years, he has been the author/co-author of over 40 articles published in intelligent system and energy conferences and SCI journals. He has been involved in the supervision of more than 10 Bachelor's and M.Sc. works in Computer Science and Electrical Engineering-Energy Systems courses. His research areas are computational intelligence, evolutionary computation, power systems, smart grids, network planning, and optimization.

Analysis of Effect of Rotor Slot Shape on Torque Ripple in Induction Motor Using FEM



A. E. Aishwarya and B. A. Sridhara

Abstract Induction motor is the most widely used motor in industry. The torque ripple is one of the important performance characteristics of the induction motor and needs to be reduced. Therefore, to maximize motor performance, torque ripple should be analyzed during the design stage. The choice of rotor slot structure is one of the factors which affects torque ripple. In this study, the effect of rotor slot shape of induction motor on the torque ripple is investigated using FEM software JMAG.

Keywords Induction motor · Torque ripple · Flux distribution · Rotor slot shapes · JMAG

1 Introduction

The induction motor (IM) was invented by Nikola Tesla in 1887. Afterward, it became a most widely used rotating machine due to its robust construction and the ability to control speed [1]. But the effect of torque ripple, noise and mechanical vibrations is the challenging issues for machine designers. Torque ripple in induction motor is due to periodic variation of reluctance of air gap with the change in rotor position [2].

In the recent years, electric vehicles (EV) are becoming popular all over the world. Three-phase AC induction motor is used in high performance electric vehicle systems. It is found that the rotor shape and the rotor slots number have important effect on torque ripple. Torque ripple in induction motor is generally undesirable as it causes vibration, noise and reduction of life of the machine [3]. To study the effect of rotor slots on torque ripple, the designer can model induction motor in FEM-based software. A computer software implementing magnetostatic study based on finite element method can be used to determine the variation of the flux and induction motor stored energy for different rotor positions [4].

A. E. Aishwarya (✉) · B. A. Sridhara
Siddaganga Institute of Technology, Tumakuru, India
e-mail: aishwarya.eranna97@gmail.com

In this study, the impact of rotor slot geometry on torque ripple of induction motor is investigated. Motor models with different geometries of rotor slots are created, and rotor slot geometry with minimum torque ripple has been found. The objective of this work is to determine the rotor slot type which produces the least torque ripple among motors with the same ratings.

Finite element method (FEM) can solve magnetostatic problems with a high degree of accuracy. In this study, motor models were created, and steady-state analysis is carried out in JMAG Express. This motor model is exported to the JMAG designer, and a 2D motor model is created and analyzed for torque ripple with different shapes of rotor slots.

2 Creation of Motor FEM Model

JMAG is finite element analysis software for electromechanical design. Preliminary design of motor is implemented in JMAG express and is exported to JMAG designer for detailed magnetostatic analysis. At the concept design stage, JMAG express is used for designing the induction motor and JMAG designer is used for transient analysis. The flow of motor design in JMAG is shown (see Fig. 1).

The steps of simulations are:

- Pre-processing: Define motor geometry and properties followed by generation of meshes.
- Processing: Execute the FEM program to solve the magnetostatic field problems.
- Post-processing: Using the results of FEM, performance parameters such as torque are obtained.

Fig. 1 Flow of motor design in JMAG

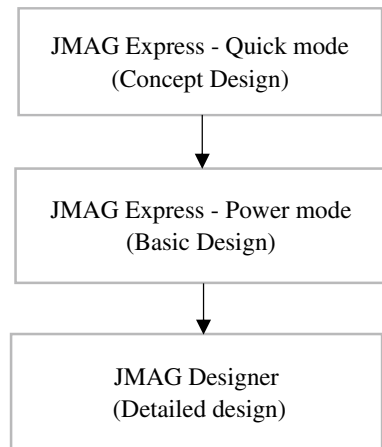


Table 1 Nominal data of motor

Parameter	Unit	Value
Rated power	kW	90
Pole pair	–	4
Number of phases	–	3
Air gap length	mm	0.7
Maximum outer diameter	mm	349

Table 2 Main stator geometry data

Parameter	Unit	Value
No. of stator slots	–	48
Outer diameter	mm	349
Inner diameter	mm	235
Tooth width	mm	6.98

Table 3 Main rotor geometry data

Parameter	Unit	Value
No. of rotor slots	–	38
Outer diameter	mm	233.6
Shaft diameter	mm	70
Slot opening width	mm	1.29

The nominal data of the induction motor under study is given in Table 1, main stator geometry data in Table 2 and main rotor geometry data in Table 3 [5].

In this study, different configurations of rotor slots of induction motor are used to analyze the torque ripple.

Initially, JMAG express is used to create the basic induction motor model and to obtain steady-state analysis results. Then, to obtain the torque ripple from motor model, transient analyses is performed using JMAG designer. Rotor slot shape type impacts the magnetic field distribution. A small variation of magnetic field distribution results in substantial difference in the performance of induction motor [3]. With the increase in slot opening width, the variation in reluctance is higher, but it is easy to insert the conductors in slot during the manufacturing.

In this work, JMAG express software is used to design the motor model. The designed induction motor models are rectangular rotor slot (see Fig. 2), oval rotor slot (see Fig. 3) and round rotor slot (see Fig. 4).

The torque–speed characteristics of induction motor with rectangular (see Fig. 5), oval (see Fig. 6) and round (see Fig. 7) rotor slots are shown.

The designed induction motor model is exported to JMAG designer. The model of induction motor in JMAG designer with rectangular rotor slot (see Fig. 8), oval rotor slot (see Fig. 9) and round rotor slot (see Fig. 10) is shown.

Fig. 2 FEM model of IM with rectangular rotor slot

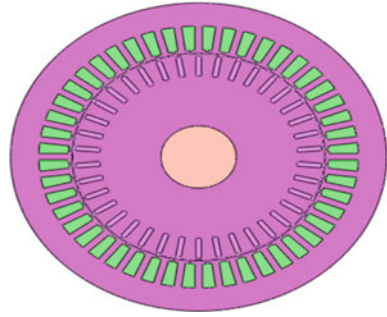


Fig. 3 FEM model of IM with oval rotor slot

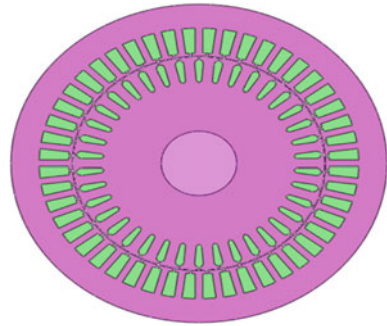


Fig. 4 FEM model of IM with round rotor slot

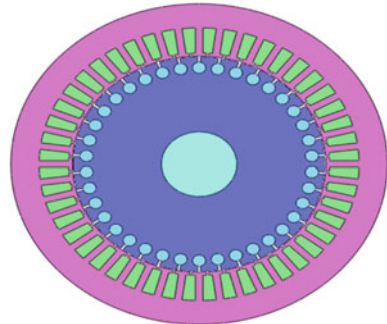


Fig. 5 Torque–speed characteristic of IM with rectangular rotor slot

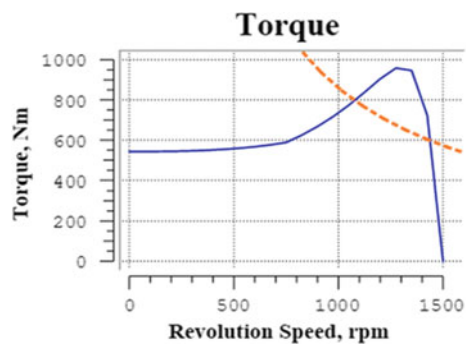


Fig. 6 Torque–speed characteristic of IM with oval rotor slot

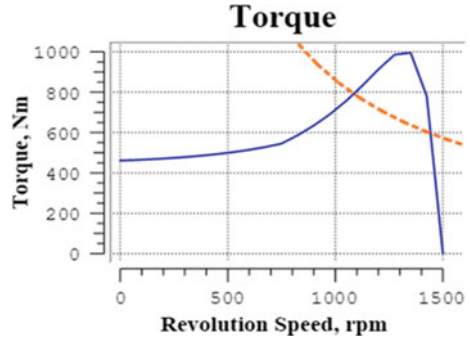


Fig. 7 Torque–speed characteristic of IM with round rotor slot

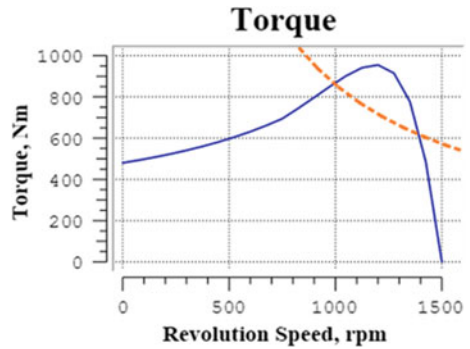
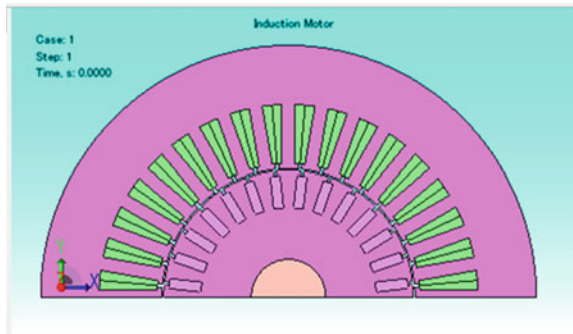


Fig. 8 Induction motor with rectangular rotor slot



3 Mesh Generation

The created model is split into number of domains by meshing, and the solution of field problems is obtained in each domain. The meshed geometries are shown for rectangular (see Fig. 11), oval (see Fig. 12) and round (see Fig. 13) rotor slots.

Fig. 9 Induction motor with oval rotor slot

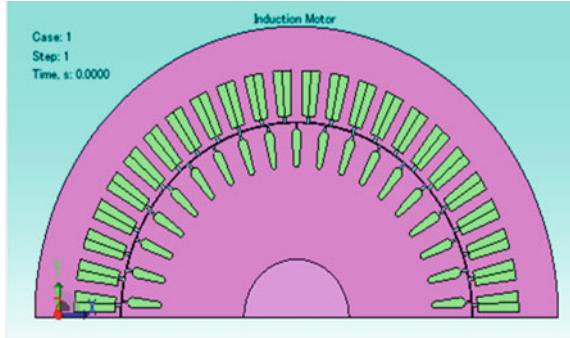


Fig. 10 Induction motor with round rotor slot

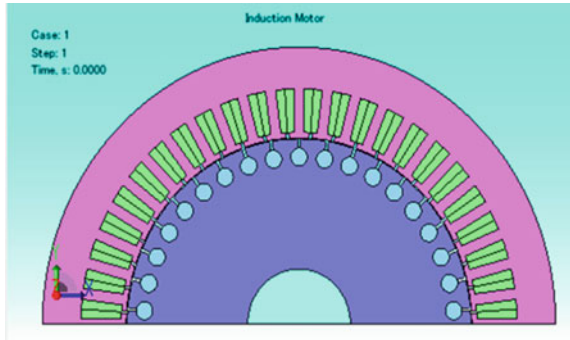
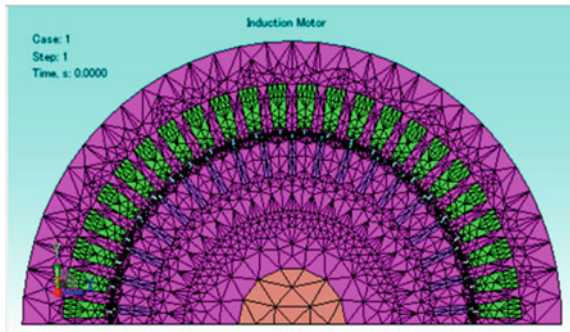


Fig. 11 Mesh generation for induction motor with rectangular rotor slot



4 Flux Distribution and Torque Ripple

The performance of induction motor is influenced by flux distribution in the air gap, and hence, the magnetic field distribution is determined by using two-dimensional FEM analysis. The flux distribution plots of IM with different rotor slots are shown (see Figs. 14, 15 and 16).

The torque ripple can be expressed as [3],

Fig. 12 Mesh generation for induction motor with oval rotor slot

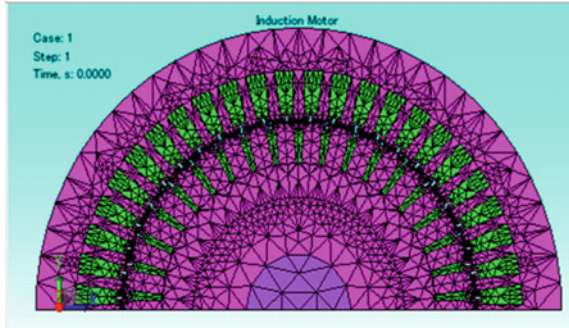


Fig. 13 Mesh generation for induction motor with round rotor slot

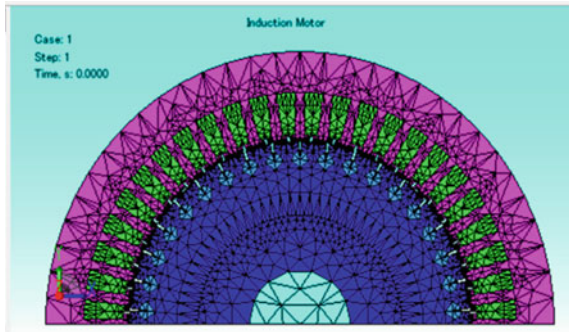
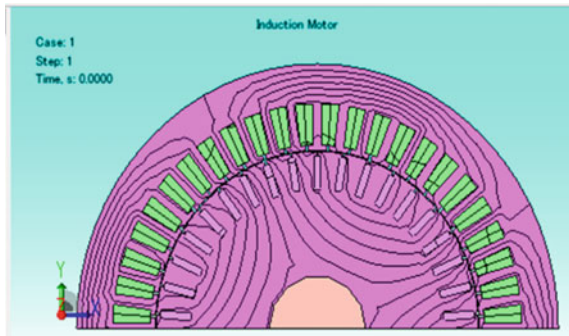


Fig. 14 Flux distribution in rectangular rotor slot



$$T_{\text{slot}} = \frac{1}{s} \phi_g^2 \frac{d\mathcal{R}}{d\theta} \tag{1}$$

where ϕ_g is air gap flux, \mathcal{R} is air gap reluctance and θ is position of rotor.

The torque ripple is mainly due to variation of stored magnetic energy in the air gap. For induction motor, the torque ripple generated by reluctance variation is a periodical waveform with respect to the mechanical rotational degree. This period is specified by,

Fig. 15 Flux distribution in oval rotor slot

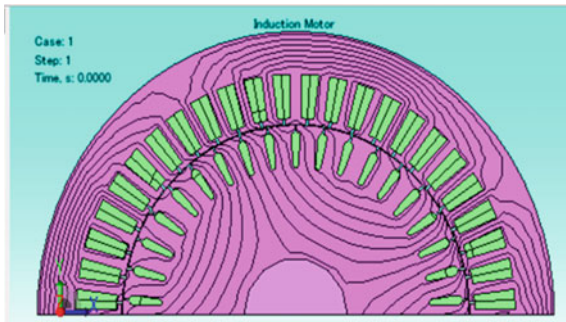
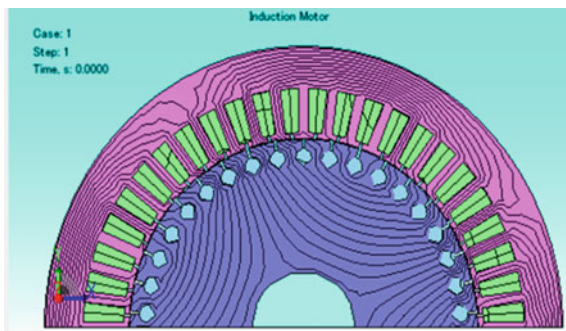


Fig. 16 Flux distribution in round rotor slot



$$\theta_{r_{\text{slot-period}}} = \frac{2\pi}{\text{lcm}(N_s, N_p)} \quad (2)$$

where 2π is one complete rotation of rotor, N_s is number of stator slots, N_p is number of poles and lcm is least common multiple.

Torque variations in one complete rotation of the rotor are shown for rectangular rotor slot (see Fig. 17), oval rotor slot (see Fig. 18) and round rotor slot (see Fig. 19). It is observed from these figures that rotor slot geometry affects torque ripple.

The peak-to-peak torque ripple of induction motor can be expressed as,

$$T_{\text{slot-pp}} = \text{Max}(T_{\text{slot}}) - \text{Min}(T_{\text{slot}})$$

Induction motor with rectangular rotor slot (see Fig. 17) and oval rotor slots (see Fig. 18) has higher torque ripple as compared to the induction motor with round (see Fig. 19) rotor slots. The torque ripple of oval rotor slot is 1%, round rotor slot is 0.75% and the rectangular rotor slot recorded torque ripple of 1.15%.

In round shape geometry, tooth width is reduced which results in lower variation in air gap length, and in turn, reluctance variation is reduced. Therefore, torque ripple is reduced in induction motors with round rotor slots. The induction motor with rectangular rotor slot (see Fig. 17) and oval rotor slot has greater torque ripple

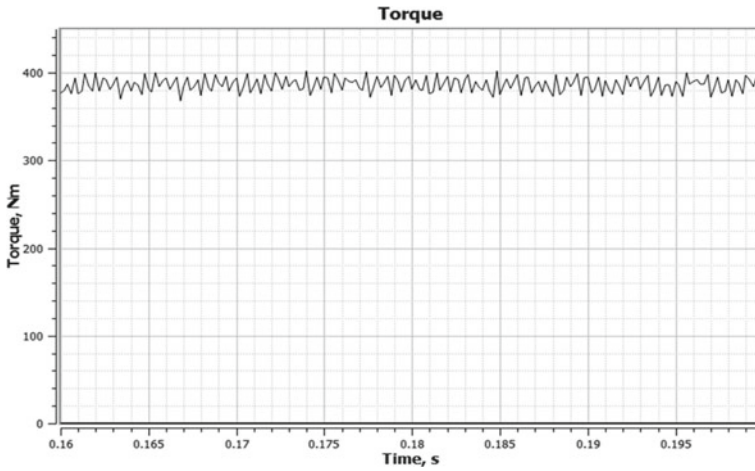


Fig. 17 Torque ripple in rectangular slot

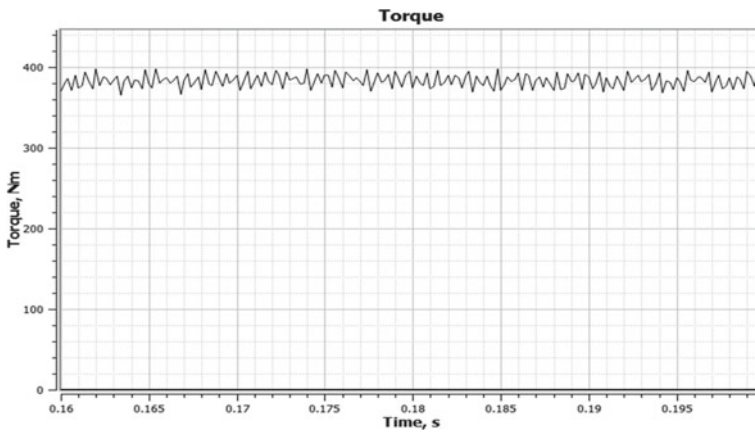


Fig. 18 Torque ripple in oval rotor slot

compared to that of round rotor slot. Hence, it is concluded that shape of the rotor slot affects the torque ripple.

5 Conclusion

In this paper, three topologies of induction motors are studied to understand the impact of rotor slot shapes on the torque ripple. Comparative analysis of induction motor with rectangular rotor slot, oval shaped rotor slot and round rotor slot is carried

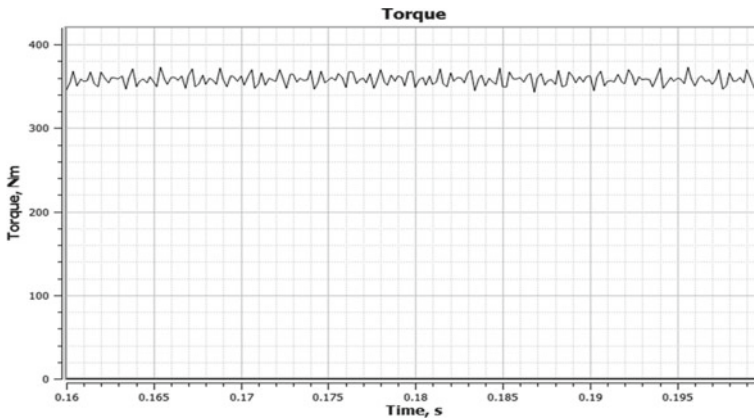


Fig. 19 Torque ripple in round rotor slot

out using JMAG. The results indicate that induction motors with round rotor slot have lower torque ripple as compared to oval shaped rotor slots and rectangular rotor slots. However, due to moment of inertia of motor and load, the effect of torque ripples on motor speed variations would be negligible.

References

1. Chitorju RKS (2009) Improved performance characteristic of induction machine with non-skewed asymmetrical rotor slot electric machines and power electronics. KTH School of Electrical Engineering, Stockholm, Sweden
2. Durmus B, Yetgin AG (2020) Analysis of the effect of rotor slot type on torque ripple in induction motor by finite element method. *El-Cezeri J Sci Eng* 7(2):536–542. <https://doi.org/10.31202/ecjse.664132>
3. Kamoun JK, Hadj NB, Chabhoub M, Ghariani M, Neji R (2013) An induction motor FEM based comparative study: analysis of two topologies. In: 8th international conference and exhibition on ecological vehicles and renewable energies (EVER)
4. Kammoun JK, Hadj NB, Ghariani M (2015) Induction motor finite element analysis for EV application, torque ripple and inter-turn circuit. *J Electr Sys*
5. Lazaridis T (2016) General design data of a three phase induction machine 90 kW squirrel cage rotor. Technical Report, pp 01–15

Comparative Analysis of Tensile Strength for Scrap Electrical Wire-Reinforced Concrete



Abhishek Kumar Gupta, Km. Shalini Kumari, and Sawan Kumar Gupta

Abstract Nowadays, the disposal of scrap is a worldwide problem because of their non-degradability, causing environmental pollution. Therefore, recycling of this type of scrap is very important for economic saving and positives effect on the environment. So in this work, an attempt is made to use scrap aluminium wire as reinforcement in concrete to increase the splitting tensile strength of concrete composite. Wire-reinforced concrete gives better results due to load distribution from matrix phase to wire and also wire acts as a crack arrester. In the fabrication process, the percentage of scrap aluminium wire is taken as 0, 1, 2 and 3% in partial replacement of sand by weight. The split tensile test is an another way for calculating the tensile strength of concrete structure. In this analysis, a cylindrical sample with standard dimension was put horizontally while the force is applied radially on surface of cylinder which results in crack propagation in vertical direction along its diameter. This tensile strength was investigated by both experimental and finite element analysis on ANSYS software 20. Finite element analysis shows a good agreement with experimental results. With the help of modelling and experimental analysis, it was found that mechanical properties of wire-reinforced concrete have increased up to 2% of wire reinforcement but on further increasing percentage of wire, mechanical properties start decreasing, Therefore, 2% of wire-reinforced concrete have maximum tensile strength. Thus, the scrap aluminium wire could be a good choice to use as a suitable reinforcement in concrete.

Keywords Concrete · Wire reinforcement · Scrap aluminium wire · Fabrication process · Tensile strength

A. K. Gupta (✉) · Km. Shalini Kumari
Harcourt Butler Technical University, Kanpur, Uttar Pradesh, India
e-mail: abhishekgupta.hbtu@gmail.com

S. K. Gupta
Ashoka Institute of Technology and Management, Varanasi, Uttar Pradesh, India

1 Introduction

In recent years, various types of electricals scrap are increasing day by day, which is harmful to the environment so recycling is very important to minimize this scrap. This scrap can be used in constructional industries to improve its performance. Other types of scrap in the form of fibres such as polyethylene fibre, carbon fibre and basalt fibre are now used in constructional and infrastructure development [1]. E-scrap involves scrap electrical and electronic equipment that reached its end life. E-scrap is more toxic than municipal scrap because it consists of more toxic materials. This type of scrap contains more than 1000 different components that are non-toxic and toxic materials such as lead, cadmium, mercury and arsenic will cause health problems if they are not managed carefully [2]. Cement concrete is extensively used for construction purposes. Cement concrete has brittle fracture characteristics so there is a high risk of the fracture without any prior information in engineering constructions. Plain concrete has limited toughness and strength to satisfy the requirement of engineering load-bearing structures. For better durability and safety, introducing toughening material such as fibres results in the improvement of the compressive strength, shear strength and fracture resistance of the reinforced concrete [3]. In the past decade, fibre-reinforced concrete has been used in constructional and building application worldwide and also carbon fibre is the most commonly used for the development of fibre-reinforced concrete material which has many advantages such as high strength, good stability, lightweight, excellent combination with cement and so on [4]. Scrap tyre is also one of the most complicated scrap materials; if not handled properly, scrap tyre can be a hazard to the environment so recycling of this type of scrap is also very significant. Scrap tyre rubber is used in concrete as reinforcement by partially replacing fine aggregate by which dynamic properties can be improved [5, 6].

An aluminium wire is most widely used in electrical and electronic purpose, wiring of households and constructional area, and when the life of this wire is over, then it becomes a scrap which is harmful to the environment. Major parts of aquatic as well as terrestrial ecosystem are affected. In the aquatic environment, aluminium works as a toxic agent on gill-breathing animals such as fish which is difficult to survive in this environment. Therefore, recycling of scrap aluminium is very important. Cost of aluminium wire is low and also has anti-corrosive and lightweight characteristics. Recycling of scrap aluminium wire for fabrication of utility product may involve a huge amount of energy, time and effort as acceptable level of purity of aluminium ingots need to be ensured. Further, the process of recycling of most of the materials leads to generation of hazardous gases causing pollution. Hence, it is a good idea to reuse the aluminium wire scrap as reinforcement in cement concrete to improve its mechanical properties in place of going for its recycling. Usage of aluminium wire by India is 18% of worldwide.

2 Literature Review

In the past, many researchers have studied to evaluate the mechanical properties of fibre-reinforced concrete (FRC) in which scrap materials are used as reinforcement in concrete to improved its mechanical properties and also to minimize this scrap which is harmful to the environment. Samindi et al. [4] have investigated that the use of steel fibre, recovered from tyre scrap, as a reinforcement in concrete, the mechanical properties such as tensile strength and flexural strength were improved and in this experiment, the percentage of steel fibre was taken as 0%, 0.5% and 1% by volume. Hameed and Ahmed [5] have reported that by using polyethylene terephthalate (PET) in a concrete, compressive strength, flexural strength and tensile strength were increased by 58, 25.59 and 130%, respectively. Sun et al. [3] experimentally studied that by using basalt fibre as reinforcement in concrete, the mechanical properties such as compressive strength, flexural strength and tensile strength were increased. Aghaee et al. [7] experimentally reported that with the use of steel fibre which was recovered from building and infrastructures projects to make lightweight structural concrete, the mechanical properties such as compressive strength, flexural strength, tensile strength and impact test were increased when compared with plain concrete and in this experiments, the percentage of fibre for all fibre-reinforced concrete specimens were taken as 0.25, 0.5 and 0.75% in volume fracture of concrete. Hameed and Shashikala investigated that by replacing 15% of fine aggregate with crumb rubber, fatigue failure load and impact resistance can be improved [8, 9]. Zheng et al. investigated the damping properties of rubberized concrete. Damping properties of concrete can be increased by replacing 20% fine aggregate with shredded rubber. These researchers studied that damping properties increased, while compressive strength decreased [10, 11]. Some researchers have reported that by using scrap electrical wire in concrete, the load-carrying capacity is increased which prevents the opening of macro-cracks and also reduced the width of micro-cracks while providing good resistance against impact and dynamic load and also increased tensile strength of wire-reinforced concrete [7]. Aluminium wire is used in various electrical and electronics purposes, wiring of households and constructional area, and when the life of this wire is over, then it becomes a scrap which is harmful to the environment. Recycling of scrap aluminium wire and fabrication into other components will involve enormous energy. Therefore, a portion of scrap aluminium wire can be planned for use as reinforcement in concrete to improve its mechanical properties [6, 12].

In the current research, scrap aluminium wire was added into concrete as a secondary raw material to test the potential sustainable construction concept. The mechanical property such as tensile strength of scrap aluminium wire-reinforced concrete was investigated by both experimental and using ANSYS software 20 after curing periods of 28 days and comparing all results.

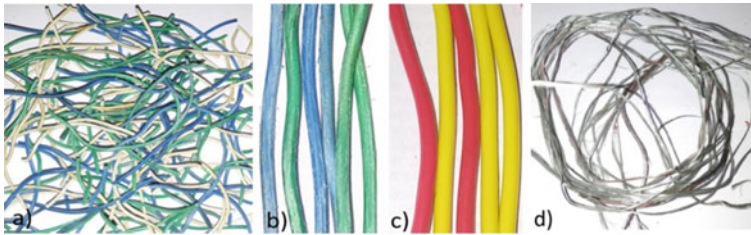


Fig. 1 a Scrap aluminium wire, b rough surface of wire, c non-rough surface of wire and d naked Al wire

3 Experimental Investigation

3.1 Materials Required

Ordinary Portland cement (OPC) of 53 grades was used for samples preparation. Specific gravity and fineness of cement are 3.15 and $227 \text{ m}^2/\text{kg}$, respectively. Good quality of river sand was used, and size of sieve, specific gravity and bulk density of sand is 4.75 mm, 2.66 and 1780 kg/m^3 , respectively. The crushed stone particle of size less than 20 mm is used as a coarse aggregate, and specific gravity and bulk density of coarse aggregate are 2.81 and 1540 kg/m^3 , respectively [9, 11]. Normal drinking water is used for making a mixture of these materials in which water–cement ratio is 0.4. In this experiment, naked and PVC-insulated scrap aluminium wire of length 60 mm and diameter 1 mm is used as reinforcement in concrete. Modulus of elasticity and Poisson’s ratio of aluminium wire are 70 GPa and 0.35, respectively [13] (Fig. 1).

3.2 Concrete Mix Design

Concrete design for M30 grade is taken according to Indian Standard Code 10262-2009 [14]. Dimension of sample for tensile strength and standard core is $150 \times 300 \text{ mm}$ and IS-5816, respectively. Mix design quantity and ratio for M30 grade concrete are given in Table 1.

Table 1 Concrete mix design [15]

Materials	Quantity (kg/m^3)	Mix ratio
Cement	350	1.00
Sand	896	2.56
Coarse aggregate	1140	3.26
Water	140	0.40

3.3 Fabrication Work

Scrap aluminium wire (both naked and PVC-insulated aluminium wire) is mixed with concrete to improve its mechanical property. The surface of PVC-insulated wire has been roughened with the help of sandpaper for enhancing the bonding of aluminium wire (fibre) with concrete (matrix). The percentage of wire is taken as 0, 1, 2 and 3% in partial replacement of sand by weight. The mechanical property such as tensile strength was determined after 28 days of curing at ambient temperature, and distribution of wire is random and aligned type. The fabrication process involves the mixing of materials, moulding, ramming, removal of freeze samples, curing and testing. Concrete samples details are shown in Table 2. Mechanical property of wire-reinforced concrete results is compared with normal concrete (i.e. 0% wire reinforcement) and also compared with finite element analysis results.

Mixing of Materials. For the preparation of normal and wire-reinforced concrete, materials are first mixed in the dry state for one minute, and during the mixing operation, scrap aluminium wire is added and all materials are mixed properly according to mix proportion as shown in Fig. 2 and the water–cement ratio of 0.4 is used [7].

Preparing the Samples. When all materials are mixed properly, then the paste of concrete is poured into a mould of the cube, cuboid and cylinder and rammed properly with the help of rammer by which porosity and air bubbles could be reduced in the casting. The mould is polished with crude oil for easy removal of freeze samples. After filling the mould, the concrete samples are strengthened with the help of a vibrating table for a period of 8 to 12 s. After 24 h under constant ambient temperature, when samples are freezes then it is removed from the mould [7, 16] (Fig. 3).

Curing of Samples. The fabricated samples for compression, flexural and tensile strength are water cured for 28 days at ambient temperature as shown in Fig. 4. During curing hydration takes place which decreases the porosity and improves the strength and durability of concrete samples as reported by Uchida and Takeyama, 2010 [17].

Table 2 Concrete samples details

Type of concrete mixture	Type of distribution of Al wire	Type of scrap Al wire
CM1	Random	Naked Al wire
CM2	Aligned	Naked Al wire
CM3	Random	Rough surface of Al wire
CM4	Aligned	Rough surface of Al wire
CM5	Random	Without rough surface of Al wire

Fig. 2 Mixing of materials



Fig. 3 Prepared samples

Fabricated sample in water

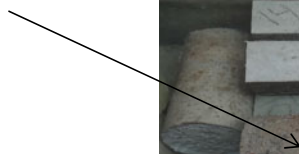


Fig. 4 Curing of samples

3.4 Experimental Set-up

Tension Test of Concrete. Tensile test of cylinder sample (150 mm diameter and 300 mm length) was performed on the universal testing machine according to IS-5816. Diametric lines are drawn on each cylinder to ensure that they are in the same plane. The splitting tensile strength is determined from Eq. (1) after 28 days of curing at ambient temperature [3].

$$T = 2P/\pi ld \quad (1)$$

In Eq. (1), T stands tensile strength, (MPa), P is the maximum applied load (N), and l and d are the length and diameter (mm) of sample (Fig. 5).

4 Finite Element Analysis

Finite element analysis (FEA) is a computer-based technique to solve a complex problem and to calculate the behaviour of mechanical structures. FEM analysis used to solve any phenomena such as vibration, stress, deflection and other behaviour. The behaviour of each element is described with a relatively simple set of equation. This element joints into a large set of the equation by which behaviour of the whole structure can be described. Process of this analysis starts with creating a geometry of the model, and then meshing is done, and after applying boundary conditions, results can be obtained [16, 18].

Fig. 5 Splitting tensile test set-up



Table 3 Materials properties

Material properties	0% WRC	1% WRC	2% WRC	3% WRC
Young's modulus, E (GPa)	27	27.9	28.45	28.23
Poisson's ratio, ν	0.20	0.2015	0.203	0.205

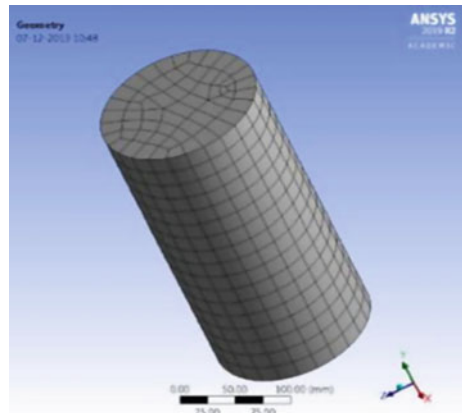
4.1 Material Properties

Material properties for each composition of concrete mixtures are required for finite element analysis. The density of cylindrical sample was 2510 kg/m^3 . Modulus of elasticity (E) and Poisson's ratio (ν) are calculated with the help of rule of mixtures for each composition of concrete mixture which is given in Table 3.

4.2 Modelling and Meshing

Modelling of cylinder was done in ANSYS 20 software. Sizes of model are same as used in experimental work. Meshing involves division into small pieces of the entire model with the help of tool available in any FEA software. The goal is to make a mesh that accurately captures the models with high-quality cells [8] (Fig. 6).

Fig. 6 Meshing on cylindrical model



5 Results and Discussion

5.1 Tensile Strength

Comparison of tensile strength results for various concrete mixtures, i.e. different wire reinforcements in concrete with ANSYS software result, is shown in Table 4 as well as in Fig. 7.

With the help of experimental analysis, it is found that tensile strength of wire-reinforced concrete has increased up to 2% of wire reinforcement because on increasing wire percentage, the bonding between wire and concrete mixture becomes good but further on increasing wire percentage, i.e. 3%, tensile strength of concrete mixture decreased as shown in Fig. 7. This happen due to poor bonding between wire and concrete mixture. Both experimental results as well as ANSYS software results is shown in Fig. 7, through which it could be analysed that experimental results are very close to the finite element analysis result which validates the obtained results.

Table 4 Comparison of tensile strength for WRC with FEA results (MPa)

Type of concrete mixture and FEA models	0% WRC	1% WRC	2% WRC	3% WRC
CM1	3.60	4.34	5.52	5.02
CM2	3.60	4.21	5.23	4.99
CM3	3.60	3.98	4.88	4.12
CM4	3.60	3.95	4.65	4.02
CM5	3.60	3.72	4.33	3.99
FEA results	3.32	5.40	7.24	4.64

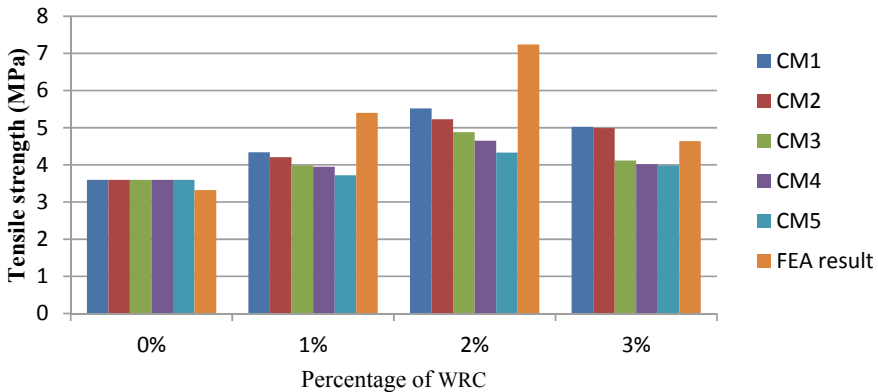


Fig. 7 Variation in tensile strength



Fig. 8 Comparison between rough and non-rough surface of wire

5.2 Comparison between Rough and Non-Rough Surface of Wire

Rough and non-rough surface of aluminium wire is used in concrete mixtures 3, 4 and 5. After experimental analysis, it could be concluded that more cement particle is attached on the rough surface of wire by which this wire exhibits better bonding with concrete when compared with non-rough surface of wire. Thus, the load-bearing capacity of the rough surface of wire is better than that of non-rough surface of wire. A similar type of work was conducted by some investigators [12] (Fig. 8).

5.3 Failure Analysis

The failure analysis of WRC with a variable percentage of wire and normal concrete is similar. In case of tensile test, a micro-crack appeared in the middle of the sample and on increasing load, the sample is broken from the middle of the cylinder as shown in Fig. 9 as reported by some researchers [3, 16].

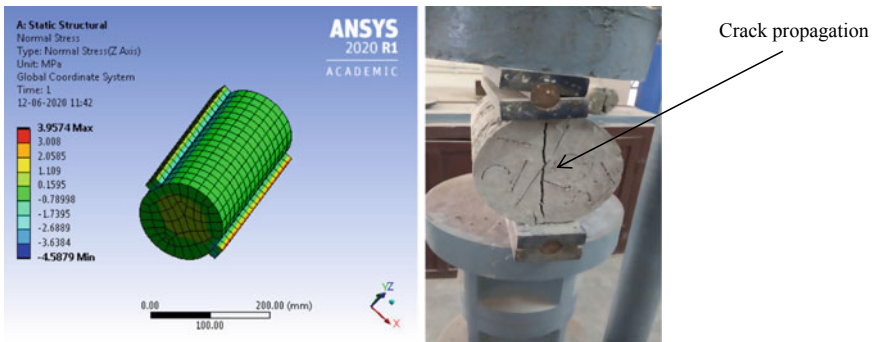


Fig. 9 FEA result and fractured sample of cylinder

6 Conclusions

In this research, modelling and experimental analysis of scrap wire-reinforced concrete were investigated and naked aluminium wire-reinforced concrete results are compared with normal concrete in which no wire is mixed. Experimental results are also validated by finite element analysis results. The following conclusions could be drawn from the present investigation.

- Tensile strength of concrete by using scrap aluminium wire was increased by 20.55, 53.33 and 39.44% when compared with normal concrete.
- An addition of 2% Al wire as reinforcement to plain cement concrete gives best results for tensile strength.
- Bare Al wire as reinforcement gives best bonding to other matrix ingredients, followed by scratched PVC-coated and unscratched PVC-coated Al wire reinforcements.
- Experimental investigation gives satisfactory results when compared with FEA results.

Hence, this research paper could be concluded that the mechanical properties of wire reinforcement concrete exhibit better results than normal concrete. So scrap wire could be a good choice to use in concrete by which economic savings and mechanical properties can be improved and also minimize the scrap which is helpful to the environment.

References

1. Sofi A, Gopu GN (2019) Influence of steel fibre, electrical waste copper wire fibre and electrical waste glass fibre on mechanical properties of concrete. *Mater Sci Eng* 513:012023
2. Kurup AR, Senthil K (2019) Novel fibrous concrete mixture made from recycled PVC fibres from electronic waste. *J Hazard Toxic Radioact Scrap* 306:11–20
3. Sun X, Gao Z, Cao P, Zhoul C (2019) Mechanical properties tests and multiscale numerical simulations for basalt fibre reinforced concrete. *Constr Build Mater* 202:58–72
4. Samarakoon SMSMK, Ruben P, Pedersen JW, Evangelista L (2019) Mechanical performance of concrete made of steel fibres from tyre waste. *Case Stud Constr Mater* 11:e00259
5. Hameed AM, Ahmed BAF (2019) Employment the plastic waste to produce light weight concrete. *Energy Procedia* 30–38
6. Sabapathy YK, Sabarish S, Nithish CNA, Ramasamy SM, Krishna G (2019) Experimental study on strength properties of aluminium fibre reinforced concrete. *J King Saud Univ-Eng Sci* 369:01–11
7. Aghaee K, Yazdi MA, Tsavdaridis KD (2014) Investigation into the mechanical properties of structural lightweight concrete reinforced with waste steel wires. University of Leeds, 0024-9831
8. Jhatial AA, Sohu S, Bhatti NUK, Lakhiar MT, Oad R (2018) Effect of steel fibres on compressive and flexural strength of concrete. *Int J Adv Appl Sci* 510:16–21
9. Hameed AS, Shashikala AP (2016) Suitability of rubber concrete for railway sleepers. *Recent Trends Eng Mater Sci* 8:32–35

10. Ceccato MR, Figueiredoa ADD (2015) Workability analysis of steel fiber reinforced concrete using slump and Ve-Be test. *Mater Res.* <https://doi.org/10.1590/1516-1439.022915>
11. Moustafa A, Mohamed AE (2015) Mechanical properties of high strength concrete with scrap tire rubber. *Constr Build Mater* 93:249–256
12. Müller T, Holschemacher K (2017) Influence of fibre type on hardened properties of steel fibre reinforced concrete. *Researchgate* 319059556
13. Hsie M, Tu C, Song PS (2008) Mechanical properties of polypropylene hybrid fiber-reinforced concrete. *Mater Sci Eng* 494:153–157
14. IS 5816, Indian Standard Code for measurement of splitting tensile strength of concrete (1959)
15. IS 10262, Indian Standard Code for mix design of concrete (2019)
16. Islam MM, Hussan M, Siddique A (2014) Finite element analysis of steel fibre reinforced concrete (SFRC): validation of experimental shear capabilities of beam. In: 10th International conference on mechanical engineering (ICME)
17. UchidaY, Takeyama T (2010) Ultra high strength reinforced concrete using aramid fiber. In: *Fracture mechanics of concrete structures*. ISBN: 978-89-5708-182-2
18. Li Y, Li Y (2019) Evaluation of elastic properties of fibre reinforced concrete with homogenization theory and finite element simulation. *Constr Build Mater* 200:301–309

IoT and Cloud Network Based Water Quality Monitoring System Using IFTTT Framework



Abhishek Kumar, Sanjay Kumar Suman, L. Bhagyalakshmi,
and Anil Kumar Sahu

Abstract An exploiting the increased ubiquity of wireless, mobile and sensor devices, the Internet of Things (IoT) has presented a potential opportunity to construct sensitive industrial systems and applications. Recent agriculture, the food processing unit of industry, environmental monitoring, security surveillance and other industries have all conducted industrial IoT initiatives. Based on IoT and cloud network technology, we built an Android mobile application to measure and report water quality. In the proposed system, multiple sensors are used to measure the presence of impurity in the water resource system. The impurity is tested in physical and chemical form. The proposed system will measure and monitor the following water parameters for analysis: potential hydrogen (pH), turbidity and temperature continuously. Furthermore, the values are stored continuously in a cloud-hosted NoSQL database named FIREBASE using IoT technology. We developed a simple user-friendly mobile application in order to access the parameter values from anywhere and at anytime based on IoT and cloud system technology. The developed mobile application uses the IoT technology and receives the parameter values from the database and displays these parameters in real time. An IoT platform named If This Then That (IFTTT) is adapted to alert the user/higher official with a voice message whenever the parameter values are not in the acceptable range. In the developed mobile application, the alert message contains the values of all the parameters and time to measurement when the quality breach has occurred.

A. Kumar
G.S Sanyal School of Telecommunication IIT Kharagpur, Kharagpur, India
e-mail: abhishek.ece14@iitkgp.ac.in

S. K. Suman
St. Martin's Engineering College, Hyderabad 500100, India

L. Bhagyalakshmi
Rajalakshmi Engineering College, Chennai, India

A. K. Sahu (✉)
Bharat Institute of Engineering and Technology, Hyderabad 501510, India
e-mail: anilsahu82@gmail.com

Keywords IOT · Cloud network · Automation · Framework · Industry system

1 Introduction

The Internet of Things (IoT) and cloud network systems are new technologies, and the rapid growth of these technologies, as well as their application for impending wireless systems, has led to the development of IoT and cloud network systems as a worldwide network infrastructure [1–3]. This communication network infrastructure is made up of a variety of interconnected devices that use sensory, communication, networking and information processing technologies [4].

Water is one of the most valuable natural resources that humanity has been given. Unfortunately, one of the most severe concerns for green globalisation is pollution. In order to ensure the quality of drinking water, it must be analysed and monitored in real time in order to ensure its safety. Water quality measurement and monitoring systems must be able to detect changes in water quality immediately and notify them to the appropriate person for further action [5, 6]. The use of IoT-based monitoring technologies makes it simple to keep track of the drinking water quality in real time. Furthermore, the client/user can monitor quality metrics at any time via a mobile phone application thanks to the integration of cloud and IoT technology [4].

Various studies have recently been published that claim to be able to remotely monitor water quality. Gokulanathan [7] created a GSM-based water quality monitoring system that uses Arduino to monitor temperature, pH and dissolved oxygen in the water for analysis. Finally, using an Internet browser application, data from sensors may be viewed. The authors of [8] proposed an IOT-based water quality monitoring system that includes multiple sensors that assess physical and chemical properties of water such as temperature, pH, turbidity and flow to analyse water quality [9]. The measured data from the sensors is processed by the core controller, which is based on Arduino. Finally, the sensor data may be seen on the Internet using a Wi-Fi configuration. Fortunately, the adoption of IoT software platforms aids in overcoming the obstacles that come with the wide range of technologies, systems, and design concepts that make up the Internet of Things [10]. IoT-based water quality measuring system will measure the following water parameters for analysis: potential hydrogen (pH), turbidity and temperature. The acidity or alkalinity of a solution is measured by the pH of that solution.

In this work, we developed a simple user-friendly water quality mobile application in order to access the parameter values from anywhere and at anytime based on IoT and cloud system technology. In the proposed system, multiple sensors are used to measure the presence of impurity in the water resource system. The impurity is tested in physical and chemical form. The proposed system will measure and monitor the following water parameters for analysis: potential hydrogen (pH), turbidity and temperature continuously.

There are three major parts of the system, which are the information management subsystem (sensor-based hardware development), the data collection subsystem

(cloud data storage) and the monitoring terminal subsystem (the mobile application). The structure and implementation of each subsystem are elaborated, and the functions of each module in the system are tested by experiments. Furthermore, the values are stored continuously in a cloud-hosted NoSQL database named FIREBASE using IoT technology. A simple user-friendly mobile application is developed in order to access the parameter values from anywhere and at anytime. The developed mobile application uses the IoT technology and receives the parameter values from the database and displays these parameters in real time. An IoT platform named If This Then That (IFTTT) is adapted to alert the user/higher official with a voice message whenever the parameter values are not in the acceptable range. The alerting message contains the values of all the parameters and the time instance at which the quality breach has been occurred.

2 System Model

The objective of this work is to develop a real-time water quality measuring and monitoring system based on IoT and cloud network. The developed mobile application is based on IFTTT framework. The system model of the proposed water quality measuring and monitoring technique is illustrated in Fig. 1. In the proposed system, we use a NODE MCU as a core processor of the system.

The NODE MCU (Wi-Fi enabled microcontroller) is the heart of the system. pH sensor, turbidity sensor and temperature sensor acts as inputs to the microcontroller. The parameter values are taken from the input sensors are pushed into the FIREBASE

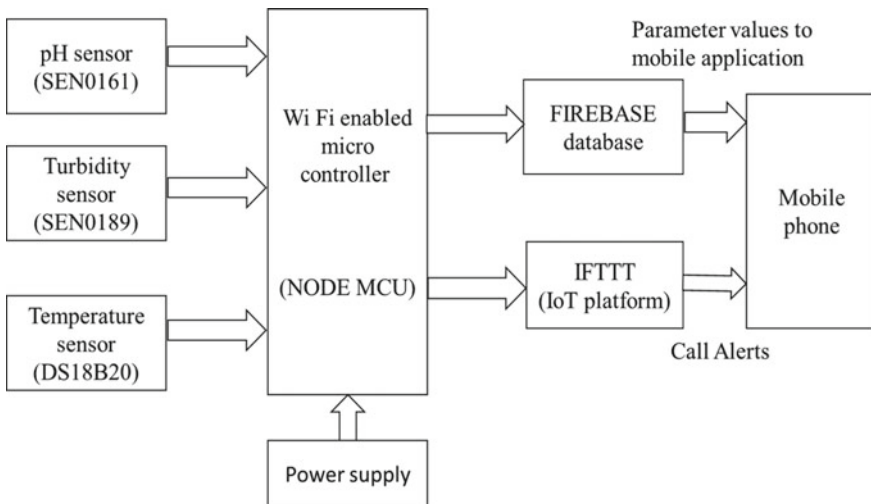


Fig. 1 The system model illustration of the proposed water quality measuring and monitoring system

database. The mobile application collects the parameter values from the database and displays them in real time. If any of the parameter values is not in the specified range, then the microcontroller is connected to the IFTTT host and then sends the user an alerting voice message/call. The voice message contains all the parameter values and also the time instance at which the quality breach has occurred.

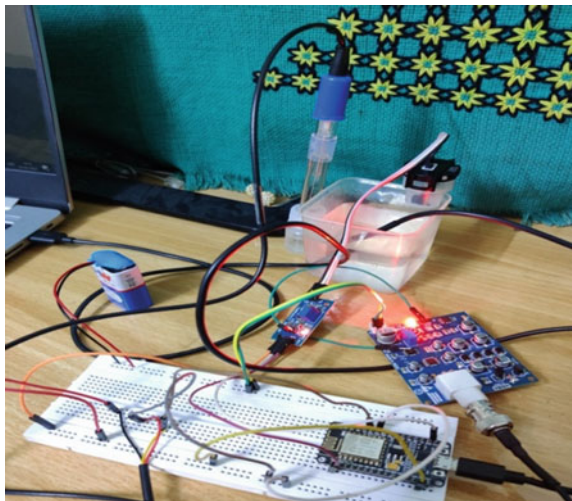
3 Prototype of Advance Water Quality Monitoring System

The developed monitoring system is based on the combination of both hardware and software systems. The hardware components used in the proposed system are as follows:

- **NODE MCU:** It is a Wi-Fi enabled microcontroller with 32-bit RISC CPU, operating voltage of 3.3 V and clock speed of 80 MHz.
- **Turbidity Sensor (SEN0189):** operating voltage of 5 V whose response time is less than 500 ms.
- **Temperature Sensor (DS18B20):** It is a stainless steel tube of 6 mm diameter by 30 mm long. The operating temperature range is $-55\text{ }^{\circ}\text{C}$ to $+125\text{ }^{\circ}\text{C}$ ($-67\text{ }^{\circ}\text{C}$ to $+257\text{ }^{\circ}\text{C}$), and the voltage associated with the sensed temperature is in the range of 3–5.5 V.
- **pH Sensor (SEN0161):** It has an operating voltage of 9 V and measuring temperature between 0 and $60\text{ }^{\circ}\text{C}$.

The hardware components and their connection to measure the parameters of drinking water are illustrated in Fig. 2.

Fig. 2 The used hardware and its connections



A set of software and application frameworks are used to access the IoT and cloud network to develop an Android-based mobile application for water quality monitoring system. The software and application framework, which are used in the proposed system, are listed below:

- **Arduino IDE:** The microcontroller is programmed using an integrated development environment.
- **FIREBASE Database:** It is a cloud-hosted NoSQL database used to store the parameter values. The data can be accessed by “n” number of clients simultaneously from anywhere and at anytime.
- **IFTTT:** If This Then That is an IoT platform used to create simple conditional statements called applets. Each applet has two parts, namely “service” and “action”. Whenever the service is triggered, the action is performed by the applet. Here, “webhooks” is considered as service and “VoIP calls” as action. So, whenever the webhook is triggered, the applet calls the user.
- **MIT App Inventor:** It is a platform used to develop software applications. A simple user-friendly mobile application has been developed which makes use of IoT technology to display all the parameter values.

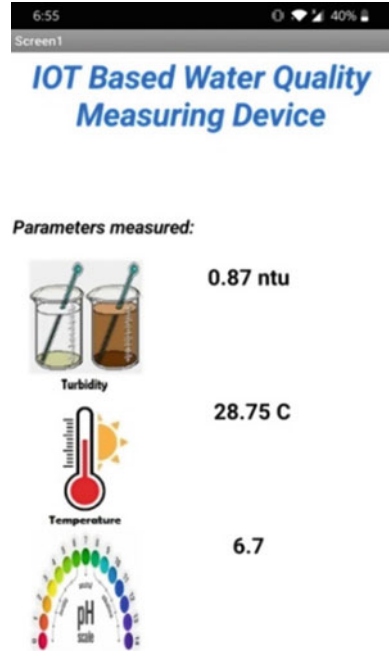
4 Andriod Logical Development Based on IFFT Framework

MIT App Inventor is one of numerous platforms for developing a mobile application that uses IoT technology. We selected MIT App Inventor for this project because it is an open-source platform that provides an intuitive, visual programming environment that allows anyone, including children, to create fully functional apps for smartphones and tablets. It enables us to construct application software (apps) for two operating systems (OS): Android and IOS, using our own code. Creating an application in MIT App Inventor usually has two phases, designer and blocks.

In the designing phase, we just have to drag the required components from the palette and drop them in the mobile screen. We can adjust the styling and properties of the components as per our desire. In order to connect to the database, we need to add FIREBASE database component to the application while creating it and include the database URL which was provided at the time of database creation. Figure 3, shows the user interface (design) of the mobile application. It displays the values of turbidity, temperature and pH parameters.

Moving on to the blocks phase (coding phase), where we write the actual functionality of our application. We will be able to see a list of blocks if we click on a component. Select the particular block that suits your purpose. In our case, the purpose of the application is to display the parameter values from the database, and whenever the values get changed in the database, the application should display the recent and updated values. To fulfil the above purpose, we have selected “**when FirebaseDb.DataChanged do**” block. It means whenever the data is changed in the

Fig. 3 A screenshot of the developed mobile application



database, the statements inside that block are executed. The entire coding/logic on which the mobile application runs is displayed in Fig. 4. The entire code basically means whenever the data in the database is changed, the same data has to be updated in the mobile application.

Figure 5 explains the flowchart of the developed system. First, the microcontroller is connected to the Wi-Fi network available, and then the parameters are read from the input sensors. The parameter values are stored in the database and displayed in the mobile application. If the quality is bad, then the IFTTT host is connected and an alerting voice message/call is sent to the registered user.

5 Real-Time Water Quality Mointoring Using the Developed Device and Android Application

In this section, we described the working satuts of the developed device and mobile application with the cases of the parameter change. In the first case, we examine the monitoring system when the given parameters are in the normal range or acceptable range. In the second case, we examine the performance of the monitoring system when the parameter value is in the abnormal range or unacceptable range. The acceptable limit for turbidity for drinking water is 1 NTU, and the acceptable ranges for

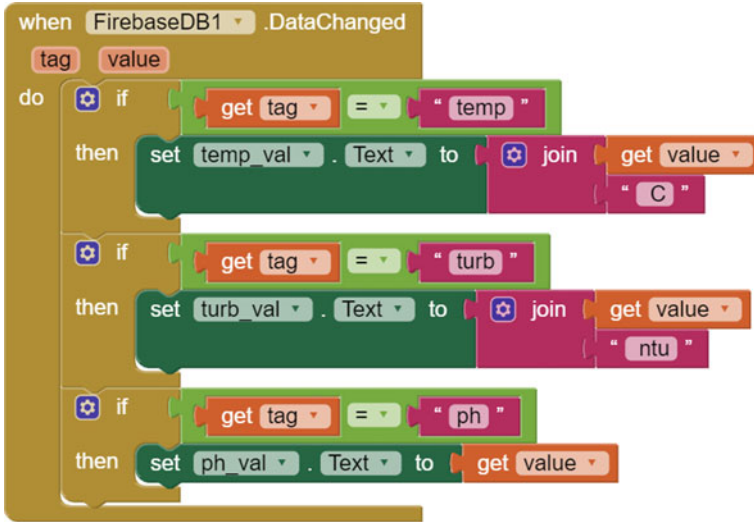


Fig. 4 A database framework for cloud network access

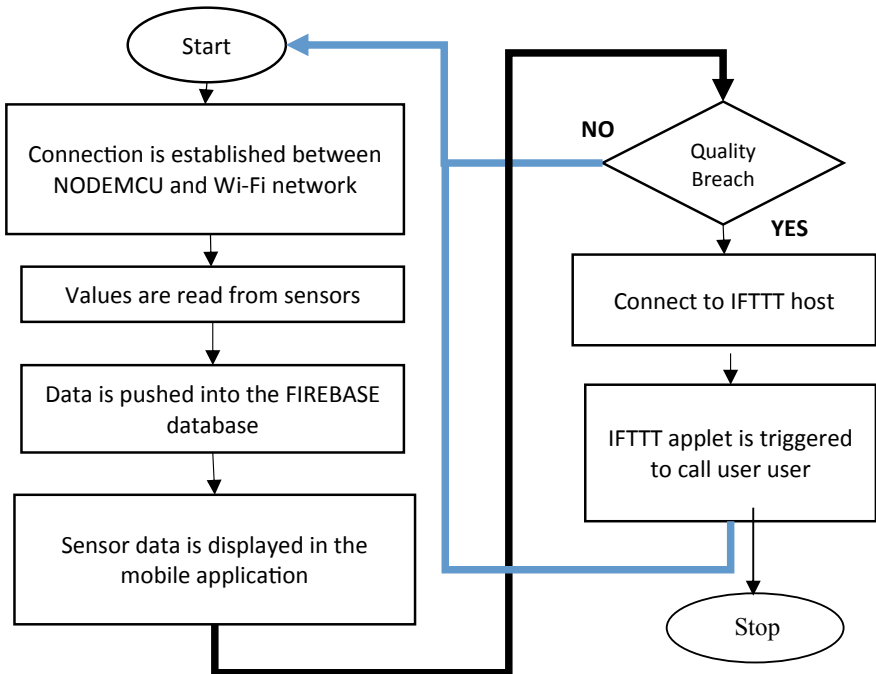
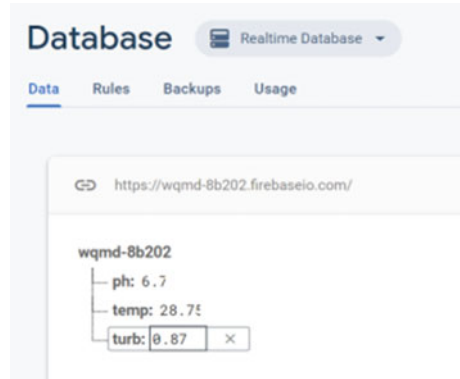


Fig. 5 Flowchart of the developed water quality monitoring system

Fig. 6 FIREBASE database to store the measure parameters



temperature and pH are 15–35 °C and 6.5–8.5, respectively. We have seen the developed mobile application and water quality monitoring systems are giving the expected performance in both cases. The detail study of both cases is presented below:

Case 1: If all the parameters values are in the acceptable range, the values are stored in the database and displayed in the mobile application. Figure 6 shows the real-time database of firebase. As it is a NoSQL database, the data is stored in key-value pairs instead of tables, and it is stored in the cloud network which can access from anytime any where with the developed mobile application.

Case 2: If any of the parameter value is not in the specified range, then the value of the parameter is communicated to the mobile application user through IFFTT framework. Next, an alerting voice message is also transmitted to the user by using VoIP protocol. In this case first, the values are stored in the database and displayed in the mobile application. Next, an alerting voice message is sent to the user through VoIP protocol, where IFTTT host is connected to the cloud network.

In Fig. 7a, it is clearly depicted that the turbidity value is out of the specified range and thus the microcontroller is connected to the IFTTT host. An alerting voice message is sent to the user to indicate about the quality breach as shown in Fig. 7b. The voice message contains all the parameter values and also the time instance at which the quality breach has occurred.. The total latency from acquiring the parameters to displaying them in the mobile application is in the order of milliseconds, which shows the application of the proposed system in upcoming wireless communication technology. As IFTTT also includes email action, it can be adapted to send alerting emails to the user/higher official whenever the water quality degrades below the predefined standards. This developed system could also be connected to a solar panel thus eliminating the need of external power supply, which may further reduce the running cost of the develop hardware.

Fig. 7 a A mobile application display showing water quality measuring parameters. **b** An alerting message when the degradation of the water quality occurred



6 Conclusions

In this work, a mobile application is developed to monitor the drinking water quality from anywhere and anytime using IoT and cloud system network. The proposed system can be used in households, industries and wherever the quality of the water is concerned. Furthermore, the developed mobile application could be used for the other monitoring application to with the designed system and sensors hardware. The mobile application is examined in both cases to check the accuracy of the application work. The system latency from the mearing the water parameter to display the alert message is in the order of the millisecond (approx. 1 ms), which shows the applicability of the system I the upcoming wireless application.

References

1. Gupta AK, Chakraborty C, Gupta B (2019) Monitoring of epileptical patients using cloud-enabled health-IoT system. *Traitement du Signal* 36(5):425–431
2. Pauget B, Dammak A (2019) The implementation of the internet of things: what impact on organizations? *Technol Forecast Soc Chang* 140:140–146
3. Dian FJ, Vahidnia R, Rahmati A (2020) Wearables and the internet of things (IoT), applications, opportunities, and challenges: a survey. *IEEE Access* 8:69200–69211
4. Varga P, Peto J, Franko A, Balla D, Haja D, Janky F, Soos G, Ficzer D, Maliosz M, Toka L (2020) 5g support for industrial iot applications—challenges, solutions, and research gaps.

- Sensors 20(3):828
5. da Luz N, Kumpel E (2020) Evaluating the impact of sampling design on drinking water quality monitoring program outcomes. *Water Res* 185:116217
 6. Almojela IF, Gonzales SM, Gutierrez K, Santos AS, Malabanan FA, Tabing JNT, Escarez CB (2020) WatAr: an arduino-based drinking water quality monitoring system using wireless sensor network and GSM module. In: 2020 IEEE region 10 conference (TENCON). IEEE, pp 550–555
 7. Gokulanathan S (2019) AGSM based water quality monitoring system using arduino. *Shanlax Int J Arts Sci Human* 6(4):22–26
 8. Amruta MK, Turkane S Solar powered water quality monitoring system using wireless sensor network. In: International multi-conference, pp 281–285. <https://doi.org/10.1109/iMac4s,2013.6526423>
 9. Bhatt J, Patoliya J (2016) IOT based water quality monitoring system. *Int J Ind Electron Electric Eng* 4(4)
 10. Dong J, Wang G, Yan H, Xu J, Zhang X (2015) A survey of smart water quality monitoring system. *ESPR* 22:4893–4906

Advanced Power Flow Management System for Electric Vehicle Charging Station



Abhishek Pratap Singh and Yogendra Kumar

Abstract In this paper, an advanced power management approach is proposed to obtain the adequate power flow control of fusion microgrid (FMG) against variable sources. The FMG is the combination of PV array system and micro gas turbine as power delivered sources. PV system has intermittent input dynamics effects in power vacillations of fusion DC microgrid. Therefore, a hybrid energy storage system (HESS), i.e., combination of battery energy storage system and supercapacitor to overcome such power fluctuations. The intermissive nature of PV system can impel the battery storage of HESS into overcharge/over discharge which again consequences in power vacillation of fusion microgrid. To avoid overcharge/over discharge of battery storage system, advanced power management system (APMS) has employed a state of charge (SOC) indicator which will protect the battery energy storage system. In this paper, to ensure the charging station voltage is constant at the DC bus terminal of FMG through a power balance between source and load with the proposed APMS. The projected method is corroborated with MATLAB /SIMULINK software.

Keywords Advanced power management system · Hybrid energy storage system · Micro gas turbine · Voltage control · Adequate power flow control · Fusion microgrid

1 Introduction

In 21st century, a new transportation sector electric vehicles are rising. To meetup the EV goals, distributed generation in the form of microgrid has installed crosswise in the country. The evolving country are deploying microgrid grid in rural areas and inaccessible locations were electrification difficult. Non-conventional sources of power like solar PV, wind energy, hydro, etc., are available abundantly. In [1, 2], the

A. P. Singh (✉) · Y. Kumar
Electrical Engineering Department, Maulana Azad National Institute of Technology Bhopal,
Bhopal, India
e-mail: asingh5130@gmail.com

admittance basic control is used for the adequate power flow of PV-diesel generator-based HMG. However, in this approach, the operational dynamics parameter of diesel generator set is not taken into account. Also, because of inclusion of diesel generator and heavy battery, this approach is not reasonable. In [3–5], the adequate management of power can be attained by governing storage system of battery that is connected to voltage source converter. Yet, the power-driven functioning dynamics of hydro generator is not taken into account by the suggested topology. The profound charging and discharging situation of battery energy storage system is ignored in the suggested power managing procedures in [6, 7] that are hardware based. In [8, 9], a multi-docks converter is accustomed for the managing the power of solar PV-battery storage system-based hybrid microgrid. In [10], for maintaining the adequate control of power flow of HMG with load fluctuation, a dynamic power management algorithm is suggested. Also, the profound discharging and charging levels of HESS are taken into account by this control process. However, this procedure does not take into account any revolving machine dynamics. In [11], for balancing load demand power, a hybrid MG structure shown in [10], and a hybrid ESS interfaced with multi-level inverter (MLI) is accustomed. However, for projected fusion microgrid based electric vehicle charging station shown in Fig.1, this procedure is not applicable. The operational parameters of hydro energy-based generators are not taken into account by the power management procedure suggested in [2, 5]. Furthermore, vast range of load power variations is not taken into account by these control procedures. Electric vehicles charging stations have categorized in slow, moderate, and fast charging modes. Charging time of EVs is crucial whenever public charging station is used. So, to maintain charging time, rated capacity of charging station must be constant irrespective of load demand because charging duration of electric vehicle is inversely proportional to charging capacity.

So, to maintain the rated capacity of charging station source active power fluctuation should be minimized. In all the literature, DC microgrid installed with battery for a DC load but ignores to manage solar power fluctuation and battery stress level. The contribution of the paper is as follows:

- A fusion microgrid based charging station power management with help of MGT, solar PV system, and HESS.
- To protect the battery from overcharging and discharging with the help of SOC indicator.

2 Modeling of Fusion Microgrid

In this section, some important equation of mathematical modelling of PV array system, micro gas turbine (MGT) based permanent magnet synchronous generator, and hybrid energy storage systems (HESS).

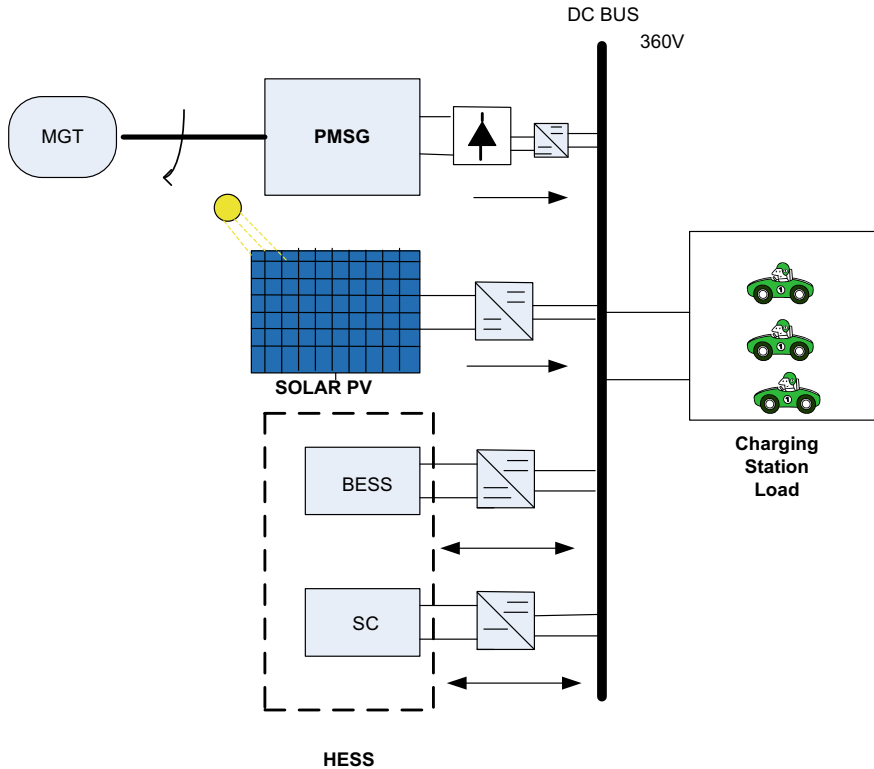


Fig. 1 Proposed electric vehicle charging station

2.1 PV Array System

PV array system is modeled with number of series and parallel modules. Desired voltage and current level of photovoltaic (PV) system depend upon the number of series and parallel modules. Maximum power point tracking (MPPT) algorithms is helps to maximize the power of PV system. This paper, incremental conductance MPPT technique is used for take-out maximum output power from the system. The incremental conductance algorithm is shown in Fig. 2. In this algorithm, the output voltage of the photovoltaic system determines by comparison with the Incremental conductance and instantaneous conductance of PV modules. If the value of conductance is equal, then it shows the maximum power point (MPP) for a particular given irradiance value (W/m^2). The power output of PV system is obtained by

$$P_{pv} = v_{pv} * i_{pv} \tag{1}$$

The duty cycle of unidirectional PV system converter is calculated by

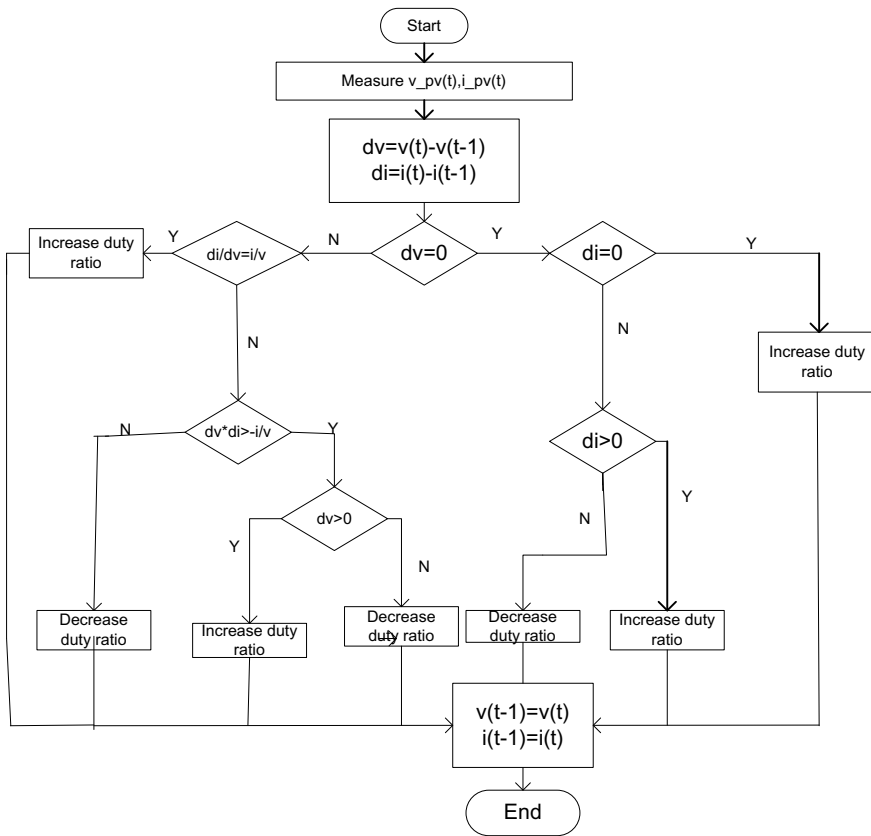


Fig. 2 Incremental conductance MPTP algorithm

$$\begin{aligned}
 Dc &= \frac{V_{dc} - V_{in}}{V_{dc}} \\
 &= 1 - 253/360 \\
 &= 0.2972
 \end{aligned}
 \tag{2}$$

The inductance of converter is calculated by

$$Lc = Dc * (V_{dc} - V_{in}) \tag{3}$$

where,

Dc = duty cycle of PV system converter

V_{in} = input voltage of PV system

V_{dc} = voltage at the bus terminal.

2.2 Modeling of Micro Gas Turbine (MGT)

The micro gas turbine has very high speed and small power capacity. MGT contributed power to FMG. The MGT with semi-Kaplan-PMSG, supply DC power to FMG without any interruption. A common type of single-reheat tandem compound turbine is used in hybrid system. The response of a steam turbine has better when compared with a hydraulic turbine due to water inertia. A simple transfer function of turbine derived by using turbine torque (ΔT_m) and control valve position (ΔV_{cv}) is follows:

$$\frac{\Delta T_m}{\Delta V_{cv}} = \frac{1 + SF_{HP}T_{RH}}{(1 + ST_{CH})(1 + ST_{RH})} \quad (4)$$

The electromagnetic torque produced by the PMSG is:

$$T_e = \frac{3P}{2} [\varphi_m i_q (L_q - L_d) i_d] \quad (5)$$

where,

P is number of poles, L_d and L_q are d_q frame inductance, i_d and i_q are d_q frame current, and φ_m is flux linkage.

2.3 Modeling of HESS

The intermittent input solar dynamics causes the voltage fluctuation of DC microgrid. To maintain the DC microgrid stable operation, HESS supports to microgrid. HESS is combination of Li-ion battery and supercapacitor. HESS compensates the source side power dynamics which is slow varying power dynamics compensated by battery storage system and very fast power variations are supported by supercapacitor (SC) storage system. But, overcharging and deep discharging of battery may harmful for battery life. Thereby a voltage limits of BSS are predefined for this work which indicates overcharging and deep discharging of BSS.

The power compensated by HESS is given by equation:

$$\Delta P_c = P_{MGT_DC} \pm P_{PV} - P_L \quad (6)$$

$$P_b = \frac{\Delta P_c}{1 + ST_b} \quad (7)$$

$$P_{SC} = \Delta P_c - P_b \quad (8)$$

where

ΔP_c = power compensated by HESS

P_b and P_{sc} = Reference's power of battery and supercapacitor, respectively

P_L = rated power capacity demand (kw)

T_b = battery response time.

3 Advanced Power Management System (APMS)

In all the literature DC microgrid installed with battery for a DC load but ignores to manage solar power fluctuation and battery stress level simultaneously.

The proposed advanced power management system shown in Fig. 3 operates based on net zero power concept, i.e., difference between local power generation and local power utilization is zero. In this paper, adequate power flow control of DC microgrid is obtained by

$$P_{MGT_DC} + P_{PV} \pm P_{ESS} - P_L = 0 \tag{9}$$

For the stable operation of hybrid microgrid. Output voltage of MG should maintain constant. That's why power generation and load demand should be equal. Optimal power flow control is obtained by

$$P_{ref}(K) = \Delta P_{PV_{j-1}} + \Delta P_{PV_j} + \Delta P_C \tag{10}$$

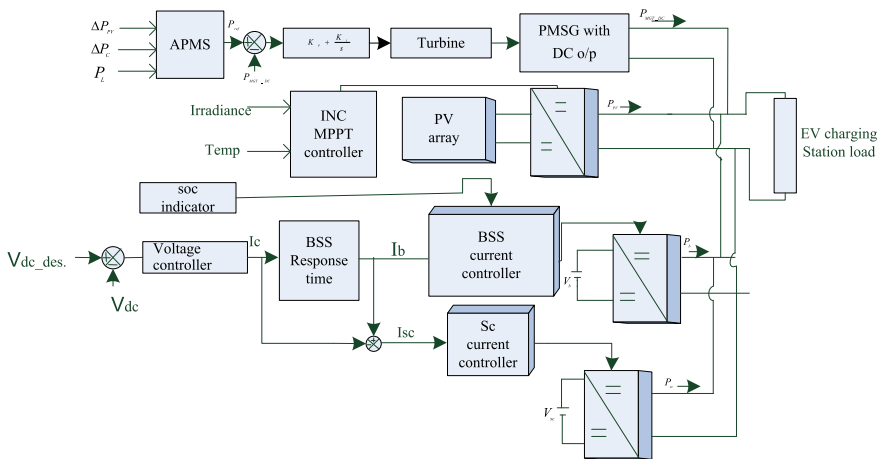


Fig. 3 Block diagram of proposed APMS

$$\Delta P_{PV_J} = P_{PV_J} - P_{PV_{J-1}} \text{ (for, } J > 1) \quad (11)$$

Power monitoring block continuously monitors the power generation and load side demand. Reference active power supported by the micro gas turbine.

4 Results and Discussion

In this section, the results are attained with APMS for power balance of a fusion microgrid. In Fig. 4a shows a constant 30 kW EV charging load demand. In Fig. 4b shown output power of photovoltaic system fluctuates in every 2 s, so after $t = 2$ s, there is no support of power from photovoltaic system. HESS has supported this source power variation to fulfill 30kW charging load demand. But, Li-ion battery has some response time so that battery cannot support instantly that's why a supercapacitor storage device is used for quick response. Figure 4c, d shown 20 kW active power support from HESS to FMG from $t = 2$ s to $t = 4$ s, respectively.

At $t = 4$ s PV array output power has abruptly risen to 20 kW. This irregularity has led the battery overcharged it's clearly shown in Fig. 4d. because of sudden increase in output power of photovoltaic system Li-ion battery has been over charged up to—13.6 kW (at $t = 4$ s). Same Li-ion battery charged with APMS reduces—10.3 kW from $t = 4$ s to $t = 5$ s as shown in Fig. 4h.

So that it is concluded from Fig. 4d, h the energy stress of battery reduces by 24.2%. The irregular behavior of PV array output power voltage of DC microgrid oscillates at $t = 2$ s and $t = 4$ s as shown in Fig. 4b. Because of voltage variation, output power of DC microgrid can varied. APMS has resolved initial voltage oscillation and voltage spike and get a smooth desired 360 V DC output voltage as shown in Fig. 4g. The total EV charging load demand is 30kW. PV array system and ESS combinedly support 20kW without any interruption in DC grid voltage. And remaining 10kW supported by micro gas turbine based permanent magnet synchronous generator as shown in Fig. 4e. Micro gas turbine supplies reference active power estimated by APMS.

5 Conclusion

The advanced power management system introduced in this paper has ensure power balance between multiple sources of fusion microgrid and load demand. Due to variation of PV array output power, microgrid output voltage fluctuates so that output power is also affects. Thus, to avoid this noxious of fusion microgrid, APMS has managed by using of battery and super capacitor based mixed energy storage system have been taken into account in this work to counteract the power fluctuations by disintegrating into slow and fast variation. Results are presented in this work; it

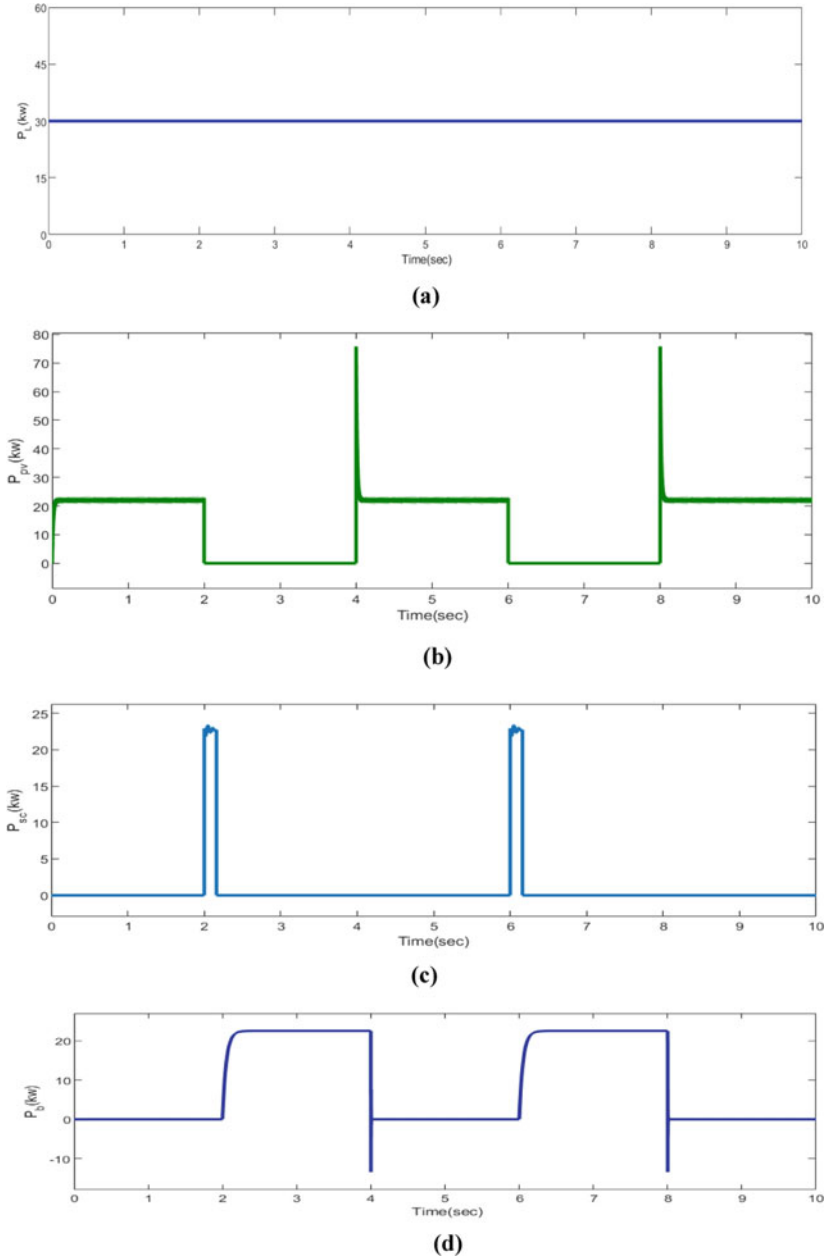
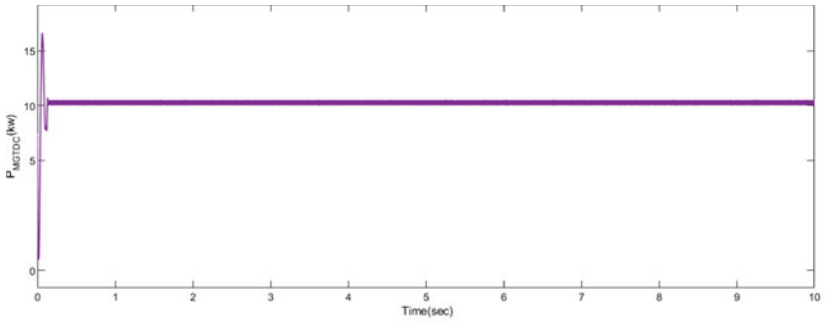
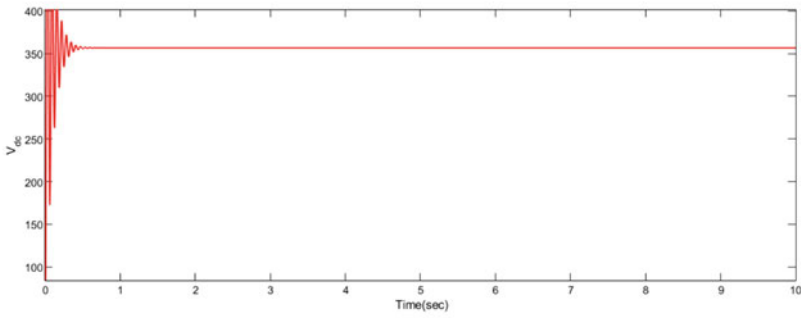


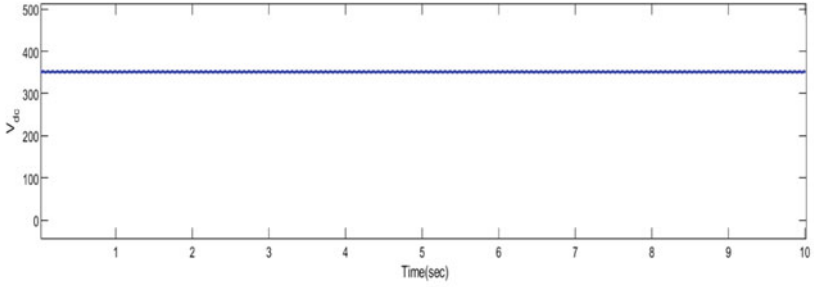
Fig. 4 **a** Constant EV charging station load demand. **b** PV array system output power. **c** Output power of supercapacitor. **d** Output power of battery without APMS. **e** DC power output of MGT based PMSG with APMS. **f** Output voltage (V_{dc}) without APMS. **g** Output voltage (V_{dc}) with APMS. **h** Output power of battery with APMS



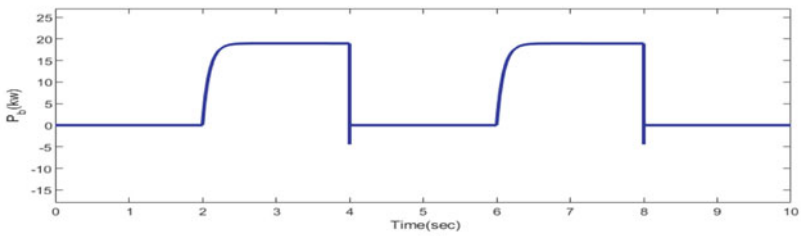
(e)



(f)



(g)



(h)

Fig. 4 (continued)

is noticed that with APMS voltage oscillation reduces and charging station power demand remains constant. Stress level is reduced to 20.7% as compared to without APMS. The slow power variation is compensated by battery, and fast power variation is compensated by super capacitor. MGT supported all the time reference power with a constant magnitude. In this paper, APMS validated only for constant charging station load. In the future, it can be extended for a variable charging station load.

Appendix

PMSG: 400 V, 30 KW, 1500 r.p.m.

MGT: fuel pressure = 358–380 kPa, fuel flow = 12 m³/h

PV array system: $v_{pv} = 255\text{V}$, $i_{pv} = 100\text{A}$

Battery Li-ion: Nominal voltage = 205 V, 140 Ah, $V_{b\text{Max}} = 220\text{V}$, $V_{b\text{Min}} = 190\text{V}$

Supercapacitor: 245 V, 120 F.

References

1. Philip J, Jain C, Kant K, Singh B, Mishra S, Chandra A et al (2016) Control and Implementation of a standalone solar photovoltaic hybrid system. *IEEE Trans Ind Appl* 52(4):3472–3479
2. Singh B, Arya SR (2012) Admittance based control algorithm for DSTATCOM in three phase four wire system. In: ICPCES 2012—2012 2nd international conference power, control embedded systems
3. Kewat S, Singh B, Hussain I (2018) Power management in PV-battery-hydro based standalone microgrid. *IET Renew Power Gener* 12(4):391
4. Seema SB (2016) Intelligent control of SPV-battery-hydro based microgrid. In: IEEE international conference power electron drives energy systems PEDES 2016, 2017, pp 1–6
5. Chandran VP, Murshid S, Singh B (2018) Power management and control of PMSG based hydro-PV-BES using CSTOGI control algorithm for autonomous micro-grid. In: 8th IEEE power India international conference PIICON 2018
6. Merabet A, Ahmed KT, Ibrahim H, Beguenane R, Ghias AMYM (2017) Laboratory scale microgrid based wind-PV-battery. *IEEE Trans Sustain Energy* 8(1):145–154
7. Prakash SL, Arutchelvi M, Jesudaiyan AS (2016) Autonomous PV-array excited wind-driven induction generator for off-grid application in India. *IEEE J Emerg Sel Top Power Electron.* 4(4):1259–1269
8. Hong J, Yin J, Liu Y, Peng J, Jiang H (2019) Energy management and control strategy of photovoltaic/battery hybrid distributed power generation systems with an integrated three-port power converter. *IEEE Access* 7:82838–82847
9. Jiang W, Fahimi B (2011) Multiport power electronic interface—concept. *Power* 26(7):1890–1900
10. Sharma RK, Mishra S (2018) Dynamic power management and control of a PV PEM fuel-cell-based standalone ac/dc microgrid using hybrid energy storage. *IEEE Trans Ind Appl* 54(1):526–538

11. Naik KR, Rajpathak B, Mitra A, Kolhe M (2020) Adaptive energy management strategy for optimal power flow control of hybrid DC microgrid. In: 2020 5th international conference on smart sustainable technology split 2020
12. Guerrero JM, Vasquez JC, Matas J, De Vicuña LG, Castilla M (2011) Hierarchical control of droop-controlled AC and DC microgrids—a general approach toward standardization. *IEEE Trans Ind Electron* 58(1):158–172
13. Deshmukh RR, Ballal MS, Suryawanshi HM, Mishra MK (2020) An adaptive approach for effective power management in DC microgrid based on virtual generation in distributed energy sources. *IEEE Trans Ind Informatics*. 16(1):362–372
14. Naik KR, Rajpathak B, Mitra A, Kolhe M (2019) Voltage stability of small hydro generator based DC microgrid. In: 2019 8th international conference on power systems transition toward sustainability smart flex grids, ICPS 2019
15. Deshmukh RR, Ballal MS, Suryawanshi HM, Talapur GG (2018) A control algorithm for energy management and transient mitigation in DC microgrid. In: 2017 national power electronics conference NPEC 2017, pp 270–275
16. Silva WDN, De Oliveira JG, Dias BH, De Oliveira LW (2019) Gas microturbines for distributed generation system. In: 2019 IEEE 15th Brazilian power electronics conference 5th IEEE south power electronics conference COBEP/SPEC
17. Moradzadeh M, Abdelaziz MMA (2020) A new MILP formulation for renewables and energy storage integration in fast charging stations. *IEEE Trans Transp Electrification* 6(1):181–198
18. Kundur P, Lauby (1994) Power system stability and control, vol 20. India McGraw Hill

Analysis of Graphene Field-Effect Transistor (GFET) as a Sensor



Arpikumar Chaudhari, Abhishek Bhowmik, Jay Patel, Achal Parikh, and Rutu Parekh

Abstract This paper studies and investigates various parameters of top-gated graphene field-effect transistors (GFET). In this paper, the study of the relationship of resistance with temperature has led to the fact that we can use GFET as a sensor. Input parameters such as length of the channel, width of the channel, and temperature are taken, and it shows a significant impact on the relationship of various other parameters such as temperature versus position, electron versus density, hole density versus position, electric field versus position, and velocity versus position. It was investigated that the resistance is having a linear relationship with the temperature which shows that the top-gated graphene field-effect transistor (GFET) can be used as a temperature sensor; the value of resistance is insignificantly changing from 2.75 to 2.5 Ω when the length of the channel is 1800 nm; and when the channel length is 1400 nm, the resistance changes from 2.57 to 2.55 Ω for temperature varying from 253 to 313 K. Secondly, by varying the temperature, the changes in field and velocity were minimal for temperature range from 100 to 300 K, the value of electric field varied from 13 to 14 V/ μm , and velocity goes from 180 to 170 km/s. The effect of other input parameters like gate length and temperature on GFET has been observed and represented graphically. The presented graphs were all simulated in the NanoHub's GFET tool.

Keywords Graphene · GFET · Electrical properties · Thermal properties · Drift–diffusion model · Sensor

1 Introduction

As per Moore's law, the transistors in a microchip are getting doubled every two years, but now there has been a limitation in the size and so following it the study of nanomaterials is emerging. Using different nanomaterials, not only is it possible to match

A. Chaudhari · A. Bhowmik · J. Patel · A. Parikh (✉) · R. Parekh
VLSI & Embedded System Group, Dhirubhai Ambani Institute of Information and
Communication Technology, Gandhinagar, India
e-mail: achalparikh2241@gmail.com

© The Author(s), under exclusive license to Springer Nature Singapore Pte Ltd. 2022
V. Mahajan et al. (eds.), *Sustainable Technology and Advanced Computing*
in *Electrical Engineering*, Lecture Notes in Electrical Engineering 939,
https://doi.org/10.1007/978-981-19-4364-5_5

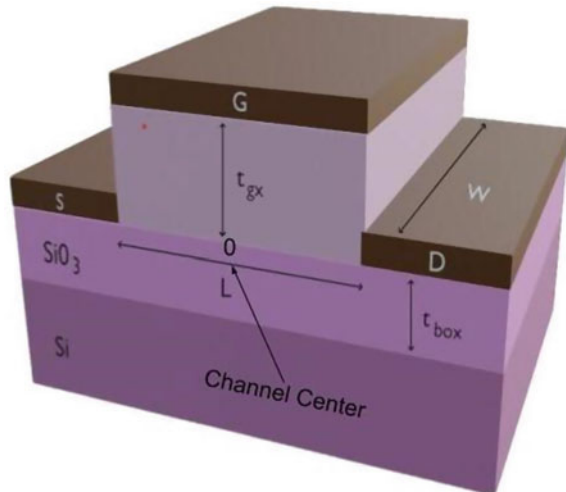
45

the limitation of size but also exploration of new useful electronics properties can be done [1]. One of the useful nanomaterials is graphene which can be used as a replica of different semiconducting materials. Graphene is among the allotropes of carbon; its carbon atoms are arranged in a single layer. These carbon atoms are organized in a honeycomb lattice with a two-dimensional arrangement. The carbon–carbon bond distance in a single graphene sheet approximates 0.142 nm. The graphene sheet’s atomic thickness is very sensitive to the local environment’s change, making it an excellent channel material in field-effect transistors used as electronic sensors. Besides, graphene is a widely researched material due to its unique properties such as zero bandgaps, also as in the formation of graphene every carbon atom is connected to other 3 carbon atoms and it is known that carbon has 4 electrons in its valence shell, and thus, due to such kind of formation there is one electron which remains free.

This free electron is responsible for graphene to have remarkable electron mobility at room temperature and high thermal conductivity; also, it has several other properties like stiffness, large surface area, impermeability to gases, etc., which helps to grow the electrical sensor market exponentially. The most straightforward and standard configuration for the graphene-based sensor is GFET, a graphene sheet with a sensing area between two metal contacts, as shown in Fig. 1. In this device, the conductivity can change using an electric field effect with a top gate, generating a very high sensitivity [2].

Due to graphene’s outstanding properties, there has been a significant amount of research in recent years. Dutta et al. discussed the electrical and thermal properties of GFET by simulating the width, electrical properties, and temperature profile of the graphene channel. It was concluded that both the electrical and thermal properties of GFET can be improved by fabricating the channel with a larger width in the GFET device [3]. An analytical work was done to study the effect of gas adsorption

Fig. 1 Schematic diagram of GFET



on GNR electrical properties, and different adsorption effects on the channel were observed and derived [4]. Another study also talks about a drift–diffusion-based GFT model for a channel length of 100 nm in Verilog-A compact for switching characteristics of GFET [5]. In another investigation, a top-gated GFET has been studied with a full numerical solution of a drift–diffusion–Poisson model. The mobilities have been deduced from the Boltzmann equations’ direct solution for charge transport in graphene by a DG method [6]. Another paper has discussed creating a graphene field-effect transistor, which has similar characteristic curves to conventional semiconductor materials with gaps based on large-area monolayer graphene [7]. A study done by Hamzah et al. on the electronic properties of GFET proved that the electrical transport in GFET is dependent on the simulation temperature as it may vary the maximum resistance in the channel of the device [8]. In another research work, the same group investigated the performance of channel length scaling in GFET using Lumerical Device Software. They have analyzed the electrical characteristics of GFET with long and short conducting channels [9].

In a research done by Hafs et al., a comparative study between experimental measurements and TCAD simulations to study the electrical properties of few-layer graphene and the approach to simulation tools is described by using the basic of band theory, Poisson’s equation, the continuity equation, and the drift–diffusion equations that are suitable for the device with small active regions [10]. In another research, simulation of dual-gate field-effect transistors based on monolayer graphene, considering essential factors such as quantum capacitance, electron–hole mobility difference, channel length, source, and drain resistance on output characteristics of the device, is analyzed [11]. The functionality of the transistor in all the regions of the operation for both hole and electron conduction was observed [12]. The model is called a dual-gate graphene FET model, and the circuit simulation has been implemented with the help of Berkeley SPICE-3.

The operation of GFET biosensors has been modeled and simulated [13]. It includes the bacterial motion in the electrolyte and also the surface charge that is induced by the charged bacterial properties. All these properties and the relationship helped in the prediction of the sensing performance of the GFET sensor. This study can serve as a guideline for the design and optimization of GFET biosensors in the future.

A research paper had surveyed recent developments in GFET considering fabrication, modeling, and simulation tools and applications, especially in sensors [14]. Another paper by Li and his team used a GFET nanosensor for the identification of COVID-19 [15]. For graphene to use as a temperature sensor, it is important to understand the relationship between electrical resistance and temperature. When the relationship between temperature and electrical conductivity is linear, it can be used as a resistive temperature detector, while a nonlinear relationship can be used as a semiconductor. Since the relationship between resistance and temperature is nonlinear as shown in Fig. 2, it can be observed that GFET can be used as a temperature sensor. Also, this result can be compared and validated with that of Davaji et al. They worked on a suspended graphene sensor, and the value of resistance differs by 0.8Ω at 293 K (20 °C) for channel length 1800 nm [16]. There is 2.6 % change in

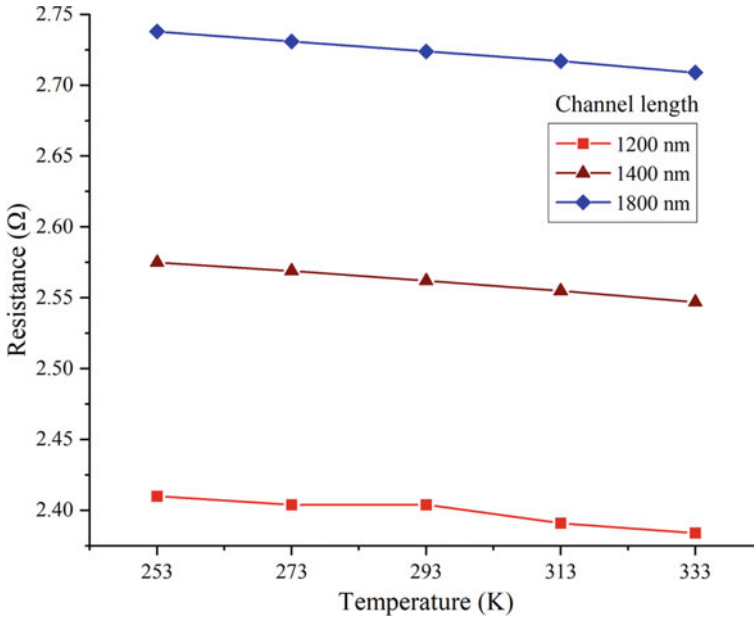


Fig. 2 Resistance versus temperature (channel length as input parameter)

resistance for temperature variation from 283 to 293 K in the suspended graphene temperature sensor, and here in GFET, it is observed that there is approx 1 % change in resistance for the same temperature variation.

Meanwhile, an experiment done by T. Hayaka and the group showed the linearity of the graph of resistance vs. temperature by varying the gate voltage for a specific range [17]. In another work using different hybrid films, the resistance vs. temperature was obtained, which also stated the linearity and decrease of resistance with increasing temperature [18].

2 Materials and Methods

This paper has used NanoHub's GFET tool to simulate graphene's thermal and electrical properties. This tool's mechanism is that the code uses the drift-diffusion approach to calculate the current vs voltage behavior of the GFET concerning the device's temperature. Other simulations that are included in this paper with the GFET tool are studying the carrier density, temperature profile, drift velocity, and electric field along the GFET channel. As shown in Table 1, different parameters are taken into account and are varied and electrical and thermal properties of GFET are observed. The main concerns are width of the channel, length of the channel, and the temperature contacts of the GFET. This simulation tool accounts for velocity

Table 1 Input parameters used for simulation in NanoHub's GFET tool

Input parameters	Values
Width of channel	1000, 1400, 1800 nm
Length of channel	1000, 1400, 1800 nm
Initial temperature	100, 300, 600 K
Dirac voltage	0 V
Maximum drain current	1 mA
Drain current step	50 μ A
Top-gated oxide thickness	0.01 μ m
Mobility	3000 ($\text{cm}^2/\text{V s}$)
Gate voltage	0.7 V

saturation at high fields, Seebeck effect at contacts, and possible device breakdown due to thermal self-heating [17].

3 Result and Discussion

The simulation results are shown below for the top-gated GFET device for all the performance parameters (width, length, and temperature). The results are simulated with a gate voltage of 0.7 V, keeping the rest of the parameters such as Dirac voltage, maximum drain current, drain current step, top-gated oxide thickness, and mobility of the tool's default values.

4 Temperature Versus Position in Channel

The temperature is highest around the center of the channel but not precisely at the center which can be seen in Fig. 3 at around $x = -0.6$ nm which is the region between the source and the center of the channel, and this is due to the contact width of source with the gate which is more than that of contact width of drain and the gate.

It has shifted the highest temperature toward 10 percent of the device length from the right side. Also, it is observed that there is a decrease in temperature at the edge of the channel. It is happening because of lateral heat transfer through the gate oxide [18]. From Fig. 3, it can be observed that when the length is increased from 1000 to 1800 nm, the graph has shifted toward the left.

In Fig. 4, it can be observed that when the width decreases from 1800 to 1000 nm, the temperature increases. It is happening due to the change in electron density. As the width decreases, there is a narrow space for the electron to move, so the electron density increases. As the electron density increases, temperature also increases because there are electrons in conflict generating heat. When width increases, there

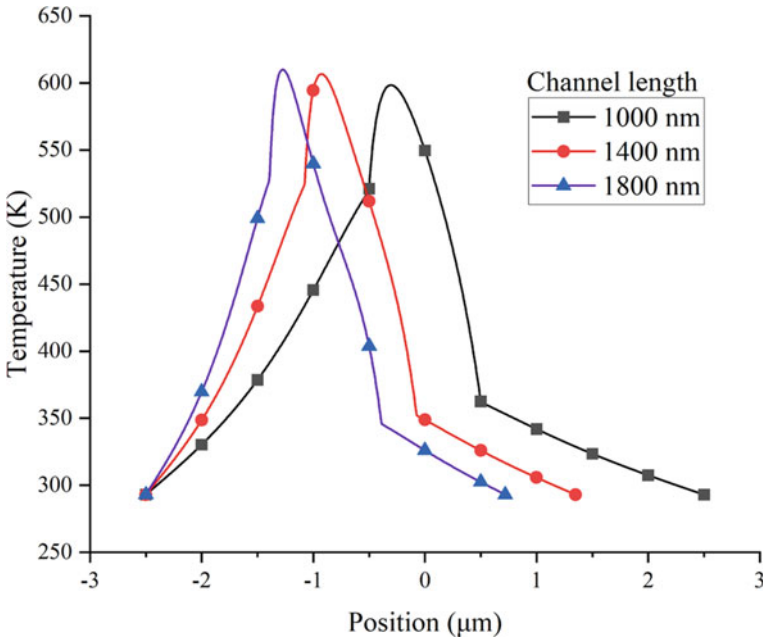


Fig. 3 Temperature versus position (length as input parameter)

is a broader space for electrons to move around, so electron density decreases; therefore, temperature decreases. Also, the results of analysis done by Dutta et al. and the investigation done here are similar; in that work, it was observed for variation for width 1000, 2000, and 3000 nm [3]. In both the experiments, it is observed that when the channel width is 1000 nm, the peak temperature near the center of the channel is around 600 K and the results are in agreement. In that analytical work, it was observed that the temperature near the center of the channel was decreasing from 600 to 375 K when the channel width was increased from 1000 to 2000 nm, and here as shown in Fig. 4, when the width is increased from 1000 to 1400 nm, the temperature falls from 600 to 450 K. And subsequently for channel width 3000 nm in that experiment, the temperature was 325 K, and here when the channel width is 1800 nm, the temperature is decreased more to 375 K.

5 Field Versus Position of the Channel

As the electric field is inversely related to the cross-sectional area, so when the width of a solid object is increased, there is a significant increase in the area. As per the observation by increasing the width of the channel, it is seen that the area increases simultaneously. As a result, it can be concluded that the electric field is also

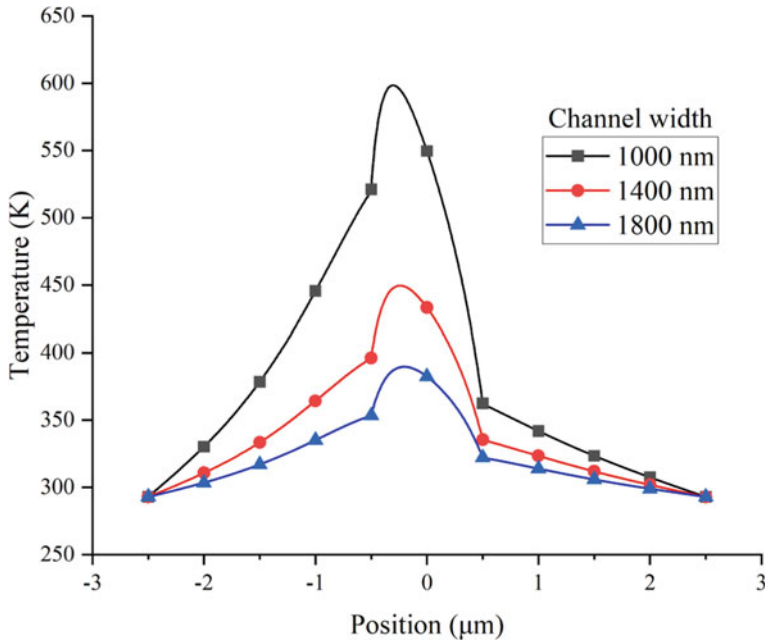


Fig. 4 Temperature versus position (width as input parameter)

inversely proportional to the channel width. From Fig. 5, it can be seen that when there is increase in the channel’s width from 1000 to 1800 nm, the electric field drops to a significant value.

Figure 6 shows that when there is an increase in the channel length from 1000 to 1800 nm, the peak electric field decreases minutely because when the channel length increases, electron density decreases. When the electron density decreases, the electric field decreases because a small amount of electrons gets saturated in a single point. Figure 7 shows that when there is increase in the temperature from 100 to 600 K, the electric field decreases in a minimal amount, because the electric field is inversely proportional to conductivity, and since in semiconductors, the temperature is inversely proportional to resistance. So when there is increase in the temperature, resistance decreases. So it can be concluded that temperature is directly proportional to conductance, and hence, it can be observed that the temperature is inversely proportional to the electric field.

6 Velocity Versus Position of the Channel

As it can be seen from Fig. 8, the charge carrier’s velocity gradually increases from source to drain (i.e, from $x = -1$ to 1 nm). At the end of the channel, the charge

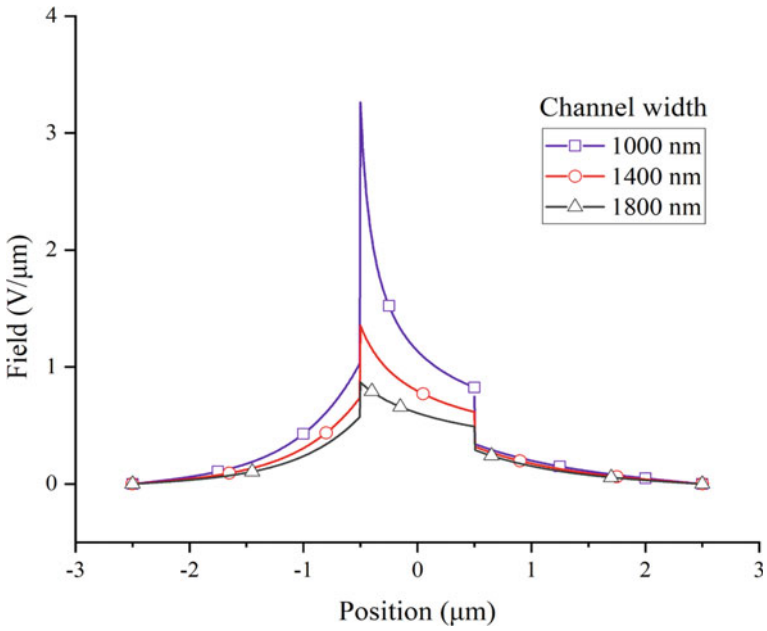


Fig. 5 Field versus position (width as input parameter)

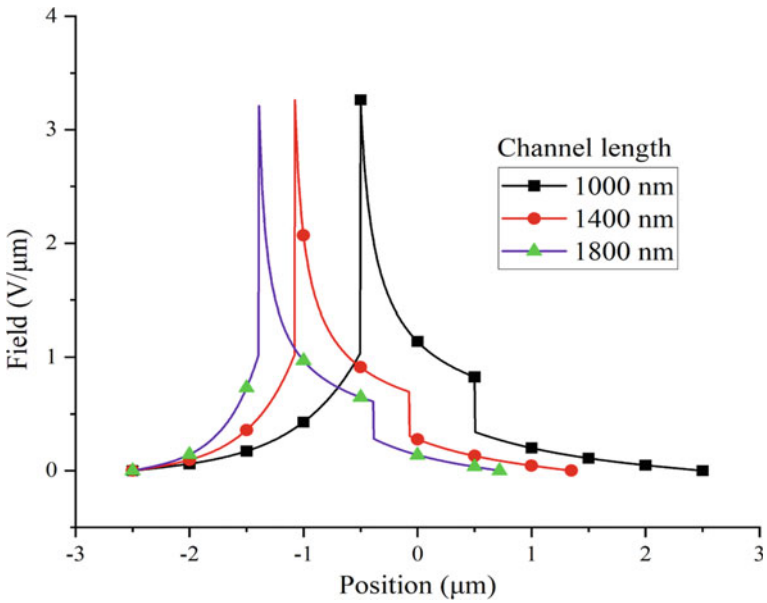


Fig. 6 Field versus position (length as input parameter)

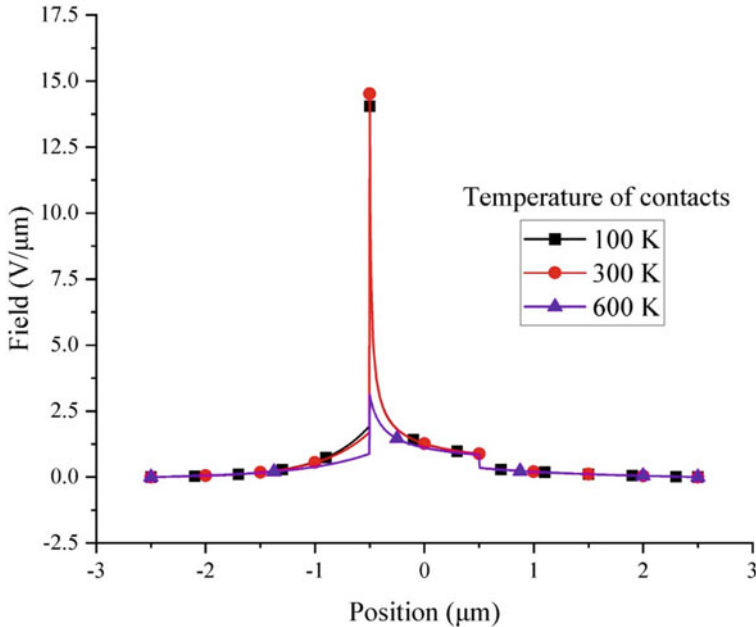


Fig. 7 Field versus position (temperature as input parameter)

carriers are jammed and they reach the drain region quickly. Therefore, in the drain region, the velocity of the charge carriers sharply increases and the carriers there collide with each other. For a graphene channel with a larger width, charge carriers have more space to travel to the drain region; therefore, the charge carrier’s velocity increases sharper concerning smaller width channels.

Figure 8 shows that when the width is increased from 1000 to 1800 nm, velocity decreases because the velocity is directly proportional to the field and also as the field decreases with increase in area or width. A research was carried out by Mohammed et al, and it was observed that by varying the channel width from 50 to 100 nm they found out the peak velocity was about 370 and 210 km/s around the center of channel, and here by investigation, it is seen that the peak velocity is around 110, 120, and 125 km/s for channel width 1000, 1400, and 1800 nm [19]. Also, another work done by Dutta et al. showed the results for velocity for width variation of 1000, 2000, and 3000 nm [3]. In that experiment, it was found out that the velocity around the center of the channel was 130 km/s, 125 km/s, and 120 km/s, respectively.

As the electric field is inversely proportional to length, therefore, when the graphene channel’s length is increasing, the electric field decreases. Since velocity is directly related to the electric field because $V_d = \mu E$ whereas $\mu =$ mobility, V_d stands for drift velocity, hence, it can be concluded that V_d is inversely proportional to length. As it is observed in Fig. 9, when the channel length is increased from 1000 to 1800 nm, it is perceived that the graph is shifted toward the left side because here

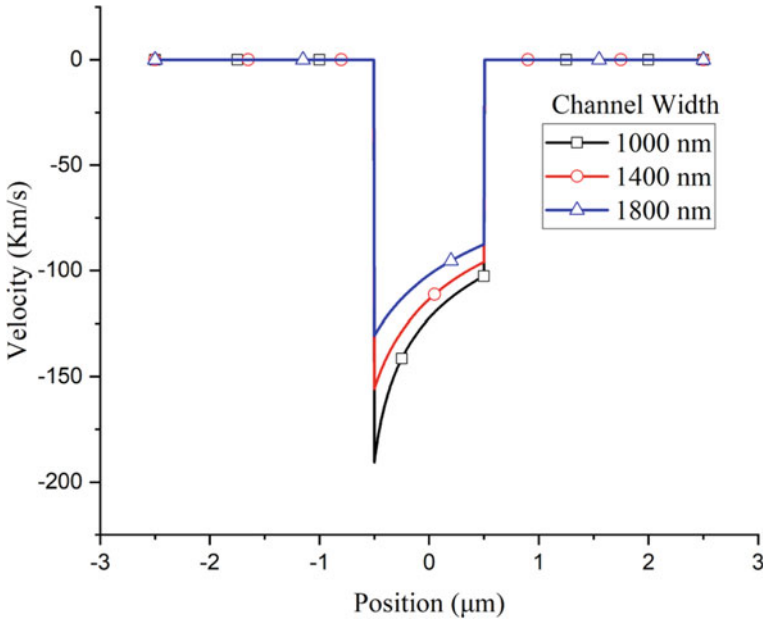


Fig. 8 Velocity versus position (width as input parameter)

position zero is the channel's center, and the scope of the position is $[-\text{length}/2, \text{length}/2]$. It is observed that the electric field is inversely proportional to temperature from the electric field versus temperature figure. Since velocity and electric field are proportional, velocity is directly related to the electric field because $V_d = \mu E$. Hence, velocity decreases as the temperature increases. In Fig. 10, when the temperature rises from 100 to 600 K, velocity decreases insignificantly.

7 Electron Density Versus Position of the Channel and Hole Density Versus Position of the Channel

When the graphene channel width increases, electron density decreases due to the electrical field being inversely proportional to the graphene channel's width. Whenever the channel's width increases, the electric field decreases, and the electron loses its energy and moves from the conduction band to the valence band, so electrons become free; hence, they are not part of channel conduction, and since graphene is a unipolar transistor, when electron density decreases, hole density inside the channel increases. Figure 11 shows that when the channel width keeps increasing from 1000 to 1800 nm, electron density starts to increase. When the channel width increases, electric lines increase [20], which implies that the number of electrons in that space increases, and hence, electron density increases. Similarly, for hole density since the

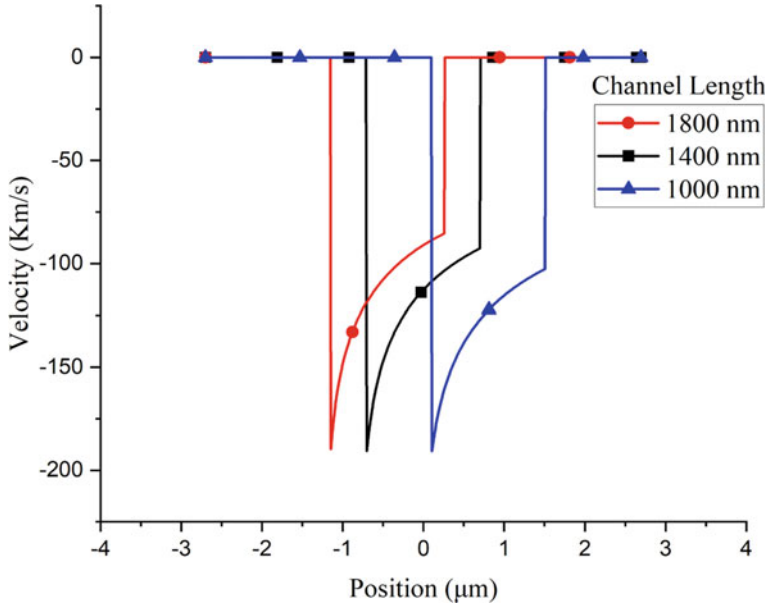


Fig. 9 Velocity versus position (length as input parameter)

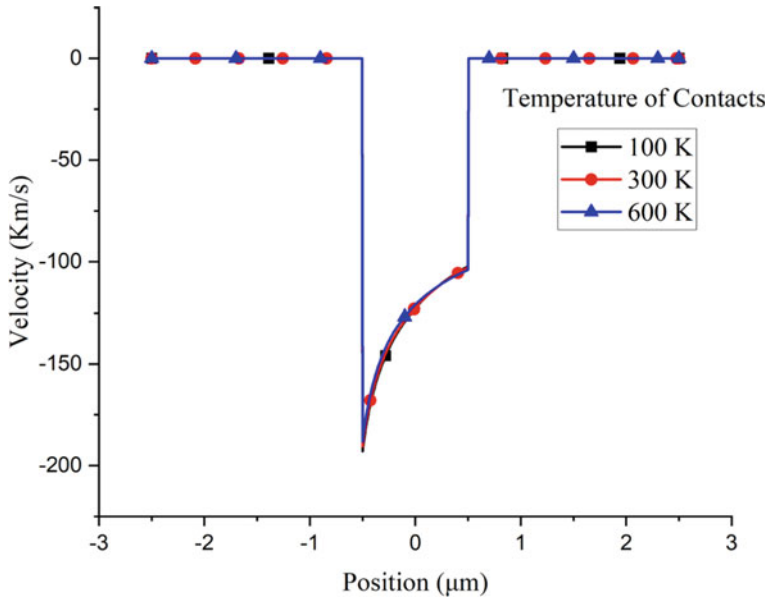


Fig. 10 Velocity versus position (temperature as input parameter)

change in channel width affects electron density. As a result, when the channel width increases, electron density increases, and a sufficient amount of electrons can fill up the holes, and because of that, hole density decreases, as it is observed in Fig. 11. Also, similar results were found in the analytical work done by Dutta et al. The variations of width in that work were 1000, 2000, and 3000 nm [3]. At 1000 nm, the hole density was around 14 P cm^{-2} and electron density was 45 P cm^{-2} for both the results; for 2000 and 3000 nm, in that experiment the hole density was 18 and 22 P cm^{-2} and the electron density was 15 and 22 P cm^{-2} ; and here for 1400 and 1800 nm, hole density is 12 and 14 P cm^{-2} and electron density is 32 and 45 P cm^{-2} .

When the length of the graphene channel increases, electron density increases, so hole density decreases. The reason behind this is the temperature. It is seen earlier that when the channel's length increases, the channel's temperature increases, so electrons get energy (Electron thermal energy $= \frac{3n_e k_B T_e}{2}$ i.e., Electron thermal energy $\propto T$) and move toward the conduction band. That is why electron density increases in the channel. In the case of hole density, when the length of the channel increases from 1000–1800 nm, more holes start to occur compared to the total number of electrons available, and hence, the graph starts to fall down, as it is shown in Fig. 12. The higher the channel length value is, the more amount of hole density remains unfilled.

Figure 13 shows that by increasing the temperature, the hole density keeps decreasing, and then, once it reaches a certain threshold level, it gets constant. The reason behind this is that whenever external energy in the form of heat is applied, electrons get energy, they move from valence band to conduction band, and as a

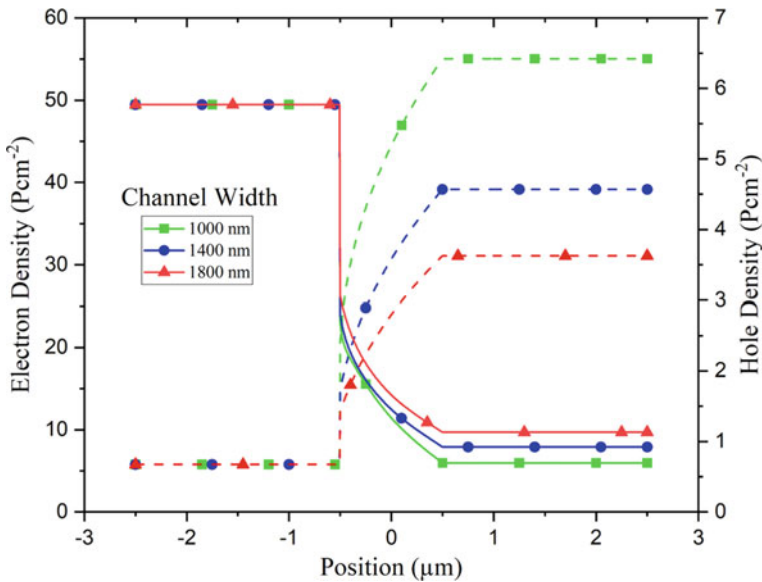


Fig. 11 Electron and hole density versus position (width as input parameter)

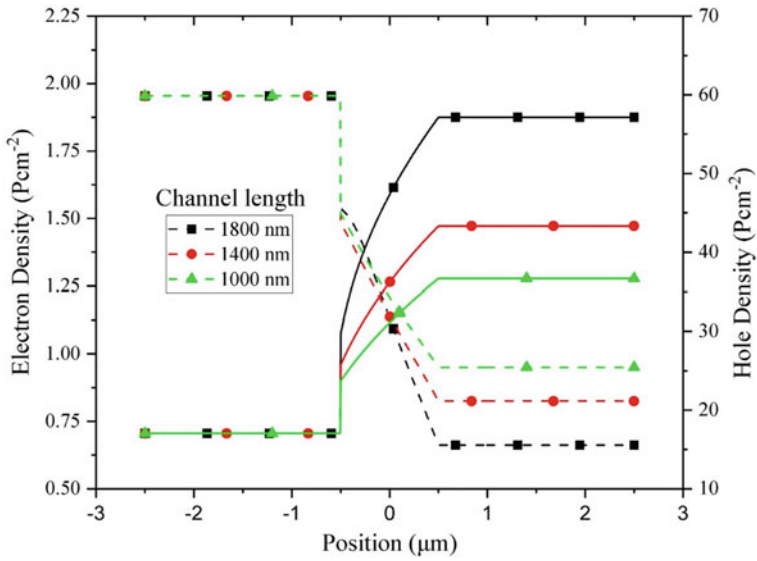


Fig. 12 Electron and hole density versus position (length as input parameter)

result, the holes get filled up by electrons, and as a result, hole density decreases and electron density increases.

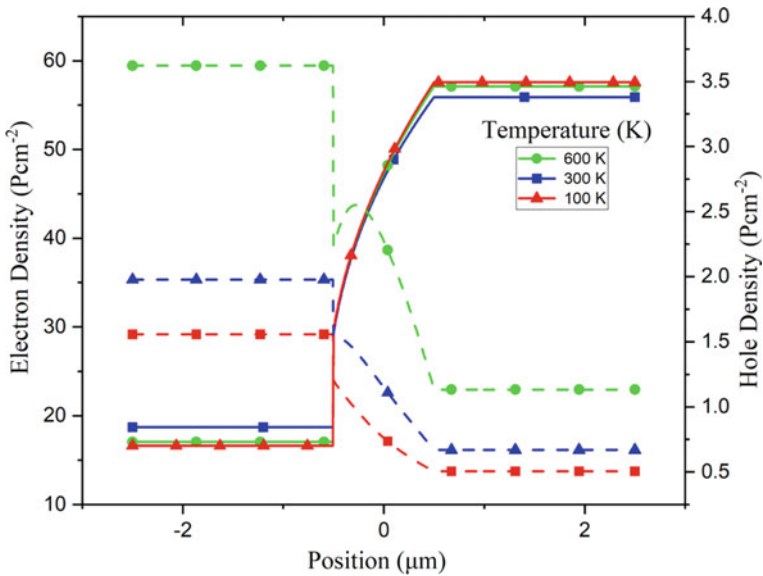


Fig. 13 Electron and hole density versus position (temperature as input parameter)

8 Conclusion

This research paper shows successful investigation on variance of electrical and thermal properties of GFET like temperature, velocity, electric field, and electron–hole density by changing other parameters like the width (1000, 1400, 1800 nm), length (1000, 1400, 1800 nm), and temperature (100, 200, 300 K) of the channel on a GFET sensor. Firstly, by increasing the width from 1000 nm to 1800 nm, the changes are very drastic like the temperature of the GFET changed from 600 to 375 K drastically, which shows that the GFET is showing very sensitive changes by a very small change in the width [21]. Also, by increasing the width, the electrical field subsequently dropped from 3 to 1 V/ μm , the velocity also dropped from 200 to 100 km/s, the electron density decreases in a significant amount from 55 to 30 P cm^{-2} (around 45 %), and hole density increases from 6 to 10 P cm^{-2} (around 66.66 %). It is also observed that by increasing the length of the channel from 1000 to 1800 nm, the electrical field was changed in a very minute amount from 3.3 to 3 V/ μm , the velocity decreased in a very significant amount from 200 to 90 km/s, the electron density increases from 1.25 to 1.8 P cm^{-2} , and the hole density falls from 0.9 to 0.6 P cm^{-2} [22]. The outcomes show that GFET is a very useful and sensitive device and the demand for it will increase exponentially in the future as it shows very sudden changes in velocity of charge carriers and field by changing the width and the length in a very small amount.

References

1. Thompson SE, Parthasarathy S (2006) Moore’s law: the future of Si microelectronics. *Mater Today* 9(6):20–25
2. Graphene (GFET) Chemical Sensors. Available at: <https://www.graphenea.com/blogs/graphene-news/graphene-field-effect-transistors-for-chemical-sensing>. Accessed Oct 2020
3. Dutta A, Fathema Farjana M, Rahman S, Mahmood ZH (2016) Simulation of the electrical and thermal properties of graphene field effect transistor
4. Pourasl AH, Ahmadi MT, Ismail R, Gharaei N (2018) Analytical modelling and simulation of gas adsorption effects on graphene nanoribbon electrical properties. *Mol Simul* 44(7):551–557
5. Sreenath R, Bala Tripura Sundari B (2016) Compact model for switching characteristics of graphene field effect transistor. In: AIP conference proceedings, vol 1724, No 1. AIP Publishing LLC, p 020013
6. Nastasi G, Romano V (2020) A full coupled drift-diffusion-Poisson simulation of a GFET. *Commun Nonlinear Sci Numer Simul* 87:105300
7. Nastasi G, Romano V (2020) An efficient GFET structure. [arXiv:2002.07067](https://arxiv.org/abs/2002.07067)
8. Selvarajan RS, Hamzah AA, Majlis BY (2017) Electrical characteristics of graphene based field effect transistor (GFET) biosensor for ADH detection. In: *Biosensing and nanomedicine X*, vol 10352. International Society for Optics and Photonics, p 103520T
9. Selvarajan RS, Hamzah AA, Yusof N, Majlis BY (2019) Channel length scaling and electrical characterization of graphene field effect transistor (GFET). *Indones J Electr Eng Comput Sci* 15:697–703
10. Hafsi B, Boubaker A, Ismail N, Kalboussi A, Lmimouni K (2015) TCAD Simulations of graphene field-effect transistors based on the quantum capacitance effect. *J Korean Phys Soc* 67(7):1201–1207

11. Abramov II, Labunov VA, Kolomeitseva NV, Romanova IA, Shcherbakova IY (2019) Simulation of graphene field-effect transistors and resonant tunneling diodes based on carbon nanomaterials. In: International conference on micro-and nano-electronics 2018, vol 11022. International Society for Optics and Photonics, p 110220F
12. Umoh IJ, Kazmierski TJ, Al-Hashimi BM (2013) A dual-gate graphene FET model for circuit simulation—SPICE implementation. *IEEE Trans Nanotechnol* 12(3):427–435
13. Wu G, Meyyappan M, Lai KWC (2018) Simulation of graphene field-effect transistor biosensors for bacterial detection. *Sensors* 18(6):1715
14. Krsihna BV, Ravi S, Prakash MD (2021) Recent developments in graphene based field effect transistors. *Mater Today Proc* 45:1524–1528
15. Li J, Wu D, Yu Y, Li T, Li K, Xiao MM, Li Y, Zhang ZY, Zhang GJ (2021) Rapid and unamplified identification of COVID-19 with morpholino-modified graphene field-effect transistor nanosensor. *Biosens Bioelectron* 183:113206
16. Davaji B, Cho HD, Malakoutian M, Lee JK, Panin G, Kang TW, Lee CH (2017) A patterned single layer graphene resistance temperature sensor. *Sci Rep* 7(1):1–10
17. Hayasaka T, Kubota Y, Liu Y, Lin L (2017) Temperature characterizations on graphene-based gas sensors. In: 2017 19th international conference on solid-state sensors, actuators and microsystems (Transducers). IEEE, pp 2103–2106
18. Huang J, Yang X, Her SC, Liang YM (2019) Carbon nanotube/graphene nanoplatelet hybrid film as a flexible multifunctional sensor. *Sensors* 19(2):317
19. Pop E, Lian F (2014) GFET tool. <https://nanohub.org/resources/gfettool>. <https://doi.org/10.4231/D3QF8JK5T>
20. Freitag M, Steiner M, Martin Y, Perebeinos V, Chen Z, Tsang JC, Avouris P (2009) Energy dissipation in graphene field-effect transistors. *Nano Lett* 9(5):1883–1888
21. Mohamad A, Awano Y (2015) graphene modulation channel-width field- effect transistors enabling high carrier velocity acceleration and bandgap introduction. *Appl Phys Express* 8(11):115102
22. Sivokon VE, Sharapova IV (2019) The melting of two-dimensional electron crystals in narrow channels. *Low-Temp Phys* 45(12):1267–1276

Optimal Location and Size of Multi-distributed Generation with Minimization of Network Losses



Akhilesh Kumar Barnwal , Shailendra Singh , and M. K. Verma 

Abstract Distribution system is one of integral part of complex power system. Power losses in distribution system branches are very high rather than power losses in transmission system branches. These higher losses lead to higher operational cost in distribution system. The advancement of technology using distributed generations has been proved to be very important in optimizing network losses, environment pollution, and reliability of power systems. The DG allocation is a mixed-integer optimization problem with nonlinearity associated. In this paper, the work optimal size location and power factor of single and multiple placements of different distributed generators have been presented. Distribution network loss has been minimized for optimal power factor, size, and location of distributed generator to be optimized. Optimum size and minimum loss have been determined. Results thus obtained have been compared with the results in the literature. The proposed method has been validated on the IEEE33-bus test system.

Keywords Distributed generation (DG) · Optimum size · Optimum location · DG types · Voltage profile · Power loss

1 Introduction

The day-by-day increase in electrical power demand, as load is increasing rapidly, has rendered the existing central generation and transmission network unable to manage such a large burden. This increasing power demand has challenged the power engineer to maintain the power system reliably, securely as well as economically [1]. Hence, it is clear that either increasing the capacity of existing transmission network or production and supply in a small—scale near the load center can cope up with these issues. Power production of small generation units dispersed across the power grid or networks is defined as distributed generation [2]. These power producing technologies have led the multidimensional research opportunities in the field of distribution

A. K. Barnwal (✉) · S. Singh · M. K. Verma
Indian Institute of Technology, Banaras Hindu University, Varanasi, India
e-mail: akhileshkb.rs.eee16@iitbhu.ac.in

© The Author(s), under exclusive license to Springer Nature Singapore Pte Ltd. 2022
V. Mahajan et al. (eds.), *Sustainable Technology and Advanced Computing in Electrical Engineering*, Lecture Notes in Electrical Engineering 939,
https://doi.org/10.1007/978-981-19-4364-5_6

system planning and operation [3]. Apart from traditional very large scale power generation utility, distributed generator installation near load center requires very less capital cost, operation cost, and maintenance cost. Distributed generators are also environment friendly, when they are used as different renewable energy technology. Renewable energy technologies which are not very new include solar generation, micro-hydro power plants, wind, geothermal generation, power from municipal waste, landfill gas, and biomass. Emerging major power source of renewable technologies comes from sea waves and tidal stream. These energy sources possess the property of lower energy density compared to fossil fuels, which leads to smaller, economic, and geographically spread power plants [4]. Benefit of effective integration of DGs includes reduced generation of central power plants, enhanced utilization of available transmission/distribution network capacity, and improved system security, more reliable operation and overall costs and pollutant gas emission reduction.

Being a conventional approach in power industry, distributed generation has a large number of definitions and terms. The term distributed generation is also known by different terminology in literature such as “embedded generation,” “dispersed generation,” and “decentralized generation” based on their geospatial locations. “Dispersed generation” and “embedded generation” are mostly popular in North-American and Anglo-American countries respectively, while Europe and Asian countries use the term “decentralized generation” [5]. According to American council of energy efficient economy sources of electricity generation which are closer to point of use are termed as “decentralized or on-site generation” contrary to large power producing central units [6]. Gas Research Institute acknowledge the term distributed generation for the amount of power production “more than 25 kW but always lesser than 25 MW” [7]. These generations can include PV solar generation, wind generation, combined heat power plant, and others. Distributed generation changes the flow of power in network and hence results in change in network losses, not only in distribution system but also for transmission network. These reductions in losses further result in reduced charges for transmission network uses by utility.

It has been shown that poor power factor size and location of DG results in increased distribution losses compared to losses with optimally located DG [8–10]. Lee et al. have presented selection of optimal locations and ratings before the integration of multiple DGs to the power grid so that minimum line losses and maximum benefits of DGs are achieved [11]. Amanifar in his paper has presented particle swarm optimizer (PSO) to achieve the minimum operating and maintenance cost, reduced line losses, and reduction in THD with optimally located and sized DG [12]. The concept of network reconfiguration by opening and closing the tie switches and maintaining the radial structure of the operational distribution network to minimize the losses and voltage deviation has been achieved in [13–17]. Mathematical modeling for reducing network losses with reconfiguration has been established in [18]. Fractal theory-based stochastic search algorithm [19] and water cycle algorithm [20] were applied to obtain a better solution in order to minimize losses while reconfiguring the distribution network in presence of DG sources. In Refs. [21–25],

method of analytical expression has been illustrated the optimality in size and location to obtain minimum distribution loss and to improve the system voltages at all nodes.

In this paper, different cases of DG allocation strategy have been presented for optimal location and size problem for minimizing real power losses while satisfying different constraints. Optimal size corresponding to optimal bus for minimum loss has been computed based on repeated load flow method with power factor. In a case where the optimal power factor, optimal location and optimal size have been calculated for minimum loss. The optimal power factor has been calculated by running load flow for different power factor. For calculation of distribution loss, load flow algorithm by backward—forward sweep is utilized [26]. The method proposed in this paper has been implemented on standard 33-bus distribution test system.

2 Problem Formulation

This paper presents the main objective to minimize the total active power losses in distribution network, i.e.,

$$\text{Minimize } P_L = \sum_{k=1}^{nb} I_k^2 * r_k \quad (1)$$

Subject to constraints:

$$V_{i,\min} \leq V_i \leq V_{i,\max} \quad (2)$$

$$\text{dg_size} \leq \text{dg_size}_{\max} \quad (3)$$

$$I_k \leq I_{k,\max} \quad (4)$$

$$\text{dg_loc}_1 \neq \text{dg_loc}_2 \neq \text{dg_loc}_3 \quad (5)$$

where P_L is total network loss, I_k and r_k is current and resistance, respectively, of branch k , nb is maximum number of branches in the network, V_i voltage at i th node. The maximum and minimum limit on voltage is $\pm 5\%$ [27]. dg_loc_1 , dg_loc_2 and dg_loc_3 are the 1st, 2nd, and 3rd location of DG placed, respectively, which must not be same in any case.

The total network loss P_L has been calculated by sum of losses in all branches of network (1) using the load flow algorithm using backward—forward sweep as given in Ghosh and Das [26]. To calculate the loss in a branch, the current flowing in that branch is multiplied by the corresponding branch resistance. The current through any particular branch is the addition of the all load currents beyond that particular

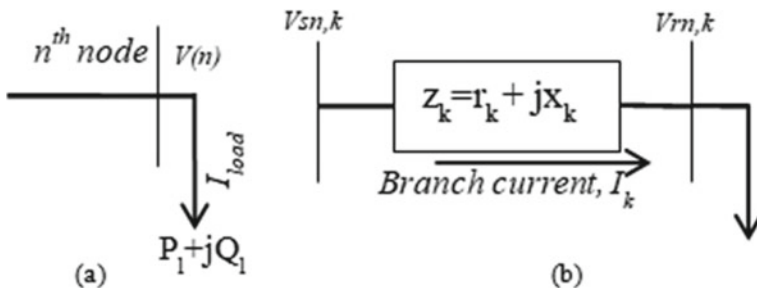


Fig. 1 **a** Current drawn by load at n th bus. **b** Voltage calculation at receiving end bus

branch, i.e.,

$$I_k = \sum_n I_{load}(n) \quad \forall n \text{ beyond branch } k \quad (6)$$

The current $I_{load}(n)$ at a particular node n is calculated by

$$I_{load}(n) = \frac{P_l(n) - jQ_l(n)}{v(n)^*} \quad (7)$$

$P_l(n)$ and $Q_l(n)$ are real and reactive power load demand at node (n), and $v(n)^*$ is complex conjugate of voltage v at node n .

The voltage at receiving end node connected with sending end node by k th branch is calculated by

$$V_{rn,k} = V_{sn,k} - I_k * Z_k \quad \forall k = 1, 2, 3 \dots nb \quad (8)$$

where $V_{rn,k}$ and $V_{sn,k}$ are voltages at receiving end node and sending end node, respectively, connected by branch k . I_k and Z_k are branch current and branch impedance of k th branch, respectively. Initially, a flat voltage profile has been assumed for each node in the network (Fig. 1).

2.1 Optimal Location and Size of DG

The optimal locations and sizes of DGs play a very crucial role for minimization of distribution network losses. At a bus, the loss is the function of injected power by DG placed at that bus, so starting from minimum DG size, if we increase the size of DG at that particular bus the losses starts decreasing till a particular DG size, which is optimal size of DG corresponding to that particular bus. Beyond this particular optimal DG size, any further increment in DG size leads to higher distribution losses, and it may overtake the losses corresponding to base case losses. Similarly, it is true

for all the buses in network. Hence, selection of DG size is very crucial as it may result in higher distribution losses. Also, the size of DG must not be more than maximum load demand and should be consumable within the distribution network boundary, otherwise there will be a large amount of loss because of design of distribution network and decreasing conductor sizes as power in passive distribution system flows in forward direction from substation to load.

DG installation for location size and minimum power loss has been calculated for different cases as below:

- A single unit of Type-3 DG rated in MVA injecting both active and reactive power has been computed.
- Losses with multi-DG placed simultaneously injecting only active power has been computed.

3 Methodology

In this section, loss calculation for Type-3 DG has been presented. Load flow has been performed to get the optimal size and location for each power factor, and corresponding loss also has been calculated. Thus, power factor for which loss is minimum has been obtained by comparing losses at other power factor. Power factor has been taken from zero to unity and has been increased in small steps of 0.02. For each power factor, different DG size has been taken into account starting from zero to 4 MW in a small step, and then, load flow has been run to calculate the losses at each bus. And thus optimal DG size, location, and optimal power factor corresponding to minimum loss are stored.

3.1 Procedure

- Step 1 Run base caseload flow using input system data.
- Step 2 Start with initial chosen size of DG, initial DG location, and initial power factor as initial solution vector and calculate the system loss.
- Step 3 Increment the size of DG in a fixed small step to get the corresponding loss.
- Step 4 If the loss found with DG size in step 3 is lesser than previous loss, update the solution vector else go to step 3 until the maximum DG size is reached.
- Step 5 Increment the DG location by one.
- Step 6 Repeat steps 2–6 until all the possible DG location have been checked and update the solution vector and corresponding loss if found lesser than previous.
- Step 7 Make an increment in previous power factor by a fixed step change.
- Step 8 Repeat steps 2 to 8 until unity power factor and update the solution vector and corresponding loss if found lesser than previous loss.
- Step 9 Print the updated solution vector and stop.

Applying the above procedure, it is also possible to get the minimum loss, optimum DG size, and location at any given power factor. In this paper, the work has been extended to obtain the minimum loss, optimal size, and location of multiple DGs injecting only real power, i.e., Type-1 DG. The procedure for placement of multiple units of Type-1 DG is as follows.

3.2 Procedure for Multi-type-1 DG Placement

- Step 1 Input the system data and run the load flow to obtain the size and location for 1st DG, as stated in previous method for unity power factor, for minimum distribution loss.
- Step 2 Store the DG size, optimal location, and minimum loss obtained for 1st DG.
- Step 3 Fix the DG of capacity/size obtained above, at their respective optimal location.
- Step 4 Repeat steps 1 and 2 to obtain the size and location, corresponding to minimum loss for 2nd DG, and then for 3rd DG also.

4 Results and Discussion

4.1 Size, Location, and Loss

The methodology is tested on standard 33-bus 32 branch test system with 2.3 MVA and 3.715 MW load at 100 MVA, 12.66 kV [17]. The test system is radial in nature. A MATLAB code has been written in the MATLAB R2018a environment to evaluate the optimal location of DG and its size to calculate the minimum loss in the network.

In Fig. 2, minimum loss at each DG location corresponding to different power factors for 33-bus system is shown. For more clarity, Fig. 2 is redrawn and shown in Fig. 3 in a more clear way for some selected power factors at 0, 0.5, 0.82, 0.9, and unity power factor. For each power factor, it is found that loss corresponding to that power factor occurs at different location and different DG size. Figure 4 is drawn for the minimum loss obtained at each power factor, which exhibits that at 0.82 power factor loss is minimum.

Case 1: For Type-3 DG injecting both real as well as reactive power, load flow for every power factor with varying DG size for each and every bus has been performed, and corresponding minimum loss is calculated which is shown in Fig. 5. It is found that at 0.82 power factor, locating 3.1 MVA capacity of DG at bus no. 6 gives the minimum loss of 61.371 kW. In Fig. 5, optimum DG size and losses corresponding to optimally located DG at each bus is shown for Type-3 DG.

In Fig. 5, optimum DG size and losses corresponding to optimum size of DG placed at each bus is shown for Type-3 DG.

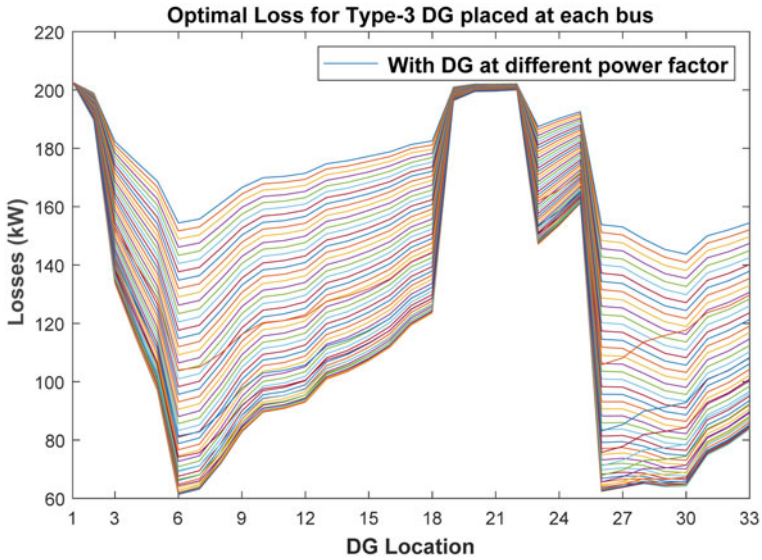


Fig. 2 Total loss with Type-3 DG at different buses at various power factors

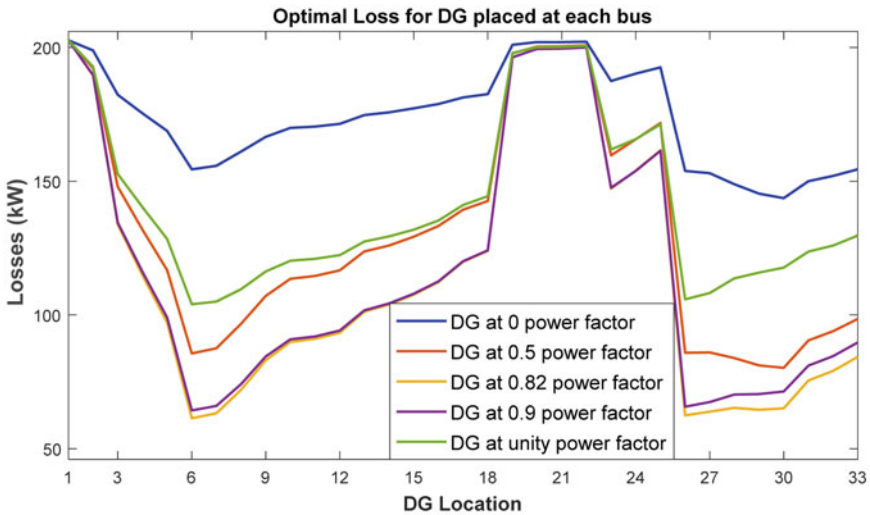


Fig. 3 Total loss with Type-3 DG at different buses for selected power factors

Case 2: As this case has been studied for multiple Type-1 DG placements in distribution network. Three successive DGs of optimum size have been placed one by one at their optimum location found with previously installed DGs, and losses have been computed as shown in Fig. 6. Thus, it is noticed that after placing 1st DG of

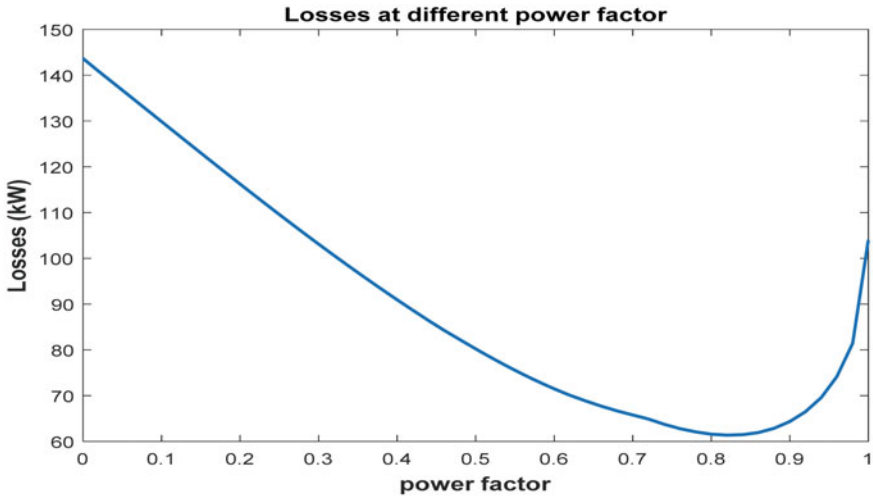


Fig. 4 Loss variation with variation in power factor

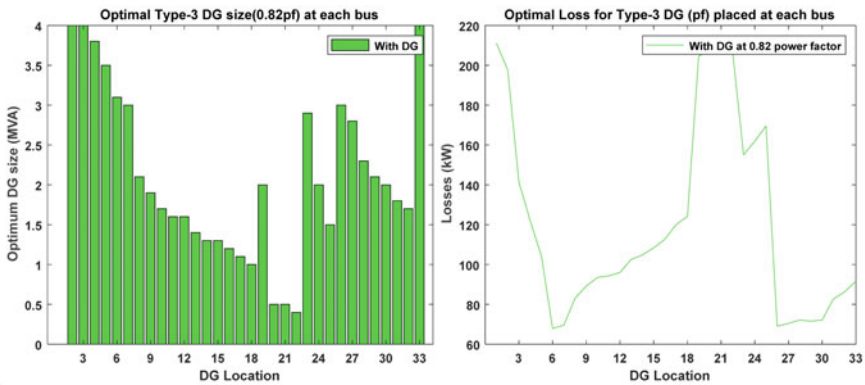


Fig. 5 Optimal size and corresponding loss for Type-3 DG at each bus

size 2.6 MW at bus no. 6, the optimal location for 2nd DG is bus no. 16 of DG size 0.4 MW reduces the losses to 93.736 kW. And for 3rd DG, it is found that 0.6 MW DG at bus no. 25 reduces the losses further to 85.989 kW.

Voltage: Voltage profile for all the cases mentioned in this paper has been calculated for each case. In Table 1, the minimum and maximum voltage obtained in each case and corresponding bus with and without DG placement is reported.

In Fig. 7, the voltage profiles for all cases have been drawn, and it is clear that using multiple numbers of Type-1 DG improves the voltage mostly as compared to Type-3 DG. In Table 1, minimum and maximum voltage and corresponding bus with and without DG are also shown.

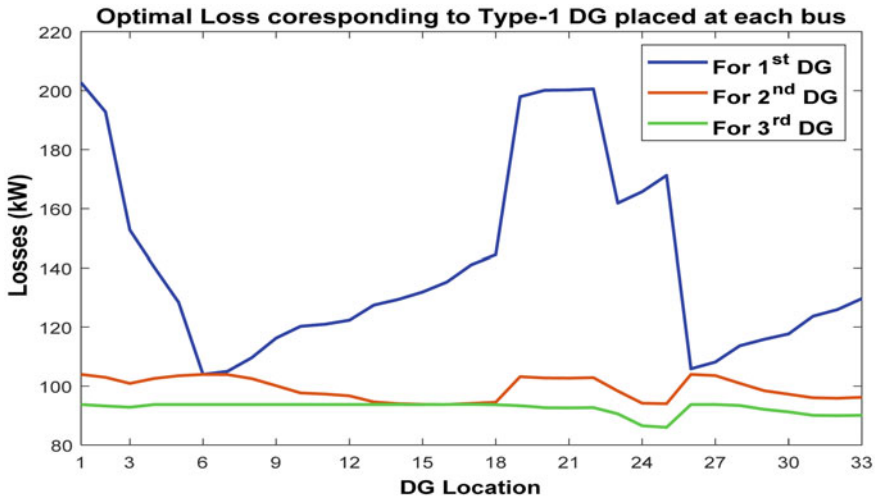


Fig. 6 Loss curve for multiple DG placements

Table 1 Voltage profile for two cases with and without DG

Cases		V_{min} (p.u.) (bus no.)		V_{max} (p.u.) (bus no.)	
		Without DG	With DG	Without DG	With DG
Case 1	1 DG	0.91309 (18)	0.96697 (18)	1.0 (1)	1.0015 (6)
Case 2	2 DG		0.96059 (33)		1.0 (1)
	3 DG		0.96291 (33)		1.0 (1)

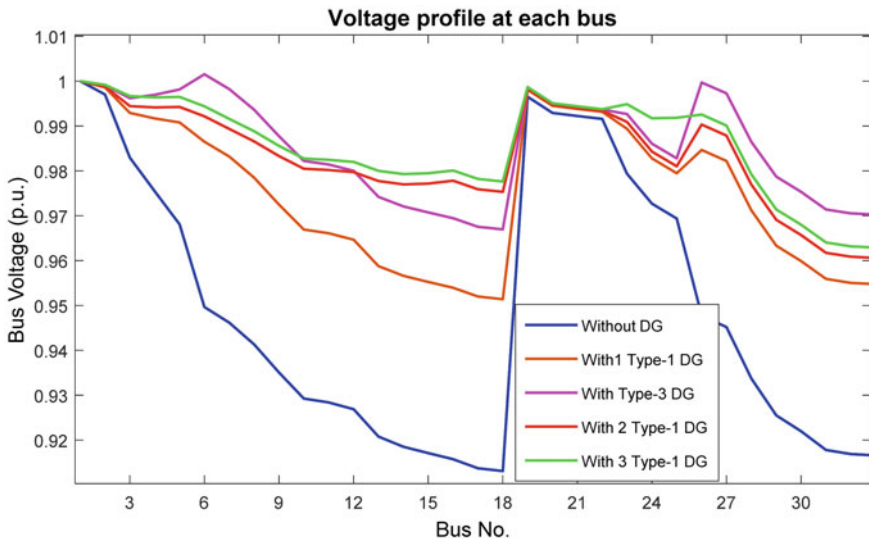


Fig. 7 Voltage curve for different cases of DG placement

Table 2 Result obtained for two cases

Cases		Base case	Case 1	Case 2	
Opt. DG location		–	6	6 and 16	6, 16 and 25
Opt. DG size	MW	–		2.6 and 0.4	2.6, 0.4 and 0.6
	MVA (pf)	–	3.1, 0.82	–	–
Loss (kW)		202.67	61.371	93.736	85.989
% Loss reduction		–	69.72	53.75	57.57
% Voltage increment			5.9	5.2	5.46

Table 3 Comparison of results

	Case 2	Multi-DG placement		
In Ref. [16]	DG size in MW (DG location)	0.1070 (18)	0.5724 (17)	1.0462 (33)
	Power loss (kW)	96.76		
	Minimum voltage	0.967		
	% Loss reduction	52.26		
Method applied in this paper	DG size in MW (DG location)	2.6 (6)	0.4 (16)	0.6 (25)
	Power loss (kW)	85.989		
	Minimum voltage (bus)	0.96291 (33)		
	% Loss reduction	57.57		

In Table 2, it is shown that loss is lowest for case 1 using Type-3 DG which reduces losses to 61.371 kW, while using multiple DGs reduces the losses in a great extent but lower than case 1. Type-3 DG reduces the losses by 69.72%, while three numbers of Type-1 DG reduce the losses by 57.57%.

A comparative study of optimal location of multiple Type-1 DG approach for maximum loss reduction is shown in Table 3, which shows that placing DG at nodes 6, 16, and 25 has reduced the losses to 85.989 kW as compared to 96.76 kW loss obtained with the meta-heuristic harmony search algorithm (HSA) [16]. And loss reduction has been improved to 57.57% as compared to 52.26% of HSA. Although it is found that voltage profile with the method applied in this paper experiences a slight decrement compared to HSA [17] but within its acceptable limit.

5 Conclusion

This paper has presented the Type-3 as well as multiple numbers of Type-1 DGs to minimize the real power losses in distribution network by injecting real or reactive power. From above discussion, it can be concluded that Type-3 DG is best suitable

for the most loss reduction which is calculated as 69.72% as can be seen in Fig. 6 and Table 2, while improvement of voltage at almost all buses after installing DG at their optimal location is well within the limit of $\pm 5\%$. Placing a single Type-3 DG improves the voltage significantly which is almost equivalent to placing two Type-1 DGs as can be seen in Fig. 7. A more improved voltage profile has been achieved with three Type-1 DG placement cases.

References

1. Alhelou HH, Hamedani-Golshan ME, Njenda TC, Siano P (2019) A survey on power system blackout and cascading events: research motivations and challenges. *Energies* 12(4):1–28. <https://doi.org/10.3390/en12040682>
2. Kumar T, Thakur T (2014) Comparative analysis of particle swarm optimization variants on distributed generation allocation for network loss minimization. In: 1st international conference on networks soft computing ICNSC 2014—proceedings, pp 167–171. <https://doi.org/10.1109/CNSC.2014.6906682>
3. Dulău LI, Abrudean M, Bică D (2014) Distributed generation technologies and optimization. *Procedia Technol* 12:687–692. <https://doi.org/10.1016/j.protecy.2013.12.550>
4. Jenkins N, Ekanayake JB, Strbac G (2010) Distributed generation. *Distrib Gener* 1–279. <https://doi.org/10.1201/b16747-16>
5. Ackermann T, Andersson G, Söder L (2001) Distributed generation: a definition. *Electr Power Syst Res* 57(3):195–204. [https://doi.org/10.1016/S0378-7796\(01\)00101-8](https://doi.org/10.1016/S0378-7796(01)00101-8)
6. ACEEE: Distributed generation. <https://www.aceee.org/topic/generation>. Last accessed 2021/07/12
7. Institute GR (1998) Distributed power generation : a strategy for a competitive energy industry. Chicago
8. Mithulananthan N, Phu LV (2004) Distributed generator placement in power distribution system using genetic algorithm to reduce losses. *Thammasat Int J Sci Tech* 9(3):55–62
9. Griffin T, Tomsovic K, Secrest D, Law A (2000) Placement of dispersed generations systems for reduced losses. In: Proceedings of the annual Hawaii international conference on system sciences
10. Jasmon GB, Lee LHCC (1991) Distribution network reduction for voltage stability analysis and loadflow calculations. *Int J Electr Power Energy Syst* 13(1):9–13. [https://doi.org/10.1016/0142-0615\(91\)90011-J](https://doi.org/10.1016/0142-0615(91)90011-J)
11. Lee SH, Park JW (2013) Optimal placement and sizing of multiple DGS in a practical distribution system by considering power loss. *IEEE Trans Ind Appl* 49(11):2262–2270. <https://doi.org/10.1109/TIA.2013.2260117>
12. Amanifar O (2011) Optimal distributed generation placement and sizing for loss and THD reduction and voltage profile improvement in distribution systems using particle swarm optimization and sensitivity analysis. In: 16th electrical power distribution conference EPDC
13. Moghaddam MJH, Kalam A, Shi J, Nowdeh SA, Gandoman FH, Ahmadi A (2020) A new model for reconfiguration and distributed generation allocation in distribution network considering power quality indices and network losses. *IEEE Syst J* 14(3):3530–3538. <https://doi.org/10.1109/JSYST.2019.2963036>
14. Merlin A, Back H (1975) Search for a minimal—loss operating spanning tree configuration in urban power distribution systems. In: Proceedings of 5th power systems computation conference Cambridge, UK
15. Srinivasa Rao R, Narasimham SVL, Ramalinga Raju M, Srinivasa Rao A (2011) Optimal network reconfiguration of large-scale distribution system using harmony search algorithm. *IEEE Trans Power Syst* 26(3):1080–1088. <https://doi.org/10.1109/TPWRS.2010.2076839>

16. Rao RS, Ravindra K, Satish K, Narasimham SVL (2013) Power loss minimization in distribution system using network reconfiguration in the presence of distributed generation. *IEEE Trans Power Syst* 28(1):317–325. <https://doi.org/10.1109/TPWRS.2012.2197227>
17. Baran ME, Wu FF (1989) Network reconfiguration in distribution systems for loss reduction and load balancing. *IEEE Trans Power Deliv* 4(2):1401–1407
18. Mahdavi M, Alhelou HH, Hatziaargyriou ND, Al-Hinai A (2021) An efficient mathematical model for distribution system reconfiguration using AMPL. *IEEE Access* 9:79961–79993. <https://doi.org/10.1109/ACCESS.2021.3083688>
19. Tran TT, Truong KH, Vo DN (2020) Stochastic fractal search algorithm for reconfiguration of distribution networks with distributed generations. *Ain Shams Eng J* 11(2):389–407. <https://doi.org/10.1016/j.asej.2019.08.015>
20. Muhammad MA, Mokhlis H, Naidu K, Amin A, Franco JF, Othman M (2020) Distribution network planning enhancement via network reconfiguration and DG integration using dataset approach and water cycle algorithm. *J Mod Power Syst Clean Energy*. 8(1):86–93 (2020). <https://doi.org/10.35833/MPCE.2018.000503>
21. Shojaei F, Rastegar M, Dabbaghjamesh M (2021) Simultaneous placement of tie-lines and distributed generations to optimize distribution system post-outage operations and minimize energy losses. *CSEE J Power Energy Syst* 7(2):318–328. <https://doi.org/10.17775/CSEEJPES.2019.03220>
22. Wang C, Nehrir MH (2004) Analytical approaches for optimal placement of distributed generation sources in power systems. *IEEE Trans Power Syst* 19(4):2068–2076. <https://doi.org/10.1109/TPWRS.2004.836189>
23. Acharya N, Mahat P, Mithulananthan N (2006) An analytical approach for DG allocation in primary distribution network. *Int J Electr Power Energy Syst* 28(10):669–678. <https://doi.org/10.1016/j.ijepes.2006.02.013>
24. Gözel T, Hocaoglu MH (2009) An analytical method for the sizing and siting of distributed generators in radial systems. *Electr Power Syst Res* 79(6):912–918. <https://doi.org/10.1016/j.epr.2008.12.007>
25. Hung DQ, Mithulananthan N, Bansal RC (2010) Analytical expressions for DG allocation in primary distribution networks. *IEEE Trans Energy Convers* 25(3):814–820. <https://doi.org/10.1109/TEC.2010.2044414>
26. Ghosh S, Das D (1999) Method for load-flow solution of radial distribution networks. *IEE Proc Gener Transm Distrib* 146(6):641–646. <https://doi.org/10.1049/ip-gtd:19990464>
27. Lee Willis H (2004) Power distribution planning reference book, 2nd edn. CRC Press, Boca Raton

Bi-q MSZSI Topology for Grid-Tied Inverter Under Ideal Grid Conditions



Anish Tiwari  and Anandita Chowdhury

Abstract This article investigates the Bidirectional aspect of quasi-modified switched Z-source inverter (Bi-q MSZSI) topology. The paper compares conventional bidirectional quasi-Z-source (Bi-q ZSI) inverter with Bi-q MSZSI highlighting the need for power exchange between grid and the batteries under balanced conditions to perform UPF and grid support operation.

Keywords Bidirectional quasi-modified switched Z-source inverter (Bi-q MSZSI) · Bidirectional quasi-Z-source inverter (Bi-q ZSI) · Voltage source converter (VSC) · Shoot-through · Duty ratio (D) · Boost factor (B) · Unity power factor (UPF)

1 Introduction

Bidirectional inverters have the potential to exchange power between the grid and the batteries. They are part of the essential link for power exchange for drive applications and grid support functionality. As per [1], the quasi-Z-source inverter (q ZSI) can handle fluctuations in load and grid voltages efficiently but has power limitations due to the wide range of discontinuous modes during battery discharging. As per [2], the use of quasi-Z-source inverters in PV systems has become quite popular, but due to some critical issues like current ripples, the author has proposed a new quasi-Z-source converter. The advantages of a quasi-Z-source include eliminating the need for extra filtering capacitors, low rating components, and reduced switching ripples. Upon comparison, Bi-q MZSIZI has a higher voltage gain, constant DC link voltage, and a lower duty cycle range with all the advantages mentioned above. In conjunction to grid integration [3, 4] the quasi-Z-source inverter is capable of

A. Tiwari (✉) · A. Chowdhury
Sardar Vallabhbhai National Institute of Technology, Surat, Gujarat 395007, India
e-mail: anishtiwari283@gmail.com

A. Chowdhury
e-mail: ac@eed.svnit.ac.in

providing auxiliary services such as power quality and load peak demand control for which dedicated expensive equipment was used earlier [5, 6]. In [7], bidirectional Z-source is implemented on PV-DG hybrid energy storage system. The author has developed a control scheme based on voltage regulation to ensure maximum power point tracking through extensive simulation to validate and evaluate the results. In [8], the need for multiple power exchange highlights for microgrid structure since the different types of loads joined to both AC and DC buses. The presence of an intermediate stage during the conversion process reduces the overall efficiency, and therefore, a bidirectional Z-source becomes a potential replacement for the task. In [9], author presents a dual-loop controller for bidirectional Z-source inverter. This control is applicable for both traction motor drive using indirect field-oriented control and grid interface inverters for regenerative braking and battery charging operations, respectively. The article [10] talks about ultracapacitor-based hybrid energy storage systems for electrical vehicles. This article uses bidirectional Z-source topology leading to better performance and low cost. Similar to above, in [11], author designed HESS based on bidirectional topology resulting in the elimination of battery converter, improving overall performance, and reducing cost. In [12], analysis of bidirectional Z-source breaker for microgrid application is presented. Here, use of LC network is to generate the commutation conditions. Z-source components offer filtering characteristics when connected in series with a power electronics converter. In [13], a sub-module constructed by combining bidirectional quasi-Z-source and half-bridge converter replaces traditional modular multilevel DC–DC converter. The bidirectional quasi-Z-source can make the input voltage of the half-bridge sub-module controllable and then solve the over-current issue of the traditional MMDDC in charge mode.

In this article, UPF and grid support features are examined for Bi-q MSZSI and compared with conventional Bi-q ZSI during balanced operation. From the above literature review, the proposed article can contribute as

1. Bi-q MSZSI provides constant DC link with reduced duty ratio ensuring more margin for modulation index. Modifications do not affect the boost factor even for bidirectional topology.
2. The topology can exchange surplus active power between the battery and the grid and meet the reactive power demand by the load during grid support.

Section 2 discusses the application-specific topological structure of Bi-q ZSI and Bi-q MSZSI for balanced grid-tied inverters applications. Section 3 shows the mathematical analysis needed to calculate the exact amount of power to be exchanged by the configuration. Section 4 gives a detailed description of the control methodology for both the Bi-q ZSI and Bi-MSZSI configurations. Section 5 discusses the simulation aspect and the results obtained. At last, a conclusion from the observations is made and references to support the above.

2 Bidirectional Z-Source Inverter Configuration

In Fig. 1, bidirectional quasi-Z-source (Bi-q ZSI) inverters replace conventional diode-switch arrangement with bidirectional switches. A major advantage of quasi-arrangement, as mentioned earlier, is reduced voltage stress on components with the ability to handle large load fluctuations.

Figure 2 provides a high gain value with a lower duty range compared to conventional Bi-q ZSI [15]. This topology has the advantage of a reduced number of components compared with typical hybrid Z-source topology for a high gain Z-source network, but in any case, the DC link is not constant.

Figure 3 of Bi-q MSZSI configuration has high gain, lower voltage stress, and components rating, lower duty range between $0 > D > 0.25$, and constant DC link with potential to exchange power between batteries and grid when desired by the network operator. The basic modified-SZSN structure [16] incorporates all the existing advantages of a quasi-Z-source network but with high gain at reduced duty values.

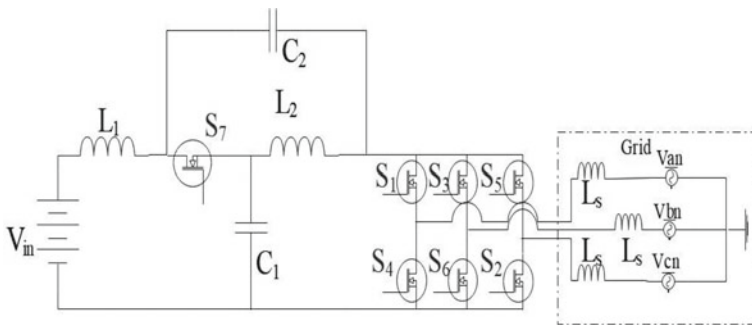


Fig. 1 Bi-q ZSI configuration for DC–AC inverter applications [13, 14]

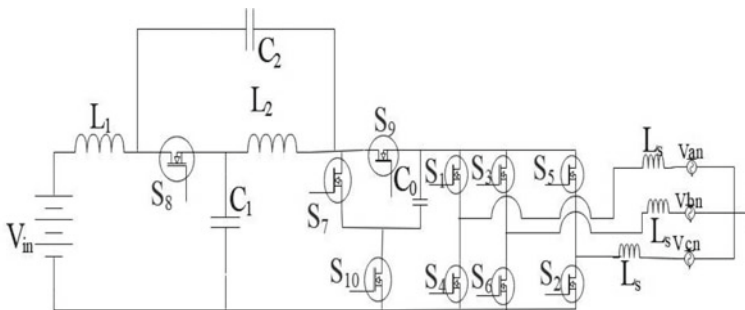


Fig. 2 Bi-q SZSI configuration for DC–AC inverter applications [15]

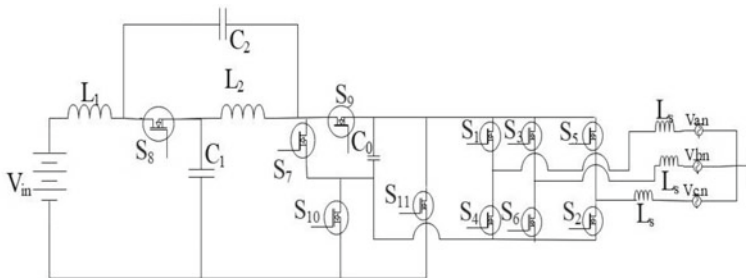


Fig. 3 Bi-q MSZSI configuration for DC–AC inverter applications

3 Mathematical Analysis

For Bi-q ZSI considering 415 V, three phases 50 Hz supply the following equations used for calculations

$$\widehat{V}_{ac} = M * B * \frac{V_i}{2} \quad (1)$$

Let us assume the duty ratio to be $D = 0.25$, $M = (1 - D) = 0.75$, then for this case, the maximum boost factor that Bi-q ZSI could provide would be

$$B = \frac{1}{1 - 2 * 0.25} = 2 \quad (2)$$

$$V_i = \frac{2 * \widehat{V}_{ac}}{M * B} = 452 \text{ V} \quad (3)$$

$$V_{dcLink} = B * V_i = 904 \text{ V} \quad (4)$$

The reference capacitor voltage is twice the peak RMS value of the desired AC output voltage. Reference current calculation, Eqs. 5 and 6, is expressed as under

$$i_d^* = \frac{2}{3} * \left(\frac{V_d * P^* - V_q * Q^*}{V_d^2 + V_q^2} \right) \quad (5)$$

$$i_q^* = \frac{2}{3} * \left(\frac{V_d * Q^* + V_q * P^*}{V_d^2 + V_q^2} \right) \quad (6)$$

From the above expressions, for active power exchange of 8 kW under unity power factor (UPF), operation desire directs axis current component of amplitude $I_d = 15.732 \text{ A}$, whereas for grid support of 6 k VAR leading and lagging reactive power exchange for ancillary services requires quadrature axis current component of amplitude $I_q = 11.7 \text{ A}$.

3.1 Calculations for Bi-q MSZI Configuration

Equation 5 shows the DC link calculation for Bi-q MSZSI configuration.

$$V_{dcLink} = \frac{V_i}{1 - 4 * D} \tag{7}$$

The duty ratio D is significantly reduced to about $D = 0.1$, enabling more margin for the modulation index. Equation 6 shows input battery voltage for grid integration.

$$V_i = (1 - 4 * 0.1) * 753.33 = 452 \text{ V} \tag{8}$$

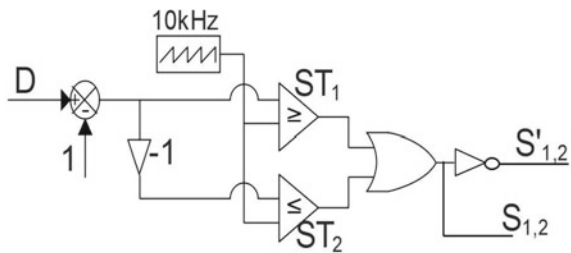
The expression for reference capacitor voltage for closed-loop operation in Bi-q MSZSI can calculate as under

$$V_C = V_i * \frac{1 - 2 * D}{1 - 4 * D} = 452 * \frac{1 - 2 * 0.1}{1 - 4 * 0.1} = 602.67 \text{ V} \tag{9}$$

4 Control Methodology

In the control methodology shown in Fig. 4, shoot-through pulses are provided directly to bidirectional IGBT switches, and negation of those switching pulses provides to other IGBT switches. The arrangement is can easily exchange active, reactive power from the grid to the battery and vice versa. A complex control circuit requires for the safe and smooth functioning of switches for the bidirectional inverter.

Fig. 4 Control scheme of Bi-q ZSI/Bi-q MSZSI for DC-AC application



5 Simulation Results

The following are the Simulink results for bidirectional quasi-Z-source configurations for active and reactive power exchange between grid and the battery (Table 1).

5.1 Simulation of Bi-q ZSI Configuration

The duty range of conventional Bi-q ZSI varies from $0 > D > 0.5$. For the double boost value of the battery, it requires a duty value of only $D = 0.25$, but the DC link is not constant evident from Fig. 5. The overall configuration is working in a continuous current (CCM) mode of operation. Significant reduction of voltage stress across the capacitors compared to basic Z-source is evident, resulting in low rating passive components. Upon observation, it is also clear that input inductor switching ripples are less compared to basic X-shaped Z-source network.

Table 1 MATLAB Simulink parameter values for Bi-q MSZSI/Bi-q ZSI

S. No.	Parameter	Value
1	L_1, L_2	5 mH
2	C_1, C_2	470 μ F
3	C_0	1000 μ F
4	V_{in}	452 V
5	D	0.25/0.1
6	f_s	10 kHz

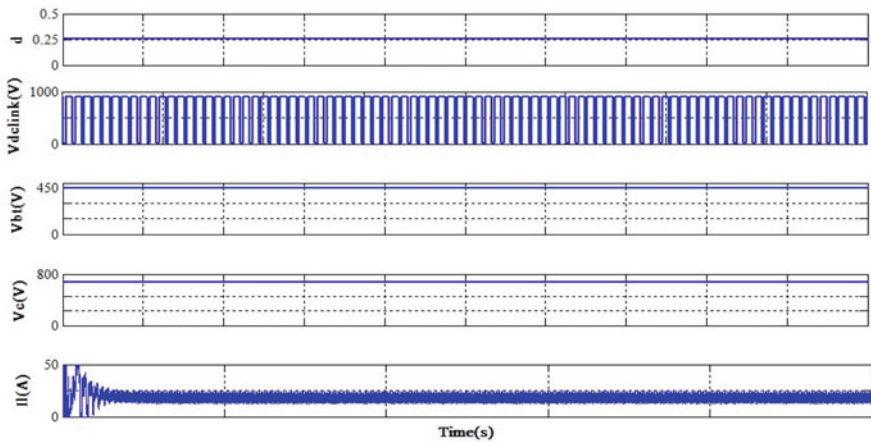


Fig. 5 DC side simulation results of Bi-q ZSI

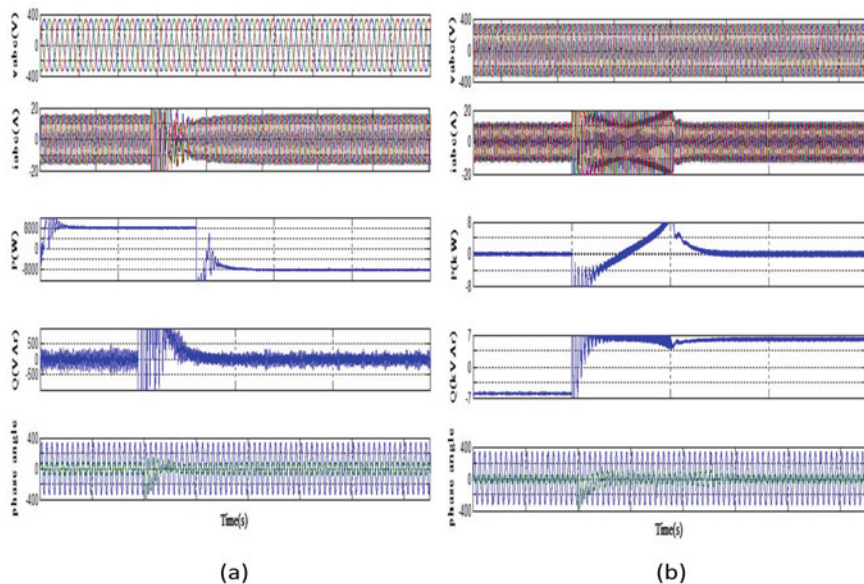


Fig. 6 Simulation results of Bi-q ZSI configuration **a** active power variations UPF operation, **b** reactive power exchange grid support feature

In Fig. 6a, step-change in direct axis component of current from positive to a negative value shown by in-phase voltage and current suggests unity power factor operation during which only the active power exchanged. After the step-change, battery voltage and current are out-of-phase suggesting surplus power storage from the grid. The total active power exchange between the grid and the battery is 8 kW.

Similarly, in Fig. 6b, step-change was observed in the quadrature axis current component. For grid support, leading capacitive current observed before the change will inject leading reactive power to support voltage sag at the nodes. Inductive lagging current will suppress voltage swell at the nodes. Total reactive power exchanged between the inverter and the grid is 6 kVAR.

5.2 Simulation of Bi-q MSZSI Configuration

Figure 7 shows that to achieve the same boost value from Bi-q MSZSI, the duty ratio value required is relatively less $D = 0.1$. The DC link observed from the simulation result is constant to about 753 V. In closed-loop operation, the PI controllers can track the reference capacitor voltage $V_c = 602.67$ V. The change in input inductor current from positive to a negative value is a mere indication of power exchange between the battery and the grid.

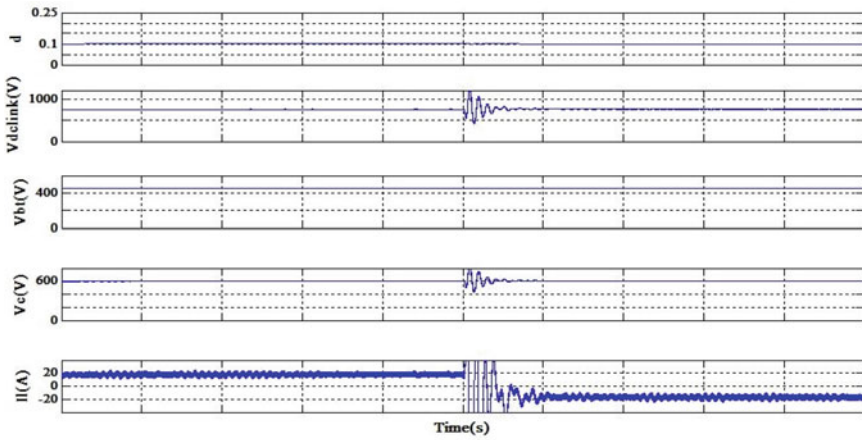


Fig. 7 DC side simulation results of Bi-q MSZSI

Figure 8a shows UPF operation of Bi-q MSZSI. The active power is varied from positive to negative 8 kW suggested by in-phase voltage and current followed by out-of-phase voltage and current. During positive to negative transition, the battery feeds active power to the grid, latter the surplus power gets stored in the battery.

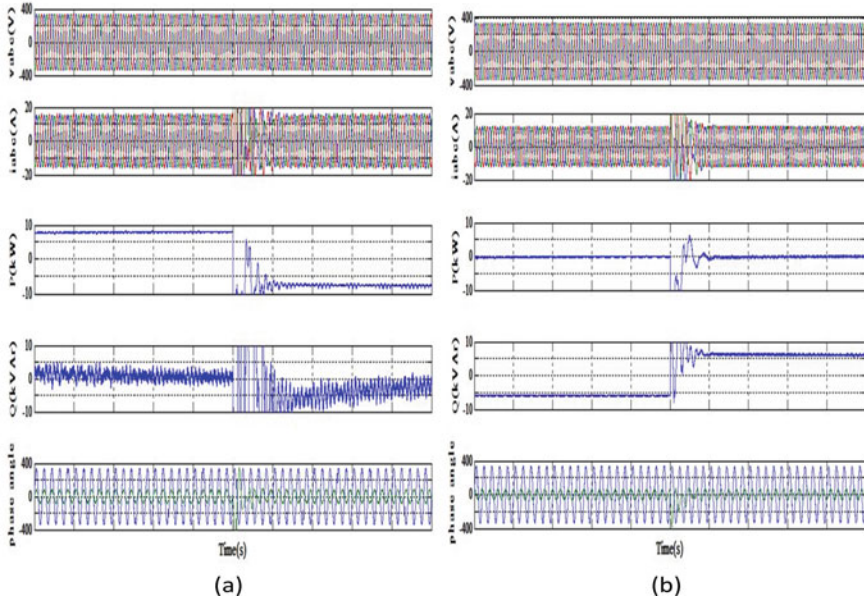


Fig. 8 Simulation results of Bi-q MSZSI configuration a active power variations UPF operation, b reactive power exchange grid support feature

Figure 8b shows reactive power exchange of Bi-q MSZSI. The step-change of 6 kVAr takes place from leading capacitive current to lagging inductive current. The battery before the change will provide reactive power for the grid support and absorb excess reactive power afterward.

6 Conclusion

From the above discussion, we may conclude that similar to Bi-q ZSI, Bi-q MSZSI can exchange power between the grid and the battery. From the analysis, Bi-q MSZSI can be well suited for various applications such as hybrid microgrid power exchange, electric vehicle regenerative braking, and renewable energy system integration for energy storage.

References

1. Ge B, Abu-Rub H, Peng FZ, Lei Q, De Almeida AT, Ferreira FJTE, Sun D, Liu Y (2012) An energy-stored quasi-z-source inverter for application to photovoltaic power system. *IEEE Trans Ind Electron* 60(10):4468–4481
2. Honarbari S, Alizadeh Bidgoli M (2020) Designing a quasi-z-source inverter with energy storage to improve grid power quality. *IETE J Res*:1–9
3. Rabkowski J (2007) The bidirectional z-source inverter as an energy storage/grid interface. In: *EUROCON 2007—the international conference on “computer as a tool”*. IEEE, pp 1629–1635
4. Vasquez JC, Mastromauro RA, Guerrero JM, Liserre M (2009) Voltage support provided by a droop-controlled multifunctional inverter. *IEEE Trans Ind Electron* 56(11):4510–4519
5. Lo Y-K, Lee T-P, Wu K-H (2008) Grid-connected photovoltaic system with power factor correction. *IEEE Trans Ind Electron* 55(5):2224–2227
6. Mastromauro RA, Liserre M, Kerekes T, Dell’Aquila A (2008) A single-phase voltage-controlled grid-connected photovoltaic system with power quality conditioner functionality. *IEEE Trans Ind Electron* 56(11):4436–4444
7. Belila A, Berkouk E-M, Benbouzid M, Amirat Y, Tabbache B, Mamoune A (2020) Control methodology and implementation of a z-source inverter for a stand-alone photovoltaic-diesel generator-energy storage system microgrid. *Electric Power Syst Res* 185:106385
8. Vigneys T, Kumarappan N (2016) Operation and control of hybrid microgrid using z-source converter in grid tied mode. In: *2016 2nd international conference on applied and theoretical computing and communication technology (iCATccT)*. IEEE, pp 318–323
9. Ellabban O, Mierlo JV, Lataire P (2010) Control of a bidirectional z-source inverter for hybrid electric vehicles in motoring, regenerative braking and grid interface operations. In: *2010 IEEE electrical power & energy conference*. IEEE, pp 1–6
10. Hu S, Liang Z, He X (2015) Ultracapacitor-battery hybrid energy storage system based on the asymmetric bidirectional z-source topology for EV. *IEEE Trans Power Electron* 31(11):7489–7498
11. Omeran KC, Mosallanejad A (2018) Smes/battery hybrid energy storage system based on bidirectional z-source inverter for electric vehicles. *IET Electr Syst Transp* 8(4):215–220
12. Savaliya SG, Fernandes BG (2019) Analysis and experimental validation of bidirectional z-source dc circuit breakers. *IEEE Trans Ind Electron* 67(6):4613–4622
13. Bi K, Liu Y, Zhu Y, Fan Q (2021) An impedance source modular dc/dc converter for energy storage system: analysis and design. *Int J Electr Power Energy Syst* 133:107261

14. Guo F, Fu L, Lin C-H, Li C, Choi W, Wang J (2013) Development of an 85-kw bidirectional quasi-z-source inverter with dc-link feed-forward compensation for electric vehicle applications. *IEEE Trans Power Electron* 28(12):5477–5488
15. Liu J, Wu J, Qiu J, Zeng J (2019) Switched z-source/quasi-z-source dc–dc converters with reduced passive components for photovoltaic systems. *IEEE Access* 7:40893–40903
16. Tiwari A, Chowdhury A (2021) Modified switched z-source topology for inverter applications. In: *Proceedings of symposium on power electronic and renewable energy systems control*. Springer, pp 31–41

ASIC Implementation of a 16-Bit Brent–Kung Adder at 45 nm Technology Node



Anmol Saxena, Vyom Saraf , and Rutu Parekh 

Abstract This paper implements a Brent–Kung adder design from register-transfer level (RTL) to Graphic Database System Information Interchange (GDSII), using Cadence Genus and Innovus tools. Brent–Kung Adder is selected with a 16-bit word size as it is considered suitable for very large-scale integration (VLSI) implementation out of the other parallel prefix adder implementation. It is provided with scan chain flip-flops which cover the overall design. This design has been implemented at 180 and 45 nm technology nodes. The design was optimized as per trade-offs between area, delay, and power. The power dissipation observed for 45 nm is $26.7 \mu\text{W}$, 0.03 ns critical path delay with $413.136 \mu\text{m}^2$ area taken up. It adheres to scalability by providing better performance metrics at 45 nm than the 180 nm technology node. For this particular implementation, the main highlight is the power consumption and the speed of the implementation, as we have illustrated below via comparison with other works through tabular means.

Keywords RTL-to-GDSII · Brent–Kung adder · Parallel prefix adders · Physical design · Simulation · Synthesis

1 Introduction

Adders as versatile, they are, they have an almost innumerable number of supporting topologies based on user and designer requirements [1, 2]. Here, the focus is on adders that are compatible with CMOS technology and are scalable. The half-adder (HA) and full-adder (FA) blocks are fundamental building blocks for various logical implementations and are very useful for, e.g., a suitable FA implementation [1] for CMOS technology using transmission gate logic (see Fig. 1a). It could be further delay optimized by forking the inputs at the terminals.

A. Saxena · V. Saraf (✉) · R. Parekh

VLSI and Embedded Systems Group, Dhirubhai Ambani Institute of Information and Communication Technology, Gandhinagar, Gujarat, India
e-mail: 201801062@daiict.ac.in

© The Author(s), under exclusive license to Springer Nature Singapore Pte Ltd. 2022
V. Mahajan et al. (eds.), *Sustainable Technology and Advanced Computing in Electrical Engineering*, Lecture Notes in Electrical Engineering 939,
https://doi.org/10.1007/978-981-19-4364-5_8

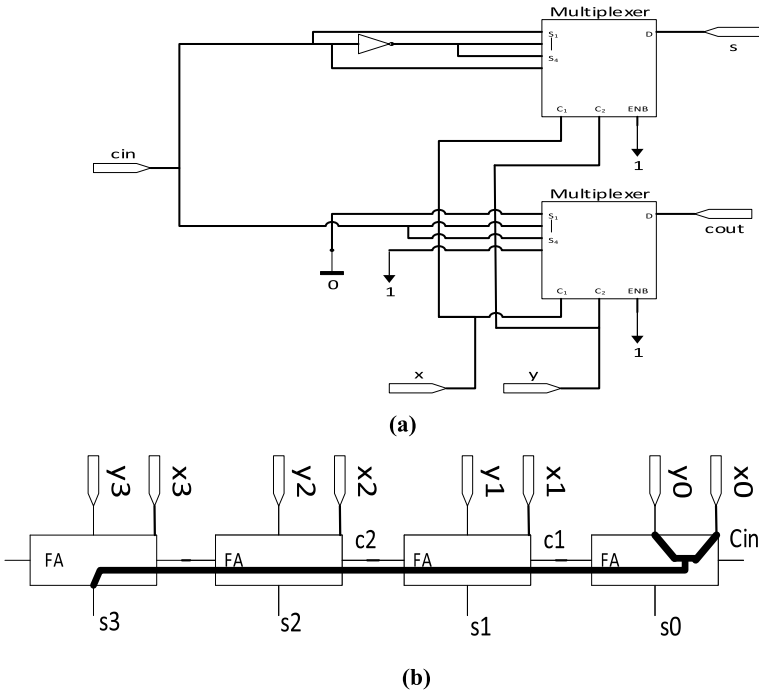


Fig. 1 Adder schematics **a** full-adder implementation suitable for CMOS. **b** Critical path for the ripple carry adder illustrated

Equation (1) denoting the sum (s) and carry-out (c_{out}), based on the inputs (x , y and carry-in, c_{in}) are as follows:

$$s = x \oplus y \oplus z \quad \text{and} \quad c = xy \vee xc_{in} \vee yc_{in} \tag{1}$$

A ripple carry adder (RCA) incorporates the FAs. This leads to a direct CMOS implementation [1, 3] where the first row constitutes 7-inverters each block-wise, and the row below comprises the 4:1 multiplexers. An n -bit ripple carry binary adder requires n FAs, with the carry-out of the i th FA connected to the carry-in input of the $(i + 1)$ th FA. The resulting n -bit adder produces an n -bit sum output and a carry-out; alternatively, C_{out} can be viewed as the most significant bit of an $(n + 1)$ -bit sum. The critical path usually starts from the x_0 and y_0 ports to the output sum port s_3 , (see Fig. 1b).

The initial port could have been c_{in} , and the destination port could have been c_{out} , but FAs are usually designed to reduce latency between their input and sum-out ports. Thus, the proposed path holds up.

Therefore, for a 4-bit RCA, the latency comes out to be:

$$T_{\text{ripple-add}} = T_{\text{FA}}(x, y \rightarrow c_{out})$$

$$+ 2 \times T_{\text{FA}}(c_{\text{in}} \rightarrow c_{\text{out}}) + T_{\text{FA}}(c_{\text{in}} \rightarrow s) \quad (2)$$

Furthermore, generalizing (3) for an n -bit RCA gives:

$$\begin{aligned} T_{\text{ripple-add}} &= T_{\text{FA}}(x, y \rightarrow c_{\text{out}}) + (n - 2) \\ &\quad \times T_{\text{FA}}(c_{\text{in}} \rightarrow c_{\text{out}}) + T_{\text{FA}}(c_{\text{in}} \rightarrow s) \end{aligned} \quad (3)$$

The delay increases linearly with n as n increases. Thus, RCA design is of time-complexity $O(n)$. Therefore, it is unfit for large input word-width. The carry computation network is a significant source of complexity and costs in designing adders [1]. A carry chain's length is the number of digit positions from where the carry is generated up to and including where it is finally absorbed or annihilated. A carry chain of length 0 thus means 'no carry production'. There is interest in the length of the longest propagation chain, which dictates the adder's latency. The expected length of the worst-case carry chain in an n -bit addition with random operands is upper-bounded by $\log_2 n$. Experimental results verify the $\log_2 n$ approximation to the length of the worst-case carry chain and suggest that $\log_2(1.25n)$ is a better estimate [1]. A carry-completion detection adder takes advantage of the $\log_2 n$ average length of the longest carry chain to add two n -bit binary numbers in $O(\log n)$ time on the average. It is essentially a ripple carry adder in which a carry of 0 is also explicitly represented and allowed to propagate between stages. Because the latency of the carry-completion adder is data dependent, the design is suitable for use in asynchronous systems. However, most modern computers use synchronous logic and thus cannot take advantage of the high average speed of a carry-completion adder. The reader is encouraged to refer to [1, 2] for appropriate coverage for more details regarding the carry-completion detection adder. For two operands, the key to fast addition is a low-latency carry network; since once the carry into position i is known, the sum digit can be determined from the operand digits x_i and y_i and the incoming carry c_i in constant time through modular addition:

$$s_i = (x_i + y_i + c_i) \bmod r \quad (4)$$

For radix-2, this is represented as:

$$s_i = x_i \oplus y_i \oplus c_i \quad (5)$$

From the point of view of carry propagation and the design of a carry network, the actual operand digits are not significant. What matters is whether a carry is generated, propagated, or annihilated (absorbed). In the case of binary addition, generate (g_i), propagate (p_i), and annihilate (absorb) (a_i) signals are characterized by the following logic equations:

$$g_i = x_i y_i \quad \text{and} \quad p_i = x_i \oplus y_i \quad \text{and} \quad a_i = x'_i y'_i \quad (6)$$

Similarly, a transfer signal (t_i) can be defined as the event that carry-out is 1 when carry-in is 1.

$$t_i = a'_i \quad (7)$$

Conceptually, the concept translates in this manner mathematically,

$$g_i = 1 \text{ iff } x_i + y_i \geq 2 \quad \text{and} \quad p_i = 1 \text{ iff } x_i + y_i = 1 \quad \text{and} \quad a_i = 1 \text{ iff } x_i + y_i < 1 \quad (8)$$

A carry network design can be generated using the above signals without using operands directly, irrespective of the radix. The carry recurrence is thus defined [see Eq. (9)]. If the carry is generated in stage i or it enters stage i and is propagated by that stage, it will enter stage $i + 1$.

The equation for carry recurrence is as follows:

$$c_{i+1} = g_i \vee c_i p_i \quad (9)$$

In most cases, p_i can be replaced by t_i if desired.

A Manchester carry chain utilizes the carry recurrence equation. For modern CMOS technology, the delay is roughly proportional to ' k^2 ' (as ' k ' pass transistors are connected in series), making it unsuitable for word-width above 8-bit. An adder design can be viewed in the generic form (see Fig. 2a) by taking advantage of generating and propagating signals defined in this section.

If the carry recurrence is unrolled, it becomes a simplified decoupled problem in implementation terms.

The unrolling is demonstrated below:

$$\begin{aligned} c_i &= g_{i-1} \vee c_{i-1} p_{i-1} \\ &= g_{i-1} \vee (g_{i-2} \vee c_{i-2} p_{i-2}) p_{i-1} \\ &= g_{i-1} \vee g_{i-2} p_{i-1} \vee c_{i-2} p_{i-2} p_{i-1} \\ &= g_{i-1} \vee g_{i-2} p_{i-1} \vee g_{i-3} p_{i-2} p_{i-1} \vee c_{i-3} p_{i-3} p_{i-2} p_{i-1} \end{aligned} \quad (10)$$

The process of unrolling goes on until c_{in} is arrived. After full unrolling, all the carries in an n -bit adder can be computed directly from the auxiliary signals (g_i, p_i) and c_{in} , using two-level AND-OR logic circuits with maximum gate fan-in of $n + 1$. Such an adder is said to have a full carry look ahead. However, as can be seen from the gate fan-in, such an adder is unsuitable for wide word length operands. This is remedied by using block generate and propagate signals but is still limited by the block size considerations, which is also a fan-in problem. Therefore, to tackle the problem of width-size of blocks, a carry operator \otimes is introduced. The carry operator \otimes can be defined (see Fig. 2b) as follows:

$$g = g'' \vee g' p'' \quad \text{and} \quad p = p' p'' \quad (11)$$

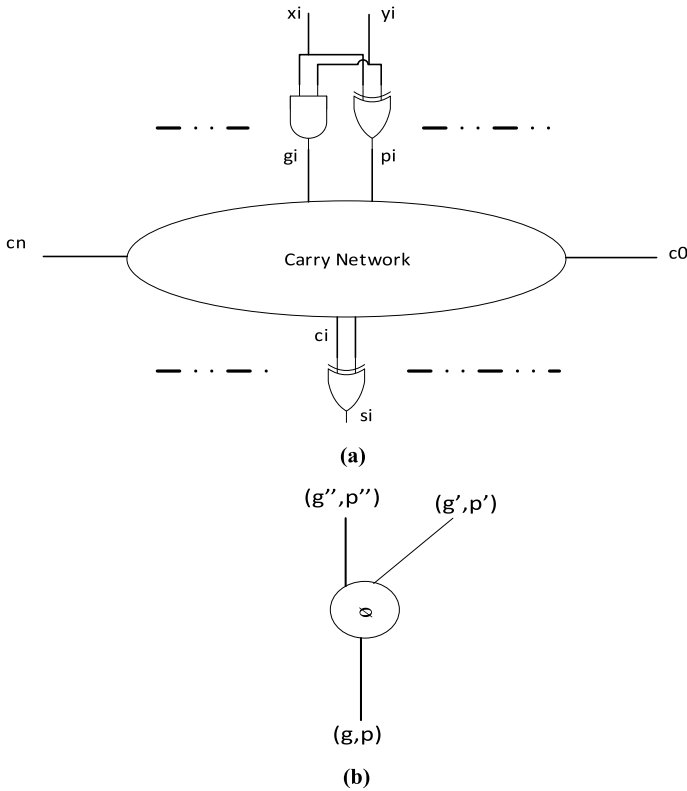


Fig. 2 **a** Block-level implementation for tree-based carry computation-intensive adders. **b** Demonstrating the \mathcal{Q} operation

Carry generation occurs if the left group generates a carry or generates a carry and the left one propagates it, while propagation occurs if both groups propagate the carry. This operator is associative but not commutative. Therefore, parallel prefix problems come into frame, which for the sum could be illustrated as follows where the variables are operands (Table 1).

The parallel prefix carry computation problem is obtained by replacing $+$ with \mathcal{Q} , and operands with (g, p) pairs. Based on this, Brent and Kung proposed a divide and conquer strategy, where the inputs are first combined pairwise to obtain a sequence of length $n/2$:

$$x_0 + x_1 \quad x_2 + x_3 \quad x_4 + x_5 \quad x_6 + x_7 \dots x_{n-2} + x_{n-1}$$

Table 1 Parallel prefix sums problem

Given	x_0	x_1	x_2
Find	x_0	$x_0 + x_1$	$x_0 + x_1 + x_2$

where j is the index for the sum-bit and input-bit being accessed (s_j, x_j).

Parallel prefix sum computation on this new sequence yields the odd-indexed prefix sums $s_1, s_3, s_5 \dots$ for the original sequence. Even-indexed prefix sums are then computed by using

$$s_{2j} = s_{2j-1} + x_{2j} \tag{12}$$

An n -input Brent–Kung parallel prefix graph will generally have a delay of $2 \log_2 n - 2$ levels and a cost of $2n - 2 - \log_2 n$ cells. It is better than Ladner–Fischer and Kogge–Stone adders due to better cell utilization and wiring congestion handling properties [4, 5]. In devising their design, Brent and Kung were motivated by reducing the chip area in the carry network’s very large-scale integration (VLSI) layout [5]. This model is used in conjunction with other models to yield hybrid solutions, meeting user requirements. Although advanced adder configurations are beyond the scope of this paper, they are mentioned in the ongoing work on this adder as it is modified and improved upon.

Let the inputs be $A = 16'hFFAB$ and $B = 16'hEF82$, and carry-in as $1'b1$. The following 2-bit vector pattern is calculated parallel allocated to black and gray cells as per-prefix generation logic where the black cells output a 2-bit vector and the gray cells, a 1-bit vector. Black cells determine the Propagate and Generate signals of the bits. The gray cell’s output is the group generating a signal used to calculate the carry of that stage. As can be seen, the verified output comes out to be $16'hEF2E$ and carry-out as $1'b1$ (see Fig. 3). Carry select adders are one of the fastest adders keeping area and delay as trade-offs [6]. A 16-bit carry select adder using Brent–Kung adder has less chip area with slightly more delay, and it is a more efficient high-speed adder among other architectures of CSLAs [7]. In [8], 16-bit regular linear Brent–Kung CSA, modified linear BK CSA, regular square root (SQRT) BK CSA, and modified

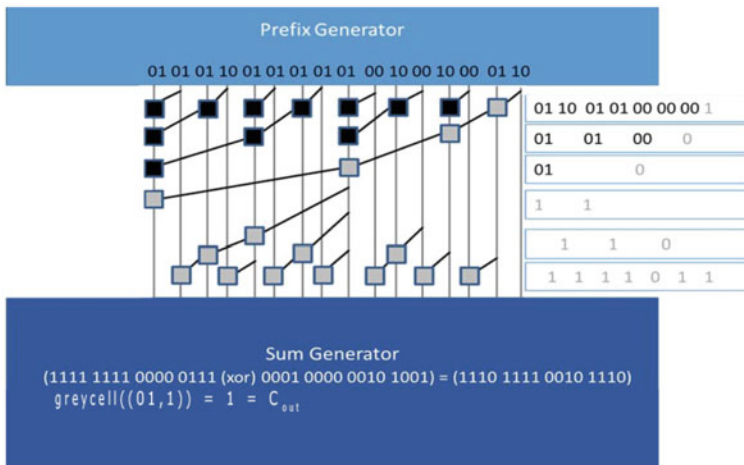


Fig. 3 Illustrating the 16-bit Brent–Kung adder in action

SQRT BK CSA are designed. The power and delay of all these adder architectures are calculated at different supply voltages from 0.6 to 1.4 V. The range of power consumption for the same is in the range (0.01–1 μ W). The optimal performance is observed around 1.2 V.

The results show that modified SQRT BK CSA is better than all other adder architectures in power but with a minor speed penalty [8]. Work in [9] validates findings in [8]. Although papers discuss improvement in design [10], there is no DFT coverage on the same. Also, although discussed, the process steps are not shown explicitly, i.e., the process to reach the final layout for adder comparisons. The same has been marked in various avenues that RTL-to-GDSII is not a very transparent process, and much needs to be done in making it more accessible for academicians and the general public alike. Thus, there is an effort to make the process as straightforward as possible. As noted in [11], Kogge–Stone adder and Ladner–Fischer adder result in faster implementations, but they are not optimized, keeping fan-in of the design as an optimizing parameter, and hence are not very suitable for VLSI implementations in their raw form [5]. It is to be noted that mixing and matching various architectures and topologies such as the former and Manchester carry and other primitive topologies may yield hybrid adder topologies that outperform the topologies in their native form. This was also noted in NVIDIA GTC 2021, where AI-based algorithms made stage-by-stage predictions to sweep in the cells to create a faster adder configuration. This paper differentiates itself but takes inspiration from [12, 13], by making inter-node observations, rather than comparing different variants of Brent–Kung adder which they have tested, as this is a regular topology, if this is to be put in one type as per [9].

2 Physical Design Flow for the Design

The synthesizable HDL code is written and functionally verified in Vivado through an appropriate test bench in a functional simulator (e.g., iSim) using behavioral simulation before utilizing it for further logical synthesis and physical design process separately in Cadence Genus and Innovus-based design flow and qFlow. The following infographic can summarize the Cadence-based design flow (see Fig. 4), and the following steps (see Fig. 5) are followed to complete the process until sign-off.

2.1 Logical Synthesis Using Genus Synthesis Solution

The RTL code as tested in Vivado HLS and a Synopsys Design Constraints (.sdc) file is written as a Tcl script to define the timing constraints such as clock definitions, and fall time and rise time are provided to the Synthesis solution program.

Here, steps of generic synthesis are done, which firstly provides an RTL schematic as per the Boolean expressions, which the design renders as the netlist. After optimization, it gives a better and more organized schematic which is mapped through

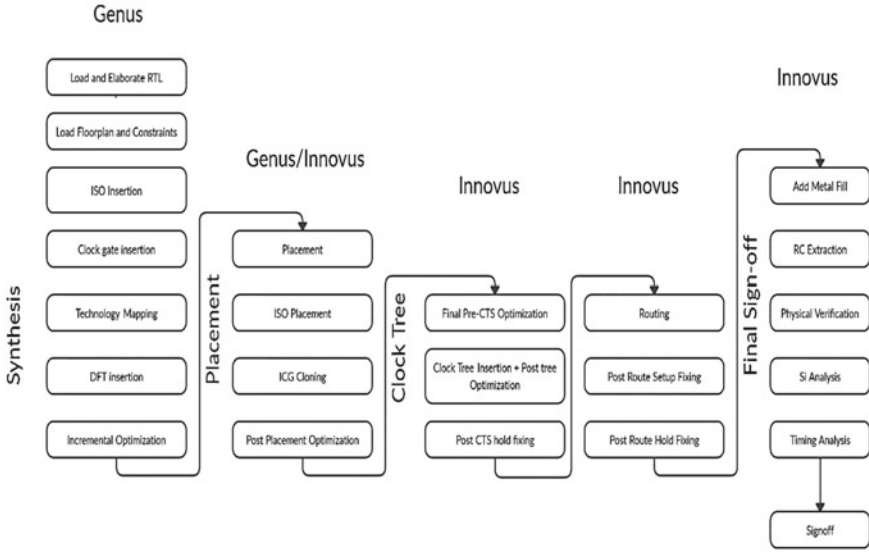


Fig. 4 Cadence EDA-based physical design flowchart

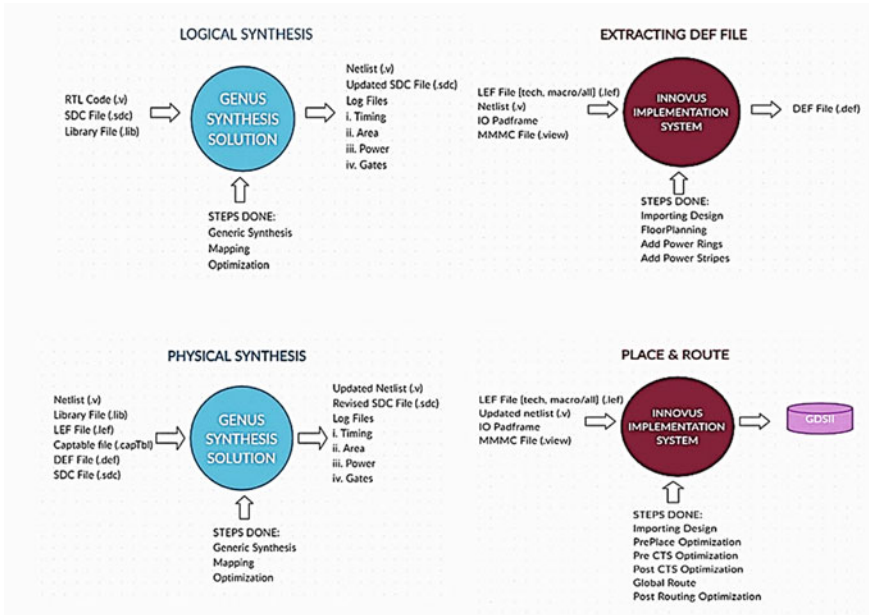


Fig. 5 Cadence EDA-based physical design flow illustrated

the library files. For making the design ‘Design for Testability’, (DFT) compatible, scan chain flip-flops are provided, at each node, at this juncture. The Synthesis solution provides an updated netlist, which incorporates the library issued cells, and the constraints provided in the .sdc file while preserving the logical integrity of the overall module. The SDC file is also updated in accordance with design deployment based on the provided library. Based on the logically synthesized netlist, timing reports, power consumption reports, and gate count reports are obtained.

2.2 Extracting DEF File from Innovus Implementation System

The Design Exchange File (DEF) is obtained by providing the Innovus implementation system with the Library Exchange File (LEF), which consists of all the required macros, library tech files, and the updated netlist. The IO pad-frames information is also provided to ensure a bounding box for the overall module. Then, the multimode multi-corner (MMMC) file is generated by specifying the nature of cells (slow, fast, typical) and RC parameters being used in the design. After importing the design, the floor-planning is done where power rings and power stripes are added to make it well defined before placing the optimally synthesized blocks inside.

2.3 Physical Synthesis Using Genus Synthesis Solution Utilizing DEF File

After having the DEF file, the synthesis steps are taken up again with Genus Synthesis, but this time, the focus is on having physical parameters be translated in the updated netlist as the capability is specified to incorporate the timing aspects of the design with more precision. After going through the synthesis steps, the updated netlist and the revised SDC file are acquired.

2.4 Placing and Routing Using Innovus

The updated netlist is then again provided to the Innovus system, after which the blocks are placed accordingly with optimization. For example, a clock tree in the design could be accommodated to eliminate skews and optimize the design further. After optimally placing the blocks, the component is routed to yield an equivalent physically laid out circuit to the specified logic and then is streamed out in Graphic Design System-II (GDSII) format. The logs generated are a complete source of information regarding the design and could be studied to make changes as required, especially while optimizing the timing through timing reports.

3 Implementation

The overall implementation requires Xilinx Vivado, Cadence Genus, and Innovus in a series of steps, as discussed below. In this implementation, the input and output capture register array (see Fig. 10) is provided to synchronize the adder with a system provided clock and run timing analysis. The prefix network (see Figs. 7 and 8) generates the block level ‘pg’ operands, which are further processed by the black and gray cells (see Fig. 9) to generate row-wise carry, propagating through the stages. The provided register array helps provide a clock path for the system, which can further be constrained through the .sdc file created for the design. If the logical elements are substituted as designed for the Brent–Kung adder algorithm with the connections (see Figs. 3 and 6), the regularity and parallelism of the structure become all so evident. Their logical aid has been discussed in the introduction section, and the reader is advised to correlate the black boxes with their contents by going back. The sum generator block is a simple XOR array (see Fig. 11).

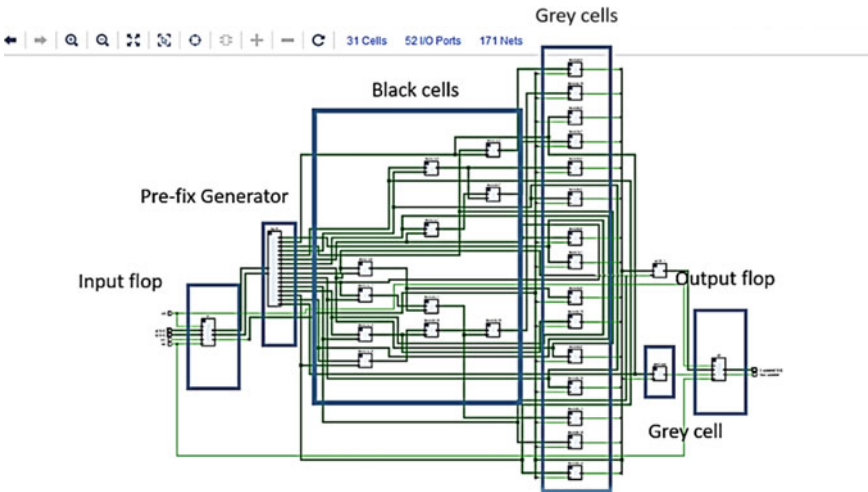


Fig. 6 HDL modules for 16-bit Brent–Kung adder

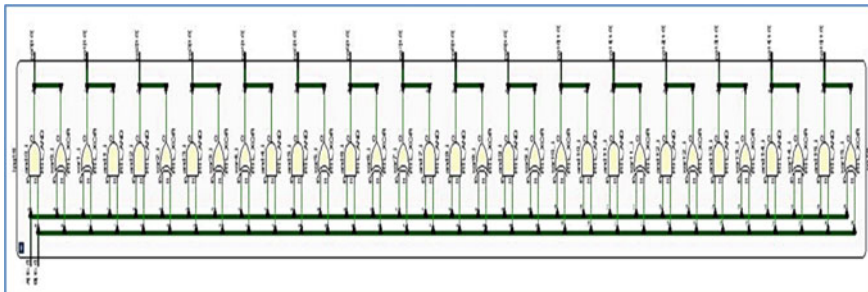


Fig. 7 Prefix generator RTL array

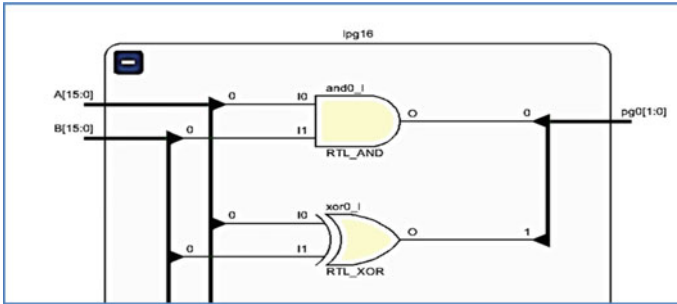
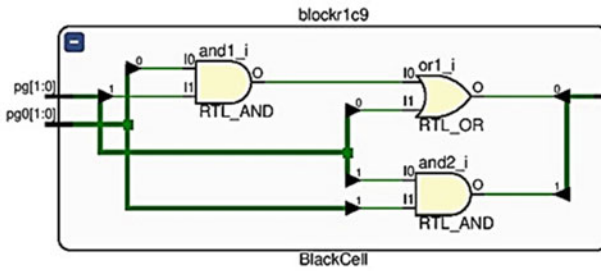
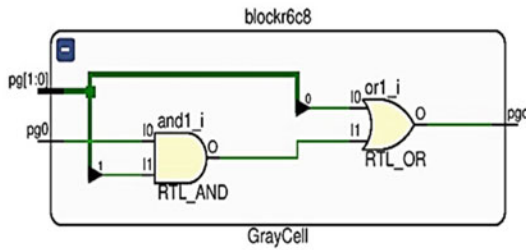


Fig. 8 Exploded view for the prefix generator

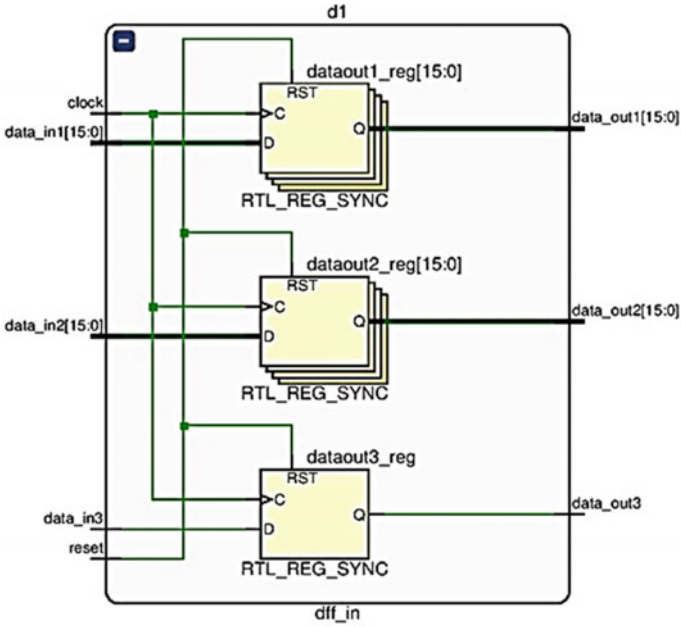


(a)

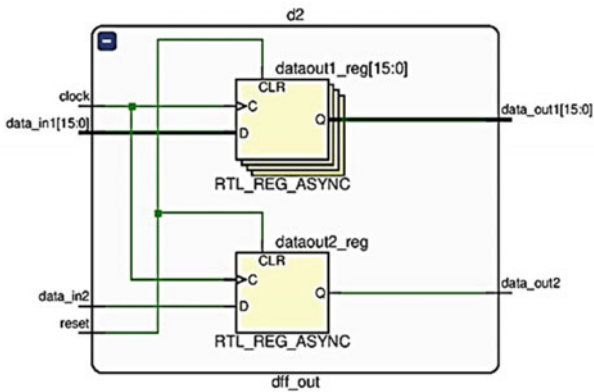


(b)

Fig. 9 Schematics for black and gray cells, the elementary computational elements of the adder. **a** Black cell, **b** gray cell



(a)



(b)

Fig. 10 Schematics for register arrays provided at I/O ports **a** input register array schematic, **b** output register array schematic

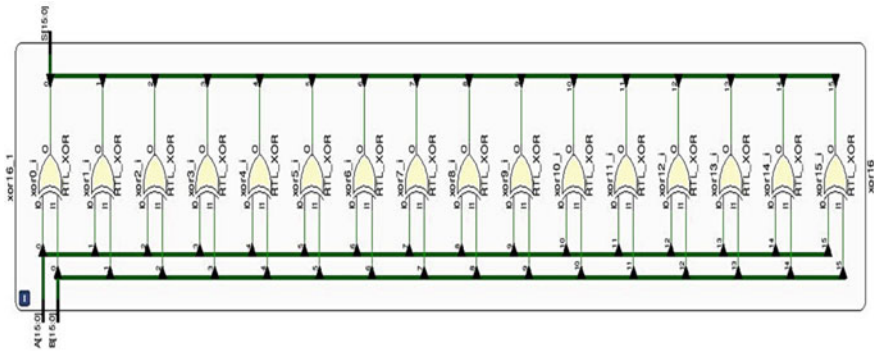


Fig. 11 Sum generator block schematic consisting of XOR array

3.1 Functional Implementation and Verification on Xilinx Vivado

The verification of the above RTL implementation is done by the provided test bench (see Fig. 12), and the behavioral simulation for the same yields favorable outputs (see Fig. 13).

3.2 Logical, Physical Synthesis, and Routing on Cadence EDA

The RTL implementation done on Vivado was for functional verification. After successfully verifying our design, Genus is utilized to do logical synthesis, and we observe a regular arrangement of cells, as DFT insertion is performed (see Fig. 14).

Hundred percentage coverage is achieved in scan chain flop insertion. Also, the synthesis notes the structural regularity and can be noticed right away after path optimization. Metal-layer 10 and 11 utilized (see Fig. 15a) and metal-layer 5 and 6 utilized (see Fig. 15b), for V_{DD} and V_{SS} , respectively, for power-stripes allocation. Similarly, the placement (see Fig. 16) and optimal routing (see Fig. 17b), for the 180 nm node are implemented. The cells are accommodated in the provided area (see Fig. 17a), not yet placed without the power stripes (see Fig. 16c).

The aspect which makes the routing an exciting part of this particular design is that the regularity and hierarchy of the Brent–Kung adder which led to a clean final layout. Cadence EDA gives us much flexibility in determining the parameters such as spacing between metal layers, the density of the lines, the grouping of the lines, and utilization of PVT corners for exhaustive experimental studies on the design and, thus, helps determine its feasibility in various use cases. The various use cases are low power, or where power is not a concern, but speed is, among many others.

Fig. 12 Test bench initialization and inputs provided **a** initialization of test bench fixture. **b** inputs for the DUT

```
module tb;

    // Inputs
    reg [15:0] a;
    reg [15:0] b;
    reg cin;
    reg clk;
    reg rst;

    // Outputs
    wire [15:0] S_updated;
    wire Cout_updated;

    // Instantiate the Unit Under Test (UUT)
    BrentKung bk16(a, b, cin, rst, clk, S_updated, Cout_updated);

    always #30 clk=~clk;

    initial begin
        // Initialize Inputs
        a = 0;
        b = 0;
        cin = 0;
        clk = 1;
        rst=1;
    end
endmodule
```

(a)

```
    // Wait 100 ns for global reset to finish
    #100;

    // Add stimulus here
    a = 16'hFFFF;
    b = 16'h0000;
    cin = 1;
    rst=0;

    #300;
    a = 16'd2017;
    b = 16'd7010;
    cin = 0;

    #300;
    a = 16'hFFAB;
    b = 16'hEF92;
    cin = 1;

end

endmodule
```

(b)

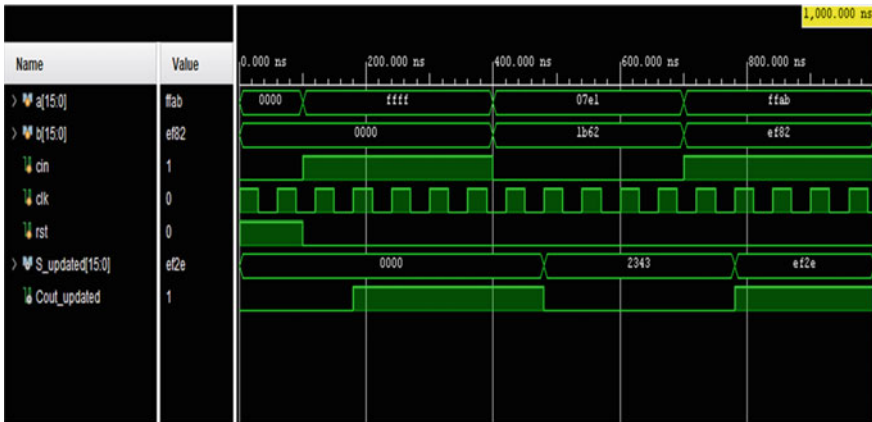


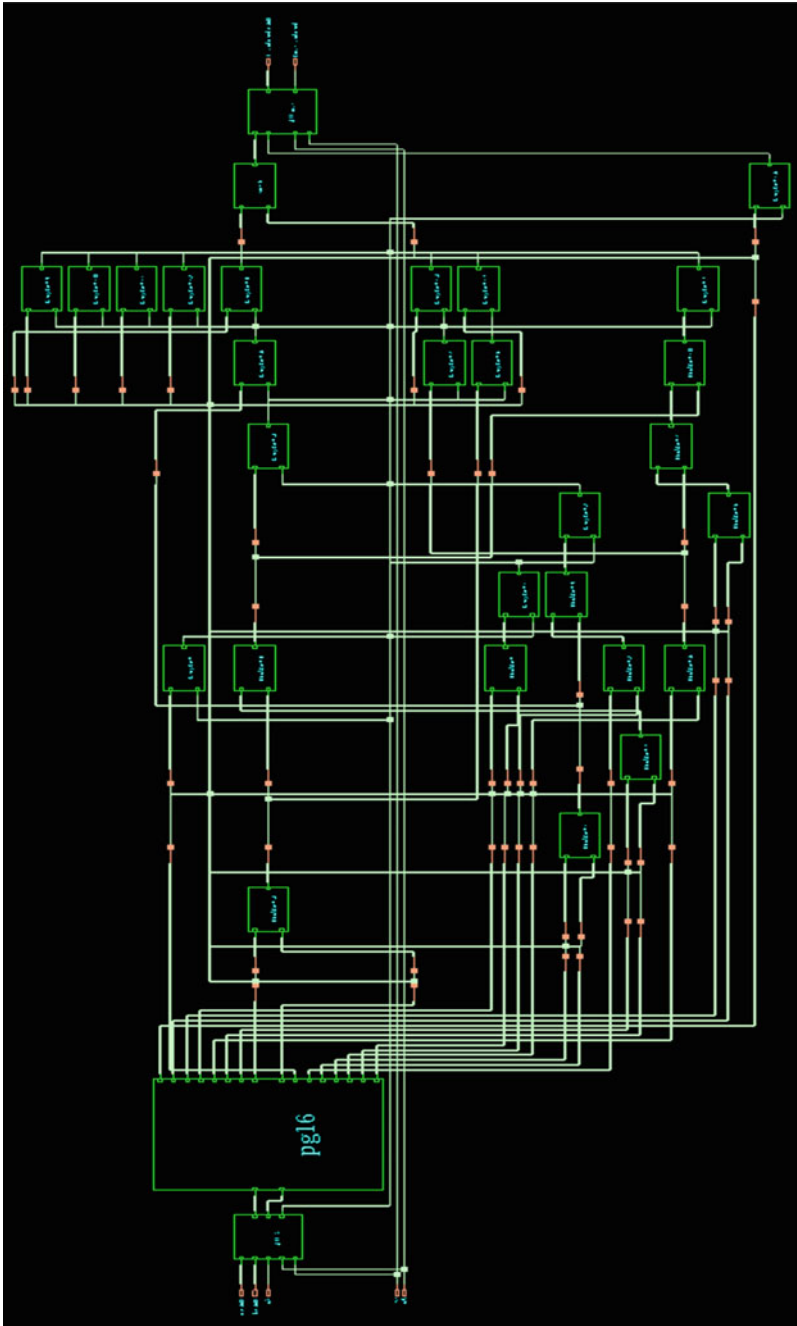
Fig. 13 Successful behavioral simulation for Fig. 12

Also, there are many libraries to explore, emphasizing speed, and, also, not being concerned with high speed; such as ‘fast’ and ‘slow’. We have homogenously utilized the ‘fast’ variants for both the 45 and 180 nm implementations.

The overall placement and global routing, along with various interconnect levels, are illustrated (see Fig. 17) to understand better how it leads to a complete ASIC implementation. In the optimized placement, the instances are physically made more compact, and there is utilization of filler cells as well, for signal strength consistency.

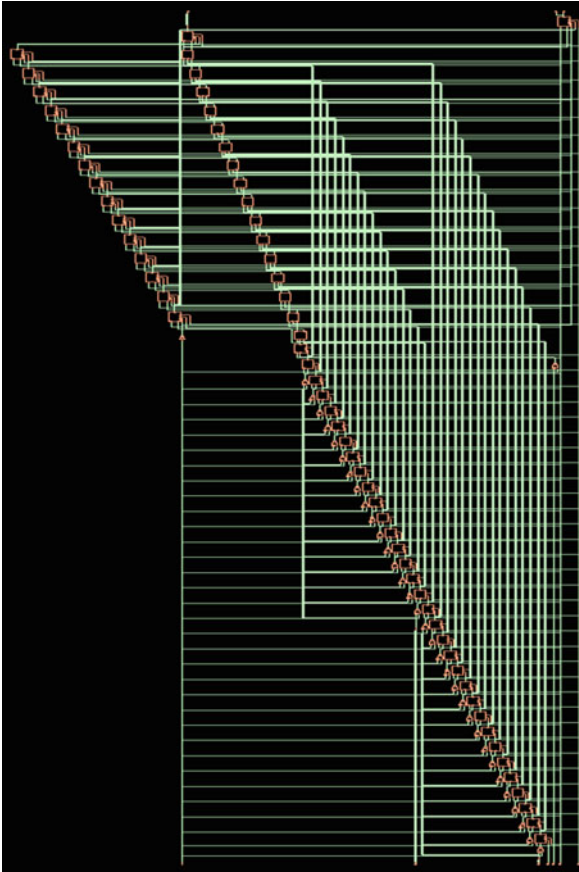
4 Results and Discussion

Insertion of inverters is observed during physical mapping at 180 nm node, which increases the overall gate count. This implies that driving strength had to be enhanced before being considered physically viable in this node. Also, area coverage is 10.3 times greater than that in 180 nm from 45 nm (see Fig. 19; Table 2). The subsystem at 180 nm can be clocked around 500 MHz, and the critical path delay observed at 45 nm is 0.03 ns (see Table 2). Another important pattern of importance that is not listed (see Fig. 18) here is the parameter leakage power, which is observed to be higher in 45 nm than 180 nm, which is expected theoretically due to shorter channel length in the former than the latter. The leakage power in 45 nm is 4 × higher than that of 180 nm implementation, which is also how the channel is scaled down from former to latter. The leakage power consumption for the 45 nm node is 24 nW. Quantum-dot cellular automata (QCA) is an alternative to CMOS and has shown promising results in particular areas. However, the delay and the power are at odds with each other, and there is an optimal solution to be arrived at or decided based on application; one can be prioritized over another. One man’s acceptable is other man’s fast or slow.



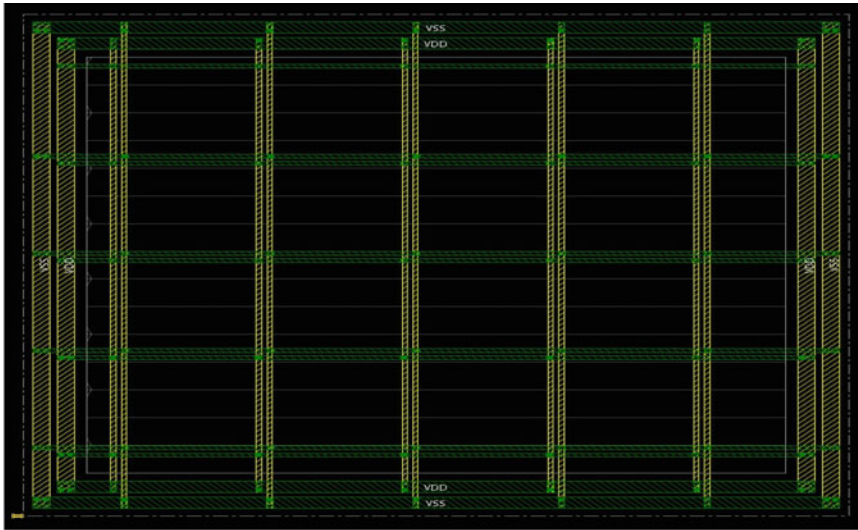
(a)

Fig. 14 Genus logical synthesis for the adder design on genus a logical synthesis on cadence genesis. **b** DFT scan flop insertion after path optimization

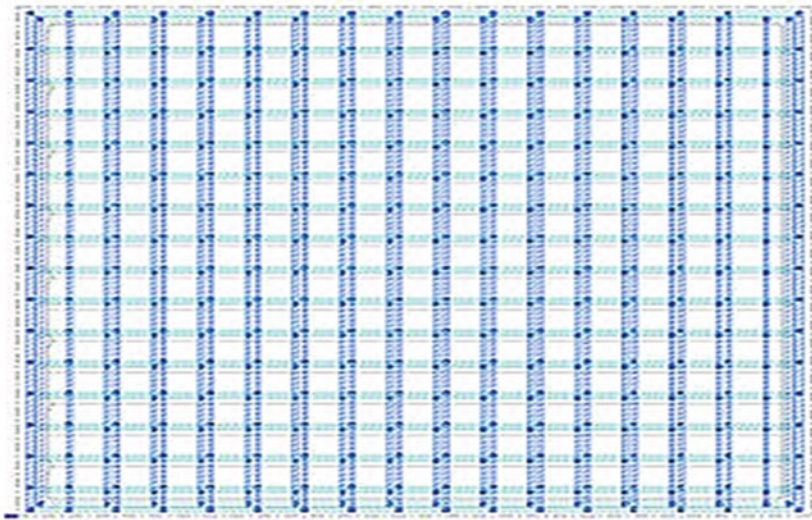


(b)

Fig. 14 (continued)

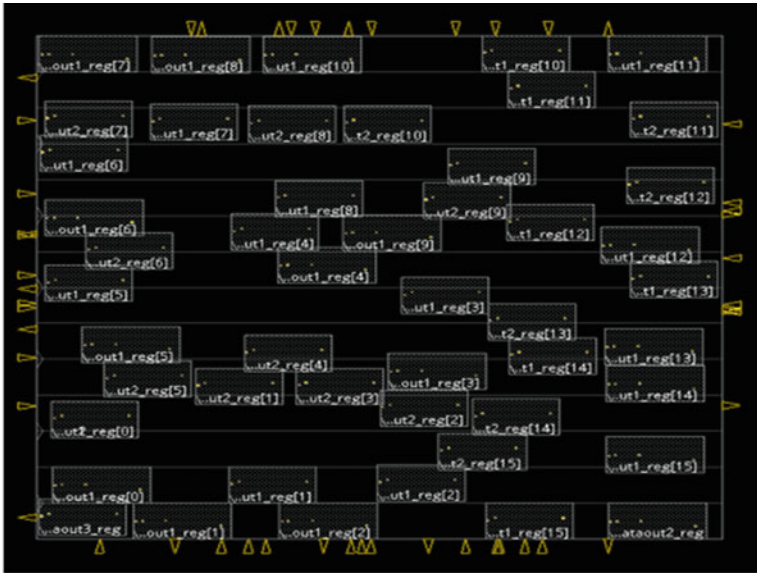


(a)

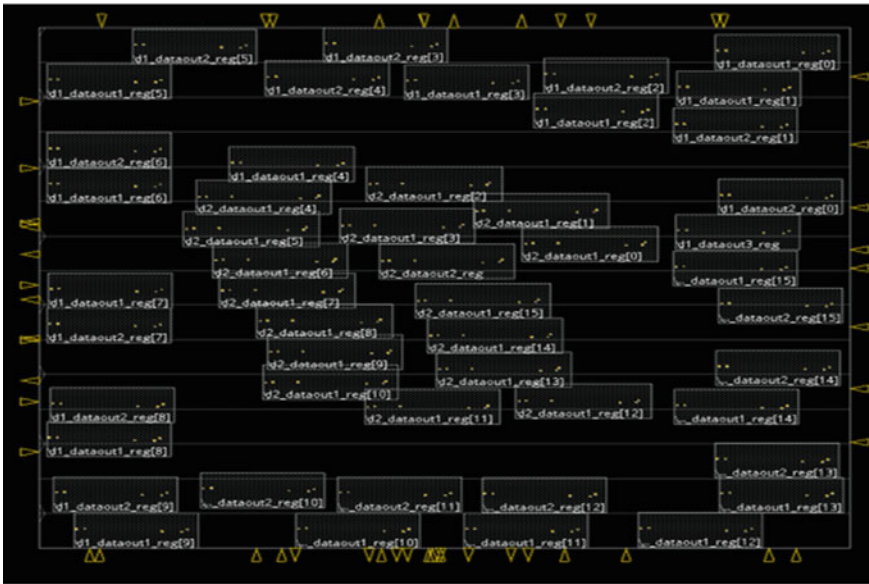


(b)

Fig. 15 Power rings and stripes allocation **a** gslib045 power rings and stripes, **b** tsmc180lib power rings and stripes

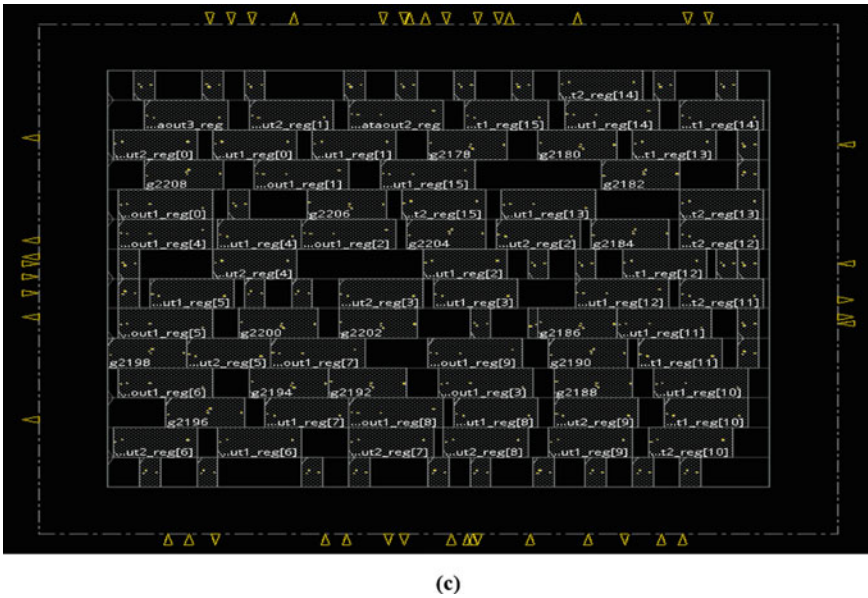


(a)



(b)

Fig. 16 Physical placement using cadence EDA tool-suite. **a** Unmapped placement, **b** mapped placement at 45 nm, **c** optimized mapped placement



(c)

Fig. 16 (continued)

The alternative technology is challenging to adopt in a mainstream manner because of the cost associated with the initial setup.

5 Conclusion

In this work, a 16-bit Brent–Kung adder has been successfully implemented for physical design (PD) flow at 45 and 180 nm technology node. Beginning from RTL code, synthesis, placement, and routing to generation of GDSII file has been executed using Cadence tool. The area, delay, and power for 45 nm are $413.136 \mu\text{m}^2$, 0.03 ns, and $26.73 \mu\text{W}$, respectively, and for 180 nm are $4254.466 \mu\text{m}^2$, 2 ns, and $513.048 \mu\text{W}$, respectively (see Figs. 18 and 19). Hence, in terms of delay, 45 nm is 66.67 times more efficient than 180 nm technology node.

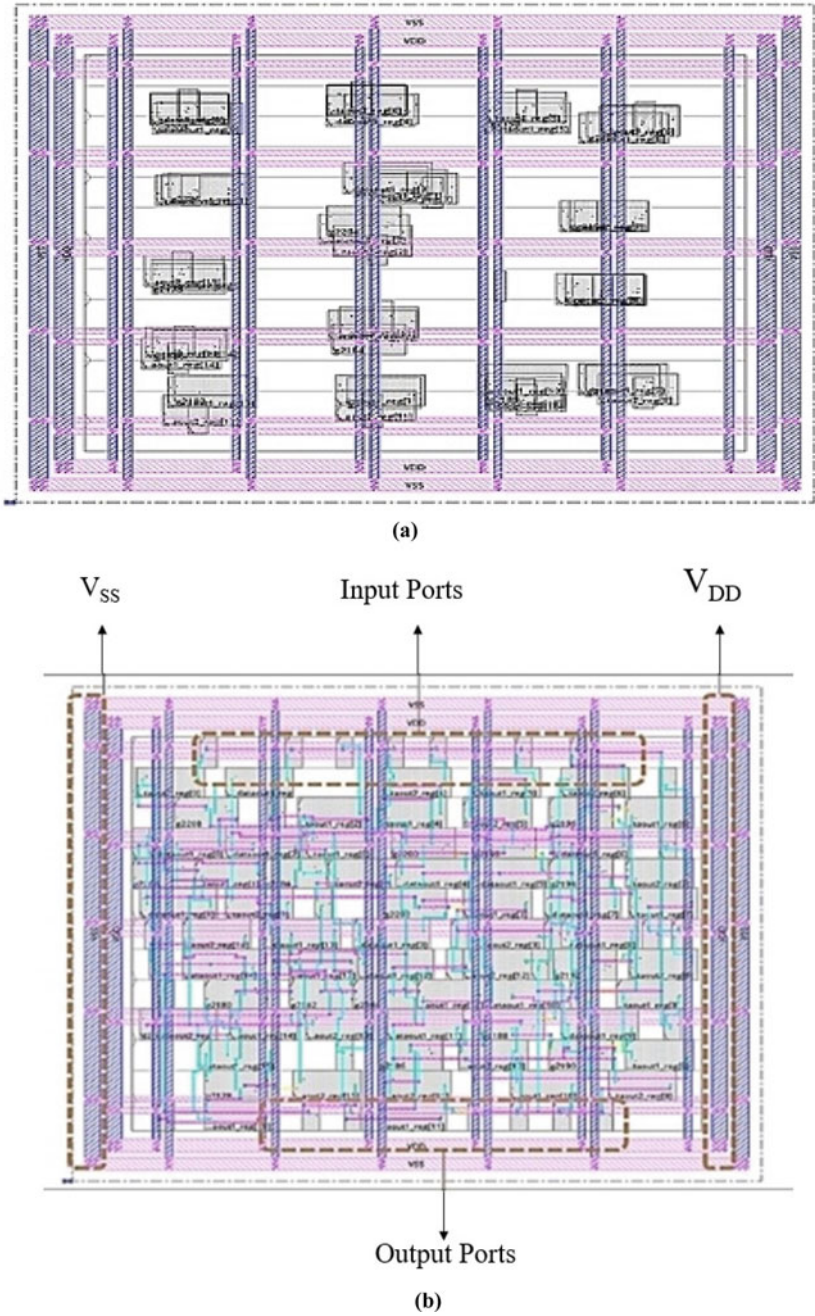


Fig. 17 Placement and routing with the inclusion of cadence EDA tool-suite. **a** Unmapped placement with power rings, **b** routed design for gsclib045

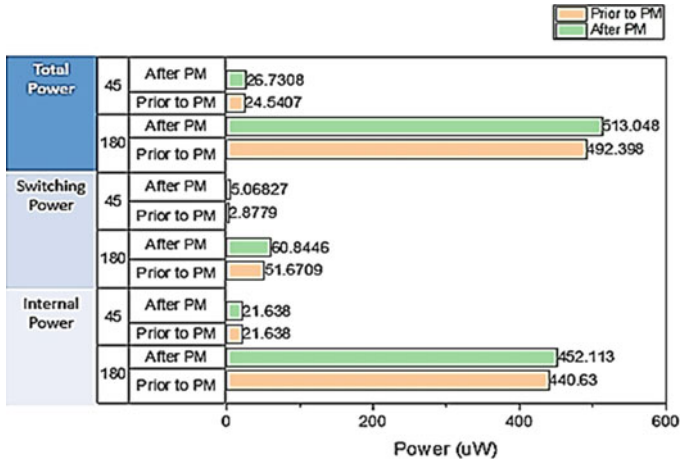


Fig. 18 Power for both the nodes after and before physical mapping (PM)

Fig. 19 Gate and instance counts after physical mapping (PM) a gate count for gsclib45, b gate count for tsmc180

Type	Instances	Area	Area %
sequential	50	285.228	69.0
inverter	1	0.684	0.2
logic	49	127.224	30.8
physical_cells	0	0.000	0.0
total	100	413.136	100.0

(a)

Type	Instances	Area	Area %
sequential	50	3266.525	76.8
inverter	23	153.014	3.6
logic	37	834.926	19.6
physical_cells	0	0.000	0.0
total	110	4254.466	100.0

(b)

Table 2 Parameters on different technology nodes

Reference	Technology node (nm)	Area (μm^2)	Delay (ns)	Power (μW)
This paper	45	413.136	0.03	26.73
This paper	180	4254.466	2	513.048
Reg. BK16 [11]	45	–	265	0.649
Reg. BK16 [14]	250	–	1.1	533
BK16 [15]	QCA	3.5508	0.008	–

References

1. Parhami B (2000) Computer arithmetic: algorithms and hardware designs. Oxford University Press, Oxford
2. Stine EJ (2004) Digital computer arithmetic datapath design using Verilog HDL. Kluwer Academic Publishers, Boston. <https://doi.org/10.5555/983751>
3. Basha MM, Pabbathi J (2016) Report on ripple carry adder power delay using Brent Kung (BK) adder. *Int J Mod Trends Sci Technol (IJMTST)* 2(8):37–40
4. Ganesan S (2015) Area, delay and power comparison of adder topologies. University of Texas Libraries, Austin. <https://doi.org/10.15781/T2F830>
5. Brent R, Kung TH (1982) A regular layout for parallel adders. *IEEE Trans Comput* C-31(3):260–264. <https://doi.org/10.1109/TC.1982.1675982>
6. Meruguboina D (2017) Efficient design of carry select adder using Domino Manchester carry chains. ProQuest Dissertations Publishing, Southern Illinois University Carbondale
7. Kumar UN, Sindhuri BK, Teja DK, Satish SD (2017) Implementation and comparison of VLSI architectures of 16 bit carry select adder using Brent Kung adder. In: 2017 innovations in power and advanced computing technologies (i-PACT), pp 1–7. <https://doi.org/10.1109/IPACT.2017.8244982>
8. Saxena P (2015) Design of low power and high speed carry select adder using Brent Kung adder. In: 2015 international conference on VLSI systems, architecture, technology and applications (VLSI-SATA), pp 1–6. <https://doi.org/10.1109/VLSI-SATA.2015.7050465>
9. Priyanka P, Nagu M (2017) Design of low power and high speed carry select adder using Brent Kung adder. *Int J Innov Technol Res (IJTR)* 5(1)
10. Gaur J, Mehra A, Kumar P, Kallakuri S (2019) 16 bit power efficient carry select adder. In: 6th international conference on signal processing and integrated networks (SPIN), pp 558–561. <https://doi.org/10.1109/SPIN.2019.8711565>
11. Turcanik M (2013) Speed comparison of the adders in FPGA. *Sci Military J* 8(1):18–23
12. Potdukhe PP, Jaiswal VD (2015) Review of carry select adder by using Brent Kung adder. *Int J Adv Res Electron Commun Eng* 4(10)
13. Vinutha R, Bharathi M, Divya D (2015) A survey on Brent-Kung, Han-Carlson and Kogge-Stone parallel prefix adders for their area, speed and power consumption. *i-manager's J Circuits Syst (JCIR)* 3(4):37–41. <https://doi.org/10.26634/jcir.3.4.5929>
14. Kowsalya P, Malathi M, Ramanathan P (2014) Low power parallel prefix adder. *Appl Mech Mater* 573:194–200. <https://doi.org/10.4028/www.scientific.net/AMM.573.194>
15. Pudi V, Sridharan K (2012) Low complexity design of ripple carry and Brent-Kung adders in QCA. *IEEE Trans Nanotechnol* 11(1):105–119. <https://doi.org/10.1109/TNANO.2011.2158006>

Autonomous Vehicles: A Detailed Bird Eye View



Ansh Jain and N. Gupta

Abstract Transportation has developed a lot in previous years, from camels and horses to conventional cars and now autonomous vehicles (AVs) or a self-driven vehicle. It is a self-apprehensive automobile that detects its current surroundings with the help of sensors and moves with less or no human intervention. Autonomous vehicles can soon come to our roads, as, a lot of research has already been done in the sector. Since very few people have commuted in an AV, one can't tell the pros and cons of AV just by the theoretical part. Initially, every research poses some issues; this is no different, but with time, it is important to solve those issues else they can gradually become a threat. The present work addresses some issues which need to be taken into consideration before AVs reach the public. These issues are not only restricted to technical but also concerns with ethics, society, and legalities. We have also focused on the pros, cons, and changes that might happen once AVs become publicly available. Is it worth spending millions of money and hundreds of hours in research? Are there more advantages of AVs than disadvantages? Is it a threat to society? Let us look at some details and aspects of AVs.

Keywords Autonomous vehicle · Self-driving vehicle · Technical and non-technical details · Issues and solutions

1 Introduction

Although the research on AV was started in the early 1980s [1], still it faces various challenges for its development in its design, control, planning, coordination, perception, and human interaction. Some of the human actions such as looking at fellow drivers or sometimes understanding sign language as waiving hand to allow other vehicle to pass etc. or allowing pedestrian to cross the road by waiving hand etc. are difficult for machines [2].

A. Jain · N. Gupta (✉)
MED,DTU, Delhi, India
e-mail: Navritigupta22@gmail.com

Artificial intelligence/machine learning has already been implemented in various fields of mass manufacturing as optimization [3] of input parameters to achieve optimized output. It ensures optimum usage of resources [4], along with optimizing consumption of energy required in a manufacturing process [5].

The automobile standardization agency, Society of Automotive Engineers (SAE), has defined six levels of automation for autonomous vehicles. There are automation levels in vehicles from 0th level (conventional cars/no automation) to 5th level (fully automated) [6]. In between are the partial automation such as speed controls, lane following assistants. Level 0–2 requires a driver all the time; level 3–4 requires a driver in difficult situations. Level 5 doesn't require a driver and is fully autonomous in all situations.

- Level 0: No driving automation: These are the conventional vehicles.
- Level 1: Assistance to driver: A single automation system like cruise control is used.
- Level 2: Partial automation: Both steering and acceleration are controlled by automation. In emergency, driver can take control any time. Tesla and Cadillac are at this level.
- Level 3: Conditional driving automation: These vehicles can detect the surroundings and act accordingly. Audi A8L falls under this category.
- Level 4: High driving automation: Along with the features of level 3, these vehicles can also intervene if there is some issue. Human has the option to override in an emergency case. NAVYA, Waymo, Magna falls under these categories.
- Level 5: Full driving automation: No human attention is required; everything is done by a vehicle even in emergency cases.

Level 5 AV would require overcoming many challenges which include social challenges, technical challenges, legal challenges, and ethical challenges. We will focus on these challenges.

One of the first notable advancements in AVs was at competition sponsored by DARPA, in which the methods were limited to slow speeds and in a not-so-crowded environment [7]. Google started its test project on AVs in 2009 [8]. In 2016, the world's first autonomous taxis was revealed by Singapore, which were operated by a software start-up named nuTonomy [9]. In 2016, Uber established an Advanced Technologies Center which began testing AVs with passengers [10, 11]. At present, Volvo, Nissan, Volkswagen, Audi, Tesla, and Ford have also started research in this sector [2]. Autonomous trucks and buses are being tested in some places [12–14]. Apple has also started research in this sector. It is expected that AVs will reach public markets by 2025–2027 [15].

In the past decade, great progress has been achieved in AVs [16, 17], and computing abilities have also been greatly improved to reduce the computation time. This was also accompanied by machine learning techniques, decision-making methods, and complex planning. Still, AVs can't operate in complex environments which need to be addressed.

AVs have sensors, radars, and LiDARs ; hence, the scenario of accidents (if caused) can be recreated, and using machine learning, AVs can learn how not to repeat it.

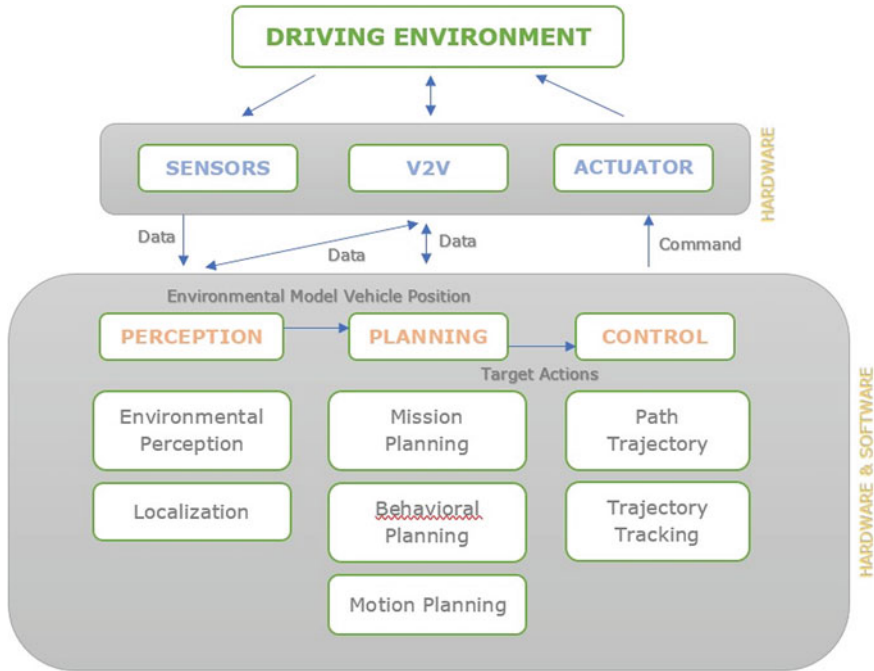


Fig. 1 Typical AV systems

Still, there are many scenarios, and most of them are different from each other, which can't be generalized.

2 Technical Details

2.1 Environment Perception System

The most suitable and representational sensors for perception systems are RADAR, LiDAR, ultrasonic, cameras, GNSS, RTK, and IMU. All of them work in the electromagnetic spectrum.

- Ultrasonic Sensor: It works in the range of 20–40 kHz. It sends sonic waves and receives the echoed wave. The time difference between the two is used to calculate the distance of the object from the sensor.
- RADAR: It works at 247,779 GHz. It sends radio waves and receives the echoed wave. The time difference between the two is used to calculate the distance of the object from the sensor.

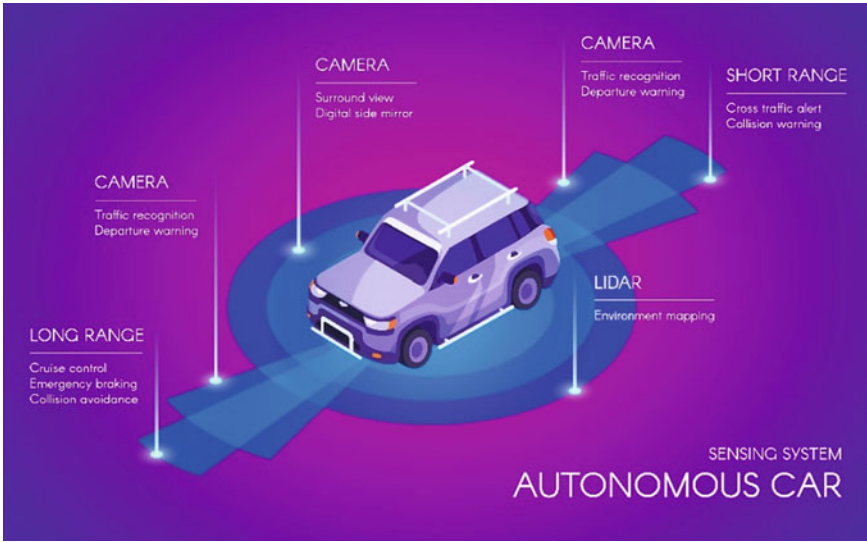


Fig. 2 Sensors and their positioning

- **LiDAR:** It works at 200 THz. It sends a light pulse and receives the echoed pulse. The time difference between the two is used to calculate the distance of the object from the sensor. They can be 2D or 3D, rotary, or solid state.
- **Cameras:** VIS cameras work in the visible spectrum, 400–780 nm. These are most commonly used in AV perception systems. A pair of VIS cameras with specified focal length can be used to calculate distance. TOF cameras are also used in detecting distance.

2.2 Position Estimation System

2.2.1 Global Navigation Satellite System (GNSS)

These technologies are used to locate the vehicles with respect to their initial point. They include a group of satellites that sends the signal about the satellite, orbital parameter, its position, etc. which is received by the vehicle. The time taken by the signal to travel from each satellite (at least four satellites) to the vehicle is used to calculate the distance from the four satellites, which helps in determining the location of the car with some error, which may be due to weather conditions, reflections, noise, synchronizations of atomic clocks, etc. This method is called the trilateration process.

Table 1 shows different GNSS and their details [18, 19].

To improve the accuracy, some methods like DGNSS, RTK, and SBAS are also developed [20].

Table 1 Various GNSS and their details [18, 19]

	BEIDOU	GALILEO	GLONASS	GPS
Coverage	Chinese	Global	Global	Global
Height (km)	21,150	23,222	19,100	26,650
Owner	China	European Union	Russia	EEUU
Period	12 h 53 m	14 h	11 h 15 m	11 h 58 m
Precision	10 m, civil 0.1 m, military	1.0 m, civil 0.01 m, advantage	7.4 m, civil 4.5 m, military	7.8 m, civil 5.9 m, military
Satellites	30 + 5	30	24	24

2.2.2 Inertial Positioning and Dead Reckoning (DR)

It is a process to estimate direction and position based on the initial position measurements. The simplest way is to use rotary sensors; at wheels and steering wheel, this technique is known as odometry [21]. Some errors like slip, lateral motion can be reduced with the help of inertial measurement units (IMUs), which comprise of gyroscope, accelerometer, and magnetometer [22].

2.3 Data Fusion Algorithm

Combining data from two or more sensors is called sensory fusion or data fusion. When more data are fused, it increases the accuracy and integrity of the system. In AV, it will help in better understanding of the environment to act accordingly.

2.3.1 Fusion Methods in Perception System

One method is to fuse data of LiDAR and stereo cameras to improve object detection. It includes two stages: (A) Hypothesis Generation: To recognize a vehicle using Haar features in depth maps and AdaBoost classifier. (B) Verification: It is done by LiDAR with a support vector machine to identify the shape of object. This has a lower false alarm rate [23, 24].

One method is to fuse MMW RADAR with camera information. This method provides a balance between computational efficiency and detection accuracy. The MMW radar initially recognizes the likely vehicle and gives a locale of interest. Symmetry detection and active contour detection of the vision processing module help to identify the vehicle. Detection rate: 92.36% and false alarm rate: 0% using a real-world dataset [25].

2.3.2 Fusion Methods in Positioning System

Generally, the Kalman filter and extended Kalman filter are most used algorithms to increase the accuracy of positioning systems.

A method is to fuse the data from the RADAR system by KF method; it is tested that the data from RADAR only are sufficient for fewer errors [26].

2.4 Testing AVs

When research on AVs started, consequently, planning, processes, and procedures for testing AV also started. The testing may be done physically or by simulation. Physical tests are comparatively not so feasible because of the guidelines, higher cost, and require more time than the simulation tests.

There are three types of simulations [27]:

- **Live:** It is an operational test to identify the systems which are damaged using real forces by stimulated firings.
- **Virtual:** It tests a complete system prototype, by computer-generated stimuli. Mainly used in developmental tests.
- **Constructive:** representation of systems using only computers.

In the automobile industry, the most accepted simulation is V-model and its variants. Although many tools have been added in simulation, yet there is no best tool for all scenarios. In some tools, the agent paradigm is also added to represent human beings as autonomous [28, 29].

One method is to use game engines and physics engines for simulation and testing. Some of the features of these simulations are physics fidelity, realism, and a scriptable environment. Still to be highly precise simulations are better than using game engines. Some engines which are used for simulations are Unity 3D, Unreal Engine, Cry Engine, Blender, Open Dynamics Engine (ODE), Bullet Physics, and NVidia PhysX.

Robotic simulations can also be used for testing if they provide modeling of all the sensors and actuators. The aspects to be considered while selecting robotic simulators are 3D rendering, external agent support [30] (Table 2).

Virtual simulation environments can also be used for more accurate results. It consists of a simulated vehicle model, simulated world, and simulated sensors. Toyota Research Institute (TRI) has developed Vehicle Platform 3.0. Google has Carcraft simulator. NVidia has developed its own platform namely NVidia drive AGX.

Table 2 Various simulators and their details

Simulator platforms	External agent	Graphical engine	License	Simulator engine
BlenSor	No	OpenGL	GPL/Open source	–
Gazebo	Yes	Ogre3D	GPL/Open source	ODE, Bullet, Simbody Art
MORSE	Yes	OpenGL	GPL/Open source	Blender, Bullet
MRDS	No	DirectX	Commercial	PhysX
USARSim	Yes	Karma	GPL	Unreal engine
V-Rep	Yes	OpenGL	GPL/Open source, commercial	ODE, Bullet, Vortex
Webots	Yes	–	Commercial	ODE

3 Non-technical Issues

3.1 Public Health Issues/Ethical Issues

There are many issues which need to be faced, some of them are as follows. A challenge is to maintain a balance between the protection of the public's safety and the manufacturer's innovation. One challenge is people would prefer to use AVs, due to their ease, over walk or cycling. The access of AVs would be only limited to the rich society as the cost of production would be high (at least in the initial stages). This is mainly because sensors like LiDARs, radars, sensors, computational devices will be used in manufacturing. People would prefer personal vehicles over public transport, leading to more usage of resources and pollution (in case of IC engines). In a forced-choice algorithm, where either a bystander or the passenger's life is at stake, who should be given a privilege.

3.2 Legal Issues

Many legal challenges also need to be addressed some of which are given. One of main challenge is Cybersecurity of vehicles, as lot of data is shared with fellow such vehicles near by. Insurance companies need come up with some new kind of solutions to the issues which will be caused because of AVs. If there is a fault and accident happen, whose fault would it be, or what actions should be taken? To find solutions to these problems the Government and lawmakers need to play their part, even in the research phase.

In 2016, US Transport Department issued the first Federal Automated Vehicles Policy, where the department stated some safety standards for testing AVs. It also

asked for system failures safeguards. These were the first few main policies which were made for autonomous vehicles.

4 Non-technical Solutions

4.1 International Standards

International standards play an important role in regulations and safety. Some of the international standards for vehicles are ISO 26262, IEC 61508. With the advancement in AVs, more standardizations must be needed for better and safer implementation of cars.

ISO 26262: ROAD VEHICLE OF FUNCTIONAL SAFETY: It is an international law regarding the safety of electronic and electrical systems in automobiles. Part 6 is solely dedicated to reliable codes.

IEC 61508: It is a global standard related to automatic protection systems, its application, design, deployment, and maintenance.

They use automotive safety integrity levels (ASILs), which measure the risk related to systems from A to D. A being least secure and D being most safe.

4.2 Testing Possibilities

All over the world, hardly, 20 countries have allowed AV testing in public roads either partially or fully; because of this, AVs are not being tested at their full pace. The other countries are either not technologically advanced or are scared of unwanted accidents due to AV in their initial phase. The solution is again to generate laws and actions against accidents so that companies would think twice before getting AVs on a public road. To compensate for it, there should also be laws that provide some motivation to the manufacturers or researchers.

5 Advantages

Autonomous vehicles will make transportation and mobility much easier and more exciting. Some of the advantages include mobility for those who don't know how to drive, lesser traffic on streets, less travel time, lesser accidents which earlier caused due to human negligence and human errors. It is estimated that autonomous cars can save 1 million lives every year.

5.1 Effect on Pollution and Environment

Since computers are much better at work than humans in various ways like, they could change gears, use clutch effectively, thus reducing fuel consumption, and hence can lead to a safer and greener environment.

They will reduce pollution because of efficient driving and various techniques possible for AVs like ‘platooning’. These things would not only reduce the pollution but also the travel cost.

5.2 Effect on Safety

Since there would be cameras, sensors in every car, they may be used to identify the criminals and thus gradually, reduce the crimes.

6 Disadvantages

6.1 Effect on Cities

It would also have various adverse effects, such as people would have no issues in traveling more and thus may shift to remote locations to enjoy more economical or bigger houses; this would further increase the dependency on cars. Lesser usage of public transport as buses and cars may lead to revenue losses to transport department and governments. Also, it would take the jobs of professional drivers, taxis, rickshaws.

6.2 Effects on Privacy

Since there would be cameras, sensors in every car that would also lead to a breach of privacy which is a debatable topic and a major concern.

7 Autonomous Taxi

An idea is of the car-sharing scheme, in which when a car becomes fully automated, it may be used as a service, rather than a commodity. In such a case a person can book an AV whenever required just like a normal cab and it will take person to his/her destination. It is estimated that one AV can replace 10 cars to help people commute.

And those who wish to buy it can send their vehicle to others once they are dropped and can call back when they wish to travel again [31].

At present, these taxis are being tested and used with controls with drivers as well so that they may take control if in case it is needed. Few cases of accidents are also reported, like Uber in March 2018, which means it need more development before it gets publicly available.

8 Conclusion

Already, artificial intelligence/machine learning-based techniques like artificial neural networks are playing very important roles in manufacturing areas, like optimization of input parameters to optimize manufacturing processes. Also, we are witnessing Industry 4.0 concept being implemented in manufacturing industry. We are witnessing an epoch in which almost everything is taking a step toward automation, and so is a vehicle, and because of this, even computer companies are also getting into this industry. This soon may lead to an integrated transportation system, where all elevators, AVs, planes, ships would come together with the help of AI.

Many technical aspects need to be solved, and training should be done properly; sensors should be fitting at every angle to minimize the blind spots. Apart from technical issues, various social, economic, legal, ethical issues also need to be taken care of, for which governments and organizations also have a large play.

There are many uncertainties about AV, its emergence, its applications. But, when it will emerge, it will affect a lot of industries, sectors, and infrastructures. As of now, these can be predicted with a little certainty but still is a very important aspect to understand the trends, threats, and issues in the near future and in a long term as well.

Research is also being conducted in the field of application of flexible manufacturing systems in automated guided vehicles (AGVs) used for material transportation in big manufacturing units across the globe.

There are more advantages to it than disadvantages, which make it worth researching it and solve the issues. Still, it is needed to be considered as a soft issue, and every aspect of it should be taken into consideration since many lives would depend on it, in terms of health and occupation and in some cases, a matter of life and death.

One major thing is to share the data, incidents with the public; this would not only allow them to give more ideas or solutions but also would provide them trust, and they would feel AVs to be more reliable. This would allow them to accept it and start using it at a faster pace.

The failure of a machine may be annoying or frustrating, but the failure of a car would lead to a life and death situation. Hence, the design, testing, and evaluation must be done carefully for public acceptance.

References

1. Hancock PA, Nourbakhsh I, Stewart J (2019) On the future of transportation in an era of automated and autonomous vehicles. In: PNAS, pp 1–8
2. Fleetwood J (2017) Public health, ethics, and autonomous vehicles. *AJPH* 107(4):1–7
3. Gupta N, Agrawal AK, Wallia RS (2019) Soft modelling approach in predicting surface roughness, temperature, cutting forces in hard turning process using artificial neural network: an empirical study. In: International conference on information, communication and computing technology. Springer, Singapore, pp 206–215
4. Gupta N, Wallia RS (2021) Predictive soft modelling of turning parameters using artificial neural network. In: Agrawal R, Jain JK, Yadav VS, Manupati VK, Varela L (eds) Recent advances in smart manufacturing and materials. Lecture notes in mechanical engineering. Springer, Singapore. https://doi.org/10.1007/978-981-16-3033-0_17
5. Aiyar HDS, Chauhan G, Gupta N (2021) Soft modelling of WEDM process in prediction of surface roughness using artificial neural networks. In: Agrawal R, Jain JK, Yadav VS, Manupati VK, Varela L (eds) Recent advances in smart manufacturing and materials. Lecture notes in mechanical engineering. Springer, Singapore. https://doi.org/10.1007/978-981-16-3033-0_44
6. SAE Intl (2016) Taxonomy and definitions for terms related to driving automation systems for on-road motor vehicles. Stand. J3016, SAE Intl, Warrendale, PA
7. Kornhauser PAL (2007) DARPA urban challenge Princeton University technical paper. Princeton University, Princeton, NJ, USA
8. Alphabet, Inc. Waymo FAQ. Available at: <https://waymo.com/faq>
9. Liang A, Durbin DA (2016) World's first self-driving taxis debut in Singapore
10. Uber. About Uber ATG. Available at: <https://www.uber.com/info/atc>
11. Uber (2016) Pittsburgh, your self-driving Uber is arriving now. Available at: <https://newsroom.uber.com/pittsburghself-driving-uber>
12. LeBeau P (2016) “Driverless” beer run; Bud makes shipment with self-driving truck. Available at: <http://www.cnbc.com/2016/10/25/driverless-beer-runbud-makes-shipment-with-self-drivingtruck.html>
13. DeVore V, Nguyen DQ (2016) Which countries are testing driverless cars?. Available at: http://www.swissinfo.ch/eng/sci-tech/future-of-transport_whichcountries-are-testing-driverless-cars-/41999484.
14. Chafkin M (2016) Uber's first self-driving fleet arrives in Pittsburgh this month. Available at: <http://www.bloomberg.com/news/features/2016-08-18/uber-s-first-self-driving-fleeta-rrives-in-pittsburgh-this-monthis06r7on>
15. <https://www.macrumors.com/roundup/apple-car/>
16. Furgale P, Schwesinger U, Ruffi M, Derendarz W, Grimmert H et al (2013) Toward automated driving in cities using close-to-market sensors: an overview of the V-charge project. In: IEEE intelligent vehicles symposium (IV). IEEE, New York, pp 809–816
17. Ulbrich S, Reschka A, Rieken J, Ernst S, Bagschik G et al (2017) Towards a functional system architecture for automated vehicles. [arXiv:1703.08557](https://arxiv.org/abs/1703.08557)
18. Eissfeller B, Ameres G, Kropp V, Sanroma D (2007) Performance of GPS, GLONASS and Galileo. In: Photogrammetric week '07. Wichmann Verlag, Heidelberg, Germany, pp 185–199
19. Chen H, Huang Y, Chiang K, Yang M, Rau R (2009) The performance comparison between GPs and BeiDou-2/compass: a perspective from Asia. *J Chin Inst Eng* 32:679–689
20. https://thesai.org/Downloads/Volume3No8/Paper_20-Techniques_to_improve_the_GPS_precision.pdf
21. Kao W-W (1991) Integration of GPS and dead-reckoning navigation systems. *IEEE*
22. Werth AJ, Shear WA (2014) The evolutionary truth about living fossils. *Am Sci* 102:434–443
23. Zhang F, Clarke D, Knoll A (2014) Vehicle detection based on LiDAR and camera fusion. In: Proceedings of the 2014 IEEE 17th international conference on intelligent transportation systems (ITSC), Qingdao, China. ISBN 9781479960774
24. Klimentjew D, Hendrich N, Zhang J (2010) Multi sensor fusion of camera and 3D laser range finder for object recognition. *IEEE*, pp 1–6

25. Wang X, Xu L, Sun H, Xin J, Zheng N (2016) On-road vehicle detection and tracking using MMW radar and monovision fusion. *IEEE Trans Intell Transp Syst* 17:2075–2084
26. De Muller FP, Diaz EM, Rashdan I (2016) Cooperative positioning and radar sensor fusion for relative localization of vehicles. In: *Proceedings of the 2016 IEEE intelligent vehicles symposium (IV)*, Gothenburg, Sweden, pp 1060–1065
27. Council NR (2001) *Statistics, testing, and defense acquisition: new approaches and methodological improvements*. The National Academies Press, Washington, DC, USA. ISBN 978-0-309-06551-1
28. Boesch PM, Ciari F (2015) Agent-based simulation of autonomous cars. In: *Proceedings of the 2015 American control conference (ACC)*, Chicago, IL, USA, pp 2588–2592
29. Kurz AY (2014) Agent-based modelling and simulation of cooperative driving. Open access master's theses. Paper 470. Available online: <https://digitalcommons.uri.edu/theses/470>
30. Koopman P, Wagner M (2016) Challenges in autonomous vehicle testing and validation. *SAE Int J Transp Saf*
31. Cohen SA, Hopkins D Autonomous vehicles and the future of urban tourism

Imperceptible Digital Image Watermarking Based on Discrete Wavelet Transform and Schur Decomposition



Anurag Tiwari and V. K. Srivastava

Abstract The excessive use of multimedia content in the past decades led to threats of illegal copying and duplication of digital contents. This paper proposes one of the solutions to this problem based on an image watermarking technique using Discrete Wavelet Transform (DWT) and Schur decomposition. The Schur decomposition takes a lesser number of computations than singular value decomposition, which makes it suitable for the decomposition of the image. In the proposed algorithm, the watermark is embedded by manipulating the Schur coefficients of the LL subband of the cover image with the Schur vectors of the watermark. In the proposed work, the properties of both DWT and Schur decomposition are combined. The proposed technique performs better against, rotation, histogram equalization attacks, and various filtering attacks. The performance of the proposed technique is evaluated using PSNR and SSIM, which shows better visual imperceptibility against various attacks. The experimental result of the proposed scheme is also compared with other prevailing techniques, and the proposed method is found more effective among the other techniques.

Keywords Image watermarking · Schur decomposition · Wavelet · Imperceptibility · Histogram equalization

1 Introduction

The excessive use of multimedia content in the past decades led to threat of illegal copying and duplication of digital content. In the recent multimedia age, the sharing of multimedia content or information like images, videos, and data with another person is widespread. Current advances in transmission invention, distribution, and

A. Tiwari (✉) · V. K. Srivastava
MNNITA, Prayagraj Teliyarganj 211004, India
e-mail: anuragt@mnnit.ac.in

V. K. Srivastava
e-mail: vinay@mnnit.ac.in

© The Author(s), under exclusive license to Springer Nature Singapore Pte Ltd. 2022
V. Mahajan et al. (eds.), *Sustainable Technology and Advanced Computing in Electrical Engineering*, Lecture Notes in Electrical Engineering 939,
https://doi.org/10.1007/978-981-19-4364-5_10

119

process have created new occasions for the unlawful modification, duplication, and spreading of digital content. In recent years, growth in digital transmission and within the cyber world has been incredibly fast, enhancing the requirement of confidentiality and authenticity of multimedia data. So digital watermarking techniques are used to solve the problem of modern digital content transmission. Digital image watermarking is defined as a scheme for embedding a watermark logo or image into the cover image using any key which will be extracted from watermarked image for copyright protection and authentication purpose [1]. In watermarking scheme, watermark can be visible or invisible. On the basis of information needed at the time of the extraction process, the watermarking techniques can be classified into three types: blind, semi-blind, and non-blind watermarking schemes [2]. In the blind types of techniques, there is no requirement of cover image only secret key is required, whereas in non-blind techniques, the cover image with the secret key both are required during extraction process. In semi-blind type of schemes, watermark bit sequence and secret key both are required [3]. Watermarking can be performed in spatial domain and transform domain. In spatial domain techniques, pixel values of cover image are modified to embed watermark, whereas in transform domain techniques, the cover image is transformed into the frequency domain and then watermark is embedded [4]. In hybrid image watermarking techniques, watermark information is embedded in both spatial domain and transform domain. The transform domain schemes have many advantages like better imperceptibility and robustness and higher payload capacity, whereas spatial domain techniques have advantages like lesser complexity and lesser cost. Wavelet-based watermarking schemes show wider scope as it is a time–frequency approach utilizes multi-resolution property [5].

Mohan et al. [6] developed a Schur-based technique that employs Schur triangular matrix to embed watermark. Liu et al. [7] suggested technique based on combination of Contourlet transform and Schur decomposition. Su et al. [8] investigated a technique based on Schur decomposition and uses dual color image watermark that employ correlation between Schur matrixes to embed the watermark. Ahmad [9] proposes a non-invertible technique in which cover image is converted into the blocks then subjected to Schur decomposition, and PN-sequences are generated to embed as watermark. Su et al. [10] suggested a primitive Schur decomposition based color image watermarking technique in which the watermark is embedded by modifying the relationship of two elements in the first column coefficient of the unitary matrix derived by Schur decomposition. This paper presents DWT and Schur decomposition-based watermarking scheme which provide better imperceptibility and robustness as well as it have lesser computational time.

This paper is arranged in following manner: In Sect. 2, the theory of DWT is explained, whereas in Sect. 3, the theory of Schur decomposition is presented, and in Sect. 4, proposed watermarking techniques are described. Section 5 contains the simulation result and finally conclusions are given in Sect. 6.

Fig. 1 DWT decomposition of image

LL2	LH2	LH1
HL2	HH2	
HL1		HH1

2 Discrete Wavelet Transform (DWT)

DWT decomposed image into four subbands, in each decomposition level which provides multi-resolution property. DWT uses based on wavelets as basis function, whereas DFT and DCT have everlasting sinusoidal or complex exponentials. Wavelets are generated by dilation and translation of mother wavelet. The DWT is mainly based on subband filtering. First original image is transformed into the four different subbands like LL1, LH1, HL1, and HH1. LL1 contains lower frequency components so it has maximum energy of image [3]. High frequency components LH1, HL1, HH1 hold the detailed information. It can be further divided into the subband by applying the second level wavelet decomposition into the LL1 subband which further provides four subbands which are LL2, LH2, HL2, and HH2. The process can be repeated to decompose image to the nth level subbands to get suitable subbands for watermarking where n is the level of decomposition. Similarly by using Inverse DWT, original image can be recovered. DWT provides suitable subband for watermarking according to human visual system. So watermark can be embedded into HL or LH subbands as they are not visible to human visible system [11, 12]. The DWT has limitation of shift invariance and phase sensitivity (Fig. 1).

3 Schur Decomposition

The Schur decomposition [9, 13, 14] provides Eigen values of pixel block easily. It can be defined for any matrix M as

$$M = U \times A \times U^T \tag{1}$$

where $M \in R^{n \times n}$ and A is upper triangular matrix and U is a unitary matrix [8, 9].

The Schur decomposition provides two matrices unitary and upper triangular matrix. The Schur decomposition can be applied on square matrices. The Schur decomposition is based on theory of unitary transformation, and it is intermediate

step of singular value decomposition (SVD) due to which it has lesser the computation time than SVD. The Schur decomposition diagonal matrices are same for A and A^T as the Eigen value of both are same. The Schur vectors are invariants to scaling. The Schur decomposition is mainly based on unitary transformation which makes so it stable. These properties make the Schur decomposition suitable for its application in image decomposition and in image watermarking as well. The watermarking information can be embedding into both the matrices either unitary matrix or upper triangular matrix but generally upper triangular matrix is preferred.

4 Proposed Watermarking Technique

The proposed watermarking algorithm is discussed in this section. In this work, a cover image as (I) of size $M \times N$ and binary watermark image as (I_w) of size $m \times n$ is considered.

4.1 Embedding Algorithm

The watermark is embedded based on procedure whose is shown in Fig. 2:

- i. Perform DWT on cover image to decompose image into four subbands LL1, LH1, HL1, and HH1.
- ii. The Schur decomposition is obtained by applying the Schur transform into the LL1 subband.

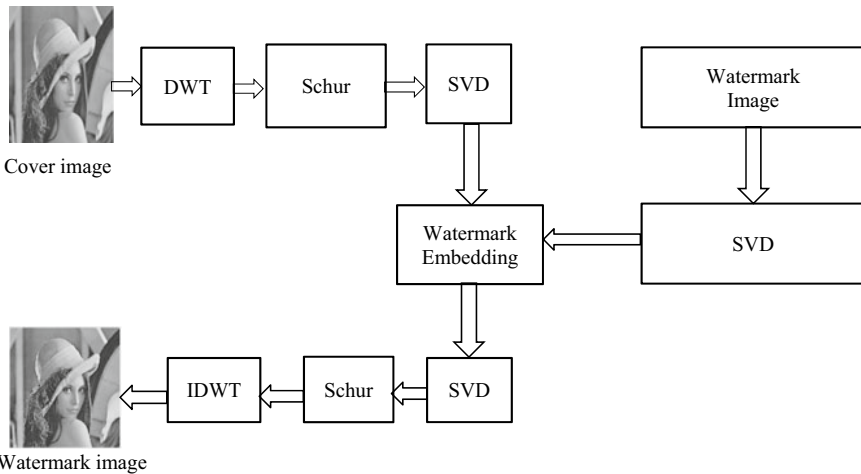


Fig. 2 Block diagram representation of proposed schemes

- iii. The upper triangular matrix of LL subband of cover image is further subjected to singular values decomposition (SVD) which gives three matrices.
- iv. The watermark image is also subjected to SVD to obtain the singular values (SV) matrices.
- v. The watermark is embedded by manipulating the SVs of cover image to SVs of watermark image

$$I_2(i, j) = I_1(i, j) + kI_w(i, j) \quad (2)$$

where k is gain factor.

- vi. Inverse process of SVD and Schur transform is applied to recover the modified LL subband.
- vii. The watermarked image is obtained by applying inverse DWT to the modified LL subband.

4.2 Extraction Process

The extraction procedure of binary watermark image is as following steps

- i. Apply DWT to obtain watermark image which results to four subband of watermarked image.
- ii. Perform Schur transform to LL subband to obtain the Schur vector matrix.
- iii. In next step, SVD is applied into the upper triangular matrix of Schur decomposition.
- iv. Extract transformed watermark image coefficients from watermarked image by applying

$$I_w(i, j) = (I_2(i, j) - I_1(i, j))/k \quad (3)$$

- v. Apply SVD to extract the watermark image.

5 Simulation Result

The effectiveness of proposed scheme is tested using various performance parameters for three images which are lena, girl, and pirates of as cover image of size 512×512 and binary watermark of size 256×256 is taken as watermark image shown in Fig. 3. Watermarked image obtained after applying the proposed algorithm is shown in Fig. 4.

The performance of the proposed algorithm is evaluated by two parameters which are as follows.

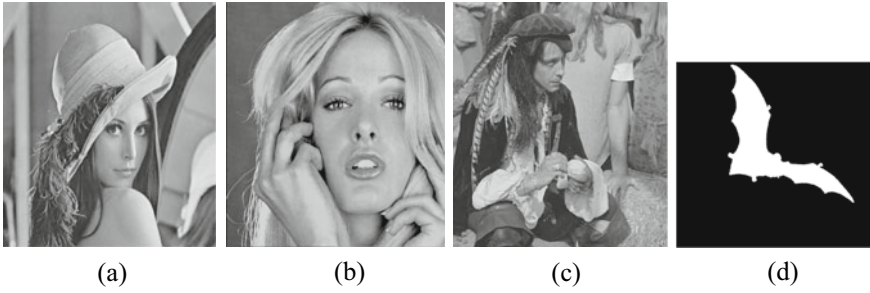


Fig. 3 Cover image **a** lena, **b** girl, **c** pirates, and **d** binary watermark

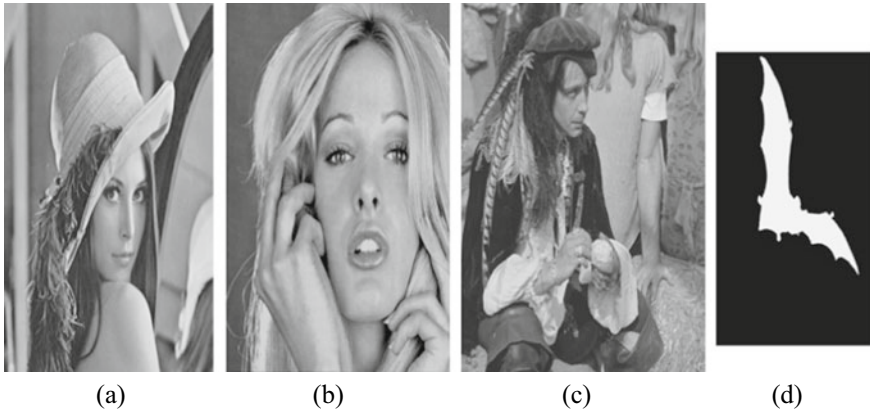


Fig. 4 Watermarked images **a** lena, **b** pirates, **c** girl, and **d** extracted binary watermark

5.1 Peak Signal to Noise Ratio (PSNR)

It is the parameter to evaluate the superiority of the watermarked image. It is ratio of peak value of signal power to noise power. PSNR used for evaluation of watermarking algorithm which is defined as:

$$\text{PSNR} = 10 * \log \frac{255^2}{\text{MSE}} \quad (4)$$

where mean square error (MSE) for gray image is given by:

$$\text{MSE} = \frac{1}{M \times N} \sum_{x=1}^M \sum_{y=1}^N [I(x, y) - W(x, y)]^2 \quad (5)$$

5.2 Structural Similarity Index Measures (SSIM)

SSIM defines the structural similarity between the cover image and watermarked image. SSIM nearer to 1 shows that structure of cover image and watermarked image are same. SSIM provides knowledge about the imperceptibility of image which is an important characteristic of watermarking algorithm.

$$SSIM(I, W_c) = \frac{\sum_{x=0}^M \sum_{y=0}^N [C(x, y) W_c(x, y)]}{\sum_{x=0}^M \sum_{y=0}^N |C(x, y)|^2} \quad (6)$$

The SSIM and PSNR evaluated after applying various types of attacks.

Noise attack: The noise affected watermarked image is obtained by applying salt and pepper type noise with variance 0.01.

Histogram equalization: Histogram equalization modifies the intensity value of image which used to improve the contrast of the image.

Filtering attack: Various types of filtering attacks like Gaussian, median, and average filtering are performed.

Geometrical attack: There exist various types of geometrical attacks like rotation, translation, etc. Performance of proposed technique is tested against rotation attack by rotation of watermarked image.

In Fig. 5, watermarked image obtained after various attacks are shown. In Fig. 6, PSNR value is plotted against gain k . Various values of parameter obtained after applying various attacks are given in Table 1.

It is clearly visible from Fig. 6, there exists an inverse relationship between the value of gain factor (k) and PSNR value. It shows the imperceptibility of watermarking scheme decreases with the increase value of k . In proposed scheme, PSNR value is greater than 30 dB for all value of k , which is more than the acceptable value of PSNR for any watermarking schemes.

Figure 7 shows the imperceptibility of proposed scheme which is better as compared to other method based on Schur decomposition proposed in [15–17].

6 Conclusion

Image watermarking scheme which is based on DWT and Schur decomposition is proposed in this paper. Binary watermark is embedded in cover image, after applying wavelet transform in LL subband. The proposed scheme shows good visual imperceptibility against various attacks. The proposed scheme shows very good PSNR and SSIM values. This algorithm can be further modified using RDWT as it has shift invariance property. Furthermore, the value of gain factor k can be optimized.

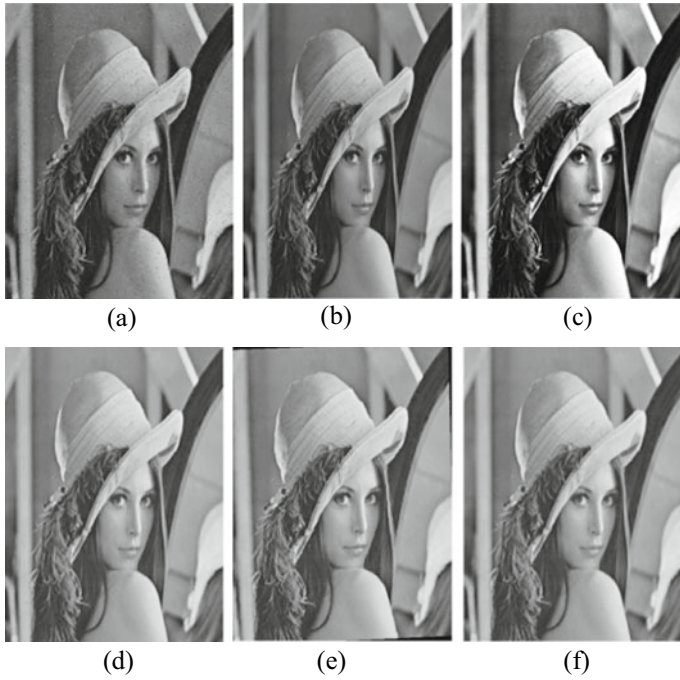


Fig. 5 Watermarked image after various attacks: **a** salt and pepper noise (0.01), **b** Gaussian noise (0.01), **c** histogram attack equalization, **d** median filter (3×3), **e** average filtering, and **f** rotation (2°)

Fig. 6 PSNR value on various values of k (gain)

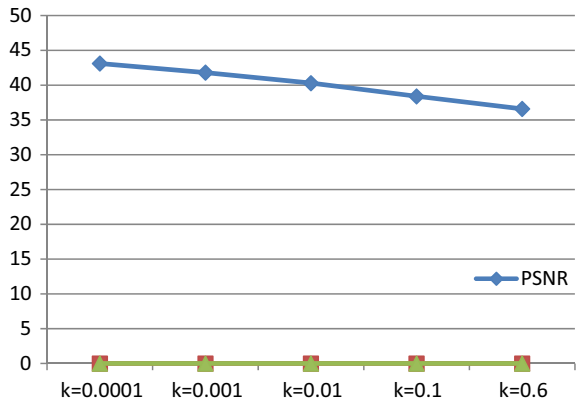
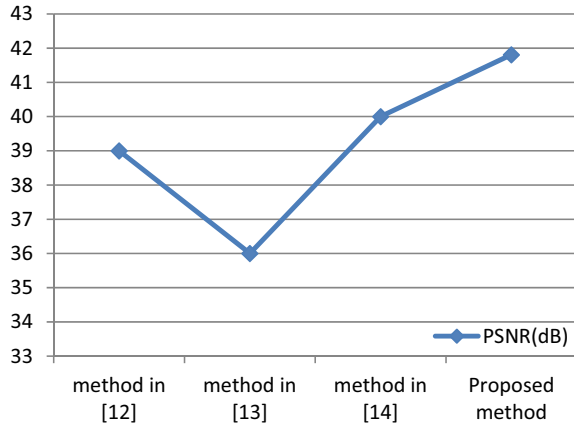


Table 1 PSNR a value and structure similarity index measure (SSIM) of various watermarked image after applying attacks

Attack	PSNR(in dB)	SSIM
Salt and pepper noise	28.06	0.8122
Median filtering (3 × 3)	30.99	0.9934
Gaussian filtering (3 × 3)	29.597	0.8602
Average filtering	30.57	0.9412
Histogram attack equalization	25.64	0.8546

Fig. 7 Comparison of PSNR values of proposed scheme with Schur-based algorithm presented in [15–17]



References

1. Khare P, Srivastava VK (2020) A reliable and secure image watermarking algorithm using homomorphic transform in DWT domain. *Multidim Syst Signal Process* 1–30
2. Rao VS, Rajendra SS, Srivastava VK (2012) A DWT-DCT-SVD based digital image watermarking scheme using particle swarm optimization. In: 2012 IEEE students' conference on electrical, electronics and computer science. IEEE
3. Khare P, Verma AK, Srivastava VK (2014) Digital image watermarking scheme in wavelet domain using chaotic encryption. In: 2014 students conference on engineering and systems, IEEE
4. Eberlein PJ (1987) On the Schur decomposition of a matrix for parallel computation. *IEEE Comput Archit Lett* 36(02):167–174
5. Haardt M, Nossek JA (1998) Simultaneous Schur decomposition of several nonsymmetric matrices to achieve automatic pairing in multidimensional harmonic retrieval problems. *IEEE Trans Signal Process* 46(1):161–169
6. Mohan BC, Veera Swamy K (2010) On the use of Schur decomposition for copyright protection of digital images. *Int J Comput Electric Eng* 2(4):1793–8163
7. Liu P et al (2010) A novel watermarking scheme in contourlet domain based on schur factorization. In: 2010 2nd international conference on information engineering and computer science, IEEE
8. Su Q et al (2012) Embedding color watermarks in color images based on Schur decomposition. *Opt Commun* 285(7):1792–1802
9. Mohammad AA (2012) A new digital image watermarking scheme based on Schur decomposition. *Multimed Tools Appl* 59(3):851–883

10. Su Q, Chen B (2017) An improved color image watermarking scheme based on Schur decomposition. *Multimed Tools Appl* 76(22):24221–24249
11. Sripradha R, Deepa K (2020) Robust and imperceptible digital image watermarking based on DWT-DCT-Schur. In: *International symposium on signal processing and intelligent recognition systems*. Springer
12. Thakkar FN, Srivastava VK (2017) A blind medical image watermarking: DWT-SVD based robust and secure approach for telemedicine applications. *Multimed Tools Appl* 76(3):3669–3697
13. Golub GH, Van Loan CF (1996) *Matrix computations*. Johns Hopkins studies in the mathematical sciences
14. Golub GH, Van Loan CF (2013) *Matrix computations*, vol 3. JHU press
15. Su Q, Yuan Z, Liu D (2018) An approximate Schur decomposition-based spatial domain color image watermarking method. *IEEE Access* 7:4358–4370
16. Vaidya P, Chandra Mouli PVSSR (2017) A robust semi-blind watermarking for color images based on multiple decompositions. *Multimed Tools Appl* 76(24):25623–25656
17. Liu X-L, Lin C-C, Yuan S-M (2016) Blind dual watermarking for color images' authentication and copyright protection. *IEEE Trans Circuits Syst Video Technol* 28(5):1047–1055

Analysis of Effective Area Radius and Its Dependency on Soil Nature in Grounding System



Aravelli S. L. K. Gopalamma  and R. Srinu Naik 

Abstract The paper is focusing on the most critical aspect in power systems from signal level to substation level, i.e., good grounding system. Like the immune system in humans, the abnormalities during unexpected overflow of critical parameters can be handled efficiently by this grounding system. The resistance of the grounding system should be low in practical (less than 5Ω). In general, we consider the provision of low resistance in designing grounding system but impedance plays major role in transient period. While installing PV plants, the grounding system designed such a way to get a less effective area radius during high front times (lightening) simply it is regarded as zone of influence effect on the protection system. It depends on the soil characteristics at the test site and respective soil treatment. This paper explains the dependency of the nature of the soil on the area affected during transients, and the performance analyzed by adopting artificial intelligence techniques. The dependency of soil properties to achieve reliable grounding grid design under zone of influence is studied. Soil resistivity value calculated to get permissible earth dissipating resistance, analysis done accordingly with several ranges of front time during transients using genetic algorithm optimization (GAO) and teacher and learner-based optimization (TLBO).

Keywords Effective area radius · GA · Grounding system · Soil treatment · TLBO · Transients

1 Introduction

From a general perspective, the grounding system is analogous to our immune system. When abnormalities occur, the way the immune system responds decide

A. S. L. K. Gopalamma (✉) · R. Srinu Naik
Dadi Institute of Engineering and Technology, Visakhapatnam, Andhra Pradesh 530046, India
e-mail: gopika.aravelli@gmail.com

R. Srinu Naik
Andhra University College of Engineering, Visakhapatnam, India

the intensity of the affected area (organ) in our body. In the same way, the performance of the grounding system during transients/lightening determines the resilient operation and lifetime of electrical equipment [1]. Whenever the electrode interacts with the soil, the performance of the protection equipment behavior becomes dynamic and depends upon the nature of the soil and environmental impacts [2]. The design of the grid and the value of design variable parameters perhaps become easy by adopting artificial intelligence techniques [3]. Several authors used different regression models for forecasting the parameters in power system/power electronic environment. Grounding grid performance becomes weird and unpredictable during transients/power frequency range [4, 5].

The dependencies of safety conditions might create severe abnormal hazards in power plants and substations. The behavior of soil under such situations can be analyzed using the concept, “effective radius” of the individual electrode affected area which is called as zone of influence [6, 7]. If the area allocated for the substation is huge, then there is no problem. However, if the design is for a new one with embedded design may create a problem [8]. By parallel connection of rods, the effective grid resistance is reduced but at transient level, the effect of inductance is more predominant. In such a scenario, one should study the dependency of these transient parameters on soil characteristics and grid impedance.

The effectiveness of spacing between electrodes under severe environmental conditions results in poor performance of the grounding grid [9]. Different shapes of optimal grid design have their own merits and demerits [10]. In this work, we assumed the vertical rod inserted in the soil having uniform properties such as resistivity and permittivity, porosity and soil stability.

Seasonal variations may result in drastic changes in soil properties such as salinity, humidity, soil stability, soil porosity and chemical composition. Sometimes these variations worsen the safety parameter values, which are responsible for personnel/industrial safety [11, 12]. Several methods are proposed to overcome the soil properties improvement those responsible for abnormalities in the power industry [13–16].

The design of limited space constraint-based non-cohesive silty soil for site explains the design model of the grid design for worst soil and limited space. The model particularly used for new embedded structure installations.

The main contribution of this work is to study the role of resistivity at transient level under uniform soil and appropriate electric properties other than soil resistivity. The dependency on the front time and radius of effective area of single vertical electrode analyzed to study the level of spacing needed between the electrodes. To analyze the values effectively application of the model adapted to artificial intelligence techniques such as TLBO and GAO.

1.1 Background

The grounding system plays a vital role in the protection of power equipment. It is essential because of the following [17, 18]

Personal safety: Personnel safety is provided by establishing a low impedance path [19] to the ground between sensitive equipment and metallic objects and pipes. High surge currents due to faults or lightning do not affect the voltage levels, which cause a shock.

Equipment protection: Protection systems for equipment such as protective devices and other internal services from sudden high fluctuations in voltage. The proper orientation devices depend on the low impedance current paths.

To reduce electrical noise: In communication, domain noise is a major problem, and it can overcome by maintaining proper voltage levels between sensitive electronic equipment provided low impedance between signal ground and earth by minimizing the interference from sources that acts as a source of noise (Fig. 1).

Table 1 represents the necessity of low resistance earthing design for different protection schemes in individual entities to industries. Moreover, this is essential for the sensitive control and automation sector, where communication plays an important role [19, 21]. Low resistance less than 5 Ω is acceptable for sensitive types of equipment in aviation/marine applications [22–24]. In industries, protection of each machinery to plant level automation needs a good governing resilient grounding system is necessary [25–27].

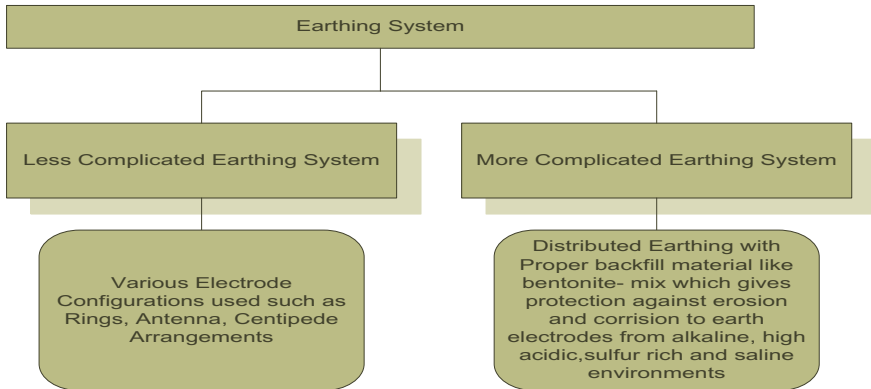


Fig. 1 General classification of earthing system [1, 20]

Table 1 General requirements of low earth resistance [5]

Item	Lightning protection	Fault protection	Signal monitoring reference	Earth electrode protection
Purpose	Dissipating lightning surge into the earth	Provides a path to fault current	Provides leakage paths for a static charge, reduces noise	Provides low resistance path
Requirements	It requires a low impedance path for low transient voltages	Low resistance path	Generates reference potential for signal voltages and sink for static charges	It provides a linking path for lightning, faults and signal reference systems connected to the earth
Designing factors	Low impedance path for high lighting surges	Low resistance and permissions for protective devices under faults	It should be designed in such a way that it should not degrade signal quality	Installed around buildings and towers to provide low resistance path

2 Role of Earth Resistance

The soil with appropriate humidity levels results in low resistive soils, which is the desirable texture of soil for good grounding grid performance tabulated in Table 2 [17].

2.1 Measurement of Earth Resistivity (Wenner Method)

Earth resistivity can be calculated in the Wenner method using the formula [28–30]

$$\rho = \frac{4\pi a R}{1 + \frac{2a}{\sqrt{a^2+4b^2}} - \frac{a}{\sqrt{a^2+b^2}}} \quad (1)$$

Table 2 Resistivity values of different soils [6]

Type of soil	Resistivity ρ (Ωm)
Wet organic soil	10
Moist soil	100
Dry soil	1000
Bedrock	10,000

Table 3 Measurement of resistivity using Wenner method; case 1: probe spacing $a = 4$

Npop/NIT	200			500			1000		
	ρ (Ω)	R (Ω)	b (m)	ρ (Ω m)	R (Ω)	b (m)	ρ (Ω m)	R (Ω)	b (m)
30	13.8	0.721	1.239	13.8	0.9064	2.4065	13.8	0.89	9.23
40	13.8	0.823	7.669	13.8	0.849	7.1557	13.8	0.874	9.1315
50	13.8	0.718	2.098	13.8	0.6183	6.0979	13.8	0.84	6.387

where $a =$ probe spacing and $b =$ depth and taking limits as $R [0.5 \ 1]$, $b = [0 \ 10]$ a varies from 4, 6, 10, respectively. Using TLBO, we got the following results below [19]

Tables 3, 4, 5 represent the values of soil resistivity under low resistance in the range of 0.5 to 1 by varying probe spacing ‘ a ’ value for different population size and maximum iterations using TLBO and GAO, respectively. In this study, we considered case 3 to analyze the dependency of the effective radius on front time and soil nature. Assuming resistivity of the soil having value nearly 180 Ω m at the test site. However, to get the low resistance, the soil treatment methods should follow or adopt different grid configurations to get soil resistivity as 31.5 Ω m. The main contribution of this work is to study the dependency of an effective area radius on the nature of the soil. So, we are not specifying the method of improving the nature of soil in this work.

Table 4 Measurement of resistivity using Wenner method; case 2: probe spacing $a = 6$

Npop/NIT	200			500			1000		
	ρ (Ω)	R (Ω)	b (m)	ρ (Ω m)	R (Ω)	b (m)	ρ (Ω m)	R (Ω)	b (m)
30	19.72	0.892	6.472	19.72	0.5475	4.648	19.72	0.566	3.135
40	19.72	0.542	8.4634	19.72	0.7741	4.609	19.72	0.9871	9.576
50	19.72	0.714	8.1574	19.72	0.8808	2.3429	19.72	0.5863	3.487

Table 5 Measurement of resistivity using Wenner method; case 3: probe spacing $a = 10$

Npop/NIT	200			500			1000		
	ρ (Ω)	R (Ω)	b (m)	ρ (Ω m)	R (Ω)	b (m)	ρ (Ω m)	R (Ω)	b (m)
30	31.9	0.603	4.2954	31.9	0.864	4.335	31.9	0.5373	3.0462
40	31.9	0.981	5.144	31.9	0.7326	2.7874	31.9	0.8143	4.9718
50	31.9	0.630	8.499	31.9	0.828	9.336	31.9	0.714	6.915

3 The Dependency of an Effective Radius on Front Time

3.1 The Expression for the Effective Radius [31]

The effective area of the buried rod/electrode in the uniform or multi-layered soil depends on the amount of fault current; it can tolerate the nature of the soil and the resistance of rod material. The impact of rod/electrode resistance is negligible. The expression for the effective radius (r_e) with respect to the parameters soil resistivity (ρ) and front time of lightning current impulse at the termination point (T) is as follows.

$$r_e = 0.34\rho^{0.42}T^{0.32} \quad (2)$$

The radius of the area affected by abnormal conditions reveals more information about the zone of influence. Under the zone of influence, the transient behavior results in impedance rather than pure resistive. The expression exposed in Eq. (1) depends only on the front time and the soil property, such as resistivity. Most of the cases, the change in permittivity effect is negligible compare with the above-specified parameters that affect the radius of the affected area. Zone of influence is nothing but the area affected under the rod when the fault current penetrates through it with the same radius. The dissipating resistance, also known as the resistance of the grid, decides the radius of an effective area. So we have to either reduce the resistivity of soil or the structure of grounding grid design.

Figure 2a represents the performance of the electrode under different soils having different properties concerning the dependency on front time and radius of an effective area for a single electrode. Figure 2b represents the performance of the buried electrode under low-high resistive variations with the area affected under constant front time. The significance of front time for a particular active community depends on the selection of electrical properties at the site area.

From Table 6, it is clear that the effective radius is reduced with soil treatment methods such as chemical treatment or with different grounding grid designs. The level of convergence using TLBO method of optimisation is lesser than GAO method. The effective radius of the area under the protection area can increase the resiliency of the power system and can reduce the interference and maintains low resistance. In this study, we have taken the front time range [1.8, 3] ms under constant permittivity and negligible temperature dependency.

Fault current

The steady state current value is the maximum fault current limit with respect to the temperature rises in the soil. The tolerable earth electrode steady state current is

$$I_{SS} = \frac{1}{R_e}(0.024\rho\Delta T) \quad (3)$$

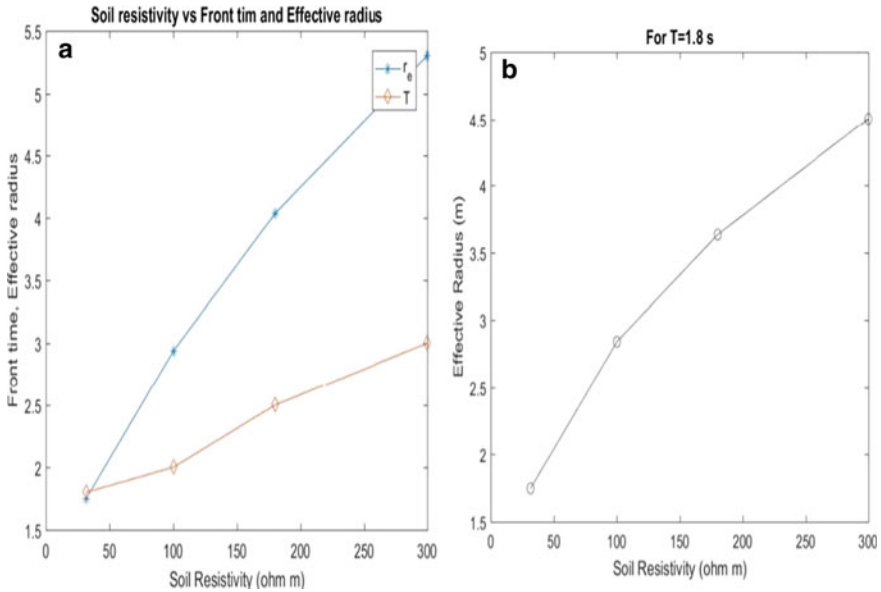


Fig. 2 **a** Characteristics of soil resistivity versus front time and effective radius. **b** Characteristics of soil resistivity versus effective radius under constant front time

Table 6 Effective radius with respect to soil resistivity

Algorithm	Soil resistivity $\rho = 180 \Omega\text{m}$		Soil resistivity $\rho = 31.5 \Omega\text{m}$	
	r_e (m)	NIT	r_e (m)	NIT
GAO	3.63	50	1.75	50
TLBO	3.63	5	1.75	5

ΔT = permissible temperature rise; R_e = electrode resistance; ρ = soil resistivity (Ω cm).

Transient current

The permissible transient current at $\Delta T = 60^\circ\text{C}$ can be calculated under dynamic t value where t represents fault duration.

$$I_t = \sqrt{\frac{1.75\Delta T}{\rho t}} \text{ amp/cm}^2 \tag{4}$$

The peak transient current which can handle by the earth electrode is expressed as

$$I_{tmax} = \pi d_e L_e I_{t60^\circ\text{C}} \text{ amps} \tag{5}$$

4 Results and Discussions

The effective radius dependency on soil resistivity parameter analyzed using TLBO and GA. Before and after treatment, we notice significant changes in soil resistivity. To check the computational convergence, the results with TLBO are compared with genetic algorithm optimization. TLBO gives better convergence, as shown in Table 6. Figures 5 and 6 represent the performance curves using the genetic algorithm for before and after soil treatment.

Figure 3a represents the performance curves of different soil structures, as mentioned in Table 2, with different soil resistive properties under constant front time for particular fault current. Figure 3b represents the dependency of the affected area radius on soil nature and its properties, soil resistivity in particular. The fault current value differs from industrial level prospects. However, its value does not depend on the area affected or zone of influence for particular earth electrode. For good soil, number of electrodes for getting low resistance is easy [33, 34]. However, it becomes tedious for high resistive soil with limited space because the zone of influence decides the spacing between the multiple electrodes in case of high resistive and dynamic soil structures (Figs. 4, 5 and 6).

Figures 7 and 8 represent the performance curves using the teacher and learner-based optimization algorithm for before and after soil treatment. The treatment of soil may be chemical or any other design considerations of rod design, such as layered rod design.

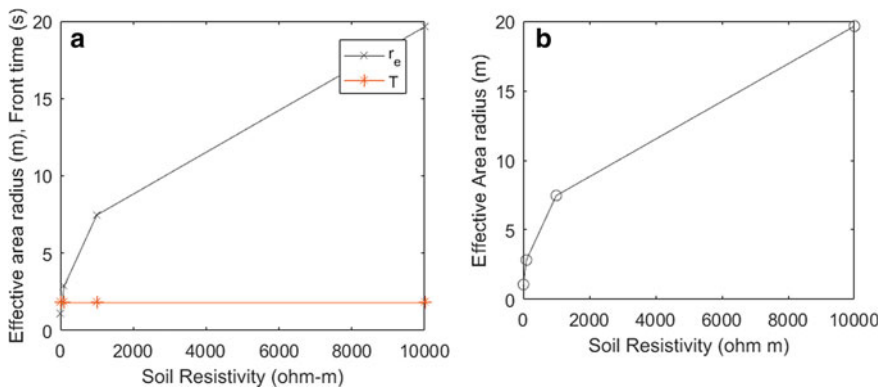


Fig. 3 **a** Characteristics of soil resistivity versus front time and effective radius. **b** Characteristics of soil resistivity versus effective radius under constant front time for different soil structures mentioned in Table 2

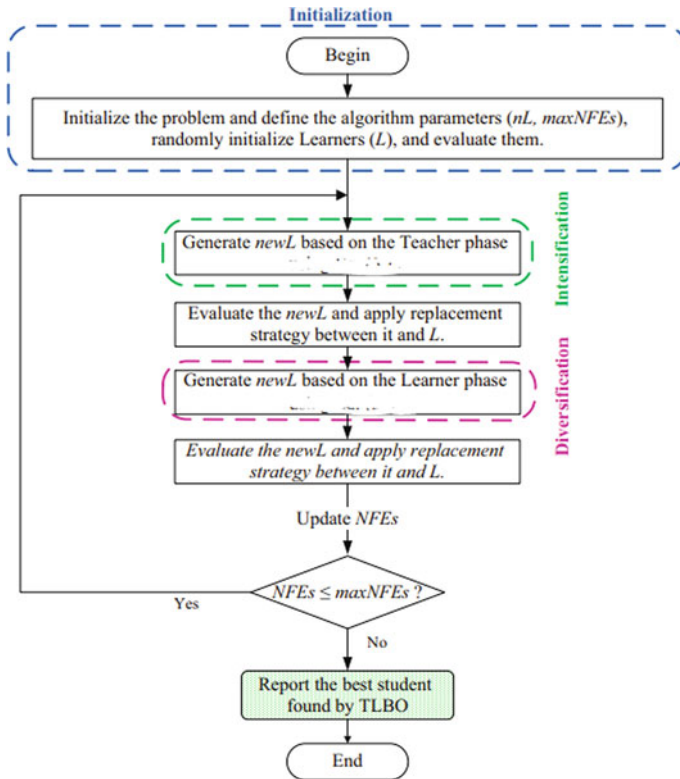


Fig. 4 Flowchart of TLBO [32]

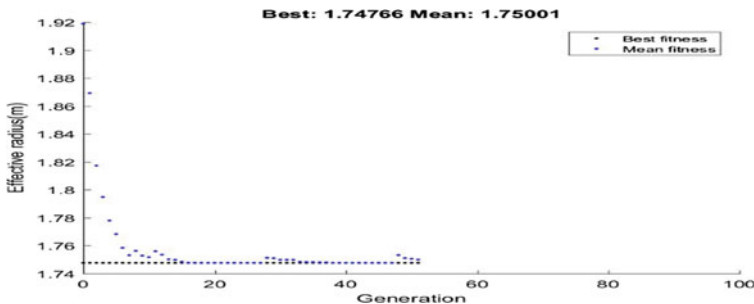


Fig. 5 Maximum iterations versus effective radius using GA (after treatment)

5 Conclusion

This paper aims to analyze the dependency of soil characteristics on the effective radius to predict the damage due to lightning over voltages. The front time of impulse

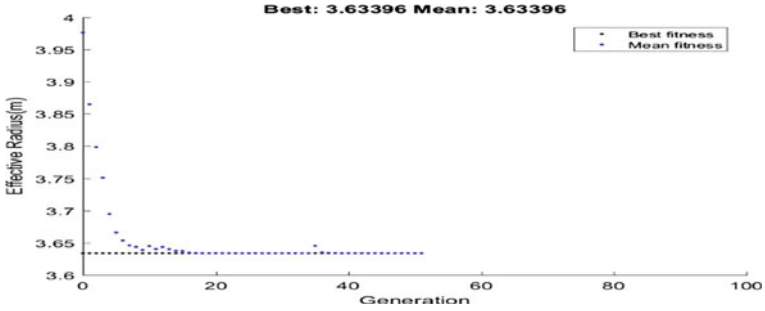


Fig. 6 Maximum iterations versus effective radius using GA (before treatment)

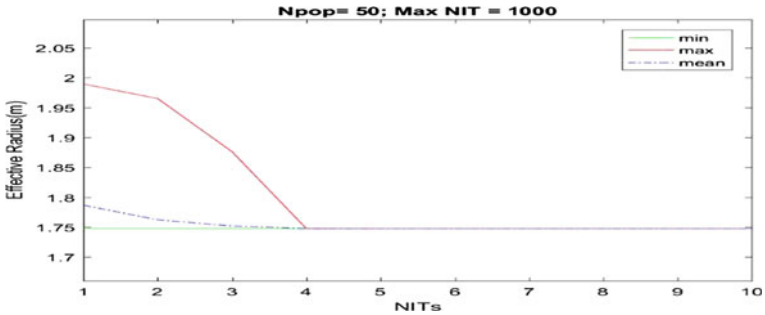


Fig. 7 Maximum iterations versus effective radius using TLBO (after treatment)

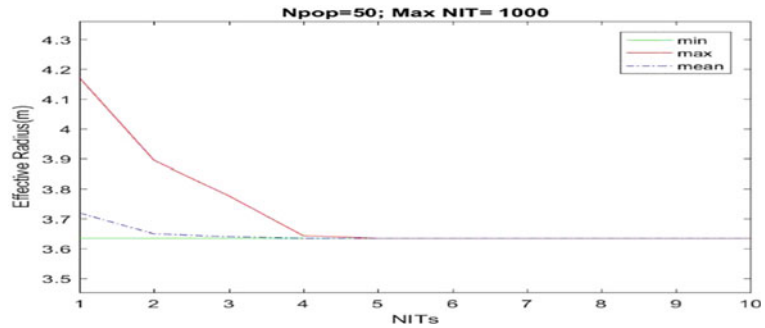


Fig. 8 Maximum iterations versus effective radius using TLBO (before treatment)

waves can result in severe abnormalities in power system equipment. With the motivation, the effective radius dependency on the parameters such as soil resistivity and front time of impulse wave studied, and the results tabulated using genetic algorithm and TLBO. The level of convergence is better while using TLBO method over GAO method. With improved soil using soil treatment methods, the effect of front time

impulse on the equipment is less, and the radius of the area affected is also less. Contributions summarized as follows:

1. Soil resistivity measurement using Wenner method has been done and analyzed the probe distance variations using TLBO optimization technique. This work exposes the dependency of probe spacing and resistivity of the soil to assess the earth resistance at the site.
2. The dependency of zone of influence and radius of the affected area on nature of soil studied considering different soil structures.
3. The results carried out using artificial intelligence techniques (TLBO) and compared the results with the genetic algorithm.
4. The role of fault current front time on zone of influence explained with necessary findings.

References

1. Lim SC, Gomes C, Ab Kadir MZA (2013) Electrical earthing in troubled environment. *Int J Electr Power Energy Syst* 47(1):117–128. <https://doi.org/10.1016/j.ijepes.2012.10.058>
2. Underwood AJ, Chapman MG (2003) Power, precaution, type II error and sampling design in assessment of environmental impacts. *J Exp Mar Bio Ecol.* [https://doi.org/10.1016/S0022-0981\(03\)00304-6](https://doi.org/10.1016/S0022-0981(03)00304-6)
3. Kara S, Kalenderli O, Altay O (2016) Optimum grounding grid design by using genetic algorithms. In: *ELECO 2015—9th international conference on electrical and electronics engineering.* <https://doi.org/10.1109/ELECO.2015.7394602>
4. Systems P, Committee E (2006) IEEE 1100:2005—IEEE recommended practice for powering and grounding electronic equipment
5. Ott HW (2009) *Electromagnetic compatibility engineering*
6. Department of Defense (1982) *Military handbook grounding, bonding, and shielding for electronic equipments and facilities Volume 1 of 2: basic theory, vol I*
7. Nowell RS (2004) *Grounding and lightning.* In: *Electric power substations engineering*
8. Hanaffi F et al (2014) Evaluation of grounding grid's effective area. In: *2014 international conference on lightning protection, ICLP 2014.* <https://doi.org/10.1109/ICLP.2014.6973157>
9. Lee HS, Kim JH, Dawalibi FP, Ma J (1998) Efficient ground grid designs in layered soils. *IEEE Trans Power Deliv.* <https://doi.org/10.1109/61.686969>
10. Colella P, Pons E, Tommasini R (2017) A comparative review of the methodologies to identify a global earthing system. *IEEE Trans Ind Appl* 53(4):3260–3267. <https://doi.org/10.1109/TIA.2017.2680399>
11. Abdullah N, Marican AMA, Osman M, Rahman NAA (2011) Case study on impact of seasonal variations of soil resistivities on substation grounding systems safety in tropical country. In: *2011 7th Asia-Pacific international conference on lightning, APL2011.* <https://doi.org/10.1109/APL.2011.6111092>
12. Heydinger AG (2003) Evaluation of seasonal effects on subgrade soils. *Transp Res Rec.* <https://doi.org/10.3141/1821-06>
13. Manikandan P (2015) Characterization and comparison studies of Bentonite and Flyash for electrical grounding. In: *Proceedings of 2015 IEEE international conference on electrical, computer and communication technologies, ICECCT 2015.* <https://doi.org/10.1109/ICECCT.2015.7225972>

14. Adesina LM, Akinbulire TO (2018) Development of an improved earthing method for power and distribution transformers substations. *Niger J Technol* 37(3):720. <https://doi.org/10.4314/njt.v37i3.22>
15. El-Tous Y, Alkhalwaldeh SA (2014) An efficient method for earth resistance reduction using the dead sea water. *Energy Power Eng.* <https://doi.org/10.4236/epe.2014.64006>
16. Glor M (2013) Modelling of electrostatic ignition hazards in industry: too complicated, not meaningful or only of academic interest? *Chem Eng Trans.* <https://doi.org/10.3303/CET1331098>
17. Committee S (2000) IEEE guide for safety, vol 2000
18. Estate M, South Africa P, Pretorius PH (2019) Principles included in lightning risk analysis
19. Nor NM, Haddad A, Griffiths H (2003) Factors affecting soil characteristics under fast transients. *Int Conf Power Syst Transients IPST 2(2003):6*
20. Joffe EB, Lock KS (2010) Grounds for grounding: a circuit-to-system handbook
21. Dong D, Zhang X, Luo F, Boroyevich D, Mattavelli P (2012) Common-mode EMI noise reduction for grid-interface converter in low-voltage DC distribution system. Conference proceedings—IEEE applied power electronics conference and exposition—APEC. <https://doi.org/10.1109/APEC.2012.6165859>
22. Tu Y, He J, Zeng R (2006) Lightning impulse performances of grounding devices covered with low-resistivity materials. *IEEE Trans Power Deliv* 21(3):1706–1713. <https://doi.org/10.1109/TPWRD.2006.874110>
23. Sekioka S, Sonoda T, Ametani A (2005) Experimental study of current-dependent grounding resistance of rod electrode. *IEEE Trans Power Deliv.* <https://doi.org/10.1109/TPWRD.2004.838660>
24. He J, Member S, Gao Y, Member S, Zeng R, Sun W (2005) Optimal design of grounding system considering the influence of seasonal frozen soil layer, vol 20, no 1, pp 107–115
25. Hasan H (2017) Characterisation of Earthing systems and materials under DC, variable frequency and impulse conditions [Online]. Available: <http://orca.cf.ac.uk/107495/>
26. Engineering E (2014) Experimental investigation of enhanced earth electrode system under high frequency and transient conditions
27. Method ST (2001) Field measurement of soil resistivity using the Wenner four-electrode method 1. Current
28. Wenner F (1916) A method of measuring earth resistivity. *Bull Bur Stand.* <https://doi.org/10.6028/bulletin.282>
29. Committee IC (1996) IEEE guide for soil thermal resistivity measurements. East
30. Pretorius PH (2018) Loss of equipotential during lightning ground potential rise on large earthing systems. In: 2018 IEEE international symposium on electromagnetic compatibility and 2018 IEEE Asia-Pacific symposium on electromagnetic compatibility, EMC/APEMC 2018. <https://doi.org/10.1109/ISEMC.2018.8393890>
31. Rao RV, Savsani VJ, Vakharia DP (2011) Teaching-learning-based optimization: a novel method for constrained mechanical design optimization problems. *CAD Comput Aided Des.* <https://doi.org/10.1016/j.cad.2010.12.015>
32. Leterme W, Tielens P, De Boeck S, Van Hertem D (2014) Overview of grounding and configuration options for meshed HVDC grids. *IEEE Trans Power Delivery.* <https://doi.org/10.1109/TPWRD.2014.2331106>
33. Grev LD, Heimbach M (1997) Frequency dependent and transient characteristics of substation grounding systems. *IEEE Power Eng. Rev.* 17(1):44. <https://doi.org/10.1109/MPER.1997.560681>
34. Dos Santos TLT, De Oliveira RMS, Sobrinho CLDSS, Almeida JF (2009) Soil ionization in different types of grounding grids simulated by FDTD method. SBMO/IEEE MTT-S international microwave and optoelectronics conference proceedings. <https://doi.org/10.1109/IMOC.2009.5427615>

Attack and Defense Methodology Against the Share Intents in Android



B. N. Arunakumari, P. Shrivathsa, and G. Vinodkumar

Abstract In today's world, almost every person owns a smartphone, out of which 83.8% are Android devices (Needham in IDC smartphone, share, 2021, [1]). Each day, there are millions of downloads of Android applications, either from trusted sources (like Google Play Store) or even from untrusted sources in the form of APKs. Due to this, a large number of users' mobiles are infected with malicious applications. According to McAfee Mobile Threat Report (2019 [2]), more than 65,000 fake apps were detected, growing in number each year. Fake apps resemble a very popular application by mimicking them in appearance and functionality, but also steal user sensitive information and/or blast the user's screen with advertisements for ad revenue. But Google Play ensures these apps are removed from time to time, as and when many users start reporting them. Furthermore, the average user may as well recognize the unusual behavior and uninstall the app. Hence, attackers have a hard time staying undetected and persist with the attack of spoofing. In this paper, we have highlighted an attack methodology (and defense), where the attacker can stay undetected and persist with his attack, which involves using the Android share feature. The share feature in Android is a very handy feature to share any content from various apps to other apps. For example, a user shares a post on Facebook with others via WhatsApp. When a user presses on the share button, a list of apps that support this share functionality is displayed to the user, through intents. This is how a typical share functionality is carried out. To utilize this feature for a persistent attack, a malicious attacker first spoofs the app's name and icon, to resemble a popular application (say WhatsApp). Next, he/she hides this app from the application listing (where all the installed apps are displayed to the user) (Android Developer Documentation on disabling the app icon from the launcher listing [3]; NexSoftSys article on hiding the app icon in the launcher programmatically, 2021 [4]). Now, when the user tries to share any content (a Facebook post), a list of possible apps to share is shown. In this list, the attacker's app will be listed with various other applications, but disguised. This will trick the user into selecting this app. When the unaware user selects this malicious app to share the content, the attacker can log/manipulate the

B. N. Arunakumari (✉) · P. Shrivathsa · G. Vinodkumar
BMS Institute of Technology and Management Bengaluru, Bengaluru, Karnataka, India
e-mail: arunakumaribn@bmsit.in

content, do unauthorized background processing as his application would be active. To remain undetected, the attacker's app calls a direct intent to the popular application (WhatsApp), which the user thinks he has selected, with the same/modified share content.

Keywords Android · Security · Share · Intent · Log · Spyware · Unauthorized processing · Malware · PHA

1 Introduction

Android, a very vastly used mobile operating system, is a system that is based on a modified version of Linux kernel and other open-source software [5, 6]. It is primarily designed for handheld mobile devices such as smartphones and tablets [1]. According to the announcement at Google I/O 2021, there are over 3 billion active Android devices all over the world [7].

Over the years, mobile phones have had many extra features inbuilt in them, other than the simple calling or SMS functionality. Google/mobile phone manufacturers support third-party developers by providing development platforms and software stores (Google Play Store/Samsung's Galaxy Store), where developers can distribute their applications. Further, many online websites share Android applications through APKs. Many untrusted websites share legitimate-looking malicious APKs that an unaware user might install unknowingly. This opens a wide avenue of attacks for an attacker.

Adversaries use malicious applications as a common attack vector to gain control of victims' mobile devices. To carry out this attack, the attacker installs a malicious application on a target mobile device, from an unofficial source in the form of APKs. They avoid placing it on an official app store due to the increased risk of detection or other policy restrictions. In the user's favor, the mobile devices are often configured to be installed only from an authorized app store, which prevents this kind of attack. It is always the technically unsound or ignorant users, who are prone to this attack. The message passing system in Android, called "intents" can become an attack surface, paving another avenue of attack for the attacker. An activity is a UI screen that is displayed to the user. Almost all activities interact with the user. Every app contains an `AndroidManifest.xml` resource file in the root of the project, which contains essential information about the application and is read by the Google Play Store and the underlying operating system, before installing.

An intent in Android is an abstract description, to perform an operation. It is mostly used to start activities, start services and send messages between two activities. Figure 1 represents the structure of the app and various ways it can interact with the Android operating system. An intent filter is an expression in an app's manifest file that specifies the type of intents that the component would like to receive. For example, by declaring an intent filter for sharing, the developer makes it possible for other apps to directly call his app to share any content. Figure 2 represents a sample

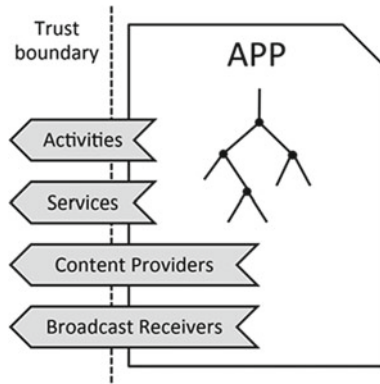


Fig. 1 Depiction of an Android app’s exported components

```
<activity
  android:name="com.android.email.activity.ComposeEmail"
  <intent-filter>
    <action android:name="android.intent.action.VIEW"/>
    <action android:name="android.intent.action.SENDTO"/>
    <data android:scheme="mailto" />
    <category android:name="android.intent.category.DEFAULT"/>
  </intent-filter>
  ...
</activity>
```

Fig. 2 Sample intent filter in AndroidManifest.xml file

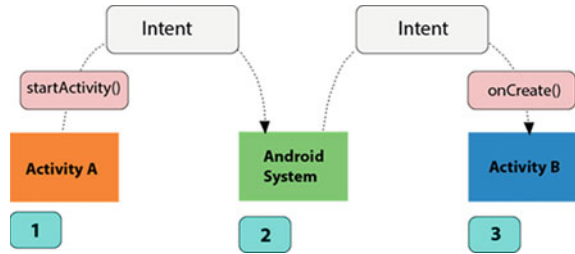
intent filter in an AndroidManifest.xml file which contains an intent filter for email intents.

When a new application is opened, an intent is called for that application. Similarly, when the share button is pressed, a share intent is called from the calling application, bundled with the content. When an intent is called, the Android sub-system searches for the right component to start. It does so by checking the intent and the respective intent filters declared in the manifest files of all the other apps installed on the device. If a match is found, the Android sub-system starts that component and sends the content of the intent to it. If many intent filters are compatible with the given intent, then an app listing is displayed to the user to choose from. Figure 3 gives a pictorial overview of the process.

2 Motivation

In the cyber-space, there is a constant war for sensitive information. The attackers constantly try to steal this information, whereas the security professionals carry out

Fig. 3 Depiction of how the intents are used to invoke activities from activity A to activity B



defense strategies to keep the attackers at bay. But still, attackers find many ways to constantly attack and come up with new innovative ways to circumvent the usual defenses and achieve their goal to steal sensitive information. Even though the defense systems are constantly updated and maintained, a new attack will almost always be discovered. The main motivation for this paper is to identify one such attack vector; which, if used by attackers, would prove to be dangerous; as it is very difficult to detect. This would also be used to have unauthorized processing on the victim's Android mobile. As stated earlier, there are a lot of downloads of infected applications through third-party sites. Even though running these infected applications, only are run when the user explicitly invokes the app from the listing. Only then the malicious activity is carried out. Some malicious apps have their original name, with the original icon, the user disregards them as adware and uninstalls them quite easily, as he realizes it was installed on his Android phone without his consent. But this kind of attack starts only when the user taps on the app, which has a very less chance of success. Hence, we propose this new methodology, where the attack takes place when the user shares any content and unknowingly selects the application, thus increasing the success rate of the attack and maintaining the covert nature. Another case is when the malicious application spoofs its identity with a known app. For example, if the malicious app takes the identity of a popular application (say WhatsApp), then when the user notices two (WhatsApp) icons next to each other with the same name and icon, he is alerted of misconduct and immediately uninstalls the duplicate; or he might as well get a technical expert's guidance on the same. Furthermore, when he/she does ignore it and selects the malicious app, and when the app does not behave the way the user expects it to, the user suspects misconduct and uninstalls the application, thus ending the attack. To counter this, the attacker removes the malicious app from the app listing that is displayed to the user; the attacker rather invokes the app process when the user shares some content, through share intents. This way, it makes it difficult to identify the malicious app, hence giving a more chance of success and rather long persistence of the attack to the attacker.

The main advantages of attacking through share intents are:

- This attack is very difficult to identify
- It has a higher rate of success for the attacker
- The victim stays infected for a longer period.

3 Literature Survey

Android security has been the focus of research efforts in the past few years. Many researchers have worked on intents and various kinds of attacks on an android device. Most of them discuss various attacks that can be performed using the vulnerabilities in the intent feature of the Android operating system. Some of the examples are discussed in the research paper, “Android Inter-App Communication: Threats, Solutions and Challenges,” University of Chinese Academy of Sciences, Beijing, China [8]. This paper states various ways the intent can be attacked by discussing implicit and explicit intent attacks. The other main research papers that were vital to the theme of this paper were “Phishing Attacks on Modern Android” [9] and “Detecting Mobile Application Spoofing Attacks by Leveraging User Visual Similarity Perception” [10]. These two papers highlighted the current threats in mobile application spoofing and phishing attacks, highlighting various attacks and defenses against them. Other research papers included innovative fuzzing methods to attack intents, as discussed in “intent Fuzzer: Crafting intents of Death,” [11]. This paper elaborates a comprehensive intent fuzzing framework with core IPC functions. We also encountered papers that discussed various defenses against intent-based attacks, which defend it from a malicious application that tries to call an implicit intent from an outside context, as discussed in [12]. It also discusses automated discovery techniques and prevention. An important resource for benchmarking vulnerabilities in Android apps called “GHERA” [13]. An automated testing tool for finding holes in Android security infrastructure called “Sealant” [14]. This technique combines static analysis of application code with run-time monitoring of IPCs through channels, which helps prevent these kinds of attacks.

In this paper, we take a different approach. Instead of discussing various methods of attacking the intents, we discuss a targeted way for an attacker to perform malicious processing and stay undetected for a persistent attack. We also list some of the general detection techniques that can be used to prevent this attack; combined with some of the general defenses that can be used to mitigate this kind of attack.

4 Proposed Methodology

For an attacker to successfully carry out the mentioned attack, he does so in these phases:

- Phase I: Install/deploy the application into the target device.
- Phase II: The user clicks on any share button to invoke a list of apps to share the content. Then, the user selects the malicious application.
- Phase III: The attacker carries out post-exploitation such as spying/unauthorized processing or logging.
- Phase IV: The attacker carries out cover-up tasks to maintain anonymity.

4.1 Implementation

To implement this kind of attack, we need an application with a covert name, as a well-known application. We use the example of a popular chatting application WhatsApp. The requirements for carrying out this attack are a malicious APK and a means to install it onto the target.

The implementation of the attack is carried out in these 4 phases:

Phase I: The attacker first creates an application that resembles WhatsApp in the name and icon, with the post-exploitation code. The requirements for the attack are for an application to be installed in the target's smartphone. The attacker uses various ways to get this specially crafted APK onto the target. Some of the ways are mentioned below:

- **Speare Phishing:** The attacker sends the APK as an attachment in an email.
- **Third-Party App Store:** The victim installs the APK from a third-party store (other than an authorized app store), which may not have a thorough examination or scanning of the app for malware or any policies implemented to prevent misconduct.
- **Speare Phishing Link Attachment:** The attacker includes a link to the APK within an email, website, text message (E.g., SMS, WhatsApp) or any other platform.
- **Unwanted Downloads:** Some malware installs other malware on the device it's installed on, automatically, without the victim noticing it.
- **Google Play Store:** Lastly, he can also manage to get this app on the play store if he can get past the Google Play security verifications.

With any one of the aforementioned techniques, the attacking application is installed on the target's phone, with the title as "WhatsApp" and with the same icon as WhatsApp.

Phase II: After the attacker gets an initial foothold by getting the application installed on the target, on the first launch, the application is hidden under plain sight by programmatically disabling it from the app listing [3, 4]—which prevents an average user from uninstalling the app easily (The user will now have to uninstall it from Settings > Apps if at all he/she wishes to remove the app). Then, the attacker waits for the target to share any content. When a share button is pressed, a list of all the apps is shown which have a share intent filter in their respective Android manifest. Here, all the apps that have this intent filter set are shown, with the attacker's malicious app being one of them; and the user picks an app from the list. For example, the target user tries to share a post on Facebook (Fig. 4). As soon as the victim clicks on the share button on the Facebook app, Facebook calls a share intent to the Android system. Since many apps share the same intent filter, a list of apps is displayed to the user. In the said list, if the target has WhatsApp installed on their device, it will be shown among other potential share options, including the attacker's covert application. When the target wishes to select WhatsApp as his share option, he is

now displayed with original WhatsApp, also with the attacker’s malicious WhatsApp (Fig. 5).

There is an equal chance that the target may select either of the apps, the original or the hoax. When the user selects the hoax app, the attacker moves on to the next phase of the attack.

Phase III: The next phase of the attack is mainly post-exploitation. As the target selected the attacker’s application, the attacker’s application is brought to the foreground. In other words, the attacker’s activity is launched and then the attacker’s

Fig. 4 Facebook post being shared

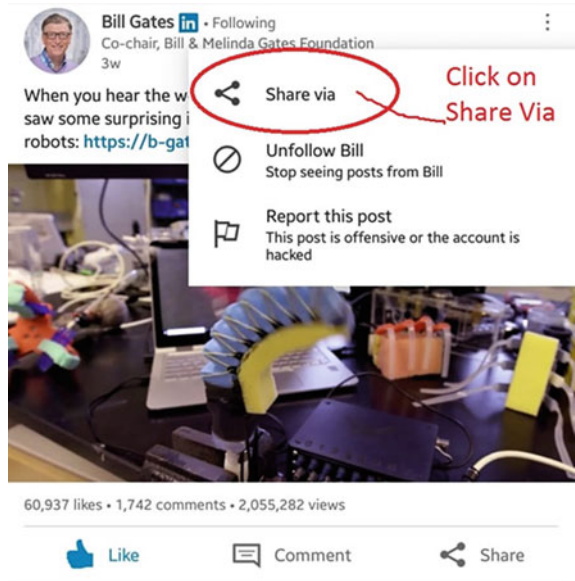
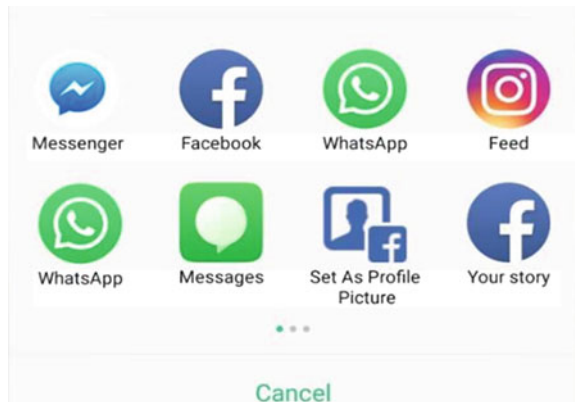


Fig. 5 Share listing of apps where there are two WhatsApp icons where one of them is malicious



post-exploitation is executed. There are various methods of post-exploitation, some of which that are more suitable for this kind of attack are listed below:

- Logging and transmitting the target's share content to the attacker's database.
- Manipulating the target's share content to include any advertisement or malicious links.
- Invoking spyware functions like:
 - Camera still image captures
 - Logging the GPS location
 - Audio recordings
 - Phonebook logging
 - Call history logging
 - SMS logging, etc.
- Invoking static shell commands, or even a reverse binding shell.
- Using the Meterpreter shell. Meterpreter is an attack payload by the Metasploit framework, that opens an interactive shell between the victim and an attacker, giving him the ability to exploit the victim's machine.

The above list is left to the imagination of the attacker; these are just to name a few.

Phase IV: The most important phase in this attack could be regarded as preserving the attack's covert nature. The target had unknowingly clicked on the attacker's application, if the target's intended action was not completed, the target may become suspicious and would alert of some wrong being. This would potentially compromise the attacker and would cause the target to analyze the situation and zeroing down the cause, potentially leading to uninstalling the application or even a system-wide scan to remove this malicious anomaly. This would be the case even if the target was not of a technical background, as he/she might consult a technical professional to "fix" the issue, spoiling the attack. Hence, to avoid this altogether, the attacker's app remains in cover by redirecting the share content which was received, back to the actual application. In this way, the target does not realize any abnormality. To achieve this, the app calls a direct intent to the WhatsApp activity with the same share content.

5 Detection and Defenses

By discussing this attack method, we now come to the results that were observed and the various defenses that can be used for this kind of attack. There is a large sum of users who download APKs off of the Internet for getting any paid apps, which are on the Google Play Store, for free. This involves a lot of risk of installing malware. There are over a million downloads for APKs through which the attacker can channel

his attack. The study shows 0.6–0.8% potentially harmful apps (PHA) were installed in the users' Android devices, from harmful websites across the globe [15, 16].

Even though these users are attacked, the attack does not usually last for long. When the user notices an anomaly in his device, like black screen flashes, and hanging of the device or even slow operation, they realize it was caused by the app that was just installed and immediately uninstalls the app; or in the extreme cases, hard reset the device; thus ending the attack. Therefore, if this attacking technique is used by an attacker, it is estimated that almost 90% of the infected victims remain infected. Also, because the installed application is removed from the app listing, the user cannot conventionally uninstall the app, through the home screen, and will have to take the tedious path of going to the Settings > Apps and searching for the application through a long list and click uninstall; which, some of the non-technical users may not find it straightforward to do so. So, even though the user notices a mishappening, they will have to be technically sound to uninstall it. This adds to more chances of the victim remaining unaware and the attack maintaining control over the victim's device.

5.1 *Detection Techniques*

This attack can be classified as a dangerous attack, as it is very difficult to detect once it has been installed on the target device. It maintains its covert nature and therefore, remains under plain sight, only invoked when any share intent is called. Therefore, it is better for the detection to happen before installing the application, as it is a tedious task to detect it afterward. To detect this attack and these kinds of attacks, we have to analyze the app before installing it and scan it to check if it contains any malicious entries in the Android manifest. Another way to detect is to check its intent filters and assess if those intent filters are genuinely used for the app. The next major thing to detect any kind of malware is to assess the permissions requested. If an app uses location, microphone, camera permission, it has to be thoroughly analyzed before proceeding further to allow the user to use the application. To detect this attack after the app has been installed, we analyze every intent that is called on the Android OS. This can be done like a scan for a specific amount of time, if not for a long time. When this scan is done, all the intents are analyzed for where one intent calls another external intent, right after it was called, which acts as middleware to other apps. This process is carried out using an intent-based communication channel.

To do this we follow certain steps.

- Detecting the usage of intent in applications, and extracting the information from the intent.
- Then, the intent communication is logged, with the source of the intent and the destination application which received the intent.
- Upon further logging, if the destination app of one intent is the source of the next intent, then we log this application.

- Finally, we display all such apps which were logged and which are possibly malicious or benign. These require special attention, hence displayed to the user.

As there are a large number of apps available in the App Store, the methods of detection also should become scalable.

5.2 Defenses Against This Attack

Defense against this attack is to detect well in advance, at the time of installation, for a misused intent filter, and to immediately abort the installation and delete the APK file from the user's device, also notifying the user of the kind of threat that the application would have caused. Also, after installation, if any application is found to be using such a technique for an attack, the application has to be force stopped immediately and uninstalled, notifying the user. The installation of a security model and service framework of the non-interference security model is to be done to strengthen the defenses against this kind of attack. In this security model, the attacker's process cannot have a covert channel of communication to access the sensitive information of the user, even after being able to execute. The attack will be stopped right in its initial stages where it cannot access any other sensitive information, where the post-exploitation can be made useless. Other than these defenses, the rest are mainly focused on defense against the installation of malicious apps on the users' devices. If the attack is stopped at the source, there is far less threatening. But even after a lot of security awareness, most of the time malicious apps find their way onto the users' devices.

Hence, we give general guidelines as defenses for preventing this kind of attack below:

- Only download apps from a trusted source. Avoid installing APKs directly, prefer installing only from the Google Play Store.
- Get alerted when you see duplicate apps in the listing, make sure to remove the one that's the hoax.
- When an application to share is selected, see if there are any redirects, usually identified by a screen transition, a white blank screen then to the actual WhatsApp page.
- Notice any delay in the opening of the app selected for share, or any slow operation of the device when the share option is selected and if you notice any, uninstall the app that was meant to be shared.
- Use any defense software like SEALANT [14], for identifying inter-app security holes and vulnerability assessment tools or repositories like GHERA [13]. Any anti-virus or anti-malware software on the device might help defend against this kind of attack.

6 Conclusion

Android security has been the major focus of research in the recent few years; there is an ever-increasing threat to Android devices. The attacks target user data and focus on full control over the user's device. There are a lot of papers that talk about vulnerabilities in Android intents, and how Android handles the intents, and how this has qualified to be an attack surface for attackers. In this paper, we highlight an avenue of attack, which is carried out in four phases. It also discusses various post-exploitation techniques that an attacker can use after having the malicious app installed on their devices, like covert logging or spying. We also discuss how the attacker can stay hidden from the victim, thus having a longer impact period. Lastly, we discuss various ways to detect this kind of attack and some of the defenses against it. We would like to conclude by saying, even though this is quite a simple attack to perform, which just shows a hoax app entry in the usual share listing, and waits for the user to tap on it; but when used in the right way, proves to be disastrous. It has a very low detection rate and a high persistent period. This attack is one of the many ways an attacker can attack an unaware victim. Thus, the users have to be very careful when installing any app on their device and do a regular clean-up of the device.

7 Future Work

In this paper, we have mainly focused on one type of intent in Android, i.e., share intents. But this can also be extended to any other type of intents, such as email intents, new activity invoking intents, etc. The attacker's covert application can be listed with different names depending on the kinds of intents, to further increase the chance of being invoked.

Another very dangerous area of having intents to be faked is the banking application intents, like Unified Payments Interface [17] (UPI) payments, where the attacker can intercept these intents and invoke a payment screen, for UPI PIN-logging and/or payment detail capturing. These are the various next avenues to be explored and for defenses to be strengthened.

References

1. Needham M (2021) IDC smartphone, share <https://www.idc.com/promo/smartphone-market-share>
2. McAfee Mobile Threat Report (2019) <https://www.mcafee.com/enterprise/en-us/assets/reports/rp-mobile-threat-report-2019.pdf>
3. Android Developer Documentation on disabling the app icon from the launcher listing https://developer.android.com/reference/android/content/pm/PackageManager#COMPONENT_ENABLED_STATE_DISABLED

4. NexSoftSys article on hiding the app icon in the launcher programmatically (2021) <https://www.nexsoftsys.com/articles/how-to-hide-application-launcher-Icon-in-android.html>
5. Android (operating system): [https://en.wikipedia.org/wiki/Android_\(operating_system\)](https://en.wikipedia.org/wiki/Android_(operating_system))
6. Application-Fundamentals. <https://developer.android.com/guide/components/fundamentals.html>
7. Cranz A (2021) The verge. <https://www.theverge.com/2021/5/18/22440813/android-devices-active-number-smartphones-google-2021>
8. Wang J, Wu H (2018) Android inter-app communication threats, solutions, and challenges. ArXiv abs/1803.05039
9. Aonzo S, Merlo A, Tavella G, Fratantonio Y (2018) Phishing attacks on modern android. In: Proceedings of the 2018 ACM SIGSAC conference on computer and communications security (CCS '18). Association for Computing Machinery, New York, NY, USA, pp 1788–1801. <https://doi.org/10.1145/3243734.3243778>
10. Malisa L, Kostiaainen K, Capkun S (2017) Detecting mobile application spoofing attacks by leveraging user visual similarity perception. In: Proceedings of the seventh ACM on conference on data and application security and privacy (CODASPY '17). Association for Computing Machinery, New York, NY, USA, pp 289–300. <https://doi.org/10.1145/3029806.3029819>
11. Sasnauskas R, Regehr J (2014) intent fuzzer: crafting intents of death. In: Proceedings of the 2014 joint international workshop on dynamic analysis (WODA) and software and system performance testing, debugging, and analytics (PERTEA) (WODA+PERTEA 2014). Association for Computing Machinery, New York, NY, USA, pp 1–5
12. Jing Y, Ahn G-J, Doupé A, Yi JH (2016) Checking intent-based communication in android with intent space analysis. In: Proceedings of the 11th ACM on Asia conference on computer and communications security (ASIA CCS '16). Association for Computing Machinery, New York, NY, USA, pp 735–746. <https://doi.org/10.1145/2897845.2897904>
13. Mitra J, Ranganath V-P (2017) Ghera: a repository of android app vulnerability benchmarks. In: Proceedings of the 13th international conference on predictive models and data analytics in software engineering (PROMISE). Association for Computing Machinery, New York, NY, USA, pp 43–52. <https://doi.org/10.1145/3127005.3127010>
14. Lee YK, Bang JY, Safi G, Shahbazian A, Zhao Y, Medvidovic N (2017) A SEALANT for inter-app security holes in android. In: 2017 IEEE/ACM 39th international conference on software engineering (ICSE), pp 312–323. <https://doi.org/10.1109/ICSE.2017.36>
15. Statista Research Department (2021) <https://www.statista.com/statistics/199698/malware-and-spyware-targeting-mobile-devices-2011/>
16. Google Android Security Report 2018 https://source.android.com/security/reports/Google_Android_Security_2018_Report_Final.pdf
17. NPCI UPI (Unified Payments Interface) <https://www.npci.org.in/what-we-do/upi/product-overview>

Comparative Study of Traffic Light and Sign Detection Techniques



Aryan Jain, Swarup Totloor, Tanisha Agarwal, M. N. Pavan Kumar, and M. L. J. Shruthi

Abstract In this paper, we look at the various approaches to traffic light and street sign detection. In the traditional image processing-based approach, we primarily use a circular Hough transform with color masks to detect traffic lights. For the more complex approach, we deploy convolution neural networks in combination with previously proposed feature extractors to aid with traffic light detection along with a confidence score. We make use of the SSD ResNet V1 trained on the COCO dataset in addition to the Inception V3 architecture trained on the ImageNet dataset. All of these experiments are performed on the Berkeley Deep Drive dataset. We compare these techniques based on parameters like accuracy, computation time, and memory usage, and highlight the advantages and disadvantages of each type.

Keywords Computer vision · Convolutional neural networks · Hough transform · Image processing · Street sign detection · Traffic light recognition

1 Introduction

Traffic light detection and street sign detection have always been central problems when it comes to the implementation of autonomous vehicles. While traditional methods of image processing have existed for quite a while, for instance, using the Hough transform with color masks for traffic lights, the recent boom in the usage of deep learning techniques like convolutional neural networks (CNNs) also proves to be an exemplary method for the detection of both traffic lights and street signs. In this paper, we aim to analyze and discuss each of these techniques and compare them with each other based on parameters like accuracy, memory usage, and computation time. Our street sign model currently identifies 3 signs in the image processing approach (shown in Fig. 1) and 1 sign in the CNN-based approach. For the analysis, we use the Berkeley Deep Drive dataset, as it provides a thorough selection of diverse

A. Jain (✉) · S. Totloor · T. Agarwal · M. N. Pavan Kumar · M. L. J. Shruthi
Department of Electronics and Communication Engineering, PES University, Bangalore, India
e-mail: Aryan.jain227@gmail.com

© The Author(s), under exclusive license to Springer Nature Singapore Pte Ltd. 2022
V. Mahajan et al. (eds.), *Sustainable Technology and Advanced Computing in Electrical Engineering*, Lecture Notes in Electrical Engineering 939,
https://doi.org/10.1007/978-981-19-4364-5_13

153

environments. We have opted for video datasets over image datasets as the model is to be incorporated for real-time applications.

We have organized our paper as given: The following section reviews and summarizes the various literature and prior work done on the various methods described above. Section 3 talks about the traditional method of detection of traffic lights and street signs using image processing techniques. The working and implementation of detection using CNNs are also presented in this section. Section 4 presents the results from the tests done on these techniques. The limitations and scope of the future work are tackled in Sect. 5. The paper is then finally concluded in Sect. 6 (Figs. 2 and 3).



Fig. 1 Signs detected



Fig. 2 a Raw image. b Color mask. c Result detection



Fig. 3 Street sign detection using the color-based approach

2 Literature Review

Omachi and Omachi [1] propose a method for the detection of traffic lights, where a specific range of red, yellow, and green pixels is chosen. To detect the traffic light, Hough transforms and Sobel filters are used. The proposed model is said to work at an accuracy of 87%. Shi et al. [2] propose a method wherein they suppress the background that increases accuracy as the model can better focus on the foreground. Charette and Nashashibi [3] put forward an approach where grayscale processing is used alongside spotlight detection. The algorithm runs in real time. Karkoub and Saripalli [4] used an algorithm based on XGBoost which works within the time limit challenges of real time. The median filter is deemed most appropriate to denoise. The illuminated light is then extracted using color segmentation techniques.

For street sign detection, Karami et al. [5] perform a comparison on image matching techniques such as SIFT, SURF, and ORB. Although ORB is observed to be the fastest algorithm, SIFT performs the best in real-world scenarios as it takes into account image rotations, affine transformations, intensity, and viewpoint change in matching features. They use the optimal constant value proposed by Lowe [6] for the SIFT algorithm. Kiran et al. [7] put forward an SVM-based model for traffic sign detection. Color segmentation techniques are applied after converting to HSV from RGB. This model performs worse in real time due to sign discoloration and viewing angles.

Arcos-Garcia et al. [8] propose an analysis for an evaluation neural networks in combination with various feature extractors. We use the results obtained on various parameters as a basis for our model selection. Wu et al. [9] propose a traffic sign detection approach based on a combination of color segmentation techniques and CNN implementation. The proposed architecture fails to do so in a lesser amount of time, making it non-implementable in real-world scenarios. Vennelakanti et al. [10] also propose a system for traffic sign detection and recognition.

In the recent times, deep learning has been used by taking neural networks. Yan et al. [11] used a YoloV5 architecture that led to high computation speeds with a slight trade-off with accuracy. Nguyen et al. [12] used deep learning for detection of traffic lights in night time which performs with 80% accuracy currently.

3 Experimentation

3.1 Detection Using Image Processing

We split the traditional image processing approach into two different parts, each for traffic light detection and street sign detection, respectively.

We deploy a color-based approach for the detection and recognition of traffic lights. The data flow of the approach is shown in Fig. 4, where we utilize the concepts of Hough transform [13]. We use Circle Hough transform to detect circular

objects, which is the case for traffic lights. The identification of the traffic lights is a combination of the color represented by the binary image with detected circular objects.

Frames extracted from the BDD dataset are fed as input to the model. The frames are converted from RGB to HSV as HSV performs better concerning real-world scenarios [14]. Based on known knowledge, three color masks are made, namely red, green, and yellow representing the colors of a traffic light. This is done by manually selecting a range in HSV that represents traffic light colors and then applying it as a mask. The mask then helps with the detection of all similar colored objects in the frame by converting the frame into a binary color space. Having detected the color, we now focus on detecting circular objects with a specific size range. To perform the detection of circular objects within the image, we use the Circular Hough transform [15]. The classified regions that satisfy the thresholding criteria are detected as traffic lights based on color values which can be seen in Fig. 2a–c.

Street sign detection is analogous to traffic light detection as both are color-based techniques. It works using FLANN [16] which takes its roots from KNN matching. It contains a collection of algorithms optimized for fast nearest neighbor search in large datasets and high-dimensional features. The model is shown in Fig. 5 which shows the data flow of implementation.

The first step is blurring the street sign. A 5×5 Gaussian mask is applied to perform blurring. This is done to overcome the issue of varying illumination. In the second step, we use the SIFT keypoint descriptors, based on Lowe's method [6] to identify key points in both templates and frames. The next step involves KNN matching, in which Hamming distances of the matched descriptors are sorted, and the matches with the lowest distance are selected. We fix the parameter for KNN by setting k to be equal to 2. This was done by iterating over different values of k

Fig. 4 Block diagram for traffic light detection using Hough transforms

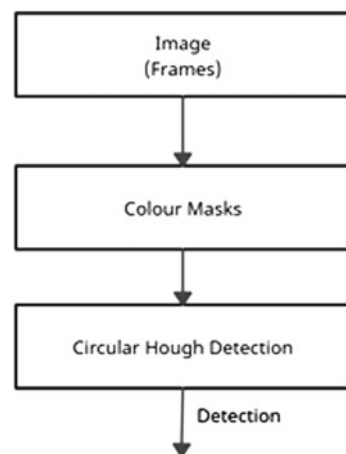
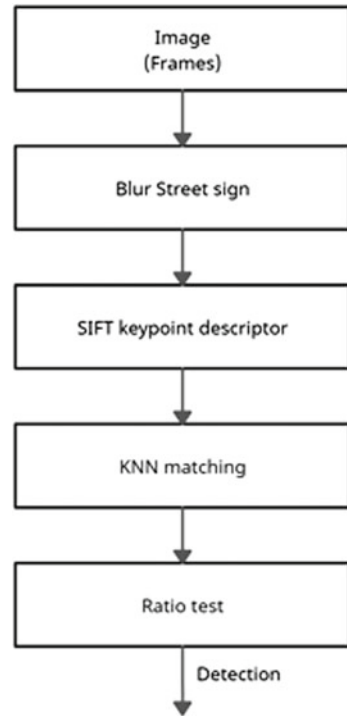


Fig. 5 Block diagram for street sign detection using SIFT



and choosing the best performing one. A larger value also compromises on computation time and memory usage. The FLANN library is used to speed up the process described. The final step is the ratio test.

It is performed with the assumption that the best matching has a much closer Hamming distance than the second best. The street sign detection can be seen in Fig. 3.

3.2 Detection Using Neural Network

Results obtained from Hough transforms were not real-world deployable, so we switched to a deep learning-based approach that gave far higher accuracies. For the identification of the traffic lights, we use a convolutional neural network that is trained on the feature vectors of the traffic light. The CNN is capable of taking raw images as input so we exploit that functionality for detection. The problem of feeding raw images as input is that the entire image is taken as a feature vector. The approach to solving the proposed problem is extracting traffic lights to use as training data. The basic flow of the model is shown in Fig. 6. Frames from the dataset as shown in Fig. 8 are fed into the feature extractor. The feature extractor used was SSD ResNet

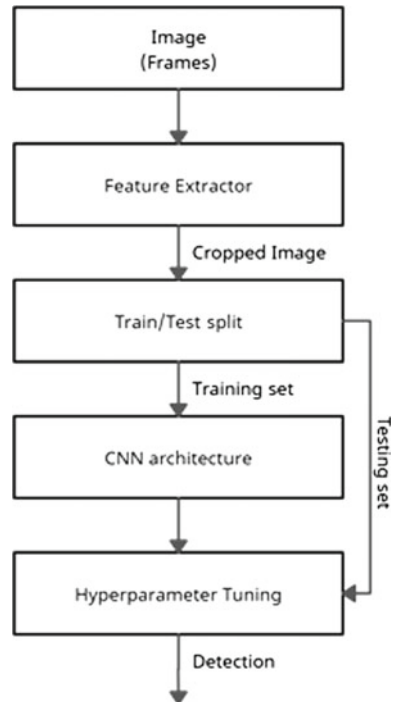
V1 [8] that had been pre-trained on the COCO dataset for the extraction of traffic lights from the frames. The breaking of feature extractor and CNN architecture helps us speed up the process and also in implementing transfer learning. These traffic lights as seen in Fig. 9 are classified into 4 segments and contain over 1800 images each (red light, yellow light, green light, and NOT traffic light) to aid the neural network. These classified subsets are then fed to the neural network for training. We perform image augmentation on all images to artificially expand the dataset without having to provide more images. The CNN architecture used for model building was Inception V3 [17] that was trained on the ImageNet dataset. This architecture provides great support for transfer learning as it does not have to perform feature extraction, which is the most computationally expensive part of the process. It consists of both symmetric and asymmetric blocks wherein the blocks perform convolutions, average and max pooling, concats, and dropouts. The loss function is taken to be categorical cross-entropy and the optimizer used is AdaDelta [18] which is then used for weight updation (Fig. 7).

Equation 1. AdaDelta formula for weight updation

$$\Delta\theta_t = -\frac{\text{RMS}[\Delta\theta]_{t-1}}{\text{RMS}[g]_t} g_t$$

$$\theta_{t+1} = \theta_t + \Delta\theta_t \quad (1)$$

Fig. 6 Traffic light identification flow



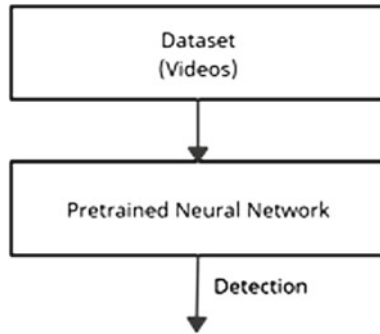


Fig. 7 Stop sign detection flow



Fig. 8 Sample frames from the dataset



Fig. 9 Extracted traffic lights

Choosing AdaDelta helps in the exclusion of the initialization of the learning rate. We then perform hyperparameter tuning on model parameters via iterative optimization to achieve higher accuracy. The best model derived from epochs after using early stopping [19] is then used on the video dataset for traffic light detection. The model also presents a confidence score with each detection demonstrated in Fig. 10 which can be used as a threshold to take actions when implementing autonomous vehicles.

This model also aids in the detection of stop signs through the use of the SSD ResNet V1 feature extractor. Through the COCO dataset, it is pre-trained for the identification of stop signs which are of great importance in real life. The block diagram for the same is shown in Fig. 7 wherein the model is run directly on the video dataset using the capabilities of TensorFlow. No further identification is required, unlike traffic light detection, therefore, an additional step was deemed unnecessary.

Fig. 10 Confidence score of prediction for traffic lights



Fig. 11 Confidence score of prediction for stop signs



A confidence score is generated that can be seen in Fig. 11 to assist with visual accuracy.

4 Results

Although through an eye test it could be observed that the CNN model is more accurate than its image processing counterpart, an analysis of metrics helps solidify that belief. In Fig. 12, we look at the model accuracy for the CNN model wherein we achieve an accuracy of 93.27%. The validation accuracy (or test accuracy) is significantly higher than the training accuracy due to image augmentation on the training set. The model has a loss of 0.243 that has been calculated via categorical cross-entropy, as mentioned before.

As this is a comparative study of models, we also compare the two proposed models based on computation time, memory usage, and accuracy. This can be seen in Fig. 13, where we normalize all parameters to fit a 0–100 scale. Some parameters are not taken into comparison as they are only relevant to one model (loss, number of epochs, number of variables, etc.)

Fig. 12 CNN model accuracy over epochs

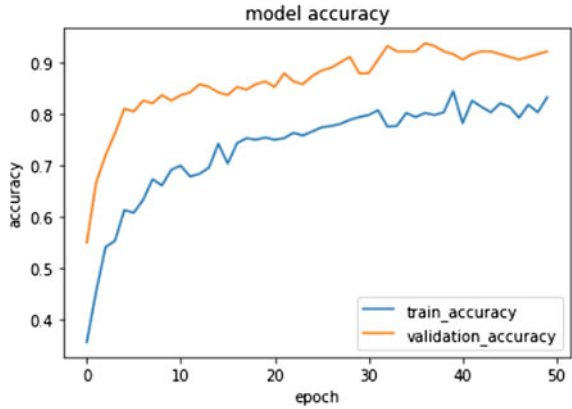
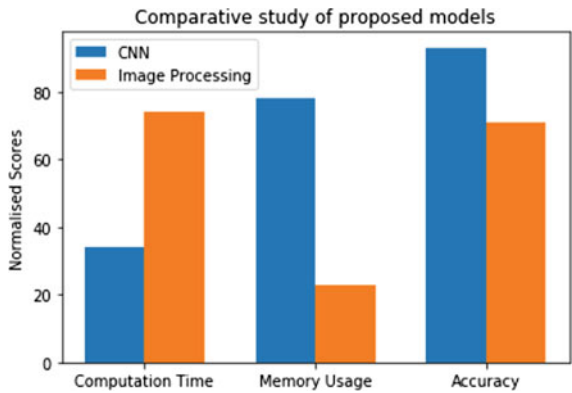


Fig. 13 Model comparison



We also discuss the case of failure for both our models. In Fig. 14a, we can see that there are two points of failure for the color segmentation model, the misclassification of red and yellow traffic lights. Although it detects the green light accurately, it also has false positives. The backlight of the car was incorrectly labeled as RED due to a similar size as that of a traffic light in the frame. A distant tree was incorrectly labeled as YELLOW due to similar reasons. In Fig. 14b, the CNN model identifies a green signboard as a green light with a high confidence score (Table 1).

Fig. 14 Incorrect detections



Table 1 Comparison of metrics

Parameter	CNN model	Traditional model
Computational time (ms)	91	194
Memory usage (MB)	~40	~146
Accuracy (%)	93.27	72.20
False positives (%)	2.7	6.32

5 Limitations and Future Work

The drawback for the image processing-based approach was the high number of false positives leading to lower precision. This could be resolved by using radial distances between traffic lights as a red traffic light is to be followed by two adjacent black circles. The color segmentation approach depends on other factors such as quality of image, angle of reflection from a traffic light with respect to image, and color of the traffic light in the country which makes it unsuitable for a real-world scenario. The street sign detection model that takes from KNN matching is time extensive making it inadequate for the real-world scenario. Only stop signs were included in this project as pre-trained models already exist and adding other street signs was beyond the scope of the current implementation.

The CNN model performed far better in terms of accuracy and had problems with the misclassification of some green signboards. This could be handled by changing the way the traffic light is extracted from the feature extractor or by inculcating a maximum size threshold for all detections. CNN also has other constraints which include overfitting to training data leading to biased results in training. The CNN model could also be scaled up to include night time detection to make a truly robust model.

6 Conclusion

In this paper, we discuss two approaches for traffic light identification and also propose a model of our own. The proposed model trained on a small portion of the BDD dataset [20] achieves an accuracy of 93.27% with a computation time of 91 ms which can be considered real time. Previous papers have performed similar tasks on other datasets having achieved slightly higher accuracies but to the best of our knowledge similar work on an extensive dataset such as the one chosen has not been carried out. We also look at how the two approaches vary on the chosen set of parameters. Although image processing models are easier to implement and use less memory, CNN models are computationally fast and perform with higher accuracy making them more suitable for the real world. Stop sign detection can be directly implemented using state-of-the-art feature extractors but for varied street signs, a color-based approach is also able to perform with moderate accuracy.

References

1. Omachi M, Omachi S (2009) Traffic light detection with color and edge information. In: 2nd IEEE international conference on computer science and information technology, pp 284–287
2. Shi Z, Zou Z, Zhang C (2016) Real-time traffic light detection with adaptive background suppression filter. In: IEEE transactions on intelligent transportation systems, pp 690–700
3. Charette Rd, Nashashibi F (2009) Traffic light recognition using image processing compared to learning processes. In: IEEE/RSJ international conference on intelligent robots and systems, pp 333–338
4. Karkoub W, Saripalli S (2019) Efficient traffic light detection for autonomous vehicles. In: Proceedings of the 5th international symposium on future active safety technology toward zero accidents
5. Karami E, Prasad S, Shehata M (2017) Image matching using SIFT, SURF, BRIEF, and ORB: performance comparison for distorted images. ArXiv: abs/1710.02726
6. Lowe DG (2004) Distinctive image features from scale-invariant keypoints. *Int J Comput Vision* 60:91–110. <https://doi.org/10.1023/B:VISI.0000029664.99615.94>
7. Kiran CG, Prabhu LV, Rajeev K (2009) Traffic sign detection and pattern recognition using support vector machine. In: 2009 seventh international conference on advances in pattern recognition, Kolkata, India, pp 87–90. <https://doi.org/10.1109/ICAPR.2009.58>
8. Arcos-Garcia A, Alvarez-Garcia JA, Soria-Morillo LM (2018) Evaluation of deep neural networks for traffic sign detection systems. *Neurocomputing*. <https://doi.org/10.1016/j.neucom.2018.08.009>
9. Wu Y, Liu Y, Li J, Liu H, Hu X (2013) Traffic sign detection based on convolutional neural networks. The 2013 international joint conference on neural networks (IJCNN). <https://doi.org/10.1109/ijcnn.2013.6706811>
10. Vennelakanti A, Shreya S, Rajendran R, Sarkar D, Muddegowda D, Hanagal P (2019) Traffic sign detection and recognition using a CNN ensemble. *IEEE Int Conf Consum Electr (ICCE) 2019*:1–4. <https://doi.org/10.1109/ICCE.2019.8662019>
11. Yan S, Liu X, Qian W, Chen Q (2021) An end-to-end traffic light detection algorithm based on deep learning. In: 2021 international conference on security, pattern analysis, and cybernetics (SPAC), pp 370–373. <https://doi.org/10.1109/SPAC53836.2021.9539934>
12. Nguyen PM, Nguyen VC, Nguyen SN, Dang LMT, Nguyen HX, Nguyen VD (2020) Robust traffic light detection and classification under day and night conditions. In: 2020 20th international conference on control, automation and systems (ICCAS), pp 565–570. <https://doi.org/10.23919/ICCAS50221.2020.9268343>
13. Hassanein AS, Mohammad S, Sameer M, Ehab Ragab M, A survey on Hough transform, theory, techniques and applications. ArXiv: abs/1502.02160
14. Mohd Ali N (2013) Performance comparison between RGB and HSV color segmentations for road signs detection. *Appl Mech Mater* 393. <https://doi.org/10.4028/www.scientific.net/AMM.393.550>
15. Rizon M, Yazid H, Saad P, Md Shakaff AY, Saad A (2005) Object detection using circular Hough transform. *Am J Appl Sci* 2. <https://doi.org/10.3844/ajassp.2005.1606.1609>
16. Vijayan V, Kp P (2019) FLANN based matching with SIFT descriptors for drowsy features extraction. *Fifth Int Conf Image Inform Process (ICIIP) 2019*:600–605. <https://doi.org/10.1109/ICIIP47207.2019.8985924>
17. Szegedy C, Vanhoucke V, Ioffe S, Shlens J, Wojna Z, Rethinking the inception architecture for computer vision. ArXiv: abs/1512.00567
18. Ruder S, An overview of gradient descent optimization algorithms. ArXiv: abs/1609.04747
19. Prechelt L (1998) Early stopping-but when? In: *Neural networks: tricks of the trade*. Springer, Berlin, pp 55–69
20. Xu H, Gao Y, Yu F, Darrell T (2017) End-to-end learning of driving models from large-scale video datasets. In: 2017 IEEE conference on computer vision and pattern recognition (CVPR)

A New Fuzzy Cascaded Controller for Hybrid Power System with Integration of FACTS Device



Ashiwani Kumar and Ravi Shankar

Abstract The integration of the FACTS device with the new fuzzy cascaded controller has been considered in this paper. Both areas contain thermal systems, biogas plants, and electric vehicles (EV), and distributed generation (DG). The renewable energy effect is considered in DG. The stored energy of an interconnected power system HVDC tie-link is utilized with inertia emulation-based control (INEC). The secondary controller is crucial to the AGC's stability. A new fuzzy controller in cascaded with (PI – FOPI^λDN) controller is proposed in this practical system. For the analysed system, a new quasi opposition lion optimization algorithm (QOLOA) has been presented to get the best controller settings. The integral time absolute error (ITAE) is used as an objective function to optimize the projected AGC mechanism. Furthermore, to boost the power transfer capabilities of the AC tie-line, a series compensator (SSSC) is connected in series with it. To demonstrate algorithm and proposed controller superiority, the results acquired utilizing the suggested approach are compared to published literature on the same platform.

Keywords AGC · QOLOA · DG · SSSC

1 Introduction

AGC plays an important part in the power system's stability. The key objective of AGC is the use of primary and secondary control to keep frequency and tie-line power deviation to zero. The effects of GRC and GDB in thermal power systems have been studied by many authors [1]. Communication delay (CD) may interrupt system stability if it is not addressed properly. Nonlinearity like GRC, GDB, BD, and CD has been tested in [2]. DG can play an essential role in response to high peak load demand. Aqua electrolyzer (AE), solar photovoltaic (SPV), wind turbine system (WTS), fuel cell (FC), battery energy system (BES), and diesel engine generator (DEG) are the most common components of DG. DG effects on power systems

A. Kumar (✉) · R. Shankar
Department of Electrical Engineering, NIT Patna, Patna, India
e-mail: ashwani@nitp.ac.in

© The Author(s), under exclusive license to Springer Nature Singapore Pte Ltd. 2022
V. Mahajan et al. (eds.), *Sustainable Technology and Advanced Computing*
in *Electrical Engineering*, Lecture Notes in Electrical Engineering 939,
https://doi.org/10.1007/978-981-19-4364-5_14

165

were investigated by [3]. Renewable energy, particularly solar and wind energy, will play a significant role in future power grid due to its low cost and technological improvement. The only issue with renewables is that they are inherently probabilistic [4]. This problem can be solved if renewable energy is hybridized with better battery energy storage. Deregulation was implemented in the power sector to increase competition and provides customers with lower-cost, higher-quality electricity. After deregulation, huge investment came in the power sector, and the quality of the power supply also improved. Following deregulation, only three types of transactions are permitted: polco, bilateral, and contract-violation transactions [5]. Electric vehicles (EV) can also play an essential role during high demand. EV power system impact was investigated in the power system in [6, 7]. The single electrical vehicle has an energy capacity of 10–30 KW, so a single EV is not suitable for AGC. For AGC, we need thousands of EV connected together [8]. EV fleet, along with conventional sources like thermal, gas, and hydro, is used in [9]. In this article, the proposed controller is used to regulate conventional sources and the EV fleet. The response in the presence of EV fleet is much better. In order to control load frequency, EV is used in [10, 11].

Electricity demand is increasing every year as a result of the rising population and industrialization. To meet increasing electricity demand, all regional grids are connected, so cheap electricity can be transferred from one region to another. For transmitting power from one control region to another, we use tie-line, which have now reached their maximum limit, so their capacity needs to be increased. In the long AC lines, there is the problem of the Ferranti effect, stability, and synchronization. To satisfy rising power demand, the ideal way is to build HVDC tie-lines in parallel with existing AC tie-lines [12]. HVDC stored energy is used in conjunction with AC/DC tie-lines in [13, 14] for interconnected power systems.

Different traditional techniques such as I, PI, and PID were employed in AGC. Many cascaded and fractional controllers were used in the literature, which shows better results than traditional computing techniques [15]. In the last few years', fractional order has been getting the attention of researchers due to its more parameter for tuning and its better result than conventional controller [16, 17]. For load frequency control, a two-degree of freedom controller is used in [18], and results are better when compared with the conventional controller like I, PI, and PID, which encourages us to use a two-degree of freedom controller [19, 20].

For controller to work better, it is necessary that its parameters need to be tuned properly. For tuning, many meta heuristic algorithm have been developed in the last few years. Cascaded PI-PID controller is optimized by bat algorithm, and its result is far superior to the classical controller like I, PI, and PID [21] for load frequency control. Fractional order PID controller is optimized by gases Brownian motion optimization in [22], and its results are encouraging for load frequency control. Chaotic ant swarm algorithm is used in [23] for tuning parameters of fraction order PID controller for AVR control. Teaching–learning-based optimization (TLBO) is used for tuning PID controllers for AVR control [24]. TLBO optimized sliding mode control is utilized in load frequency control of multi-connected power systems [25]. For the proposed power system, the fruit fly approach [26] is utilized to optimize

the PIDN controller parameters. Hybrid bacterial foraging optimization algorithm along with particle optimization algorithm is used to tune PI controller for AGC [27]. Water wave optimization is used in [28] to tune the cascaded controller for AGC. Maziar Yazdani proposed the lion optimization algorithm (LOA) in 2016 [30]. LOA is the most recent optimization algorithm that focuses on a lion's ability to find prey and maintain a healthy lifestyle. In LOA, along with a normal lion, a quasi-opposition-based lion is also used to find the right solution, which needs a compact search space. Therefore, the solution achieved by initialization is closer to the optimum solution because the almost quasi-opposite number is used instead of a pseudo-random number. Consequently, the number of iterations needed for the ideal solution is smaller than the other initialization method.

2 System Investigated

In a deregulated context, the AGC is employed in multi-source power systems. Figure 1 depicts the suggested test system. A thermal system, gas system, DG, and aggregate electric vehicle are included in Area-1 and Area-2. Solar photovoltaic (SPV), wind turbine system (WTS), diesel engine generator (DEG), battery energy storage system (BESS), fuel cell (FC), aqua electrolyzer (AE), and flywheel energy storage system (FESS) are among the components of the DG. In both regions, nonlinearity, such as GDB, GRC, and BD, is taken into account in thermal plants. In Area-1, the participation factors for thermal, DG, and gas are 0.5, 0.3, and 0.2, respectively, and the same is true in Area-2. When EV is fully charged, it can act as a source, and charged below a certain value, it can act as a load. Due to the increasing interconnection of control area and increasing power demand tie-line power transfer capability needs to be increased. Tie-line power capability can be improved by adding AC-line or HVDC line in parallel to the existing AC-line. It is better to go for an HVDC tie-line, as it is more economical and has a less technical issues. Using INEC, the HVDC tie-stored line's energy can be used for frequency adjustment. In this paper, HVDC stored energy has been used for frequency regulation. FACTS device can also be used to increase the transfer capability of AC tie-lines. The SSSC is modelled with an AC tie-line in this research and used to improve the tie-power line's transmission capability. Deregulation was implemented in the power sector in order to increase competition. Following deregulation, a large amount of private investment came into the electricity system, resulting in improved power quality. Independent system operator (ISO) manages all transactions between GENCO and DISCO.

3 Proposed Controller

The proposed controller consists of a fuzzy controller in cascade with (PI – FOPI³DN). The membership function is shown in Fig. 2, and the fuzzy membership

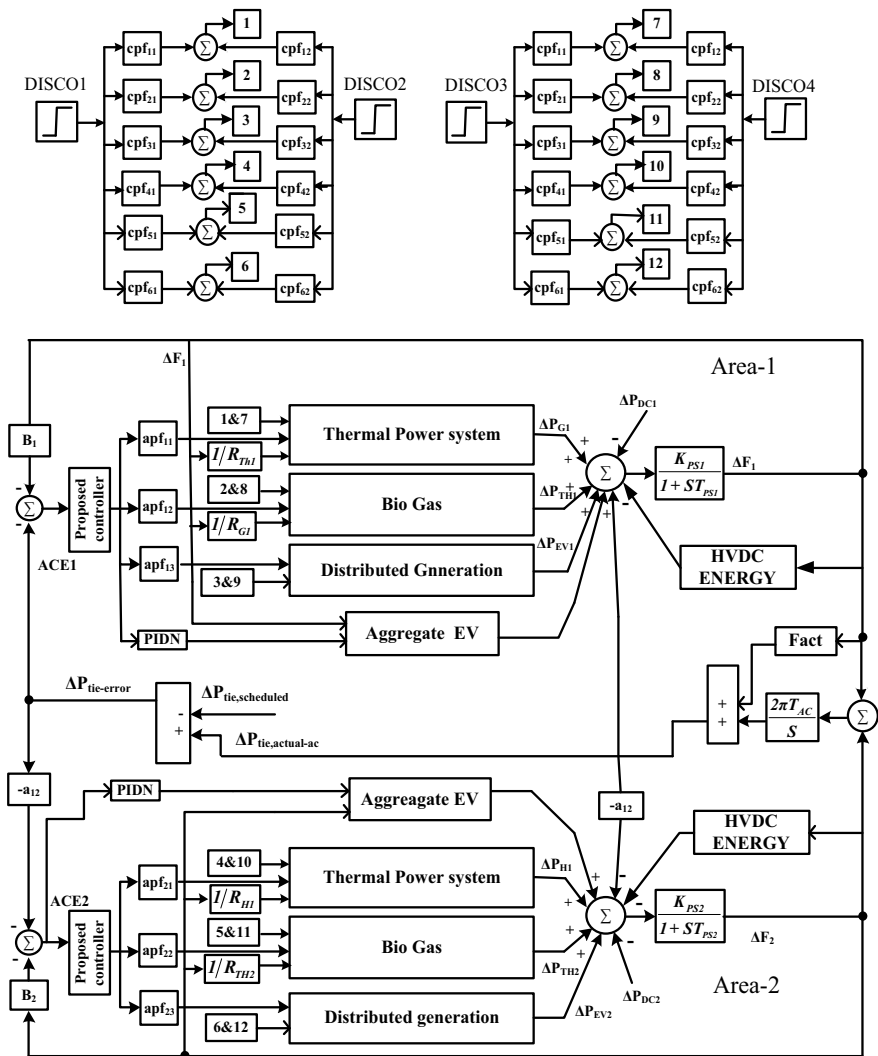


Fig. 1 Two areas test system

rule base is shown in Table 1. Figure 3 depicts the fuzzy cascaded controller. The proposed cascaded controller is shown in Fig. 4.

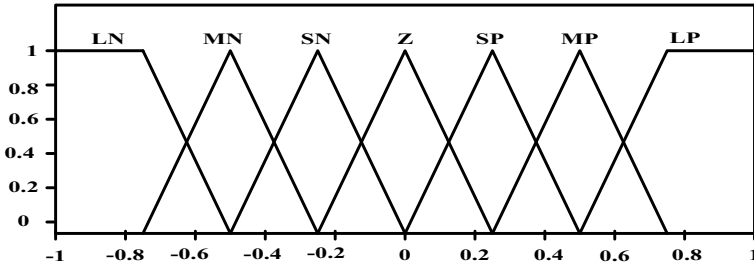


Fig. 2 Membership function for input and output of FLC

Table 1 Rule for fuzzy membership

ACE	ACE						
	LN	MN	SN	Z	SP	MP	LP
LN	LP	LP	LP	MP	MP	SP	Z
MN	LP	MP	MP	MP	SP	Z	SN
SN	LP	MP	SP	SP	Z	SN	MN
Z	MP	MP	SP	Z	SN	MN	MN
SP	MP	SP	Z	SN	SN	MN	NL
MP	SP	Z	SN	MN	MN	MN	NL
LP	Z	SN	MN	MN	NL	NL	NL

Fig. 3 Fuzzy cascaded controller

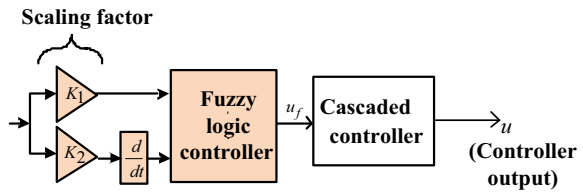
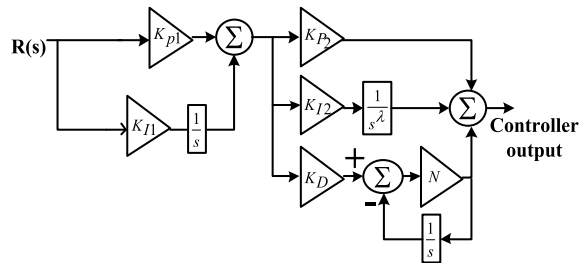


Fig. 4 Proposed cascaded controller (PI – FOPI^λDN)



4 Result and Analysis

The suggested test system is simulated in a restructured power environment using the MATLAB/Simulink toolbox. In the suggested test system, a GDB of 0.0006 pu is used, and 10% of GRC is used to decrease and raise generation in the thermal power system. For the simulation study, N_{EV} stands for the number of electric vehicles. In idle state, 10,000 EVs are examined. Two scenarios are taken. Scenario-1 is evaluated in absence of FACTS and HVDC energy, whereas scenario-2 is in the presence of FACTS and HVDC energy. The proposed QOLOA is shown in Fig. 5.

4.1 PBT Case

In the event of PBT, DISCO can obtain power from GENCO in the area where DISCO is located. In this case, one area's load disturbance is 1%, while the other area's load disturbance is 0%. The fuzzy controller in cascaded with (PI – FOPI^λDN) makes up the control unit. The controller gain is optimized using QOLOA. PBT response is shown in Fig. 6.

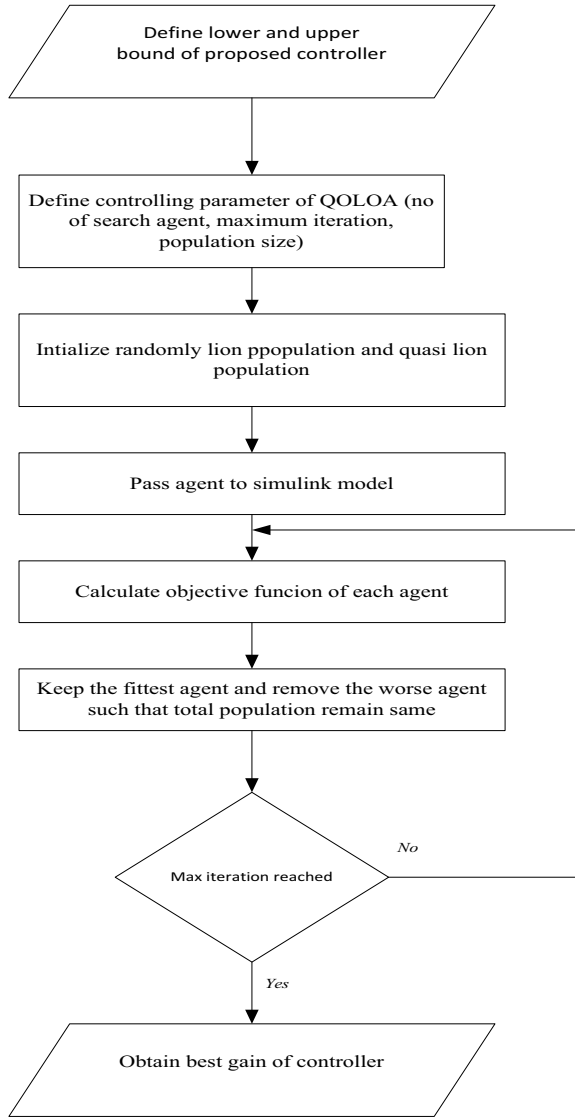
4.2 BBT Case

In the case of BBT, the DISCO can draw power from any GENCO. The load disturbance in each location is 1% in this scenario. The fuzzy controller in cascaded with (PI – FOPI^λDN) makes up the control unit. The controller gain is optimized using QOLOA. BBT response is shown in Fig. 7.

4.3 CVT Case

In this case, DISCO takes more power than what it has contracted for. The un-contracted power is taken from GENCO, in which area DISCO is situated. The load disturbance in Area-1 is 1%, and the un-contracted load is 0.001 pu. The fuzzy controller in cascaded (PI – FOPI^λDN) makes up the control unit. The system response for the CVT case is shown in Fig. 8.

Fig. 5 Procedure for QOLOA



4.4 Comparison with Previous Work

The paper simulated result for PBT case is compared with a recent paper on AGC by et al. [29] on the same platform. From Fig. 9, it is clear that the proposed controller outperforms in settling time and deviation.

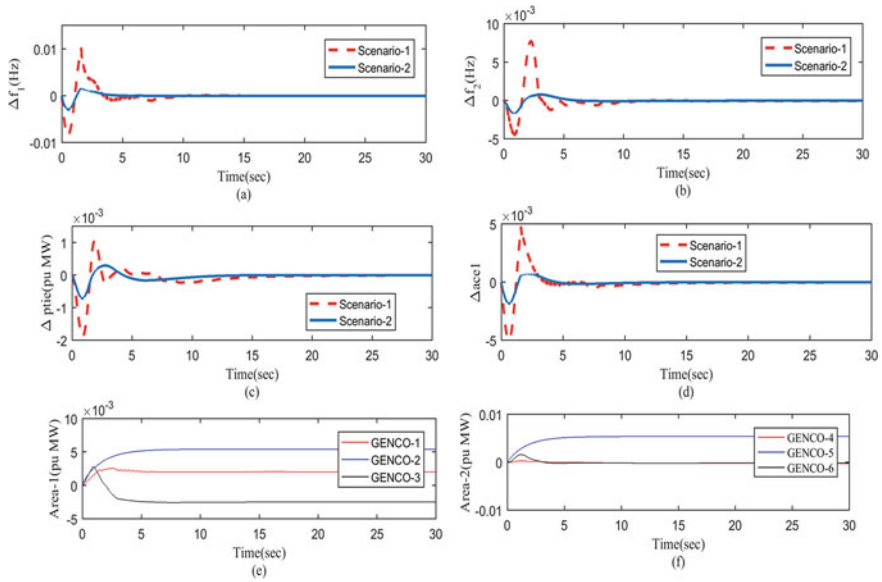


Fig. 6 Response for PBT case **a** Δf_1 deviation, **b** Δf_2 deviation, **c** ΔP_{tie} deviation, **d** Δace_1 deviation, **e** Area-1 GENCO output, and **f** Area-2 GENCO output

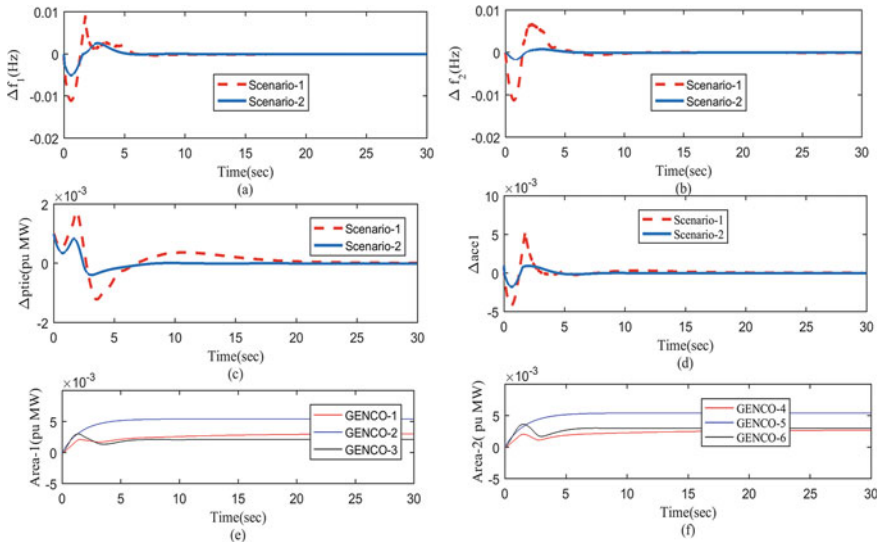


Fig. 7 Response for BBT case, **a** Δf_1 deviation, **b** Δf_2 deviation, **c** ΔP_{tie} deviation, **d** Δace_1 deviation, **e** Area-1 GENCO output, and **f** Area-2 GENCO output

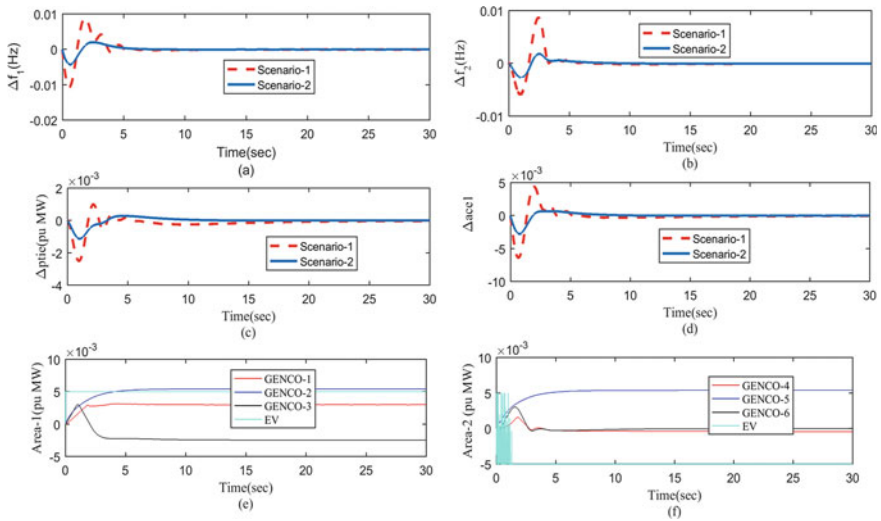


Fig. 8 Response for CVT case, **a** Δf_1 deviation, **b** Δf_2 deviation, **c** ΔP_{tie} deviation, **d** Δace_1 deviation, **e** Area-1 GENCO output, and **f** Area-2 GENCO output

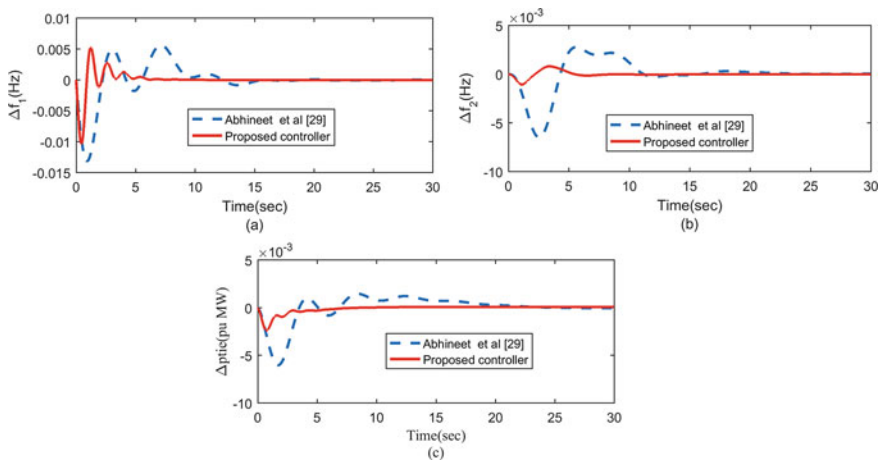


Fig. 9 System response for PBT case, **a** Δf_1 deviation, **b** Δf_2 deviation, and **c** ΔP_{tie} deviation

5 Conclusion

The paper attempts to improve the response of hybrid power system by use of fact devise and HVDC stored energy. A new fuzzy controller in cascaded with (PI – FOPI²DN) is used, and result shows the superiority of the controller. A new QOLOA algorithm is used to optimize controller gain. From the response of PBT case, BBT

case and CVT case, it can be concluded that all responses settle around ten seconds and undershoot and overshoot improves in scenario-2, which shows the superiority of algorithm and controller. Paper has been compared from recent literature on the same platform to show its superiority.

References

1. Tan W, Chang S, Zhou R (2017) Load frequency control of power systems with nonlinearities. *IET Gener Transm Distrib* 11(17):4307–4313
2. Daraz A, Suheel AM, Hazile M, Ishan ul haq, Zafer F, Nurulfiqah NM (2020) Improved-fitness dependent optimizer based FOI-PD controller for automatic generation control of multi-source interconnected power system in deregulated environment. *IEEE Access* 8:197757–197775
3. Saha A, Saikia LC (2018) Combined application of redox flow battery and DC link in restructured AGC system in the presence of WTS and DSTS in distributed generation unit. *IET Gener Transm Distrib* 12(9):2072–2085
4. El-Hameed MA, Elkholy MM, El-Fergany AA (2019) Efficient frequency regulation in highly penetrated power systems by renewable energy sources using stochastic fractal optimizer. *IET Renew Power Gener* 13(12):2174–2183
5. Shankar R, Chatterjee K, Bhushan R (2016) Impact of energy storage system on load frequency control for diverse sources of interconnected power system in deregulated power environment. *Electr Power Energy Syst* 79:11–26
6. Bhatt P, Roy R, Ghoshal SP (2010) Optimized multi area AGC simulation in restructured power systems. *Electr Power Energy Syst* 32:311–322
7. Debbarma S, Dutta A (2017) Utilizing electric vehicles for LFC in restructured power systems using fractional order controller. *IEEE Trans Smart Grid* 8(6):2554–2564
8. Khooban MH, Niknam T, Blaabjerg F, Dragicevic T (2017) A new load frequency control strategy for micro-grids with considering electrical vehicles. *Electr Power Syst Res* 143:585–598
9. Oshnoei A, Khezri R, Muyeen SM, Oshnoei S, Blaabjerg F (2019) Automatic generation control incorporating electric vehicles. *Electr Power Compon Syst* 0(0):1–13
10. Rocha Almeida PM, Soares FJ, Lopes P (2015) Electric vehicles contribution for frequency control with inertia emulation. *Electr Power Syst Res* 127:141–150
11. Sbordone D, Bertini I, Di Pietra B, Falvo MC, Genoveseb A, Martirano L (2015) EV fast charging stations and energy storage technologies: a real implementation in the smart micro grid paradigm. *Electr Power Syst Res* 120:96–108
12. Rakhshani E, Rouzbehi K, Elsharty MA, Cortes PR (2017) Heuristic optimization of supplementary controller for VSC-HVDC/AC interconnected grids considering PLL. *Electr Power Compon Syst* 45(3):288–301
13. Zhu J, Guerrero JM, Hung W, Booth CD, Adam GP (2014) Generic inertia emulation controller for multi-terminal voltage-source-converter high voltage direct current systems. *IET Renew Power Gener* 8(7):740–748
14. Prakash A, Murali S, Shankar R, Bhushan R (2019) HVDC tie-link modeling for restructured AGC using a novel fractional order cascade controller. *Electr Power Syst Res* 170:244–258
15. Saikia LC, Sahu SK (2013) Automatic generation control of a combined cycle gas turbine plant with classical controllers using firefly algorithm. *Electr Power Energy Syst* 53:27–33
16. Pan I, Das S (2015) Fractional-order load-frequency control of interconnected power systems using chaotic multi-objective optimization. *Appl Soft Comput* 29:328–344
17. Pan I, Das S (2016) Fractional order AGC for distributed energy resources using robust optimization 7(5):2175–2186
18. Debbarma S, Saikia LC, Sinha N (2014) Robust two-degree-of-freedom controller for automatic generation control of multi-area system. *Electr Power Energy Syst* 63:878–886

19. Li M, Zhou P, Zhao Z, Zhang J (2016) Two-degree-of-freedom fractional order-PID controllers design for fractional order processes with dead-time. *ISA Trans* 61:147–154
20. Raju M, Saikia LC, Sinha N (2018) Maiden application of two degree of freedom cascade controller for multi-area automatic generation control. *Int Trans Electr Energy Syst* e2586
21. Dash P, Saikia LC, Sinha N (2015) Automatic generation control of multi area thermal system using Bat algorithm optimized PD–PID cascade controller. *Electr Power Energy Syst* 68:364–372
22. Zamani A, Masoud Barakati S, Yousofi-Darmian S (2016) Design of a fractional order PID controller using GBMO algorithm for load–frequency control with governor saturation consideration. *ISA Trans* 64:56–66
23. Tang Y, Cui M, Hua C, Li L, Yang Y (2012) Optimum design of fractional order controller for AVR system using chaotic ant swarm. *Expert Syst Appl* 39:6887–6896
24. Chatterjee S, Mukherjee V (2016) PID controller for automatic voltage regulator using teaching–learning based optimization technique. *Electr Power Energy Syst* 77:418–429
25. Mohanty B (2015) TLBO optimized sliding mode controller for multi-area multi-source nonlinear interconnected AGC system. *Electr Power Energy Syst* 73:872–881
26. Shankar R, Kumar A, Raj U, Chatterjee K (2018) Fruit fly algorithm-based automatic generation control of multiarea interconnected power system with FACTS and AC/DC links in deregulated power environment. *Int Trans Electr Energy Syst* e2690
27. Panda S, Mohanty B, Hota PK (2013) Hybrid BFOA–PSO algorithm for automatic generation control of linear and nonlinear interconnected power systems. *Appl Soft Comput* 13:4718–4730
28. Dahiya S, Singh Parmar KP (2021) A novel fractional order proportional integral derivative plus second-order derivative controller for load frequency control. *Int J Sustain Energy* 40(3):235–252
29. Prakash A, Kumar K, Parida SK (2020) PIDF(1+FOD) controller for load frequency control with SSSC and AC–DC tie-line in deregulated environment. *IET Gener Transm Distrib* 14(14):2751–2762
30. Maziar Y, Fariborz J (2016) Lion optimization algorithm (LOA): a nature-inspired meta-heuristic algorithm. *J Comput Design Eng* 3:24–36

MATLAB GUI-Based Partial Discharge Localization in Power Transformers Using UHF Acoustic Method



Avinash S. Welankiwar and Sagar Kudkelwar

Abstract Partial discharge (PD) problem is getting more attention day by day due to its severity toward insulation deterioration and internal arcing problems. In this paper, PD detection is illustrated with the help of a case study conducted on a power transformer by using ultra high frequency (UHF) injection and acoustic method combined with high frequency current transducer (HFCT) to get more accurate results. This method is getting more popular day by day due to its accuracy in PD detection. This paper represents the mathematical approach of UHF acoustic method for the localization of PD in MATLAB GUI environment. Field testing is done on 100 MVA 400/220 kV interconnecting transformer at 400 kV receiving station, and the obtained results are compared with the output of mathematical algorithm in MATLAB software. Results reveal the effective visualization of the possible position of the PD in the transformer tank in terms of x , y and z coordinates.

Keywords Partial discharge · Power transformers · UHF acoustic method · MATLAB GUI · PD localization algorithm

1 Introduction

The power transmission is conducted at high voltages and extra high voltages which contribute to reduction of both transmission, distribution and system complexity. As the operating voltage level is increased, proper dielectric strength is necessary for the protecting the equipment. PD is found as a principal cause that, in the course of its continuous operation, silently damages insulation of electric appliances such as transformers, cables, alternators, current (CT) and transformers (PTs). [1, 2]. Hence, it becomes necessary for monitoring of PD in high-voltage power apparatus

A. S. Welankiwar (✉) · S. Kudkelwar
Department of Electrical Engineering, G. H. Rasoni Institute of Engineering and Technology,
Nagpur, India
e-mail: avinash.welankiwar@raisoni.net

S. Kudkelwar
e-mail: sagar.kudkelwar@raisoni.net

to maximize its life [3–5]. PD is a dielectric localization breakdown which bridges the electrode insulation. Several solid, liquid and gaseous materials for insulation are used in high-voltage electrical systems. The power system insulators are not 100% perfect. The presence of air bubbles or voids degrades the insulator quality. The insulation property degrades mainly due to electrical, mechanical and thermal stresses [6, 7]. PD detection is now the most well-accepted quality management tool in factories and at locations. Various PD measuring techniques use verity of different PD-phenomenal parameters, such as electric discharge currents, dissolved gas analysis or acoustic emission sensors (UHF). The main advantage of an acoustic PD measurement is that PD can be detected without the transformer being shut down and that a PD source can be located with accuracy of centimeter to a few decimeters [8–10]. The electric method (IEC60270) includes use of coupling condenser used for the calibration in terms of picocoulomb (pC) of other PD measurement systems. This method is unsuitable for onsite PD testing because of some disadvantages [11].

The aim of this paper is to develop GUI for visualization of PD event inside the transformer tank using PD positioning algorithm in MATLAB software. Organization of this paper is as follows: Sect. 2 consists of UHF sensor positioning and related methodology based on mathematical equations for PD localization. Section 3 focuses on real-time case study of a 400/220 kV power transformer used for executing the algorithm, and results are elaborated. Section 4 concludes the paper.

The contribution of this work is, PD localization algorithm is designed in MATLAB and GUI is developed. Acoustic PD testing is conducted on 100 MVA, single phase (R) 400/220 kV single phase interconnecting transformer is discussed in case study section. Results of the case study are compared with MATLAB GUI output. Work presented in this paper will help to visualize the PD position in transformer tank.

2 PD Detection Using UHF Acoustic Method

Acoustic method is non-destructed and electromagnetic noise resistant. The principle of this method is sound waves detection originated from PD inside the insulation. A sound wave originated from PD within a transformer travels to an acoustic emission (AE) sensor attached to the outer body of tank wall through different materials. Signal received at the AE sensor has to be processed to get the PD position [12–14]. The PD location can be computed by using the time of arrival (TOA) between the sensors [15, 16].

2.1 PD Detection Using UHF Acoustic Method

Figure 1 shows placing AE sensors on the transformer tank by taking proper scale of measurement using magnets. Thus, it gives the sensor positions in terms of Cartesian coordinates (x, y, z) .

Figure 2 shows sensor positioning on different sides of tank to locate the PD. Minimum three sensors are required for the PD detection. Any one sensor and its position can be taken as reference [1, 2].

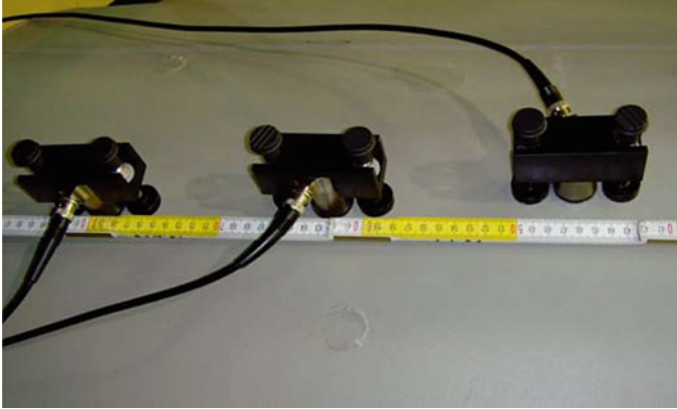


Fig. 1 Placing sensors on transformer using magnets [1]

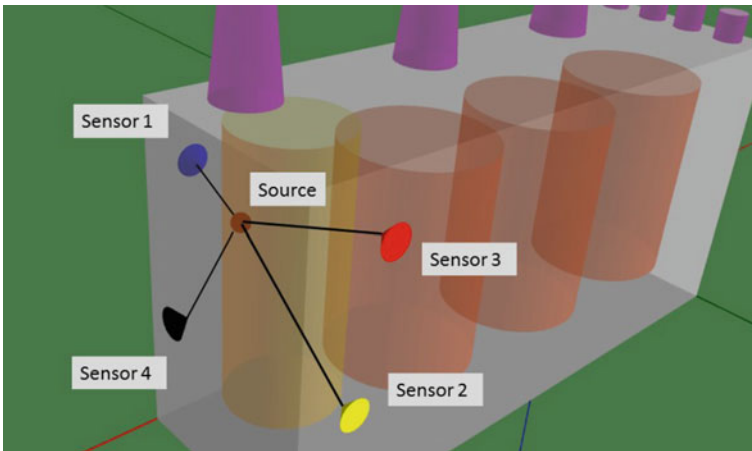
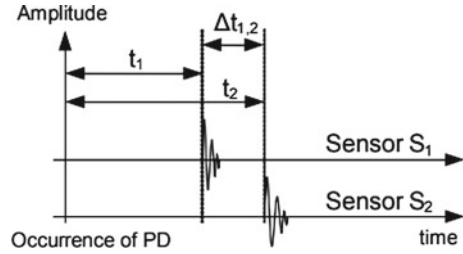


Fig. 2 Sensors placed at different positions on transformer tank [1]

Fig. 3 Representation of TOA at sensors 1 and 2 [17]



2.2 Time Difference of Arrival (TDOA)

TOA of sensor 1 (t_1) is defined as time required by the traveling wave to reach the sensor 1. In similar way, t_2 can be defined. TDOA is the difference between TOA of the two sensors and is shown in Fig. 3.

TDOA of sensors 1 and 2 is given by Eq. (1),

$$\Delta t_{12} = t_1 - t_2 \quad (1)$$

2.3 PD Localization

Sensors placed on the transformer can be represented by Eqs. (2)–(5),

$$(x - x_1)^2 + (y - y_1)^2 + (z - z_1)^2 = (Vs \times T_1)^2 \quad (2)$$

$$(x - x_2)^2 + (y - y_2)^2 + (z - z_2)^2 = (Vs \times T_2)^2 \quad (3)$$

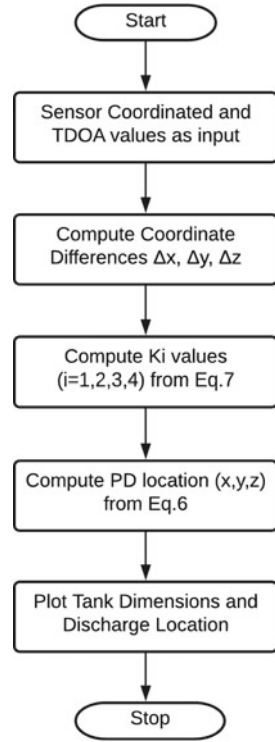
$$(x - x_3)^2 + (y - y_3)^2 + (z - z_3)^2 = (Vs \times T_3)^2 \quad (4)$$

$$(x - x_4)^2 + (y - y_4)^2 + (z - z_4)^2 = (Vs \times T_4)^2 \quad (5)$$

Here, (x_1, y_1, z_1) are the coordinates of sensor 1. T_1 is time of arrival of sensor 1. Similarly, other sensor coordinates and T_2, T_3, T_4 can be defined. PD coordinates can be found out by Eq. (6),

$$\begin{bmatrix} x \\ y \\ z \end{bmatrix} = - \begin{bmatrix} x_{14} & y_{14} & z_{14} \\ x_{24} & y_{24} & z_{24} \\ x_{34} & y_{34} & z_{34} \end{bmatrix} \times \begin{bmatrix} r_{14} \\ r_{24} \\ r_{34} \end{bmatrix} r_4 + \frac{1}{2} \begin{bmatrix} r_{14}^2 - K_1 + K_4 \\ r_{24}^2 - K_2 + K_4 \\ r_{34}^2 - K_3 + K_4 \end{bmatrix} \quad (6)$$

Fig. 4 PD positioning flowchart



where (x, y, z) are the position of the PD source, (x_{i4}, y_{i4}, z_{i4}) are the coordinate difference of the reference sensor ($i = 4$) and sensor 4 ($i = 1,2,3$), r_{i4} is the TDOA between sensor i and sensor 4 ($i = 1,2,3$), r_4 indicates the position of sensor 4 from PD origin, and K_i is calculated as per Eq. (7),

$$K_i^2 = x_i^2 + y_i^2 + z_i^2 \tag{7}$$

Algorithm is developed to find the solution of Eq. (6) and executed in MATLAB software with the different sensor positions [3, 4, 6]. Overall mathematical flow is shown in the flowchart in Fig. 4

3 Case Study

Field testing was done on 100 MVA, single phase (R) 400/220 kV interconnecting transformer located at 400 kV substation Koradi, Nagpur (India), with PDTP500A test equipment. Tank size of the transformer is 3000 mm × 5000 mm × 10,000 mm. Acoustic emission (AE) sensors were mounted at turret of transformer and of the

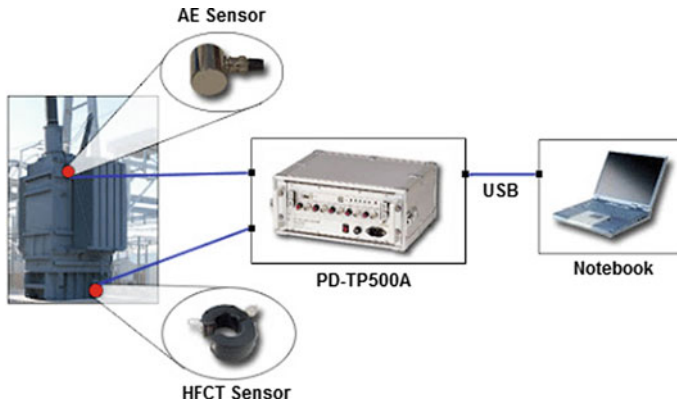


Fig. 5 System configuration with PDTP500A

HFCT sensor mounted at grounding. AE sensors were mounted at different locations to find the PD activities in the transformer. This system is based on ultrasound detection of acoustic signals emitted and electrical signals from the discharges. It consists of five inputs; four of AE sensor and one HFCT sensor that detects the PD signals simultaneously and compares these signals to determine origin of the PD phenomena is shown in Fig. 5.

3.1 Testing at HV Side (400 kV)

Figure 6 shows the HV Side, 400 kV of the transformer; AE sensors were mounted at the structure of the transformer. Figure 7 shows no PD activities are detected. Also, HFCT has not detected any PD activities at the neutral grounding of ICT.

Fig. 6 400 kV HV side view



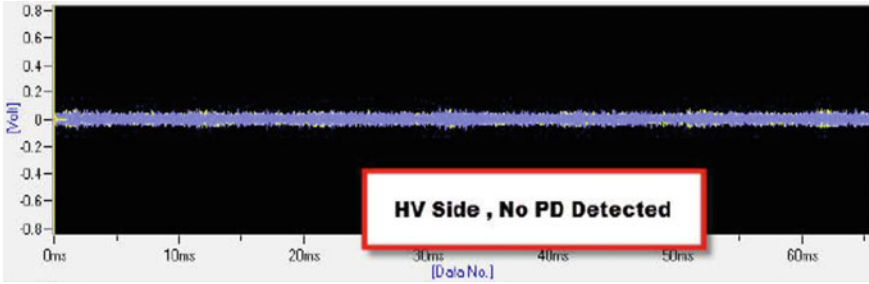


Fig. 7 Online testing result

In MATLAB, four sensor coordinates and the respective values of TDOA were simulated, and GUI shown no results for the PD is indicated in Fig. 8. Sensor coordinates (in mm) are Sensor 1 located at [7000, 0, 3000], Sensor 2 located at [7000, 0, 5000], Sensor 3 located at [4000, 0, 5000] and Sensor 4 located at [4000, 0, 3000]. TDOA values with respect to sensor 1, T12, T13 and T14 are found to be zero. Similarly, tests are conducted on LV and OLTC side but no PD activity is confirmed by online testing and MATLAB.

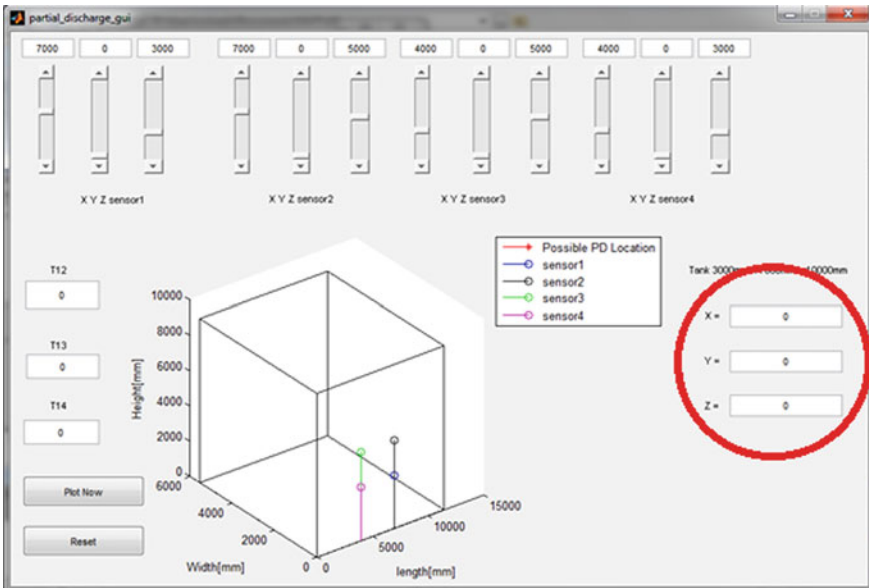


Fig. 8 Output of GUI on HV side showing no PD activity

3.2 PUMP Side

Figure 9 shows AE sensors mounted on pump side of the transformers. Figures 10 and 11 show PD activity detected at regular intervals found at the pump side. PD activity is measured as $66.4 \mu\text{V}$ and localized using PDTPA500A at coordinates ($x = 10,087.4, y = 4011.41, z = 8013.77$). MATLAB algorithm has localized the PD at ($x = 10,083.48, y = 4000, z = 8001.24$) in mm (Fig. 12).

Error in the measurement is found as 3.92 mm at x coordinate, 11.41 mm at y coordinate and 12.63 mm at z coordinate. Error is relatively small because MATLAB is localizing the PD on the basis of mathematical equations only. Technical parameters of the UHF and HFCT sensors are not considered in GUI that are important to recognize PD pattern.

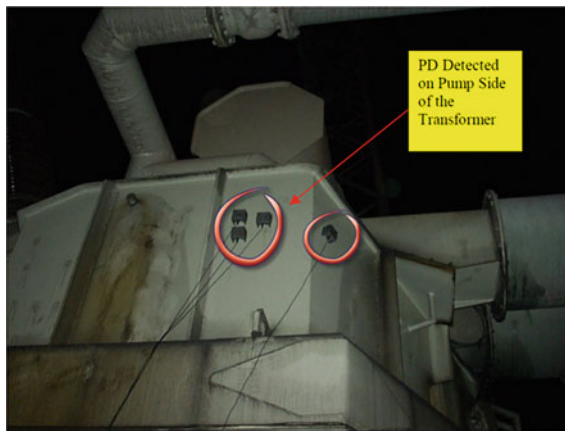


Fig. 9 UHF sensors mounted pump side view of transformer

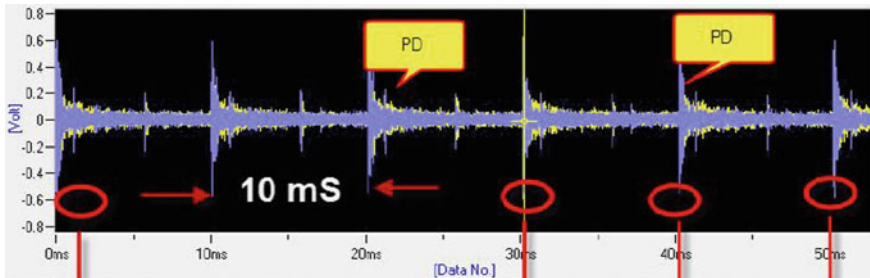


Fig. 10 PD activity at pump side by AE sensor number 3 and 4

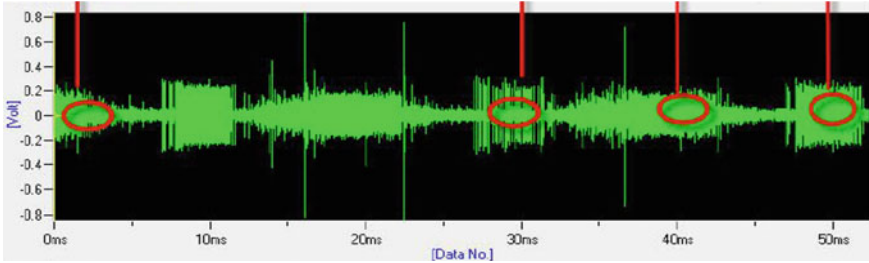


Fig. 11 HFCT sensor showing the PD activities

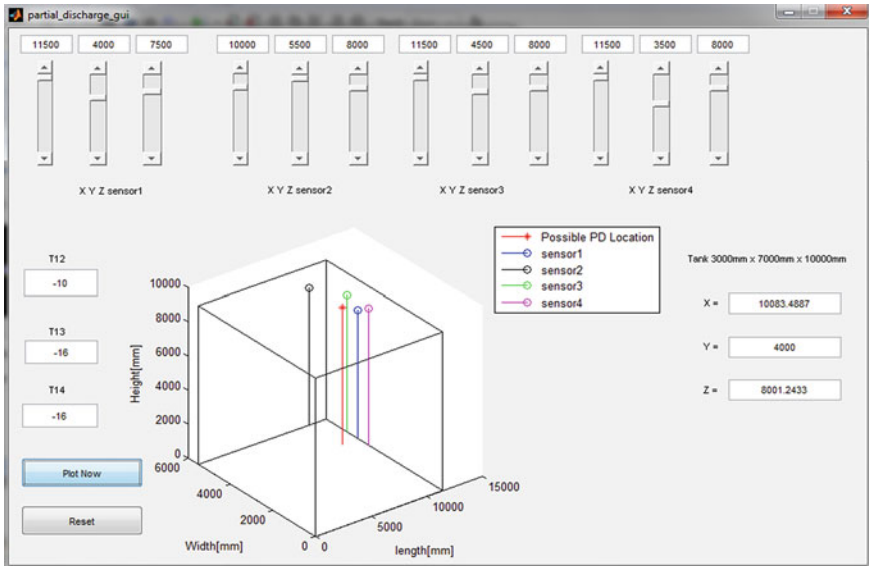


Fig. 12 GUI showing PD activity

4 Conclusion

PD causes consistent insulation deterioration of power transformers under continuous operating cycle. It is to conclude that GUI developed in MATLAB software based on PD positioning algorithm has successfully localized PD on the basis of sensor coordinates and TDOA values as input and the results were matching satisfactorily with the online testing results obtained by PDTP500A. The main advantage of UHF acoustic method is increased sensitivity of PD detection and localization. Algorithm for GUI presented in this paper can be combined with TDOA calculation algorithm based on energy criterion to reduce the manual inputs of TDOA values and to get more simplified visualization of PD source in the tank by just changing sensor positions.

Acknowledgements I would like to thank Er. Mukesh Tatte, Asst. Engineer, 400 kV substation, Koradi (India), and Er. D. P. Ashtikar, DY.EE 400 kV Substation Waluj, Aurangabad (India), for giving me valuable inputs, sharing their expertise and support for this work.

References

1. Hoek SM, Kraetge A, Hummel R, Kessler O, Winter P, Broniecki U, Kästner B (2012) Localizing partial discharge in power transformers by combining acoustic and different electrical methods. In: 2012 IEEE international symposium on electrical insulation. IEEE, pp 237–241
2. Coenen S, Tenbohlen S, Markalous SM, Detection of partial discharges in power transformers using UHF PD measurements and acoustic measurements
3. Coenen S, Müller A, Beltle M, Kornhuber S (2011) UHF and acoustic partial discharge localisation in power transformers. In: International symposium on high voltage engineering (ISH)
4. Sinaga HH (2012) Detection, identification and localization of partial discharges in power transformers using UHF techniques. PhD thesis, The University of New South Wales Australia
5. Lazarevich AK (2003) Partial discharge detection and localization in high voltage transformers using an optical acoustic sensor. Doctoral dissertation, Virginia Tech
6. Win SS, Aung MM, Swe W (2011) Partial discharge detection and localization in power transformers. In: The 8th electrical engineering/electronics, computer, telecommunications and information technology (ECTI) association of Thailand-conference 2011. IEEE, pp 673–676
7. Cavallini A, Ramos CGA, Montanari GC, Rubio-Serrano J, Garcia-Souto JA (2011) Comparison of ultrasonic, electrical and UHF characteristics of partial discharge emission in oil/paper insulation systems. In: 2011 annual report conference on electrical insulation and dielectric phenomena. IEEE, pp 440–443
8. Gross DW, Soeller M (2012) On-site transformer partial discharge diagnosis. In: 2012 IEEE international symposium on electrical insulation. IEEE, pp 558–564
9. Sarkar DK, Koley B, Roy NK (2015) Localization of partial discharge source in high voltage apparatus using multiple UHF sensors. In: 2015 international conference on energy, power and environment: towards sustainable growth (ICEPE). IEEE, pp 1–5
10. Azirani MA, Ariannik M, Werle P, Akbari A (2019) Enhancing the accuracy of partial discharge localization in power transformers using the UHF measurement technique. In: 2019 IEEE electrical insulation conference (EIC). IEEE, pp 58–62
11. IEEE Guide for the Measurement of Partial Discharges in AC Electric Machinery, IEEE P1434/D1.1, 4 Oct 2010
12. Singsathien J, Suwanasri T, Suwanasri C, Ruankon S, Fuangpian P, Namvong W et al (2017) Partial discharge detection and localization of defected power cable using HFCT and UHF sensors. In: 2017 14th international conference on electrical engineering/electronics, computer, telecommunications and information technology (ECTI-CON). IEEE, pp 505–508
13. Dukanac D (2018) Application of UHF method for partial discharge source location in power transformers. IEEE Trans Dielectr Electr Insul 25(6):2266–2278
14. Judd MD, Yang L, Hunter IB (2005) Partial discharge monitoring of power transformers using UHF sensors. Part I: sensors and signal interpretation. IEEE Electr Insul Mag 21(2):5–14
15. Chakravarthi MK, Giridhar AV, Sarma DS (2019) Localization of incipient discharge in power transformer using UHF sensor. In: 2019 international conference on high voltage engineering and technology (ICHVET). IEEE, pp 1–3

16. Mao Y, Ding Y, Wu J, Chen J (2020) Research on partial discharge detection technology for power transformers. In: 2020 IEEE 4th conference on energy internet and energy system integration (EI2). IEEE, pp 3956–3959
17. Li Y, Chen D, Li L, Zhang J, Li G, Liu H (2017) Study of comparison between ultra-high frequency (UHF) method and ultrasonic method on PD detection for GIS. In: IOP conference series: earth and environmental science, vol 94, No 1. IOP Publishing, p 012086

A Study and Investigation of Structural Parameters of Vertically Aligned Carbon Nanotube Arrays as a Thermal Interface Material



Ayush Nirwal, Rushabh Agrawal, Ragini Meena, Aayush Raval, Akash Parmar, and Rutu Parekh

Abstract Carbon nanotubes (CNTs) have high thermal conductance and the potential to be the thermal interface material (TIM) of the future. This paper presents how various structural parameters like mean height, a fractional standard deviation of height, a fractional standard deviation of space, and an outer diameter of CNT arrays affect the contact area and the tip contact resistance (TCR) between the heat sink and vertically aligned CNTs (VACNTs) using the simulation tool. The simulation tool is based on the bead-spring model, and it counts van der Waals interactions between the heat sink and VACNT. It is investigated that by changing the fractional standard deviation of height from 0 to 0.05, TCR increases from 62.26–319.52 mm²K/W. It is also observed that by changing an outer diameter from 40 and 72 Å, tip contact resistance decreases from the range of 124.68–62.26 mm²KW⁻¹ that is a decrement of 62.42 mm²KW⁻¹, and by changing an outer diameter from 40 to 400 Å, TCR decreases from 124.68–4.49 mm²KW⁻¹. These types of simulation results show that the mean height and the fractional standard deviation of space do not show a drastic change in TCR value, but the fractional standard deviation of height and the outer diameter of multi-walled CNT in VACNT are among the primary parameters which drastically change TCR value while slightly changing them.

Keywords Heat dissipation · Thermal interface material (TIM) · Thermal coupling · Compressive stress · Thermal conductivity

1 Introduction

Thermal interface materials are a category of products used to aid thermal conduction between mechanically mated surfaces (two regions with one or more parts that contact each other) such as a semiconductor device and a heat sink, for example, a thermal interface material (TIM) between silicon die and a heat spreader is shown in Fig. 1.

A. Nirwal · R. Agrawal · R. Meena · A. Raval · A. Parmar (✉) · R. Parekh
VLSI and Embedded System Group, Dhirubhai Ambani Institute of Information and Communication Technology, Gandhinagar, India
e-mail: akash.parmar9122@gmail.com

Various types of materials are used as thermal interface materials like Arctic silver 5 (AS-5), Matrix, Arctic Alumina, ceramic, Arctic Silver Thermal Adhesive, Arctic Alumina thermal adhesive, silicone and non-silicone heat sink compounds, pads, gap fillers, and epoxies [1]. To enhance the heat transfer between the two surfaces, a thermal interface material aims to fill the gaps between surfaces in contact with a substance that has improved thermal conduction and reduced thermal resistance between contacting surfaces. Higher thermal conductivity implies thermal interface material to allow better heat flow than one with lower thermal conductivity. Various structural formations are used for TIMs like gap pads-fillers, conductive adhesives, and thermal greases. Multiple properties are taken into consideration for a TIM depending on its application, including adhesiveness, viscosity, coefficient of thermal expansion (CTE), bond line thickness, rework ability, and longevity. However, major ones include through-plane conductivity and thermal contact resistance. CNTs, due to their high thermal conductance, have the potential to be TIM. CNT-based TIMs are among the most recognized ones, owing to the fact that their high values of thermal conductance along their axis provide outstanding thermal coupling. Grease-based TIMs and gap filler pads show a decrease in thermal resistance when under compressive stress, but structural deformations are irreversible [2] and cause degradation in overall performance over time. Carbon-loaded polymer and CNT nanostructures also show a decrease in thermal resistance under compressive stress but have high tensile strength [3, 4].

The vertically aligned structure of carbon nanotube arrays has thermal conductivity of over $200 \text{ Wm}^{-1} \text{ K}^{-1}$ compared to a bulk sample of randomly aligned single-walled carbon nanotubes structured, which has noticed thermal conductivity of $35 \text{ Wm}^{-1} \text{ K}^{-1}$ [5]. Han and Fina observed that for aligned CNTs, thermal conductivity is much higher compared to un-aligned CNTs [6]. In the bundle of CNT arrays,

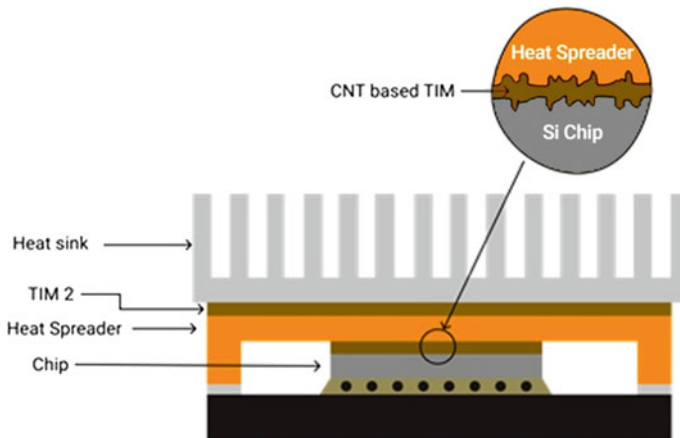


Fig. 1 Schematic application of thermal interface materials in electronic packages. The figure shows CNT-based TIM between heat spreader-SINK and Si chip (source)

thermal conductivity is more dependent on tube–tube interconnections and CNT structural defects. Randomly aligned CNTs have more entanglement than vertically aligned CNTs, resulting in high thermal resistance and low thermal conductivity [5]. So, VACNTs have high thermal conductivity compared to randomly aligned CNTs. So, the vertically aligned structure of CNT arrays is better than randomly aligned CNTs as thermal interface material. Vertically aligned carbon nanotube arrays (VACNT) can be used as thermal interface material because each CNT-pristine has high thermal conductivity ~ 1000 W/mK [7]. So, VACNT shows hope for better results as a TIM. Jun Xu and T. Fisher synthesized dense and vertically oriented CNT arrays on a silicon wafer using plasma-enhanced chemical vapor deposition and used it as TIM [8]. It is observed that dry CNT arrays generate minimum thermal interface resistance of 19.8 mm²W/K and for Cu-PCM-Si (PCM-phase change material) interface has a resistance range from 52.2 to 16.2 mm²K/W, while the Cu-PCM-CNT-Si interface has a minimum interface resistance value 5.2 mm²K/W at 0.35 MPa pressure [8]. It was also concluded that the PCM-CNT array has higher thermal conductivity than PCM. Peacock et al. synthesized vertically aligned carbon nanotube on silicon surface using chemical vapor deposition process, and noticed interfacial thermal resistance of CNT-solder composite was 0.458 cm²K/W at a 20 psi while 0.425 cm²K/W at a pressure of 50 psi [9]. Yao et al. grew a high-quality vertically aligned carbon nanotube and made it a TIM sample that has thermal boundary resistance from 11.6 ± 0.5 mm²K/W to 3.4 ± 0.1 mm²K/W [10]. These types of experiments promise vertically aligned carbon nanotube arrays (VACNTs) as next-generation thermal interface material. Recent advancement in the fabrication process of chemical vapor deposition (CVD) [10] allows us to get optimally aligned carbon nanotube (CNT) nanostructures with their aligned axis on the surface of the heat source itself seen in Fig. 2.

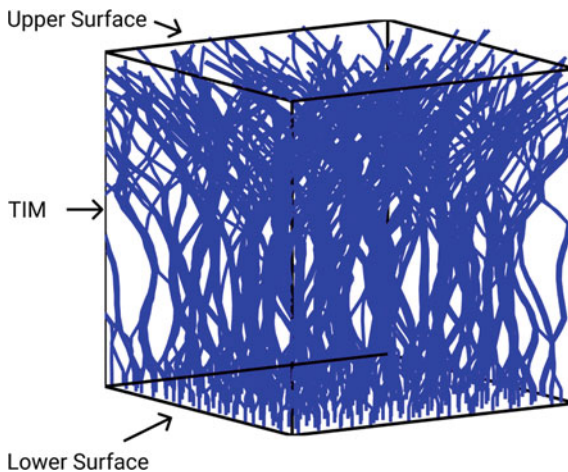


Fig. 2 Structure of VACNT: One end of an array of CNTs is fabricated to the lower surface, and the other end is freely suspended along the upper surface [13]

One problem with using CNT arrays' vertically aligned structure is that not all CNT arrays are in contact with the sink material as they slightly vary in height. Ping et al. mentioned that only 3%–15% of CNTs arrays contributed to thermal transport [11]. They also observed that for VACNT arrays on a silicon surface, total thermal resistance is $16 \text{ mm}^2\text{KW}^{-1}$, while thermal contact resistance is $14 \text{ mm}^2\text{KW}^{-1}$. Simulations of vertically aligned CNTs arrays were carried out, and experiment results show that CNT–CNT contact conductance is less important than CNT-substrate contact conductance and thermal conductivity [12]. It was also concluded that CNT-substrate contact is the main bottleneck to reduce the performance of vertically aligned CNTs as TIM, and thermal conductivity is dependent on diffusive resistance and pressure-dependent array height. So, in this paper, the main concentration is on how various structural parameters like mean height, a fractional standard deviation of height, a fractional standard deviation of space, and an outer diameter of CNT arrays affect the tip contact resistance and the contact area between TIM and sink under compressive stress/strain.

2 Methodology

Sadasivam et al. use the bead-spring model of reference [14] and microwave plasma chemical vapor deposition technique for simulating the vertically aligned CNTs structure for experiments [12] and creating the simulation tools [13]. The simulation tool [13] uses the bead-spring model of CNT and takes van der Waals interaction into account to model the physical and thermal behavior of the CNT nanostructure [14, 15]. The vertically aligned CNTs arrays have van der Waals interactions with an upper surface shown in Fig. 2. The length of individual CNTs and spacing between them present in the nanostructure are taken as a Gaussian distribution, while the outer diameter is taken as a constant value throughout the structure [16]. The different parameters are varied individually to observe their respective effects on the tip contact resistance under different compressive stress/strain. In Table 1, all input parameters and their values are mentioned, which are used in the simulation tool [13]. The tip contact resistance of the lower surface with the CNT arrays is nominal compared to the tip contact resistance between the upper surface and CNT arrays because a covalent bond exists between the lower surface and CNT arrays, while a weak van der Waals force exists between the upper surface and CNT arrays. The reader can refer to reference [13] to learn more about the tool and refer to reference [10] for further details about structure. So here, consider tip contact resistance as tip contact resistance between the upper surface and CNT arrays.

Table 1 Input parameters

Input parameters	Simulation values
Mean height (in Å)	5000
Fractional standard deviation of height	0
Number of CNTs on each side	4
Average spacing (in Å)	1200
Fractional standard deviation in spacing	0.2
Equilibrium spacing between beads (in Å)	1000
Outer diameter (in Å)	72
Number of walls	6
Fractional length	0.3
Mean vertical inclination	30
Fractional standard deviation in vertical inclination	0.1
Young's modulus of CNT (in Pa)	1e12
Cut off distance (in Å)	2000
Number of steps before dump	50,000
Stopping tolerance for energy (eV)	0.0000000000000001
Stopping tolerance for force (eV/Å)	0.0001
Number of indentation steps	5
Indentation step size (in Å)	100
Contact resistance per unit area (in m ² K/W)	10e-8
Indenter force constant (eV/Å ³)	1e3
Bending stiffness scale parameter	1

3 Results and Discussions

The results are simulated by varying one parameter or two parameters under compressive stress/strain during simulations, while other parameters' values are taken as the default value, which is shown in Table 1. Out of all the input parameters, mean height, the fractional standard deviation of height, the fractional standard deviation of space, and an outer diameter were varied for the simulation results. According to simulation results, graphs were plotted for tip contact resistance and contact area.

3.1 Effect of Compressive Stress/Strain on Contact Area and on Tip Contact Resistance

Figure 3a, b is generated by merging two graphs: (1) Contact area versus strain, (2) Stress versus strain. In Fig. 3a, b, strain is taken in the x -axis because it is common for both graphs, while compressive stress and contact area are taken in two different y -axes. Figure 3a, b shows how compressive stress generates compressive strain in VACNT structure and how compressive strain affects the contact area between the upper surface and CNT arrays.

Figure 4a, b is generated by merging two graphs: (1) Tip contact resistance versus stress, (2) Tip contact resistance versus strain. In Fig. 4a, b, tip contact resistance is taken in the x -axis because it is common for both graphs, while compressive stress

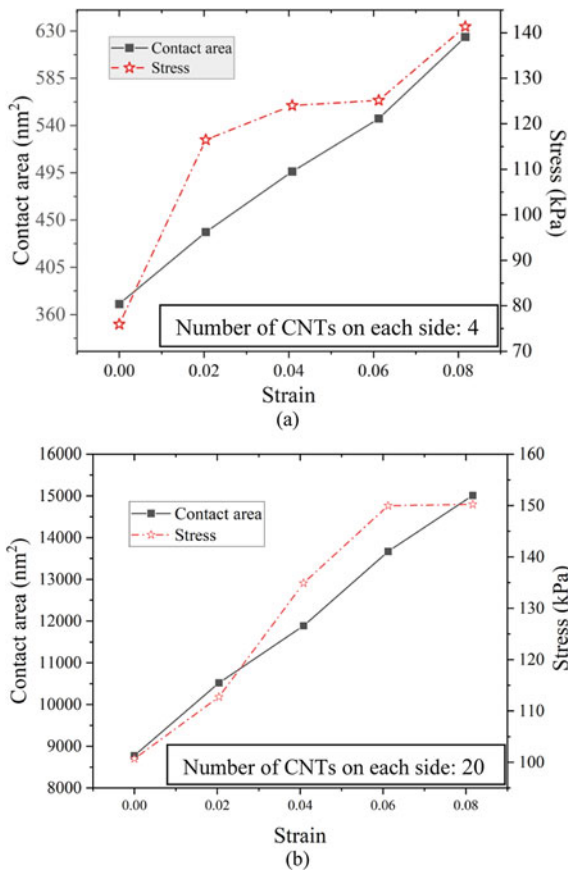


Fig. 3 **a** Contact area versus strain and stress versus strain for VACNT with mean height equals 500 nm and number of CNTs on each side equals 4. **b** Contact area versus strain and stress versus strain for VACNT with mean height equals 500 nm and number of CNTs on each side equals 20

and compressive strain are taken in two different y-axes. Figure 4a, b shows how compressive stress and compressive strain affect the tip contact resistance between the upper surface and CNT arrays. Figures 3a and 4a are obtained from applying compressive stress on VACNT structure with CNT arrays of a mean height of 500 nm, and the number of CNTs on each side is 4, so the total number of CNTs is 16. Figures 3b and 4b are obtained from applying compressive stress on VACNT structure with CNT arrays of a mean height of 500 nm, and the number of CNTs on each side is 20, so the total number of CNTs is 400.

Figure 3a, b shows that contact area increases with increasing compressive strain. Figure 4a, b shows a decrease in thermal contact resistance (TCR) with increased compressive strain. VACNT arrays make point-type contact with the substrate,

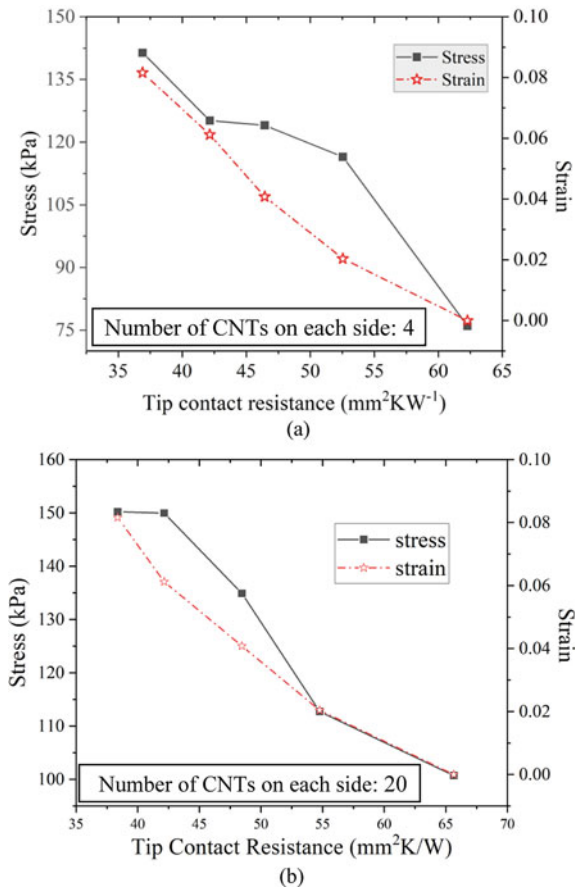


Fig. 4 **a** Change in tip contact resistance on increasing compressive stress and strain for VACNT with mean height equals to 500 nm and the total number of CNTs equals to 16. **b** Change in tip contact resistance on increasing compressive stress and strain for VACNT with mean height equals to 500 nm and the total number of CNTs equals to 400

which means VACNT makes only vertical tip-point contact using weak van der Waals without any compressive stress/strain. It is also observed that tip inclination, percentage of CNTs in contact with the upper surface, and total tip contact area increase with increasing compressive stress [12]. VACNT arrays' mean tip angle increases with the upper surface due to applied compressive stress means that VACNT arrays vertical tip bent during compressive stress/strain [5, 12]. It is also observed that bent horizontal tips of VACNT arrays make line contact with the substrate, which significantly increases the contact area with the upper surface. So, increasing strain increases the contact area of CNT arrays with the sink. Due to more contact area, more van der Waals interaction is happening between the CNT arrays and sink surface, which decreases the tip contact resistance and increases the viability of this nanostructure to be used as TIM.

It is observed when the total number of CNT is 16, to increase the compressive strain from 0.02 to 0.06, the additional compressive stress of 8.68 kPa is required, which is the change of compressive stress from 116.47 to 125.16 kPa. Moreover, when the total number of VACNT equals 400, to increase the compressive strain from 0.06 to 0.08, the additional compressive stress of 0.248 kPa is required, which is the change of compressive stress from 149.97 to 150.21 kPa. This observation shows that sometimes a significant change in compressive strain for VACNT structure requires a meager change in compressive stress. From Fig. 3a, b, it is observed that the starting portion of the stress–strain curve is rapidly increasing, and after one point, some part of the stress–strain curve is slightly increasing. This type of behavior and flattening in the stress–strain curve in VACNT is also observed by Sadasivam et al. [12] and Maschmann et al. [17]. The flattening in the stress–strain curve is due to collective buckling in VACNT arrays. All the CNT arrays are buckled [4] due to compressive strain, and Maschmann et al. observed well-organized collective buckling for the top surface of VACNTs [17]. Additional buckling was also observed near the lower surface for 650 and 1200 μm mean height [17]. Figure 3a, b shows the buckling effect on both VACNT structures despite the difference in the total number of CNTs. From Fig. 3a, b, it is observed that to get a buckling effect, more number of VACNTs structure required more stress than less number of VACNTs structures. The buckling happens because of so much compressive stress/strain on this type of aligned arrays structure like VACNT has.

Sadasivam et al. got 0.06 strain for 150 kPa stress on VACNT structure which has a mean height of 500 nm and total number of CNTs equal to 400 [12]. A similar result is observed for VACNT structure with a mean height of 500 nm and a total number of CNTs equal to 400 required 149.97 kPa stress for 0.06 strain in VACNT structure according to simulated result (see stress–strain curve in Fig. 4b). Sadasivam et al. also compared the simulation base stress–strain curve and experimental base stress–strain curve to observe that the simulation base tangential modulus for different realizations varies between 2.5 to 4 MPa, which is close to the experimental base tangential modulus [12]. Due to compressive strain, higher frequency phonon mode increases [18]. The diffusive resistance shows a weak dependence on applied pressure [16], but the thermal conductivity and thermal diffusivity of CNTs decrease because of buckling [16, 18]. Additionally, if the outer shell of a multi-walled CNT breaks, then

thermal conductivity changes drastically [19]. It was also observed that too much stress might bend or break some CNTs in the structure, and a defected VACNT structure does not transfer phonons fast compared to pristine VACNT [20].

3.2 Effect of Mean Height of VACNT Arrays on Contact Area and on Tip Contact Resistance

Here, a VACNT nanostructure follows a Gaussian distribution, with mean and fractional standard deviation as parameters in the simulation tool [13]. The changes in the tip contact resistance are analyzed by taking different values of a mean height (300 nm, 400 nm, 500 nm, 600 nm). Figure 5a, b is generated from the simulation results for different mean heights. For 300 nm, 400 nm, 500 nm, and 600 nm of mean height, the tip contact resistance, respectively, is 28.40 mm²K/W, 32.84 mm²K/W, 36.90 mm²K/W, and 45.36 mm²K/W (see in Fig. 5b for zero compressive strain). It could be observed that tip contact resistance slightly increases with an increase in the mean height. The diffusive resistance increases with an increase in the mean height of the CNT arrays [16], and for different thermal conductivity, the diffusive resistance value is in order of 1 mm²K/W [4].

Figure 5a, b shows that as compressive strain increases, the contact area increases, and the tip contact resistance decreases because of more contact area available, and more van der Waals interaction is happening between the CNT array tip and the upper surface. From Fig. 5a, b, it can be observed that the contact area is inversely proportional to tip contact resistance. In analytical work, it was observed that thermal conductivity for vertically aligned multiwall carbon nanotube decreases with an increase in mean height because as the height increases, defect density also increases in CNT arrays, which reduces thermal conductivity for longer CNT arrays [21]. Recent research and development on VACNT shows that post-growth treatment and quality-controlled synthesis, including thermal annealing and coating with a thermal conductive layer, optimizes VACNT arrays' quality with high thermal conductivity and less defect density [11]. The high-quality VACNT arrays with less defect density have a thermal conductivity in order of 10 Wm⁻¹ K⁻¹ which is better than many available commercial TIMs [11].

3.3 Effect of Fractional Standard Deviation of Height of VACNT on Contact Area and on Tip Contact Resistance

The fractional standard deviation (SD) of height distribution is also a structural parameter whose effect on tip contact resistance is observed by changing it in small and large gaps (0, 0.05, 0.06, 0.07, 0.1). Figure 6a shows significant changes in the

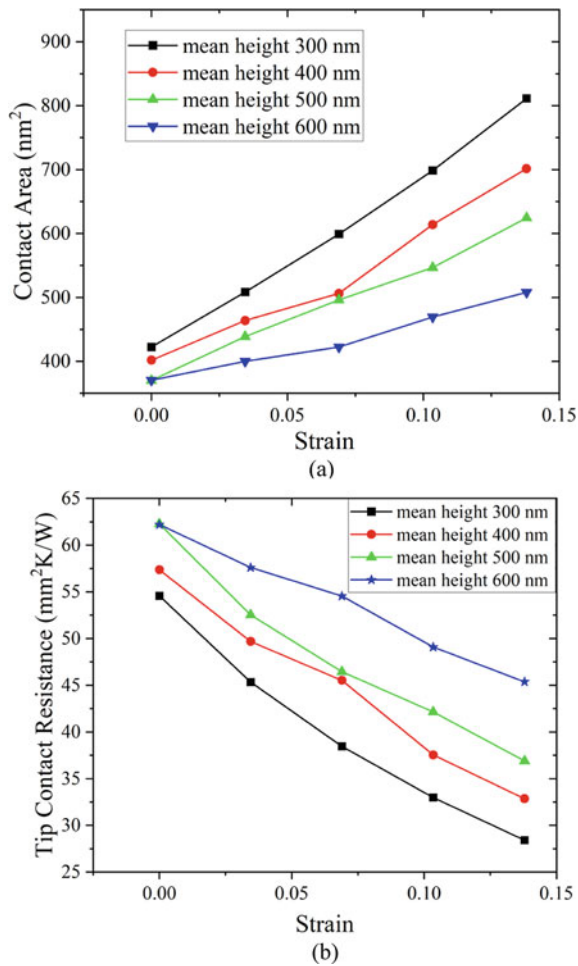
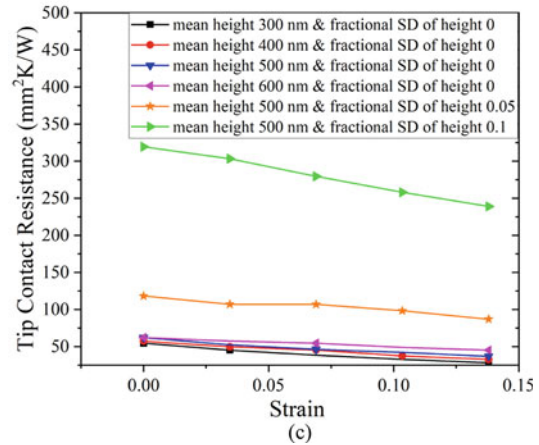
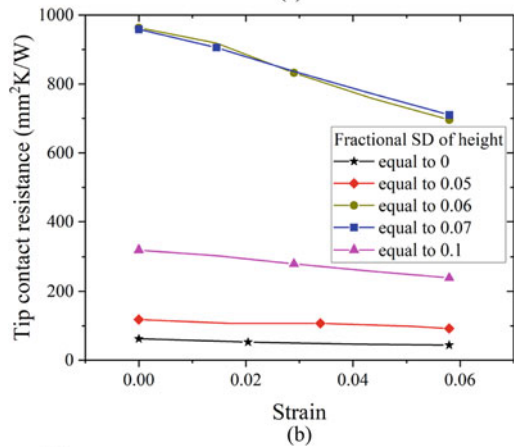
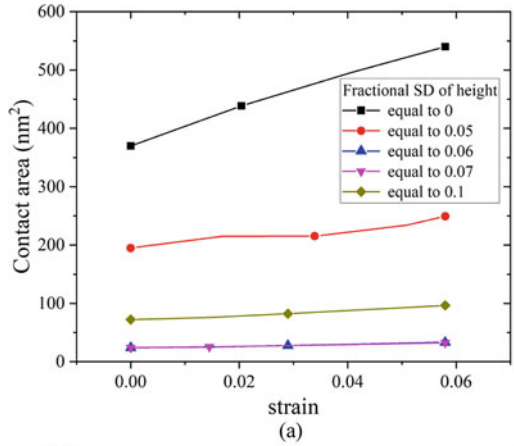


Fig. 5 **a** Contact area versus strain for different mean height. **b** Tip contact resistance versus strain for different mean height

contact area, and Fig. 6b shows the effect on the tip contact resistance for different values of the fractional standard deviation of height with a fixed mean height of 500 nm. From Fig. 6c, for a VACNT structure with the fractional standard deviation of height equal to 0, when a mean height increases from 300 to 500 nm, tip contact resistance slightly increases from 54.56 to 62.26 mm²K/W. From Fig. 6c, for a VACNT structure with a mean height equal to 500 nm, when the fractional standard deviation of a height slightly increases from 0 to 0.05, tip contact resistance significantly increases from 62.26 to 319.52 mm²K/W even without any type of stress/strain. So, the fractional standard deviation of height is an important parameter to design VACNTs as TIM.

Fig. 6 a Contact area versus strain of VACNT as TIM on varying fractional standard deviation (SD) of height for mean height equals to 500 nm. **b** Tip contact resistance versus strain of VACNT as TIM on varying fractional standard deviation of height for mean height equals to 500 nm. **c** Tip contact resistance versus strain of VACNT as TIM on varying mean height and fractional standard deviation of height



As the fractional standard deviation of height is 0, almost all CNTs are in contact with the sink material, and a very high contact area is available (see Fig. 6a for the fractional standard deviation of height equals 0) (structural deformation is also taken into account). So, the least tip contact resistance is available when the fractional standard deviation of height is 0 which is analyzed in Fig. 6b for the fractional standard deviation of height equal to 0. When the fractional standard deviation of a height slightly changes, the number of CNTs with mean height and the number of CNTs with different heights significantly vary according to Gaussian distribution and standard deviation. So, it is observed that the number of CNTs with direct contact with the sink significantly changes. It is also observed that contact area and tip contact resistance also considerably change compared to the value of contact area and tip contact resistance when the fractional standard deviation of height is 0 (see in Fig. 6a, b). If TCR increases, then total thermal resistance increases, and thermal conductivity and thermal diffusivity decrease [19].

3.4 Effect of Fractional Standard Deviation of Space Between CNTs on Contact Area and on Tip Contact Resistance

This parameter represents how regularly the CNTs are arranged in the nanostructure. In the simulations, these values of the fractional standard deviation of space are changed in a certain range (0, 0.2, 0.3, 0.4, 0.7).

It can be observed from Fig. 7a, b that tip contact resistance slightly increases with an increase in the fractional standard deviation of spacing (see Fig. 7b), and contact area decreases with an increase in the fractional standard deviation of space (see Fig. 7a). Hence, it can be said that more regular structures will be a superior choice for thermal interface material. However, the changes in TCR values are insignificant and slightly changed (in order of 10 s with a change of 0.1 in fractional Standard Deviation of spacing) (see Fig. 7b). Thus, this parameter would not so much matter for tip contact resistance. It was observed that the overall thermal conductivity of the VACNT structure increases but not linearly with an increase in packing density [11, 19].

3.5 Effect of Outer Diameter of VACNT Arrays on Contact Area and on Tip Contact Resistance

Contact area significantly increases with an increase in the outer diameter of VACNT (see in Fig. 8a) because each CNT is bringing more area in contact with the sink material as the outer diameter increases. When an outer diameter is 40 Å, the contact area is 184.78 nm², and tip contact resistance is 124.68 mm²KW⁻¹. When the outer diameter is 400 Å, the contact area is 5125.7 nm², and tip contact resistance is

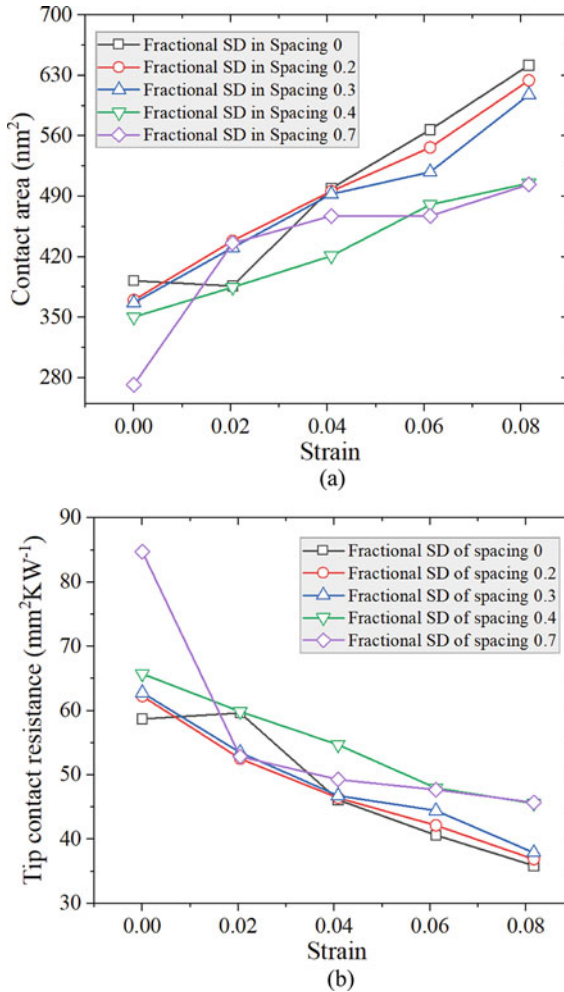


Fig. 7 a Contact area versus strain of VACNT as TIM on varying fractional standard deviation (SD) of space for mean height 500 nm and average spacing 120 nm. **b** Tip contact resistance versus strain of VACNT as TIM on varying fractional standard deviation of space for mean height 500 nm and average spacing 120 nm

4.49 mm²KW⁻¹ which shows a drastic change in the contact area and tip contact resistance.

It can be observed from Fig. 8a, b that this structural parameter would be one of the primary parameters and should be subjected to maximization to decrease tip contact resistance. As outer diameter increases, the effect of strain significantly increases for the contact area (see Fig. 8a). The tip contact resistance follows an inverse pattern with respect to the contact area and substantially decreases with increasing outer diameter (see Fig. 8b). As the outer diameter increases, the thermal conductivity of

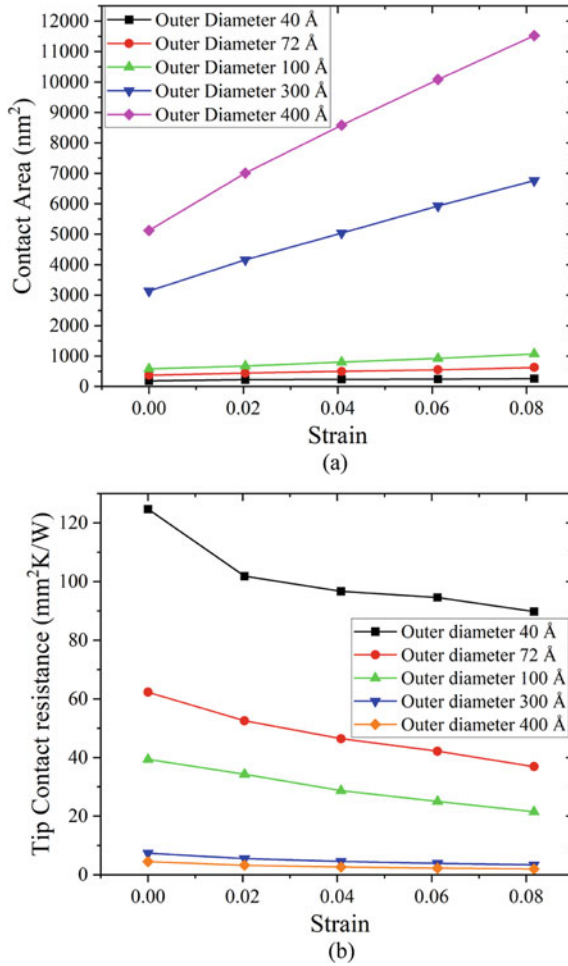


Fig. 8 **a** Contact area versus strain of VACNT as TIM on varying outer diameter for mean height equals to 500 nm. **b** Tip contact resistance versus strain of VACNT as thermal interface material on varying outer diameter for mean height equals to 500 nm

individual MWCNT decreases, but aligned contacts between CNTs in VACNT can significantly increase the thermal conductivity of CNTs array structure [22].

4 Conclusion

This research paper shows the effect of various structural parameters on contact area and tip contact resistance under different compressive stress/strain conditions. This

paper presents a quantitative analysis and the most accurate results for contact area and TCR on the effect of changing specific structural parameters under different compressive stress/strain. Out of the studied parameters, a fractional standard deviation of height and the outer diameter of CNTs in the nanostructure can be taken as one of the primary parameters to maximize CNTs contact area and minimize thermal contact resistance for VACNT as thermal interface material (TIM) because thermal contact resistance is a bottleneck to use VACNT as TIM. It is investigated that by varying mean height from 300 to 500 nm, tip contact resistance slightly increases from 54.56 to 62.19 $\text{mm}^2\text{K/W}$, so increasing in the mean height leads to a slight increase in tip contact resistance (TCR). While slight changes in the standard deviation of height from 0 to 0.05, tip contact resistance significantly increases from 62.26 to 319.52 $\text{mm}^2\text{K/W}$, and the increment in TCR value is 410.25%. The fractional standard deviation of spacing does not give a significant difference in tip contact resistance because it is observed a change of 0.52 $\text{mm}^2\text{KW}^{-1}$ from 62.78 to 62.26 $\text{mm}^2\text{KW}^{-1}$ that is only a 0.82% variation on tip contact resistance for the decrement of 0.1 on fractional standard deviation from 0.3 to 0.2. Hence, mean height and fractional standard deviation of space should not consider optimizing tip contact resistance. It is observed when the outer diameter of CNT arrays varies between 40 to 72 Å; the tip contact resistance varies in the range of 124.68–89.74 $\text{mm}^2\text{KW}^{-1}$ to 62.26–36.90 $\text{mm}^2\text{KW}^{-1}$ under different stress/strain situations which is a decrement of 52.84–62.42 $\text{mm}^2\text{KW}^{-1}$ over the change of 32.8 Å of outer diameter. If the outer diameter changes from 40 to 400 Å, then tip contact resistance changes from 124.68 to 4.49 $\text{mm}^2\text{KW}^{-1}$ that is a 96.40% decrease in tip contact resistance without any compressive stress. As mentioned earlier in Sect. 3.5, tip contact resistance dramatically decreases as the outer diameter increases. It is also possible to maintain good thermal conductivity for a larger outer diameter in the VACNT structure. So, the fractional standard deviation of height and outer diameter of CNT arrays are crucial parameters to increase the contact area and to optimize the tip contact resistance.

References

1. Jaiswai P, Dwivedi C (2011) Thermal interface materials used for improving the efficiency and power handling capability of electronic devices: a review. *Int J Innov Technol Creative Eng* 1(5):1–9
2. BOYD corporation: Types of thermal interface material, reusability of thermal grease. <https://www.boydcorp.com/resources>
3. Ohayon-Lavi A, Buzaglo M, Ligati S, Peretz-Damari S, Shachar G, Pinsk N, Riskin M, Schatzberg Y, Genish I, Regev O (2020) Compression-enhanced thermal conductivity of carbon loaded polymer composites. *Carbon* 163:333–340
4. Sadasivam S, Hodson SL, Fisher TS (2013) Microstructure-dependent heat transfer modeling of carbon nanotube arrays for thermal interface applications. In: *Heat transfer summer conference*, vol 55478. American Society of Mechanical Engineers, p V001T03A045
5. Peacock MA, Roy CK, Hamilton MC, Johnson RW, Knight RW, Harris DK (2016) Characterization of transferred vertically aligned carbon nanotubes arrays as thermal interface materials. *Int J Heat Mass Transf* 97:94–100

6. Han Z, Fina A (2011) Thermal conductivity of carbon nanotubes and their polymer nanocomposites: A review. *Prog Polym Sci* 36(7):914–944
7. Berber S, Kwon YK, Tománek D (2000) Unusually high thermal conductivity of carbon nanotubes. *Phys Rev Lett* 84(20):4613
8. Xu J, Fisher TS (2006) Enhancement of thermal interface materials with carbon nanotube arrays. *Int J Heat Mass Transf* 49(9–10):1658–1666
9. Yao Y, Tey JN, Li Z, Wei J, Bennett K, McNamara A, Joshi Y, Tan RL, Ling SN, Wong CP (2014) High-quality vertically aligned carbon nanotubes for applications as thermal interface materials. *IEEE Trans Compon Packag Manuf Technol* 4(2):232–239
10. Wang M, Wang X, Moni P, Liu A, Kim DH, Jo WJ, Sojoudi H, Gleason KK (2017) CVD polymers for devices and device fabrication. *Adv Mater* 29(11):1604606
11. Ping L, Hou PX, Liu C, Cheng HM (2019) Vertically aligned carbon nanotube arrays as a thermal interface material. *APL Mater* 7(2):020902
12. Sadasivam S, Hodson SL, Maschmann MR, Fisher TS (2016) Combined microstructure and heat transfer modeling of carbon nanotube thermal interface materials. *J Heat Transf* 138(4)
13. Wang Y, Sadasivam S, Fisher TS (2015) Combined microstructure and heat transfer modeling of carbon nanotube thermal interface materials. <https://nanohub.org/resources/thermomechcnt>. <https://doi.org/10.4231/D3SN0152F>
14. Buehler MJ (2006) Mesoscale modeling of mechanics of carbon nanotubes: self assembly, self-folding, and fracture. *J Mater Res* 21(11):2855–2869
15. Zhibanov AI, Pogorelov EG, Chang YC (2010) Van der Waals interaction between two crossed carbon nanotubes. *ACS Nano* 4(10):5937–5945
16. Sadasivam S (2016) Atomistic and mesoscopic simulations of heat transfer across heterogeneous material interfaces. Doctoral dissertation, Purdue University
17. Maschmann MR, Zhang Q, Du F, Dai L, Baur J (2011) Length dependent foam-like mechanical response of axially indented vertically oriented carbon nanotube arrays. *Carbon* 49(2):386–397
18. Nakarmi S, Unnikrishnan VU (2020) Understanding size and strain induced variabilities in thermal conductivity of carbon nanotubes: a molecular dynamics study. *Mech Adv Mater Struct* 1–9
19. Lin W, Shang J, Gu W, Wong CP (2012) Parametric study of intrinsic thermal transport in vertically aligned multi-walled carbon nanotubes using a laser flash technique. *Carbon* 50(4):1591–1603
20. Zhou Q, Meng F, Liu Z, Shi S (2013) The thermal conductivity of carbon nanotubes with defects and intramolecular junctions. *J Nanomater*
21. Jakubinek MB, White MA, Li G, Jayasinghe C, Cho W, Schulz MJ, Shanov V (2010) Thermal and electrical conductivity of tall, vertically aligned carbon nanotube arrays. *Carbon* 48(13):3947–3952
22. Yang J, Waltermire S, Chen Y, Zinn AA, Xu TT, Li D (2010) Contact thermal resistance between individual multiwall carbon nanotubes. *Appl Phys Lett* 96(2):023109

Review on Reliability Assessment in Power System



Bansi R. Kanzariya, Trisha Parekh, Kartavi Patel, Mithilesh G. Solanki, Neeraj Kumar Singh, Atul Kumar Yadav, Mahshooq Abdul Majeed, Lalit Tak, and Vasundhara Mahajan

Abstract Reliability analysis is one of the major parts in the study of the power system. This paper comprehensively reviews all aspects where reliability analysis plays a vital role including cyber networks, renewable energy sources, and distribution systems. The cyber portion contains the cyber power system model, failures of information and communication networks, various reliability assessment methods, and cost reliability measures. Reliability techniques of hybrid energy sources, uncertainty, and risk evaluation have been explored. It describes the effect of component failure in the distribution system, sensitivity analysis, and methodology for reliability. Lastly, it delivers a brief description of the microgrid, its challenges, and its reliability. This review paper is expected to provide reliability enhancement strategies and their benefits in summary to upgrade the infrastructure of our modern power systems.

Keywords Power system reliability · Smart grid · ICT network · Cyber security · Renewable resources · CPPS model · Distribution systems

1 Introduction

Reliability plays a crucial role in every field. It is the probability of a device performing a given task within indicated timeframe. The major purpose of studying reliability in the power system is to make the system more economical and to transfer optimum electricity to consumers. To fulfill this, there are some analytical techniques to evaluate reliability. These are fault trees, binary decision diagrams, and Markov chains techniques. Although fault tree has been widely utilized to build an analytical model of the system, this method has several demerits including lack of modeling

B. R. Kanzariya · T. Parekh · K. Patel · M. G. Solanki
Electrical Engineering Department, Pandit Deendayal Energy University, Gandhinagar, India

N. K. Singh · A. K. Yadav · M. A. Majeed · L. Tak · V. Mahajan (✉)
Electrical Engineering Department, Sardar Vallabhbhai National Institute of Technology, Surat, India
e-mail: vasu.daygood@gmail.com

power and arrangement time rises dramatically with the size of the system which needs to be modeled. However, a new particular method for the productive analysis of both static and dynamic fault trees is introduced in [1]. As in case of the conventional reliability evaluation, the long-term performance of a power system has been evaluated. However, for time varying performance the value of its constant failure rate is not able to impact in an operational time frame. Based upon online operation details which is provided by Energy Management Systems (EMS), for real-time atmosphere this paper describes the perception of operational reliability. An evaluation framework of operational reliability is suggested systematically. Failure rates can be affected by distinct parameters such as components' inherent conditions, environmental conditions, and operating electrical conditions. Thus, it is essential to consider in their operational reliability models. For real-time evaluation, a unique algorithm is specified to satisfy the confinement necessity. The basis for operational reliability is presented methodically in [2]. Development of software and reliability evaluation tools are useful to implement the functions. It warns when reliability of system is undesirably low and further obtains information regarding risk on the system [3].

As we go further toward the development of modernization of smart grid, two networks need to be involved for the calculation of reliability. The first is information and communication technology, and the second is the physical power system network. The ICT network includes parameters such as sensors, monitoring function, and communication equipment. Meanwhile, the physical power system network consists of generators, transformers, switches, circuit breakers, etc. Whereas ICT network comes in the power system, it is mandatory to take cyber security as a leading aspect to make the system more reliable. Freshly, in the United States, the phenomenon of cyber-attack occurred on a colonial pipeline in the year 2021. As the ratio of cyber-attack in the network is rising day by day, the modernization of the smart grid which contains all these cyber elements has a higher risk of failure. Because the faulty elements in the physical power system are easier to trace rather than in a cyber network. Some type of failures in cyber components seems normal and work properly and will come whenever a malfunction happens in the system. Therefore, it is necessary to research and take appropriate actions in this direction to prevent losses of revenue and many more causes. Thus, by merging both these two networks the main network cyber-physical power system is targeted to achieve the optimal power flow to decrease the cyber-attacks and vulnerabilities of it and above all enhancing the reliability of this network. The relationship between cyber security and reliability is dominant factors to understand and described in [4]. The failure of any network impacts on optimal power flow, cost, and reliability. The paper [5] presents reliability modeling of power system with protection system failures. It is essential to study these factors so that finding a solution of this problem can establish more reliable system in upcoming days. To take this point into account, [6] describes the importance of reliability for generating system. The conception of proposed node (link) reliability method and results is explained in [7].

The scope of this review paper can be devoted as follows: Sect. 2 represents the reliability analysis of three networks. The cyber part includes a discussion of the cyber

power system model, impact of communication failure and its approaches, and risk evaluation techniques. As moving toward renewable sources, the notion of uncertainty plays a key role; thus, this paper gives the basic overview of fuzzy set, alpha cut, and Mamdani fuzzy logic system to understand uncertainty. It introduces various techniques of reliability for hybrid energy sources. Furthermore, it explains the risk evaluation in the distribution system, sensitivity analysis, the effect of component failure in the distribution system, the concept of microgrid and challenges, reliability modeling, reliability enhancement strategies, and benefits. Section 3 of this review paper reveals the discussion of this review paper. Section 4 provides the conclusion and potential future work of the paper.

2 Related Work

As mentioned earlier in the introduction part the necessity of studying cyber technology, the classification of cyber-attacks is classified in [8]. The impact of cyber-attack on system is evaluated by taking time as a prime parameter two novel indices which is proposed in [9]. Protection algorithm regarding intelligent weighted trust is suggested for sensor system of a smart grid in [10]. Advance gray wolf optimization approach is proposed in [11] to detect the cyber-attack. To protect system against cyber-attacks and malfunctions of devices, the cyber power system model [12] is illustrated in Fig. 1. This paper describes a brief introduction of cyber power system model.

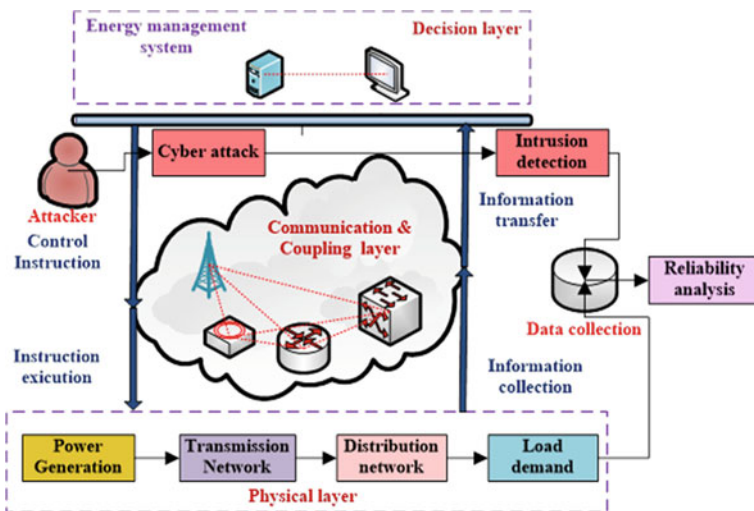


Fig. 1 Cyber power system model

2.1 Cyber Power System Model

1. Power layer: It is the bottom layer of the cyber-physical power system model which is linked to communication and coupling layer. It consists of all electrical equipment such as generators, transformer, lighting arresters, circuit breakers, and switches.
2. Communication and coupling layer: It is middle layer of CPPS model that is connected to both decision layer and power layer. It is composed of communication and interface instruments. Interface devices in this network consist of several other communication devices and also connect them. Thus, it is clear that not working of the interface devices in this network will affect the efficiency and performance of the decision-layer functions. This is a reason why modeling of communication and coupling layer plays an important role to operate effectively a CPPS.
3. Decision layer: In decision layer, there are several functions operated for the effective working of the CPPS model. Further, evaluation of smart grid does not include manual systems. For example, numerical relay. It can be programmed via a computer. An attacker may attack on relay or any devices, deforming values, injecting false data in the grid. False injection data in the grid is more vulnerable. It may mislead the equipment to take the incorrect decision that can result in major malfunction or sometimes black out. The failure of the decision equipment may affect its correctness. For false data injection attack, an artificial neural system detection method is explained in [13].

2.2 Concept of Interdependency

The interdependency is the precise and proper activity of one component which relies on the properties and working of some other components. In cyber network, there are four types of interdependency categories. The concept of reliability evaluation of smart grid utilizing direct cyber power interdependency is covered in this research paper [14, 15]. As concluded from CPPS model, cyber and physical network are interconnected by information network. Fig. 1 reveals the interconnection of these systems. Thus, it can be said that reliability of equipment of information network can affect the reliability of other networks. To enumerate the reliability of monitoring function, this paper provides a brief over view of method.

2.3 Component Reliability Index

$$R(t) = Q(T > t) = \int_t^{\infty} x(t)dt \quad (1)$$

$$x(t) = 1 - R(t) \quad (2)$$

where $R(t)$ is the probability of the system that will not operate properly under determined conditions and duration of time t and $x(t)$ is the complement of $R(t)$, that means system does not work nicely.

2.4 Reliability Block Diagram Based on Component Logic

A system can be categorized into three sections:

- (1) Series system: If a system contains n modules and all modules are working properly, then the system is called as series or tandem system.
- (2) Parallel system: In system of n module, if one module works ordinarily, then system is called as parallel system.
- (3) Voting system: A system is said to be voting system, if it obeys this condition for r ($1 \leq r \leq p$).

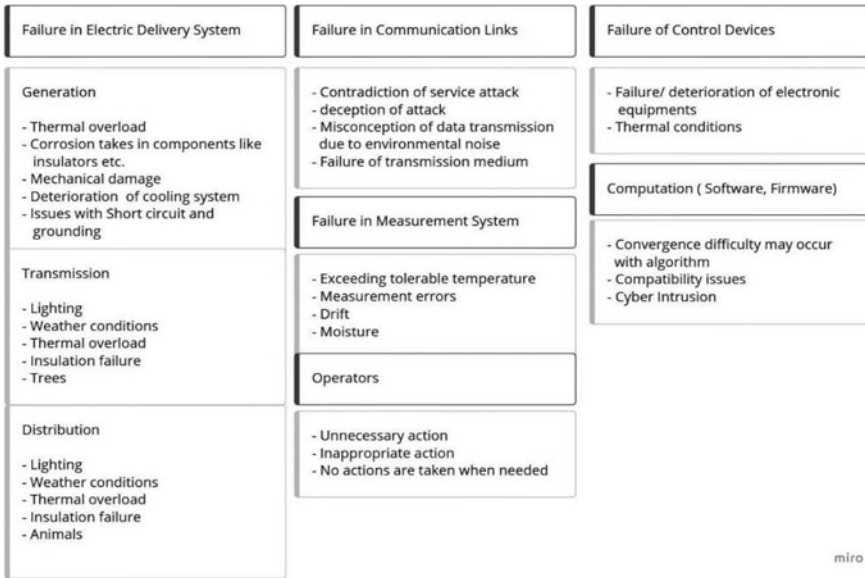
2.5 Impacts of Failure of Communication Network

Failure of any component of any network affects the overall performance of the system. Figure 2 represents the major failure sources of the smart grid. It discusses the system where chances of failure can take place such as electric delivery system, control equipment, measuring network, communication links, and other errors like computation along with operator actions. However, this review paper is mainly concentrated on the impacts of the failure of ICT networks [16]. As the failure of this network may be the case, loss of restraint over a stable operation, communication, and decision components can be root of failure for some of the cause such as:

Constituent Failure: There is a possibility of failing cyber and decision-making equipment such as routers and servers. When it occurs, it impacts communication or decision devices, and as a result, these devices may not be able to take appropriate actions in the power system operation.

Cyber Unavailability: Communication should not hinder because of link unavailability, packet loss, and delay without any physical failure. This affects the decision process of devices, and it tends to weaken power system reliability.

Cyber Intrusion: This comes via communication and coupling layer or decision layer. The decision process could be disrupted by malicious manipulation of information. Cyber intrusion should be modeled as an integral part of the decision blunders for efficient reliability modeling. Hence, the impact of cyber intrusion on power system reliability requires to be integrated.



miro

Fig. 2 Major failure sources in smart grid

The numerical approach to access this cause is optimal power flow, and another method is the implementation of control operation which is presented in the paper [17]. Although this review paper will provide some bullet points to understand. Optimal power flow is an algorithm that discovers the optimum operating point with respect to its target function. During the procedure of optimizing target function, the optimal power flow synchronously decodes the power flow equations and maintains the working conditions within specified limits. Which OPF schemes should be utilized will depend upon the system's structure and the connections between devices. As the name suggested, in centralized OPF all detail is accumulated and observed in the central unit. The considerable dissimilarities between these two are that separately issue is resolved, and all network participants intend to adhere particular solution, and later on, more than one decision-makers solve their own issues based on unique cost functions and constraints. In the case of centralized systems, each separate equipment requires bidirectional communication with the server. While in distributed systems, each IED should mandatorily directly with a subset of peer IEDs in order to take suitable action. Communication is more significant and difficult to handle in a distribution system than centralized. As main work of communication system is to protect, operate system efficiently and control the power system to make more lossless system. Thus, local area network, wide area network, and metropolitan network are suggested. Degraded operation of power system may cause undesirable events. In smart grid, the hardware and software both are necessary to take into consideration to protect the system from inconvenient events such as loss of control, loss of revenue and many more. Thus, the paper [17] shows various condition which

may lead to loss of control. Reliability evaluation utilizing monitoring functions in information system is explained in [18]. To obtain successful results in real time, a case study which is implemented on the IEEE-30 bus system to evaluate the effects of monitoring function on the power system is introduced. Whereas the reliability of the CPPS changes by distinct positions of the transmission lines in the physical system. Hence, the conclusion can be given as the failure of this systems in the varied places will differ with the values of the reliability of the CPPS. After researching in this area, it is concluded that after considering CPPS fusion reliability assessment can more efficiently analyze the reliability of the network. Nowadays, the digital communication has a major contribution to the power system. It is example of cyber-physical device in the smart grid, and with the help of architecture and critical clearing time, risk analysis has been obtained in [19]. While to measure reliability in power communication network an exciting complex network theory approach and to make system strong enough against cyber-attack, the most commonly used analytical method attack tree is proposed in [20, 21], respectively.

Markov model for ICT system is utilized to find the probability of security-based mis-operation of ICT components [22]. It includes three scenarios such as repair rates and detected failure, undetected failure and repair rates, and spurious trip and repair rates of ICT component. The operating states are as follows:

- (1) Normal state: In this, all constituent of ICT network will work correctly.
- (2) Failure, detected: The dependability-based mis-operation (DBM) of constituent is discovered and resolved before it becomes source any undesirable events.
- (3) Failure, undetected: In this, constituent’s DBM failure is not discovered yet, resulting in the scheme failed to work when it is required.
- (4) Spurious trip: An ICT network constituent will work when there is no need for it and causing overall security-based mis-operation (SBM).

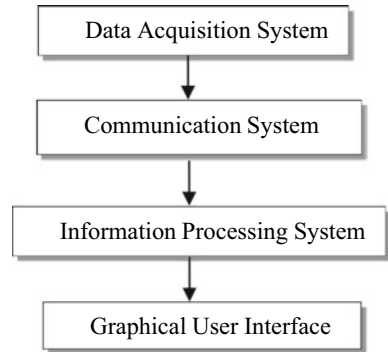
To understand the operation of these states, Table 1 shows the risk level analysis for ICT components via the Markov model.

The protection of power system is becoming a complex task as the majority of task is associated with information and communication network. Thus, more dependency on ICT systems for its resiliency results in information failure or even sometimes

Table 1 Risk level analysis for ICT components using Markov model

Risk level	ICT states			
	Normal	Failure, detected	Failure, undetected	Spurious trip
No	1	NA	0	0
Low	0	1	0	0
	0	1	0	1
Medium	0	0	0	1
High	0	0	1	1

Fig. 3 The information chain constituting organization of components



malicious attack. For safety purpose, [23] studies the main parameters of ICT structure. The prime classification of ICT systems and influence of all possible failures are estimated in [24]. The paper [25] proposes techniques that detect the failure in the ICT system and discusses the probability of major faults such as blackouts. On load curtailments to find the probability of ICT failure rates, sequential Monte Carlo simulation (SMCS) is essential factor to elaborate. The outcomes of test can get via a small-scale power system which is explained in [26]. There are few types of the components establishing ICT infrastructure. Fig. 3 illustrates information chain constituting organization of components. These components should be operated as designed to support operator's decision-making.

2.6 Strategic Reliability Analysis

Few models have been proposed for power system reliability evaluation [5, 27]. There are two possible sites such as reliability and budget based. In a reliability-based vision asserts, utility must acquire a particular stage of reliability. Further, the user can question SRA to present the strategic budget prerequisites. Whereas a budget-based sites provides chance to the user to make reliability budget for upcoming years and accordingly to have SRA enumerate the consequences. Presently, there are total five achievable aims [28, 29].

2.7 Assessment Methods

The popular metrics such as CIF, CID, SAIFI, SAIDI, ASAI, and EENS. CIF and CID are utilized to compute the reliability of distribution systems [30]. The number of constant interruptions for an average customer can be evaluated by SAIFI. The total energy which is going to be decreased can be termed as EENS [31]. Generally,

distribution optimization models are derived for analytical reliability assessments. Electric utility SCADA systems are found useful for reliability evaluation [32].

2.8 Cost Reliability Measures

Evaluation reliability considering electricity pricing is discussed [33]. Based on the classical theory of economic analysis, the predicated steady-state cost can be derived by below formula.

$$\text{Predicated cost} = \sum C_i * \pi_i, \quad i \in \Omega \quad (3)$$

where C_i is the average cost rate co-related with state i [34].

3 New Techniques and Conceptions Proposed for Power System Reliability

In our day-to-day life generally, two types of protection failures are observed by technicians. One more reliability modeling is described in [35], which introduces aging effects of components. Methods such as IIM, TST, and TA are studied, and outcomes are compared for producing inter-arrival time sequence [36]. Selection of methods according to model simplicity and simulation time requisites, IIM is selected as best method out of three methods. The paper [37] represents hands-on calculation of reliability and safety characteristics. Further, there are some recent growths on reliability measure which is discussed in [38]. An optimization model is planned under uncertainty which is proposed in [32]. Accurate techniques on time-dependent source are represented in [39]. The paper [40] describes the methods for performance of electric power communication network. In networks, there are several types of networks in real time, for example, series, parallel, mesh network, etc. [41] reveals method to evaluate mesh network reliability to provide higher quality of services and to deploy a better network. The arrangement of series and shunt also effects the reliability of transmission system; the approaches are mentioned [42]. The IEEE test system has been modified which include RTS transmission modification representing modern power system [43].

4 Risk Evaluation

To identify chances of failure in the system, risk estimation is a prime step in the direction of a reliable and economical system. The proposed algorithm is suggested

to evaluate cyber power reliability which includes methods such as P -table, state mapping, and cyber power link. This portion of risk evaluation considers complex network theory as its major point and represents the methods for risk evaluation in ICT network [44]. The first task to calculate the risk of mal-operation is to check the event to be analyzed and its consequences. All faulty or perilous events should be contemplated to analyze it. Let us assume, only one event at a time takes place, and all consequences are equalized to one. The shortest path algorithms will be beneficial, finding the shortest path between source and target via some component. However, in some cases, the reliable path and the operational path are different. Sometimes, shortest paths could not be competent to fulfill the performance. Thus, the system reliability index is taken as a solution for more efficient performance.

5 Reliability of Hybrid Energy Systems

Renewable energy contains a lot of energy strength. It has main natural power sources such as solar, wind, tidal, biomass, and geothermal. Since past few years, plenty amount of growth has occurred in solar and wind energy. For large-scale renewable sources, reliability analysis is described [45]. For small isolated systems, energy utilization is discussed via PV and wind in [46]. However, the development of tidal and biomass has not been popular yet in the world. Whereas the thought of combining both solar and wind renewable energy sources with the smart grid has secured a lot of attention from the researchers as well as marketers in technology and business perspective. The conclusion of the study state that the inter connection of both energy systems into the grid will strengthen the performance. Therefore, the study in this area is concentrated on the hybrid energy system reliability analysis work in [47]. This review paper will deliver a short overview of techniques. The first is alternative model creating techniques. Researchers have provided a discussion regarding hybrid energy system failures. To enumerate the chances of failures by recursive method, discrete distributions are impactful. Further, the large failure rate can be found by constant distribution. This evaluation is also good with the increasing size of the hybrid system. The second is the two-parameter alpha model technique which works according to its flowchart. And the third method is the suggested fuzzy fault tree-based technique. This method will first collect the related data and recognize the problems and arrangements to resolve it. Steps will include all possibilities from subevent to top event. The concept of reliability importance measures for generating system, the methods for reliability analysis such as reliability indices and Welch's test are applied to historical data, and the results of it are discussed in [48]. Clustering algorithm is proposed for risk evaluation of renewable energy sources in [49]. Approach for integrated transportation system has been proposed incorporation electric vehicle [50]. Whenever renewable energy sources are used in the systems, energy storage plays a significant part. As a result, developing consistent reliability evaluation methodologies that integrate energy storage capabilities in assessment is required. A sequential Monte Carlo simulation method can be used for integrating energy storage capability in generating

capacity adequacy measurement of such systems [51]. Using appropriate risk indices like loss of load expectation (LOLE) and loss of energy expectation (LOEE) [52], the system risk is assessed. There are two elementary methods to measure these indices, one being the direct analytical methods and other is the Monte Carlo simulation.

6 Uncertainty

Renewable energy sources are weather-dependent sources, as sometimes due uncertainty such as climate change affects forecasting. To address uncertainty in real world and enable upgrading precise energy time series forecasting, disparate approaches have been developed. Pekaslan and Wagner [53] capture different approaches modeled to minimize information loss by generating uncertainty interval along with not decreasing the results of FS-value to a numeric value. This review paper gives a short view of these methods. According to [53], fuzzy set (FS) theory can be given as “A fuzzy set is a class with a continuum of membership grades.” Here, FS is shaped in a reference frame (Y) by membership function (MF) that affiliated with each component $y \in Y$. The membership grade $\mu_k(y)$ varies in the range $[0, 1]$.

$$k = \{ y, (\mu_k(y)) | \forall y \in Y \} \tag{4}$$

where $\mu_k(y)$ is the membership degree of y on the FS

$$[\mu]\alpha = \{ \forall y \in Y | \mu(y) \geq \alpha \} \tag{5}$$

The concept of Mamdani FLS is described in [54]. The detailed information about intervals is mentioned [55].

7 Approach and Effect of Component Failure in Distribution Systems

For simplicity, the power system is divided into three parts: generation, transmission, and distribution. Essential fault incidence matrix (FIM) can conclude from enumeration of the reliability indexes of distribution systems. The components that influence system reliability can be classified into two sections: quantifiable and non-quantifiable system structure parameters. Using direct partial derivation, sensitivity indexes of the quantifiable parameter can be calculated. Whereas transformation of FIMs are helpful to discover the non-quantifiable network. As sensitivity analysis is an indispensable step to quantify the effect of each component’s failure event on system reliability and recognize the link which is not strong in the system, this can provide valuable information to magnify reliability. There are two classifications of

sensitivity calculation methods, the finite difference technique or perturbation technique and the partial derivation method. Reliability sensitivity indexes are evaluated by partial derivation with respect to the components such as the component failure rate, the fault maintenance time, the power line capacity, and the generator capacity. Currently, the research and study mainly focus on derivation operation on the transmission system to calculate the sensitivity index. No partial derivation method exists for distribution systems. The reason is that the distribution system has an entirely different network structure from the network structure of the transmission system such as the operation mode, the protection practice, the load transfer, and the fault restore process. In this paper, a brief introduction of FIM to calculate reliability is given. The effects of component failure in the distribution system are mentioned as:

- (1) If fault component in system is removed, then only load can be restored; otherwise, it disconnects all power supply paths to the load.
- (2) Due to fault, disconnection of paths to utility takes place, but after fault isolation of faulty component, a load can be restored either from the main power supply or alternative supply.

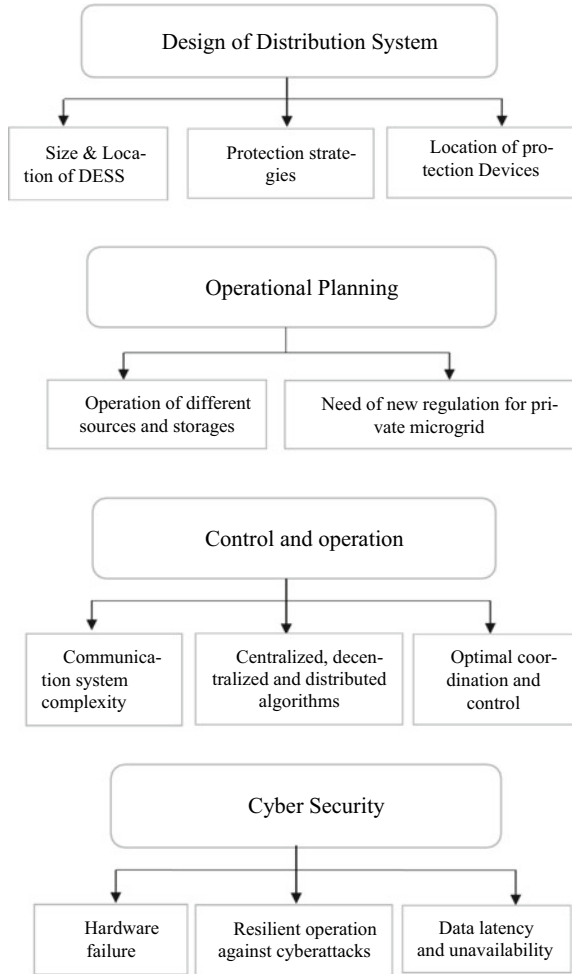
7.1 Risk Evaluation in Distribution System

If cyber component failures and changes of their reliabilities can be calculated systematically, then the total number of risks embedded in ICT system can be found. Thus, sensitivity analysis methods in a distribution system based on the impact of competent failure in the power system are sensitivity of a circuit breaker installation position, sensitivity of a disconnecting installation position of switch, and sensitivity of automation transformation of selected manual switches which are further discussed in [56]. An efficient assess to improve the SAIFI is to diminish the failure rates of these components by updating the equipment or installing breakers. An efficient measure to improve SAIDI and EENS indexes is to reduce the failure rates of these components by updating the equipment or installing switches.

8 Reliability of Microgrid

Nowadays, the concept of the microgrid has caught the eye of researchers. It is an economical and ideal invention of the grid which contains energy sources such as power supply and, in advance, an energy storage system to support abnormal loads. It can be a direct current, alternative, or hybrid system based on a primary source. For stable and continuous operation of the microgrid, it requires the support of cyber elements. Resources of distributed energy and circuit breakers are delivered to cyber and the physical system. The circuit breakers are distinctively modeled by Markov process. The reliability modeling of the cyber-physical microgrid which contains the penetration process of cyber element failure on the physical element and

Fig. 4 Induced challenges in microgrid



Markov three-state model of circuit breakers are informed in [22]. Microgrid induced challenges such as design of distribution system, operational planning, cyber security, control, and operation are explained in Fig. 4.

9 Reliability Enhancement Strategies

This portion of this review paper introduces some techniques to upgrade the reliability of modern renewable power systems. To analyze the reliability of such a system, it is divided into three stages of component, subsystem, and system levels. Power electronics equipment like power converters, transformers, protection relays,

wind turbines, and solar arrays is part of the subsystem which is connected to the component level. By analyzing the failure rate of this, the life cycle of these devices can increase. In subsystem, the reliability of equipment can be affected by operating conditions, temperature changes, and control strategy. To upgrade reliability of any equipment level, an important aspect such as working and effect of environmental conditions and the control strategy are essential for equipment's design. At the power system level, the accessibility of subsystems is of high significance. Failure frequency and duration of maintenance are associated with availability. It can be recovered by diminishing the failure rate or maintenance period. It requires designing of components for reliability. Hence, modeling of reliability would guide to abate failure rate or change the maintenance duration. Overall system reliability can intensify based on the reliability of power sources via the power and energy management strategies. It is mandatory to create an accurate model of devices which impacts the system's reliability from the security perspective.

10 Benefits

The study on distribution network would be helpful, as it determines what will be the effect of installing unique DG sizes at different spots from substation on reliability indices. Further, it states the difference between establishing a large-scale and several small-scale distributed DGs.

- (1) System reliability indices can improve via small-scale distributed DGs rather than an aggregated large-scale DG. As it relies on the locations of DGs, the number of customers, and the sizes of the burden, it is noted that the value of index will improve most when the aggregated DG is located at a point at which line terminates. Further, index value will improve even if DGs are placed near to the termination of line. Although it will be comparatively lower at the end of the line.
- (2) Overall system reliability indices do not affect by establishing alike size of one or more aggregated DG at the same location. As a greater number of DGs are established, the reliability indices can modify for the burden points. Because even if one of them fails during operation, remaining DG can assist the burden points partially.

Some methods are expressed to boost the reliability, feasibility, and resiliency of the power grid [57–64].

11 Discussion

This paper comprises the fundamentals of reliability in the conventional and modern power system. It notifies the various impacts of failure or malfunctions of components on the overall reliability of the entire network. The multilayer structure of the modern power system has been explained. It concludes the interconnection of all networks. The concept of interdependency is introduced. For stable, economical, and continuous operation of power system, the impact of the failure of components in the cyber network, physical power system, and communication network is studied and mentioned an appropriate technique such as attack tree, RBD, fault tree analysis, Fuzzy logic, and complex network theory.

To find the chances of failure of ICT components in the CPPS system, the Markov model has also been discussed. Few categories of the components constituting ICT infrastructure have been plotted, and strategic reliability analysis is mentioned. An accurate approach for time-dependent sources to analyze reliability is represented including modern approaches in reliability power systems. Although risk evaluation techniques such as RBD, complex network, and based network topology are less practical in a real-world scenario to analyze large networks as the excessive computational power requires. Thus, the shortest path algorithm is being used. To transfer maximum electricity to utility, the basic idea of optimal power flow is discussed for a centralized system. The substantial difference between centralized and distribution systems has been discussed. Methods for reliability analysis are described. The new attractive notion of the microgrid in modern power has been explained. Furthermore, the challenges which may appear on the power system due to microgrid are presented. The risk evaluation in the distribution system, reliability enhancement strategies in modern power systems, and benefits are also discussed. At the end, a distribution network planning is described which will result in improvement in reliability indices.

12 Conclusion and Potential Future Work

This review paper presents the perception of reliability, its requirement, techniques, assessment methods, its benefits, and recent advances in techniques. This paper contributes a paramount role to find the reliability of cyber-physical power systems, hybrid energy of the system, distribution system, and in a microgrid. Along with that, it determines all challenges, impact of failure, or malfunctioning of elements in modern power system. It also includes strategic reliability analysis in which few assessment methods have also been discussed. By observing previous work on the reliability analysis, we addressed some future work. It should explore the era of reliability modeling for more accurate, efficient performance. While in cyber power physical system, the risk evaluation and component failure are the future scopes to furnish a reliable power system. As it is proved that Markov's model depends on the failure of the current state as opposed the past information. Future work could focus

on preclusive maintenance modeling to examine its necessity on the components of the station. Hence, electricity supply and operating cost will get affected with the help of this. The value electricity supply will increase mean while operating cost will decrease. The uncertainty of renewable energy sources has required some future work for accurate results. As microgrid is new notion, the reliability of modern power systems is another topic that requires a lot of attention from the researchers.

References

1. Gulati R, Dugan JB (1997) A modular approach for analyzing static and dynamic fault trees. IEEE
2. Bagen, Billinton R (2005) Impacts of energy storage on power system reliability performance. IEEE, pp 494–497
3. Sun Y, Cheng L, Wang P (2010) Overview of power system operational reliability. IEEE, pp 166–171
4. Lei H, Chen B, Butler-Purry KL, Singh C (2018) Security and reliability perspectives in cyber-physical smart grids. IEEE
5. Jiang K, Singh C (2011) New models and concepts for power system reliability evaluation including protection system failures. IEEE
6. Niu M, Xu NZ, Kong X, Ngini HT, Ge YY, Liu JS et al (2021) Reliability importance of renewable energy sources to overall generating systems. IEEE Access
7. Li Q, Cao Z, Tanveer M, Pandey HM, Wang C (2015) An effective reliability evaluation method for power communication network based on community structure. IEEE
8. Aravinthan V, Balachandran T, Ben-Idris M, Fei W, Kapourchali MH (2018) Reliability modeling considerations for emerging cyber-physical power systems. IEEE Access
9. Singh NK, Mahajan V (2021) Analysis and evaluation of cyber-attack impact on critical power system infrastructure. Smart Sci 9(1):1–13
10. Singh NK, Gupta PK, Mahajan V (2020) Intrusion detection in wireless network of smart grid using intelligent trust-weight method. Smart Sci 8(3):152–162
11. Singh NK, Mahajan V (2020) Detection of cyber cascade failure in smart grid substation using advance grey wolf optimization. J Interdisc Math 23(1):69–79
12. Peyghami S, Palensky P, Blaabjerg F (2020) An overview on the reliability of modern power electronic based power systems. IEEE
13. Gupta P, Singh N, Mahajan V (2021) Intrusion detection in cyber-physical layer of smart grid using intelligent loop based artificial neural network technique. Int J Eng 34(5):1250–1256
14. Falahati B, Fu Y, Wu L (2012) Reliability assessment of smart grid considering direct cyber-power interdependencies. IEEE
15. Marashi K, Sarvestani SS, Hurson AR (2017) Consideration of cyber-physical interdependencies in reliability modeling of smart grids. IEEE
16. Vongsingthong S, Smachat S (2014) Internet of things: a review of applications and technologies. Suranaree J Sci Technol 21(4):359–374
17. Falahati B, Kargarian A, Fu Y (2013) Impacts of information and communication failures on optimal power system operation. IEEE
18. Ni M, Li M (2018) Reliability assessment of cyber physical power system considering communication failure in monitoring function. IEEE
19. Huang H, Davis K (2018) Power system equipment cyber-physical risk assessment based on architecture and critical clearing time. IEEE
20. Bertini GJ (2001) Strategic reliability analysis. IEEE, pp 887–890
21. Davis KR, Davis CM, Zonouz SA, Bobba RB, Berthier R, Garcia L, Sauer PW (2015) A cyber-physical modeling and assessment framework for power grid infrastructures. IEEE

22. Zhu W, Panteli M, Milanović JV (2018) Reliability and vulnerability assessment of interconnected ICT and power networks using complex network theory. *IEEE*
23. Panteli M, Kirschen DS (2011) Assessing the effect of failures in the information and communication infrastructure on power system reliability. *IEEE*
24. Ding M, Han P (2006) Reliability assessment to large-scale power grid based on small-world topological model. *IEEE*
25. Singh C, Jiang K (2009) The concept of power unit zone in power system reliability evaluation including protection system failures. *IEEE*
26. Baharum A, Alwan FM (2013) A case study of reliability and performance of the electric power distribution station based on time between failures. *IEEE*
27. Singh C, Jiang K (2011) New models and concepts for power system reliability evaluation including protection system failures. *IEEE*, pp 1845–1855
28. Ikechukwu UK, Okechukwu UK, Ngang NB (2021) Improving power system stability in distribution network with intelligent distributed generation scheme. *Am J Eng Res (AJER)*
29. Sanghvi AP (1982) Strategic planning for power system reliability and vulnerability: an optimization model for resource planning under uncertainty
30. Wang Y, Li W (2010) Reliability analysis of wide-area measurement system. *IEEE*, pp 1483–1491
31. Li Z, Wu W (2019) Analytical reliability assessment method for complex distribution networks considering post-fault network reconfiguration. *IEEE*
32. Bruce AG (1998) Reliability analysis of electric utility SCADA systems. *IEEE*
33. Yang H, Wang L, Zhang Y, Tai HM, Ma Y, Zhou M (2019) Reliability evaluation of power system considering time of use electricity pricing. *IEEE*
34. Da Silva AL, Anders GJ (2000) Cost related reliability measures for power system equipment. *IEEE*, pp 654–660
35. Singh C, Kim H (2010) Reliability modeling and simulation in power systems with aging characteristics. *IEEE*
36. How to check the reliability of a model in power systems?
37. How to hand-calculate system reliability and safety characteristics (1975) *IEEE*
38. Kuo W, Zhu X (2012) Some recent advances on importance measures in reliability. *IEEE*
39. Singh C, Kim Y (1988) An efficient technique for reliability analysis of power systems including time dependent sources. *IEEE*
40. Zhang R, Zhao Z, Chen X, Li J (n.d.) Design and implementation of a RBD-based algorithm for reliability analysis of electric power communication network. *IEEE*
41. Lin C-M, Teng H-K, Yang C-C, Weng H-L, Chung M-C, Chung C-C (2010) A mesh network reliability analysis using reliability block diagram. *IEEE*
42. Yang K, Lin C, Liu H, Sun R (2014) Effect of series and parallel compensation on operating reliability of transmission system
43. Barrows C, Bloom A, Jorgenson J, Krishnamurthy D (n.d.) The IEEE reliability test system: a proposed 2019 update. *IEEE*
44. Zhu W, Han M, Milanović JV, Crossley P (n.d.) Methodology for reliability assessment of smart grid considering risk of failure of communication architecture. *IEEE*
45. Lai Y, Li G (2013) Reliability assessment for power systems with large-scale renewable energy sources. *IEEE*
46. Karki R, Billinton R (2001) Reliability/cost implications of PV and wind energy utilization in small isolated power systems. *IEEE*, pp 368–373
47. Akhtar I, Kirmani S, Jameel M (2021) Reliability assessment of power system considering the impact of renewable energy sources integration into grid with advanced intelligent strategies. *IEEE Access*
48. Agalgaonkar YP, Hammerstrom DJ (2017) Evaluation of smart grid technologies employed for system reliability improvement: Pacific Northwest smart grid demonstration experience. *IEEE Power Energy Technol Syst J*
49. Yang W, Cao M, Ge P, Hu B, Qu G, Xie K et al (2020) Risk-oriented renewable energy scenario clustering for power system reliability assessment and tracing. *IEEE Access*

50. Hou K, Xu X (2015) A reliability assessment approach for integrated transportation and electrical power systems incorporating electric vehicles. *IEEE*
51. Zhang T, Wang C, Luo F, Li P, Yao L (2020) Analytical calculation method of reliability sensitivity indexes for distribution systems based on fault incidence matrix. *J Mod Power Syst Clean Energy*
52. Ahmed NA, Miyatake M, Al-Othman AK (2008) Hybrid solar photovoltaic/wind turbine energy generation system with voltage-based maximum power point tracking
53. Pekaslan D, Wagner C (2020) Uncertainty-aware forecasting of renewable energy sources. *IEEE*, pp 240–246
54. Zadeh L (1965) Fuzzy sets. *Inf Control* 8(3):338–353
55. Mamdani EH, Assilian S (1975) An experiment in linguistic synthesis with a fuzzy logic controller. *Int J Man Mach Stud* 7(1):1–13
56. Guo J, Liu W, Zhang FR (2017) Reliability assessment of a cyber physical microgrid system in Island mode. *CSEE*
57. Waseem MP (2009) Reliability benefits of distributed generation as a backup source. *IEEE*
58. Yadav AK, Mahajan V (2019) Reliability improvement of power system network with optimal transmission switching. In: 2019 IEEE 1st international conference on energy, systems and information processing (ICESIP). pp 1–6
59. Yadav AK, Mahajan V (2019) Transmission line switching for loss reduction and reliability improvement. In: 2019 International conference on information and communications technology (ICOIACT). pp 794–799
60. Yadav A, Mudgal S, Mahajan V (2020) Monte Carlo simulation application in composite power system reliability analysis
61. Yadav AK, Mudgal S, Mahajan V (2020) Transmission switching based available transfer capability assessment to make system network reliable. pp 27–32
62. Yadav AK, Mudgal S, Mahajan V (2019) Reliability test of restructured power system with capacity expansion and transmission switching. pp 1–6
63. Yadav AK, Mahajan V (2019) Transmission system reliability evaluation by incorporating STATCOM in the system network. pp 198–203
64. Yadav AK, Tak L, Mahajan V (2021) Customer-operated solar photovoltaic system to improve the system and customer reliability: solar photovoltaic system incorporation for reliability analysis of composite system. In: Computational methodologies for electrical and electronics engineers. IGI Global, pp 175–185

Synchronization of Optimized Traffic Signals Designed by Webster Method Along Six Intersections of Raipur City from Sharda Chowk to Telibandha Chowk



Bhavesh Kumar Kashyap, Harshit Mishra, Shubham Tiwary, Abhishek Bisen, Mayank Verma, Anurag Wahane, and Alok Kumar Jain

Abstract Over the last decade, large cities have experienced haphazard industrialization and country-wide urbanization. As a outcome, the urban population must travel long distances in the shortest amount of time. To manage travel demand, the intersection should provide the least amount of barrier to traffic flow to reduce travel time. These days, efforts are being made all over the world to safeguard the environment and save the planet. An attempt is made to investigate numerous crossings to reduce delays at these studied intersections. The areas considered for the study consists of Raipur's city busiest intersections, i.e., Sharda Chowk to Telibandha Chowk. In the initial phase, gathering data collected from different intersections analyzing the cycle length, signal type by using the Webster method. The second phase of work is based on accurate green timing for pedestrians. The third phase of work is done with the floating car method for synchronization of the traffic signal at each intersection. It was concluded that synchronization results in cost and time-efficient traffic movement for the road users giving lesser travel durations and low chances of collision thus ensuring smooth traffic operation.

Keywords Synchronization · Webster method · Floating car method · Pedestrian timing

1 Introduction

The study route selected along the major intersection (Sharda Chowk to Telibandha—3.13 km) serves the huge traffic community in Raipur city making the need for proper signal design a mandatory need. The synchronization of these major intersections of the city will be benefited not only by time and money but also in terms of safety and violation against traffic rules. Thus, synchronization of traffic signal timing at the selected study stretch will allow the smooth functioning of traffic flow. Webster

B. K. Kashyap (✉) · H. Mishra · S. Tiwary · A. Bisen · M. Verma · A. Wahane · A. K. Jain
Shri Shankaracharya Institute of Professional Management and Technology, Raipur, India
e-mail: bhaveshkashyap99@gmail.com

method [1] is used for the optimization of traffic timings; thus, more efficient signal timings can be achieved. The journey time is then calculated by the floating car method to calculate the required journey speed through which synchronization can be done. Kushwah et al. [2] examined traffic signal coordination at Bhopal. The time-based coordination is established for current traffic by offsetting signal time for particular junctions where actuated signal controller mechanism deals with the demand of traffic flow and timings are set out. Rafidi and Hamid [3] studied the synchronization of traffic systems for better performance along Penang, Malaysia. However, the vehicle density as well as traffic timings is recorded out in order to plan proper reconsideration of timing along the considered road track. Raifidi and Hamid [3] studied about synchronization of a signal system for better performance along Penga Road, Malaysia. However, the density of vehicles and traffic timings were recorded out to plan proper reconsidered timing of traffic lights for the Penga road. Goliya and Jain [4] investigated a case study for the ring road, Indore for which data collection is done with the Webster method, and synchronization has been carried out for nine intersections to minimize the traffic delay.

Raj [5] studied four junctions at Outer Ring Road of the most fast-growing city Bengaluru, namely Kamakya Intersection, Kathriguppe intersection, Janathba-zar junction, and Hoskerehalli crossing located in Banashankari. The traffic volume counts for the weekdays were recorded on each approach lane, and signal times were synchronized with Webster's method [1]. The author concluded that after synchronization almost a 50% increase in traveling speed was seen due to lack of red time. Jilani et al. [6] synchronized the signals at Helmet Circle, Sal Junction and Mam Nagar, Ahmedabad, from different observations made through video survey and field survey during the process. Since, after the designing of cycle lengths, major differences were seen so to remove the whole bias; the average of the cycle length was taken thus reducing the distortion arriving due to congestion. Gaurav and Goliya [7] have worked on synchronized the optimized signals to improve the level of service at intersections on MR-10 Road. Twelve intersections on a stretch of 8.4 km were studied and designed. It was concluded that 13.71 kmph speed increased from Radisson Square to Lavkush Square and 12.71 kmph speed increased from Lavkush Square to Raddisson Square after the synchronization. Also, CO₂ emission is estimated to reduce by 2.29 million kg per annum. Vinod Kumar and Pavithra [8] studied the signal design at West Church Circle and Gandhi Road Circle, Tirupati, by IRC method and optimized by Webster's method [1] to help in reducing the accident rates at the intersections due to congestion and conflict between vehicles. The comparison of green times by IRC method and trial cycle method was presented.

Sanket and Davara [9] examined the signal time of the KKV junction, Rajkot, to lower the cycle length of signal and the time of each approach. The video recording approach for volume counting and the Webster method [1] for signal optimization has been implemented. The cycle length of KKV intersection is reduced from 250 to 157 s. Roshandeh et al. [10] examined the methodology data on the Chicago area for travel demand, designs, and signal timings for main intersections. Easa and Cheng [11] established a probabilistic method for pedestrian's characteristics to collect data

for 14 intersections. Pimentel et al. [12] applied to a pedestrian using data collected by a pedestrian as input to the model, and a sudden increase in density is observed.

Hamilton [13] deals with the promotion of transportation reliability and timing for the signal which balances overcrowding. Sharma et al. [14] studied to analyze red-light violation under traffic conditions due to timer. Gaurav and Goliya [7] synchronized the transitions between Devesh Naka intersection to Rajeev Gandhi intersection, Eastern Ring Road, Indore, which is about 14.6 km long and comprises 11 transitions. The results include saving of 241 kl petrol and 340 kl diesel per annum and reduction of CO₂ emission by 1.50 million kg per annum. Yun and Park [15] study the development of stochastic optimization for actuated traffic signal by implementing an algorithm with better schemes.

2 Objective for Synchronization of Traffic Signal

The involvement of proper signal timings, a continuation of signals, conveniences for both bicyclist and side walkers in pedestrian, good lightings in crossings and better drainage system impart overall progress in a journey with signalizing. For proper signalizing, the Webster method is applied to reduce delay in seamless traveling along with the pedestrians. This research work will provide cost and time-efficient traffic movement for the road users giving lesser travel durations and low chances of collision thus ensuring smooth traffic operation. The first phase of the study is gathering of data from the intersection for understanding the type of signal system at each and signal cycle length by the Webster method. The second phase of work is based on accurate timing for pedestrians. The third phase of work is done with a floating method for synchronization of the traffic signal at each intersection.

3 Study Specifications and Approach for Synchronization of Traffic Signal

The study area consists of major intersections of Raipur city accommodating a total length of 3.13 km. The study area comprises of six intersections, namely Sharda Chowk, Jaistambh Chowk, Kutchery Chowk, Ghadi Chowk, Bhagat Singh Chowk, and Telibandha Chowk. Each intersection has a four-phase signalized traffic system. The reason behind selecting these intersections is as these intersections possess a large traffic volume of Raipur city (Figs. 1 and 2).

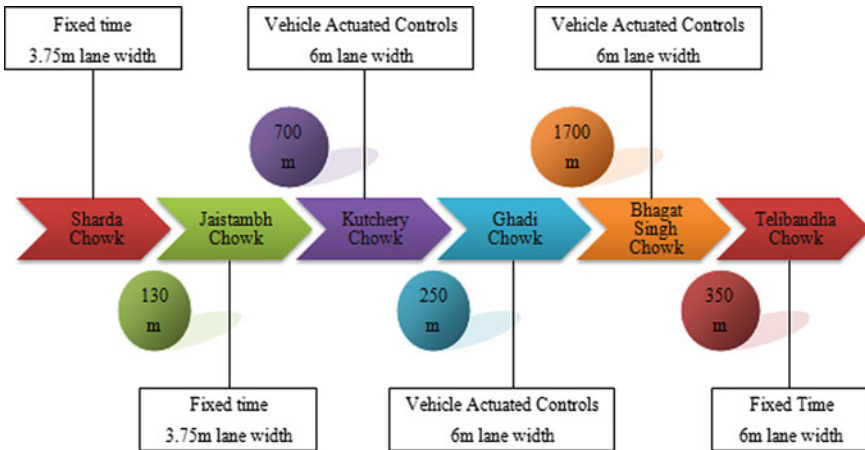


Fig. 1 Sequence of intersections surveyed and their details

3.1 Traffic Survey Procedure and Approach for Data Collection and Designing

The study consists of the collection of preliminary data and traffic survey analysis for six intersections, i.e., Sharda Chowk (SC) having 4 approaches which are Tatyapara Chowk (TPC), Jaistambh Chowk (JC), Banjari Chowk (BC) and Gurunanak Chowk (GNC). Similarly, for JC, i.e., SC, Kutchery Chowk (KC), Gol Bazar (GB), and Moudhapara (MP). Four approaches of KC are JC, Ghadi Chowk (GC), Moti Bagh (MB), and Mekahara (MH). For GC, the approaches are KC, Bhagat Singh Chowk (BSC), Raj Bhavan (RB), and Civil Court (CC). The approaches of BSC are GC, Telibandha Chowk (TBC), CM House (CMH), BTI ground (BTIG). Last TBC has 4 approaches, i.e., BSC, Gurudwara (GW), Canal linking road (CLR), Katora Talab (KT). Traffic volume has been recorded during their peak hours (10:00–12:00 am and 6:00–8:00 pm) for 4 days which consist of 2 weekdays and 2 weekends at each intersection. The type of traffic, i.e., whether the vehicles are light or heavy commercial, decides the type of PCU values to be adopted as per the road congress. After computing the normal flow rate, these values were converted to PCU per hour (Fig. 3).

Saturation flow rates are estimated for each flow direction from 20 min of recording during a green time, and average data are calculated by averaging morning and evening data. Cycle lengths are then estimated for each intersection by Webster’s method [1], and green time is also then calculated for each phase. Journey time is then estimated by conducting the floating car method. Six trips were made throughout the study stretch with 3–3 trips in each direction (Sharda Chowk to Telibandha Chowk—Telibandha Chowk to Sharda Chowk). The synchronization was then done for each intersection signal after the calculation of journey speed and time needed for traveling within the intersections (Tables 1 and 2) (Fig. 4).

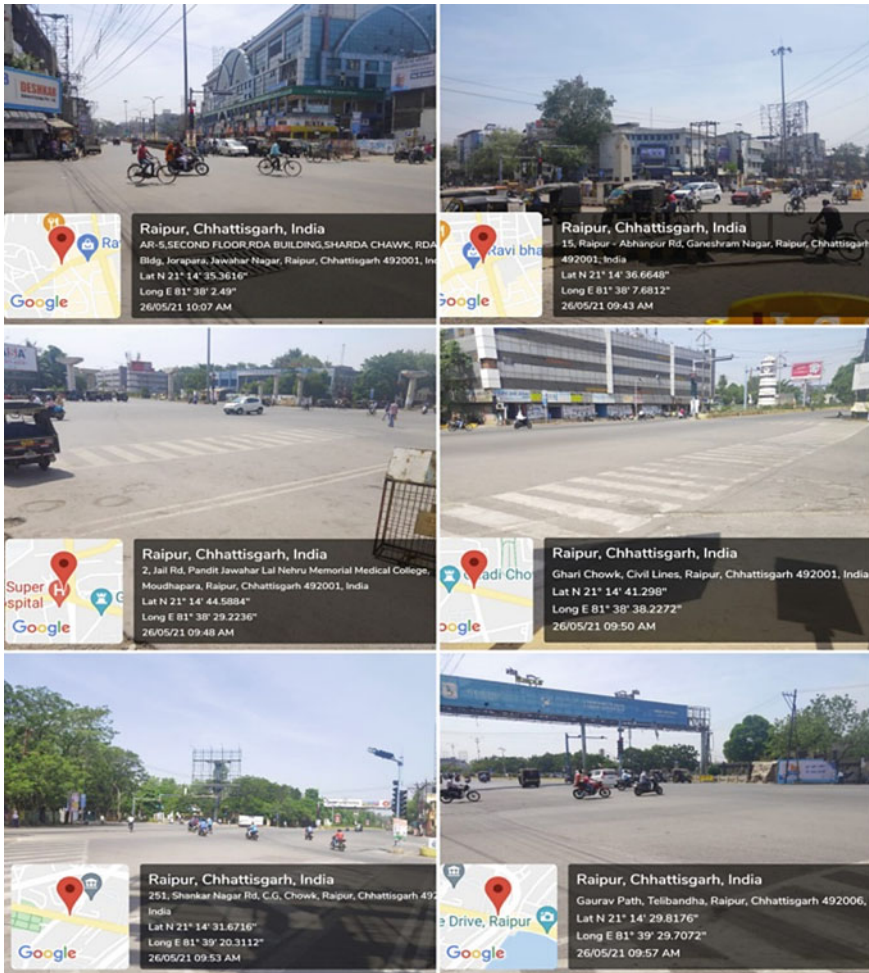


Fig. 2 Geo-tagged locations of studied intersection

Fig. 3 General sequence for synchronization of traffic signal

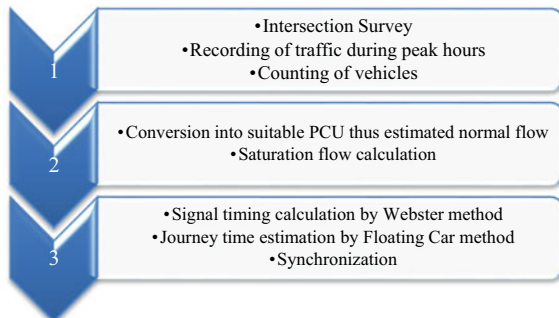


Table 1 Traffic survey data for all locations

Intersections	Green (sec.)	Amber (sec.)	Red (sec.)	Current cycle length (s)	Road width (m)	Type of signal system
SC to TPC	43	3	104	150	3.75	Fixed time
SC to JC	43	3	104			
SC to BC	36	3	111			
SC to GNC	19	3	128			
JC to SC	37	5	108	150	3.75	Fixed time
JC to KC	37	5	108			
JC to GB	25	5	120			
JC to MP	22	5	123			
KC to JC	22	8	90	120	6	VAC
KC to GC	19	8	93			
KC to MB	27	8	85			
KC to MH	17	8	95			
GC to KC	27	5	78	110	6	VAC
GC to BSC	30	5	75			
GC to RB	7	5	98			
GC to CC	12	5	93			
BSC to GC	19	3	98	120	6	VAC
BSC to TBC	35	3	82			
BSC to CMH	23	3	94			
BSC to BTIG	22	3	95			
TBC to BSC	44	5	88	137	6	Fixed time
TBC to GW	28	5	104			
TBC to CLR	28	5	104			
TBC to KT	20	5	112			

3.2 Design Calculation Utilized for Traffic Signal

The optimum signal cycle is given by the relation:

$$C_o = \frac{1.5 L + 5}{1 - Y} \tag{1}$$

where

L = total lost time per cycle, sec = $2n + R$

n = number of phases and R = all-red time or red-amber time

Table 2 Traffic design data for all locations

Intersections	Normal flow (PCU/hr)	Saturation flow (PCU/hr)	2 * n + all-red time	Cycle length	g	Amber	Green	Red
SC to TPC	1307	5651.21	16	120	32	3	31	86
SC to JC	1737.2	6362.8	16	120	38	3	37	80
SC to BC	500.2	3850	16	120	19	3	18	99
SC to GNC	261.2	2173.81	16	120	17	3	16	101
JC to SC	1764.9	8042.7	16	100	27	3	26	71
JC to KC	1346.8	7145.85	16	100	23	3	22	75
JC to GB	979.9	5463.8	16	100	22	3	21	76
JC to MP	1000.5	8678.72	16	100	15	3	14	83
KC to JC	1068.15	5086.43	16	110	27	3	26	81
KC to GC	966.5	5685.29	16	110	22	3	21	86
KC to MB	814.5	4072.50	16	110	26	3	25	82
KC to MH	860.35	5735.67	16	110	20	3	19	88
GC to KC	615.4	2930.48	16	100	25	3	24	73
GC to BSC	746	3390.91	16	100	27	3	26	71
GC to RB	237.2	1976.67	16	100	15	3	14	83
GC to CC	314.9	2099.33	16	100	18	3	17	80
BSC to GC	918.7	3674.80	16	120	35	3	34	83
BSC to TBC	897.45	5609.06	16	120	22	3	21	96
BSC to CMH	1073.35	8256.54	16	120	18	3	17	100
BSC to BTIG	812.6	3869.52	16	120	29	3	28	89
TBC to BSC	1335.8	4947.41	16	120	38	3	37	80
TBC to GW	624.85	4463.21	16	120	20	3	19	98
TBC to CLR	1071.3	8927.50	16	120	17	3	16	101
TBC to KT	1092.55	4966.14	16	120	31	3	30	87

Here,

$$Y = y_1 + y_2 \quad (2)$$

$$y_1 = \frac{q_1}{s_1} \quad (3)$$

$$y_2 = \frac{q_2}{s_2} \quad (4)$$

$$G_1 = \frac{y_1}{Y}(C_o - L) \quad (5)$$

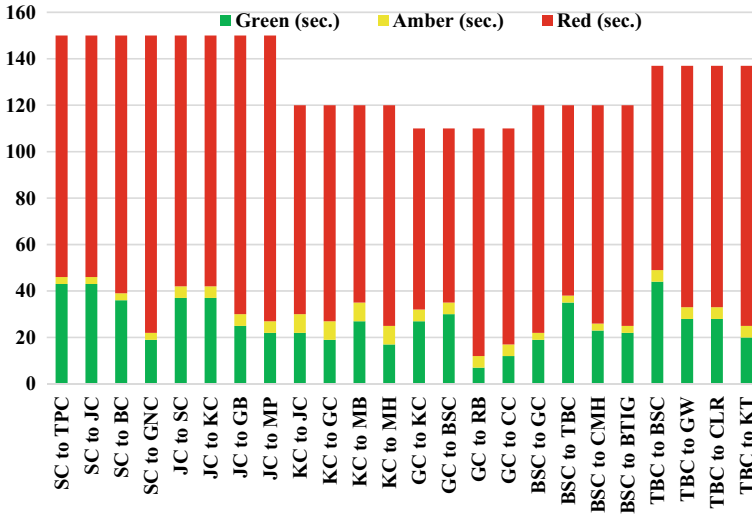


Fig. 4 Traffic signal based on survey data

$$G_2 = \frac{v_2}{Y} (C_0 - L) \tag{6}$$

4 Evaluating the Pedestrian Timings for the Study Area

The pedestrian movement has been majorly obtained at Sharda Chowk and Jaistambh Chowk; thus, pedestrian green times have to be designed for these two intersections. The widths of these junctions are 7.5 m. The guidelines for recommendations followed for pedestrian’s timings are from IRC 93:1985 [16]. The pedestrian green time allocated for intersections is $(7.5/1.2 + 7)$ equal to 13.25 s say 14 s. Therefore, pedestrian green time for pedestrian movement of 14 s is provided (Fig. 5).

Here, all the vehicles traveling along major roads are asked to travel at preassigned speed, and signal timings of junctions are adjusted in such a way that none of the vehicles on major roads of the study stretch experience the red signal and thus allow seamless travel of vehicles along the study stretch (Fig. 6).

5 Evaluation by Floating Car Method

To evaluate the effectiveness of the project, existing journey speed, running speed, and delays at the study stretch are examined by floating car method during the peak

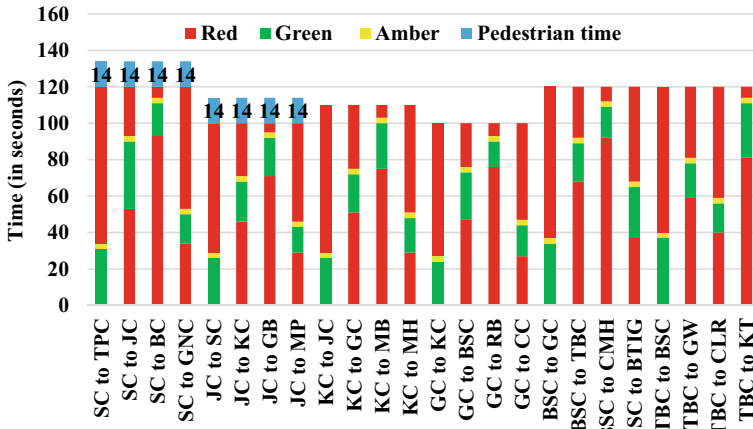


Fig. 5 Design traffic signal for intersections

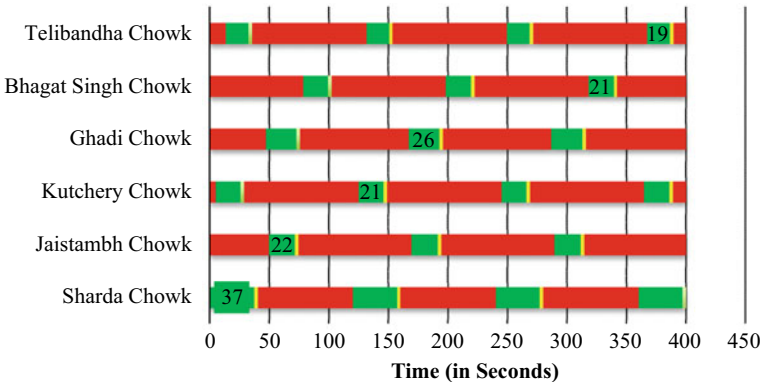


Fig. 6 Synchronization of the signal timings

hour of traffic flow where no. of vehicles met with opposite direction and no. of vehicles overtaking and overtaken by the test vehicle are noted and analyzed in which notations used are n_y = average no. of vehicles overtaking the test vehicle minus the no. of vehicles overtaken when the test is in the direction of the stream, n_a = average no of vehicles in the direction of the stream when the test vehicle travels in the opposite direction, t_w = average journey time, in minutes when the test vehicle is traveling with the stream, t_a = average journey time, in minutes when the test vehicle is running against the stream, and q = Average volume = $(n_a + n_y)/(t_a + t_w)$, t = average journey time = $t_w - (n_y/q)$ (Table 3).

Therefore, journey speed = journey length/journey time.

Table 3 Different responses obtained by the floating car method

Particulars	Along Sharda to Telibandha	Along Telibandha to Sharda
Average no. of vehicles overtaking the test vehicle	14	23
Average no. of vehicles overtaken by the test vehicle	15.33	23
n_y	-1.33	0
n_a	161.67	186
t_w	5.13 min	6.37 min
t_a	6.37 min	5.13 min
Average volume q	13.94 veh/min	16.17 veh/min
Journey length	3.13 km	3.13 km
Average journey time, t	5.22 min	6.37 min
Average journey speed	36 kmph	29.5 kmph
Average delay	1.4 min	1.74 min
Average running time = Average journey time—Average delay	3.82 min	4.63 min
Average running speed	50 kmph	41 kmph

Therefore, journey speed from Sharda Chowk to Telibandha Chowk and Telibandha Chowk to Sharda Chowk is found to be 36 kmph and 29.5 kmph, respectively, with a suitable delay of 1.4 min and 1.74 min. After the synchronization has been done, journey speed increases by about 39% for Sharda Chowk to Telibandha Chowk and 39% for Telibandha Chowk to Sharda Chowk with no stoppage of vehicles at any part of the study stretch. Since the synchronization has been done, the static delay caused due to encountering the red time signal is ideally zero. The synchronization is done for 50 kmph for much efficient flow and more reduction in the journey time. The below table shows the time required to travel between each of the intersections when traffic moves with the design speed of 50 kmph (Table 4).

6 Conclusions

- The optimized signal timings by Webster's method provide lesser cycle lengths thus giving lesser stoppages.
- Low red time stoppages provide lesser chances of mental frustration and a low risk of red-light running.
- Journey time is reduced by synchronizing the route signal timings. Journey time is reduced from 5.22 to 3.82 min when traveling from SC to TBC and from 6.37 to 4.63 min when traveling from TBC to SC.

Table 4 Time required between two intersections

Intersection	Distance (km)	Time (s)
Sharda Chowk (SC)		
	0.13	9.36
Jaistambh Chowk (JC)		
	0.7	50.4
Kutchery Chowk (JC)		
	0.25	18
Ghadi Chowk (GC)		
	1.7	112.4
Bhagat Singh Chowk (BSC)		
	0.35	25.2
Telibandha Chowk (TC)		
Total	3.13	225.36

- Keeping the design speed of 50 kmph, the timings are synchronized at each of the six intersections.
- About a 39% increase in journey speed is observed after the removal of delays at intersections due to synchronization.
- Since there is no delay, thus, there will be no idling of vehicles. Due to this, the idle fuel consumption of traffic flow is reduced leading to the economy for the transport users.
- No idling also results in lesser gas emissions thus proving synchronization as an environmentally beneficial method.
- No traffic congestion will be encountered even for the low width intersections, i.e., Sharda Chowk and Jaistambh Chowk.
- The need for pedestrian timings was observed at Sharda Chowk and Jaistambh Chowk for which after evaluating 14 s green-pedestrian time was allotted.

References

1. Kadiyali DLR (2015) Transportation engineering, 2016th ed. Khanna Publishing
2. Kushwah N, Natariy R, Jaiswal A (2015) Traffic signal coordination for effective flow of traffic: a review. *Int J Sci Res Dev* 3:1803–1806
3. Rafidi MAA, Hamid AHA (2014) Synchronization of traffic light systems for maximum efficiency along Jalan Bukit Gambier, Penang, Malaysia. *SHS Web Conf* 6:1–5
4. Goliya HS, Jain NK (2012) Synchronization of traffic signals a case study-Eastern ring road, Indore. *Int J Adv Technol Civ Eng* 5:2231–5721
5. Shambhavi S, Raj P (2018) Traffic signal synchronization—a case study : Bengaluru ring road. *Int J Eng Technol Sci Res* 5:696–711
6. Jilani G, Modi M, Mitra A, Joshi PT (2017) Synchronization of traffic light system for maximizing efficiency along helmet circle, Sal junction and Mam nagar

7. Gaurav D, Goliya H (2016) Synchronization of traffic signals a case study—Mr-10 road, Indore. *Int J Sci Res* 5:871–875
8. Vinod Kumar R, Pavithra M (2016) Design of traffic signals at closely spaced intersections in Tirupati. *Int J Adv Res* 4:1663–1670
9. Sanket H, Davara MPP (2016) Improvement of signalized urban intersection through optimization of signal timing. *Glob Res Dev J Eng* 82–89
10. Roshandeh AM, Levinson HS, Li Z, Patel H, Zhou B (2014) New methodology for intersection signal timing optimization to simultaneously minimize vehicle and pedestrian delays. *J Transp Eng* 140:1–10
11. Easa SM, Cheng J (2013) Reliability analysis of minimum pedestrian green interval for traffic signals. *J Transp Eng* 139:651–659
12. Pimentel RL, Araújo MC, Braga Fernandes Brito HM, Vital de Brito JL (2013) Synchronization among pedestrians in footbridges due to crowd density. *J Bridg Eng* 18:400–408
13. Hamilton BA (2009) Improving traffic signal management and operations : a basic service model
14. Sharma A, Vanajakshi L, Girish V, Harshitha MS (2012) Impact of signal timing information on safety and efficiency of signalized intersections. *J Transp Eng* 138:467–478
15. Yun I, Park B (2012) Stochastic optimization for coordinated actuated traffic signal systems. *J Transp Eng* 819–829
16. IRC 93:1985 (1985) Guidelines on design and installation of road traffic signals

Comparison Between Incremental Conductance MPPT of Two-Phase Interleaved Boost Converter and Boost Converter Using MATLAB Simulink



Boga Jyothi, Sudheer Vinnakoti, Madisa V. G. Varaprasad,
and S. Leela Tejaswini Kavya

Abstract In this paper, a comparison between incremental conductance (InC), maximum power point tracking (MPPT) of two-phase interleaved boost converter, and boost converter using Simulink is presented. The incremental conductance (InC) maximum power point tracking (MPPT) is utilized in solar sources using a direct control technique. This paper presents the design and simulation of an interleaved boost converter, a boost converter using incremental conductance, and an MPPT algorithm with PV sources. The results are attained for the PV system simulation for different irradiation levels.

Keywords Maximum power point tracking (MPPT) · Incremental conductance method (InC) · Interleaved boost converter (IBC) · Boost converter

1 Introduction

Because of the depletion of fossil fuel, its value upward thrust and environmental effect on electricity era have compelled humans to show into renewable power sources consisting of sun electricity era, wind electricity, biomass, and hydro. The solar electricity era has many advantages consisting of much less renovation, no noise, no wear and tear, and green nature. The Charanka Solar Park in India with a capability of 214 MW is keeping 2nd area with inside the listing, and it is also Asia's biggest PV plant [1].

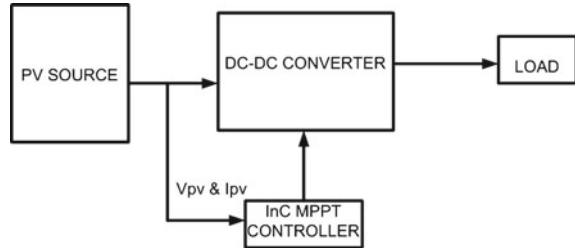
The photovoltaic modules are made from silicon cells. The effectiveness of the PV system predominantly based on the working point of the graphical plot of PV

B. Jyothi (✉) · M. V. G. Varaprasad · S. Leela Tejaswini Kavya
Vignan's Institute of Information Technology, Visakhapatnam, India
e-mail: jyothi_chinni2002@yahoo.com

B. Jyothi
KLEF, Vijayawada, Andhra Pradesh, India

S. Vinnakoti
RAGHU Engineering College, Visakhapatnam, India

Fig. 1 PV system using an InC MPPT-based block diagram



module. The key tasks of the PV system may contain are the MPPT. To improve the effectiveness of the PV system, a huge types of MPPT algorithm techniques were progressed.

Among them, the easy and successful way to obtain the maximum power can be provided by fractional—open-circuit voltage and short-circuit current strategies, but they arise in power loss due to they need repeated interruptions or short-circuit current for reference. Among the MPPT algorithms, P&O, and InC are extensively used. The Hill climbing, P&O is need elementary maintenance and simple to apply. A disturbance in the duty ratio of the power converter is introduced by hill-climbing strategy and is too exciting due to its simple construction. However, steady-state fluctuations consistently take place which may increase power loss [2–12, 13].

The P&O algorithm swings near the MPP at steady state. The enhancement of the algorithm effects in lagging reply, i.e., improper tracking under rapid climatic disorders, and during cloudy days, the efficiency of the algorithm decreases. Due to excessive tracking reliability at steady state, the incremental conductance (InC) algorithm is used, and at frequently changing atmospheric conditions, it also provides good adaptability (Fig. 1).

A DC–DC converter works as an interface for MPP operation, either implemented by using direct duty ratio or through voltage reference control with the support of a PI controller. Different DC–DC converter topologies like step-down converter, step-up converter, step-down—step-up converter, cuk converter, and sepic converter are used for individual PV systems.

An error signal is generated by InC method, and this value is zero at the maximum power point and is not zero at maximum of the remaining working points. The voltage reference control from MPPs which is near to zero with the help of a PI controller. Hence, $P-I$ controller is excepted, and the direct duty ratio is corrected in the algorithm.

2 Mathematical Model of PV Module

Silicon cells are used to make up the photovoltaic modules. The silicon solar cells under open-circuit conditions give around 0.7 V output voltage. The module current rating is based on the size of the individual cells.

A current source (I_{PV}), a diode (D), and series resistors (R_s) are placed in the appropriate circuit for a simplified structure of a PV cell, as shown in Fig. 2.

From Kirchhoff's law, output current from the equivalent circuit is followed as

$$I = I_{PV} - I_d \tag{1}$$

Equation 1 can be rewritten in the following way:

$$I = I_{PV} - I_S \left\{ \exp\left(\frac{q}{AkT_C N_S} V + IR_{se}\right) - 1 \right\} \tag{2}$$

where

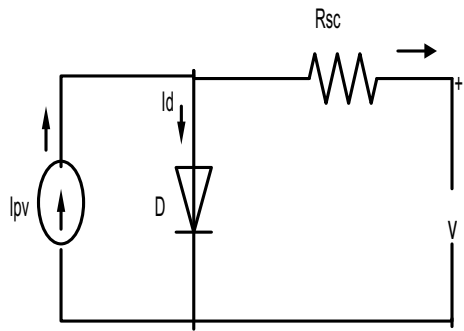
$$I_{PV} = [I_{SC} + K_I(T_C - T_r)] \cdot G \tag{3}$$

$$I_S = I_{rs} \left(\frac{T_C}{T_r}\right)^3 \exp\left[\frac{qE_g}{Ak} \left(\frac{1}{T_C} - \frac{1}{T_r}\right)\right] \tag{4}$$

$$I_{rs} = \frac{I_{SC}}{\exp\left(\frac{q}{AKT_C(n)N_S} V_{OC}\right) - 1} \tag{5}$$

A resistor R_p and a diode are linked in parallel in the typical structure of the PV cell. The resistance R_p is normally neglected in the modeling of PV cells because it is having very high value. To build up a solar PV module, we have to connect number of these cells are in series.

Fig. 2 PV cell equivalent circuit



3 Incremental Conductance

The PV power (P_{PV}) and PV voltage (V_{PV}) variations drive the incremental conductance MPPT. The PV module's P - V characteristics curve with MPP is shown in Fig. 3.

It utilizes the following equation.

$$\frac{\Delta P_{PV}}{\Delta V_{PV}} = \frac{\Delta V_{PV} I_{PV}}{\Delta V_{PV}} = I_{PV} + V_{PV} \frac{\Delta I_{PV}}{\Delta V_{PV}} = \frac{\Delta I_{PV}}{\Delta V_{PV}} = -\frac{I_{PV}}{V_{PV}} \tag{6}$$

where ΔI_{PV} is the PV current.

$-\frac{I_{PV}}{V_{PV}}$ is the instantaneous conductance, and $\frac{\Delta I_{PV}}{\Delta V_{PV}}$ is the incremental conductance in this equation. The maximum PV output power can be obtained when

$$I_{PV} + V_{PV} \frac{\Delta I_{PV}}{\Delta V_{PV}} = 0$$

From Fig. 2, we can derive has

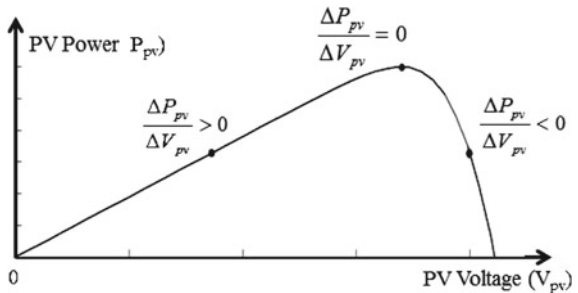
$$I_{PV} + V_{PV} \frac{\Delta I_{PV}}{\Delta V_{PV}} = 0 \text{ or } \frac{\Delta I_{PV}}{\Delta V_{PV}} = 0 \text{ at MPP} \tag{7}$$

$$I_{PV} + V_{PV} \frac{\Delta I_{PV}}{\Delta V_{PV}} > 0 \text{ or } \frac{\Delta I_{PV}}{\Delta V_{PV}} > 0 \text{ at MPP's left - hand side} \tag{8}$$

$$I_{PV} + V_{PV} \frac{\Delta I_{PV}}{\Delta V_{PV}} < 0 \text{ or } \frac{\Delta I_{PV}}{\Delta V_{PV}} < 0 \text{ at MPP's right - hand side} \tag{9}$$

The method changes the duty ratio (D) of its converter by continually tracking the PV output using Eqs. (7), (8), and (9) to increase or decrease the perturbation (D). Figure 4 depicts the incremental conductance flowchart.

Fig. 3 PV module P - V characteristics



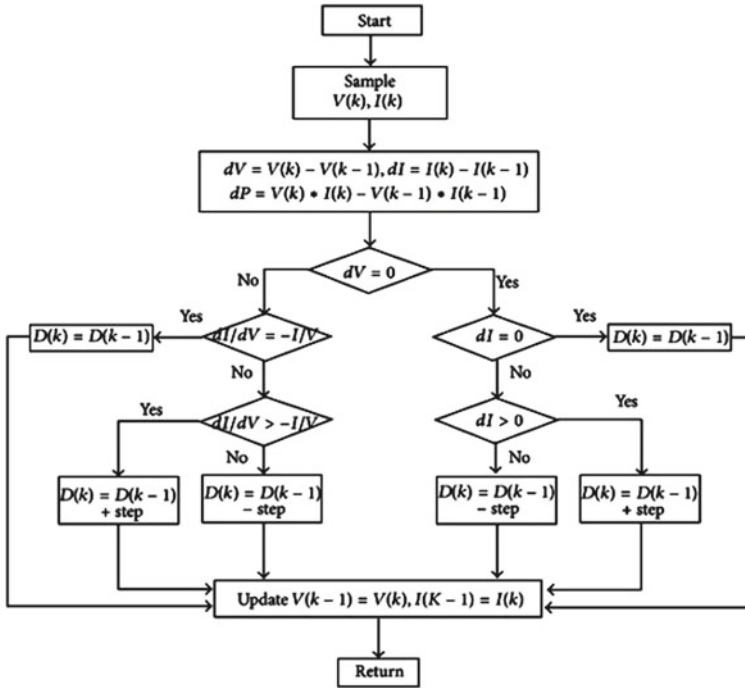


Fig. 4 Flowchart of InC MPPT algorithm

4 DC-DC Converter

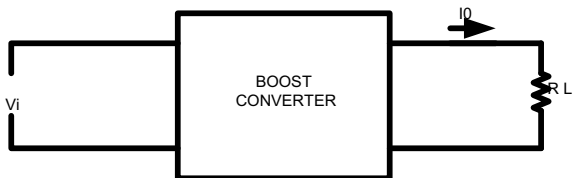
We compare boost converters with two-phase interleaved boost converters in this research.

4.1 Boost Converter

A boost converter's voltage output is more compared with the input voltage. Hence, the converter is called as "boost" converter (Fig. 5).

For ideal boost converter conditions,

Fig. 5 RL load on a boost converter



$$P_0 = P_i = V_0^2/R_2 = V_0 * I_0 \tag{10}$$

Also

$$V_0 = V_i/1 - D \tag{11}$$

$$D = 1 - V_i/\sqrt{P_I R_L} \tag{12}$$

4.2 Two-Phase Interleaved Boost Converter

The interleaved DC/DC converters are more reliable than single-phase converters [14]. Two standard converters are paralleled in the two-phase IBC. With 180° phase shift, the two-phase IBC switches are turned ON. The current sharing technique is used to reduce the input ripple current and output ripple voltage in the IBC circuit. When the converter’s duty cycle is set to 50%, in the theoretical point of view, the input current ripple is zero because the switches are controlled by a total of 180° phase shifts between them [15, 16] (Fig. 6).

The following equations are used to compute component values.

$$L = \frac{V_S}{f_S \Delta I_L} D \tag{13}$$

$$C = \frac{I_0}{f_S \Delta V_0} D \tag{14}$$

D is the converter’s duty cycle, which can be calculated using

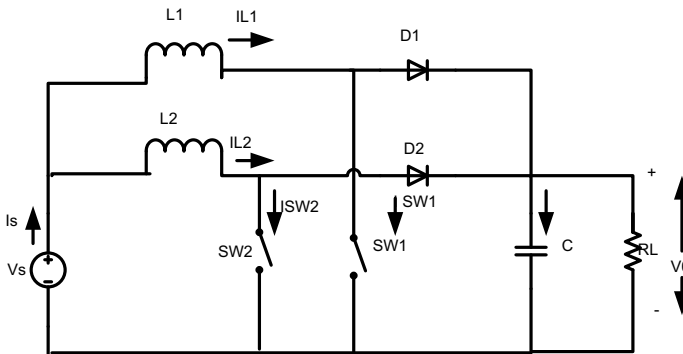


Fig. 6 Circuit diagram of two-phase IBC

$$D = 1 - \frac{V_s}{V_0} \tag{15}$$

5 Simulation Results

The $P-V$ characteristics for 500, 1000, 600 W/m^2 are plotted in Fig. 7, and the comparison of InC MPPT between two—phase IBC and boost converter is simulated. For various irradiances, the following results were found (Figs. 8, 9 and 10; Table 1).

Fig. 7 P-V characteristics

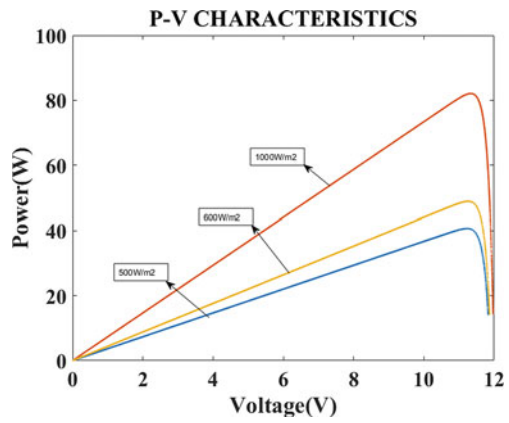


Fig. 8 Voltage of two-phase IBC and boost converter

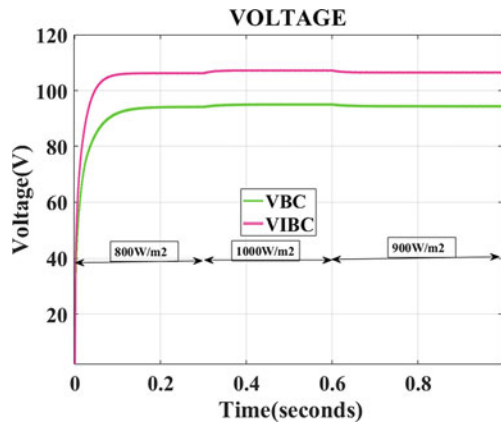


Fig. 9 Current of two-phase IBC and boost converter

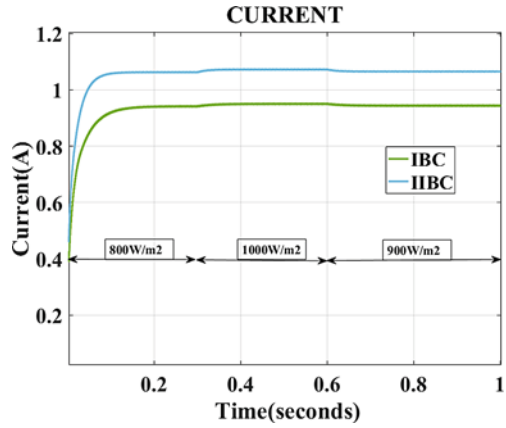


Fig. 10 Power of two-phase IBC and boost converter

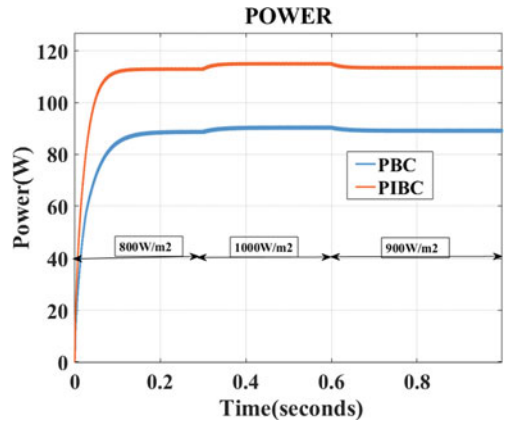


Table 1 Incremental conductance using interleaved boost converter (IBC) and boost converter (BC)

Irradiance	IBC output voltage (V)	IBC output current (A)	IBC output power (W)	BC output voltage (V)	BC output current (A)	BC output power (W)
800	106.3	1.063	112.9	94.05	0.9405	88.45
1000	107.2	1.072	115	94.9	0.949	90.06
900	106.5	1.065	113.5	94.27	0.9427	88.87

6 Conclusion

This study presents a simulation of InC. MPPT of two-phase IBC and boost converter. The model is run under various irradiation conditions to obtain the results. For all of

the selected scenarios, the suggested MPPT algorithm enhances PV panel efficiency, and the two-phase IBC circuit works at a duty cycle near to 50%.

References

1. Sheik Mohammed S, Devaraj D (2015) Simulation of incremental conductance MPPT based two-phase interleaved boost converter using MATLAB/simulink. *IEEE Trans* 978-1-4799-6085-9/15 ©2015
2. Kumar H, Tripathi RK (2012) Simulation of variable incremental conductance method with direct control method using boost converter. *IEEE*. 978-1-SS4673-0455-9/12 ©2012 IEEE
3. Erickson RW, Maksimovic D (2001) *Fundamentals of power electronics*, 2nd ed. Kluwer Academic Publishers, Norwell, MA
4. Hohm DP, Ropp ME (2003) Comparative study of maximum power point tracking algorithms. *Prog Photovoltaics: Res Applic Nons II*:47–62
5. Tsai H-L, Tu C-S, Su Y-J (2008) Development of generalized photovoltaic model using MATLAB/SIMULINK. In: WCECS, San Francisco, USA
6. Maity S, Varaprasad MVG (2018) An efficient PV power optimizer with reduced EMI effects: map based analysis and design technique. *IEEE Trans Energy Convers* 33(2):546–555
7. Varaprasad MVG, Maity S (2019) Development of current sensor less photovoltaic MPPT Tracker. In: International conference on computer, electrical and communication engineering (ICCECE)
8. Varaprasad MVG, Maity S (2018) Development of observer-based photovoltaic MPPT tracker under shading conditions. In: *IEEE India international conference on power electronics (IICPE)*
9. Varaprasad MVG, Maity S (2018) Microcontroller-based current sensorless photovoltaic MPPT tracker. In: *IEEE India international conference on power electronics (IICPE)*
10. Varaprasad MVG, Ravi Sankar RS, Alice Mary K (2013) Reduction of torque and flux ripple of 3- Φ asynchronous machine using multilevel inverter. *Int J Adv Res Electr Electron Instrum Eng* 2(2):4781–4793
11. Varaprasad MVG, Arundhati B, HemaChander A, PhaniTeja B (2021) Design and implementation of a modified H-bridge multilevel inverter with reduced component count. In: *Machine intelligence and soft computing. Advances in intelligent systems and computing*, vol 1280. Springer Publisher, pp 321–334
12. Arundhati B, Madisa VGV, Vijayakumar G (2021) Novel topology for 9-level H bridge multilevel inverter with optimum switches. In: *Machine intelligence and soft computing. Advances in intelligent systems and computing*, vol 1280. Springer Publisher, pp 419–433
13. Dadashzadeh H, Khosroshahi AE, Hosseini SH (2017) A digital predictive controller for a SEPIC-based battery charger in photovoltaic power systems. In: *IV international electromagnetic compatibility conference (EMC Turkiye)*, pp 1–6. <https://doi.org/10.1109/EMCT.2017.8090371>
14. Khosroshahi A, Abapour M, Sabahi M (2015) Reliability evaluation of conventional and interleaved DC–DC boost converters. *IEEE Trans Power Electron* 30(10):5821–5828. <https://doi.org/10.1109/TPEL.2014.2380829>
15. Khosroshahi AE, Mohammadpour Shotorbani A, Dadashzadeh H, Farakhor A, Wang L (2019) A new coupled inductor-based high step-up DC–DC converter for PV applications. In: *20th workshop on control and modeling for power electronics (COMPEL)*, pp 1–7. <https://doi.org/10.1109/COMPEL.2019.8769630>
16. Khosroshahi AE, Wang L, Dadashzadeh H, Ardi H, Farakhor A, Shotorbani AM (2019) A two-stage coupled-inductor-based cascaded DC–DC converter with a high voltage gain. In: *IEEE Canadian conference of electrical and computer engineering (CCECE)*, pp 1–5. <https://doi.org/10.1109/CCECE.2019.8861768>

A Novel Converter for Bidirectional Power Flow in Hybrid Electric Vehicle Systems Using ANN Controller



C. H. Mohan Murali Krishna, R. S. Ravi Sankar, Madisa V. G. Varaprasad, and K. K. Deepika

Abstract In a hybrid electric vehicle system, a bidirectional DC–DC converter (BDC) is a device that connects a first voltage source (FVS), second voltage source (SVS), and a DC-bus voltage at various levels. This proposed converter is operated in two modes: the first one is a source powering mode, and the second one is a regeneration mode, as well as power flow management in both directions. In addition, the dual-source low-voltage buck/boost mode allows for independent power flow management between two sources. This converter is controlled by feedback control using an artificial neural network to meet the two modes of operation. The simulated results of the system are present with less steady-state error, peak overshoot, and less settling time in both modes of operation of the converter.

Keywords Hybrid electric vehicle (HEV) · Two battery voltage sources · Bidirectional DC/DC converter · Artificial neural network

1 Introduction

Nowadays, transportation systems play a crucial role in the entire world. The majority of them drive automobile with internal combustion engines (ICE). Using the ICE has resulted in and continues to result in major issues like air pollution, global warming, and the rapid depletion of the world's petroleum resources. The three types of vehicles suggested to replace conventional cars with ICE are fuel cell vehicles (FCV), electric vehicles (EV), and hybrid electric vehicles (HEV). The performance of fuel cell and electric vehicles falls well short of what is required. As a result, the focus of advanced

C. H. Mohan Murali Krishna · R. S. Ravi Sankar · M. V. G. Varaprasad (✉) · K. K. Deepika
Vignan's Institute of Information Technology, Visakhapatnam, Andhra Pradesh, India
e-mail: mvgvaraprasad@gmail.com

C. H. Mohan Murali Krishna
e-mail: mohanchippada5@gmail.com

R. S. Ravi Sankar
e-mail: satyaravirai2001@gmail.com

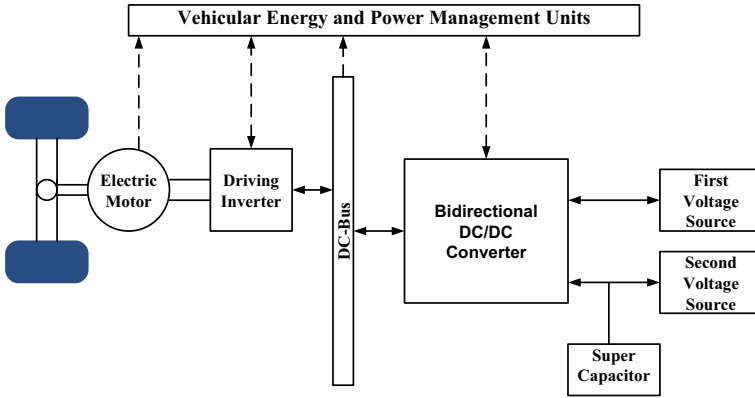


Fig. 1 Basic block diagram for a hybrid electric vehicle (HEV) power system

vehicle technology development has shifted to HEVs [1–3]. By utilizing an energy storage system, hybrid electric vehicles can reduce fuel consumption in a variety of ways, including collecting energy during braking, downsizing the engine, operating the engine more effectively, and turning off the engine when it is not in use. [4–8] In advanced HEVs, regenerative braking is employed to convert the vehicle’s kinetic energy into electric energy, rather than dispersing it as heat energy like standard brakes do. Furthermore, it comprises a component with a high energy density, such as super capacitors (SCs), which avoid peak energy transients during acceleration and regenerative braking systems [9–18]. SCs may store and release regenerative energy during deceleration and acceleration, producing extra power. Figure 1 shows a basic block diagram for a hybrid electric vehicle (HEV) power system.

The main idea of the system design is that it links two DC energy sources with different voltage levels. The power flow among both energy sources, and also the current flows from the DC-bus to the voltage sources, is all managed individually.

This paper is organized in such a way that in Sect. 2, the architecture and operating modes of the dual converter are illustrated. The control technique of the converter is narrated in Sect. 3. Finally, in Sect. 4, the validation of the proposed vehicle is projected with simulation results.

2 Architecture and Operating Modes

In the illustration, V_{HB} , V_{FVS} , and V_{SVS} stand for high bus voltage, first voltage source (FVS), and second voltage source (SVS), respectively. The FVS and SVS control loops were turned on and off using two bidirectional power switches in this architecture. The voltage gain between low-voltage sources V_{FVS} and V_{SVS} is developed using a pump capacitor (C_{cp}) that separates the voltage with active switches (M_1, M_2, M_3, M_4) and two inductors (L_f, L_s). C_{cp} eliminates the need for an extremely

high duty ratio by reducing voltage stress across switches. The bidirectional switches (S , S_{FVS} , S_{SVS}) enable the circuit's four-quadrant functioning, which allows the flow of power control between two low-voltage sources, V_{MVS} and V_{AVS} , as well as the suppression of positive and negative voltages. As indicated in Fig. 2, the bidirectional switches (S_w , S_{MVS} , S_{AVS}) are MOSFETs connected in obverse direction. Table 1 describes the BDC concepts and operation modes.

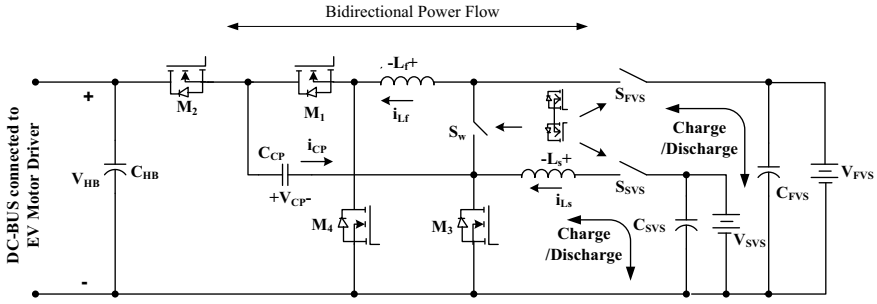


Fig. 2 Dual-battery energy storage in BDC architecture

Table 1 Conduction status of devices for various operation modes

Operation modes	Switches are ON	Switches are OFF	Control switches	Synchronous rectifiers (SR)
Dual low-voltage sources powering mode (Accelerating, $x_1 = 1$, $x_2 = 1$)	S_{FVS}, S_{SVS}	S_w	M_3, M_4	M_1, M_2
DC-bus energy-regenerative mode at high voltage (braking, $x_1 = 1$, $x_2 = 1$)	S_{FVS}, S_{SVS}	S_w	M_1, M_2	M_3, M_4
Dual low-voltage sources buck mode (FVS to SVS, $x_1 = 0$, $x_2 = 0$)	S_{FVS}, S_{SVS}	M_1, M_2, M_4	S_w	M_3
Dual low-voltage sources boost mode (FVS to SVS, $x_1 = 0$, $x_2 = 0$)	S_{FVS}, S_{SVS}	M_1, M_2, M_4	M_3	S_w

2.1 Dual Low-Voltage Sources Powering Mode

The switch has been flipped in this mode of operation, the switches (S_{MVS} , S_{AVS}) have been turned on, and the dual low-voltage sources (V_{FVS} , V_{SVS}) provide energy to connected loads and the DC-bus, as shown in Fig. 3. M_3 and M_4 switches on the bottom side are controlled by active switching with a 180° phase shift angular position, whereas M_1 and M_2 switches on the top side are synchronous rectifiers.

Four circuit stages are featured in Fig. 4. Dual-sources low-voltage powering mode steady-state waveforms with a duty ratio greater than 50%, as illustrated in Fig. 3b, and the operation can be stated quickly as follows.

- (a) **Stage 1** [$t_0 < t < t_1$]: The time period at this point is $(1 - D_t)T_s$. As shown in Fig. 4a, switches M_1 and M_3 are on, whereas switches M_2 and M_4 are off. The voltage across the first inductor L_f , which drops linearly from its original value,

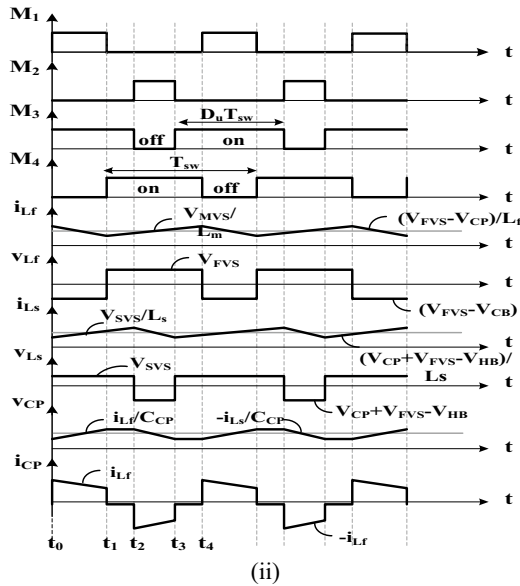
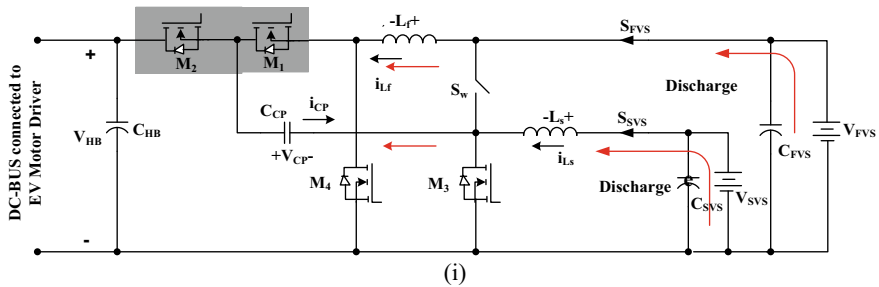


Fig. 3 a Schematic diagram, b waveforms of BDC's dual low-voltage sources powering mode

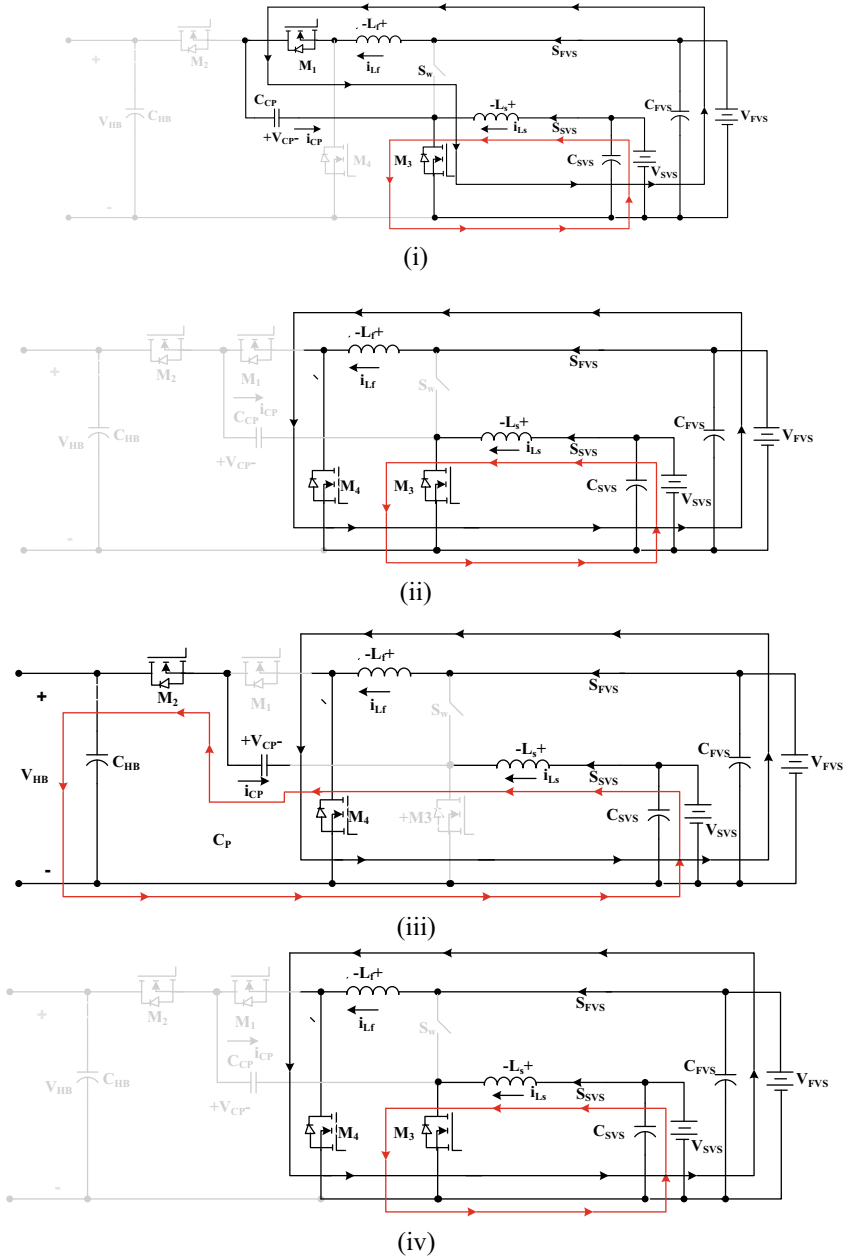


Fig. 4 Circuit stages of BDC's dual low-voltage sources powering mode

is represented by the differential between the charge pump voltage V_{CP} and the lower side voltage V_{FVS} , whereas the voltage across the second inductor L_s charged by the energy source V_{SVS} increases linearly. The voltage across the inductors L_f and L_s in stage 1 is denoted by

$$L_f \frac{di_{L_f}}{dt} = V_{SVS} - V_{CP} \quad (1)$$

$$L_s \frac{di_{L_s}}{dt} = V_{SVS} \quad (2)$$

- (b) **Stage 2** [$t_1 < t < t_2$]: The time interval at this stage is $(D_t - 0.5)T_s$; the M_3 and M_4 switches are on, while the M_1 and M_2 switches are off, as shown in Fig. 4b. The lower side voltages, V_{FVS} and V_{SVS} , are located between the first and second inductors, and inductor currents are linearly increased. Under stage 2, the voltage between the inductors L_f and L_s is indicated by

$$L_f \frac{di_{L_f}}{dt} = V_{FVS} \quad (3)$$

$$L_s \frac{di_{L_s}}{dt} = V_{SVS} \quad (4)$$

- (c) **Stage 3** [$t_2 < t < t_3$]: The time interval at this stage is $(1 - D_t)T_s$; M_1 and M_3 switches are off, while M_2 and M_4 switches are on, as shown in Fig. 4c. Under stage 3, the voltage between the inductors L_f and L_s is indicated by

$$L_f \frac{di_{L_f}}{dt} = V_{FVS} \quad (5)$$

$$L_s \frac{di_{L_s}}{dt} = V_{CP} + V_{SVS} - V_{HB} \quad (6)$$

- (d) **Stage 4** [$t_3 < t < t_4$]: The time interval at this stage is $(D_t - 0.5)T_s$; the M_3 and M_4 switches are on, while the M_1 and M_2 switches are off, as shown in Fig. 4d. Under stage 4, the voltage across the inductors L_f and L_s is denoted by

$$L_f \frac{di_{L_f}}{dt} = V_{FVS} \quad (7)$$

$$L_s \frac{di_{L_s}}{dt} = V_{SVS} \quad (8)$$

2.2 Regenerative Mode at High Voltage

In the regenerative mode, the motor's kinetic energy is returned to the voltage sources, and the regeneration energy can be more than the battery's storage capability, with the additional energy used to charge the storage devices. On the higher side, active switching regulates the current through the inductors, i.e. M_3 and M_4 switches with a 180° phase shift angle, while the lower side switches, M_1 and M_2 , act as synchronous rectifiers, increasing the converter's conversion performance. As we can observe in Fig. 5a.

The duty ratio of the energy-regenerating mode at DC-bus high-voltage steady-state waveforms is less than 50%. Their four circuit stages are illustrated in Fig. 6, and the stage-wise operation is summarized as:

- (a) **Stage 1** [$t_0 < t < t_1$]: It is indicated in Fig. 6a. The time interval is $D_1 T_s$. Switches M_1 and M_3 are turned on, but switches M_2 and M_4 are turned off. Voltage across the main inductor, L_m , drops linearly from its original value. It is represented by the differential between the charge pump voltage V_{CP} and the lower side voltage V_{FVS} , whereas the voltage across the auxiliary inductor L_a charged by the energy source V_{AVS} increases linearly. The voltage across the inductors L_f and L_m in stage 1 is denoted by

$$L_f \frac{di_{Lf}}{dt} = V_{FVS} - V_{CP} \quad (9)$$

$$L_s \frac{di_{Ls}}{dt} = V_{SVS} \quad (10)$$

- (b) **Stage 2** [$t_1 < t < t_2$]: The time interval at this stage is $(0.5 - D_1)T_s$; the M_3 and M_4 switches are on, while the M_1 and M_2 switches are off, as shown in Fig. 6b. Positive lower side voltages, V_{MVS} and V_{AVS} , are located between the first and second inductors, where inductor currents increase linearly. Under stage 2, the voltage between the inductors L_f and L_s is indicated by:

$$L_f \frac{di_{Lf}}{dt} = V_{FVS} \quad (11)$$

$$L_s \frac{di_{Ls}}{dt} = V_{SVS} \quad (12)$$

- (c) **Stage 3** [$t_2 < t < t_3$]: The time interval is $D_1 T_s$ at this stage, with M_1 and M_3 switches off and M_2 and M_4 switches on, as shown in Fig. 6c. The differential between the lower side voltages V_{FVS} and the charge pump voltages V_{CP} indicates the voltage across the main inductor L_f , and the lower side voltage V_{SVS} and its level are negative. Under stage 3, the voltages across the inductors L_f and L_s are denoted by:

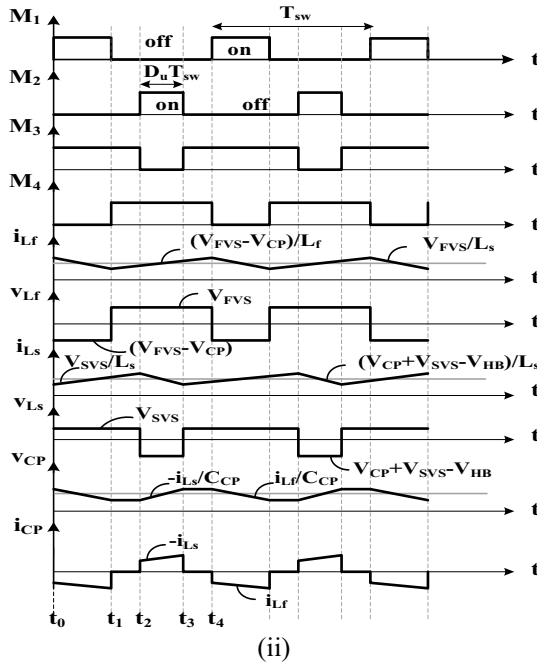
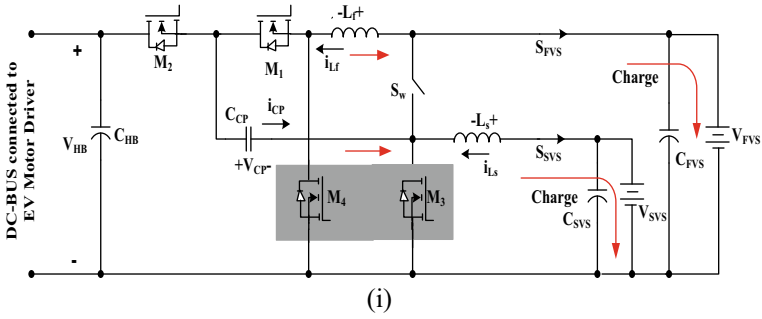


Fig. 5 a Schematic diagram, b waveforms of BDC’s DC-bus high-voltage energy-regenerative mode

$$L_f \frac{di_{L_f}}{dt} = V_{FVS} \tag{13}$$

$$L_s \frac{di_{L_s}}{dt} = V_{SVS} + V_{CB} - V_{HB} \tag{14}$$

(d) **Stage 4** [$t_3 < t < t_4$]: The time interval at this stage is $(0.5 - D_1)T_s$; the M_3 and M_4 switches are on, while the M_1 and M_2 switches are off, as shown in Fig. 6d. Under stage 4, the voltage across the inductors L_f and L_s is denoted by:

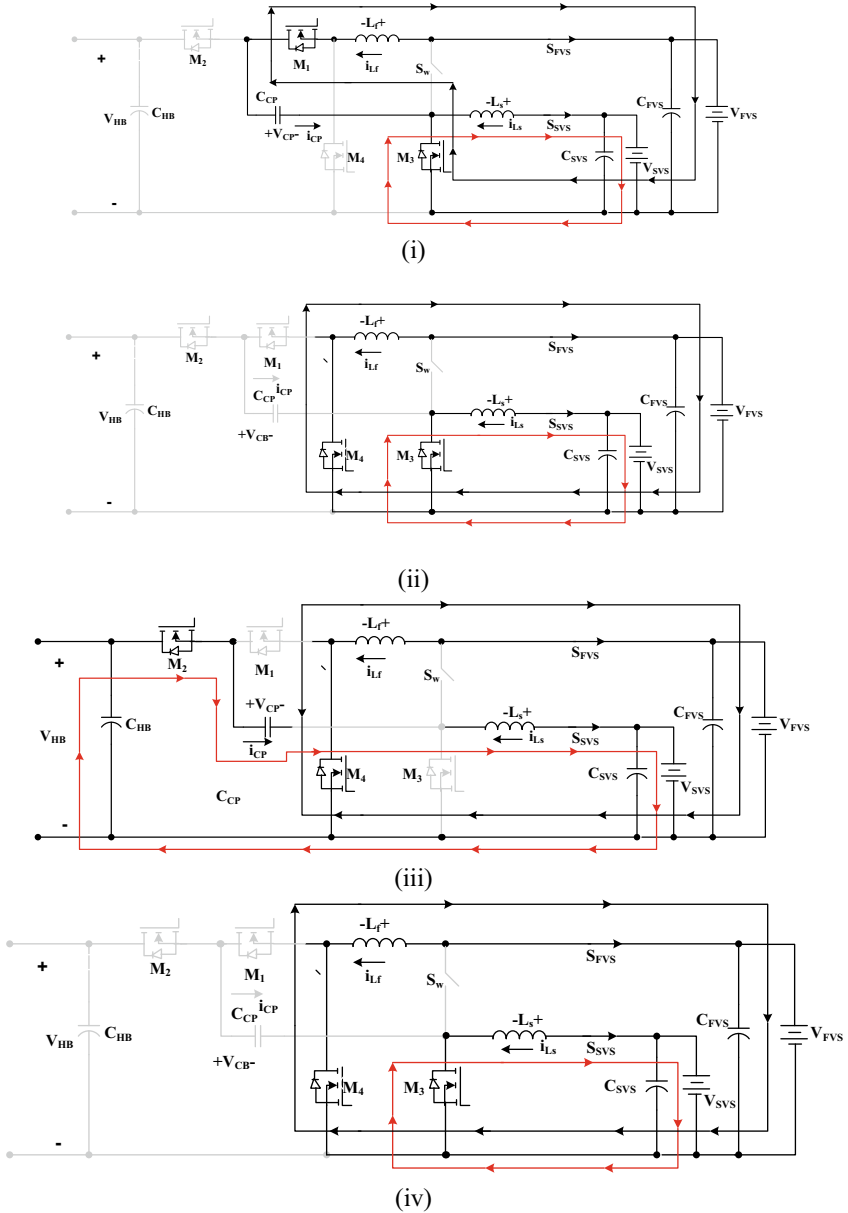


Fig. 6 Circuit stages in regenerating mode at high voltage

$$L_f \frac{di_{Lf}}{dt} = V_{FVS} \quad (15)$$

$$L_s \frac{di_{Ls}}{dt} = V_{SVS} \quad (16)$$

2.3 Buck/boost Mode with Dual Low-Voltage Sources

In this mode, energy stored in the first voltage source is transferred energy to the second voltage source and vice versa [16], as we can observe in Fig. 7a.

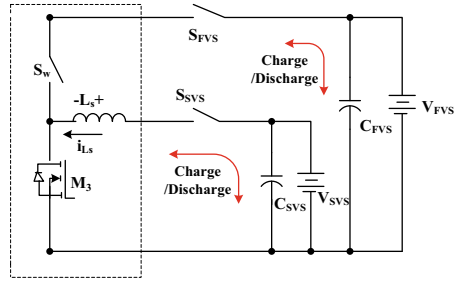
If the duty cycle of active switch S_w is controlled, as shown in Fig. 8, the buck converter will operate as power flows from the first voltage source to the second voltage source. It depicts the dual low-voltage sources buck mode's planned BDC circuit stages. If the duty cycle of switch M_3 is regulated, the converter will operate in boost mode, as shown in Fig. 9, which depicts the expected BDC circuit stages for the dual low-voltage sources boost mode and transferring power from the second voltage source to the first voltage source.

3 Converter Control

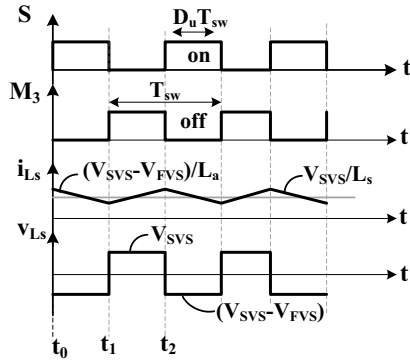
Figure 10 shows the block diagram of the feedback-loop control technique, which comprises choosing a vehicle strategic level and mode of BDC to govern pulse width modulation switching schemes. The BDC controller's many operating modes are depicted in Fig. 11. As indicated in the closed loop controller architecture, the vehicular key level necessitates power demand (P_{Dem}), vehicle voltage, and power management units, which serve as input signals to the BDC mode selection. The management unit's overall results improve the utilization of voltage sources to meet the power train's power demand, which satisfies the needs of the driver. As can be seen in Fig. 10, the currents in inductors i_{L_m} and i_{L_a} are calculated and compared to the reference converter currents. Different driving states of power demand and voltage sources are used to determine the vehicle condition in this mode of controller operation (V_{FVS} , V_{SVS}). Then, using an artificial neural network, it chooses the appropriate i_{L_mRef} or i_{L_aRef} current references to control the power switches S_w , M_1 , M_2 , M_3 , and M_4 . The pulse width modulation (PWM) switching methods transform the duty cycle into regulated gate signals for the active switches (S_w , M_1 , M_4), and the BDC controller's switch selectors (s_1 , s_2) are employed in many operating modes.

The i_{L_mRef} is used to regulate the power flowing from 2LV to HV or HV to 2LV on dual low and high DC-buses voltage sources, whereas the i_{L_aRef} is also used to regulate the power flowing from the first to the second voltage source and vice versa (i.e. V_{FVS} to V_{SVS} or V_{SVS} to V_{FVS}) as shown in Fig. 10,

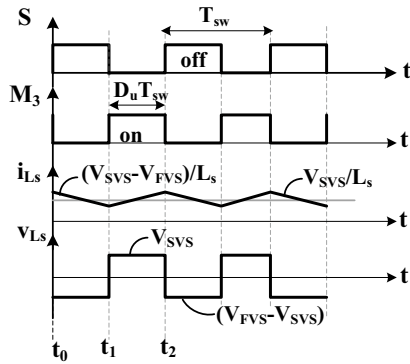
Fig. 7 BDC's dual low-voltage sources buck/boost mode



(i). Schematic Diagram.

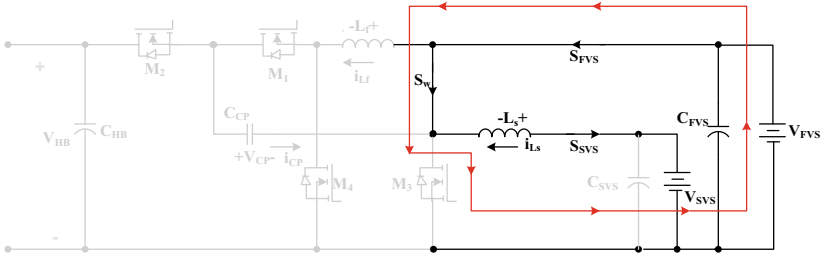


(ii). Buck-mode stable-state waveforms.

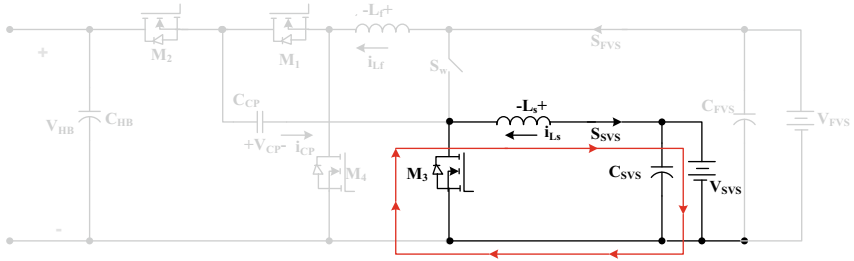


(iii). Boost-mode stable-state waveforms.

when the vehicle is in moving state ($P_{Dem} > 0$), the control loop $s = 1$ in the controller i_{LM} is activated, and it operates in two modes: accelerating and braking, as seen in the controlled switches in Table 1. If both conditions are not met, it returns to the reassign mode to operate the very next percipience of switching mode. Furthermore, while the vehicle is in a halting condition ($P_{Dem} < 0$), the control loop $s_1 = 0$ in the controller i_{La} will work in two modes, buck and boost, as illustrated in the controlled switches in Table 1. The voltages of V_{FVS} (96 V) and V_{SVS} (48 V)

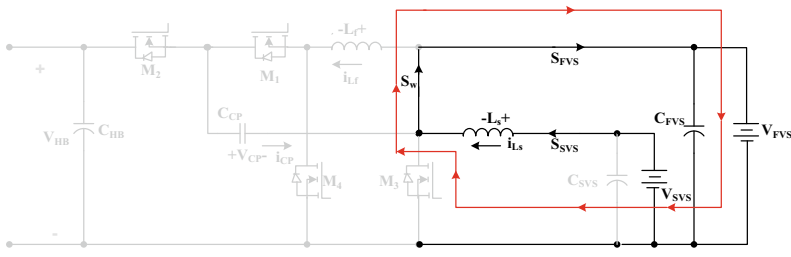


(i). Stage 1

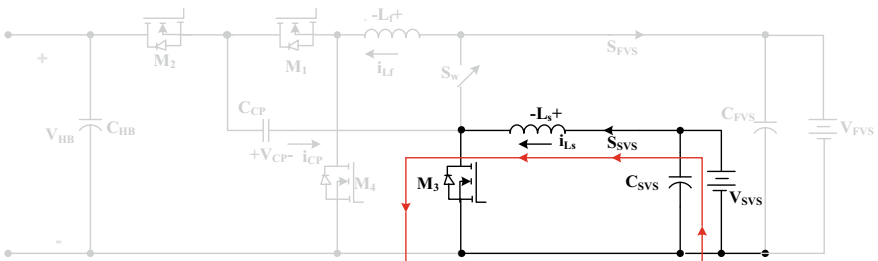


(ii). Stage 2

Fig. 8 a Stage 1, b stage 2



(i). Stage 1



(ii). Stage 2

Fig. 9 a Stage 1, b stage 2

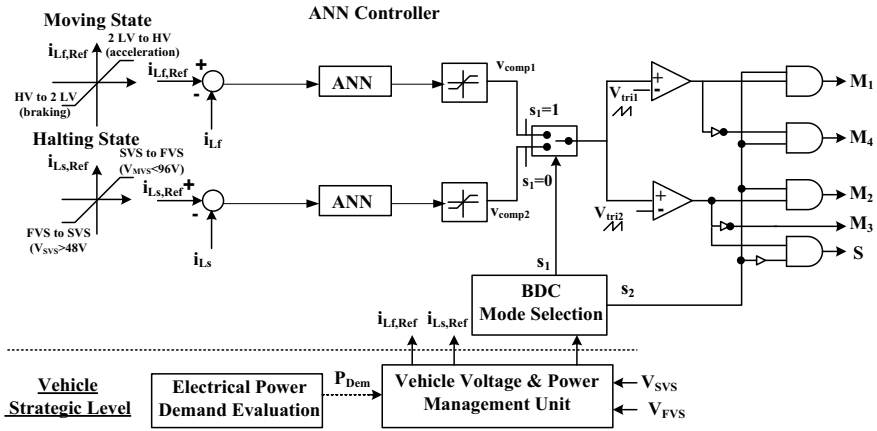


Fig. 10 Block diagram for feedback-loop control technique

are used to perceive mode change in this halting condition. When the V_{FVS} is less than 96 V during boost mode, $i_{LaRef} > 0$, and power flows from the V_{SVS} to the V_{FVS} . When the V_{SVS} is less than 46 V in buck mode, $i_{LaRef} < 0$ sends power from the V_{FVS} to the V_{SVS} . If neither of these conditions is met, the system reverts to the reassign mode, which is used to process the next perception of mode switching. Figure 12 shows the modelling of ANN controller.

4 Simulation Results

The simulation model is provided in Fig. 2 to validate the feasibility and performance of the BDC converter topology with dual battery. It is modelled in MATLAB/Simulink, and the system’s four operation modes are investigated; Table 2 contains the system parameters.

The traction motor was powered by both sources, which increased the two input voltages, as shown in Fig. 14. As a result, the DC-bus voltage V_{HB} of 430 V was influenced by both sources. The dual low-voltage sources’ power mode waveforms are depicted below. Figure 13 shows the gate pulses delivered to switches M_1, M_2, M_3 , and M_4 , while the inductor currents of i_{L_f} and i_{L_s} are shown in Fig. 14. Figures 15 and 16 depict the gate pulses and inductor current and output voltage in DC-bus energy-regenerative mode at high voltage.

The power transfer by the DC-bus towards the main and auxiliary voltage sources is shown in Fig. 16. The input power flowed in the opposite direction as the inductor currents i_{L_f} and i_{L_s} . V_{FVS} and V_{SVS} were about 96 and 48 V on the lower side output voltages, respectively.

Using dual low-voltage sources, simulated waveforms of gate signals, inductor currents, and output voltage for buck and boost modes are shown in Figs. 17 and 18. In

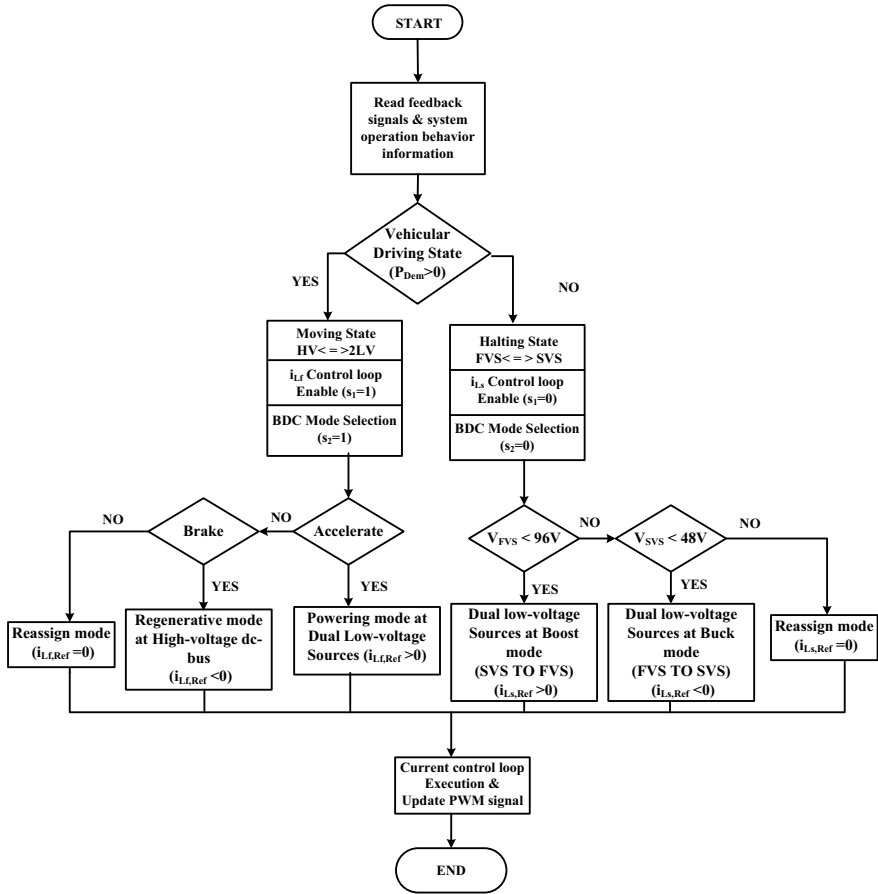


Fig. 11 Flow chart for the planned BDC's multiple working modes

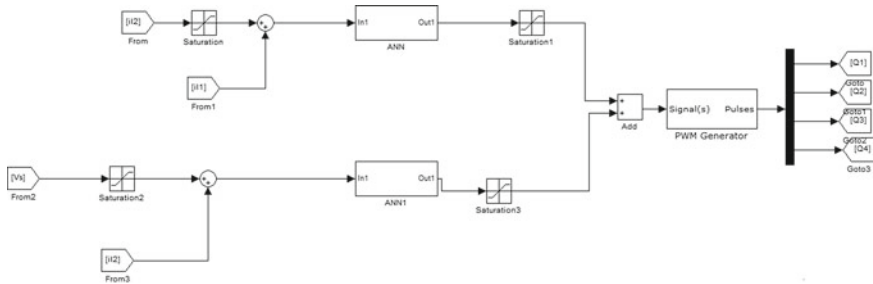


Fig. 12 Modelling of ANN controller

Table 2 Parameters and ratings of the HEV system

Parameters	Ratings
Inductors	$L_f = L_s = 250 \mu\text{H}$
High-side capacitor	$C_{\text{HB}} = 1880 \mu\text{F}$
Low-side capacitor	$C_{\text{FVS}} = C_{\text{SVS}} = 400 \mu\text{F}$
Charge pump capacitor	$C_{\text{CP}} = 10 \mu\text{F}$
ESR of inductance	$R_{L_f} = R_{L_s} = R_L = 50 \text{m}\Omega$
ESR of capacitance	$R_{\text{CB}} = 20 \text{m}\Omega$ $R_{\text{FVS}} = R_{\text{SVS}} = 50 \text{m}\Omega$
Line resistance	$R_{\text{FVS}} = 12 \text{m}\Omega$ $R_{\text{SVS}} = 6 \text{m}\Omega$
First voltage source	FVS = 96 V
Second voltage source	SVS = 40 V

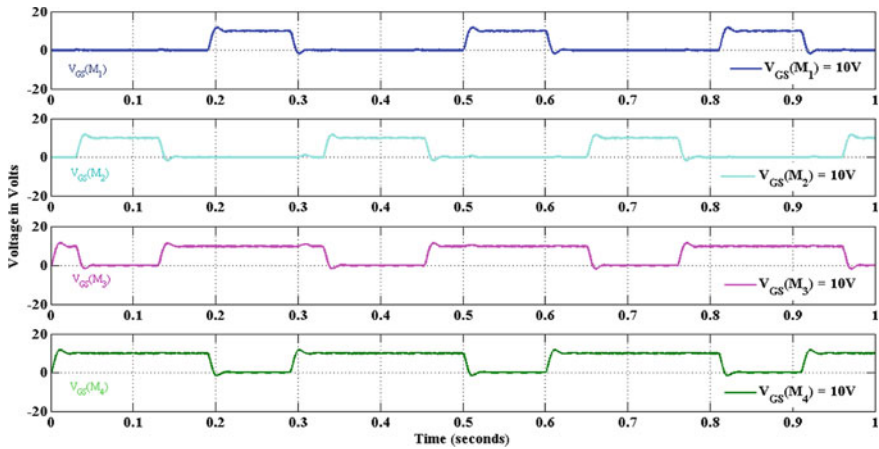


Fig. 13 Gate signals in powering mode

Fig. 17, the currents in the inductor are inverted from those in Fig. 18, demonstrating that the concept can handle bidirectional power to flow between the second and first voltage sources. Finally, all of the simulation results were consistent with the stable-state prognostication study. The waveforms of regulated current step variations for the conceptual design in the higher-voltage energy-regenerative mode and the dual low-voltage sources powering mode and are shown in Figs. 19 and 20. In order to transmit energy from the dual lower side sources to the higher-side DC-bus, the current in the inductor i_{L_f} and the higher-side current i_{HB} were adjusted, as illustrated in Fig. 19. Figure 20 shows the negative current output waveforms. The power flow was effectively inverted, as seen in Fig. 20.

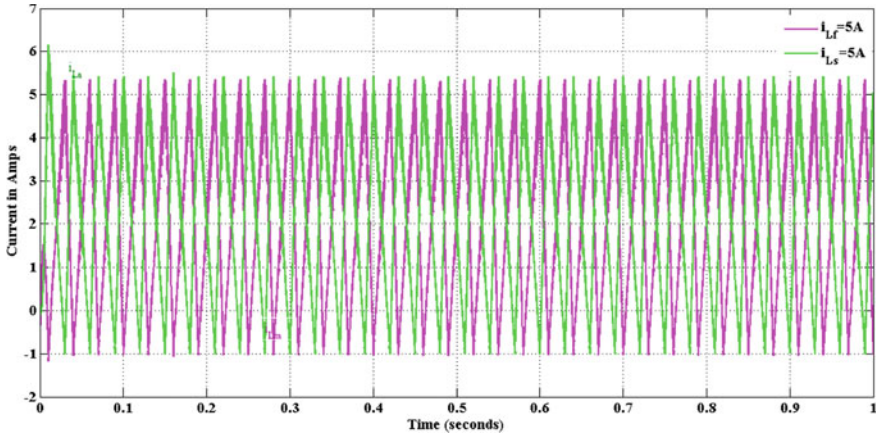


Fig. 14 Inductor current waveform in powering mode

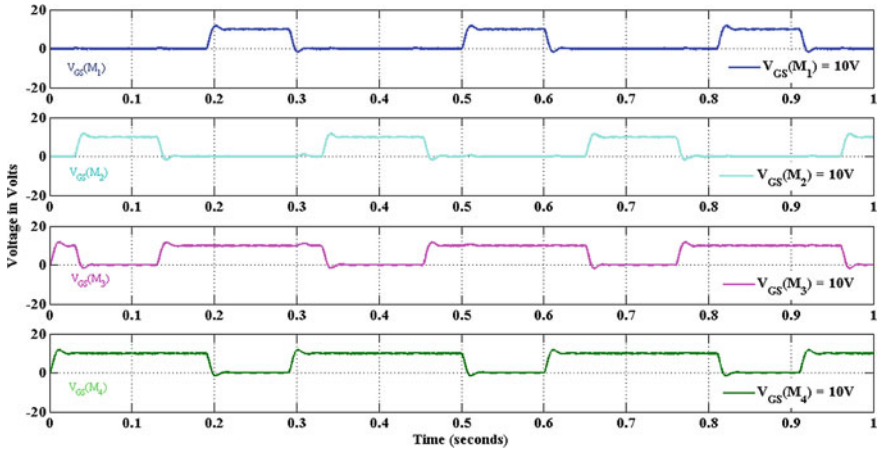


Fig. 15 Gate signals in regenerative mode

Figures 21 and 22 show the waveforms of regulated current step variations for the conceptual model for the dual low-voltage sources buck and boost modes, respectively. The higher-side current i_{FVS} and the inductor current i_{Ls} were altered to distribute energy between two low-voltage source currents. The inductor current i_{Ls} and the first voltage source current i_{FVS} were controlled to transmit the power from the second voltage source to the first voltage source. In Fig. 21, the output waveforms of negative current were effectively inverted, and in Fig. 22, the power flow was effectively inverted.

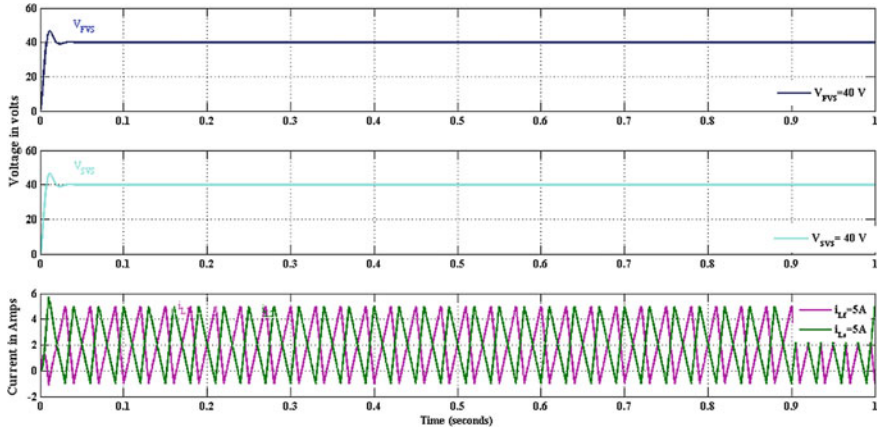


Fig. 16 Output voltages and inductor currents

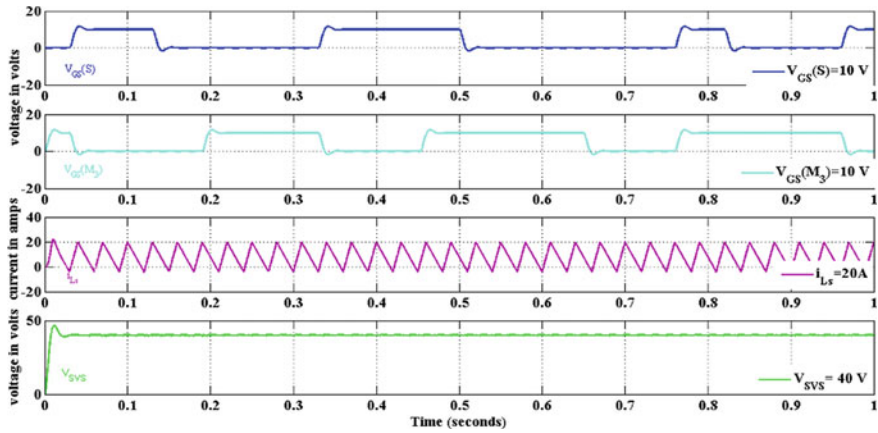


Fig. 17 Gate signals, output voltage, and inductor currents for buck mode

The ANN controller has a significantly faster rising time and processing speed than the PI controller, and the ANN controller has reduced current ripples in the current signal. As compared to the PI controller [17, 18], the artificial neural network gives better performance.

5 Conclusions

Dual-battery voltage sources were integrated with higher-voltage DC-buses of varying voltage levels using the BDC architecture. Various forms of power transfer

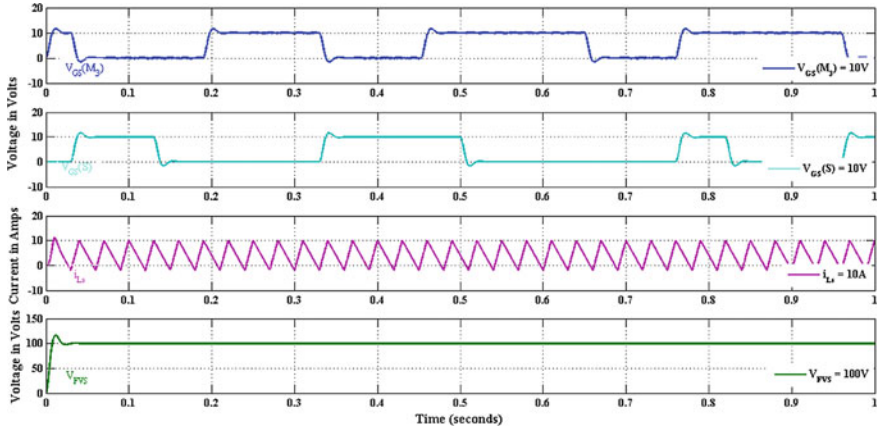


Fig. 18 Gate signals, output voltage, and inductor currents for boost mode

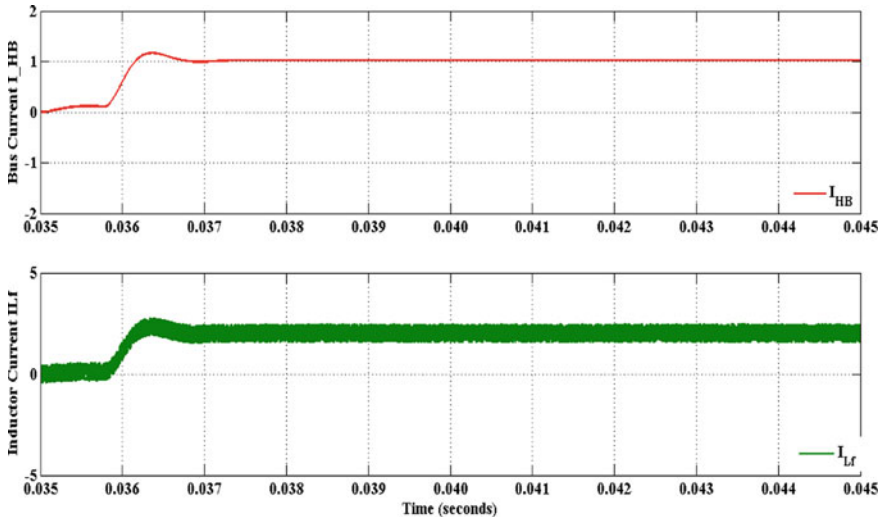


Fig. 19 Regulated current step variations in inductor currents at dual low-voltage sources

were used to discuss the circuit architecture and operational concepts of the BDC. A controlled DC–DC voltage static converter was investigated using the neural network. The method shows that the ANN outperforms the PI. The higher damping performance of the neural controllers allows the system to be operated closer to its stability limit in steady state while still staying stable after several disturbances. In addition, the neural network has a quicker processing speed than PI controllers, resulting in a faster rising time, no overshoot, and no steady-state inaccuracy.

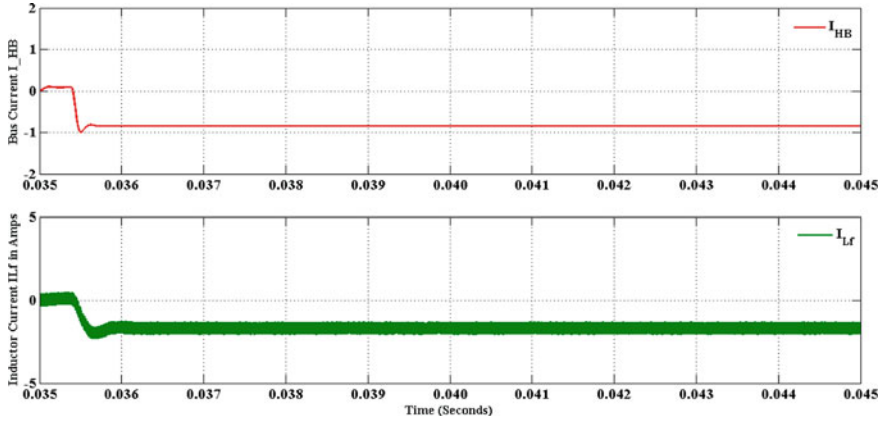


Fig. 20 Regulated current step variations in inductor currents at high bus voltage

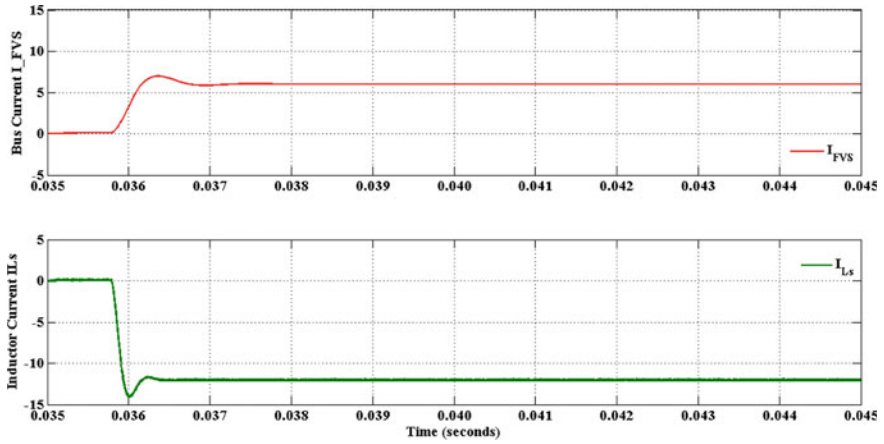


Fig. 21 Regulated current step variations in inductor currents at buck mode

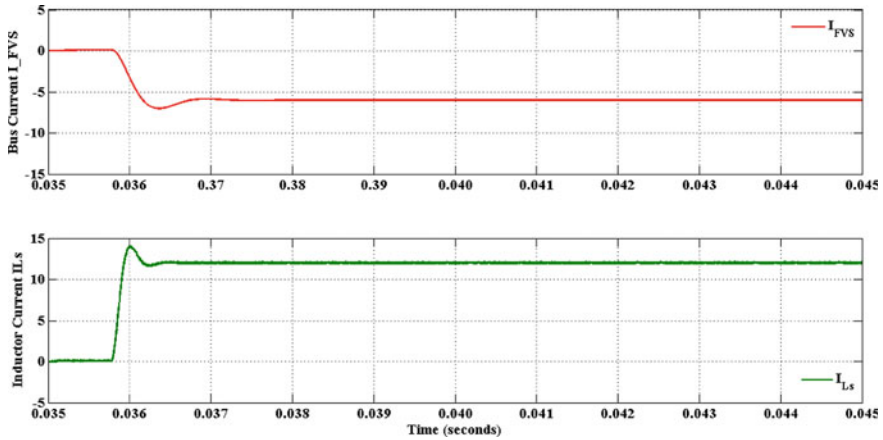


Fig. 22 Regulated current step variations in inductor currents at boost mode

References

1. Ni L (2010) Energy storage and management for a small series plug-in hybrid electric vehicle. Thesis for the doctor of philosophy, University of Nebraska
2. Chan CC (2010) Electric, hybrid, and fuel-cell vehicles: architectures and modeling. *IEEE Trans Veh Technol* 59(2):589–598
3. Thounthong P, Chunkag V, Sethakul P, Davat B, Hinaje M (2009) Comparative study of fuel-cell vehicle hybridization with battery or supercapacitor storage device. *IEEE Trans Veh Technol* 58(8):3892–3904
4. Khaligh A, Li Z (2010) Battery, ultracapacitor, fuel cell, and hybrid energy storage systems for electric, hybrid electric, fuel cell, and plug-in hybrid electric vehicles: state of the art. *IEEE Trans Veh Technol* 59(6):2806–2814
5. Rajashekara K (2013) Present status and future trends in electric vehicle propulsion technologies. *IEEE J Emerg Sel Top Power Electron* 1(1):3–10
6. Schaltz E, Khaligh A, Rasmussen PO (2009) Influence of battery/ultracapacitor energy-storage sizing on battery lifetime in a fuel cell hybrid electric vehicle. *IEEE Trans Veh Technol* 58(8):3882–3891
7. Hintz A, Prasanna UR, Rajashekara K (2015) Novel modular multiple-input bidirectional DC–DC power converter (MIPC) for HEV/FCV application. *IEEE Trans Industr Electron* 62(5):3163–3172
8. Lai C-M, Lin Y-C, Lee D (2015) Study and implementation of a two-phase interleaved bidirectional DC/DC converter for vehicle and dc-microgrid systems. *Energies* 8(9):9969–9991
9. Lai CM (2016) Development of a novel bidirectional DC/DC converter topology with high voltage conversion ratio for electric vehicles and DC-microgrids. *Energies* 9(6):410
10. Bauman J, Kazerani M (2008) A comparative study of fuel-cell–battery, fuel-cell–ultracapacitor, and fuel-cell–battery–ultracapacitor vehicles. *IEEE Trans Veh Technol* 57(2):760–769
11. Ehsani M, Gao Y, Emadi A (2009) Modern electric, hybrid electric and fuel cell vehicles: fundamentals, theory, and design. CRC Press
12. Haihua Z, Khambadkone AM (2008) Hybrid modulation for dual active bridge bi-directional converter with extended power range for ultracapacitor application. In: Industry Applications Society Annual Meeting (IAS'08). IEEE, pp 1–8
13. Moreno J, Ortúzar ME, Dixon JW (2006) Energy-management system for a hybrid electric vehicle, using ultracapacitors and neural networks. *IEEE Trans Industr Electron* 53(2):614–623

14. Tao H, Duarte JL, Hendrix MA (2008) Three-port triple-half-bridge bidirectional converter with zero-voltage switching. *IEEE Trans Power Electron* 23(2):782–792
15. Bhattacharya T, Giri VS, Mathew K, Umanand L (2009) Multiphase bidirectional flyback converter topology for hybrid electric vehicles. *IEEE Trans Industr Electron* 56(1):78–84
16. Maity S, Varaprasad MVG (2018) An efficient PV power optimizer with reduced EMI effects: map-based analysis and design technique. *IEEE Trans Energy Convers* 33(2):546–555
17. Lai C, Lin YJ, Hsieh MH, Li JT (2016) A newly-designed multiport bidirectional power converter with battery/supercapacitor for hybrid electric/fuel-cell vehicle system. In: 2016 IEEE Transportation Electrification Conference and Expo, Asia-Pacific (ITEC Asia-Pacific), pp 163–166. <https://doi.org/10.1109/ITEC-AP.2016.7512941>
18. Lai C, Cheng Y, Hsieh M, Lin Y (2018) Development of a bidirectional DC/DC converter with dual-battery energy storage for hybrid electric vehicle system. *IEEE Trans Veh Technol* 67(2):1036–1052. <https://doi.org/10.1109/TVT.2017.2763157>

Multiple Optimal Solutions for Optimal PMU Placement Using Graph Theory



Chejarla Madhu Kishore Devara and Matam Sailaja Kumari

Abstract This paper presents a graph theory-based novel optimal PMU placement strategy. The proposed strategy provides complete feasible solution space by working on binary connectivity matrix. The binary connectivity matrix is built using graph theory. Multiple optimal solutions are obtained from the feasible solution space. Multiple optimal solutions will provide choice to the operators to choose a particular optimal solution which has a good fit to the considered other minor objectives rather than providing single optimal solution. The proposed approach is tested on IEEE-14 and IEEE-30-bus system. It is observed that, the proposed method guarantees complete set of multiple global optimal solutions.

Keywords Optimal PMU placement · Graph theory · PMU

1 Introduction

Advancements of power system in various ways such as integration of renewables, deregulation of electrical utility, and independent players participation in electricity markets are happening all over the world for meeting the rising demand and to decrease the carbon footprint. This makes the grid more dynamic than ever. Therefore, real-time monitoring of the grid has become very essential. Supervisory control and data acquisition-based (SCADA) measurement system is not fit for dynamic monitoring of the grid due to its low arrival rate.

To further enhance the real-time monitoring of the grid, the deployment of PMUs has been warranted. PMUs provide very accurate time-synchronized voltage and incident current phasors of the lines at the installed bus. Sampling rate of PMUs is much higher than SCADA. It is not recommended to install PMUs in all buses due to its high installation cost and lack of sufficient communication infrastructure. Therefore, optimal strategies are required for deploying PMUs into the system. The following literature explains the proposed optimal strategies for deploying PMUs into the grid.

C. M. K. Devara (✉) · M. S. Kumari
National Institute of Technology, Warangal, India
e-mail: cmk@student.nitw.ac.in

© The Author(s), under exclusive license to Springer Nature Singapore Pte Ltd. 2022
V. Mahajan et al. (eds.), *Sustainable Technology and Advanced Computing in Electrical Engineering*, Lecture Notes in Electrical Engineering 939,
https://doi.org/10.1007/978-981-19-4364-5_21

267

In [1], A two step approach is proposed, In first step, to choose the PMU number, bisection search is used. In the second step, simulated annealing technique is used to get PMU locations. In [2], pareto optimal solution is provided using non-dominated sorting algorithm. In [3], objective function formulation for minimizing number of PMUs has been presented using binary connectivity matrix. Procedure for adding additional constraints into the formulation is also presented.

In [4], constrained formulation for optimal PMU placement (OPP) problem is presented by considering power injection and flow measurements and zero injection measurements. In [5], first time channel limits are considered for providing optimal OPP solution. In [6], quadratic objective function is formulated considering two objectives such as minimization of number of PMUs and maximization of redundancy and also presented procedure for modifying constraints for PMU and transmission line outage. Weighted sum multi-objective formulation is done in [7] and is solved using particle swarm optimization technique.

For identifying critical buses, concept of criticality is presented in [8]. PMU locations are pre-assigned to the identified critical buses while obtaining optimal set. By considering all constraints, a modified binary PSO-based algorithm is presented in [9] for obtaining the optimal solution. Multiple optimal solutions are presented in [10] by using exponential binary PSO algorithm. In [11], recursive tabu search is used for minimizing OPP problem. Pareto optimal solutions are provided [12] by using biogeography optimization algorithm. OPP problem is optimized converting six objectives into single objective in [13]. In [14], semidefinite programming is used for formulating the OPP problem. To the formulated objective, OPP solution is provided considering channel limits in [15]. In [16], OPP solution for different depth of observabilities is presented. In [17], two indices are developed for providing optimal multi-stage solution.

Five indices are proposed in [18]. These indices are used while obtaining optimal solution. Exhaustive search approach is proposed in [19] for obtaining the optimal solution. In [20], both topological and numerical observability conditions are checked while obtaining optimal solution.

In [21], multi-stage solution is provided for maximizing percentage of observability at each stage using PMU relocation scheme. Artificial bee colony algorithm is used in [22] for providing optimal solution. In [23], two objectives, i.e., observability and state estimation accuracy are considering while providing the optimal solution. In [24], constriction factor—particle swarm optimization (CF-PSO) is used to provide optimal solution for various contingencies. In [25], hybridized PSO—gravitational search algorithms are used for providing optimal solution. In [26], accuracy variance of state estimation is used as one of the objective for providing optimal solution. In [27], preexisting condition of SCADA measurements is used for obtaining optimal solution

All the works presented above provided single optimal solution by considering system observability as a major criteria. In [10], importance of multiple solutions is discussed and failed to provide complete set of multiple solutions.

This paper proposes a novel graph theory-based optimal PMU placement strategy for providing complete set of multiple optimal solutions. The proposed method works

on binary connectivity matrix for providing multiple optimal solutions with out using any meta-heuristic or classical techniques.

The reminder of the paper is constructed as follows. Section 2 illustrates the graph theory-based OPP method. Description of the variables, flowchart and step by step algorithm of the proposed method is presented in Sect. 3. Section 4 presents discussion on case study results. Finally, Sect. 5 concludes the article.

2 Illustration of Graph Theory Based OPP Method

In the literature, OPP problem is formulated as a minimization problem. The basic objective function is presented in Eq. (1).

$$f(X) = \sum_{i=1}^N C_{PMU_i} \cdot x_i \tag{1}$$

Subjected to

$$\text{Rank}(H) = N \tag{2}$$

(or)

$$\text{BC} \cdot X = b \tag{3}$$

where

- C_{PMU_i} i th bus PMU installation cost
- x_i = 1 If PMU is installed at i th bus
= 0 If PMU is not installed at i th bus
- N Number of buses
- H Design matrix
- BC Binary connectivity matrix
- b $N \times 1$ unit vector
- X $N \times 1$ vector having x_i as an entity.

A 7-bus system shown in Fig. 1 is used for illustrating the graph theory-based OPP method. Feasible solution space is obtained by working on the binary connectivity matrix. Binary connectivity matrix corresponding to the 7-bus system is shown in Eq. (4)

$$\text{BC} = \begin{bmatrix} 1 & 1 & 0 & 0 & 0 & 0 & 0 \\ 1 & 1 & 1 & 0 & 0 & 1 & 1 \\ 0 & 1 & 1 & 1 & 0 & 1 & 0 \\ 0 & 0 & 1 & 1 & 1 & 0 & 1 \\ 0 & 0 & 0 & 1 & 1 & 0 & 0 \\ 0 & 1 & 1 & 0 & 0 & 1 & 0 \\ 0 & 1 & 0 & 1 & 0 & 0 & 1 \end{bmatrix} \tag{4}$$

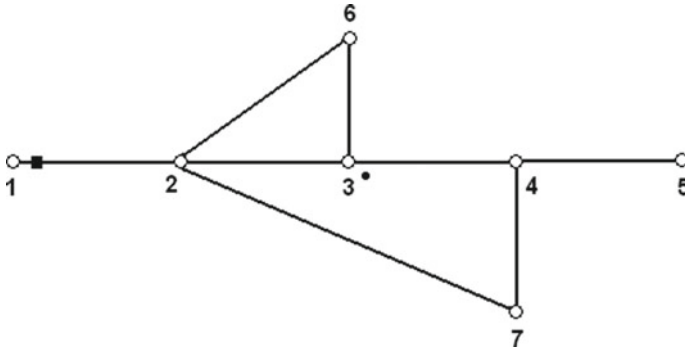


Fig. 1 7-bus system

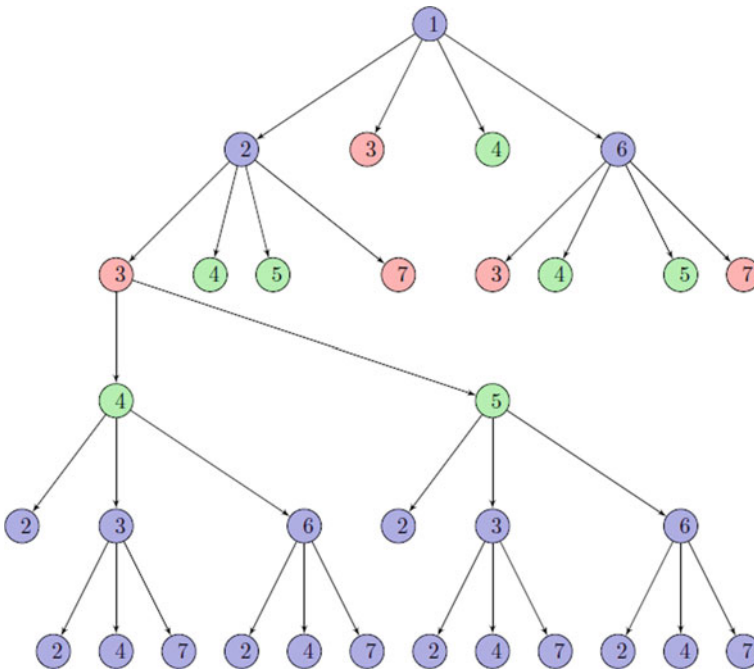


Fig. 2 Node 1 tree

Start from the first row 1 of the binary connectivity matrix. The number of non-zero entities decides how many trees are to be formed. From row 1, for making the bus 1 observable, there are two possibilities. One is placing PMU at bus 1, and other is placing PMU at bus 2. Start with the bus 1. Placement of PMU at bus 1 observes bus 1 and bus 2. From the first column of the binary connectivity matrix check for continuity of the 1's. Stop where it ceases to exist one. Continuity of ones gives the information about the observing capacity of the PMU placed. Therefore, placing PMU at bus 1 has continuity upto 2nd row.

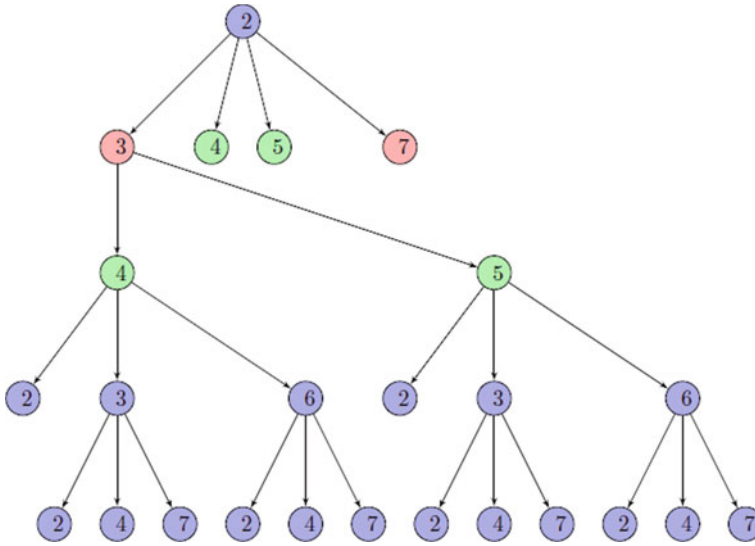


Fig. 3 Node 2 tree

Check for non-zero entities in the next row where discontinuity happens, to further go down. These non-zero entities are the possibilities to install PMUs for making corresponding row number bus observable. Here, in this case, 2, 3, 4, 6 are the possibilities. Place the PMU at bus 2. Again, look for discontinuity of ones. Again, get the new possibilities for installing PMU to make the corresponding row number bus observable. Here, in this case, 3, 4, 5, 7 are the new possibilities for installing PMU to make the corresponding row number bus observable. By repeating the abovesaid process will give the complete feasible set for OPP problem. Solution tree starting at bus 1 and bus 2 is given in Figs. 2 and 3. Table 1 is reporting the complete feasible solution space for the illustrated 7-bus system using the proposed method.

3 Algorithm of the Proposed Method

The flowchart of the proposed algorithm is given in Fig.4. The following are the description of variables used in the flowchart.

Node vector (n): It is vector which stores column number of non-zero elements corresponding to selected row.

Ex: $n = [1 \ 2 \ 0 \ 0 \ 0 \ 0]$.

Depth of penetration vector (d): It is a vector which stores row number upto which stored column number in 'n' is having continuity of ones. Apart from that it also stores the information about how many times this vector need to visit, in $d(nc, N + 1)$ entity and how many times it already visited in, $d(nc, N + 2)$ entity.

Table 1 Feasible solution space

No. of PMUs	No. of solutions	Placement sites
2	2	2-4, 2-5
3	10	1-2-4, 1-2-5, 1-3-4, 1-4-6, 2-3-4, 2-3-5, 2-4-6, 2-5-6, 2-4-7, 2-5-7
4	21	1-2-3-4, 1-2-3-5, 1-2-4-6, 1-2-5-6, 1-2-4-7, 1-2-5-7, 1-3-4-7, 1-3-4-6, 1-3-4-5, 1-3-5-7, 1-4-6-7, 1-4-5-6, 1-5-6-7, 2-3-4-7, 2-3-4-6, 2-3-4-5, 2-3-5-7, 2-3-5-6, 2-4-6-7, 2-4-5-6, 2-5-6-7
5	17	1-2-3-4-7, 1-2-3-4-6, 1-2-3-4-5, 1-2-3-5-7, 1-2-3-5-6, 1-2-4-6-7, 1-2-4-5-6, 1-2-5-6-7, 1-3-4-6-7, 1-3-4-5-6, 1-3-5-6-7, 1-4-5-6-7, 2-3-4-6-7, 2-3-4-5-6, 2-3-5-6-7, 2-3-4-5-7, 2-4-5-6-7
6	6	1-2-3-4-6-7, 1-2-3-4-6-7, 1-2-3-4-5-6, 1-2-3-5-6-7, 1-2-3-4-5-7, 1-2-4-5-6-7, 1-3-4-5-6-7

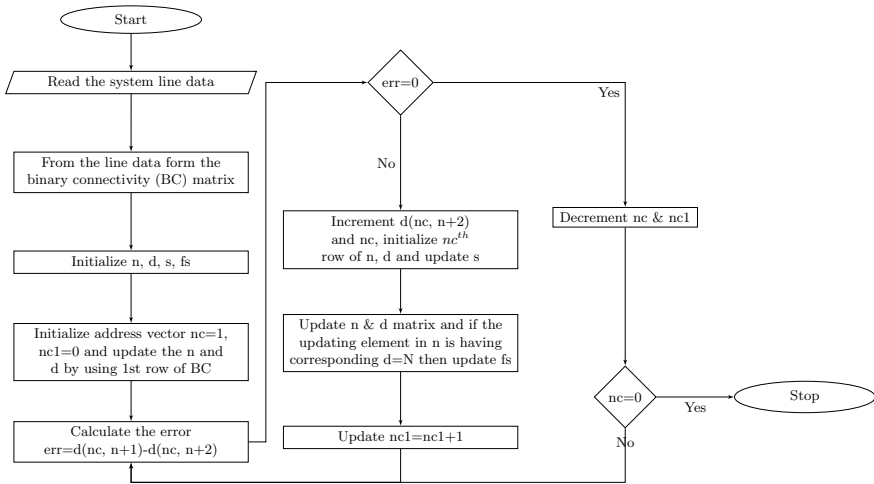


Fig. 4 Flowchart of graph theory-based OPP method

Ex: $d = [2\ 3\ 0\ 0\ 0\ 0\ 2\ 0]$.

Temporary solution updater (s): s is a $1 \times N$ vector, which stores solution temporarily.

Ex: $s = [1\ 0\ 0\ 0\ 0\ 0]$.

Final solution updater (fs): fs is a $1 \times N$ vector, which stores final solution.

Table 2 Comparison of results for IEEE-14-Bus system

Method	No. of PMUs	No. of solutions	Placement sites
Proposed method	4	5	2-6-7-9, 2-6-8-9, 2-7-11-13, 2-7-10-13, 2-8-10-13
EBPSO [9]	4	4	2-6-7-9, 2-6-8-9, 2-7-10-13, 2-8-10-13

3.1 Algorithm

1. Initialize node vector (n), depth of penetration vector (d), solution storer (s), final solution vector (fs)
2. Update the first row of n and d by selecting 1st row binary connectivity matrix (BC), initialize address vector $nc = 1$, $nc1 = nc$
3. Calculate the error = $d(nc, N + 1) - d(nc, N + 2)$
4. If error is not zero increment $d(nc, N + 2)$ and nc , initialize n th row of n , d matrix, and update the s matrix
5. update the n and d matrix and if the updating element into n is having corresponding d element is equal to N then update fs
6. update $nc1 = nc1 + 1$
7. if error = 0 then decrement nc and $nc1$
8. If $nc = 0$ stop the process. Otherwise go to step3.

4 Case Study and Results

The efficacy of the proposed method is tested on IEEE-14-bus and 30-bus systems for base case. For coding the proposed algorithm, MATLAB software is used.

From Table 2, the proposed method is providing all five optimal solutions for IEEE-14-bus system where as EBPSO method provided only four optimal solutions. From the results, it is observed that the proposed method has the ability to provide complete set of multiple optimal solutions.

From Table 3, for IEEE-30-bus system, the proposed method providing 734 solutions. Only, five solutions presented in Table 3 where as all the methods in the literature provided single optimal solution. These all solutions provided in the literature are the subset of the multiple optimal solution space obtained by the proposed method.

By running the proposed algorithm, one will get complete set feasible solution space to an OPP problem. This feasible solution space will be pruned to get complete set of multiple optimal solutions. Whereas in case of obtaining optimal solution, using meta-heuristic techniques or classical will give one solution for every run. Multiple runs may or may not give different optimal solutions.

The proposed method is obtaining multiple optimal location of PMUs without using any conventional or heuristic optimization techniques and by working only

Table 3 Comparison of results for IEEE-30-Bus system

Method	No. of PMUs	No. of solutions	Placement sites
Proposed method	10	734	3-5-8-9-10-12-19-23-25-30, 2-4-6-9-10-12-15-18-25-27, 1-2-6-9-10-12-15-19-25-27, 1-2-6-9-10-12-15-18-25-27, 2-4-6-9-10-12-15-19-25-27
ILP based [6], IMS MBPSO [10]	10	1	2-4-6-9-10-12-15-19-25-27
BPSO [7]	10	1	2-4-6-9-10-12-15-18-25-27
BSP [14]	10	1	1-2-6-9-10-12-15-18-25-27
Exhaustive search [19]	10	1	1-2-6-9-10-12-15-19-25-27

on the binary connectivity of the matrix. From the results, it is observed that the optimal PMU placement problem is having many global optimal points rather than single global optimal point. Therefore, OPP problem is a specialized optimization problem having many global optimal solutions. The proposed method guarantees complete set of multiple global optimal solutions. These multiple optimal solutions would give the operator freedom to choose an optimal solution which has a good fit to the considered other monitor objectives.

5 Conclusions

This paper proposes a novel graph theory-based optimal PMU placement algorithm for providing multiple optimal solutions. The proposed method purely works on binary connectivity matrix without using any heuristic or conventional optimization techniques. The proposed method has the ability to provide complete set of optimal solutions. Multiple optimal solutions would give the choice to the operators to choose an optimal solution which has good fit to the considered other minor objectives rather than providing a single optimal solution. From the results, it is observed that the optimal PMU placement problem is having many global optimal points rather than single global optimal point. Therefore, OPP problem is a specialized optimization problem having many global optimal solutions. The proposed method guarantees complete set of multiple global optimal solutions. As the algorithm progresses, the solution vector length is increasing. Because of this, computers with low RAM capacity are not sufficient to run the algorithm for higher-order systems.

References

1. Baldwin TL, Mili L, Boisen MB, Adapa R (1993) Power system observability with minimal phasor measurement placement. *IEEE Trans Power Syst* 8(2):707–715
2. Milosevic BD, Begovic M (2002) Nondominated sorting genetic algorithm for optimal phasor measurement placement. *IEEE Power Eng Rev* 22(12):61
3. Xu, B, Abur, A (2004) Observability analysis and measurement placement for systems with PMUS. In: IEEE PES power systems conference and exposition, vol 2, pp 943–946
4. Gou B (2008) Optimal placement of PMUS by integer linear programming. *IEEE Trans Power Syst* 23(3):1525–1526
5. Korkali M, Abur A (2009) Placement of PMUS with channel limits. In: 2009 IEEE power energy society general meeting, pp 1–4
6. Chakrabarti S, Kyriakides E, Eliades DG (2009) Placement of synchronized measurements for power system observability. *IEEE Trans Power Delivery* 24(1):12–19
7. Ahmadi A, Alinejad-Beromi Y, Moradi M, Optimal PMU placement for power system observability using binary particle swarm optimization and considering measurement redundancy. *Exp Syst Appl* 38(6):7263–7269 (2011) [Online]. Available: <http://www.sciencedirect.com/science/article/pii/S0957417410013886>
8. Pal A, Sanchez-Ayala GA, Centeno VA, Thorp JS (2014) A PMU placement scheme ensuring real-time monitoring of critical buses of the network. *IEEE Trans Power Delivery* 29(2):510–517
9. Rahman NHA, Zobaa AF (2017) Integrated mutation strategy with modified binary PSO algorithm for optimal PMUS placement. *IEEE Trans Industr Inf* 13(6):3124–3133
10. Maji TK, Acharjee P (2017) Multiple solutions of optimal PMU placement using exponential binary PSO algorithm for smart grid applications. *IEEE Trans Ind Appl* 53(3):2550–2559
11. Koutsoukis NC, Manousakis NM, Georgilakis PS, Korres GN (2013) Numerical observability method for optimal phasor measurement units placement using recursive Tabu search method. *IET Gen Transm Distrib* 7(4):347–356
12. Jamuna K, Swarup K (2012) Multi-objective biogeography based optimization for optimal PMU placement. *Appl Soft Comput* 12(5):1503–1510 [Online]. Available: <http://www.sciencedirect.com/science/article/pii/S1568494612000075>
13. Müller HH, Castro CA (2016) Genetic algorithm-based phasor measurement unit placement method considering observability and security criteria. *IET Gen Transm Distrib* 10(1):270–280
14. Korres GN, Manousakis NM, Xygkis TC, Löfberg J (2015) Optimal phasor measurement unit placement for numerical observability in the presence of conventional measurements using semidefinite programming. *IET Gen Transm Distrib* 9(15):2427–2436
15. Manousakis NM, Korres GN (2016) Optimal PMU placement for numerical observability considering fixed channel capacity: a semidefinite programming approach. *IEEE Trans Power Syst* 31(4):3328–3329
16. Nuqui RF, Phadke AG (2005) Phasor measurement unit placement techniques for complete and incomplete observability. *IEEE Trans Power Delivery* 20(4):2381–2388
17. Dua D, Dambhare S, Gajbhiye RK, Soman SA (2008) Optimal multistage scheduling of PMU placement: an ILP approach. *IEEE Trans Power Delivery* 23(4):1812–1820
18. Sodhi R, Sharieff MI (2015) Phasor measurement unit placement framework for enhanced wide-area situational awareness. *IET Gen Transm Distrib* 9(2):172–182
19. Chakrabarti S, Kyriakides E (2008) Optimal placement of phasor measurement units for power system observability. *IEEE Trans Power Syst* 23(3):1433–1440
20. Sodhi R, Srivastava S, Singh S (2010) Optimal PMU placement method for complete topological and numerical observability of power system. *Electr Power Syst Res* 80(9):1154–1159 [Online]. Available: <http://www.sciencedirect.com/science/article/pii/S0378779610000647>
21. Wen MHF, Xu J, Li VOK (2013) Optimal multistage PMU placement for wide-area monitoring. *IEEE Trans Power Syst* 28(4):4134–4143

22. Li S, Meng Z (2017) Optimal PMU placement based on improved binary artificial bee colony algorithm. In: 2017 IEEE transportation electrification conference and expo, Asia-Pacific (ITEC Asia-Pacific), pp 1–6
23. Singh SP, Singh SP (2018) A novel multi-objective PMU placement method for power system state estimation. In: International electrical engineering congress (IEEECON), pp 1–4
24. Shafiullah M, Hossain MI, Abido M, Abdel-Fattah T, Mantawy A (2019) A modified optimal PMU placement problem formulation considering channel limits under various contingencies. *Measurement* 135:875–885 [Online]. Available: <http://www.sciencedirect.com/science/article/pii/S0263224118311862>
25. Laouid AA, Rezaoui MM, Kouzou A, Mohammedi RD (2019) Optimal PMUS placement using hybrid PSO-GSA algorithm. In: 2019 4th international conference on power electronics and their applications (ICPEA), pp 1–5
26. Sun L, Chen T, Chen X, Ho WK, Ling K, Tseng K, Amaratunga GAJ (2019) Optimum placement of phasor measurement units in power systems. *IEEE Trans Instrum Meas* 68(2):421–429
27. Manousakis NM, Korres GN (2020) Optimal allocation of phasor measurement units considering various contingencies and measurement redundancy. *IEEE Trans Instrum Meas* 69(6):3403–3411

LVRT Performance Enhancement of Multi-machine Power System with High Penetration of Wind Energy Sources Considering Fault Current Limiters



Chintan R. Mehta and Santosh C. Vora

Abstract The low voltage ride through (LVRT) is the ability of wind farms to remain connected in synchronism with the power grid during the disturbance in the power system. The literature proposes various techniques for LVRT improvement of grid-connected wind farms by considering the single machine infinite bus (SMIB) system. The behavior of the power system having multiple synchronous generators, asynchronous generators and loads needs to be observed for the system-level fault as the effectiveness of any solution cannot be extrapolated to large systems only by verifying it on the SMIB system. The fault current limiters (FCLs) are widely used in literature to improve the LVRT requirement of wind farms. This paper compares the operation of different types of FCLs by considering a system-level fault at the weak bus in a multi-machine power system. The effects of FCLs on generator buses during the symmetrical fault are presented and analyzed in the paper.

Keywords Doubly fed induction generator · Fault current limiter · Low voltage ride through · Multi-machine power system · Wind farms

1 Introduction

Carbon-free environment-friendly energy sufficiency is one of the goals of sustainable development, and it is the major driving force for energy-related research. Moreover, as per United Nations' #17 sustainable development goals to transform the world, goal #7 deals with affordable and clean energy. The fast depletion of fossil-fuel-based resources and exponential rise in energy demand has made renewable energy research inevitable. Of the viable renewable sources, viz. wind energy, solar energy and geothermal resources, etc., wind energy is the prominent and fast-developing energy source. Some of the advantages of wind energy are low maintenance cost of structure and machine, maximum power extraction, wind availability in

C. R. Mehta (✉) · S. C. Vora

Department of Electrical Engineering, Institute of Technology, Nirma University,
Ahmedabad 382481, India

e-mail: chintan.mehta@nirmauni.ac.in

several parts of the world for long hours and no air pollution. As per the world wind energy association, the total wind energy capacity has reached 589 GW [1]. The wind turbine generators (WTGs) are classified as fixed-speed WTGs and variable-speed WTGs (VSWT). From the available VSWT, doubly fed induction generator (DFIG) is gaining more popularity as compared to fixed-speed induction generator (FSIG) because of its better power extraction capacity, higher efficiency, decoupled active and reactive power control, the requirement of small rating converters and lower maintenance [2]. However, in case of the grid fault, DFIGs are adversely affected as its stator winding is directly connected with the grid. The terminal voltage of DFIG reduces much below the nominal value during the fault, resulting in high fault current through the converters which will severely affect the life of its converters [3]. As the penetration of wind energy is increasing exponentially in the power grid and to protect the grid against severe system disturbances, the transmission system operators have introduced stringent grid code requirements. According to various grid codes, wind farms must remain connected to the network even during the faults [4]. To achieve the LVRT requirements of DFIG-based wind farms, the solutions proposed should protect the rotor side converter and DC link capacitor. The solution should also provide the required reactive power support to the grid during the system fault [5].

According to the literature, the LVRT enhancement of DFIG-based WTs can be classified into the following two main categories

- Modification in control system/strategy for the DFIG converters.
- Auxiliary hardware application.

Demagnetization current method [6], virtual damping flux-based control [7] and sliding mode control [8] are a few of the methods proposed in the literature to fulfill the LVRT requirements of DFIG-based WTs. The methods with modification in the control system of DFIG converters cannot ensure the LVRT performance requirements in severe voltage collapse, and they need proper tuning of control parameters. Moreover, these techniques can be used only for new installations of wind farms. A review of various testing tools under hardware and software-based categories has been analyzed [9]. This review helps to understand the challenges in the testing and implementation of wind turbines in the present day.

The commonly used auxiliary hardware application is a crowbar-based system [10]. The crowbar can protect the rotor side converter (RSC) and grid side converter (GSC); however, with the activation of the crowbar the DFIG acts as a conventional induction generator and demands large reactive power from the grid. Thus, it affects the voltage profile of the system and the power system's stability gets adversely affected. The other auxiliary hardware method proposed is reactive power injection using STATCOM [11]. The STATCOM provides the reactive current immediately after the fault to improve the voltage profile, but it cannot protect the RSC and DC link. Unified inter-phase power controller (UIPC) [12] and series grid side converter [13] are the few other auxiliary hardware to meet and improve LVRT requirements, but these techniques require full-rated converters and transformers so the overall cost is increased.

Series dynamic braking resistor technique with DFIG-based wind farm [14] and different types of fault current limiters are proposed in literature to achieve the LVRT improvement of DFIG-based WTs. The non-superconducting fault current limiter comprising of diode bridge is proposed in [15]. To improve the performance of the system, a nonlinear controller is introduced where RMS voltage at PCC and the direct current through bridge path are compared with the threshold value of the voltage and current, unlike the case where only RMS voltage at PCC was compared with the threshold value [15]. The series combination of resistance and inductance in parallel to a diode bridge circuit is proposed in [16]. The LVRT improvement is shown by comparing the results with the series dynamic braking resistor technique. The series combination of resistance and capacitor in parallel to a diode bridge circuit is proposed in [5]. The LVRT improvement is shown by comparing the results with bridge-type fault current limiter [16]. The capacitive DC reactor type of FCL is introduced in [17], which is a modified version of conventional DC reactor type FCL.

The concept of the series resonance-based FCL was introduced in [18] only for limiting fault currents in synchronous generator-based SMIB system. The technique of estimating parameters of resonance type FCL for protection and stability analysis of power systems having synchronous generators is proposed in [19]. The authors of [20] have proposed the modified series resonance type of FCL (MSRFCL) by meaningfully modifying the series resonance type FCL by introducing the resistor for energy dissipation, inductor–capacitor for restricting current, oscillations and reactive power support, respectively.

Among the above-mentioned solutions, the applications of fault current limiters (FCL) are observed to be an effective solution for enhancing the LVRT performance requirement and it also restricts short circuit current peak for induction generators during faults. The application of FCLs as a solution toward the grid connection of wind power plants (WPPs) allows wind farms (WF) to remain in service, even if the network fault current exceeds the rated peak. Moreover, an effective FCL connected to the WPP reduces the voltage sag at the PCC during a fault.

The literature available mostly discusses the performance of FCLs for the WPPs connected to the grid as a single machine infinite bus (SMIB) system. However, the effects of FCLs for system-level fault on the multi-machine power system having other synchronous generators are not depicted in the literature. The authors have considered a Western System Coordinating Council (WSCC) 3-generator 9-bus system and modified it to incorporate the DFIG wind farm and the FCL for the simulation-based demonstration. The symmetrical fault is simulated at the weakest bus, and the effectiveness of FCLs is compared.

This paper is organized as follows:

- Section #2 presents the mathematical modeling of the important component for transient analysis.
- Section #3 discusses the concept of a modified series resonance type of fault current limiter.
- Section #4 discusses the selection of FCL parameters.

- Section #5 represents the system description of the DFIG-based wind farm connected to the grid in a multi-machine system.
- Section #6 discusses simulation results and a comparison of the MSRFCL with CBFCL and the case with no controllers in the system.
- Section #7 summarizes the research work.

2 System Component Modeling

2.1 Equivalent Circuit of Induction Machine

Wind turbine modeling depends on various geometrical and physical aspects. In this paper, the authors have considered the electrical behavior of the system. The equivalent circuit model corresponds to Park’s model of the induction generator which is shown in Fig. 1 [21]. Based on this model, the stator and rotor voltages and fluxes are expressed [5].

$$\vec{v}_s = R_s \vec{i}_s + \frac{d\vec{\Psi}_s}{dt} + j\omega_s \vec{\Psi}_s \tag{1}$$

$$\vec{v}_r = R_r \vec{i}_r + \frac{d\vec{\Psi}_r}{dt} - j(\omega_s - \omega_r) \vec{\Psi}_r \tag{2}$$

$$\vec{\Psi}_s = L_s \vec{i}_s + L_m \vec{i}_r \tag{3}$$

$$\vec{\Psi}_r = L_r \vec{i}_r + L_m \vec{i}_s \tag{4}$$

In Eqs. (1) to (4), \vec{v}_s and \vec{v}_r are stator voltage and rotor voltage, respectively, while R_s and R_r represent stator and rotor resistances (in Ω), respectively, ω_s and ω_r represent supply angular frequency and rotor angular frequency (in rad/s), respectively, \vec{i}_s and \vec{i}_r are stator current and rotor current, respectively, and ψ term represents

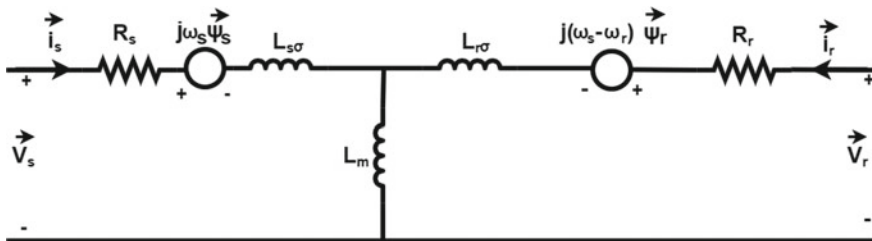


Fig. 1 Equivalent circuit of an induction machine for transient analysis

flux linkages. Neglecting the stator and rotor resistance and by using Eqs. (1) and (2)

$$\frac{L_m}{L_s} \vec{v}_s = -\sigma \frac{d\vec{i}_r}{dt} - j\sigma L_r(\omega_s - \omega_r) \vec{i}_r + j\omega_r \frac{L_m}{L_s} \vec{\psi}_s \quad (5)$$

Here, $\sigma = 1 - L^2m/L_sL_r =$ Leakage factor, while L_s and L_r are the stator and rotor leakage inductance in (H), respectively, and L_m is magnetizing inductance.

In steady-state condition, \vec{v}_s is approximately equal to $j\omega_r\vec{\psi}_s$ and the term $\frac{d\vec{i}_r}{dt}$ is equal to zero.

Based on these conditions, Eq. (5) can be derived as

$$\frac{L_m}{L_s} \vec{v}_s = -j\sigma L_r(\omega_s - \omega_r) \vec{i}_r + \vec{v}_r \quad (6)$$

At the instant of fault, the value of stator flux and rotor current is constant because of the continuity of magnetic flux and inductor current. So from Eq. (6), a stator voltage change is given as

$$\frac{L_m}{L_s} \Delta\vec{v}_s = -\sigma \frac{d\vec{i}_r}{dt} + \Delta\vec{v}_r \quad (7)$$

With higher voltage drop (i.e., $\Delta\vec{v}_s$ is large), high current will flow from rotor and it will affect the performance of RSC and GSC of DFIG.

2.2 The Rotor Side Controller (RSC)

Rotor side controller is an IGBT-based power electronic converter connected between slip rings and a DC link capacitor. It is used to control active and reactive power.

2.3 The Grid Side Controller (GSC)

The grid side controller (GSC) is an IGBT-based power electronic converter connected between the DC link capacitor and the grid side of DFIG. This converter maintains a constant power factor at the PCC.

2.4 Synchronous Generator Modeling

The modeling of synchronous generators with a controller is not reproduced here, and its voltage, current and flux linkage equations under normal and transient conditions are very well deliberated in [22, 23].

3 Fault Current Limiter (FCL)

The modified series resonance fault current limiter (MSRFCL) is shown in Fig. 2. The MSRFCL comprises a bridge part and the shunt part. The bridge part comprises a diode bridge ($D_1 - D_4$), power electronic switch (S), dc reactor L_{dc} with very less resistance R_{dc} and a free-wheeling diode (D_f).

The power electronic switch normally comprised of IGBT is connected in the normal working condition. The current takes the path $A - D_1 - L_{dc} - R_{dc} - S - D_4 - B$ in the first half cycle, and in the second half cycle, the line current takes the path $A - D_3 - S - R_{dc} - L_{dc} - D_2 - B$. So, the current from L_{dc} and R_{dc} flows in the same direction. The detailed description of the working of MSRFCL is depicted in [24]. As the impedance of the shunt section is very high during normal operating conditions, the current passing through the shunt path is insignificant.

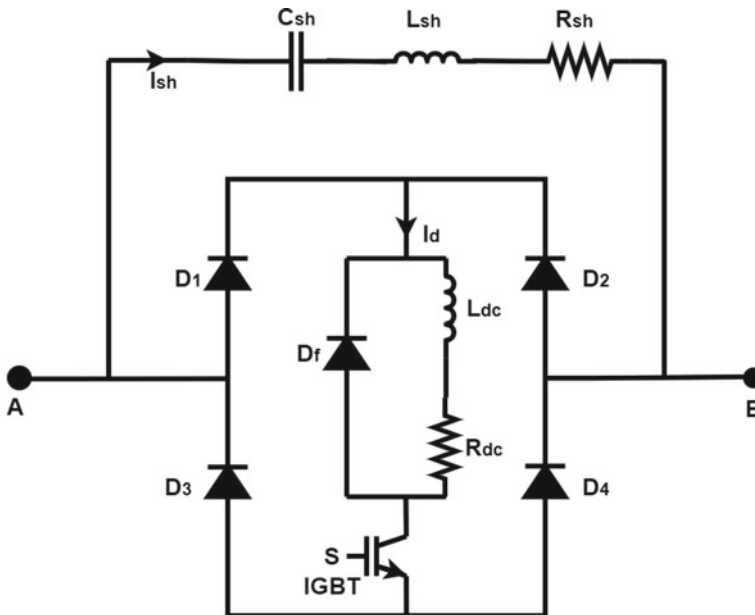


Fig. 2 Single-phase representation of MSRFCL

During the system fault, the current increases abruptly, but the rate of rise of the current is reduced by the dc reactor L_{dc} which protects the power electronic switch from high di/dt. The shunt section comprises the series combination of resistance, inductor and capacitor and functions based on the concept of series resonance. The shunt path consists of a bypass current limiting inductor L_{sh} in series with a resistor R_{sh} and capacitor C_{sh} as shown in Fig. 2. The R_{sh} limits the fault current and dissipates the excess energy from the system which helps improve the transient stability of the power system. The inductor L_{sh} limits the rate of rise of line current, and the capacitor C_{sh} helps to improve reactive power support to the system and also improves the system's voltage profile during faulty conditions. The controller design for the FCL is described in [25]. The comparison of the proposed MSRFCL with CBFCL [5], BFCL [16] and PRBFCL [3] by considering SMIB system is presented in [25].

4 FCLs for Transient Stability Improvement Analysis of Multi-machine Power System

The SMIB system helps in understanding the machine behavior under consideration but it does not offer a response of other machines connected in the system in the event of the faults, changes in generation or load, loss of line, etc. It becomes essential to introduce renewable generation in multi-machine systems, simulate various cases and analyze the behavior of synchronous and asynchronous generators for such cases and, further, offer a genuine solution(s) to improve machine performance on various counts. The behavior of the power system having multiple synchronous and asynchronous generators and loads needs to be observed for the fault at the system level. The effectiveness of any solution cannot be extrapolated to large systems only by verifying it on the SMIB system. To address this issue, a multi-machine power system is presented in this paper to demonstrate the effects of fault current limiters for transient stability analysis of the power system. To show the effectiveness of the FCLs, faults are simulated at a weak bus of the system.

The analysis is presented for a 3L-G fault. The WSCC system is selected as a multi-machine power system [22, 26], and it is modified to accommodate the DFIG wind farm and is shown in Fig. 3.

To consider the large penetration of wind energy-based generation, a synchronous generator at bus #2 is replaced by an equivalent capacity of coherent aggregated DFIG-based wind farm. Bus #5 is a weak bus of the standard system. To analyze the effects of FCL on system-level fault in a multi-machine system, the performance of MSRFCL is compared with CBFCL [5] and the case where no FCLs (no controller) are installed in the multi-machine power system. All these systems are simulated in the PSCAD/EMTDC. For transient stability analysis, a wind speed of 11 m/s is considered to be constant for the short fault duration. A symmetrical fault (3L-G) is simulated on bus #5. Fault instant is 10 s. Fault duration is considered as 150 ms but

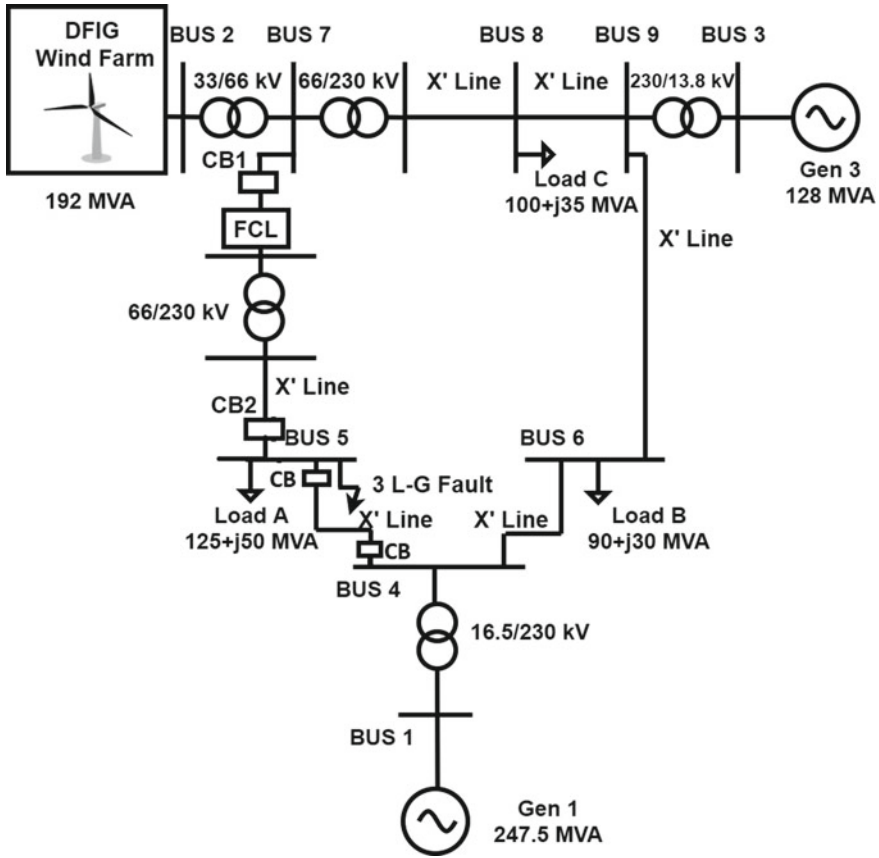


Fig. 3 Modified WSCC #3-generator #9-bus test system

relevant circuit breakers CB1 and CB2 open and isolate the line in 100 ms where FCL is connected and re-closes after removal of fault at 10.65 s.

5 FCL Parameter Selection for Multi-machine Power System

For the multi-machine power system, the power output from the wind farm under steady-state condition is 163 MW. The FCL is connected between bus #7 and bus #5. The power flow in the transmission line connecting bus #7 and bus #5 is 84 MW under steady-state condition. The current in the said line is calculated to be

$$I_{sh} = \frac{84 \times 10^6}{66 \times 10^3 \times \sqrt{3}} = 735 \text{ A}$$

Based on the value of I_{sh} , the resistance of shunt path R_{sh} in FCL is calculated as per [16].

$$R_{sh} = \frac{84 \times 10^6}{3 \times 735 \times 735} = 52 \text{ } \Omega/\text{phase}$$

Accordingly, the per phase value of R_{sh} is selected as $52 \text{ } \Omega$. The capacitance of the shunt path C_{sh} is chosen as $40 \text{ } \mu\text{F}$ per phase, and based on the concept of series resonance, L_{sh} is derived as 176 mH .

The value of inductor L_{dc} and R_{dc} is considered as 1 mH and $0.2 \text{ m}\Omega$, respectively. The values of C_{sh} and L_{sh} are based on the trade-off between the realizable value and Q factor.

6 Simulation Results

The simulation results of RMS voltage (phase), active power, reactive power and RMS current of all the three generators at bus#1, #2 and #3 are presented and analyzed for fault duration and FCL presence.

Figure 4 depicts the RMS voltages of all generators during pre-fault, fault and post-fault conditions. RMS voltage in steady-state condition is 1 pu. When no FCLs are installed in the system, in the event of symmetrical fault at bus #5, the voltage at bus #2 falls to 0.39 pu. However, when the FCLs have installed in the system the voltage profile at all the generator buses gets improved significantly.

With the MSRFCL, the voltage improves to 0.84 pu as compared to 0.68 pu in a case with CBFCL. It is evident from Fig. 4b that the insertion of the inductor with the capacitor leads to reduced voltage swing on all the generator buses. Generator #1, being a swing generator, undergoes an insignificant voltage dip (Fig. 4a). The RMS voltage at generator #3 is improved from 0.707 pu for the case of no FCL to 0.86 pu with MSRFCL as seen from Fig. 4c.

Figure 5 represents the active power at all the generator buses. Active power output from generator #2 in its steady-state condition is 1.63 pu at bus #2. As seen from Fig. 5b, the active power output during fault at bus #2 dips to 0.58 pu in the case where no FCL is installed in the system. However, with the insertion of FCLs, the generator active power improves significantly. Apparent from the graphs of Fig. 5b, MSRFCL gives less power swing as compared to the CBFCL. As seen in Fig. 5a, generator #1 supplies active power even during the fault interval with the MSRFCL. A careful investigation shows that with the MSRFCL the variation in active power output of generator #3 is also reduced as compared to the case of CBFCL Fig. 5a, c.

Figure 6 focuses on reactive power output at generator buses. The variation in reactive power is also reduced at all the buses with FCLs. The reactive power offered

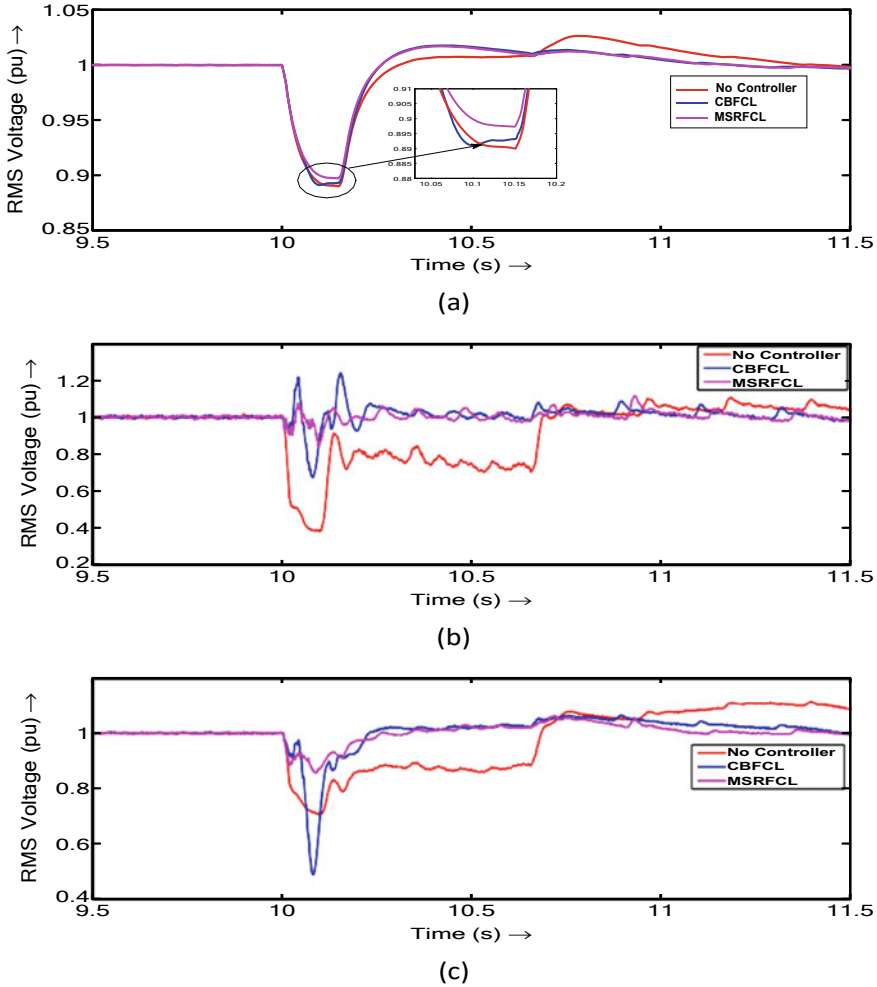


Fig. 4 RMS voltages at generator buses 3L-G fault a bus #1; b bus #2; c bus #3

by CBFCL is up to 1.70 pu compared to 0.74 pu by MSRFCL. It is noted that being the R-C circuit the CBFCL offers more reactive power at bus #2, (Fig. 6b) bringing greater swing in RMS voltages at bus #2.

Figure 7 shows a comparison of RMS currents at the generator buses. In the fault condition, the peak value of the RMS current shoots to 3.1 pu from its base value of 1.63 pu in the absence of a series device at bus #2, which is limited 2.24 pu with the MSRFCL, better as compared to CBFCL. The results of bus #1 are almost similar for all the cases. At bus #3 where the base current is 0.85 pu, during the fault the peak value of current touches 1.61 pu for the case of no FCL and improves to 1.29 pu in MSRFCL (seen in Fig. 7c).

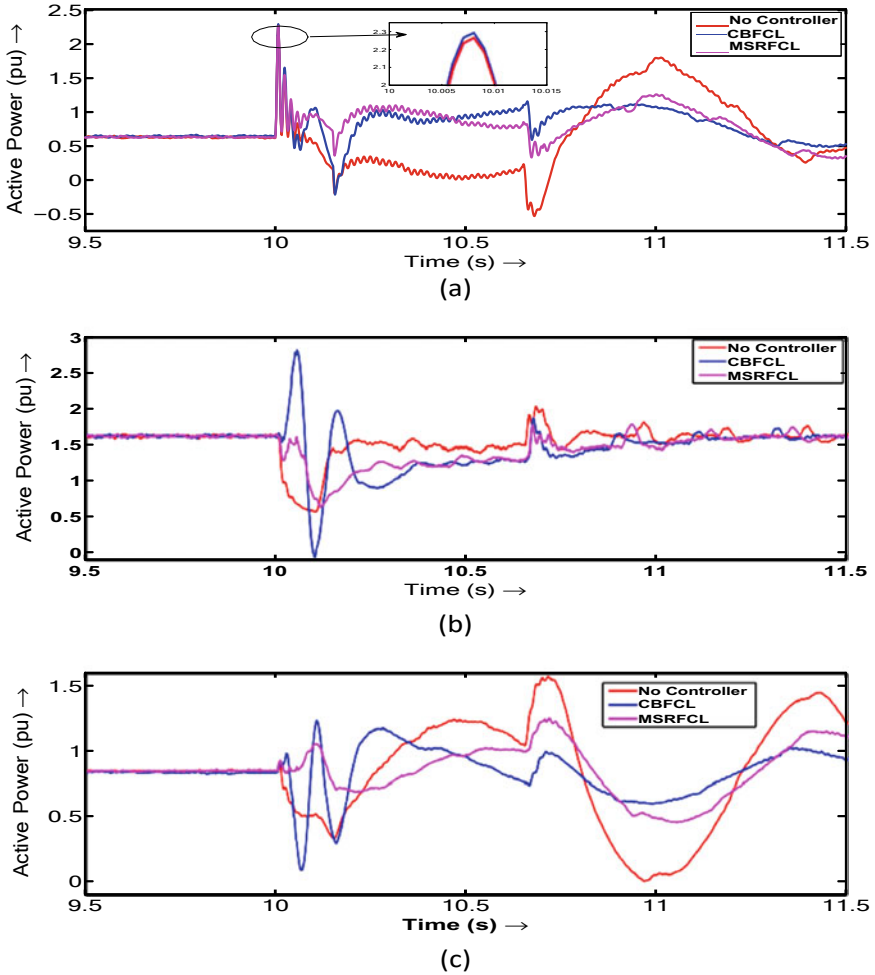


Fig. 5 Active power output at generator buses during 3L-G fault a Bus#1; b bus#2; c bus #3

The DC link voltage of coherent aggregated DFIG wind farm is presented in Fig. 8. The DC link voltage swing post-fault clearance is in the band of 0.53 kV when no FCL is connected. With the CBFCL, the swing is in the band of 0.35 kV, and with the MSRFCL, it is the minimum at 0.26 kV. The lesser variation in the DC link voltage will protect the DC link capacitor and converters of DFIG.

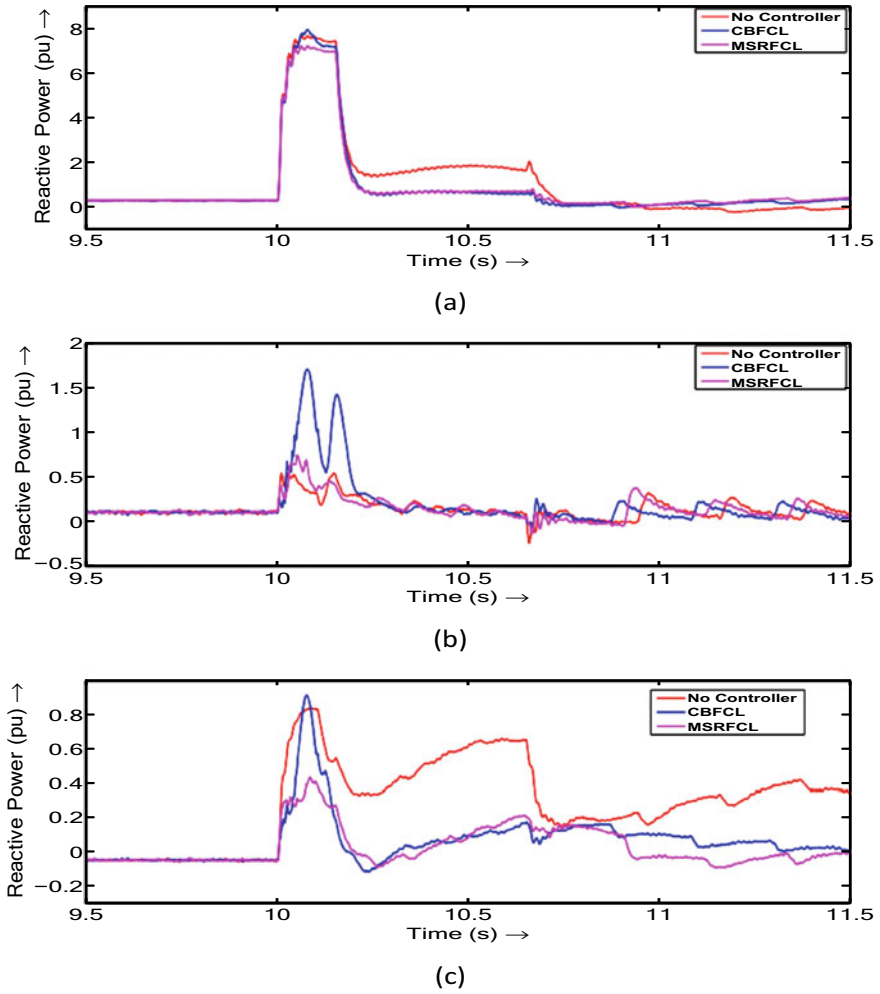


Fig. 6 Reactive power at generator buses for 3L-G fault a Bus #1; b bus #2; c bus #3

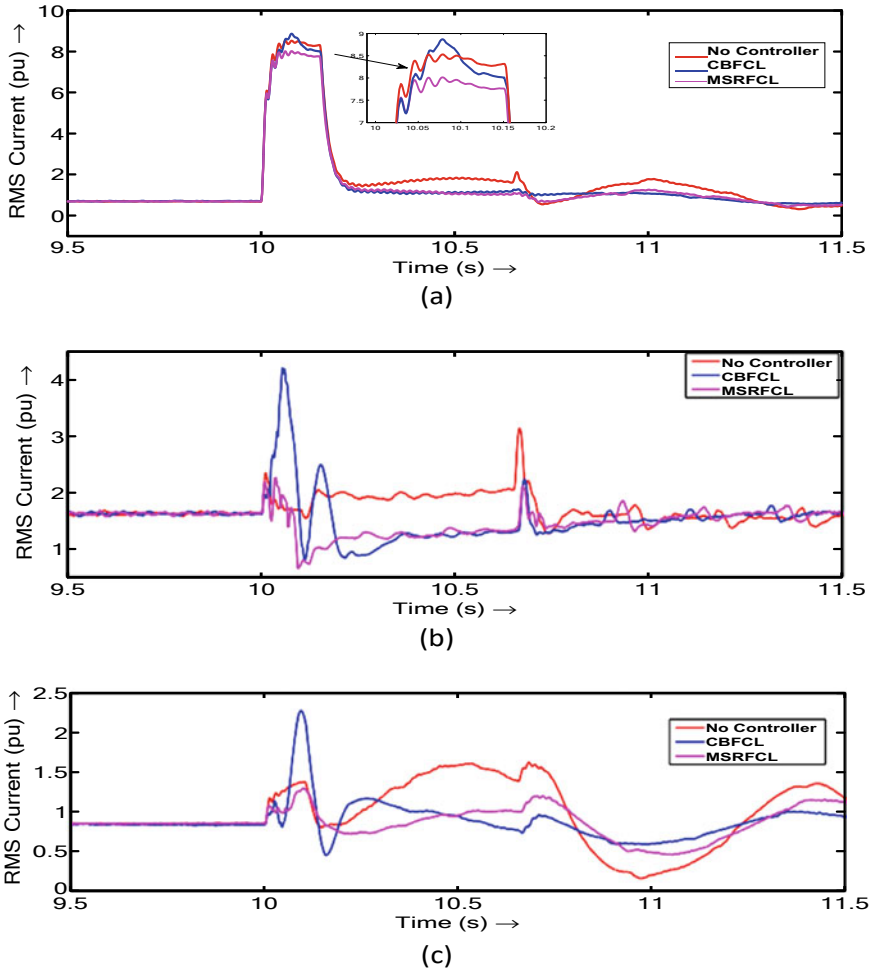


Fig. 7 RMS current at generator buses for 3L-G fault a Bus #1; b bus #2; c bus #3

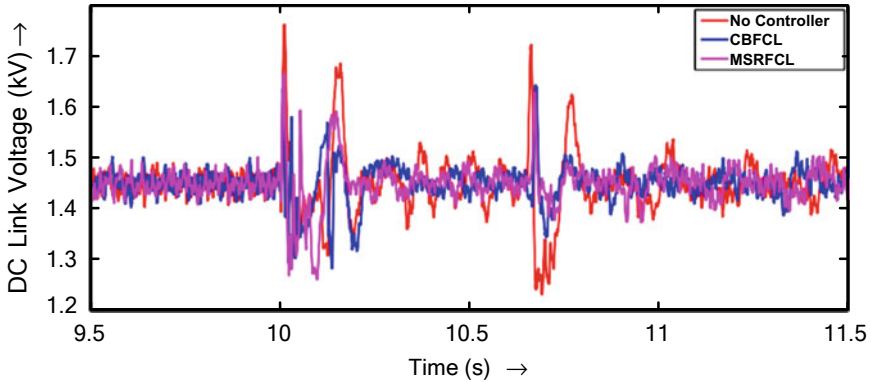


Fig. 8 DC link voltage response for 3L-G fault at bus #5

7 Results Comparison for 3L-G Fault at Bus #5 in Multi-machine Power System

The following tables show the comparison of all the performance indicators for the fault duration (150 ms) of all FCLs used for the 3L-G fault at bus #5, and boldface letters indicate the superior performance among the parameters. The MSRFCL proves its superior performance on all parameters besides slightly lower reactive power. The latter is compensated in terms of the narrow band of voltage variations at all the system buses during fault (Tables 1, 2 and 3).

Table 1 Comparison of performance parameters at bus #1

Type of fault current limiter	V_1 (RMS) pu	P_1 (Range) pu	Q_1 (Peak) pu	I_1 (Peak) pu
No controller	0.89	-0.51 to 2.26	7.63	8.52
CBFCL	0.89	-0.21 to 2.29	7.89	8.86
MSRFCL	0.90	0.37-2.26	7.18	8.01

The bold face letters indicate the superior performance among the parameters for various FCLs

Table 2 Comparison of performance parameters at bus #2

Type of fault current limiter	V_3 (RMS) pu	P_3 (Range) pu	Q_3 (Peak) pu	I_3 (Peak) pu
No controller	0.39	0.58 to 2.02	0.55	3.10
CBFCL	0.68	-0.04 to 2.78	1.70	4.13
MSRFCL	0.84	0.65-1.77	0.74	2.24

The bold face letters indicate the superior performance among the parameters for various FCLs

Table 3 Comparison of performance parameters at bus #3

Type of fault current limiter	V_3 (RMS) pu	P_3 (Range) pu	Q_3 (Peak) pu	I_3 (Peak) pu
No controller	0.70	0–1.56	0.83	1.61
CBFCL	0.49	0.1–1.22	0.91	2.26
MSRFCL	0.86	0.46–1.24	0.43	1.29

The bold face letters indicate the superior performance among the parameters for various FCLs

8 Conclusion

The research literature available so far offers LVRT performance improvement by various types of FCLs on the SMIB. In this paper, the performance of MSRFCL is compared with that of CBFCL and the case where no controllers are used in the multi-machine power system using PSCAD/EMTDC for system-level symmetrical fault at a weak bus. The following are the noteworthy points derived from the simulation results.

1. The MSRFCL enhances the transient stability of a multi-machine power system having DFIG-based wind farm. It is also feasible to introduce such FCL in the existing power system for LVRT improvement.
2. Insertion of an inductor in series with resistance–capacitor in the MSRFCL, the oscillations in RMS current are reduced as evident from the results. Also, the oscillations in voltage and active power are reduced and the system stabilizes faster as compared to the case with CBFCL.
3. The effect on the other synchronous generators connected at bus #1 and bus #3. From the simulation results, it is observed that the performance of synchronous generator connected at bus #3 is improved with the MSRFCL as compared to CBFCL. Naturally, the effects were not expected for swing generator #1.

References

1. Hiremath R, Moger T (2020) Comprehensive review on low voltage ride through capability of wind turbine generators. *Int Trans Electr Energy Syst* 30:1–39. <https://doi.org/10.1002/2050-7038.12524>
2. Rashid G, Ali MH (2017) Nonlinear control-based modified BFCL for LVRT capacity enhancement of DFIG-based wind farm. *IEEE Trans Energy Convers* 32:284–295. <https://doi.org/10.1109/TEC.2016.2603967>
3. Hossain MK, Ali MH (2016) Transient stability augmentation of PV/DFIG/SG-based hybrid power system by parallel-resonance bridge fault current limiter. *Electr Power Syst Res* 130:89–102. <https://doi.org/10.1016/j.epsr.2015.08.016>
4. Benali A, Khiat M, Allaoui T, Dena M (2018) Power Quality Improvement and low voltage ride through capability in hybrid wind-PV farms grid-connected using dynamic voltage restorer. *IEEE Access* 6:68634–68648. <https://doi.org/10.1109/ACCESS.2018.2878493>

5. Firouzi M, Gharehpetian GB (2018) LVRT performance enhancement of DFIG-based wind farms by capacitive bridge-type fault current limiter. *IEEE Trans Sustain Energy* 9:1118–1125. <https://doi.org/10.1109/TSTE.2017.2771321>
6. Zhou L, Liu J, Zhou S (2015) Improved demagnetization control of a doubly-fed induction generator under balanced grid fault. *IEEE Trans Power Electron* 30:6695–6705. <https://doi.org/10.1109/TPEL.2014.2382603>
7. Zhu R, Chen Z, Wu X, Deng F (2015) Virtual damping flux-based LVRT control for DFIG-based wind turbine. *IEEE Trans Energy Convers* 30:714–725. <https://doi.org/10.1109/TEC.2014.2385966>
8. Liu X, Han Y, Wang C (2017) Second-order sliding mode control for power optimisation of DFIG-based variable speed wind turbine. *IET Renew Power Gener* 11:408–418. <https://doi.org/10.1049/iet-rpg.2015.0403>
9. Jerin ARA, Kaliannan P, Subramaniam U (2018) Testing of low-voltage ride through capability compliance of wind turbines—a review. *Int J Ambient Energy* 39:891–897. <https://doi.org/10.1080/01430750.2017.1340337>
10. Pannell G, Atkinson DJ, Zahawi B (2010) Minimum-threshold crowbar for a fault-ride-through grid-code-compliant DFIG wind turbine. *IEEE Trans Energy Convers* 25:750–759. <https://doi.org/10.1109/TEC.2010.2046492>
11. Ashok Kumar L, Indragandhi V (2020) Power quality improvement of grid-connected wind energy system using facts devices. *Int J Ambient Energy* 41:631–640. <https://doi.org/10.1080/01430750.2018.1484801>
12. Firouzi M, Gharehpetian GB, Mozafari SB (2017) Application of UIPC to improve power system stability and LVRT capability of SCIG-based wind farms. *IET Gener Transm Distrib*. <https://doi.org/10.1049/iet-gtd.2016.1758>
13. Yao J, Li H, Chen Z et al (2013) Enhanced control of a DFIG-based wind-power generation system with series grid-side converter under unbalanced grid voltage conditions. *IEEE Trans Power Electron* 28:3167–3181. <https://doi.org/10.1109/TPEL.2012.2219884>
14. Okedu KE, Muyeen SM, Takahashi R, Tamura J (2012) Wind farms fault ride through using DFIG with new protection scheme. *IEEE Trans Sustain Energy* 3:242–254. <https://doi.org/10.1109/TSTE.2011.2175756>
15. Hossain ME (2017) Performance analysis of diode-bridge-type non-superconducting fault current limiter in improving transient stability of DFIG based variable speed wind generator. *Electr Power Syst Res* 143:782–793. <https://doi.org/10.1016/j.epsr.2016.09.020>
16. Rashid G, Ali MH (2015) Transient stability enhancement of doubly fed induction machine-based wind generator by bridge-type fault current limiter. *IEEE Trans Energy Convers* 30:939–947. <https://doi.org/10.1109/TEC.2015.2400220>
17. Shahbabaee Kartijkolaie H, Radmehr M, Firouzi M (2018) LVRT capability enhancement of DFIG-based wind farms by using capacitive DC reactor-type fault current limiter. *Int J Electr Power Energy Syst* 102:287–295. <https://doi.org/10.1016/j.ijepes.2018.04.031>
18. Hagh MT, Naderi SB, Jafari M (2010) New resonance type fault current limiter. In: 2010 IEEE international conference on power and energy, pp 507–511. <https://doi.org/10.1109/PECON.2010.5697635>
19. Sirisha ANRL, Pradhan AK (2017) Parameter estimation of resonant fault current limiter for protection and stability analysis. *IEEE Trans Power Syst* 32:2288–2295. <https://doi.org/10.1109/TPWRS.2016.2608904>
20. Mehta CR, Vora SC (2020) Transient stability enhancement of multi-machine hybrid power system employing modified series resonance type fault current limiter. *Int J Emerg Technol* 11:858–866
21. Morren J, de Haan SWH (2007) Short-circuit current of wind turbines with doubly fed induction generator. *IEEE Trans Energy Convers* 22:174–180. <https://doi.org/10.1109/TEC.2006.889615>
22. Anderson PM, Fouad AA (2002) *Power system control and stability*, 2nd edn. <https://doi.org/10.1109/9780470545577>.
23. Kundur PS (2006) *Power system stability and control*, 2nd edn, McGraw Hill

24. Mehta CR, Nathani BD, Deshpande PD, Vora SC (2019) Effects of fault current limiters in transient stability performance of hybrid wind farm. *Int J Eng Adv Technol* 9:2768–2775. <https://doi.org/10.35940/ijeat.b2277.129219>
25. Mehta CR, Shah YS, Vora SC (2020) Performance analysis of fault current limiters for low voltage ride through improvement of DFIG based wind farms. In: 2020 21st National power systems conference NPSC 2020, pp 3–8. <https://doi.org/10.1109/NPSC49263.2020.9331863>
26. Sauer PW, Pai MA, Chow JH (2017) *Power system dynamics and stability: with synchro phasor measurement and power system toolbox 2e*. <https://doi.org/10.1002/9781119355755>

Comparative Analysis of Electromagnetic Forces on Two Different Structures of Sen Transformer



Dhrupa Patel  and Anandita Chowdhury 

Abstract The Sen Transformer (ST) has been introduced as a smart power flow controller as it controls active and reactive power independently, which is equivalent to UPFC. The utilization of ST is not only limited to transmission lines but has expanded into distribution lines also. Many problems, like voltage sag, voltage swell, and voltage flickering, can be mitigated by ST. In the distribution line, the Sen Transformer also controls active and reactive power flow. To operate ST in the real power system, it is advisable to perform several tests on that motivate to analyze electromagnetic forces on the ST structure, as taps of ST change rapidly for impedance regulation. In the proposed work, two different structures of ST, one is simple ST, and another is magnetic equivalent circuit-based (MEC) ST, have been designed in ANSYS. The electromagnetic forces that occur in the ST windings were calculated using finite element analysis. The demonstrated results are with three different conditions: (1) steady state current (SSC), (2) inrush current (IC), and (3) short-circuit current (SCI).

Keywords Distribution line · Electromagnetic forces · Finite element method · Magnetic equivalent circuit · Sen Transformer

1 Introduction

Dr. Kalyan Sen invented the Sen Transformer in 2003 to control active and reactive power separately [1]. The ST has unique capabilities as a power flow regulating transformer in which time tested components are used like on-load tap changers. Impedance regulation is the most cost-effective architecture for controlling active and reactive power separately [2]. The Sen Transformer has the ability like smart

D. Patel (✉) · A. Chowdhury
Sardar Vallabhbhai National Institute of Technology, Surat, India
e-mail: d17el002@eed.svnit.ac.in

A. Chowdhury
e-mail: ac@eed.svnit.ac.in

power flow controller. The power grid needs line impedance regulation and phase angle regulation in the smart power flow controller [3].

The influence of ST on the real-world power system must be investigated, which encourages developing a nonlinear electromagnetic transient model for comprehensive analysis. The geometry-based magnetic equivalent circuit (MEC) approach is utilized to model multi-winding transformers, which include permeance elements, magnetomotive force (MMF), and flux path [4]. As the ST regulates active and reactive power selectively by changing load tap changers in an AC transmission line, the tap changing algorithm has been developed in [5]. In that, FORTRAN code is used to interface with the ST PSCAD/EMTDC software model to change the position of the specific compensating voltage and its phase angle. In [6], detailed transient model of ST has been developed with salient features, i.e., the effect of mutual coupling in ST secondary windings has been ignored to make it more simple and realistic, so that nonlinear characteristics are also ignored.

When current passes through the transformer windings, electromagnetic forces are produced due to interactions between the current flowing through it and leakage flux. In abnormal conditions like inrush current or short-circuit current, transformer winding may deform, displace, or rupture, resulting in substantial mechanical changes arising in the assembly of the transformer. As a result, the winding problems indicated in [7] have an impact on the characterization of power transformer electromagnetic forces. Sometimes, multiple short circuits can happen in the real power system; thus, the cumulative impact of numerous short circuits may change the winding structure. In [8], research on the winding displacement has been studied on transformer windings due to multiple short circuits. In [9], the electromagnetic forces on the power transformer were predicted using the 3D finite element approach in a single line-to-earth fault condition with the magnetic flux density analysis and magnetic vector potential. The axial and radial forces have been computed in the transient state with good agreement results of numerical and analytic values. Authors in [10] describe the evolution technique of electromagnetic forces on a medium-frequency transformer in detail, taking into account different fault scenarios such as magnetic inrush current (MIC) and magnetic short-circuit current (MSC). The problem of excessive electromagnetic force generated by the MIC and MSC will be solved to a great extent by using the appropriate interleaved winding. Authors in [11] propose that for the safe functioning of a power system, proper transformer design and study of short circuit stress on the high voltage winding is a significant matter, resulting in winding displacement in both vertical and horizontal directions. In various short circuit settings, the computation of radial electromagnetic forces produced in the low voltage windings of the power transformer has been investigated, leading to the conclusion of the ability to withstand short-circuit current given in [12].

In the present work, two different structures of Sen Transformer, i.e., simple ST and MEC-based ST, have been designed in ANSYS Maxwell to perform FEM analysis. The analysis of electromagnetic forces in various conditions like steady-state current, inrush current, and short-circuit current is described. To regulate voltage and impedance rapidly for controlling active and reactive power, ST must have the

capability to perform satisfactory operations in all abnormal conditions of the power system.

2 Sen Transformer

The Sen Transformer is proved as a smart power flow controller so that to place it in the real power system, its operations in all normal and abnormal conditions have been checked and observed. Thus, ANSYS Maxwell is used to design and analyze ST performance and reliability of its structure. Basically, the “Sen” transformer (ST) is a single-core, multi-winding, three-phase transformer consisting of two units; one is an exciter unit, and the other one is a compensating-voltage unit. The exciter unit has three-phase star connected windings, and the compensating unit has nine windings, which can be connected as shown in Fig. 1. On the first, second, and third limbs of ST, a_1 - a_2 - a_3 , b_1 - b_2 - b_3 , and c_1 - c_2 - c_3 windings are mounted, respectively, which inject compensating voltage. In ST, the in-phase component of the winding injects voltage in series to increase the line voltage magnitude, and the out-of phase component of the windings reduces the line voltage magnitude of the transmission line. Tap changers can vary the magnitude and angle. The combinations of different windings are performed in specific roles to insert inductive or capacitive effects in the transmission or distribution lines to regulate the impedance of the line. The basic model of the Sen Transformer is shown in Fig. 1.

In the proposed work, two different structures have been designed in ANSYS Maxwell 3D; one is the basic model of ST, which is mentioned as a simple ST. The other is magnetic equivalent circuit-based ST, which is mentioned with MEC-based ST.

3 Electromagnetic Force

When a current-carrying conductor of transformer windings is put in a magnetic field, electromagnetic forces are exerted due to the interaction of the magnetic field and electric current. As shown in the equation below, the electromagnetic force is determined by taking the vector product of current density and magnetic field density.

$$F = J \times B \tag{1}$$

Where

F force in Newton (N)

J current density in A/m^2

B magnetic flux density in Tesla (T)

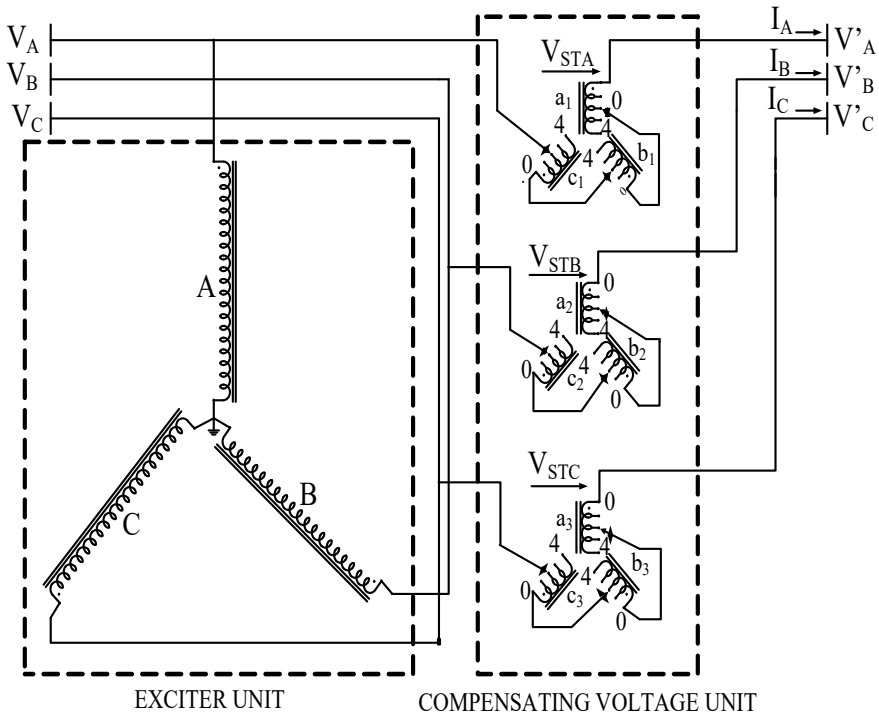


Fig. 1 Basic model of SEN transformer

Two components exist in the magnetic field vector: the radial and axial components, leading to the resultant electromagnetic force.

3.1 Axial Force

$$F_a = J_a \times B_r \tag{2}$$

The axial force results from the interaction between the radial components of magnetic flux and current density. An axial force is produced when magnetic field lines are radially oriented in the transformer, and it is parallel with the winding height. The distribution of flux lines in such a way that transformer windings experience opposite forces at the winding ends. The axial forces at the top and bottom winding ends are in opposite directions; as a result, in the axial direction, the conductor tends to bend and act on the coil clamping ring and other clamping structures. Both radial and axial forces result in failure of the insulator, leading to arc formation and dielectric breakdown.

The calculation of radial and axial forces is as follows in 3D FEM analysis. Radial force is exerted in the x-direction while axial force is exerted in the z-direction.

$$F_x = \iint (J \times B_z) \bullet h \bullet dx \bullet dz \quad (3)$$

$$F_z = \iint (J \times B_x) \bullet h \bullet dx \bullet dz \quad (4)$$

At the mean diameter of the transformer limb, the mean radial flux density and the radial force are given by,

$$B_r = 4\pi \times 10^{-7} \frac{a(NI)}{2l_{eff}} \text{ (T)} \quad (5)$$

$$F_r = \frac{2\pi(NI)^2}{h} D_m \times 10^{-7} \text{ (N)} \quad (6)$$

The mean axial force density and axial force are given by,

$$B_a = \frac{4\pi(NI)}{10^4} \text{ (T)} \quad (7)$$

$$F_a = \frac{2\pi a(NI)^2}{l_{eff}} \pi D_m \times 10^{-7} \text{ (N)} \quad (8)$$

where

- h height of the winding (mm)
- D_m mean diameter of the transformer limb (mm)
- l_{eff} effective length of the radial flux (mm)
- l_{eff} 0.222 h
- a fractional differences in winding heights.

3.2 Radial Force

$$F_r = J_r \times B_a \quad (9)$$

The interaction of the axial components of magnetic flux with the current density produces the radial force. It generates mutual repulsion between primary and secondary windings. The flux at mid-winding height is, for the most part, parallel to the winding height. The inner winding is subjected to compressive stress, whereas the outer winding is subjected to tensile tension. The radial force has been evenly distributed across the entire winding region; however, windings at the two ends are weaker. The forces in the inner and outer windings are in opposite directions.

4 Simulations

To analyze the performance of both structures of ST, i.e., simple ST and MEC-based ST, ANSYS Maxwell is used to simulate the model with different winding arrangements. The effect of inrush current and short-circuit current has been illustrated, and electromagnetic force and flux distribution are demonstrated.

A 25 KVA, 11/11 kV, three-phase, core type ST is modelled of both the structure to carry out results. The installation purpose of ST is on the distribution side to regulate impedance and voltage for power flow control and mitigation of voltage fluctuation. For that dimension of ST has been calculated, and based on that, it is modelled using specified data as per Table 1. To regulate the voltage and impedance of line, a continuous change of ST taps has been operated; as a result, the current flowing in the ST windings also changes rapidly. The effect of this phenomenon is reflected in the ST structure as inrush current flows in the windings also continuously change. Sometimes, due to the rapid change in taps of ST, two or more turns may short circuit; as a result, heavy short-circuit current will flow. In that event, the investigation of the electromagnetic force is needed.

In the simple ST, the arrangement of windings is such that of the normal power or distribution transformer, i.e., inner side exciting winding and outer side compensating windings are placed. To design the simple ST, ample data is required to get a precise result, whereas, in MEC-based ST, normalized core parameters are used as it requires less physical data. Hence, the calculation of the dimensions of ST has been found to be easier in MEC-based ST. The two different windings of ST, i.e., exciting winding and compensating winding, are mounted vertically, as shown in Fig. 2. Different tap arrangements are specified on the compensating winding, which has been operated to regulate the voltage or impedance of the line, as mentioned earlier. As a result, the effect of inrush and short-circuit current has to be taken into account. In ANSYS Maxwell, both structures of ST are modeled, and different excitation values have

Table 1 Specification of ST

Quantity	Value (unit)
Rated power	25 KVA
Rated current	1.25 A
Rated frequency	50 Hz
Rated voltage (exciting winding)	11 KV
Rated voltage (compensating winding)	11 KV
Numbers of turns	110
Winding material	Copper
Core material	M125_27
Lamination thickness	0.33 mm
Quantity	Value (unit)
Rated power	25 KVA

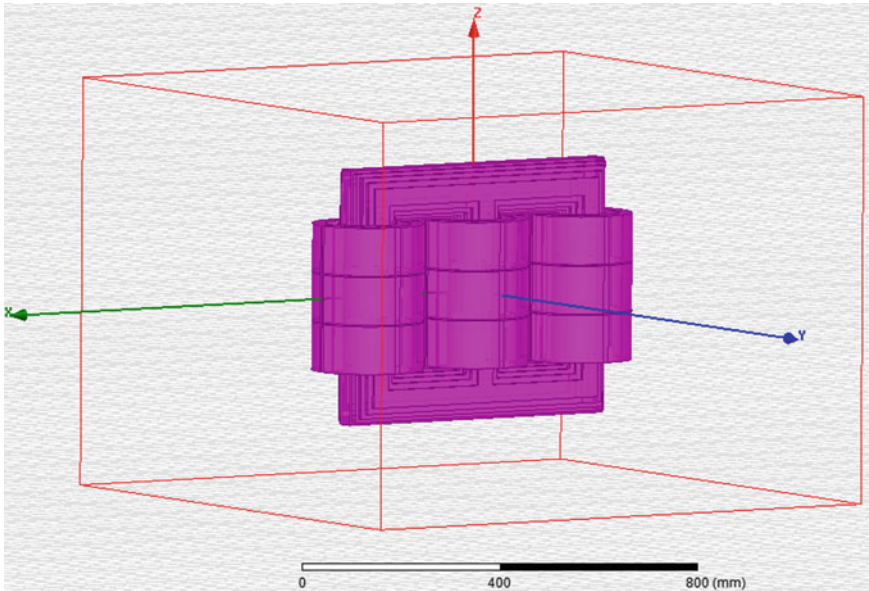


Fig. 2 3D model of simple ST

been assigned by calculating SSC, IC, and SCC. Hence, electromagnetic forces are produced accordingly. The specification of the ST model is tabulated in Table 1.

The 3D model of simple ST is illustrated in Fig. 2, in which exciting windings are placed nearer to the core and compensating windings are wound over the exciting windings. In Fig. 3, mesh plot of the simple structure of ST has been shown. It is mentioned over here that more numbers of mesh elements are given more accurate results.

Figure 4 describes the deviation of electromagnetic force along with the winding height in simple ST. (a) axial force under SSC, (b) radial force under SSC, (c) axial force under IC, (d) radial force under IC, (e) axial force under SCC, and (f) radial force under SCC. In which from Fig. 4a, b, it is observed that axial force is maximum at the top and bottom of the windings, whereas the radial force is maximum at the middle part of the windings; hence, the value of the exerted forces are less due to the steady-state current. Besides, in Fig. 4c, d, the value of axial force and radial force is ten times higher due to inrush current than the steady-state current. The reason for behaving that way is that the inrush current value is much higher than the steady-state current for a while. Figure 4e, f show the exerted axial and radial electromagnetic forces, respectively, whose magnitude increases drastically up to 500–1000 times due to heavy short-circuit current flow through the ST windings.

The ANSYS Maxwell FEM results of simple ST show that the short-circuit current is more critical to failure or damage of the windings compared with the inrush current; hence, suitable clamping and robust structure can reduce the electromagnetic forces and failure of the ST windings.

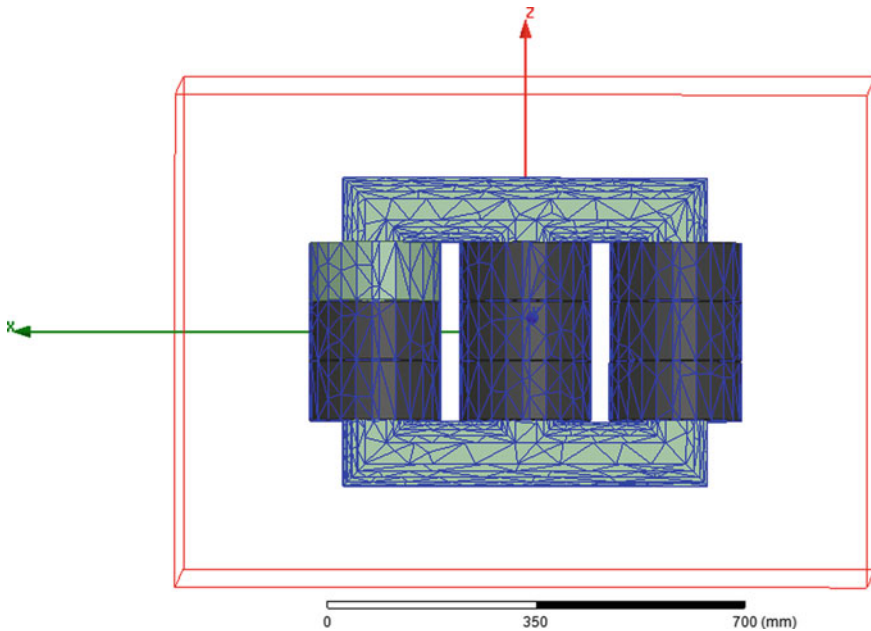


Fig. 3 Mesh plot in 3D model of simple ST

The 3D model of MEC-based ST is illustrated in Fig. 5, in which exciting windings are placed on the upper side of the core and compensating windings are wound on the lower side of the core. In Fig. 6, the mesh plot of the MEC-based ST has been shown. It is mentioned over here that more numbers of mesh elements are given more accurate results.

Figure 7 describes the deviation of electromagnetic force along with the winding height in MEC-based ST. (a) axial force under SSC, (b) radial force under SSC, (c) axial force under IC, (d) radial force under IC, (e) axial force under SCC, and (f) radial force under SCC. In which from Fig. 7a, b, it is observed that axial force is maximum at the top and bottom of the windings, whereas the radial force is varied over the height of the windings; hence, the value of the exerted forces are less due to the steady-state current.

Besides, in Fig. 7c, d, the value of axial force and radial force is ten times higher due to inrush current than the steady-state current. The reason for behaving that way is that the inrush current value is much higher than the steady-state current for a while. Figure 7 e, f show the exerted axial and radial electromagnetic forces, respectively, whose magnitude increases drastically up to 500–1000 times due to heavy short-circuit current flow through the ST windings. It is noted here that radial force is not maximum at the middle of the winding, but it is maximum at only one point of the winding, which is a better result than the simple ST.

In the simple structure of ST, the amount of axial and radial electromagnetic forces is very high as compared to the MEC-based structure of ST, which is tabulated in

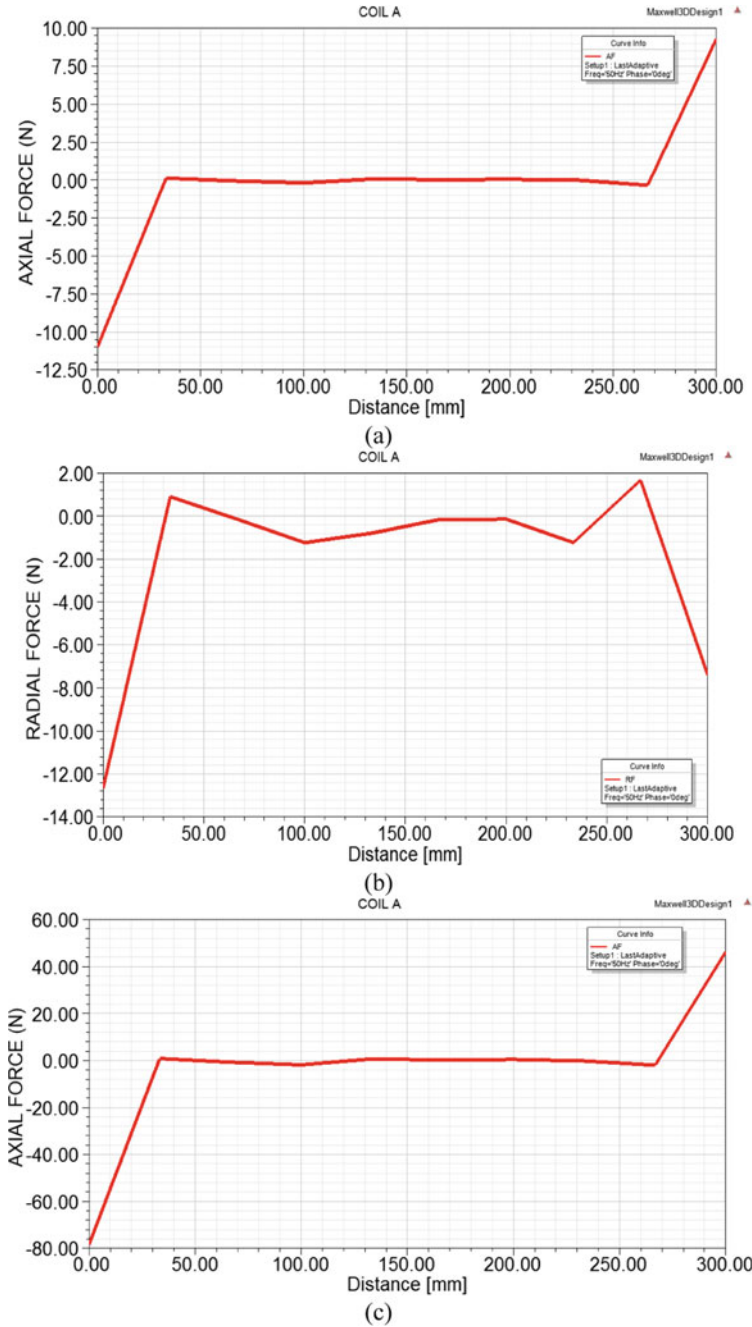
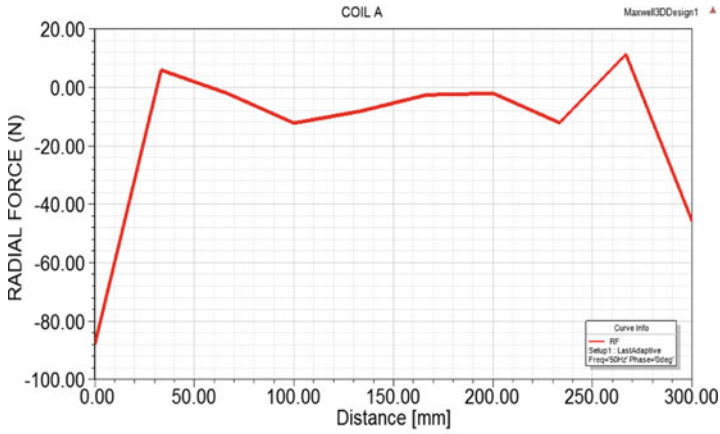
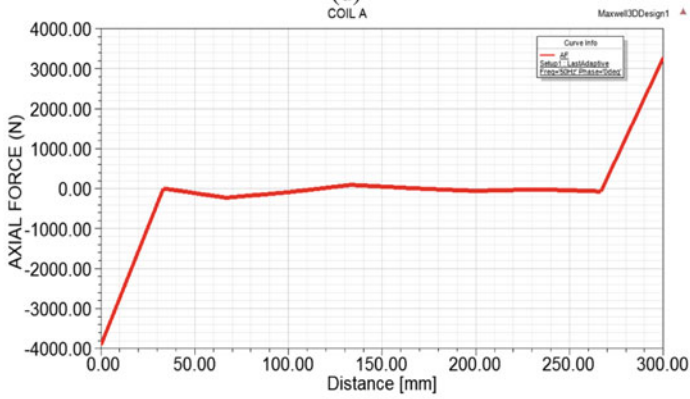


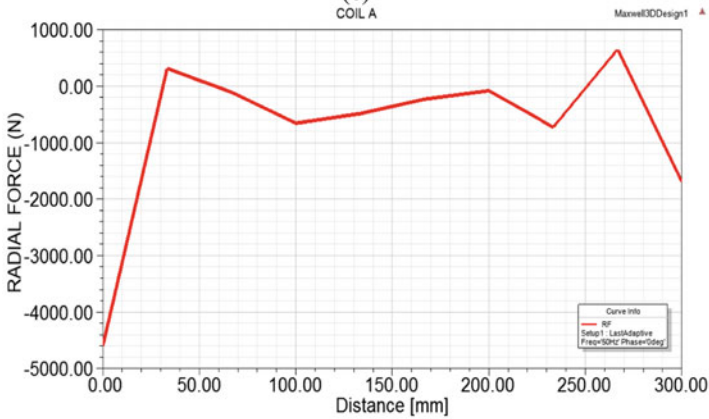
Fig. 4 Deviation of electromagnetic forces along the winding height in simple ST. **a** axial force under SSC, **b** radial force under SSC, **c** axial force under IC, **d** radial force under IC, **e** axial force under SCC, **f** radial force under SCC



(d)



(e)



(f)

Fig. 4 (continued)

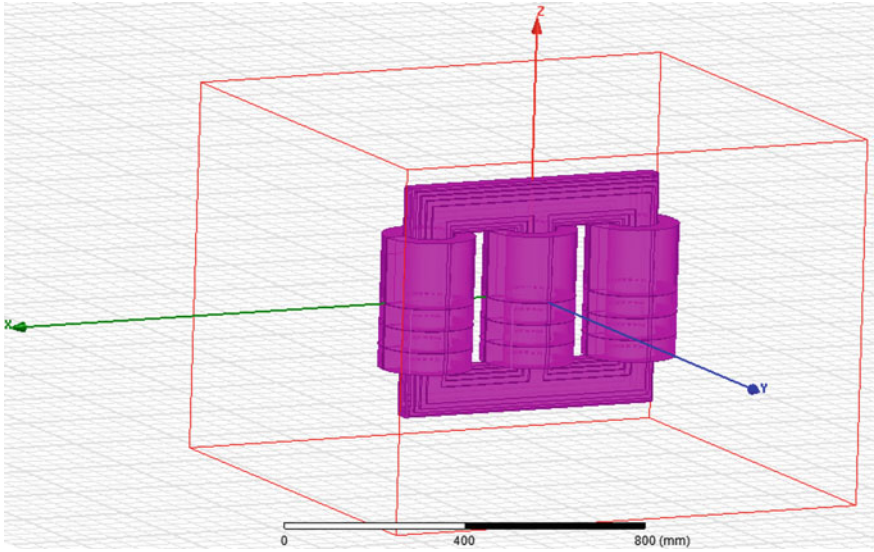


Fig. 5 3D model of MEC based ST

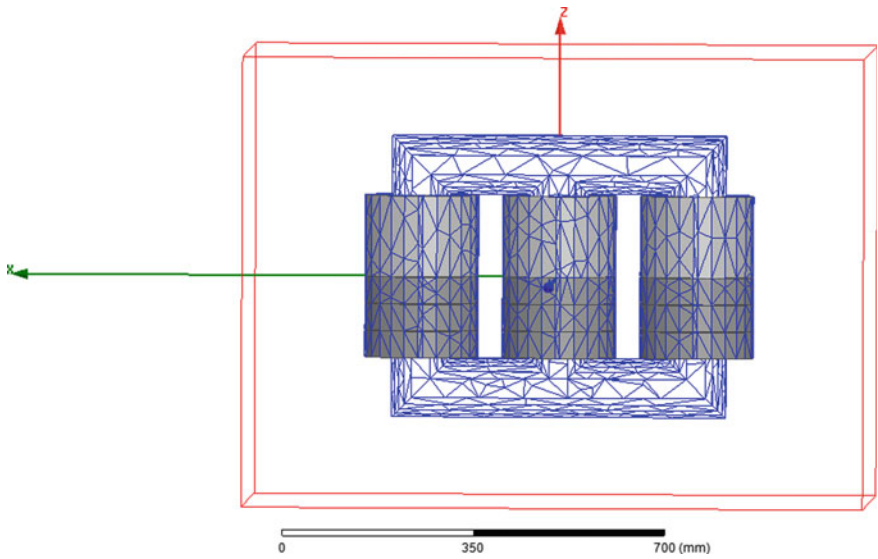


Fig. 6 Mesh plot in 3D model of MEC based ST

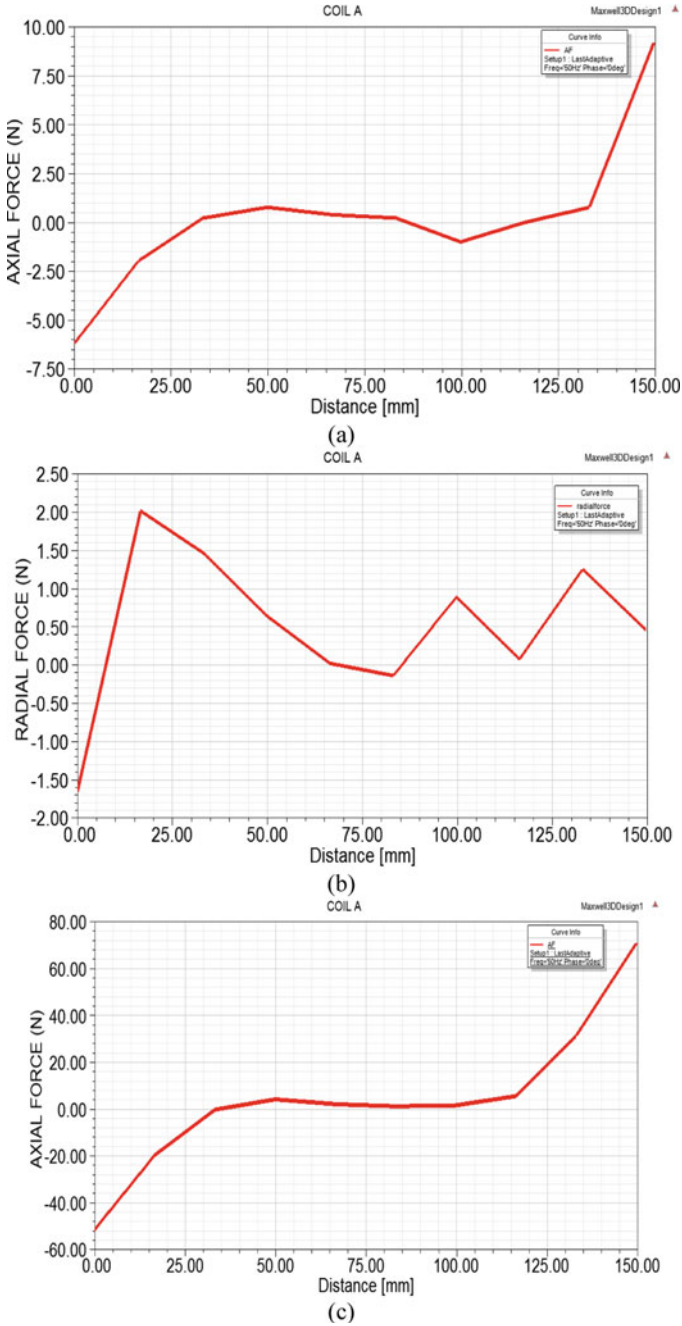
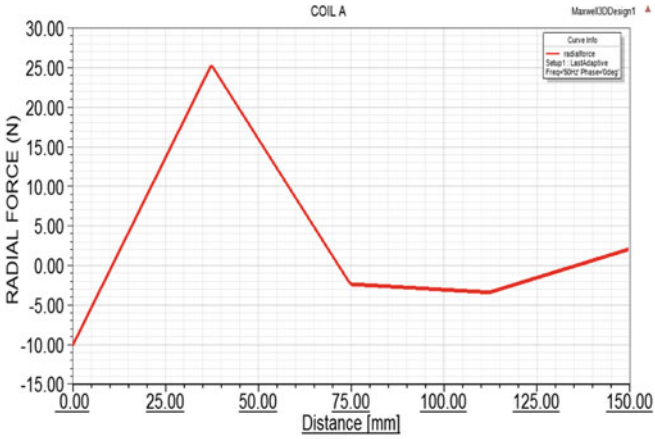
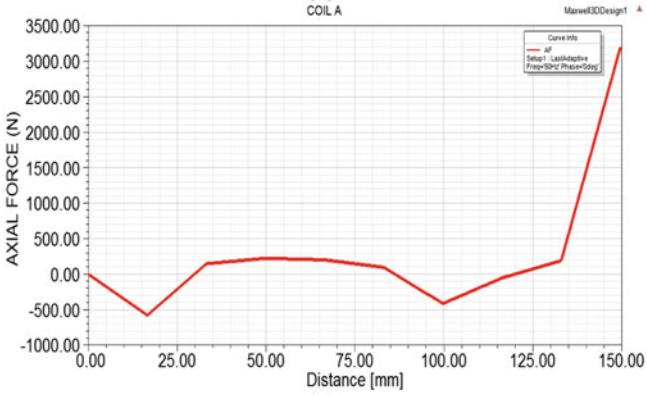


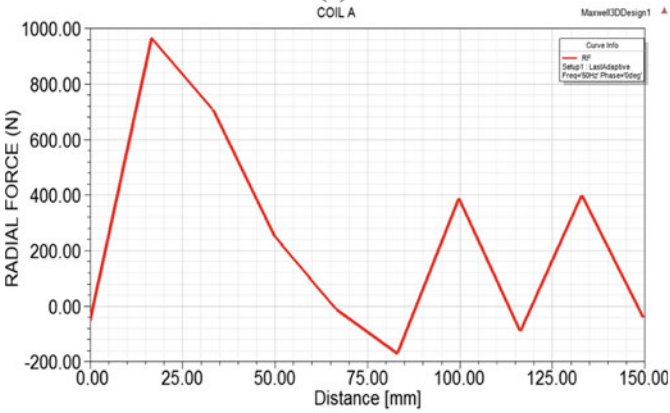
Fig. 7 Deviation of electromagnetic forces along the winding height in MEC-based ST. **a** axial force under SSC, **b** radial force under SSC, **c** axial force under IC, **d** radial force under IC, **e** axial force under SCC, **f** radial force under SCC



(d)



(e)



(f)

Fig. 7 (continued)

Table 2 Result of axial forces in simple ST

Distance (mm)	AF in (N) during SSC	AF in (N) during IC	AF in (N) during SCC
0	-11.03	-78.35	-3908.8
30	0.11	0.75	349
65	-0.06	-0.79	-230.19
100	-0.20	-1.89	-91.81
135	0.05	0.59	91.02
165	0.01	0.11	7.57
200	0.03	0.36	-59.44
230	-0.19	-0.25	-17.12
265	-0.352	-2.06	-73.17
300	9.29	46.17	3274.1

Tables 2 and 3. Whereas in MEC-based ST, the windings are mounted vertically, hence production or formation of ducting can be avoided, but due to axial force, deformation of windings may arise; as a result, the height of the winding may change. The results of electromagnetic forces are tabulated in Tables 4 and 5, for MEC-based ST, respectively. All the graph and tabulated results of both the structures are the winding height (i.e., distance) versus axial or radial force have been mentioned.

The electromagnetic force exerted in three different conditions (i) steady-state condition, (ii) inrush current condition (iii) short circuit condition are tabulated at the specific distance on the height of the winding. It is clearly observed that the magnitude of the force increases noticeably in inrush current and short-circuit conditions compared to MEC-based ST. In ST, due to frequent changes in taps, the value of inrush current is also seriously considered. For the satisfactory function of ST, MEC-based ST has been designed, and its structure will be developed more robust and used more numbers of clampers.

Table 3 Result of radial forces in simple ST

Distance (mm)	RF in (N) during SSC	RF in (N) during IC	RF in (N) during SCC
0	-12.66	-88.03	-4604.4
30	0.89	5.79	-306.34
65	-0.16	-2.23	-113.03
100	-1.25	-12.34	-661.56
135	-0.08	-8.29	-491.18
165	-0.17	-2.69	-237.40
200	-0.15	-2.16	-85.65
230	-1.25	-12.237	-731.76
265	1.67	11.15	645.75
300	-7.42	-45.96	-1701

Table 4 Result of axial forces in MEC based ST

Distance (mm)	AF in (N) during SSC	AF in (N) during IC	AF in (N) during SCC
0	-6	-51	0
15	-2	-19	-578
30	0.22	0	146
50	0.77	4	222
65	0.39	2	200
80	0.22	1	94
100	-0.99	1.5	-414
115	0.04	5.5	-53
130	0.7	31	188
150	9.16	70	3187

Table 5 Result of radial forces in MEC based ST

Distance (mm)	RF in (N) during SSC	RF in (N) during IC	RF in (N) during SCC
0	-1.64	-10	0
15	2.01	24	844
30	1.45	25	630
50	0.63	2.5	252
65	0.020	-0.9	32
80	-0.139	-2.68	-100
100	0.88	-2.01	365
115	0.075	4.6	-33
130	1.25	1.48	374
150	0.45	2.01	7

5 Conclusion

Investigations of electromagnetic forces are presented in this work. Here, two different structures of the Sen Transformer are designed in ANSYS Maxwell 3D. Electromagnetic forces in three different conditions, i.e., steady-state condition, inrush current condition, and short-circuit condition, has been investigated using the finite element method. It is observed that MEC-based ST's structure offers a lower amount of electromagnetic force with all three conditions. The MEC-based ST offers 40% less amount of electromagnetic force than simple ST. To regulate voltage and impedance of the transmission or distribution line, frequent tap changing occurs in ST. Due to that, high inrush current and sometimes short-circuit also may flow, which is an unavoidable process in the operation of ST. The purpose of the research work is to require a robust structure of ST to be manufactured to get long-lasting and satisfactory operation of ST. In MEC-based ST, windings are mounted vertically,

so the radial force will not create a duct between the windings, but axial force can deform the windings in the vertical direction. As a result, the structure has to be more accurately designed than an ordinary power or distribution transformer.

References

1. Sen KK, Sen ML (2003) Introducing the family of “Sen” transformers: a set of power flow controlling transformers. *IEEE Trans Power Delivery* 18(1):149–157
2. Sen KK, Sen ML (2016) Unique capabilities of Sen transformer: a power flow regulating transformer. In: 2016 IEEE power and energy society general meeting (PESGM), Boston, MA, 2016, pp 1–5
3. Sen KK, Sen ML (2015) SMART power flow controller for smarter grid applications. In: 2015 IEEE power & energy society general meeting, Denver, CO, 2015, pp 1–5
4. Liu J, Dinavahi V (2017) Nonlinear magnetic equivalent circuit-based real-time sen transformer electromagnetic transient model on FPGA for HIL emulation. In: 2017 IEEE power & energy society general meeting, Chicago, IL, pp1–1
5. Faruque MO, Dinavahi V (2007) A tap-changing algorithm for the implementation of “Sen” transformer. *IEEE Trans Power Delivery* 22(3):1750–1757
6. Asghari B, Faruque MO, Dinavahi V (2008) Detailed real-time transient model of the “Sen” transformer. *IEEE Trans Power Delivery* 23(3):1513–1521
7. Behjat V, Shams A, Tamjidi V (2018) Characterization of power transformer electromagnetic forces affected by winding faults. *J Oper Autom Power Eng* 6(1):40–49. <https://doi.org/10.22098/joape.2018.2436.1210>
8. Li HK (2013) Simulation of power transformer windings displacement caused by multiple short-circuit forces. *Appl Mech Mater* 268–270:1341–1344
9. Ahn H, Lee J, Kim J, Oh Y, Jung S, Hahn S (2011) Finite-element analysis of short-circuit electromagnetic force in power transformer. *IEEE Trans Ind Appl* 47(3):1267–1272
10. Huang P, Mao C, Wang D (2017) Analysis of electromagnetic force for medium frequency transformer with interleaved windings. *IET Gener Transm Distrib* 11. <https://doi.org/10.1049/iet-gtd.2016.1586>
11. Ahmad A, Javed I, Nazar W, Asim MM (2016) Short circuit stress analysis using FEM in power transformer on H-V winding displaced vertically & horizontally. *Alexandria Eng J* 57. <https://doi.org/10.1016/j.aej.2016.10.006>
12. Zheng HB et al (2013) Computation of radial electromagnetic forces on power transformer LV windings due to short-circuit currents. *Adv Mater Res* 732–733:1069–1073

Eunoia: A Website for Self-CBT and Psychotherapy



Dhruv Rastogi, Shubhangi Thakur, and Leena Singh

Abstract Cognitive behaviour therapy (CBT) is an effective treatment strategy for a variety of mental and emotional health disorders, such as anxiety and depression. CBT aims to assist you in recognising and challenging harmful ideas as well as learning practical self-help techniques. Internet technology is a viable addition to traditional therapy delivery because of its high penetration, capacity to gather and analyse data, and ability to engage with people. With the various CBT apps and websites, it is discovered that most of them required membership or hiring a therapist online in order to use CBT. They had resources added to them, but most of them lacked an appropriate structure or methodology. The objective of this paper is to achieve privacy, accessibility, and time-saving. In this paper, the online support for the delivery of Self-CBT is provided by a website called “Eunoia,” which gives numerous questionnaires to help patients identify difficult events or conditions in their lives, as well as worksheets and other resources such as chatbot for the patient’s therapy. This website focuses on interpersonal issues, emotional dysregulation, relationship issues, and workplace issues, and it can help in figuring out where the negative thoughts come from and how to utilise the worksheets as homework to work on emotions and thoughts. The questionnaire findings are calculated quite precisely. There is no correct answer in these questionnaires, thus the answer choice involves different points. Users of this Self-CBT website can complete their homework without the burden of lugging papers and worksheets around with them. Eunoia, the Self-CBT website, has yielded unexpected outcomes. Participants in this study went through stage 1 of Self-CBT, where they are required to complete questionnaires that assisted them in recognising their negative thoughts. They are quite pleased with the outcome.

D. Rastogi · S. Thakur · L. Singh (✉)
Amity School of Computer Science and Engineering, Amity University, Noida, Uttar Pradesh 201301, India
e-mail: lsingh1@amity.edu

D. Rastogi
e-mail: dhruv.rastogi1@s.amity.edu

S. Thakur
e-mail: shubhangi.thakur1@s.amity.edu

Keywords Self-CBT · Psychotherapy · Mental wellness · Cognitive behaviour therapy · Eunoia

1 Introduction

Cognitive therapy (CT), or cognitive behaviour therapy (CBT), was pioneered by Dr. Aaron T. Beck in the 1960s, while he was a psychiatrist at the University of Pennsylvania [1]. It seeks to understand the patient's ideas and behavioural patterns and to alter their underlying dysfunctional beliefs utilising a range of goal-oriented techniques. Patients with depression and anxiety disorders benefit the most from CBT compared to other methods of treatment. Face-to-face meetings with a therapist are at the heart of CBT, followed by homework assignments in which the patient implements CBT interventions prescribed by his therapist on his own. Patients perform their homework using pen and paper. This is inconvenient, and it may lead to a habit of procrastinating on the homework. The therapists, on the other hand, may find it tedious to go over homework worksheets in order to obtain the necessary information.

Internet technology is a viable addition to traditional therapy delivery because of its high penetration, capacity to gather and analyse data, and ability to engage with people. When patients are required to complete homework as part of their therapy, the enhanced interaction and degree of engagement that Internet give when compared to pen-and-paper is also essential. The Internet has enormous potential in areas such as health-related education and awareness, with the ability to reduce procedural costs and effort for both healthcare staff and patients. In 2009, the developing world accounted for 64% of all mobile phone users. The number of mobile phone subscriptions is expected to rise to around 7.3 billion in 2014, according to a study by the International Telecommunications Unit [2]. This encourages businesses and individuals to adopt mobile technologies in order to improve health and healthcare services [3]. The rise of mobile medical apps is one such example. Individuals can use mobile medical apps to manage their own health and wellness or gain access to useful information at any time [3]. According to reports, app usage increased by 40% during the pandemic, reaching an all-time high of more than 200 billion hours in April 2020. Despite the fact that this is a global trend, statistics in individual countries vary. In India, for example, time spent in apps increased by 35% from Q4 2019 to Q2 2020. Italy and Indonesia both experienced 30% and 25% growth, respectively. Time spent in apps increased by 15% in the United States. Consumers spent a record \$27 billion on apps in the second quarter, up to 15% year over year and up to 25% to \$10 billion on Android [4]. The use of homework, in which patients regularly practise strategies given by the therapist in face-to-face treatment sessions, is a crucial element in all CBT therapies. Patients are usually given worksheets and handouts to help them with their homework. Each face-to-face session begins with a review of past assignments and concludes with the assignment of new homework [5].

With the various CBT apps and websites, it is discovered that most of them required membership or hiring a therapist online in order to use CBT. They had

resources added to them, but most of them lacked an appropriate structure or methodology. To fill that void, we created a Self-CBT website. It includes surveys, a chatbot, worksheets, and a wealth of other resources to help patient get the most out of their therapy. It focuses on interpersonal issues, emotional dysregulation, relationship issues, and workplace issues, and it can help in figuring out where the negative thoughts come from and how to utilise the worksheets as homework to work on emotions and thoughts. These types of problems are common in the general public, which may make early testing and validation of any modifications easier. Patients can also use the website's chatbot to get answers to their health-related questions.

2 Literature Review

Earlier projects which come so close to achieving Self-CBT were CBT-I Coach [6] and CBT Assistant [7], although they lack in providing a full Self-CBT. CBT Assistant mentions homework delivery and activity tracking, which is a very efficient way to carry out homework, but to get the homework assigned and to sort out the negative thoughts, the patient still needs to see a therapist, which the patient can do on their own by filling out the questionnaires. These questionnaires are similar to those used by therapists. CBT-I Coach focuses on insomnia and does a good job of monitoring sleep and medications, but it lacks the patient's conversation and interaction, which is an important part of CBT and keeps the patient motivated; possible solutions could have included a chatbot or some resources to keep the patient motivated.

Similar models and mobile applications are previously discussed, which also focused on one specific mental illness rather than treating the negative thoughts that cause that illness, which is what CBT is all about. Jayachandran and Shyamala [8] discussed some previous apps, such as "Catch it," lacked systematic advancement while introducing their own effective algorithm. Alanzi et al. [9], proposed a model for diabetes CBT treatment; however, its algorithm felt more static. As with diabetes, people may have a higher rate even if they do not consume sugar from outside sources; in this case, the results are less accurate. Research by Fletcher et al. [10] introduces a method of performing CBT using sensors, which explains a very creative and effective method of performing CBT for drug addiction and PTSD. Researchers like Dino et al. [11] and Patel et al. [12] discussed the chatbots and their effectiveness in CBT. While it is true that chatbots do help a lot, a patient cannot completely rely on CBT on the chatbot. Mattila et al. [13] demonstrate the use and effectiveness of a mobile diary to record thoughts and reminders; it is an important step in CBT, but it is not complete. While, an interesting way to compute CBT results is applied in a research done by Hur et al. [14], which uses scenario-based mobile application to perform CBT.

3 Objectives

Current Self-CBT websites or applications lack of fully self-contained therapy. Homework completion is crucial step for this therapy, which is traditionally performed by pen-and-paper or in presence of the therapist. Not only is this inconvenient for the patients, but they may also consider it to be embarrassing to do in public. Smart gadgets, rather of continuously referring to and scribbling on their workbooks, would be far more practical and commonplace nowadays. Internet assistance can also make it easier for the therapist to analyse data obtained from the individual. Information gathered and outcomes are displayed in a much more appealing manner, reminders can be made, and reports can be examined by both patients and therapists. While this can be accomplished manually using existing pen-and-paper methods, it requires a significant amount of time and work. In this paper, Eunoia a Self-CBT website, is introduced to address issues mentioned above, resulting in increased privacy, dependability, accessibility, and proper time management.

4 Methodology and Features

CBT with a therapist is preceded by a series of questions designed to assist the patient get motivated to participate in therapy and recognise negative thoughts. The therapist then provides the patient worksheets to perform on their own based on the answers to those questions [1]. These worksheets are created in such a manner that it makes individuals understand and find out what is giving them problems, and once they realise it, they do the activities advised by the therapist. Users of this Self-CBT website can complete their homework without the burden of lugging papers and worksheets around with them. Their performance is seen using a variety of quizzes, and based on their results, they can complete their homework papers. Tons of audio files and lectures are added to the resources to keep them motivated. In the event that someone need assistance, a health bot is introduced to help with health-related issues and to recommend what the patient should do. While conversing with the bot, a to-do list option is also available, which is used to note down the activities assigned. There is also a filtered option to look for therapists nearby based on users' needs, which displays verified and attested services.

4.1 *Proceeding of Questionnaires and Evaluating the Results*

In Eunoia, there are six questionnaires. Each questionnaire provides a distinct purpose and assists the patient in identifying concerns. It is useful for both patients who want to do CBT on their own and patients who want to do it in the traditional way because it gives users an idea of what is wrong in their life and helps them identify negative

thoughts; it is completely up to them whether to continue it on their own or go see a therapist. The questionnaire findings are calculated quite precisely. There is no correct answer in these surveys, thus the answer choice involves different points. Depending on the number of possibilities, answer selections are marked with a 4-3-2-1-0 or 3-2-1-0 points pattern. The lower the point, the better is the mental health; high points indicate that users have major troubles and should visit a therapist; yet, in some questionnaires, high values indicate the contrary.

The results are calculated natively and provide patients with insight into their negative thoughts. Because there is no correct answer in this inquiry, each choice carries a different set of points. The lower the point, the better the users' performance and the fewer troubles users have. Except in the "Self-Compassion" and "Relationship Satisfaction" questionnaires, where the contrary is true: the bigger the number of points, the better users are doing and having fewer issues.

4.2 Resources and Worksheets

Homework is an essential part of cognitive behaviour therapy (CBT) and other evidence-based therapies for psychological disorders. Homework assignments, which are created collaboratively during therapy sessions, can be utilised by clients to practise new abilities, coping mechanisms, and modifying problematic beliefs. Homework in therapy research has yielded several significant findings that may be interpreted collectively using a technique known as meta-analysis. A meta-analysis is a statistically summarised summary of a corpus of research. It can be used to determine the average effect of psychotherapy homework on treatment results across multiple studies. The results of a meta-analysis listed below highlight the value of homework in therapy: results from 16 research and an updated analysis of 23 studies indicated that greater compliance linked to improved treatment outcomes among individuals who got homework assignments during therapy [15]. Depending on the method employed to quantify compliance, the effect sizes ranged from small to medium. Taken together, the evidence demonstrates that adding homework to psychotherapy improves its effectiveness and that clients who complete homework assignments on a frequent basis have better mental health results. Worksheets that patients can use to complete their homework are added and a few extra resources to keep the patients motivated and the therapy enjoyable.

4.3 Interactive Health Bot and To-Do List

An interactive health bot that can address health-related issues is also featured. This bot is created with the Azure Bot API and is hosted on Azure. The bot also responds to COVID-19-related difficulties, as the patient may be experiencing headaches because of COVID-19 rather than stress. Creation of bot and assignment of replies is done

using the Azure flow chart system. The Azure bot flow chart is simple to use and aids in the organisation of responses.

Figure 1 shows the conversation with the bot. In Fig. 1d, it can be seen that the bot asks for the patient's gender and age first, in order to offer the most precise and effective results. During the interaction, Fig. 1a the bot also asks the patient if they have been exposed to or have been in the presence of someone who has tested positive for COVID-19. The bot then continues the conversation by asking how the patient has been feeling recently Fig. 1c, and finally, the bot delivers a quick overview of the results and recommends the best care Fig. 1b.

A reminder or to-do list application is also included so that users can add tasks to it and be reminded of them anytime they enter the website. Because the data is now stored on the local device, the tasks does not disappear even if they reload the webpage. So they can see the reminders till and unless they open the page on another device. It is a very essential tool because many patients forget about their tasks and need to be reminded of them. As with Self-CBT, doing the assignments and tasks is an important and valuable component of the process.

5 Design and Implementation

5.1 Design

In this section, Eunoia is designed in a straightforward yet effective manner. All of the features are essential components of Self-CBT. On the homepage, a list of the various questionnaires that had to completed in order to begin the Self-CBT can be seen. Now, at the end of each questionnaire, results are given that gives an idea of what aspect of the lifestyle is causing to have negative thoughts. Following that, there are worksheets that can be completed on your own, as well as a plethora of resources to keep the motivation to continue with the therapy. While all of this self-work may appear to be exhausting, a chatbot is included to address the health concerns. A to-do list is also included to keep track of the activities that people enjoy doing.

5.2 Implementation

Eunoia has the questionnaires and a scoring system that evaluates what the negative thoughts might be, taking into account all of the other parameters. Each questionnaire has its own scoring system; there are no correct answers, only a constructive approach to the outcome. Then, we included worksheets and resources from various psychological health centres. Atom integrated development environment (IDE) and blocs are used to create the entire website. Then, after feeling compelled to add some

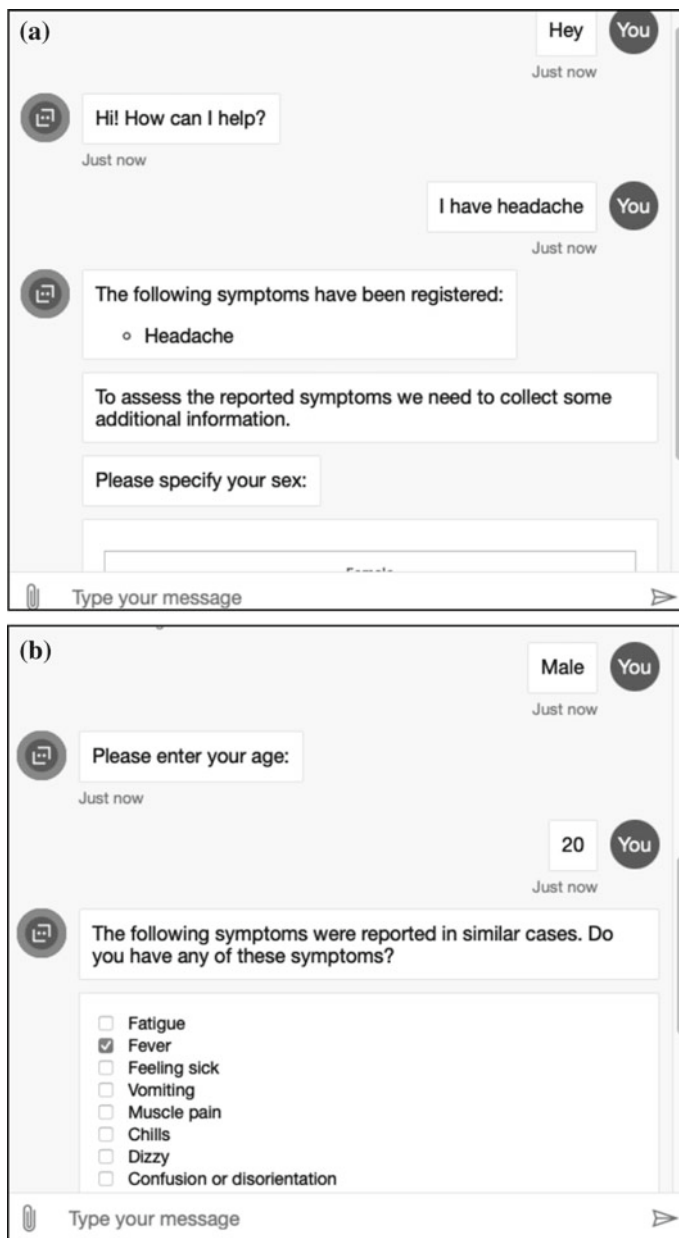


Fig. 1 a Intro with bot, b informing bot about the issue, c checking with the COVID-19 symptoms, d report generated by the bot

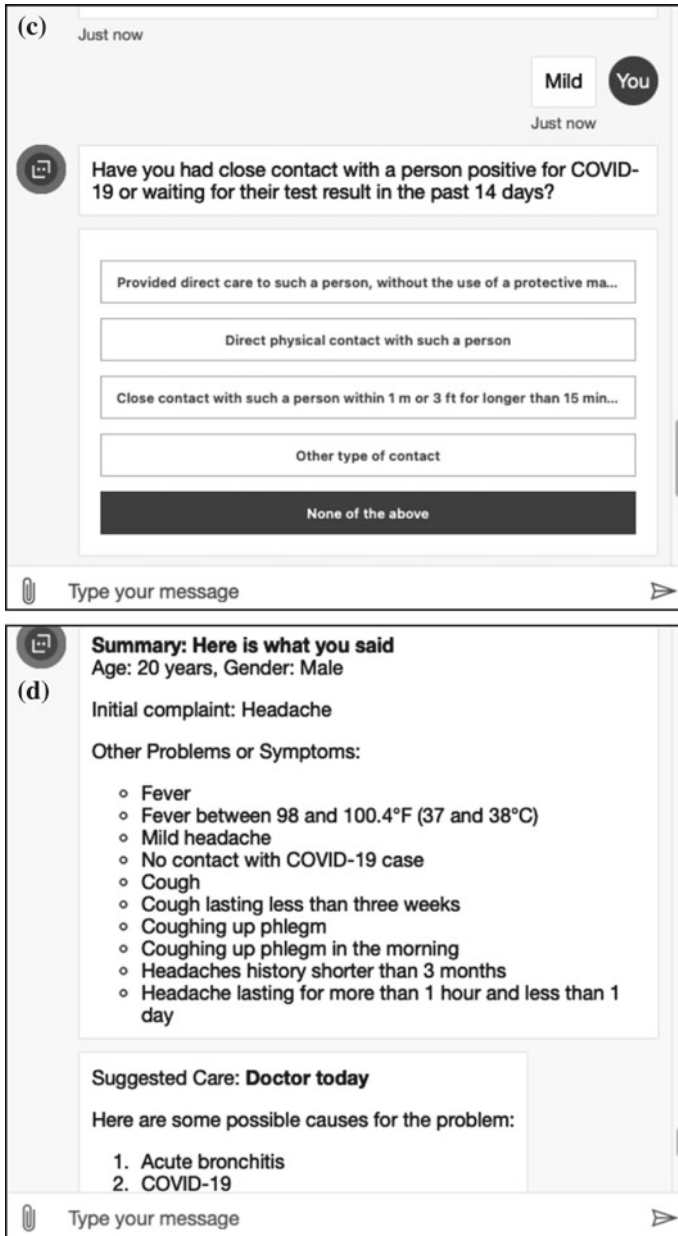


Fig. 1 (continued)

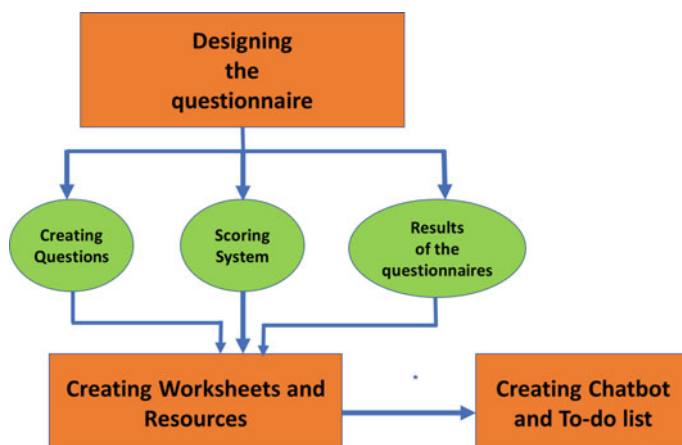


Fig. 2 Workflow of implementation

interactivity, a health chatbot using Microsoft Azure Health Chatbot, which is effective and can be integrated with a great deal of customisation is added. It has been customised and added to the website, along with a JavaScript to-do list application. The workflow of implementation is shown in Fig. 2.

6 Results

Eunoia, the Self-CBT website, has yielded unexpected outcomes. In stage 1 of Self-CBT, participants are required to complete questionnaires that assisted them in recognising their negative thoughts. Participants in this Self-CBT study went through stage 1 of CBT for Eunoia. They are quite pleased with the outcome. As shown Fig. 3, the participants represented a wide range of backgrounds. Almost all of them are inhabitants of other nations; 8% from India, Poland, Finland, Canada, Spain, 25% from United States of America and 33% from Germany (Fig. 3a) demonstrating Eunoia's global acceptance. The participants are likewise of a certain age; the majority are teenagers, but a few proportions comprised adults as well (Fig. 3b). Although the survey did not include participants of age older than 26, it can yield the same performance among them as well. This demonstrates that Self-CBT is applicable to all age groups and can be as effective as other treatments, regardless of the patient's age. The need for participants to be of different ages and from different regions is crucial. As there are certain traits or characteristics displayed by people from a specific age group or region, which could not have demonstrated how the Self-CBT is globally effective. Gender characteristics are also considered. The survey had 75% female respondents, 16.7% male respondents, and 8.3% gender-fluid respondents (Fig. 3c). Despite the fact that females outnumbered males, both genders were pleased with the

results. Some individuals completed many questionnaires, while others completed only one. The demographic data is depicted in Fig. 3.

Eunoia shows satisfactory results, with astounding ratings (Fig. 3d) by participants. Below are some of the reviews given by the participants:

1. It felt very simple and was easy to understand.
2. Great questionnaires and website! I would just suggest adding a timeframe to the questionnaires if possible. I liked how the questionnaire gave a score and explanation of the score at the end. Maybe there can be an option for the client to print this score and the questions and answers so they can discuss with their therapist?
3. The website is really pretty and clean, I love it. At the end of the relationship quiz, I reflected myself this really helped me.
4. The design and layout of the website was very pleasing to the eye, and it was very easy to navigate. Also, I was satisfied with the result of my questionnaire, for it really reflected who I am.

Figure 3e depicts the features of existing CBT apps, which include a plethora of options. Although having more features are always a plus, the sequence in which CBT is performed is not shown in all of those apps. CBT is carried out by analysing negative thoughts, and in Eunoia, it is carried out by questionnaires. Following that, the patient is required to reflect on their results and complete the worksheets provided by the therapist, which are also included in Eunoia, and a chatbot is available for additional assistance. This systematic procedure makes therapy execution easier for both the patient and the therapist.

7 Conclusion and Future Scope

The objective of research is achieved by following the successful completion of Stage 1 by number of participants. Users' data is kept private, and they believe the website is more trustworthy because it includes verified resources from around the world. Users perceived that they could perform CBT at any time, making it more accessible and time-saving. All of this adds up to achieving the research's goals.

CBT is the most effective therapy, which when done by your own makes it more effective. Traditional CBT had been hard to carry out these days, and people are preferring Self-CBT over traditional CBT. The role of technology had played an important role in order to make the experience of CBT far better for the patients and makes things easier according to their needs. In the future, we plan to add time frames to all quizzes so that patients can track their progress or compare their scores to previous scores, as well as make changes to the website's appearance.

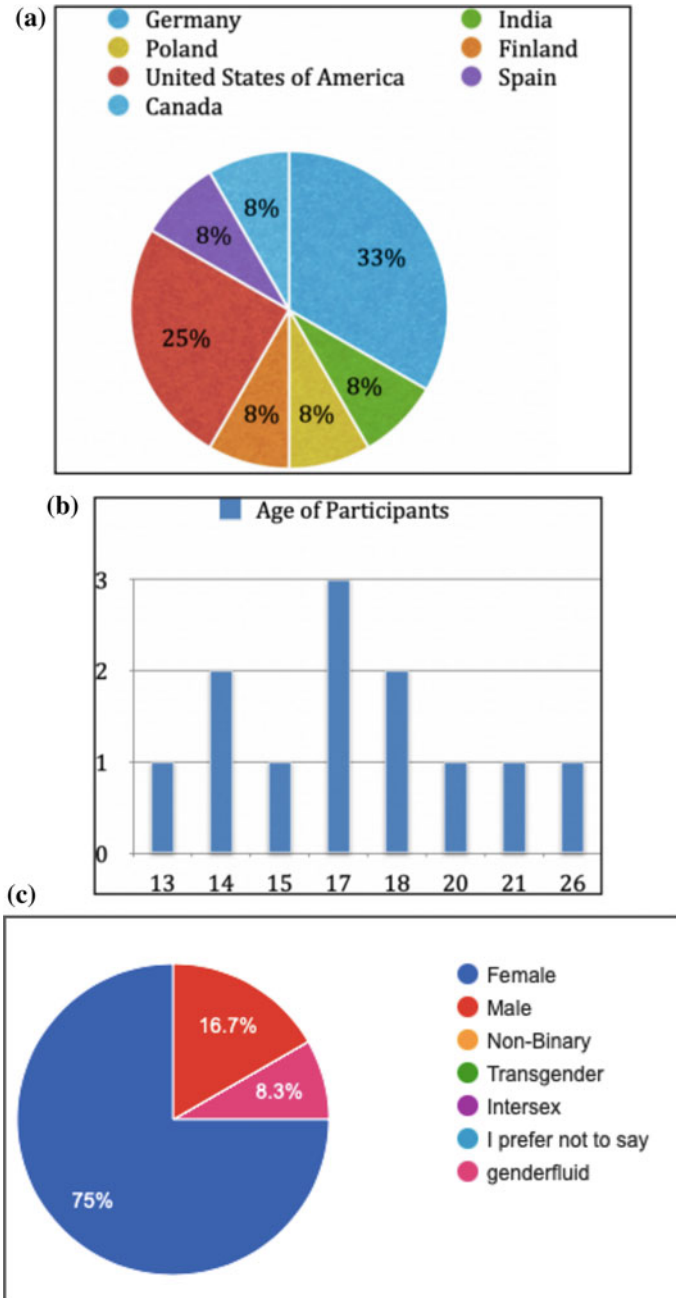


Fig. 3 a Country of participants, b age of participants, c gender of participants, d ratings of Eunoia by participants, e data of functions of existing CBT apps

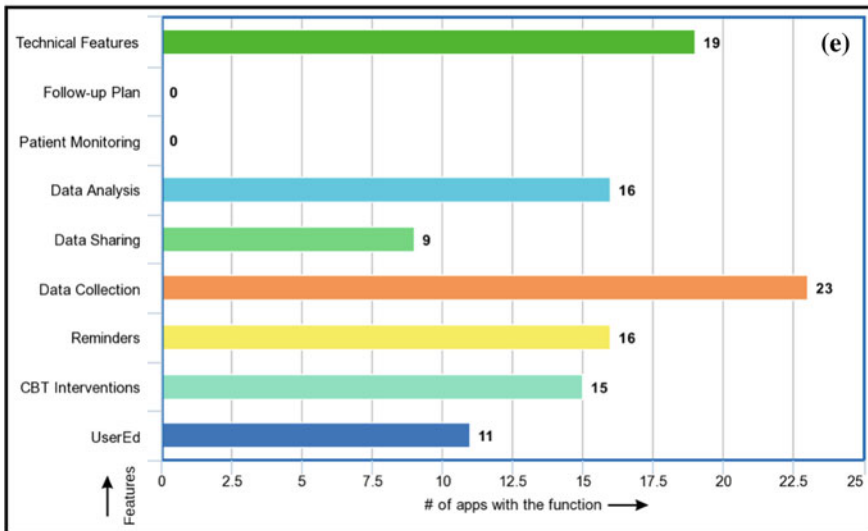
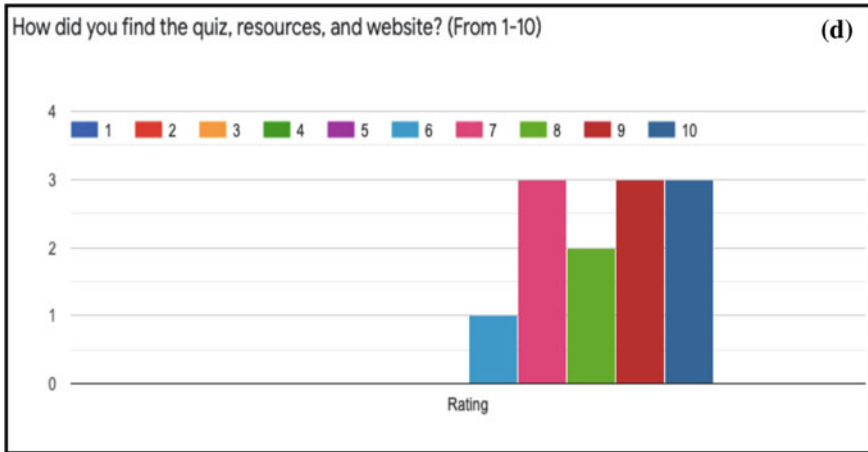


Fig. 3 (continued)

References

1. Beck Institute for Cognitive Behavior Therapy (2021) <https://beckinstitute.org/about-beck/history-of-cognitive-therapy>
2. International Telecommunication Unit (2013) The world in 2013: ICT facts and figures. <http://www.itu.int/en/ITU-D/Statistics/Pages/facts/default.aspx>
3. U.S. Food and Drug Administration (n.d.) Policy for device software functions and mobile medical applications (2019). <https://www.fda.gov/regulatory-information/search-fda-guidance-documents/policy-device-software-functions-and-mobile-medical-applications>
4. Natanson E (2020) Healthcare apps: a boon, today and tomorrow. <https://www.forbes.com/sites/eladnatanson/2020/07/21/healthcare-apps-a-boon-today-and-tomorrow/?sh=2337b2e51bb9>

5. Barlow DH (2007) *Clinical handbook of psychological disorders: a step-by-step treatment manual*, 4th edn. Guilford Press, New York
6. Kuhn E, Weiss BJ, Taylor KL, Hoffman JE, Ramsey KM, Manber R, Gehrman P, Crowley JJ, Ruzek JI, Trockel M (2016) CBT-I coach: a description and clinician perceptions of a mobile app for cognitive behavioral therapy for insomnia. *J Clin Sleep Med* 12(04):597–606
7. Michelle TQY, Jarzabek S, Wadhwa B (2014) CBT assistant: MHealth app for psychotherapy. In: 2014 IEEE global humanitarian technology conference—South Asia satellite (GHTC-SAS), pp 135–140
8. Jayachandran CM, Shyamala K (2017) Kohonen SOM deployment in android app-based cognitive behavioral therapy for personality disorders. In: 2017 World congress on computing and communication technologies, pp 255–257
9. Alanzi TM, Istepanian RSH, Philip N (2014) An integrated model for cognitive behavioural therapy for mobile diabetes self-management system. In: 36th Annual international conference of the IEEE engineering in medicine and biology society, pp 5393–5396
10. Fletcher RR, Tam S, Omojola O, Redemske R, Fedor S, Moshoka JM (2011) Mobile application and wearable sensors for use in cognitive behavioral therapy for drug addiction and PTSD. In: 5th International conference on pervasive computing technologies for healthcare (Pervasive health) and workshops, pp 202–203
11. Dino F, Zandie R, Abdollahi H, Schoeder S, Mahoor MH (2019) Delivering cognitive behavioral therapy using a conversational social robot. In: IEEE/RSJ international conference on intelligent robots and systems (IROS), pp 2089–2095
12. Patel F, Thakore R, Nandwani I, Bharti SK (2019) Combating depression in students using an intelligent ChatBot: a cognitive behavioral therapy. In: IEEE 16th India council international conference (INDICON), pp 1–4
13. Mattila E, Parkka J, Hermersdorf M, Kaasinen J, Vainio J, Samposalo K, Merilahti J, Kolari J, Kulju M, Lappalainen R, Korhonen I (2008) Mobile diary for wellness management—results on usage and usability in two user studies. *IEEE Trans Inf Technol Biomed* 12(4):501–512
14. Hur JW, Kim B, Park D, Choi SW (2018) A scenario-based cognitive behavioral therapy mobile app to reduce dysfunctional beliefs in individuals with depression: a randomized controlled trial. *Telemed E-Health* 24(9):710–716
15. Sussex Publishers (n.d.) How much does homework matter in therapy?. <https://www.psychologytoday.com/za/blog/cbt-and-me/201704/how-much-does-homework-matter-in-therapy>

Performance Evaluation of Basic, Modified, and Advanced DC-DC Boost Converters Used with PV System



Dilip Yadav and Nidhi Singh

Abstract This paper presents the performance analysis and comparison of various DC-DC converters that are utilized to step up the output voltages in DC system. These converters are classified as basic, modified, and advanced boost DC-DC converter. Its capability to transform a low-level voltage to a high-level voltage or vice versa is an advantage in power electronics. To transform its voltage level value, various types of converters are used (basic converters) like boost, buck-boost, SEPIC (single end primary inductor converter), Zeta, and Cuk converter, but these converters lag in some performance parameters, so modified converters were preferred. The modified DC-DC converter used in this paper is interleaved, integrated boost-Cuk (IBC), modified SEPIC converter (MSC), single-switch converter (SSC), and two-switch buck-boost (TSBB) converter. Recently developed advanced boost converters are switched-capacitor boost converter (SCBC) and a stackable switching boost converter (SSBC) which are utilized nowadays in various applications. MATLAB/Simulink software is used in this paper, to simulate (compare) and analyze the output performances of different converters. In last, all the performance parameters were compared and concluded that in the basic converter SEPIC and Cuk converter, in modified converter interleaved and IBC converter, and in advanced DC-DC boost developed converter, switched-capacitor boost converter can be used in a PV system. The analysis of SEPIC, interleaved, and SCBC is also shown on PV system using fuzzy logic-based MPPT and concluded that SCBC has a better response as in output the ripple is very less in comparison to two other fuzzy logic-based converters.

Keywords Interleaved converter · SEPIC converter · Switch capacitor boost converter · PV system · Fuzzy logic MPPT

D. Yadav (✉) · N. Singh
Department of Electrical Engineering, Gautam Buddha University, Greater Noida, India
e-mail: dilipyadav.eng@gmail.com

N. Singh
e-mail: nidhi@gbu.ac.in

1 Introduction

A DC-DC power converter is utilized for many power-based applications nowadays that include power supplies for laptops, telecommunication, renewable energy, PV system as well as for driving the different DC loads, DC motor drives, etc. Power electronic converters have become more popular because of their application in sustainable renewable energy. In renewable energy, solar power application is increasing at a high rate worldwide, and in that, power electronic devices are playing a vital role by transforming the voltage level for different applications like charge pumps, energy harvest for photovoltaic systems and wind turbines, solar chargers, DC microgrid applications, in the context of different voltage levels, telecommunication power supply, etc. These power electronic converters deal with the control, conversion, and conditioning of electric power. DC-DC converter changes one DC voltage level to another by stepping up or stepping down the voltage level. “Buck” converter is used to reduce input DC voltage level and “boost” converter is used to increase input DC voltage level [1]. Step-up DC-DC converter topology involves temporarily saving input energy [2].

The converter is majorly classified as basic, modified, and advanced converter. Figure 1 represents the classification of different DC-DC converters used in this paper for the performance analysis and comparison. Converters are designed such that they are capable to step up and then step down the voltage level, without changing its power capability [1–3]. Basic converters include boost [4], buck, buck-boost [5–7], Cuk [6], Zeta [6], and single end primary inductor converter (SEPIC) for various power applications [8].

Furthermore, some changes in design parameters and few circuit modifications enhance the performance of the basic converter and are called modified converters. Modified converters include integrated boost-Cuk (IBC), SSC (single-switch converter), modified SEPIC converter (MSC), two-switched buck-boost (TSBB), and interleaved [9–13]. The modified converters have different output performances and properties because of their separate circuit diagrams and different

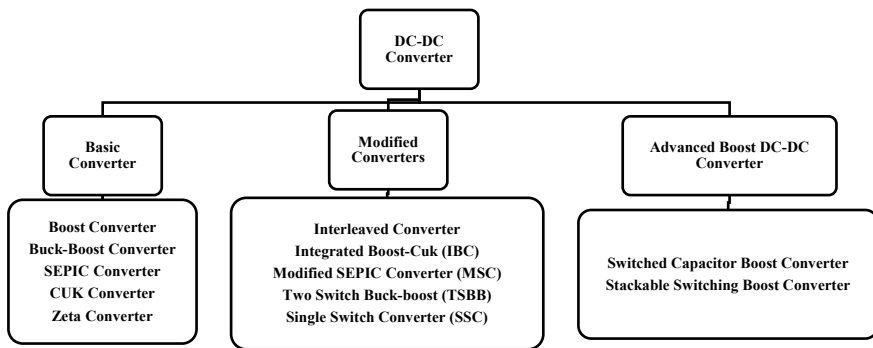


Fig. 1 Classification of DC-DC converter

design parameters. These act as a filter with an integrator circuit, which reduces the ripples and increases the circuit output performance.

The recently developed advanced set-up DC-DC converter included stackable switching boost converter (SSBC) and switched-capacitor boost converter (SCBC) [14, 15]. These converters were designed such that they can be utilized for a grid-connected PV system and stand-alone system. The low voltage output cannot directly feed to the grid-connected system or for any power applications [15]. Therefore, various types of DC-DC converters can be utilized with PV system applications [6, 16, 17].

Ayop et al. [4] studied the effects of inductor series resistance, transistor resistance, and capacitor series resistance. Gorji et al. [5] define the major advantage of bidirectional DC-DC converter to a grid-connected system. Soedibyoto et al. [6] compare the MPPT performance of four types of converters: buck-boost, Cuk, SEPIC, and Zeta. Siouane et al. [7] said that buck converters can be transformed to buck-boost converters without losing performance. Basha et al. [18] utilized MATLAB/Simulink to show the SEPIC converter in action. The working principle of SEPIC, Zeta, and landsman converters was discussed in Basha [16]. Maroti et al. [8] proposed a novel SEPIC converter construction for PV applications with greater voltage gain than the conventional SEPIC converter. Kumar et al. [9] integrated boost-Cuk converter, which is used for PV applications. Fu et al. [10] combined boost and buck-boost converters. Jung et al. [11] suggested two-switch buck-boost (TSBB) converter features less conduction and switching components than a typical TSBB converter, resulting in lower energy losses. Lin and Zhang [12] proposed a switched-capacitor boost converter with a better voltage gain and improved efficiency. Azer and Emadi [13] proposed a generalized state-space average for interleaved converters. Tran et al. [14] illustrate SCBC in two modes of operation CCM and DCM. Thuan et al. [14] demonstrated the functioning of a switched-capacitor-based high boost DC-DC converter using MPPT techniques. According to Vijay et al. [15], the requirements for converter connection include the maximum power point, efficiency, control power fed into the grid, and low total harmonic distortion. Basha et al. [17] utilized SEPIC and Zeta converters for motor drive application. Smyej and Cheriti [19] used Simulink to build a fuzzy logic controller that uses voltage output as feedback to improve the dynamic performance of boost DC-DC converters.

The study and overview of the DC-DC converter given in different papers provide different perspectives. However, past literature does not provide evidence of a systematic comparative study of all DC-DC converters for PV systems under similar practical conditions [5–19]. In this paper, an overview of different DC-DC converters used in a PV system is given. Parameters of the DC-DC converter are calculated by using its mathematical formula for each topology. Every DC-DC converter has a different topology and arrangement of elements with its advantages and disadvantages, which can be helping hands to the researchers.

2 Different DC-DC Converters

The three most basic topologies used in DC-DC converter are boost (step-up) [4], buck [7] (step-down), and buck-boost [7, 10] (step-down/step-up). “Buck” reduces the input DC voltage level and “boost” to increase the input DC voltage level. Buck-boost converter has the property of buck as well as boost. The DC-DC converters are classified as simple (basic), modified, and advanced DC-DC boost converters.

2.1 Simple (Basic) DC-DC Converter

A boost converter [18] or step-up chopper is one of the simplest types of converters or chopper.

In a boost converter, an inductor is connected at the input side and a capacitor is connected at the output terminal of the converter to make the output voltage constant and ripple-free. Figure 2a represents the boost converter diagram, and its application is used to regulate switch mode power supplies, regenerative braking of DC motors. The circuit diagram of a buck-boost converter [7] is seen in Fig. 2b, and the buck-boost circuit is easy to construct, but it differs slightly from the boost converter circuit seen in Fig. 2a, b. The buck-boost converter has an inverting output voltage which raises converter costs. It is used in self-regulating power supplies and the battery power systems.

Cuk [6] converter is an improved version of the buck-boost converter, it can also operate as a buck converter as well as a boost converter by varying duty cycle, and Fig. 2c shows the circuit for Cuk converter. Cuk converter consists of an extra pair of inductors and capacitors known as coupling inductor and coupling capacitor for filter purposes. Similar to buck-boost, it also provides inverting output voltage; because of these extra pairs of capacitors, the inductor circuit becomes slightly complex and

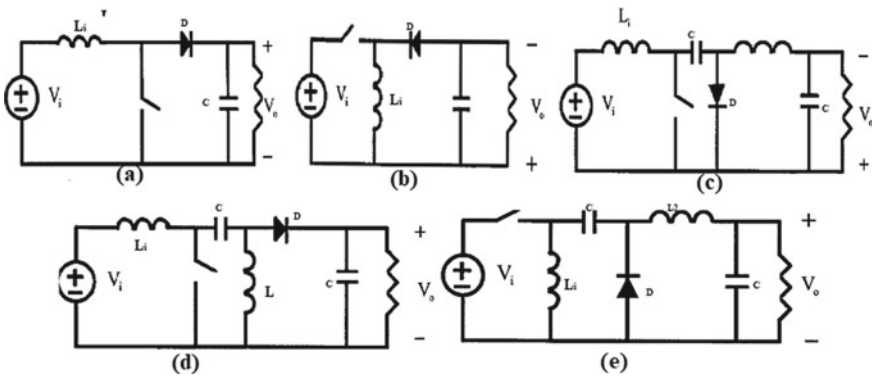


Fig. 2 Basic DC-DC converter **a** Boost converter. **b** Buck-boost converter. **c** Cuk converter. **d** SEPIC converter. **e** Zeta converter

costlier. It is used as a voltage regulator in a hybrid solar-wind energy system where input voltage depends on the speed of wind and sun.

SEPIC [8, 16, 18] converter can also operate as a buck converter as well as a boost converter by varying duty cycles. SEPIC converter consists of an extra pair of inductors and capacitors known as coupling inductors and coupling capacitors used for filter purposes. The circuit design of the SEPIC converter is different from the Cuk converter shown in Fig. 2d. Due to extra filtering, output performance becomes better, and although the circuit is slightly complex, still cost is moderate for the converter. SEPIC converter is widely used in LED lighting, battery-operating types of equipment, and handheld devices.

Figure 2e represents the Zeta converter [6, 16, 17], and Zeta converter can also operate as a buck converter as well as a boost converter by varying duty cycle. Zeta converter also consists of an extra pair of inductors and capacitors. The circuit design of the Zeta converter is highly complex and slow operating in nature. The cost of the Zeta converter is also high because of its complex circuit design and used in switched-mode power supplies and for photovoltaic systems.

2.2 Modified DC-DC Converter

Modified DC-DC converter was improved form of a basic converter, in which its few parameters were improved. There are many modified DC-DC converters; in this paper, 5(five) improved or modified converters have been covered. In Fig. 3a, an interleaved converter [19] circuit diagram is shown, and interleaved converter is a non-isolated low input ripple DC-DC converter, which can provide the high DC-DC step-up voltage from low input. It provides a higher voltage gain, better regulation, reduced voltage stress, and improved efficiency. Two inductors attached at the input side reduce the current ripples in the starting, and the capacitor at the output terminal tries to keep the output voltage level constant. It is used in fuel cell systems, BLDC motor drives, and hybrid vehicles.

In Figure 3b, an IBC [9] circuit diagram is shown. For obtaining the high voltage DC gain, IBC converters are used. Its efficiency is similar to boost and performance as the Cuk converter. The advantage of this converter is that it provides high efficiency with lessor regulation at the output voltage and is used for solar PV applications. Figure 3c represents the circuit diagram of MSC [19]. Modified SEPIC converter is a modified version of the SEPIC converter, and it is mainly introduced for high voltage applications. MSC consists of a single switch, three inductors, and three capacitors. Modified SEPIC converter is a third-order DC-DC converter because of its complex circuit design but output performance is better than traditional SEPIC converter.

The circuit diagram of the two-switch buck-boost is seen in Fig. 3d (TSBB). It can switch between boost, buck, and buck-boost modes. The number of conduction components and switching semiconductors in this converter is lower than in a traditional TSBB, resulting in less power loss during operation. Figure 4 represents the single-switch converter circuit diagram. SSC [10] is a cascaded connection of boost

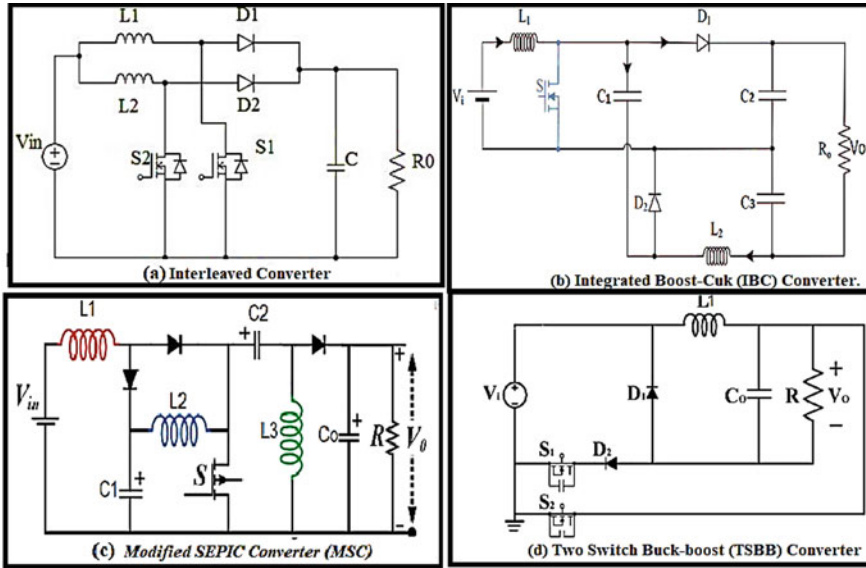


Fig. 3 The circuit diagram a Interleaved converter. b Integrated boost-Cuk (IBC) converter. c Modified SEPIC converter (MSC). d Two-switch buck-boost (TSBB) converter

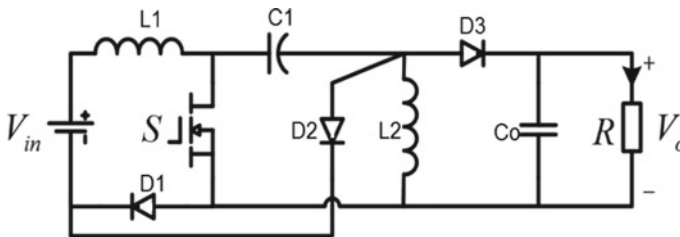


Fig. 4 Circuit diagram of the SSC

and buck-boost. The circuit of this converter is more like a SEPIC converter, with an equal number of inductors and capacitors like the Cuk and SEPIC converter. Just one switch is utilized in this converter, which efficiently improves the circuit structure.

2.3 Advanced Boost DC-DC Converter

A switched-capacitor boost converter (SCBC) consists of a single switch (IGBT/MOSFET), five diodes (D_1 - D_5), a single inductor, five capacitors, and a resistive load, and structure of SCBC is given in Fig. 5a.

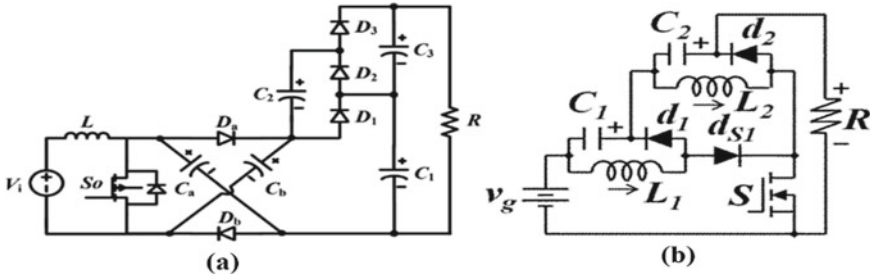


Fig. 5 Advanced DC-DC boost converter a SCBC and b SSBC

SCBC has an advantage of using switched-capacitor converter as they have high voltage gain with less stress on the power device so that the losses can be minimized in the output and efficiency can be increased with that operation, and control is easy in SCBC as only one switch is used for operation [14, 15]. Another converter in this section is known as stackable switching boost converter. SSBC converter is given in Fig. 5b. The number of capacitors used in SSBC is more than in the SCBC converter. The advantages of using the SSBC include low voltage tension in both capacitors and a flexible design that allows the converter’s configuration to be conveniently extended and, as a result, its gain to be improved by piling more switching cells [12, 15]. These converters are more appropriate for PV applications where a converter of a smaller size with high efficiency is needed.

3 Fuzzy Logic Controller

Fuzzy logic is a method of interfacing with electrical processes that move to a digital system, which seems to be well-defined discrete numeric values, over a continuous range of values. Fuzzy logic appears to be weak or imprecise logic [19] as it depends on human knowledge. The fuzzy controller’s concepts are divided into three major stages: input, processing, and output. Sensor or other outputs, such as shifting to the correct membership functions and truth values, are mapped by the output phase. The compiling cycle allows for each rule and assigns a score to each rule before approximating the results. One of the most essential elements of fuzzy logic systems is the sequential nature of the rules. Fuzzification, knowledge base, decision-making logic, and defuzzification are the major components of the FLC. Because the set of rules and their ranges have an impact on the FLC controller value, membership functions should be allocated with care. The main advantages are that they are not designed according to a mathematical model of a converter, can work with inaccurate inputs, and are robust. The importance of the fuzzy logic in the industry leads to intensive research to effective applications of fuzzy logic to embedded systems, and there are introduced many different hardware and software implementations of fuzzy logic [20].

4 Designing Parameters of PV Panel and Converter

In PV array, 3 parallel and 17 series strings are considered to achieve 240 V at the input side of the converter. And common values for each converter consider as input voltage 240 V, output voltage 402 V, resistive load 200 Ω , and switching frequency 25 kHz. The output of the PV array is the input of the DC-DC converter. The PV panel is integrated with a different converter. For that PV module, SunPower PL-PLT-63L-BLK-U is used in MATLAB/Simulink. The specification of the PV module is given below:

- Power at STC(W)—63
- V_{oc} (V)—14.5
- I_{sc} (Amp)—5.5
- V_{mp} (V)—11.9
- I_{mp} (Amp)—5.3
- Solar irradiation—1000 W/meter square
- Temperature—25-degree centigrade
- Effect of wind, humidity, and the temperature of panel is constant AM = 1.5.

4.1 Specification of Different DC-DC Converter

The modeling of the DC-DC converter is based on few important components that run the circuit as per the working principle. Any converter has 4 basic components, i.e., capacitor (C_{in}), connected across the PV source side of the converter to bypass the current ripple produced by the inductor. A DC-link capacitor (C_o) bypasses the ripple current. An inductor (L_i) and resistive load (R) act as the output of the converter. These parameters are mentioned in Table 1 and are adopted for the modeling of the basic converter, where D is the converter duty cycle. L_i and L_1 are the input inductor and coupling inductor, C_{in} is the input capacitor, and C_o is the output side capacitor which is used to make output voltage constant.

Table 2 represents the value of parameters that are adopted for the modeling of different modified converter [10–13], where D is the converter duty cycle, L_1, L_2, L_3 are the coupling inductor, and C_1, C_2, C_3 are the coupling capacitor. C_o is the output

Table 1 Parameters of basic converters

Component	Boost	Buck-Boost	SEPIC	Cuk	Zeta
D	0.4	0.62	0.62	0.627	0.6
L_i (mH)	46	50	50	50	35
L_1 (mH)	–	–	50	50	35
C_{in} (μ F)	–	33	33	33	11
C_o (μ F)	20	33	33	12	78

Table 2 Parameters of modified DC-DC converter

Component	Interleaved	IBC	MSC	TSBB	SSC
D	0.4	0.25	0.47	0.62	0.47
L_1 (mH)	46	50	50	50	50
L_2 (mH)	46	50	50	–	50
L_3 (mH)	–	–	50	–	–
C_1 (μ F)	–	33	33	–	33
C_2 (μ F)	–	20	33	–	–
C_3 (μ F)	–	20	–	–	–
C_o (μ F)	20	–	20	20	20

Table 3 Parameters of advanced DC-DC converter

Component	SCBC	SSBC
D	0.3	0.41
L_1 (mH)	50	50
L_0 (mH)	–	50
L_2 (mH)	50	–
C_1 (μ F)	0.46	20
C_2 (μ F)	0.46	20
C_a (μ F)	0.06655	–
C_b (μ F)	0.06655	–
C_c (μ F)	0.06655	–

side capacitor to obtain the output voltage constant. MSC has more components than the other 4 converters, which sometimes becomes a disadvantage for the circuit in terms of losses and size. Table 3 represents the values of parameters adopted for the modeling of the advanced-based DC-DC converter [14] 22, 23], where D is the converter duty cycle. L_1, L_o, L_2 are the inductor, and $C_1, C_2, C_3, C_a, C_b, C_c$ is the coupling capacitors.

In the case of switched-based boost converter, $C_a = C_b = C_c$, and $C_1 = C_2$, whereas in SSBC, $L_1 = L_o$ and $C_a = C_b$ with 5 diodes. All the values of the component used in SSBC and SCBC are calculated by the mathematical formula and proper naming with calculation [14, 15].

5 Simulation of Different DC-DC Converters

MATLAB/Simulink R2015a software version is used to examine the output performance of the different converters. Few of the parameters are kept constant in all the cases like input voltage, current, irradiation, temperature, load, switching frequency,

sample time, operation time period, and panel parameters (V_{oc} , I_{sc} , R_{sh} , R_{se} , ideality factor, number of series and parallel cell).

5.1 Basic Converter

Figure 6 represents the layout of boost converter, buck-boost, Zeta, Cuk, and SEPIC converter. From the performance perspective, all models are having an input voltage of 240 V, and the output for all the converters is set to be about $400 \pm 3n =$ volts for the resistive load of 200 ohms. The values of the converter parameters like an inductor and a capacitor are calculated by using mathematical calculations. Power, voltage, and current waveform are obtained for all the converters. Figure 7a represents the voltage output waveform for all the basic converters, Fig. 7b represents the current, and Fig. 7c shows the power obtained from different basic converter sections. To obtain a clear curve and to analyze, the basic converters are operated for $t = 0.2$ (time period). From the simulation results, buck-boost and Cuk converter gives inverting output voltage. Using such a converter has the disadvantage of increasing the converter's cost by inverting the output voltage. Ripple voltage for all converters is less than 1%, and minimum ripples are in Cuk and Zeta converter. SEPIC converter has the advantage of an extra capacitor which helps in reducing the voltage stress on the circuit, and it gives better input-output isolation. Ripple and noise are less in the circuit which improves the performance of the system (Table 4).

5.2 Modified DC-DC Converter

The layout of the modified converter implemented in MATLAB is shown in Fig. 8, having (a) two-switch buck-boost converter, (b) modified SEPIC converter, (c) single-switch converter, (d) interleaved converter, and (e) integrated boost-Cuk converter. The modification was done such that the efficiency increases and the size of the system can be reduced. From the performance perspective, all models are having an input of 240 V, and the output for all the converters is set to be 400 ± 3 for the resistive load of 200 ohms. Power, voltage, and current waveforms are obtained for all the converters. Figure 9a–c shows the power, voltage, and current output waveform for all the modified converters.

In Fig. 9, the interleaved converter provides a well-regulated voltage and efficiency (91%) as in the boost converter. Ripple in output voltage and the current waveform are reduced up to less than 0.3% in IBC converter. The IBC converter also provides a well-regulated output voltage so that it requires very small regulation. The efficiency of the IBC converter is very high around 91% as that of interleaved. Most of the output performance is similar to the interleaved converter. Ripple in output voltage and the current waveform are less than 1% in MSC. The modified SEPIC converter requires more regulation because its less regulated output voltage and the efficiency of the

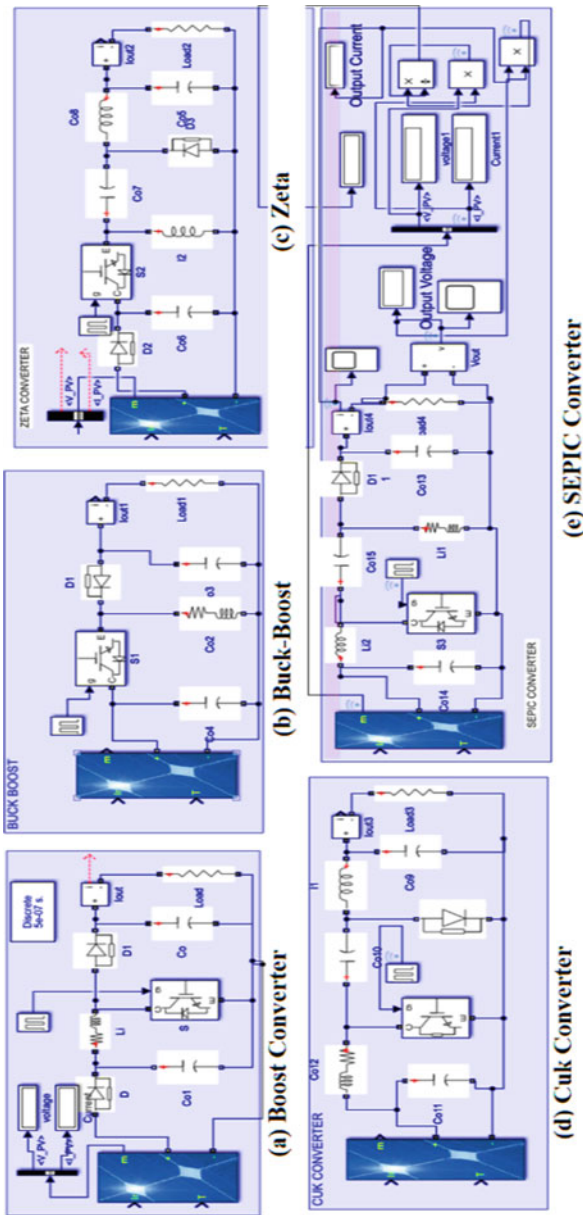


Fig. 6 Different basic converters layout **a** Boost, **b** buck-boost, **c** Zeta, **d** Cuk converter, and **e** SEPIC converter

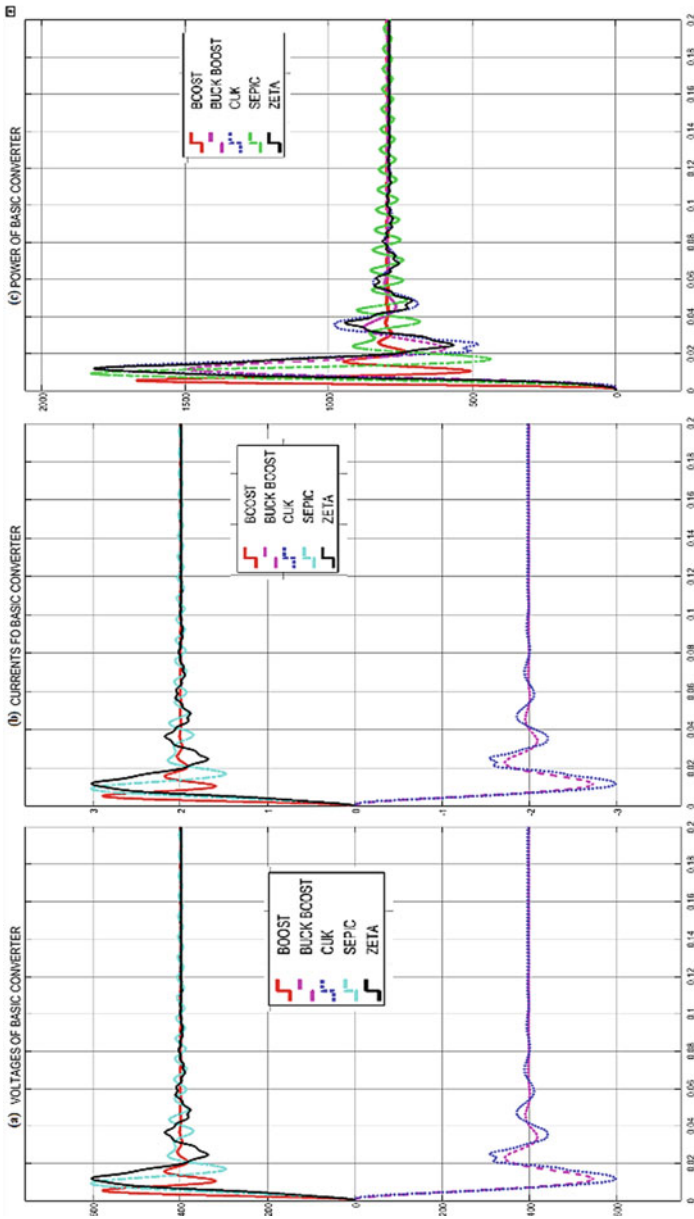


Fig. 7 a Voltage, b current, and c power waveforms for different basic converters

Table 4 Analysis of basic DC-DC converters performance

Converters output boost	Boost	Buck-boost	SEPIC	Cuk	Zeta
Vin (V)	240.5	239.6	239.4	239.4	241
Vout (V)	399.5	-399.4	400	-397.0	397.3
Inverting	No	Yes	No	Yes	No
Ripple voltage	1.8	1.171	0.2069	0.016	0.3166
Maximum power (W)	798.3	797.8	810.8	788.3	790.4
Pulsating	Yes	Yes	Yes	Slightly	Smooth
Rise time	3.55 μs	19.14 μs	1.25 ms	1.87 ms	1.32 ms
Efficiency (%)	91.21	80.4	82.83	80.38	81.5
Circuit design	Easy	Easy	Easy	Hard	Complex
Inductor used	1	1	2	2	2
Capacitor used	2	2	3	3	2
Diode used	2	1	1	1	2
IGBT used	1	1	1	1	1
Cost	Low	Moderate	Moderate	High	Very High

MSC are around 80% similar to the simple SEPIC converter. The TSBB converter requires less regulation around 3 V, and the efficiency of the TSBB converter is around 83%. The output of the SSC requires regulation around 5 V. And the efficiency of the single-switch converter is around 80% similar to the simple converter.

The size of the converter also plays an important role, so in IBC with 4 elements as shown in Fig. 8, the efficiency of 91% has been attained with a smaller number of ripples in output. If we talk about overall efficiency, output voltage, maximum power, ripple, rise time, and circuit design and then Interleaved, IBC, and SSC have a better response. All are non-inverting. Table 5 shows the brief comparison between the modified DC-DC converters.

5.3 Advanced DC-DC Boost Converter

In the advanced boost converter, there are two converters SCBC and SSBC. The layout of the basic converter implemented in MATLAB is shown in Fig. 10, having SCBC and SSBC. Though the size of the converter has been increased due to an increase in elements, the output response has been increased at a high rate with efficiency. Figure 11a is the voltage output waveform for all the SSBC and SCBC converters, Fig. 11b represents the current, and Fig. 11c shows the power obtained from different basic converter sections. To obtain a clear curve and to analyze, the basic converters are operated for $t = 0.2$ (time period).

In Fig. 11, the SSBC converter has output somewhat near to the SCBC converter, but the transient occurring in the SCBC is more and the settling time is also more than

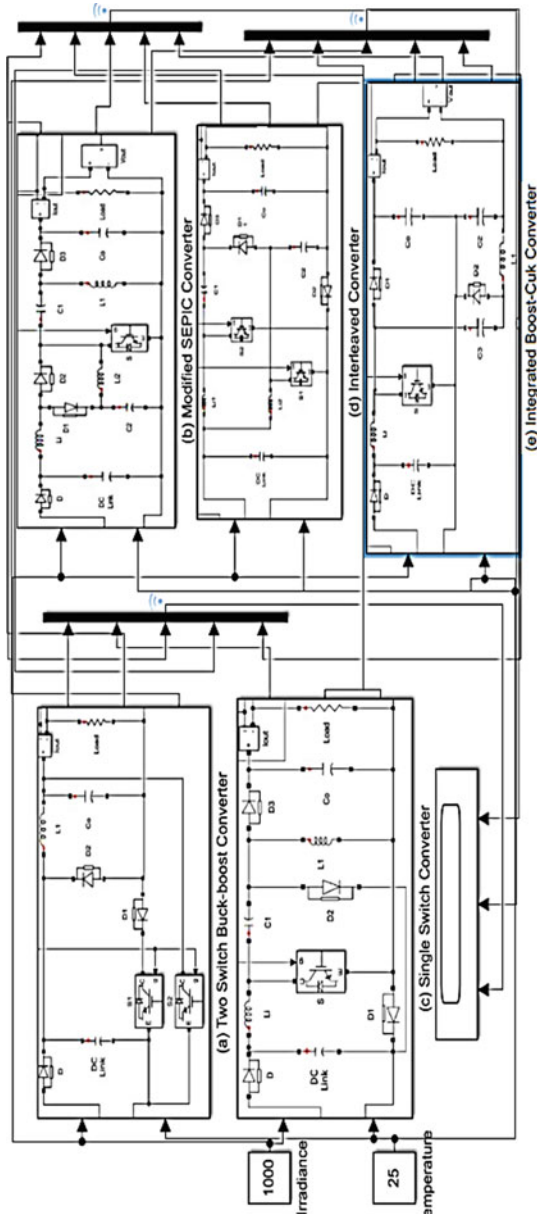


Fig. 8 Modified DC-DC converter **a** TSBC, **b** MSC, **c** SSC, **d** interleaved, and **e** IBC converter

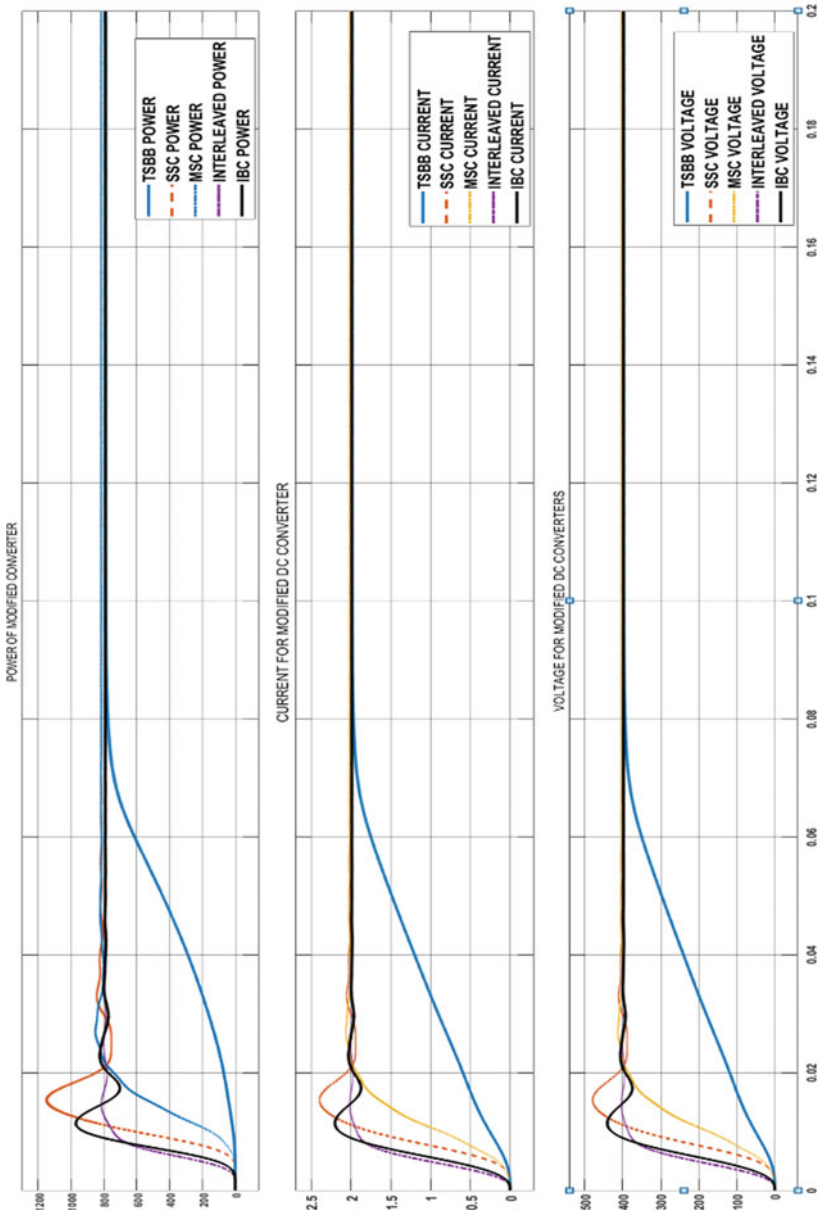


Fig. 9 Modified DC-DC converter output in terms of power, current, and voltage

Table 5 Modified DC-DC converter performance analysis

Converter output	Interleaved	IBC	MSC	TSBB	SSC
Vin (V)	239.9	239	236.55	239	236.55
Vout (V)	398.5	398	404.1	398.7	404
Ripple voltage (V)	1.2	1.1	2.7	3	2.7
Operating time (S)	0.05	0.07	0.12	0.11	0.06
Max. power (W)	795.8	793.8	821.7	794.9	821.7
Pulsating	Less	Less	Medium	High	Medium
Rise time	5.39 ms	4 ms	11.81 ms	52.2 ms	5.45 ms
Efficiency (%)	91	91	80	83	80
Inductor used	2	1	2	1	2
Capacitor used	3	3	3	1	3
Diode used	3	3	4	3	4
IGBT used	2	1	1	2	1
Circuit design	Easy	Easy	Complex	Easy	Easy

the SCBC converter. The waveform of SCBC is quite smooth, and stability is high in comparison to the SSBC converter. This converter has a higher capability with fewer ripples in the output. Table 6 is the brief comparison of these two converters in terms of ripples, maximum power, and rise time, and the efficiency of the SCBC converter is maximum of all the converters about 95.13%. The maximum power it can draw is 834 watts with an output voltage of 407.6 V. The size of the converter has its importance in designing the converter, the total inductor, and capacitor used for the SCBC converter that are 2 and 6 in number as shown in Fig. 11. SCBC shows a higher and better response in comparison with the SSBC converter.

From Table 4, 5, and 6, after comparison, it can be seen that in basic converter the performance is better in between boost, buck-boost, SEPIC, Cuk, and Zeta. SEPIC converter has better performance than CUK converter, and CUK converter has better performance than boost converter. In the modified converter, interleaved converter has better response and performance than IBC, IBC are better than the SSC converter, and SSC is better than MSC-based converter. In advanced DC-DC boost converter, SCBC converter has the best response than all converters. The performance analysis is carried on basis of ripple voltage, efficiency, maximum power, operating time/rise time, number of elements used with less size, and design circuit.

From Tables 4, 5, and 6, the three most efficient converters at 0.6 duty cycle are interleaved, SEPIC, and SCBC converter.

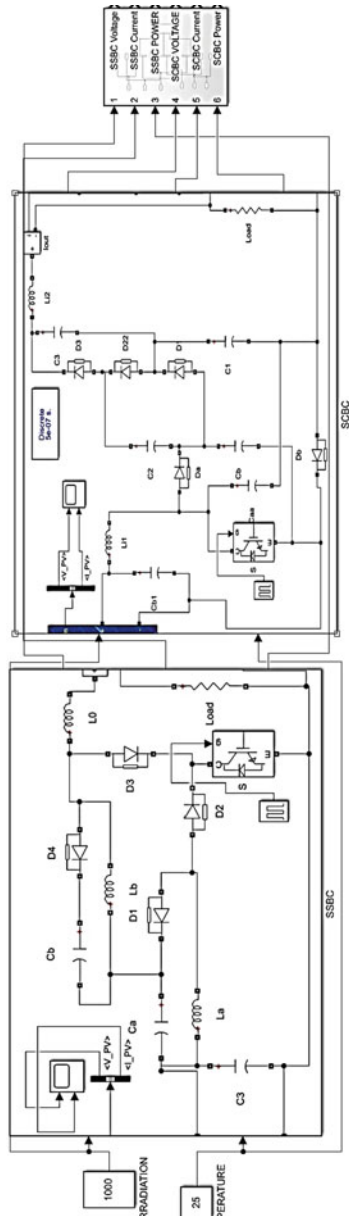


Fig. 10 Advanced DC-DC boost converter SCBC and SSBC

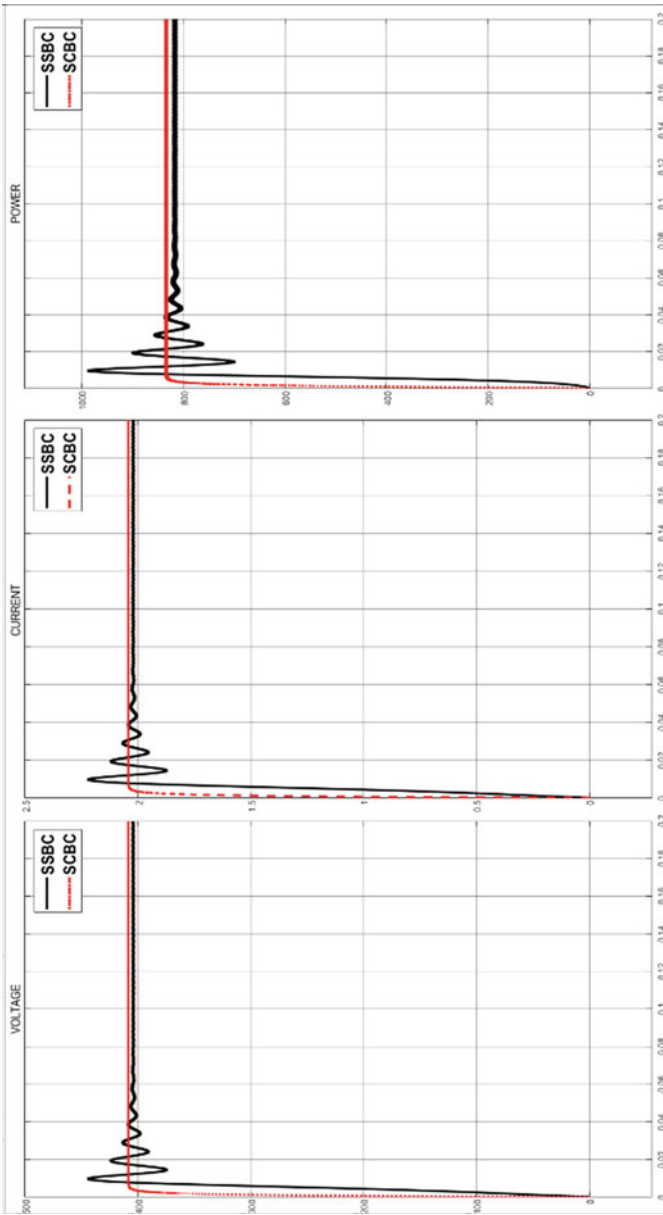


Fig. 11 Voltage, current, and power response for SCBC and SSBC

Table 6 Performance analysis of advanced DC-DC boost converters

Converters output	SSBC	SCBC
Vin (V)	238.5	240.05
Vout (V)	405.2	407.6
Inverting/non-inverting	Non-inverting	Non-inverting
Ripple voltage (V)	2.5	1.8
Operating time (S)	0.0097	0.020
Maximum power (W)	819.2	834.4
Pulsating nature	Pulsating	Non-pulsating
Rise time	5.843 μ s	3.357 μ s
Number of inductor	3	2
Number of capacitor	3	6
Number of diodes	4	5
Number of IGBT	1	1
Efficiency (%)	89.25	95.13
Circuit design	Complex	Complex

5.4 Fuzzy Logic Controller with Interleaved, SEPIC, and SCBC Converter

For the three models, an FLC-based system is designed which have two inputs, i.e., is in terms of voltage and power, and one output that is duty cycle. The membership function plot is in terms of *VS* (*very small*), *S* (*small*), *M* (*medium*), *H* (*high*), and *VH* (*very high*); total 25 sets of rules have been designed on which the FLC will work. Parameters like input solar power, boost converter (inductor, capacitor), and load value have been kept constants for all the cases of converter specified in Tables 4, 5, and 6. Table 7 represents the output obtained for the three different converters. Figure 12 shows the ruler view of the fuzzy logic controller for the given converter. Figure 13 shows the Simulink model of three converters on which the FLC-based MPPT technique is used.

Interleaved, SEPIC, and SCBC converter and the voltage, current, and power curve are shown in Fig. 14. The result for the given converter shows that for the given input of 239.4 V system the SEPIC converter output voltage is increased to 399.1 V with the transient value of 2.071, whereas interleaved converter has the output value of 397.7 V with the transient value of 4.13 V. In the case of advanced DC-DC converter, SCBC-based converter has an output voltage of 399.4 V with the negligible transient value of 0.004 V in the output value of voltage current and power. From the result obtained for the three different converters, it can be concluded that with FLC-based MPPT technique Interleaved have better performance in terms of power but the transient value is very high, SEPIC converter has less output power but the voltage value is higher than interleaved converter with less transient value,

Table 7 Performance analysis of interleaved, SEPIC, and SCBC with FLC controller

Converter output	Interleaved	SEPIC	SCBC
Vin (V)	239.9	239.4	240.05
Vout (V)	395.5	397.3	399.7
Maximum power	790.8	723.8	693.4
Number of inductor	2	Easy	2
Number of capacitor	3	2	6
Number of diodes	3	3	5
Number of IGBT	2	1	1
Circuit design	Easy	Moderate	Complex
Transient (V)	4.13	2.071	0.004
Rise time	17.931 ms	52.896 ms	3.263 ms
Efficiency	93.5	78.93	79.6

and SCBC-based converter has highest output voltage with the negligible transient in the output curve of voltage power and current.

6 Conclusion

In this paper, a comparative study, analysis of different DC-DC converters is done. These converters are broadly classified as a basic DC-DC converter, modified DC-DC converter, and advanced boost DC-DC converter. All converters were designed for 240 V input PV voltage. In basic converter, boost, buck-boost, SEPIC, Cuk, and Zeta DC-DC converters were simulated with a PV system and their response was analyzed. SEPIC and Cuk converters were found most suitable among basic DC-DC converters for PV application. In modified converters, interleaved, IBC, MSC, TSBB, and SSC have non-inverting output voltage, which reduced additional devices required to invert the output voltage as in a basic converter. From the response obtained, the performance of interleaved and IBC is found suitable among the modified converter for implementing it with PV applications. In advanced DC-DC boost converter, SSBC and SCBC came into existence to reduce the problem that was taking place in boost converter. SCBC is more preferred as its performance is better than other converters. When these most suitable converters, namely interleaved, SEPIC, and SCBC converter, are used with the FLC-based MPPT controller, it is found that interleaved-based converters have better power than the other two converters. Based on transient, rise time, and output voltage, it was concluded that the SCBC converter has a better response than the other two converters.

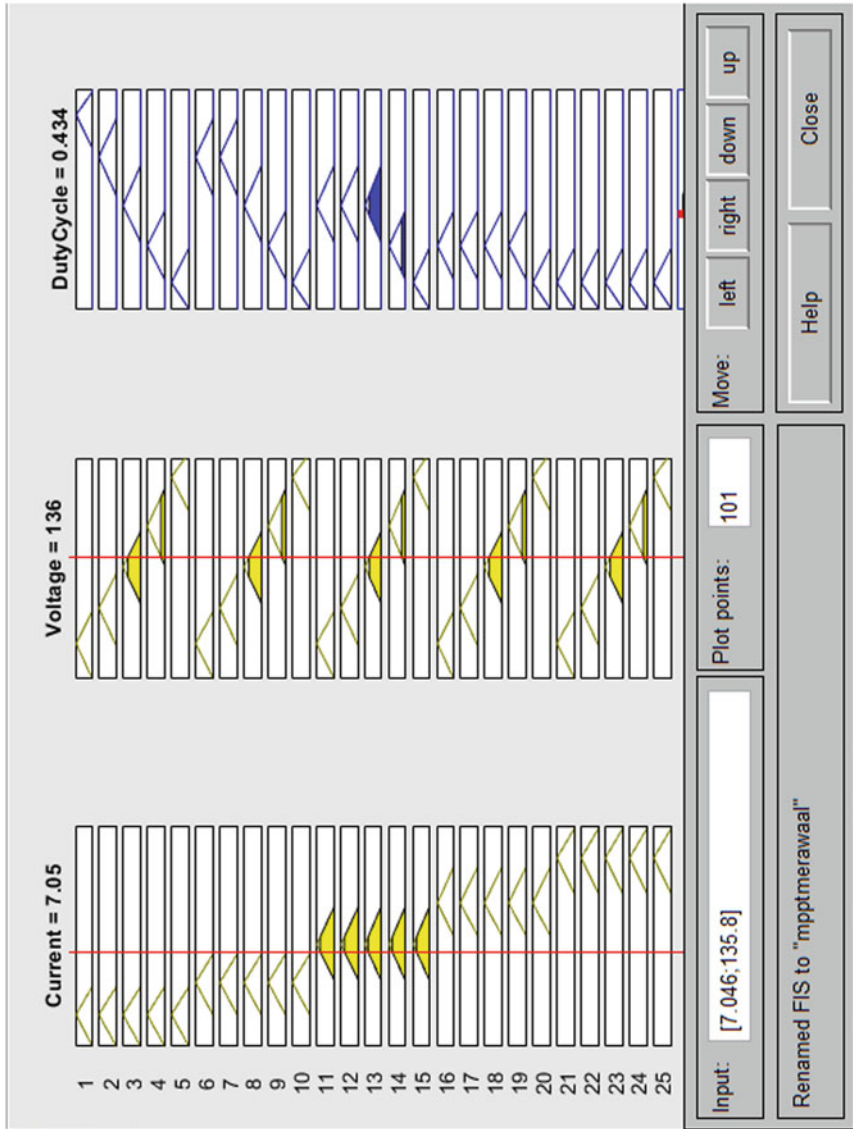


Fig. 12 Ruler view of the fuzzy logic controller

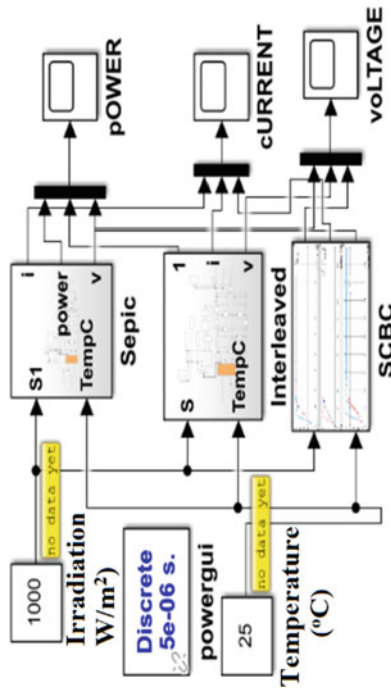


Fig. 13 Simulink model for Interleaved, SEPIC, and SCBC converter with FLC controller

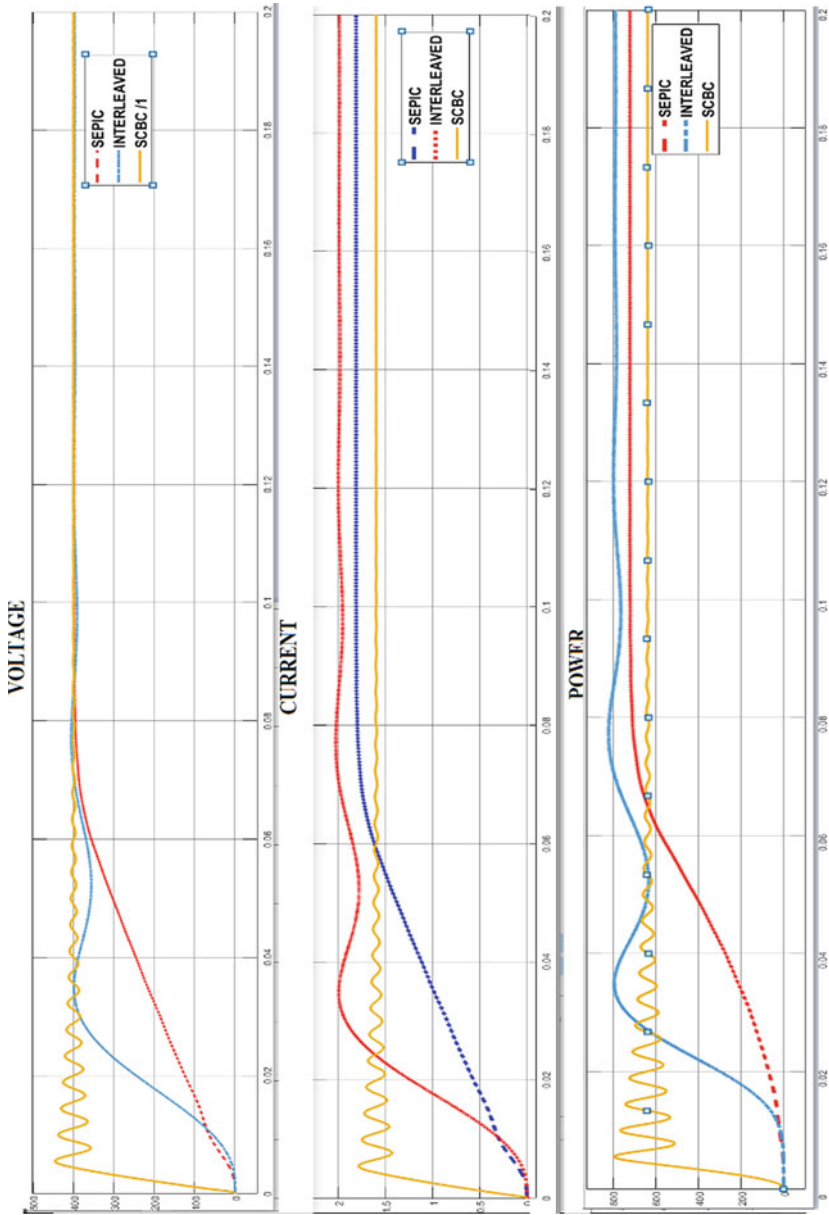


Fig. 14 Voltage, current, and power response for interleaved, SEPIC, and SCBC

References

1. Bimbhra PS (2003) Power electronics. Published by Khanna
2. Forouzesh M, Siwakoti YP, Gorji SA, Blaabjerg F, Lehman B (2017) Step-up DC-DC converters: a comprehensive review of voltage-boosting techniques, topologies, and applications. *IEEE Trans Power Electron* 32(12):9143–9178. <https://doi.org/10.1109/TPEL.2017.2652318>
3. Rashid MH (2011) Power electronics handbook: devices circuits and application, 3rd edn. Elsevier, Burlington, MA, USA
4. Ayop R, Tan CW (2018) Design of boost converter based on maximum power point for photovoltaic applications. *Sol Energy* 322–335
5. Gorji SA, Sahebi HG, Ektesabi M, Rad AB (2019) Topologies and control schemes of bidirectional DC-DC power converters: an overview. *IEEE Access* 7:117997–118019
6. Soedibyo, Budi Amri B, Ashari M (2015) The comparative study of buck-boost, cuk, SEPIC and Zeta converters for maximum power point tracking photovoltaic using P & O method. In: 2nd International conference on information technology, computer and electrical engineering (ICITACEE), Indonesia
7. Siouane S, Jovanovic S, Poure P (2018) Service continuity of PV synchronous buck/buck-boost converter with energy storage. *Energies* 1369
8. Maroti PK, Padmanaban S, Holm-Nielsen JB (2019) A new structure of high voltage gain SEPIC converter for renewable energy applications. *IEEE Access* 7:89857–89868
9. Kumar K, Ramesh Babu N, Prabhu KR (2017) Analysis of integrated boost-cuk high voltage gain DC-DC converter with RBFN MPPT for solar PV application. In: International conference on innovations in power and advanced computing technologies [i-PACT], Vellore, India
10. Fu J, Zhang B, Qiu D, Xiao W (2014) A novel single-switch cascaded DC-DC converter of boost and buck boost converters. In: IEEE 16th European conference on power electronics and applications, Lappeenranta, Finland
11. Jung HY, Kim SH, Moon B, Lee S-H (2018) A new circuit design of 2-switch buck-boost converter. *IEEE Access* 6:47415–47423
12. Lin G, Zhang Z (2019) Low input ripple high step-up extendable hybrid DC-DC converter. *IEEE Access* 7:158744–158752
13. Azer P, Emadi A (2020) Generalized state space average model for multi-phase interleaved buck, boost, and buck-boost DC-DC converters: transient, steady-state and switching dynamics. *IEEE Access* 8:77735–77745
14. Tran VT, Nguyen MK, Choi YO, Cho GB (2018) Switched-capacitor-based high boost DC-DC converter. *Energies*
15. Sood VK, Abdelgawad H (2019) Power converter solutions and controls for green energy. Distributed energy resources in microgrids, Academic Press
16. Basha CH, Rani C, Odofin S (2018) Analysis and comparison of SEPIC, Landsman and Zeta converters for PV fed induction motor drive applications. In: Proceedings of the 2018 international conference on computation of power, energy, information and communication (ICCPEIC), Chennai, India
17. Basha CH, Rani C, Odofin S (2018) Analysis and comparison of SEPIC, Landsman and Zeta converters for PV fed induction motor drive applications. In: International conference on computation of power, energy, information and communication, pp 327–334
18. Hussaia CH, Basha N, Rani C (2020) Different conventional and soft computing MPPT techniques for solar PV systems with high step-up boost converters: a comprehensive analysis. *Energies*

19. Smyej M, Cheriti A (1999) Fuzzy logic controller for a DC-to-DC converter. In: Engineering solutions for the next millennium. 1999 IEEE Canadian conference on electrical and computer engineering, vol 2, pp 1020–1023
20. Leso M, Zilkova J, Girovsky P (2018) Development of a simple fuzzy logic controller for DC-DC converter. In: IEEE 18th international power electronics and motion control conference (PEMC)

Energy and SLA-Aware VM Placement Policy for VM Consolidation Process in Cloud Data Centers



Dipak Dabhi and Devendra Thakor

Abstract The use of cloud services in recent times increased drastically. Satisfying the appeal for cloud services requires an enormous number of data centers that use colossal energy. These data centers create high carbon dioxide by-products in the climate and high functional expenses for the cloud service provider. The strategy for lessening energy utilization in the server is called virtual machine consolidation (VMC). The VMC procedure helps to improve the performance of Physical Machine (PM) by closing down underutilized PM without infringement Service Level Agreement (SLA). The VMC procedure is divided into four policies: underload detection of the host, overload detection of a host, selection of the host for migration, and placement of VM on the destination host. The virtual machine placement (VMP) methodology is fundamental in controlling energy consumption and SLA infringement by choosing a precise host for VM placement. This work proposed energy and SLA-aware VM placement (ESVMP) policy, which identifies the placement based on medium utilizing PM instead of lower utilized PM. We execute and compare our proposed ESVMP policy with other existing placement policies like the first fit (FF), least fit (LF), modified best fit decreasing (MBFD), and power-aware best fit decreasing (PABFD). We execute our experiment using the PlanetLab dataset on the CloudSim toolkit and compare simulation results. The results indicate that our policy ESVMP policy outperforms compared to standard policies.

Keywords VM consolidation · VM placement · Power-aware best fit decreasing · Modified best fit decreasing · First fit · Least fit · Modified VM placement

D. Dabhi (✉) · D. Thakor
Chhotubhai Gopalbhai Patel Institute of Technology, Uka Tarsadia University, Bardoli, India
e-mail: dipakdabhi11@gmail.com

D. Thakor
e-mail: devendrathakor@gmail.com

1 Introduction

In cloud computing, many data centers are used to serve user requests over the globe [1]. This large amount of scattered data centers absorbs a high volume of energy and produces carbon emissions in an environment similar to the aviation industry. Also, the high demand for cloud services will exponentially increase the data centers' energy consumption over time, so there is a need for lower energy consumption and less carbon emission-aware efficient technique [2, 3].

The VMC process is divided into four parts: (a) detection of host overloaded, (b) detection of underloaded host, (c) selection of VM, and (d) placement of VM. Figure 1 shows VM consolidation algorithm classifications.

The VMC process will address this issue and provide a solution [2, 4]. Cloud data center has a large number of hosts to serve the user request. Whenever a host utilization reaches its limit, it will affect the Service Level Agreement (SLA) and system performance. So, detection of overload PM algorithms will identify the overloaded PM [5]. Also, it is essential to identify the underloaded PM because for saving energy, it transfers the load from the underutilized PM to other PMs, and the underloaded PM will be put on sleep/shutdown mode [6, 7]. For that, it uses the detection of underload host algorithms. The VM selection algorithm identifies the VM which is liable for overload host and selects this VM for migrating to another host [8, 9]. The VMP policy is used to detect the best destination PM for the selected VM to migrate.

VMP policy will play a vital role in identifying the best possible destination PM to migrate VM. If the destination PM selection goes wrong, destination PM utilization reaches its maximum limit and violates the SLA performance [10, 11]. So, in that

Host Overload Detection Algorithm	Static Threshold (Th)	Median Absolute Deviation (MAD)	Interquartile Range (IQR)	Local Regression (LR)	Robust Local Regression (LRR)
Host Underload Detection Algorithm	Host with Minimum Utilization				
VM Selection Algorithm	Minimum Migration Time (MMT)	Random Choice (RC)	Maximum Correlation (MC)	Minimum Utilization (MU)	
VM Placement Algorithm	First Fit (FF)	First Fit Decreasing (FFD)	Best Fit Decreasing (BFD)	Worst Fit Decreasing (WFD)	Power Aware Best Fit Decreasing (PABFD)

Fig. 1 VM consolidation algorithms

case, the VMC process is repeated till the overutilized PM is converted to normal utilized PM. The more significant number of migrations also affects the performance of the server. To efficiently utilize resources and minimize the SLA violation, it is required to place VM effectively on PM in the data center. This process will be called VM placement. This article proposed the new VM placement policy named energy and SLA-aware VM placement policy (ESVMP) to find destination hosts effectively. The simulation-generated result is applied to assess the performance of the existing methods with the newly proposed method.

2 Related Work

This section discussed various mechanisms that claim to reduce energy consumption by efficiently allocating resources, using proper VM selection, efficient VM placement, better load balancing techniques, etc. [11]. The virtual machine placement problem is being well advised as one of the most promising research issues in achieving energy efficiency in cloud computing. The VM placement policy implementation is situated on two criteria [12]. The primary is established on the Quality-of-Service approach, in which efficient utilization of computing resources is a concern. The second is the power utilization-based approach, in which energy consumption is reduced using the shutdown of the underutilized host [13, 14].

Beloglazov [4] proposed an energy-aware best fit decreasing-based policy. This strategy sorts VMs to diminish CPU use and appoints the most immaterial effect on power utilization by new designation. It will give better outcomes in power utilization with other standard arrangements, yet the average SLA infringement and the number of VM movements are high. Dubey et al. [10] proposed an efficient service best fit decreasing policy, which produces a better result than the first fit and best fit policy to decrease the execution time and placement failure rate. However, power consumption and several VM migration are still higher.

Liu et al. [15] proposed an efficient QoS and energy-aware dynamic VMC method with four algorithms corresponding to different VM consolidation stages. Alboaneen et al. [5] proposed a glowworm swarm improvement VM migration strategy to limit the energy and SLA infringement. A glowworm creates extra luciferin, implies close to the genuine designation, and has a high target point esteem. It applies to looking for VM, which devours less energy and SLA infringement. The arrangement results in contrasts and PABFD, and it gives better outcomes. Nonetheless, it is not compared with the most recent VM migration policy.

Zhou and Buyya et al. [8] look at the most recent VM placement strategies like MBFD, EcoCloud, GRANITE, LOAD, and ACS. The subsequent semantics demonstrate that every strategy execution is acceptable in energy utilization or SLA violation; however, no arrangement is better than others in all cases. Moges et al. [14] proposed many adequate VM placement policies like energy-aware first fit decreasing algorithm, power-efficient best fit decreasing algorithm, and medium fit power-efficient decreasing algorithm. The proposed calculation is executed on the

actual cloud platform Open-Stack Neat. The proposed new strategy creates the best outcome contrasted with PABFD, first fit, worst fit, best fit, and others. There is a requirement for the strategy to keep up with the tradeoff between power consumption and infringement of SLA.

3 Proposed Work

The current VMC policies consume more energy use and produce high carbon emissions in the cloud data center. We propose efficient energy and SLA-aware VM placement (ESVMP) policy that identifies the host’s proper selection for VM migration. The flowchart of the proposed ESVMP policy is shown in Fig. 2.

Our proposed ESVMP policy first identifies the available host list and VM list that needs placement. The list of VM is sorted in descending sequence as per the CPU utilization of the VM. Now, it calculates the maximum usage of each VM and checks the host in the host list for whether it is suitable for the selected VM. It checks that host utilization should not be zero, and after the allocation of VM to the destination host, it should not be overutilized. Next, it calculates the host utilization without a new VM and checks if the current host utilization is greater than the max

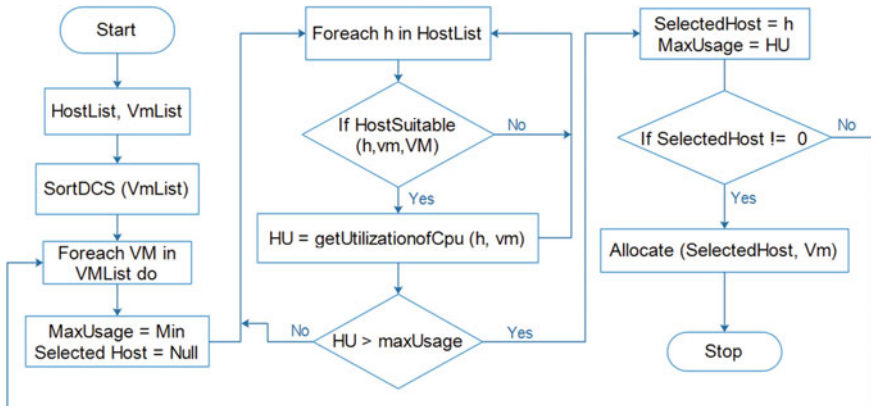


Fig. 2 Energy and SLA-aware VM placement policy flowchart

usage of VM it will select for migration, and VM will allocate to the selected host. This process system migrates VM to the destination host, which is medium loaded, and it must not be underloaded and overloaded after migration. It can serve the user request through the minimum number of the host and save energy. Also, it takes care of the minimum number of VM migration and SLA violation. The proposed policy algorithm steps are mention below.

Algorithm 1: Energy and SLA-aware VM placement policy (ESVMP)

Input: vmList, hostList

Output: selectedHost

- 1) sort vmList in the order of decreasing CPU utilization;
- 2) **foreach** vm in vmList **do**
- 3) MaxUsage = Min;
- 4) selectedHost = Null;
- 5) **foreach** host in hostList **do**
- 6) **if** host has enough resource for vm **then**
- 7) hostUtilization = host.getUtilizationofCpu();
- 8) **if** hostUtilization > MaxUsage **then**
- 9) selectedHost = host;
- 10) MaxUsage = hostUtilization;
- 11) **end if**
- 12) **end if**
- 13) **end**
- 14) **end**
- 15) **if** selectedHost Null **then**
- 16) add (selectedHost, vm) to vmPlacement;
- 17) **end**

Our proposed ESVMP policy will be compared with some existing policies like power-aware best fit decreasing (PABFD), modified best fit decreasing (MBFD), first fit (FF), and least fit (LF). To assess the proposed VM placement policies with other policies, we perform a series of experiments on the different real-time datasets and provide a detailed result analysis that proves that our policy performs best compared to other policies. The CloudSim toolkit is used for modeling virtualized data centers and simulation [15].

4 Experimental Environment

4.1 Experimental Setup

For the simulation environment, we utilized 800 physical heterogeneous hosts, in which 400 hosts have HP ProLiant ML110 G4, and the other 400 hosts will be HP ProLiant ML110 G5 type. The definite property of hosts is given in Table 1 [16, 17].

Table 1 Server detail

Server	HP ProLiant ML110 G4	HP ProLiant ML110 G5
CPU model	Intel Xeon 3040	Intel Xeon 3075
Processor (MIPS)	1860	2660
Number of cores	2	2
Memory (GB)	4	4
Network bandwidth (GB/s)	1	1

Table 2 VM detail

VM type	Core	CPU (MIPS)	Memory (MB)
High-CPU medium	1	2500	870
Extra large	1	2000	1740
Small	1	1000	1740
Micro	1	500	613

Table 3 Energy consumptions of server

Server	Sleep	0%	10%	20%	30%	40%	50%	60%	70%	80%	90%	100%
HP G4	10	86	89.4	92.6	96	99.5	102	106	108	112	114	117
HP G5	10	93.7	97	101	105	110	116	121	125	129	133	135

The exact property of hosts is given in Table 1 [16, 17]. The virtual machine also plays a vital role in process migration decisions. VM Configuration Table 2 shows VM design for this examination dependent on changing CPU and RAM. The power utilization by the server is estimated in Kilowatt each hour. Table 3 shows detail of the energy usage by servers at a different level of utilization [8, 18].

4.2 Datasets

The real dataset we utilized in this series of trials was gathered from the CoMon project, which has PlanetLab's foundation checking program [3, 16]. The PlanetLab dataset has ten different days of workload traces, and detailed characteristics are shown in Table 4 [4, 12]. In our experiment, we used all the datasets for evaluation.

Table 4 Dataset detail

Dataset Name	20110303	20110306	20110309	20110322	20110325	20110403	20110409	20110411	20110412	20110420
No. of host	800	800	800	800	800	800	800	800	800	800
No. of VM	1052	898	1061	1516	1078	1463	1358	1233	1054	1033

4.3 Evaluation Parameters

In this experiment, we use some of the well-known evaluation parameters used by most researchers to evaluate the VMC policy performance.

Energy consumption (EC): The EC parameter represents the overall energy consumed by the data center [1, 17, 19].

VM migrations (VMM): This measurement shows the absolute number of moved VMs. The higher number of VM migration violates more SLAV, and performance will degrade [20, 21].

SLA violation (SLAV): It indicates compromise with QoS. To calculate overall SLA violation, it used two different parameters like SLA violation per active host (SLATAH) and SLA violation due to migration (PDM). When the host arrives at 100%, the framework cannot satisfy the CPU demands, violating the SLA, which is known as SLATAH, and the metric formula is given in Eq. 1 [4, 9]. Many migrations will affect the system's performance, PDM, and the metric calculation formula is given in Eq. 2 [4, 5]. We can calculate overall SLA through SLATAH and PDM, and the metric formula is given in Eq. 3 [4, 7].

$$SLATAH = \frac{1}{N} \sum_{i=1}^N \frac{T_{S_i}}{T_{A_i}} \quad (1)$$

$$PDM = \frac{1}{M} \sum_{j=1}^M \frac{C_{d_j}}{C_{r_j}} \quad (2)$$

$$SLAV = SLATAH * PDM \quad (3)$$

$$ESLAV = EC * SLAV \quad (4)$$

Energy consumption and SLA violation (ESLAV): Any VMC framework should keep up with the tradeoff among EC and SLAV, so we calculate the tradeoff among EC and SLAV through Eq. 4 [9, 11]. In the given formula, the M and N address the absolute of PMs and VMs in data centers, respectively; T_{S_i} is the period when the PM usage of CPU comes to 100%; T_{A_i} represents the total time of the active host. C_{d_j} indicates the performance degradation by migration of VMs. C_{r_j} is the total CPU capacity requested by selected VMs [8, 20].

5 Experimental Results and Analysis

An experiment was carried out using ten different days of PlanetLab workload traces. We consider the default IQR policy as VM allocation policy, MC as default VM selection policy, and other parameters the same for all experiments. The experiment

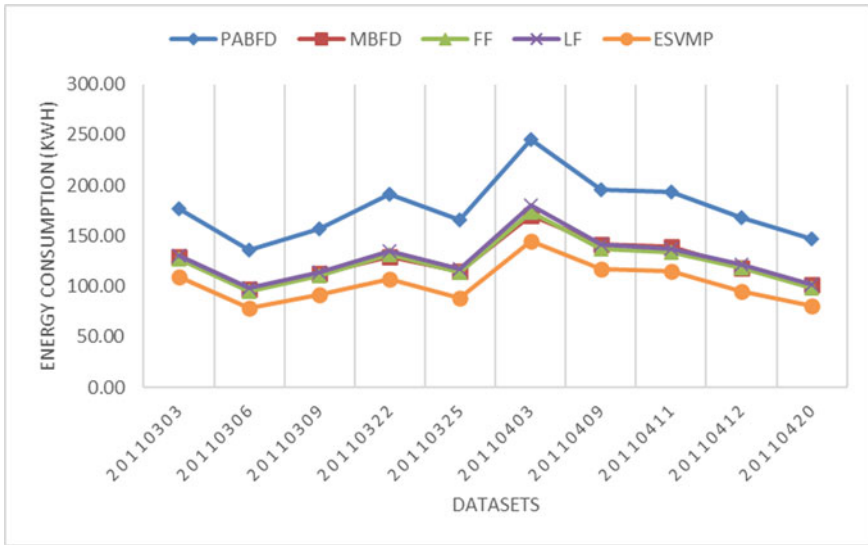


Fig. 3 EC for PlanetLab dataset

was performed for five different VM placement policies for ten different datasets, so fifty experiments will be carried out. For the comparative analysis, we represent results of three parameters, energy consumption, SLA violation, and ESLAV, which indicate the tradeoff between EC and SLAV.

Energy consumption (EC): The experiment results are shown in Fig. 3, Tables 5 and 6. The experiment results indicated that our proposed energy and SLA-aware VM placement (ESVMP) consumes less energy than other standard policies. It will give a better result for all datasets with an average of 53%, 20%, 18%, and 21%, respectively, of PABFD, MBFD, FF, and LF policy. Our modified policy finds the better destination hosts for migrating VM on the medium loaded host and checks the condition whether after the migration destination host is not overloaded.

The SLA violation parameter results are shown in Fig. 4, Tables 7 and 8. It indicates that our proposed placement scheme generates less SLA violation in almost all cases than other policies. Our proposed policy will generate higher SLATAH but minimize the PDM, so overall SLA violation will clearly show that the violation will decrease compared to standard policy because of placement modification. It will give a lower SLA violation for all datasets with an average of 27%, 20%, 15%, and 18% of PABFD, MBFD, FF, and LF policy.

The energy and SLA violation (ESLAV) parameter indicates the tradeoff between energy and SLA violation, as shown in Fig. 5, Tables 9 and 10. The ESLAV results show that the proposed modified placement policy performs better in all ten datasets. The lower ESLAV indicates good results in terms of energy and SLAV. It will give a lower ESLAV for all datasets with an average of 78%, 40%, 33%, and 39% of PABFD, MBFD, FF, and LF policy. It indicates that acceptance of our policy in both

Table 5 EC for PlanetLab dataset

Dataset	PABFD	MBFD	FF	LF	ESVMP
20110303	177.10	129.91	127.38	130.81	109.41
20110306	135.49	97.62	95.52	98.14	78.10
20110309	156.64	113.15	110.71	114.15	91.91
20110322	191.16	129.78	131.30	135.29	107.58
20110325	165.80	115.34	113.96	116.89	88.36
20110403	245.78	169.96	174.04	179.93	144.44
20110409	196.13	141.86	137.09	141.25	117.53
20110411	193.26	139.11	133.56	137.44	115.31
20110412	168.31	118.72	118.11	121.22	95.61
20110420	147.37	102.05	98.02	101.84	81.04

Table 6 EC results compared with ESVMP for PlanetLab dataset

Dataset	PABFD	MBFD	FF	LF
20110303	-47.2524	-17.1297	-15.1764	-17.8129
20110306	-53.7332	-22.2167	-20.0618	-22.7409
20110309	-52.0832	-20.7159	-18.5507	-21.581
20110322	-55.9607	-18.7085	-19.8666	-22.8219
20110325	-60.9373	-26.4886	-25.3021	-27.7945
20110403	-5 1.9402	-16.2319	-18.5886	-21.8857
20110409	-50.1127	-18.756	-15.3612	-1 8.3287
20110411	-50.5247	-1 8.7097	-14.6705	-17.5142
20110412	-55.0953	-21.5666	-21.0583	-23.6296
20110420	-58.0827	-22.9529	-18.9628	-22.746
Average	-53.5722	-20.3476	-18.7599	-21.6855

energy and SLA violation case is more. All the above parameters discussed, like EC, SLAV, and ESLAV, indicate that our policy performs better with a standard policy.

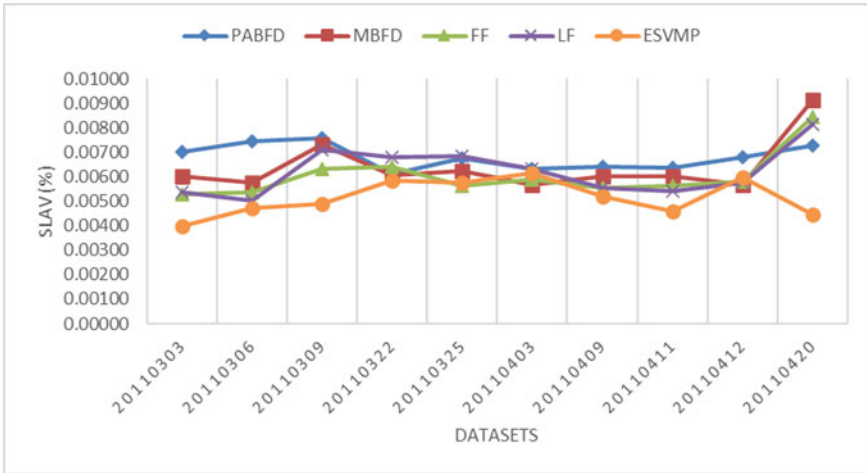


Fig. 4 SLAV for PlanetLab dataset

Table 7 SLAV for PlanetLab dataset

Dataset	PABFD	MBFD	FF	LF	ESVMP
20110303	0.00701	0.00600	0.00529	0.00538	0.00398
20110306	0.00744	0.00576	0.00538	0.00503	0.00470
20110309	0.00756	0.00734	0.00634	0.00709	0.00490
20110322	0.00609	0.00608	0.00642	0.00681	0.00587
20110325	0.00675	0.00626	0.00562	0.00685	0.00576
20110403	0.00632	0.00568	0.00590	0.00631	0.00617
20110409	0.00640	0.00600	0.00553	0.00554	0.00518
20110411	0.00638	0.00601	0.00561	0.00543	0.00461
20110412	0.00680	0.00567	0.00580	0.00578	0.00600
20110420	0.00730	0.00916	0.00844	0.00817	0.00447

Table 8 SLAV results compared with ESVMP for PlanetLab dataset

Dataset	PABFD	MBFD	FF	LF
20110303	-55.0459	-40.4807	-28.0973	-29.744
20110306	-45.0657	-20.2434	-13.3757	-6.70199
20110309	-42.7493	-39.8055	-25.5661	-36.5487
20110322	-3.71458	-3.48483	-8.9126	-14.7724
20110325	-15.9075	-8.30778	2.435407	-17.3565
20110403	-2.51733	8.158913	4.381977	-2.3837
20110409	-21.0355	-14.6466	-6.39836	-6.57034
20110411	-32.2227	-26.3406	-19.643	-16.3511
20110412	-12.5139	5.54536	3.395974	3.617696
20110420	-48.1787	-68.9417	-61.6294	-58.5903
Average	-27.8951	-20.8547	-15.3409	-18.5401

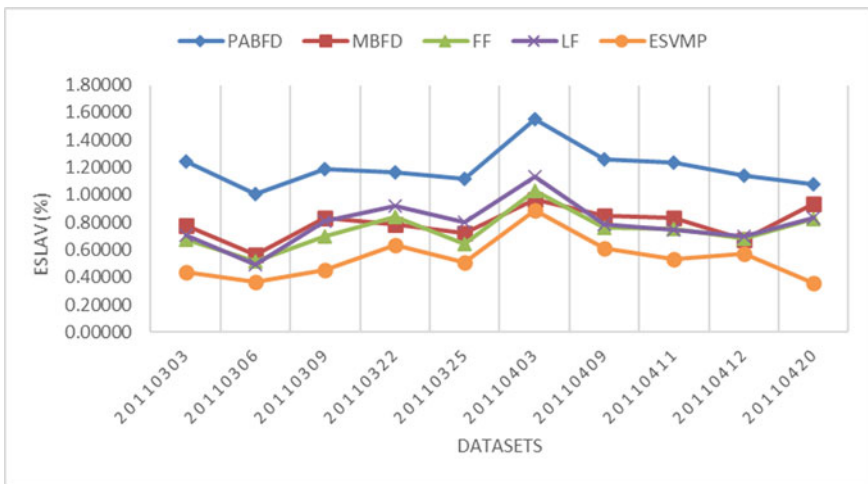


Fig. 5 ESLAV for PlanetLab dataset

Table 9 ESLAV for PlanetLab dataset

Dataset	PABFD	MBFD	FF	LF	ESVMP
20110303	1.24124	0.78009	0.67325	0.70309	0.43581
20110306	1.00766	0.56241	0.51351	0.49347	0.36724
20110309	1.18491	0.83004	0.70151	0.80950	0.45040
20110322	1.16470	0.78888	0.84272	0.92089	0.63152
20110325	1.11981	0.72178	0.64045	0.80104	0.50885
20110403	1.55417	0.96583	1.02715	1.13628	0.89064
20110409	1.25560	0.85154	0.75758	0.78190	0.60923
20110411	1.23285	0.83563	0.74967	0.74626	0.53144
20110412	1.14410	0.67354	0.68466	0.70116	0.57336
20110420	1.07579	0.93517	0.82760	0.83161	0.36189

Table 10 ESLAV results compared with ESVMP for PlanetLab dataset

Dataset	PABFD	MBFD	FF	LF
20110303	-96.0524	-56.6287	-42.8172	-46.9352
20110306	-93.1592	-41.988	-33.2147	-29.3311
20110309	-89.8321	-59.2989	-43.5999	-57.0057
20110322	-59.3668	-22.1572	-28.6524	-37.28
20110325	-75.0266	-34.606	-22.902	-44.613
20110403	-54.2802	-8.09979	-14.2356	-24.2378
20110409	-69.3213	-33.1747	-21.7062	-24.8243
20110411	-79.5113	-44.502	-34.0681	-33.6246
20110412	-66.4637	-16.0693	-17.694	-20.0548
20110420	-99.3136	-88.3975	-78.3044	-78.7137
Average	-78.2327	-40.4922	-33.7194	-39.662

6 Conclusion

In cloud computing, energy consumption by data centers is high, so many researchers are committed to addressing the problem. VMC is one technique used to hold down the energy used in the cloud data centers by limiting the hosts to serve the user request. In this study, we address the issue of VM placement by proposing a new efficient energy and SLAV-aware VM placement (ESVMP) strategy. The investigation was performed on proposed and standard methodologies for ten consistent PlanetLab datasets. The exhibition of the proposed strategy is to improve further energy utilization and SLA infringement contrasted with standard policies. Our proposed ESVMP algorithm shows better performance with less power consumption (EC) of all datasets average by 53%, 20%, 18%, and 21%, and it also violates less SLA (SLAV) by 27%, 20%, 15%, and 18% and minimizes the tradeoff between EC and SLAV (ESLAV) with an average of 78%, 40%, 33%, and 39% compared to PABFD, MBFD, FF, and LF algorithms. So based on performance results, we can state that our proposed ESVMP algorithms outperform compared to PABFD, MBFD, FF, and LF. As a future direction, we will try to work on the real implementation of the proposed algorithm.

References

1. Addya SK, Turuk AK, Sahoo B, Sarkar M, Biswash SK (2017) Simulated annealing based VM placement strategy to maximize the profit for cloud service providers. *Eng Sci Technol Int J* 20(4):1249–1259
2. Baskaran N, Eswari R (2018) Adaptive threshold-based algorithm for multi-objective vm placement in cloud data centers. In: *International conference on frontier computing*. Springer, Singapore, pp 118–129
3. Mapetu JPB, Kong L, Chen Z (2021) A dynamic VM consolidation approach based on load balancing using Pearson correlation in cloud computing. *J Supercomput* 77(6):5840–5881
4. Beloglazov A (2013) Energy-efficient management of virtual machines in data centers for cloud computing (Doctoral dissertation)
5. Alboaneen DA, Tianfield H, Zhang Y (2016) Glowworm swarm optimisation algorithm for virtual machine placement in cloud computing. In: *2016 Intl IEEE conferences on ubiquitous intelligence & computing, advanced and trusted computing, scalable computing and communications, cloud and big data computing, internet of people, and smart world congress*. IEEE, pp 808–814
6. Singh P, Sengupta J, Suri PK (2019) A novel approach of virtual machine consolidation for energy efficiency and reducing sla violation in data centers. *Int J Innovative Technol Exploring Eng* 8:547–555
7. Gohil B, Shah S, Golechha Y, Patel D (2016) A comparative analysis of virtual machine placement techniques in the cloud environment. *Int J Comput Appl* 156(14)
8. Hamdi N, Chainbi W (2019) A survey on energy aware VM consolidation strategies. *Sustain Comput Inform Syst* 23:80–87
9. Gohil BN, Gamit S, Patel DR (2021) Fair Fit—a load balance aware VM placement algorithm in cloud data centers. In: *Advances in communication and computational technology*. Springer, Singapore, pp 437–451
10. Dubey K, Nasr AA, Sharma SC, El-Bahnasawy N, Attiya G, El-Sayed A (2020) Efficient vm placement policy for data centre in cloud environment. *Soft Comput Theor Appl* 301–309

11. Renugadevi T, Geetha K, Prabakaran N, Siano P (2020) Carbon-efficient virtual machine placement based on dynamic voltage frequency scaling in geo-distributed cloud data centers. *Appl Sci* 10(8):2701
12. Moges FF, Abebe SL (2019) Energy-aware VM placement algorithms for the OpenStack Neat consolidation framework. *J Cloud Comput* 8(1):1–14
13. Yun HY, Jin SH, Kim KS (2021) Workload stability-aware virtual machine consolidation using adaptive harmony search in cloud datacenters. *Appl Sci* 11(2):798
14. Wang H, Tianfield H (2018) Energy-aware dynamic virtual machine consolidation for cloud datacenters. *IEEE Access* 6:15259–15273
15. Liu Y, Sun X, Wei W, Jing W (2018) Enhancing energy-efficient and QoS dynamic virtual machine consolidation method in cloud environment. *IEEE Access* 6:31224–31235
16. Jangiti S, Ram ES, Sriram VS (2019) Aggregated rank in first-fit-decreasing for green cloud computing. In: *Cognitive informatics and soft computing*. Springer, Singapore, pp 545–555
17. Nazir B (2018) QoS-aware VM placement and migration for hybrid cloud infrastructure. *J Supercomput* 74(9):4623–4646
18. Li Z, Yu X, Yu L, Guo S, Chang V (2020) Energy-efficient and quality-aware VM consolidation method. *Futur Gener Comput Syst* 102:789–809
19. Zhou Q, Xu M, Gill SS, Gao C, Tian W, Xu C, Buyya R (2020) Energy efficient algorithms based on VM consolidation for cloud computing: comparisons and evaluations. In: *2020 20th IEEE/ACM international symposium on cluster, cloud and internet computing (CCGRID)*. IEEE, pp 489–498
20. Khattar N, Singh J, Sidhu J (2020) An energy efficient and adaptive threshold VM consolidation framework for cloud environment. *Wireless Pers Commun* 113(1):349–367
21. Li H, Li T, Shuhua Z (2018) Energy-performance optimisation for the dynamic consolidation of virtual machines in cloud computing. *Int J Serv Oper Inf* 9(1):62–82

Analysis and Prevention of Denial of Service Attacks in Smart Grid Using IoT



Harsh Kakadiya , Janavi Popat, Neeraj Kumar Singh , Lalit Tak , Mahshooq Abdul Majeed , Soumya Mudgal, and Vasundhara Mahajan 

Abstract Smart grid and its undiscovered cyber vulnerabilities have arisen requirement of efficient and reliable methods for prevention, protection, detection and repairation. The article classifies and discusses different methods of performing denial of service (DoS) and distributed denial of service (DDoS) attacks and analyzes Packet Internet Groper (PING)/Internet Control Message Protocol (ICMP) flooding method in smart grid using a hardware prototype. Methods of prevention of bandwidth depletion and resource depletion attacks are classified and discussed in brief.

Keywords Denial of service attack · Distributed denial of service attack · Prevention · Smart grid

1 Introduction

Introduction of integrating information and communication technology (ICT) with the existing power grid and making it smart is to provide a reliable and faster communication network which allows bidirectional flow of energy as well as information [1, 2]. This makes it a cyber-physical power system (CPPS) which is vulnerable to malicious attacks that affects the availability, integrity, confidentiality, accountability and consequently, the reliability of the system [3]. Compared with the moderately simpler conventional power system, the research on security of smart grid is in underlying stage [4]. When a fault occurs in the conventional power system, it is generally due to physical failure but along with having physical uncertainties, smart grid is vulnerable to communication and cyber-based attacks too. This expands research areas for protection of smart grid from cyber-attacks, prevention and detection of them, as well as efficient repairing methods after attack is happened [5].

Denial of service (DoS) and distributed denial of service (DDoS) are the most common type of malicious attacks which affect availability of the power system. It

H. Kakadiya · J. Popat · N. K. Singh · L. Tak · M. A. Majeed · S. Mudgal · V. Mahajan (✉)
Electrical Engineering Department, Sardar Vallabhbhai National Institute of Technology, Surat,
Gujarat, India
e-mail: vmahajan@eed.svnit.ac.in

Table 1 Difference between DoS and DDoS attacks

Denial of service	Distributed denial of service
Victim is attacked using only one device	Victim is attacked by numerous devices
Detection is easier compared to DDoS as only one IP address is associated	Detection of attack is difficult compared to DoS as multiple IP addresses are associated
Effectiveness is lesser compared to DDoS	Effectiveness of attack is multiplied by adding devices

aims to revoke the user access from a particular web server, website or a device by flooding them. Both attacks have purpose but follows different methods to attack the victim system which are listed in Table 1.

Section 2 describes various techniques and taxonomy of DoS and DDoS attacks in CPPS. Section 3 includes literature survey of prevention techniques for DoS and DDoS attacks. In this article, ICMP flooding is analyzed. Section 4 narrates hardware prototype used for the experiment and how Internet of Things (IoT) devices are analogous elements of smart grid. In Sect. 5, attack is analyzed using mobile application and command line.

2 Classification and Taxonomy of DoS and DDoS Attacks

DoS and DDoS attacks can be performed by various flooding techniques which are classified in hierarchical structure as shown in Fig. 1.

In Fig. 1, these are classified in two major categories, 1. bandwidth depletion attack and 2. resource depletion attack [6].

In bandwidth depletion attacks, the victim network is flooded by various methods, further classified as direct flooding and amplification-based flooding. Direct flooding is further classified depending upon which network protocol layer is attacked, i.e., User Datagram Protocol (UDP) flood [7], Internet Control Message Protocol (ICMP)/Packet Internet Groper (PING) flood [8] and Domain Name System (DNS) flood [9]. In amplification-based flooding, attacker sends messages to broadcast Internet Protocol (IP) address, and the sub networks attacked by attacker, send a reply to the victim system which results in amplification of data and congestion of bandwidth [10, 11].

Resource depletion attacks refer to targeting resources of the victim system [12], i.e., server or process which in turn makes the victim system unable to provide the service. Protocol exploitation flooding and reflection-based flooding are main types of resource depletion attacks. Protocol exploitation flooding includes synchronize (SYN) flood, acknowledge (ACK) flood, SYN ACK flood and ACK PUSH flood, and Smurf attack is an example of reflection-based flooding [13].

Attacks in CPPS can be classified in four categories based on their taxonomy: 1. cyber based, 2. network based, 3. physical based and 4. communication based

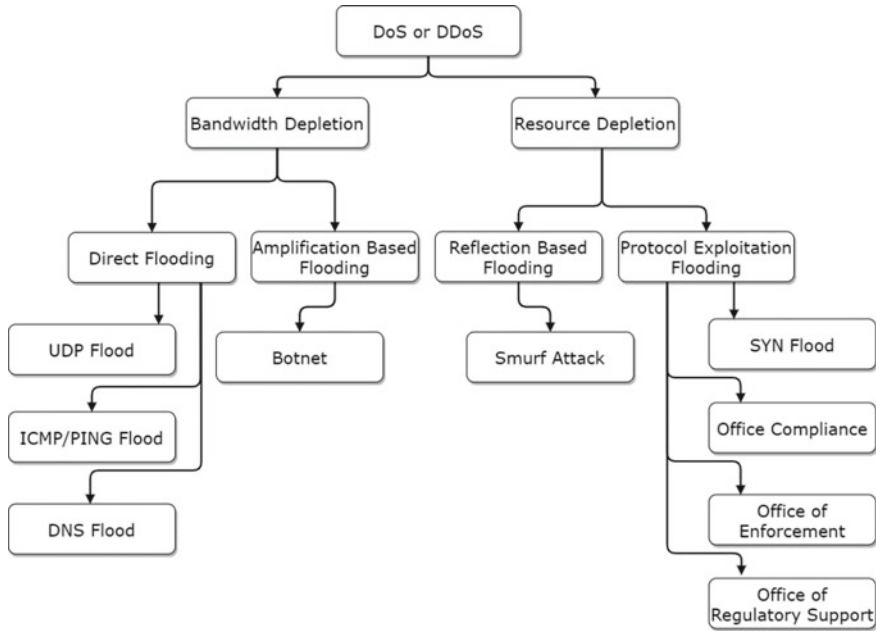


Fig. 1 Classification of DoS and DDoS attacks

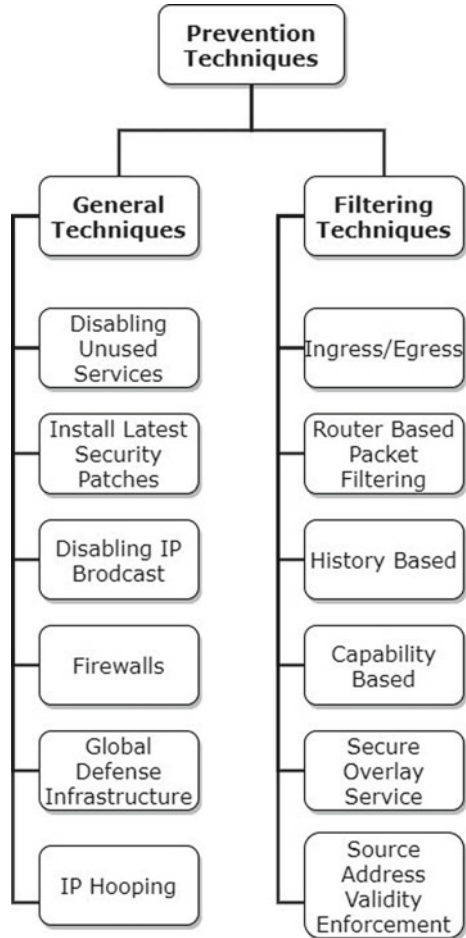
[1]. DoS and DDoS attacks are main network-based attacks. They make the virtual network inaccessible without altering physical communication system. This makes the system unavailable for victim and results in loss of information, time and money. Taxonomy of DoS and DDoS attacks are further classified based on scanning methods, spoofing methods, target and impact [14].

3 Prevention of Denial of Service and Distributed Denial of Service Attacks in Smart Grid

Prevention methods for DOS or DDOS are mainly classified in two categories as shown in Fig. 2 [15, 16]:

General methods of prevention refer to the basic precaution which can be taken by the user in order to prevent the DoS or DDoS attack. Disabling unused services decreases the number of vulnerable nodes which reduces the chances of exploitation. Latest security patches remove known security ports [17]. Disabling IP broadcast ensures prevention against ICMP flood and Smurf attacks [18]. Firewalls can prevent simple attacks but are not efficient enough to prevent the attack on web server [19, 20]. Global defense infrastructure is hypothetical concept refers to installing security filters in important router which is not feasible due to variation of security policies

Fig. 2 Classification of prevention methods of DoS and DDoS attacks



according to administration [21]. IP hooping ensures prevention from DoS and DDoS attacks which are based on IP addresses because the method changes the IP address within a pre-specified range [21, 22].

Ingress filtering reduces the traffic by restricting IP address with different domain prefix [23], while egress filtering allows only assigned IP address to leave the network [24, 25]. Router-based packet filtering is advanced version of ingress filtering which filters only spoofed IP addresses [26, 27]. In history-based IP filtering, frequent source IP addresses are kept in IP Address Database (IAD) and the packets other than part of IAD are dropped [28, 29]. In capability-based filtering, packets are assigned their capability by destination and when congestion takes place, packets without capability might get dropped [30, 31]. Secure Overlay Service (SOS) architecture allows communication between victim and specified users only [32]. Using Source

Address Validity Enforcement (SAVE), routers can update the information of source IP address and can block the data packets with another IP address [33].

4 Proposed System and Its Description

Two NodeMCU ICs are used, one as station (STA) mode and another as soft access point (soft AP) mode which contains Wi-Fi chipset known as ESP8266. In AP mode, it creates a Wi-Fi network which acts as a server for other devices. It sets Service Set Identifier (SSID), IP address and password through which other devices can be connected and it can also deliver web pages to all the connected devices under its own network. It allows to connect maximum five devices to the network. In both soft AP and station mode, NodeMCU can create and deliver webpages to all connected devices, but in station mode, it uses connected Wi-Fi router as server and in the soft AP mode, it has its own Wi-Fi server.

The station model is connected with several various LEDs which can be controlled through the AP. In a smart grid, various electrical appliances are connected to the network which is signified by LEDs in our prototype. In the proposed prototype, LEDs can be controlled using NodeMCU as shown in Fig. 3. But when DoS or DDoS attack takes place, the user loses the control which is equivalent to the loss of data in the smart grid.

For constructing algorithm and uploading the program into NodeMCU using USB cable, Arduino IDE was used. Arduino IDE is an open source software with huge set of libraries available. Libraries required for the purpose are ESP8266WiFi and ESP8266WebServer. Pointer variables *ssid and *password are mandatory to create its own web server. Local IP addresses, gateway and subnet are assigned to NodeMCU used in AP mode. Other IoT devices can be connected with it by accessing the IP

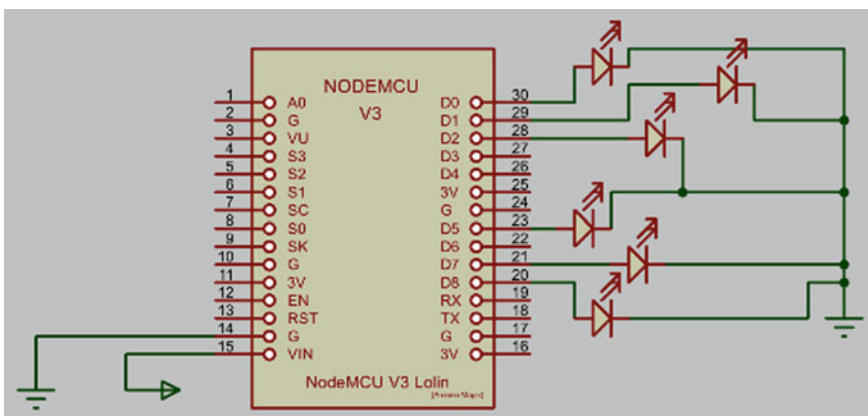


Fig. 3 NodeMCU circuit

address using the SSID and password assigned to it. ESP8266WebServer command allows configuring the IoT device with server on port 80.

Source Code:

```
#include <ESP8266WiFi.h>
#include <ESP8266WebServer.h>
const char* ssid = "Your_User_Name";
IPAddress local_ip(192,168,1,1);
IPAddress gateway(192,168,1,1);
IPAddress subnet(255,255,255,0);
ESP8266WebServer server(80);
```

5 Procedure to Get Access on Remote Terminal Unit

As shown in Figs. 4 and 5, in DoS attack, only one attacker is indulged, while DDoS uses multiple attackers.

Figure 6 describes how malware devices get access to the victim and data loss occurs. After getting connected to network, IPCONFIG command is used to get Layer 3 information (generally layer 3 contains network layer information) which contains IP address, default gateway and subnet mask. As shown in Fig. 7, server was pinged by getting address of default gateway.

Ping mobile application was used to send data packets of size 64 bytes through ICMP and flood the network as shown in Fig. 8. By using command line, attacker can ping server with data packets of 32 bytes using following command as shown in Fig. 9:

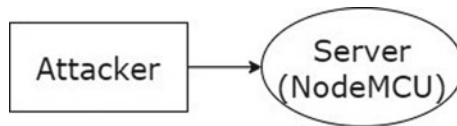


Fig. 4 Flow of denial of service attack

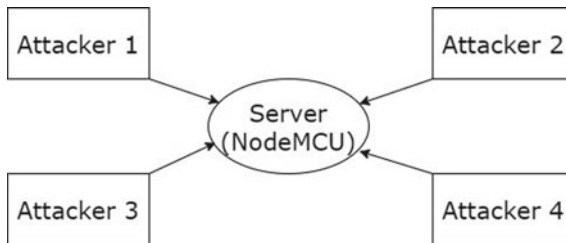


Fig. 5 Flow of distributed denial of service attack

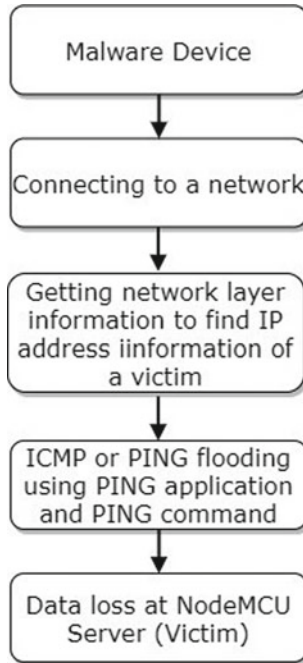


Fig. 6 Flow of attack in experiment

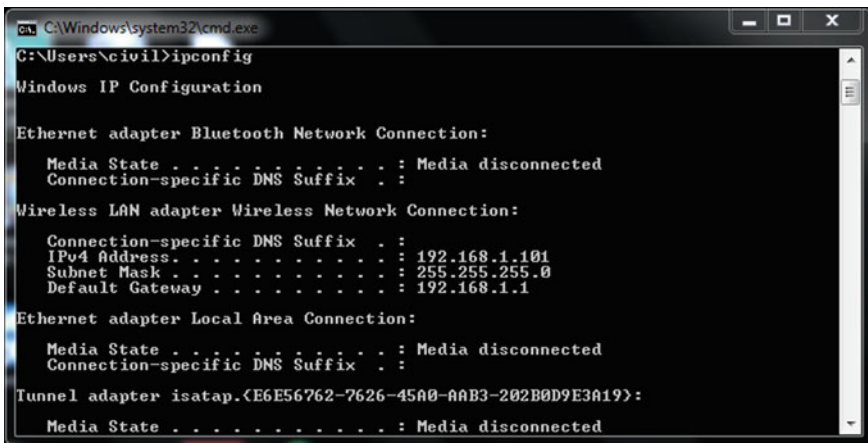


Fig. 7 Getting information of IP address

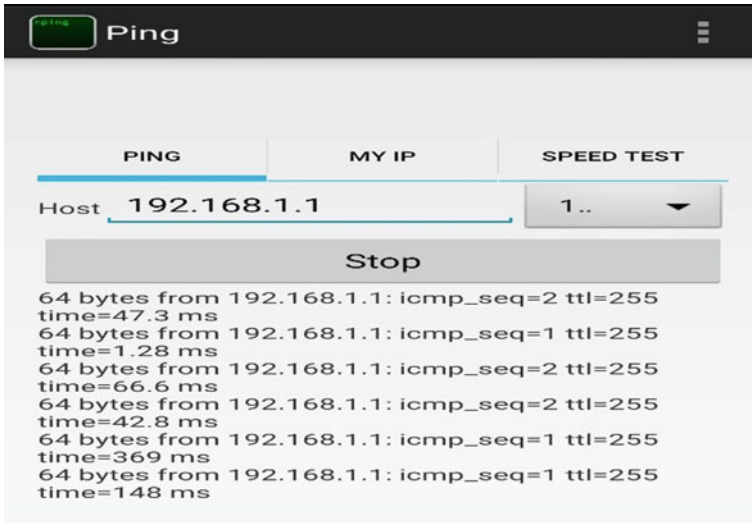


Fig. 8 ICMP flooding using ping application

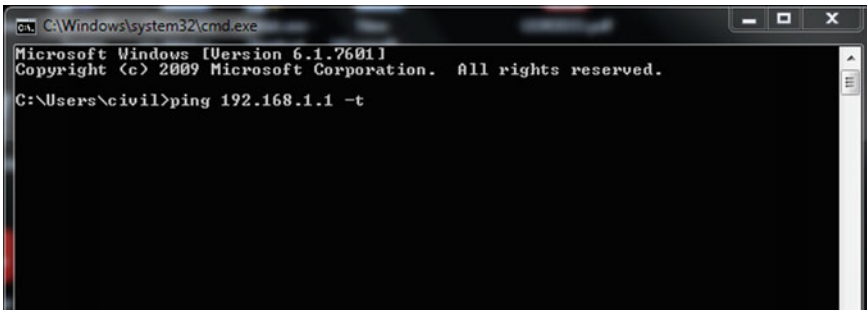


Fig. 9 PING flooding command

```
ping 192.168.1.1 -t
```

Where, ping command is used to send data packets to the victim, “192.168.1.1” is victim’s IP address, -t stands for sending infinite data packets.

Infinite data packets of 32 bytes are sent to the specified IP address which is evidenced in Fig. 10.

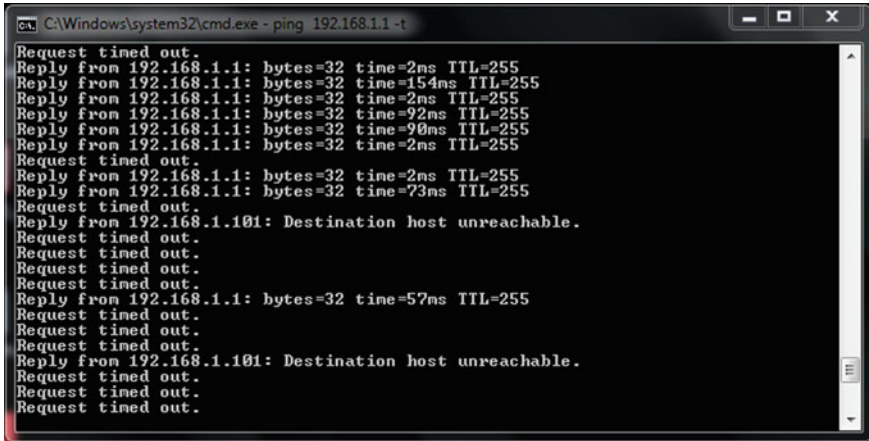


Fig. 10 PING flooding using command line

6 Proposed Method for Prevention

In this experiment, a password is added which makes the network private and only those who know it can get access. Other malware devices or attackers who do not know password, cannot connect to network. So chances of malware intrusion in the network can be decreased (Fig. 11).

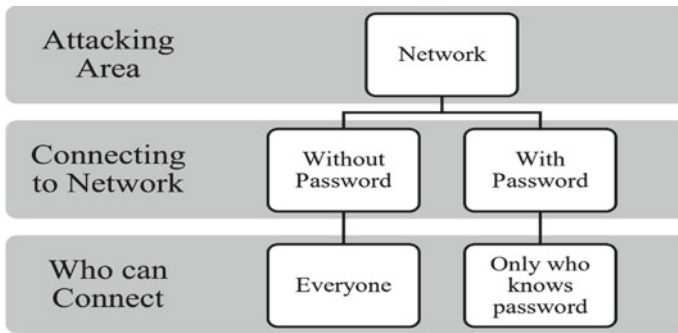


Fig. 11 Prevention using password

7 Conclusion

In this article, a network analogous to a smart grid is proposed using IoT devices. Availability of power plays a crucial role in our day-to-day lives. For the continuous operation of CPPS, it is necessary to prevent malicious DoS and DDoS attacks. Analyzing the vulnerabilities in the network is an essential step before researching its prevention. These attacks can take place by various methods among which ICMP/PING flooding was analyzed. In these flooding, attackers can use mobile application as well as command line interface by which services becomes inaccessible to victims. In order to prevent these attacks, general prevention technique to make the network private using password was used. By preventing the malware devices to access the network, vulnerabilities can be reduced to some extent. Prevention and detection techniques become more reliable when a device with high power capacity is used as a server. This research can be further expanded by implementing more suitable prevention and detection techniques.

References

1. Musleh AS, Chen G, Dong ZY (2020) A survey on the detection algorithms for false data injection attacks in smart grids. *IEEE Trans Smart Grid* 11(3):2218–2234. <https://doi.org/10.1109/TSG.2019.2949998>
2. Popat J, Kakadiya H, Tak L, Singh NK, Majeed MA, Mahajan V (2021) Reliability of smart grid including cyber impact: a case study. In: Singh R, Singh AK, Dwivedi AK, Nagabushan P (eds) *Advances in computer and electrical engineering*. IGI Global, pp 163–174. <https://doi.org/10.4018/978-1-7998-3327-7.ch013>
3. Singh NK, Mahajan V (2021) Analysis and evaluation of cyber-attack impact on critical power system infrastructure. *Smart Science* 9(1):1–13. <https://doi.org/10.1080/23080477.2020.1861502>
4. Wang Q, Tai W, Tang Y, Ni M (2019) Review of the false data injection attack against the cyber-physical power system. *IET Cyber-Phys Syst* 4(2):101–107. <https://doi.org/10.1049/iet-cps.2018.5022>
5. Singh NK, Mahajan V (2019) Smart Grid: cyber attack identification and recovery approach. In: 2019 2nd International conference on innovations in electronics, signal processing and communication (IESC), Shillong, India, pp 1–5. <https://doi.org/10.1109/IESPC.2019.8902401>
6. Sonar K, Upadhyay H, A survey: DDOS attack on Internet of Things, p 7
7. Kolahi SS, Treseangrat K, Sarrafpour B (2015) Analysis of UDP DDoS flood cyber attack and defense mechanisms on Web Server with Linux Ubuntu 13. In: 2015 International conference on communications, signal processing, and their applications (ICCSPA'15), Sharjah, United Arab Emirates, pp 1–5. <https://doi.org/10.1109/ICCSPA.2015.7081286>
8. Conta A, Deering S, Internet control message protocol (ICMPv6) for the Internet protocol version 6 (IPv6) specification, p 55
9. Rastegari S, Saripan MI, Rasid MFA (2009) Detection of denial of service attacks against domain name system using neural networks. [arXiv:0912.1815](https://arxiv.org/abs/0912.1815) [cs]. Accessed 11 Oct 2021. (Online). Available: <http://arxiv.org/abs/0912.1815>
10. Kambourakis G, Moschos T, Geneiatakis D, Gritzalis S (2008) Detecting DNS amplification attacks. In: Lopez J, Häggerli BM (eds) *Critical information infrastructures security*, vol. 5141. Berlin, Heidelberg: Springer Berlin Heidelberg, pp 185–196. https://doi.org/10.1007/978-3-540-89173-4_16

11. Bhosale KS, Nenova M, Iliev G (2017) The distributed denial of service attacks (DDoS) prevention mechanisms on application layer. In: 2017 13th International conference on advanced technologies, systems and services in telecommunications (TELSIKS), Nis, Oct 2017, pp 136–139. <https://doi.org/10.1109/TELSIKS.2017.8246247>
12. Douligeris C, Mitrokotsa A (2004) DDoS attacks and defense mechanisms: a classification. In: Proceedings of the 3rd IEEE international symposium on signal processing and information technology (IEEE Cat. No.03EX795), Darmstadt, Germany, 2004, pp 190–193. <https://doi.org/10.1109/ISSPIT.2003.1341092>
13. Kumar S (2007) Smurf-based distributed denial of service (DDoS) attack amplification in Internet. In: Second international conference on internet monitoring and protection (ICIMP 2007), San Jose, CA, USA, pp 25–25. <https://doi.org/10.1109/ICIMP.2007.42>
14. Gu Q, Liu P, Denial of service attacks. p 28
15. Zargar ST, Joshi J, Tipper D (2013) A survey of defense mechanisms against distributed denial of service (DDoS) flooding attacks. *IEEE Commun Surv Tutor* 15(4):2046–2069. <https://doi.org/10.1109/SURV.2013.031413.00127>
16. Gupta BB, Joshi RC, Misra M (2012) Distributed denial of service prevention techniques. [arXiv:1208.3557](https://arxiv.org/abs/1208.3557) [cs]. Accessed 11 Oct 2021. (Online). Available: <http://arxiv.org/abs/1208.3557>
17. Geng X, Whinston AB (2000) Defeating distributed denial of service attacks. *IT Prof* 2(4):36–42. <https://doi.org/10.1109/6294.869381>
18. Lau F, Rubin SH, Smith MH, Trajkovic L (2000) Distributed denial of service attacks. In: SMC 2000 conference proceedings. 2000 IEEE international conference on systems, man and cybernetics. “cybernetics evolving to systems, humans, organizations, and their complex interactions” (Cat. No.00CH37166), Nashville, TN, USA, vol 3, pp 2275–2280. <https://doi.org/10.1109/ICSMC.2000.886455>
19. Gupta BB, Joshi RC, Misra M (2009) Defending against distributed denial of service attacks: issues and challenges. *Inf Secur J A Global Perspect* 18(5):224–247. <https://doi.org/10.1080/19393550903317070>
20. Rengaraju P, Ramanan VR, Lung C-H (2017) Detection and prevention of DoS attacks in software-defined cloud networks. In: 2017 IEEE conference on dependable and secure computing, Taipei, Taiwan, pp 217–223. <https://doi.org/10.1109/DESEC.2017.8073810>
21. Zhang G, Parashar M (2006) Cooperative defence against DDoS attacks. *J Res Pract Inf Technol* 38(1):16
22. Chang RKC (2002) Defending against flooding-based distributed denial-of-service attacks: a tutorial. *IEEE Commun Mag* 40(10):42–51. <https://doi.org/10.1109/MCOM.2002.1039856>
23. Alqurashi RK, Al-harathi OS, Alzahrani SM (2020) Detection of IP spoofing attack. *Int J Eng Res Technol* 13(10):2736. <https://doi.org/10.37624/IJERT/13.10.2020.2736-2741>
24. Murdoch SJ, Seng D, Schafer B, Mason S, The sources and characteristics of electronic. p 51
25. Du P, Nakao A (2010) DDoS defense deployment with network egress and ingress filtering. In: 2010 IEEE international conference on communications, Cape Town, South Africa, May 2010, pp 1–6. <https://doi.org/10.1109/ICC.2010.5502654>
26. Kim Y, Lau WC, Chuah MC, Chao HJ (2006) PacketScore: a statistics-based packet filtering scheme against distributed denial-of-service attacks. *IEEE Trans Dependable Secure Comput* 3(2):141–155. <https://doi.org/10.1109/TDSC.2006.25>
27. Park K, Lee H (2001) On the effectiveness of route-based packet filtering for distributed DoS attack prevention in power-law internets. *SIGCOMM Comput. Commun Rev* 31(4):15–26. <https://doi.org/10.1145/964723.383061>
28. Zhou C, Leckie C, Ramamohanarao K (2009) Protecting SIP server from CPU-based DoS attacks using history-based IP filtering. *IEEE Commun Lett* 13(10):800–802. <https://doi.org/10.1109/LCOMM.2009.090840>
29. Peng T, Leckie C, Ramamohanarao K (2003) Protection from distributed denial of service attacks using history-based IP filtering. In: IEEE international conference on communications, 2003. ICC '03, Anchorage, AK, USA, vol 1, pp 482–486. <https://doi.org/10.1109/ICC.2003.1204223>

30. Duran-Sindreu M, Choi J, Bonache J, Martin F, Itoh T (2013) Dual-band leaky wave antenna with filtering capability based on extended-composite right/left-handed transmission lines. In: 2013 IEEE MTT-S international microwave symposium digest (MTT), Seattle, WA, USA, pp 1–4. <https://doi.org/10.1109/MWSYM.2013.6697379>
31. Anderson T, Roscoe T, Wetherall D (2004) Preventing Internet denial-of-service with capabilities. *SIGCOMM Comput Commun Rev* 34(1):39–44. <https://doi.org/10.1145/972374.972382>
32. Keromytis AD, Misra V, Rubenstein D (2002) SOS: secure overlay services. *SIGCOMM Comput Commun Rev* 32(4):61–72. <https://doi.org/10.1145/964725.633032>
33. Li J, Mirkovic, Mengqiu Wang, P. Reiher, and Lixia Zhang (2002) SAVE: source address validity enforcement protocol. In: Proceedings. Twenty-First annual joint conference of the IEEE computer and communications societies, New York, NY, USA, vol 3, pp 1557–1566. <https://doi.org/10.1109/INFCOM.2002.1019407>

Convolutional Neural Network-Based Contemporaneous Human Facial Expression Identification



B. K. Harsha, M. L. J. Shruthi, and G. Indumathi

Abstract In this paper, we discuss the use of facial expression in tandem with feature extraction and neural network to recognize distinct facial emotions like happy, sad, angry, surprised, and neutral. We look at the limitations of existing emotion identification algorithms using convolutional neural networks on CK+ and modified FER13 datasets and achieved decent prediction. Expression recognition utilizing a brain activity system is more difficult and time-consuming than facial emotion recognition using CNN. Alongside with recognizing the user's emotion, the paper also aims to analyze and generate an emotion log file comprising all of the emotions recorded with a time stamp. We have achieved 97.87% accuracy on FER13 dataset, and for CK+ dataset in testing, we got 94.93% of accuracy.

Keywords Real time · Emotion recognition · Convolutional neural network · Emotion analyzer · Emotion logging

1 Introduction

Considering face is one of our most significant resources, the face has also been nicknamed “the organ of emotion,” and it is true that it reveals important information about our own feelings as well as those of others. How important are human emotion in real life: A person's emotions can have a significant impact on how he or she think experiences in life can push us to act and affect the big and small decisions we make throughout our lives. Using sophisticated photo dispensation techniques, a machine can assess the feelings on a human face using emotion recognition. To understand

B. K. Harsha (✉)

Department of ECE, VTU RC, CMR Institute of Technology, Bengaluru, Karnataka, India
e-mail: harsha405@gmail.com

M. L. J. Shruthi

Department of ECE, PES University, Bengaluru, Karnataka, India

G. Indumathi

Department of ECE, VTU RC, Cambridge Institute of Technology, Bengaluru, India

more about what a video or photograph of a person's face tells us about them, many firms have been experimenting with a combination of advanced mathematics and image processing approaches that have evolved in the previous decade. With the help of CNN, this paper aims to recognize emotions in real time by developing an automated system that analyzes human facial expressions.

The work is distributed as, in Sect. 2, the focus is on the existing literature of the emotion recognition systems which states about strengths, results, and limitations of some of the existing models. In Sect. 3, we discuss about the proposed approach, convolutional neural network [1] used in along with its different basic and activation layers. In the fourth section, we discuss about the implementation details, the modules, and the packages used in the system. In Sect. 5, we discuss about experimental outcomes of the model.

2 Related Work

Without knowing about some of the previously existing literatures and their pros, cons, and limitations, it is not good to make any justifications on any model. Hence, in this section, we briefly take a note on some of the previously existing literatures that help us in improving our model by knowing the results and their limitations.

Many attempts have been made to create automatic facial expression [2] analysis tools [3] because they have applications in a variety of fields, including robotics, medicine, driving assist systems, and lie detectors [4–6]. The fundamental facial expressions, independent of the person's culture is discussed in [7]. Recent research on facial recognition technology, FERET dataset, Sajid et al. [8] examined the effect of geometry of the face for measuring and assessment of age. Convolutional networks can be used to solve a variety of issues, such as excessive makeup [9], expression, and poses [10]; the most important is lie detection.

For face emotion recognition in students, Lasri et al. [1] suggested a convolutional neural network model. The proposed model includes two fully connected layers as well as four convolutional layers and four maximum pooling layers. Using a Haar-like detector, children's faces are input, and their emotions are classified into surprise, fear, disgust, sadness, happiness, rage, and neutrality.

Oktavia et al. [11] present a study on emotion recognition in humans based on Electroencephalogram (EEG) categorization. The basic concept is to capture the EEG data and then analyze the emotions. They detected the expression with an accuracy of 87.5%. The research has its own limits, such as the expensive equipment utilized, which has a complex operational process. Their classification was limited to happy and sad emotions only.

Ayvaz et al. [12] present a paper on expression identification system applied to faces, with an idea to identify the human motion based on machine learning algorithms. The paper claims to have better expression recognition rates. This concludes that KNN and SVM-based machine learning algorithms give the best accuracy rates.

Tang et al. [13] suggested a FER system that uses the KNN algorithm to estimate the effectiveness of classroom teaching by analyzing students' emotions with face as input. The work claims good results, but the system has certain flaws, such as the emotion prediction step being slow when using vast data and the system being sensitive to data scale and irrelevant information.

In Taghi et al. [14], a work has been presented to identify face using Gabor filter to extract features. The work presented that the Gabor filters can be used to extract features aligned to specific angles from photos. The work was carried out using the JAFFE dataset; the authors were able to attain a 91 percent accuracy rate. Because of the Gabor filters feature dimension, it takes an excessive amount of time to extract features. The vector is rather long and has a lot of characteristics that are redundant. The downside of the recognition rate in the proposed is due to redundancy.

Ghaffar [15] proposed a facial emotion recognition system using CNN. The was intended to detect seven emotions using JAFFE and KDEF datasets and achieved maximum accuracy rate of 78% using combined datasets. They understood preprocessing stage is more important from getting poor results due to loss of many features in preprocessing stage.

3 Proposed Approach

The plan of action is explained for analyzing human face expressions using CNN. The algorithm first detects the face in the collected frame, which is then cropped and normalized to a size of 224×224 . The CNN model uses these facial photos as input. The face expression recognition findings are the final product that is belonging to one among the anger, neutral, happy, sad, or surprise emotions. The model flow of the planned activity is as depicted in Fig. 1.

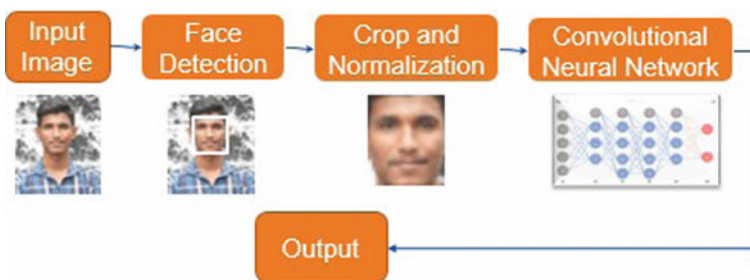


Fig. 1 Model flow of emotion recognition system

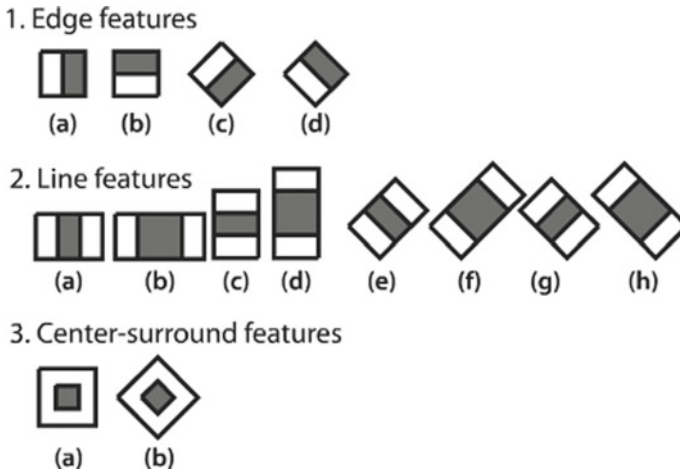


Fig. 2 1(a), 1(b), 1(c), 1(d) are the edge features. 2(a), 2(b), 2(c), 2(d), 2(e), 2(f), 2(g), 2(h) are the line features, and 3(a), 3(b) are the center-surround features of the Haar cascade filters [16]

3.1 Usage of Haar Cascade for Face Detection

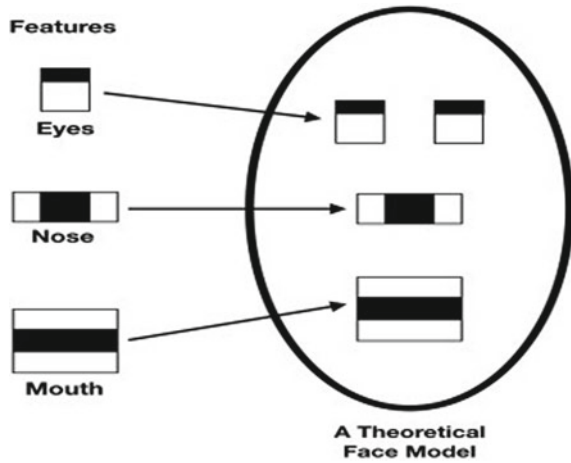
Haar cascade is an object identification algorithm that detects faces in photos or real-time video. The Haar cascade is a form of “filter” that extracts features from images, comparable to the concept of the convolutional kernel. Haar characteristics are a type of filter that looks alike. Figure 2 which can be visualized as 1 is the edge features of the Haar cascade filters; 2 shows the different line features of the Haar cascade filters, while 3 is the center-surround features of the Haar cascade filters [16].

In feature extraction, a training dataset is used to determine which features of a face should be examined by the algorithm [17]. A function is trained using machine learning techniques through a massive number of true and false images. The theoretical face with the help of Haar cascade can be visualized as in Fig. 3.

3.2 Convolutional Neural Network (CNN)

The terminology stated is a branch of artificial neural network that is specifically built using deep learning, CNNs can do both generative and descriptive tasks and are often used in image and video processing, machine learning, and also recommendations.

Fig. 3 Facial diagram based on theory [17]



3.3 Skins Used

In our work, we make use of three skins, namely convolution skin, pooling skin, and fully connected skin:

Convolution Skin

In convolution layer, operation that is performed is convolution on input image or output of the previous layer using a kernel matrix. The convolution operation can be done multiple times on the input image pixel to have an appropriate image frame for further processing. The mathematical formula for convolution operation is given as in Eq. 1.

$$net(t, f) = (x * w)[t, f] = \sum_{\forall m} \sum_{\forall n} x[m, n]w[t - m, f - n] \quad (1)$$

Pooling Layer

In mathematics, pooling is essentially a down sampling. As a result, each feature map has a reduced dimensionality yet preserves the most critical features. Different types of pooling are possible. Some of them are sum down sampling, max down sampling, and average down sampling. In this work, max down sampling is used as pooling layer to minimize dimensionality because it mainly focuses on the recognizable edge or feature from the pixel of the image. In this pooling method, down sampling is done by selecting maximum value from within the selected $m \times m$ region. This significantly reduces the size maintaining the important features.

Fully Connected Skin

On the output skin, there is an activation function for the multi-layer perception (MLP). The skin terminology “Fully Connected” corresponds to the understanding

of linking of every previous layer neuron to every following layer neuron. The fully connected layer identifies the target correctly using a classifier.

3.4 *ReLU and Softmax Activation Functions*

Rectified linear unit functions (ReLU) are used to introduce nonlinearity into our model. The ReLU function's mathematical formula is given in Eq. 2.

$$R(z) = \max(0, z) \quad (2)$$

The last function of activation used for prediction of classification is softmax. The function of softmax is to predict the most suitable or featured result from the set of possible outputs. We use only one softmax layer which is at the end so that it can predict the most appropriate emotion.

3.5 *MobileNet (Version2)*

MobileNet v2 [18] is developed by Google. MobileNetV2 employs the depthwise separable convolutions (DSCs) technique for portability, not only improving the problem of information destruction in nonlinear layers in convolution blocks by using linear bottlenecks but also introducing a new structure known as inverted residuals to preserve the information. The complete architecture of our proposed model is designed according to the flow can be seen in the below Fig. 4.

4 Implementation

Here, we discuss about the implementation of the work carried out, viz., data acquisition, imported modules, and transfer learning using MobileNet v2 usage.

4.1 *Data Acquisition*

There are two phases in the stage of data acquisition: training phase and testing phase.

Training phase

FER2013 dataset [3] is used to train our model. The FER2013 dataset consists of 35887 photos. Some of the images of FER2013 are shown in Fig. 5. All the faces in the database are normalized to 48×48 (Fig. 6).

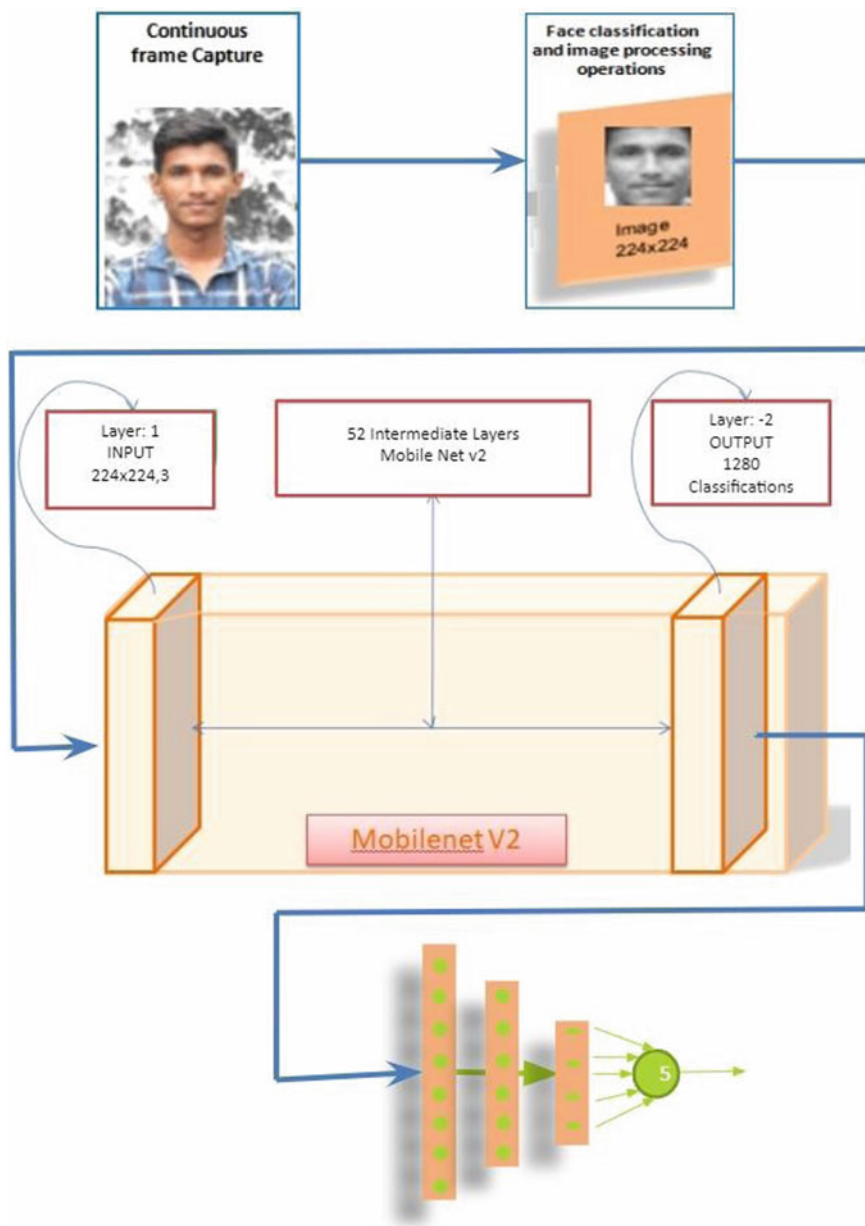


Fig. 4 Architectural view of the planned model



Fig. 5 FER2013 dataset sample images [19]



Fig. 6 CK+ dataset sample images [21]

The FER2013 dataset has 35887 images, and it comprises of 7 emotions, namely angry, disgust, fear, happy, neutral, sad, and surprised. In each of the category, the count of members of images are as shown in Table 1.

Testing phase

We use the CK+ dataset [20] to test our trained model. It has images of 981 individuals with age range 18–50 years, with a combination of genders and ethnicities. All the faces in the database are normalized to 640 × 480.

Table 1 Count of images in each category of emotion in FER2013 dataset

Emotion Label	Emotion	Number of images
0	Angry	4953
1	Disgust	547
2	Fear	5121
3	Happy	8989
4	Neutral	6198
5	Sad	6077
6	Surprise	4002

Table 2 Count of images in each emotion category of CK+ dataset

Label name	Category	Count of images	Number of images used for testing the model
0	Angry	135	45
1	Contempt	54	–
2	Disgust	177	18
3	Fear	75	–
4	Happy	207	69
5	Sad	84	28
6	Surprise	249	83

The CK+ dataset has 981 images, and it comprises of 7 emotions. The count of images in each emotion category are as shown in Table 2. It also shows the number of images that have been utilized in the testing phase.

4.2 Imported Modules

Human faces were detected using the Haar cascades method using the OpenCV library. It was constructed using Keras and TensorFlow, a high-level API for convolutional neural networks. We then utilized Haar cascade library for detecting multiple faces in the continuous frames captured from the Webcam.

4.3 Transfer Learning Using MobileNet V2

MobileNet v2 [18] has several sets of layers which has to be modified to get required number of classifications. It was developed to classify image as one of 1000 classifications or labels. Therefore, it has to be modified to classify the image into one of five classifications. We use 0th layer as input which accepts the image of $224 \times 224 \times 3$, i.e., 224×224 is a pixel resolution of the image, and 3 represents as it is an RGB image. The last second layer is used as our output which will be further modified to classify image up to five classifications.

Three more dense layers of the requisite size have been added, in the designed CNN model. ReLU function is used to provide nonlinearity; finally, the activation function softmax is used, to estimate the classification. The three dense layers are of size [128, 64, 5].

ANGRY	64	0	52	19	0	
HAPPY	0	207	0	0	0	
NEUTRAL	2	1	35	1	0	
SAD	12	0	61	11	0	
SURPRISE	0	0	31	0	218	
	ANGRY	HAPPY	NEUTRAL	SAD	SURPRISE	

Fig. 7 Confusion matrix

5 Results

As stated, FER13 is used for training purpose. From the experimental observations, it is found to have achieved 97.87% of training accuracy in detecting the emotion from the mentioned dataset. Similarly, for CK+ dataset in testing, we got 94.93% of accuracy.

5.1 Confusion Matrix

This matrix is used to compare the performance of the state-of-the-art techniques. Figure 7. shows the confusion matrix for the five emotion considered. As can be seen from our model’s success in predicting happy and surprised faces, but, it does a lousy job of predicting sad expressions since it confuses with the angry emotions.

5.2 User Interface

During the implementation phase of our trained model, we developed a user interface using OPENCV library. The interface was developed for various purposes. In Fig. 8, we can have an insight view of our user interface.

When the model is run, the system opens a user camera console which consists of different functional keys such as play/pause, status, read log, and quit keys. On the very left top corner, we have status tab which shows the current status of the emotion; on left bottom corner, there is a play/pause (space) key to pause or resume the activity; on the right top, we have r key through which we can log the emotion details into a

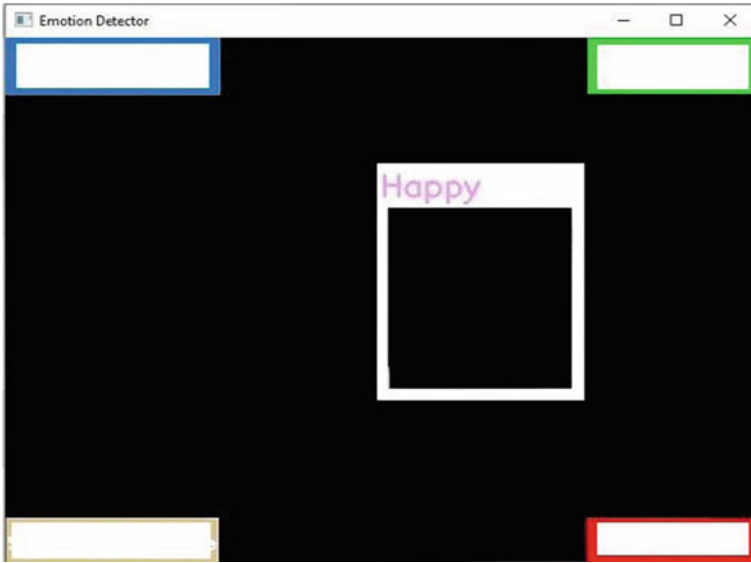


Fig. 8 User interface window

separate file; at right bottom, we have q key to quit the overall activity and exit from the interface. The OpenCV will detect the face/faces using Haar detection method and mark a rectangular/squared box around the face which has pixel width of 10.

We captured some of our live expressions using our emotion recognition system. Some of the outputs of our user interface are shown in Fig. 9 (a) Sample output of happy face, (b) Sample output of angry face, (c) Sample output of neutral face and (d) Sample output of sad face.

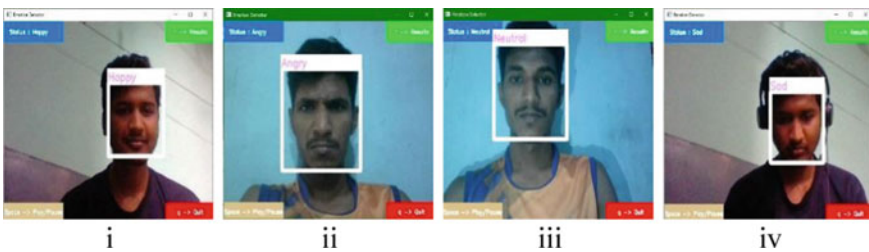


Fig. 9 a Sample output of happy face, b Sample output of angry face, c Sample output of neutral face, and d Sample output of sad face

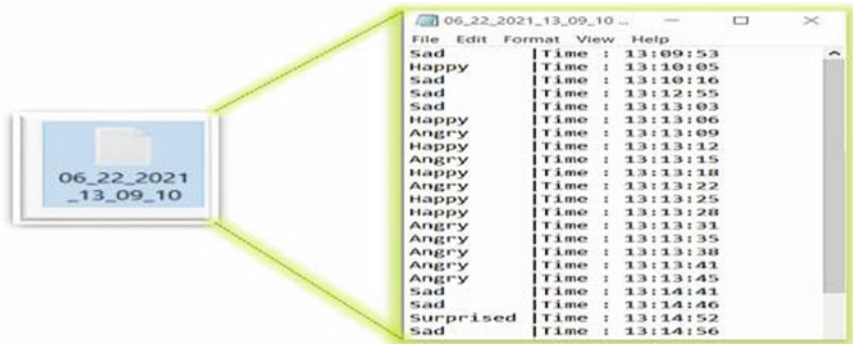


Fig. 10 Sample look of the log file

5.3 Log File Generation

The log file is a record containing log of emotions at particular interval of time. The dominant emotion present in the interval is logged in to the file along with the time stamp. When we process the generated log file, we can find out the dominant emotion during the use of application. The log file generated during the use of application is entitled in the format of date time as shown in Fig. 10. The log file helps in finding the emotion in that particular interval of time.

5.4 Performance Comparison

Table 3 shows the comparison of our model with SOTA. The accuracy obtained is the best in the proposed algorithm using Eq. 3.

$$\text{Accuracy} = \frac{R_{\text{classification}}}{R_{\text{classification}} + W_{\text{classification}}} \tag{3}$$

Table 3 Comparison with other methods

	Number of moods considered	Key frame	Accuracy obtained (%)
Proposed	5	Edge based	97.87
FERC [22]	5	Edge based	96.00
Jung [23]	7	Fixed frame	91.44
Zang [24]	7	Last frame	97.78

The applications of emotion recognition systems are plenty; one popular among many is real-time emotion recognition of user while playing video game. It is important to remember that video games are built with a certain target market in mind, and that they are intended to elicit, user feedback, which is to be included into the final product throughout the testing phase. When a user is playing a game, facial emotion detection can be used to determine what feelings they are experiencing in real time, without having to go through the entire video.

6 Conclusion

In the present paper, work has been carried out on detection of facial emotions based on Haar cascade and convolutional neural network using MobilenetV2. Added to these are the three dense layers as an extension to improve the results. This project works to detect emotions as well as stores its log with time stamp. Comparative results provide a satisfactory improvement in the results obtained with an achieved accuracy of 97.87%. The detection rate is good with emotions like happy and surprise. The model's performance can be improved by setting stringent factors to detect angry and sad emotions accurately.

References

1. Lasri I et al (2019) Facial emotion recognition of students using convolutional neural network. In: 2019 3rd international conference on intelligent computing in data sciences (ICDS), <https://doi.org/10.1109/ICDS47004.2019.8942386>
2. Zhao X et al (2016) Peak-piloted deep network for facial expression recognition. Lecture notes in computer science (including Subseries lecture notes in artificial intelligence and lecture notes in bioinformatics). vol 9906 LNCS. pp 425–442, https://doi.org/10.1007/978-3-319-46475-6_27
3. Zahara L et al (2020) The facial emotion recognition (FER-2013) dataset for prediction system of micro-expressions face using the convolutional neural network (CNN) algorithm based Raspberry Pi. In: 2020 5th international conference on informatics and computing (ICIC), 2020. <https://doi.org/10.1109/ICIC50835.2020.9288560>
4. Zafar B et al (2018) A novel discriminating and relative global spatial image representation with applications in CBIR. Appl Sci 8(11):1–23. <https://doi.org/10.3390/app8112242>
5. Ali N et al (2018). A hybrid geometric spatial image representation for scene classification. <https://doi.org/10.1371/journal.pone.0203339>
6. Ali N et al (2016). A novel image retrieval based on visual words integration of sift and surf. <https://doi.org/10.1371/journal.pone.0157428>
7. Ekman P, Friesen WV (1971) Constants across cultures in the face and emotion. J Pers Soc Psychol 17(2):124–129. <https://doi.org/10.1037/H0030377>
8. Sajid M et al (2019). The impact of asymmetric left and asymmetric right face images on accurate age estimation. <https://doi.org/10.1155/2019/8041413>
9. Sajid M et al (2018). Data augmentation-assisted makeup-invariant face recognition. <https://doi.org/10.1155/2018/2850632>

10. Ratyal N, Taj I, Bajwa U, Sajid M (2018) Pose and expression invariant alignment based multi-view 3D face recognition. *KSII Trans Internet Inf Syst* 12(10):4903–4929. <https://doi.org/10.3837/tiis.2018.10.016>
11. Oktavia NY, Wibawa AD, Pane ES, Purnomo MH (2019) Human Emotion Classification Based on EEG Signals Using Naïve Bayes Method. In: *Proceedings 2019 international seminar on application for technology of information and communication Industry 4.0 retrospect, prospect and challenges (iSemantic)*, 2019. pp 319–324 <https://doi.org/10.1109/ISEMANTIC.2019.8884224>
12. Ayvaz U, Gürüler H, Devrim MO (2017) Use of facial emotion recognition in e-learning systems. *Information Technologies and Learning Tools* 60(4):95. <https://doi.org/10.33407/itl.v60i4.1743>
13. Tang C, Xu P, Luo Z, Zhao G, Zou T (2015) Automatic facial expression analysis of students in teaching environments lecture notes in computer science (including subseries lecture notes in artificial intelligence and lecture notes in bioinformatics), vol 9428, pp 439–447 https://doi.org/10.1007/978-3-319-25417-3_52
14. Zadeh MMT, Imani M, Majidi B (2019) Fast facial emotion recognition using convolutional neural networks and gabor filters. In: *2019 IEEE 5th conference on knowledge based engineering and innovation KBEI 2019*, pp 577–581, <https://doi.org/10.1109/KBEI.2019.8734943>
15. Ghaffar F (2020) Facial emotions recognition using convolutional neural net, pp 7–12 <https://arxiv.org/ftp/arxiv/papers/2001/2001.01456.pdf>
16. Viola P, Jones M (2001) Rapid object detection using a boosted cascade of simple features. In: *Proceedings of the 2001 IEEE computer society conference on computer vision and pattern recognition*, vol 1. <https://doi.org/10.1109/CVPR.2001.990517>
17. Tabora V (2021) Face detection using opencv with haar cascade classifiers | by Vincent Tabora becoming human: artificial intelligence magazine. <https://becominghuman.ai/face-detection-using-opencv-with-haar-cascade-classifiers-941dbb25177>. Accessed 1 Sep 2021
18. Sandler M, Howard A, Zhu M, Zhmoginov A, Chen L-C (2018) MobileNetV2: inverted residuals and linear bottlenecks. in *2018 IEEE conference on computer vision and pattern recognition*, pp 4510–4520. <https://doi.org/10.1109/CVPR.2018.00474>
19. Sambare M (2021) FER-2013 | Kaggle <https://www.kaggle.com/msambare/fer2013?select=test>. Accessed 1 Sept 2021
20. Lucey P, Cohn JF, Kanade T, Saragih J, Ambadar Z, Matthews I (2010) The Extended Cohn-Kanade Dataset (CK+): A complete dataset for action unit and emotion- specified expression. In *2010 IEEE computer society conference on computer vision and pattern recognition-workshops*, pp 94–101. <https://doi.org/10.1109/CVPRW.2010.5543262>
21. Shawon A (2021) CKPLUS | Kaggle <https://www.kaggle.com/shawon10/ckplus>
22. Mehendale N (2020) Facial emotion recognition using convolutional neural networks (FERC). *SN Appl Sci* 2(3):1–8. <https://doi.org/10.1007/s42452-020-2234-1>
23. Jung H, Lee S, Yim J, Park S, Kim J (2015) Joint fine-tuning in deep neural networks for facial expression recognition. In: *Proceedings of the IEEE international conference on computer vision*, vol 2015 Inter, pp 2983–2991, <https://doi.org/10.1109/ICCV.2015.341>
24. Zhang K, Huang Y, Du Y, Wang L (2017) Facial expression recognition based on deep evolutionary spatial-temporal networks. *IEEE Trans Image Process* 26(9):4193–4203. <https://doi.org/10.1109/TIP.2017.2689999>

Photovoltaic Maximum Power Point Tracking Using Artificial Neural Network and PI Controller



Hocine Abdelhak Azzeddine, Djamel-eddine Chaouch, Mourad Hebali, Ahmed Labaoui, Youcef Islam Djilani Kobibi, and Benaoumeur Ibari

Abstract This article outlines the development of a photovoltaic maximum power point tracker (MPPT) based on a radial basis function artificial neural network (RBF ANN) and a boost converter controlled by a proportional integrator (PI) controller. The photovoltaic panel single diode model is used to create the training data for the proposed artificial neural network and then to validate the simulation results. The artificial neural network is then used as a voltage reference generator for a DC–DC boost converter controlled by a PI controller to extract the maximum power available from the photovoltaic panel. The simulation results show that the developed MPPT has enhanced performance even in case of rapid change in temperature and solar irradiance levels.

Keywords MPPT · Photovoltaic · Artificial neural network

1 Introduction

Energy production is a challenge of great importance for the future. Demand for energy of industrialized countries is clearly set to continue growing while the countries developing will need more and more energy to carry out their development [1]. In this context, solar energy could be a real solution of energy supplies of these countries while respecting environment and sustainable development requirements. Among the techniques of solar energy harvesting, photovoltaic systems are by far the most used nowadays [2]. A photovoltaic panel directly converts solar energy into a direct electrical current using semiconducting material that exhibits the photovoltaic effect. A photovoltaic panel exhibits nonlinear current–voltage characteristics, and for any given operating conditions, there is a unique operating point defined by its corresponding current (I_{mpp}) and voltage (V_{mpp}) where the panel output power is at its maximum [3]. This point is commonly known as the maximum power point (MPP). Maximizing the efficiency of power by tracking this point is decisive to overcome

H. A. Azzeddine (✉) · D. Chaouch · M. Hebali · A. Labaoui · Y. I. D. Kobibi · B. Ibari
Mustapha Stambouli University of Mascara, Mascara, Algeria
e-mail: hocine.azzeddine@univ-mascara.dz

© The Author(s), under exclusive license to Springer Nature Singapore Pte Ltd. 2022
V. Mahajan et al. (eds.), *Sustainable Technology and Advanced Computing in Electrical Engineering*, Lecture Notes in Electrical Engineering 939,
https://doi.org/10.1007/978-981-19-4364-5_29

393

the higher investment required for the installation of a photovoltaic system [4]. To this end, a photovoltaic system must be able to control a static converter used as an interface between PV panel and the load in a way to enforce the panel to operate at its maximum power point [3]. This solution is called maximum power point tracking. A maximum power point tracker uses an algorithm which continuously provides the V_{mpp} and/or the I_{mpp} values [5]. The most common algorithms have many drawbacks: the perturb and observe method exhibits a bad dynamic response; the increment conduction method requires complex control circuitry; and the extremum seeking control method suffers from the complexity of its implementation and the necessity to measure small signals [6, 7]. Moreover, artificial intelligence neural networks are expected to predict accurately and quickly the maximum power point of a solar panel without needing its parameters or knowledge of the complicated relationships between system inputs and outputs [6]. During the last decade, many published works focus on the use of artificial neural networks for photovoltaic applications: prediction and estimation of solar power potential [6–8], system sizing [9], photovoltaic panel modeling [10], system control [11], and maximum power point tracking [12, 13]. In this work, a radial basis function neural network is developed, tested, and used in a system for extracting the maximum power of a photovoltaic panel.

2 System Configuration

2.1 Photovoltaic Panel Modeling

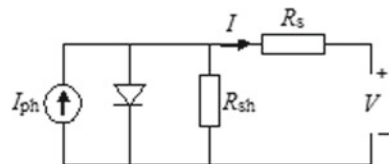
The single diode electrical model shown on Fig. 1 is used to modeling the photovoltaic panel. This model is quite simple and offers a good accuracy [14].

The model is governed by the following equation:

$$I = I_{\text{ph}} - I_s \left(\exp\left(\frac{q(V + R_s I)}{AKT}\right) - 1 \right) - \frac{V + R_s I}{R_{\text{sh}}} \quad (1)$$

where I is the output current of the photovoltaic cell (A), V is the output voltage of the photovoltaic cell (V), T is the cell temperature (K), I_{ph} is the photo current of the diode (A), I_s is the reverse saturation current of the diode (A), q is the electron charge (1.602×10^{-19} C), A is a diode ideality factor between 1 and 2, k is the Boltzmann's

Fig. 1 PV cell model



constant (1.381×10^{-23} J/K), R_s is the series cell resistance (Ω), and R_{sh} is the shunt cell resistance (Ω) [15, 16]

Equations (2) and (3) show the temperature dependence of the photo current and the saturation current of the diode, respectively [14].

$$I_{ph} = \frac{G}{G_{ref}}(I_{sc} + a_i(T - T_{ref})) \tag{2}$$

where I_{sc} is the cell’s short-circuit current at standard conditions test (STC) (A), a_i is the cell’s short-circuit current temperature coefficient (A/K), T_{ref} is the standard temperature (298 K), G is the solar irradiance (W/m^2), and G_{ref} is the standard solar irradiance ($1000 W/m^2$).

$$I_s = \frac{I_{sc} + a_i(T - T_{ref})}{\exp\left(\frac{V_{oc} + a_v(T - T_{ref})}{AKT}\right) - 1} \tag{3}$$

where V_{oc} is the standard cell’s open circuit voltage (V) and a_v is the voltage temperature coefficient (V/K).

The relationship between the current I (A) and the voltage V_m (V) of a photovoltaic module consisting of N photovoltaic cells in series is expressed as in Eq. (4) [15, 17].

$$I = I_{ph} - I_s \left(\exp\left(\frac{q(V_m + R_s I)}{NAKT}\right) - 1 \right) - \frac{V_m + R_s I}{R_{sh}} \tag{4}$$

To fitting the photovoltaic panel current–voltage curve, the Newton–Raphson method is applied. For a given voltage value, the model can be written as follow:

$$f(I) = I - I_{ph} - I_s \left(\exp\left(\frac{q(V_m + R_s I)}{NAKT}\right) - 1 \right) - \frac{V_m + R_s I}{R_{sh}} = 0 \tag{5}$$

The Newton–Raphson method is used to find the root of the function $f(I)$. The principle of the method is as follow: starting with an initial value I_0 , the algorithm executes the following iterations:

$$I_{i+1} = I_i + \frac{f(I)}{f'(I)} \tag{6}$$

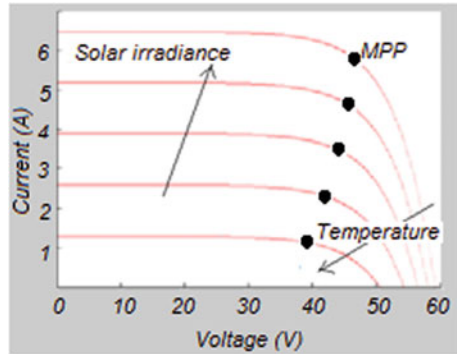
where $f'(I)$ is the derivate of the function $f(I)$. The algorithm is stopped if the difference of two succeeding iterations values is less than a predefined threshold.

In this work, the SunPower® photovoltaic panel is used. The main electrical data of this photovoltaic panel taken from its datasheet are summarized in Table 1.

Table 1 SunPower® 300 photovoltaic panel parameters

Parameter	Value
Open circuit voltage at STC, V_{oc}	64 V
Short-circuit current at STC, I_{sc}	5.87 A
Temperature coefficient of open circuit voltage, a_v	-0.1766 V/K
Temperature coefficient of short-circuit current a_i	0.0035 A/K

Fig. 2 PV module current–voltage characteristics



The datasheet provides, in addition, the open circuit voltage, the current at maximum power and the open circuit voltage values at 20 °C and 800 W/m²; and some measured current–voltage curves at different operating conditions. The others model parameters are adjusted against simulation by comparison between several current–voltage curves generated by the mathematical model, and the data and curves provided in the SunPower® 300 photovoltaic module datasheet. The following values are well suited to our photovoltaic module: $A = 1.7$, $R_s = 0.1 \Omega$, and $R_{sh} = 10 K\Omega$.

Figure 2 shows the photovoltaic panel nonlinear behavior under varying climatic conditions. On a given curve, there is a single point defined by its voltage and current where the power delivered by the photovoltaic panel is at its maximum. This point (MPP) changes when the operating conditions change.

2.2 DC–DC Boost Converter

The operating point of a photovoltaic system is defined by the photovoltaic panel current–voltage curve and the load line intersection. To extract the maximum power of the panel, it is essential to maintain the operating point very close to the maximum power point. This is not a simple task, once the maximum power point all the time changes when solar irradiance and temperature level change. The solution is, therefore, to allow the system to change the load line for the panel so that the operating

point is very close to the maximum power point. This is possible if a static converter is interposed between the PV module and the load. The converter duty cycle must be controlled so that, when temperature or solar irradiance changes, the impedance seen by the photovoltaic panel corresponds to the desired operating point. For our system, a DC–DC boost converter operating in a continuous mode is used.

2.3 PI Controller

The control scheme is simple, and it controls the input voltage of the boost converter (the output voltage of the PV panel) (Fig. 3).

For this, a single loop control suffices. One output of the radial basis function artificial neural network (the V_{mpp} value) is a signal which is compared with the actual output voltage of the PV panel in order to generate the control signal required to control the boost converter and drive the PV panel to its MPP through a PI controller. When the boost input voltage (the PV output voltage) tends to be lower or higher than the reference voltage (V_{mpp}) delivered by the artificial neural network, the control loop increase or decrease the duty cycle and, thereby, controls the boost input voltage at the maximum power voltage. Compared to other published works, our control schema controls a single parameter. To control the boost converter output voltage and current, other control loops must be added as needed.

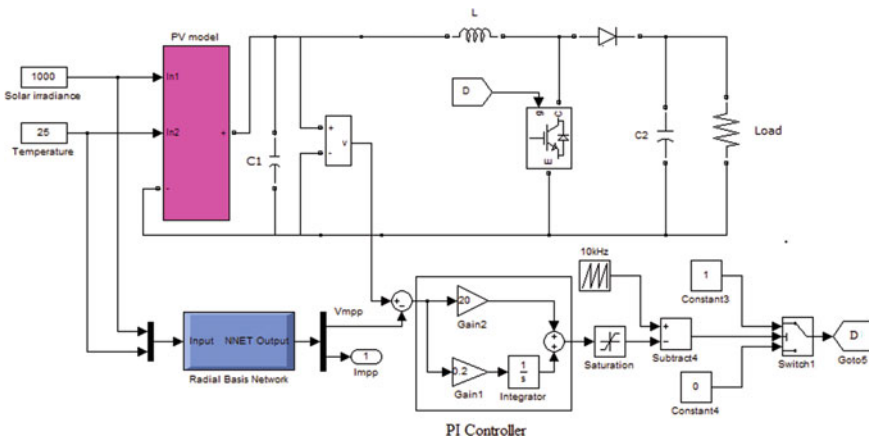


Fig. 3 Overall proposed MPPT system

3 Proposed Artificial Neural Network

3.1 Basics of Radial Basis Function Artificial Neural Network

Inspired by the neural structure of the brain, artificial neural networks (ANN) can be used in intelligent systems since they are able to learning and solving problems from examples previously chosen [18, 19]. Radial basis function (RBF) artificial neural networks are easy to implement, and they generalize well and they are insensitive to noisy data [20]. The decisive advantage of artificial neural networks is their ability to model the behavior of photovoltaic systems without need the complicated mathematical models governing input and output variables systems [21].

The structure of a radial basis function network has three layers with completely different roles [22]. The input layer is made up of input nodes, also called source nodes. The second layer (a hidden layer) has a high enough number of neurons; each neuron performs a nonlinear transformation of the input, by means of a radial basis function [23, 24]. The output layer is a linear combination of the hidden input nodes. A radial basis function neural network is fully connected: every neuron in each layer is connected to every other neuron in the next layer [24]. Synaptic weights between the input layer and the hidden layer networks have a unit value.

Figure 4 shows a structure diagram of a radial basis function neural network with n input nodes, m hidden layer nodes, and one output layer node. Each node in the hidden layer is a Gaussian function defined by its center c_j and its radius r_j in accordance with Eq. (7).

$$h_j(x) = \exp\left(-\frac{(x - c_j)^2}{2r_j^2}\right) \tag{7}$$

Fig. 4 RBF artificial neural network structure

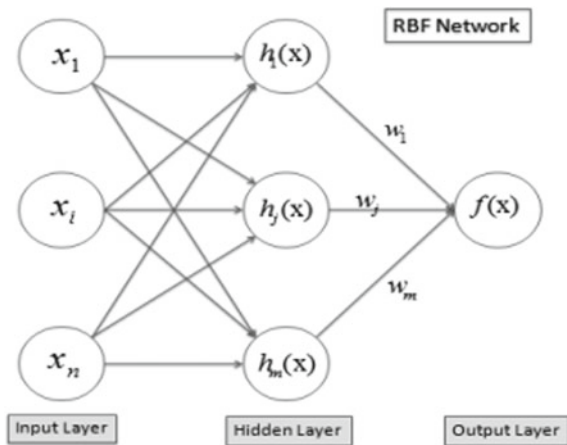
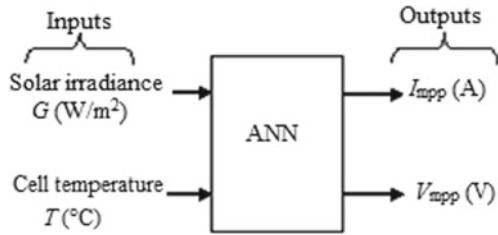


Fig. 5 Proposed ANN inputs/outputs



where x is a scalar input.

The output node is given by the equation

$$f(x) = \sum_{j=1}^m w_j h_j(x) \tag{8}$$

where w_j is the weight of the synapse connecting the hidden node of rank j to the output node.

In short, RBF network process learning is divided into two stages. The learning process begins with determining the number of neurons in the hidden layer, and the center and radius of each neuron using an unsupervised method. After, by means of a supervised technique, the weights of the output layer connections are adjusted [24].

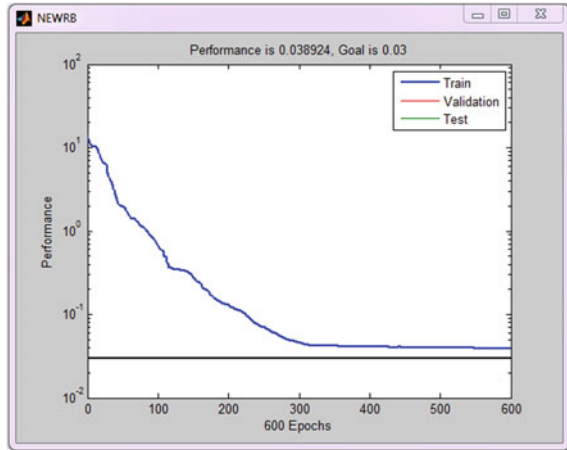
3.2 Design of the Proposed Artificial Neural Network

The proposed neural network is designed in such a way to have as sensory input units the temperature and the solar irradiance measurements, and as outputs the corresponding I_{mpp} and V_{mpp} values (Fig. 5).

3.3 Training Data Generation

I_{mpp} and V_{mpp} values for different temperature and solar irradiance conditions obtained using the single diode model detailed above are used as examples to train the proposed artificial neural network. Values of cell temperature are chosen between 0 and 70 °C, while the solar irradiance values are chosen between 50 and 1000 W/m². Training set consists of a matrix of data, where each column corresponds to a variable (temperature, solar irradiance, I_{mpp} , and V_{mpp}).

Fig. 6 Training error evolution



3.4 Training of the Proposed ANN

During the training process, the artificial neural network parameters are adjusted in order to make the actual ANN outputs (predicated V_{mpp} and I_{mpp} values) close to the target outputs (V_{mpp} and I_{mpp} values of the data training set). The learning is stopped when the desired accuracy defined by the mean squared error goal is reached. A good accuracy was reached after 600 iterations for a mean square error goal fixed at 0.03 and a spread of the radial basis function value equal to 1 (Fig. 6).

In this step, the network's ability to generalize is tested. A network generalizes well when it gives acceptable results for input conditions not encountered during the phase of learning. So, the designed neural network is used to predict several maximum power points of the photovoltaic module for temperature and solar irradiance levels other than training data set. To be validated, results are compared to those estimated by the one diode model at the same climatic conditions (Fig. 7).

It is clear that maximum power points predicted by the proposed ANN are very close to those calculated by the single diode model. So we can state that the proposed artificial neural network has very good performances and therefore, for any cell temperature and solar irradiance conditions, it can predict the maximum power point of the photovoltaic panel with a very good accuracy.

4 Simulation Results

The proposed neural network will be used to provide the reference voltage to control the input voltage of a boost converter connected to a photovoltaic panel and controlled using a PI controller. The system will be tested for very rapid changes in temperature

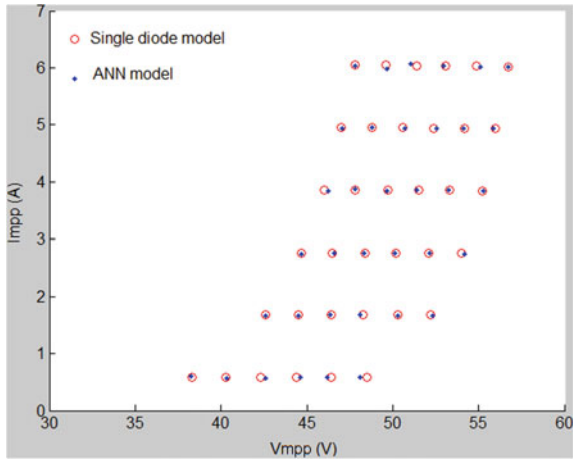


Fig. 7 ANN generalization ability

and solar irradiance. Figure 8 shows the temperature and solar irradiation profiles used for the test.

Figure 9 shows the panel output voltage response, while Fig. 10 shows the panel output current response.

It is clear that the system exhibits good dynamic and static performances. Even in the event of rapid changes in temperature and solar irradiance, the proposed MPPT can find quickly and accurately the new maximum power point.

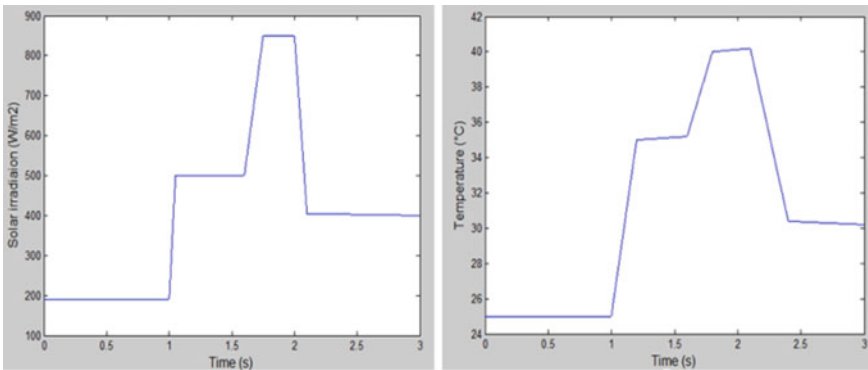


Fig. 8 Solar irradiance and temperature profiles for the MPPT test

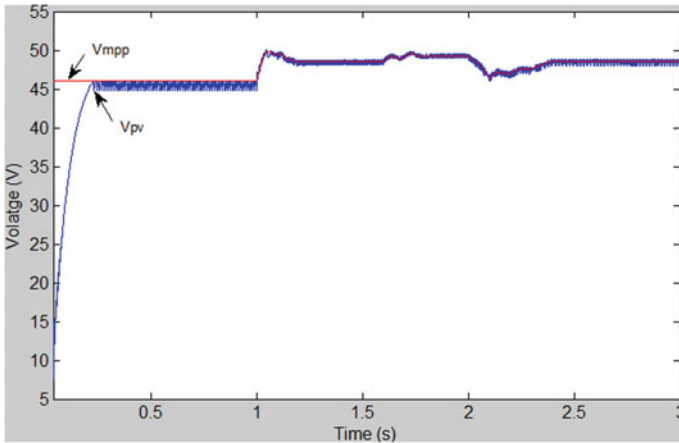


Fig. 9 Voltage response

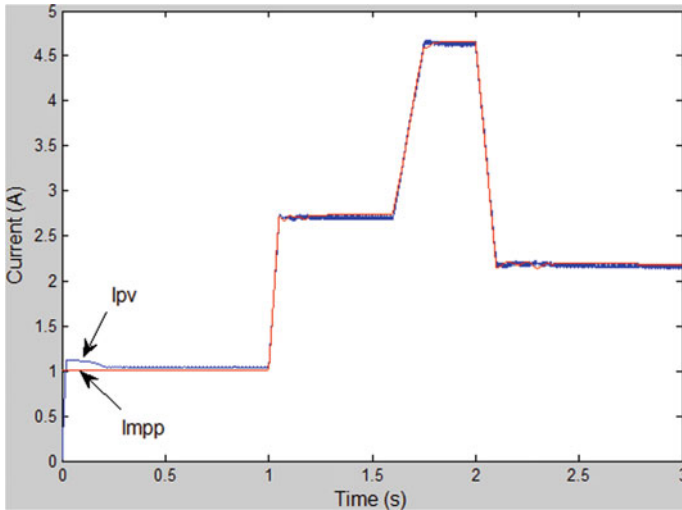


Fig. 10 Current response

5 Conclusion

A photovoltaic maximum power point tracker can be easily synthesized by means of an artificial neural network and a PI controller. The trained neural network provides the reference voltage value and/or the reference current value while the PI controller controls a static converter inserted between the photovoltaic panel and the load such a way that the operating point is very close to the photovoltaic panel maximum power point. The simulation results show that the MPPT has good performances even in

case of rapid change of temperature and solar irradiances conditions. The decisive advantage of the proposed MPPT over conventional techniques such as perturb and observe technique is its precision and reliability in the event of operating conditions fast change. This work is the first phase of a research on grid connected photovoltaic systems.

References

1. Gielen D, Boshell B, Saygin D, Bazilian M, Wagner N, Gorini R (2019) The role of renewable energy in the global energy transformation. *Energy Stra Rev* 24:38–50
2. Li Y, Witharana S, Cao H, Lasfargues M, Huang Y, Ding Y (2014) Wide Spectrum solar energy harvesting through an integrated photovoltaic and thermoelectric system. *Particulogy* 15:39–44
3. Rekioua D, Matagne E (2012) Optimization of photovoltaic power system: modelization, simulation and control. Springer, London
4. Reisi AR, Moradi MH, Jamasb S (2013) Classification and comparison of maximum power point tracking techniques for photovoltaic system: a review. *Renew Sustain Energy Rev* 19:433–443
5. Esram T, Chapman PL (2007) Comparison of photovoltaic array maximum power point tracking technique. *IEEE Trans Energy Convers* 22(2):439–449
6. Bhatnagar P, Nema RK (2016) Maximum power point tracking control techniques: state-of-the-art in photovoltaic applications. *Renew Sustain Energy Rev* 23:224–241
7. A Linares-Rodriguez JA Ruis-Arias D Pozo-Vasquez (2013) An artificial neural network ensemble for estimating global solar radiation from Meteosat satellite images. *Energy* 61:636–645
8. Notton G, Paoli C, Vasileva S, Nivet ML, Canaletti JL, Cristofari C (2012) Estimation of hourly global solar irradiation on tilted planes from horizontal one using artificial neural networks. *Energy* 39:166–176
9. Mellit A (2007) Modeling and simulation of a stand-alone photovoltaic system using an adaptive artificial neural network: proposition for a new sizing procedure. *Renew Energy* 32:285313
10. Bonanno F, Capizzi G, Graditi G, Napoli C, Tina GM (2012) A radial basis function neural network based approach for the electrical characteristics estimation of a photovoltaic module. *Appl Energy* 97:356–961
11. Hong CM, Chen CH (2014) Intelligent control of grid-connected wind-photovoltaic hybrid power systems. *Electr Power Energy Syst* 55:554–561
12. Punitha K, Devaraj D, Sakthivel S (2013) Artificial neural network based modified incremental conductance algorithm for maximum power point tracking in photovoltaic system under partial shading conditions. *Energy* 62:330–340
13. Liu YH, Liu CL, Huang JW, Chen JH (2013) Neural-network-based maximum power point tracking methods for photovoltaic systems operating. *Sol Energy* 89:42–53
14. Celik AN (2011) Artificial neural network modelling and experimental verification of the operating current of mono-crystalline photovoltaic modules. *Sol Energy* 85:2507–2517
15. Mirić S, Nedeljković N (2015) The solar photovoltaic panel simulator. *Revue Roumaine des Sciences et Techniques, Série Électrotechnique et Énergétique* 60(3):273–281
16. Azzeddine HA, Chaouch D, Khiari B, Tioursi M (2016) An offline trained artificial neural network to predict a photovoltaic panel maximum power point. *Revue Roumaine des Sciences et Techniques, Série Électrotechnique et Énergétique* 61(3):255–257
17. Quaschnig V, Hanitsch R (1996) Numerical simulation of current-voltage characteristics of photovoltaic systems with shaded solar cells. *Sol Energy* 56(6):513–520

18. Kalogirou SA, Şencan A (2010) Artificial intelligence techniques in solar energy applications. In: Manyala R (ed) *Solar collectors and panels, theory and applications*. Intech, pp 315–340
19. Sumathi S, Kumar LA, Surekha P (2015) *Solar PV and wind energy conversion systems: an introduction to theory, modeling with MATLAB/SIMULINK and the role of soft computing techniques*, 1st edn. Springer
20. Yu T, Xie T, Paszczynski S, Wilamowski BM (2011) Advantages of radial basis function networks for dynamic system design. *IEEE Trans Ind Electron* 58(12):5438–5450
21. Mellit A, Kalogirou SA (2008) Artificial intelligence techniques for photovoltaic applications: a review. *Prog Energy Combust Sci* 34:574–632
22. Haykin S (1999) *Neural network: a comprehensive foundation*, 2nd edn. Pearson
23. Karabacak K, Cetin N (2014) Artificial neural networks for controlling wind-PV power systems: a review. *Renew Sustain Energy Rev* 29:804–827
24. Kasabo N (1998) *Foundations of neural networks, fuzzy systems, and knowledge engineering*. The MIT Press, London

Performance Analysis of DGFET, MESFET, and SOI on Varying Device Intrinsic Input Parameters



Isha Desai, Jhanvi Shroff, and Rutu Parekh

Abstract In this paper, we systematically evaluate the performance of DGFET, MESFET, and SOI by varying different device intrinsic input parameters and perform simulations to determine which one has the best functionality and dependency. The performance for the three devices in the paper is compared by varying channel length, temperature, and top oxide thickness. The simulation is done using a quasi-three-dimensional quantum-corrected semi-classical Monte Carlo transport simulator for conventional and non-conventional MOSFET devices. Based on the simulations we performed, it was observed that all three devices are a significant improvement over bulk MOSFET, and it was also noticed that SOI outperforms both DGFET and MESFET which shows great promises for certain input parameters. MESFET outperforms DGFET in most scenarios. SOI has 24.89% better drain current than DGFET, which increases to nearly 80% with increase in channel length from 20 to 30 nm. However, SOI has 34.93% better drain current than DGFET when temperature is 300 K and top oxide thickness 1 nm but reduces to 21.51% and 31% for 400 K temperature and a top oxide thickness of 1.5 nm, respectively. It is also observed that at device width of 22 nm, conduction band value for SOI is 0.00047, whereas the value for MESFET at the same device width is 0.17, which corresponds to the fact that SOI has lower barrier lowering than MESFET.

Keywords MOSFET · DGFET · MESFET · SOI · Channel length · Temperature · Top oxide thickness

I. Desai (✉) · J. Shroff · R. Parekh
Dhirubhai Ambani Institute of Information and Communication Technology, Gandhinagar,
Gujarat, India
e-mail: 201801107@daiict.ac.in

J. Shroff
e-mail: 201801198@daiict.ac.in

R. Parekh
e-mail: rutu_parekh@daiict.ac.in

1 Introduction

To overcome the shortcomings of MOSFET, several field-effect transistors were introduced. One of the trending areas for the design of sub-50 nm transistors is the double-gate MOSFET (DGFET). Node transistor measurements have to be reduced to contain potential developments, contributing to some transistor feature drawbacks. Many of these issues can be solved to give effectual circuit output by using the double-gate process. The use of double-gate transistors in analog circuit design provides significant enhancements over traditional single-gate CMOS design as we go for further scaling down [1]. The significant distinction between the MESFET and MOSFET, which is also a surface unit, is that a MOSFET is normally off until the gate is introduced to a voltage greater than the threshold. In comparison, until a sizable reverse voltage is applied to the gate to shut off the conducting channel, the MESFET is normally on. However, if the thickness of the channel layer (or epilayer) is made very thin, the MESFET will be turned off unless a forward voltage is applied to the gate. The normally on MESFET will be highlighted here [2]. Like ICs, metal oxide semiconductor field-effect transistors (MOSFETs) have also been used as the main technologies. Therefore, to increase the efficiency of transistors, the silicon on insulator (SOI) approach was proposed. The SOI MOSFET transistors have gained interest in addition to providing high-frequency parameters due to their production method being compliant with traditional CMOS transistors and providing several advantages like higher trans-conductance, improved parasitic capacitance, reduced short-channel effects, and improved subthreshold slope. Si CMOS, CNT FET, graphene nanoribbon FET, Ge/Si nanowire FET, all kinds of tunnel FETs, n-Ge FET, and Ga(In)Sb are some of the better alternatives to MOSFET (Fig. 1).

The method used here is based on a perturbation theory around thermodynamic equilibrium and leads to a quantum field formalism in which the size of an electron depends upon its energy. The simulator uses different self-consistent event-biasing schemes for statistical enhancement in the Monte Carlo device simulations [3, 4]. There is much research done on DGFET, MESFET, and SOI. A study done by Goyal and Sah investigated the performance of double-gate MOSFET on impact of various engineering [5]. They showed that because of the decrease in channel length of MOSFET, a short-channel effect arises, and to minimize it and maximize the performance of the device, double-gate MOSFET is the most beneficial option. A study by Chakrabarti et al. analyzed double-gate MOSFET based on oxide thicknesses, doping concentrations, gate voltages, and temperature effect to determine at which setting does double-gate MOSFET best functions [6]. Comprehensive research and comparison have been done in Vardhan [7] in which it was shown that MESFET performed better than MOSFET when compared to some input parameters. Modeling of classical SOI MESFET has been studied in Sarvaghad-Moghaddam et al. [8]. A comparative study between SOI MOSFET and MOSFET has been presented in Aziz et al. [9] which shows that to overcome the problems of lower gate leakage current, nominal threshold voltage, and lower drain-induced barrier lowering, a SOI MOSFET combats short-channel effects by burying in silicon substrate an oxide

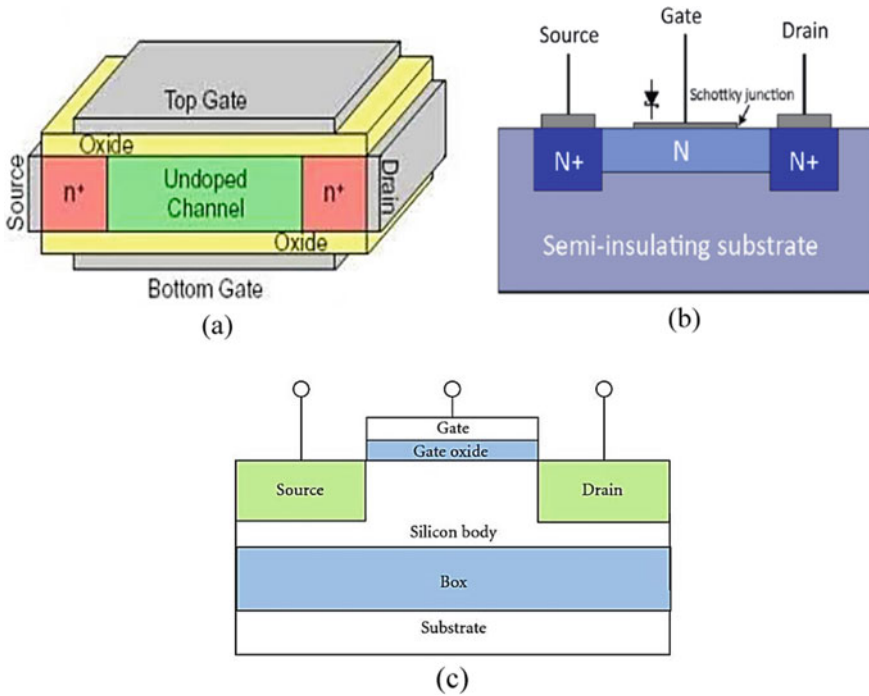


Fig. 1 Schematic of **a** DGFET, **b** MESFET, **c** SOI

layer. Improvement in electrical characteristics of silicon on insulator (SOI) transistor using graphene material has been presented in Karbalaei et al. [10].

The main aim of this paper is to compare the three devices, DGFET, SOI MOSFET and MESFET. In this paper, comparison has been made between double-gate MOSFET, MESFET, and SOI MOSFET based on I_d-V_g curve, electric field, electron density, hole density, electron energy, electron velocity, charge density, conductance band, and doping density all against device width by varying top oxide thickness, temperature, and channel length. The simulations have been performed on the tool ‘QuaMC2D’ [11].

2 Materials and Method

Table 1 shows the input parameters available in the tool for DGFET, MESFET, and SOI and those that are varied to study the effect have been marked. Out of all the input parameters, those, which were varied in values and plotted, are as follows: (a) Channel length (b) Operating temperature and (c) Top oxide thickness. The temperature will be varied for 200 and 400 K. The top oxide thickness will be altered for 1 and 1.5 nm. Similarly, the channel length will be varied for 20 and

Table 1 Device structural input parameters and material properties

Device/Parameters	DGFET	MESFET	SOI
Source/drain length (nm)	6	25	25
Channel length (L_{ch}) (nm)	20, 30	20, 30	20, 30
Gate contact length (nm)	9	25	25
Channel thickness (nm)	3	20	5
Top oxide thickness (T_{ox}) (nm)	1, 1.5	–	1, 1.5
Bottom oxide thickness (nm)	1	150	150
Device width (nm)	1000	1000	1000
Ambient temperature (K)	200, 400	200, 400	200, 400
Source voltage (V)	0	0	0
Drain voltage (V_d) (V)	0.4	1	1
Gate voltage (V_g) (V)	0.4	–0.1	1
Substrate voltage (V)	0	0	0
Substrate thickness (nm)	–	100	100

30 nm. These graphs will be studied and analyzed in detail. The reason that top oxide thickness, temperature, and channel length have been chosen as the varying parameters is because that oxide thickness plays a crucial role in determining the capacitance of the FET, and the temperature determines the quantity of free electrons, and the channel length accounts in the distance between the source and the drain. These factors affect the FET in many ways and cause variations in simulations for different parameters. Amount of doping in source, drain, and channel has been set by us and has not been varied.

3 Results and Discussion

The paper evaluates the three devices based on the following output parameters.

3.1 I_d – V_g Curve

The I_d – V_g curve plots the logarithmic values of drain current (I_d) against gate voltage (V_g).

Effect of Varying Channel Length

Figure 2a shows the impact of different channel length, L_{ch} on the I_d response curves at drain voltage, V_d equal to 0.4 V when the change in gate voltage, V_g is shifted from 0 to 5 V. From the curves, it is observed that I_d magnitude is significantly increased

as the L_{ch} is reduced from 30 to 20 nm. The shorter-channel length improves the current flow due to less resistance in the channel region [12].

Effect of Varying Temperature

There is a significant decrease in the charge carrier mobility in the channel as the temperature keeps on increasing, which as a result decreases the current passing in the channel as seen in Fig. 2b. When operating at a nominal supply voltage, the propagation delay increases as the temperature is increased and as a result, decreasing the current in the channel while increasing the electric field [13].

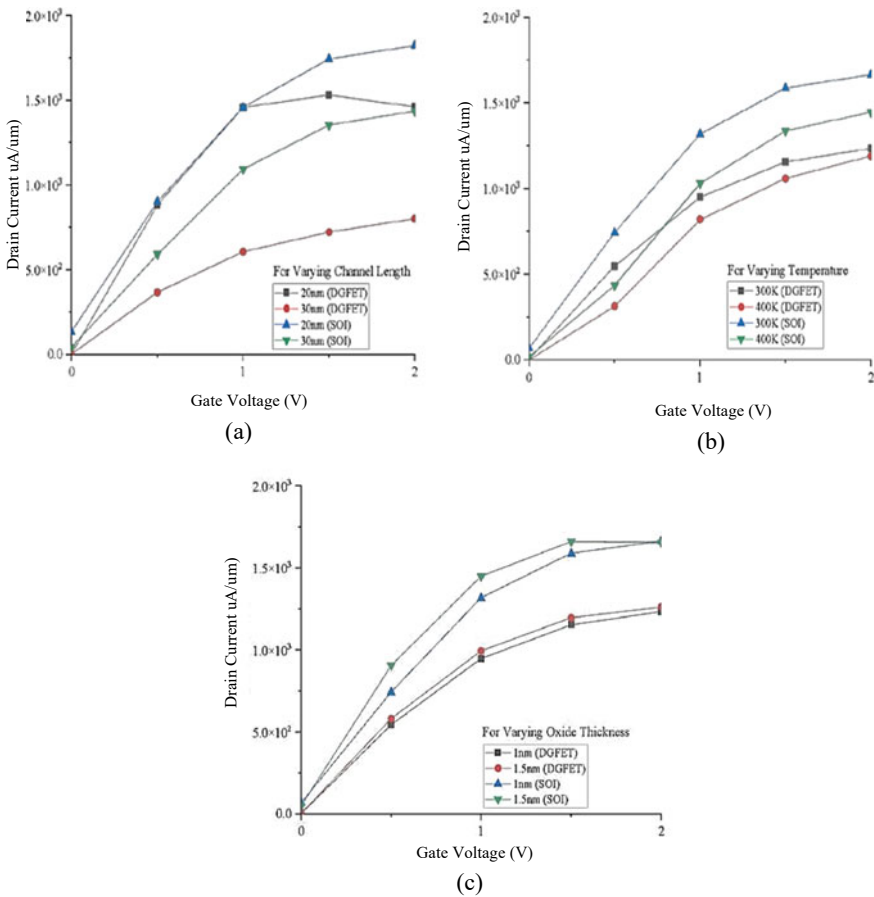


Fig. 2 I_d-V_g curve for DGFET and SOI for variation in **a** channel length; **b** temperature; **c** top oxide thickness

Effect of Varying Top Oxide Thickness

With the decreases in oxide thickness, the capacitance increases at different values of the gate voltage. But, the electrons start tunneling at the T_{ox} of 1.4 nm resulting in a large I at V_d of 0.4 V, increasing the drain current [14].

3.2 Electric Field

It is the electric property associated with each point in a space when charge is present in any form. FETs use an electric field to control the flow of current.

Effect of Varying Channel Length

The shorter channel length improves the current flow due to less resistance in the channel region. At the start and end of the channel, the electric field will decrease as the channel length increases as shown in Fig. 3a. Due to discontinuity in the DG structure's surface potential, there is observed to be a great reduction in the peak of the electric field at the drain-channel junction. When we compare this with the DG structure, this leads to a reduced hot-carrier effect [12].

Effect of Varying Temperature

It is observed that the propagation delay increases as the temperature is increased and as a result decreasing the current in the channel while increasing the electric field as evident in Fig. 3b. This is observed when the voltage supply is very low [15].

Effect of Varying Top Oxide Thickness

It is observed that the propagation delay increases as the oxide thickness is increased, but there is little to none variation in the electric field as shown in Fig. 3c. This is observed when the voltage supply is very low [15].

3.3 Electron Density

It refers to the modulation of the electrical conductivity of a material by the application of an external electric field. In a metal, the electron density that responds to applied fields is so large that an external electric field can penetrate only a very short distance into the material.

Effect of Varying Channel Length

The peak majority carrier concentration coincides with the channel region that has the lowest electric field as evident in Fig. 4a [12]. Also, refer to Fig. 3a.

Effect of Varying Temperature

At low temperatures, almost no intrinsic electron-hole pairs exist, and the donor electrons and atoms are bound together forming an ionization region. On increasing

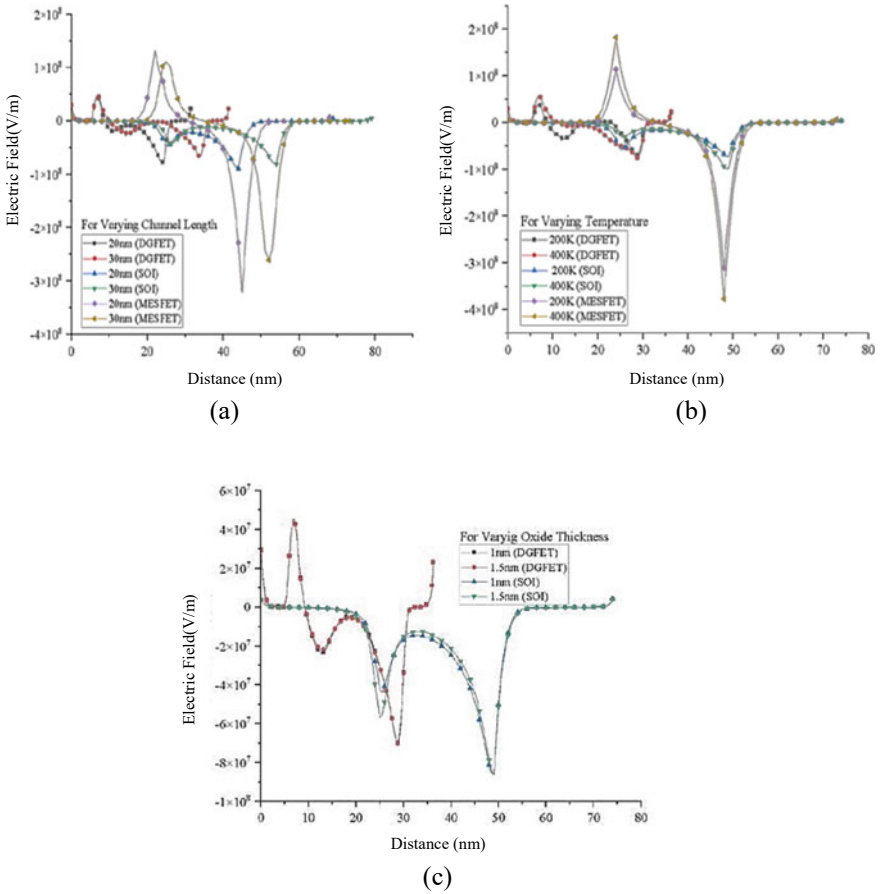


Fig. 3 Electric field versus device width curve for DGFET, MESFET, and SOI for variation in **a** channel length; **b** temperature; **c** electric field versus device width curve for DGFET and SOI for variation in top oxide thickness

the temperature, increased ionization occurs, and ionization of all donor atoms takes place. Here, the electron density is largely determined by doping. In an extrinsic region, where every dopant is ionized, increasing the temperature produces no increase in electron density. However, in an intrinsic region, where intrinsic carriers that are generated thermally at higher temperatures, they easily outnumber the dopants and electron density increases with temperature [16] as shown in Fig. 4b.

Effect of Varying Top Oxide Thickness

Low oxide thickness results in a weaker dependence of back bias on threshold voltage in the channel. Since the threshold voltage is directly proportional to the thickness of the oxide layer [17], it can be concluded that an increase in oxide thickness increases the electron density.

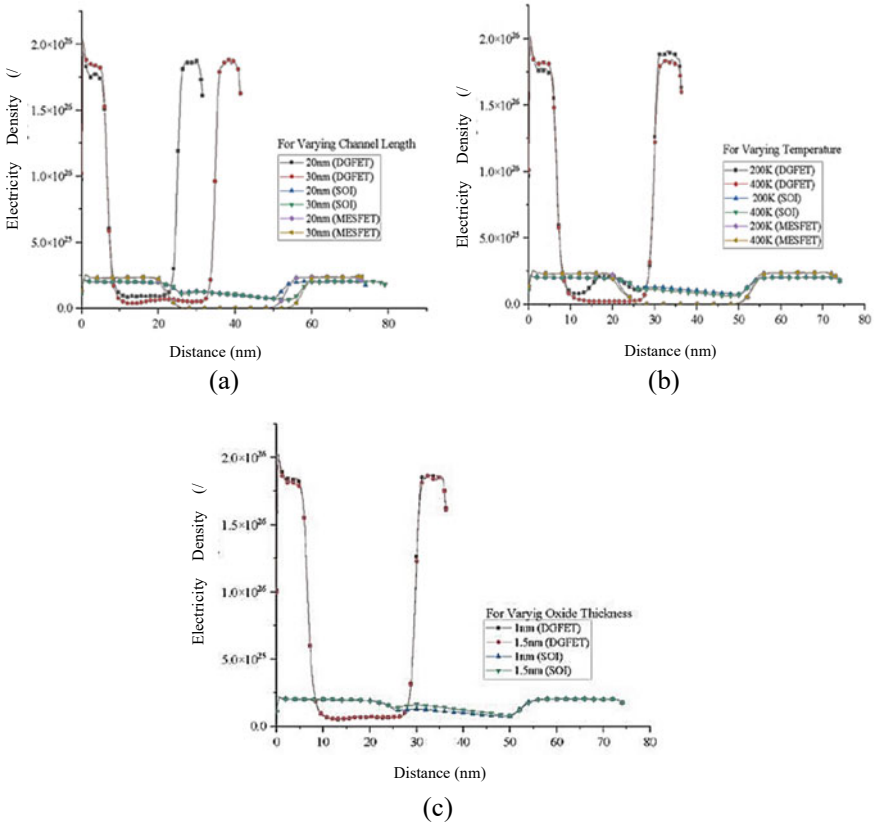


Fig. 4 Electron density versus device width curve for DGFET, MESFET, and SOI for variation in **a** channel length, **b** temperature, **c** electron density versus device width curve for DGFET and SOI for variation in top oxide thickness

The values of top oxide thickness used here; 1 and 1.5 nm are extremely small, but we can still see in Fig. 4c that SOI has greater electron density at thickness 1.5 nm than at thickness 1 nm.

3.4 Hole Density

Hole density in a FET is the number of holes in the devices, which are yet to be filled by an electron.

Effect of Varying Channel Length

Increase in channel length leads to an increase in hole density as visible in Fig. 5a. There are spikes when entering and leaving the channel, partly due to sudden change

in hole density. Increase in channel length leads to higher hole density as there is a bigger depletion region [18].

Effect of Varying Temperature

An increase in temperature increases hole density, while a decrease in temperature decreases hole density as seen in Fig. 5b. This is partly due to increase in electron velocity as electrons have more energy to leave the channel to create more holes.

Effect of Varying Top Oxide Thickness

Variation in thickness has negligible effect on DGFET. On the other hand, SOI seems to show an increase in hole density as top oxide thickness decreases as seen in Fig. 5c. It is likely due to the fact that top oxide is only above the channel (not source and drain).

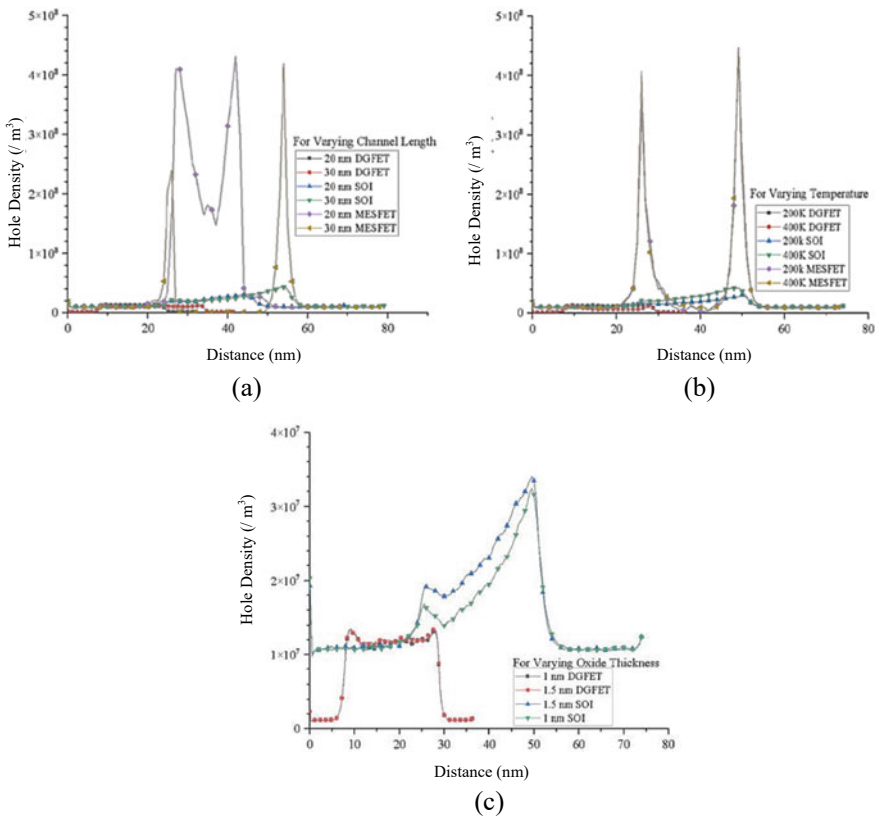


Fig. 5 Hole density versus device width curve for DGFET, MESFET, and SOI for variation in **a** channel length, **b** temperature, **c** hole density versus device width curve for DGFET and SOI for variation in top oxide thickness

3.5 Electron Energy

It is the potential difference between electron acceleration in the ionization source and electron ionization.

Effect of Varying Channel Length

It can be seen from Fig. 6a that as the channel length is shortened, the electron energy seems to increase. This is due to the fact that as the channel length is decreasing, the channel resistance tends to decrease and that leads to a rise in velocity, which in turn leads to rise in energy [19].

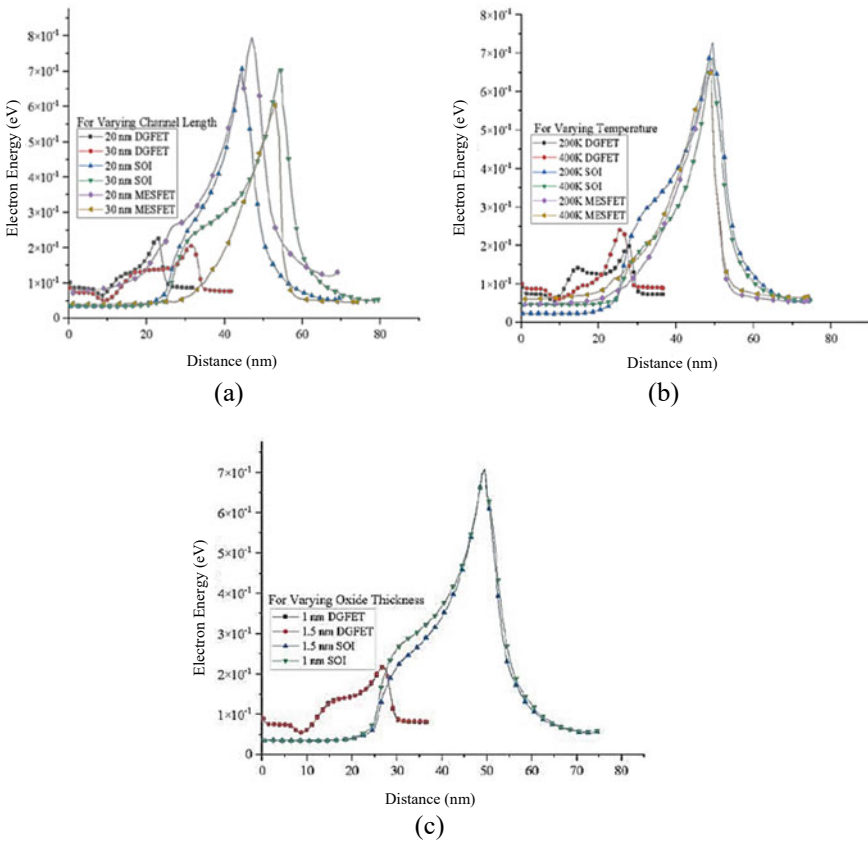


Fig. 6 Electron energy versus device width curve for DGFET, MESFET, and SOI for variation in **a** channel length; **b** temperature; **c** electron energy versus device width curve for DGFET and SOI for variation in top oxide thickness

Effect of Varying Temperature

Higher temperature leads to a higher peak value of energy. It can be seen from Fig. 6b that the device with the higher temperature reached a bigger peak than the same device at a lower temperature. However, we can also observe that the device operating on the lower temperature starts increasing in energy quicker and maintains that energy for a longer period of time. Average electron energy through the length of the device is more when operating a lower temperature [19].

Effect of Varying Top Oxide Thickness

Varying the oxide thickness does not seem to have any notable changes in the electron energy of any of the devices as they produce almost identical results to their counterparts. SOI is completely identical, while we see a slight increase in DGFET as seen in Fig. 6c, as it increases in energy a little quicker when the channel length is reduced [19].

3.6 Electron Velocity

Electron velocity is attained by charged particles, in a material due to an electric field. When electrons are subjected to an electric field, they do move randomly, but they slowly drift in one direction.

Effect of Varying Channel Length

As the channel length is decreasing, the electron velocity seems to rise, but this is not the case for all. At nanoscale, the linearity relation does not seem to hold. As devices get smaller, there is increase in electric field, and now, the carriers have a higher velocity in the channel. As velocity gradually reaches saturation velocity, there does not exist a linear relation at high fields between electron velocity and electric field [20, 21].

Effect of Varying Temperature

It is observed that the charge carrier mobility is decreased as there is an increase in the temperature which leads to a drop in electron velocity in the FET devices. This can be seen in Fig. 7b. Also, this reduces effective current through the channel [13].

Effect of Varying Top Oxide Thickness

Variation in thickness has negligible effect on DGFET. SOI again shows increase in electron velocity as oxide thickness is decreased as seen in Fig. 7c. This is because as oxide thickness gets larger, carrier tunneling and electron velocity become less dependent on the applied electric field [21].

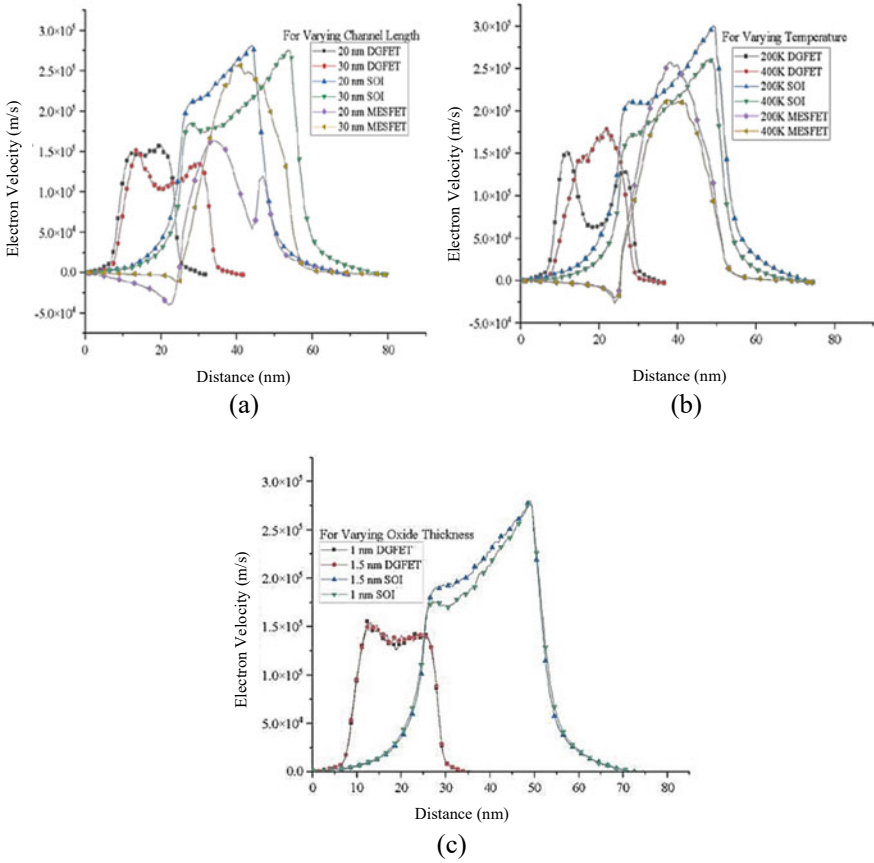


Fig. 7 Electron velocity versus device width curve for DGFET, MESFET, and SOI for variation in **a** channel length; **b** temperature; **c** electron velocity versus device width curve for DGFET and SOI for variation in top oxide thickness

3.7 Doping Density

It is the concentration of some dopant, e.g., of laser-active ions in a laser gain medium. It can be specified in different ways. Doping density has remained constant to what was set for simulations for source, drain, and channel for all changes in channel length, temperature, and top oxide thickness.

3.8 *Conduction Band*

It is the band of electron orbitals that electrons can jump up into from the valence band when excited.

Effect of Varying Channel Length

Conduction band increases with increase in channel length as seen in Fig. 9a. Conduction band is found lowest in the device with or without lower barrier lowering [22].

Effect of Varying Temperature

As shown in Fig. 9b, with an increase in temperature, the band gap energy decreases. This is because crystal lattice expands, and the interatomic bonds are weakened. The weaker interatomic bonds mean that less energy is required to break a bond and get an electron in the conduction band (Fig. 8).

Effect of Varying Top Oxide Thickness

The lesser the top oxide thickness, the more the band gap energy decreases, and less energy will be required for an electron to move to the conduction band. The top oxide thickness values taken here are small to see a notable difference, but we do notice a difference in SOI, as seen in Fig. 9c for top oxide thickness of 1.5 and 1 nm in channel length.

3.9 *Charge Density*

It is a measure of accumulated electric charge in a given region. It is dependent on how charge is distributed, and it can be both negative and positive.

Effect of Varying Channel Length

The resistance in FET devices is voltage dependent since the charge density inside the channel depends on gate voltage [23]. As we go to short-channel lengths, it is observed that as the drain and the source now support the charge in the depletion region, the threshold voltage also begins to decrease [24]. Simulation can be seen in Fig. 10a.

Effect of Varying Temperature

At lower values of gate to source voltage, the drain current increases with decrease in temperature. As the drain voltage increases, the voltage drop across the oxide near the drain terminal decreases, which means that the included inversion charge density near the drain also decreases.

Effect of Varying Top Oxide Thickness

There is not much effect of top oxide thickness on the charge density in source or drain as clearly visible from Fig. 10c, but in channel, with increase in top oxide

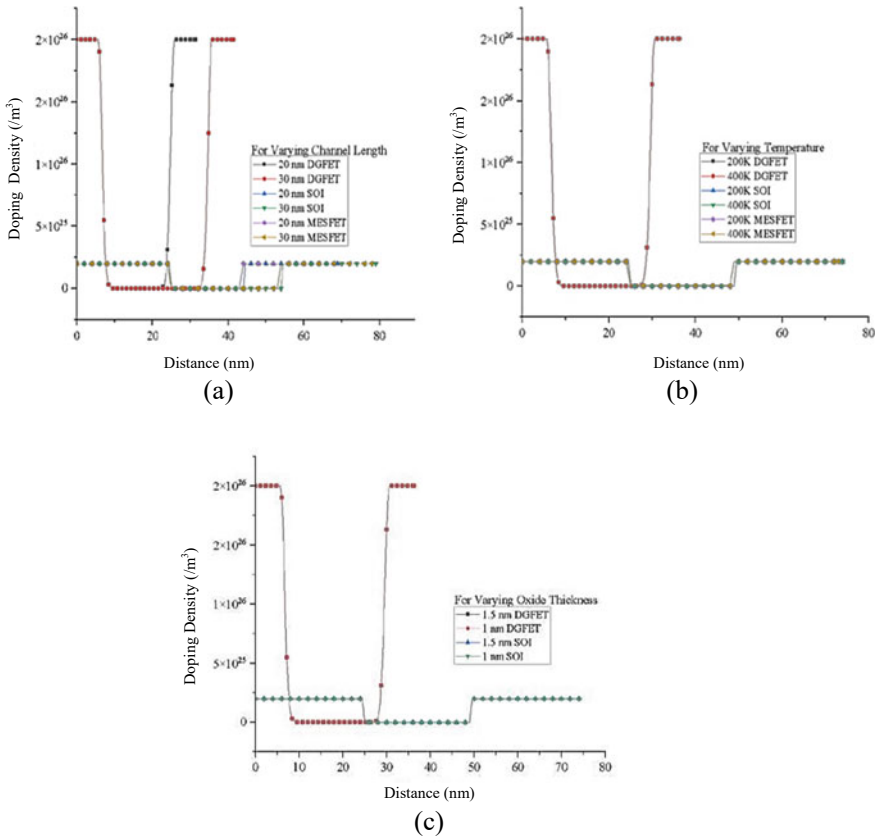


Fig. 8 Doping density versus device width curve for DGFET, MESFET, and SOI for variation in **a** channel length; **b** temperature; **c** doping density versus device width curve for DGFET and SOI for variation in top oxide thickness

thickness, charge density increases which is expected as there will be potential of more charge concentration.

4 Conclusion

For simulating quantization effects in double-gate MOSFET, MESFET, and SOI MOSFET to detect which device performs better, a quantum field approach was adapted and was utilized quite successfully in order to capture the simulation results for the output parameters that were considered for this paper. By results of simulations that were performed for this project, we clearly conclude that SOI MOSFET is much better than MESFET and DGFET for the input parameters that were varied for

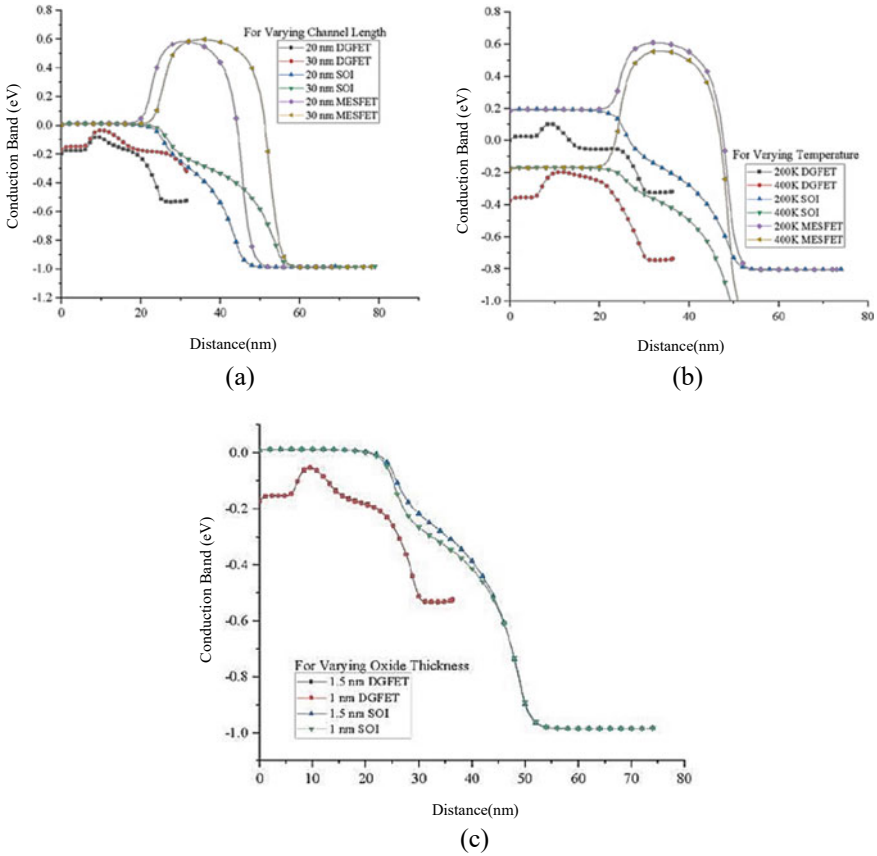


Fig. 9 Conduction band versus device width curve for DGFET, MESFET, and SOI for variation in **a** channel length; **b** temperature; **c** conduction band versus device width curve for DGFET and SOI for variation in top oxide thickness

most simulations. MESFET outperformed DGFET, and all three devices significantly outperformed bulk MOSFET. SOI has 24.89% better drain current than DGFET, which increases to nearly 80% with an increase in channel length from 20 to 30 nm. However, SOI has 34.93% better drain current than DGFET when temperature is 300 K and top oxide thickness 1 nm, but it reduces to 21.51% and 31% for 400 K temperature and a top oxide thickness of 1.5 nm, respectively. It is also observed that at device width of 22 nm, conduction band value for SOI is 0.00047, whereas the value for MESFET at the same device width is 0.17, which corresponds to the fact that SOI has lower barrier lowering than MESFET.

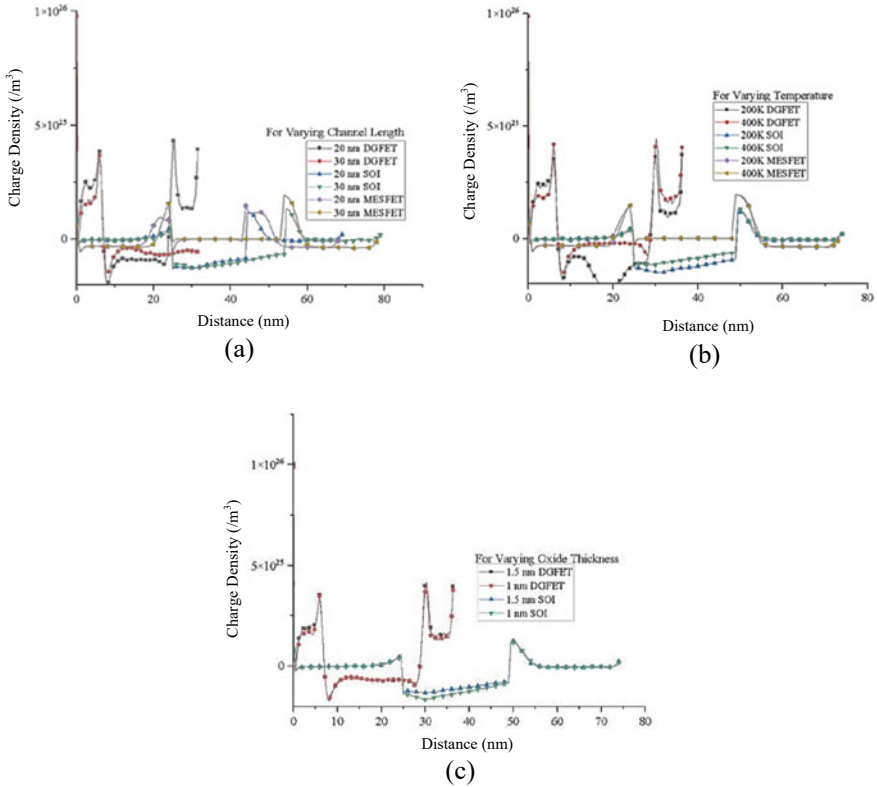


Fig. 10 Charge density versus device width curve for DGFET, MESFET, and SOI for variation in **a** channel length; **b** temperature; **c** charge density versus device width curve for DGFET and SOI for variation in top oxide thickness

References

1. Gupta SK, Pathak GG, Das D, Sarma C (2012) Design and simulation of a two stage OP-AMP using DG MOSFETs for low power and low voltage applications. *Int J Wisdom Based Comput* 1(3):60–63
2. Sun Z, Erickson N, Sun J, From R, Fan J (2019) Monte Carlo: particle simulation for electrical and thermal analysis of a MESFET using the finite-element approach. In: *IEEE MTT-S international conference on numerical electromagnetic and multiphysics modeling and optimization (NEMO)*, pp 1–4
3. Ahmed SS, Ringhofer C, Vasileska D (2005) Parameter-free effective potential method for use in particle-based device simulations. *IEEE Trans Nanotechnol* 4(4):465–471
4. Vasileska D, Ahmed SS (2005) Narrow-width SOI devices: the role of quantum-mechanical size quantization effect and unintentional doping on the device operation. *IEEE Trans Electron Devices* 52(2):227–236
5. Goyal N, Sah N (2018) Review article on impact of various engineering on double gate MOSFET. *Int J Electr Electron Comput Sci Eng* 5(2):2348–2273, 2454–1222

6. Chakrabarti H, Maity R, Maity NP (2019) Analysis of surface potential for dual-material-double-gate MOSFET based on modeling and simulation. *Microsyst Technol* 25(12):4675–4684
7. Mahabadi SJ, Moghadam HA (2015) Comprehensive study of a 4H–SiC MES–MOSFET. *Physica E* 74:25–29
8. Sarvaghad-Moghaddam M, Orouji AA, Ramezani Z, Elhoseny M, Farouk A (2019) Modelling the spice parameters of SOI MOSFET using a combinational algorithm. *Clust Comput* 22(2):4683–4692
9. Aziz MA, Salehuddin F, Zain ASM, Kaharudin KE, Radzi SA (2014) Comparison of electrical characteristics between Bulk MOSFET and Silicon-on-insulator (SOI) MOSFET. *J Telecommun Electron Comput Eng* 6(2):45–49
10. Karbalaie M, Dideban D, Heidari H (2019) Improvement in electrical characteristics of Silicon on Insulator (SOI) transistor using graphene material. *Results Phys* 15:102806
11. QuaMC2D. <https://nanohub.org/resources/quamc2d>. Last accessed on 2021/10/30
12. Kaharudin K, Salehuddin F, Zain A, Roslan AF (2019) Effect of channel length variation on analog and RF performance of junctionless double gate vertical MOSFET. *J Eng Sci Technol* 14(4):2410–2430
13. Sinha SK, Chaudhury S (2013) Impact of oxide thickness on gate capacitance—a comprehensive analysis on MOSFET, nanowire FET, and CNTFET devices. *IEEE Trans Nanotechnol* 12(6):958–964
14. Temperature affects the Fermi distribution. <http://www.ece.utep.edu/courses/ee3329/ee3329/Studyguide/ToC/Fundamentals/Carriers/explain.html>. Last accessed on 2021/10/30
15. Radzi NM, Sanudin R (2017) Effect of oxide thickness variation in sub-micron NMOS transistor. In: IOP conference series. Materials science and engineering (online), vol 226, no 1
16. Callister WD (2018) Materials science and engineering an introduction, 8th ed. Wiley
17. Vardhan H (2015) Effects of gate length and oxide thickness on DG-MOSFET. *Int Res J Eng Technol* 2(8)
18. Assad F, Ren Z, Vasileska D, Datta S (2000) Lundstrom: on the performance limits for Si MOSFETs: a theoretical study. *IEEE Trans Electron Devices* 47(1):232–240
19. Choi BK, Park KH, Han KR, Kim YM, Lee H (2007) Threshold voltage modeling of double-gate MOSFETs by considering barrier lowering. *J Semicond Technol Sci* 7(2):76–81
20. Dixit S, Singh RK, Singh AK (2019) Short channel effects and their mitigation. *Int J Appl Eng Res* 14:0973–4562
21. Liu H, Neal AT, Ye PD (2012) Channel length scaling of MoS₂ MOSFETs. *ACS Nano* 6(10):8563–8569
22. The Field Effect Transistor. <https://www.mhhe.com/engcs/electrical/neamen01/etext/ch05.pdf>. Last accessed 2021/10/30
23. MOSFET-Short Channel Effects. <https://nptel.ac.in/content/storage2/courses/117101058/downloads/Lec-8.pdf>. Last accessed 2021/10/30
24. FET Temperature Effects. <https://coefs.unc.edu/dlsharer/files/2012/04/J8a.pdf>. Last accessed 2021/10/30

Distraction of Experienced Drivers at a Construction Site Using Eye Tracker



Kamini Gupta, Piyush Miglani, Purva Dua, Amit Agarwal ,
and Neelima Chakrabarty

Abstract More than a million people die and many more are injured every year in road crashes. There are various factors, which affect the chances of a road traffic injury, and many of them can be avoided/ improved to limit the exposure to vulnerable road users. Distraction in traffic is another risk, which is another major concern for planners and policymakers. Driver distraction can result from various factors/sources, which can be from inside a vehicle or outside a vehicle. External distractions may arise due to building/ structure/ people/ activities/ billboards (i.e., road side advertising) along the road, and a driver is attracted to them. The present study attempts to study the distraction patterns of experienced drivers due to external factors (e.g., construction site). The case study is chosen as Ashram intersection in Delhi. A road safety audit of that construction site was performed. Distraction pattern of drivers have been captured using wearable eye-tracker and processed for pre-defined zones. Fixation patterns are analyzed for approach transition, working, and terminal transition zones. The combined heat maps are used to provide an estimated distraction of all the drivers superimposed onto a single frame. The study exhibits that the highly skilled drivers are only marginally affected by the construction site; however, the distraction can be further minimized if recommendations of road safety audits are implemented correctly.

Keywords Road safety · Eye tracker · Construction site · Distraction

K. Gupta · N. Chakrabarty
CSIR-Central Road Research Institute, New Delhi, India

P. Miglani · P. Dua · A. Agarwal (✉)
Indian Institute of Technology Roorkee, Roorkee, India
e-mail: amitfce@iitr.ac.in

P. Miglani
e-mail: pmiglani@ce.iitr.ac.in

P. Dua
e-mail: pdua@ce.iitr.ac.in

1 Introduction

1.1 Background

About 11% of the world's accidents-related deaths happen in India, i.e., about 150,000 persons every year, which accounts for about 0.77% of the nation's GDP [1]. Over speeding, careless driving, drunk driving, wrong side, and signal jumping, etc., are the main causes of accidents. About 65% of the accidents occurred on the straight road section, where the drivers become less attentive (or distracted). Typically, a driver needs to pay attention for the whole duration of driving, more explicitly to traffic and other road users), road signs, traffic signals, road surface, potholes, sand/gravel on the surface, etc. Thus, road safety management, safer roads and mobility, safe vehicles, road user behavior, and post-crash care are the five pillars of road safety. India is taking bold and innovative steps to tackle its road safety challenges.

1.2 Driver Distraction

Distraction is the major factor, and this is particularly challenging nowadays, where a wide spectrum of technologies (e.g., use of touch screen panel or infotainment system, use of digital maps for the route navigation, adjusting the temperature, etc.) have been introduced into the car environment may be dash mounted or wearable. Typically, distraction is an event, which causes a driver to focus on an activity other than remain focused on driving [2]. There could be a person/ object within/ outside of the vehicle, which induces a shift in the driver's attention. This distraction could be cognitive (mind off from driving), manual (hands off the steering), auditory and visual (eyes off the road). As a consequence of automation in the vehicle technology, the various types of distraction caused by secondary tasks that drivers have to manage have increased over the years, hence increasing distracted driving or sometimes due to road scenarios. The distraction leads to an increase in the reaction time, and longer reaction times may steer to accidents. A few studies studied the behavior of the drivers to evaluate the impact on the reaction time using driving simulators [3–5]. Similarly, Choudhary and Velaga [4] used driving simulator to study the pedestrian crossing event during use of a mobile phone. An increase in reaction time by 40%, 95%, 137%, and 204% for simple conversation, complex conversation, simple texting, and complex texting while driving was found [4]. Clearly, an increased reaction time is a result of distraction. Driver distraction is also a common reason for road accidents, therefore, in this study, focus is on driver distraction at one of the construction sites in Delhi using eye tracker.

1.3 Past Studies Using Eye Tracking

There are many studies that attempted to study the reaction time, speed, lane positioning, etc., (i.e., performance measures) of the drivers using a driving simulator [3, 4, 6–9]. A few other studies looked at the psychological responses using the driving simulator and in real-world conditions [10]. In addition to driving simulators, eye movements of the drivers can be studied to understand the pattern in case of fatigue, distraction, carelessness, etc. A few studies attempted to use eye tracker to study psychological factors, distractions, etc. Typically, two devices are used for such purposes, i.e., glasses and dashboard based. The former is placed on the head of the driver as a helmet or regular glasses. The latter is more suitable, when no physical contact should be made with the driver, i.e., installed on the dashboard of a vehicle and sensors placed in the helmet/ glasses/dashboard track the eye movement. A review of various studies is presented, which aims to perceive the cognitive function of eyes, to exhibit movement patterns of eyes [11]. Further, the study demonstrates the use of various eye trackers under various driving conditions. The literature lacks understanding of eye fixation, gazing pattern/ direction, reaction time, impact of monotonous driving conditions, etc. A few studies used eye tracker under a controlled environment (i.e., a driving simulator) [12, 13]. The former study confirms that the eye-tracking might provide the cognitive load estimation of the driver. The latter study compares the reaction times of racing and non-racing drivers using eye trackers using a racing simulator.

In a study, which uses FACELab eye tracker under controlled conditions on a driving simulator, found that the fixation time for older (experienced) drivers is longer than younger (newer) drivers [14]. In the similar direction, PERCLOS (“Percentage of Eyelid Closure Over the Pupil Over Time”) and ACES (“Average Eye Closure Speed”) are combined to propose an algorithm, which detects driver fatigue [15]. Fatigue is a major problem due to monotonous driving conditions. Eye tracking methodology can also be used to study the psychological behavior [16]. In another study, it is shown that with the help of eye monitoring, the quality of infrastructure can be evaluated toward road safety [9]. Similarly, gazing patterns are studied to understand the driver awareness at an urban intersection [8].

Overall, very few studies have attempted to use eye tracker to study the eye movement, gazing pattern of drivers under various conditions (e.g., distraction due to vehicle automation, fatigue, construction work along the roads, etc.). In a study, Indian drivers were asked to drive a vehicle on a driving simulator and wearing eye trackers. The study attempted to study the violations [17]. Similarly, another study attempted to study the distraction patterns on Indian roads using a driving simulator [18]. The authors found that the gaze percentage of all drivers were above 90%, and the average fixation duration for 25–30, 31–35, and 36–40 years are 73%, 70%, and 80%, respectively.

1.4 Problem Statement

A review of driver's distraction using eye-tracking highlights the need for distraction studies using eye tracker in real conditions [19]. Since roadside construction activities are likely to intensify the chances of roadside hazards, the distraction of drivers due to such activities needs to be studied. The scope of the study is limited to study the distraction patterns of the highly experienced drivers in a metro city.

1.5 Objectives of the Study

The objectives of this work are to

- study the distraction of very experienced (expert) drivers in real conditions due to construction work along with an arterial and
- perform the road safety audit of the construction site.

For this, the eye movement data is collected using an eye tracker in the field.

2 Study Area and Methodology

Figure 1 shows the various steps involved in this study. These steps are explained in subsequent sections.

2.1 Site Selection

Ashram intersection in Delhi is selected for the present study. It serves very high traffic and has stop-and-go conditions during peak hours. Figure 2a shows the top view of the site. A flyover is already functional, and an underpass is being constructed at this location. The length of the underpass is 750 m. Two approach arms, perpendicular to the flyover are, Faridabad side and India gate side having an approach-based signal during construction. On each approach, a signal is installed, which are functioning as roundabout signals.

The construction site is very unsafe. In the work zones, the recommended guidelines (IRC:SP:55-2014) are not followed strictly (see Sect. 3). Thus, road users, specifically, non-motorized users are vulnerable.

Five different zones are considered during the whole driving trip. These are approach transition zone, working zone, two traffic signals (approach to Bhogal and near Ashram metro station), and termination (or terminal transition) zone. Figure 3 shows the five different zones. It is a total of around 540 m journey, the length

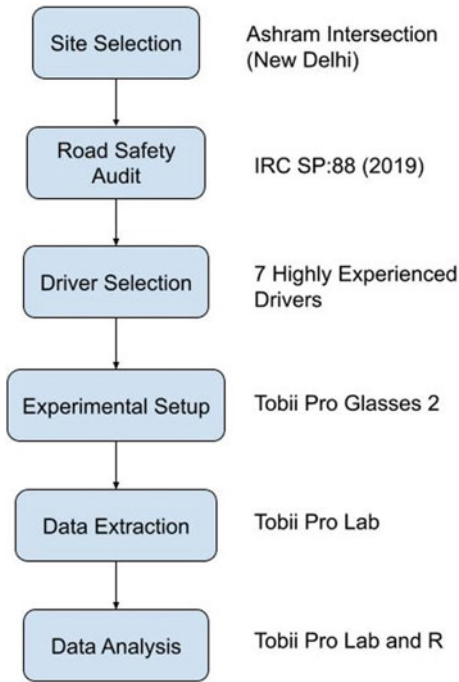


Fig. 1 Methodological steps

between two consecutive zones is as given in Table 1. The tests were conducted during afternoon hours in broad daylight and peak traffic hours. Originally, the road consisted of three lanes in each direction, but due to construction, only one lane or two lanes were available at different sections of the road.

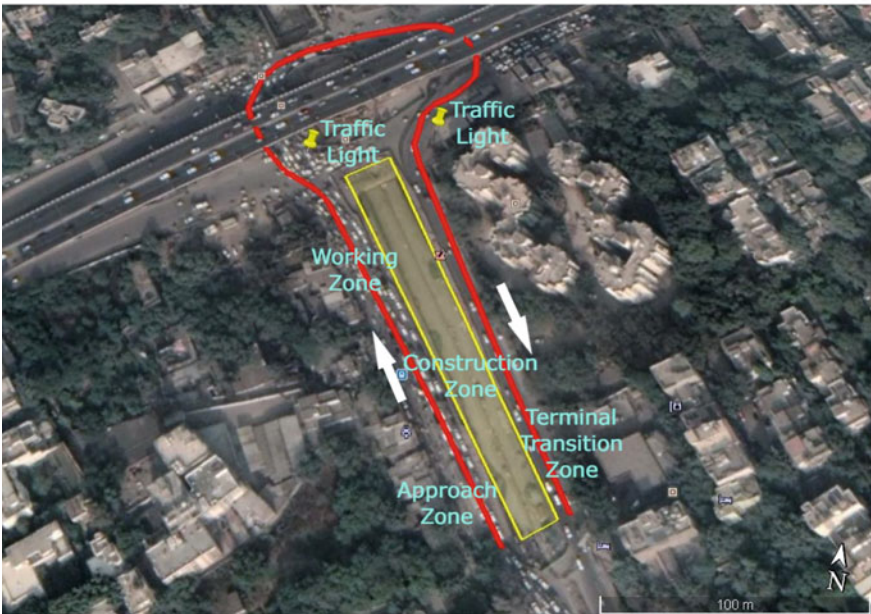
The route was unknown to the drivers. If this is not the case, the distraction patterns are likely to differ due to the knowledge of the surroundings (see [7] for impact of route familiarity). Since the primary focus of the study is distraction at the construction site, only three zones are used for analysis, i.e., approach transition zone, working zone, and terminal zone.

2.2 Driver Selection

In this study, seven skilled, male, 25–40 years old drivers are selected. These drivers were very experienced, and driving is part of their long-term job. The mean annual mileage-driven is 150,000 km, and mean driving experience is 11.5 years. The Keystone eye viewer is used to test the vision of the drivers in all aspects. All the drivers had an acceptable range of vision. These drivers were asked to wear the eye



(a) Top view of Ashram Intersection



(b) Markings for selected segment, including construction site

Fig. 2 Ashram intersection, Delhi and different zones for analysis



Fig. 3 Areas of interests for the study

Table 1 Details of the zones

Zone	distance(in m)
Approach transition zone	51
Working zone	98
Traffic signal 1	27
Traffic signal 2	100
Terminal transition zone	160

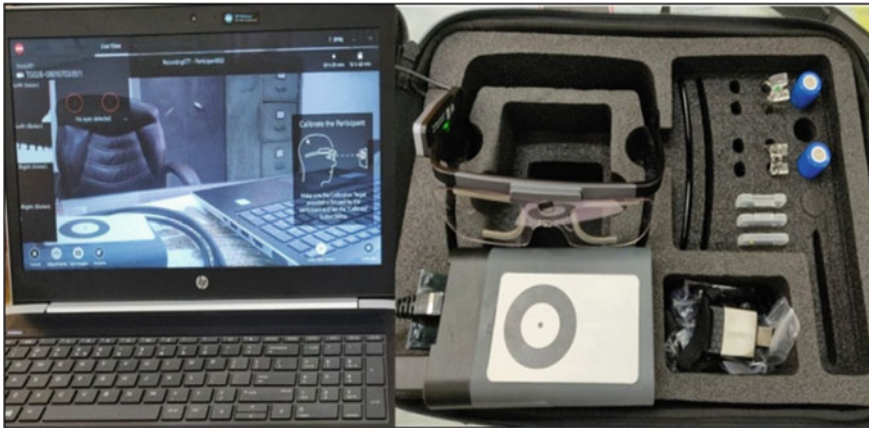


Fig. 4 Tobii Pro eye tracker controller and glasses

tracking glasses (see Sect. 2.3 for experimental set up) and drive a car on a pre-defined route. The marked zone in Fig. 2b is the selected segment of the trip. All drivers followed the same route at different times.

2.3 *In-Field Experimental Set up*

The eye tracker is a device that can be used as a regular-glasses, while driving on a simulator or in real-world conditions. It can also be used while riding a bicycle or motorcycle. At first, the device is self-calibrated before the start of the recording, for each participant. This was performed using a calibration card. The device is connected with a recording unit (pocket friendly), which stores the data on-the-go in a memory card. At first, the driver undergoes a practice session on a driving simulator and/ or on a controlled stretch so that drivers become comfortable with the device. The data was collected during daytime (≈ 30 min trip time) in Nov., 2020, i.e., after the first wave of the COVID-19 pandemic. The traffic conditions were close to the pre-Covid levels, which is also observed by looking at the traffic conditions in the videos/ images; therefore, the results are unlikely to be affected by the COVID-19 pandemic.

In this study, Tobii Pro Glasses 2¹ are used (see Fig. 4). It has four eye cameras (two on each side), gyroscope and accelerometer sensors, scene outward-facing camera with 90° field of view.²

¹ See <https://www.tobii.com/product-listing/tobii-pro-glasses-2/>

² <https://www.tobii.com/siteassets/tobii-pro/accuracy-and-precision-tests/tobii-pro-glasses-2-accuracy-and-precision-test-report.pdf> for technical details (e.g., accuracy, precision, etc.) of the sensors.

2.4 Data Extraction

In order to analyze the data, recorded data is processed using a dedicated software Tobii Pro Lab.³ The extraction of eye-tracker metrics needs manual efforts (i.e., first selection of a discrete screen out of the recorded video, creating events of gazing and fixation pattern on the screenshot, creating heat maps, etc.). Therefore, the results are prepared for three AOIs. Following measurements are extracted:

- Eye movement type: At first, it is tested if eyes not found properly or saccade (rapid movement of eyes) occurs or fixation is high/ low.
- Gaze sample percentage (portion of recording for which one or both eyes were found); an eye tracker with 50 Hz frequency has 50 samples per second, it is unlikely that 100% of the samples can be used to calculate gaze points due to blinking or any other reasons.
- Weighted gaze samples: About 100% if both eyes found for full recording, 50% if both eyes for 50% of recording and one eye for half of the recording

3 Road Safety Audit

A road safety audit was done prior to the experiment to identify the safety concerns at a construction site. Typically, IRC:SP:55-2014 provides guidelines to address the traffic management in work zones and IRC:SP:88-2019 provides guidelines for road safety audit. A few safety concerns are shown in Fig. 5. The findings of the road safety audit and risk levels are tabularized in Table 2. Clearly, if the risk level is very high for any safety concerns, these are essential and should be fixed immediately. High-risk level concerns are highly desirable. For instance, the traffic management plan, which is essential for smooth traffic flow, is missing, thus imposing greater risk to the drivers and causing delays. Furthermore, to inform the drivers about the construction zones, warning signs should be provided in advanced warning zones. Chevron and hazard markings are missing, which is a very high safety risk, especially in low lights.

4 Results

4.1 Impact of Construction Activities

The video data from one of the drivers is not able to capture the approach zone, working zone, and terminal transition zone, thus, excluded from the analysis. For the analysis, data from six drivers is used. Five drivers used the same path (see Fig. 2)

³ <https://www.tobii.com/product-listing/tobii-pro-lab/>



Fig. 5 Safety concerns identified during road safety audit

Table 2 Findings of the road safety audit

Safety concern	Risk level
Traffic management plan is missing Prior information of work zone missing Chevron and hazard marking missing GI sheet to separate working area with traffic (very dangerous)	Very high
Incomplete zebra crossing Improper advance warning zone Improper approach transition tapering	High
No new jersey barrier Poor condition of road Improper diversion signs No/ improper facility/marking for NMT users	High

and one driver passed through the first three zones (i.e., went straight toward India gate, see Fig. 2) only. The average time to cover the five zones (from approach to terminal) of length about 600 m, is 9 min 17 s. It ranges from 6 min 25 s to 12 min 38 s, which should typically take about 1–1.5 min. Clearly, the higher travel time is a consequence of congestion due to construction activities and traffic signals.

Figure 6 shows the box plots of gazing sample percentage for various zones and for the whole journey. This number is given in %, and represents active seeing, i.e., portion of recording for which one or both eyes were found. A lower value is possibly due to the blinking of eyes, waving head, low light, or other reasons and is undesirable

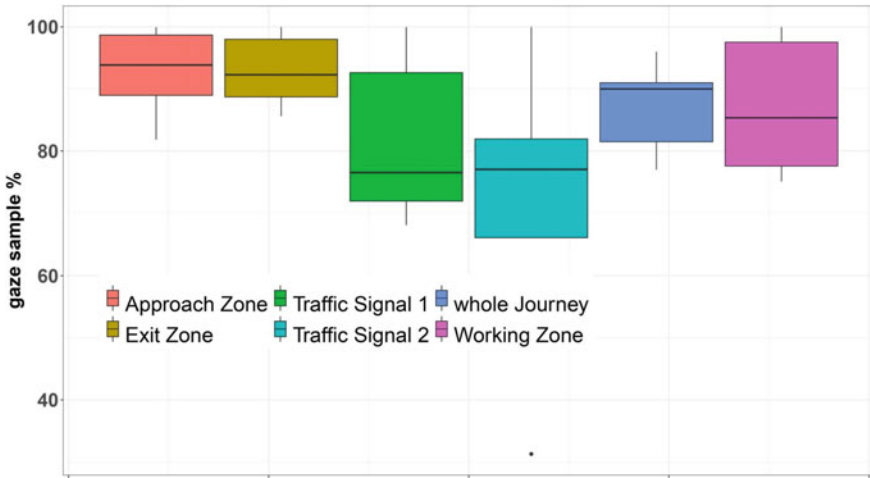
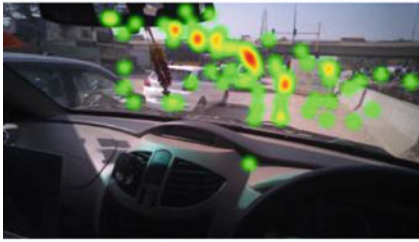


Fig. 6 Gaze sample percent for different zones and whole journey

while driving. From Fig. 6, it can be observed that the gaze sample percentage is very high except for the traffic signals. At traffic signals, i.e., in a stand-still condition, it is most likely that the drivers will be closing eyes to relax or looking away than the field of view of the camera.

Figure 7 shows the heat maps produced using the gaze plot for working, traffic signal 1, and terminal transition zones. The heat map shows the points where the driver was looking. The red color denotes higher frequency at a point, whereas green is showing fewer gaze points. From Figs. 7a, c, it can be observed that the driver is not focused and looking at many points in the approach zone than in the terminal transition zone. During the approach, drivers are likely to be inquisitive due to new route (and new information)/hazard information, whereas in the terminal transition zone, the driver is accustomed to the area and possible hazards. A plausible interpretation is that if proper signage, markings are provided at a construction site (see Sect. 3), drivers are more likely to understand it quickly (very less or no fixation) and may not be interested in collecting information related to area and plausible hazard. Thus, ignoring the provision of signage, marking, etc., are likely to create distraction for the drivers. Further, the heat map for traffic signal (see Fig. 7b) indicates that the driver is attempting to look at the traffic signal and at the same time, he is distracted due to movement on the flyover (i.e., unwanted information) rather than focusing on the signal or road.



(a) Heat map for working zone



(b) Heat map for traffic signal 1 zone



(c) Heat map for terminal transition zone

Fig. 7 Heat map of a driver in various zones

4.2 Analysis for Areas of Interest

In order to understand the distraction pattern of these drivers, three areas of interest are defined. These are in the approach zone, working zone, and terminal zone. In each of these zones, for every frame, an area is specified (like a polygon) where the number of fixation, fixation duration, etc., are counted. The area is selected such as to identify the distraction due to the construction site. Figure 8 shows the areas of interest for three zones.

The interval time and fixation duration for six drivers are shown in Fig. 9. The former is time spent by a driver in each zone, and the latter is time of fixation in the pre-defined areas of interest (see Fig. 8). Higher is the fixation duration, more distracted is the driver. From Fig. 9, it can be observed that the fixation duration is pretty low in all zones except for one driver, whose fixation is higher in the working zone (i.e., driver 'r88'). Interestingly, three drivers in the approach zone, two drivers in terminal transition zones, and one driver in the working zone are not distracted at all, i.e., they are not attempting to collect the new information about route/ possible hazards. The number of fixations is also very low for these drivers, this indicates that the skilled drivers are very less distracted due to construction sites. These drivers are more focused on the road.

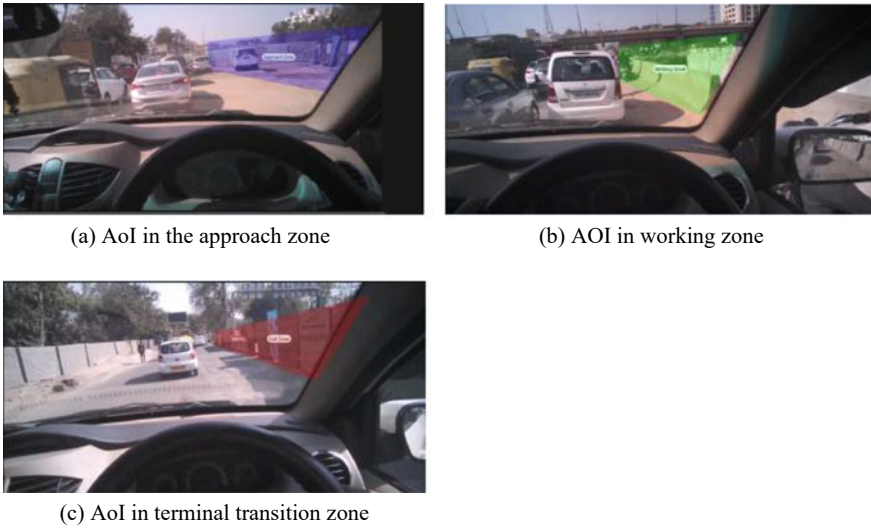


Fig. 8 Area of interests defined for distraction analysis

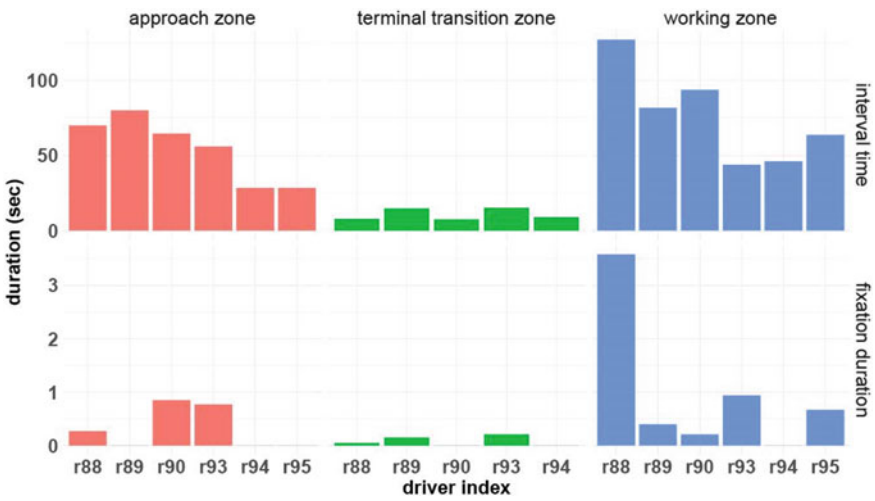


Fig. 9 Interval time and fixation duration in AoIs



Fig. 10 Combined heat maps for five zones considered in the present study

4.3 Combined Heat Maps

In order to see the overall distraction pattern in the five zones, the heat maps of individual drivers are superimposed in one image.⁴ The final heat maps are shown in Fig. 10. Following can be observed:

- The construction activities have affected the very skilled driver marginally (i.e., experienced drivers are more attentive on the road rather than collecting more information from the adjacent working areas). That means, the novice drivers will be affected most and may lead to accidents.

⁴ These superimposed heat maps are approximates due to the fact that no two drivers can have identical spatial trajectories.

- The traffic signal 2 is immediately after a ‘U’ turn (see Fig. 2), which has led to diversified gazing. This indicates the confusion among the drivers. Thus, the traffic signal may need to be redesigned.
- In the terminal transition zone, almost all drivers are very focused, i.e., in absence of construction activities, drivers are focused. Another interpretation is that the drivers are used to the working area and therefore not looking at many points. However, most of the drivers were attentive in the approach transition zone, therefore, least distraction is the most appropriate explanation.

5 Conclusions

Distracting activities while driving are common and can result in driving errors, which ultimately affects the safety of road users. As driver’s exposure to distraction (maybe in-vehicle or external distraction) is high, policies that include education and innovative enforcement practices are required to decrease the adverse outcomes.

The present study attempts to look on the distraction of experienced drivers due to construction work along the road using an eye-tracker device. In this study, it has been found out that:

- The average time to cover the five zones (from approach to terminal) of length about 600 m, is 9 min 17 s, which should typically take about 1–1.5 min. It is because of congestion due to construction activities and traffic signals.
- At the construction site, the road safety guidelines by IRC:SP:88-2019 and IRC:SP:55-2014 were not followed, which increases the risk for the road users.
- Higher is the fixation duration on the adjacent work areas, more distracted is the driver, i.e., a driver is collecting more information about the route/hazard, etc. However, this can be reduced substantially, if standard guidelines are followed in work zones. Except, one driver, whose fixation is higher in the working zone, all other drivers have a marginal effect due to the construction work. This is likely to be an effect of their extensive experience.
- Drivers are more distracted and looking at many more points in the approach zone (inquisitive) than in the terminal transition zone (used to with the route).
- The traffic signal close to Ashram intersection, which is immediately after a ‘U’ turn (see Fig. 2), which has led to diversified gazing. This indicates the confusion among the drivers and pedestrians.

In summary, at the selected site, selected drivers were very less distracted since they are skilled drivers. Thus, the results obtained in this study can be used as a reference to study the distraction of novice/ untrained drivers, which is likely to be affected most and may lead to accidents.

6 Future Scope

Though this work summarizes the findings for a construction site in Delhi, the similar distraction characteristics can be observed for experienced drivers in other cities. Due to paucity of time, the selected sample size was only seven drivers and of the same age groups of (commercial category) drivers. In the future, more sample size (male and female drivers; novice and experienced) can be taken with different environmental settings in simulated as well as in-field conditions to draw more concrete conclusions for policy recommendations. In addition to the eye tracker, ECG, and thermal cameras can allow a better interpretation of cognitive processes while driving.

Acknowledgements The authors wish to thank the Director of the CSIR-CRRI, Prof. Satish Chandra, for his continuous encouragement, and support. The authors wish to thank Tobii Pro for providing two free licenses of Tobii Pro Lab for a month.

References

1. MoRTH. Road accidents in India 2019 (2019) Technical report, ministry of road transport and highways
2. Pettitt M, Burnett G, Stevens A (2005) Defining driver distraction. In: World congress on intelligent transport systems, San Francisco
3. Boyle LN, Lee JD (2010) Using driving simulators to assess driving safety. *Accid Anal Prev* 42(3):785–787. <https://doi.org/10.1016/j.aap.2010.03.006>
4. Choudhary P, Velaga NR (2017) Modeling driver distraction effects due to mobile phone use on reaction time. *Transp Res Part C: Emerg Technol* 77:351–365. <https://doi.org/10.1016/j.trc.2017.02.007>
5. Underwood G, Crundall D, Chapman P (2011) Driving simulator validation with hazard perception. *Transport Res F: Traffic Psychol Behav* 14(6):435–446. <https://doi.org/10.1016/j.trf.2011.04.008>
6. Alavi SS, Mohammadi MR, Soori H, Ghanizadeh M (2017) The cognitive and psychological factors (personality, driving behavior, and mental illnesses) as predictors in traffic violations. *Iran J Psychiatry* 12(2):78–86. <https://www.ncbi.nlm.nih.gov/pmc/articles/PMC5483241/>
7. Hu Y, Liu H, Zhu T (2019) Influence of spatial visual conditions in tunnel on driver behavior: considering the route familiarity of drivers. 11(5):168781401985366. <https://doi.org/10.1177/1687814019853661>
8. Stapel J, El Hassnaoui M, Happee R (2020) Measuring driver perception: combining eye-tracking and automated road scene perception. 001872082095995. <https://doi.org/10.1177/0018720820959958>
9. Vetturi D, Tiboni M, Maternini G, Bonera M (2020) Use of eye tracking device to evaluate the driver's behaviour and the infrastructures quality in relation to road safety. *Transp Res Procedia* 45:587–595. <https://doi.org/10.1016/j.trpro.2020.03.053>
10. Johnson MJ, Chahal T, Stinchcombe A, Mullen N, Weaver B, Bedard M (2011) Physiological responses to simulated and on-road driving. *Int J Psychophysiol* 81(3):203–208. <https://doi.org/10.1016/j.ijpsycho.2011.06.012>
11. Kapitaniak B, Walczak M, Kosobudzki M, Jóźwiak Z, Bortkiewicz A (2015) Application of eye-tracking in drivers testing: a review of research. *Int J Occup Med Environ Health* 28(6):941–954. <https://doi.org/10.13075/ijomeh.1896.00317>

12. Palinko O, Kun AL, Shyrovkov A, Heeman P (2010) Estimating cognitive load using remote eye tracking in a driving simulator. In: Proceedings of the 2010 symposium on eye-tracking research & applications—ETRA '10. ACM Press. <https://doi.org/10.1145/1743666.1743701>
13. van Leeuwen PM, de Groot S, Happee R, de Winter JCF (2017) Differences between racing and non-racing drivers: a simulator study using eye-tracking. PLoS one 12(11):e0186871. <https://doi.org/10.1371/journal.pone.0186871>
14. Fildes BJ, Charlton J, Muir C, Koppel S (2007) Driving responses of older and younger drivers in a driving simulator. In: 51st Annual proceedings association for the advancement of automotive medicine, 2007
15. Lang L, Qi H (2008) The study of driver fatigue monitor algorithm combined PERCLOS and AECS. In: 2008 International conference on computer science and software engineering. IEEE, 2008. <https://doi.org/10.1109/csse.2008.771>
16. Mele ML, Federici S (2012) Gaze and eye-tracking solutions for psychological research. Cogn Process 13(S1):261–265. <https://doi.org/10.1007/s10339-012-0499-z>
17. Thakur V, Gupta K, Chakrabarty N, Chopra T (2019) Approach to driver visual behaviour using eye tracker. In: 6th Colloquium on transportation systems engineering and management, SVNIT Surat
18. Thakur V, Gupta K, Chakrabarty N, Velumurgan S (2019) Distraction pattern of driver using eye tracker on Indian Roads. In: 5th conference of the transportation research group of India, Bhopal
19. Ojstersek TC, Topolsek D (2019) Eye tracking use in researching driver distraction: a scientometric and qualitative literature review approach. J Eye Mov Res 12(3). <https://doi.org/10.16910/jemr.12.3.5>

Detailed Economic Analysis of Solar Rooftop Photovoltaic System: Case Study of Institutional Building



Kritika Kohli, Saurabh Kumar Rajput, and Sulochana Wadhvani

Abstract Energy conservation has become an important part of a country's economic growth. Our country, India, is committed to generating electricity through unconventional methods. The most extensively used renewable energy source is solar PV. A lot of money is invested in solar photovoltaic systems. Thus, rooftop photovoltaic systems require economic analysis. An economic analysis of a 100 kWp grid-connected solar rooftop PV system is presented in this research. Cost–benefit analysis, calculation of payback period, and analysis of electricity bills are covered in the study. After the cost–benefit analysis, the payback period is 5.5 years. After analysis of the electricity bills, it was seen that the maximum demand, running charges, and power factor decreases after the installation of the system. The average power factor before installation of the system was 0.963 and after the installation is 0.9143.

Keywords Photovoltaic (PV) · Economic analysis · Cost–benefit · Payback period · Power factor

1 Introduction

Non-conventional energy sources produce clean energy. Solar energy is widely used and has a good potential of producing electricity [1]. Solar PV has the largest share among all the renewable energy resources in most parts of the world, including India [2]. In India, solar capacity has risen from 2.6 GW to over 36 GW in recent years. [3]. Since solar PV technology has increased immensely, economic analysis becomes important. Various studies have been carried out in different parts of the world including India on the same. Economics of a 120 kW photovoltaic system showed that the system was highly efficient with payback period 5.24 years and internal rate of return 31.88%. It was observed that the system degradation factor has an important role in economic analysis. It was finally concluded that the Middle Eastern part of the world had great potential for installing solar photovoltaic system

K. Kohli (✉) · S. K. Rajput · S. Wadhvani
Department of Electrical Engineering, MITS, Gwalior, Madhya Pradesh, India
e-mail: kohlkritika1@gmail.com

© The Author(s), under exclusive license to Springer Nature Singapore Pte Ltd. 2022
V. Mahajan et al. (eds.), *Sustainable Technology and Advanced Computing in Electrical Engineering*, Lecture Notes in Electrical Engineering 939,
https://doi.org/10.1007/978-981-19-4364-5_32

441

[4]. In the last few years, Europe has grown rapidly in the PV market. A study has been done to evaluate the economic parameters in seven European countries with different schemes and different types of solar PV systems. It was observed that the size of the system had a significant effect on profitability. It was also seen that Germany, Italy, Spain, and Greece were the countries that had good potential to install PV systems due to favorable conditions. But overall, in most cases, the systems came out to be not profitable [5]. A PV system in Jeddah, Saudi Arabia was studied. The size of the system was estimated to be 12.25 kW. It was seen that performance ratio of the system was low because of the high solar cell temperature at that place which further affects the efficiency of solar cell. Performance ratio was 78%. Capacity factor was found out to be 22%. Economic analysis was done and it was estimated that the net present value was \$4378 and payback period was 14.6 years [6]. A 2.1 kW system at Norwegian University was analyzed. The levelized cost of energy was calculated and it came out to be US \$0.246/kWh which was much higher than the tariff in Norway. But feed-in-tariff and some financial support can increase the development of PV systems. Less sunlight and other climate factors may reduce the system's economic utility [7]. Systems were evaluated economically and environmentally in several Italian locations. Less CO₂ emissions were measured by reducing net present value and internal rate of return. The annual average insolation value and the design philosophy applied influenced the outcomes. The design principle also affects the performance of the PV plants. The results obtained by using both the design principles, i.e., the principle of first year and principle of economic maximization were almost similar [8]. A study for the University of Jordan has been done. Different types of solar PV systems like fixed axis, single axis, and double axis was studied. Two different engineering models, BOT and EPC, were taken into account while doing the study. The fixed axis system utilizing the EPC model was shown to be more advantageous with a 3-year payback period and an IRR of 32%. In the BOT model, the single axis system had the best payback period of 8.5 years [9]. Three different types of buildings in two different states with different price plans were studied. Some economic indicators were used to evaluate the economic benefits of using the PV system in these buildings. It was concluded that building 2 had better results in state A and building 3 had better results in state B. Investment was not profitable in both the states as payback period was more than 20 years [10]. The performance of a 27 kW grid-connected system was observed in Suriname. The PR and CF were found to be 74.5 and 15%, respectively. The NPV of the project was estimated as \$-110,527. The results showed that since the payback period is much more than the lifetime of the system, the system under study was not economically feasible. Moreover, the levelized cost of energy of the system was found out to be 3.5 times more than the current price of energy in that place [11]. A 1 MWp PV system in Adam, Oman was analyzed. The yearly yield factor of the system is 1875.1 kWh/kWp. The PV system's capacity factor was 21.7%. The energy cost was found to be roughly 0.2258 USD/kWh, with a 10-year payback period [12]. Along the southern coast of Iran, different cities were selected, and it was seen whether these places were suitable for developing PV plants or not. The results showed that the selected cities were good sites for installing PV plants and single axis system

came out to be the most economical. The cost of electricity was also determined for various types of tracking systems [13]. Another 5kWp grid-connected system was studied in Iran. Different parameters were determined. The LCOE of the system was very high. A new dynamic FIT strategy was given which was even suitable for other developing nations [14]. Analysis of off-grid PV for a typical household building (power consumption-9.57 units/day) and typical hostel building (Total power consumed per day = 600 kWh) was done. Lifetime profit (in 25 years) and payback for household building was found to be Rs. 3 lakh and 10.5 years and for hostel building, it was Rs. 1.95 crores and 10 years [15]. A study has been done on 110 kWp system Bhopal, India. The main idea of this study was to design the system and evaluates the economics of the proposed system. Payback period and net present value were calculated. Payback was 8.2 years and NPV was 1.12 [16]. The cost of electricity (COE) and payback period of four different systems in Lucknow, India hve been analyzed. System 1 (5 kWp) had cost of electricity-5.44 INR/kWh (30 years lifespan 5% interest rate) and payback period-13.36 years. System 2 (198 kWp) had COE-2.94 INR/kWh and payback period-6.87 years. System 3 (75 kWp) and system 4 (50kWp) had COE and payback period 2.88 INR/kWh and 6.71 years and 3.23 INR/kWh and 7.12 years, respectively [17]. Economic examination of solar energy systems such as sun drying, solar heating, and solar distillation units are covered in [18].

The objectives of the paper are as follows:

1. To do energy analysis of a 100 kWp PV system taking into account the degradation of PV modules.
2. To perform cost–benefit analysis for 25 years.
3. To calculate the payback period of the system.
4. Electricity bill analysis, power quality analysis, and comparison of fixed and running charges before and after the installation of the PV system.

The following is a breakdown of the paper’s structure:

Section 2 is system description.

Section 3 covers the methodology for economic analysis.

Section 4 of the paper is the result and discussion.

Section 5 of the paper is the conclusion.

2 System Description

The study system is 100 kWp PV at rooftop of institute building (26.23152 N, 78.20533 E). The location has extreme climatic conditions. Summer is very hot, humidity also increases, and winter is very cold. The PV system installed in the institution is divided into two parts. Each part is 50 kW with 154 panels and a 50 kW inverter. The effective area of each module is $1.955 \times 0.982 \text{ m}^2$ and produces 320 W peak power. PV modules are made by connecting solar cells. It is made of semiconductor material. When sunlight strikes solar cells, the photovoltaic effect

Table 1 Rating of PV module

Peak power	320 Wp
Open circuit voltage	46.56 V
Rated voltage	37.85 V
Short circuit current	9.05 A
Rated current	8.46 A
Module efficiency	16.49%

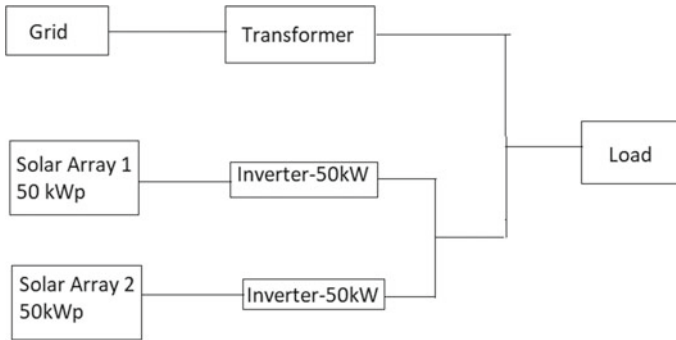


Fig. 1 Systematic diagram of grid-connected solar PV system

produces electricity. The power output is a direct current supply that is transformed to an alternating current supply by an inverter. Metering is accomplished by net metering. Net metering assumes that the power generated by the PV plant is utilized first by the linked load. When the electricity produced by the PV plant exceeds the linked load, the excess PV produced power is fed back into the grid. When the electricity produced by the PV plant is less than the linked load, the extra demand is met by grid supply.

The grid-connected solar PV rooftop system consists of 308 PV modules. The rating of each module is given in Table 1.

The supply voltage from the grid to the college is 33 kV, and the contracted demand is 350 kVA. Institute load is connected to a 500 kVA transformer and hostel load is connected to a 315 kVA transformer (Fig. 1).

3 Economic Analysis of the System

Cost–benefit (CB) analysis

The economic analysis and calculation of the payback period of the system are done by cost–benefit (CB) analysis. In CB analysis, annual savings are calculated for the

lifetime of the system (i.e., 25 years). Annual savings can be calculated by subtracting the annual cost from the annual benefits. The annual cost is the money that is spent on the system in a year (operation and maintenance cost). Annual benefit is the amount that is saved by generating electricity by a solar PV system. The amount of money saved is the amount it would have cost if the number of units generated by the PV system would have been taken from the grid supply. For calculating annual benefits, we need to find unit generation (kWh) of the system or how many units of electricity does the system generates in a year.

The following formula can be used for calculating the annual unit generation (kWh) of the solar PV system.

$$\text{Unit generation} = \text{system output} \times \text{capacity utilization factor} \\ \times 24 \text{ hours} \times 365 \text{ days} \quad (1)$$

where capacity utilization factor is the ratio of actual output to the maximum possible output.

By knowing the unit generation of the system and unit price of electricity, we can find the annual benefits, i.e., savings in the electricity bills (Tables 2 and 3). For more accurate results, system degradation factor and escalation in the unit price of electricity are taken into account.

$$\text{Annual savings} = \text{Annual benefit} - \text{Annual cost} \quad (2)$$

Calculation of simple payback period

Payback period is the time (in years) required for the initial investment of the system to be recovered. In order to calculate and analyze the simple payback time of the 100 kWp grid-connected solar PV system, annual savings at the end of each year are

Table 2 Component wise cost of solar PV plant

SN	Component	Cost (Rs)
1	Solar panels	2,041,446
2	Solar inverter	343,500
3	Electrical items (DC/AC cables, earthing cable, earthing strip, earthing kit, ACDB junction box, MCCB box, MC 4 solar cable connector, lightning arrester, etc.)	704,480
4	Civil and mechanical items (mounting structure, foundation, hardware, etc.)	687,904
5	Services (installation, commissioning, design, transport, freight, etc.)	165,760
	Total component cost	3,943,090
	GST on supply (5%)	197,154
	GST on service (18%)	709,756
	Net cost payable	4,850,000

Table 3 Energy analysis for 25 years

Year	Output (%)	Output (kW)	Unit (kWh) generation
2020	100.00	100.00	131,400
2021	98.00	98.00	128,772
2022	97.22	97.22	127,747.08
2023	96.44	96.44	126,722.16
2024	95.67	95.67	125,710.38
2025	94.90	94.90	124,698.6
2026	94.14	94.14	123,699.96
2027	93.39	93.39	122,714.46
2028	92.64	92.64	121,728.96
2029	91.90	91.90	120,756.6
2030	91.17	91.17	119,797.38
2031	90.44	90.44	118,838.16
2032	89.71	89.71	117,878.94
2033	89.00	89.00	116,946
2034	88.28	88.28	115,999.92
2035	87.58	87.58	115,080.12
2036	86.88	86.88	114,160.32
2037	86.18	86.18	113,240.52
2038	85.49	85.49	112,333.86
2039	84.81	84.81	111,440.34
2040	84.13	84.13	110,546.82
2041	83.46	83.46	109,666.44
2042	82.79	82.79	108,786.06
2043	82.13	82.13	107,918.82
2044	81.47	81.47	107,051.58

analyzed (Table 4). We need to find the time required to make the savings equal to the amount invested.

4 Result and Discussion

In our study, the initial investment of the entire system is Rs. 4,850,000, and operation and maintenance cost is taken as 2.5% of the initial cost. It is considered that the output of the system is reduced by 2% after the first year, and after the second year, it is reduced by 0.8% every year. Escalation in the unit price of electricity is taken as 3.84%. With the increasing scarcity of fossil fuels, the unit price of electricity

Table 4 Cost–benefit analysis for 25 years

Year	Unit (kWh) generation	Unit cost with escalation	Benefit (Rs.)	O&M cost (Rs.)	Saving (Rs.)
2020	131,400	7.10	932,940	121,250	811,690
2021	128,772	7.37	949,389.60	121,250	828,139.60
2022	127,747.08	7.66	977,999.63	121,250	856,749.63
2023	126,722.16	7.95	1,007,406.98	121,250	886,156.98
2024	125,710.38	8.25	1,037,739.16	121,250	916,489.16
2025	124,698.6	8.57	1,068,915.37	121,250	947,665.37
2026	123,699.96	8.90	1,101,072.67	121,250	979,822.67
2027	122,714.46	9.24	1,134,244.93	121,250	1,012,994.93
2028	121,728.96	9.60	1,168,341.21	121,250	1,047,091.21
2029	120,756.6	9.97	1,203,943.30	121,250	1,082,693.30
2030	119,797.38	10.35	1,239,902.88	121,250	1,118,652.88
2031	118,838.16	10.75	1,277,510.22	121,250	1,156,260.22
2032	117,878.94	11.16	1,315,528.97	121,250	1,194,278.97
2033	116,946	11.59	1,355,404.14	121,250	1,234,154.14
2034	115,999.92	12.03	1,395,479.04	121,250	1,274,229.04
2035	115,080.12	12.49	1,437,350.70	121,250	1,316,100.70
2036	114,160.32	12.97	1,480,659.35	121,250	1,359,409.35
2037	113,240.52	13.47	1,525,349.80	121,250	1,404,099.80
2038	112,333.86	13.99	1,571,550.70	121,250	1,450,300.70
2039	111,440.34	14.53	1,619,228.14	121,250	1,497,978.14
2040	110,546.82	15.09	1,668,151.51	121,250	1,546,901.51
2041	109,666.44	15.66	1,717,376.45	121,250	1,596,126.45
2042	108,786.06	16.27	1,769,949.20	121,250	1,648,699.20
2043	107,918.82	16.89	1,822,748.87	121,250	1,701,498.87
2044	107,051.58	17.54	1,877,684.71	121,250	1,756,434.71

is increasing every year [19]. Considering the past 3 years' electricity bills, the escalation in electricity pricing is observed as 3.84%. The capacity utilization factor is taken as 15%. The cost–benefit analysis of the 100 kW grid-connected rooftop system for the next 25 years (the life of the system is considered as 25 years) is given in Table 4.

The cost for lightning protection and overvoltage protection installation has been considered in the total cost of the system. The cost of these components (Rs 704,480) is covered in electrical items, as mentioned in Table 2.

As per the calculation, the total savings at the end of the fifth year will be Rs. 4,299,225.37 and at the end of the sixth year will be Rs. 5,246,890.74. Since the initial investment is Rs. 4,850,000; therefore, the payback period will be approximately 5.5 years.

Table 5 Comparison of payback period with variation in unit cost of electricity

Variation in unit cost of electricity	Payback period
Unit cost with escalation 3.84%	5.5 years
Unit cost not increased	6.5 years
Unit cost increased for next 10 years and then kept constant	5.5 years

Savings after first year: Rs. 811,690.

Savings after second year: Rs. 811,690 + Rs. 828,139.60 = Rs. 1,639,829.60.

Savings after third year: Rs. 811,690 + Rs. 828,139.60 + Rs. 856,749.63 = Rs. 2,496,579.23.

Savings after fourth year: Rs. 811,690 + Rs. 828,139.60 + Rs. 856,749.63 + Rs. 886,156.98 = Rs. 3,382,736.21.

Savings after fifth year: Rs. 811,690 + Rs. 828,139.60 + Rs. 856,749.63 + Rs. 886,156.98 + Rs. 916,489.16 = Rs. 4,299,225.37.

Savings after sixth year: Rs. 811,690 + Rs. 828,139.60 + Rs. 856,749.63 + Rs. 886,156.98 + Rs. 916,489.16 + Rs. 947,665.37 = Rs. 5,246,890.74.

Payback period when escalation in the unit cost is considered is 5.5 years. If unit price is not increased, payback period comes out to be 6.5 years (Table 5).

Analysis of electricity bills

In our study, analysis of electricity bills is also done. The solar PV rooftop system was installed in November 2019. A summary of the electricity bills from February 2019 to March 2021 is given in Table 6.

From the analysis, it can be seen that maximum demand has decreased after the installation of the solar PV system. The average maximum demand (kVA) before installation was 334.5 kVA and after the installation was 152.625 kVA. Also, it is evident that the power factor has decreased after the installation of the system. The average power factor before installation of the system was 0.963 and after the installation is 0.9143. It is a disadvantage that the power factor slightly decreases. The power factor of PV produced power majorly depends on inverter output power with respect to its rated power. During the morning and evening time, the PV generation is very low in comparison to the rated power of solar inverter [20, 21]. This reduces the average monthly power factor of the plant. It is clear from Table 6 that the fixed and running charges have also decreased after the installation of the solar PV system. Running charges has decreased from an average of Rs. 692,138.15 to an average of Rs. 293,981.875. Average electricity bill before the system was installed is Rs. 871,867 and the average electricity bill after the installation is Rs. 432,020.

Table 6 Summary of electricity bill

Month	Contracted demand (kVA)	Maximum demand (kVA)	Power factor	Running charges (Rs.)	Fixed charges (Rs.)	Total bill (Rs.)
Feb 2019	350	209	0.96	520,504.5	159,637.5	680,142
Mar 2019	350	168	0.96	409,553.5	159,637.5	569,191
April 2019	350	365	0.97	704,925.5	161,787.5	866,713
May 2019	350	405	0.96	918,260.5	181,137.5	1,099,398
June 2019	350	432	0.96	801,820.5	198,552.5	1,000,373
July 2019	350	435	0.95	675,898.5	200,487.5	876,386
Aug 2019	350	420	0.96	828,188.5	193,827.5	1,022,016
Sept 2019	350	415	0.97	922,832	200,675	1,123,507
Oct 2019	350	294	0.97	677,638	170,775	848,413
Nov 2019	350	202	0.97	461,760	170,775	632,535
Dec 2019	350	169	0.96	437,496	170,775	608,271
Jan 2020	350	219	0.98	503,892	144,900	648,792
Feb 2020	350	166	0.97	457,408	144,900	602,308
Mar 2020	350	163	0.93	304,115	144,900	449,015
April 2020	350	72	0.87	125,354	–	125,354
May 2020	350	81	0.85	132,436	289,800	422,236
June 2020	350	180	0.89	–	144,900	–
July 2020	350	195	0.93	264,372	144,900	409,272
Aug 2020	350	177	0.92	321,656	144,900	466,556
Sept 2020	350	159	0.94	326,106	144,900	471,006
Oct 2020	350	162	0.89	312,596	144,900	457,496
Nov 2020	350	106	0.86	262,061	144,900	406,961
Dec 2020	350	130	0.92	272,953	144,900	417,853
Jan 2021	350	172	0.95	381,330	147,850	529,180
Feb 2021	350	153	0.91	324,731	148,050	472,781
Mar 2021	350	138	0.86	277,188	148,050	425,238

*Fixed charges of April 2020 are considered in bill of May 2020

5 Conclusion

The installation cost of the grid-connected solar PV rooftop system is very high. Since we invest a lot of money in the system, it becomes important to carry out economic analysis. It becomes important to analyze the payback period and other economic benefits. If the system is able to recover the invested amount in less than the lifetime (25 years) of the system, the system is considered to be economically

feasible and efficient. Lesser the payback back period, the more efficient the system is.

1. In our study, the solar PV rooftop system has capital investment of Rs. 4,850,000. Economic analysis of the system is done by energy analysis, cost–benefit analysis, analyzing electricity bills, and by calculating the simple payback period.
2. Payback calculation is done by considering capacity utilization factor (CUF) equal to 15%, escalation in the unit price of electricity is taken as 3.84%, and O&M cost is taken as 2.5% of the initial cost. Considering this, the simple payback time is 5.5 years.
3. After analyzing the electricity bills, it was seen that the maximum demand decreases after the installation of the system. The power factor slightly decreases which is a disadvantage. The average power factor before installation of the system was 0.963 and after the installation is 0.9143. Measures should be taken to improve the power factor.
4. Fixed and running charges also decreased after the installation of the solar PV system. Average electricity bill before the system was installed is Rs. 871,867, and the average electricity bill after the installation is Rs. 432,020.
5. Since the payback is 5.5 years which is very less than the lifetime of the system, the system installed is economically efficient. Although the system under the study is economically efficient, the efficiency of the PV system can be further improved by proper maintenance of the system.

References

1. Twidel J, Weir T (2006) Renewable energy resources, 2nd edn. Taylor and Francis Publication, New York
2. IEA (2019) World energy outlook 2019. IEA, Paris. <https://www.iea.org/reports/world-energy-outlook-2019>
3. Ministry of New and Renewable Energy (MNRE). <https://mnre.gov.in>
4. Bakhshi-Jafarabadi R, Sadeh J, Dehghan M (2020) Economic evaluation of commercial grid-connected photovoltaic systems in the Middle East based on experimental data: a case study in Iran. In: Sustainable energy technologies and assessments, pp 37
5. Ramírez F, Honrubia-Escribano A, Gómez-Lázaro E, Pham D (2017) Combining feed-in tariffs and net-metering schemes to balance development in adoption of photovoltaic energy: comparative economic assessment and policy implications for European countries. Energy Policy 102:440–452
6. Imam A, Al-Turki Y, Sreerama Kumar R (2020) Techno-economic feasibility assessment of grid-connected PV systems for residential buildings in Saudi Arabia—a case study. Sustainability (Switzerland) 12(1)
7. Adaramola M (2015) Techno-economic analysis of a 2.1 kW rooftop photovoltaic-grid-tied system based on actual performance. Energy Convers Manage 101:85–93
8. Cucchiella F et al (2013) Environmental and economic analysis of building integrated photovoltaic systems in Italian regions. J Clean Prod. <https://doi.org/10.1016/j.jclepro.2013.10.043>

9. Ayadi O, Al-Assad R, Al Asfar J. Techno-economic assessment of a grid connected photovoltaic system for the University of Jordan. *Sustain Cities Soc.* <https://doi.org/10.1016/j.scs.2018.02.011>
10. Zeraatpisheh M, Arababadi R, Pour M (2018) Economic analysis for residential solar PV systems based on different demand charge tariffs. *Energies* 11:3271. <https://doi.org/10.3390/en1112327>
11. Raghoebarsing A, Kalpoe A (2017) Performance and economic analysis of a 27 kW grid-connected photovoltaic system in Suriname. *IET Renew Power Gener* 11(2):1545–1554
12. Kazem H, Albadi M, Al-Waeli A et al (2017) Techno-economic feasibility analysis of 1 MW photovoltaic grid connected system in Oman. *Case Stud Thermal Eng* 10:131–141
13. Mohammadi K, Naderi M, Saghaififar M (2018) Economic feasibility of developing grid-connected photovoltaic plants in the southern coast of Iran. *Energy* 156:17–31
14. Bakhshi R, Sadeh J (2018) Economic evaluation of grid-connected photovoltaic systems viability under a new dynamic feed-in tariff scheme: a case study in Iran. *Renew Energy* 119:354–364. <https://doi.org/10.1016/j.renene.2017.11.093>
15. Sharma P, Bojja H, Yemula P (2016) Techno-economic analysis of off-grid roof top solar PV system. IEEE. ISBN 9781509001286
16. Shukla A, Sudhakar K, Baredar P (2016) Design, simulation and economic analysis of standalone roof top solar PV system in India. *Solar Energy* 136:437–449
17. Yadav S, Bajpai U. Energy, economic and environmental performance of a solar rooftop photovoltaic system in India, *Int J Sustain Energy.* <https://doi.org/10.1080/14786451.2019.1641499>
18. Tiwari G (1984) Economic analysis of some solar energy systems, pp 131–135
19. Rajput SK (2017) *Solar energy—fundamentals, economic and energy analysis*, 1st edn. ISBN: 978-93-81125-23-6
20. Rampinelli GA, Gasparin FP, Bühler AJ, Krenzinger A, Romero FC (2015) Assessment and mathematical modeling of energy quality parameters of grid connected photovoltaic inverters. *Renew Sustain Energy Rev* 52:133–141. ISSN 1364-0321. <https://doi.org/10.1016/j.rser.2015.07.087>
21. Elkholy A (2019) Harmonics assessment and mathematical modeling of power quality parameters for low voltage grid connected photovoltaic systems. *Solar Energy* 183:315–326. ISSN 0038-092X, <https://doi.org/10.1016/j.solener.2019.03.009>

Multi-agent System for Energy Management of Renewable Energy in Domestic Cooking



M. Lakshmi Swarupa, G. Divya, and V. Ch. S. N. Lavanya

Abstract As we are using many home appliances day by day, the energy consumption is increasing. As fossil fuels are depleting and demand is increasing, it is important to move toward renewable energy even in domestic areas. Energy used for cooking is in large amount in developing countries. Almost 80% of energy which among household is used as cooking energy in rural areas. This cooking need is substituted with biofuels such as fuelwood, charcoal, agro-residues and dung cakes. Many efforts have been taken specially in India to use biofuels and renewable energy for domestic cooking. In this paper, energy trapped from solar is used as source of energy for induction stove. Induction stove is widely used in recent days because of its high efficiency and safety. Induction cooking uses the principle of electromagnetic induction. By inducing eddy currents in the coil, the coil gets excited in the ferromagnetic material to cause heating (MNES in Annual Report: 1993–94. Ministry of Non-Conventional Energy Sources (MNES), Government of India, New Delhi, India [1]). This paper aims to design a solar powered induction cooktop that is supplemented by the mains power using half-bridge topology and control the power output by varying operating frequency both by simulation and hardware implementation.

Keywords Induction cooking · Solar powered · Half-bridge circuit · Microcontroller · Battery charging circuit · MATLAB-Simulink · PROTEUS

1 Introduction

Solar energy is a clean source of energy which will help the world from avoiding use of non-renewable energy sources such as coal. For domestic applications, induction heating is widely used. It is also a clean, efficient, low cost and performance oriented

M. L. Swarupa · G. Divya (✉) · V. Ch. S. N. Lavanya (✉)
EEE Department, CVR College of Engineering, Hyderabad, India
e-mail: divya.gongidi@cvr.ac.in

V. Ch. S. N. Lavanya
e-mail: Chaya.lav@gmail.com

[2]. In general, induction heating is mainly used in industries for melting, brazing and hardening [3]. Now, the existing option of domestic cooking is solar cookers. Even though many research papers have reported, biogas plants and cookstoves with new features are still far away from their respective potential. Solar cookers are also contributing their part in meeting domestic needs. It is ideal to improve the technology of solar cooker as India is blessed with sunshine and can meet the requirements of energy. In this reference, an attempt has been made to analyze the utilization potential of this technology for domestic cooking in India, which helps in assessment of their future potential of planning energy sector in country. It is important to mention that the actual potential of renewable energy devices in case of domestic cooking may change with time depending on changes in number of households in country, biomass feedstock availability and other renewable resources.

In general, main portion of the cooking energy requires low temperature. So solar cookers are known to be very good source of having low thermal energy. Average countries, annual mean daily solar radiation received is in the range of 5–7 kwm²/day. In India, box type solar cooker is the one which is standardized [4] for boiling and baking of food (Fig. 1).

In this paper, assumption of few households is considered for box type solar cooker for domestic cooking. The above estimation is done by assuming solar cooker cannot completely replace existing cooking options but will surely save certain amount of fuel when it is used for domestic cooking. In other way, it is assumed that if all the cooking device requirements of above conditions are satisfying, then solar cookers are its potential users.

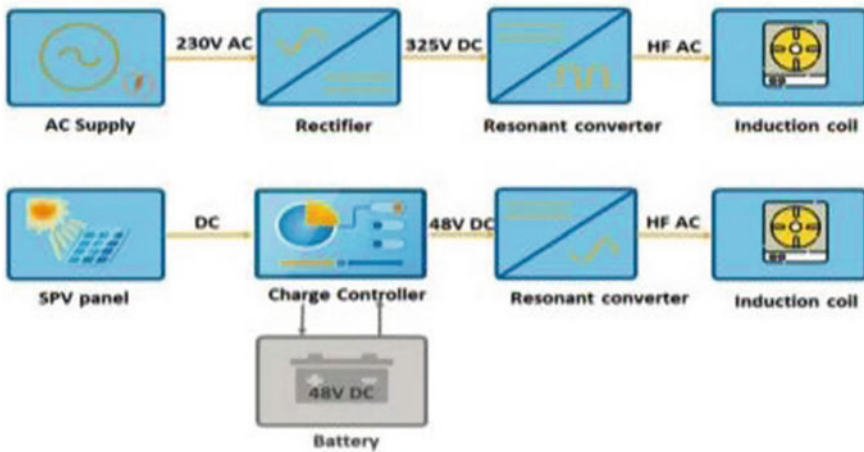


Fig. 1 Time variation of cumulative number of box type solar cookers existing in country

2 Induction Heating

Induction heating is being used nowadays for domestic appliances, as it is clean, gives high efficiency and is low cost advanced semiconductor device, it gives high performance [5]. In industries, induction heating is used for brazing, hardening and melting [6]. 80% of the magnetic field which is created between the coil and pan is transferred to coil [4]. Domestic and commercial cooker will give quick warming by saving energy with different range of temperatures [9]. Induction heating is done by electromagnetic induction in which the ferromagnetic materials are heated electrically. Among many applications of induction, cooking is one. Induction cooking uses a principle of magnetic induction in which eddy currents are induced in the coil which in turn excites the ferromagnetic materials to cause heating effect. Many converter topologies are their which can efficiently produce time varying magnetic field that is needed for induction heating.

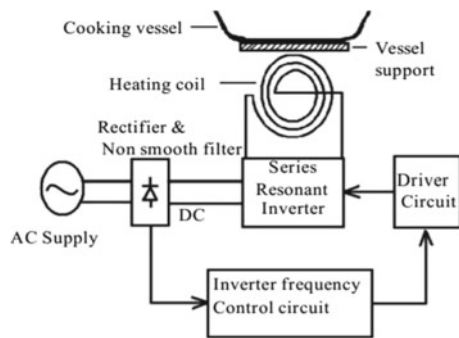
In this paper, principle of working of induction heaters/cookers is presented. Different topologies of solar electricity-based DC induction cookers like resonant converter and the voltage source inverters of full bridge inverter, and quasi resonant topology have been reviewed.

3 Principle of Operation of Solar Induction

Solar induction cooker uses a solar panel, which charges the battery by giving variable DC. By using inverter circuit, the DC from the battery is converted to high frequency AC voltage. Alternating flux produced in magnetic core produces eddy currents and hysteresis losses also. Due to high efficiency and safety of induction cooking, it is used widely nowadays (Fig. 2).

Induction cooker is initially supplied with energy as fuel from solar panel, and solar panel is controlled using a controller. The energy from solar panel can be used immediately for induction cooker or store in the form of DC for future use. The stored energy can be converted into high frequency AC form by using inverter to use the

Fig. 2 Basic circuit if induction cooking



saved energy later. This high frequency current produces a high frequency alternating magnetic field by induction coil. By placing cooking pan close to induction coil will induce eddy current in pan. This results in production of heat on pan surface. In this way, internal resistance of the pan will result in dissipation of heat. Finally, it is the pan which helps in heating and cooking process but not the heater.

Advantages of induction cooker:

- Heat radiation is only produced by induction cooker
- Coil stays cool, so it will be safer
- High efficiency, so gives low electricity bills
- Gives constant power output
- No danger of electric shock in cooking pan
- Has flexible temperature control
- When compared with microwave-oven induction cooker is cheaper
- No need of any special utensils, regular kitchen steel utensils are enough.

4 Energy Management System of Solar Induction Cooker

There are three types of cooktops available in the market: gas, electric and induction.

- Gas: It has burner on top and uses gas (LGP or PNG) to burn a flame that is used to cook food
- Electric: It has a coil that heats up because of resistance. It generates electricity to heat and cook food.
- Induction: It uses electricity as well as magnetic property of steel to directly heat the cooking vessels (Fig. 3).

In this paper, it is also explained regarding the thermal storage, which is present in food also, even if battery is not used. So, the cook can use the cooking appliances inside house also. Therefore, even without battery, the solar e-cooker system has many advantages when compared with conventional solar cooker.

The expenses of 500 Wp roof top panel with its fitting and fixing

$$C(\text{PV}) = 300[0.1/(1 - (1 + 0.1)^{-20}) + 0.05] = \text{Rs. } 3500 \text{ per year (approx.)} \quad (1)$$

Amount of energy produced by panel for an average of daily insolation of 4.5 kWh/m² (assumptions of insolation are considered from paper studies) is 821.25 × 0.8 = 657 kWh.

Cost of energy is approximated to

$$C(\text{solar PV electricity}) = 50.23/657 = \text{Rs. } 5.355/\text{kWh} \quad (2)$$

The cost of energy production will depend on sunshine and interest rate. The average time of cooking is assumed to be 4 h per day with average power delivery

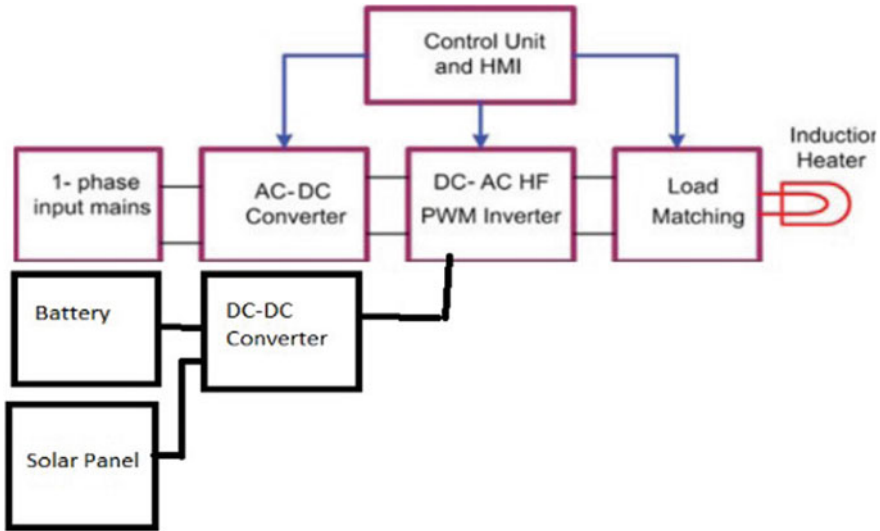


Fig. 3 Block diagram of solar induction cooking

of 300 W, and the monthly cost of electricity for cooking is approximated to be

$$C(\text{cooking}) = 0.0765 \times 0.3 \times 4 \times 30 = \text{Rs. } 192.78/\text{month}$$

5 Simulation Model and Results

The major aim of this paper is to develop a multi-agent system for energy management of renewable energy in domestic cooking. Multi-agent system can solve problems that are very difficult or impossible for an individual agent or a monolithic system. Intelligence technique for taking decisions can be methodic, functional, procedural approaches, algorithmic search or reinforcement learning.

The main aim of this project is to set an intelligent habitat system by considering which components will be able to take decisions and optimize energy consumption through intercommunication. The method should not affect the inhabitant comfort with respect to the application.

Also, the application of multi-agent system (MAS) was investigated as key technology to provide a distributed flexible micro-network control. In multi-agent technique, each function of system will be assigned to a separate agent, which provides a higher modularity and greater autonomy compared to traditional system of solar-based induction cooking. These agents will closely link and communicate with each other.

The initial analysis of the solar-based cooking system is done by using 555 timers. The driver circuit for induction cooking is also developed with the help of the same 555 timers. Simulation of driver circuit using 555 timer is done by MATLAB-Simulink (Figs. 4, 5 and 6).

The MOSFET will be ON for 20% of the cycle and OFF for 80% of the cycle. The graph is recorded for every 20 KHz frequency. The simulation results of multi-agent system is shown below. The main circuit is simulated with three sources solar battery and a adopter, which are used for domestic cooking purpose (Figs. 7, 8, 9 and 10).

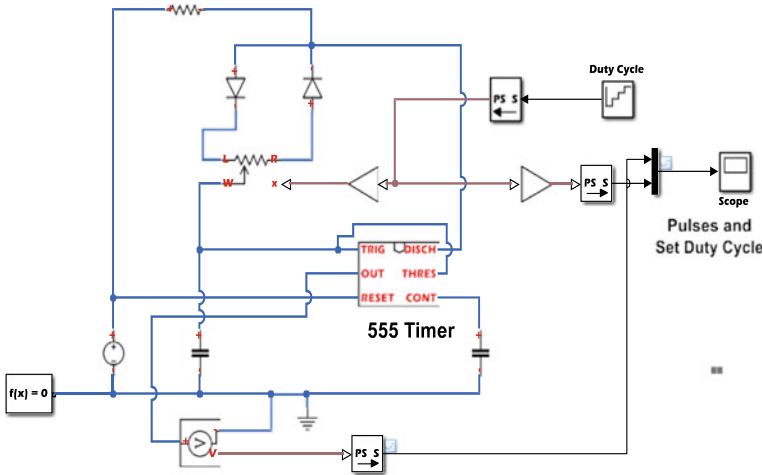


Fig. 4 555 timer circuit diagram to generate PWM pulses

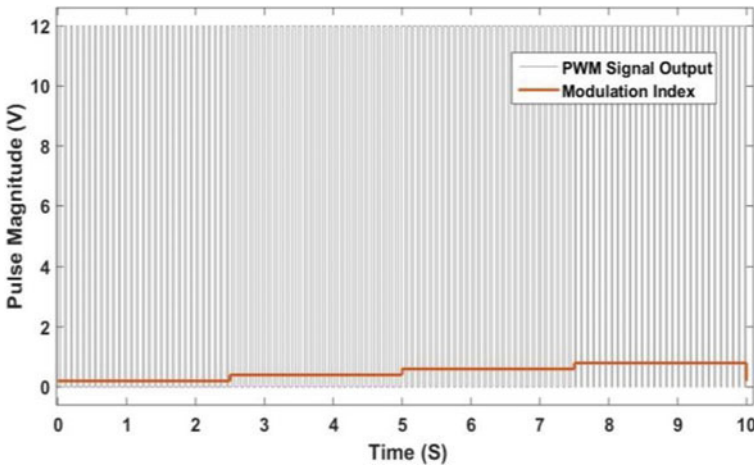


Fig. 5 555 timer PWM pulses for different modulation index

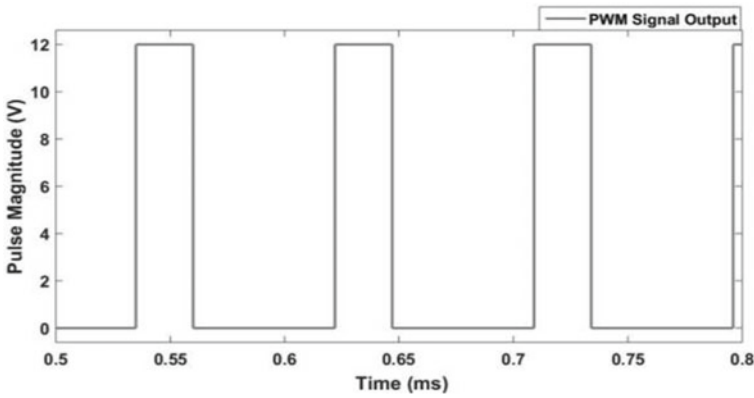


Fig. 6 555 timer PWM pulses for 25% modulation index

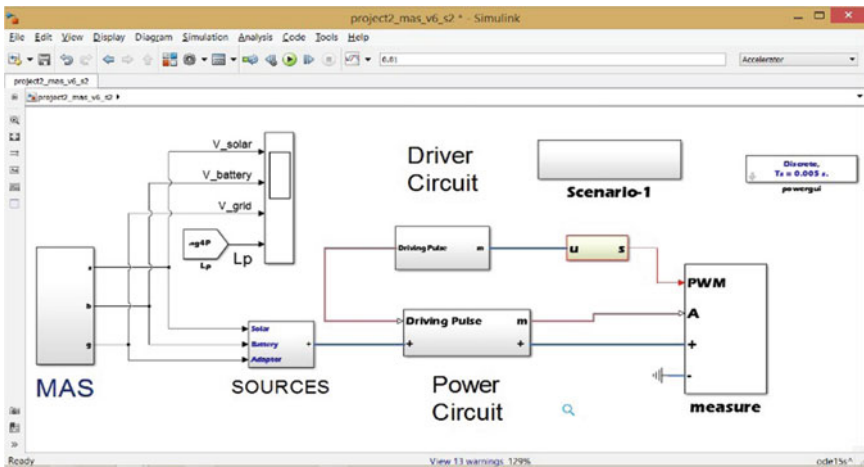


Fig. 7 Main circuit

Considering load is constant at 4000 W as peak, also grid is not available, solar power and battery are available. A threshold value of 5000-watt peak is considered and categorized as low power and high power (If the value is less than or equal to 5000 peak, then it is low power, if value is more than 5000 peak, then consider it as high power) (Fig. 11).

Solar power has been delivered at 48V and battery also has the terminal voltage at 48V, whereas grid voltage is zero as it is not considered in this scenario (Fig. 12). Figure 13 shows the load response to the first case executed in the simulation.

Input information is taken by multi-agent system and given to the central controller. The central controller unit will take decision depending on the algorithm

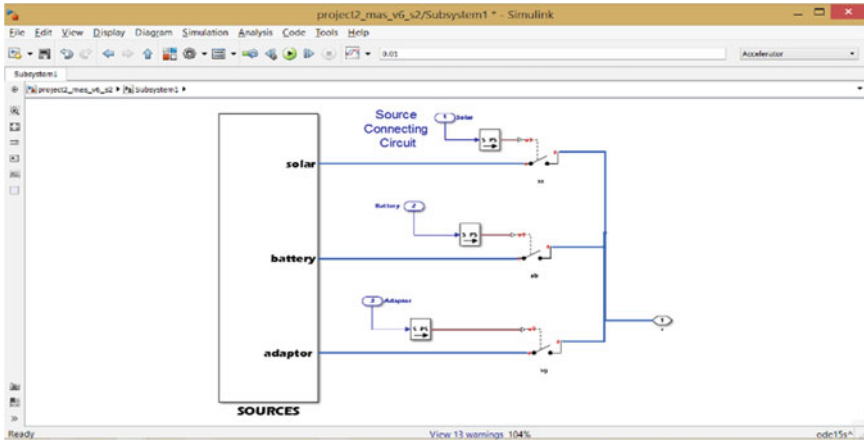


Fig. 8 Connection of sources to main power circuit

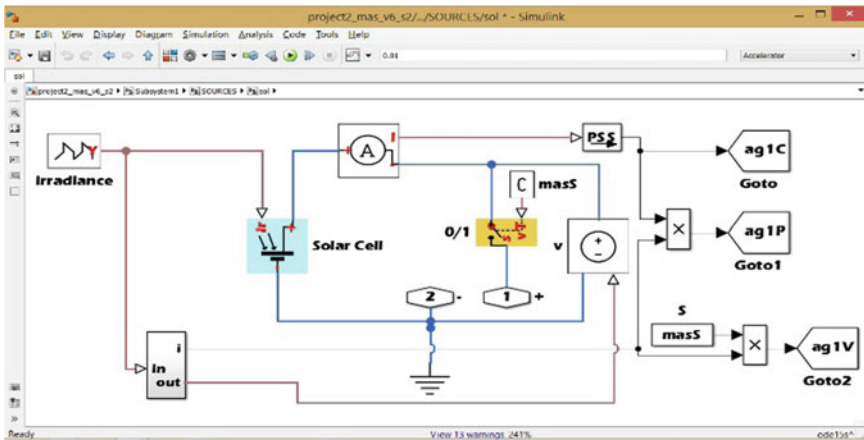


Fig. 9 Subsystem of solar source

output. The decision will be in the form of turning a particular source as ON/OFF (Figs. 14, 15, 16, 17, 18, 19 and 20; Tables 1, 2, 3 and 4).

During the time $t = 0$ to 0.006 s, it is observed that solar power which is generated is sent to the load, as the requirement is below the threshold values in 5000 W type. In this period, the input to solar PV is kept at 1000 W per meter.

At time t is equal to 0.006 s solar insolation level drops to 500 W per meter square, and hence, power needed by the load cannot be generated, the same is communicated to central multi-agent system. The grade is used as second option in multi-agent system; the voltage across the adapter will cross the threshold limit of 47 V. The power levels will increase because the adapter output is 52 V, it means more power can be generated from the source (Figs. 21 and 22).

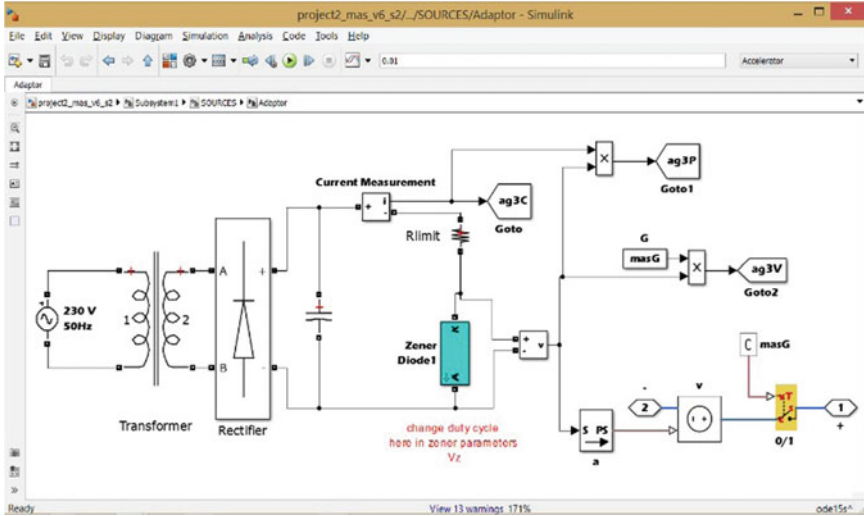


Fig. 10 Subsystem of adaptor circuit

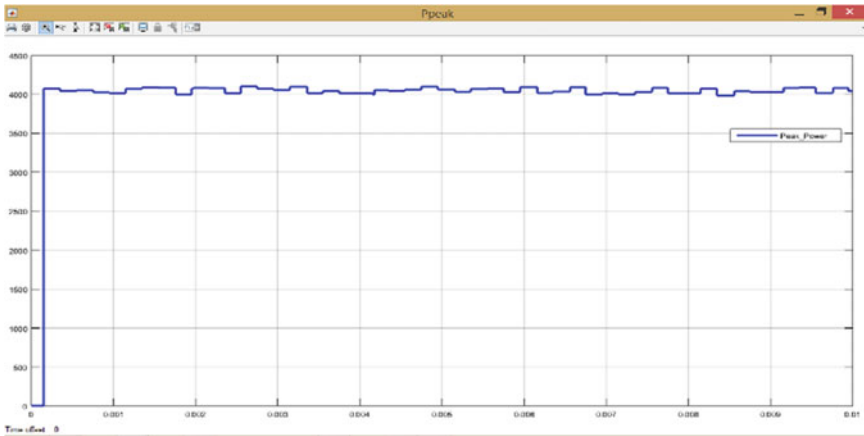


Fig. 11 Load power requirement

This paper addresses the main challenges of solar e-cooking with respect to energy cost, energy consumption and energy conservation. The energy cost for cooking is very low in insulated stoves and pans, and these can be used in applications of both grid and off-grid case. The main technical challenge for this research is cooking food at low power and within reasonable time, also issue of change in cooking habits. According to the understandings made, there is no need for changing the cooking procedure of rice, vegetables or meat but frying will be difficult. From the cost analysis, it is found that integration of solar e-cooking in case of solar home system

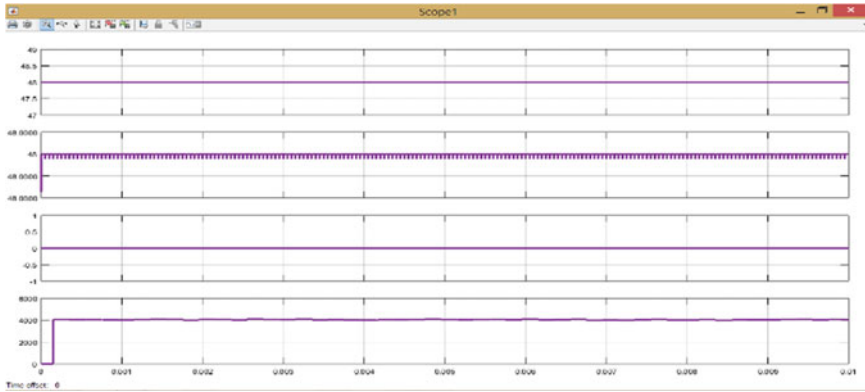


Fig. 12 Voltage profile of sources and load power

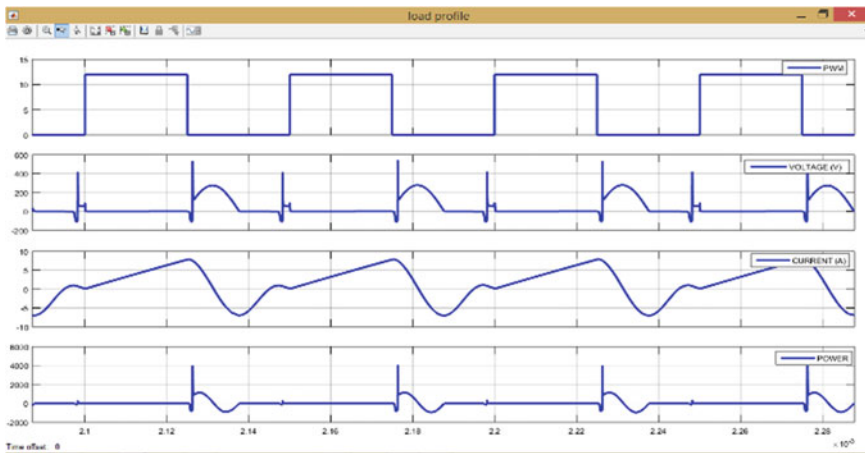


Fig. 13 Load response to first case executed in the simulation

can be improved by increasing the size of PV panel, and battery can be cost effective when compared with normal cooking cost. Also, by increasing the power capacity of solar home system enables the households to use more equipment like fans for cooling, small refrigerators, etc. This enhances the quality of life of users. The results obtained are verified with compact and low cost efficient 500 W prototype design. In the comparison process, it is found that efficiency of the proposed converters exceeds more than 92% with full load condition due to reduction in THD.

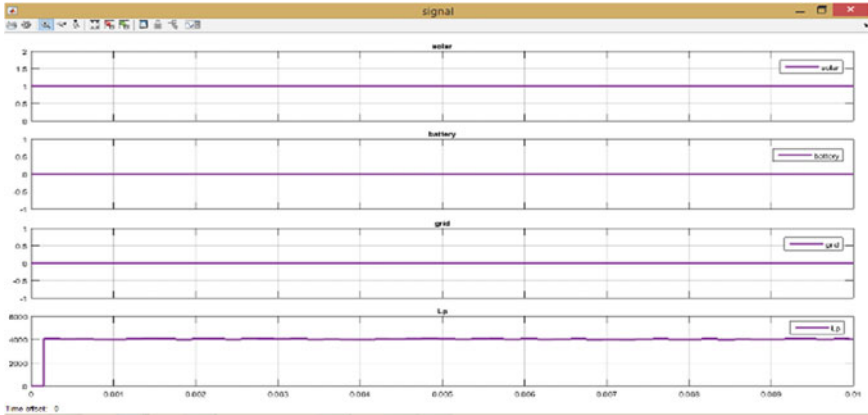


Fig. 14 MAS output, switching ON/OFF sources

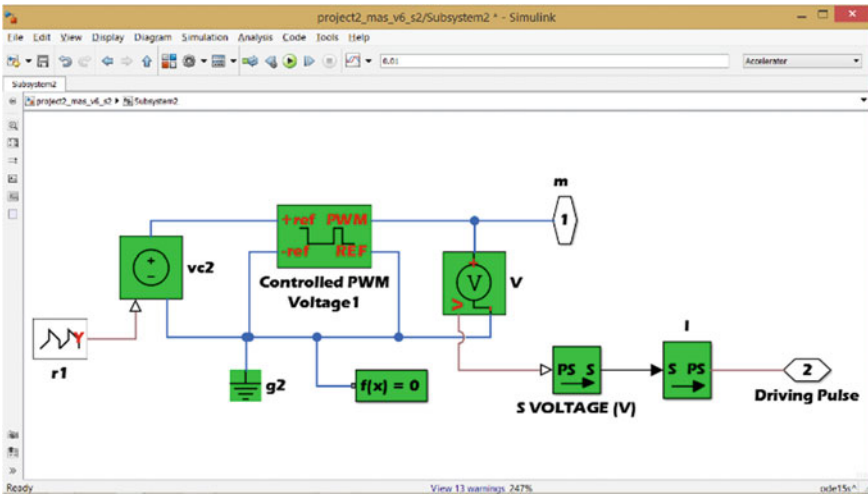


Fig. 15 Driver circuit

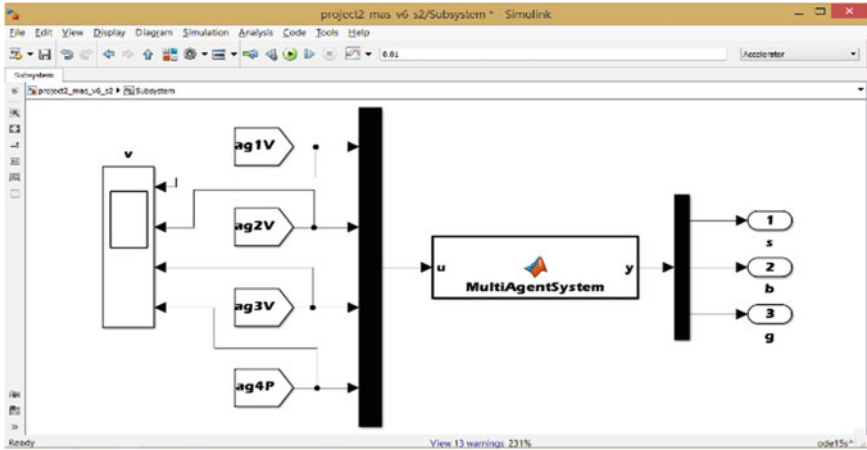


Fig. 16 Multi-agent system central controller

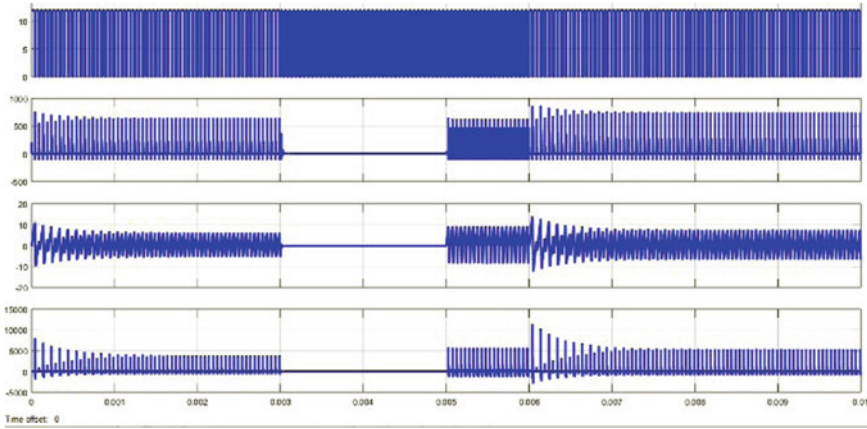


Fig. 17 Voltage, current and power at the load side

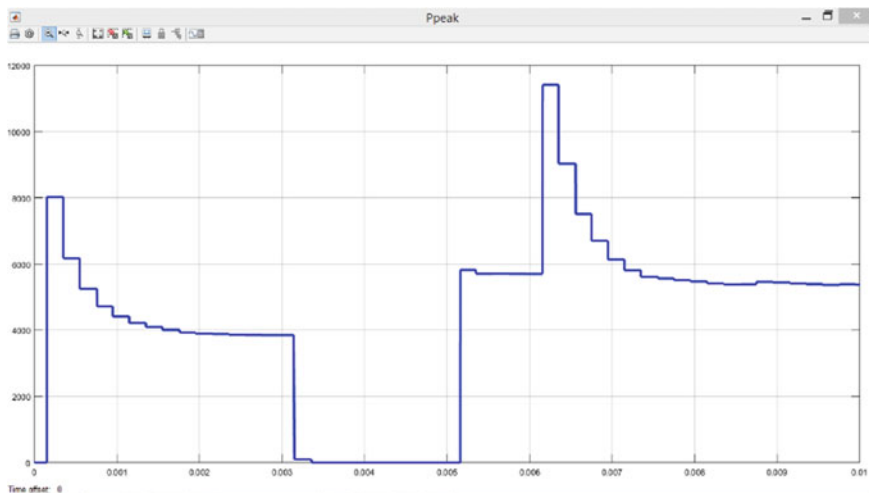


Fig. 18 Load power versus time

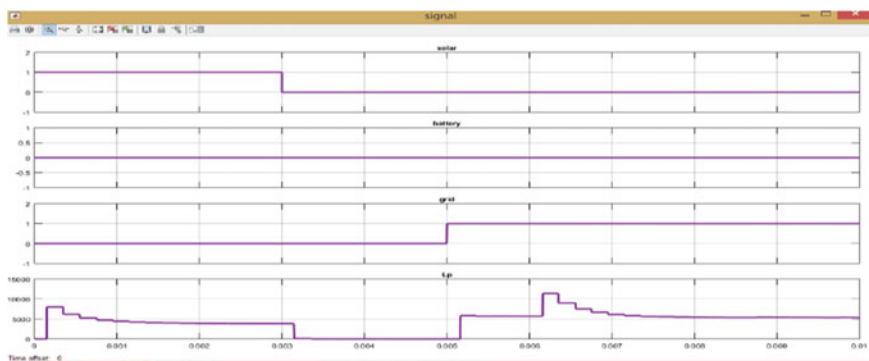


Fig. 19 MAS decision making output: sources

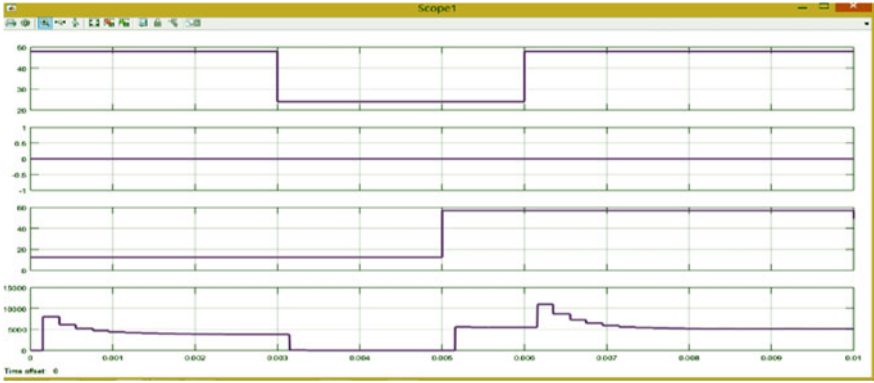


Fig. 20 Voltage levels of sources connected to the system

Table 1 Solar parameters

From time (ms)	To time (ms)	Insolation (H in Watts/m ²)
0	3	500
3.01	6	1000
6.01	10	1000

Solar source parameters (1 = ON or 0 = OFF)
 MAS to Solar = 1; MAS to Battery = 1; MAS to GridG = 1

Table 2 Drive duty cycle parameters

From time (ms)	To time (ms)	Duty cycle (%)
0	3	75
3.01	6	50
6.01	10	75

Table 3 Solar parameters

From time (ms)	To time (ms)	Insolation (H in Watts/m ²)
0	3.33	1000
3.33	6.66	1000
6.66	10	500

Solar control parameters (1 = ON or 0 = OFF)
 MAS to Solar = 1; MAS to Battery = 1; MAS to Battery = 1;
 MAS to GridG = 1

Table 4 Driver-duty cycle parameters

From time (ms)	To time (ms)	Duty cycle (%)
0	3.33	50
3.33	6.66	75
6.66	10	50

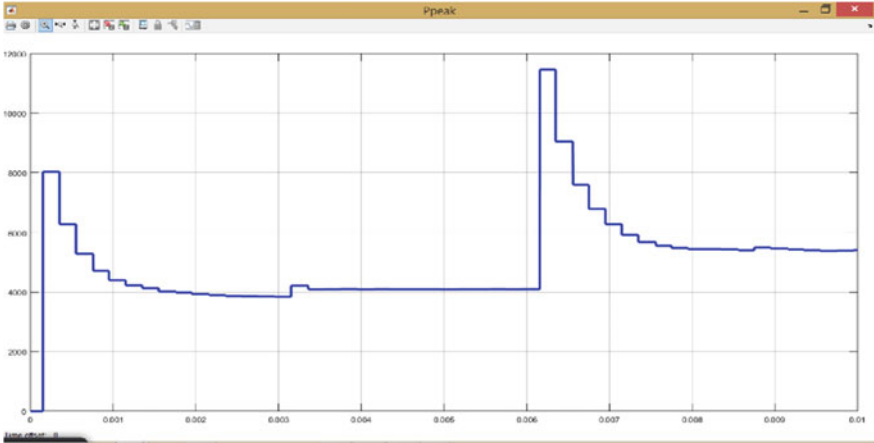


Fig. 21 Power requirement of load

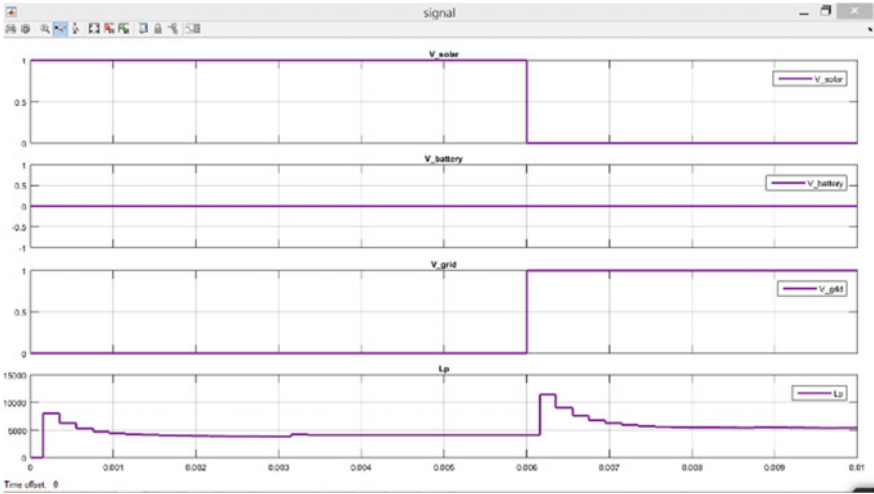


Fig. 22 MAS-based decision made, based on source availability and load power required

References

1. MNES (1994) Annual report: 1993–94. Ministry of Non-Conventional Energy Sources (MNES), Government of India, CGO Complex, Lodhi Road, New Delhi (India)
2. Mani A, Rangarajan S (1981) Solar radiation over India. Allied Publishers, New Delhi (India)
3. Rubab S, Kandpal TC (1997) Box type solar cooker vs other options for domestic cooking: a financial evaluation. *Int J Ambient Energy* 18(3):121
4. Coster E, Myrzik J, Kruimer B, Kling W (2011) Integration issues of distributed generation in distribution grids. *Proc IEEE* 99(1):28–39
5. Mühlbauer A (2008) History of induction heating and melting. Vulkan-Verlag GmbH

6. Clement K, Haesen E, Driesen J (2009) Analysis of the impact of plug-in hybrid electric vehicles on the residential distribution grids by using quadratic and dynamic programming. In: Proceedings of 24th international battery, hybrid and fuel cell electric vehicle symposium and exhibition (EVS 24)

Hourly Load Forecasting Using Sequence-to-Sequence LSTM-Based Deep Machine Learning Model



Mahshooq Abdul Majeed , Soumya Mudgal, Lalit Tak , Janavi Popat, Harsh Kakadiya, Neeraj Kumar Singh , and Vasundhara Mahajan 

Abstract The operational reliability of power system highly invests in the accurate load forecasting techniques. The complexity and grey lie not only in the accurate forecast of load but also in understanding the temporal and long-term dependencies of features that affect the load. Long short-term memory (LSTM) is a deep machine learning model which aces in understanding the sequential temporal and long-term dependencies in the data. The sequence-to-sequence LSTM model proposed in this paper uses data obtained from real-world utilities and weather service providers for hourly forecast of load for a period of 3 days with very high accuracy.

Keywords Long short-term memory · Load forecasting · Machine learning · Deep learning · Day-ahead forecast

1 Introduction

Ever since the establishment of an operational power system, humans have been struggling to keep the operation smooth and maintenance minimum by proper planning of the system. Time series load forecasting is in fact the most essential step in the maintenance, operation and control of power systems. Load forecasting can be of two types: long-term and short-term load forecasting. Short-term forecasting allows in the smooth operation and maintenance of power system by including the seasonal fluctuations, while long-term forecasting allows for the proper planning and expansion of the existing power system.

Even though the existing power system is constantly being updated and upgraded to make it more reliable, the complexity and uncertainty still exist due to the unwithering time varying load and with the introduction of EVs and renewables into the grid. The variance in load depends on factors like, time of day, season, type of

M. A. Majeed · S. Mudgal · L. Tak · J. Popat · H. Kakadiya · N. K. Singh · V. Mahajan (✉)
Department of Electrical Engineering, Sardar Vallabhbhai National Institute of Technology Surat,
Gujarat 395007, India
e-mail: vmahajan@eed.svnit.ac.in

© The Author(s), under exclusive license to Springer Nature Singapore Pte Ltd. 2022
V. Mahajan et al. (eds.), *Sustainable Technology and Advanced Computing in Electrical Engineering*, Lecture Notes in Electrical Engineering 939,
https://doi.org/10.1007/978-981-19-4364-5_34

469

day (weekends and working days), temperature, wind pressure, wind direction, etc. [18, 22]. The acquaintance of the aforesaid characteristics that define the load at a moment is not being properly taken into consideration in conventional time series load forecasting models like autoregressive integrated moving average (ARIMA) [2].

Machine learning opens the doors to such load forecasting problems, where the load at a moment is based on the temporal dependencies of various inputs/features. The attention gained by machine learning models like artificial neural network (ANN), support vector machines (SVM), random forest (RF) and recurrent neural network (RNN) is tremendous owing to its unique feature dependency and relationship learning capability.

Deep learning has gained the attention of the researchers due to its unique qualities. It is a method in which multiple artificial neural networks are stacked up in multitudes and advanced stochastic optimization techniques are used to perform machine learning tasks [5, 12] depending on the number of layers the feature extraction quality, performance and the learning ability varies. Hochreiter and Schmidhuber [9] introduced LSTM which is an inoculation of memory element to RNN. The memory element in LSTM provides a perfect platform for sequence learning and thus has a huge upper hand over conventional RNN. The applications of LSTM have a wide-range, starting from natural language translation [19], image captioning [10, 14, 21] and speech recognition [6].

The qualities of LSTM allow it to learn the seasonal variations and dependencies of the load with the inputs [7, 16, 20]. Thereby accumulating the seasonal characteristics of ARIMA in a more simplified manner. The researchers in [11] tested a LSTM-based model for residential load forecasts. In [15], it was observed that when a residential charge of 1 min ahead is predicted, the sequence-to-sequence architecture based in LSTM is superior to the normal LSTM. In the study [13], a concatenated LSTM consisting of two neural LSTM networks was created, which improves the performance significantly in comparison with one LSTM. In [17], LSTM was used to capture the dynamic feature of wind field with 5% error.

In this paper, sequence-to-sequence LSTM model is used to forecast load for a period of 3 days and evaluate its performance using metrics such as mean absolute error (MAE), root mean squared error (RMSE), mean absolute percentage error (MAPE) and R^2 . This paper is organized as follows. Section 2 describes the proposed LSTM model. The data used for forecasting is discussed in Sect. 3. Implementation of the model is discussed in Sect. 4. The results obtained from the implemented model are analysed in Sect. 4.1. The paper is concluded in Sect. 5.

2 Sequence-to-Sequence LSTM Model

RNNs are sequence-based models which have the ability to make temporal dependencies between the previous and the current information. For load forecasting which is a time series problem, this could mean that a decision taken at previous time could affect the decision taken at the present time. But the problem of long-term dependen-

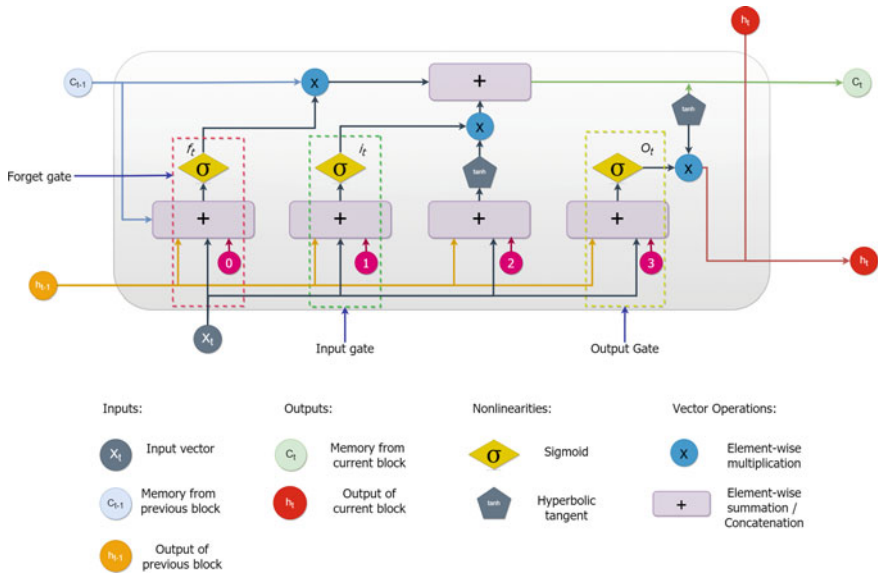


Fig. 1 Basic cell structure of LSTM

cies and vanishing gradient degraded the performance of RNN [1, 8]. These problems are overcome by the inclusion of a memory cell, and further improvement is done by adding a forget gate [4].

The basic cell structure of LSTM is shown in Fig. 1. The memory cell of LSTM consists of forget gate (FG_t), input gate (IG_t) and output gate (OG_t). The various steps involved in LSTM are:

• **Forget gate:**

$$FG_t = \sigma(W_{FG} \cdot [H_{t-1}, X_t] + B_f) \tag{1}$$

- FG_t Output value of forget gate in the range of 0–1.
- W_{FG} Weight of forget gate.
- H_{t-1} Output value of previous instant.
- X_t Input value at the current instant.
- V_{FG} Bias of the forget gate.

The property of forget gate is to decide which information needs attention and which can be ignored. $X(t)$ and $H(t - 1)$ are passed through the sigmoid function which generates values between 0 and 1. A value closer to 1 indicates that the part of the old output is necessary.

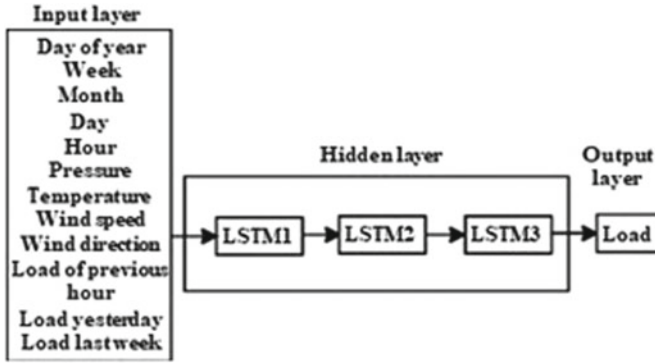


Fig. 2 Architecture of sequence-to-sequence LSTM based forecasting model

• **Input gate and candidate cell state:**

$$IG_t = \sigma(W_{IG} \cdot [H_{t-1}, X_t] + B_{IG}) \tag{2}$$

$$\tilde{C}_t = \tanh(W_{CIG} \cdot [H_{t-1}, X_t] + B_{CIG}) \tag{3}$$

- IG_t Output value of input gate in the range of 0–1.
- W_{IG} Weight of input gate.
- B_{IG} Bias of the input gate.
- W_{CIG} Weight of candidate input gate.
- B_{CIG} Bias of candidate input gate.

The property of the input gate is to update the cell status. It involves two steps. First, $X(t)$ and $H(t - 1)$ are passed into the sigmoid function. Second, $X(t)$ and $H(t - 1)$ are passed into a tanh function. The output from both the activation functions is then multiplied for determining the candidate cell state \tilde{C}_t .

• **Current cell state:**

$$C_t = FG_t * C_{t-1} + IG_t * \tilde{C}_t \tag{4}$$

The property of current cell state is to store the information from the new state. C_t has value in the range of 0–1.

• **Output gate:**

$$OG_t = \sigma(W_{OG} \cdot [H_{t-1}, X_t] + B_{OG}) \tag{5}$$

- W_{OG} Weight of output gate.
- B_{OG} Bias of the output gate.

Output gate contains value for the next $H(t - 1)$.

• **Output value of LSTM:**

$$H_t = OG_t * \tanh(C_t) \tag{6}$$

The above equations provide the sequential step in which the output of an LSTM cell is obtained. Figure 2 provides the architecture of the LSTM model used in this paper for forecasting. The actual data contains timestamps and its corresponding load, wind speed, temperature and pressure. Additional data like day of year, week, month, day and hour is extracted from the timestamp. Load of the previous hour, load of yesterday of the same hour and load of last week of the same hour are other data's that are extracted from the load values in actual data. These are then scaled to the range of -1 to 1 and are reshaped from 2D to 3D array. Input for load previous hour is taken from the output of the previous input. Thus, this model turns out to be a sequence-to-sequence forecasting LSTM model.

3 Dataset

The dataset is obtained from [3]. It contains load data for a period of four years from 2017 to 2021. The various other data that the dataset contains are actual values of wind speed, wind direction, temperature and humidity, and forecasted values of wind speed, wind direction, temperature and humidity.

For training the system, the forecasted values of wind speed, wind direction, temperature and humidity are used. Apart from these, week number, day, hour and month are extracted from the timestamp provided in the dataset.

4 Implementation

LSTM1, LSTM2 and LSTM3 are three sequentially connected LSTM networks each having 100 nodes, and the output layer consists of a densely connected LSTM layer of single node. Callback function is used to train the model which helps to retain the best weights corresponding to each training epoch. Then, the best weights which give out minimum error are loaded on to the model to forecast load for 24, 48 and 72h. The errors in the prediction are then calculated using metrics such as MAE, RMSE, MAPE and R^2 . MAE is calculated as follows:

$$\text{MAE} = \frac{1}{n} \sum_{i=1}^n |\hat{y}_i - y_i| \quad (7)$$

RMSE is calculated as follows:

$$\text{RMSE} = \sqrt{\frac{1}{n} \sum_{i=1}^n (\hat{y}_i - y_i)^2} \quad (8)$$

MAPE is calculated as follows:

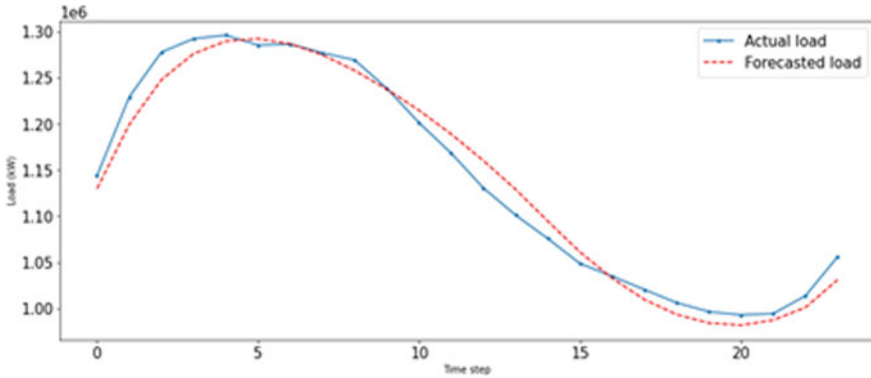


Fig. 3 Forecasted and actual values for 24-h load forecasting using sequence-to-sequence LSTM

$$MAPE = \sum_{i=1}^n \frac{\hat{y}_i - y_i}{y_i} \times 100 \tag{9}$$

R^2 is calculated as follows:

$$R^2 = 1 - \frac{\sum_{i=1}^n (y_i - \hat{y}_i)^2 / n}{\sum_{i=1}^n (\bar{y}_i - \hat{y}_i)^2 / n} \tag{10}$$

where

- y_i Actual load value
- \hat{y}_i Predicted load value
- \bar{y}_i Average load value.

R^2 values ranges from 0 to 1, a value closer to 1 indicates that there is minimum error between the actual and forecasted values of load. For MAPE, a value closer to zero is the best solution.

4.1 Results and Discussion

The dataset discussed in Sect. 3 is used to train the proposed model and the hourly load is forecasted. Table 1 shows the hourly error calculation for 24-h load forecast. Figures 3, 4 and 5 depict the actual and forecasted load waveforms for 24, 48 and 72 h, respectively. Table 2 gives the error metrics used for evaluating the performance of the load forecasting model for 24, 48 and 72 h. It can be observed that the proposed sequence-to-sequence LSTM model yields a MAPE of 1.235%, 1.238% and 1.16% and R^2 score of 0.979, 0.978 and 0.982 for 24, 48 and 72 h, respectively.

Table 1 Error calculation for 24-h load forecasting using sequence-to-sequence LSTM model

Hour	Actual load (MW)	Forecasted load (MW)	Absolute error	Absolute percentage error	Squared error
1	1143.771432	1129.608478	14.162954	1.238267857	200.589266
2	1228.988432	1199.12871	29.859722	2.429617824	891.6029979
3	1277.612432	1247.704246	29.908186	2.340943564	894.4995898
4	1292.200932	1276.037711	16.163221	1.250828768	261.2497131
5	1295.953432	1289.489546	6.463886	0.498774558	41.78182222
6	1285.201932	1292.078221	6.876289	0.535035688	47.28335041
7	1286.284932	1286.642147	0.357215	0.027771063	0.127602556
8	1276.822432	1274.684364	2.138068	0.167452259	4.571334773
9	1269.148432	1257.699797	11.448635	0.902072186	131.0712434
10	1238.363432	1237.411379	0.952053	0.076879935	0.906404915
11	1201.108432	1214.577509	13.469077	1.121387265	181.4160352
12	1168.052932	1188.753126	20.700194	1.77219657	428.4980316
13	1130.367932	1159.977295	29.609363	2.61944471	876.7143773
14	1100.914932	1128.832454	27.917522	2.535847338	779.3880346
15	1075.527432	1094.409641	18.882209	1.755623189	356.5378167
16	1048.474432	1060.890143	12.415711	1.184169172	154.1498796
17	1034.669932	1032.502089	2.167843	0.209520247	4.699543273
18	1020.234932	1009.421993	10.812939	1.059847949	116.9196498
19	1005.990932	993.2577251	12.7332069	1.265737741	162.134558
20	996.3214321	984.0772322	12.2441999	1.228940732	149.9204312
21	992.7724321	981.6740017	11.0984304	1.117922904	123.1751573
22	994.2224321	987.1590493	7.0633828	0.710442912	49.89137658
23	1013.446932	1000.858706	12.588226	1.242119898	158.4634338
24	1055.880432	1030.938833	24.941599	2.362161306	622.0833607

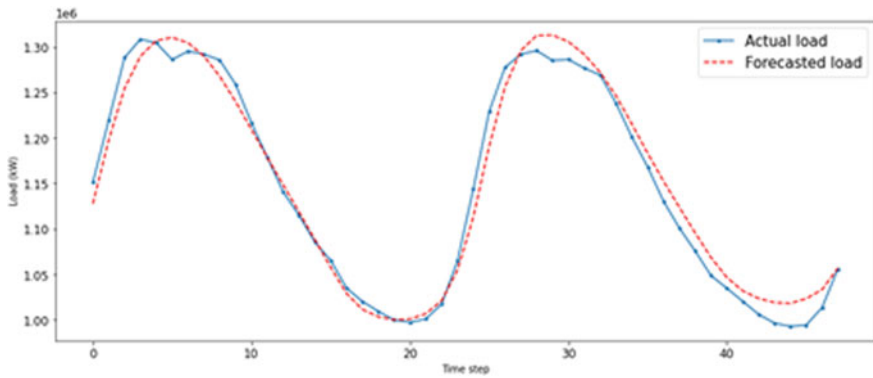


Fig. 4 Forecasted and actual values for 48-h load forecasting using sequence-to-sequence LSTM

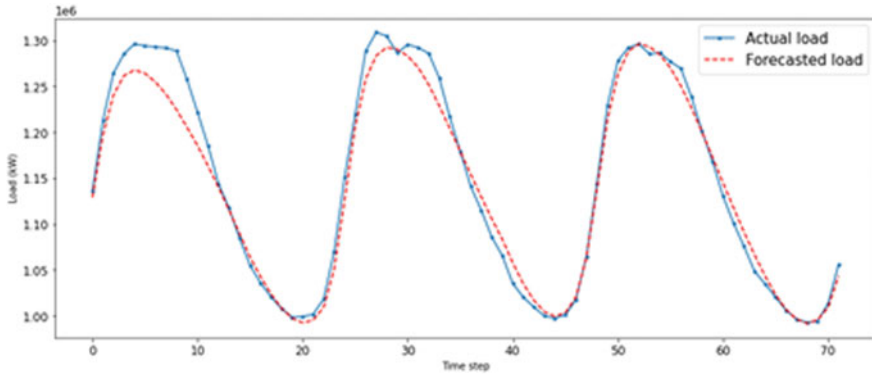


Fig. 5 Forecasted and actual values for 72-h load forecasting using sequence-to-sequence LSTM

Table 2 Error metrics of load forecasting using sequence-to-sequence LSTM model

	24 h prediction	48 h prediction	72 h prediction
MAE	13.957	14.228	13.926
RMSE	16.63	17.195	19.116
MAPE (%)	1.2355	1.2389	1.165
R^2	0.97957	0.97857	0.9822

5 Conclusion

Load forecasting is the torchbearer for the initial step towards expansion, maintenance and operation of power system. The nonlinear time series nature of load makes forecasting using conventional methods like ARIMA tiresome as it does not completely incorporate the sequence nature embedded in the data. LSTM, a deep machine learning model, which perfectly suits for application like sequence learning is used to forecast load. The proposed sequence-to-sequence LSTM model forecasts hourly load for a period of 3 days with MAPE less than 1.25% and R^2 score very near to 1, these values substantiates the high accuracy of the forecasting model.

References

1. Bengio Y, Simard P, Frasconi P (1994) Learning long-term dependencies with gradient descent is difficult. *IEEE Trans Neural Netw* 5(2):157–166. <https://doi.org/10.1109/72.279181>
2. Box GE, Jenkins GM, Reinsel GC, Ljung GM (2015) *Time series analysis: forecasting and control*. Wiley. <https://doi.org/10.1002/9781118619193>
3. Farrokhhabadi M (2020) Day-ahead electricity demand forecasting: post-covid paradigm. <https://doi.org/10.21227/67vy-bs34>

4. Gers FA, Schmidhuber J, Cummins F (2000) Learning to forget: continual prediction with LSTM. *Neural Comput* 12(10):2451–2471. <https://doi.org/10.1162/089976600300015015>
5. Goodfellow I, Bengio Y, Courville (2016) *A deep learning*. MIT Press
6. Graves A, Jaitly N (2014) Towards end-to-end speech recognition with recurrent neural networks. In: *International conference on machine learning*. PMLR. <https://doi.org/10.5555/3044805.3045089>
7. He W (2014) Deep neural network based load forecast. *Comput Model New Technol* 18(3):258–262. <https://doi.org/10.3390/en10010003>
8. Hochreiter S (1998) The vanishing gradient problem during learning recurrent neural nets and problem solutions. *Int J Uncertainty Fuzziness Knowl Based Syst* 6(02):107–116. <https://doi.org/10.1142/S0218488598000094>
9. Hochreiter S, Schmidhuber J (1997) Long short-term memory. *Neural Comput* 9(8):1735–1780. <https://doi.org/10.1162/neco.1997.9.8.1735>
10. Karpathy A, Fei-Fei L (2015) Deep visual-semantic alignments for generating image descriptions. In: *Proceedings of the IEEE conference on computer vision and pattern recognition*, pp 3128–3137
11. Kong W, Dong ZY, Hill DJ, Luo F, Xu Y (2017) Short-term residential load forecasting based on resident behaviour learning. *IEEE Trans Power Syst* 33(1):1087–1088. <https://doi.org/10.1109/TPWRS.2017.2688178>
12. Kong W, Dong ZY, Jia Y, Hill DJ, Xu Y, Zhang Y (2017) Short-term residential load forecasting based on LSTM recurrent neural network. *IEEE Trans Smart Grid* 10(1):841–851. <https://doi.org/10.1109/TSG.2017.2753802>
13. Kuan L, Zhenfu B, Xin W, Xiangrong M, Honghai L, Wenxue S, Zijian Z, Zhimin L (2017) Short-term CHP heat load forecast method based on concatenated LSTMs. In: *2017 Chinese automation congress (CAC)*. IEEE, pp 99–103. <https://doi.org/10.1109/CAC.2017.8242744>
14. Mao J, Xu W, Yang Y, Wang J, Huang Z, Yuille A (2014) Deep captioning with multimodal recurrent neural networks (m-RNN). *arXiv preprint arXiv:1412.6632*
15. Marino DL, Amarasinghe K, Manic M (2016) Building energy load forecasting using deep neural networks. In: *IECON 2016-42nd annual conference of the IEEE industrial electronics society*. IEEE, pp 7046–7051. <https://doi.org/10.1109/IECON.2016.7793413>
16. Ouyang T, He Y, Li H, Sun Z, Baek S (2017) A deep learning framework for short-term power load forecasting. <https://doi.org/10.1109/TETCI.2018.2880511>. *arXiv preprint arXiv:1711.11519*
17. Qin Y, Li K, Liang Z, Lee B, Zhang F, Gu Y, Zhang L, Wu F, Rodriguez D (2019) Hybrid forecasting model based on long short term memory network and deep learning neural network for wind signal. *Appl Energy* 236:262–272. <https://doi.org/10.1016/j.apenergy.2018.11.063>
18. Raza MQ, Khosravi A (2015) A review on artificial intelligence based load demand forecasting techniques for smart grid and buildings. *Renew Sustain Energy Rev* 50:1352–1372. <https://doi.org/10.1016/j.rser.2015.04.065>
19. Sutskever I, Vinyals O, Le QV (2014) Sequence to sequence learning with neural networks. In: *Advances in neural information processing systems*, pp 3104–3112. <https://doi.org/10.5555/2969033.2969173>
20. Tian C, Ma J, Zhang C, Zhan P (2018) A deep neural network model for short-term load forecast based on long short-term memory network and convolutional neural network. *Energies* 11(12):3493. <https://doi.org/10.3390/en11123493>
21. Vinyals O, Toshev A, Bengio S, Erhan D (2015) Show and tell: a neural image caption generator. In: *Proceedings of the IEEE conference on computer vision and pattern recognition*, pp 3156–3164
22. Zhao J, Liu X (2018) A hybrid method of dynamic cooling and heating load forecasting for office buildings based on artificial intelligence and regression analysis. *Energy Build* 174:293–308. <https://doi.org/10.1016/j.enbuild.2018.06.050>

Symmetrical Pulse Width Modulation Technique for Harmonic Elimination in PWM AC Voltage Regulator Using Random Search Method



M. S. Patil and A. S. Koshti

Abstract A random search (RS) method of optimization has been implemented in SPWM AC voltage regulator. This method gives trial solutions for the optimization model using random number generators for the decision variables. The symmetrical pulse width modulation (SPWM) strategy is used to obtain required voltage (50 Hz) with minimum harmonic. In SPWM, RS method is used for obtaining multiple switching angles maintaining symmetry of pulse width in both positive and negative half cycle. Angles for on/off instant are obtained from RS, and the waveforms of output voltages and frequency spectra of AC voltage regulator are obtained using PSIM software. The statistics for mean and standard deviation for objective function of one specific case is also discussed.

Keywords SPWM · AC voltage regulator · Harmonics elimination · RS

1 Introduction

Voltage requirement of appliances varies as per the customer's demand. The applications such as line conditioners, speed control of pumps, and industrial heating require variable AC voltages at different time intervals according to user's demand. Conventionally, it is achieved by using induction voltage regulator, by changing taps on transformer. But, due to advancement of power electronics-based circuits, it is possible to control voltage very quickly. PWM strategy is suggested in [1, 2] used for control of AC voltage. SPWM technique uses solid-state switching devices to control voltage. Such devices will provide the advantages such as fast response and compactness [3]. Along with these advantages, they inject harmonics and make distorted voltage waveforms. The higher-order harmonics has most detrimental effect on the system components such as heating of winding of transformer, false or spurious operation, and trips of fuses and circuit breakers; utility meters may record measurements incorrectly resulting higher billing to consumers. So, it is a crucial task to minimize such

M. S. Patil (✉) · A. S. Koshti

EED, R.H. Sapat College of Engineering Management, Studies and Research, Nashik, India
e-mail: mamatapatil2898@gmail.com

© The Author(s), under exclusive license to Springer Nature Singapore Pte Ltd. 2022
V. Mahajan et al. (eds.), *Sustainable Technology and Advanced Computing*
in *Electrical Engineering*, Lecture Notes in Electrical Engineering 939,
https://doi.org/10.1007/978-981-19-4364-5_35

479

higher-order harmonics. This can be minimized by suitably selecting the values of firing angles such that SPWM AC voltage regulator will give desired output voltage across load with no harmonic content present in it. That is why this issue is refracted as an optimization and discussed in [4–13]. The values of firing angles at which SPWM AC voltage regulator will give minimum harmonics are calculated by using RS. The optimization of RS is discussed in [14, 15]. This paper suggests RS for obtaining required voltage (50 Hz) with minimum harmonic in SPWM AC voltage regulator. Angle for on/off is optimized using RS. This paper presents harmonic elimination up to 19th order, and for that purpose, ten pulses per quarter cycle are applied to SPWM AC voltage regulator.

2 Working Principle of SPWM AC Voltage Regulator

SPWM AC voltage regulator with switch arrangement is shown in Fig. 1. Load is connected to source through switch D1-S1-D3 during ON time in + ve half cycle, and D5-S2-D7 provides freewheeling in off period. During ON time, in –ve cycle, it is done by D2-S1-D4, and freewheeling is done by D6-S2-D8 in off period. S1 is made ON at angles $\alpha_1, \alpha_3, \alpha_5, \dots, \alpha_{m-1}$, respectively and made OFF at $\alpha_2, \alpha_4, \alpha_6, \dots, \alpha_m$ per quarter cycle. The output voltage of the SPWM AC voltage regulator with ‘ n ’ pulses per half cycle is shown in Fig. 2 for ($m = 2$).

Voltage across load is expressed using Fourier series as:

$$V_{out} = V_{dc} + \sum_1^n B_n \sin(n\theta) + \sum_1^n A_n \cos(n\theta) \tag{1}$$

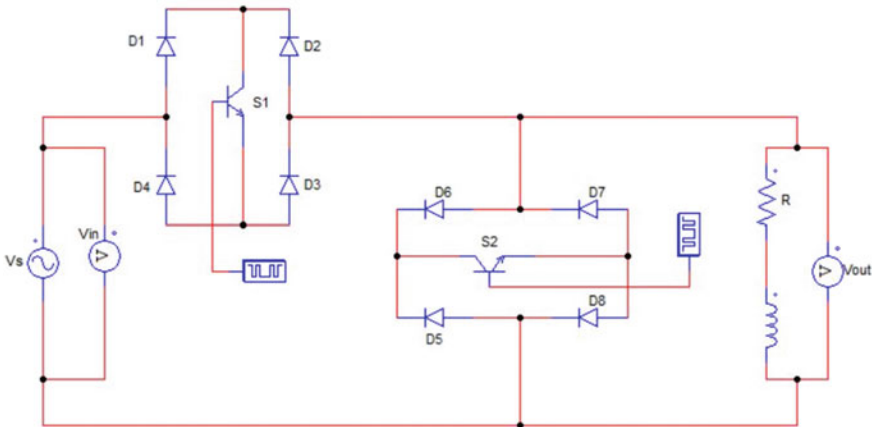


Fig. 1 SPWM AC voltage regulator with switch arrangement

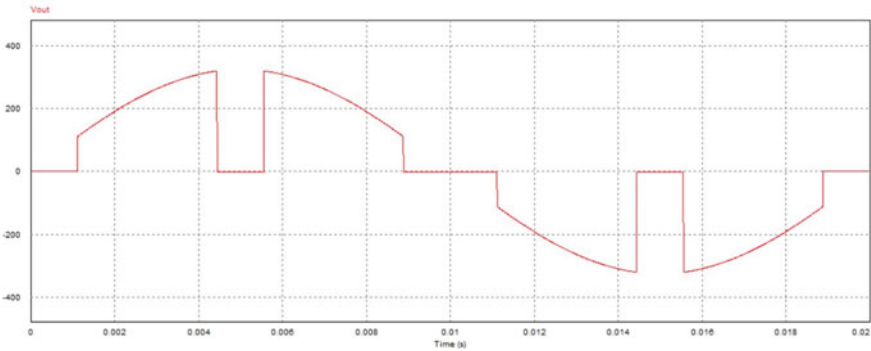


Fig. 2 Output voltage of SPWM AC voltage regulator for one pulse per quarter cycle ($m = 2$)

where $\theta = \omega t$,

It is noticed that $V_{dc} = 0$ and all terms related with A_n and even terms of B_n are zero in view of symmetry in quarter cycle

$$V_{out} = \sum_1^n B_n \sin(n\theta); \quad n = 1, 3, 5, 7, 9, 11, 13, 15, 17, 19, \dots \quad (2)$$

And B_n is given by

$$B_n = \frac{2V_m}{\pi} \left[\frac{\sin(n-1)\theta}{(n-1)} - \frac{\sin(n+1)\theta}{(n+1)} \right]_{\alpha_1, \alpha_3, \alpha_5, \alpha_7, \alpha_9, \dots, \alpha_{m-1}}^{\alpha_2, \alpha_4, \alpha_6, \alpha_8, \alpha_{10}, \dots, \alpha_m} \quad (3)$$

where, $n \neq 1$

The value of B_1 is given by

$$B_1 = \frac{2V_m}{\pi} \left[\theta - \frac{\sin \theta}{2} \right]_{\alpha_1, \alpha_3, \alpha_5, \alpha_7, \alpha_9, \dots, \alpha_{m-1}}^{\alpha_2, \alpha_4, \alpha_6, \alpha_8, \alpha_{10}, \dots, \alpha_m} \quad (4)$$

The output of SPWM AC voltage regulator in terms of voltage (50 Hz) and harmonic component up to 19th order is given by

$$J = (V_d - B_1)^2 + \sum_{i=3}^{19} (B_i)^2 \quad (5)$$

where

V_d = Desired voltage (max value)

B_1 = Fundamental component (max value)

3 Algorithm Based on RS Method for Evaluation of Optimum Switching Angles for SPWM AC Voltage Regulator

This paper deals with a RS-based optimization algorithm for solving optimization problem. RS method provides inherent advantage of control variables found in the limit. The algorithm for RS is as follows:

Step 1: Start with trial solution α_i , set $i = 1$

Step 2: The values of α_i can be calculated by the formula

$$\alpha_i = X_{\min} + (X_{\max} - X_{\min}) \text{rand};$$

where, $X_{\min} = 0$

$$X_{\max} = \pi/2$$

Step 3: Compute objective function $F(\alpha_i)$

$$F(\alpha_i) = (Vd - B_1)^2 + \sum_{j=3}^{19} (B_j)^2$$

Step 4: Generate new solution at α_{i+1}

Step 5: Compute objective function at $f(\alpha_{i+1})$

$$F(\alpha_{i+1}) = (Vd - B_1)^2 + \sum_{j=3}^{19} (B_j)^2$$

Step 6: Convergence check

Step 7: Obtain optimal solution as

$$([\alpha_{\text{opt}}] = [\alpha_i])$$

Step 8: Repeat step 4–6 until the termination criteria are not satisfied.

4 Results and Discussion

The circuit diagram is as shown in Fig. 1 is same for all cases; only, the firing angles are inserted according to our requirement. If one pulse per quarter cycle is applied to AC voltage regulator, then only one, i.e., 3rd harmonic gets eliminated. If two pulses per quarter cycle are applied to AC voltage regulator, then three 3rd, 5th, 7th harmonics get eliminated. That means if ‘ m ’ angles per quarter cycle are applied to AC voltage regulator, then ‘ $m-1$ ’ harmonics get reduced. Similarly, the procedure is followed for next harmonics. This paper deals from one pulse per quarter cycle to five pulses per quarter cycle. The 230 V (rms) or 325.26 V (max), 50 Hz AC supply is considered for each case with the load of $R = 50\Omega$, $XL = 37.48\Omega$ with 0.8 lagging

power factor. For the expected fundamental frequency voltage with minimum number of odd order harmonic component, the algorithm is given in Sect. 3 is executed, and optimal values of switching angles are obtained. The values of optimal switching angles $\alpha_1, \alpha_2, \alpha_3, \alpha_4, \alpha_5, \alpha_6, \alpha_7, \alpha_8, \alpha_9,$ and α_{10} are obtained from MATLAB software by RS method. The switching angles and obtained harmonic components are presented from Tables 1, 2, 3, 4, 5, 6, 7, and 8. Once the optimal switching angles are obtained, then they are inserted into PSIM software, and based on that switching angles, the waveforms of output voltages and frequency spectra of AC voltage regulator are obtained using PSIM software. It tested for $V_d = 0.1-0.5$ p.u. at 0.8 p.f. loading condition. The Figs. 2, 4, 6, 8, and 10 show the output voltage waveforms having one pulse per quarter cycle, two pulses per quarter cycle, three pulses per quarter cycle, four pulses per quarter cycle, and five pulses per quarter cycle, respectively. Figures 3, 5, 7, 9, and 11 show frequency spectra for one pulse per quarter cycle, two pulses per quarter cycle, three pulses per quarter cycle, four pulses per quarter cycle, and five pulses per quarter cycle, respectively, of voltage harmonics for particular case $V_d = 0.1$. Statistics for mean and standard deviation for twenty run for objective function at 0.8 p.f. with $V_d = 0.1$ p.u. is shown in Table 9 is obtained by RS method.

Table 1 Obtained switching angles and voltages for one pulse per quarter cycle ($m = 2$) with p.f. = 0.80 lagging

Desired voltage (p.u.)	Obtained by RS			
	α_1 (rad)	α_2 (rad)	B_1 (p.u.)	B_3 (p.u.)
0.1	0.9949	1.0976	0.0978	0.0001
0.2	0.9384	1.1470	0.1976	0.0015
0.3	0.8787	1.2072	0.3002	0.0012
0.4	0.8243	1.2541	0.4026	0.0018
0.5	0.7671	1.3028	0.4966	0.0042

Table 2 Obtained switching angles and voltages for two pulses per quarter cycle ($m = 4$) with p.f. = 0.80 lagging

Desired voltage (p.u.)	Obtained by RS							
	α_1 (rad)	α_2 (rad)	α_3 (rad)	α_4 (rad)	B_1 (p.u.)	B_3 (p.u.)	B_5 (p.u.)	B_7 (p.u.)
0.1	0.6387	0.7146	1.2497	1.3121	0.1107	0.0050	0.0053	0.0060
0.2	0.5124	0.6355	1.1700	1.2719	0.1607	0.0229	0.0004	0.0312
0.3	0.5543	0.7418	1.1596	1.3348	0.2871	0.0131	0.0251	0.0111
0.4	0.5341	0.7186	1.1599	1.3457	0.3938	0.0002	0.0044	0.0119
0.5	0.5295	0.7946	1.0995	1.4117	0.4847	0.0322	0.0366	0.0326

Table 3 Obtained switching angles for three pulses per quarter cycle ($m = 6$) with p.f. = 0.80 lagging

Desired voltage (p.u.)	Obtained by RS					
	α_1 (rad)	α_2 (rad)	α_3 (rad)	α_4 (rad)	α_5 (rad)	α_6 (rad)
0.1	0.0157	0.0401	0.9486	0.9582	1.3510	1.3686
0.2	0.0169	0.0973	0.1521	0.1660	0.1691	0.1732
0.3	0.3213	0.5109	0.7971	0.9918	1.2370	1.4700
0.4	0.3217	0.5833	0.7128	1.0544	1.1883	1.5276
0.5	0.1689	0.7592	0.7732	1.0684	1.0787	1.5543

Table 4 Obtained output voltages for three pulses per quarter cycle ($m = 6$) with p.f. = 0.80 lagging

Desired voltage (p.u.)	Obtained by RS					
	B_1 (p.u.)	B_3 (p.u.)	B_5 (p.u.)	B_7 (p.u.)	B_9 (p.u.)	B_{11} (p.u.)
0.1	0.1010	0.0128	0.0001	0.0020	0.0015	0.0046
0.2	0.1885	0.0028	0.0044	0.0057	0.0067	0.0071
0.3	0.2837	0.0499	0.0284	0.0003	0.0239	0.0064
0.4	0.4339	0.0413	0.0035	0.0555	0.0283	0.0159
0.5	0.5065	0.0067	0.0135	0.0074	0.0397	0.0027

Table 5 Obtained switching angles for four pulses per quarter cycle ($m = 8$) with p.f. = 0.80 lagging

Desired voltage (p.u.)	Obtained by RS							
	α_1 (rad)	α_2 (rad)	α_3 (rad)	α_4 (rad)	α_5 (rad)	α_6 (rad)	α_7 (rad)	α_8 (rad)
0.1	0.1868	0.2184	1.1446	1.1514	1.2628	1.2680	1.4736	1.4787
0.2	0.1959	0.3281	0.7046	0.7544	1.0125	1.0948	1.3629	1.4378
0.3	0.3927	0.5171	0.7314	0.7968	1.0319	1.1485	1.3433	1.4854
0.4	0.1977	0.3068	0.6677	0.7301	1.1141	1.3353	1.4226	1.4937
0.5	0.4088	0.5010	0.7243	0.7968	0.9823	1.1251	1.3405	1.4813

Table 6 Obtained output voltages for four pulses per quarter cycle ($m = 8$) with p.f. = 0.80 lagging

Desired voltage (p.u.)	Obtained by RS							
	B_1 (p.u.)	B_3 (p.u.)	B_5 (p.u.)	B_7 (p.u.)	B_9 (p.u.)	B_{11} (p.u.)	B_{13} (p.u.)	B_{15} (p.u.)
0.1	0.0913	0.0077	0.0088	0.0148	0.0000	0.00974	0.0073	0.0072
0.2	0.2077	0.0174	0.0089	0.0428	0.3902	0.0055	0.0050	0.0015
0.3	0.3027	0.0313	0.0003	0.0296	0.0050	0.0378	0.0474	0.0062
0.4	0.4135	0.0301	0.0005	0.4804	0.0112	0.0478	0.0176	0.0030
0.5	0.4783	0.0608	0.0101	0.0063	0.0045	0.0807	0.0058	0.0622

Table 7 Obtained switching angles for five pulses per quarter cycle ($m = 10$) with p.f. = 0.80 lagging

Desired voltage (p.u.)	Obtained by RS									
	α_1 (rad)	α_2 (rad)	α_3 (rad)	α_4 (rad)	α_5 (rad)	α_6 (rad)	α_7 (rad)	α_8 (rad)	α_9 (rad)	α_{10} (rad)
0.1	0.0269	0.0500	0.1995	0.2726	0.8735	0.8952	1.4070	1.5911	1.4315	1.4495
0.2	0.0969	0.1263	0.1666	0.1785	0.3103	0.3284	0.8558	0.8565	1.1684	1.1760
0.3	0.0897	0.0970	0.2086	0.2158	0.3001	0.3040	0.5062	0.5202	0.8232	0.8437
0.4	0.3193	0.3675	0.6573	0.7431	0.9653	1.0591	1.2274	1.3369	1.4377	1.5352
0.5	0.5677	0.7008	0.8276	0.9524	0.9740	0.9870	1.0800	1.2326	1.3732	1.5175

Table 8 Obtained output voltages for five pulses per quarter cycle ($m = 10$) with p.f. = 0.80 lagging

Desired voltage (p.u.)	Obtained by RS									
	B_1 (p.u.)	B_3 (p.u.)	B_5 (p.u.)	B_7 (p.u.)	B_9 (p.u.)	B_{11} (p.u.)	B_{13} (p.u.)	B_{15} (rad)	B_{17} (p.u.)	B_{19} (p.u.)
0.1	0.0638	0.0031	0.0070	0.0268	0.0314	0.0033	0.0052	0.0070	0.0020	0.0169
0.2	0.0198	0.0057	0.0071	0.0191	0.0007	0.0065	0.0033	0.0099	0.0074	0.0012
0.3	0.0295	0.0229	0.0082	0.0085	0.0124	0.0015	0.0152	0.0067	0.0235	0.0067
0.4	0.3893	0.1169	0.0302	0.0269	0.0101	0.0138	0.0065	0.0195	0.1012	0.0082
0.5	0.5101	0.0731	0.0730	0.0389	0.0090	0.0011	0.0749	0.0185	0.0136	0.0340

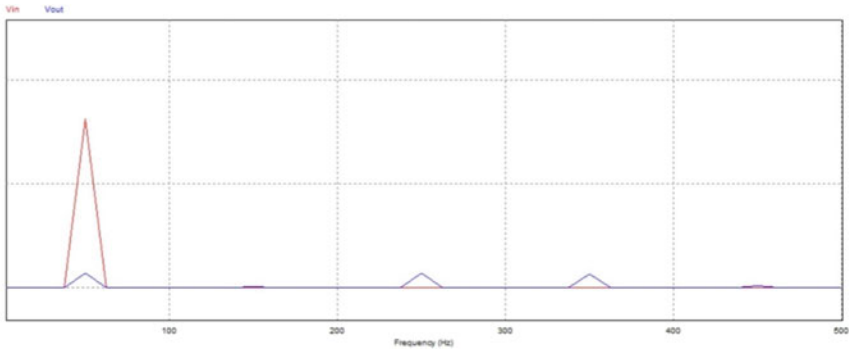


Fig. 3 Frequency spectra for one pulse per quarter cycle at $V_d = 0.1$ p.u. at 0.8 p.f. (lagging)

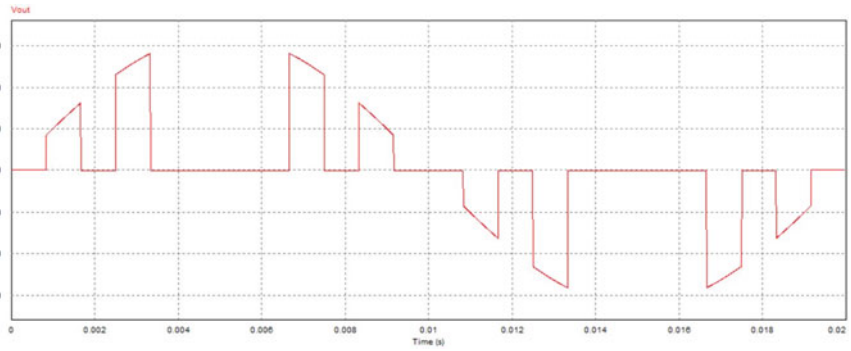


Fig. 4 Output voltage of SPWM AC voltage regulator for two pulses per quarter cycle ($m = 4$)

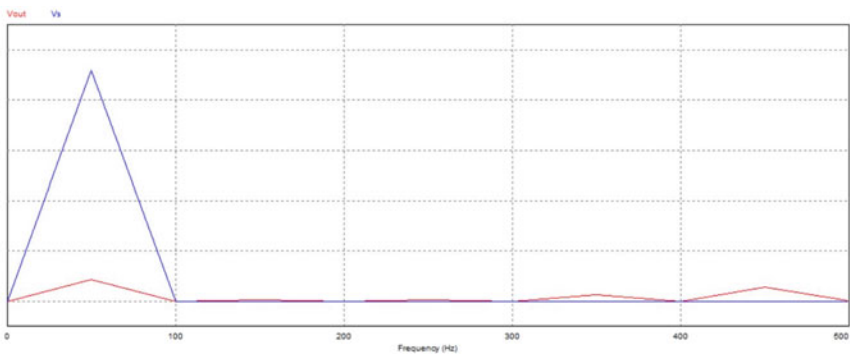


Fig. 5 Frequency spectra for two pulses per quarter cycle at $V_d = 0.1$ p.u. at 0.8 p.f. (lagging)

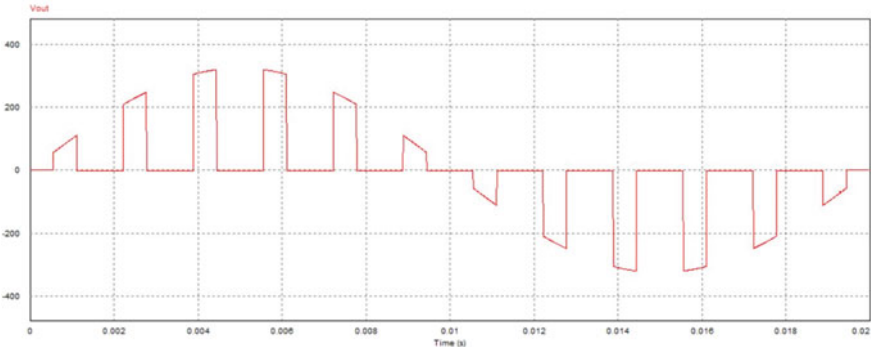


Fig. 6 Output voltage of SPWM AC voltage regulator for three pulses per quarter cycle ($m = 6$)

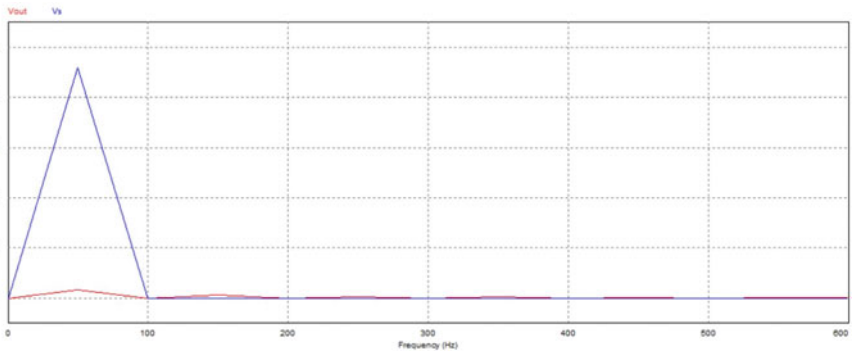


Fig. 7 Frequency spectra for three pulses per quarter cycle at $V_d = 0.1$ p.u. at 0.8 p.f. (lagging)

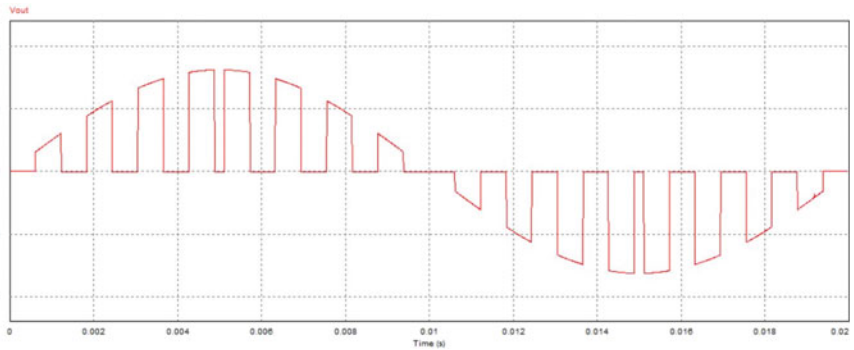


Fig. 8 Output voltage of SPWM AC voltage regulator for four pulses per quarter cycle ($m = 8$)

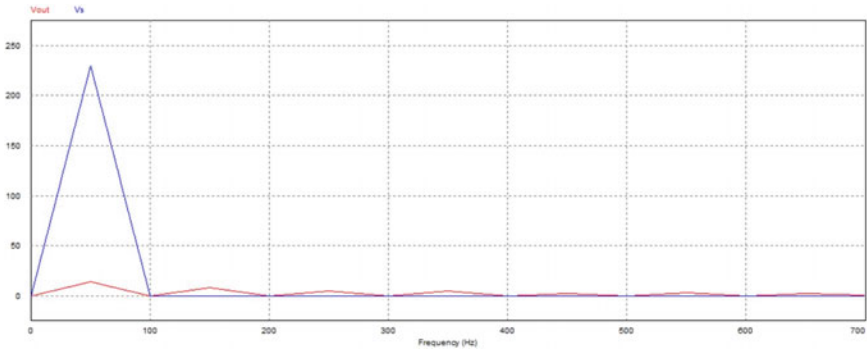


Fig. 9 Frequency spectra for four pulses per quarter cycle at $V_d = 0.1$ p.u. at 0.8 p.f. (lagging)

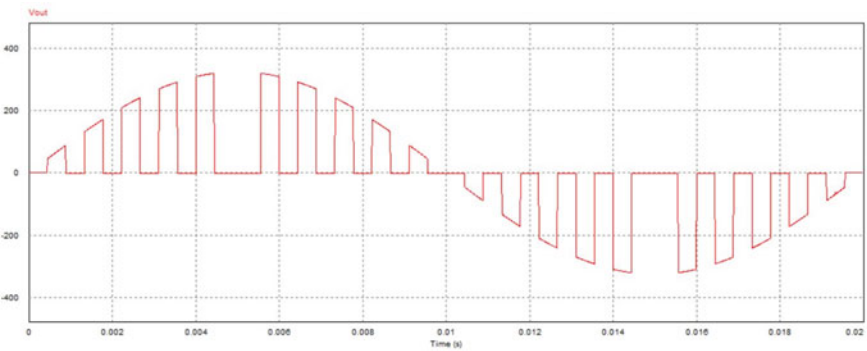


Fig. 10 Output voltage of SPWM AC voltage regulator for five pulses per quarter cycle ($m = 10$)

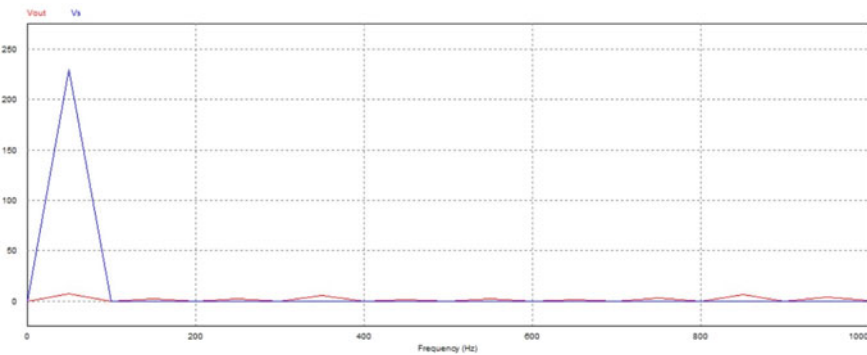


Fig. 11 Frequency spectra for five pulses per quarter cycle at $V_d = 0.1$ p.u. at 0.8 p.f. (lagging)

Table 9 Statistics for mean and standard deviation for twenty run for objective function (Y_{\min}) at 0.8 p.f. with Vd = 0.1 p.u., i.e., 23 V

No. of runs	Y_{\min}	α_1 (deg)	α_2 (deg)	α_3 (deg)	α_4 (deg)	$(Y_{\min} - Y_{\text{avg}})^2$
1	11.1392	35.9920	39.4021	69.8790	72.7936	0.3836
2	17.2351	46.2779	49.3819	74.3632	77.0812	29.9900
3	14.5039	36.5976	40.9488	71.6072	75.1787	7.5366
4	9.8485	32.4679	35.4812	69.9541	72.7190	3.6484
5	13.7550	33.5970	36.1464	70.7825	74.6267	3.9856
6	12.7157	36.8955	40.7599	71.8621	75.8171	0.9160
7	7.4861	32.9573	36.1493	70.0109	73.6455	18.2542
8	10.8471	37.4548	39.9969	70.2098	73.6364	0.8308
9	13.8611	32.8623	36.9794	68.3226	72.9157	4.4205
10	11.1210	32.0883	37.0787	69.5192	72.9349	0.4065
11	9.1881	36.1278	39.3883	71.6557	75.4192	6.6074
12	4.3440	34.2572	37.7621	69.4025	73.0583	54.9762
13	10.9391	34.7323	38.0315	71.2087	75.3706	0.6715
14	13.7905	35.3336	39.2852	70.3230	73.2385	4.1286
15	11.9420	31.9106	35.8038	68.4416	72.8020	0.0336
16	6.0509	33.1955	37.3059	70.2243	74.3879	32.5778
17	11.2085	40.5691	43.9129	70.4933	73.9771	0.3026
18	10.6766	30.9490	35.7528	69.9994	74.0237	1.1707
19	14.6230	34.4305	37.0412	72.4147	76.0678	8.2047
20	19.8667	50.7535	54.1668	76.1831	78.5776	65.7412
	$Y_{\text{avg}} = 11.7586$					$\sum(Y_{\min} - Y_{\text{avg}})^2 = 244.7865$

$$\text{Standard Deviation } (\sigma) = \sqrt{\frac{1}{(NR - 1)} \left[\sum Y_{\min, i} - Y_{\text{avg}} \right]^2}$$

where

$Y_{\min, i}$ = minimum value of objective function at i th iteration

Y_{avg} = average value of objective function

NR = total number of runs

$$\sigma = \sqrt{\frac{1}{(20 - 1)} [244.7865]^2} = 3.5893$$

$$\text{Standard deviation of mean}(s) = \frac{\sigma}{\sqrt{NR}} = \frac{3.5893}{\sqrt{20}} = 0.8025$$

5 Conclusion

In this paper, random search optimization is proposed for harmonic elimination of SPWM AC voltage regulator. The values of switching angles are obtained from MATLAB software by RS algorithm. Based on the switching angles which are obtained from RS, the waveforms of output voltages and frequency spectra of AC voltage regulator are obtained using PSIM software. If ' m ' angles per quarter cycle are applied to AC voltage regulator, then ' $m-1$ ' odd order harmonics get eliminated. This paper presents work from one pulse per quarter cycle to five pulses per quarter cycle. Also, the statistics for mean and standard deviation for twenty run for objective function at 0.8 p.f. is presented. From this paper, it is conclude that the RS method works efficiently for output voltage regulation along with harmonic elimination.

References

1. Choe G-H, Wallace AK, Park M-H (1989) An improved PWM technique for AC Choppers. *IEEE Trans Power Electron* 4(4):496–505
2. Revankar GN, Trasi DS (1977) Symmetrically pulse width modulated AC chopper. *IEEE Trans Ind Electron Control Instrum* 24(1):39–44
3. Addoweesh KE, Mohamadein AL (1990) Microprocessor based harmonic elimination in chopper type AC voltage regulators. *IEEE Trans Power Electron* 5(2):191–200
4. Sundareswaran K, Pavan Kumar A (2005) Performance enhancement of PWM AC chopper using random search method. *J Inst Eng (India)* 85(4):228–230
5. Arya LD, Koshti A, Bhatt PK (2007) Mitigation of harmonics content in PWM AC chopper using particle swarm optimization (PSO) and implementation on artificial neural network. *IE (I) J-EL* 87:32–36
6. Sundareswaran K, Kumar AP (2004) Voltage harmonic elimination in PWM AC chopper using genetic algorithm. *IEEE Proc Electr Power Appl* 151(1):26–31
7. Al- Othman AK, Ahmed NA, AlSharidah ME, AlMekhaizim HA (2013) A hybrid real coded genetic algorithm—pattern search approach for selective harmonic elimination of PWM AC/AC voltage controller. *Electr Power Energy Syst* 44:123–133
8. Al-Othman AK, Ahmed NA, Al-Kandari M, Ebraheem HK (2007) Selective harmonic elimination of PWM AC/AC voltage regulator using hybrid RGA-PS approach. *Int J Electr Comput Syst Eng* 227–233
9. Ghorpade DB, Koshti A, Halve SM (2020) Reduction of selective harmonics in PWM AC chopper using TLBO. In: *Advances in power and control engineering, lecture notes in electrical engineering*, vol 609
10. Lang T-J, O'Connell RM, Hoft RG (1997) Inverter harmonic reduction using Walsh function harmonic elimination method. *IEEE Trans Power Electron* 12(6):971–982
11. Swift F, Kamberis A (1993) A new Walsh domain technique of harmonic elimination and voltage control in pulse-width modulated inverters. *IEEE Trans Power Electron* 8(2):170–185
12. Patel H, Hoft R (1973) Generalized techniques of harmonic elimination and voltage control in thyristor inverters: part 1—harmonic elimination. *IEEE Trans Ind Appl* 9:310–317

13. Patel H, Hoft R (1974) Generalized techniques of harmonic elimination and voltage control in thyristor inverters: part 2—voltage control techniques. *IEEE Trans Ind Appl* 10:666–673
14. Solis FJ, Wets RJ-B (1981) Minimization by random search techniques. *Math Oper Res* 6(1):19–30
15. Sundareswaran K, Sankar P, Palani S (2014) Application of random search method for maximum power point tracking in partially shaded photovoltaic systems. *IET Renew Power Gener* 8(6):670–678

Design of Three-Phase, 400 Hz Power Supply Using Three-Level T-Type Topology



Gayatri Kher, M. T. Shah, and Vinod Patel

Abstract This paper proposes the design of 400 Hz power supply using T-type, three-level inverter topology. T-type topology is investigated for 400 Hz power supply which is generally used in aircraft application. To generate this power supply, T-type inverter is controlled by space vector pulse width modulation (SVPWM) technique. The design of output passive filter with its damping components is also given in this paper to reduce the harmonics from the output of the given system. The performance of T-type multi-level inverter is simulated with balanced three-phase resistive and inductive load of 110 kW and also with balanced three-phase resistive load of 55 kW. Various performance parameters like output voltage, output current, its %THD, etc., are discussed using PSIM as simulation tool. Hardware prototype of this simulated system is also implemented. This hardware design employs a high-performance digital signal processor (DSP) from Texas Instruments. At last, the simulated results are verified with the experimental results which are taken from the hardware prototype.

Keywords T-type inverter · SVPWM · Aircraft power supply · Harmonics · Switching loss

1 Introduction

Nowadays, single-phase, three-phase, and DC power supplies in defense and military applications are one of the core competencies of the aegis power supply system team. Power at 400 Hz, which is generally used in many applications like aircraft, military equipment, submarines, spacecraft, etc. [1]. In above applications, reduction of weight and size of whole system are essential. A high-frequency power supply

G. Kher · M. T. Shah (✉)

Electrical Engineering Department, Institute of Technology, Nirma University, Ahmedabad, India
e-mail: manisha.shah@nirmauni.ac.in

V. Patel

DGM, Research and Development, Amtech Electronics India Limited, Gandhinagar, India

allows more power to be access for the same size and weight of the motor. The size of the power supply is inversely proportional to switching frequency, and switching losses are directly proportional to it. So, there is always tread-off between size and efficiency of the power supply [2]. In the proposed work, 400 Hz is taken as optimum switching frequency. Power at 400 Hz has many advantages like higher efficiency, lower noise, high reliability, and less THD [3]. Almost all aircraft systems use 115 V AC supply with 400 Hz or 28 V DC. For the lighting purposes, 26 V AC is also used in some of the aircraft system [2].

Multi-level inverters have become more popular choice over two-level inverters due to their advantages such as reduced switch rating, improved harmonic profile, etc. Multi-level inverter also have few disadvantages like segregated dc power bank requirement in cascaded H-bridge inverters, giant capacitor bank needed in flying capacitor inverters, and voltage unbalancing in neutral point clamped (NPC) inverter [4]. To overcome the limitations of NPC inverter, advanced NPC inverter or also known as T-type inverter is becoming more plausible. Since this T-type inverter abolish all the issues which are faced by the conventional three-level inverters, it become a substitute solution with many benefits like uncomplicated operation and few numerals of switching devices [5]. At medium frequency range, T-type topology is much more effective than two-level and three-level NPC inverters [6, 7]. As compared to the NPC inverter, clamping diode requirement is completely eliminated in this T-type topology [8]. Furthermore, it also needs less number of discriminated gate driver circuit than conventional three-level topologies because of the common emitter switching configuration [9].

Different PWM techniques have the same approach and that is to reduce the THD of the output current [10]. With the evolution of microcontroller, SVPWM method has become one of the most prior method to control the three-phase converter. All the disadvantages of the conventional PWM schemes were solved by SVPWM technique. Easy digital implementation and broad linear modulation range for the output line voltage are remarkable feature of SVPWM scheme [11].

2 System Schematic Diagram of 400 Hz Power Supply

The system schematic diagram of 400 Hz power supply is demonstrated in Fig. 1. Three-level T-type inverter is employed to procreate 400 Hz power supply. Three-phase, 415 V, 50 Hz power is supplied to the three-phase diode bridge rectifier circuit. DC choke is connected at the end of the three-phase diode bridge rectifier to reduce the total harmonic content and smooth the DC bus voltage. Two capacitors are fitted in series at the DC-link, which are used to subdue the fluctuations in the DC bus capacitors voltage.

Three-phase T-type inverter is made by three T-type IGBT modules. At the middle point of the DC bus capacitors, the middle point of the T-type IGBT modules are connected. A three-phase filter is fitted between the inverter and load to lower the

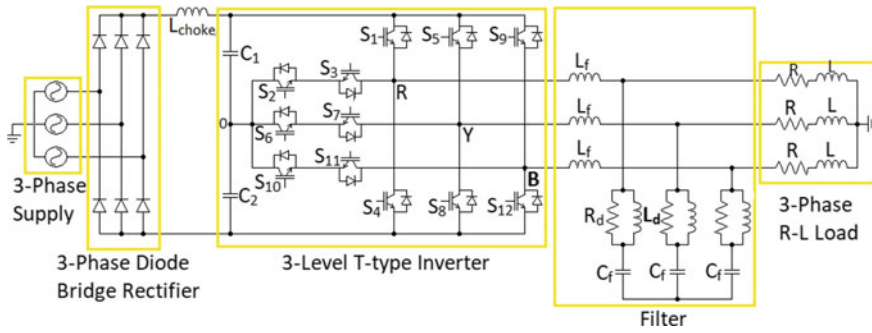


Fig. 1 System schematic diagram of 400 Hz power supply

THD in the output voltage. At the end, three-phase load is connected after the filter configuration which having the rating of 110 kW, 350 V, 180 A.

2.1 Three-Level T-Type Inverter

The conventional two-level voltage source converter topology is expanded with an active, bi-directional switches to the dc bus middle point [12]. The one leg of the T-type inverter is display in Fig. 2. It comprises four switches (S1, S2, S3, and S4). Switches S2 and S3 are connected in common emitter configuration. Both switches are connected in this manner because the common emitter pattern required only one additional gate driver circuit for one leg, adding up total three additional gate driver circuit is needed in three-level T-type inverter as compared to the two-level voltage source converter (VSC). The switching pattern of one leg of T-type inverter is shown in Table 1.

Fig. 2 One leg of T-type inverter

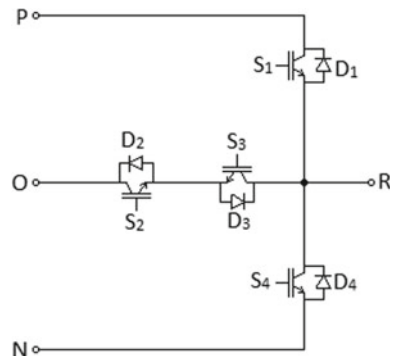


Table 1 Switching table of T-type inverter

Switching state	Device status				Pole voltage V_R
	S_1	S_2	S_3	S_4	
+	ON	ON	OFF	OFF	$+V_{dc}/2$
0	OFF	ON	ON	OFF	0
-	OFF	OFF	ON	ON	$-V_{dc}/2$

2.2 Calculation of DC Choke

Consider the input supply voltage 415 V and its variations is taken of 10%, efficiency is 96% and the power factor of the system is 0.85. The input power $P_{i/p}$ can be calculated using (1).

$$P_{i/p} = \frac{P_o}{\eta} = \frac{109119.2008}{0.96} = 113.6658 \text{ kW} \quad (1)$$

The input current $I_{i/p}$ is calculated using (2).

$$I_{i/p} = \frac{P_{i/p}}{(\sqrt{3} * V_{i/p} * \cos \phi)} = 186.0382 \text{ A} \quad (2)$$

The value of AC choke (L) can be found out using (3) from the value of the (2). Take the voltage drop across the inductor is 3% and neglect the value of resistance from the impedance of the system. Take the supply frequency is 50 Hz.

$$\text{AC Choke, } L = \frac{V_{i/p}}{2 * \pi * f * I_{i/p}} = 123.0488 \mu\text{H} \quad (3)$$

The value of DC choke can be found out using the value of AC choke and it is shown in (4). Its value is 1.732 times the value of AC choke, which is mentioned below:

$$\text{DC Choke} = \sqrt{3} * \text{AC Choke} = \sqrt{3} * 123.0488 = 213.126 \mu\text{H} \quad (4)$$

Hence, the standard value of DC choke is taken as 220 μH .

2.3 Passive Filter Design

Passive LC low pass filter is used to diminish lower order harmonic from the outcome of the inverter. When the frequency of the both components L_f and C_f are matched,

resonance will be created which can cause system unstable [13]. Damping components R_d and L_d are connected with L_f and C_f filter components to avoid resonance in the system. So many passive damping configurations are available; each having its own characteristic. To avoid resonance, damping resistor R_d is fitted in cascaded manner with shunt filter capacitor C_f , but larger resistance reduces the attenuation and increase the losses [14]. So, damping inductor L_d is connected in parallel with damping resistor R_d . Low-frequency components are flowing through the L_d and high-frequency components are flowing through the R_d because inductive reactance will increase as frequency is increases.

2.4 Calculation of Output Filter

The capacitance value is selected depending on the amount of reactive power which is suck up by the LC output filter. The value of capacitor is to select in such a way that it helps in improving power factor. The value of output filter capacitor (C_f) can be found out using (5) [15].

$$C_f = \frac{\alpha * P_o}{2 * \pi * f * V_o^2} = 42.87 \mu\text{F} \quad (5)$$

where α = Reactive Power Factor and is less than 15% and the selected value is 0.12, f = Output line frequency, P_o = Rated output power, V_o = Rated output voltage

Hence, the standard selected value of the output filter capacitor is taken as 40 μF .

The value of output filter inductor (L_f) can be found out using (6) [15].

$$L_f = \frac{1}{4 * \pi^2 * C_f * f_r^2} = 70.36 \mu\text{H} \quad (6)$$

where C_f = Output filter capacitor, f_r = Resonance frequency [12]

After performing various iteration, the selected resonance frequency is 3 kHz. Hence, the standard selected value of the output filter inductor is 70 μH .

The selection of damping resistance is such that it allows low amplitude and high switching frequency current through it. This will cause less ($I^2 * R$) losses and hence less power dissipation. The value of damping resistance (R_d) can be found out using (7) [16].

$$R_d = \frac{1}{6 * \pi * f_r * C_f} = 0.44 \Omega \quad (7)$$

Hence, the standard selected value of the damping resistance is 0.5 Ω .

Table 2 Ratings of various components used in simulation

Parameter	Variable	Value
Nominal output power	P_o	110 kW
DC choke	L	220 μ H
DC-link capacitance	C	2 * 20.4 mF
Switching frequency	f_s	12,800 Hz
Output filter inductance	L_f	70 μ H
Output filter capacitance	C_f	40 μ F
Damping resistance	R_d	0.5 Ω
Damping inductance	L_d	50 μ H
Load	R_L	3-Phase, 350 V, 180 A

The damping inductor presents low impedance at power frequency which will reduce the current passing through the damping resistor. The resistive or heat losses decreases with increase in the value of inductance [16]. The value of damping inductance (L_d) can be found out using (8).

$$L_d = \frac{R_d}{2 * \pi * \frac{f_r}{2}} = 46.68 \mu\text{H} \quad (8)$$

The standard selected value of the damping inductance is 50 μ H.

Table 2 shows the variable and its value which are used in simulation.

2.5 The Control Strategy of the Three-Level T-Type Inverter

The space vector pulse width modulation (SVPWM) gives better harmonic spectrum and 15% more utilization of DC bus as compared to popular sinusoidal pulse width modulation (SPWM) technique [17]. In order to attain above motives, the control strategy of the T-type three-level inverter is implemented which is shown in Fig. 3. The control algorithm is realized via digital signal processor.

For the control scheme implementation, two-line voltages are sensed which is in ABC reference frame. Based on the switching frequency and number of samples, angle θ is calculated. Using this angle θ , sensed three-phase output voltage is transformed into orthogonal rotating reference frame (d -axis and q -axis) using Clarke and park transformation from ABC \rightarrow $\alpha\beta \rightarrow$ dq. Using of above calculated quantities, magnitude of the reference vector is found out [18].

With the use of $\alpha\beta$ components, three voltage vector's formula is developed. These three vectors are now used for the controlling action. Actual voltage is compared with the reference voltage vector and the generated error signal is given to the proportional-integral (PI) controller [19]. PI controller is used to minimize the error between the magnitude of two quantities which are reference voltage and actual voltage to zero.

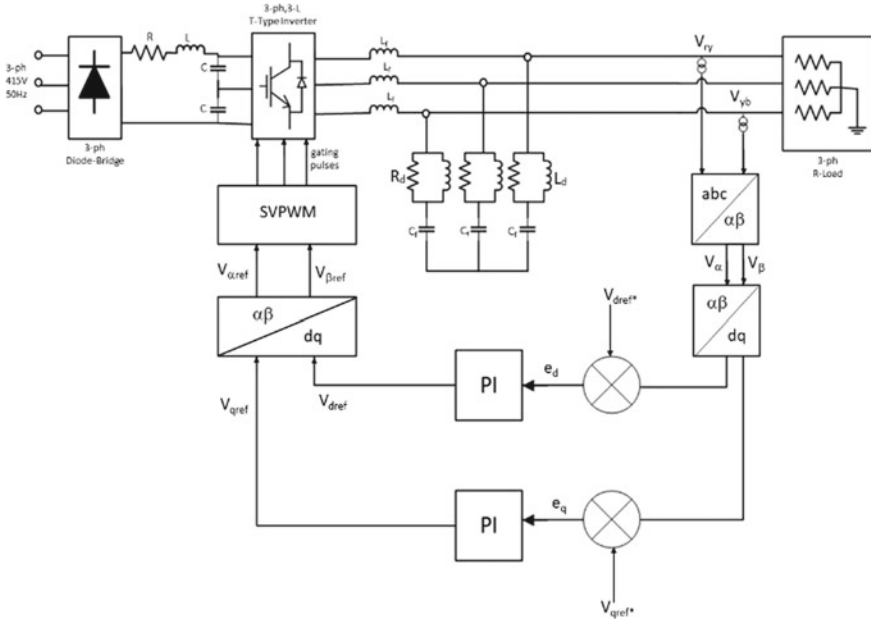


Fig. 3 Control strategy of the three-level T-type inverter system

All the controlling action are performed in dq frame. The outcome of the PI controller is converted into the three-phase control voltages V_a , V_b , and V_c by using inverse park and Clarke transformation [20]. Hence, the three-phase modulation signal R_{pwm} , Y_{pwm} and B_{pwm} is generated which is shown in Fig. 5. DSP will be performing every controlling process required to control switching action and will generate the gate pulses based on the code dump in it. The DSP is used in this hardware is of 32 bit. At the end, the procreated PWM signals are applied to the gate driver circuit to drive the IGBTs to achieved required control output by performing the control scheme in closed loop manner (Fig. 4).

3 Simulation Analysis and Result Discussion

The simulation of whole system is made in Powersim (PSIM) software tool. In simulation, all the components used in the system are ideal. Hence, there is minor difference one can observe in simulation results and practical results. Total time is set at 0.3 s to run the simulation. Some of the waveforms are shown below.

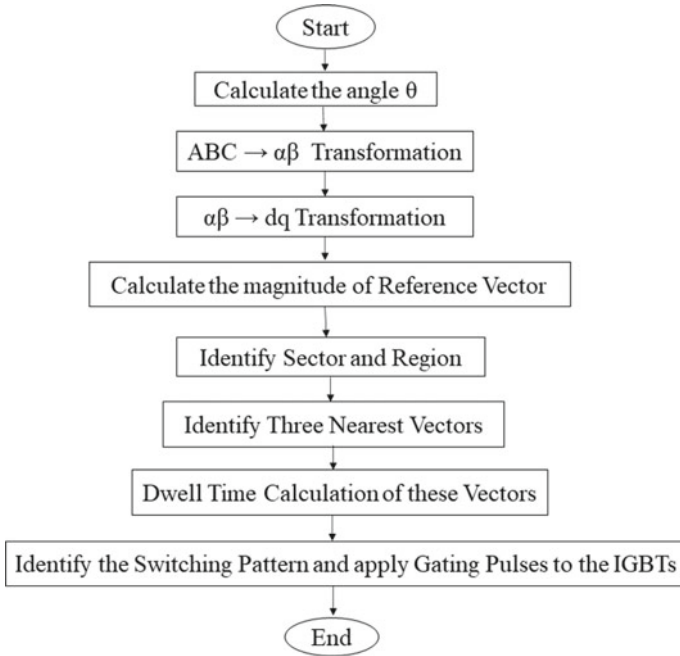


Fig. 4 Flow chart of SVPWM control scheme

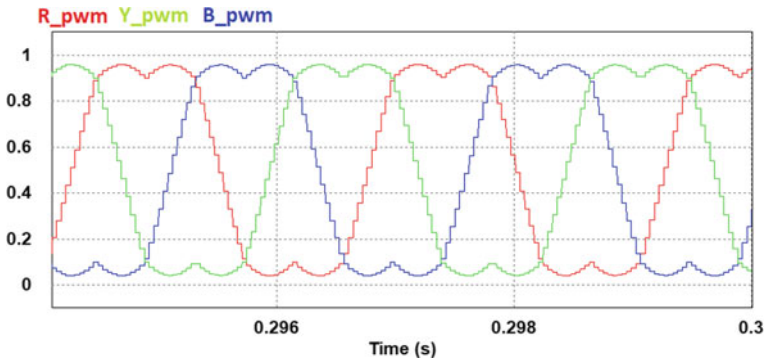


Fig. 5 Three-phase modulating signals

3.1 Results Under No-Load Condition

The wave shape of inverter line voltage is present in Fig. 6. It is five-level wave shape. The harmonic content in this wave shape is much lesser than the traditional two-level inverter with the alike switching frequency. The RMS value of this voltage is 367.157 V.

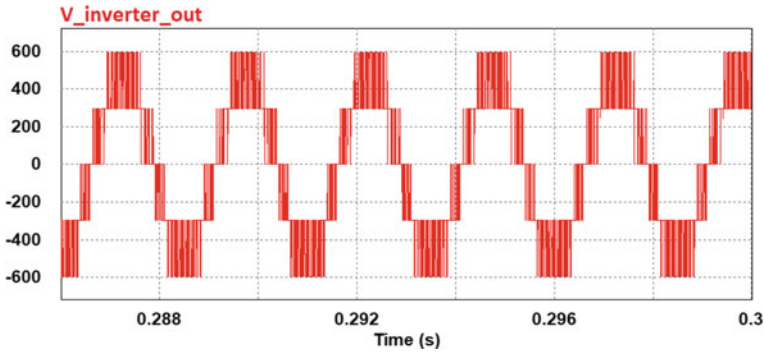


Fig. 6 Inverter line to line voltage before the filter

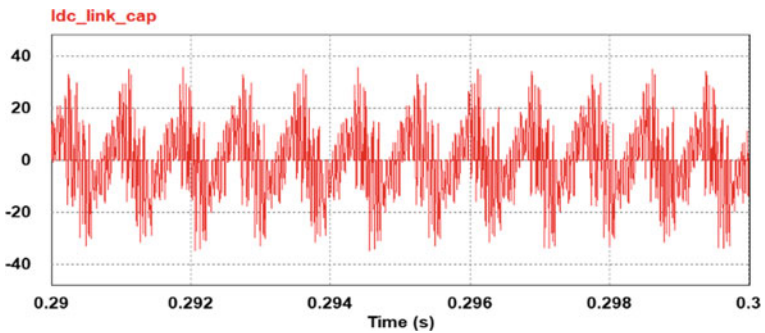


Fig. 7 DC bus capacitor current

The waveform of the current flowing through the DC bus capacitor is present in Fig. 7. It has a RMS magnitude of 11.863 A. These capacitors are initially charged with some amount of voltage level to achieve the fast response of the system.

The waveform of current which is flowing through the filter inductor and filter capacitor is display in Fig. 8. In this both elements, same amount of the current is flowing. The RMS magnitude of the current is 21.496 A.

The waveform of current which is flowing through damping resistor R_d is display in Fig. 9. In this component, very high-frequency current would flow. The RMS magnitude of this current is 8.45 A.

The waveform of output terminal voltage between the two phases R and Y is display in Fig. 10. The RMS magnitude of this voltage is 347.43 V and has a frequency of 400 Hz.

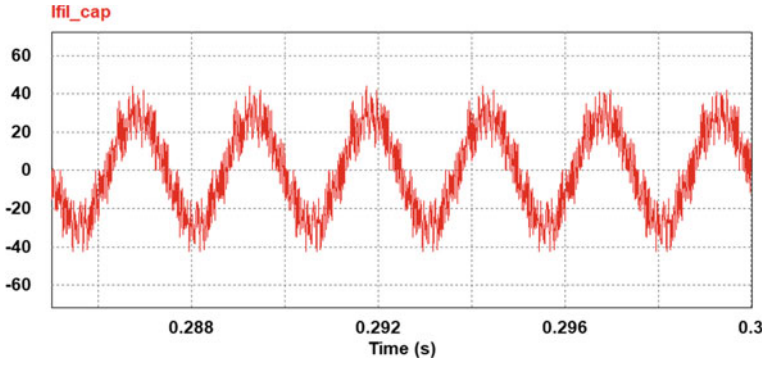


Fig. 8 Current flowing through L_f and C_f

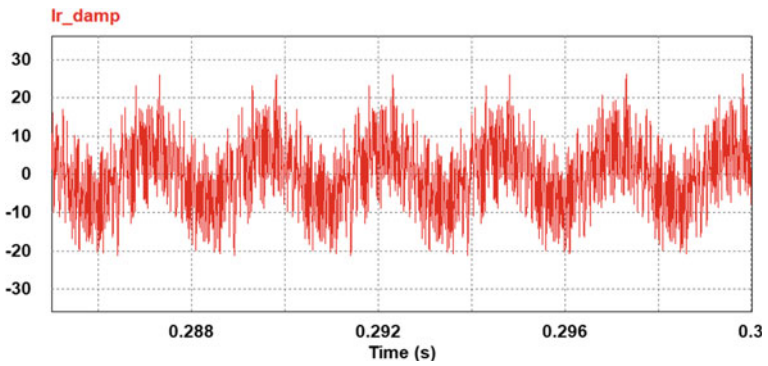


Fig. 9 Current flowing through damping resistor R_d

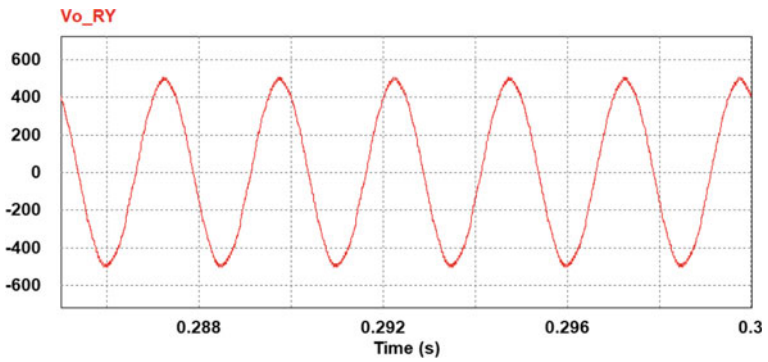


Fig. 10 Output voltage V_{ry} after the filter

3.2 Results Under Full-Load Condition with R-Load

In this condition, at the output terminal of the system, 110 kW resistive load is connected. The various parameters of the load are 350 V, 180 A, 110 kW, three-phase balanced resistive load. It is connected to understand the system behavior under linear load condition. Various performance parameter like output terminal voltage, output terminal current, it's total harmonic distortion, etc., are discussed in this section.

The waveform of theta is present in Fig. 11. It is varying between the ranges of 0–6.2831. The limit band is provided between the 0 and 2π . Using this evaluated value of theta (θ), $\sin \theta$, and $\cos \theta$ will be determined which is further used in Clarke and Park transformation.

The wave shapes of three modulating vectors which are m_1 , m_2 , and m_3 are shown in Figs. 12, 13 and 14, respectively. They are used for sextants selection and its region detection. The magnitude of vectors m_1 and m_2 are found out using modulation index and magnitude of $\cos \theta$ and are varying with different sectors. Vector m_3 is the vector summation of two vector m_1 and m_2 . These three vectors compute the duty cycle of the gating pulses, which are applied to the switches of the inverter.

The direct axis and quadrature axis component's wave shape is shown in Fig. 15. These two quantities are transformed from three-phase AC quantities to two-phase DC quantities. Clarke transformation is used for three-phase to two-phase transformation. The phase angle between these two quantities is 90° .

The waveform of the collector to emitter voltage across the switching devices S_1 , S_4 , S_2 , and S_3 and of the one leg of T-type inverter is shown in Figs. 16, 17, 18 and 19, respectively. The voltage across the S_1 , S_4 , S_2 , and S_3 during the off condition is 362 V, 361 V, 162 V, and 162 V, respectively.

The inverter line voltage is demonstrated in Fig. 20. It is five-level wave shape. With the same switching frequency, the harmonic content in this wave shape is much

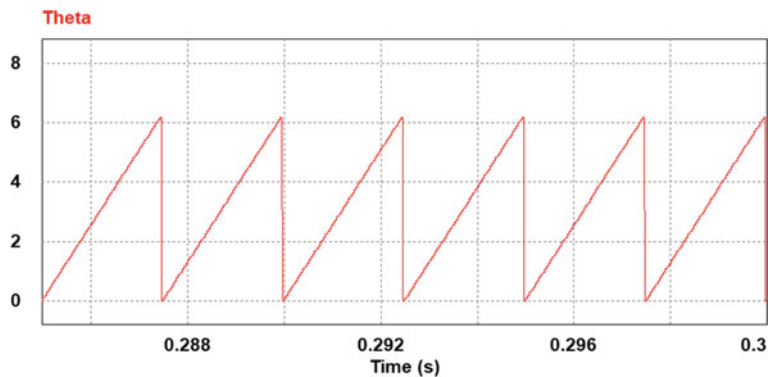


Fig. 11 Waveform of theta

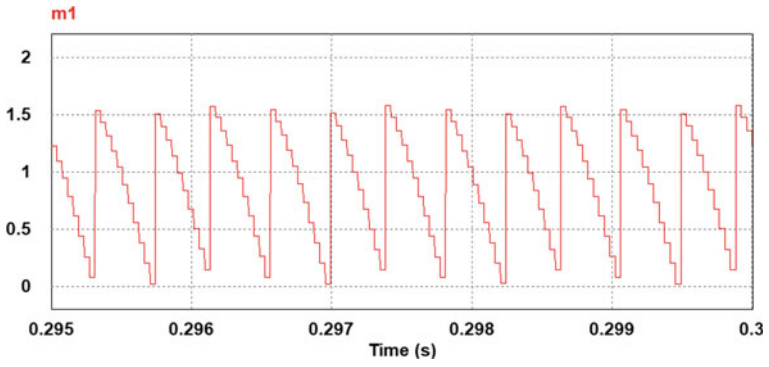


Fig. 12 Modulating wave m1

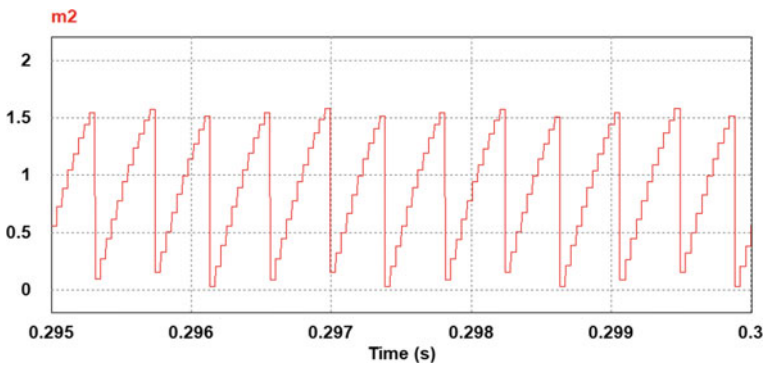


Fig. 13 Modulating wave m2

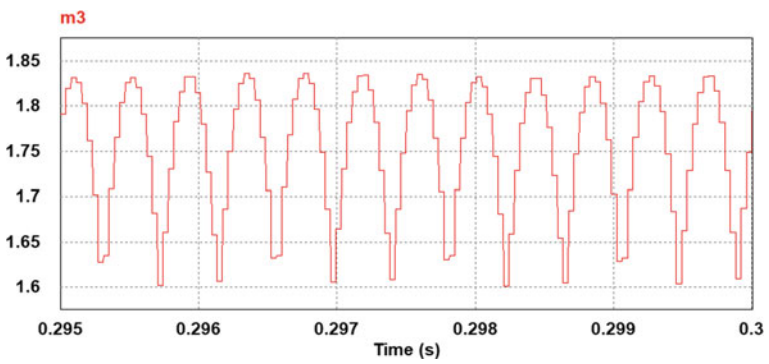


Fig. 14 Modulating wave m3

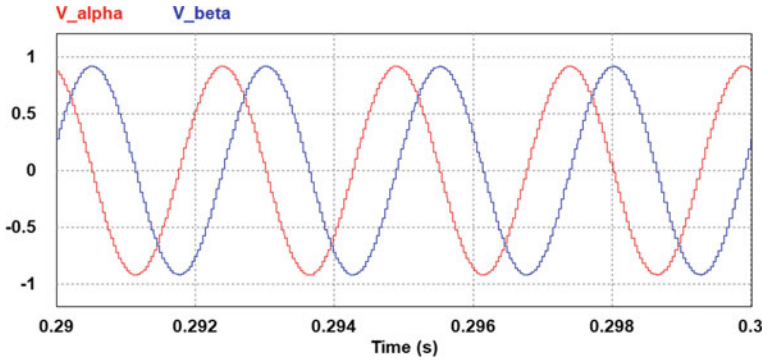


Fig. 15 Wave shape of V_{α} and V_{β}

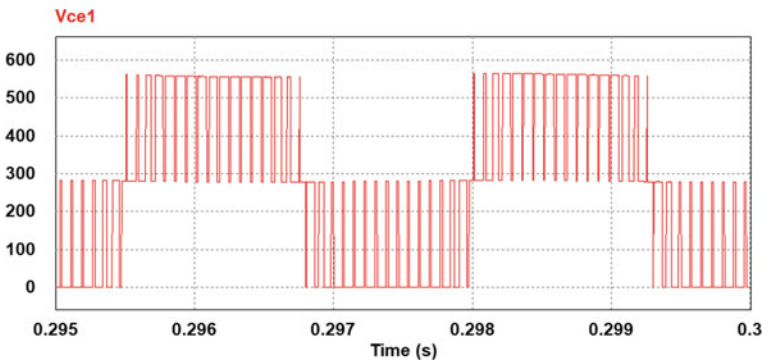


Fig. 16 Collector to emitter voltage across switch S_1

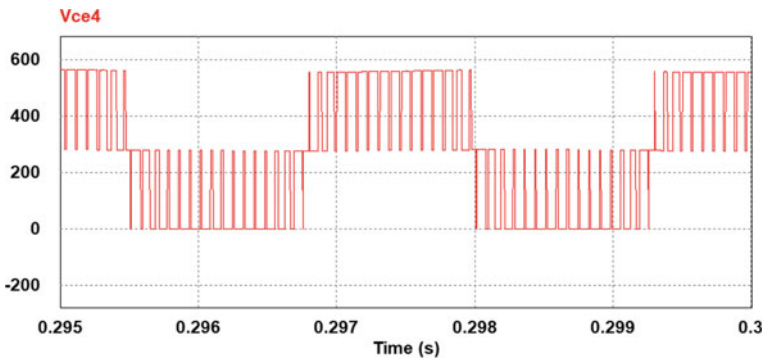


Fig. 17 Collector to emitter voltage across switch S_4

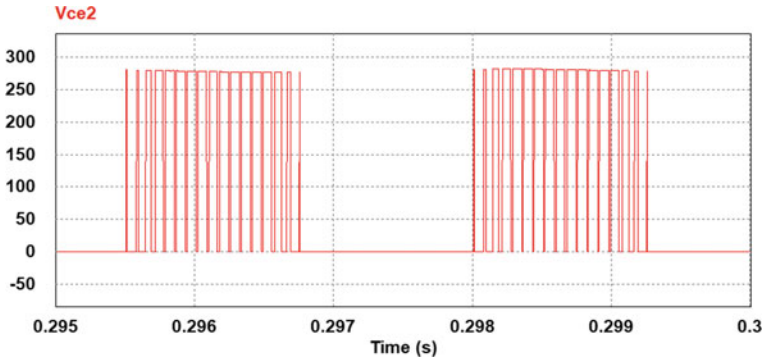


Fig. 18 Collector to emitter voltage across switch S_2

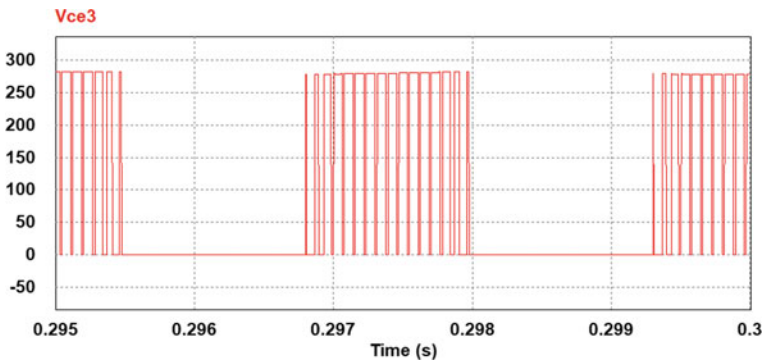


Fig. 19 Collector to emitter voltage across switch S_3

more lesser than the traditional two-level inverter. The RMS value of this voltage is 362.953 V.

The waveform of DC-link capacitor bus voltage is display in Fig. 21. It's having the magnitude of 558.971 V and has ripple frequency of 300 Hz.

The RMS magnitude of the DC-link capacitor current is 203.175 A with the 300 Hz ripple frequency. The waveform of current which is flowing through the DC-link capacitor is present in Fig. 22.

The wave shape of output RMS load voltage is shown in Fig. 23. It's having the magnitude of 348.383 V with the 400 Hz frequency. After performing it's FFT analysis, the calculated THD of this output load voltage is 1.675% which can meet the IEEE519-2014.

The waveform of output RMS load current is shown in Fig. 24. The RMS magnitude of load current is 179.102 A with the frequency of 400 Hz. After performing it's FFT analysis, the calculated THD of this output load current is 1.657% which can meet the IEEE Standard 519-2014.

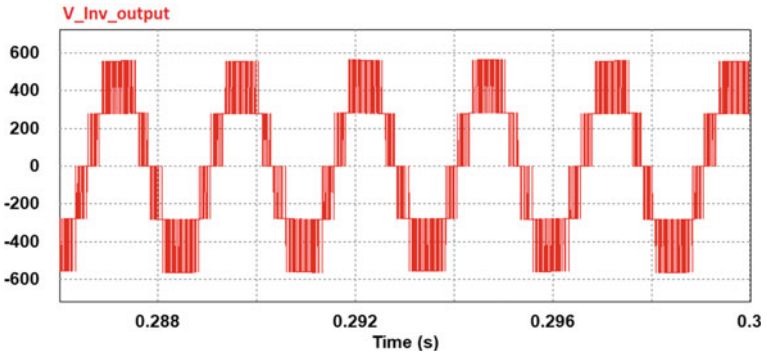


Fig. 20 Inverter line to line voltage before the filter

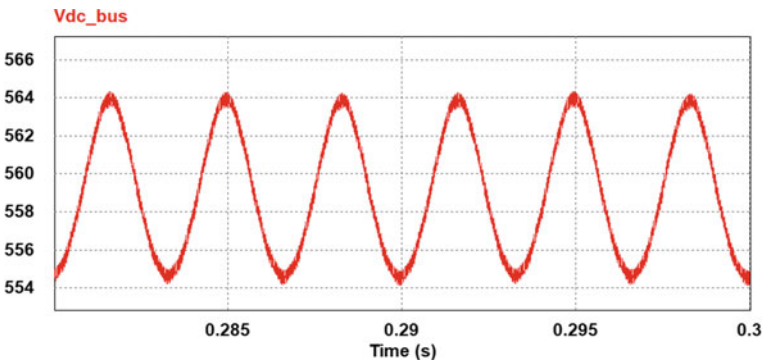


Fig. 21 DC bus capacitor voltage

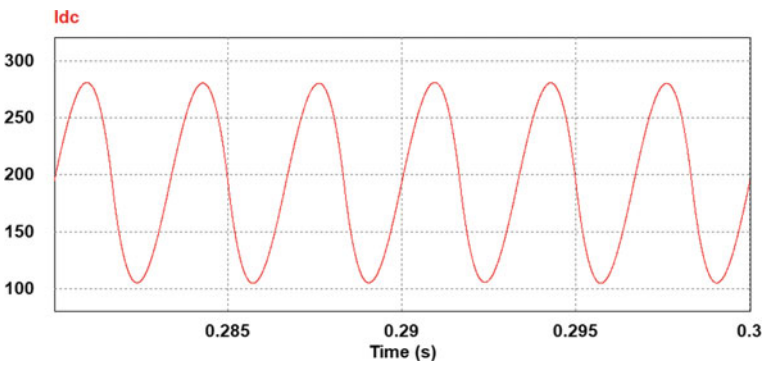


Fig. 22 DC bus capacitor current

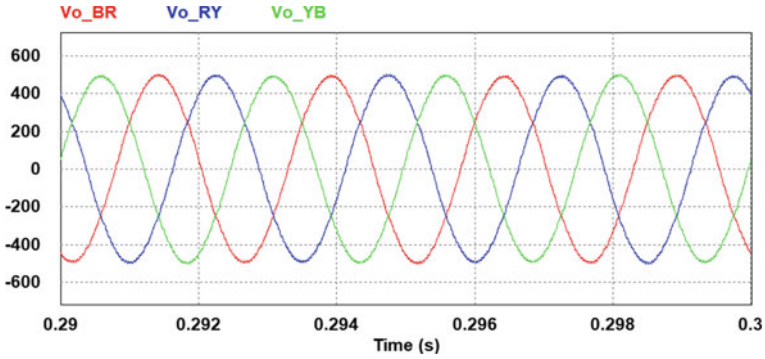


Fig. 23 Three-phase output load voltage after the filter

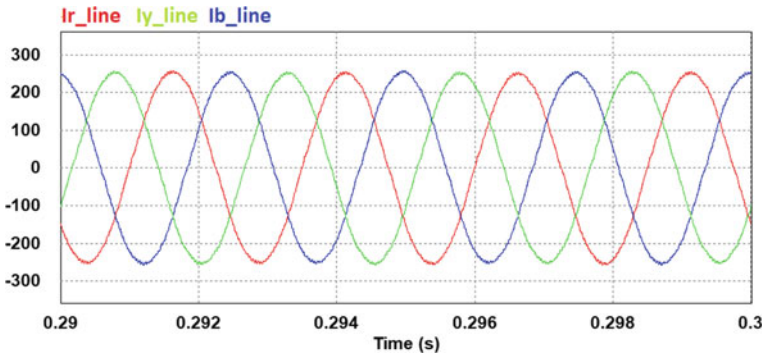


Fig. 24 Three-phase output load current after the filter

3.3 Results Under Half-Load Condition with R-Load

In this condition, half value of the full load which is of 55 kW resistive load is connected at the output terminal of the system. The parameters for this load are 350 V, 90.72 A, 55 kW, and three-phase balanced resistive load. It is connected to understand the system behavior under linear load condition. Inverter output voltage, DC bus voltage waveforms have same magnitude and that's why not discussed here in this section.

The RMS magnitude of the DC-link capacitor current is 115.779 A with the 300 Hz ripple frequency. The waveform of current which is flowing through the DC link capacitor is present in Fig. 25.

The wave shape of output RMS load voltage is shown in Fig. 26. It's having the magnitude of 348.184 V with the 400 Hz frequency. It is more distorted wave shape, and the THD for this output load voltage is 2.268% which is more compared to the full-load condition.

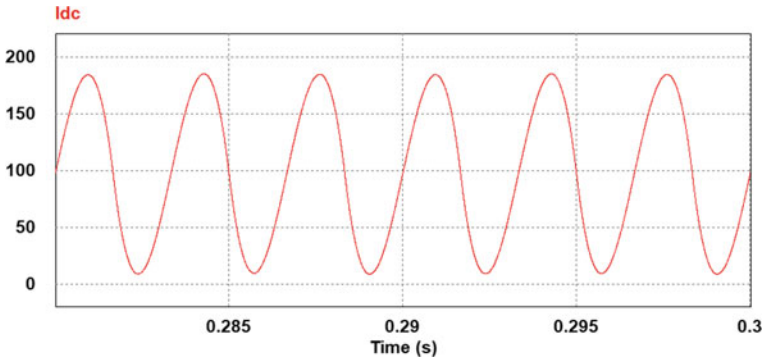


Fig. 25 DC bus capacitor current

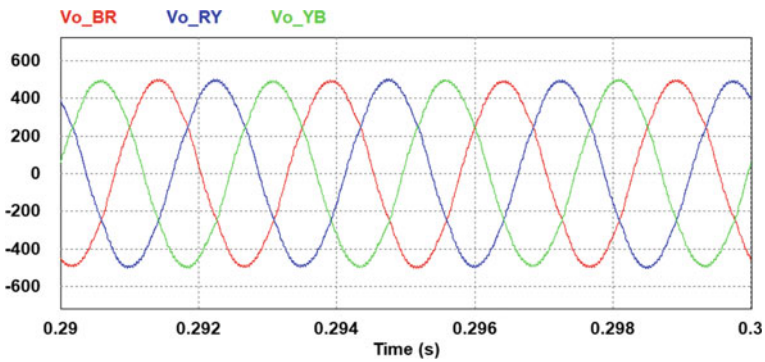


Fig. 26 Three-phase output load voltage after the filter

The waveform of output RMS load current is shown in Fig. 27. The RMS magnitude of load current is 90.236 A with the frequency of 400 Hz. It is more distorted wave shape, and the THD for this output load current is 2.286% which is more compared to the full-load condition load current.

3.4 Results Under Full-Load Condition with R-L Load

In this condition, at the output terminal of the system, 110 kW R-L load is coupled. The various parameters of the load are 350 V, 180 A, 110 kW, three-phase balanced R-L load. It is observed that, as compared to R-Load, less distortion is observed in output load current with R-L Load. Figure 1 shows the 400 Hz system with R-L Load. The magnitude of inductance is taken of 0.5 μ H. After simulated this system, it is observed that, minor changes are observed only in output load voltage and output

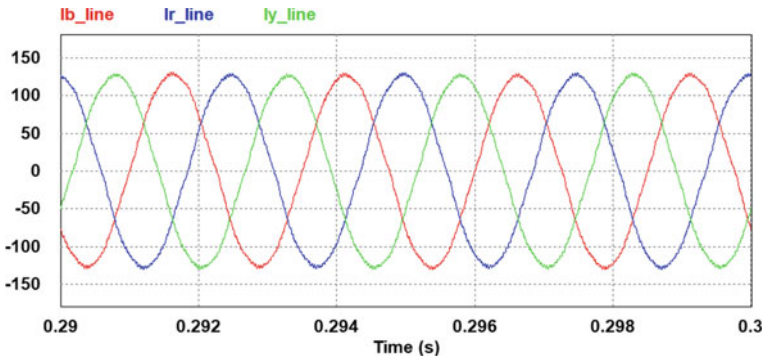


Fig. 27 Three-phase output load current after the filter

load current. Other parameters have same value. That's why it is not shown in this subsection.

The wave shape of output RMS load voltage is shown in Fig. 28. It's having the magnitude of 348.359 V with 400 Hz frequency. After performing its FFT analysis, the calculated THD of this output load voltage is 1.6817% which can meet the IEEE519-2014.

The waveform of output RMS load current is shown in Fig. 29. It's having the value of 179.079 A with the frequency of 400 Hz. After performing its FFT analysis, the calculated THD of this output load current is 1.552% which can meet the limit of IEEE Standard 519-2014.

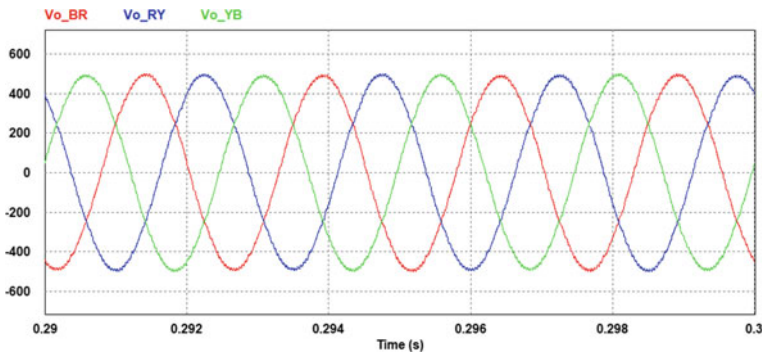


Fig. 28 Three-phase output load voltage after the filter

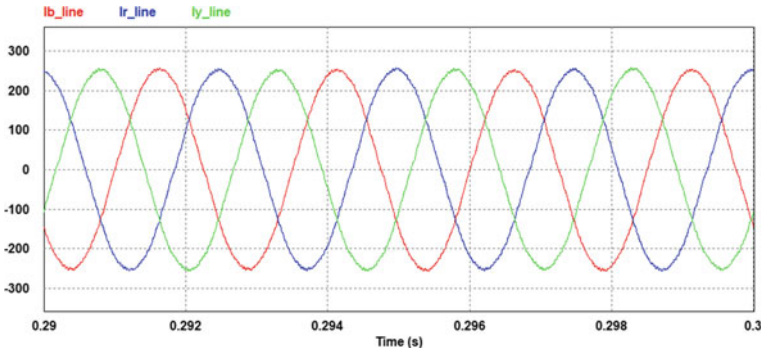


Fig. 29 Three-phase output load current after the filter

4 Experimental Results and Discussion

The results are taken out during no-load condition. The waveform of inverter output line voltage V_{ry} is present in Fig. 30. It is five-level waveform with the RMS value of 371 V having the frequency of 400 Hz. Less distortion is observed in the inverter output voltage wave shape when it's number of levels is increased.

The wave shape of output terminal voltage during no-load condition is shown in Fig. 31. It has the RMS magnitude of 355 V with the frequency of 400.3 Hz. By rising the number of levels of the inverter terminal output, one can get the output same as pure sinusoidal waveform.

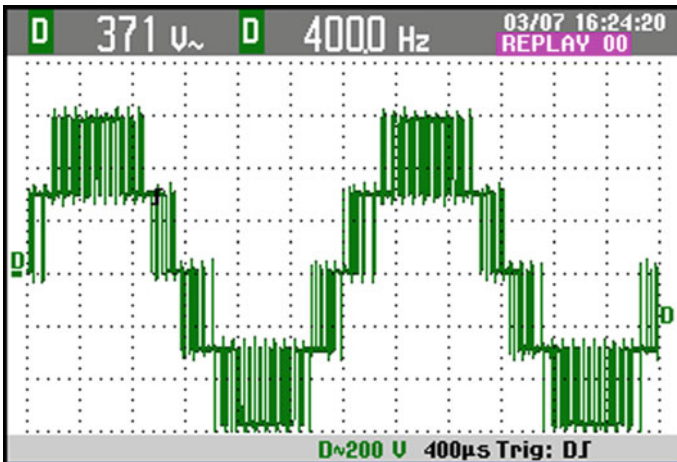


Fig. 30 Inverter output line voltage V_{ry}

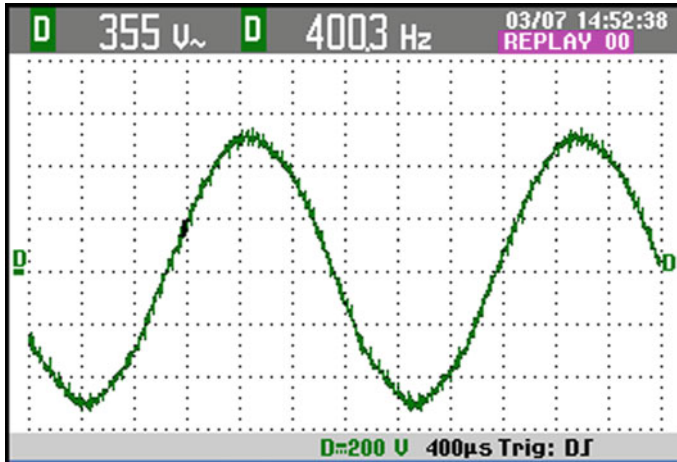


Fig. 31 Output terminal voltage at no-load condition

Due to used of multi-level converter, which gives staircase kind of waveform at output, THD is reduced. This will further reduces the size of filter components to get more sinusoidal output voltage.

At the output side, filter is connected. Even when there is no load is connected, some amount of current is always flowing through the filter components to charge the filter capacitor. Figure 32 shows the waveform of current which is flowing through L_f and C_f . From both component, same current is flowing. It's having the magnitude of 21.4 A. High-frequency component can't flow through the L_d because as the frequency will increase, inductive reactance must be increased which oppose the flow of current from it. So, in this component, low-frequency component will flow.

To eliminated the above problem which is faced in L_d which do not allow high-frequency component flowing from itself, one resistor having small value is connected in shunt with L_d . The job of the damping resistor R_d is to eliminate the occurrence of resonance. So, now high-frequency components are flowing through the damping resistor R_d .

The waveform of current which is flowing through the damping resistor R_d is shown in Fig. 33. It's having the magnitude of 7.5 A. One disadvantage to connecting this component in filter configuration is that heat losses are produced in it.

5 Conclusion

In this paper, a 110 kW, three-level T-type topology for the low-voltage and high-efficiency applications is designed and implemented with no-load, with R-Load, and with R-L Load. Reduced switching devices count concept makes T-type topology more suitable for economical cost structure and efficiency. The proposed system

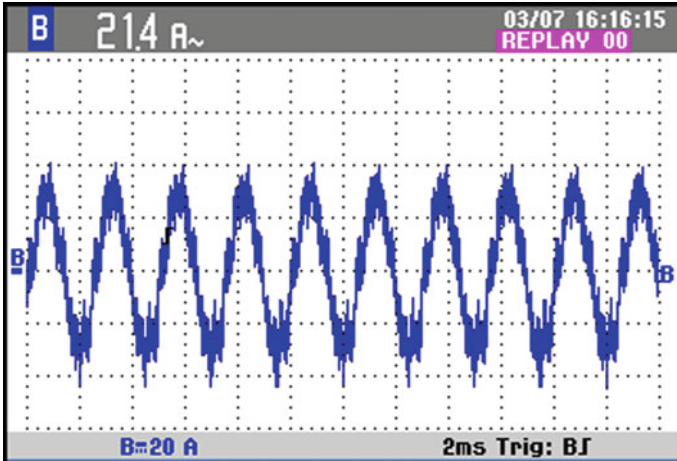


Fig. 32 Current flowing through L_f and C_f

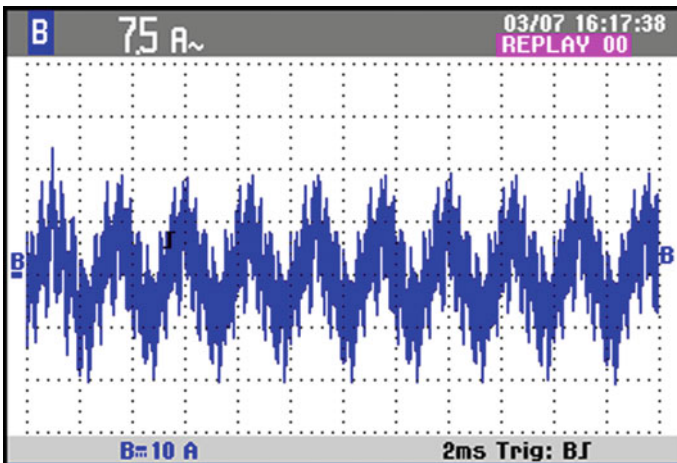


Fig. 33 Current flowing through damping resistor R_d

is validated through the Powersim (PSIM) software. The performance parameters like output voltage, output load current, and % total harmonic distortion is also found out. The %THD of output voltage is 1.675% and %THD of output current is 1.657% with R-Load, whereas the %THD of output voltage is 1.682%, and %THD of output current is 1.552% with R-L Load, which matches the limits described in the international standard like IEEE519-2014. It is observed that less distortion is observed in output current with R-L Load as compared to R-Load. Hardware prototype of the simulated system is also implemented. Presented hardware results are in-line with the simulation results as expected.

References

1. Su X, Liu J (2011) Design of 400HZ mid-frequency static switch power employing PWM. Department of Basic Experiment Naval Aeronautical and Astronautical University Yantai, China
2. Why we use 400Hz power supply in aircraft. Available: <https://www.academia.edu/4768401>
3. Liu CX, Ma WM, Sun C, Hu WH (2013) Research on harmonics suppression in high power middle frequency 400Hz inverter. Naval University of Engineering, APPEEC, in press
4. Altin N, Sefa I, Komurcugil H, Ozdemir S (2018) Three-phase three-level T-type grid-connected inverter with reduced number of switches. In: 2018 6th International Istanbul smart grids and cities congress and fair
5. Ozdemir S (2016) Z-source T-type inverter for renewable energy systems with proportional resonant controller. *Int J Hydrogen Energy* 41(29):12591–12602
6. Schweizer M, Friedli T, Kolar JW (2013) Comparative evaluation of advanced three-phase three-level inverter/converter topologies against two-level systems. *IEEE Trans Industr Electron* 60(12):5515–5527
7. Choi UM, Blaabjerg F, Lee KB (2015) Reliability improvement of a T-Type three-level inverter with fault-tolerant control strategy. *IEEE Trans Power Electron* 30(5):2660–2672
8. Xing X, Chen A, Wang W, Zhang C, Li Y, Du C (2015) Space vector modulated for z-source three-level T-type converter with neutral voltage balancing. In: *IEEE applied power electronics conference and exposition (APEC)*, pp 833–840
9. Xuan Y, Tian M, Song X, Chen W, Yang X (2015) Design and implementation of a high power three-level T-type inverter for a photovoltaic system. In: *9th International conference on power electronics-ECCE Asia*. 63 Convention Center, Seoul, Korea
10. Tolunay B (2012) Space vector pulse width modulation for three-level converters—A LabVIEW implementation. Uppsala Universitet
11. Mishra A, Save S, Sen R (2014) Space vector pulse width modulation. *Int J Sci Eng Res* 5(2)
12. Schweizer M, Kolar JW (2013) Design and implementation of a highly efficient three-level T-type converter for low-voltage applications. *IEEE Trans Power Electron* 28(2):899–907
13. Ahmed KH, Finney SJ, Williams BW (2007) Passive filter design for three-phase inverter interfacing in distributed generation. In: *Proceedings of IEEE 5th international conference-workshop on compatibility in power electronics*, pp 1–9
14. Wang TCY, Ye Z, Sinha G (2003) Output filter design for a grid-interconnected three-phase inverter. GE Global Research Center, NY 1209, USA
15. Jayaraman M, Sreedevi VT (2018) Design of a passive damped filter for harmonic reduction in multilevel inverters used in PV applications. School of Electrical Engineering, VIT University, Chennai, India
16. Azani H, Massoud A, Williams BW (2015) An LCL filter-based grid-interfaced three-phase voltage source inverter: performance evaluation and stability analysis. Qatar University, Electrical Engineering Department
17. Patel SV, Shah MT (2012) Three-phase front end converters and current control techniques for unity power factor. In: *Nirma university international conference on engineering, (NuiCONE)*, 6–8 Dec 2012. Ahmedabad, India, pp 1–6
18. Rani DS, Appaprao A (2011) A space vector PWM scheme for three level inverters based on two-level space vector PWM. *Int J Power Syst Oper Energy Manage (IJPSOEM)* 1(1)
19. Seo JH, Choi CH, Hyun DS (2001) A new simplified space vector PWM method for three level inverters. *IEEE Trans Power Electron* 16(4):545–550
20. Jana KC, Chowdhury SK, Biswas SK (2013) Performance evaluation of a simple and general space vector pulse-width modulation-based M-level inverter including over-modulation operation. *IET Power Electron* 6(4):809–817

An Overview of Recently Developed Liquefaction Mitigation Methods



Md Asad Ahmad and Yamin Wasti

Abstract Soil liquefaction is one of the major concerns in granular soil. Traditional methods are found to be effective, but with the availability of new materials and their application in liquefaction, mitigation has been studied as one of the good alternatives that need to be used. With the development of science and technology and multidisciplinary research, it is observed that there are many other materials which are still available which can be used, like nanomaterials, biomaterials, air injection, and various studies are listed in which these methods applications and consequences have been noted. Following are the parameters that are being noted like reduction of excess pore water pressure, settlement of nearby structures, economical options, and environment friendly.

Keywords Biomaterials · Liquefaction · Mitigation · Nanomaterial · Recycled material

1 Introduction

Liquefaction is one of the major consequences of earthquake-induced damage. Once liquefaction is induced due to any reason like static and dynamic forces for the case of saturated sandy soil, then it will pose a major problem to the collapse of structures, loss of life, and property. Liquefaction is mainly observed after the earthquake occurrence. One of the major reasons for liquefaction is the increase of pore water pressure and reduction of the effective stress to zero and sandy soil appears like a fluid [1]. This has caused increased geotechnical engineers to think about the possibilities to minimize the liquefaction mechanism. Ground improvement techniques

M. A. Ahmad

Department of Civil and Construction Engineering, National Taiwan University of Science and Technology, Taipei 10607, Taiwan
e-mail: mdasadbtech@gmail.com

Y. Wasti (✉)

Department of Civil Engineering, Aligarh Muslim University, Aligarh 202002, India
e-mail: yaminwasti6309amu@gmail.com

are one of the ways by which liquefaction effects can be eliminated. Some of the articles suggested that liquefaction is affected by the physical characteristics of the soil like the coefficient of uniformity, Fine's content, soil density, and others [2].

Various studies have been done in the past in order to improve liquefaction resistance using existing plant roots, metal strips, and bars. Usage of metal strips may affect ductility, and it affects various environmental factors [3, 4]. Further, plants roots gave a poor response in terms of durability. Some suggestions are regarding dynamic compaction, but it affects the surrounding structure and this method is limited for shallow depth not for deep layers. Therefore, still an investigation is need to be carried out in order to get a method that prevents liquefaction [5–9].

These days, grouting is done with cement and some chemicals are used like epoxy, acrylate, sodium silicate, etc., foundation densification, gravel columns, foundation replacement, and dewatering. Since research is being done and methods are getting modified, but this leads to high construction cost [1, 10]. Apart from these, the environmental factor is one of the major concerns that is being affected when chemicals and cement are used [11–16]. Therefore, it is necessary to carry out the research in this area to take into account all of the factors like sustainability, environment friendly, no damage to existing structures, low cost, and non-polluting [17, 18].

With the advancement of science and technology and multidisciplinary research, some methods are proposed such as:

- Induced partial saturation
- Microbial geotechnology
- Passive site remediation

Meanwhile, new liquefaction mitigation technologies, such as air injection, nano-material suspension grouting, bio cementation, biogas, and liquefaction mitigation employing various geomaterials, have been developed based on the concepts stated above [17, 19–23]. These methods have been developed as a result of advancements in new materials.

In order to get a better understanding of the progress made in liquefaction resistance, various studies are of newly developed material will be discussed in this article.

2 Methods Newly Developed

2.1 Nanomaterials

Nanomaterials have shown better performance in the field of geotechnical engineering. It is mainly because of the very tiny particle size which can penetrate very small void size and very high-pressure grouting is not required, consequently leading to less environmental destruction when compared with conventional methods. Following are the nanomaterials which are used and listed below:

- Colloidal silica
- Bentonite
- Laponite

From the analysis, it is found that these materials are also non-toxic to groundwater. Therefore, in this section main focus will be on its usage and effects.

2.1.1 Colloidal Silica

Colloidal silica size ranges between 2 and 100 nm and is produced when silica acids are saturated, it is also an aqueous mixture. CS compounds are stabilized from gel formation with alkali solutions during the production process. The ionization of nanoparticles by alkaline solutions causes them to oppose each other. By diminishing these repulsive forces, coagulation based on particle interaction is generated, culminating in the creation of an occur simultaneously of siloxane (Si–O–Si) bonds to link soil particles together and restrict porous fluids. The viscosity of the colloidal silica stabilizer, the hydraulic gradient, and the hydraulic conductivity of the liquefiable soil are the primary parameters that determine colloidal silica transfer in liquefiable sand. In addition, the amount of silica in the solution, p-H, the size of the silica particles, ionic strength, and the temperature of the solution all affect how long the gel takes to develop (Fig. 1).

Colloidal silica offers low initial viscosity, regulated gel durations, strong long-term mechanical stability, and minimal disruption to infrastructure, according to studies conducted in the past. Electrical inter-particle forces control the activity and fabric development of nanoparticles, while chemical interaction continues after the first resonating gel state is established. As a result, continued linking enables the gel’s strength to rise over time. Apart from these, colloidal silica is found to have diverse characteristics like chemically and biologically inert, superb durability, and one of the qualities which makes it eco-friendly is its non-toxic property. Due to the above-listed properties, colloidal silica when present in small concentrations leads to a reduction in liquefaction of sands by keeping grains together and a reduction in pore fluids. It has also been found in one of the experiments that the strength of sand mixed

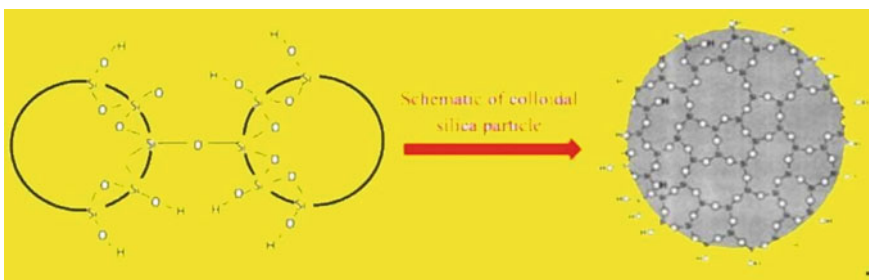


Fig. 1 Development of siloxane bond [23]

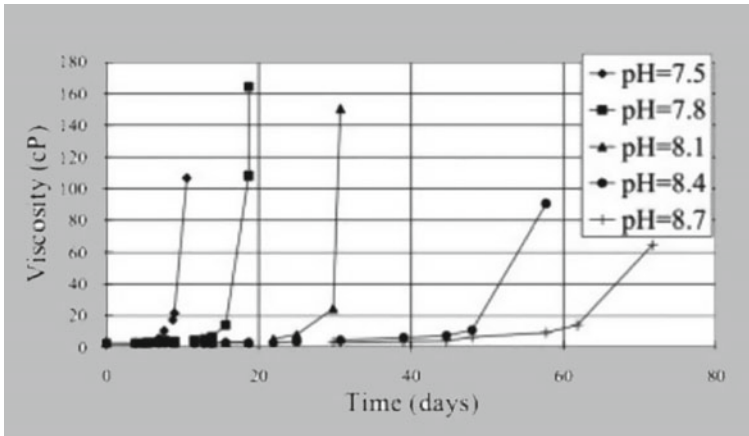


Fig. 2 CS gel 5% by wt. at ionic conc. of 0.1 N [4]

with colloidal silica increases with the increase in its concentrations. Similarly, shear strength would increase with the passage of time [10]. Moreover, sand mixed with colloidal silica has unconfined compressive strength was proportional to the colloidal silica particle concentration up to a maximum of 400 kPa. Despite colloidal silica being found to be a useful approach for enhancing sand strength, the permeability of the sand which is treated declined in a roughly log-linear manner with increasing CS concentration down to a minimum of $2 * 10^{10}$ mm/s. From this, it can be observed that colloidal silica cannot be used for a very large area. One of the researchers found that by using colloidal content as 5% by wt. and a pH value between 7.5 and 8.7 can effectively control the uniform distribution over a large area and sufficient liquefaction resistance [24] (Fig. 2).

2.1.2 Bentonite

It is formed by the breakdown of volcanic ash which is basically an absorbent clay. Nowadays, it is one of the filler materials. Because of its thixotropic characteristics in water, bentonite suspensions are particularly effective in improving the performance of granular soils as pore fluids. Bentonite is simple to get by, inexpensive, and environmentally beneficial. Content of the clay, pH, ionic strength of the H_2O , and type of cation and anion are the key influences on bentonite rheological qualities. As a result of these changes, the bentonite suspensions will appear in several “states,” such as sol, attractive gel, repulsive gel, and sediment [25]. Further, bentonite has the ability to increase liquefaction resistance. Since it is known that bentonite poses rheological properties of fluids and when bentonite gel formed in pores leads to restrain the motion during earthquakes. As a result, when bentonite is dispersed it will have a higher viscosity, higher initial yield strength, and gelation time is very short and consequently affect the coefficient of permeability of the granular soil

[18, 26]. As it provides poor transmission in large areas, a study is conducted with 0–5% sodium pyrophosphate, then significantly improved rheological properties are noted. Furthermore, when more than 5% by wt. of bentonite is used then a significant liquefaction resistance is observed [20, 21].

2.1.3 Laponite

Laponite is a synthetic smectic clay and when dispersed in water forms a thixotropic gel behavior. It is around one-tenth of sand particles (diameter = 25 nm, thickness = 1 nm). It is highly plastic and when compared with bentonite, it can be up to 1100% more plastic [27, 28]. Apart from high plasticity and small-size characteristics, it is also environment friendly that is non-toxic in behavior [29]. Concentration, PH, and ionic strength are the main factors that affect its dispersion. One of research, studied that pyrophosphate and polyethylene oxide on effects its aggregation and gelation on laponite while dispersion [5].

Further, it is noted that positive and negative charged surfaces with the above polymers can delay the gelation time. As a result of the foregoing qualities, laponite can be equally dispersed in pores [10]. Apart from that, it is studied that with the passage of time laponite combines and form a particle size greater than clay with the passage of time and shows solid-like properties. One of the results reports that 1% laponite mixing is equal to 3% bentonite in the liquefaction resistance [14] (Fig. 3).

Furthermore, various experiments (Resonant column test, static and dynamic triaxial tests) are done in order to know the properties and it is observed ten times enhancing the number of cycles when used with bentonite [6]. Moreover, studied the behavior of storage modulus and finally concluded that sand treated with bentonite will effectively prevent the phenomenon of liquefaction (Figs. 4 and 5).

Finally, it concluded that laponite is one of the ways to prevent liquefaction without harming the environment.

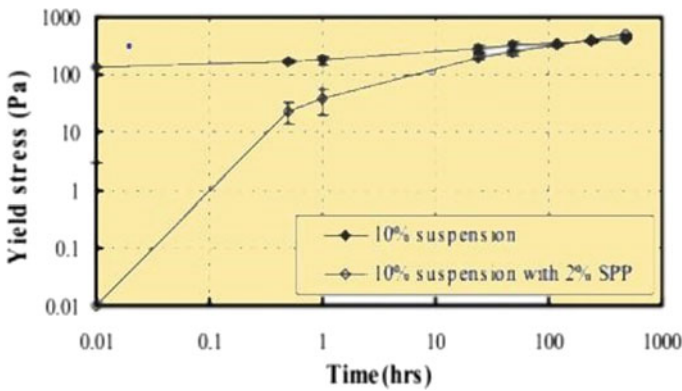


Fig. 3 Bentonite with and without admixtures [30]

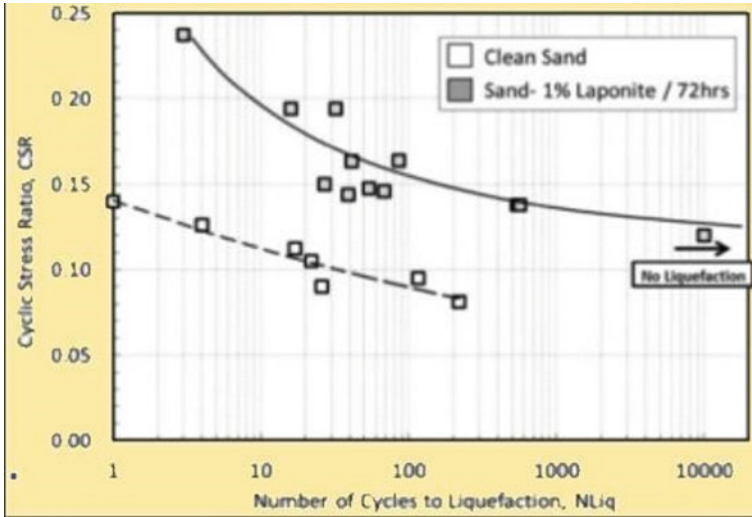


Fig. 4 CSR of clean sand and sand with laponite [1]

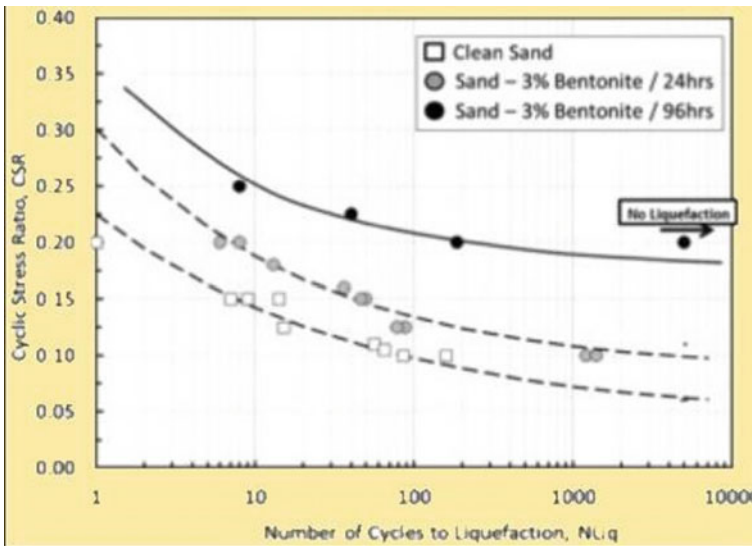


Fig. 5 CSR of clean sand with Bentonite [1]

From the use of the above three nanomaterials, these materials are good for liquefaction prevention. Apart from that, these materials are much better in performance and cost aspects. Chemicals and cement used traditionally are harmful to the environment and more expensive than these nanomaterials. The reason for the low cost is that for the same amount of liquefaction mitigation, only a small amount of nanomaterials

is required. Following are the properties that are enhanced by the use of nanomaterials are most important thing is strength, swelling index, settlement, volumetric strength, compressibility, and liquefaction risk. Researchers also expect that with the continuing research and advancement in science and technology, nanomaterials will be available at a lower cost. Therefore, in geotechnical engineering, nanomaterials will solve the economic outcomes.

2.2 Recycled Materials

These days, it is found in the surrounding that construction waste has no scrap value and is found abundant in the environment. Similarly, tire waste and glass have continually increased. Therefore, researchers started to use these materials in the backfill in order to control liquefaction in the sand.

An undrained cyclic triaxial test is conducted using discarded tire chips. It is found that with increasing tire chips content up to 50%, it can increase resistance liquefaction potential. Further, it is noted that with the increase in the tire content relative density decreases and these tires also prevent the generation of excess pore water pressure [7]. It is found that seismic waves decay in the tire chips as backfill because of the increase in the damping ratio in the liquefiable sand. A 1 g shaking table model test is conducted to study the variation of using tire chips at different percentages in saturated sand and it is observed that a reduction in the pore water pressure but augmented damping ratio with increasing content of tire chips (Fig. 6).

Glass is one of the renewable resources which is abundant in nature. Unconfined compressive strength tests and direct shear tests are conducted with 3% glass fiber for cement-treated sand to study the optimum mechanical properties [9]. It is studied that the strength increases with the increase in curing time because cement and glass fiber covered the entire sample area. Following properties are enhanced like pull-out strength, ductility, axial or shear deformations, and tensile strength. All of the materials are considered satisfactory for ecological and economic considerations. Apart from that, these materials are satisfactory in performance when these materials are used in backfill to prevent the floating of the pipe. Tire chips give good results in case of ease of compaction, good permeability, and efficacy in terms of limiting pile displacement. Further, it concludes that the concrete and recycled glass found appropriate materials for backfill materials [25].

Therefore, in order to conserve resources and resist liquefaction use an eco-friendly method that is discussed above. The majority of the research discussed, however, is still at the experimental stage and requires further investigation [1, 10].

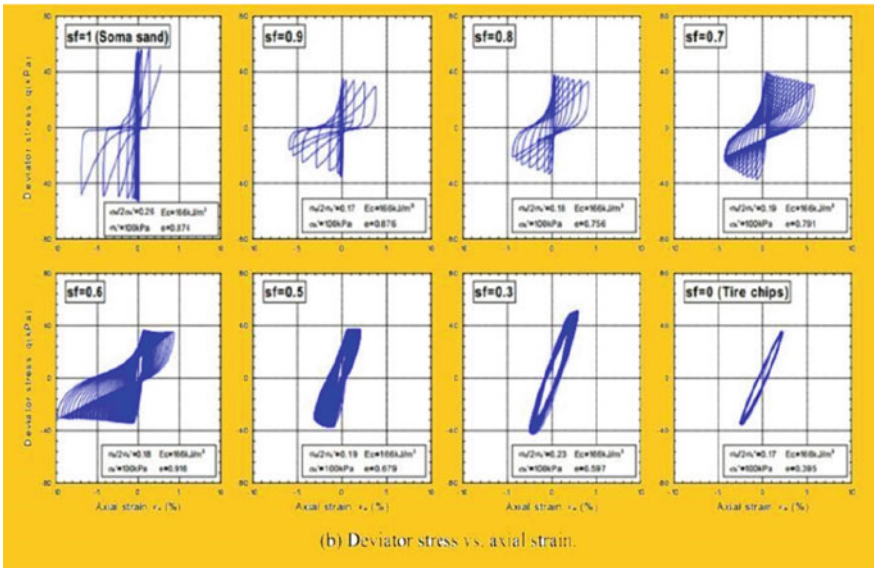
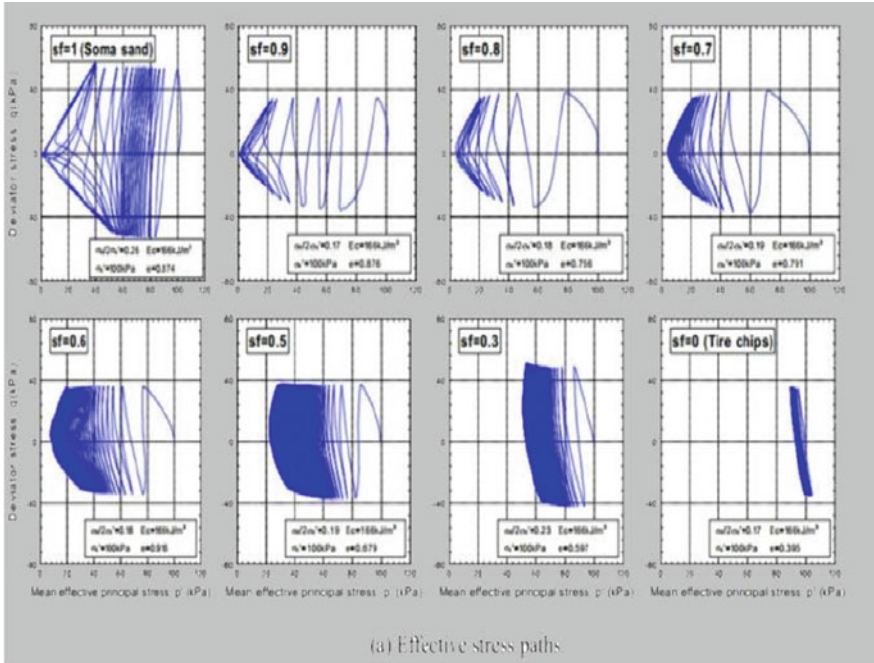


Fig. 6 Results of undrained cyclic shear test [22]

2.3 *Biological Materials*

In the last several years, the use of biological materials is promoted instead of using chemicals and other materials. These materials are good in liquefaction resistance and also prevent damages that is associated with earthquake loading [27]. The mechanism of binding sand with the use of biological materials with nutrients, microorganisms, MICP with calcite, and dissolved calcium source. This whole process is called bio cementation [28]. Microorganisms and nutrients affect the series of chemical reactions. It was also confirmed in one of the studies that MICP is one of the eco-friendly and pollution-free options. While doing the triaxial test, it is observed that parameters like cyclic strength, liquefaction resistance, and stiffness of the sand increase, however, properties like settlement and pore water pressure decrease [11].

2.4 *Partial Saturation Method*

We know that in recent times, hundreds of studies are conducted on the liquefaction reduction in the case of saturated sand. Five methods come into the picture are:

- Air Injection
- Sand compaction pile
- Electrolysis
- Biogas released from the bacteria
- Some chemical methods which produce tiny gas bubbles

In air injection, it was studied using a centrifuge model at high confining pressure and the results were like settlement reduced for a shallow foundation, excess pore water pressure restrained, and liquefaction resistance enhanced [12–14].

3 Cost

Cost includes various parameters that need to be listed such as the location where it is used, treatment range, etc. Therefore, the qualitative cost is difficult to determine. Some of the methods are still in the laboratory stage and still not practically applied. Further, the cost is also estimated based on the following consideration like economical application, sustainable development, and non-polluting means eco-friendly. A few reviews are listed below:

- Using nanomaterials, the obtained unit cost is higher, but the overall cost is much higher when taking into account minimal disturbance, good permeability, etc. [16].
- Use of recycled materials is one of the alternatives is one the economical ways because instead of wasting in landfills it can be used underneath footing, as a

backfill material, and on embankments. Tire chips are found to be one the suitable material [15].

- Biomaterials are found to be one of the substitutes which are cheap in comparison to chemical grouting, but it is used under restricted environmental conditions.
- In case of partial saturation when done with air injection it can be an economical option because air is used in place of chemicals.

4 Conclusion

The methods stated above are newly developed ways based on scientific and technological advancements as well as multidisciplinary research, and it has been discovered that traditional methods are inefficient and harmful to the environment. Further, these methods are found to be economical and environmentally friendly, and the usage of waste materials is one of the best options. Very few researches are being done on the durability of newly developed methods which needs to be further explored.

References

1. Ochoa-Cornejo F, Bobet A, Johnston CT, Santagata M, Sinfield JV (2014) Liquefaction 50 years after anchorage 1964; how nanoparticles could help prevent it. In: NCEE 2014 10th U.S. national conference on earthquake engineering: frontiers of earthquake engineering
2. Huang Y, Wen Z (2015) Recent developments of soil improvement methods for seismic liquefaction mitigation. *Nat Hazards* 76(3):1927–1938
3. Huang Y, Wang L (2016) Experimental studies on nanomaterials for soil improvement: a review. *Environ Earth Sci* 75(6)
4. Gallagher PM, Lin Y (2005) Column testing to determine colloidal silica transport mechanisms
5. Ochoa-Cornejo F, Bobet A, Johnston CT, Santagata M, Sinfield JV (2016) Cyclic behavior and pore pressure generation in sands with laponite, a superplastic nanoparticle. *Soil Dyn Earthq Eng* 88:265–279
6. Gill KS, Choudhary AK, Jha JN (2010) Copyright ASCE 2010 GeoShanghai 2010 international conference geotechnical special publication. ASCE 204–205:34–41
7. Kaneko T, Orense RP, Hyodo M, Yoshimoto N (2013) Seismic response characteristics of saturated sand deposits mixed with tire chips. *J Geotech Geoenvironmental Eng* 139(4):633–643
8. Terms and conditions privacy policy copyright © 2021 Elsevier B.V. All rights reserved. Scopus® is a registered trademark of Elsevier B.V. p 2021
9. Ateş A (2016) Mechanical properties of sandy soils reinforced with cement and randomly distributed glass fibers (GRC). *Compos Part B Eng* 96:295–304
10. Huang Y, Wang L (2016) Laboratory investigation of liquefaction mitigation in silty sand using nanoparticles. *Eng Geol* 204:23–32
11. Han Z, Cheng X, Ma Q (2016) An experimental study on dynamic response for MICP strengthening liquefiable sands. *Earthq Eng Vib* 15(4):673–679
12. Zeybek A, Madabhushi SPG (2017) Centrifuge testing to evaluate the liquefaction response of air-injected partially saturated soils beneath shallow foundations. *Bull Earthq Eng* 15(1):339–356
13. Peng E, Zhang D (2017) Prevention of liquefaction of saturated sand using biogas produced by *pseudomonas stutzeri*. *DEStech Trans Mater Sci Eng (ictim)*

14. Eseller-Bayat E, Yegian MK, Alshawabkeh A, Gokyer S (2013) Liquefaction response of partially saturated sands. I: experimental results. *J Geotech Geoenvironmental Eng* 139(6):863–871
15. El Howayek A, Bobet A, Johnston CT, Santagata M, Sinfield JV (2014) Microstructure of sand-laponite-water systems using cryo-SEM. 693–702
16. Ahmad F, Yahaya AS, Safari A (2016) Development of low cost soil stabilization using recycled material. *IOP Conf Ser Mater Sci Eng* 136(1)
17. Bao X, Jin Z, Cui H, Chen X, Xie X (2019) Soil liquefaction mitigation in geotechnical engineering: an overview of recently developed methods. *Soil Dyn Earthq Eng* 120:273–291, Elsevier Ltd
18. Santagata M et al (2014) Rheology of concentrated bentonite dispersions treated with sodium pyrophosphate for application in mitigating earthquake-induced liquefaction. *Appl Clay Sci* 99:24–34
19. Tsai MH, Chen JY, Kang SC (2019) Ask Diana: a keyword-based chatbot system for water-related disaster management. *Water (Switzerland)* 11(2)
20. *Geo-Frontiers 2011* © ASCE 2011 677. pp 677–686
21. El Mohtar CS, Bobet A, Drnevich VP, Johnston CT, Santagata MC (2014) Pore pressure generation in sand with bentonite: from small strains to liquefaction. *Geotechnique* 64(2):108–117
22. [https://doi.org/10.1061/41108\(381\)44](https://doi.org/10.1061/41108(381)44)
23. Conlee CT, Gallagher PM, Boulanger RW, Kamai R (2012) Centrifuge modeling for liquefaction mitigation using colloidal silica stabilizer. *J Geotech Geoenvironmental Eng* 138(11):1334–1345
24. Graybeal B, Tanesi J (2008) A cementitious long-life wearing course to reduce frequency of maintenance works on high-traffic roads. *Transp Res Arena Eur* 1561:454–461
25. Tanaka H, Meunier J, Bonn D (2004) Nonergodic states of charged colloidal suspensions: repulsive and attractive glasses and gels. *Phys Rev E Stat Nonlinear Soft Matter Phys* 69(3 1):1–6
26. Xu H, Zhu W, Qian X, Wang S, Fan X (2016) Studies on hydraulic conductivity and compressibility of backfills for soil-bentonite cutoff walls. *Appl Clay Sci* 132–133:326–335
27. DeJong JT, Fritzges MB, Nüsslein K (2006) Microbially induced cementation to control sand response to undrained shear. *J Geotech Geoenvironmental Eng* 132(11):1381–1392
28. Akimana (2016) *Geo-Chicago 2016 GSP* 269 458. pp 458–466
29. Bao X, Jin Z, Cui H, Chen X, Xie X (2019) Soil liquefaction mitigation in geotechnical engineering: an overview of recently developed methods. *Soil Dyn Earthq Eng* 120:273–291
30. Rugg DA, Yoon J, Hwang H, El Mohtar CS, Asce AM (2011) Undrained shearing properties of sand permeated with a bentonite suspension for static liquefaction mitigation

Review on Cybersecurity and Major Cyberthreats of Smart Meters



Mithilesh G. Solanki , Kartavi S. Patel , Bansri R. Kanzariya ,
Trisha H. Parekh , Neeraj Kumar Singh , Atul Kumar Yadav ,
Mahshooq Abdul Majeed , Lalit Tak , and Vasundhara Mahajan 

Abstract With the substantial increase in implementation of green technology across all sectors worldwide to overcome energy loss, attributes such as reliability, efficiency, productivity, and security become very crucial for a system. Especially with the integration of IoT and smart features into a system alongside the evolution of Internet, cybersecurity and privacy of an individual component should be taken into important consideration. A smart grid comprises wireless network components exposed to cyber-attacks, smart meters being one the most vulnerable part of an advanced metering infrastructure. An advanced metering infrastructure enables two-way communication for automatic meter readings (AMR) and transmits data through wireless network. To counter cyber-attacks afflicting the network of AMI and functioning of a smart meter, additional intrusion detection methods are implemented into the grid network. The review includes cybersecurity concerns associated with smart meters along with an in-depth insight to some major cyber-attacks and their aftermath.

Keywords Cybersecurity · Cyber-attacks advanced metering infrastructure (AMI) · Smart meters · Denial-of-service (DoS) · False data injection (FDI) · Man-in-the-middle (MitM)

1 Introduction

With the increasing demand for automation and smart systems, terms like reliability, efficiency, emission, productivity, privacy, etc., are being focused upon. With the sustainable energy system, these features are expected along with additional smarter

M. G. Solanki · K. S. Patel · B. R. Kanzariya · T. H. Parekh
Electrical Engineering Department, School of Technology, Pandit Deendayal Energy University,
Gandhinagar, India

N. K. Singh · A. K. Yadav · M. A. Majeed · L. Tak · V. Mahajan (✉)
Electrical Engineering Department, Sardar Vallabhbhai National Institute of Technology, Surat,
India
e-mail: vasu.daygood@gmail.com

attributes, thus bringing the smart grid into the limelight. Thus, according to ‘The smart grids country report 2019’ 16 countries around the globe have implemented smart grid systems.

These smart grids are stout to load fluctuations as well as supply–demand imbalances. With an additional feature of two-way communication between consumer and distributor, a smart grid outperforms a conventional power system with more reliability, more efficient electricity usage [1], improved sustainability, and more controllability. With all the essential features of a smart system namely measuring, monitoring, controlling, and managing, a smart grid tends to have all these features with the management of generation, transmission, distribution, storage, and consumption of energy, with the help of electrical grids, communication network, hardware, and software. Implementation of advanced metering infrastructure in a smart grid increases the system’s reliability and economics and the system’s resilience against attacks, threats, and component failures in the system, hence maintaining a continuous uniform power structure.

Smart meters are one of the key components of advanced metering infrastructure and are a customer side technology. With the power of a computer and capabilities to connect itself to the cyber world, it increases system efficiency, system reliability, system controllability with increase in possibility of cyber vulnerability and cyber-attacks [2]. Being a cyber-physical system, it gets exposed to cyber-attacks.

This paper intends to provide a systematic understanding of advanced metering infrastructure, smart meters, and its cybersecurity, also covering three of the most critical cyber-attacks on smart meters. Section 2 of the paper states the basics and a brief background of cybersecurity in the advanced metering infrastructure (AMI), Sect. 3 contains details about advanced metering infrastructure (AMI) and the advantages of its implementation into the smart grid, Sect. 4 deals with security of smart meters, Sect. 5 discusses the types of attacks on a smart meter infrastructure and different intrusion detection techniques have been summarized, and finally, Sect. 6 concludes the findings of this paper.

2 Cybersecurity

The very base of advanced metering infrastructure is constructed on integrated information and communication technologies for its wireless communication network and data management system in the power grid/smart grid (Table 1).

Real-time data monitoring, two-way communication feature, and system communication in the network are enabled by the implementation of information and communication technologies, but ICT is greatly subject to the threat of cyber-attacks and thus making cybersecurity a very crucial point for an advanced metering infrastructure. A network connected system that operates on software and runs commands over the same are unfortified toward cyber-attacks, thus with the exponential growth in the application of smart system valuable personal and public data comes at threat of breach, data manipulation, theft, etc. And with the basic built-in security features

Table 1 History of major attacks on smart meters

Attack	Year	Attacker	Attack type	Affected users	Attack duration
Colonial pipeline attack	2021	Dark side	Ransomware		≈6 days
AWS DDoS attack	2020	Unknown	DDoS		≈3 days
Singapore’s health sectors breach	2019	Unknown	Data breach	1.5 million	≈3 years
British airways cyber-attack	2018	Unknown	Supply chain	0.38–0.50 million	
Equifax	2017	U.S. government alleges members of the People’s Liberation Army (China)	MitM	147 million	76 days
The MiraiKrebs and OVH DDoS attacks	2016	Unknown	DDoS		≈7 days

of a smart grid, it becomes an even more tempting and effortless target for an attack. Thus, additional methods are implemented to counter the cyberthreats and built an overall stronger network system. Smart meters are not only limited to the power system but has varied application for water, gas, and air—conditioning metering as well, the attack’s year wise revenue loss is shown in Fig. 1. The attacks types that have taken place in the past over smart meters are discussed in the later sections of the paper. Some of the major attacks have been listed in Table 1, along with the types of attack and causalities, the after math of these attacks and the huge number of fatalities demonstrate the amplitude of importance for implementation of cybersecurity measures in an advanced metering infrastructure.

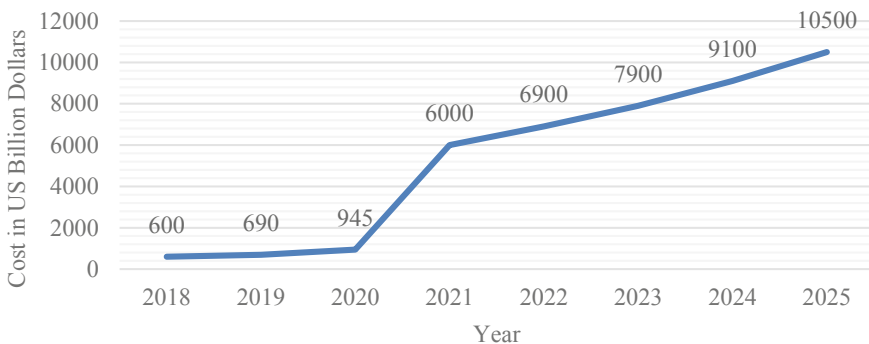


Fig. 1 Cybercrime damage cost

3 AMI—Advanced Metering Infrastructure

For the establishment of a smart grid system, a series/line-up of subsystems should be constructed first. In the smart grid chain, output of one subsystem serves as an input to the succeeding one for data management and improvement in the operation of the smart grid. An advanced metering system provides two-way communication and thus providing a relationship base between the consumer and provider [3].

AMI constitutes of multiple components, smart meters, as well as the entire communication network along with data management system. Such advanced metering infrastructure establishes communication with the load end and provides real-time stamped system information and transmits the data to the service provider/metering host system as well as for data management for storage and analysis [4, 5]. A data management system would perform the functions of data collection, storage, analysis, and system management by providing information in a brief and apt form for the service provider [6].

There are many more prospects for the utilization of an advanced metering system, for example, the same aspect can be applied to the water network, gas network, telecommunication network alongside electricity distribution networks [3]. With the right set of measurement devices and embedded controllers, one can implement the advanced metering system to any distribution channel/network [7]. For our review paper, we shall be further elaborating on our observations on the electrical distribution aspect of an advanced metering system. The key advantages of implementing an advanced metering system are listed below:

- **Managing Supply and Demand:** With accurate advanced metering, power resourcing is done more efficiently. Customers can avail details to their consumption and avail price incentives as per the norms thus, balancing the demand and peak loads which accounts for greater and adequate management of supply
- **Distribution Network Management:** Future demand and usage can be predicted by the data collected by AMI. The same can be used for new transformers' procurement parameters to manage the peak load conditions. The real-time readings can be further utilized to detect and prevent outages in the smart grid, and thus restoration back to normal conditions can be achieved faster, thereby reducing the duration and frequency of outages and contributing to the reduction in revenue loss.
- **Varying Tariff/Dynamic Pricing (pricing structure):** AMI data can help formulate business strategies such as consumer incentive programs and other ways to make the entire smart grid consumer-friendly, provide consumer incentives to utilize off-peak hours for high energy demanding chores, etc. Thus, implementation of varying tariff hours can encourage off-peak usage of energy.
- **Improved Data Quality:** Transcription errors and data reading errors can be reduced, thus eliminating redundant data from the system owing greatly to the reduction in billing errors and thus saving millions in consumer host disputes. The billing period need not be fixed with the use of AMI, with real-time data transmission, consumers can access their usage history and information immediately and

the same applies to the service provider, the hassle of manual meter data reading and delay in data update can be terminated. All these factors contribute to a better customer service policy for the service provider.

Numerous other benefits of AMI consist of protection from loss of data and revenue due to theft or a cyber-attack. Thus, applying AMI to its fullest capacity can leverage consumers and service providers at many domains/parameters/factors.

With data transmission at regular intervals, the host is prone to receive huge amounts of data; thus, storage of the metered data becomes a challenge for the service provider. The biggest challenge for the transition of conventional grid to smart grid is the long-term financial commitment that comes into picture with wide-area AMI implementation and smart meter installations. The installations cost of smart meters may seem extremely costly and inconvenient to the general public; thus, utilities may face heavy oppositions during the grid transition. In-order for the smart grid to function adequately, ensuring network security for smart meters and AMI is of utmost importance, thus constituting a challenge for the utility personage.

Smart metering holds a crucial position in the AMI; it communicates data such as power consumed, load fluctuations, etc., back to the service provider. It also holds the capability of providing visual details to the consumers as well, regarding consumption and energy usage as well as pricing information conveyed by the service provider [7]. Smart meters record and transmit detailed consumption of a user and thus is vulnerable to attacks; one can manipulate and steal data as the transmission from a smart meter is wireless, making it more vulnerable to cyber-attacks [6, 8]. At present almost all the smart meters communicate through the ZigBee communication protocol [9]. It is easy to install and supports a large number of nodes and with its short working period, it results in low power consumption for operation yet it has a few vital disadvantages such as a low bandwidth for communication and a meshed data network with low network stability. ZigBee is less complex as compared to Bluetooth but is not secure or fast enough like Wi-Fi and does not have end devices available yet. To counter the dilemmas, a wireless version of BACnet has been a prominent communication protocol as compared to ZigBee [10].

3.1 AMI: Networking

Another crucial segment of the advanced metering system is the network over which the data communication is structured. It conducts the transmission of the metering data from smart meters to the central data management system [8] and vice-versa as AMI supports two-way communication including real-time measures, voltage measurement, load control, etc.

Thus, it offers utility providers with enormous data transfer capabilities through the transmission network along with data security nevertheless maintaining the accuracy and precision of the metered data [5].

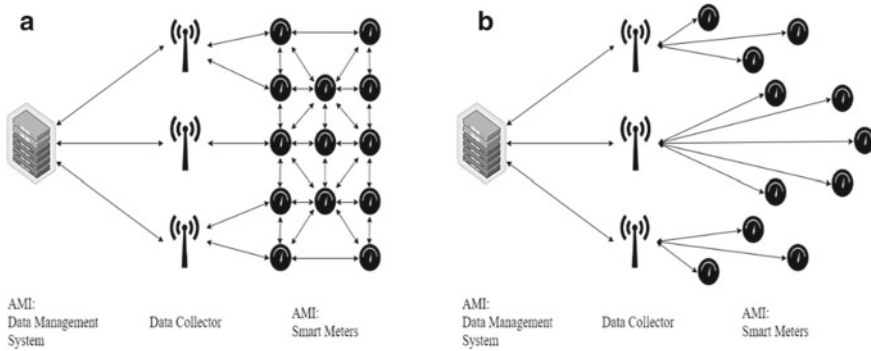


Fig. 2 a Mesh network and b point-to-multipoint network

As per the implementational observations, two types of networks are adapted by AMIs for data communication, namely mesh network and point-to-multipoint network. Figure 2 shows the AMI communication network [11]. The multipoint network allows the service provider to connect with multiple smart meters at a time even at a significant range. It also takes into use the licensed radio frequency, unlike the mesh network [12].

Several communication links pass the data from various endpoints onto the connected grid router where all the meter data are collected, and commands from a control center are sent on a specific path from the connected grid router to the control target. If any of the aging of the components, from the specified path, go rogue the network topology will intuitively set itself to its preselected configuration.

3.2 AMI: Data Management System

The data obtained from the smart grid owes to a great volume, data variations, and even data velocity, referring to the speed at which data is transferred and processed. To manage such a huge amount of data, relevant management and processing procedures are applied to the IoT [13] of the smart grid [14].

For an electrical smart grid, such applications are expected to run all day long to provide real-time applications to monitor and analyze the smart meter characteristics to counter any incipient faulty behavior in the smart grid.

3.3 AMI: Smart Meters

Smart meters are an integral part of the advanced metering infrastructure (AMI) [3]. It allows two-way communication for varied purposes, apart from its basic purpose of

recording power usage [15]. It has many advanced features as compared to conventional power meters. Figure 3 shows the comparison between metering architecture of conventional meters and smart meters [16]. Each smart meter can communicate the collected information at frequent intervals at a continual rate and transmits the data through ethernet connectivity to a central data management center, where the data is utilized to calculate the energy consumption and other parameters such as energy flow in and out of the system [17]. Smart meters are capable of tracking and recording surrounding information, like temperature, humidity, light, motion, etc., with accuracy and precision, providing better stability for data management, it can also accept commands from both consumers and service providers and can respond accordingly [11, 18, 19]. Smart meters consist of all the components, and a basic CPU consists of namely RAM, microprocessor, data storage unit, along with many sensors and modules to measure different parameters like current, voltage, temperature, humidity, motion, a module for information transmission to communicate with the host and other smart devices, analogue to digital converters, energy management system, etc. The collected data from smart meters is sent to a data management system through a communication network for storage, load monitoring, and for future analysis purposes, which is accessible by the service provider, utilities, or authorized third-party user [11, 20]. Presently, network architecture like WiMax, ZigBee, Cellular, or powerline cables is used, with ZigBee [21] being a prominent choice for a mesh-style smart meters network due to its short communication range and to provide end-device communication [5, 7].

Many smart meters have crucial warning features programmed within the system which can be accessed by the service provider and can be altered as per need. A smart meter also can regulate different efficacies to the maintain balance in the system during unstable conditions.

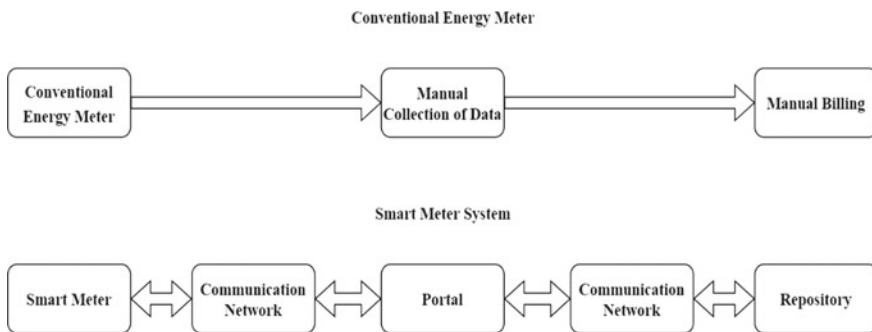


Fig. 3 Data transmission difference between a conventional meter and a smart meter

4 Cybersecurity of Smart Meters

With the advancements in technology and implementation of Internet-of-Things in every aspect of human life, the smart power system has become a crucial part of it as well as for the whole nation. But with the whole network relying on one communication topology invites malicious attacks, threats, data breaches, and condemning acts of cybercrime which can lead to network systems' divergence. With the damage/shut down of the power system, the nation can face an economic crisis. Thus, cyber-physical security [22, 23] is required in a smart grid. Cyber-attacks observed on the electricity, gas, and air-conditioning are depicted in Fig. 4. The attacks were recorded at different location around the globe by public.

Comprehensively, the smart grid fundamental security requirements [24] can be mentioned as follows:

- *Integrity*: Prevention of data temperament during transmission and maintaining the authenticity of the source data [8]. Unauthorized data manipulation or destruction of data can cause financial and privacy deprivation to both, user as well the service provider [7]. Repetitive data flow or controlled messages and absurd sensor values are the indications of the system being under attack and results in loss of integrity of data and disrupt crucial data exchange in the system [24]. The integrity of the data does not necessarily project the validity of the data, and it only signifies that the received data is the same as the source data [14].
- *Availability*: Exclusivity in providing accessibility to authorized personnel only, but easy to acquire from the communication network among the system. The availability of data can be compromised by an event such as Denial-of-service (Dos) attacks. This can lead to disruption of data transmission; it can also cause the system to collapse and accessibility to the advanced metering system which on the further end will affect the power distribution network.

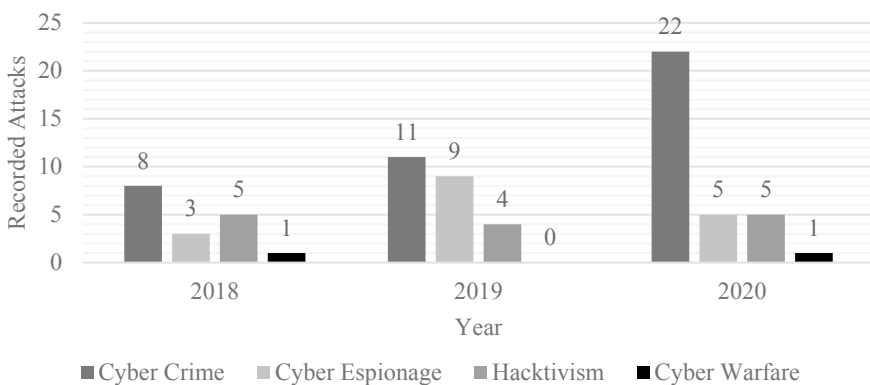


Fig. 4 Recorded attacks on electricity, gas steam, and air-conditioning

- *Confidentiality*: Intentional or unintentional disclosure of personal data should not occur. The transmitted data, as well as the stored data accessibility, should be restricted for unauthorized users to protect the privacy and security of the user and the service provider, and violation of the same can lead to data breach. With the increase in the easy availability of the Internet and smart devices, the eminence of confidentiality has intensified as well.
- *Accountability*: In a smart grid, even a single rogue smart meter will lead to invalid data transmission to the service provider, denial in holding the responsibility for the malicious act falls under accountability attack threat. The purpose behind the same can be for data manipulation of the smart meter; thus, the smart grid security must be resisted by both hardware as well as software attacks. To address data accountability and data confidentiality, a quantum cryptography-based approach in a smart grid has been proposed by Xin et al. in [25].

In the smart grid, the smart meter being a customer side technology is the most easily accessible cyber-physical device, hence is the most vulnerable to cyber-physical attacks. Different attack techniques are listed in Fig. 5.

4.1 False Data Injection (FDI)

False data injection (FDI) is one of the most critical cyber-attacks on smart meters which directly affects the measurement data compromising its confidentiality and authenticity. The tampered data can compromise the grid's state estimation and can cause a power outage. It can severely increase the energy distribution cost. Many detection solutions have been proposed for FDI attacks in [26]. In [27] deep belief network is used to extract the behavior and characteristic of FDI attacks with some logical assumptions. In [28, 29], based on spatial-temporal model detection of FDI attack is determined, relation between smart grid components is establish to detect the attack [30].

4.2 Denial-of-Service (DoS)

Denial-of-Service attacks target a network by loading the smart meters with a profuse amount of data signals causing communication blockage between the user and service provider [31]; this can result in low service availability and further lead to a breakdown in the AMI. When more than one sources are under raid, the attack is termed Distributed Denial-of-Service (DDoS) [20, 32]. By targeting multiple hosts, the effects of a DDoS attack can be spread out, complicating the resilience of the AMI toward such attacks. The prime target of a DDoS attack can be multiple hosts as well as an entire network. DDoS attacks can be classified into flooding attacks and vulnerability attacks. Flooding attacks target the Transmission Control Protocol

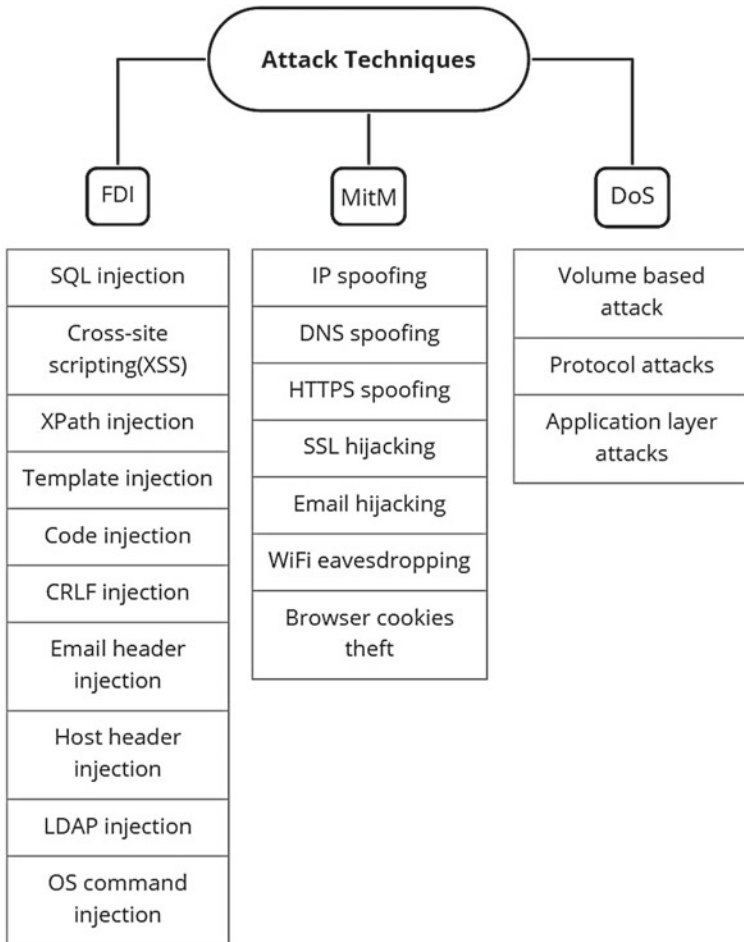


Fig. 5 Different attack techniques for the listed attack types

(TCP), while vulnerability attacks deploy malicious packets of false data that target the weak components of an AMI. Defense methods to counter a DoS/DDoS attack have been proposed by Asri and Pranggono [33] and Wei et al. [34]. The authors of the following paper have introduced a Java-based intelligent agent component (IAC) for the early detection of a DoS attack. Honeypots can be employed as a defense mechanism as well, Batesian Honeypot model distinguishes a malicious attack from the legitimate transmissions, such detection mechanisms can be employed in an advanced metering infrastructure for intrusion detection of DoS/DDoS attacks.

4.3 *Man-in-the-Middle (MitM)*

Man-in-the-middle (MitM) is an intelligent attack where the attacker positions himself in between consumer and service provider, to either eavesdrop or impersonate one of the targets. MitM is a high confidentiality breaching attack where measurement data, device protocol, and other confidential information may get leaked [21]. An attacker can perform every action authorized personnel can perform. In [35], a lightweight physical unclonable function (PUF)-based authentication model is used between two nodes which detects and eliminates MitM attack. In [36], they have used a One-way memory Attestation Protocol (OMAP) for the detection of attackers on the network. As Checksum transmission is one-way and each checksum is used once it is impossible for an attacker to perform MitM attack, thus prevention from MitM attacks. Explaining the consequences of a MitM attack [37] performs a MitM attack on a power factor correction unit to perform an intentional false tripping of the entire feeder. Further, MitM attack can be prevented by using strong encryption on access point. In Table 2, an overview of the three major attacks with the target, cause, and the after math of the attacks is listed.

5 Intrusion Detection

One of the most crucial and widespread counter mechanisms against cyber-attacks on the advanced metering system is the detection of attacks and threats and building a resilient structure hostile to unusual behavior [38]. Attack detection can be settled in two ways; anomaly based detection where the deployed technique tries to determine deviations from the normal usage pattern as intrusion, detection methods include support vector machine (SVM) [39, 40], neural networks [41], genetic algorithms, decision trees, graph theories [42], classification and regression trees (CART), etc. [43]. The misuse type detection uses profound patterns of attacks and vulnerabilities base for intrusion detection, uses pattern recognition techniques for the same. Here, we shall be briefing upon just the anomaly based detection techniques [18, 43]. Numerous machine learning algorithms techniques [44] can be employed for anomaly based intrusion detection, the ensemble technique where multiple learning algorithms are combined and trained based on their specificity to maintain the overall detection accuracy.

In [18], one of such technique has been proposed, where in the initial steps of intrusion detection, support vector machine [39] is installed, and in the second stage, time failure propagation graph (TFPG) which validates if the detected intrusion is caused by system failure or is a definite cyber-attack [45].

The support vector machine is a supervised machine learning algorithm. It functions by deploying a hyperplane that differentiates dataset by plotting the data in n -dimensions [46]. The vector data points which on removal cause the hyperplane to shift are called support vectors. The technique of finalization of hyperplane through

Table 2 Critical cyber-attacks on smart meter

Type of attack	Target of attack	Cause of attack	Aftermath of the attack
False data injection (FDI) [27–29]	Performing FDI to alter energy meter data for personal benefit (typically reducing the usage amount from the customer side or increasing the usage amount from the service provider side)	Breaching and tampering communication signal between the smart meter and data management system	Can cause unnecessary load shedding to the power system impacting the security and economics of the power system
Denial-of-Service (DoS/DDoS) [9, 20, 33, 34]	Such an attack is performed with the objective of bringing down a portion of an entire network by compromising smart meters leading to consumers staying devoid of essential services	Overburdening a network can cause a smart meter to obstruct the incoming and outgoing signals from the network, causing a complete shut out of the attacked SM from the smart grid	The shutdown of a network or a segment can lead to substantial losses due to a shortfall of essential services, consumers, as well as service providers, may face serious consequences
Man-in-the-Middle (MitM) [21, 35–37]	To Perform malicious activity, to compromise integrity, to jeopardize consumer privacy	A weakly secure access point like a communication network, weakly protected SMS can help attacker breach communication	Data being communicated can be illegally accessed, transferring data can tamper, and can also damage or shut down the system by false command

datasets has proven useful in rapid classification with lesser computational power [47]. The mathematical functions used for data structurization in SVM algorithms are called kernels. Kernels can be classified into two basic classes; local kernels wherein the closer support vectors influence the hyperplane and affect the SVM model, and global kernel, where support vectors can affect from a larger distance and can impact the kernel value. A few basic kernels are string kernel, tree kernel, graph kernel, homogenous/inhomogeneous polynomial kernel, etc. [48].

The SVM can be employed to detect intrusions such as Denial-of-service (Dos), probe, user to root (U2R), remote to user (R2L), etc. [49]. The scikit-learn library in Python is profoundly used for machine learning algorithms, SVM can be employed by the usual structure; import library, object creation, fitting model, and prediction

timed failure propagation graphs (TFPG) are causal models that capture the timely aspects of failure propagation in dynamic systems [50]. This technique is used to present the failure behavior of a system and provides us the system operation during failure and faults. Thus, TFPG can be used to optimally diagnose or predict failure in a synchronous system as well as for forming correspondence between abnormal

behaviors and attack types, i.e., interrelation between the cause and the effect of an attack [45]. TFPG in intrusion detection is used to compare the detected abnormal behavior with the pre-defined intrusion attack events and determine that the intrusion detected is an actual cyber-attack or a system failure within the AMI.

6 Conclusion

This paper elaborates on the structure of advanced metering infrastructure (AMI), further focusing on smart meters and its cybersecurity. It describes the need for cybersecurity in a smart system. Moving forward, details, and after-effects of prominent attacks have been discussed. Cyber-attack techniques and past cyber-attacks with their after-effects are briefly described in the next section. Detection of such attacks plays a crucial role in smart meter security. Intrusion detection is a fundamental step to counter cyber-attacks, briefing intrusion detection system (IDS) use of SVM and TFPG model for detection and classification for such attacks has been discussed. In conclusion, this paper is intended to motivate future researchers for the development of efficient and advanced intrusion detection systems (IDS) for smart meters.

References

1. Taow-klang C, Pattanasethanon S (2008) Using of artificial light combination with daylight in interior. (Thai). *Asia-Pacific J Sci Technol* 13(5):597–605
2. Geetha A, Jamuna K. Smart metering system, pp 1047–1051
3. NETL modern grid strategy: Advanced metering infrastructure. US Department of Energy Office of Electricity and Energy Reliability, 2008
4. Mohassel RR, Fung A, Mohammadi F, Raahemifar K (2014) A survey on advanced metering infrastructure. *Int J Electr Power Energy Syst* 63:473–484
5. Grochocki D, Huh JH, Berthier R, Bobba R, Sanders WH, Cárdenas AA, Jetcheva JG. AMI threats, intrusion detection requirements and deployment recommendations, pp 395–400
6. Wang X, Yi P (2011) Security framework for wireless communications in smart distribution grid. *IEEE Trans Smart Grid* 2(4):809–818
7. Tweneboah-Koduah S, Tsetse AK, Azasoo J, Endicott-Popovsky B (2018) Evaluation of cybersecurity threats on smart metering system. In: *Information technology-new generations*. Springer, pp 199–207
8. Yan Y, Qian Y, Sharif H, Tipper D (2012) A survey on cyber security for smart grid communications. *IEEE Commun Surv Tutor* 14(4):998–1010
9. Shuaib K, Trabelsi Z, Abed-Hafez M, Gaouda A, Alahmad M (2015) Resiliency of smart power meters to common security attacks. *Procedia Comp Sci* 52:145–152
10. Aravinthan V, Namboodiri V, Sunku S, Jewell W. Wireless AMI application and security for controlled home area networks, pp 1–8
11. Khattak AM, Khanji SI, Khan WA. Smart meter security: vulnerabilities, threat impacts, and countermeasures, pp 554–562
12. Yan Y, Qian Y, Sharif H, Tipper D (2012) A survey on smart grid communication infrastructures: motivations, requirements and challenges. *IEEE Commun Surv Tutor* 15(1):5–20
13. Jaradat M, Jarrah M, Bousselham A, Jararweh Y, Al-Ayyoub M (2015) The internet of energy: smart sensor networks and big data management for smart grid. *Procedia Comp Sci* 56:592–597

14. Gunduz MZ, Das R. Analysis of cyber-attacks on smart grid applications, pp 1–5
15. Kabalci Y (2016) A survey on smart metering and smart grid communication. *Renew Sustain Energy Rev* 57:302–318
16. Depuru SSSR, Wang L, Devabhaktuni V, Gudi N. Smart meters for power grid—challenges, issues, advantages and status, pp 1–7
17. Shahinzadeh H, Hasanalizadeh-Khosroshahi A (2014) Implementation of smart metering systems: challenges and solutions. *TELKOMNIKA Indo J Electr Eng* 12(7):5104–5109
18. Sun C-C, Cardenas DJS, Hahn A, Liu C-C (2020) Intrusion detection for cybersecurity of smart meters. *IEEE Trans Smart Grid* 12(1):612–622
19. Ueno T, Sano F, Saeki O, Tsuji K (2006) Effectiveness of an energy-consumption information system on energy savings in residential houses based on monitored data. *Appl Energy* 83(2):166–183
20. Unsal DB, Ustun TS, Hussain S, Onen A (2021) Enhancing cybersecurity in smart grids: false data injection and its mitigation. *Energies* 14(9):2657
21. Sharma K, Saini LM (2015) Performance analysis of smart metering for smart grid: an overview. *Renew Sustain Energy Rev* 49:720–735
22. Mahmud R, Vallakati R, Mukherjee A, Ranganathan P, Nejadpak A. A survey on smart grid metering infrastructures: threats and solutions, pp 386–391
23. Singh NK, Gupta PK, Mahajan V (2020) Intrusion detection in wireless network of smart grid using intelligent trust-weight method. *Smart Sci* 8(3):152–162
24. Cleveland FM. Cyber security issues for advanced metering infrastructure (AMI), pp 1–5
25. Miao X, Chen X. Cyber security infrastructure of smart grid communication system, pp 1–4
26. Drayer E, Routtenberg T (2019) Detection of false data injection attacks in smart grids based on graph signal processing. *IEEE Syst J* 14(2):1886–1896
27. Pu Q, Qin H, Han H, Xia Y, Li Z, Xie K, Wang W. Detection mechanism of FDI attack feature based on deep learning, pp 1761–1765
28. Chen P-Y, Yang S, McCann JA, Lin J, Yang X (2015) Detection of false data injection attacks in smart-grid systems. *IEEE Commun Mag* 53(2):206–213
29. Kallitsis MG, Bhattacharya S, Michailidis G. Detection of false data injection attacks in smart grids based on forecasts, pp 1–7
30. Singh NK, Mahajan V (2021) End-user privacy protection scheme from cyber intrusion in smart grid advanced metering infrastructure. *Int J Crit Infrastruct Protect*:100410
31. Jamal T, Haider Z, Butt SA, Chohan A (2018) Denial of service attack in cooperative networks. *arXiv preprint arXiv:1810.11070*
32. Mahjabin T, Xiao Y, Sun G, Jiang W (2017) A survey of distributed denial-of-service attack, prevention, and mitigation techniques. *Int J Distrib Sens Netw* 13(12):1550147717741463
33. Asri S, Pranggono B (2015) Impact of distributed denial-of-service attack on advanced metering infrastructure. *Wirel Pers Commun* 83(3):2211–2223
34. Wei L, Rondon LP, Moghadasi A, Sarwat AI. Review of cyber-physical attacks and counter defense mechanisms for advanced metering infrastructure in smart grid, pp 1–9
35. Aruna Gawade NS (2020) MITM attack prevention using PUF authentication in smart grid. *Int J Adv Sci Technol* 29(3):12321–12331, 03/30
36. Song K, Seo D, Park H, Lee H, Perrig A. OMAP: one-way memory attestation protocol for smart meters, pp 111–118
37. Hadjidemetriou L, Tertytchny G, Karbouj H, Charalambous C, Michael MK, Sazos M, Mani-atakos M. Demonstration of man in the middle attack on a feeder power factor correction unit, pp 126–130
38. Yadav SA, Kumar SR, Sharma S, Singh A. A review of possibilities and solutions of cyber attacks in smart grids, pp 60–63
39. Suthaharan S (2016) Support vector machine. In: *Machine learning models and algorithms for big data classification*. Springer, pp 207–235
40. Widodo A, Yang B-S (2007) Support vector machine in machine condition monitoring and fault diagnosis. *Mech Syst Signal Process* 21(6):2560–2574

41. Gupta P, Singh N, Mahajan V (2021) Intrusion detection in cyber-physical layer of smart grid using intelligent loop based artificial neural network technique. *Int J Eng* 34(5):1250–1256
42. Singh NK, Mahajan V (2020) Detection of cyber cascade failure in smart grid substation using advance grey wolf optimization. *J Interdiscip Math* 23(1):69–79
43. Jyothsna V, Prasad R, Prasad KM (2011) A review of anomaly based intrusion detection systems. *Int J Comp Appl* 28(7):26–35
44. Tsai C-F, Hsu Y-F, Lin C-Y, Lin W-Y (2009) Intrusion detection by machine learning: a review. *Expert Syst Appl*
45. Ofsthun SC, Abdelwahed S. Practical applications of timed failure propagation graphs for vehicle diagnosis, pp 250–259
46. Noble WS (2006) What is a support vector machine? *Nat Biotechnol* 24(12):1565–1567
47. Joachims T (1999) Svmlight: support vector machine. SVM-light Support Vector Machine 19(4). University of Dortmund. <http://svmlight.joachims.org/>
48. Zhang J (2015) A complete list of kernels used in support vector machines. *Biochem Pharmacol (Los Angel)* 4:2167–0501
49. Kotpalliwar MV, Wajgi R. Classification of attacks using support vector machine (SVM) on KDDCUP'99 IDS database, pp 987–990
50. Abdelwahed S, Karsai G. Practical considerations in systems diagnosis using timed failure propagation graph models, pp 129–136

A Brief Review of Different Estimation Methods of SOC for Li-ion Battery



Mona Rani and Supriya Jaiswal

Abstract Considering the effects of increasing pollution causing greenhouse gas (GHG) emission, leading to global warming and depletion of fossil fuels has opened the way globally toward the use of hybrid and battery electric vehicles (BEVs). The vehicle manufacturing sector has already entered in the manufacturing of EVs, hence reducing the environmental problems globally. Also, the need for energy storage system has appeared to be an important concern. In this regard, Li-ion batteries because of their significant characteristics including faster charging, lower self-discharging, longer lifespan, light-in-weight, and higher energy density have appeared to be the best choice. SOC which shows the battery remaining capacity is the principal states of the battery and hence required to be observed efficiently to increase the conduction and life span of batteries. This paper comprehensively reviews the estimation techniques involved in the estimation of SOC of Li-ion batteries. Along with the categorization of the methodologies, explanation of the different methods with their advantages and disadvantages has been discussed for their application in the on-line BMS. Also, the review focuses on the different challenges and parameters with their feasible proposals for the SOC estimation and organization of an efficient BMS for the future EVs application.

Keywords Li-ion battery · Battery management system (BMS) · State of charge (SOC) · Battery modeling · SOC estimation

1 Introduction

The increase in pollution and rise in fuel prices have raised the concern globally to reduce the usage of fuel-driven vehicles. The harmful carbon effusion from the internal combustion engine (ICE)-based vehicles has caused rise in greenhouse gases (GHG) and global warming [1]. To provide a solution toward green transportation, use of renewable sources such as solar, wind, and hydro energy can be suggested.

M. Rani · S. Jaiswal (✉)
National Institute of Technology, Hamirpur, Himachal Pradesh, India
e-mail: supriya@nith.ac.in

© The Author(s), under exclusive license to Springer Nature Singapore Pte Ltd. 2022
V. Mahajan et al. (eds.), *Sustainable Technology and Advanced Computing in Electrical Engineering*, Lecture Notes in Electrical Engineering 939,
https://doi.org/10.1007/978-981-19-4364-5_39

543

However, the intermittent and unregulated nature of supply restricts its implementation for powering the transportation sectors. Hence, all these reasons have driven the researchers, automobile industries and their consumer's interest toward the electric vehicles (EV) [2].

The use of rechargeable batteries for the energy storage in EVs is the right choice nowadays. Due to some of the significant features of batteries, such as high efficiency, lower self-discharge rate, higher working cell voltage, higher power density, low pollution, portability in hybrid electric vehicles and industrial applications, they are the apt choice for the energy storage systems [3]. Some of the available options are lead-acid, nickel metal hydride (NiMH), and Li-ion batteries. Among them Li-ion batteries possess some special features such as longer lifespan, lightweight, faster charging, higher energy density, and higher efficiency which makes them popular and widely in use. Proper control and management of battery packs is the primary requisite for their longer life expectancy and good performance [3, 4]. Any undesirable operation inside the battery such as variation in the temperature range or overcharging/over discharging may deteriorate the life of battery. Since battery packs consist of series or parallel connection of hundreds of cells together to fulfill the requirement of high amount of voltage, current, and power of the automobiles. Therefore, special care must be taken during their operation and need to be protected from any physical damage. In this regard, the battery management system (BMS) helps in protecting the batteries from any physical damage, cell unbalancing, controls thermal degradation for the safety, and long-lasting performance of batteries. It consists of following techniques, i.e., battery modeling, state estimation, and battery control for the proper functioning of batteries [3]. For the design of battery and utilization in EVs, it is important to know about its state of charge (SOC) and state of health (SOH). SOC which indicates the remaining capacity of battery and SOH which indicates the age/health of battery which are two different states of battery which can easily be estimated by the systematic use of BMS [2]. Since SOC is the ratio of available capacity to maximum capacity and represents the remaining capacity of battery, so it helps in increasing the battery life by protecting it from overcharging/discharging and helps in saving the energy. The battery states are then regulated and monitored by (BMS) which includes different algorithms and uses scientific models consisting of hardware and software. Since battery is the storage system of chemical energy and to reach out to this energy directly is not possible. Hence, this leads to difficulty in the accurate estimation of SOC [4]. Since battery has nonlinear and time varying characteristics, hence computation of SOC instantaneously is very difficult. The inaccurate estimation of SOC will give wrong indication of overcharging/discharging situations of battery. So great care must be taken while measuring SOC. Till now researchers and scholars have propounded various methods. But the errors and the reliability in the SOC estimation create differences in these methodologies. These methods have been classified into five categories as shown in Fig. 1. Table 1 presents the merits and demerits of different SOC estimation methods. Majorly Li-ion batteries are used in EVs. These are used for propelling wide range of EVs such as aircraft, electric cars, and hybrid vehicles because of their less weight. The other applications include their use in electronic daily use appliances such as DSLR camera, scientific calculators,

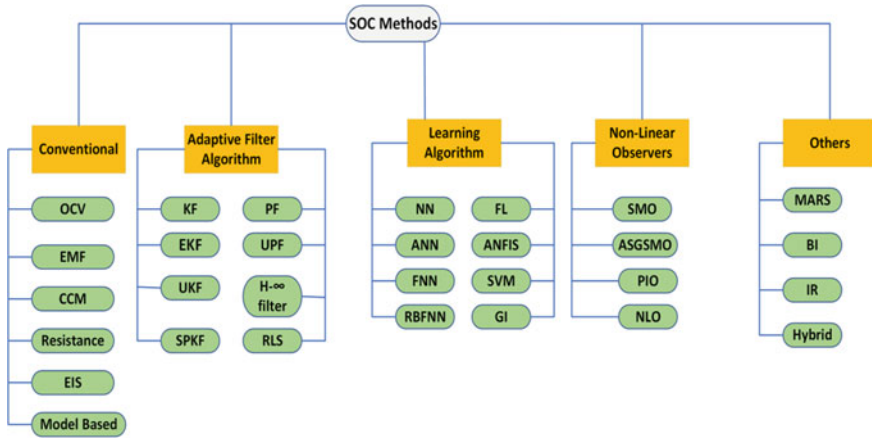


Fig. 1 Classification of SOC methodologies

mobile phones, and most of the consumer electronics devices. These are harnessed in cardiac pacemakers, the power tools such as cordless drills, saws and various garden equipment such as hedge trimmers etc.

This paper has been organized into following sections: In Sect. 2, a brief explanation of BMS is done. In Sect. 3, different models of battery are explained. In Sect. 4, different SOC estimation methods with their merits and demerits are explained. And Sect. 5 gives the conclusions and recommendation about suitable estimation technologies.

2 Battery Management System

A systematic BMS is required for the protection of the battery from aging, thermal defects, and any physical damage hence estimating, regulating, and measuring the SOC of the battery with great precision. Since Li-ion battery provides greater performance due to their longer lifespan, high voltage generation, hence need to be protected from any accident. The BMS comprises of sensors, controllers, and actuator that are managed and directed by different models, algorithms, and signals. In [16], the parts of BMS are classified into hardware and software which is represented in Fig. 2.

3 Battery Modeling

The SOC estimation requires an effective battery model. Various models have been designed but electrochemical model (EM) and equivalent circuit model (ECM) are

Table 1 Merits and demerits of SOC methods

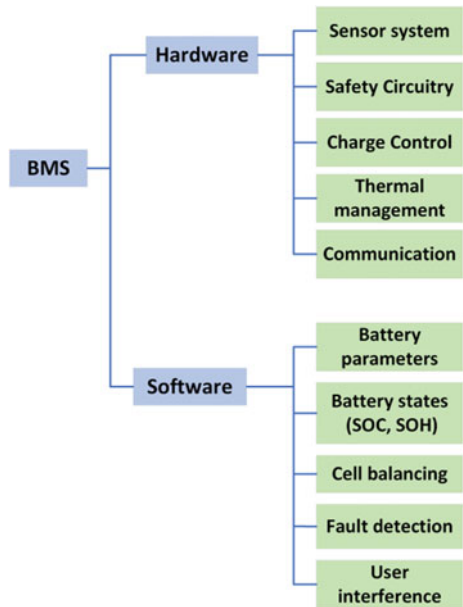
Methods	Merits	Demerits
CCM [5]	Simple to use. Power consumption low	Accuracy decreases due to some disturbances. Applicable when initial SOC value known leading to accumulation of errors
OCV [6]	Simple to use. Provides higher accuracy	Only applicable to vehicles at rest. Flat region in the SOC curve makes it unsuitable for estimation of SOC
KF [7]	Self-correcting nature decreasing the variation in current. Higher accuracy while determining the states containing some surface disturbances like noises headed by Gaussian disturbances	Direct implementation for the estimation of states of nonlinear system is not possible. High computational cost
EKF [8]	Provides high accuracy while estimating nonlinear states of the system	Causes error during linearization
UKF [8]	Provides good accuracy while estimating a highly nonlinear system of third order. During computation of the mathematical equation Jacobian matrix and Gaussian noise are not required	Occurrence of unknown errors or disturbances and the inaccuracy of system model decreases its accuracy
AEKF [9]	High accuracy in the estimation of SOC of the battery	Highly complex computation and high computational cost
H_{∞} filter [10]	Shows reasonable performance regarding precision, computational cost, and time duration	Hysteresis, temperature issues, and aging factor affect the precision level of the model
Sigma point Kalman filter (SPKF) [1]	Shows similar computation as EKF without the involvement of Jacobian matrices	Highly complex computation and computational cost
NN [11]	Capable of working for the nonlinear system	For the storage of trained data, large memory unit required

(continued)

Table 1 (continued)

Methods	Merits	Demerits
Fuzzy logic (FL) [12]	Efficiently operates in a nonlinear dynamic system. Easily forecasts an appropriate precision level regarding temperature, aging, and charging factors	Computation is highly complex. Require very costly processing unit
Multivariable adaptive regression spline (MARS) [13]	Accuracy level high	Starting and at the end of SOC interval accuracy diffuses
Hybrid [14]	Provides better and authentic result and decreasing the monetary value of the system	Highly complex computation. Integrating two or more methods together increases the difficulty level
Genetic algorithm (GA) [15]	Precision level high. Strong enough against the noise factors	Highly complex computation. Excellent regulation of the variables required for the productive outcome

Fig. 2 Block diagram of BMS in EVs



often employed. The EM expresses the electrochemical reaction undergoing inside the battery for which knowledge in the field of electrochemistry is required. Also, as this method uses time-varying partial differential equation containing huge number of undefined variables leading to complexity in the computation, hence, this is suitable for the battery designing and for reviewing the battery performance. Another model

is the ECM, since battery has a complex polarization feature so the models having increased number of parallel RC networks joined in series must be highly precise. Also, increase in the order causes rise in the model complexity. Therefore, keeping in mind about the accuracy and the model complications, a second order Thevenin RC model has been used here. The designing of the ECM's is done basically for the vehicle management control and the development of BMS [17, 18], also it consists of a fewer number of variables. The ECM is a circuit consisting of different key elements including resistance (R), capacitance (C), and source voltage connected in series-parallel way. This model is inherent and incisive, manageable, and intelligent and easy to form the state space equation which is appropriate for examining the battery simulation and in finding its parameters [19, 20]. Hence, this is the commonly used method in the estimation of SOC of the battery. The different ECM models are Rint model, Thevenin model, PNGV model, and GNL-model.

The Rint model diagram is represented in Fig. 3a [21]. This model is very easy to implement, and uncomplicated comprising of an ideal source voltage E and a series connected internal resistance R_0 . But since its accuracy level is low so it is unable to reflect the electrochemical reaction undergoing inside the battery cell. Hence, this is practically not acceptable. Another is the first order Thevenin model Fig. 3b [22]. It includes an open circuit voltage source V_{OCV} , a capacitance representing the polarization capacitance C_{P1} and counterfeits the effect of diffusion happening in the batteries charging/discharging operation, a polarization resistance R_{P1} charging/discharging current I_{b1} , an internal resistance R_t , and a battery terminal voltage V_t . Also, it overcomes the constraints coming from Rint model showing effective features of the battery to a certain level. But since battery action is very complicated so the effectiveness of this model with a single RC branch is finite. Hence, it is unable to display the effect of diffusion effectively and other parameters affecting battery performance.

In partnership for a new generation of vehicle (PNGV) battery model Fig. 3c [23], a plate capacitor C_b is connected in the Thevenin first order RC model leading to an increased accuracy, but it is very tough in finding battery variables and causes complication in the computation, hence this model is not worth to use it in real-time estimation of SOC rationally. Another is the GNL-model shown in Fig. 3d [24]. This is the combination of all the above models, Rint model, Thevenin model, and PNGV. Since it comprises of several resistances and capacitances, thus increasing the order and causing complexity in the computation. So, the application of this model in the estimation of SOC in real time is not feasible.

So, after the complete analysis and keeping in mind the merits and demerits of the above methods Thevenin model with second order RC network Fig. 4 is the right choice for the estimation of SOC, since as the parallel RC network figure rises, then precision of the feedback coming from the dynamic battery prognosis increases.

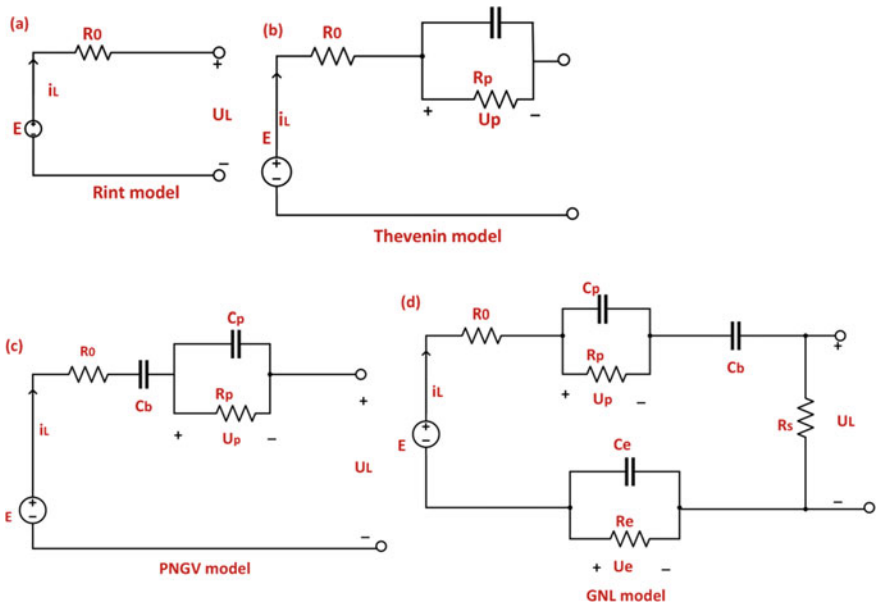
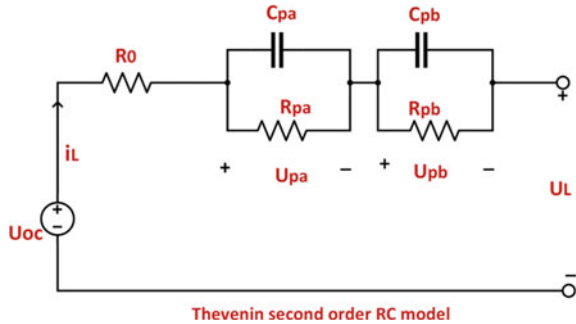


Fig. 3 Different battery models

Fig. 4 Thevenin second order RC model



4 Estimation Methods of State of Charge

SOC is the salient feature of the battery and plays an important role to achieve better performance is described as the ratio of available capacity to maximum capacity and represents the remaining capacity of battery as the percentage of total charge/capacity at which battery is currently at, so it helps in increasing the battery life by protecting it from overcharging/discharging and helps in saving the energy. But the estimation of SOC directly is not possible, since battery is the storage system of chemical energy and to access this energy directly is not possible. So various methods have been founded for SOC estimation. One of them is, with

the help of battery voltage and current which is one of oldest approach to estimate SOC. Another is the coulomb counting method which includes integration of charging/discharging current w.r.t time. The accurate information about SOC is very crucial for the better performance of battery since this information is applied in BMS to sense the overcharging/discharging condition so that we can stop the battery from charging/discharging on time to protect it from any damage. Various methods with their merits and demerits have been discussed below.

4.1 Conventional Methods

This method estimates SOC by making use of the physical properties of battery such as voltage (V), current (I), and temperature (T) and computes them forming mathematical equations or by forming any correlation between them.

Coulomb Counting Method (CCM)

This is an elementary method which shows the relation between SOC and the charging/discharging current. This is the commonly used method for the estimation of SOC due to its simplicity and is easily carried out in battery energy storage system (BESS) without consuming much power. Also, the demand for the hardware is easily accessible [5]. The integration of the battery current with time during the battery charging or discharging period is done.

The mathematical equation is given below: -

$$\text{SOC}(t) = \text{SOC}_{\text{initial}} - \frac{1}{C_{\text{rated}}} \int_0^t \eta i(t) dt \quad (1)$$

where C_{rated} is nominal capacity, η is the charging/discharging or columbic efficiency, $i(t)$ is the battery current, and $\text{SOC}_{\text{initial}}$ is the initial SOC value [25].

But due to various constraints like current, noise, temperature, and unknown interferences and since it is an open loop system, hence the accuracy level decreases [16]. Since, the reliability of this method is merely dependent upon the exact value of the initial estimated SOC value since occurrence of any error in the initial SOC value will influence the entire estimates and will remain throughout the operation. Besides this, the computational errors might affect the current sensors upon which the precision level is hugely dependent, hence affecting the battery performance [26]. So instead of using individually, it is applied along with other methods.

Open Circuit Voltage Method (OCV)

For the SOC computation by OCV, battery requires adequate rest time to acquire equilibrium condition. Generally, there exists a linear correlation between SOC and OCV, but this relation varies within the batteries since it relies upon the material and

size of the batteries. So, for the SOC estimation in this method continuously measures the cell voltage and proportionally gets the SOC from the table. But practically, this method has some built in problem as it requires longer rest period for the equilibrium condition and for the precise voltage evaluation and the sensors require high level of resolution. Due to hysteresis property of batteries, OCV rises highly while charging and slows down while discharging, hence special attention required while calculating the charging/discharging voltage [6]. However, this method can be merged with other methods and noise-filtering techniques to measure CCM method shown in Eq. (1) [27].

Internal Resistance Method (IR)

The internal resistance which is a DC resistance is the ratio of voltage and current variation over a small interval of time (≤ 10 ms), thus expressing the battery capacity in DC. So, by varying current over a small-time duration voltage is calculated and the battery capacity is expressed in DC. The small duration of time is taken to express the ohmic reaction and the polarization effect [1]. And if the duration becomes more than 10 ms, then error occurs in the computed resistance value. Further, with a wide range of SOC value, there is a marginal change in the internal resistance, hence causing problem while examining. Though its highly precise and provides fine workability while estimating the SOC but this is possible only during the end duration of discharging [28]. Because of all these reasons, this method is rarely in use for the SOC computation.

4.2 Adaptive Filter Method

Kalman Filter Method (KF)

A highly developed and vastly explored method capable of eliminating the various undefined imprecise constraints irrespective of its huge computational cost is currently growing strong enough. Due to its self-correcting property one of its significant properties, it can bear a huge current variation. It is used in the field of aerospace, automobile technologies, navigator tracking, and radar tracking. It uses mathematical equations in state space form which forecasts and improves the current state repeatedly during the operation and assesses the cell dynamics in the discrete-time form. This method treats each cell as a dynamic system consisting of cell temperature and current as input and output is the terminal voltage. Basically, the main aim is to put required unknown parameter in the form of state vector x_k and this will lead KF to instinctively figure out the best approximate of its current value. Here, as a state in the vector x_k , SOC needs to be involved and in the derivation of the equation w_k and v_k are taken as mutually uncorrelated white Gaussian random process with zero mean and covariance matrices. For the estimation of SOC, this method presents a recursive solution by using linear optimal filtering. To find minimum mean squared deviation of true state, a comparison between input and output is done. This model comprises

of a process equation which forecasts the present state x_k from previous state x_{k-1} , and another is a measurement equation this upgrades present state to merge with its real value [7].

State equation: $x_{k+1} = A_k x_k + B_k u_k + w_k$.

Measurement equation: $y = C_k y_k + D_k u_k + v_k$.

where x represents the system state, u represents control input, w is the process noise, y is the measurement input, v is the measurement noise, and A , B , C , D represent covariance matrices varying with time and explain the dynamics of battery.

In [29], the BMS which consists of an RC model of battery in the designing of KF is used. By transforming the mathematical equations obtained from the RC model to state space form, hence describing the dynamic features of the battery. The estimated root mean squared (RMS) error (1.92×10^{-4}) from the result comes out to be very small in comparison with the measured error (91.0013 V). In [30], the results of KF with OCV are merged and CCM is implemented to rectify the undesirable elements affecting the battery operation. So, the use of KF, hence enhanced the precision of SOC by CCM in the battery leading to an error of $\pm 1.76\%$.

This method has an advantage that it precisely estimates the states troubled by extrinsic disruption like noise controlled by Gaussian distribution. But for the estimation of states of nonlinear system, it cannot be used, and the computation of the mathematical equation becomes very complicated.

Extended Kalman Filter Method (EKF)

Since battery has nonlinear characteristic KF operates better for linear system, hence an improved version of KF, i.e., use of KF with linear time-varying system known as EKF method is introduced. It operates in nonlinear system without the use of initial SOC value. The battery model is linearized using first order Taylor series and partial differential equation. At every interval of time state space model is linearized, hence equating the estimated value with the measured battery terminal voltage to rectify the estimated variables for SOC. But when the situation arises of extreme nonlinearity, the precision level decreases since first order Taylor series does not operate properly in a highly nonlinear conditions leading to linearization error [8]. The EKF algorithm is shown in Fig. 5, [31]. In [10], EKF with a nonlinear battery model is used for the computation of SOC. The nonlinear model comprises of a second order RC network with a nonlinear OCV connected in series, hence decreasing the consequences of process and measurement noise. This model results produce increased accuracy for the SOC estimation with unspecified initial SOC value.

4.3 Learning Algorithm

Neural Network

It is a very ingenious mathematical tool having high flexibility and self-directed learning ability for signifying the complex nonlinear model. It does not rely upon

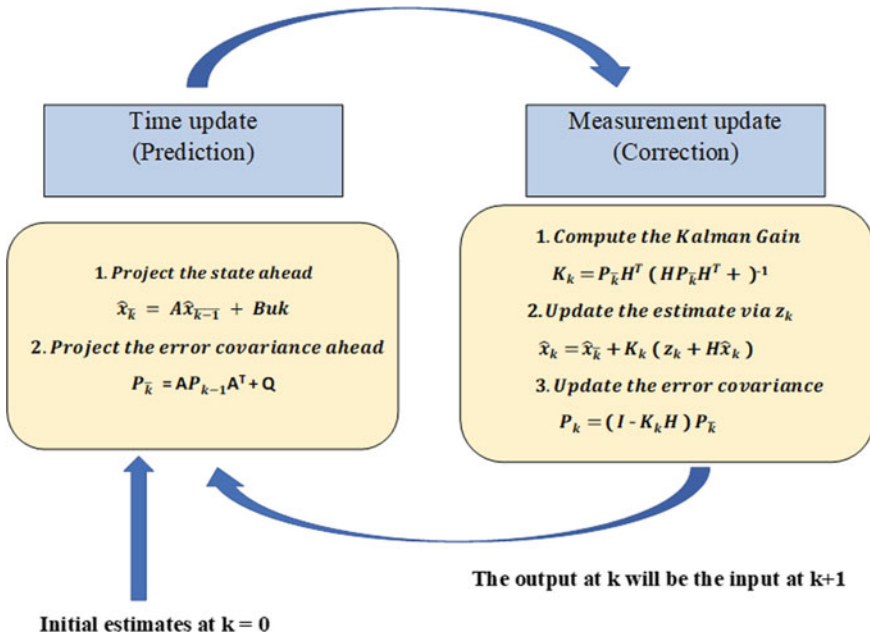


Fig. 5 Operation of EKF

internal battery state or initial SOC value whereas makes use of the trained data for the estimation of SOC. It comprises of three layers one is input layer, output layer, and one or more hidden layer as illustrated in Fig. 6, [11]. It uses terminal voltage, temperature, and discharging current as the input and output as SOC for the formation of NN of Li-FePO₄ battery. It is efficient enough to operate effectively in nonlinear state of battery during battery charging/discharging. But this method needs prominent storage system. Since, training requires storage of considerable volume of statistics, thus overburdening the whole system. In [32], proposed a battery model based on EKF and involving the hysteresis effect on OCV. Then, SOC is estimated by joining the NN with EKF, thus providing better results while estimating the precision level producing an error just less than 1%. In [33], radial basis function NN (RBFNN) is proposed when the system consists of insufficient data information while estimating the SOC. So, it comes out to be a very convenient mathematical tool. Hence, while forming a battery model considering process speed and precision this method comes out to be very productive.

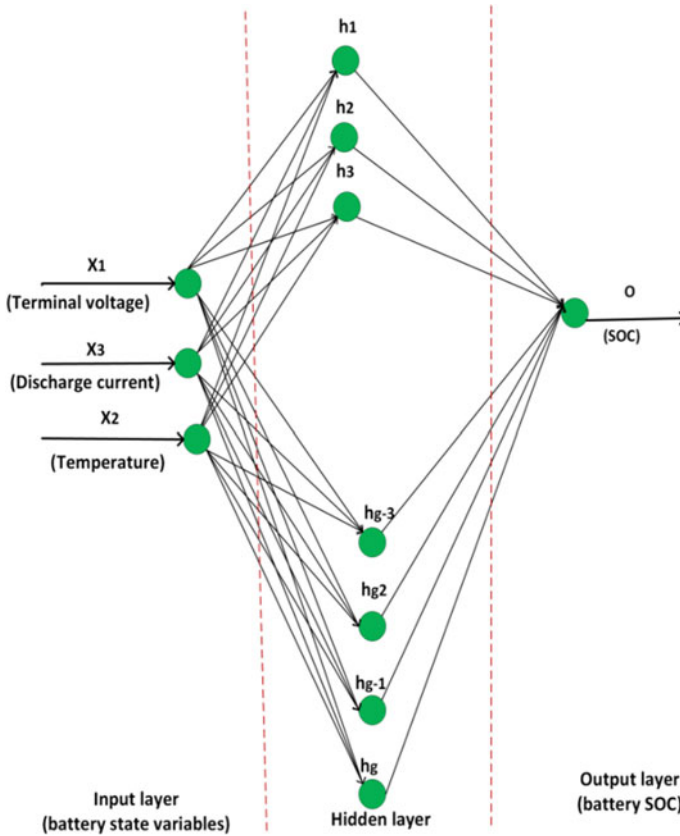


Fig. 6 Neural network diagram

5 Conclusion and Recommendation

This paper critically reviews the different methods of SOC estimation and brings out the various issues associated with their application in the EVs. The use of Li-ion battery has been highly stressed upon in this paper because of their longer life span, high energy density, and high voltage generating capacity. The significance of BMS in the battery, its easy and reliable operation is also elucidated here. After analyzing the different methods, it has been founded that conventional methods are simple in application but temperature, aging, and other foreign factors affect them. Also, it has been observed that adaptive algorithm is able to evaluate the non-dynamic states of battery with high level of accuracy, low computational cost, and with increased efficiency. But this method is affected by the complex computation and poor robustness. Another approach is learning algorithm which efficiently operates in the nonlinear dynamic system keeping in view the noise, temperature, and aging factors, but it requires large memory storage system for the trained data and suffers

from complex computation. Due to the complex electrochemical reaction, higher vulnerability and different internal external factors of an Li-ion battery causing a serious problem in the accurate estimation of SOC.

Due to various external and internal factors such as electrochemical reaction taking place inside the battery causes difficulty estimation of SOC accurately which has become a very challenging task. So, this paper specifies the various reasons which are affecting the accuracy level of SOC estimation. Hence, this will provide help to the automotive manufacturers to recognize suitable estimation method for the implementation and the researchers to find better solutions in reducing these issues.

References

1. Hannan MA, Lipu MSH, Hussain A, Mohamed A (2017) A review of lithium-ion battery state of charge estimation and management system in electric vehicle applications: challenges and recommendations. *Renew Sustain Energy Rev* 78(2017):834–854
2. Anair D, Mahmassani A (2012) State of charge. electric vehicles. In: *Global warming emissions and fuel-cost savings across the United States*. Union of Concerned Scientists, Cambridge, MA. Retrieved from http://www.ucsusa.org/assets/documents/clean_vehicles/electric-car-globalwarming-emissions-report.pdf
3. Liu K, Li K, Peng Q, Zhang C (2019) A brief review on key technologies in the battery management system of electric vehicles. *Front Mech Eng* 14(1):47–64
4. Rivera-Barrera JP, Muñoz-Galeano N, Sarmiento-Maldonado HO (2017) SoC estimation for lithium-ion batteries: review and future challenges. *Electronics* 6(4):102. <https://doi.org/10.3390/electronics6040102>
5. Zhang R, Xia B, Li B, Cao L, Lai Y, Zheng W, Wang H, Wang W, Wang M (2018) A study on the open circuit voltage and state of charge characterization of high-capacity lithium-ion battery under different temperature. *Energies* 11(9):2408
6. Roscher MA, Sauer DU (2011) Dynamic electric behavior and open-circuit-voltage modeling of LiFePO₄-based lithium-ion secondary batteries. *J Power Sources* 196(1):331–336
7. Xu L, Wang J, Chen Q (2012) Kalman filtering state of charge estimation for battery management system based on a stochastic fuzzy neural network battery model. *Energy Convers Manage* 53(1):33–39
8. Hu X, Sun F, Zou Y (2013) Comparison between two model-based algorithms for Li-ion battery SOC estimation in electric vehicles. *Simul Model Pract Theory* 34:1–11
9. He H, Xiong R, Zhang X, Sun F, Fan JinXin (2011) State-of-charge estimation of the lithium-ion battery using an adaptive extended Kalman filter based on an improved Thevenin model. *IEEE Trans Veh Technol* 60(4):1461–1469
10. Zhu Q, Xiong N, Yang M-L, Huang R-S, Guang-Di H (2017) State of charge estimation for lithium-ion battery based on nonlinear observer: an H ∞ method. *Energies* 10(5):679
11. He W, Williard N, Chen C, Pecht M (2014) State of charge estimation for Li-ion batteries using neural network modeling and unscented Kalman filter-based error cancellation. *Int J Electr Power Energy Syst* 62:783–791
12. Huang D, Feng D (2009) The prediction of SOC of lithium batteries and varied pulse charge. In: *2009 International conference on mechatronics and automation*. IEEE, pp 1578–1582
13. Antón JCA, Nieto PJG, de Cos Juez FJ, Lasheras FS, Vega MG, Gutiérrez MNR (2013) Battery state-of-charge estimator using the SVM technique. *Appl Math Modell* 37(9):6244–6253
14. Cheng KWE, Divakar BP, Wu H, Ding K, Ho HF (2010) Battery-management system (BMS) and SOC development for electrical vehicles. *IEEE Trans Veh Technol* 60(1):76–88
15. Xu J, Cao B, Chen Z, Zou Z (2014) An online state of charge estimation method with reduced prior battery testing information. *Int J Electr Power Energy Syst* 63:178–184

16. Xing Y, Ma EWM, Tsui KL, Pecht M (2011) Battery management systems in electric and hybrid vehicles. *Energies* 4(11):1840–1857
17. Yanli L, Sheng CZD (2014) Estimation of state of charge of lithium-ion battery based on finite difference extended Kalman filter. *Trans China Electrotech Soc* 29(1):221–228
18. Meyer M, Komsiyiska L, Lenz B, Agert C (2013) Study of the local SOC distribution in a lithium-ion battery by physical and electrochemical modeling and simulation. *Appl Math Model* 37(4):2016–2027
19. Waag W, Fleischer C, Sauer DU (2014) Critical review of the methods for monitoring of lithium-ion batteries in electric and hybrid vehicles. *J Power Sources* 258(2014):321–339
20. Meng J, Luo G, Ricco M, Swierczynski M, Stroe D-I, Teodorescu R (2018) Overview of lithium-ion battery modeling methods for state-of-charge estimation in electrical vehicles. *Appl Sci* 8(5):659
21. He H, Xiong R, Fan J (2011) Evaluation of lithium-ion battery equivalent circuit models for state of charge estimation by an experimental approach. *Energies* 4(4):58–598
22. Wu B, Chen B (2014) Study the performance of battery models for hybrid electric vehicles. In: 2014 IEEE/ASME 10th international conference on mechatronic and embedded systems and applications (MESA). IEEE, pp 1–6
23. Feng J, He YL, Wang GF (2013) Comparison study of equivalent circuit model of Li-ion battery for electrical vehicles. *Res J Appl Sci Eng Technol* 6:3756–3759
24. Fang J, Qiu L, Li X (2017) Comparative study of Thevenin model and GNL simplified model based on kalman filter in SOC estimation. *Int J Adv Res Comput Eng Technol* 6(2017):1660–1663
25. Hannan MA, Azidin FA, Mohamed A (2014) Hybrid electric vehicles and their challenges: a review. *Renew Sustain Energy Rev* 29(2014):135–150
26. Ng KS, Moo CS, Chen YP, Hsieh YC (2009) Enhanced coulomb counting method for estimating state-of-charge and state-of-health of lithium-ion batteries. *Appl Energy* 86(9):1506–1511
27. Truchot C, Dubarry M, Liaw BY (2014) State-of-charge estimation and uncertainty for lithium-ion battery strings. *Appl Energy* 119(2014):218–227
28. Lu L, Han X, Li J, Hua J, Ouyang M (2013) A review on the key issues for lithium-ion battery management in electric vehicles. *J Power Sources* 226:272–288
29. Ting TO, Man KL, Lim EG, Leach M (2014) Tuning of Kalman filter parameters via genetic algorithm for state-of-charge estimation in battery management system. *The Scien World J* 2014
30. Yatsui MW, Bai H (2011) Kalman filter based state-of-charge estimation for lithium-ion batteries in hybrid electric vehicles using pulse charging. In: 2011 IEEE vehicle power and propulsion conference. IEEE, pp 1–5
31. Plett GL (2004) Extended Kalman filtering for battery management systems of LiPB-based HEV battery packs: part 3. State and parameter estimation. *J Power Sources* 134(2):277–292
32. Chen Z, Qiu S, Masrur MA, Murphey YL (2011) Battery state of charge estimation based on a combined model of Extended Kalman Filter and neural networks. In: The 2011 international joint conference on neural networks. IEEE, pp 2156–2163
33. He W, Salkind AJ, Craig F, Pritpal S, Terrill A, Reisner DE (1999) Determination of state-of-charge and state-of-health of batteries by fuzzy logic methodology. *J Power Sources* 80(1–2):293–300

Various Machine Learning Techniques to Diagnose Alzheimer's Disease—A Systematic Review



Narmada Kari, Sanjay Kumar Singh, and S. Velliangiri

Abstract Alzheimer's disease (AD) is a variety of diseases related to dementia. This disease is very dangerous since it can cause death to the patient gradually if time is moved on. There is no medicine or treatment to cure this disease completely. AD is a neurodegenerative disease. This is mostly affected to the elder age people. Initial diagnosis is very important for AD. There are several treatments available but none of them cures completely. Image processing plays a vital role here. Always the combination of brain imaging and clinical treatment helped the medical technology or patients to move further. This paper gives a survey of some of the best papers written from 2005 to 2021. This paper reviews various techniques, where authors used for feature extraction and the machine learning process. This paper also discusses the results obtained using various techniques.

Keywords (MRI) "Magnetic resonance imaging" · (PET) "Positron emission tomography" · (DTI) "Diffusion tensor imaging" · (MCI) "Mild cognitive impairment" · (SVM) "Support vector machine" · (ANN) "Artificial neural network"

1 Introduction

Alzheimer's disease (AD) is the most powerful disease which affects humans. Approximately, 100 million populations are affected by this disease by 2021. This can be exponentially increased by 2050 [1, 2]. Generally, AD is affected after 60 years of age but recently, cases are noted between 30 and 50 years of age also. AD can be viewed in the young age having gene mutation. AD is mainly affected by the brain [3–5]. All the structural and functional operations in the brain will be affected.

N. Kari (✉) · S. K. Singh
Amity University Rajasthan, Jaipur, Rajasthan, India
e-mail: narmadakari@gmail.com

S. Velliangiri
B V Raju Institute of Technology, Narasapur, Telangana, India

(MCI) “mild cognitive impairment” is the starting stage of AD, but not all MCI affected patients are affected by AD. The conversion of patients from MCI to AD is done by medical imaging and (BPS) “blood plasma.” To perform any research database is important. There are many databases available on AD [6–9]. The most commonly used databases are ADNI, AIBL, OASIS, and J-ADNI. These databases have longitudinal and structural studies. Operating MRI images are very difficult, so an open-source excellent software was designed named SPM “statistical parametric mapping” which helped many researchers to obtain prominent results in this area. This software was developed by (WCH) “Welcome Center for Human.” SPM is used for (VBM) “voxel-based morphometric data.”

According to the International Diabetes Federation, around 463 million people between the ages of 20 and 79 are affected by diabetes in 2019. Depression affects diabetic patients, causing nerve damage. From the past decade, machine learning techniques also played a vital role in treating AD. There are many classification techniques available but the most commonly used techniques are (SVM) “support vector machine,” (ANN) “artificial neural networks,” and (DL) “deep learning,”

The variation between the SVM and ANN is global and local optimization. Feature extraction and classification are important steps in any technique [11–13]

These combinations help to analyze the image easily. If the database is very large, then deep learning is the best option for image analysis. Many researchers use ensemble methods for obtaining greater accuracy. The MRI image is a three-dimensional structure so the MRI dataset is high [14–17]. So to operate MRI image, efficient techniques are required for accurate results [3, 18, 19]. Advanced feature extraction and classification techniques are used for image analysis. Recently, many researchers used deep learning and provided the best results for AD. Some of authors and their results are discussed below.

Authors Litjens et al. published a survey paper on image analysis using deep learning. They concluded that even though deep learning is estimated as black boxes, many researchers used and obtained promising accuracy. They also stated that some statistical techniques are available to calculate the uncertainty of a network [1].

Shen et al. also published a review on AD with deep learning, which helped many new researchers to choose the techniques for their research [2].

Jose et al. worked on neurological imaging; they provided information about the techniques used for treating the disorders in the brain. They described that machine learning is accurate for neurological disorders in the brain. Many authors used this paper as a base paper for their research [3].

Pellegrini et al. worked on dementia and cognitive impairment. They reviewed machine learning techniques used to treat dementia and CI from 2006 to 2016. Many machine learning algorithms were used in between this period from various domains [4].

Rathore et al. also surveyed many papers and stated the suitable feature extraction and classification techniques used for treating and diagnosing AD [5].

This paper reviewed many selective papers and presented the techniques most commonly used.

- SVM
- ANN
- Ensemble methods.

This paper reviews the techniques used for the diagnosis of AD. The application-based survey is presented with ensemble methods.

2 SVM “Support Vector Machine”

SVM is the most commonly used technique in any dimensional data. This technique is used in image processing, speech processing, video processing, etc. SVM is used in classification and regression operations [7, 8]. (SRM) “structural risk minimization” can be combined with SVM and produce the best results. SVM always uses the theory of large margin for classification which is shown in Fig. 1. The decision function is given in the expression as

$$f(y) = \text{sign}(w^T y + b) \tag{1}$$

w : weight vector b : bias function.

Many researchers use kernel functions for the classification of nonlinear inputs. Factors like time are taken for training and ability of generalization were further increased by changing the factors in SVM or combining various factors with SVM. Some of the other efficient technique in SVM is (TWSVM) “twin support vector machine,” (LSTSVM) “least square-based support vector Machine,” etc. [20]. These algorithms helped the researchers to get prominent results in the treatment of AD. The detailed kernel classification is shown in Fig. 2. And the authors used SVM for the diagnosis of AD with various modality, and feature extraction techniques are given in Table 1.

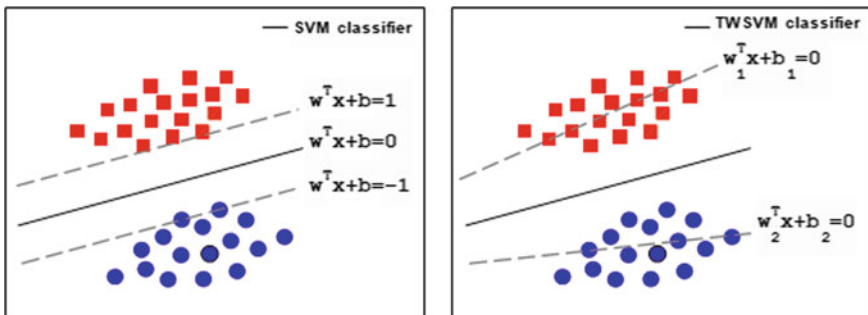


Fig. 1 Plot showing SVM and TWSVM classification

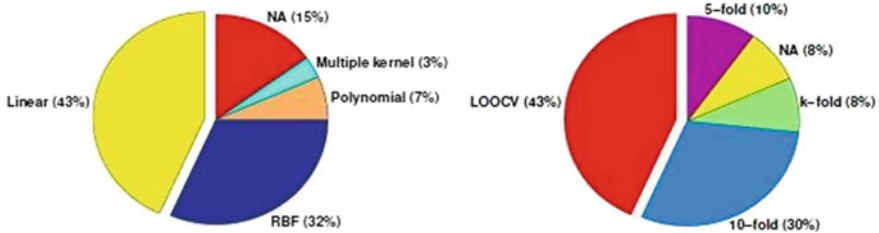


Fig. 2 Kernel classifications

The table also describes the datasets and accuracy obtained through suitable techniques. In Fig. 2, the NA is not an available kernel, polynomial is used for multiple classifications of AD. Data overfitting is done by using (RBF) “radial base function.” A linear kernel is very simple to classify. (LOOCV) “leave one out cross-validation” is also a classification technique used by SVM in AD. Folds are used for classification, where generally 5 or 10 is used. k -fold is where k is an integer from 1 to 20.

3 ANN “Support Vector Machine”

ANN is the most common technique used in recognition, segmentation, representation, etc. ANN is very widely used by many researchers. In ANN, the most advanced machine learning algorithms are applied. If the data is nonlinear, easily it can be modeled by ANN [7]. The review of a few papers is given in Table 1. The most common algorithms used for AD are given as

- MTL “Multi-task learning”
- MKL “Multi-kernel learning.”

FNN is where the data is passed from input to output from the hidden layers. RN is where the outputs are dependent on the present and past inputs. There are some feedback connections in the network. Deep neural network architecture is considered for the diagnosis of AD.

4 DL “Deep Learning”

Deep learning is an advanced technology used in almost all fields. This works on a multi-layered network as shown in Fig. 3. The data is trained in complex structures. Deep learning is classified into two types.

- FFN “Feedforward networks”

Table 1 Comparison of papers on SVM, for diagnosis of AD

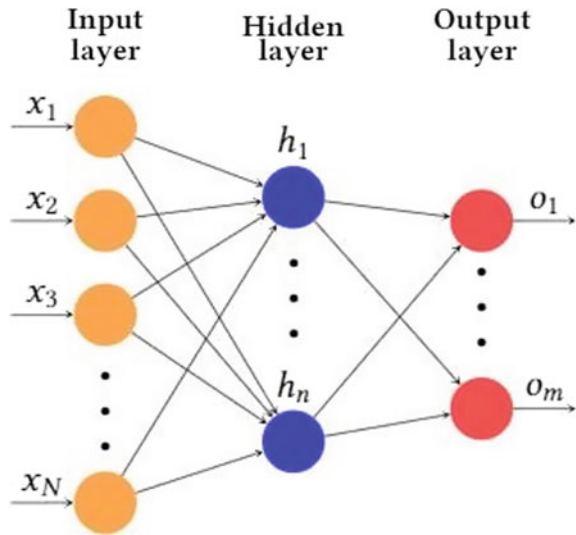
S. No	Authors	Modality	Extraction of features	Machine learning	Dataset	Validation	Performance			Year
							Acc (%)	Sens (%)	Spec (%)	
1	Richhariya et al. [6]	Audio or speech signal	MFCC	USVM	75 CN-50 MCI-25	fivefold	92	-	85	2020
2	Gabor et al. [7]	Audio or speech signal	MFCC	SVM (Linear)	75 CN-50 MCI-25 MAD-25	fivefold	80	-	75.9	2019
3	Jinhua et al. [8]	fMRI	RF-score	SVM	96 CN-24 eMCI-24 IMCI-24 AD-24	fivefold	93.8	-	-	2019
							95.8			
							95.8			
							87.5			
91.7										
4	Peng et al. [9]	sNP + PET + SMRI	VM + IF	SVM multiple kernel	189 CN-47 eMCI-93 AD-49	tenfold	96.1	97.3	94.9	2019
5	Zhang et al. [10]	DTI	LDH + SVM + RFE	SVM linear	75 CN-24 eMCI-75 IMCI-39 AD-48	LOOCV	89.9	-	-	2018
							100			
							92.98			
							97.7			
6	Paraskevaidi et al. [11]	Blood plasma	PCA-LDA	SVM	41 CN-15 eAD-11 IAD-15	LOOCV	-	84	86	2018
								84	77	

(continued)

Table 1 (continued)

S. No	Authors	Modality	Extraction of features	Machine learning	Dataset	Validation	Performance			Year					
							Acc (%)	Sens (%)	Spec (%)						
7	Mazaheri et al. [12]	EEG	TFRs	SVM RBF	36 CN-11 Meinc-10 Mele-15	LOOCV	-	80	95	2018					
											sMRI (T1)	PCA + PSO	361 CN-92 sMCI-82 pMCI-95	tenfold	69.23
															76.92
		85.71													
		57.14													

Fig. 3 Deep learning



- RN “Recurrent networks” (Table 2).

5 Ensemble Methods

The discussed three techniques come under ensemble methods. Figure 4 shows (LOOCV) “leave one out cross-validation” which is also a classification technique used by SVM in AD. Folds are used for classification where generally 5 or 10 is used. k -fold is where k is an integer from 1 to 20.

Best papers who worked on fMRI, PET, sMRI, SPECT, MRI, MRI+PET, and others are shown in the chart. Many researchers worked on sMRI [7].

The various modalities used by the researchers are shown in Fig. 4. Complex networks are used and stated as

- SAE “Stacked autoencoders”
- DBN “Deep belief networks”
- CNN “Convolutional neural networks.”

6 Research Gap

As 52 papers are reviewed and in which around 20 papers are compared with the parameters like modality technique, feature extraction technique, machine learning, dataset, validation, performances, and published year. After the analysis of the research, a wide gap can be observed to diagnose AD by using various techniques.

Table 2 Comparison of papers on ANN, for diagnosis of AD

S. No.	Authors	Modality	Extraction of features	Machine learning	Dataset	Validation	Performance			Year
							Acc (%)	Sens (%)	Spec (%)	
1	Fritsch et al. [13]	Linguistic data	n-gram	LSTM	266 CN-98 AD-168	LOOCV	85.6	–	–	2019
2	Subrata et al. [14]	CT	ROI	ANN	20 CN-11 AD-9	–	100	100	100	2019
3	Cui et al. [15]	sMRI (T1)	VBM	ANN + BGRU	427 CN-229 AD-128	fivefold	89.69	86.87	92.58	2018
4	Van Veen et al. [16]	FDG + PET	VBM	LGMLVQ	304 CN-82 PD-146 AD-76	–	–	79.23 91.47 84.7	68.15 91.45 86.63	2018
5	Zhou et al. [17]	sMRI (T1)	Atlas	TrAdaBoost	543 CN-103 MCI-245 AD-195	–	93.75 95.2	87.5 95.2	100 95.3	2018
6	Cheng et al. [18]	sMRI (T1)	VBM	rMLTFL	543 CN-103 MCI-245 AD-195	tenfold	82.4 76.3 76.7	86.7 73.4 61.4	73.8 78.6 81.8	2018

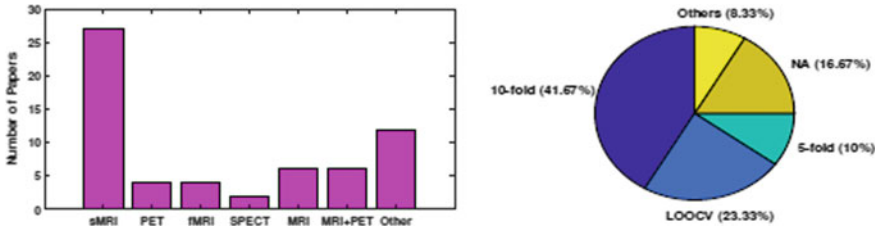


Fig. 4 Image modalities and cross-validation

One of the areas is SVM, here many authors used SVM but still, there is a need to improve the performance by using advanced methodology and algorithms. So this paper suggests to use any SVM technique on any type of image which can provide the best results. Various models of SVM can be used like admin SVM, data SVM, node SVM, system SVM, etc.

7 Proposed Methodology

Firstly, AD image is fixed and the image is converted to a 2D or 3D grayscale. The image is further promised results segmented to the particular area where the segmentation is needed, i.e., where the area is affected by AD. Next, the segmented image is processed and some features are extracted and stored. The extracted features are trained for further classification. As all the features are not used techniques like PCA, etc., can be used to select or reduce the features. Lastly, the features are classified and accuracy can be calculated. Many algorithms can be used for all these processes but suitable techniques need to be considered for obtaining.

8 Future Scope

Targets are very important in the research. One of the basic targets is MCI versus AD. Many researchers worked on CN versus MCI and other possible combinations but very few researchers focused on MCI versus AD. So there is a future scope on this target for the performance evaluation. New researchers should focus on AD which occurs at a young age individually; the AD can be different so the diagnosis needs to be done on individuals. The researchers need to create a database of similar symptoms of AD to treat it easily. This is named a multi-modal diagnosis. They should even consider real-time problems and treatment that need to be done. Denoising techniques can be added to remove the noise in the AD images to 3D images from 2D images which give a clear view of the areas affected by AD.

9 Conclusion

This paper reviews the diagnosis of AD based on SVN, ANN, DL, and ensemble techniques. Various kernel functions are discussed. Other learning methods are briefed while applying MRI images. This research is very needful for beginners to start their research. As per the results, SVM is very commonly used and obtained optimal results. ANN is versatile. DL is more flexible and can be easily used for any type of inputs. Compared to ANN, DNN the SVM is more user-friendly and can be interfaced with any modules. Feature selection and feature reduction are also easy using SVM. A researcher needs to divide the extraction, selection, and classification process equally.

References

1. Litjens G, Kooi T, Bejnordi BE, Setio AAA, Ciompi F, Ghafoorian M, Laak JAVD, Van Ginneken B, Sanchez CI (2017) A survey on deep learning in medical image analysis. *Med Image Anal* 42(2017):60–88
2. Shen D, Guorong W, Suk H-I (2017) Deep learning in medical image analysis. *Annu Rev Biomed Eng* 19(2017):221–248
3. Mateos-Perez JM, Dadar M, Lacalle-Aurioles M, Iturria-Medina Y, Zeighami Y, Evans AC (2018) Structural neuroimaging as clinical predictor: a review of machine learning applications. *NeuroImage: Clin*
4. Pellegrini E, Ballerini L, Del Maria C, Hernandez V, Chappell FM, Gonzalez-Castro V, Anblagan D, Danso S, Munoz-Maniega S, Job D, Pernet C et al (2018) Machine learning of neuroimaging for the assisted diagnosis of cognitive impairment and dementia: a systematic review. *Alzheimer's Dementia: Diag Assess Dis Monit* 10(2018):519–535
5. Rathore S, Habes M, Iftikhar MA, Shacklett A, Davatzikos C (2017) A review on neuroimaging-based classification studies and associated feature extraction methods for Alzheimer's disease and its prodromal stages. *Neuroimage* 155(2017):530548
6. Richhariya B, Tanveer M, Rashid AH (2020) Diagnosis of Alzheimer's disease using Universum support vector machine-based recursive feature elimination (USVM-RFE). *Biomed Sig Process Control* 59:101903. ISSN 1746-8094. <https://doi.org/10.1016/j.bspc.2020.101903>
7. Gosztolya G, Vincze V, Toth L, Pakaski M, Kalman J, Hoffmann I (2019) Identifying mild cognitive impairment and mild Alzheimer's disease based on spontaneous speech using ASR and linguistic features. *Comput Speech Lang* 53(2019):181–197
8. Sheng J, Wang B, Zhang Q, Liu Q, Ma Y, Liu W, Shao M, Chen B (2019) A novel joint HCPMMP method for automatically classifying Alzheimer's and different stage MCI patients. *Behav Brain Res*
9. Peng J, Zhu X, Wang Y, An L, Shen D (2019) Structured sparsity regularized multiple kernel learning for Alzheimer's disease diagnosis. *Pattern Recogn* 88:370–382
10. Zhang Y-T, Liu S-Q (2018) Individual identification using multi-metric of DTI in Alzheimer's disease and mild cognitive impairment. *Chin Phys B* 27(8):088702
11. Paraskevaidi M, Morais CLM, Halliwell DE, Mann DMA, Allsop D, Martin-Hirsch PL, Martin FL (2018) Raman spectroscopy to diagnose Alzheimer's disease and dementia with Lewy bodies in blood. *ACS Chem Neurosci* 9(11):2786–2794
12. Mazaheri A, Segaeert K, Olichney J, Yang J-C, Niu Y-Q, Shapiro K, Bowman H (2018) EEG oscillations during word processing predict MCI conversion to Alzheimer's disease. *Neuroimage: Clin* 17:188–197; Bi X, Shu Q, Sun Q, Xu Q (2018) Random support vector machine cluster analysis of resting-state fMRI in Alzheimer's disease. *PloS one* 13(3):e0194479

13. Fritsch J, Wankerl S, Noth E (2019) Automatic diagnosis of Alzheimer's disease using neural network language models. In: ICASSP 2019–2019 IEEE international conference on acoustics, speech, and signal processing (ICASSP). IEEE, pp 5841–5845; Cabral C, Morgado PM, Costa DC, Silveira M, Alzheimer's Disease Neuroimaging Initiative et al (2015) Predicting conversion from MCI to AD with FDG-PET brain images at different prodromal stages. *Comp Biol Med* 58:101–109
14. Kar S, Majumder DD (2019) A novel approach of diffusion tensor visualization based neuro fuzzy classification system for early detection of Alzheimer's disease. *J Alzheimer's Dis Rep Prepr* 1–18
15. Cui R, Liu M, Li G (2018) Longitudinal analysis for Alzheimer's disease diagnosis using RNN. In: 2018 IEEE 15th international symposium on biomedical imaging (ISBI 2018). IEEE, pp 1398–1401
16. van Veen R, Martinez LT, Kogan RV, Meles SK, Mudali D, Roerdink JBTM, Massa F, Grazzini M, Obeso JA, Rodriguez-Oroz MC et al (2018) Machine learning-based analysis of FDG-PET image data for the diagnosis of neurodegenerative diseases. In: APPIS, pp 280–289
17. Zhou K, He W, Xu Y, Xiong G, Cai J (2018) Feature selection and transfer learning for Alzheimer's disease clinical diagnosis. *Appl Sci* 8(8):1372
18. Cheng B, Liu M, Zhang D, Shen D, Alzheimer's Disease Neuroimaging Initiative et al (2018) Robust multi-label transfer feature learning for early diagnosis of Alzheimer's disease. *Brain Imag Behav*:1–16
19. Shen D, Wu G, Suk H-I (2017) Deep learning in medical image analysis. *Ann Rev Biomed Eng* 19:221–248
20. Cortes C, Vapnik V (1995) Support vector machine. *Machine Learn* 20(3):273–297

Technical Aspect of Water Resource Management of Aligarh District



Nazish Mohammad, Mahfooz Alam, and Mubeen Beg

Abstract For ages, water resource systems have helped both people and the economy. These systems provide a wide range of services. Despite this, many parts of the globe are unable to fulfill even the most basic drinking water and sanitation demands. Many of these water resource systems are also incapable of supporting and maintaining robust biodiverse ecosystems. The primary goal of this interdisciplinary study is to evaluate the technical aspects of water resource management in Aligarh, a district of Uttar Pradesh, India, by examining how water resources can be managed while taking anthropogenic factors (population, economic growth, and stability) and environmental constraints into account (climate change). A concerted effort is being undertaken to establish the city's water resource management demands as well as alternative possibilities for effective water resource management. One of the main features of this article is the comparison between the city's total water demand versus total availability from various sources, as well as their quality. Most of the data were gathered from the UP Jal Nigam, Aligarh, and the Aligarh Municipal Corporation.

Keywords Water management · Gap bridging · Aligarh · Jal Nigam Aligarh · Nagar Nigam Aligarh · Public demand · Quality parameters · Safety limits

N. Mohammad (✉) · M. Alam · M. Beg
Civil Engineering Department, Zakir Husain College of Engineering and Technology, Aligarh
Muslim University, Aligarh, India
e-mail: nazishmohammad2013@gmail.com

M. Alam
e-mail: mahfooz.aalam123@gmail.com

M. Beg
e-mail: raisbeg2013@gmail.com

1 Introduction

Water, a valuable natural resource, is essential for the existence of life on Earth. Water is required for irrigation, electricity generation, navigation, industry, residential needs, and wildlife. Inadequate water resources endanger the ecology. Crops, plants, woods, vegetative cover, and pasture are all water dependent. Furthermore, assessing water quality is critical for determining the appropriateness of various applications. A good irrigation system makes a country self-sufficient in terms of its people's food needs. A poorly managed water supply may cause socioeconomic difficulties. People-to-people, region-to-region, and country-to-country conflicts over water resources strain tie and cause political and socioeconomic issues. Aligarh district is in western Uttar Pradesh and encompasses a tiny portion of the Ganga-Yamuna Doab. It is located between latitudes 27035' and 28010' N and longitudes 770 29' 00'' and 780 36' 00'' E, and is part of the India Toposheet Nos. 53H, L, and 54E surveys. The district's northern boundary is parallel to the Bulandshar district. In the northeastern part of the district, the Ganga River creates a natural boundary between Aligarh and Budaun, while the Yamuna in the northwest defines the state border between Uttar Pradesh and Haryana. The Aligarh district has a total area of 3650 km², which is split into five tehsils and 12 community development units. There are 122 Nyay Panchayats in the district, with 855 g Sabhas, and 1210 villages. Santhana Bosu [1], Gupta et al. [2], Pradhan et al. (2001), Mahapatra and Mishra [3], Rahman [4], Khan [5], Beg and Khan [6], Chatterjee and Jha [7], and others have suggested various solutions and techniques for water conservation via direct rainwater conservation, in situ moisture conservation, water harvesting and using irrigation technology for harvested water, and through agronomic and engineered solutions. The water issue is not a passing occurrence to be dealt with in the manner of a crisis management approach. It needs long-term and sustainable solutions that go beyond the tenure of decision-makers in government (Wim van der Hoeck 2001) (Fig. 1, Map of District Aligarh).

1.1 *Population Growth of Aligarh and Increasing Demand for Water*

The number of inhabitants of Aligarh in 2021 is expected to be 1,244,591. Aligarh had a headcount of 139,477 people in 1950. Aligarh has increased by 34,037 people during 2015, a 2.81% yearly increase. The latest release of the UN World Urbanization Prospects presents these population figures and forecasts. The district's water demand is quickly increasing as a result of this rapid population boom, and the city's water consumption has changed radically, posing a serious threat to several sections of Aligarh. It necessitates careful planning and implementation of appropriate strategic alternatives. The paradigm shift from water resource development to water resource management is better realized through reorganizing and strengthening



Fig. 1 Administrative map of district Aligarh

existing institutions for optimal service delivery and resource sustainability. An integrated approach to water resource management is currently becoming popular. It must change its service delivery plan to comply with the national water policy of 2002, which focuses on providing everyone with safe and sufficient drinking water. Prioritize rainwater collecting and conservation, followed by technical treatment alternatives and institutional measures for better local management (Fig. 2, <https://www.census2011.co.in/census/city/112-aligarh.html#:~:text=As%20per%20provisional%20reports%20of,males%20and%20430%2C016%20are%20females>).

1.2 A Framework of the City’s Water Resource Management

Two different government bodies are responsible for various activities performed within the city. They often share each project and development scheme and cooperate to secure the proper functioning of water distribution and its management. But, in a broader way, each government body serves different roles of water resource management and planning, briefly explained below in the table.

Planning and design	Construction	O&M
UP Jal Nigam Aligarh	UP Jal Nigam Aligarh	Nagar Nigam Aligarh

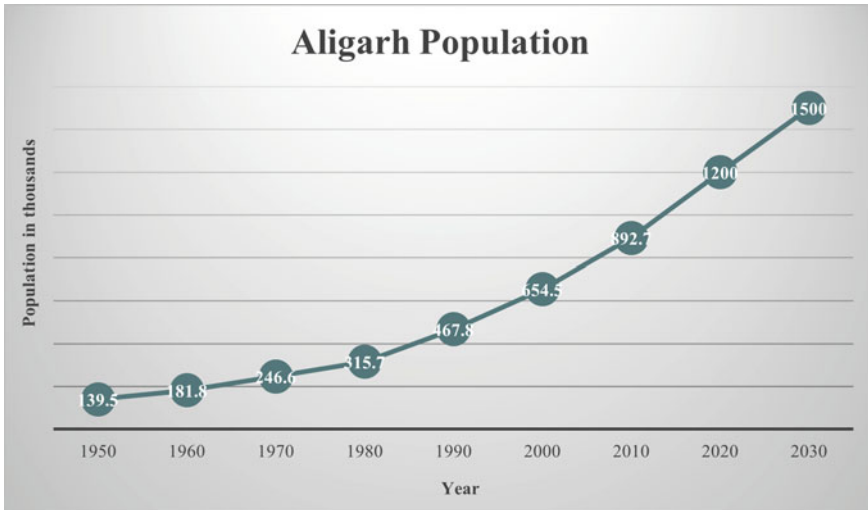


Fig. 2 Year-wise population of Aligarh

The projects will be carried out by the nodal agency Jal Nigam Aligarh, in compliance with orders from the state government and the Government of India, and minor projects, such as branch lines and pipeline gaps, will be carried out by Nagar Nigam Aligarh. The projects will be implemented by parastatal entities in accordance with federal and state government mandates. Nagar Nigam Aligarh will oversee smaller projects such as branch lines and pipeline gaps. The incorporation of various authorities might be one of the major causes of disputes in the city's water resource development schemes, as well as the several abandoned water projects, inefficiency, and delays in implementation. Once the difference between existing service levels has been calculated, objectives will be created to close the gaps in order to attain universal coverage. These objectives will be based on actions done in various ongoing programs and projects. This might include an assessment of the sector's present institutional structure. The data on each zone will be employed to determine the gaps. These zone-by-zone service gaps will be put together to yield district-level service gaps.

Aligarh city has 36.9% coverage of water supply connection having a mound benchmark of 100%, total supply at present is 88.32 MLD, supplying 90 LPCD having a mound benchmark of 135 LPCD. There is no system of metering of water supplied at present, and it is planned to achieve 100% metering by 2030. The quality of water is 88.32% as most of the water is taken from groundwater resources, and only, chlorination has to be done. There is a total of 92 tube wells catering to the demand of the district. The district is divided into 15 zones with a total of 127,789 households of which 52,830 households have tap water connections and 74,959 households are without tap water connections. The households with no tap water connection usually rely on submersible pumps and hand pumps for the withdrawal of water. District uses elevated reservoirs and direct pumping for the supply of water. Nagar Nigam Aligarh

has a water capacity of 88.32 MLD and a storage capacity of 25,030 KL; thus, there is a storage capacity disparity of 4410 KL in NNA. The overall length of the water supply pipeline in NNA is 721 km, while the total length of the road is 811 km, with a 90-km gap at the city level. Aligarh's city road length is 811 km. Pipelines have not been through every street. A 90-km pipeline is expected for universal water delivery coverage. A demand of 147.55 MLD currently exists, with a source imbalance of 33.31 MLD. New tube wells must be constructed to close the gap. A project called 24 new tube well 3 rebore is now underway at a cost of 9.29 crores. It was originally scheduled to be finished in 2017; however, owing to unforeseen circumstances, the project is still underway with an 80% completion status. Through well-planned information, education, and communication (IEC) programs, the Nagar Nigam Aligarh must make its people aware of the value of drinking water and make efforts by having meetings and registering water connections through advertisements. Due to damaged and leaky pipelines, there is a significant problem with non-revenue water (NRW). Proper and bad maintenance, a lack of management, and low-quality appurtenances beneath the earth are the most frequent cause. The district's NRW level is 21.40, and it needs to be decreased for the district's water supply system to perform and disperse efficiently. The Nagar Nigam Aligarh, on the other hand, is checking this to level 0.

1.3 Dynamics of Aligarh's Water Resource

Most of the city's demand is catered by groundwater reserves. There are few canals and river systems available in the Aligarh district. Due to scarcity of surface source, groundwater resource is depleted for domestic as well as industrial use. Dissection of Aligarh District shows that there is the availability of ponds, few canals, and no rivers to cater to the water demand which is explained from a column shown below (Fig. 3, showing surface source of water).

Most of the water supply plans and schemes are based on groundwater reserves. In the zone of saturation, groundwater is found in the pore spaces of fissure material. Groundwater in the Aligarh district occurs at shallow depths under water table conditions, while deeper aquifers are in a constrained state of disposition, with impenetrable clay beds functioning as confining layers. Due to excessive and continuous use of groundwater, its level fluctuates and worsens day by day. According to the report of National Hydrograph Stations last conducted in the year 2012, in most of the districts, a fall in water level can be seen which indicates the adversity of using groundwater use. Use also rapidly increased due to drastic changes in the district's population, resulting in heavy exhaustion of water reserves. There was a fall of around half a meter in groundwater level in 2012, but now, we have come too far, and it is 2021 and by observing all the factors like population growth, monsoon delay, climate change, less precipitation, urbanization, lack of management programs, and lack of awareness among people, would have caused a serious and drastic fall in groundwater level in the area. According to a pre-monsoon depth to water map based on National Hydrograph Stations and State Government Wells, depth to water ranges between

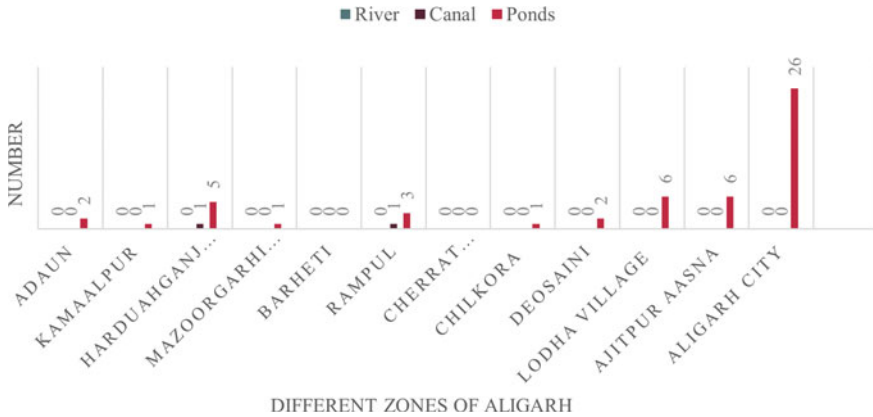


Fig. 3 Surface sources of water

2.50 and 12.56 m. Shallow water levels of 5–10 m may be found in the Jawain and Akrabad blocks of the Upper Ganga Canal, as well as the major branch canal in the Tappal, Khair and Gonda blocks. In the center section of the 16 districts, Aligarh town in Lodha block and Dhanipur block also had the deepest water level of more than 12 m. The water level in the rest of the area is 10–15 m below ground level. Water levels in the post-monsoon period range between 1.86 and 12.9 m below ground level, according to a perusal of post-monsoon data. In the eastern and western regions, the Ganga and Yamuna rivers, as well as the main canals and their distributaries, have water levels of less than 5 m (shallow). In Jawain block, along the Upper Ganga Canal, the lowest water level was 1.86 m below ground level. The water table varies in response to recharge or outflow from the phreatic aquifer. The aforementioned components have a direct effect on the quantity of fluctuation. The replenishment occurs mostly during the rainy season (June to September), whereas the withdrawal occurs during the rest of the year. These changes, however, are not proportional to the national level. These may be addressed by appropriate infrastructure, responsibility, and accountability inside the business in question, as well as public awareness.

2 Data Collection

In situ data are collected from various blocks of the district of Aligarh, which are Dhanipur, Jawan, Lodha, and Aligarh city. This data are collected in a well-organized pattern with a fixed interval of time. Data are solely based on study area details like extant water resource infrastructure, land use, population detail, number of schools, ponds, average annual precipitation, and water required for irrigation, industrial as well as domestic demand. The standard of living of the people of Aligarh is also considered while taking data from the field. Data were taken in several blocks of

Aligarh district for a qualitative investigation of different properties of local water, as portrayed in the figure. To have a better understanding of the locations of water resources within the focused area, information was gained from two government bodies, namely Jal Nigam Aligarh and Nagar Nigam Aligarh. Vikas Bhawan, Aligarh, and Tehsil Koil provided us about land use, the number of villages, the ratio of irrigated land to unirrigated land, barren land, the type of soil, the total area of Aligarh district, and most importantly, they provided us with a number of ponds and their location, tube wells, manual pumps, and municipally-owned water tanks.

2.1 Quantitative Analysis of Data

All the sources which contribute to the water demand of the district are collectively calculated and given in the table below, which was collected through in situ surveys all over the district, and results have been formed accordingly. The available quantity is calculated by dividing the groundwater availability by separate areas of concern. Aligarh is situated in the center of the Ganga plain in the Ganga–Yamuna interfluvial zone. The Upper Ganga canal, which runs from N–W to S–W on the drainage divide, breaks the district into two areas. The quantity of available water from 45 ponds in the district is derived from the data of Vikas Bhawan Aligarh and Tehsil Koil. The required quantity of water in the Aligarh district is the function of domestic water requirements like bathing, drinking, and washing, institutional requirements, public use requirements, industrial requirements, and the lifestyle of the population. Individual per capita demand in the district is 135 LPCD, conforming to the Indian standard code of “BASIC REQUIREMENTS FOR WATER SUPPLY, DRAINAGE, AND SANITATION” (IS1172:1993). However, Aligarh supplies only 90 LPCD to households based on their storage capacity, water deficiency, water distribution network, and lifestyle of people. Also, they have planned to reach the target of supplying 135 LPCD by 2023. They are introducing new projects and schemes to overcome this gap. While analyzing all the data, it should be kept in mind that Aligarh replenishes most of the water from groundwater resources alone. There are no significant contributions to rivers, lakes, and canals (Tables 1, 2, 3, 4, and 5).

Table 1 Collective data of Dhanipur block

S. No.	Villages	Available quantity (ha-m)	Required quantity (ha-m)
1	Adaun	1030.2297	1701.32619
2	Eisanpur	127.8276	153.7865
3	Kamaalpur	250.8284	268.4816
4	Harduaganj	1468.1549	1925.8949
Total		2877.0406	4049.48919

Table 2 Collective data of Jawan block

S. No.	Villages	Available quantity (ha-m)	Required quantity (ha-m)
1	Manzoorgarhi	320.9025	228.4646
2	Barheti	497.8545	501.6467
3	Rampur	312.5652	330.6564
4	Cherrat	785.5623	816.4627
Total		1916.8845	1877.2304

Table 3 Collective data of Lodha block

S. No.	Villages	Available quantity (ha-m)	Required quantity (ha-m)
1	Chilkora	123.142	70.5632
2	Deosaini	339.6497	287.541
3	Lodha	504.1522	602.452
4	Ajitpur Asna	130.2330	134.155
Total		1097.1769	1094.7112

Table 4 Data of Aligarh city

S. No.	Town	Available quantity (ha-m)	Required quantity (ha-m)
1	Aligarh city	9012.4512	9542.1234

Table 5 Collective data of Aligarh district

S. No.	Block	Available quantity (ha-m)	Required quantity (ha-m)
1	Dhanipur	2877.0406	4049.48919
2	Jawan	1916.8845	1877.2304
3	Lodha	1097.1769	1094.7112
4	Aligarh city	9012.4512	9542.1234
Total		17,780.5938	20,613.04338

2.2 A Comparison Between Previous Data (Published in 2014) and Current Data

Variation in available water in a district does not show much variation because schemes and programs to improve the district's water capacity have only recently begun, and many of them are still in the works. Also, there is no increment in the number of ponds, and the district still totally relies on groundwater reserves. It means that the district has not increased its water capacity noticeably from 2014 (as published in a research paper) to 2021 (Fig. 4).

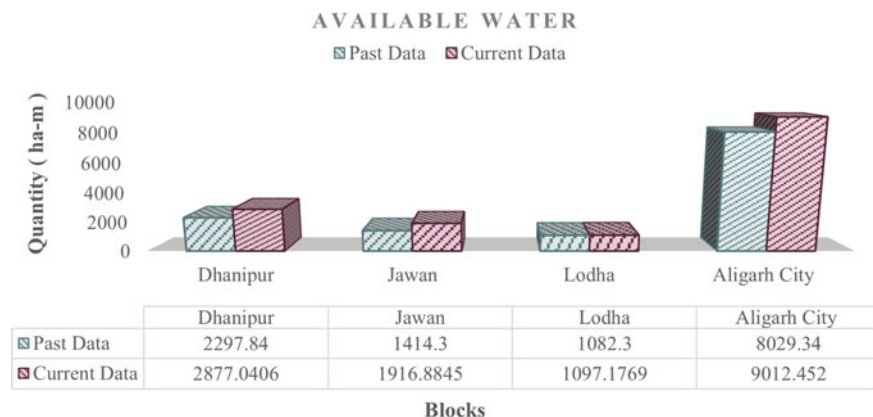


Fig. 4 Comparison between previous and current data of available water

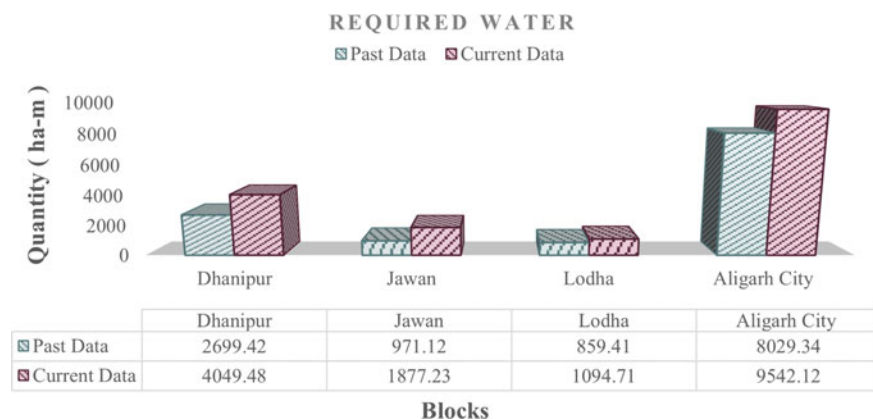


Fig. 5 Comparison between previous and current data of required water

The overall analysis of the data shows that there is a clear deficiency of water at present, and the district has to take the essential steps to mitigate this deficiency between the available quantity and the required quantity. Among the four blocks, two blocks, namely Dhanipur and Aligarh City, are in critical condition. Dhanipur block has greater water problems because of its rapid growth in population and industrialization at present. Although, in overall comparison, the gap is not that much which cannot be checked by implementing suitable means like water harvesting, leakage control, runoff control, and pollution control (Fig. 5).

Table 6 Quality parameters of Aligarh district

Block	Alkalinity (ppm)	TH	Cl	pH	TDS (ppm)	Quality
Dhanipur	305	70	154	7.0	560	Good
Jawan	300	82	182	7.4	510	Good
Lodha	355	87	168	7.1	516	Good
Aligarh city	297	78	159	7.3	498	Good

2.3 *Qualitative Analysis of Data*

The quality of water in the Aligarh district is examined through descriptive analysis and laboratory tests in conformity with Indian Standards for “Drinking Water as per BIS standards (IS 10500–2012) (Second Revision).” All water quality indices (in ppm) expected for safe drinking water were tested in the samples obtained from groundwater and surface sources, including alkalinity, total hardness, chloride, fluoride, pH, and total dissolved solids, as per BIS guidelines (TDS). The following locations and ponds were specified for their compatibility and convenience (Table 6).

2.4 *Comparison Between Test Values and Recommended Values by IS 10500: 2012 for Safe Drinking*

By comparing in situ chemical and physical water characteristics conforming to Indian standard codes, it can be concluded that Aligarh’s water quality parameters are not of great concern right now; also, all the physical and chemical parameters are not beyond cause for rejection limits. As mentioned earlier in the paper that the district uses mostly groundwater for daily consumption and use, and groundwater is not that polluted generally. So, it can be inferred that as the district is using groundwater reserves that is why they almost get safe drinking water. Also, a couple of treatment plants are there which only do preliminary treatment of water like chlorination and aeration.

3 **Result and Discussion**

The comparison between available water demands and required capacity is done for all blocks of the district. Most of the blocks show deficiencies, while some fulfill the requirements. It is evident from Table 1 and Table 4 that Dhanipur and Aligarh city blocks are in a state of water gap and must be taken care of. However, by seeing

Table 5, it is quite obvious that the Aligarh district as a whole has a deficiency of water.

As far as water quality parameters are concerned, it is potable, safe, and fit for drinking. Though some parameters exceed the permissible limit, they are not beyond cause for rejection as suggested by Indian standards. In ponds, alkalinity, TDS, chloride, and hardness are beyond the limit of cause for rejection in accordance with Indian standards.

4 Conclusion

The purpose of this research was to assess the potential of Aligarh district's current water resources and their four surrounding blocks in light of the growing population density in the study region, and the following findings were reached:

Water resources in the district are sufficient for the Lodha and Jawan blocks, where the Dhanipur and Aligarh city blocks show a great deficiency of the latest sources due to an increase in population and lifestyle changes. For any district to have a well-established system of water distribution, sustainable development and management play a vital role that cannot be negotiated. However, there is a lack of sustainable management in the Aligarh district. Groundwater resources are scarce and limited, so thefts and random use of water resources may exacerbate the problem. Farmers either depend on rainwater or irrigation water to cultivate their fields, so runoff from rainwater would be highly useful to them as they could easily meet the demand for water through it. Waterborne diseases are not frequent in the district as they directly pump the water from soil interstices. The crops in the district are not such that flooding of water in the field is required. The water pumped out from the ground is safe to drink without any secondary treatment as it sufficiently conforms to the water quality parameters of Indian standard codes. This information could help water managers monitor hydrological and irrigation systems, predict how much water is left to be used at the next sub-basin/sub-system, and aid the district administration in the fight against waterborne diseases.

References

- 1 Santhana Bosu S (1999) "Interbasin issues on sharing water resources", Presented in National Seminar on "Irrigation in 2050-Challenges ahead", Irrigation management Training Institute, Thuvakudy, March 1-2
- 2 Gupta VP, Sharma RP, Goyal RK (2000) Theme 6-16-impact assessment of conservation measures in arid areas-A case study of Osian-Bigmi (Jodhpur) watershed. National Institute of Hydrology
- 3 Mahapatra MK, Mishra RK (2005) Groundwater contamination in Subarampur and Nuapada districts of Orissa. *Poll Res* 24(4):863-865

- 4 Rahman A (2006) Assessing income-wise household environmental conditions and disease profile in urban areas: study of an Indian city. *Geo J* 65(3):211–227
- 5 Khan TA (2011) Trace elements in drinking water and their possible health effects in Aligarh city, India. *J Water Resour Prot* 3:522–530
- 6 Beg M, Khan WA (2014) Water resources management and sustainable development of Tehsil Koil (District Aligarh) UP, India-A Case Study
- 7 Chatterjee R, Jha BM (2006, February) Methods for estimation of replenishable ground water resources adopted in India. In: International conference on ground water for sustainable development, vol 174. New Delhi
8. Government of India (GOI): Report of National Commission for Integrated Water Resources Development 2015; Report of the working group on major and medium irrigation Programmes for the Tenth Five-year Plan, Ministry of Water resources, central Water Commission, October 2011; Draft Report of the Working Group on Major & Medium irrigation for the Tenth Five Year Plan, Irrigation Department (Uttar Pradesh), 2011; Census, Planning Commission; Report of Central Pollution Control Board (CPCB); Groundwater resources of India, CGWB, 2017
9. Down to Earth (2008). <http://www.downtoearth.org.in/>, <http://www.downtoearth.org.in/>

Flood Modelling and Simulation Using iRIC Model for Dhom Dam on Krishna River



Shaikh Neha Anjum Nisar and Aditya P. Nilawar

Abstract Flooding occurs when a river's flow is quite high, and the water spreads over active and inactive flood plains due to natural or artificial causes, inflicting property damage, as well as loss of livestock and human life. Inundation, drainage congestion owing to urbanization, and bank erosion are the main issues in India when it comes to floods. Flood modelling is one-dimensional or two-dimensional predictions of water level flows and flood depth using computer techniques. The International River Interface Cooperative (iRIC) programme was employed in this work, which is a river flow and riverbed variation analysis package with many solutions. A historic flood in Wai taluka, Satara district, Maharashtra, was studied using the Nays2DFlood solver, which simulates two-dimensional plane flow. Dam discharge data, as well as digital elevation model (DEM) data, is fed into the model. Based on simulated results, it is found that in 2019, Wai was highly prone to flood having the maximum value of 5.32 m. Also this model identified the critical locations of flow velocity and water surface elevation. As a result, the Nays2DFlood solver may be used to determine the flood extent in urban catchments.

Keywords Flood · iRIC · Nays2DFlood · Flood modelling · Flood depth

1 Introduction

Flooding occurs when a river's flow is quite high, and the water spreads over active and inactive flood plains due to natural or artificial causes, inflicting property damage, as well as loss of livestock and human life. When it comes to floods in India, the main challenges are inundation, drainage congestion due to development, and bank erosion [1]. The unstable and non-uniform flow of a flood wave in a river channel is a highly intricate occurrence [2].

S. N. A. Nisar (✉) · A. P. Nilawar
Department of Civil Engineering, Shri Guru Gobind Singhji Institute of Engineering and Technology (SGGS IE & T), Nanded 431605, India
e-mail: shaikhneha228@gmail.com

Not only did the flow change over time as the wave moved downstream, but also did the channel characteristics and the amount of lateral inflow and outflow. As a result, the problem's analytical solution becomes rather difficult [3].

The technique of limiting a real phenomenon or process with a set of mathematical formulas is known as modelling. Many areas of flood control rely heavily on flood modelling [4].

Flood modelling underpins several elements of flood risk management, including warning and forecasting, design, appraisal, asset management, and floodplain zoning to guide suitable development, flood mapping to promote community awareness. The use of computer tools to estimate water levels, flows, and flood depth in one or two dimensions is known as flood modelling.

The phrase "flood model" refers to a raster-based digital model in which cell values correlate to river levels during a flood. The way catchment processes are represented (deterministic or stochastic), and how the watershed is spatially discretized is used to characterize models (lumped or distributed). The routing models that estimate flood wave propagation over a river channel were built using continuity, momentum, and data-driven methodologies [5].

2 iRICNays 2D Flood

Professor Yasuyuki Shimizu (Hokkaido University) and Dr. Jonathan Nelson (USGS) founded the International River Interface Cooperative (iRIC) in 2007 with the goal of developing a software platform called iRIC for numerical simulation of flow and morph dynamics in rivers, as well as providing seminars and educational material to support that software. Nays2Dflood is a two-dimensional flood flow simulation modelling application that uses boundary-fit coordinates or a rectangular coordinate system to convert to a general curvilinear coordinate system. There are several subwindows: pre-processing, which prepares the input and sets the calculation conditions, solver, which executes the simulation, and post-processing, which displays the results [6].

The application does not need river channel data; it can work with digital elevation model (DEM) data as input. By considering the background image, it is simple to set upstream and side inflow points over terrain [7].

The bottom friction of the river is set using Manning's roughness coefficient because the model is unable to define multiple parameters for boundary conditions. This model has been used to simulate floods in small and medium-sized rivers, and it can also be used to replicate flood processes in developed countries [6].

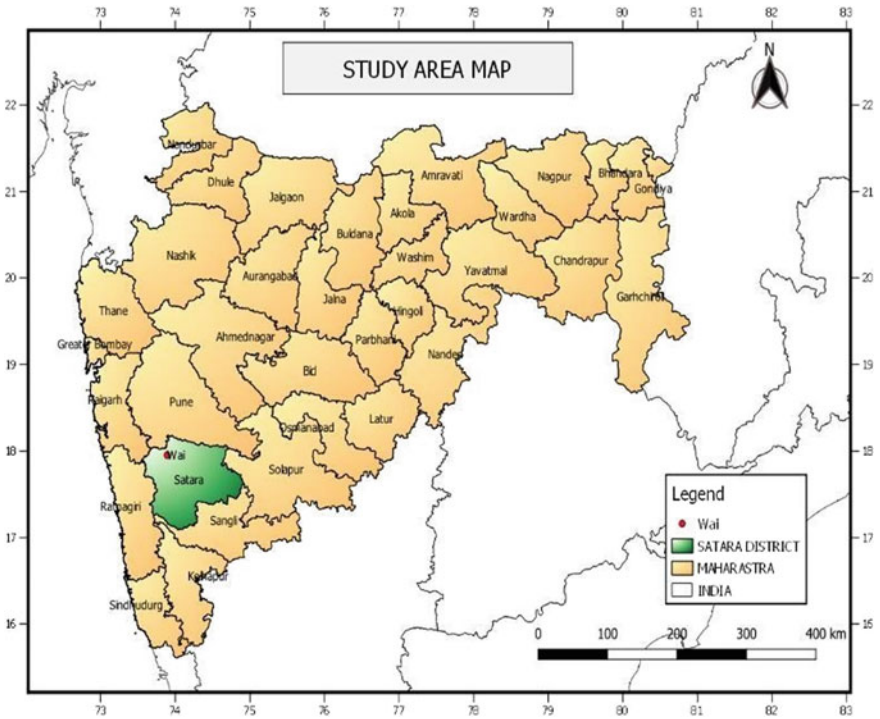


Fig. 1 Study area map

3 Area of Study

Dhom is a hamlet in Maharashtra’s Wai taluka, Satara district. Dhom is 7.9 km from Wai, the taluka’s main town. Dhom is 37.9 km from Satara, the district’s main city. And it is 155 km from Mumbai, the state capital. Dhom, Wai, Menawali, Bhogaon, Eksar, Kolan, and other nearby villages include Dhom, Wai, Menawali, Bhogaon, Eksar, Kolan, and others (Fig. 1).

4 Methodology

4.1 Collection of the Data

- Geographical data
- Hydrological data.

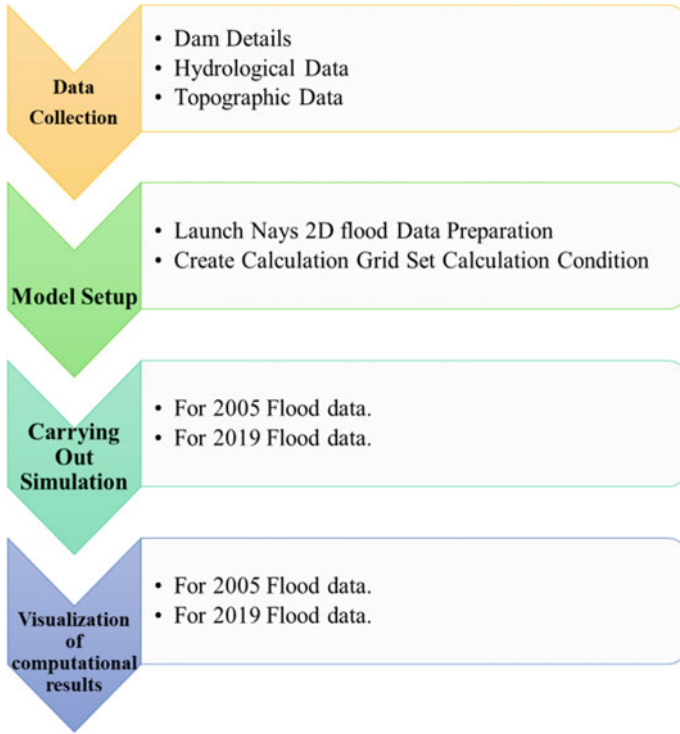


Fig. 2 Methodology flow chart

The topographic data for the study was downloaded from open access SRTM-1s DEM, which corresponds to about 30 m grid size at the equator. Figure shows the topographic image (DSM) of the study area. Hydrological data such as flood releases from Dhom dam of the year 2005 and 2019 has been collected from the Satara Irrigation Circle, Satara, Government of Maharashtra (Fig. 2).

4.2 Basic Flow Equations

Before being transferred to a general curvilinear coordinate system, the following is the basic equations in a rectangular coordinate system (x, y) [6].

$$\frac{\partial h}{\partial t} + \frac{\partial(hu)}{\partial x} + \frac{\partial(hv)}{\partial t} = q + r$$

$$\frac{\partial(hu)}{\partial t} + \frac{\partial(hu^2)}{\partial x} + \frac{\partial(huv)}{\partial y} = -hg \frac{\partial H}{\partial x} - \frac{\tau_x}{\rho} + D^x$$

$$\frac{\partial(vh)}{\partial t} + \frac{\partial(huv)}{\partial x} + \frac{\partial(hv^2)}{\partial y} = -hg \frac{\partial H}{\partial y} - \frac{\tau_y}{\rho} + D^y$$

$$\frac{\tau_x}{\rho} = C_f u \sqrt{u^2 + v^2}$$

$$\frac{\tau_y}{\rho} = C_f v \sqrt{u^2 + v^2}$$

$$D^x = \frac{\partial}{\partial x} \left[V_t \frac{\partial(uh)}{\partial x} \right] + \frac{\partial}{\partial y} \left[V_t \frac{\partial(uh)}{\partial y} \right]$$

$$D^y = \frac{\partial}{\partial x} \left[V_t \frac{\partial(vh)}{\partial x} \right] + \frac{\partial}{\partial y} \left[V_t \frac{\partial(vh)}{\partial y} \right]$$

where h is water depth, t is time, u is flow velocity in the x -direction, v is flow velocity in the y -direction, g is gravitational acceleration, H is water surface elevation, r_x is riverbed shear stress in the x -direction, r_y is riverbed shear stress in the y -direction, C_f is the riverbed friction coefficient, V_t is the eddy viscosity coefficient, ρ is the density of water, q is inflow through a box culvert, q , a sluice pipe or a pump per unit area, and r is rainfall [6].

4.3 Model Set Up

Following is the pre-processing window after the setting the calculation conditions like creating the calculation grid, the inflow boundary conditions, the initial water surface profile, setting the time condition, setting riverbed roughness coefficient, and setting the occupy, setting for the box culvert. Setting for the box culvert (Fig. 3).

5 Results and Discussion

This Chapter discusses about the results obtained after the simulation of past flood data of the year 2019 for Dhom dam on Krishna river by using iRIC-Nays2DFlood solver. The results are shown in the form of table and figures which can be used to access the flood situation of Krishna river in Wai taluka. It is observed that 8 villages in Wai taluka get affected due to flood release of Dhom dam. Simulated results are obtained in the form of maximum depth, water surface elevation, and velocity, as shown in Table 1. From observing the post-processing window in iRIC-Nays2DFlood solver, it has been found that Wai is highly prone to flood having the maximum value of 5.32 m. Validation of the results is our future work. From observing the post-processing window in iRIC-Nays2DFlood solver, it has been found that maximum value of water surface elevation, which is 645.63 m, is observed at Dhom which can

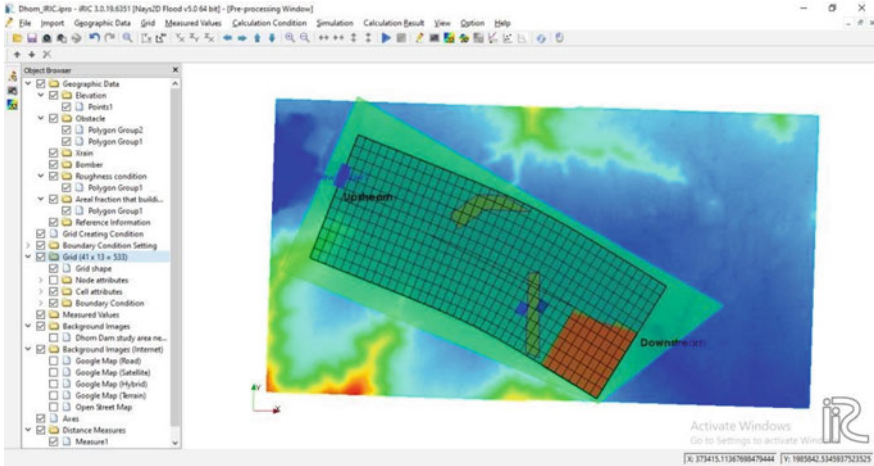


Fig. 3 Pre-processing window of the model

Table 1 Effect of flood on downstream villages

Village	Location of river bank	Maximum depth in (m)	Water surface elevation in (m)	Maximum velocity in (m/s)
1. Dhom	Left bank	0.77	645.63	2.31
2. Eksar	Right bank	0.95	642.28	0.34
3. Bhogaon	Left bank	0.94	643.55	0.34
4. Menawali	Left bank	2.01	642.19	0.18
5. Navechiwadi	Left bank	4.50	637.56	0.35
6. Wai	Left bank	5.32	637.55	0.31
7. Madhli Ali	Left bank	3.04	639.10	0.19
8. Wai Rural	Left bank	3.57	637.56	0.25

be seen in Figs. 4, 5, and 6 The 2D post-processing window shows the maximum flow velocity which is 2.31 m/s occurs at Dhom.

6 Conclusions

The Nays2DFlood solver with iRIC was found to be very useful for simulating and modelling of past flood event in Wai taluka. From the post-processing window, it can be seen that for 2019 flood scenario, the maximum depth was 5.32 m in Wai and minimum depth 0.77 m at Dhom village. Maximum value of water surface elevation, which is 645.63 m, is observed at Dhom, and minimum water surface elevation is 637.55 m at Wai maximum flow velocity which is 2.31 m/s occurs at Dhom and

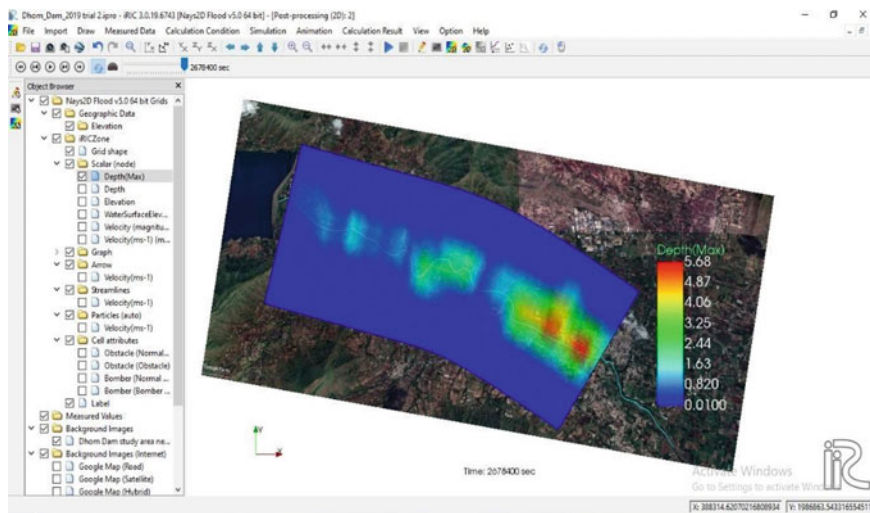


Fig. 4 2D post-processing window showing maximum depth

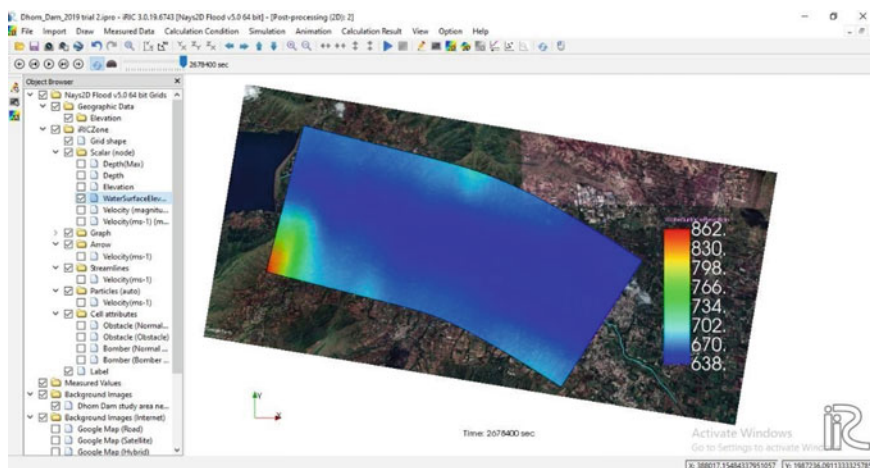


Fig. 5 2D post-processing window showing value of water surface elevation

minimum velocity is 0.18 m/s at Menawali. It is found that 8 villages in Wai taluka are prone to flood. Flood forecasting study can be done if the forecasted data (river discharge and precipitation) is used as input to this model. The results will make possible to avoid constructing buildings in hazards zone.

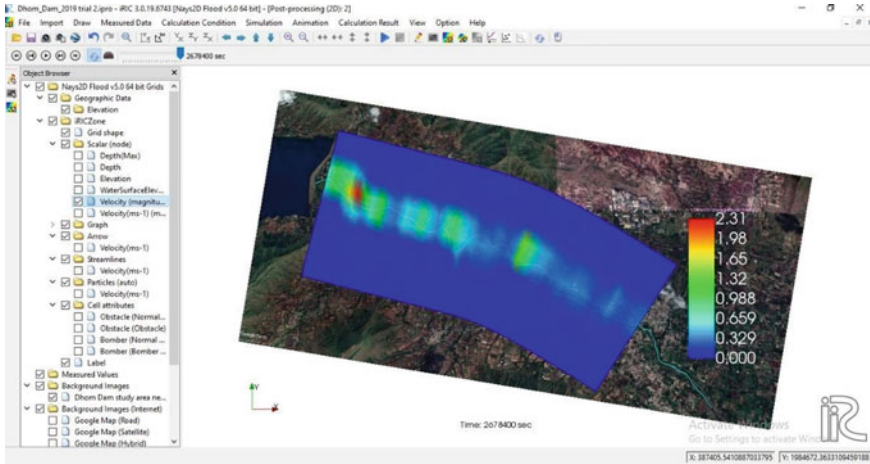


Fig. 6 2D post-processing window showing the maximum flow velocity

References

1. ChandraRupa R, Mujumdar PP (2019) Flood modelling: recent Indian contributions. *Proc Indian Nat Sci Acad* 85:705–722
2. Wongs S, Vichiensan V, Piamsa-nga N, Nakamura S (2019) Urban flooding and adaptation to climate change in Sukhumvit area, Bangkok, Thailand. In: *International conference on urban drainage modelling*, pp 644–648
3. Singh A, Dawson D, Trigg M, Wright N (2021) A review of modelling methodologies for flood source area (FSA) identification. *Nat Hazards* 1–22. <https://doi.org/10.1007/s11069-021-04672-2>
4. Shokory JAN, Sakai K (2016) Flood modeling and simulation using iRIC: a case study of Kabul City. In: *3rd European conference on flood risk management*, vol 7, no 04003, pp 1–6
5. Gharbi M, Dartus D (2016) Comparison of 1D and 2D hydraulic models for floods simulation on the Medjerda River in Tunisia. *J Mater Environ Sci* 7(8):3017–3026
6. Nays2DFlood solver manual (2015)
7. Kumar S, Kaushal DR, Gosian AK (2018) Hydrodynamic simulation of urban storm water drain (Delhi city, India) using iRIC model. *J Appl Res Technol* 16:67–78

A Review on Performance and Reliability Aspects of Photovoltaic Modules



Neha Kumari, Sanjay Kumar Singh, and Sanjay Kumar

Abstract The photovoltaics are potentially capable to provide service adequately for 25 years. Photovoltaic (PV) is usually considered as one of the reliable component of PV system. However, to estimate the long-term performance and reliability of a photovoltaic module under diverse terrestrial and outdoor conditions, performance analysis is required. However, it is not desirable to wait for 25 years to establish the reliability and performance of the module. To resolve this, accelerated tests are carried out in the laboratory by replicating the field conditions to understand the behavior of PV modules under these conditions. The paper discuss various photovoltaic technologies, performance parameters, different degradation in PV module, and accelerated stress testing method to analyze the reliability of photovoltaic. This paper would help PV manufacturers, researchers, academicians, and energy generating members to develop reliable PV systems in the future.

Keywords Photovoltaic technologies · Performance parameters · Efficiency · Reliability · Accelerated stress test

1 Introduction

The current energy generation system comprises fossil fuel, renewable energy, and nuclear energy, which is not secure and reliable. Among all these, renewable energy is sustainable and secure energy source [1]. Solar photovoltaic technology serves to be clean, reliable, and affordable sources of renewable energy. Today, photovoltaic is being used to power a small calculator to a large space satellite. It is anticipated that photovoltaic will rule the energy source globally by 2025, with 60% capacity addition by PV module [2]. The installed and grid-connected global capacity solar PV power

N. Kumari (✉) · S. K. Singh
Amity University Rajasthan, Jaipur, India
e-mail: neesingh0187@gmail.com

S. Kumar
UIET, Himachal Pradesh University, Shimla, H.P, India

extended to 480 GW in the year 2018 showing year to year increase of 20% with year 2017 with 386 GW and compound annual growth rate(CAGR) of approximate 43% since year 2000. Considering plenty resource available, potential market, and cost affordability, the solar PV is anticipated to be ruling overall renewables growths over next decade. Also, IRENA’s REmap estimates that the installation of solar PV could grow almost six fold over next decades leading to global cumulative capacity of 2840 GW by 2030 and increasing by eighteen times leading to 8519 GW by 2050. Figure 1 shows cumulative solar PV capacity from 2000 to 2050 with historical and future expected projection statistics [3].

The performance of PV is greatly affected by the occurrence of degradations in field PV modules. The literature has shown the annual approximately 0.6–0.7% degradation and beyond this leading to concern the manufacturer. Degradation can be categorized as long term or short term depending upon the mechanism involved [4]. Commonly observed degradations in the last 10 years are summarized in the paper by Kim et al. [5].

The data concluded hotspot being most dominant degradation over last 10 years followed by internal circuit (IC) discoloration. Other noticed degradations are glass breakage, encapsulant discoloration, fractured cells, PID, and others including such as IC failure and junction box problem which is represented in Fig. 2.

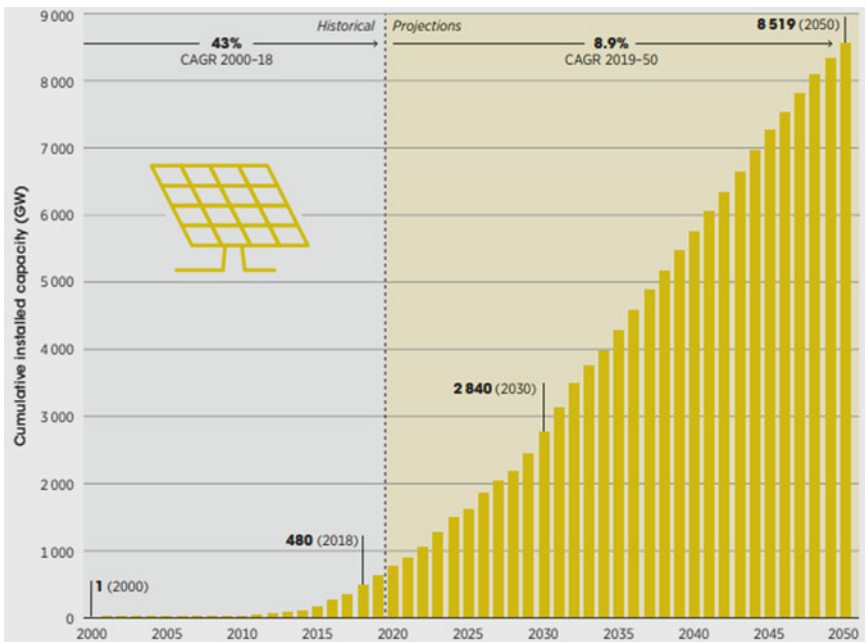
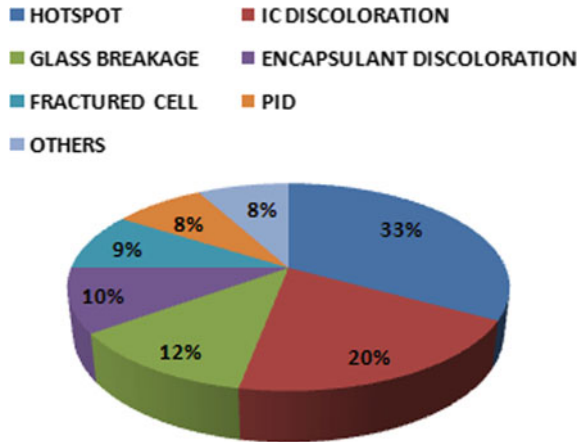


Fig. 1 Cumulative solar PV capacity from 2000 to 2050 with historical and future expected projection statistics [3]

Fig. 2 Significant degradation modes in last 10 years [5]



1.1 PV Markets Top Ten Market in 2020

The Chinese market showed an improvement with 48.2 GW installation in year 2020 after two years of market contraction signifying 35% of the worldwide market. The European Union took second position in the list with 19.6 GW annual installation in 2020. The USA showed hike in market of 19.2 GW followed by Vietnam overwhelming 11KW installations. Last in top five was Japan with an estimate of 8.2 GW installation showing improvements in market condition as compared to 2019 and 2018. Indian market experienced contraction down to around 5 GW. Korea and Australia markets showed stability with 4.1 GW installation, Brazil with 3.1 GW annual installation with the most active market in Latin America. Germany showed growing year with 4.9 GW of added installation and Netherlands sustained with large PV installation of 3.0 GW. Several such as France, Turkey, and Mexico left the top 10 list for annual installation [6]. The list of top 10 countries representing installations and total installed capacity in 2020 is shown in Fig. 3.

2 Photovoltaic Parameter

The most critical parameters of photovoltaic (PV) are: technology, efficiency, and reliability.

2.1 Photovoltaic Technology

Silicon is the principle technology in photovoltaic cells. The silicon-based solar cells are expensive; therefore, a lot of research is focused on finding new technologies to

FOR ANNUAL INSTALLED CAPACITY				FOR CUMULATIVE CAPACITY		
1		China	48,2 GW	1		China 253,4 GW
(2)		European Union	19,6 GW	(2)		European Union 151,3 GW
2		United States	19,2 GW	2		United States 93,2 GW
3		Vietnam	11,1 GW	3		Japan 71,4 GW
4		Japan	8,2 GW	4		Germany 53,9 GW
5		Germany	4,9 GW	5		India 47,4 GW
6		India	4,4 GW	6		Italy 21,7 GW
7		Australia	4,1 GW	7		Australia 20,2 GW
8		Korea	4,1 GW	8		Vietnam 16,4 GW
9		Brazil	3,1 GW	9		Korea 15,9 GW
10		Netherlands	3 GW	10		UK 13,5 GW

Fig. 3 Top 10 countries representing installations and total installed capacity in 2020 [6]

minimize the material cost. For the same reason, thin film technology can be an appropriate option [7]. Another way out for silicon is PV fabrication using polymer or organic material having advantages of low cost, ecofriendly, and light-weighted, but with a problem of low efficiency [8]. The various photovoltaic technologies can be classified as given in Fig. 4.

Crystalline Silicon Photovoltaic. Crystalline silicon PV is the workhorse of photovoltaics covering up the maximum of the solar cell industry with the highest efficiency among other technologies. On the top, the material silicon is available in nature easily as a raw material. These are classified as monocrystalline and polycrystalline. The monocrystalline silicon PV cells are sliced from a single crystal in form of very thin wafers and are high purity with high conversion efficiency. But the manufacturing process of this PV is complicated making it expensive. However, polycrystalline PV is manufactured by using many crystals of silicon in one PV cell. These are

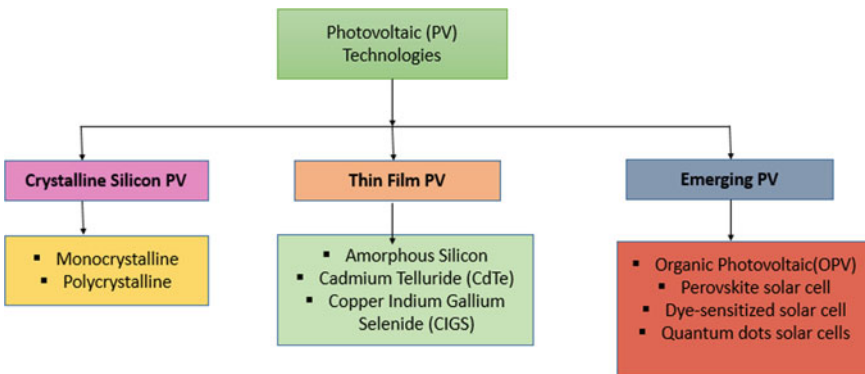


Fig. 4 Different photovoltaic technologies

less expensive due to less complicated manufacturing processes and less efficient than monocrystalline solar cells. Despite having high efficiency, this technology has a scope of improvement in the following areas—lowering the cost of crystalline silicon modules to achieve a good profit margin, minimizing metallic impurities, and developing thinner wafers.

Thin Film Photovoltaic. The other type of photovoltaic is fabricated by depositing a thin semiconductor layer on top of a substrate made up of glass, metal, or plastic substrate, therefore, making it less expensive. As the material required is very little, these types of solar cells can be manufactured very thin around 35–260 nm [9]. These technologies comprise two main families—one the silicon-based comprising amorphous silicon and the other is non-silicon-based thin film PV comprising cadmium telluride (CdTe) and copper-indium-gallium-selenide (CIGS). The amorphous silicon PV holds an advantage of low cost and flexible substrate but with a drawback of low conversion efficiency and is widely used in an application in calculators, electronics, and solar garden. The two key properties of CdTe technology are—firstly it has an appropriate bandgap of 1.5 eV and secondly good optical absorption coefficient [10]. Although the manufacturing process like spraying or decomposing the material makes it cheap, the use of cadmium is a toxic metal and can be unhealthy for the environment and workers. The other type of thin film photovoltaic is CIGS is a high efficient substitute for commercial solar modules on large-scale installation. CIGS is a flexible material that can be manufactured by deposition on a substrate like metal foils, glass, and polymer making them lightweight.

Organic Photovoltaic. These PV are still in its emerging phase. These PV cells are fabricated using organic/polymer compounds. In this way, the functions of PV cells like transparency, color, and band gaps can be enhanced. Although these solar cells have low efficiency but have the advantages of mechanical flexibility and cost-efficient low-temperature manufacturing process. The building-integrated PV utilizes organic PV due to color tuning property and the ability to work as transparent devices [11]. The benefits of organic photovoltaic are—low-cost manufacturing, abundant building block materials, and flexible substrate. Organic photovoltaic cells are of two types: small molecules organic PV cells (polyacenes, phthalocyanines, and squarenes as electron-donating system) and polymer-based organic PV cells (P3HT, MDMO-PPV, and PC60BM, PC70BM) [12].

Next-Generation Photovoltaic. In many new technologies, photovoltaic technologies have been worked upon tremendously like—quantum dots, hybrid organic–inorganic materials, and dye–sensitized solar cells proving more options with better efficiencies in the future. Quantum-dot photovoltaic uses nanocrystals made up of semiconductor materials as absorber materials for better performance. Perovskite solar cells, which are hybrid metal halide, are drawing attraction due to their slim design, low-temperature processing, and lower price with good excellent properties of light absorption. Also, these cells are flexible, lighter in weight, and semitransparent. The dye-sensitized solar cell is hybrid organic–inorganic cell that comprises small molecular absorber dyes which imitate the natural photosynthesis process of absorbing light. The dye is the photoactive material generating electricity sensitized by light.

2.2 Efficiency

The conventional and most common solar photovoltaics are crystalline silicon technology holding the maximum percentage of global market. The laboratory conversion efficiency of crystalline silicon cells is over 25% and over 20% for single crystal and multi-crystalline, respectively. The commercial PV module has achieved efficiencies from 18 to 22% under standard test condition (STC). The theoretical efficiency of amorphous silicon is about 15% but practical efficiency range from 6 to 11% [13]. The recorded laboratory-scale efficiency for CdTe photovoltaic cells is 22.1% by First Solar. However, commercial module efficiency of approximately 18% is recorded at the end of the year 2020. The laboratory-scale cell efficiency of the CIGS module has exceeded 20% but commercial efficiency is in the range of 12–14%. The third generation solar cells comprise organic photovoltaic achieved efficiency of about 11% [12]. The new emerging technologies such as perovskite photovoltaic have improved efficiency ranging from 3% in 2009 to 25% in 2020. The efficiency of present dye-sensitized PV extends up to 12%. The reader can get more information about different photovoltaic technologies through an efficiency chart from 1976 to the present by an efficiency chart by National Renewable Energy Laboratory (NREL) in Fig. 5.

Performance assessment of PV system. The performance of PV system is highly influenced by factors like solar radiation, humidity, atmospheric temperature, geographical conditions, and landscape wind speed. The temperature of the panel surface is a one of the critical environmental parameter that impacts the generated output of PV panel by fluctuating its electrical parameters, like open-circuit voltage (V_{OC}), short circuit current (I_{SC}), maximum power output (P_M), and fill factor (FF) [14]. Each technology of PV array is observed to assess its performance as per IEC standard 61724. Performance parameters are specified to examine the photovoltaic system in reference to energy production [15]. The most important performance parameters which present the overall performance of PV system are:

Total Energy generated by PV Array. The total energy generated, daily ($E_{DC,d}$), monthly ($E_{DC,m}$), and yearly ($E_{DC,y}$) by a PV array over a period of time is given by (1), (2), and (3), respectively.

$$E_{DC,d} = \sum_{h=0}^{24} E(DC, h) \quad (1)$$

$$E_{DC,m} = \sum_{d=1}^n E(DC, d) \quad (2)$$

$$E_{DC,y} = \sum_{m=1}^{12} E(DC, m) \quad (3)$$

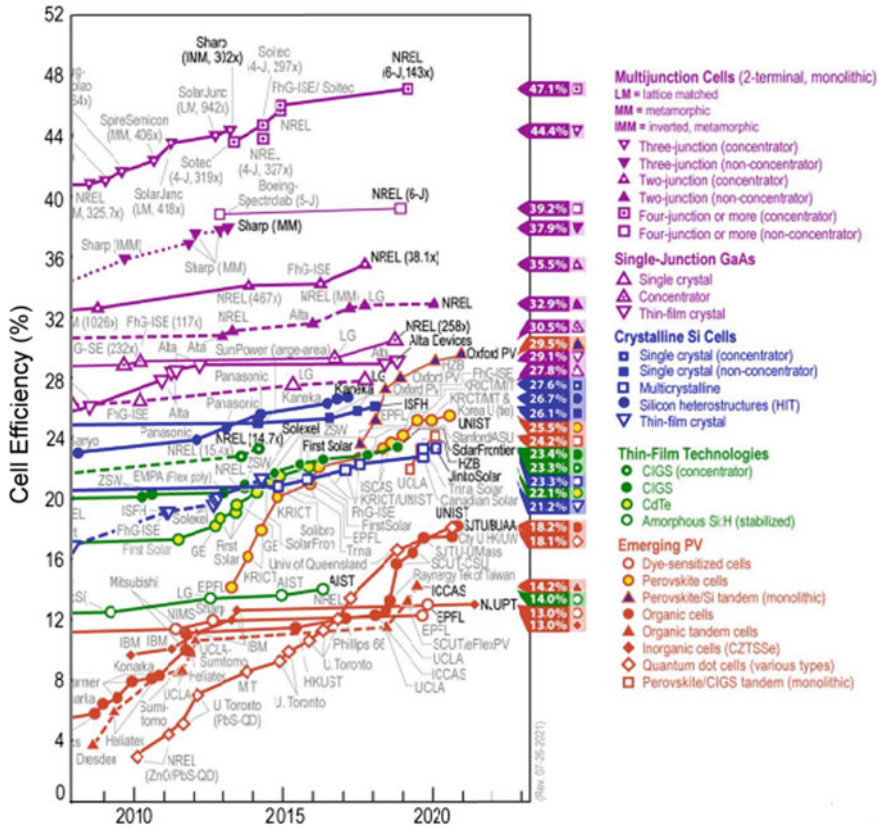


Fig. 5 Efficiency chart presented by National Renewable Energy Laboratory (NREL)

where $E(DC, h)$ is the hourly (h) DC Output, $E(DC, d)$ monthly DC energy output, $E(DC, m)$ yearly DC energy output, and n is the days in one month (m) [16].

Array Yield (Y_A). Equation (4) defines array yield as the ratio of total DC output generated (E_{DC}) by the PV array for a definite period comprising day, month, or year to the rated output power of PV array ($P_{PV, RATED}$).

$$Y_A = \frac{E_{DC}}{P_{PV, RATED}} \tag{4}$$

Reference yield (Y_R). It is evaluated by the ratio of total in-plane solar radiation, S_R (kWh/m^2) divided by the reference irradiance, H_R (kW/m^2) given by (5).

$$Y_R = \frac{S_R}{H_R} \tag{5}$$

Performance ratio (P_{RA}). Equation 6 defines performance ratio as array yield (Y_A) divided by reference yield. This performance parameter is used to find estimate the long-term change in the PV system and decline in P_{RA} values are signs of loss in performance

$$P_{RA} = \frac{Y_A}{Y_R} \quad (6)$$

2.3 Reliability—Accelerated Stress Test (Method to Investigate the Reliability)

Reliability is an essential element of continuous growth in the solar photovoltaic market. Solar electricity provides a cost-effective availability in the market due to constant improvement in solar technology and manufacturers providing performance warranty of photovoltaic of 25 years. A reliable PV module has a high probability to give its output as the intended function. The accelerated stress test contributes to minimize early failure and improvement in these testing procedures ensures the PV modules reliability and durability when working in outdoor conditions. Along with these tests analysis of the PV product, weakness is done which would further benefit manufacturer and consumer for selecting the product that will last longer in the field [17]. After knowing the list of degradation and failures, the test is developed that duplicate the real-time failure conditions for a short period. The main aim of these tests should be—to develop the accelerated stress test that replicates the same failure conditions as in the field, secondly to estimate the approximate time for execution of accelerated stress test to replicate the module exposure in the field, and finally, the degradations should be duplicated in a similar manner faced by fielded modules while creating accelerated test [18]. An accelerated stress test is carried out by increasing the intensities of the testing variables like ultraviolet light, temperature, humidity, voltage, or mechanical load. These reliability tests cause changes in parameters, and these changes are analyzed to observe the failure modes [19]. To make sure high quality, the photovoltaic panels goes through certification. The organization IEC—International Electrotechnical Commission—has laid certain standards. For conventional crystalline silicon PV modules, the IEC 61215 standard is implemented, and for thin film PV modules, the IEC 61646 standard is used. These standards include tests under a few fixed conditions, which are discussed in this section. Few methods of accelerated stress test for the solar photovoltaic module are:

Thermal cycling. The thermal cycling accelerated test as detailed in the standard of IEC 61215 is used to understand whether a solar photovoltaic module can tolerate the temperature variation occurring in changing climatic conditions. This may occur due to the reason that different materials used in fabrication have different temperature expansion coefficients and get stressed due to temperature variation. Due to this,

different components tend to contract and expand at different rates in the same climatic condition. The accelerated stress test is performed according to IEC 61215:2005 standards. The target of the test is to investigate the effect of temperature change taking place on PV modules from 85 to -40 °C. The test finds out the impact of temperature cycling creating interfacial stress that may even damage the module and cause loss of performance. This test can identify problems like broken connectors and cells and solder bond failures [17]. It also analyzed that cell connector breakage is one of the main reasons for module degradation [20]. Kawai et al. observed solder bond failure along with bypass diode failure after performing 600 thermal test cycles resulting due to implementation of inappropriate design and quality management issues of photovoltaic [21]. Schiller compared the accelerated thermal cycle test with the standard thermal cycle test to assess novel interconnections concepts. The results do not show much difference from the outputs of both the tests [22]. Khan et al. presented a comparison of failure and degradation in a c-Si PV module attached with and without a concrete slab by thermal cycling stress test [23]. A study by Perez et al. showed a variation in the performance of PV modules when it is new and after the thermal cycling test due to degradation. The output showed a power decline in the range of 1.4% up to 7.6% from its initial conditions [24].

Damp Heat test. This test outcomes the effect of long-term humidity contact on PV module and is executed in keeping with the IEC standards 61215 and IEC 61646, in which modules are exposed to 85 °C of temperature with 85% of relative humidity in the climatic chamber for 1000 h. The combination of high humidity and temperature stresses different PV module layers and provides information about behavior changes and performance of the module when placed in the field. As high temperature and humidity are climatic conditions in tropical and subtropical areas, the PV modules experience such high temperature and humidity. To assess the PV module reliability and durability, the damp heat test imitates failure and degradation mechanism that take place in the field. The damp heat tested PV module results in a drop in power output. A study by Morita et al. showed that the moisture reaching solar cell through penetrating polymer weaken adhesive bonds at the interface further leading delamination [22]. Park et al. investigated the correlation between effective humidity with ambient temperature and humidity on exposing PV modules to damp heat testing [25]. Zhu et al. investigated variations of solar cell parameters through damp heat testing and noticed modules showing degradation and solar cell equivalent circuit parameters [26]. Silicon PV module having polyethylene film showed a stable performance after damp heat test with testing parameters to be 85 °C and 85% relative humidity for 4000 h, but with a significant decrease in efficiency after test [27]. Bheemreddy et al. developed a reliability model for analyzing the field life of CIGS photovoltaics by performing damp heat tests at different temperature and humidity values. The result showed that adding a time exponent term in the developed model for life prediction can prove a significant way of improving the accurateness of field life prediction [28].

Ultraviolet (UV) Light. The qualifying test IEC 61215 for crystalline silicon PV and IEC 61646 for thin film PV and IEC 61730-2 consist of UV preconditioning test in

which the modules are kept at a temperature range of 60 ± 5 °C and subjected to 15 kWh/m^2 with a wavelength in the range of 280 and 385 nm with at least 5 kWh/m^2 between 280 and 320 nm. The UV irradiance in the test should not cross 250 W/m^2 and should have uniformity of $\pm 15\%$. Laboratory test result showed that temperature accelerated the process of degradation while ultraviolet radiations are responsible for the discoloration in PV modules. The study has shown that exposure to UV radiation can damage a passivated silicon-oxide interface causing an increased recombination process [29]. Osterwald et al. reported a linear relationship between short circuit current degradation rates and UV radiation exposure on 5 years fielded commercial crystalline silicon PV modules [30]. The experiment result showed a good optical transmission of silicon encapsulants than EVA encapsulant proving silicon a stable encapsulant on UV exposure [31]. The EVA undergoes yellowing and browning along with corrosion of solder bonds and electrical contacts are also notice on UV exposure [32] causing an increase in leakage current through the encapsulant [33]. An analysis showed the loss of performance in dye-sensitized solar cells caused by UV exposure [34]. The UV test is used to analyze the materials used in encapsulation to evaluate their optical transmission and mechanical strength. The available qualifying standards are not adequate to evaluate the UV radiation effect on the PV module and do not give a confident answer about the longevity of the PV module. A test performed on silicon photovoltaic devices on UV exposure showed degradation in polymeric encapsulation causing a decline in output power. Also, it accelerates aging in amorphous silicon modules with a change in material color. UV radiation tests do not analyze bare crystalline silicon photovoltaic confidently [35]. A UV radiation activated degradation causes a decrease in the photocurrent most likely due to the reason of damage of the charge extraction layer is observed in a study showing the UV radiation affecting multilayer organic photovoltaic [36].

Static and Dynamic Mechanical Loads. Using static loads, the mechanical load test for the solar photovoltaic module evaluates the combined effects of wind and snow load. Issues such as the role of size and thickness of module front glass, framing and mounting setups, and stability of solder joints are studied under this test. Micro-crack is a critical issue in crystalline silicon modules. Apart from static, there are other conditions dynamic in nature and are tested by dynamic load test. The standards IEC 61215 and IEC 61646 are used for a static load test. Dynamic loads result in the fatigue of materials of PV cells and connecting wires [37]. An experiment performed by Koch et al. in 2010, concluded that the Dynamic mechanical load test impacts the solder joints, failure in the electrical circuit resulting in output power of monocrystalline test modules. However, increased micro-cracks along with broken cells are observed in static mechanical load tests resulting in 2% higher power loss [38]. In 2019, a mechanical loading experimental resulted on two different types of PV amorphous silicon and organic PV observed a decline in the open-circuit voltage V_{oc} [39].

Hail Test. The hail test is significant for PV quality and safety issues as in many geographical areas; hails can cause damage to the panels. A few of the possible issues that can be identified with this test are broken cells and glasses, micro-cracks,

and structural deformation. Semi-flexible types of PV modules have been tested more subjected to hail impacts than rigid PV [40]. The effect of hail on the photovoltaic module may even result in loss of efficiency. Experimental result evaluated after hail test on the PV modules showed a decline in power generation efficiency by 11% [41]. Hails not only break the panel but also reduces the output of the photovoltaic module leads affecting the longevity of PV module to the development of a reliable protective system. Hail can even cause energy loss as high as 30% [42]. The experimental results indicated that PV modules are damaged to a level causing irreversible effects like micro-cracks and a decline in generated power from 2.33 to 4.83% [43].

3 Conclusion

There are tremendous renewable energy resources present and solar PV is one among them to generate electricity. The most important parameter of solar PV is defined by technology, efficiency, and reliability. Photovoltaic technologies are continuously emerging about the material, design fabrication, and many more so that the efficiency is improved. Reliability becomes an important parameter for the success of PV modules in the market place. To maintain all these parameters, accelerated stress tests are developed to predict behavior, failure mechanism, lifetime, and reliability of PV products when placed in practical conditions. In situ accelerated testing methods are conducted for variable conditions, and the measurement of various module characteristics is recorded during the stress test. The paper provides an overview of three critical parameters of solar PV and contributes to the development efforts of a reliable solar PV.

References

1. (2009) Peak people: the interrelationship between population growth and energy resources. Energy Bull. <https://www.resilience.org/stories/2009-04-20/peak-people-interrelationship-between-population-growth-and-energy-resources/>. Last accessed 2021/9/28
2. International Energy Agency (2020) Renewable. <https://www.iea.org/reports/renewables-2020>. Last accessed 2021/9/28
3. International Renewable Energy Agency, IRENA (2019) Future of solar photovoltaic: deployment, investment, technology, grid integration and socio-economic aspects (A Global Energy Transformation: paper). https://irena.org//media/Files/IRENA/Agency/Publication/2019/Nov/IRENA_Future_of_Solar_PV_2019.pdf. Last accessed 2021/10/14
4. da Fonseca JEF et al (2020) Degradation analysis of a photovoltaic generator after operating for 15 years in southern Brazil. Sol Energy 196:196–206
5. Kim J et al (2021) A review of the degradation of photovoltaic modules for life expectancy. Energies 14(14):4278
6. International Energy Agency (2021) Snapshot of PV global markets. <https://iea-pvps.org/snapshot-reports/snapshot-2021/>. Last accessed 2021/10/14
7. Mc Cann MJ et al (2001) A review of thin-film crystalline silicon for solar cell applications. Part 1: native substrates. Sol Energy Mater Solar Cells 68(2):135–171

8. Gorter T, Reinders AHME (2012) A comparison of 15 polymers for application in photovoltaic modules in PV-powered boats. *Appl Energy* 92:286–297
9. Vrieland JAM et al (2012) Applicability of X-ray fluorescence spectroscopy as method to determine thickness and composition of stacks of metal thin films: a comparison with imaging and profilometry. *Thin Solid Films* 520(6):1740–1744
10. Morales-Acevedo A (2006) Thin film CdS/CdTe solar cells: research perspectives. *Sol Energy* 80(6):675–681
11. Dyer-Smith C, Nelson J (2012) *Organic solar cells-practical handbook of photovoltaics* 2nd edn. Academic Press
12. Office of energy efficiency and renewable energy-organic photovoltaics research. <https://www.energy.gov/eere/office-energy-efficiency-renewable-energy>
13. Kafui AD, Seres I, Farkas I (2019) Efficiency comparison of different photovoltaic modules. *Acta Technol Agric* 22:5–11
14. Vergura S, Acciani G, Falcone O (2012) A finite-element approach to analyze the thermal effect of defects on silicon-based PV cells. *IEEE Trans Ind Electron* 3860–3867
15. Marion B et al (2005) Performance parameters for grid-connected PV systems. In: Conference record of the thirty-first IEEE photovoltaic specialists conference, pp 1601–1606
16. Li C (2018) Comparative performance analysis of grid—connected PV power systems with different PV technologies in the hot summer and cold winter zone. *Int J Photoenergy* 2018
17. Wohlgenuth JH, Kurtz S (2011) Reliability testing beyond qualification as a key component in photovoltaic’s progress toward grid parity. In: International reliability physics symposium
18. Climatic tests. <http://www.pytest.cz/en/tests/thermal-cycling-test>. Last accessed 2021/9/28
19. Kumari N, Singh SK (2021) A study of commonly observed degradation methods in photovoltaic modules. In: IEEE technically sponsored international conference on advancements in electrical electronics communication computing and automation ICAECA 2021
20. How temperature cycling degrades photovoltaic-module performance. <https://spie.org/news/3177-how-temperature-cycling-degrades-photovoltaic-module-performance?SSO=1>. Last accessed 2021/9/28
21. Schiller CH et al (2019) Accelerated TC test in comparison with standard TC test for PV modules with ribbon, wire and shingle interconnection. In: 36th European photovoltaic solar energy conference and exhibition, pp 995–999
22. Khan F, Rezgui BD, Kim JH (2020) Reliability study of c-Si PV module mounted on a concrete slab by thermal cycling using electroluminescence scanning: application in future solar roadways. *Materials (Basel)* 13(2)
23. Perez, A (2019) Performance of photovoltaic modules after an accelerated thermal cycling degradation test. *PHM_CONF* 11(1)
24. Morita K (2003) Degradation factor analysis of crystalline-Si PV modules through long-term field exposure test. In: 3rd world conference on photovoltaic energy conversion, pp 1948–1951
25. Park NC, Oh WW, Kim DH (2013) Effect of temperature and humidity on the degradation rate of multicrystalline silicon photovoltaic module. *Int J Photoenergy*
26. Zhu J et al (2016) Changes of solar cell parameters during damp-heat exposure. *Prog Photovolt: Res Appl* 24(10):1346–1358
27. Hara K, Jonai S, Masuda A (2015) Crystalline Si photovoltaic modules functionalized by a thin polyethylene film against potential and damp-heat-induced degradation. *RSC Adv* 5(20):15017–15023
28. Bheemreddy V et al (2018) Life prediction model development for flexible photovoltaic modules using accelerated damp heat testing. In: IEEE 7th world conference on photovoltaic energy conversion (WCPEC) (A joint conference of 45th IEEE PVSC, 28th PVSEC & 34th EU PVSEC), pp 1249–1251
29. Ruby DS, Schubert EK (1991) The effects of concentrated ultraviolet light of high-efficiency silicon solar cells. In: The conference record of the twenty-second IEEE photovoltaic specialists conference—1991, 1991, pp 111–117
30. Osterwald CR (2003) Degradation in weathered crystalline-silicon PV modules apparently caused by UV radiation. In: 3rd world conference on photovoltaic energy conversion, pp 2911–2915

31. Kempe MD (2009) Accelerated stress testing of hydrocarbon-based encapsulants for medium-concentration CPV applications. In: 34th IEEE photovoltaic specialists conference (PVSC), pp 001826–001831
32. Kempe MD et al (2007) Acetic acid production and glass transition concerns with ethylene-vinyl acetate used in photovoltaic devices. *Sol Energy Mater Sol Cells* 91(4):315–329
33. Kempe M et al (2010) Types of encapsulant materials and physical differences between them. Golden, Colorado, NREL
34. Poskela A (2021) Extreme sensitivity of dye solar cells to UV-induced degradation. *Energy Sci Eng* 1(1):19–26
35. Shamachurn H, Betts T (2016) Experimental study of the degradation of silicon photovoltaic devices under ultraviolet radiation exposure. *J Solar Energy*
36. Patel JB et al (2019) Effect of ultraviolet radiation on organic photovoltaic materials and devices. *ACS Appl Mater Interfaces* 11(24):21543–21551
37. Weiss KA (2009) Measurement and simulation of dynamic mechanical loads on PV-modules. *Proc SPIE—Int Soc Opt Eng* 7412:41203–41211
38. Koch S et al (2010) Dynamic mechanical load tests on crystalline silicon modules. In: 25th European photovoltaic solar energy conference and exhibition/5th world conference on photovoltaic energy conversion, Spain, pp 3998–4000
39. Dai Y et al (2019) Continuous performance assessment of thin-film flexible photovoltaic cells under mechanical loading for building integration. *Sol Energy* 183:96–104
40. Corrado M, Infuso A, Paggi M (2017) Simulated hail impacts on flexible photovoltaic laminates: testing and modeling. *Meccanica* 52(6):1425–1439
41. Makarskas V (2019) Simulation study of hail impact on photovoltaic modules. In: IEEE 7th IEEE workshop on advances in information, electronic and electrical engineering (AIEEE), pp 1–4
42. Gupta V (2019) Impact of hailstorm on the performance of PV module: a review. *Energy Sources. Part A* 1–22
43. Kilikevičien K et al (2019) A research of the energy losses of photovoltaic (PV) modules after hail simulation using a newly-created testbed. *Energie* 1(2):4537

A Game-Theoretic Approach for Enabling Peer-to-Peer Sharing of Rooftop Solar Energy



Nilesh Hadiya , Shashank Vyas, Falti Teotia, and Rohit Bhakar

Abstract Rooftop solar (RTS) has emerged as a widely utilized mode of decentralized Energy resource. Net metering and feed-in tariffs are among the preeminent examples that compensate prosumers for injecting their excess solar generation into the grid. However, the real value of this clean source of power is not always ensured by these mechanisms, and the consumers remain under-compensated for the value they bring to the system. Peer-to-peer Energy Sharing Mechanism (P2PESM) with rooftop Solar Energy can provide a level-playing field for prosumers by providing appropriate prices for their excess Energy through adequate Energy and cost-sharing mechanism, With prices remaining in regulatory limits. The above-mentioned mechanism can incentivize residential consumers to adopt RTS. This paper presents a game theory-based approach wherein cooperative game theory-based shapley value approach is used to find the most appropriate internal buying and selling prices with a fair distribution of benefits among consumers, with a proper performance index for an analysis carried out for an institutional campus-based set up in India.

Keywords Solar energy · Energy markets · Game theory

1 Introduction

Recently there has been an increasingly larger share of new generation resources such as rooftop PV, micro-wind turbines, and Energy storage devices (batteries and electric cars, etc.) being connected to the low voltage grid [1]. With the increasing share of generation resources being added at the distribution end, the traditional

Supported by The Energy and Resources Institute.

N. Hadiya (✉) · S. Vyas · R. Bhakar
Department of Electrical Engineering, Malaviya National Institute of Technology Jaipur, Jaipur
302017, India
e-mail: 2018psm5481@mmit.ac.in

F. Teotia
The Energy and Resources Institute, New Delhi, India

© The Author(s), under exclusive license to Springer Nature Singapore Pte Ltd. 2022
V. Mahajan et al. (eds.), *Sustainable Technology and Advanced Computing in Electrical Engineering*, Lecture Notes in Electrical Engineering 939,
https://doi.org/10.1007/978-981-19-4364-5_44

603

boundaries between generation, transmission, and distribution are fast disappearing [2]. However, the proliferation of distributed generation resources which has put the electric grids on the threshold of a paradigm shift [3]. With decreasing cost of Energy storage solutions, there are opportunities to invest in transmission or storage—the choice between “Generation + Transmission + Distribution” and “Distributed Generation + Storage + Distribution” is becoming a real one to make [4]. This is even more relevant in regions where transmission and distribution losses are high as distributed generation reduces network losses [5]. The power flow in distribution system [6]. This new topology opens the door for power exchange between customers, forcing utilities to find new revenue sources. This will largely impact the existing business model of the utility industry [7].

Distributed and dispersed generation produce electricity near the particular load they are intended to serve, such as a residential home or commercial building [8]. This is a complementary alternative to the production of electricity at large centralized plants and subsequent transmission (often over long distances) to the consumer [9]. Distributed generation may serve a single structure, such as a home or business, or it may be part of a microgrid (a smaller grid that is also tied into the larger electricity delivery system), such as at a major industrial facility, a military base, or a large college campus [10]. Distributed generation of electricity would not only reduce the demand-supply gap but would also enable consumers to become “prosumers” wherein they would feed electricity into the grid and earn credits/revenue [11]. However, now with rooftop PV on customer premises being connected to the grid, a customer can inject electricity into the grid that the utility can sell to any customer on the network [12]. Traditional customer who was only a buyer of electricity has become a producer and a consumer—“prosumer” now. A prosumer generates electricity through RE sources, which are intermittent, consume the same electricity, and feed excess energy to the grid [13]. These changes indicate the need for a separate Energy market for the full utilization of RE sources.

For India, The Electricity (Amendment) Bill, 2020 [14] under sections 126, 135, and 164 permits state distribution utilities to commission a third member to distribute electricity on its behalf in their service area with the approval of the appropriate State Commission. Also, India is heading to start the Real-Time Market [15] to foster the integration and trading of renewables. This would incentivize the creation of a new local Energy market paradigm for prosumers and utilization of decentralized distributed generation like rooftop solar. This would reduce RTS intermittency and make them as a flexible source. The main aim of local Energy market would be to satisfy local demand with local supply of RTS. In this market, third-person (retailer, aggregator, or Discom) would handle the exchange of RTS from prosumers inside Energy sharing area or outside Energy sharing area. In [16] authors have identified the importance of LEM as mitigation of market power, creation of flexibility and ancillary services, proper utilization of REs, and support to medium-size RE power plants. To achieve these goals of the local Energy market P2PESM is one of the best models.

Within P2PESM, peers can transact Energy with each other within the Energy sharing area, at the same time import for consumers and the export for prosumers

can be compensated for. In such a scenario, it is more likely that the peers will have an objective of social welfare maximization rather than individual profit maximization, which shows, P2PESM as an efficient demand management technique. As, the Indian government has announced a target for 15% of vehicle sales to be electric by 2022 and has introduced a significant incentive program, called Faster Adoption and Manufacturing of Hybrid Electric Vehicles (FAME), in which there is a scope to include community-level rooftop solar as a demand flexibility option [17]. In this regard, P2PESM can act as a reliable flexible source to satisfy the upcoming peak in the system. P2P Energy sharing is a paradigm that can ensure that the “true” value of the rooftop solar system is provided to the consumer. Both at the technical and commercial sides, it can prove to be beneficial to the distribution utilities also. Accordingly, significance on designing an effective P2P Energy trading Mechanism has been reported in the literature. From a limited number of actual case studies to modeling and simulation studies, the research reported has mostly focused on pricing mechanisms to ensure either the benefits to the consumers or, in a few studies, benefits to the utilities and advantages to both, in a very few studies. Most of them have made use of popular electricity pricing methods to determine the buying and selling prices in a P2P setup while some have also used non-cooperative and cooperative game theory to find them. However, because of the P2P Energy sharing paradigm being proposed in this paper, the following research gaps have been observed in this paper:

- Actual meter data corresponding to import and export of electricity on an institutional campus
- Clear identification between Peer-to-Peer Energy Trading and Peer-to-Peer Energy Sharing
- Season-wise clustering of meter data could not be observed and hence the variation in consumption/export trends has been observed at a macro-level that may provide some clue toward a possible relation with pricing
- Shapley value or Cooperative game theory has been used to determination of selling and buying prices.

2 P2P Energy Exchange Mechanism: Two Paradigms

The majority of dilemmas discussed in the literature relate to determining the optimal or appropriate compensation to renewable Energy with increasing demand while also considering the reliability of supply. Peer-to-Peer Energy Exchange Mechanism (P2PEEM) allows peers having distributed Energy resources to coordinate with each other to ensure the right incentive for RE adoption and to optimize local supply and demand, and balance the power flow since the exchange of Energy between peers has now been adequately accounted for even in scheduling and dispatch of power for the distribution utility.

There are two approaches to implement P2PEEM, keeping in view the conflicting interests of peers within the Energy sharing area.

1. **Real-time P2P Energy Trading Mechanism (P2PETM):** The principal purpose of this mechanism is to maximize individual profit. In this mechanism, peers will try to maximize their profit; consumers will try to reduce their bills by bidding lower prices, and prosumers will try to increase their revenue by asking higher prices for their RTS Energy. Suitable mathematical approaches for P2PETM include Non-Cooperative Game theory-based methods and Double Auction (DA) mechanism, which also work on the principle of "Individual Profit Maximization". According to the bid and ask requests collected, the internal trading price can be identified, which will dynamically change based on the peer's adverse interests.
2. **Peer-to-Peer Energy Sharing Mechanism (P2PESM):** In this arrangement, fundamentally, the peers are following an agreement of cooperation for Energy sharing. This mechanism focuses more on the proper utilization of RE with the win-win approach for all the parties involved. This mechanism can provide fair and feasible internal buying and selling prices. The basic premise of this mechanism is proper, fair, and accounting of the benefits of green Energy to each of the stakeholders involved, instead of fair trading, which depends on market clearing and leaves a few small prosumers without a proper price match. On the other hand, this mechanism advocates for the adoption of efficient Energy and cost-sharing models, which are agreed upon by each peer within the Energy Sharing Area (ESA). According to these models, the peers will attempt to maximize their respective objective functions; for example, consumers can secure a coalition with prosumers to reduce their bills and the same for prosumers to increase their revenue from RTS Energy. However, cooperation between each peer is a predominant factor for this mechanism. Accordingly, there is no requirement for bid and ask prices because internal buying and selling prices depend upon the volume of import and export Energy, retail tariff, and feed-in tariff. Figure 1 shows a schematic diagram of the major actors and the processes involved in a P2P Energy Sharing Mechanism.

As shown in Fig. 1, prosumers who consume and generate energy, and consumers who only consume Energy are the peers for P2PESM. The DISCOM of that particular area would provide a physical and virtual platform for P2PESM. Peers are abode by virtual agreements for coalitions between them for Energy sharing within Energy sharing area. These virtual agreements can be written on smart contracts and blockchain distributed ledger technology in which every transaction within peers can be recorded and stored within the blockchain platform and entirely handled by DISCOM.

The next section describes the electricity consumption and solar generation profile of the institutional campus in India. The basic theory of shapley value and how they have been applied to this P2PESM have also been explained.

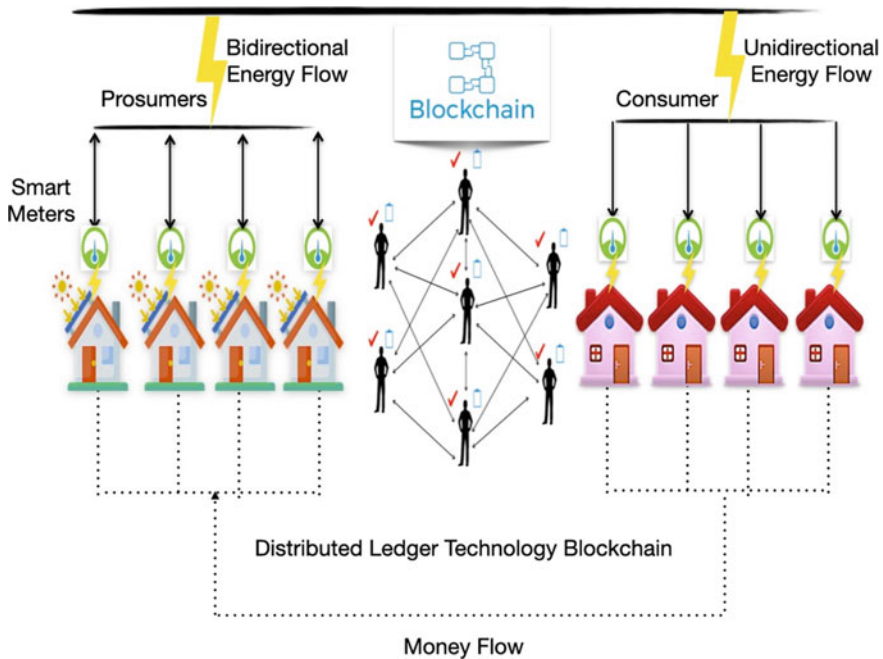


Fig. 1 A schematic diagram representing the actors and the process involved in a P2PESM

3 Case Study

For this study, the Indian Institute of Technology (IIT) Kanpur case has been used. As part of the National Smart Grid Mission, IIT Kanpur developed a smart city within its campus that comprises 11 substations of the IIT Kanpur power distribution network. These substations collectively feed around 10.5 MW load of the institution receiving input supply from a 33/11 kV substation and connected to various 11 kV/440 V distribution transformers liable for feeding a residential load of IIT Kanpur. The project directed at promoting a smart city prototype and R&D platform for smart distribution systems. The project area comprises three substations for implementing substation automation on residential flats for enabling a smart home system configuration with a robust communication system. Grid-connected solar PV was installed for RE integration on rooftops of the flats. As far as the grid-connected solar PV installation is considered, 20 locations with 5 KWp capacity rooftop solar plants were selected for implementation. Amidst these places, four houses are equipped with Energy storage.

3.1 Local Grid Assets

Local grid assets can be classified as prosumers, implemented with RTS on their premises, and consumers with their demand patterns that can be affected by increasing consumption of green Energy. In this mechanism, peers are indirectly connected to the local distribution network. Each peer should be equipped with bidirectional digital meters that will record instantaneous outflow and inflow of RTS Energy and log in the average value of imported and exported Energy over a standard billing time interval, like 30 or 15 min. Each peer will need to forecast their own consumption and generation of Energy to plan the potential coalition-based optimization of Energy management in P2PESM and receive compensation/benefits.

Out of the 20 prosumers, data relating to 12 efficient prosumers has been taken for this study. The houses having rooftop solar with Energy storage was not considered. The 12 prosumers selected were divided into two groups, each group consisting of three consumers and three prosumers. Data for the one-year duration—June 2018 to July 2019 collected for the study. This data has segregated into winter, summer, and monsoon seasons. prosumers were decided based on their export and import from 6:30 AM to 6:30 PM, the solar hours. The electricity demand time-series data was available in a time step of 30 min. The solar generation data in kWh was available at every 5 min. Accordingly, for prosumers, the resulting export data was converted into a 30 min kW time series by multiplying the kWh values by 60/5. These values were then multiplied by 0.5 to again convert into kWh values.

Since all the consumers had rooftop solar systems, to generate a completely “import” based profile, the metered-data values for prosumers were converted by following formulas,

- Solar generation = Export + self-consumption
- Self-consumption = Solar Generation – Export
- Total demand = Import + self-consumption from Solar Energy.

The 12 peers were divided into two groups according to their import and export levels as.

Group 1

- Three prosumers – Export of RTS Energy less than and equal to 10 kWh per day
- Three consumers – Import of Energy in the range of 15–25 kWh per day.

Group 2

- Three prosumers – Export of RTS Energy 10–15 kWh per day
- Three consumers – Import of Energy in the range of 25–30 kWh per day.

3.2 ICT Framework

Solar generation, Energy import, and export data need to be collected using smart meters attached to each consumer’s premises. Apart from Energy accounting and settlements, this data is further used to forecast future inflow and outflow of Energy. With these forecast values, peers can predict their compensations from P2PESM, which moreover incentivizes more trustworthy demand management. An enabling digital platform, required for such a mechanism, can be handled by the utility, which can be provided with the right to use peers’ data for better utilization of RE.

As shown in Fig. 2, within the IITK campus, these peers have been implemented with smart meters, which give data associated to voltage, current, power factor, output power and export, and import power. These locations are within the 2 km area on the campus. Data from these Smart meters have been accumulated by 13 Data Concentrated Units (DCUs) with some time delay with each smart meter. The data from DCUs fed into the server (cloud) with the use of ethernet. This data is pulled in JSON format and fed into excel. This IT infrastructure will be more suitable for implementing Blockchain Distributed Ledger Technology. Distribution network’s power security and reliability guaranteed by the IITK control room. Here four places are equipped with hybrid inverter Energy storage. Moreover, there is a Distribution box with wifi contractors connected to the router and operates by a mobile device. This technology facilitated users with alternatives for the use of Energy from Energy storage, which establishes the concept of P2PEEM.

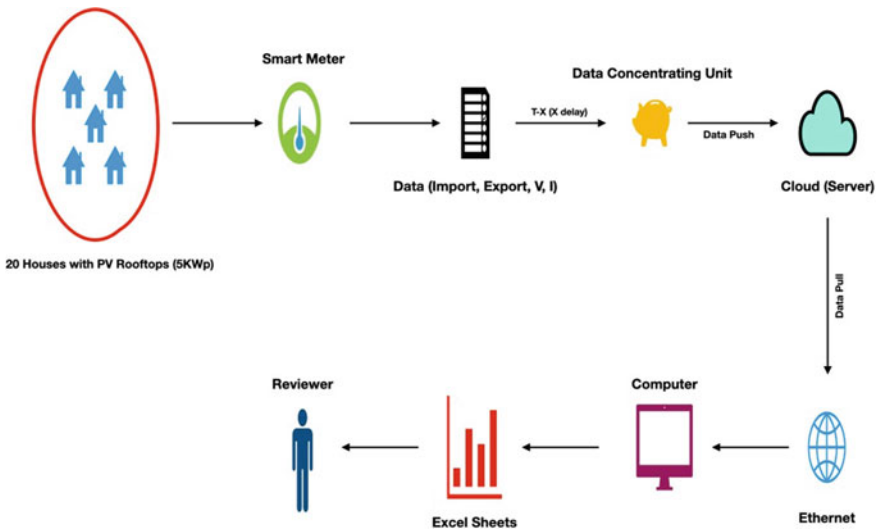


Fig. 2 A schematic diagram representing the ICT infrastructure and process involved in an IITK campus

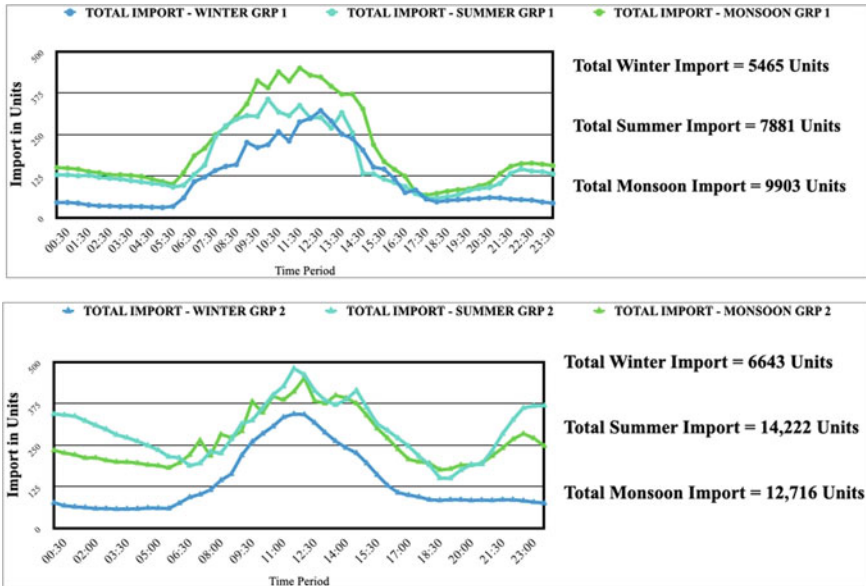


Fig. 3 A graphical representation of import pattern of consumers for three seasons

Figure 3 shows the total season-wise import for all the consumers in groups 1 and 2 over the year. Figure 4 shows the season-wise total import and export of prosumers in groups 1 and 2 over the year. Both the patterns have been shown as a daily curve, cumulated over the year.

3.3 Energy Sharing Model

The reliability of P2PESM can be estimated by coalitions between different peers and cooperative behavior that influences the determination of the internal trading prices. The suitability and applicability of these coalitions depend upon the benefits earned from them. The principal purpose of P2PESM is to maximize each peers' benefit by the Energy outflow of each prosumer that will be distributed among consumers according to their demand contributions. This Energy Sharing Mechanism can further increase the participation power of each peer. The Energy sharing component has been modeled using a simple, effect, and practically implementable method whose description as follows.

In this model, Energy sharing among peers is done on the basis of volume of Energy consumed. The underlying objective is efficient social welfare maximization within the Energy sharing area. For $i = 1, 2, 3, \dots, n$ consumers and $j = 1, 2, 3, \dots, p$ prosumers, the Energy consumed by a prosumer at time t of the P2P sharing $Ee_{j,t}$ process is in proportion to the total Energy imported from the grid in that time

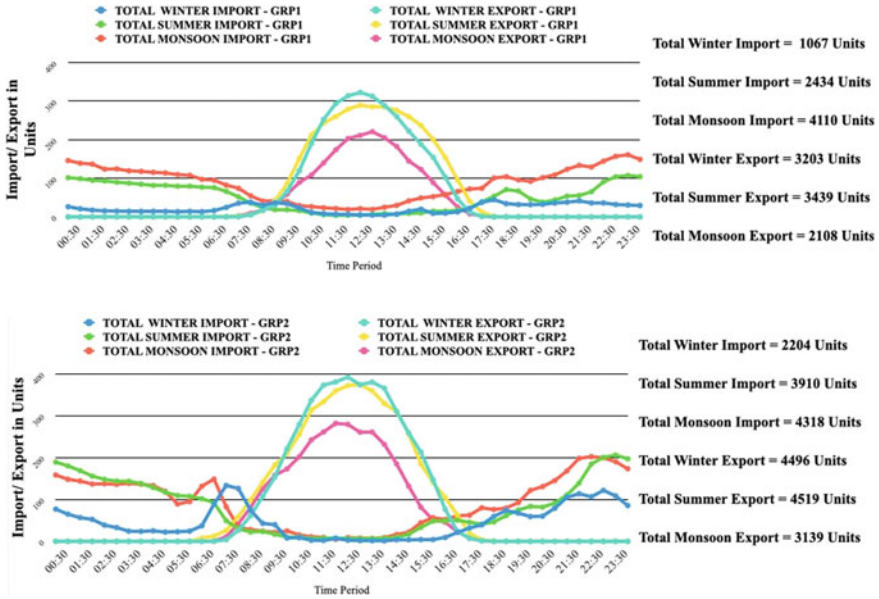


Fig. 4 A graphical representation of import and export pattern of prosumers for three seasons

period. consumer’s consumption from export Energy (CCE) can be expressed as in (2)

$$CCE_{(t)} = Ee_{(j,t)} \times Ei_{(i,t)} \div \sum_{i=1}^n Ei_{(i,t)} \tag{1}$$

Figure 5 gives the illustration of an example to show RTS Energy sharing between consumers. In this example, a Prosumer is equipped with RTS Export of P units, and consumers possess demand of $X, Y,$ and Z Units. According to Eq. 2 RTS export Energy will be distorted among consumers.

3.4 Cost-Sharing Model

Cost-sharing models (CSM) indicate opportunity cost, which can be earned by peers with the use of P2PESM. These models use different logics to identify internal buying and selling prices for peers, which will be the most feasible for prosumers and consumers. Here price cap limits are [2, 9], and internal buying and selling prices are between these limits. A CSM indicates payment rules and relates to the internal buying and selling price for the given volume of export and import, according to the price cap fixed to allow Energy accounting within its price boundaries. The price

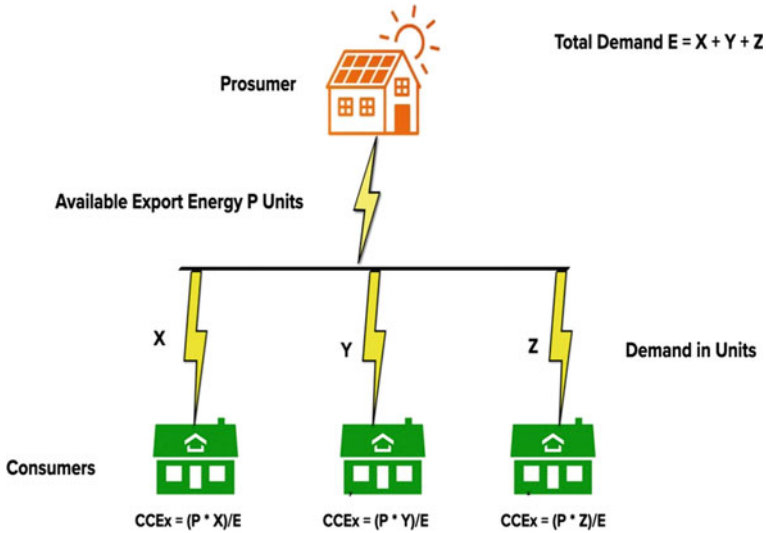


Fig. 5 A schematic representation of the energy sharing mechanism

range should be between retail tariff of electricity (for a particular consumer category or the lowest among all categories, if sharing happens between different consumer categories) and feed-in tariffs (the price offered to un-accounted excess Energy from net metering at the end of each financial year), which can ensure benefits to each peer in P2PESM. Following the main objective, cost-sharing models should ensure fairness in terms of benefit distribution. Therefore, a CSM should take into account the volume of outflow and inflow of RTS Energy, Retail tariff, and feed-in tariff and make use of appropriate mathematical approaches and algorithms to implement logic.

Cooperation Game Theory: Shapley Value

Cooperation Game Theory (CGT), also called as coalition GT or Transferable Utility [18] is an extension of the game theory where cooperation between players is possible. In these types of cooperative games, each player has the same interests. It aims to determine how much payoff each player will get if various coalitions improve the overall payoff of the Game. In CGT, each player will co-operate with other players to increase overall payoff of the Game. A certain amount of payoff will be associated with each coalition, which will again get distributed among the players, including negative payoffs (Cost) [19]. In CGT, players are self-motivated to participate in coalitions because each player will get more benefits when compared to being alone.

In recent years, coalition game theory has been an influential asset for the electricity market, notably in the sectors of smart grid, carbon emission, local Energy trading, renewable integration. In [20], they used canonical coalition games to propose P2P Energy trading to confirm the stability of the coalition and the benefit of peers for the social coalition. Authors in [21] proposed an efficient peer-to-peer

Energy trading model for the reduction of CO₂ emissions and the price of electricity within prosumers. The stability of this model has been verified by the coalition game theory approach, which is considered as an influential solicitor to model the local Energy market. The model in [22] further expanded the work in which they suggested stackelberg cooperative game theory, which builds stability of prosumers' coalitions with the use of novel and well-built stackelberg equilibrium.

There are many types of indices used in CGT; however, shapley value has been proposed in this paper for the fair distribution of benefits within players. Lloyd Shapley had first presented the concept of shapley value in 1951 [23]. Shapley value has the potential to implement compliance and check the feasibility of coalitions between players. The main aim of shapley value is to provide a fair allocation of benefits within the players who have participated in a coalition [24]. The allocation of the payoff depends upon the marginal contribution of each player. As more players participate in the coalition, more benefits will be distributed among players. It can be termed as Meritocracy Fairness of coalition game theory [25]. It has many applications in Business profit sharing, Machine Learning, Online marketing, etc. [26].

Applications of shapley value in electricity markets have been reported in the literature [27] wherein the cooperation between sellers and buyers has been analyzed based on coalition GT using asymptotic shapley value (to reduce computation, when a large number of peers introduced) for fair distribution of revenue between peers. In [28], the authors proposed different pricing mechanisms for peer-to-peer Energy trading with shapley value. This study indicates that the best results in terms of benefits sharing in CGT can be achieved with shapley value. It also proposed a fairness index, which measures how efficient other methods are in comparison to shapley value. The article [29] concentrates on the shared operation of a microgrid and its holding utility and suggested that using shapley value, and daily generation cost can be depreciated. In [30], the authors used a game theory-based mathematical approach: shapley value to minimize the deficits of power and Energy in various regions of India. They concluded that with shapley value, fair allocation on the availability and requirement of Energy could be done while satisfying peak demand. In [31], authors have used cooperative game theory with shapley value to allocate the carbon obligation between the generation side and demand side and have confirmed that shapley value has the potential to utilize the carbon abatement of all pertinent players thoroughly.

Definition of Shaley Value [31]

For N a finite set of players indebted by i , $N = 1, 2, 3, \dots, n \forall S \subseteq N$. The Shapley value is the Greek letter φ . To be more complete the Shapley value for the player i is written like that also written as $\varphi(i)$.

The Core [32]

“The core can accomplish the stability of a coalition and the grand coalitions”. It can be stated that the core of a game is a set of all stable payoffs. With the core's

availability, the players' will not have any incentives to leave a coalition, if these three conditions will be satisfied:

The Shapley value can thus be defined as follows:

For given a coalition game (N, v) , there is an individual payoff division $x(v) = \varphi(N, v)$ that shares the full payoff of the grand coalition and that meets the Symmetry, Dummy player, Efficiency, and Additivity axioms.

$$\phi_i(N, v) = \frac{1}{N!} \sum_{S \subseteq N/\{i\}} |S|!(|N| - |S| - 1)! [v(S \cup \{i\}) - v(S)] \quad (2)$$

This captures the ‘‘Marginal Contribution’’ of agent I , averaging over all the different sequences according to which the grand coalition could be built up,

- F For any such sequence, player i 's marginal contribution when added: $(v(S \cup \{i\}) - v(S))$.
- Weight this quantity by the $|S|!$ ways the set S could have been formed before i 's addition
- Weight this quantity by the $(|N| - |S| - 1)!$ ways the remaining players could be added.
- Sum over all possible sets S
- Sum over all possible sets S and average by dividing by $N!$: the number of feasible orders of all the players.

There are some Axioms of Shapley value [32] that prove the fairness property of Shapley value like symmetry, additivity, and efficiency. After obtaining the Shapley value, the main question is that, Under what payment divisions would the players require to create the grand coalition? The answer would be, if and only if the payment contour is, extracted from a set called the core.

1. The coalition bill of two or more players should be less than the sum of each player's bills.
2. The grand coalition bill should be less than the sum of all the player's bills.

If all these conditions satisfy a given shapley value, it can be called total distribution rationality [33]. Also, it can be concluded that for a given shapley value, if the core is nonempty, then for players, there will be no incentives to leave the coalition as they will receive a fair cost allocation with coalition stability.

The cost-sharing model applies the concepts of coalition game theory, as explained above. To apply cooperation game theory—shapley value as a cost-sharing mechanism for P2P Energy Exchange Mechanism, ‘‘Coalitions’’ between different peers are the essential parts of it. The number of coalitions and the value of a coalition is essential to determine first. If the number of coalitions can be identified by:

p = Number of Prosumers in Coalition and q = Number of Consumers in Coalition, then the value of a coalition can be calculated by:

$$\text{Value of Coalition} = \sum_{t=1}^T \left\{ \sum_{i=1}^p \sum_{j=1}^q [E_{I(pq)}^{P2P} - E_{E(pq)}^{P2P}] \right\} \tag{3}$$

where $p \subseteq i, q \subseteq j$ Based on the formula in (3), different possible coalitions for peers group 1 and group 2 can be calculated for a given case. For example, if a set of players in one group form a coalition $N = 1, 2, 3$ and there are three players in another similar coalition, then the number of possible coalitions is $2^6 = 64$. Accordingly, the various number of coalitions are possible, from zero-player coalition to six-player coalition, for this case, since the number of players in a coalition, based on grouping, can be six. A zero-player coalition $V(\emptyset)$ indicates the number of dummy players, who contribute their value to the coalition. For this scenario value of the dummy player = 0. Similarly, a single-player coalition $V(i)$ contains individual payoffs for each player for peer-to-peer and Energy sharing model (ESM) as explained in previous sections. The payoff will be the bill for consumers, and for prosumers, the payoff will be revenue. Coalition value of consumers: $V(1), V(2), V(3)$ Coalition value of prosumers: $V(4), V(5), V(6)$.

A two-player coalition $V(i1, i2)$ will contain coalitions payoff values between consumer to consumer, prosumer to prosumer, and consumer to prosumer. In the case of a consumer-to-consumer, prosumer-to-prosumer payoff will add according to their payoffs. For example for a consumer-to-consumer coalition payoff, $V(12) = [V(1) + V(2)]$. For a prosumer-to-prosumer coalition payoff, $V(45) = [V(4) + V(5)]$. In the case of a consumer to prosumer, according to the Energy sharing model, shared export will be deducted from import for each player’s specific coalition. For instance, a consumer-to-prosumer coalition payoff will be expressed as,

$$V(14) = [(Total\ import\ of\ player\ 1) - (Energy\ shared\ by\ 4\ to\ 1)] \times Retail\ Tariff$$

In this way, the three-player coalition, four-player coalition up to six-player coalition is possible. The value of coalitions is in terms of payoff (INR), here negative values are for revenue earned by selling RTS excess Energy and positive value for billed units for import units of Energy. From these coalition values, there is a requirement of fair distribution of benefits coming from coalitions between peers. It can be done by shapley value, which proves beneficiary applications of this mechanism.

4 Results

By using the formula given in Eq. (1) above, and using $N = 6$, the shapley values for the players arranged in the two groups can be derived as given in Tables 1 and 2, respectively.

Here, the positive values stand for bill in INR and negative values represent revenue in INR. The applicability and stability of coalitions can be identified by “The Core”. A payoff vector x is in the core of a coalition game (N, v) iff,

Table 1 Shapley values—Group 1

Players	Winter	Summer	Monsoon
ϕ1	6626	9093	15,813
ϕ2	9321	10,348	17,936
ϕ3	8565	11,070	14,605
ϕ4	−3371	−7890	−3085
ϕ5	−4234	−3287	−3394
ϕ6	−5931	−4059	−5229

Table 2 Shapley values—Group 2

Players	Winter	Summer	Monsoon
ϕ1	9712	18,510	19,578
ϕ2	5318	14,853	16,753
ϕ3	7720	13,739	15,628
ϕ4	−6276	−7440	−4283
ϕ5	−5472	−6577	−5048
ϕ6	−7563	−7249	−6551

$$\forall S \subseteq N, \sum_{I \in S}^N Xi \geq v(s) \tag{4}$$

The number of payoffs to the player in any sub-coalition *S* should be more than they could receive. The core is in the core of a coalition game if and only if the following conditions are true:

1. The grand coalition bill should be less than the sum of all the player’s bills.
2. The player’s payoff value should be less than his/her value.

Tables 3 and 4 show the applicability of shapley value and the establishment of shapley value. As shown in this table in Fig. 6, for group 1, each peer gets more profits with cooperation game theory, and shapley value gives fair distribution, and the core gives the stability of this mechanism. As per the table, savings for each peer

Table 3 Season-wise savings in bill and status of the core in group 1

Players	Winter	Summer	Monsoon	The core
ϕ1	2130	3179	2888	Non empty
ϕ2	4258	3982	2769	Non empty
ϕ3	4943	5234	2630	Non empty
ϕ4	1670	4288	2028	Non empty
ϕ5	2326	1791	2178	Non empty
ϕ6	3135	2279	3286	Non empty

Table 4 Season-wise savings in bill and status of the core in group 2

Players	Winter	Summer	Monsoon	The core
ϕ_1	6992	6601	4375	Non empty
ϕ_2	3336	5428	3824	Non empty
ϕ_3	5527	4483	3657	Non empty
ϕ_4	3303	4225	2608	Non empty
ϕ_5	2856	3746	3033	Non empty
ϕ_6	4160	4257	3963	Non empty

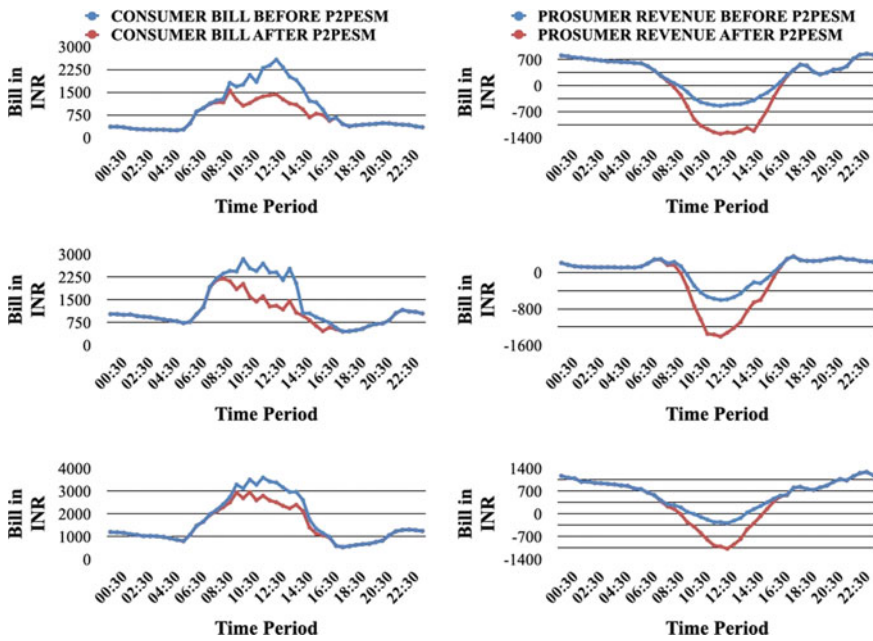


Fig. 6 Comparison of benefits derived from P2PESM for group 1 over three seasons

is between 2000 and 6000 INR for group 1, as in group 1, import and export values for each peer is small compared to that in group 2. As shown in the table in Fig. 7, for group 2 profit range is 2000–7000 INR. Moreover, The core for all peers is nonempty means there is the availability of the core prove this mechanism stable as no peers have any incentive to leave this coalition and further incentive for future coalitions.

The internal Buying and selling prices can be determined by following equations

$$C_{p2p}^{buy} = \left[(C_{Buyer} - E'_I \times C_{rt}) / E_J^{P2P} \right] \tag{5}$$

$$C_{p2p}^{sell} = \left[(C_{Seller} - E'_E \times C_{nm}) / E_E^{P2P} \right] \tag{6}$$

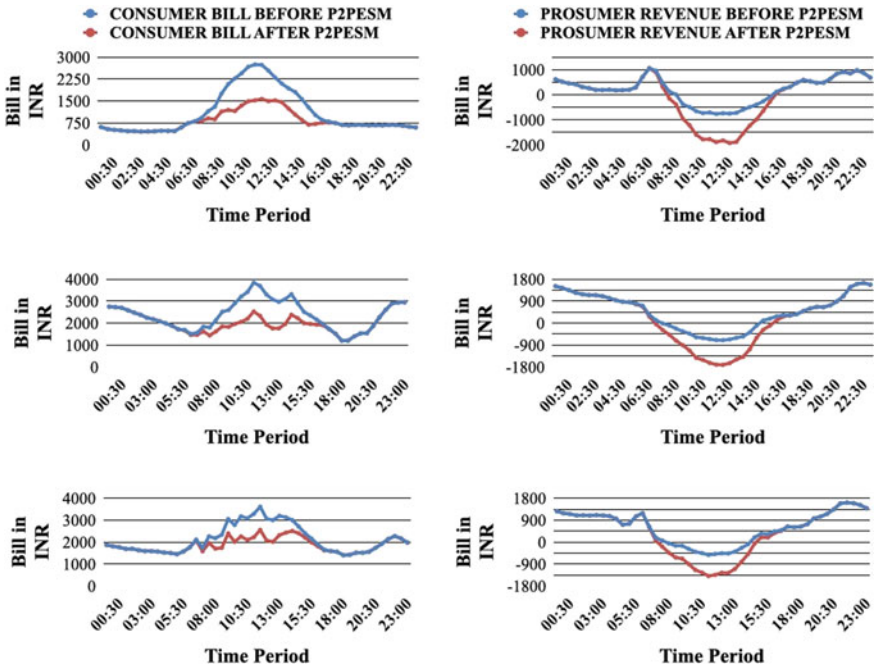


Fig. 7 Comparison of benefits derived from P2PESM for group 2 over three seasons

For this case, C_{rt} is INR 8/kWh and C_{nm} is INR 2/kWh as applicable for the IIT-K campus. To find internal buying and selling price inputs the values required are of—volume of import and export of peer, retail tariff and incentive tariff (Net metering compensation).

Tables 5 and 6 show the internally calculated buying and selling prices for groups 1 and 2, respectively.

Table 5 Internal selling and buying prices for group 1

Seasons	P2P buying price	P2P selling price
Winter	4.34	4.34
Summer	4.13	4.61
Monsoon	4.07	5.55

Table 6 Internal selling and buying prices for group 2

Seasons	P2P buying price	P2P selling price
Winter	3.99	4.60
Summer	4.34	4.70
Monsoon	4.22	5.06

In Fig. 6, the graphs represent the accumulated sum of all consumer's bills and all prosumers revenue for three seasons, which has been compared with before the P2PESM scenario for group 1. As shown in this figure, in winter, after using P2PESM with shapley value, the consumers' total bill reduces to 25%, and prosumers' total revenue increases to 138%. For the summer season, consumers' total bill is reduced to 18%, and prosumers' revenue increased to 78%. The monsoon season, reduction in consumer bill was recorded as 10%, and prosumers' revenue increased to 26%. A similar analysis is shown in Fig. 7 for group 2. In this figure, the graphs represent the cumulative sum of consumer's bills and prosumers revenues for three seasons, which has been compared with before the P2PESM scenario for group 2. A scan is observed; in winter, after using P2PESM with shapley value, consumers' total bill reduces to 26%, and prosumer's total revenue increases to 147%. For the summer season, consumers' total bill gets reduced to 14.53%, and prosumers' revenue increases to 55%. For monsoon season reduction in consumers, the bill is recorded as 12%, and prosumers' revenue increased to 34%.

Figure 8 graphs explain the cumulative sum of the total bill of peers before and after P2PESM using shapley value. For group 1, the total bill's reduction is 24%, and for group 2, this reduction is approximately 23.3%.

Calculation of performance Index:

It indicates to what extent the model has touched the potential value included in the P2P Energy sharing, depending upon parameters like Value min, Value max, and

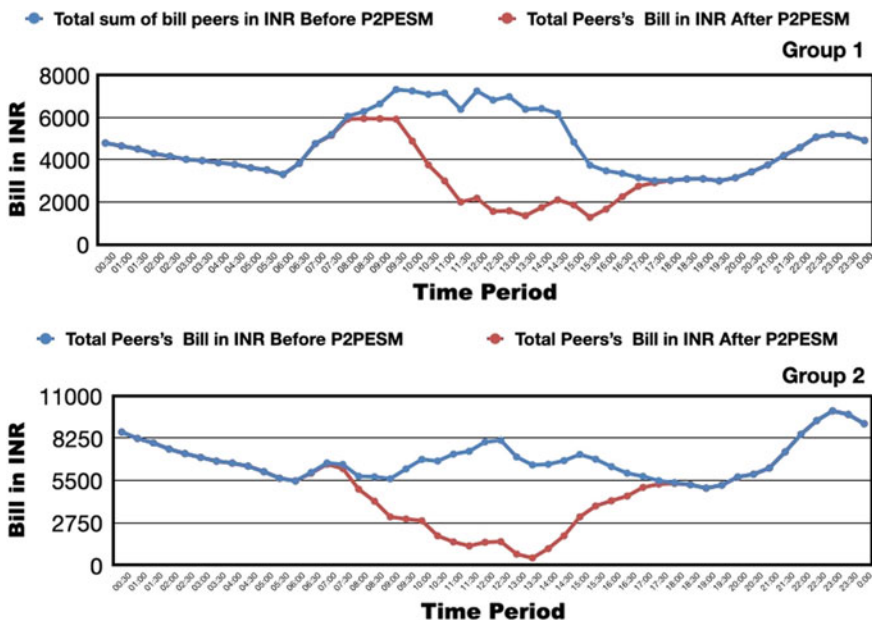


Fig. 8 Comparison of benefits derived by peers from P2PESM for both the groups over three seasons

Table 7 Calculation of performance index

Performance index (%)	Winter	Summer	Monsoon
Group1	100	92	75
Group2	90	94	86

Income, or Cost due to P2P.

$$\text{Performance Index} = \frac{\left(\frac{\text{Income}}{\text{Cost}_{\text{ESR}}}\right) - \text{Value Min}}{\text{Value Max} - \text{Value in}} \tag{7}$$

For a high-Performance Index (PI) value, the difference between import and export Energy and price within the Energy sharing region (ESR) should be low.

The performance index takes a value within [0, 1]. The higher the index is, the more reliable the P2P Energy sharing model brings more economic benefits to the peer’s population. If the index equals to 1, it demonstrates that the model has tapped all the values contained in the Energy sharing area. As shown in the table in Table 7, the utilization of demand symbolizes that the import volume of Energy comes from the export volume of RTS Energy. The purpose behind low utilization of volume is export volume being more than the import volume. When this export Energy is compensated based on grid net-metered price or import volume is more than the export volume of RTS, this excess import volume will be satisfied based on a retail tariff. According to the utilization of import and export volume, after using the Cooperation Game theory shapley value, the performance index for this mechanism is almost 90%.

Settling each unit of Energy exported by prosumers and that consumed by consumers is an essential and most-essential activity in a P2PESM. Based on the forecast values, and each peer has to abide by coalition agreements, Energy is shared at the community level, and benefits are distributed, respectively. This whole Energy Sharing Mechanism can be built upon distributed ledger technology—blockchain. These coalition agreements can be written in smart contracts and digitally signed by each peer. The specific period for which utility allows to operate P2PESM, export Energy from prosumers’ premises can be distributed among consumers with an efficient Energy sharing model. This Energy sharing model has been built based on available import and export volumes of peers.

According to their demand multiplying factor, each consumer will get their shares of export Energy, which gives a guarantee to each consumer to get a share of export Energy according to their demand, rather than other models in which most Energy transactions occur one to one manner. More coalitions will bring more benefits and social welfare among peers. Here coalition means approval of peers (sharing agreements) on sharing Energy between them. As we concentrate on a win-win approach, after coalition sharing of bills must be fair. Fair in terms of benefits due to coalitions must reflect in their bills. As cooperation game theory with shapley value mainly focuses on the fairness of coalitions, it perfectly suits this scenario. P2PESM game theory can give a theoretical base for the model, and shapley value can provide a

fair distribution of bills among peers, and the core can give surety of stability. The principal purpose of using shapley value in this model is to find the most economical, fair, and stable internal buying and selling prices for purposed P2PESM. Here, shapley value gives fair bill to each peer according to their import and export; from these values, consumers' buying price for P2PESM can be identified by the division of P2PESM bill of consumers by import Energy volume, and prosumers' revenue can be identified by the division of P2PESM revenue of prosumers by export Energy. These internal buying and selling prices are fair and stable, which can be assured by the performance index.

5 Conclusion

The entire study of the P2PESM model shows sufficient potential compared to Net Metering. With a win-win strategy in P2PESM, each entity can achieve its objectives. Applicability of P2PESM over Net Metering can be explained as follows (Confirmed by Utilities),

- Enhanced generation from rooftop solar depreciates the volume of electricity to be transmitted to local communities, which satisfies the local demand with diminishing distribution losses and defers investment on stream upgrades with the improvisation of quality of supply.
- It can encourage rooftop solar, which will offer to meet the RPO of the DISCOM with New Revenue Streams: (1) Wheeling charges, (2) Billing, and transaction fees.
- This will save cross-subsidies, loss in revenue due to T&D losses, reduce infrastructure necessary, and contribute to meeting Renewable Purchase Obligation (RPO) targets as promised, and residential consumers will not be obligated entities.
- CGT-shapley value provides the fair and stable distribution of benefits within the Energy sharing area, which leads to a reduction in consumer's bills and increases the revenue of prosumer from RTS. For promoting solar rooftops for the cross-subsidized consumers, P2PESM offers incentives and a sense of participation from consumers and prosumers to participate in trading, encouraging consumers to install solar panels on their rooftops.
- The introduction of Battery Energy Storage Station (BESS) to peers can even be more beneficial as a consumer will have the choice not to trade or trade depending upon the storage Source of Charging. The excess Energy of consumers having BESS could be sold during peak time, helping DISCOM to manage the peak demand better.
- If DISCOM has a daily peak during solar hours or it buys expensive power than its Average Power Purchase Cost (APPC) during the daytime, then it will add to savings.

- It can help to utilize electric mobility on a broad scale by providing an efficient Energy management system with efficient demand management schemes
- With the use of Blockchain Distributed Ledger Technology can make transactions faster, better secured, and trackable Simplify billing at charging stations with Automize the secure transaction of power and money among prosumers, consumers, and DISCOM can actively aware of power flow within its network (starting point to the ending point of Energy).
- Enable consumers to watch their electricity contracts and consumption data with instantaneous billing and settlement by scale-up prepaid meters with BC—DLT platform.

Nevertheless, some challenges exist to implement this model. like,

- **Proper regulatory framework:** The sector is regulated with particular conditions involving the consumer mix, competition, and other concerns, affecting all segments of the value chain. Consequently, for the consumers to engage in electricity sales/purchases among themselves and for peer-to-peer transactions to take place seamlessly, relevant provisions will have to be introduced to the extent of allowing such sales/purchases among the consumers.
- **Sharing/Trading protocol development:** Protocol development is the most crucial step, including tariff determination, revenue sharing, and profit distribution, forecasting and scheduling of the power to be traded roles and definition
- **Interoperability of software and hardware:** The integration of blockchain technology with the current architecture available in terms of interoperability is of crucial importance. This is mainly in the case of possibly outdated software or hardware available with the utility, which may not be compatible with blockchain technology.
- **User acceptability and education:** Lack of social awareness regarding this mechanism will have to be overcome through multiple awareness programs. Despite these efforts, consumers may express reluctance to accepting this technology.

For future scope, P2PEEM empowered with Energy storage can give added flexibility for this model, which may provide exciting results to prove P2PEEM as an efficient flexibility source. Due to P2PEEM, there will be an extension of the bidirectional flow in the distribution network. How it will influence today's network quality constraints also would be an exciting topic to learn.

Acknowledgments The authors acknowledge the financial support provided by the Department of Science and Technology, the Government of India, and the U.S. Department of Energy under the UI-ASSIST project.

References

1. The National Academic Press (2017) Enhancing the resilience of the nation's electricity system
2. IRENA (2019) Innovation landscape for a renewable future: solutions to integrate variable re-newables
3. Martin C, Starace F, Tricoire FP (2017) The future of electricity new technologies transforming the grid edge
4. Dhawan K, Pillai RK (2017) ISGF—Smart grid handbook
5. EIA. <https://www.eia.gov>. Last accessed 4 2015
6. Burke MJ, Stephens JC (2018) Political power and renewable Energy futures: a critical review. *Energy Res Soc Sci*
7. Lacroix M. <https://electricEnergyonline.com>. Last accessed 4 2018
8. U.S. Department of Energy (2017) EIA—Modelling distributed generation in the buildings sectors
9. Cox S, Gagnon P, Stout S, Zinaman O, Watson A, Hotchkiss E (2016) Distributed generation to support development focused climate action
10. EPA. <https://www.epa.gov>. Last accessed 4 2017
11. Yanine F, Sa' nchez-Squella A, Barrueto A, Parejo A, Cordova F, Rother H (2019) Grid tied distributed generation systems to sustain the smart grid transformation: tariff analysis and generation sharing
12. Singh R, Sethi R, Mazumdar R (2019) Solar rooftop: perspective of Discos
13. Parag Y, Sovacool BK (2016) Electricity market design for the prosumer era
14. The Electricity (AMENDMENT) Bill (2020). <https://powermin.nic.in>. Last accessed 2020
15. Framework for real-time market for electricity. CERC. Last accessed 2020
16. Teotia F, Bhakar R (2016) Local energy markets: concept, design and operation. In: 2016 national power systems conference (NPSC) on proceedings. IEEE, pp 1–6
17. CEA.:National Electricity Plan. (2018)
18. Argoneto P, Renna P (2011) Innovative tools for business coalitions in B2B applications: how negotiation, auction and game theory can support small and medium-sized business in e-business
19. Chatain O (2016) Cooperative and non cooperative game theory
20. Tushar W, Saha TK, Yuen C, Liddell P, Bean R, Poor HV (2018) Peer-to-peer energy trading with sustainable user participation: a game theoretic approach. *IEEE Access* 94–119
21. Tushar W, Saha TK, Yuen C, Imran Azim M, Morstyn T, Vincent Poor H, Niyato D, Bean R (2020) A coalition formation game framework for peer-to-peer energy trading. *Appl Energy*
22. Tushara W, Saha TK, Yuen C, Morstyn T, McCulloch MD, Vincent Poor H, Wood KL (2019) A motivational game : theoretic approach for peer-to-peer energy trading in the smart grid. In: *Computer science and game theory*
23. Roth AE (1988) The shapley value
24. Rosenbusch AP (2001) Fairness considerations in cooperative games
25. Kolker A (2007) The concept of the shapley value and the cost allocation between cooperating participants
26. Landinez-Lamadrid DC, Ramirez-Ríos DG, Rodado DN, Negrete KP, Combata Niño (2017) Shapley value : its algorithms and application to supply chains. In: *INGE CUC*
27. Lee W, Xiang L, Schober R, Wong VWS (2014) Direct electricity trading in smart grid: a coalitional game analysis. *IEEE J Sel Areas Commun*
28. Pilling R, Chang SC, Luh PB (2017) Shapley value based payment calculation for energy exchange between micro- and utility grids. In: *Games*
29. Priya Esther B, Sathish Kumar K, Gokul Krishnan G, Venkatesh S (2017) Fair allocation of energy and power using shapley value to reduce deficit in regions of Indian grid. *Indian J Sci Technol*
30. Chen L, Sun T, Zhou Q, Feng D (2017) IECON 2017—43rd annual conference of the IEEE industrial electronics society. In: Editor F, Editor S (eds) *A Shapley value based method for allocating carbon obligation between generation side and demand side in power system 2017*, pp 1–13

31. Branzei R, Dimitrov D, Tijs S (2008) Models in cooperative game theory. *Games*
32. Han L, Morstyn T, McCulloch M (2019) Estimation of the shapley value of a peer-to-peer energy sharing game using coalition stratified random sampling. In: *Computer science and game theory*
33. Bhakar R, Sriram VS, Padhy NP, Gupta HM (2010) Probabilistic game approaches for network cost allocation. *IEEE Trans Power Syst*

Recent Technological Advances in Solar Photovoltaic System and Its Applications in Building Integrated Photovoltaic System



Noorul Islam, Aslam Nat, and Rashid Ahmed Khan

Abstract Energy has become an integral part of our life. The fossil fuel present in the environment is very much limited. On the other hand, fossil fuel emits harmful gases such as carbon dioxide, Chlorofluorocarbon (CFC), carbon monoxide, and others which harmed flora and fauna. Therefore, the concern for renewable energy application has become more vital due to the depletion of fossil fuels, rising global warming, and increased consumption of energy. Renewable energy aims to reduce pollution levels, enhancing the local economy and community sustainability. Solar energy is the most promising alternative energy source since it has various advantages over other renewable energy sources. The sun is an unquenchable source of energy capable of addressing all energy requirements of humankind. The solar energy concept has been around for a long time, and technological advancements will make it endure for a longer period. The PV-Effect is a mechanism that can produce an electric current when sunlight strikes the limiting layer of semiconductor materials. A photovoltaic (PV) system is a semiconductor device that produces electricity when exposed to luminosity. A PV module is made up of several solar cells that are coupled in parallel and series. This paper provides an extensive study of advancements in energy extraction techniques from a solar panel, analysing solar PV systems under diverse circumstances. PV technology is hastily evolving compared to alternative renewables, consequently leading to the Building Integrated Photovoltaics (BIPV) systems playing a significant role in the generation of electrical energy. BIPV system is a preferred choice as a building integrated solar energy storage system. It has been categorised into three subparts: Grid-connected BIPV system, BIPV system with a

N. Islam

Department of Electrical Engineering, ZH College of Engineering and Technology, Aligarh Muslim University, Aligarh 202002, India

A. Nat

Department of Computer, Control, and Management Engineering, Sapienza University of Rome, 00185 Rome, Italy

R. A. Khan (✉)

Department of Electrical Engineering, National Taiwan University of Science and Technology, Taipei 10607, Taiwan

e-mail: rashidkhan6417@gmail.com

solar battery, and PV-Trombe wall. The BIPV mechanism simultaneously acts as a material for the envelope of the building and power extraction from.

Keywords Building integrated photovoltaics (BIPV) · Chlorofluorocarbon (CFC) · Photovoltaic (PV) module · Maximum power point tracker (MPPT)

1 Introduction

Energy is one of the most significant components of a country's prosperity and economic development. The electricity demand is increasing rapidly due to an increase in the human population across the globe. For sustainable and clean energy, the whole world is switching towards renewable energy sources. The fossil fuel-based generation of electrical energy has several negative effects on the environment as it produces harmful greenhouse gases which deteriorate the environment. Considering this detrimental effect on the environment, the generation of electrical energy from solar energy sources reduces the emission of harmful gasses to a great extent.

Consequently, the use of solar PV panels increases across the globe. Solar energy is one of the optimal ways to this problem—solar irradiance results in the generation of different types of energy. Either the irradiance is directly used in the generation of electrical energy or indirectly uses solar energy through passive heating and active heating. In direct conversion, the solar insolation is converted into electrical energy through a solar PV module. Generally, the efficiency of solar photovoltaic modules restricts to 15–20% only. Many research experiments are accomplished to enhance the output efficiency of a solar PV module system. Many new technologies and efforts are being implemented in developing the solar PV system. Besides the many advantages of solar PV systems, the demerits of Solar PV technology are being encountered during the advancement of solar PV technologies. Some critical issues are the lower efficiencies of the solar cell, skilled workforce, proper infrastructure absence, high installation cost. The research and the studies in this field have paved the way for the advancement of new technologies.

The solar photovoltaic system tops the list of widespread technologies of renewable energy which transform solar radiation into electrical energy. The major positives of solar photovoltaic energy are lower operating and maintenance costs, zero pollutant emissions, mitigating the global warming issue. Solar energy can be transformed into electrical energy and thermal energy with the aid of different technologies. The solar PV cells are used to convert the incident solar radiation directly into electricity [1–7]. Only a small part of the irradiance is transformed into electricity. At the same time, the major portion of this light increases the cell temperature by converting it into heat, thus reducing its performance. With the help of solar collectors and concentrators, the incident lights can be converted into thermal energy. Besides the numerous advantages, a few shortcomings and problems of PV technology are its low efficiency and climatic dependencies such as ambient temperature, solar irradiance,

humidity, speed of wind, hail, and dust accumulation on the surface of photovoltaic module [8–13]. These climatic parameters can highly affect their performance.

In a few last years, researchers used variant semiconductor materials and different technologies in designing the solar photovoltaic cell having low cost and efficiency of conversion is high [14–18]. Conventional solar PV modules, manufactured from Si-crystalline wafer modules, are bulkier, and the weight is also high, which causes transportation from one place to another a greater challenge. Generally, these are large size solar PV modules cover with glass sheets [19–21]. A greater weight, bulky, and massive solar PV panels acquire a greater space and a large roof to accommodate these massive panels when there is an application of high power [22–24].

The building is a dominant contributor of worldwide electricity consumption and carbon emission, approximately 40% of world energy consumption. Mitigation of greenhouse gas emission, excess carbon emission across multiple dimensions is essential to enhancing the climate viability for future generations. The possibility of renewable power generation at the construction site was examined to optimise energy consumption and distribution infrastructure. This offers an opportunity to alleviate the associated harmful emissions from expanding energy utilisation of non-renewable sources. BIPV system offers an opportunity by allowing clean energy production from various incorporated building design elements [25]. BIPV decreases the environmental damage caused by conventional energy sources and is a viable approach to facilitate the rising environmental and economic expenses of energy generation from fossil fuels.

This paper has been categorised in nine sections. The introduction has been discussed in Sect. 1. Modelling of solar PV module has been discussed in Sect. 2. Different MPPT Techniques has been presented in Sect. 3. Section 4 gives the a brief introduction to building integrated photovoltaic module. Integration of BIPV is explained in Sect. 5. The economical aspects are discussed in Sect. 6. In Sect. 7 strategic benefits of BIPV is explained. The factors of improvements in BIPV presented in Sect. 8 and in the last section of the paper, the conclusion and future aspects are provided.

2 Modelling of Solar PV Module

In a solar PV module or cell, the energy conversion at the solar PV cells do not produce either voltage or current. It takes place by the photoelectric effect. Many solar cells combine to form a solar PV module. These cells are connected in series to raise the output voltage significantly, and the solar cell is coupled in parallel to boost the output current. The researcher had proposed many equivalent models of a solar photovoltaic cell. Figure 1 depicts a solar photovoltaic module cell with a single diode model. The solar PV cells do not produce either voltage or current signal; the circuit comprises a diode linked in parallel with the current source. The series and the parallel resistance are connected in parallel. I_{PV} is the current generated from the PV module, which is influenced by solar insolation and temperatures. The I_{PV} will

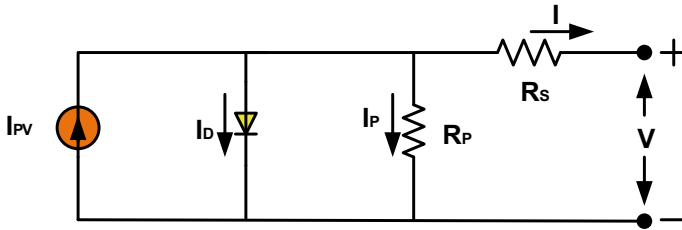


Fig. 1 Single diode model for a solar PV cell

be greater when the solar insolation has a greater intensity. The solar PV module’s behaviour is nonlinear because of the presence of the current I_{Diode} in the circuit. the output current can be derived by Kirchoff’s Current Law (KCL).

$$I = I_{PV} - I_{Diode} - I_{Parallel} \tag{1}$$

It is expressed as

$$I = I_{PV} - I_0 \left[e^{\left(\frac{q(V+I \cdot R_s)}{aKT} \right)} - 1 \right] - \frac{V + I \cdot R_{Series}}{R_p} \tag{2}$$

where

- I Current through the solar PV cell
- I_{PV} Solar Insolation current
- I_{Diode} Diode current
- $I_{parallel}$ Current through R_p
- V output voltage
- $R_{parallel}$ Parallel resistance and
- R_{Series} Series resistance
- a Ideality factor of the diode
- T Cell Temp (Kelvin)
- K Boltzmann constant (1.380×10^{-23} J/K)
- q Charge on electron (1.602×10^{-19} °C).

The current in a solar photovoltaic module can be expressed as follows. If the factor of temperature and irradiance is taken into the consideration

$$I_{PV} = (I_{PV, n} + K \cdot \Delta T) \frac{G}{G_N} \tag{3}$$

where

- G operating condition irradiance
- G_N Nominal condition irradiance
- ΔT is the temperature variance between the actual and nominal temperatures.

When the solar photovoltaic module is exposed to solar insolation, there may be a possibility that some area or part of the solar PV module get a low intensity of solar insolation as compared to other area or part, this phenomenon is called partial shading conditions. the above mention phenomenon is more likely to occur due to appearance of shadow of tall rise buildings, Trees, and nearby objects—partial shading condition consequences in complicated solar PV characteristics and revealing numerous peaks. These methods or techniques can be utilised under partially shaded atmospheric conditions and suddenly varying conditions to determine the maximum power delivered.

3 Maximum Power Point Tracker (MPPT)

Typically, the efficiency of Solar PV module has an output efficiency nearby 15%-22%. Many factors are responsible for decreasing the panel’s output efficiency, some of their orientation of panel, topographical location, temperature, humidity, rate of dust accumulation, and many other factors. To boost or enhance the efficiency of the solar PV module, Power electronic devices accompanying by Maximum Power Point Tracker (MPPT). MPPT controllers are responsible for the extraction of maximum power from the solar PV module. The implementation of MPPT significantly improves the output performance of the solar PV module. Different algorithms are being implemented for tracking the maximum power point (MPP) adequately. The main drawback or limitation with the MPPT existing is that they track the maximum power slowly. Consequently, the output Efficiency of the solar PV module deteriorates. Figure 2 shown a basic block diagram for MPPT integrated solar PV module [26].

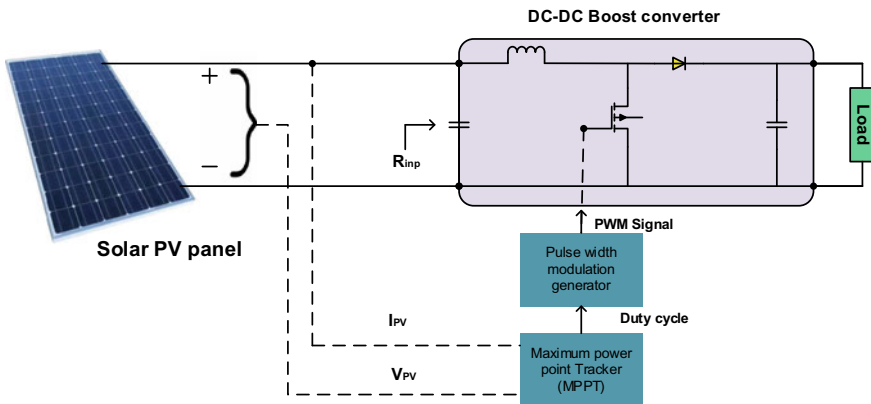


Fig. 2 Basic block diagram of MPPT for a solar PV module

The various techniques have been implemented for maximum power point tracker and are classified as stochastic-based techniques, Artificial intelligence techniques, and conventional techniques. In a traditional MPPT approach, incremental conductance and perturbation and observation (P&O) are hill climbing-based techniques. For uniform solar irradiation, two strategies are used: fractional open-circuit voltage and short-circuit current. Under Partial shading, due to the existence of multiple peaks in the PV characteristic, the maximum power point tracking efficiency deteriorates.

Various artificial intelligence techniques stochastic algorithms have been implemented because of the conventional method interfacing. All the techniques are influenced by the biological structure and as well as nature. It incorporates firefly algorithm (FA), Fuzzy Logic Control (FLC), Cuckoo Search (CS), Differential Evolution (DE), Artificial Neural Network (ANN), Genetic Algorithm (GA), Particle Swarm Optimisation (PSO). The technique mentioned above is implemented in extracting the maximum power under the condition of partial shading condition (PSC) and differing the atmospheric condition. Amongst all the different maximum power point trackers, one possesses less complexity, is cheap, minimum fluctuation in the output power.

4 Building Integrated Photovoltaic (BIPV) System

As global demand and emphasis on clean and non-contaminating power and energy efficiency increase, zero-emission buildings quickly attract interest. To become low energy or zero-emission house, it must collect energy from its neighbouring environment. Hence solar radiation has been one of the probable choices. BIPV systems, in which solar cells are structured inside the climate enclosures and use solar radiation to generate electricity, seem to be a productive and adaptable technique to achieve these objectives in terms of aesthetics, technical, and economic solutions. The BIPV systems complement standard construction materials and elements such as roofs and faces and the building's climate enclosure [27, 28]. BIPV mechanisms are either regarded as a legitimate structural element or architecturally integrated into building design. THEREFORE, the BIPV method simultaneously acts as a material for the envelope of the building and an energy generator. BIPV also mentions the building attached photovoltaic (BAPV) systems, including BIPV foil, panels, tiles, and other solar cell glazing elements. Therefore, this study links current technology and scientific energy exploration tomorrow by examining and exploring potential future approaches and research opportunities for the BIPV system [29] (Fig. 3).

5 Photovoltaic Cell Integration in Buildings

BIPV cells can be integrated into sloping rooftop buildings, flat rooftops, facades, and solar shielding structures. PV cells can also be mounted on or above existing rooftop surfaces or walls. BIPV systems substitute the outer skin of the existing structure,



Fig. 3 Building integrated PV system

functioning as both a climatic barrier and a source of energy. Several factors must be addressed and analysed when integrating PV cells into the external building structure. The primary aspect is ensuring an air space under photovoltaic modules to provide airflow to reduce solar cell temperature. The second factor to look for is the efficiency of solar cell efficiency at higher temperature levels, specifically for mono and polycrystalline Si cells. One other factor is the tendency of BIPV towards current and new constructions, as solar cells must naturally obey the roof or wall inclination to be incorporated solutions. During the integration of BIPV systems, more considerations should be taken into account during the geographical location and sun orientation and coverage area [30].

6 Economical Aspects of BIPV System

PV panels require a substantial amount of space for installation; space-saving technologies like BIPV may be the best way to address the accompanying budgetary burden. Incorporating PV elements into goods such as roof systems, window frames, awnings, and curtained facades allows for cost savings by replacing typical construction elements with PV components at nominal expenditures. Moreover, since BIPV is still a long way from becoming a viable technology, uncertainty over BIPV and its application is another crucial issue. There are several aspects behind this uncertainty: safety aspects, life cycle assessment, installation, integration aspects, architectural aspects, durability, possibility to offer excess electricity to the grid, and others [28, 31].

The expenditure of a PV system will decrease over time as technological improvements enhance, resulting in a reduced price for each kW, which would be an impactful step towards making PV product implementation and structural integration commercially viable even without tax incentives. When evaluating potential alternative energy sources, the energy payback period plays a crucial role; it explains how long it takes the photovoltaic system to generate the same amount of power as consumed

to build it. The embodied electric power of the system must be evaluated to establish the energy payback period.

7 BPIVs Strategic Benefits

The infrastructure facade mainly comprises brickwork, glazes, coverings and fenestrations, and other elements, including shading elements and parapets. All of these construction components offer the opportunity to customise integrate PV systems in the buildings. BIPV is a versatile innovation. Therefore, it is usually established for more than one application. As a result, BIPV signifies that it can perform various functions as an exterior element, such as thermal protection and glare shielding. Three classes recognised for this additional function or literature contribute to the exterior design of the building exterior, economic benefits, and environmental consequences [32].

7.1 The Design-Related Benefits Include

1. Views and natural light options for light transfer and communication with the outside world
2. Serve as reinforced safety glass
3. Thermal and wind isolation
4. Single-way refraction acts as a visual cover, shading modulation
5. Substitution of conventional products such as stonework.

7.2 Economic Benefits

1. Elimination of the requirement for long-distance transmission and distribution of electricity from power stations
2. Additional assembling and installation expenses are reduced, yielding in on-site electricity and a reduction in overall building material cost
3. Reduced land consumption for energy generation
4. Mitigate infrastructure and operational capital expenditure
5. Savings in both materials and labour via grid integration.

7.3 Environmental Benefits

1. Reduced carbon emissions

2. Reduced conventional energy dependency
3. Secure Authentication of Power Grid
4. Sound protection up to 25 dB Noise damping.

8 Improvement Factors of BPIV System

8.1 PV Development

PV material and technological advancements would have an even greater impact on the growth of BIPV in the near term. This seems to be especially significant when you can customise solar cell compositions and building incorporation methods from research based on the Photovoltaic system. In the approaching BIPV solutions to be created, the progress in these technologies and their increased efficiency will inevitably be exploited.

8.2 New BIPV Materials and Technologies

Research pathways for prospective future PV technologies can lead to discoveries that can be applied into BIPV in numerous fields such as Modules of incredible efficiency, Organic modules based on ultra-low costing and moderate productivity, Solar concentrate or solar trapping systems integrated into the photovoltaic cell surface, and underlying components, Versatile ultra-light thin-film solar cell, and few more considerable aspects.

8.3 Solar Cell Concentrators

Numerous Photovoltaic Panels surface solutions can be considered to increase solar cell efficiency. Different mechanisms of solar radiation absorption may be incorporated in the domain. In the conventional sense, solar concentrators are arrays of photovoltaic modules mounted on massive mobile structures that are always facing the sun. As a result, one can visualise creating an outer surface capable of gathering as much renewable energy as if the entire exterior surface were coated with a PV substance. One technique for high solar cell efficiency is to create or stack solar cells, so-called sandwiched solar cells, using various substance layering and cells with various spectral absorption to collect as much solar light as possible.

8.4 *Texture of Inverted Pyramid*

Another technique for more efficient energy extraction is the inverted pyramid texturing of a photovoltaic module. The tremendous light-capturing characteristics of the pyramid pattern are induced by these three effects: (1) Significantly raise solar ray pathway length through the cell, capturing a greater portion of the solar energy entering the cell before leaving the molecule. (2) Reduced reflection of the frontal panel by offering a triple rebound for a proportion of entering solar rays. (3) enhance the quality of sunlight reflected from a rear surface by a whole internal reflection around the frontal surface well above the critical angle.

9 Conclusion and Future Aspects

There are various issues in general and specific terms with the framework of BIPV customisation, and various researchers have addressed these obstacles. To begin with, BIPV is still in its early stages of technological advancement; it has to achieve its maximum efficiency, and research demonstrates that design codes and application standards are still not fully recognised. The analysis has only shown the huge variances in BIPV exterior modification methodologies and techniques. This makes it potentially difficult to develop an analytical framework and demands certain implications. Thermal monitoring and aesthetics were highlighted as being the most often investigated BIPV facade modification objectives. However, the various tactics employed in each of these cases necessitated the employment of specialised manufacturing methods that have yet to be widely standardised.

Further research should be conducted to formulate the evaluation of adaptable BIPV and develop a strategy implementation model. The objective of this paper is just to assess the prospect of optimising BIPV. Additional research potentials for precise evaluation of data are the customisation of cost difficulties, climatic or geographical uses.

References

1. Kasaeian A, Khanjari Y, Golzari S, Mahian O, Wongwises S (2017) Effects of forced convection on the performance of a photovoltaic thermal system: An experimental study. *Exp Thermal Fluid Sci* 85:13–21
2. Saygin H, Nowzari R, Mirzaei N, Aldabbagh LBY (2017) Performance evaluation of a modified PV/T solar collector: a case study in design and analysis of experiment. *Solar Energy* 141:210–221
3. Wang S, Shi J, Chen H-H, Schafer SR, Munir M, Stecker G, Pan W, Lee J-J, Chen C-L (2017) Cooling design and evaluation for photovoltaic cells within constrained space in a CPV/CSP hybrid solar system. *Appl Therm Eng* 110:369–381

4. Chinamhora T, Cheng G, Tham Y, Irshad W (2013) PV panel cooling system for Malaysian climate conditions. In: International conference on energy and sustainability
5. Chandel SS, Agarwal T (2017) Review of cooling techniques using phase change materials for enhancing efficiency of photovoltaic power systems. *Renew Sustain Energy Rev* 73:1342–1351
6. Su D, Jia Y, Alva G, Liu L, Fang G (2017) Comparative analyses on dynamic performances of photovoltaic–thermal solar collectors integrated with phase change materials. *Energy Convers Manage* 131:79–89
7. Zhu L, Boehm RF, Wang Y, Halford C, Sun Y (2011) Water immersion cooling of PV cells in a high concentration system. *Sol Energy Mater Sol Cells* 95(2):538–545
8. Rosa-Clot M, Rosa-Clot P, Tina GM, Scandura PF (2010) Submerged photovoltaic solar panel: SP2. *Renew Energy* 35(8):1862–1865
9. Han X, Wang Y, Zhu L (2011) Electrical and thermal performance of silicon concentrator solar cells immersed in dielectric liquids. *Appl Energy* 88(12):4481–4489
10. Sun Y, Wang Y, Zhu L, Yin B, Xiang H, Huang Q (2014) Direct liquid-immersion cooling of concentrator silicon solar cells in a linear concentrating photovoltaic receiver. *Energy* 65:264–271
11. Xiang H, Wang Y, Zhu L, Han X, Sun Y, Zhao Z (2012) 3D numerical simulation on heat transfer performance of a cylindrical liquid immersion solar receiver. *Energy Convers Manage* 64:97–105
12. Zhu L, Raman A, Wang KX, Anoma MA, Fan S (2014) Radiative cooling of solar cells. *Optica* 1(1):32–38
13. Cao C, Li H, Feng G, Zhang R, Huang K (2016) Research on PV/T-air source heat pump integrated heating system in severe cold region. *Procedia Engineering* 146:410–414
14. Mojumder JC, Ong HC, Chong WT, Izadyar N, Shamsirband S (2017) The intelligent forecasting of the performances in PV/T collectors based on soft computing method. *Renew Sustain Energy Rev* 72 (2017): 1366–1378.
15. Islam N, Mohammad K, Khan RA, Sarwer Z, Sarwar A (2021) Symmetrical and asymmetrical multilevel inverter topologies with reduced device count: a review. In: 2021 2nd international conference for emerging technology (INCET). IEEE, pp 1–6
16. Benganem M, Al-Mashraqi AA, Daffallah KO (2016) Performance of solar cells using thermoelectric module in hot sites. *Renew Energy* 89:51–59
17. Najafi H, Woodbury K (2012) Feasibility study of using thermoelectric cooling modules for active cooling of photovoltaic panels. In: ASME international mechanical engineering congress and exposition, vol 45226. American Society of Mechanical Engineers, pp 1743–1751
18. Ahadi S, Hoseini HR, Faez R (2014) Using of thermoelectric devices in photovoltaic cells in order to increase efficiency. *Ind J Sci Res* 2(1):20–26
19. Najafi H, Woodbury KA (2013) Optimisation of a cooling system based on Peltier effect for photovoltaic cells. *Sol Energy* 91:152–160
20. Farooqui SA, Khan RA, Islam N, Ahmed N (2021) Cuckoo search algorithm and artificial neural network-based MPPT: a comparative analysis. In: 2021 IEEE 8th Uttar Pradesh section international conference on electrical, electronics and computer engineering (UPCON). IEEE, pp 1–5
21. Van Sark WGJHM (2011) Feasibility of photovoltaic thermoelectric hybrid modules. *Appl Energy* 88(8):2785–2790
22. Whitburn G (2012) Exploring green technology, fundamental advantages and disadvantages of solar energy
23. Peplow M (2014) Organic synthesis: the robo-chemist. *Nature* 512:20–22. <https://doi.org/10.1038/512020a>
24. Khan RA, Farooqui SA, Khan MH, Sarfraz M, Luqman M, Khan M (2022) Dust deposition on PV module and its characteristics. In: The effects of dust and heat on photovoltaic modules: impacts and solutions. Springer, Cham, pp 59–95
25. Heinstein P, Ballif C, Perret-Aebi LE (2013) Building integrated photovoltaics (BIPV): review, potentials, barriers and myths. *Green* 3(2):125–156

26. Khan AI, Khan RA, Farooqui SA, Sarfraz M (2021) Artificial neural network-based maximum power point tracking method with the improved effectiveness of standalone photovoltaic system. In: AI and machine learning paradigms for health monitoring system: intelligent data analytics, 86:459
27. Jelle BP (2016) Building integrated photovoltaics: a concise description of the current state of the art and possible research pathways. *Energies* 9(1):21
28. Tsai HL, Hsu CY, Hsieh FS, Chiang YH (2013) Design and performance evaluation of building integrated photovoltaic/thermal (BIPVT) air collector. In: 2013 IEEE 39th photovoltaic specialists conference (PVSC). IEEE, pp 1492–1494
29. Mehravaran A, Derhem A, Nassereddine M (2019) Building-integrated photovoltaics (BIPV) for residential and industrial properties. In: 2019 Advances in science and engineering technology international conferences (ASET). IEEE, pp 1–6
30. Sechilariu M, Wang B, Locment F (2012) Building integrated photovoltaic system with energy storage and smart grid communication. *IEEE Trans Industr Electron* 60(4):1607–1618
31. Biyik E, Araz M, Hepbasli A, Shahrestani M, Yao R, Shao L, Essah E, Oliveira AC, Del Cano T, Rico E, Lechón JL, Atl, YB (2017) A key review of building integrated photovoltaic (BIPV) systems. *Eng Sci Technol Int J* 20(3):833–858
32. Attoye DE, Tabet Aoul KA, Hassan A (2017) A review on building integrated photovoltaic façade customisation potentials. *Sustainability* 9(12):2287

Performative Analysis on Ion-Sensitive Field-Effect Transistor by Varying Intrinsic Parameter



Keval Thakrar, Parth Katrodiya, Dhruvam Panchal, Hitarth Bharad, Jaimin Vaghela, Sai Deepak, and Rutu Parekh

Abstract This paper studies the effects on the performance of silicon-based and germanium-based ISFET by varying the device parameters. The ENBIOS-2D Lab of nanoHUB has been used for simulation. Parameters like temperature, channel length, and gate oxide thickness are varied. These parameters are varied to study I-V transfer characteristic curves of Si-based and Ge-based devices, effect on potential along x -direction as well as z -direction and carrier concentration. Variation of device temperature from 273.15 to 323.15 K shows there is a direct relation of drain current with the device temperature. Si-based devices show 107% current increase and Ge-based devices show 13.65% current increase when temperature increases from 273.15 to 323.15 K at 0.5 V gate voltage. Comparing the results of Si-based devices at different temperatures of 273.15 and 323.15 K, the carrier concentration increases massively by about 53 times at the bottom center of the channel with this increase in temperature, while potential at this point is unaffected. The length of the ISFET channel is varied from 200 to 1000 nm and the thickness of gate oxide from 3 to 15 nm. An increase in the potential of 174% along z -direction is observed at the bottom center of the channel when gate oxide thickness increases from 3 to 15 nm. Simulations of all these parameters show an inverse relation of drain current with channel length as well as gate oxide thickness. After analyzing the results, the effects on each parameter and the magnitude of these effects were identified based on the material used in the ISFET device.

Keywords MOSFET · ISFET · Bio-FET · Simulation · Carrier concentration

1 Introduction

In 1970, Dutch engineer Piet Bergveld studied the MOSFET and adapted it into a sensor for electrochemical and biological applications which led to the invention

K. Thakrar · P. Katrodiya (✉) · D. Panchal · H. Bharad · J. Vaghela · S. Deepak · R. Parekh
VLSI and Embedded System Group, Dhirubhai Ambani Institute of Information and
Communication Technology, Gandhinagar, India
e-mail: parthkatrodiya3108@gmail.com

of ion-sensitive FET (ISFET). BioFET, Electrolyte-gated organic FET (EGOFET), and some other emerging devices are derivations of ISFET. BioFET is a biosensor described as a self-contained integrated device capable of providing specific quantitative or semi-quantitative analytical information. This is done using a biological receptor that comes in contact with an electrochemical transduction element [1]. Measurement of the concentration of H_3O^+ ions is represented on the pH scale, which is a vital factor affecting many chemical reactions as well as biochemical activities, and hence it is very important to measure pH accurately. Before the invention of BioFET, glass electrode sensors were used to sense the change in pH in the solution. However, due to the limitations of the glass electrode sensor and cost, it made the way for BioFET. BioFET acts as an intrinsic amplifier that reflects a larger change in current from a comparatively smaller change in surface potential. Silicon-based biosensors have gained a lot of attention in the field of bioanalytical applications due to their characteristics like speed, miniaturization, sensitivity, and low cost. Carbon-based organic semiconductor materials can be used in such a biosensor as a sensing membrane. Carbon-based materials that are derived from a specific arrangement of carbon atoms are extensively used as transducing materials due to their unique properties and nanostructures [2]. An important subtype of BioFET is an EGOFET. In this biosensor, an organic semiconducting channel is capacitively coupled with the gate electrode utilizing an electrolytic solution [3]. Enzyme-based-ISFET is working on the principle of pH-sensitive ISFETs in which during an enzymatic reaction the concentration of hydrogen ions is proportional to the level of the substrate.

Furthermore, the Ion-sensitive field-effect transistor (ISFET) has been used in many applications. Some of these are DNA sensing where the DNA strand binds to the gate surface of ISFETs. This changes the charge in the surface potential due to the negative charge of DNA, allowing DNA sensing [4]. Electro-immunological sensing, the antibody recognizing antigen is coated onto the gate of an immuno-ISFET which is used for the detection of the antibody. And due to the specificity of the antigen-antibody interaction antibodies are the most commonly used capture agents to identify and quantify individual analytes [5].

A significant amount of research is done in studying the transfer characteristics of ISFET devices to the change in pH of electrolytes. That is, drain current (I_D) as a function of the reference voltage (V_{ref}) and drain-source voltage (V_{DS}) for different pH scales [6]. Also, there is a notable study on the effects on device sensitivity by varying the gate oxide thickness and buried oxide thickness of SOI-ISFET using its behavioral macro-model proving that thicker buried oxide and thinner gate oxide increase the dual-gate sensitivity of the device [7]. Additionally, there has also been an in-depth comparative analysis done on the performance of ISFET due to different sensing films such as Al_2O_3 -gate, SiO_2 -gate, Ta_2O_5 -gate, etc. The sensitivity of Ta_2O_5 is the highest and that of SiO_2 is the lowest. Such device sensitivity is based on threshold voltage due to the variation in electrochemical parameters like surface site density and dissociation constants [8]. To overcome this barrier and achieve greater sensitivity, other membranes like Si_3N_4 , Al_2O_3 , and HfO_2 can be utilized [9]. An ISFET's channel current is highly modulated by ion concentration in electrolytes [10].

Further, it is known that a slow and monotonic change in the threshold voltage of ISFET is observed at the interface between the insulator and the electrolyte. This effect of drift is studied in detail [11]. Moreover, it is known that pH measuring sensitivity can be significantly increased by using pH buffer solutions containing counter-ions beyond a specific size, which is validated by measuring the pH response of an extended gas ISFET pH sensor [12]. Also, the temperature instability of ISFET devices is quite complicated that cannot be overlooked. Moreover, it is estimated that a variation of 7 K in temperature around the room temperature corresponds to a change in 1 pH value of electrolyte [11]. While considering the sensitivity, the concept of the Nernst limit restricts the sensitivity of SiO₂ sensing at 59 mV/pH [13]. Furthermore, considerable work is also done in the simulation and modeling of temporal and temperature dependence of ISFET electrochemical and device parameters are studied. Considering the temperature and temporal drift, the transfer characteristics of the device from extracted parameters and experimentally reported values to match accurately [14, 15]. Another study models and simulates BioFETs as well as deploy them on nanoHUB explaining the working of the device by 2D and 3D multi-scale models [16].

This paper presents the nature and characteristics of ISFET in different situations. Different sections of this paper include the application and scope of ISFET and BioFET devices, the working principle of these devices as well as the effect on device performance as a result of changes in various device parameters. A detailed analysis of these results is presented by varying channel length, gate oxide thickness, and temperature for silicon-based and germanium-based sensors that are simulated on the nanoHUB tools [17, 18]. This paper presents a comparative study of Si-based and Ge-based ISFET devices under different physical conditions and varying parameters. A study and investigation of various parameters like drain current vs voltage for different temperatures, channel lengths and gate oxide thickness, carrier concentration and potential along horizontal as well as vertical axes for varying temperature, channel length, and gate oxide thickness, as well as carrier concentration for varied drain voltage, have been implemented and simulated. This helps to optimize the device's performance. It can be applied to decide the dimensions and material of the device for a particular sensing application. Further, it can be applied for pH sensing as well as developing more effective biosensors for a wide range of medical applications.

2 Working of ISFET and Simulation Framework

ISFET and MOSFET are fundamentally very similar and hence, work on the same principle. The difference between the two is that the standard gate electrode of MOSFET is replaced by a reference electrode in contact with the gate oxide and an ion-sensitive membrane as displayed in Fig. 1. Between these, is present, an electrolyte that completes the gate-source circuit of the ISFET device when voltage is applied at the reference electrode [19]. A barrier, which is sensitive to hydrogen ions,

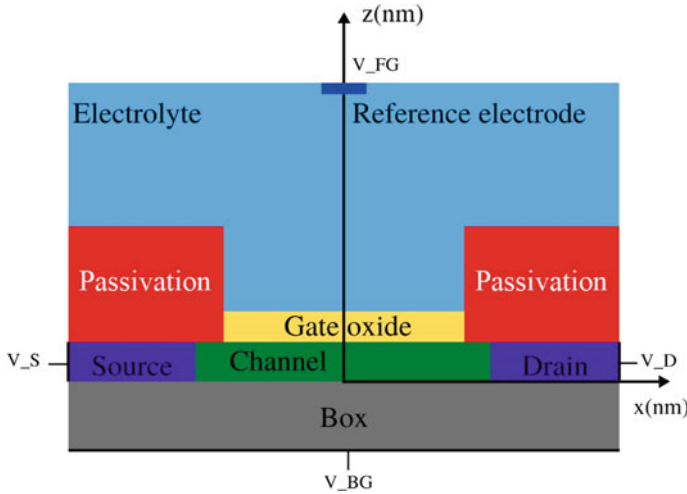


Fig. 1 Schematic of an ISFET

separates the gate electrode from the channel. Also, a gap allows the pH measurement of the electrolyte that comes in contact with the sensitive barrier. Here, z equal to 0 nm represents the bottom point of the channel, and z equal to 20 nm represents the top of the channel.

When the ions bind to the gate, it leads to a change of electric charges on the gate terminal. The site-binding model can be used to explain the oxide surface charge. It describes the equilibrium between the Si-oxide surface sites and H^+ ions in the electrolyte solution. As explained by the site-binding model, the SiO_2 oxide surface can donate and accept protons at the oxide-electrolyte interface. Due to this change in charge, there is an accumulation or depletion of carriers. Due to the dependence of the channel conductance on the gate voltage applied, the applied fluid gate voltage (V_{FG}) is analogous to the electric field generated due to the binding of ions to the gate [20].

The tool used for simulation of various parameters is ENBIOS-2D Lab of nanoHUB [17, 18]. This tool illustrates and simulates an ion-sensitive field-effective transistor (ISFET) in two dimensions. The physical system is modeled with the Poisson/Boltzmann (DC) and Poisson/Nernst/Planck—Poisson/Drift/Diffusion (AC small-signal) equations coupled to the site-binding charge model equations at the Electrolyte/Insulator interfaces (Table 1).

3 Results and Discussions

This paper studies and investigates the change in behavior of BioFET parameters like drain current, carrier concentration along x -direction (DC), potential along

Table 1 Simulation parameters of ISFET device

ISFET input parameters	Values
Channel length	200, 1000 nm
Gate oxide thickness	3, 15 nm
Temperature	273.15, 323.15 K
Semiconductor film thickness	20 nm
BOX thickness	100 nm
V_{DS}	0.05 V
V_{BG}	0 V
Electrolyte	NaCl
Concentration of NaCl	0.01 mol/L
pH of NaCl	7
Insulator material	SiO ₂

the x -direction, carrier concentration along z -direction (DC), and potential along z -direction; with variation in channel length, gate oxide thickness and temperature. Additionally, there is also a simulation presenting carrier concentration along z -direction with varying drain-source voltage.

3.1 I-V Characteristics of ISFET Device

Studying the transfer characteristics of the device, from Fig. 2a, it is observed that variation in current is proportional to change in temperature. As temperature increase mobility of ions increase due to kinetic energy and since the mobility of ions is proportional to the current flowing in the device, an increase in current is observed according to the following formula:

$$I_D = \frac{1}{2} C_{ox} \mu_{eff} W_{eff} / L_{eff} [2(V_{GS} - V_{TH}) V_{DS} - V_{DS}^2] \tag{1}$$

where

- I_D Transistor drain current (A)
- C_{ox} Gate dielectric capacitance per unit area (F/m²)
- μ_{eff} effective carrier mobility (m²/V_s)
- W_{eff} effective channel width (m)
- L_{eff} effective channel length (m)
- V_{GS}, V_{DS} gate-source and drain-source voltages (V)
- V_T transistor threshold voltage (V).

It can be observed from Fig. 2a that as the channel length increases, the current decreases. A shortening of the length of the channel region results in increased drain current as well as a reduction in device resistance and vice versa. This can be

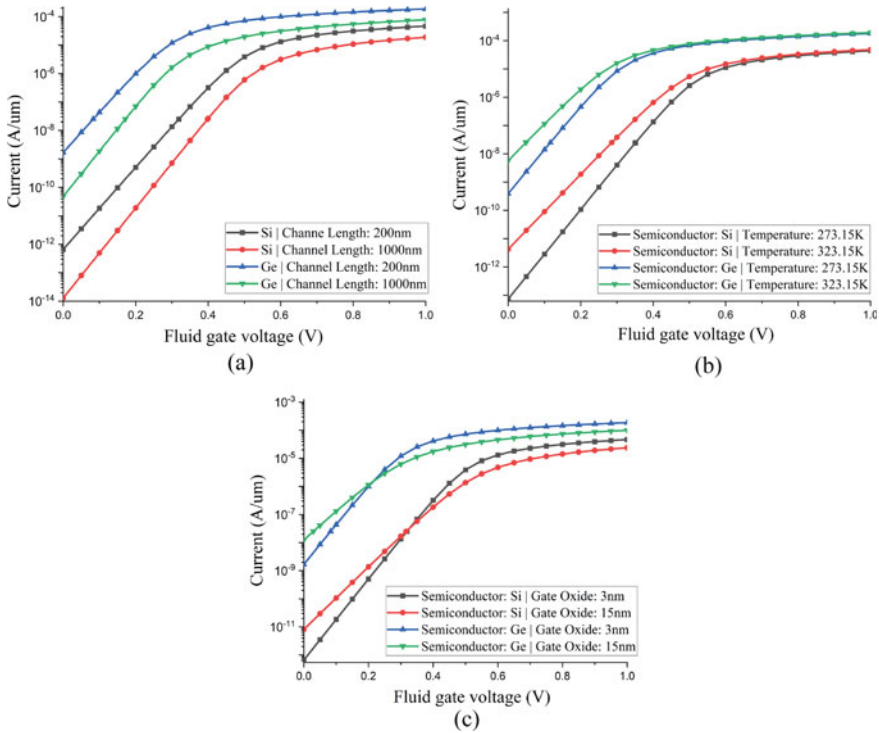


Fig. 2 I_D - V_{FG} curve. **a** Varying channel length, **b** varying temperature, **c** varying gate oxide

supported by Eq. 1 drain current (I_D) is inversely proportional to the length of the channel (L). As seen, in the graph, the current decreases from 46.4 to 19.99 μA and 186.25 to 78.02 μA in Si and Ge, respectively at 1 V. In a similar study by Noh et al. reports that drain current at around 1 V (isothermal point) decreases from 406 μA to 219 μA with an increase in channel length (considering constant width of the channel) [21, 22]. Although the behavior of the I-V curve is similar the difference in magnitude is because of variation in dimensions of channel length and gate oxide thickness. Further comparing it with [7], the drain current is found to be 4.5 μA at pH equal to 8 and 5.25 μA at pH equal to 6 at 1 V gate voltage. These findings are in accordance with the above graph but with a variation in magnitude because of different device parameters.

Figure 2b depicts the graph of drain current vs gate voltage for Si-based and Ge-based ISFET devices at 273.15 and 323.15 K temperatures. The graphs for both of these devices coincide at higher voltages for these temperature values. This can be explained by the fact that with increasing temperature, threshold voltage decreases. At low gate voltage, the drain current is more for a higher temperature. It is possible to achieve the same amount of current at lower voltage with increasing temperature. The off-state drain leakage increases with an increase in temperature as well as

voltage. Thus, as temperature increases, off-state current also increases, and then the value of current is almost the same for both. In addition to this, Narang et al. studied the effect of change in pH of electrolyte on drain current and states that the current decreases with an increase in pH for the same value of voltage and vice versa [23].

From Fig. 2c, it is observed that as the gate oxide thickness increases, the current flowing through the device decreases. This can be explained by the fact that incrementing thickness gives a lower oxide capacitance (C_{OX}) and the ratio of drain capacitance to total capacitance is increased. Because the lower oxide capacitance and the control of drain on the channel are increased, the drain current is increased with an increase of voltage. But at low gate voltage due to low threshold voltage and high off current, by increasing the oxide thickness, the current is also increased.

3.2 Carrier Concentration and Potential Curve Along the x-Direction

Understanding the concentration of charge carriers under changing device parameters provides a better idea of device performance. Since carrier concentration affects the mobility of carriers, it, in turn, affects the current in the channel. This current change impacts the delay factor of the device which is a primary factor considered to measure the sensitivity of ISFET [24]. From Fig. 3a, it is observed that the concentration of electrons in the vicinity of the source and drain remains unaffected by the variation in temperature. However, there is a significant difference observed in the region between source and drain. The number of electron-hole pairs varies proportionally with the temperature thus varying the conductivity proportionally to the temperature.

From Fig. 3b, it is observed from the graph that the concentration of electrons remains unaffected in the source and drain region by the variation in channel length. Although, a drop in concentration is observed as the channel contains a free flow of current, which is from -100 to 100 nm as shown in Fig. 1. Moreover, there is also a higher hole concentration as compared to electrons as the channel is a p -type semiconductor, which has holes as the majority of careers. From Fig. 3c, it is observed that as the gate oxide thickness increases, capacitance in the channel also increases. An increase in capacitance increases the conductivity and thereby increases the concentration of electrons in the channel. Further, a decrease in surface potential is observed with an increase in the pH of the electrolytic solution and vice versa [23].

3.3 Carrier Concentration Along z-Direction

Analysis of carrier concentration along z -direction along the width of the channel to get a better idea of carrier mobility. Carrier mobility affects the delay of the device

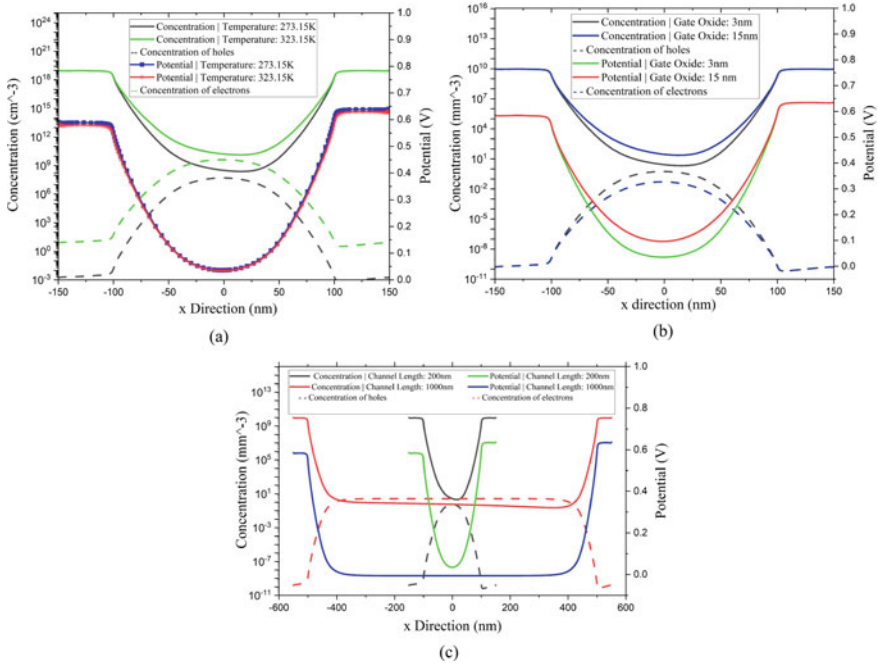


Fig. 3 Carrier concentration and potential curve along x-direction. **a** Varying temperature, **b** varying channel length **c** varying gate oxide

which directly affects the sensitivity of ISFET devices, as discussed earlier. It is clear from Fig. 1 that Fig. 4a ranges from the bottom point of the channel to the top point. The characteristic observed is linear. Channel is a *p*-type semiconductor, so the majority of charge carriers are holes, and hence, the concentration of holes increases from the bottom of the channel to the top. It is observed that the concentration of electron-hole pairs increases proportionally to the temperature since the conductivity increases with an increase in temperature. In Fig. 4b, as explained above, the number of holes increases as the number of electrons decreases. Additionally, as the channel length increases, electron concentration decreases as the per-unit electron count decreases due to an increase in channel length. As a result of which, the hole count increases. From Fig. 4c, it is observed that as the gate oxide thickness increases, capacitance in the channel also increases. An increase in capacitance increases the conductivity and thereby increases the concentration of electrons in the channel.

3.4 Potential Along z-Direction

It is already known that FETs are power-efficient devices. Since the power of these devices depends on their voltage, it is essential to study the voltage performance

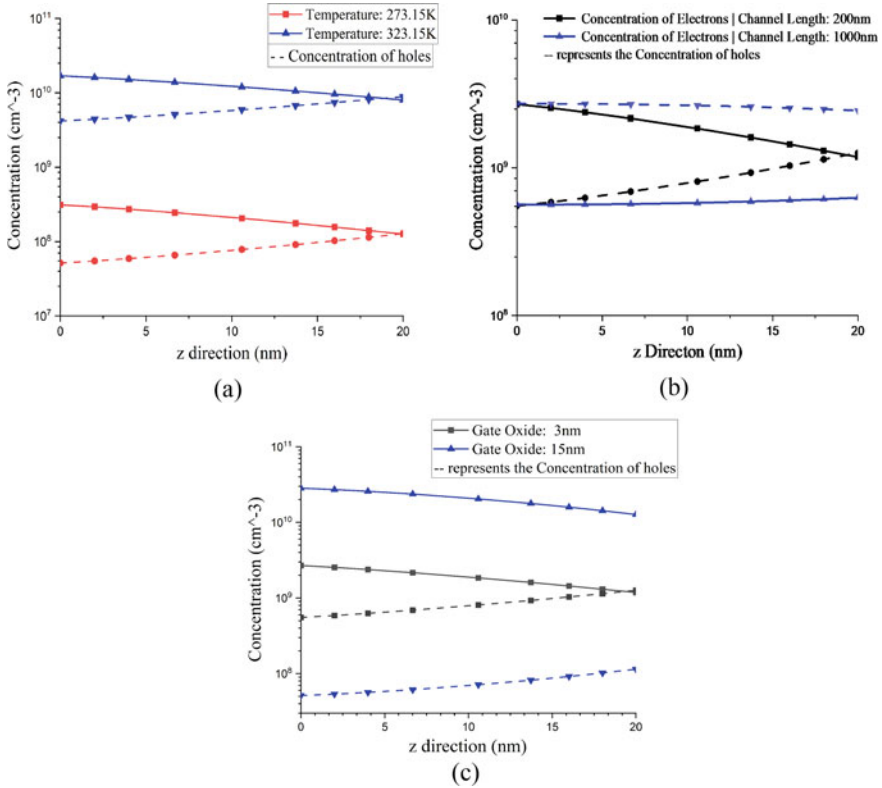


Fig. 4 Carrier concentration along z-direction. **a** Varying temperature, **b** varying channel length, **c** varying gate oxide thickness

of these devices. Surface potential is an important factor in sensing ions and pH measurement which is a primary application of ISFET devices based upon its working principle. From Fig. 5a, it can be observed from the graph that voltage remains the same even though the temperature varies as the temperature does not affect the voltage of the device. In Fig. 5b, as it is known, the voltage depends upon the concentration of electrons in the gate region of the device, and as per the graph of carrier concentration, the concentration of electrons decreases in the channel as the channel length increases. Hence, the voltage also decreases as the channel length increases. In Fig. 5c, as discussed earlier that carrier concentration increases as the gate oxide thickness increases, an increase in voltage too, is observed, as the gate oxide thickness increases since the voltage are directly proportional to the carrier concentration of the device as per Eq. 2 of capacitance given below.

$$C = q/V = \epsilon_0 A/d \tag{2}$$

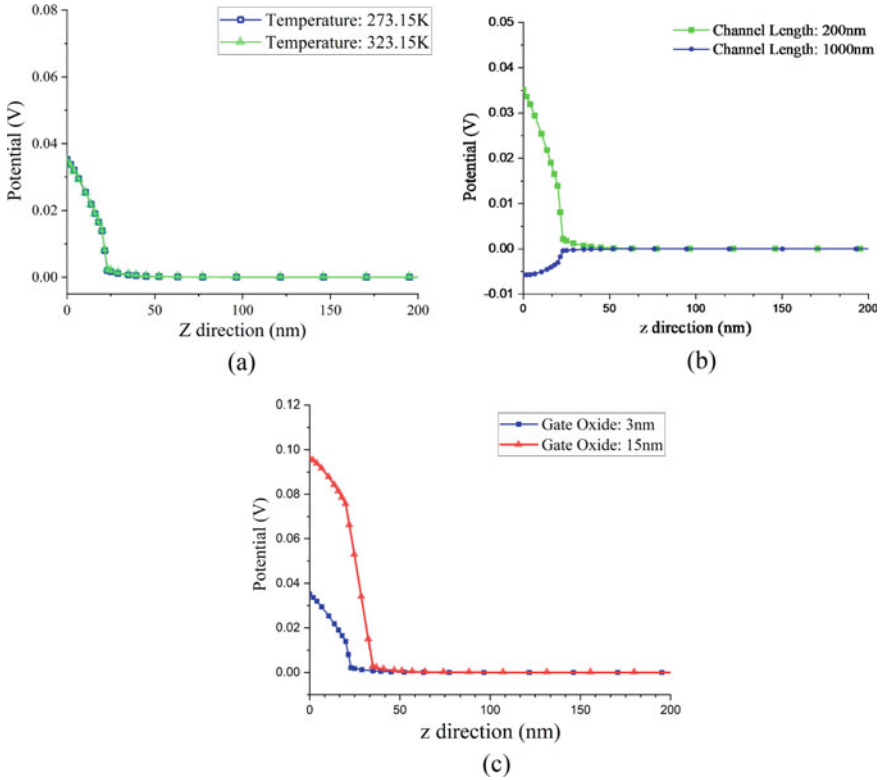


Fig. 5 Potential along z-direction. **a** Varying temperature, **b** Varying channel length, **c** varying gate oxide thickness

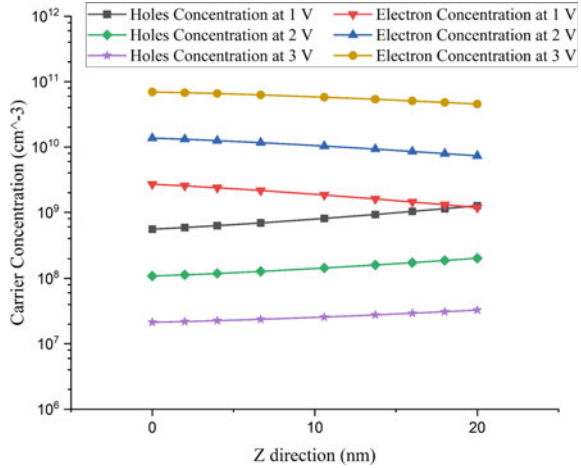
where

- C is Capacitance
- q is Charge
- V is Voltage
- A is the Area of the oxide film
- d is an Oxide film thickness
- ϵ_0 is the electric constant ($\epsilon_0 \approx 8.854 \times 10^{-12} \text{ F m}^{-1}$).

3.5 Carrier Concentration Along z-Direction for the Varied Drain Voltage

Analysis of carrier concentration along z-direction along the width of the channel to get a better idea of carrier mobility to analyze the sensitivity of ISFET. Figure 6 shows the concentration of carriers along the z-direction of ISFET devices with varying

Fig. 6 Carrier Concentration along z-direction with varying drain- source voltage (V_{DS}) $V_{DS} = 1\text{ V}$, $V_{DS} = 2\text{ V}$, $V_{DS} = 3\text{ V}$



drain voltage. The concentration of charge carriers is almost equal at relatively lower drain voltage (V_{DS} equals 1 V). As drain-source voltage is increased to 2 V, the concentration of holes increases, and that of electrons decreases. Furthermore, as the voltage is increased to 3 V, the trend continues resulting in a further increase of hole concentration and lower electron concentration. As a positive voltage is connected to the drain of the device, the concentration of holes increases with an increase in the magnitude of this connected voltage.

4 Conclusion

This paper discusses the comparative analysis between silicon-based ISFET and germanium-based ISFET. For the analysis, temperature, gate oxide thickness, and channel length were varied, and drain current, carrier concentration along the x-direction, potential along the x-direction, carrier concentration along the z-direction, and potential along z-direction were measured. Simulations show that drain current is directly proportional to temperature. For a temperature increase from 273.15 to 323.15 K, in Si-based device, current increases from 2.59 to 5.37 μA at 0.5 V gate voltage while for Ge-based device, current increases from 67.75 to 77 μA at 0.5 V gate voltage. This drain current for both temperatures approaches the same value as voltage increases, it is 48.47 μA for Si-based devices and 192 μA for Ge-based devices at 1 V. Similarly, there is a direct relation of temperature with carrier concentration. While potential along the z-direction does not depend on the temperature at all. Further, as channel length is increased from 200 to 1000 nm, for Si-based ISFET, current decreases from 46.44 to 18.99 μA , and for Ge-based ISFET, it increases from 186.25 to 78.02 μA at 1 V gate voltage. This increased channel length also results in a drop of voltage along z-direction as well as the carrier concentration,

hence an inverse relation. Furthermore, as gate oxide thickness increases from 3 to 15 nm, drain current decreases from 46.44 to 23.08 μA for Si-based ISFET while current drops from 186.24 to 99.54 μA for Ge-based ISFET at 1 V gate voltage. This increase in gate oxide thickness also results in an increased voltage along z -direction till the oxide-electrolyte interface of the device which slowly drops to 0 V thereafter. Similarly, the concentration of carriers increases with an increase in gate oxide thickness. Carrier concentration along z -direction also increases steadily with an increase in drain voltage from 1 to 3 V as shown by the simulations.

It was observed that the amount of change due to the change in parameters was similar between Si-based and Ge-based ISFET but since the initial values for the two were different the amount of change compared to the initial value was higher in Ge-based ISFET devices. Hence, one of these parameters or a combination of them can be varied to achieve a certain result and the material for the ISFET can be chosen based on how much change is required to achieve the result.

References

1. Thévenot DR, Toth K, Durst RA, Wilson GS (2001) Electrochemical biosensors: recommended definitions and classification. *Biosens Bioelectron* 16(1–2):121–131
2. Sung D, Koo J (2021) A review of BioFET's basic principles and materials for biomedical applications. *Biomed Eng Lett* 1–12
3. Tibaldi A, Fillaud L, Anquetin G, Woytasik M, Zrig S, Piro B, Mattana G, Noël V (2019) Electrolyte-gated organic field-effect transistors (EGOFETs) as complementary tools to electrochemistry for the study of surface processes. *Electrochem Commun* 98:43–46
4. Ingebrandt S, Han Y, Nakamura F, Poghossian A, Schöning MJ, Offenhäusser A (2007) Label-free detection of single nucleotide polymorphisms utilizing the differential transfer function of field-effect transistors. *Biosens Bioelectron* 22(12):2834–2840
5. Lupp PB, Sokoll LJ, Chan DW (2001) Immunosensors—Principles and applications to clinical chemistry. *Clin Chim Acta* 314(1–2):1–26
6. Dinar AM, Zain AM, Salehuddin F, Attiah ML, Abdulhameed MK (2019) Modeling and simulation of electrolyte pH change in conventional ISFET using commercial Silvaco TCAD. In: IOP conference series: materials science and engineering, vol 518, no 4. IOP Publishing, p 042020
7. Padhye M, Sinha S, Sharma R, Mukhiya R (2017) Design and simulation of SOI-ISFET macromodel using SPICE. In: International workshop on the physics of semiconductor and devices. Springer, Cham, pp 789–796
8. Sinha S, Rathore R, Sinha SK, Sharma R, Mukhiya R, Khanna VK (2014) Modeling and simulation of ISFET microsensor for different sensing films. In: ISSS international conference on smart materials, structures and systems
9. Jang HJ, Cho WJ (2011) High performance silicon-on-insulator based ion-sensitive field-effect transistor using high-k stacked oxide sensing membrane. *Appl Phys Lett* 99(4):043703
10. Bousse L, De Rooij NF, Bergveld P (1983) Operation of chemically sensitive field-effect sensors as a function of the insulator-electrolyte interface. *IEEE Trans Electron Devices* 30(10):1263–1270
11. Moser N, Lande TS, Toumazou C, Georgiou P (2016) ISFETs in CMOS and emergent trends in instrumentation: a review. *IEEE Sens J* 16(17):6496–6514
12. Parizi KB, Xu X, Pal A, Hu X, Wong HP (2017) ISFET pH sensitivity: counter-ions play a key role. *Sci Rep* 7(1):1–10

13. Lu CH, Hou TH, Pan TM (2017) High-performance double-gate α -InGaZnO ISFET pH sensor using a HfO₂ gate dielectric. *IEEE Trans Electron Devices* 65(1):237–242
14. Sinha S, Sahu N, Bhardwaj R, Ahuja H, Sharma R, Mukhiya R, Shekhar C (2020) Modeling and simulation of temporal and temperature drift for the development of an accurate ISFET SPICE macromodel. *J Comput Electron* 19(1):367–386
15. Sinha S, Bhardwaj R, Sahu N, Ahuja H, Sharma R, Mukhiya R (2020) Temperature and temporal drift compensation for Al₂O₃-gate ISFET-based pH sensor using machine learning techniques. *Microelectron J* 97:104710
16. Heitzinger C, Kennell R, Klimeck G, Mauser N, McLennan M, Ringhofer C (2008) Modeling and simulation of field-effect biosensors (BioFETs) and their deployment on the nanoHUB. *J Phys: Conf Ser* 107(1):012004 (IOP Publishing)
17. Pittino F, Selmi L (2014) Use and comparative assessment of the CVFEM method for Poisson-Boltzmann and Poisson–Nernst–Planck three dimensional simulations of impedimetric nano-biosensors operated in the DC and AC small signal regimes. *Comput Methods Appl Mech Eng* 278:902–923
18. Hoxha A, Scarbolo P, Cossetini A, Pittino F, Selmi L (2016) ENBIOS-2D Lab
19. Dutta JC (2012) Ion sensitive field effect transistor for applications in bioelectronic sensors: a research review. In: 2012 2nd National conference on computational intelligence and signal processing (CISP). *IEEE*, pp 185–191
20. Lee CS, Kim SK, Kim M (2009) Ion-sensitive field-effect transistor for biological sensing. *Sensors* 9(9):7111–7131
21. Noh NIM, Yusof KA, Zolkapli M, Abdullah AZ, Abdullah WFH, Herman SH (2013) Effect of channel width-to-length ratio on isothermal point of MOSFET-ISFET structure. In: RSM 2013 IEEE regional symposium on micro and nanoelectronics. *IEEE*, pp 130–133
22. Wang Y, Yang M, Wu C (2020) Design and implementation of a pH sensor for micro solution based on nanostructured ion-sensitive field-effect transistor. *Sensors* 20(23):6921
23. Narang R, Saxena M, Gupta M (2017) Analytical model of pH sensing characteristics of junctionless silicon on insulator ISFET. *IEEE Trans Electron Devices* 64(4):1742–1750
24. Khakifirooz A, Antoniadis DA (2008) MOSFET performance scaling—Part I: historical trends. *IEEE Trans Electron Devices* 55(6):1391–1400

Alignment Format for Semantic Translation



Paweł Szmeja, Wiesław Pawłowski, Maria Ganzha, Marcin Paprzycki,
and Katarzyna Wasielewska-Michniewska

Abstract Abundance of vastly heterogeneous, high-volume/high-velocity data producers/consumers, predominantly caused by proliferation of IoT-based solutions, results in an urgent need for efficient semantic interoperability solutions. Hence, the need to solve the problems of domain understanding, domain formal representation, and expression of mappings between different data models arise. In this contribution, we present an alignment format called IPSM-AF, for persisting correspondences between ontologies that can be used for semantic translation. Specifically, alignments represented using the IPSM-AF can be efficiently parsed and consumed by the IPSM tool, which performs the actual translation (possibly on streaming data). The proposed format is compliant with the Alignment API format, level 2.

Keywords Semantic translation · Semantic stream processing · Ontology · Alignments · Internet of Things

1 Introduction

The rise of the Internet of Things [2, 18], in which “everything” can be connected, and used as data publisher or subscriber, leads to new challenges in data processing. IoT-based solutions either already are or very soon will be one of the foundational ingredients of almost every modern technological solution. Concepts such as Smart City, Smart Grid, or Supervisory Control and Data Acquisition (SCADA) systems are just a few, but prominent examples. With rapidly growing number of deployed IoT artifacts (platforms, applications, devices), one of the key problems is the ability to understand, integrate, and uniformly process data, materializing/existing in

P. Szmeja · M. Ganzha · M. Paprzycki · K. Wasielewska-Michniewska
Systems Research Institute, Polish Academy of Sciences, Newelska 6, 01-447 Warsaw, Poland

W. Pawłowski (✉)

Faculty of Mathematics Physics and Informatics, University of Gdańsk, Wita Stwosza 57, 80-308 Gdańsk, Poland

e-mail: wieslaw.pawlowski@ug.edu.pl

different formats and semantics, often in heterogeneous domains. The task of data format conversion/translation, also called *syntactic translation*, is reasonably well understood, and there are many tools, both open-source and commercial, that support it. Data interoperability/integration at the level of semantics, on the other hand, poses a much bigger challenge, especially in IoT environments where, naturally occurring, high volume/velocity, heterogeneous data *streams* have to be considered and efficiently handled. The viability and the need for integration of heterogeneous data streams in IoT, including real-time analytics, is well demonstrated, understood, and often includes semantic data [14]. The solutions are, however, limited to systems that already implement common semantics and operate on directly interoperable and exchangeable data. Communication between semantically incompatible systems requires the addition of semantic translation.

The problem of “meaningful communication” (data exchange) between IoT artifacts becomes even more pronounced over time. Typically, initial deployments of IoT ecosystems exist within homogeneous, domain- or vendor-specific “silos,” which do not need to communicate externally. For instance, companies *X* and *Y* installed smog monitoring ecosystem, while companies *A*, *B*, and *C* provided (in the same city) infrastructure for electric scooters rental (with GPS sensors build into them, to be able to track their location). Each company used its own data representation and semantics to deal with geospatial data. Now, the City would like to combine information from both ecosystems to develop a novel user-centric application, where smog data is combined with scooter location to help user decide, which road to take. Here, for all practical purposes, it cannot be mandated, that either the providers of the smog alert data, or the electric scooter rental companies, are required to reengineer their systems to adapt the geospatial data model to the one used by the other (or to yet another data model that the City is supporting). Situations like this are becoming more and more common, as numerous IoT-based solutions/services are being combined to provide users with ubiquitous “smart environments.”

In our earlier works [8, 9], we have proposed a viable solution to the semantic interoperability problem, based on the concept of a *semantic mediator*, offering (streaming) *semantic translation* capabilities for data. The mediator takes “translation rule-sets” as arguments, and by “applying” them, creates appropriate *translation channels*. An efficient and scalable [12] implementation was subsequently created within the INTER-IoT project [7, 17],¹ and later further enhanced and adopted as the “kernel part” of the interoperability solution for the ASSIST-IoT project.² The architecture of the *Inter-Platform Semantic Mediator* (IPSM) utilizes a concept of *modular central ontology*, to minimize the number of necessary translation rule-sets. Since the data models of artifacts are assumed to be formally represented in the form of an ontology,³ it is natural to consider (partial) *alignments* between these ontologies, and the central ontology, as the basis for the rule-sets. “Partiality” of the

¹ <http://www.inter-iot-project.eu>.

² <https://assist-iot.eu/>.

³ Comprehensive discussion concerning what needs to be done if the original local data representation is not ontology-based can be found in [5, 11].

alignments reflects the fact that *only* the information that is to be communicated/exchanged between pertinent artifacts needs to be taken into account. This, in turn, is a consequence of the assumption that all details of data streams that are to be translated, are fully known to the IoT ecosystems developers. As a consequence, the alignments required for the translation do not have to cover complete data models of communicating artifacts and therefore have reasonable both size and complexity. As a result, translation time is limited, as it involves only information needed in the context of a given “type of conversation.” Here, note that this assumption, which is grounded in real-world scenarios observed during the INTER-IoT project (and the remaining six EU projects from the same call) makes an important difference in what follows. While there exists a body of research, which includes, also, an ontology matching competition,⁴ it focuses on establishing relationships between complete data models. While this academic problem is very challenging and stimulating, it is not necessarily required to facilitate semantic interoperability between IoT deployments, where data streams are produced, exchanged, and consumed.

Whereas in ontology matching competitions, the main use of an alignment format is to enable direct comparison between outputs of different automatic or semiautomatic tools [16], it is not required to be human-readable, highly expressive, and “executable” as input for data transformation. In other words, the requirements that it answers do not fully cover the challenges of dynamic data translation in IoT, which, for us, was the starting point.

The focus of this paper, and its main contribution, is to discuss an alignment format introduced for formally representing and persisting mappings between different semantic domain models that are consumed by the IPSM tool, to perform semantic translation. Since the initial version, described in [21], both the alignment format and the IPSM tool have been updated and extended in different ways. In particular, support for an elegant, concise, and much more readable/comprehensible syntax, based on the RDF Turtle was added. As will be shown, while there exists a large body of work devoted to ontology alignments and their representation, they seem to be slightly off the mark, when application of semantic technologies to *streaming translation* is concerned. The aim of this work is not only to propose the format but also to show how the IPSM-AF can be used in real-world applications. Examples will be based on actual pilot implementations that have been delivered during the INTER-IoT project. To this effect, we proceed as follows. First, we will discuss existing approaches for persisting alignments, then we will introduce the alignment format that we propose, and finally, we will conclude by giving examples of its application.

⁴ <http://oaci.ontologymatching.org/>.

2 Quest for the Mapping Language

Even though ontologies are said to provide a “formal specification of a shared conceptualization” [1], in real-life, models of concepts represented in ontologies can differ in many ways. A domain can be perceived from different perspectives, depending on the modeling purpose or/and approach. Starting from the most simple cases—the same term can describe different concepts, or different terms can be used to denote the same concept. The simplest example can be expressing the same term in different languages, e.g., *name* and *Vorname*, using abbreviations, e.g., *temperature* and *temp*, or using synonyms, e.g., *car* and *automobile*. More involved differences can result from the adoption of different modeling paradigms and/or granularity levels, e.g., address with all components contained in a text literal, or address decomposed into attributes like country, city, street, house and flat number, or decision what should be represented by a concept and what by a property. Of course, the list of examples continues and is easy to construct.

The process of discovering relations/correspondences between entities originating from a pair of ontologies, such as classes, properties, or individuals, is called *aligning* or *matching*. Because of the possible modeling differences between ontologies, the matching task can be (and in most cases is) highly non-trivial, even though some guidelines and patterns have been identified and described in the literature [19, 20]. The result of the matching process is called an *alignment*. At a very abstract level, an alignment can be seen as a set of correspondences, i.e., triples (e_A, r, e_B) , where e_A and e_B are entities from ontologies A and B , respectively (or expressions that use said entities), and r is a relation, such as *subsumption* and *equivalence* [4, 24]. Alignments have been utilized as the basis for many ontology-related operations such as ontology merging, query rewriting, or data integration.

In order to “apply” the correspondences forming the alignment to any task, however, they have to be represented/persisted using a *mapping language*. Obviously, a particular choice of the mapping language highly depends on the intended application scenario, but also on the complexity and the level of sophistication of the correspondences constituting the alignment. The more involved the alignment correspondences are, the more *expressive* mapping language they require.

Within the INTER-IoT project, we were interested in utilizing alignments in the process of *semantic translation* of (high velocity) *streams* of IoT-originated data. Here, let us note that, to the best of our knowledge, alignments have not been directly applied in such a scenario before. Therefore, we have started our quest for the “right” mapping language by considering the available options. In [10], we have analyzed existing tools for ontology matching. Here, one of their most important features was the mapping languages they used to persist the matching results (as these matchings were to be used in the dynamic translation process). We have found that, although in some cases alignments were encoded in different application-specific formats, the standard way to express mapping(s) between (complete) ontologies is to use the Alignment API format [3].

Apart from the Alignment API, there were, of course, also other possibilities to consider. The technologies relevant to our needs were not limited to those, that directly express alignments, but also included those, that are capable of expressing mappings between any ontologically described data, or even one-way transformations, that could potentially be used to build alignments. Consequently, the research included alignment, mapping or transformation languages and technologies for OWL or RDF, such as SPARQL,⁵ its extension SPARQL Inference Notation (SPIN),⁶ Semantic Web Rule Language (SWRL),⁷ ShEx,⁸ SHACL,⁹ SILK [25], RDF Mapping Language (RML)¹⁰ and RMLEditor [13], Simple Knowledge Organization System (SKOS)¹¹ [15], and even the Web Ontology Language OWL¹² itself. However, there were three important aspects/features of the needed mapping language that we were particularly interested in. We wanted it to: (1) be expressive, in particular allowing flexible *value processing/transformation*; (2) provide clean and *comprehensible* syntax for expressing alignments; (3) have tools that would support it in our scenario (translation of streaming data). Upon in-depth analysis, we have established that none of, just listed, “secondary” options met all three of these requirements at once. Therefore, they have been excluded from further considerations.

The Alignment API format that we identified as the most widely used (and possibly useful for our purpose) defines several *levels*, where higher level indicates higher expressiveness. Specifically, the available levels are: 0—not depending on any particular language correspondences between discrete entities (identified by URIs), 1—replaces pairs of entities by pairs of sets (or lists) of entities, 2—directional, and language-dependent, sets of expressions of a particular language with variables in these expressions.

Unfortunately, as we have established in our work, and reported in [10], even if a tool produced Alignment API compliant mapping, it was on level 1 (only simple correspondences without transformations). Moreover, even then, we did not find any tool that could consume such alignment file and perform automatic translation based on the defined mappings.

On the other hand, there is a detailed description language for expressing alignments on the Alignment API format level 2. It is the EDOAL (Expressive and Declarative Ontology Alignment Language¹³ [3, 4]). In principle, it allows to represent complex correspondences, to precisely describe the relation between the entities including: construction, restrictions, transformations, and conditions for equivalence. However, from the point of view of our intended application, i.e., streaming semantic

⁵ <https://www.w3.org/TR/sparql11-overview/>.

⁶ <https://www.w3.org/Submission/spin-overview/>

⁷ <https://www.w3.org/Submission/SWRL/>

⁸ <https://shex.io/>

⁹ <https://www.w3.org/TR/shacl/>.

¹⁰ <https://rml.io/>

¹¹ <https://www.w3.org/TR/skos-reference/>

¹² <https://www.w3.org/TR/owl2-overview/>.

¹³ <http://alignapi.gforge.inria.fr/edoal.html>.

translation, it did not offer enough support for the “transformations,” which according to the official documentation are “still work in progress.” Moreover, although EDOAL allows to state *directionality* of individual mappings, it does not express it explicitly in the alignment’s header, which seems important and natural in the context of (streaming) translation. Our investigation also showed that there were no alignment creation tools that would actually use the full expressive power of EDOAL format for their output.¹⁴ Therefore, we had to accept the fact, that alignments will need to be mostly “handcrafted.” Moreover, in most cases, we could not assume that they will be created by experienced ontology engineers. Therefore, we needed a mapping language, which would seem familiar and understandable to a “working software engineer.” As its name suggests, EDOAL mainly (although not exclusively) supports the *declarative* style of defining mappings. This style, although elegant and often more concise, tends to be considerably more difficult to understand and use by practitioners than the *imperative/procedural* one. This aspect became also an important factor in our quest.

Consequently, we have decided to design a dedicated mapping language that will be sufficiently expressive and will have comprehensible syntax dedicated to semantic translation. The proposed solution, called IPSM Alignment Format (IPSM-AF), is compliant with the Alignment API format, allows to express complex correspondences involving, e.g., transformations, supports the imperative/procedural style of defining alignments, and is directly supported by the Inter-Platform Semantic Mediator (IPSM) translation tool. Among advantages of being compliant with the Alignment API are the possibility to store alignments in the Alignment Server,¹⁵ which enables different actors to share available alignments, networks of ontologies, and ontology matching methods.

3 IPSM Alignment Format

Although semantically annotated data can be, in principle, expressed in many different ways, today, the unquestionable standard is the Resource Description Framework (RDF).¹⁶ Therefore, we have decided that the alignment format should follow the assumption that data is expressed in the form of RDF graphs, whereas IPSM-AF allows to persist translation rules between (selected fragments of) RDF graphs that express the pair of underlying ontologies. For the format to be flexible and expressive, IPSM-AF was defined as a level 2 Alignment API format extension. Therefore, it is language-dependent and allows specifying compound constructs. In particular, while designing it we have assumed that it should:

¹⁴ The situation has not changed much, ever since, as recently confirmed in [23, 24].

¹⁵ <http://alignapi.gforge.inria.fr/server.html>.

¹⁶ <https://www.w3.org/RDF/>.

- be able to express mappings of sets of expressions, e.g., RDF graphs (not only individual triples or entities),
- allow using *variables* for expressing RDF graph patterns,
- utilize callable *functions*, to perform value transformations, e.g., concatenate strings, apply regular expression to select part of the value, perform arithmetic operations, etc.
- enable expressing restrictions on datatypes, both in source and in target patterns,
- be able to remove parts of the source RDF graph and to add new elements to it.

It should be stressed that these assumptions were based, in large part, on the requirement analysis of the use cases of the INTER-IoT project. Therefore, they are grounded in real-world needs of streaming semantic translations, in IoT ecosystems.

To introduce the proposed format, let us start by considering the overall structure of an IPSM-AF alignment, expressed in RDF/XML as shown in Listing 1. The main element—an *align:Alignment*—contains three “sections,” giving the alignment *metadata*, specifying the *steps*, i.e., the ordering, in which individual mappings should be considered, and defining the mappings themselves. The namespace prefixes that are used in the examples that follow are expanded in Table 1.

```
<rdf:RDF xmlns="http://www.inter-iot.eu/sripas#" % other xml namespaces % >
  <align:Alignment>
    %-----%
    % alignment metadata %
    %-----%
    % alignment "steps" %
    %-----%
    % alignment mappings %
    %-----%
  </align:Alignment>
</rdf:RDF>
```

Listing 1 IPSM-AF - alignment structure

The *metadata* section, as illustrated in Listing 2, provides the *title* and *version*, specifies *creator* and gives a short *description* of the alignment. These items, in particular the name, version, and creator, allow for tracking changes and using versioning schemes, which are necessary procedures in any evolving ecosystem. Since the IPSM-AF is compliant with the Alignment API, the metadata section also needs to specify the needed Alignment-API-specific properties. In particular, the *align:level* whose value “2IPSM,” states that the alignment is on “level 2” in the Alignment API terminology. The elements *align:onto1* and *align:onto2*, structure of which is also defined by the Alignment API Format, specify the *source* and *target* ontologies, for the alignment, respectively. The IPSM-AF alignments are always considered to be unidirectional—mapping entities of the ontology *align:onto1* to entities of the ontology *align:onto2*. Here, the source ontology can be that of the IoT artifact and the target ontology can be a central ontology, used in the ecosystem. This assumption allows the creator to focus on the translation-targeted task, without the need to consider “reversibility” of the individual mappings defined by the alignment. If translation is needed in both directions then two alignments should be created. The

last metadata item, presented in Listing 2, is the element *sripas:cellFormat*, which specifies syntax used for representing RDF graph patterns, contained in the alignment mappings. By default, it is RDF/XML but IPSM also supports Turtle, which is more concise and readable.

```
<dcelem:title> % alignment title % </dcelem:title>
<exmo:version> % alignment version % </exmo:version>
<dcelem:creator> % alignment creator % </dcelem:creator>
<dcelem:description> % alignment description % </dcelem:description>

<align:level>2IPSM</align:level>
% other Alignment API specific metadata %

<align:onto1> % source ontology specification % </align:onto1>
<align:onto2> % target ontology specification % </align:onto2>

<sripas:cellFormat>
  <iiot:DataFormat rdf:about="&sripas;turtle"/>
</sripas:cellFormat>
```

Listing 2 IPSM-AF alignment metadata

The alignment *steps* section (see, Listing 3) allows to specify the *default* order, in which specific mappings of the alignment should be considered (“applied”), possibly allowing any of them to be used more than once or, perhaps, excluded from the translation (i.e., not used at all). When defining a specific *translation channel*, based on the alignment, the IPSM tool allows to overwrite the default sequence of steps, if needed. Each step (represented by the *sripas:step* element) refers to a specific mapping within the alignment via its *identifier* represented by URI. The idea of steps reflects the *procedural* style of IPSM-AF that makes the format more accessible for the less “semantically proficient” users.

```
<sripas:steps rdf:parseType="Literal">
  <sripas:step sripas:order="1" sripas:cell="cell_id"/>
  % more alignment steps %
</sripas:steps>
```

Listing 3 IPSM-AF - alignment steps specification

```
<align:map>
  <align:Cell rdf:about="&sripas;cell_id">
    <align:entity1 rdf:datatype="&xsd:string">
      % source RDF graph pattern %
    </align:entity1>
    <align:entity2 rdf:datatype="&xsd:string">
      % target RDF graph pattern %
    </align:entity2>
    <align:relation>=</align:relation>
    % optional transformations, filters and typing restrictions %
  </align:Cell>
</align:map>
```

Listing 4 IPSM-AF - alignment map/cell

The mappings section of the alignment consists of a sequence of *align:map* elements, each containing a single *cell*, defining a specific correspondence between two *entities* (or compound entity descriptions). Entity can be a class, instance/individual,

Table 1 Namespaces in IPSM-AF

Prefix	Namespace
sripas	http://www.inter-iot.eu/sripas#
var	http://www.inter-iot.eu/sripas:node_
pred	http://www.inter-iot.eu/sripas:pred_
align	http://knowledgeweb.semanticweb.org/heterogeneity/alignment#
dcelem	http://purl.org/dc/elements/1.1/
exmo	http://exmo.inrialpes.fr/align/ext/1.0/#
xsd	http://www.w3.org/2001/XMLSchema#

object, or datatype property. Cells are elements, in which all the mapping logic of the alignment is expressed. The structure of a cell has been outlined in Listing 4. Within *align:entity1*, the source RDF graph pattern is specified that is matched against input ontology. The *align:entity2* defines the target structure of the result of the mapping. When the alignment cell is used/applied, by a translator tool, then any RDF content matching the pattern in the *align:entity1*, will be modified into an RDF graph matching the pattern from *align:entity2*. To relate parts of the source and the target RDF graph patterns, IPSM-AF utilizes *variables* appearing in the *entity1* that can be later referenced from the *entity2* and, possibly, also used by the optional cell components, described in the next paragraph. Variables should belong to the namespace *var*. For instance, *var:A* is expanded to http://www.inter-iot.eu/sripas:node_A. Variables can be used in places of data and object properties' values. They serve as placeholders for values/entities that match the pattern. Additionally, each mapping cell can have optional elements: *sripas:transformation*, *sripas:filters*, and *sripas:typings*. These allow to, respectively, perform function calls during cell application, filter entities based on datatypes, and assign datatypes to entities in the target RDF graph. Listing 5 shows the structure that is to be used to include optional elements. If, for example, in the transformation, a reference to a SPARQL function is passed, the tool that consumes IPSM-AF content should be able to use any RDF library that supports SPARQL to apply the function to arguments specified by the *sripas:param* elements. For instance, the IPSM internally utilizes Apache Jena, which makes it possible to define and employ arbitrary external function libraries, thanks to the ARQ query engine.

```

<sripas:transformation rdf:parseType="Literal">
  <sripas:function about="{function name}">
    <sripas:param order="1" val="{simple value}"/>
    <sripas:param order="2" about="{variable URI}"/>
    % more parameter descriptions %
    <sripas:return about="{variable URI}"/>
  </sripas:function>
  % more function application descriptions %
</sripas:transformation>
<sripas:filters rdf:parseType="Literal">
  <sripas:filter about="{variable URI}" datatype="{datatype}"/>
  % more filters %

```

```

</sripas:filters>
<sripas:typings rdf:parseType="Literal">
  <sripas:typing about="{variable URI}" datatype="{datatype}" />
  % more typings %
</sripas:typings>

```

Listing 5 IPSM-AF - optional cell properties

4 Basic Translation Constructs

Thus far we have introduced the general structure of alignments, expressed in IPSM-AF, and indicated that the “translation cells” are the “workhorse” of the semantic translation. Let us now discuss some basic constructs that can be used within such translation cells. These constructs can be further composed, to define more complex patterns and correspondences, to be matched against the input data (RDF graphs). Since every RDF graph is a set of *triples*, “atomic” translations that can be applied to such graphs work on triples. Let us start with the case of translating just the *predicate* connecting the subject and the object of a triple. Listing 6 shows an example, in which the predicate of all matching triples will be changed from *ont1:hasName* to *ont2:hasVorname*.

```

<align:Cell rdf:about="{&sripas;name_mapping_example}">
  <align:entity1 rdf:datatype="{&xsd;string}">
    var:X ont1:hasName var:Y .
  </align:entity1>
  <align:entity2 rdf:datatype="{&xsd;string}">
    var:X ont2:hasVorname var:Y .
  </align:entity2>
  <align:relation>=</align:relation>
</align:Cell>

```

Listing 6 IPSM-AF triple mapping

Let us now assume that our goal is to “translate” a specific URI. In any alignment cell both *entity1* and *entity2* are RDF graph patterns, i.e., sets of RDF triple patterns. Therefore, to change the URI we need to explicitly use it in the *entity1* triple pattern, and substitute it with the “replacement” URI in the *entity2* pattern. Listing 7 presents a cell defining such a translation. In this example, *ont1:res1* is equivalent to *ont2:res1* in the target ontology.

```

<align:Cell rdf:about="{&sripas;uri_mapping_example}">
  <align:entity1 rdf:datatype="{&xsd;string}">
    var:X a sofa:Observation ;
    sofa:hasResult ont1:res1 .
  </align:entity1>
  <align:entity2 rdf:datatype="{&xsd;string}">
    var:X a sofa:Observation ;
    sofa:hasResult ont2:res1 .
  </align:entity2>
  <align:relation>=</align:relation>
</align:Cell>

```

Listing 7 IPSM-AF URI mapping

Listing 8 shows an example of a mapping where, in the target semantics, we want to specify new named entity, generated based on an entity from the source ontology, matched by a variable. To create the named entity, a standard SPARQL IRI function is used.

```
<align:Cell rdf:about="&sripas;named_entity_example">
  <align:entity1 rdf:datatype="&xsd:string">
    var:elem a pt:Element ;
    pt:hasDeviceId var:device_id .
  </align:entity1>
  <align:entity2 rdf:datatype="&xsd:string">
    var:device a iiot:IoTDevice, sosa:Sensor ;
    iiotex:hasLocalId var:device_id .
  </align:entity2>
  <align:relation>=</align:relation>
  <sripas:transformation rdf:parseType="Literal">
    <function about="IRI">
      <param order="1" about="&var;device_id"/>
      <return about="&var;device"/>
    </function>
  </sripas:transformation>
</align:Cell>
```

Listing 8 IPSM-AF named entity

When creating an alignment, it is often necessary to remove triples matching a given triple pattern. An example of a cell defining such a “translation” is depicted in Listing 9. The “removal” is achieved by mapping the source triple pattern to an empty pattern.

```
<align:Cell rdf:about="&sripas;triple_removal_example">
  <align:entity1 rdf:datatype="&xsd:string">
    var:X ont1:hasName var:Y .
  </align:entity1>
  <align:entity2 rdf:datatype="&xsd:string">
  </align:entity2>
  <align:relation>=</align:relation>
</align:Cell>
```

Listing 9 IPSM-AF remove part of a graph

Finally, Listing 10 shows an example of adding new triples to an RDF graph. The original triple is preserved, but two additional are included. Here, we assume that the values of variables *var:V* and *var:Z* can be calculated from the result of applying the cell transformation (otherwise, the cell would be ill-formed).

```
<align:Cell rdf:about="&sripas;adding_new_triples">
  <align:entity1 rdf:datatype="&xsd:string">
    var:X ont1:hasName var:Y .
  </align:entity1>
  <align:entity2 rdf:datatype="&xsd:string">
    var:X ont1:hasName var:Y .
    var:X ont1:hasFirstName var:V .
    var:X ont1:hasName var:Z .
  </align:entity2>
  <align:relation>=</align:relation>
  <sripas:transformation rdf:parseType="Literal">
    % transformation %
  </sripas:transformation>
</align:Cell>
```

Listing 10 IPSM-AF add triples to a graph

It is important to note, that application of the alignment cell translates all the triples of an RDF graph that match the *align:entity1* graph pattern, preserving at the same time all the unmatched ones.

Based on analysis of the literature, requirements analysis of the use cases of the project pilots, and implementation of semantic translation within their scope we believe that the above-presented set of transformations covers majority of practical needs. However, it should be stressed that the proposed approach is flexible and can easily be extended to capture additional practical needs.

5 Example

Let us now illustrate the usage of IPSM-AF format, by presenting a fragment of an alignment between a port ontology, that describes (among others) meteo stations and data they produce, and a suitably extended Generic IoT Platform Ontology (GOIoTP ontology¹⁷). The GOIoTP is a modular core ontology developed during the INTER-IoT project, which allows describing various aspects of IoT deployments, such as devices, platforms, observations, units and measurements, location, services, and users. GOIoTP imports and uses parts of several standard ontologies, such as SSN/SOSA,¹⁸ GeoSPARQL,¹⁹ and NASA SWEET units.²⁰ Since GOIoTP is a core ontology, it has been further extended to form the Generic Ontology for IoT Platforms Extended (GOIoTPex)—a vertical module that imports the GOIoTP ontology, and augments and “fills” selected stub concepts from GOIoTP with more specific classes, properties, and individuals. In short, GOIoTPex ontology extends GOIoTP with terms required in the concrete instantiations of the INTER-IoT solution. In particular, it serves as a central ontology for semantic translations executed within the INTER-IoT pilot applications, where both IPSM-AF and IPSM were utilized to provide a flexible and efficient semantic interoperability solution.

As discussed in [9], depending on the application/domain needs, practically any ontology can be selected as the central one, since the choice does not influence the semantic translation engine. However, semantic engineer should keep in mind that central ontology should: (i) cover all “topics” of conversations in the ecosystem, (ii) be clear enough to enable querying and reasoning done directly on it, and (iii) contain subject-specific modules that can be independently maintained and versioned. In this respect, GOIoTPex can be seen as an excellent “foundational” central ontology for any IoT-centric ecosystem.

¹⁷ <https://inter-iot.github.io/ontology/>.

¹⁸ <https://www.w3.org/TR/vocab-ssn/>.

¹⁹ <https://www.ogc.org/standards/geosparql>.

²⁰ <http://sweet.jpl.nasa.gov/2.3/reprSciUnits.owl>.

Table 2 Prefixes used in the examples

Prefix	Namespace
	<i>Source</i>
port	http://inter-iot.eu/syntax/WSO2Port#
	<i>Target</i>
vp	http://inter-iot.eu/LogVPmod#
iiot	http://inter-iot.eu/GOIoTP#
iiotex	http://inter-iot.eu/GOIoTPex#
geo	http://www.opengis.net/ont/geosparql#
ogis	http://www.opengis.net/def/sf/
sosa	http://www.w3.org/ns/sosa/
meteo	http://www.inter-iot.eu/wso2port/weather/stations/

The example alignment consists of just two mappings (cells). Both refer to an ecosystem, in which meteorological data is important and, in addition, artifacts forming the ecosystem might be interested in data arriving from specific “registered” meteo stations. In the first mapping, we are interested in translating RDF messages exchanged within the ecosystem that represents meteo station “registration.” The second mapping should enable translation of RDF graph structures into actual measurements coming from meteo stations. In both cases, we shall utilize the GOIoTPex as the target ontology. We assume that input data is represented in a (simple) *port* ontology expressing “flat” data coming from the port platform. Both examples (with some simplifications) originate from the INTER-IoT project pilot, in which data gathered by different IoT platforms is published and processed in an INTER-IoT ecosystem, deployed at the Port of Valencia, in Spain. The ontologies/prefixes used in the example alignment are listed in Table 2.

Let us start with the first example, in which a message describing a meteo station registration needs to be translated from the *port* ontology, and expressed in terms of the central ontology. In Listing 11, a meteo station called “P.Felipe” is characterized by a set of datatype properties (expressed using RDF Turtle notation).

```
[ ] a port:Element ;
port:haslatitude "26.94442"^^xsd:float ;
port:haslongitude "19.29351"^^xsd:float ;
port:hasmeteoStationId "2"^^xsd:int ;
port:hasname "P.Felipe" .
```

Listing 11 “P.Felipe” meteo station metadata

Alignment cell given in Listing 12 contains RDF graph patterns that generate correspondences (translation rules) that “match” any meteo station registration message, and produce its counterpart, expressed in terms of the GOIoTPex ontology.

```
<align:Cell rdf:about="&sripas;1_meteo_stations">
```

```

<align:entity1 rdf:datatype="xsd:string">
  var:elem a port:Element ;
  port:haslatitude var:lat ;
  port:haslongitude var:long ;
  port:hasmeteoStationId var:id ;
  port:hasname var:name .
</align:entity1>
<align:entity2 rdf:datatype="xsd:string">
  var:station a vp:MeteoStation, iiot:IoTDevice, sosa:Sensor ;
  iiotex:hasLocalId var:id ;
  iiot:hasName var:name ;
  iiot:hasLocation [
    a iiot:Location ;
    geo:asWKT var:geopos
  ] .
</align:entity2>
<align:relation>=</align:relation>
<sripas:transformation rdf:parseType="Literal">
  <function about="STR">
    <param order="1" about="&var;id"/>
    <return about="&var;sid"/>
  </function>
  <function about="CONCAT">
    <param order="1" val="&meteo;"/>
    <param order="2" about="&var;sid"/>
    <return about="&var;id_uri"/>
  </function>
  <function about="IRI">
    <param order="1" about="&var;id_uri"/>
    <return about="&var;station"/>
  </function>
  <function about="STR">
    <param order="1" about="&var;lat"/>
    <return about="&var;slat"/>
  </function>
  <function about="STR">
    <param order="1" about="&var;long"/>
    <return about="&var;slong"/>
  </function>
  <function about="CONCAT">
    <param order="1" val="Point("/>
    <param order="2" about="&var;slat"/>
    <param order="3" val=" " />
    <param order="4" about="&var;slong"/>
    <param order="5" val=")"/>
    <return about="&var;geopos"/>
  </function>
</sripas:transformation>
<sripas:filters rdf:parseType="Literal">
  <filter about="&var;lat" datatype="xsd:float"/>
  <filter about="&var;long" datatype="xsd:float"/>
  <filter about="&var;slat" datatype="xsd:string"/>
  <filter about="&var;slong" datatype="xsd:string"/>
</sripas:filters>
<sripas:typings rdf:parseType="Literal">
  <typing about="&var;geopos" datatype="ogis:wktLiteral"/>
</sripas:typings>
</align:Cell>

```

Listing 12 Alignment cell mapping meteo station “registration”

The message from Listing 11, when matched against the pattern from *entity1*, establishes appropriate “variable bindings” that are subsequently utilized/referenced in *entity2*, *transformation*, and *filters* sections of the cell. The structure of the RDF graph of the message together with the “variable bindings” is depicted in Fig. 1.

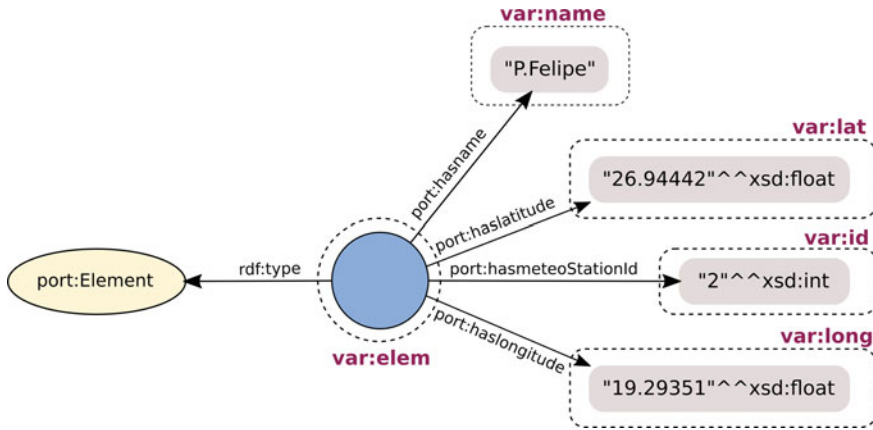


Fig. 1 RDF graph of the registration message

Because of the structure of the RDF graph pattern from *entity2* (Listing 12), and the created variable bindings, an instance of *vp:MeteoStation*, *iiot:IoTDevice*, and *sosa:Sensor* needs to be generated from the value that was matched by the *var:id* variable. This way, a numerical property of a blank node, representing a meteo station in the source data, is translated into an identifier (URI) of an entity representing the station in the target ontology. Therefore, in transformations sections, functions are called to cast it into string (STR), concatenate it with proper prefix (CONCAT), and generate the URI (IRI). The result is stored in the *var:station* variable that is referenced in the graph pattern from *entity2*. The source *port:hasname* property is mapped to the *iiot:hasName* property from the target (central) ontology.

The third important part of the mapping is defining the correspondences between geospatial data representations. Properties *port:haslatitude* and *port:haslongitude* are mapped onto *iiot:hasLocation* property, from GOIoTPEX, with value being an instance of *iiot:Location* that has *geo:asWKT* property. Geospatial data, in the WKT format, needs to be computed (concatenated), which is done by applying the CON-

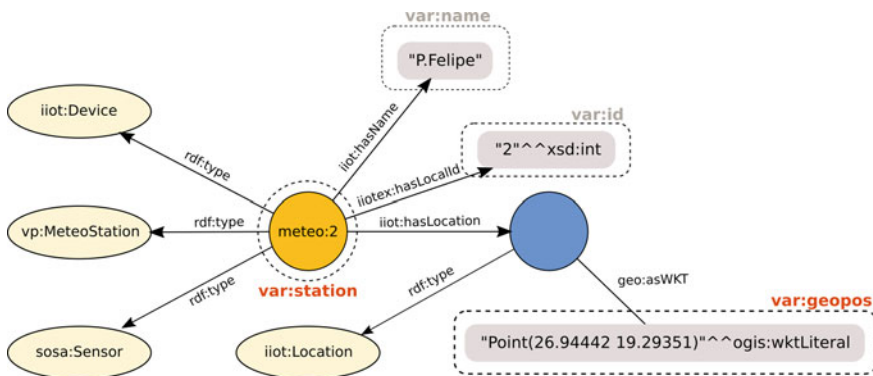


Fig. 2 RDF graph of the translated registration message and IPSM-AF variable bindings created by the alignment cell

CAT function that is called from the *transformation*. CONCAT takes as parameters string values; therefore, the STR function is called first, on source variables *var:lat* and *var:long*. Note that, in this case, *sripas:filters* and *sripas:typings* are used to include type filters and assign *ogis:wktLiteral* to the output variable. Figure 2 shows the structure of the translated RDF graph of the “registration” message, together with the variable bindings.

The result of the translation, represented in RDF Turtle notation, is given in Listing 13.

```
meteo:2 a vp:MeteoStation , iiot:IoTDevice , sosa:Sensor ;
  iiot:hasLocation [
    a iiot:Location ;
    geo:asWKT "Point(26.94442 19.29351)"^^ogis:wktLiteral
  ] ;
  iiot:hasName "P.Felipe" ;
  iiotex:hasLocalId "2"^^xsd:int .
```

Listing 13 “P.Felipe” registration message after translation

The second example shows a mapping between meteorological data (observation) expressed in different semantics. Listing 14 shows sample RDF instance of an observation.

```
[ ] a port:Element ;
  port:hasdate "2020-07-15T09:50:01.000Z" ;
  port:hasmeasurementId "3181710"^^xsd:int ;
  port:hasmeteoStationId "9"^^xsd:int ;
  port:haspressure "1025.552"^^xsd:float ;
  port:hasseaTemperature "0.0"^^xsd:float ;
  port:haswindDirection "177.4603"^^xsd:float .
```

Listing 14 RDF instance representing meteorological observation

The instance, with a given numerical measurement identifier, is described with date and identifier of the station it originated from and includes measured values for pressure, temperature, and wind direction. The cell, for mapping observation data, is presented in Listing 15. The mapping defines how to transform input RDF graph, based on the *port* ontology, into an output RDF graph, based on the GOIoTPEX ontology, with additional module for the meteorological data. The RDF graph structures, for the instance and the variable bindings that result from matching the alignment cell, are depicted in Fig. 3.

```
<align:Cell rdf:about="&sripas;1_weather_measurement">
  <align:entity1 rdf:datatype="&xsd:string">
    var:elem a port:Element ;
    port:hasmeasurementId var:meas_id ;
    port:hasmeteoStationId var:station_id ;
    port:hasdate var:date ;
    port:haswindDirection var:direct ;
    port:hasseaTemperature var:seatemp ;
    port:haspressure var:pressure .
  </align:entity1>
  <align:entity2 rdf:datatype="&xsd:string">
    var:station a vp:MeteoStation , iiot:IoTDevice , sosa:Sensor ;
    iiotex:hasLocalId var:station_id .
    var:measurment a sosa:Observation , vp:WeatherMeasurement ;
    iiotex:hasLocalId var:meas_id ;
```

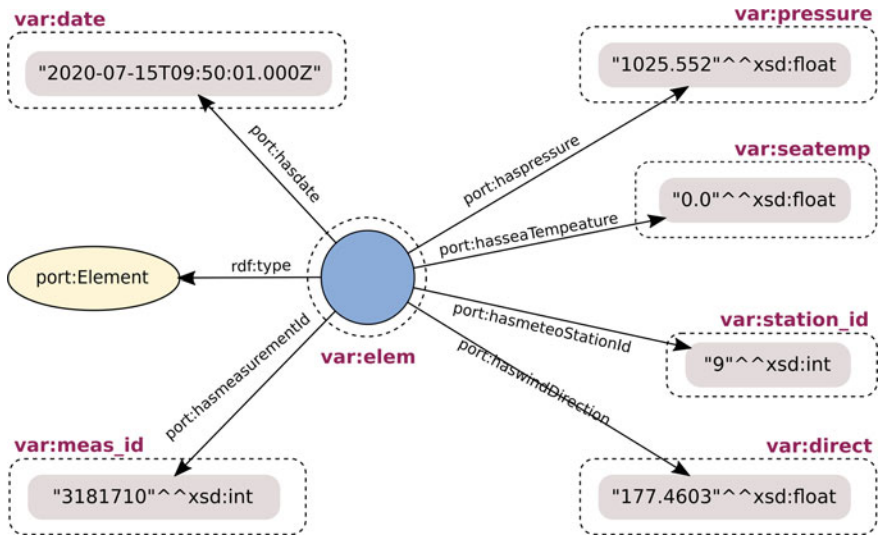


Fig. 3 RDF graph of the meteorological observation

```

sosa:madeBySensor var:station ;
sosa:hasResult [
  a sosa:Result, vp:WindDirection ;
  iiot:hasResultValue var:direct
], [
  a sosa:Result, vp:SeaTemperature ;
  iiot:hasResultValue var:seatemp
], [
  a sosa:Result, vp:Pressure ;
  iiot:hasResultValue var:pressure
] ;
sosa:resultTime var:date .
</align:entity2>
<align:relation>=</align:relation>
<sripas:transformation rdf:parseType="Literal">
  <function about="STR">
    <param order="1" about="&var;station_id"/>
    <return about="&var;sid"/>
  </function>
  <function about="CONCAT">
    <param order="1" val="&meteo;"/>
    <param order="2" about="&var;sid"/>
    <return about="&var;sid_uri"/>
  </function>
  <function about="IRI">
    <param order="1" about="&var;sid_uri"/>
    <return about="&var;station"/>
  </function>
  <function about="STR">
    <param order="1" about="&var;meas_id"/>
    <return about="&var;mid"/>
  </function>
  <function about="CONCAT">
    <param order="1" about="&var;id_uri"/>
    <param order="1" val=""/>
    <param order="2" about="&var;mid"/>
  </function>

```

```

        <return about="&var;meas_id_uri"/>
    </function>
    <function about="IRI">
        <param order="1" about="&var;meas_id_uri"/>
        <return about="&var;measurment"/>
    </function>
</sripas:transformation>
<sripas:typings rdf:parseType="Literal">
    <sripas:typing about="&var;date" datatype="&xsd;dateTimeStamp"/>
</sripas:typings>
</align:Cell>

```

Listing 15 Alignment cell for translation of meteorological observations

Next, the alignment is applied to transform the data, and the resulting output is as in Listing 16.

```

<http://www.inter-iot.eu/wso2port/weather/stations/9/3181710>
  a sosa:Observation , vp:WeatherMeasurement ;
  iiotex:hasLocalId "3181710"^^xsd:int ;
  sosa:hasResult [
    a sosa:Result , vp:WindDirection ;
    iiot:hasResultValue "177.4603"^^xsd:float
  ] ;
  sosa:hasResult [
    a sosa:Result , vp:SeaTemperature ;
    iiot:hasResultValue "0.0"^^xsd:float
  ] ;
  sosa:hasResult [
    a sosa:Result , vp:Pressure ;
    iiot:hasResultValue "1025.552"^^xsd:float
  ] ;
  sosa:madeBySensor meteo:9 ;
  sosa:resultTime "2020-07-15T09:50:01.000Z"^^xsd:dateTimeStamp .

meteo:9
  a vp:MeteoStation , iiot:IoTDevice , sosa:Sensor ;
  iiotex:hasLocalId "9"^^xsd:int .

```

Listing 16 Output for translation of meteorological observation

In the translation, identifiers of measurement and meteo station are transformed from numerical values into entities using IRI function applied to the source variables identifiers concatenated with prefixes. Meteo station is an instance of *iiot:IoTDevice*, *sosa:Sensor*, *vp:MeteoStation*, whereas measurement is an instance of *sosa:Observation*, *vp:WeatherMeasurement*. An observation is annotated with a reference to the specific sensor (meteo station), by which it was taken, as well as a result time and three results with values and classes, which indicate what was actually measured (Fig. 4).

6 Concluding Remarks

With the growing popularity of IoT-based solutions, big data processing, and systems integration, the need arose not only to be able to express correspondences (alignments) between data models, but also to use them in practices to realize needed (pos-

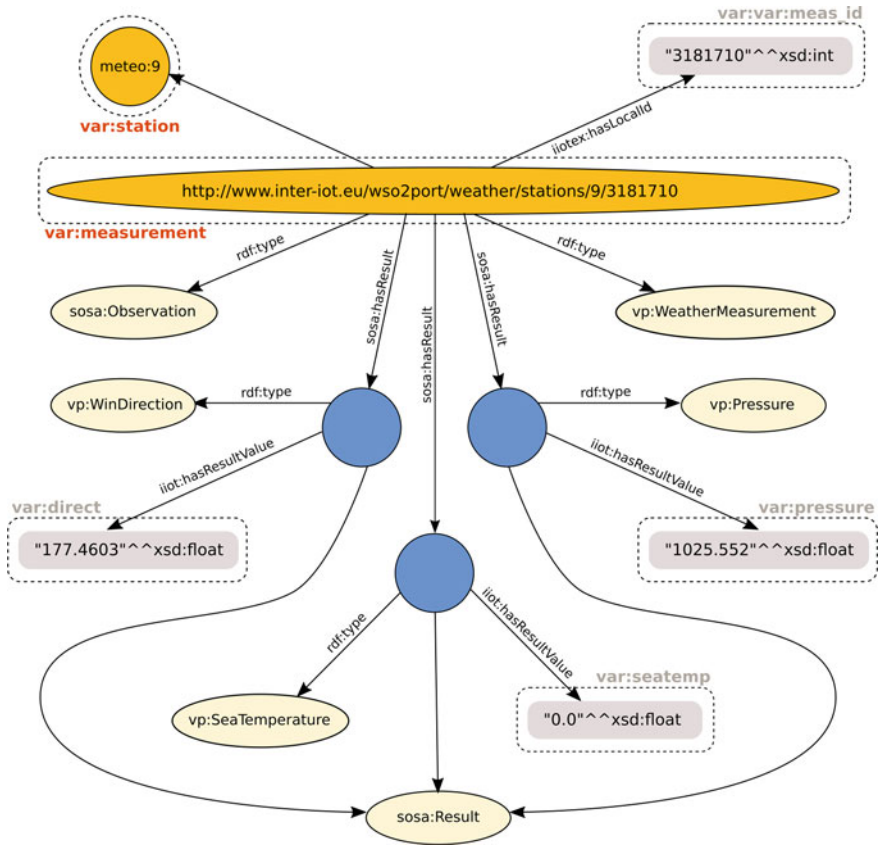


Fig. 4 RDF graph of the translated meteorological observation

sibly streaming) translations. Alignments should be persisted in a machine-readable format that can be automatically consumed by software tools, but is also easy to pick-up by humans. Here, IPSM-AF proves to be an expressive language for defining alignments that can be used by IPSM which automatically executes semantic translation. IPSM-AF was tested in two pilot applications and open call projects where different requirements for semantic translation needed to be fulfilled. Compliance with well-known Alignment API format enables alignments expressed in IPSM-AF to be consumed (if required after adjusting) by other semantic translators that may be developed in the future.

Outside of the validation of IPSM-AF in the INTER-IoT project [17], the format is supported by a rich number of concrete “recipes”²¹ and guides for practical usage,²²

²¹ <https://inter-iot.readthedocs.io/projects/inter-iot-cookbook/en/latest/inter-layer/ds2ds/recipes/alignment/>.

²² <https://inter-iot.readthedocs.io/projects/inter-iot-cookbook/en/latest/inter-layer/ds2ds/appendices/products/>.

including deeply analyzed examples, e.g., for mapping of geolocation data [6], as well as comparison with other possible alternatives [22].

The complete source code for the Inter-Platform Semantic Mediator (IPSM) can be freely obtained from the INTER-IoT official code repository²³ on GitHub. The easiest way to test/use IPSM is to follow the IPSM Docker image deployment instructions available from the INTER-IoT IPSM documentation site.²⁴

Acknowledgments This research was partially supported by the European Union’s “Horizon 2020” research and innovation program as part of the “Interoperability of Heterogeneous IoT Platforms” (INTER-IoT) project under the Grant Agreement No. 687283.

References

1. Borst WN (1997) Construction of engineering ontologies for knowledge sharing and reuse. Ph.D. thesis. University of Twente, Enschede, Netherlands. base-search.net (ftunivtwente:oai:doc.utwente.nl:17864)
2. Cousin P (ed) Internet of Things success stories, series 1-3. Internet of Things European Research Cluster (IERC) and Smart Action, 2014–2015
3. David J, Euzenat J, Scharffe F, Trojahn dos Santos C (2011) The alignment API 4.0. *Semantic Web* 2(1):3–10
4. Euzenat J, Shvaiko P (2013) *Ontology matching*, 2nd edn. Springer
5. Ferdinand M, Zirpins C, Trastour D (2004) Lifting XML schema to OWL. In: Koch N, Fraternali P, Wirsing W (eds) *Web engineering—4th International Conference. ICWE 2004*, Munich, Germany, 26–30 July 2004, Proceedings. Springer, Heidelberg, pp 354–358
6. Ganzha M, Paprzycki M, Pawłowski W, Szymeja P, Wasielewska K (2017) Alignment-based semantic translation of geospatial data. In: *Proceedings of 3rd International conference on advances in computing, communication & automation (ICACCA)*
7. Ganzha M, Paprzycki M, Pawłowski W, Szymeja P, Wasielewska K (2017) Semantic interoperability in the Internet of Things: an overview from the INTER-IoT perspective. *J Netw Comput Appl* 81:111–124
8. Ganzha M, Paprzycki M, Pawłowski W, Szymeja P, Wasielewska K (2017) Streaming semantic translations. In *Proceedings of 21st international conference on system theory, control and computing ICSTCC. IEEE*, pp 1–8
9. Ganzha M, Paprzycki M, Pawłowski W, Szymeja P, Wasielewska K (2017) Towards semantic interoperability between Internet of Things platforms. In: Gravina R, Palau CE, Manso M, Liotta A, Fortino G (eds) *Integration. Interconnection, and interoperability of IoT systems*. Springer, Cham, pp 103–127
10. Ganzha M, Paprzycki M, Pawłowski W, Szymeja P, Wasielewska K, Fortino G (2016) Tools for ontology matching—Practical considerations from INTER-IoT perspective. In: *Proceedings of the 8th international conference on internet and distributed computing systems*, vol 9864 of LNCS. Springer, pp 296–307
11. Ganzha M, Paprzycki M, Pawłowski W, Szymeja P, Wasielewska K, Palau CE (2017) From implicit semantics towards ontologies—Practical considerations from the INTER-IoT perspective (submitted for publication). In: *Proceedings of 1st edition of globe-IoT 2017: towards global interoperability among IoT systems*

²³ <https://github.com/INTER-IoT/ipsm-core>.

²⁴ <https://inter-iot-ipsm.readthedocs.io/en/latest/Deployment/Docker-image/>.

12. Ganzha M, Paprzycki M, Pawłowski W, Szymeja P, Wasielewska K, Solarz-Niesłuchowski B, de Puga García JS (2018) Towards high throughput semantic translation. In: Fortino G, Palau CE, Guerrieri A, Cuppens NCF, Chaouchi H, Gabillon A (eds) *Interoperability, safety and security in IoT*. Springer, Cham, pp 67–74
13. Heyvaert P, Dimou A, De Meester B, Seymoens T, Herregodts A-L, Verborgh R, Schuurman D, Mannens E (2018) Specification and implementation of mapping rule visualization and editing: MapVOWL and the RMLEditor. *J Web Semantics* 49:31–50
14. Kharlamov E, Kotidis Y, Mailis T, Neuenstadt C, Nikolaou C, Özçep Ö, Svingos C, Zheleznyakov D, Ioannidis Y, Lamparter S, Möller R, Waaler A (2019) An ontology-mediated analytics-aware approach to support monitoring and diagnostics of static and streaming data. *J Web Semantics* 56:30–55
15. Miles A, Matthews B, Wilson M, Brickley D (2005) SKOS core: simple knowledge organisation for the web. In: *Proceedings of the 2005 international conference on dublin core and metadata applications: vocabularies in practice, DCMI'05*. Dublin Core Metadata Initiative, pp 1–9
16. Mohammadi M, Rezaei J (2020) Evaluating and comparing ontology alignment systems: an MCDM approach. *J Web Semantics* 64:100592
17. Palau CE, Fortino G, Montesinos M, Exarchakos G, Giménez P, Markarian G, Castay M, Fuart F, Pawłowski W, Mortara M, Bassi A, Gevers F, Ibañez G, Huet I (eds) (2021) *Interoperability of Heterogeneous IoT platforms—A layered approach*. Internet of Things. Springer
18. Perera C, Liu CH, Jayawardena S, Chen M (2015) Context-aware computing in the Internet of Things: a survey on Internet of Things from industrial market perspective. In: *CoRR*. abs/1502.00164
19. Scharffe F (2009) *Correspondence patterns representation*. Ph.D. thesis. University of Innsbruck
20. Scharffe F, Zamazal O, Fensel D (2014) Ontology alignment design patterns. *Knowl Inf Syst* 40:1–28, 7
21. Szymeja P, Ganzha M, Paprzycki M, Pawłowski W, Wasielewska K (2018) Declarative ontology alignment format for semantic translation. In: *3rd International conference on Internet of Things: smart innovation and usages (IoT-SIU 2018)*. IEEE Xplore, pp 1–6
22. Szymeja P, Prud'hommeaux E (2021) ShExMap and IPSM-AF—comparison of RDF transformation technologies. In: *Intelligent systems, technologies and applications, Proceedings of sixth ISTA 2020, India*. Springer, Berlin, Germany, pp 29–46
23. Thiéblin E (2019) *Automatic generation of complex ontology alignments*. Ph.D. thesis. Institut de Recherche en Informatique de Toulouse, Toulouse, 10 2019
24. Thieblin E, Haemmerlé O, Hernandez N, dos Santos CT (2019) Survey on complex ontology matching. *Semantic Web*
25. Volz J, Bizer C, Gaedke M, Kobilarov G. Silk—A link discovery framework for the web of data. *LDOW*, 538

Topical Classification of Food Safety Publications with a Knowledge Base



Piotr Sowinski, Katarzyna Wasielewska-Michniewska, Maria Ganzha, and Marcin Paprzycki

Abstract The vast body of scientific publications presents an increasing challenge of finding those that are relevant to a given research question, and making informed decisions on their basis. This becomes extremely difficult without the use of automated tools. Here, one possible area for improvement is automatic classification of publication abstracts according to their topic. This work introduces a novel, knowledge base-oriented publication classifier. The proposed method focuses on achieving scalability and easy adaptability to other domains. Classification speed and accuracy are shown to be satisfactory, in the very demanding field of food safety. Further development and evaluation of the method are needed, as the proposed approach shows much potential.

Keywords Publication classification · Ontology · Named entity linking · Systematic literature review · Food safety

1 Introduction

In modern science, we are confronted with a fast-growing body of publications, where finding the “relevant ones” is becoming increasingly challenging. To address the problem, evidence-based decision-making (EBDM) [3] was proposed, where one of the forms of research used is the systematic review (SR), which uses scientifically

P. Sowinski (✉) · M. Ganzha
Warsaw University of Technology, Warsaw, Poland
e-mail: piotr.sowinski@mini.pw.edu.pl

M. Ganzha
e-mail: maria.ganzha@pw.edu.pl

P. Sowinski · K. Wasielewska-Michniewska · M. Ganzha · M. Paprzycki
Systems Research Institute, Polish Academy of Sciences, Warsaw, Poland
e-mail: katarzyna.wasielewska@ibspan.waw.pl

M. Paprzycki
e-mail: marcin.paprzycki@ibspan.waw.pl

© The Author(s), under exclusive license to Springer Nature Singapore Pte Ltd. 2022
V. Mahajan et al. (eds.), *Sustainable Technology and Advanced Computing in Electrical Engineering*, Lecture Notes in Electrical Engineering 939,
https://doi.org/10.1007/978-981-19-4364-5_48

rigorous methods to identify, select, assess, and summarize multiple works [20]. Systematic reviews are increasingly used to summarize the state-of-the-art and to guide the direction of future research [2]. While SRs are very reliable, due to the required time and expertise, producing them quickly proved to be a challenge [26]; e.g., a study is typically included in a systematic review 2.5–6.5 years after publication [14]. This all points to the need of SR automation. While some parts of an SR require creativity and expertise, others can be automated [26].

This work discusses the use of semantic technologies and natural language processing to aid automation of SR in the field of food safety. More specifically, the described system facilitates relevance screening by classifying articles according to their topic(s). Having an article described by its title, abstract, and, optionally, unstructured keywords, the aim is to assign to it topics drawn from a knowledge base (KB). Here, potential advantage of using a semantic KB is explored, because of the meaning and the context provided by the ontology [22].

The proposed solution was evaluated in the food safety domain, which presents a unique challenge in automatic SR, as it involves a wide variety of topics from multiple fields of science necessitated by the integration of heterogeneous sources of information [4, 27]. On the other hand, there are numerous ontologies available for biology, chemistry, and medicine domains [28], which can be incorporated to reason about food safety.

2 Related Works

Food safety is a relatively unexplored domain in text classification-oriented research. However, documents in this domain draw terminology from numerous biomedical sciences. Thus, one may expect to encounter similar characteristics to those present in related areas. For diseases and drugs, issues with entity linking usually stem from the many ways in which a single entity can be represented in text [18]. There are examples of similar morphology but different meaning: “ADA-SCID (adenosine deaminase deficiency)” and “X-SCID (X-linked combined immunodeficiency diseases).” There are also examples of entirely different morphology, but similar semantic meaning, e.g., “Kaplan Plauchu Fitch syndrome” and “acrocraniofacial dysostosis.” Moreover, the numerous obscure abbreviations can vary between publications, bringing importance to the context. Finally, very few labeled datasets are available, making supervised methods unfeasible [30].

On the other hand, in biomedical sciences there are many well-structured ontologies that may be used in entity linking [1, 30]. There is a relatively large body of research concerning entity linking for medical reports and publications [18]. However, these works usually focus on linking text to thesauri or taxonomies, such as MeSH¹ that are less expressive than full ontologies. Moreover, these methods are often evaluated using benchmark datasets that provide researchers with training

¹ <https://www.nlm.nih.gov/mesh/introduction.html>.

data for supervised models. Nonetheless, even very sophisticated methods, based on BERT, can struggle to correctly perceive context and resolve ambiguous entities. Especially hard are situations where the model is asked to identify terms that occur rarely within the training corpus [10]. Finally, modern supervised approaches have very high hardware requirements.

Furthermore, there are a few solutions addressing the classification problem in the biomedical domain. Here, we outline most relevant to the presented work.

NCBO Annotator² is an ontology-based tool for entity linking in biomedicine. Being a part of the BioPortal,³ it supports all ontologies published there. The Annotator uses basic string matching to find entities with names similar to those occurring in the text. Results are further enhanced with concept expansion and ontology mappings [15]. Here, the method is unsupervised and can handle hundreds of ontologies at the same time. However, the system lacks the ability to handle morphological variants and more complicated disambiguation cases.

Neural Concept Recognizer [1] links entities from medical ontologies. It is based on the idea that both text and ontologies can be embedded into a vector space and one can compute similarity metrics between vectors to find matching terms. Text is vectorized using word embeddings and a convolutional neural network. Concept embeddings are established with respect to the taxonomical structure of the ontology. Training is performed on an artificially made dataset, derived from labels present in the ontology. The approach allows training the classifier based only on the ontology and allows easy adaptation to a different domain. It is also claimed that the system can handle novel synonyms, contrary to rule- or dictionary-based solutions. However, the authors point to the inability of the model to perceive context and a relatively slow performance.

The CSO Classifier [22] is an automatic classification system for computer science publications. Although it does not focus on the biomedical sciences, its general idea seems applicable to other domains as well. It uses the Computer Science Ontology of research topics, with a taxonomical structure [23]. The system consists of three modules. The syntactic module preprocesses the text and searches for n-grams, with high Levenshtein similarity to terms in the ontology. This is to find topics that are explicitly mentioned in the document. The semantic module aims at retrieving topics that are semantically related, but not explicitly mentioned. Part of speech tagging and a simple grammar rule are used for extracting candidate text spans to be analyzed. Next, word embeddings (via word2vec) are used to find semantically similar terms in the ontology. The most relevant topics are selected by ranking them using a metric that considers the frequency with which they occur in the document and how “diverse” were their mentions. Finally, in postprocessing, the terms most frequently occurring in the corpus are discarded and the remaining list of topics is enhanced by including direct ancestors of the terms from the ontology. According to the authors, the CSO Classifier outperforms other topic detection methods in terms of recall, by also including topics that are only implied in text but not explicitly stated.

² <https://bioportal.bioontology.org/annotator>.

³ <https://bioportal.bioontology.org/>.

3 Dataset Preparation

Let us now describe datasets that were used in our work. For constructing a corpus of food safety publications, two popular sources were used: PubMed⁴ and the European Food Safety Authority (EFSA) Journal.⁵ For both sources, articles relevant to food safety were found and their metadata retrieved.

3.1 PubMed

To retrieve the metadata from PubMed, the Entrez API client, from the Biopython package, was used [5]. Articles in PubMed are described using MeSH, which through its hierarchical structure groups descriptors into categories. Our search was limited to articles that use the “food safety” MeSH descriptor, and any of its children; 77,348 articles were found, of which 61,941 had available abstracts. Table 1 shows how often descriptors from a given MeSH category were used to point to articles in the corpus. The analysis was performed using SPARQL queries on MeSH and article metadata, imported into a Blazegraph quad store.⁶

It can be observed that food science is *not* the dominant area. Even in [A] and [C] categories, terms associated with the digestive system are not the most frequent. Among frequent terms, not related to food science, are organisms, chemicals, investigative techniques, phenomena and processes, health care, and geo-location. Thus, it is obvious that *food safety touches upon a very diverse set of topics and involves complex relations*. Hence, when choosing ontologies for describing this domain, a very wide spectrum of topics has to be included.

To identify additional keywords that were not provided explicitly with the publications, named entity linking (NEL) of abstracts, against the UMLS metathesaurus, was performed with the scispaCy [21] library. The used model was based on BERT architecture (`en_core_sci_scibert`), and the linker was targeting a ~785k entity subset of UMLS. Finally, entity occurrence frequency in abstracts was summarized. The method identified 48,083 unique entities in 61,941 abstracts. The results contain some obvious misclassifications—for example 28,253 abstracts are to refer to mental concentration (attention concentration), which is a very uncommon topic in food safety. These occurrences most likely refer to the concentration of substances, which is a frequent topic in food safety literature. Barring the misclassifications, many of the frequently identified keywords refer to investigative techniques, risk assessment, and statistics (e.g., *levels, concentration, detection, contamination, association, significance, prevalence*). Most other entities are typically within the scope of MeSH (biology, chemistry, medicine).

⁴ <https://pubmed.ncbi.nlm.nih.gov/>.

⁵ <https://www.efsa.europa.eu/en/publications>.

⁶ <https://blazegraph.com/>.

Table 1 Descriptor usage by category for PubMed articles

Category	# descriptors
Anatomy [A]	26,050
<i>including:</i>	
Fluids and secretions	4790
Cells	4691
Plant structures	3770
Digestive system	2519
Organisms [B]	119,840
Diseases [C]	45,388
<i>including:</i>	
Infections	15,672
Animal diseases	5046
Digestive system disorders	4205
Chemicals and drugs [D]	209,783
Analytical, diagnostic and therapeutic techniques (...) [E]	101,766
<i>including:</i>	
Investigative techniques	81,670
Psychiatry and psychology [F]	5513
Phenomena and processes [G]	128724
Disciplines and occupations [H]	12752
Anthropology, education, sociology (...) [I]	8712
Technology, industry, and agriculture [J]	69,369
<i>including:</i>	
Food and beverages	35,432
Technology, industry, and agriculture	31,536
Humanities [K]	1079
Information science [L]	6161
Named groups [M]	9822
Health care [N]	111,808
Geographicals [Z]	30,474

3.2 EFSA

EFSA metadata is available via a free API,⁷ which allows retrieving abstracts and associated keywords. As the primary focus of EFSA is food safety, all available articles were retrieved. Of 10,088 publications, 6684 had available abstracts.

Provided keywords are not structured, which prohibits analysis that was performed using MeSH descriptors. On the other hand, these keywords are not restricted by a controlled vocabulary, and thus, a rudimentary frequency analysis may show

⁷ <https://openapi-portal.efsa.europa.eu/>.

often used terms that were not identified previously. Among the most common keywords that are not directly within the scope of food science are *risk assessment*, *safety*, *health claims*, *MRL* (maximum residue levels), *QPS* (qualified presumption of safety), *exposure*, *quarantine*, *children*, *data collection*, *confirmatory data*, European Union member states, and various EU legislative documents. The latter appeared in contributions dealing with regulation compliance. It should be noted that nearly 67% of keywords appear only once, while 14% appear twice. These rarely appearing terms are mostly specific chemicals, processes, and organisms.

Entity linking against UMLS was performed for the retrieved abstracts, using the same method as with the PubMed corpus. For 6684 abstracts, 13,200 unique entities were found. As in PubMed, there were many misclassified terms that are unlikely to appear frequently in the corpus. The used NEL method is based on simple n-gram vectorization of mentions and lacks the necessary context required to successfully disambiguate some terms. Additionally, it failed to identify terminology specific to the EFSA dataset (e.g., *European Commission*, *MRLS*, *MON*), due to UMLS lacking these terms. On the other hand, typical biomedical terms were identified easily. Often found were references to food products, ingredients, organisms, age groups, chemicals, and diseases.

3.3 Summary

From the preliminary analysis, it is obvious that dictionaries (ontologies) used in food safety should span a wide scope of biomedical topics. Moreover, the preliminary NEL results obtained using scispaCy strongly suggest that disambiguating of named entities in texts may require the system to better perceive the context in which the term appears and how is it related to other terms.

4 Ontologies

While initial results suggest that the use of semantic technologies could be beneficial to the task of publication classification, there is no public food safety ontology available. However, there are ontologies describing related fields, such as food science. One example is FoodOn—a comprehensive food ontology [9], available through NCBO's BioPortal [28]. FoodOn has numerous mappings to other ontologies in the BioPortal,⁸ which allows them to be used jointly. FoodOn is also a part of OBO Foundry,⁹ guaranteeing application of several quality-improving guidelines [25], especially important when using multiple ontologies at a time.

⁸ <https://bioportal.bioontology.org/ontologies/FOODON/?p=mappings>.

⁹ <http://obofoundry.org/>.

As shown previously, food safety publications touch upon many diverse topics within the biomedical domain. The number of available biomedical ontologies is also high—NCBO’s BioPortal claims to host 846 ontologies. Without the help of domain experts, the only viable method for ontology selection (and use) would have to be based on data-driven analysis of topics found in publications. Such analysis can be based on data gathered from PubMed, thanks to the presence of structured MeSH descriptors. Those descriptors can be mapped to related entities in other ontologies, using mappings from the BioPortal.

For each of the 11,693 MeSH descriptors, present in the corpus, mappings to all BioPortal ontologies were retrieved. The initial focus was on ontologies from the OBO Foundry. Actively maintained ontologies with comprehensive documentation were prioritized. Additionally, several upper level ontologies were included (e.g., BFO, IAO, RO). The selected OBO ontologies are listed below, ordered alphabetically by their abbreviations.

- Anatomical Entity Ontology (**AEO**)¹⁰
- Agronomy Ontology (**AGRO**)¹¹
- Apollo Structured Vocabulary (**APOLLO-SV**)¹²
- Basic Formal Ontology (**BFO**)¹³
- BRENDA tissue/enzyme source (**BTO**)¹⁴
- Common Anatomy Reference Ontology (**CARO**)¹⁵
- Chemical Entities of Biological Interest (**CHEBI**)¹⁶
- Chemical Methods Ontology (**CHMO**)¹⁷
- Cell Ontology (**CL**)¹⁸
- Human Disease Ontology (**DOID**)¹⁹
- Drug Ontology (**DRON**)²⁰
- Human developmental anatomy ontology (**EHDAA2**)²¹
- Environment Ontology (**ENVO**)²²
- Food-Biomarker Ontology (**FOBI**)²³
- FoodOn²⁴

¹⁰ <http://www.obofoundry.org/ontology/aeo.html>.

¹¹ <https://github.com/AgriculturalSemantics/agro>.

¹² <https://github.com/ApolloDev/apollo-sv>.

¹³ <http://basic-formal-ontology.org/>.

¹⁴ <http://www.obofoundry.org/ontology/bto.html>.

¹⁵ <https://github.com/obophenotype/caro/>.

¹⁶ <https://www.ebi.ac.uk/chebi/>.

¹⁷ <http://obofoundry.org/ontology/chmo.html>.

¹⁸ <https://obophenotype.github.io/cell-ontology/>.

¹⁹ <https://disease-ontology.org/>.

²⁰ <https://github.com/ufbmi/dron>.

²¹ <http://obofoundry.org/ontology/ehdaa2.html>.

²² <http://environmentontology.org/>.

²³ <http://www.obofoundry.org/ontology/fobi.html>.

²⁴ <https://foodon.org/>.

- Gazetteer (**GAZ**)²⁵
- Gene Ontology (**GO**)²⁶
- Human Phenotype Ontology (**HP**)²⁷
- Information Artifact Ontology (**IAO**)²⁸
- Mammalian Phenotype Ontology (**MP**)²⁹
- NCBI organismal classification (**NCBITaxon**)³⁰
- Ontology for Biomedical Investigations (**OBI**)³¹
- Phenotype And Trait Ontology (**PATO**)³²
- Population and Community Ontology (**PCO**)³³
- Plant Experimental Conditions Ontology (**PECO**)³⁴
- Plant Ontology (**PO**)³⁵
- Relation Ontology (**RO**)³⁶
- Symptom Ontology (**SYMP**)³⁷
- Uberon³⁸
- Units of measurement ontology (**UO**)³⁹
- Experimental condition ontology (**XCO**)⁴⁰

This set of ontologies covers 4031 out of 11,693 (34.5%) MeSH descriptors present in the corpus (271,714 out of 872,838 (31.1%) descriptor occurrences). This relatively low coverage contrasts with the very wide range of topics these ontologies cover. This is possibly due to MeSH being designed for indexing publications, and thus having terms oriented toward more general topics instead of granular concepts. For example, one of the frequently occurring MeSH descriptors is *Fishes*, an imprecise term that does not have a strict definition. The NCBITaxon ontology includes many species of fish (and their biological taxonomy), but not this particular term. Other OBO Foundry ontologies also describe specific terms very well, but lack the more general/imprecise ones.

²⁵ <http://obofoundry.org/ontology/gaz.html>.

²⁶ <http://geneontology.org/>.

²⁷ <http://www.obofoundry.org/ontology/hp.html>.

²⁸ <https://github.com/information-artifact-ontology/IAO/>.

²⁹ http://www.informatics.jax.org/vocab/mp_ontology/.

³⁰ <http://obofoundry.org/ontology/ncbitaxon.html>.

³¹ <http://obi-ontology.org/>.

³² <http://obofoundry.org/ontology/pato.html>.

³³ <https://github.com/PopulationAndCommunityOntology/pco>.

³⁴ <http://www.obofoundry.org/ontology/peco.html>.

³⁵ <http://www.obofoundry.org/ontology/po.html>.

³⁶ <https://oborel.github.io/>.

³⁷ <http://symptomontologywiki.igs.umaryland.edu/>.

³⁸ <http://uberon.github.io/>.

³⁹ <https://github.com/bio-ontology-research-group/unit-ontology>.

⁴⁰ https://rgd.mcw.edu/rgdweb/ontology/view.html?acc_id=XCO:0000000.

One way to cope with this issue would be to include an additional, “meta-level” biomedical ontology. MeSH could play this role, but it has several significant drawbacks. First, being a thesaurus, it is less expressive than ontologies. Second, its non-standard structure hinders its reuse with OWL ontologies that adhere to different design principles. Ultimately, the Systematized Nomenclature of Medicine Clinical Terms (SNOMED CT) was selected. It covers well the “general” biomedical terms and contains very expressive relations [8].

To integrate it with OBO Foundry ontologies, the terminology was converted to OWL⁴¹ and inserted into a knowledge base. Next, connections between identical (or related) terms in OBO Foundry ontologies and SNOMED CT were created, using two sources of mappings. Some OBO ontologies already contained cross-database references to SNOMED CT—these references were normalized and converted to `skos:closeMatch` relations. Additionally, all mappings for SNOMED CT were retrieved from the BioPortal API. In total, 43,595 unique mappings were inserted into the KB, covering 37,999 of all 354,318 entities (10.7%) in SNOMED CT. From here, the combined OBO Foundry with SNOMED CT knowledge base will be referred to as **OBO/SNOMED**.

MeSH descriptor coverage was then re-evaluated. The new set of ontologies covers 7696 out of 11,693 (65.8%) MeSH descriptors, which constitutes 569,104 out of 872838 (65.2%) descriptor occurrences. The twenty most frequently occurring, yet uncovered MeSH descriptors include *food contamination*, *food microbiology*, *food safety*, *pesticide residue*, and other terms directly related to food safety. This implies that the constructed ontology is still incomplete in this regard. This problem is not solvable with the immediately available resources, and solving it is out of scope of this contribution.

The knowledge graph was inspected for inconsistencies and other issues that may hamper the classification algorithm. The first discovered issue was the lack of consistency among cross-ontology references. They are supposed to connect similar/identical terms originating from different ontologies. Some such references are specified with loose annotation properties pointing to textual identifiers, not their URIs. Some target terms did have their identifiers attached using another annotation property, but many did not. These problems were mitigated with SPARQL UPDATE queries that transformed OBO references into traversable `skos:closeMatch` properties. Note that these issues are known and their detailed discussion can be found in the work of Laadhar et al. [16]. Other issues, e.g., triples with properties pointing to erroneous URIs, object properties referring to literal values, and annotation properties referring to objects, were also fixed with SPARQL queries. Such errors would decrease the accuracy of the method, due to it relying on the ontology for domain knowledge.

At the end, the OBO/SNOMED graph became relatively large, containing almost 49 million triples. Handling such a large dataset presents significant challenges. Therefore, the graph was inspected for triples of little value to text-based information retrieval. Unnecessary information was removed including provenance informa-

⁴¹ <https://github.com/IHTSDO/snomed-owl-toolkit>.

tion, metadata, links to external databases, and more. This resulted in a graph with approximately 25 million triples.

5 Proposed Approach

Let us now describe the method used to perform topical publication classification. Proposed approach is based on the following assumptions. (1) Classification should be as accurate as possible. (2) Solution should be fast and scalable, as target ontologies, depending on the discipline, can have tens of millions of triples. (3) The method should robustly cope with larger-than-memory datasets, without significant performance degradation. (4) Solution should be easily applicable to any domain. This implies reliance on the information contained in the KB, while “domain-specific code” should be limited to a minimum.

Figure 1 presents an overview of the method. First, using named entity recognition (NER), mentions are identified in the text (Sect. 5.1). Then, for each mention, a set of candidate entities is produced, based on a full-text query to a search engine (Sect. 5.2). Neighborhoods of candidates are taken into account, using an algorithm that exploits the semantic meaning of relations between entities (Sect. 5.3). Candidates are compared to the mention, and each is assigned a similarity score (Sect. 5.4). Additionally, connections between candidates are used to discard the least coherent choices (Sect. 5.5). Finally, the list of entities is enhanced using information from the KB, and the final set of terms most relevant to the publication is returned (Sect. 5.6). Let us now describe each operation in more detail.

5.1 *Named Entity Recognition*

The first stage of the method identifies mentions, in publication abstracts that may correspond to “entities of interest.” In later stages, these mentions will be linked to the entities in the knowledge base. There are several ready solutions to this problem in the biomedical domain, such as the scispaCy biomedical pipeline (`en_core_sci_lg`), which achieves a 69% F₁ score in NER, on the very demanding MedMentions dataset [21], and it was chosen to be used here. The final set of mentions is additionally extended with explicitly provided keywords, which are available for the EFSA corpus.

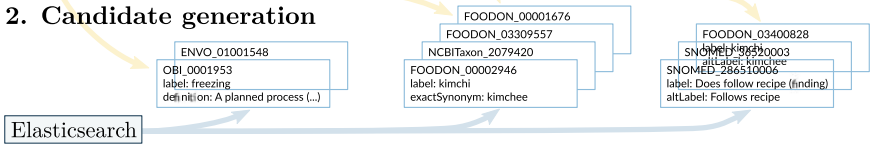
5.2 *Candidate Generation*

Selecting candidate entities for a mention is not trivial when the number of entities in the KB is large; e.g., OBO/SNOMED is too large to be loaded into memory

1. Named entity recognition

The **supercooling degree (SD)**, which refers to the difference between the **ice nucleation temperature** and **freezing point** of **kimchi**, varies depending on the type of **kimchi**, **manufacturer**, **recipe**, and **manufacturing season**.

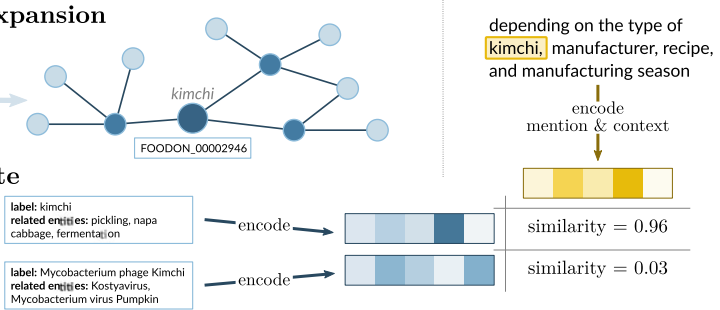
2. Candidate generation



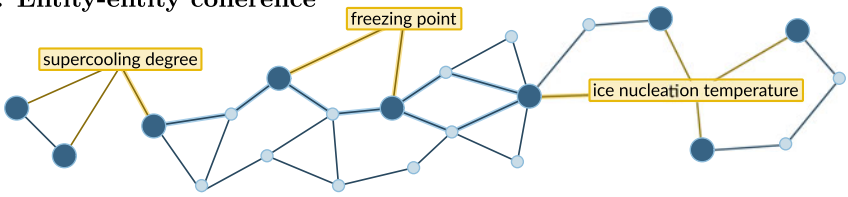
3. Graph expansion



4. Candidate ranking



5. Entity-entity coherence



6. Candidate selection and results enhancement

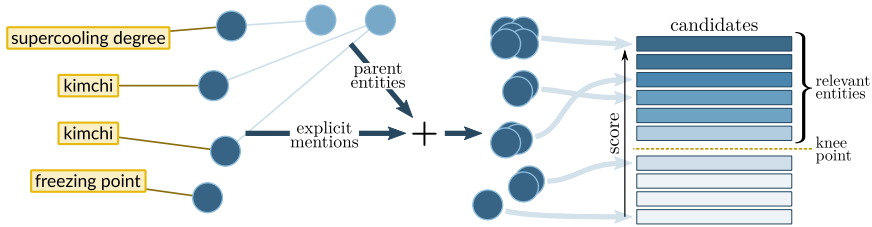


Fig. 1 Overview of the method

of a standard computer. Thus, Elasticsearch⁴² was used for candidate generation. Specifically, an Elasticsearch index was constructed, fields of which depended on types of text properties present within the KB. The unique identifier for each record in the index is simply the entity's URI. For each type of text property, a numeric weight was assigned for use when searching, to indicate how relevant the field is expected to be. Additionally, several fields are included for caching results of compute-intensive operations, described in detail in Sects. 5.3 and 5.6. Finally, the constructed index for the OBO/SNOMED knowledge base consists of 3,739,476 valid entity linking targets.

5.3 Graph Expansion

A candidate entity does not provide context information by itself—it is necessary to look at related entities to obtain a better sense of what it describes. This “graph expansion” approach was used successfully in a textual entailment system [29]. Before attempting to design an algorithm for this problem, KB was examined and several observations were made.

- **O1:** Traversing the graph only along the edges' original directionality may be too limiting. For example, with the `rdfs:subClassOf` relations this would result in only traversing the class hierarchy upward. Thus, the algorithm should traverse edges in both directions.
- **O2:** Processing large graphs with long-tail distributions of node degrees is challenging [11]. Encountering a vertex with a large number of neighbors forces the algorithm to visit all of them. Moreover, the relative amount of information a neighbor provides can vary considerably. Within large KBs, one can find entities with numerous connections (e.g., many instances of one class), which makes the meaning of such an entity intuitively less “concentrated.” Conversely, an entity with fewer connections is more likely to have a more concrete and relevant meaning.
- **O3:** Similarly, if an entity has many connections of type A, but very few of type B, the B-type edges are likely to provide more “focused” information. For instance, the *analgesic* class from CHEBI is connected to 65 substances that can be used as analgesics. When expanding from the *analgesic* entity, they may introduce “noise.” On the other hand, connections such as *analgesic is a subclass of drug* do provide important contextual information.
- **O4:** Finally, different types of properties have different meanings and can be intuitively translated to connections of varying importance. For example, the `skos:closeMatch` relation implies greater similarity than `rdfs:subClassOf` or `obo:RO_0002604` (is opposite of).

Based on these observations, the following formula for calculating edge weights (w_{rel}) was proposed (3).

⁴² <https://www.elastic.co/what-is/elasticsearch>.

$$l(o) = |(s', p', o) \in \text{KB} \cup (o, p', o') \in \text{KB}| \tag{1}$$

$$g(s, p, d) = \begin{cases} |(s, p, o') \in \text{KB}| & \text{if } d = \text{'spo' } \\ |(s', p, s) \in \text{KB}| & \text{if } d = \text{'ops' } \end{cases} \tag{2}$$

$$w_{\text{rel}}(s, p, o, d) = w_p l(o)^{f_l} g(s, p, d)^{f_g} \tag{3}$$

Here, s, p, o (subject, predicate, object) is a triple from the KB that may be inverted to allow traversing the graph in either direction (**O1**). In such case, the d parameter is set to ops to indicate the inversion, otherwise it is spo . The final weight consists of three components:

- w_p —the constant base weight for property p (**O4**). The base weights have to be picked manually, based on the user’s expertise, ontology documentation, and the use of the property in practice. The value typically ranges from 0.1 for very close, identity-like ties to 4, for the loose connections.
- $l(o)$ —the total number of links to and from the object of the triple (**O2**). By considering only the number of links of the object, the algorithm discourages visiting nodes with high cardinality, while leaving the node is not penalized. This is additionally scaled by a tunable parameter, f_l (0.5 by default).
- $g(s, p, d)$ —the number of links from subject s , through predicate p , in direction d (**O3**). This is also scaled by a parameter, f_g (0.5 by default).

In the equations, s', p', o' refer to (respectively) any subject, predicate, and object matching the given triple pattern. Expressions in the form of (s, p, o) indicate triple patterns present in the KB.

To compute w_{rel} effectively, the following approach is used. First, for each node x in the KB, $l(x)$ is calculated and the result inserted back into the graph. Next, a list of all (s, p, o) triples in the KB is generated, along with their $l(s)$ and $l(o)$. The list is enhanced with inverted triples, to enable traversing edges in both directions. This results in a list that may be much larger than the system memory available, which necessitates careful processing of the data (in parts). To be able to perform grouping operations effectively, the list is sorted on disk and repartitioned by s , producing partitions that can be safely grouped in isolation. Then, it is grouped by s, p , and d , which corresponds to the $g(s, p, d)$ function. Computing w_{rel} is straightforward now and is done by iterating over all obtained groups. For each group, only c_{max} (4 by default) connections with lowest weights are kept. The partitioned data is processed in parallel using the Dask Python library [6].

The algorithm outputs a list of triples with weights that when inserted into the KB yield a weighted, traversable graph. A weighted graph can be more generally framed as an attribute graph, where any edge between two nodes (a triple) can be annotated with additional information. Blazegraph implements a solution to this

called Reification Done Right (RDR), in which any triple can be either the object or the subject of another triple [12].

Perhaps the most obvious solution to finding neighboring entities in the knowledge graph would be to employ SPARQL queries; however, this would be hardly a typical use case for this language. A better fit would be a Gather-Apply-Scatter (GAS) algorithm, similar to the PowerGraph approach [11]. GAS allows one to write high-performance, parallel graph analytics algorithms. Blazegraph implements this approach⁴³ via a Java API. The graph expansion algorithm was implemented using this method and compiled as a Blazegraph plugin. The algorithm obtains edge weights of triples using RDR. The code is a modified version of the breadth-first search algorithm, taking into account maximum allowed traversal depth and maximum distance of found neighbors. The search is executed in parallel, across multiple threads.

As the neighborhood of an entity depends solely on the ontology, and not the particular search being made, it is possible to perform graph expansion for each possible candidate beforehand, to speed up classification. Then, the neighboring entities are saved to the Elasticsearch index, along with the distances to them (in the `related_entities` and `related_entities_weights` fields). This removes the need to run and query Blazegraph during runtime, improving classification speed and reducing the overall memory footprint.

5.4 Candidate Ranking

Obtained candidate entities are then rated by their relevance to the mention. The algorithm should consider both the context in which the mention appears, as well as the neighborhood of the candidate entity within the KB. The proposed solution uses two types of text vector representations—semantic and lexical. The semantic component employs word embeddings provided by the `scispaCy` library. While word embeddings have superior performance to lexical-based methods, one must also consider that out-of-vocabulary words will not produce a vector and thus cannot be compared. Here, for scientific texts, it is unreasonable to expect the embedding model to cover all possible words, some of which may be highly specialized and/or rarely occurring. Hence, the lexical component is introduced, based purely on character-level similarity between text fragments. To construct a lexical vector, the text fragment is split into 3–4 character n -grams. Next, the unique n -grams are grouped by their hashes and counted.

To compute the score of a candidate, its and all of its neighbors' text properties are vectorized. This produces two matrices, $L_{n \times m_l}$ and $S_{n \times m_s}$, for lexical and semantic vectors, respectively. Here, n is the number of all text properties from all entities that are taken into account. The number of columns depends on the length of the vectors. The matrices are L2-normalized row-wise, with the exception of zero-length

⁴³ https://github.com/blazegraph/database/wiki/RDF_GAS_API.

vectors. Additionally, a vector of distances to related entities is retrieved (w_e), with values starting from zero (for the candidate entity itself). As described in Sect. 5.2, text properties can have varying importance, which is considered here in the form of w_p , a vector of property weights. Finally, the similarity between the mention and other text fragments is calculated in bulk using (4).

$$d = w_p \frac{w_l a(Ll) + w_{sm} a(Ss_m) + w_{sc} a(Ss_c)}{1 + w_e} \quad (4)$$

$$a(x) = (1 + \exp(\alpha - \beta x))^{-2} \quad (5)$$

Here, l , s_m , s_c refer to the lexical vector of the mention, its semantic vector, and the semantic vector of the sentence the mention is in (its context), respectively. It is assumed that these vectors are L2-normalized. Moreover, w_l , w_{sm} , w_{sc} are tunable weights for the three components. Next, raw cosine similarity values are put through the activation function a , presented in (5). It is a case of the generalized logistic function. Its purpose is to discard low similarity scores and “promote” good matches. The α and β parameters can be tuned to control its steepness and translation along the X axis. The function will return values from the $(0, 1)$ interval. Equation (4) produces an n -length vector of similarity scores between the mention and each of the considered text fragments. The score is accumulated by simply summing the elements of the vector d . The actual code for calculating this formula uses several performance optimizations, such as a lookup table for the activation function. Additionally, numerically heavy routines were compiled using the Numba JIT compiler [17].

To further speed up classification, the feature vectors for text from the KB are pre-computed during indexing. They are then stored and retrieved during classification, minimizing the amount of text processing at runtime. The cached vectors can take up large amounts of memory. For the OBO/SNOMED KB, problems occurred even on a computer with ~ 32 GB of memory, and for other KBs, required memory may increase further. This is solved by storing the vectors using the Lightning Memory-Mapped Database (LMDB),⁴⁴ which offers very high random-read performance and supports concurrent reads. This approach, however, necessitates the use of an SSD as the backing storage medium, as traditional hard drives are unsuitable for rapid random reads.

As a result of this step, for each mention, an ordered list of candidates with assigned scores is obtained. The greater the score, the more likely the candidate is to be a good match for the mention.

⁴⁴ <https://symas.com/lmdb/>.

5.5 Entity-Entity Coherence

To help disambiguate named entities, the entity-entity coherence algorithm, introduced by Hoffart et al. [13], is used, albeit with several modifications—most notably the preprocessing stage is different. Original entity-entity coherence values are based on Wikipedia article similarity, which produces a dense similarity matrix. This would be hard to implement efficiently here, given the high complexity of algorithms computing all-pairs distance matrices in graphs.

Therefore, first, the highest scoring candidate entities across all mentions are selected, to discard noisy low-confidence scores. A sparse similarity matrix is constructed, which represents how closely candidates are related to each other. This is established by effectively approximating the shortest path between each pair of the candidates, using their cached neighborhoods from the graph expansion step. Resulting matrix will not be very dense. However, the most important connections should be present. Finally, the set of candidates is narrowed down by greedily removing the least strongly connected candidates. The algorithm outputs a mapping of candidate entities to boost values, scaled to be greater or equal to 1. This boost is used to multiply the scores of those entities, possibly changing the ordering of candidates for each mention. The candidate ranking lists are then sorted again, to account for this change.

To enhance the performance of the method, several additional “bookkeeping” data structures and optimizations are introduced. Additionally, the last stage of the algorithm, being heavy in numerical computations, is compiled using the Numba JIT compiler.

5.6 Candidate Selection and Results Enhancement

Having identified and ranked candidate entities for each mention, the final step is to determine the most relevant terms that describe the publication. The classification result should also include concepts that are not explicitly mentioned in the text. This is achieved by using a technique similar to the one employed in the CSO Classifier [22], where the final set of terms is enhanced with “parent” entities, higher up in the “semantic hierarchy.” Depending on the ontology, this may translate to, for example, a subclassing relationship or the `skos:broader` property. The list of parent entities is established using a SPARQL query with parameters, which allow for specifying parent properties or inverse parent properties, to accommodate both approaches to expressing such relationships. Additionally, each parent is given a weight $w_p = links^{-\alpha}$, where $\alpha \in (0, 1)$. Here, *links* is the total number of links the parent has and α is a scaling factor, set to 0.3 by default. These parent entities along with their weights are saved to Elasticsearch during indexing, in the `parent_entities` and `parent_entities_weights` fields. This information is later retrieved during classification.

Similarly to the CSO Classifier, the ranking algorithm aggregates the top-scoring candidates across mentions, increasing their score based on how frequently they were identified in text and with what diversity (number of unique mention lemmas). From the final list of candidates, only a portion is kept using, which is by finding the “knee point” in the distribution of scores. The knee is established using the Kneedle algorithm, which can adjust to different situations robustly [24] and is shown to perform significantly better than any fixed cutoff value.

5.7 Summary

The presented method makes extensive use of preprocessing to offload most of the computationally intensive tasks to run-only-once jobs and, in turn, speed up classification. Part of the data is cached in Elasticsearch, which is accessed over an HTTP API, with only two batch requests per classified document. The encoded text vectors’ significant size would make transporting them over HTTP inefficient. Thus, they are stored in an embedded database (LMDB), which achieves zero-copy reads, owing to its memory-mapped architecture.

Adaptability to other domains is achieved through the extensive use of configuration settings and modular design. One can easily create new mention detectors, semantic vector encoders, and lexical vector encoders, with a few lines of Python code. Other aspects of the classifier, such as the various tunable parameters of algorithms presented above, can be changed using a YAML configuration file. The process of retooling the entire pipeline to an entirely new domain is largely reduced to changing the configuration file and providing an appropriate ontology.

6 Experimental Results

A thorough quantitative classification accuracy evaluation of the classifier could not be performed, due to the lack of a labeled dataset. Thus, the scope of the assessment was limited to identifying obvious misclassifications that would negatively impact the precision metric. For this purpose, articles from the EFSA and PubMed datasets were classified and selected results examined manually. Table 2 presents example output of the method, with two identified errors highlighted in bold.

It can be observed that the method performs generally well, albeit it tends to frequently return terms that do not seem to have much importance, such as *species*, *application*, *food*, and *population*. Usually, it is able to perceive context, but can still fail in some cases when understanding of the entire sentence is needed for correctly identifying the mention. Unfortunately, this is hard to achieve with simple word embeddings. However, rarely occurring and very specific terms such as taxa, geographic locations, and chemicals are identified easily and seemingly with good accuracy.

Table 2 Example classification of a food safety PubMed article [7]

URI	Label	Mention lemmas	Score
obo:CHEBI_26208	Polyunsaturated fatty acid	Blood fatty acid, plasma fatty acid, fatty acid profile	82.88
obo:NCBITaxon_29073	Ursus maritimus	Polar bear, polar bear intake	43.93
obo:CHEBI_35366	Fatty acid	Fatty acid	33.97
obo:ENVO_02500036	Environmental pollution	Pollution	33.86
obo:GAZ_00052766 ⁵¹	Illoqqortoormiut	East Greenland, Ittoqqortoormiit	32.30
obo:CHEBI_5692	Hexachlorobenzene	Hexachlorobenzene	31.69
obo:OBI_0000181	Population	Population	29.20
obo:GAZ_00001507	Greenland	Greenland	27.75
obo:NCBITaxon_9709	Phocidae	Seal	25.13
snomedct:19314006	Seal (organism)	Seal	22.48
obo:FOODON_03411343	Whale	Whale	22.45
snomedct:733446001⁵²	Canadian (ethnic group)	canadian	22.18
snomedct:226365003	N-3 fatty acid (substance)	n-3 fatty acid	19.81
obo:CHMO_0002820	Concentration	Concentration	19.73
obo:CHEBI_34852	Mirex	Mirex	17.69
obo:CHEBI_61204	Docosapentaenoic acid	Docosapentaenoic acid	17.29
obo:CHEBI_34623	Chlordane	Chlordane	16.85
obo:CHEBI_27208	Unsaturated fatty acid	Blood fatty acid, plasma fatty acid, fatty acid profile	16.62
snomedct:223503004⁵³	North America (geographic location)	North	16.27
obo:PATO_0000025	Composition	Composition	14.90
obo:UBERON_0001969	Blood plasma	Plasma	14.72
obo:FOODON_03412406	Bear	Polar bear, polar bear intake	14.49
obo:GAZ_00228284	Northwest Atlantic Ocean coastal waters of Greenland	Greenland	13.87

5 more results omitted

^a Illoqqortoormiut is an alternative name of Ittoqqortoormiit. The classification is correct.

^b Misclassification: The text refers to the “Canadian guideline levels,” not the ethnic group of Canadians.

^c Misclassification: The text refers to Northern Greenland (the North), not the North America. Although Greenland is in fact considered to be a part of North America, this “technically correct” entry is probably just the result of coincidence

The performance of the method was measured on a modern Linux workstation with a 3.6 GHz 6-core CPU, 32 GB of system memory, and an NVMe SSD rated at 480,000 IOPS. From the EFSA and PubMed corpora, 50 publications were selected randomly and classified in batch. Only the wall clock time taken by classification was measured, excluding the time required to load the code and the models into memory. The experiment was repeated ten times. Classifying the entire EFSA batch

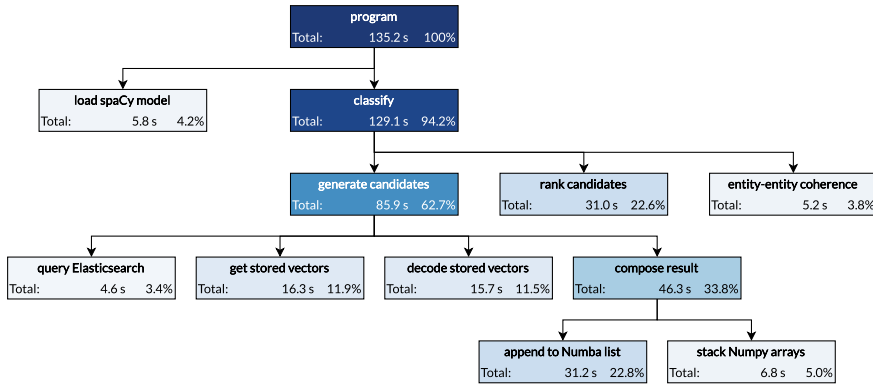


Fig. 2 Profiler diagram for classifying 50 EFSA publications in a batch

took 78.48 s in average, with the mean time to classify a publication at 1.57 s. For PubMed, classifying the batch took 80.49 s on average.

To examine possible bottlenecks, the classification of a batch of 50 EFSA publications was profiled using cProfile. The results are presented in Fig. 2, with only the most important calls included.

Over 60% of the program’s execution time is spent generating candidates, which seems counter-intuitive, as this should be simply a matter of querying Elasticsearch. Querying is indeed present here (taking up only 3.4% of the total time), but for efficiency reasons, several other operations are performed as well. LMDB is queried for the stored lexical and semantic vectors (11.9%). These vectors have to be then decoded with the pickle protocol to Python objects (11.5%). Finally, the found candidates and their neighbors are rearranged into data structures optimized for the later stages (33.8%).

This last step can be especially confusing, raising question why such seemingly simple operation requires so much time. The main reason is that code compiled with Numba, in later stages, requires its input data structures to be Numba-compatible. This necessitates “boxing” of Python objects to be performed at some point, which incurs a performance hit. Another option would be not to use Numba, but that would make the program even slower. Another compute-intensive step is candidate ranking, where most of the time is spent in optimized numerical routines.

7 Conclusions

The proposed method is an adaptable, scalable, and performant solution to the topical publication classification problem, easily handling KBs containing millions of entities. Classification results seem satisfactory, although a detailed evaluation remains to be performed on a labeled dataset. The method is robust, modular base which

can be iteratively improved, to achieve better accuracy. In particular, further research into candidate generation and how the algorithm perceives the context of both the abstract and the knowledge base is needed.

Regarding classification speed, substantial improvements could be made by parallelizing the code. However, currently this could not be easily done, due to the Python Global Interpreter Lock (GIL), which prevents the simultaneous execution of multiple Python interpreter threads [19]. There is also a significant amount of overhead involved at several steps, necessitated by transitioning from interpreted to native code. The only reasonable solution to these problems would be to drop pure Python as the implementation language altogether in favor of C++ or Cython, which will be investigated in future research.

Additional materials and data related to this work, as well as the most important algorithms mentioned above, were published on GitHub.⁵⁴

References

1. Arbab A, Adams DR, Fidler S, Brudno M (2019) Identifying clinical terms in medical text using ontology-guided machine learning. *JMIR Med Inform* 7(2):e12,596
2. Aromataris E, Riitano D (2014) Constructing a search strategy and searching for evidence. *Am J Nurs* 114(5):49–56
3. Baba VV, HakemZadeh F (2012) Toward a theory of evidence based decision making. *Manag Decis*. <https://doi.org/10.1108/00251741211227546>
4. Boqvist S, Söderqvist K, Vågsholm I (2018) Food safety challenges and one health within Europe. *Acta Vet Scand* 60(1):1–13
5. Cock PJ, Antao T, Chang JT, Chapman BA, Cox CJ, Dalke A, Friedberg I, Hamelryck T, Kauff F, Wilczynski B et al (2009) Biopython: freely available Python tools for computational molecular biology and bioinformatics. *Bioinformatics* 25(11):1422–1423
6. Dask Development Team: Dask: Library for dynamic task scheduling (2016). <https://dask.org>
7. Deutch B, Pedersen H, Hansen J (2004) Dietary composition in Greenland 2000, plasma fatty acids and persistent organic pollutants. *Sci Total Environ* 331(1–3):177–88
8. Donnelly K et al (2006) SNOMED-CT: the advanced terminology and coding system for eHealth. *Stud Health Technol Inform* 121:279
9. Dooley DM, Griffiths EJ, Gosal GS, Buttigieg PL, Hoehndorf R, Lange MC, Schriml LM, Brinkman FS, Hsiao WW (2018) FoodOn: a harmonized food ontology to increase global food traceability, quality control and data integration. *NPJ Sci Food* 2(1):1–10
10. Fraser KC, Nejadgholi I, De Bruijn B, Li M, LaPlante A, Abidine KZE (2019) Extracting UMLS concepts from medical text using general and domain-specific deep learning models. *arXiv preprint arXiv:1910.01274*
11. Gonzalez JE, Low Y, Gu H, Bickson D, Guestrin C (2012) Powergraph: distributed graph-parallel computation on natural graphs. In: 10th USENIX symposium on operating systems design and implementation (OSDI 12), pp 17–30
12. Hartig O, Thompson B (2014) Foundations of an alternative approach to reification in RDF. *arXiv preprint arXiv:1406.3399*
13. Hoffart J, Yosef MA, Bordino I, Fürstenau H, Pinkal M, Spaniol M, Taneva B, Thater S, Weikum G (2011) Robust disambiguation of named entities in text. In: Proceedings of the 2011 conference on empirical methods in natural language processing, pp 782–792

⁵⁴ <https://github.com/Ostrzyciel/food-safety-classif>.

14. Jonnalagadda SR, Goyal P, Huffman MD (2015) Automating data extraction in systematic reviews: a systematic review. *Syst Control Found Appl* 4(1):78
15. Jonquet C, Shah N, Youn C, Callendar C, Storey MA, Musen M (2009) NCBO annotator: semantic annotation of biomedical data. In: *International semantic web conference, poster and demo session*, vol 110
16. Laadhar A, Abrahão E, Jonquet C (2020) Investigating one million XRefs in thirty ontologies from the OBO world. In: *11th international conference on biomedical ontologies (ICBO)*
17. Lam SK, Pitrou A, Seibert S (2015) Numba: a LLVM-based Python JIT compiler. In: *Proceedings of the second workshop on the LLVM compiler infrastructure in HPC*, pp 1–6
18. Li H, Chen Q, Tang B, Wang X, Xu H, Wang B, Huang D (2017) CNN-based ranking for biomedical entity normalization. *BMC Bioinform* 18(11):79–86
19. Meier R, Gross T (2019) Reflections on the compatibility, performance, and scalability of parallel Python. In: *Proceedings of the 15th ACM SIGPLAN international symposium on dynamic languages*
20. Morton S, Berg A, Levit L, Eden J et al (2011) *Finding what works in health care: standards for systematic reviews*. National Academies Press, Washington, DC
21. Neumann M, King D, Beltagy I, Ammar W (2019) ScispaCy: fast and robust models for biomedical natural language processing. In: *Proceedings of the 18th BioNLP workshop and shared task. Association for computational linguistics*, Florence, Italy, pp 319–327. /DOIurl10.18653/v1/W19-5034. <https://www.aclweb.org/anthology/W19-5034>
22. Salatino AA, Osborne F, Thanapalasingam T, Motta E (2018) The CSO classifier: ontology-driven detection of research topics in scholarly articles. In: *International conference on theory and practice of digital libraries*. Springer, pp 296–311
23. Salatino AA, Thanapalasingam T, Mannocci A, Osborne F, Motta E (2018) The computer science ontology: a large-scale taxonomy of research areas. In: *International semantic web conference*. Springer, pp 187–205
24. Satopää V, Albrecht JR, Irwin DE, Raghavan B (2011) Finding a “kneedle” in a haystack: Detecting knee points in system behavior. In: *2011 31st international conference on distributed computing systems workshops*, pp 166–171
25. Smith B, Ashburner M, Rosse C, Bard J, Bug W, Ceusters W, Goldberg LJ, Eilbeck K, Ireland A, Mungall CJ et al (2007) The OBO Foundry: coordinated evolution of ontologies to support biomedical data integration. *Nat Biotechnol* 25(11):1251–1255
26. Tsafnat G, Glasziou P, Choong MK, Dunn A, Galgani F, Coiera E (2014) Systematic review automation technologies. *System Rev* 3(1):74
27. Uyttendaele M, De Boeck E, Jacxsens L (2016) Challenges in food safety as part of food security: lessons learnt on food safety in a globalized world. *Procedia Food Sci* 6:16–22
28. Whetzel PL, Noy NF, Shah NH, Alexander PR, Nyulas C, Tudorache T, Musen MA (2011) BioPortal: enhanced functionality via new web services from the national center for biomedical ontology to access and use ontologies in software applications. *Nucleic Acids Res* 39(suppl_2):W541–W545
29. Yadav S, Pallagani V, Sheth A (2020) Medical knowledge-enriched textual entailment framework. In: *Proceedings of the 28th international conference on computational linguistics*, pp 1795–1801
30. Zheng JG, Howsmon D, Zhang B, Hahn J, McGuinness D, Hendler J, Ji H (2015) Entity linking for biomedical literature. *BMC Med Inform Decis Mak* 15(S1), S4

Comparative Study of Different Types of Slab Structures



Pranav Mene and Aditya P. Nilawar

Abstract As the population grows and civilization develops, the need for industrialization and building construction grows rapidly. Demand of construction is particularly high in construction of residential and commercial buildings. A flat slab is commonly used in the construction of commercial and residential buildings. Flat slab structure is efficient as compared to other types of slab structure in terms of economy, architectural system, simple formwork methods, efficient use of spaces, and shorter construction of time. In flat slab structural arrangement, the slab is directly supported on the column, and the load is transferred directly to the column and then to the foundation. The objective of the present study covers behavioral study of multi-story buildings having different slab structure. The amount of steel and concrete use, costing of structures, nodal displacement, bending moment, and analysis of different structures are compared by using STAAD Pro V8i software as per IS 456:2000. Fe-415 steel grade and M25 grade of concrete are considered. In this present study, analysis and design of flat slab or plate slab, conventional slab, grid, or waffle slab for G+4 building in seismic zone III having medium soil condition are considered. Analysis of structure is concluded using STAAD Pro V8i software which saves lot of time as compared to manual calculations. The results show that flat slab structure is efficient as compared to other slab structures for given G+4 structure.

Keywords Slab structures · Flat slab · Grid slab · Analysis of slab structure

P. Mene (✉) · A. P. Nilawar
Department of Civil Engineering, SGGSIET, Nanded, Maharashtra, India
e-mail: 2020mse019@sggs.ac.in

A. P. Nilawar
e-mail: apnilawar@sggs.ac.in

© The Author(s), under exclusive license to Springer Nature Singapore Pte Ltd. 2022
V. Mahajan et al. (eds.), *Sustainable Technology and Advanced Computing in Electrical Engineering*, Lecture Notes in Electrical Engineering 939,
https://doi.org/10.1007/978-981-19-4364-5_49

695

1 Introduction

In this modern developing era, India at present is fastest growing country [1]. We notice the large construction activities taking place. As a result of rise in population, development of infrastructures is necessity. In order to neutralize, this demand development in infrastructure is must. To overcome this problem, high-rise structure is one of the solution. Frame structures are basically used to build high-rise or multi-storied structures. In frame structures, impact of horizontal loads and vertical loads is one of the considerable factors. This makes study of horizontal and vertical loads more important. Absolute analysis, design, modeling, and slab construction are needed. Loads are transferred to beams and supported by columns. There are different factors which need to be considered for choosing particular type of slab. Purpose of structure and economy of total construction are important parameter to be considered.

To design structure, several types of slabs generally conventional, flat, and grid slabs are used [2]. When slab is maintained by beams and columns called as beam slab construction. Such types of constructions are also known as conventional slab structure. Dimensions of slab and support conditions further classify it as one way and two way slab system.

When slab is directly maintain by column to avoid visual and light interference [3]. The slab structures without beams but directly supported on columns are flat slab structures. Flat plate slab or flat slab is also known as beamless slab since beams are not present. Grid slab is concrete slab type, which is having rectangular grids with sides on support condition. Grid slab is also known as waffle slab [4]. Grid slab is used mainly where column interference should avoid up to some extent the places like auditorium, parking.

For modeling, analysis, and design of different slab structures, STAAD Pro V8i software is used in this work. Validation considered for STAAD Pro V8i software is very high as more than 90 international codes of steel, concrete, and timber are considered in this software. It is easy to use and has interactive interface, which allows the user to draw the different models, input the load values, and provide support conditions. Accordance with the specified criteria assigned, analysis the structure and designs the members with reinforced cement concrete as per Indian standard code is concluded in this present work. The objective of the present study covers the comparison of overall cost of different slab structure for concrete and steel by analyzing structure, seismic behavior of the structure, and behavior of multi-story buildings having different slabs using STAAD Pro V8i software.

2 Related Work

In 2017, Bhatia and Golait [5] studied the comparative study of square, hexagonal, and octagonal geometry of different slab structure is done. Slab structure includes

conventional, flat, and grid slab structures. STAAD Pro V8i software is used for analysis and design of structure mentioned. Code of Indian standard IS 1893–2002 (Part 1) used for analysis of earthquake resistant structure, the researcher in the paper concluded that the frame with flat slabs conveniently provides more safety to the designers. All types of slab system mentioned in paper show the result of story drift is within the permissible limits while flat slabs showed better results when compared to other system. The response reduction factor is important parameter considered for variation of cost.

In 2018, Khan and Jeelani [6] used Etabs software to analyze and design the different slab structures. Methods of analysis of a structure used in the paper are linear static method and time history earthquake analysis method. Structures of $G + 2$ and $G + 7$ models are used to analyze slab structures in this paper. Researcher concluded in this paper that there is a steady increase in the values of lateral forces from bottom story to top story. As the seismic zone rises from zone II to IV, the story shear increases. As the seismic zone rises from II to IV, the story drift increases. The highest story displacement is increases as the seismic zone rises from II to IV.

In 2018, Thu Htun et al. [7] study slab structure of flat type using panel and slab structure exclusive of panels. Behavioral study of slab structure of flat type using panel and slab structure of flat plate without panels are studied by using ETABS software by static earthquake analysis. The slabs are designed, and the differences of slab stresses are studied by SAFE software. The design code used for study is ACI 318–08. They have concluded from this study that the story shear in slab structure of flat plate is more than slab structure of flat slab. Story drift and displacement in flat slab are also more than that of flat plate. The difference in the moment values in flat slab structure and flat plate structure is almost 40%.

In 2019, Yadav and Khalotiya [8] studied about performance of structure in different earthquake zones. The structure considered in the paper is irregular multi-storied structure having flat slab. Researcher found gap in research that the dynamic analysis of various structures has been assessed but as far as the RC flat slab with irregular structure is concerned, and no work has been reported. They concluded that these contributions help to visualize the problem faced by way of RC flat slab from a new perspective.

In 2020, Nishanth et al. [9] worked on different slab system structure subjected to gravity load and lateral load using $G + 6$ story model. In this study, four different slab structure which is load bearing wall structure, conventional two way slab structure, flat slab of plate type, and grid slab for commercial structure building analyzes and compared by utilizing ETABS software. The design and analysis of slab system are done as per Indian standards. Authors concluded that the amount of concrete quantity needed for the flat plate slab structure is lowest which 21% is less than load bearing wall structure which has highest quantity of concrete requirement as compared to other slab structures. Story displacement for the load bearing wall slab system is lowest which 92.6% is less than conventional slab system which has highest story displacement as compared to other slab systems. Base shear for the flat slab system is lowest which 44.5% is less than load bearing wall system which has highest base shear as compared to other slab systems.

In 2020, Nassar and Al-Qasem [10] conclude the study of flat plate slab structure, slab solid structure, conventional slab structure of type one way and two way is done using residential building model of 14.3×13.3 m dimension model. Software used for modeling and analysis of structure in this paper is ETABS v.16. Results in this paper show that the plate slab system is more cost-effective as compared to slab solid structure and conventional slab structure. Plate slab structure reduces structure height by 10–15% than other slab systems. Plate slab structure reduces 7% costing as compared to solid slab system. Flat plate slab system reduces 4% costing as compared to conventional of one way type slab structure. Flat plate slab structure reduces 3.33% costing as compared to conventional slab structure of two way type.

3 Statement of Project

3.1 Geometric Details of Structure

1. Dimension of building: L-15 m B-15 m H-15 m
2. Model type: G + 4 residential building
3. Beam: L-0.23 m B-0.23 m
4. Column: L-0.4 m B-0.4 m
5. Thickness of slab: 0.150 m (150 mm)
6. Grid size: 1 m
7. Meshing method: standard
8. Target element size for mesh: 1 m
9. No. of bays: 5
10. Dimension of bay: L-3 m B-3 m H-3 m.

3.2 Material Detail of Structure

1. Concrete: M25
2. Steel: Fe415
3. Density of concrete: 25kN/m^3 or 2549.29 kg/m^3 .

4 Methodology

4.1 Modeling

Modeling of slab structures consists of a G + 4 story executed on STAAD Pro V8i software by utilizing IS 1893:2002 and IS 456:2000.

1. Grid size selected for modeling of structure using structure wizard software is 1 m.
2. Type of slab selected as conventional slab or flat slab or grid slab as per required.
3. Meshing method-standard.
4. Target element size for meshing-1 m.

4.2 Load Combinations

The gravity load and lateral loads are taking into account for design and analysis of multistoried slab structures.

Dead Load	Considered as per IS 875 (part 1):1987. Self weight factor: 1. Plate load: 4.75kN/m ² or 484.36 kg/m ² .
Live Load	Considered as per IS 875 (part 2):1987.
Seismic Load	Considered as per IS 1893 (part 1):2002. Zone value-0.16 (zone 3). Response reduction factor-5. Importance factor of building-1.5 Rock and soil factor-1. Structure type-1. Damping ratio-0.05. Time period of structure-0.42 s.
Load Combinations	1.2[DL + LL + EQX]. 1.2[DL + LL + EQZ].

4.3 Cost of Structure

Cost of structure is mainly comprises of steel and concrete cost. Unit cost considered from Indiamart Website and S.O.R.

$$\text{Unit cost of concrete} = 4500/\text{m}^3 \text{ (RMC)}$$

$$\text{Unit cost of steel} = 42 \text{ Rs/kg}$$

$$\text{Conventional slab structure—Concrete} = 4500 \times 268 = \text{Rs } 120,600$$

$$\text{Steel} = 42 \times 21,792 = \text{Rs } 915,264$$

$$\text{Total cost} = 12,06,000 + 91,524 = \text{Rs } 21,21,264.$$

$$\text{Flat slab structure—Concrete} = 4500 \times 172.8 = \text{Rs } 777,600$$

$$\text{Steel} = 42 \times 9330 = \text{Rs } 391,860$$

Total cost – $12,06,000 + 91,524 = \text{Rs } 11,69,460.$

Grid slab structure—Concrete – $4500 \times 426.7 = \text{Rs } 1920,150$

Steel – $42 \times 37,717 = \text{Rs } 15,84,114$

Total cost – $12,06,000 + 91,524 = \text{Rs } 35,04,264.$

5 Results and Discussion

5.1 Maximum Nodal Displacement

Maximum nodal displacement (millimeters) in all directions for different slab structures is as shown in Fig. 1.

5.2 Maximum Bending Moment

Maximum bending moment (kNm) in all directions for different slab structures is as shown in Table 1.

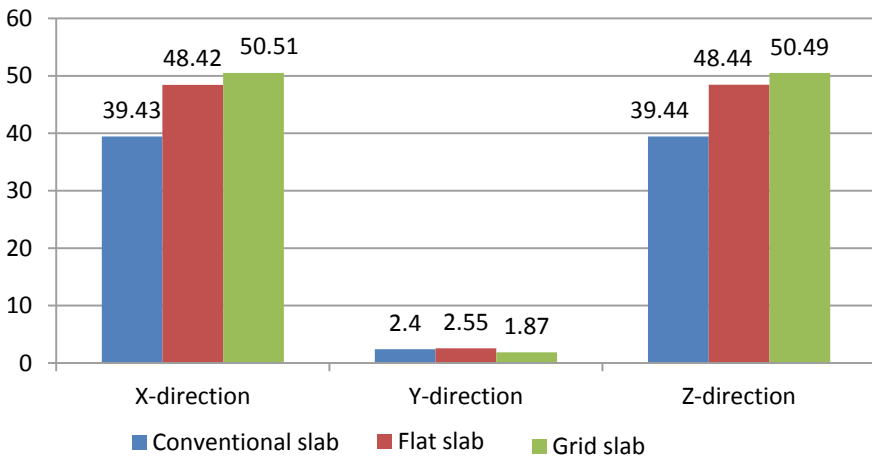


Fig. 1 Comparative study of maximum nodal displacement (mm) in all directions

Table 1 Comparative study of maximum bending moment (kNm) in all directions

Maximum bending moment (kNm)	Manual calculation	Software calculation
Conventional slab	60.22	67.91
Flat slab structure	52.23	75.45
Grid slab structure	75.62	83.50

5.3 Quantity of Steel

Required quantity of steel (kg) for different slab structures is as shown in Fig. 2.

5.4 Quantity of Concrete

Required quantity of concrete (m³) for slab structures is as shown in Fig. 3.

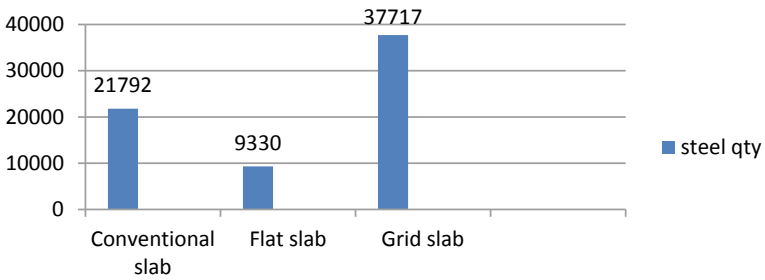


Fig. 2 Comparative study of quantity of steel (kg) in different slab structures

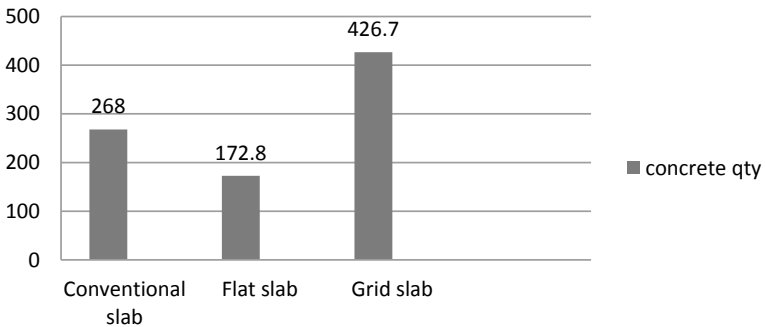


Fig. 3 Comparative study of quantity of concrete (m³) in different slab structures

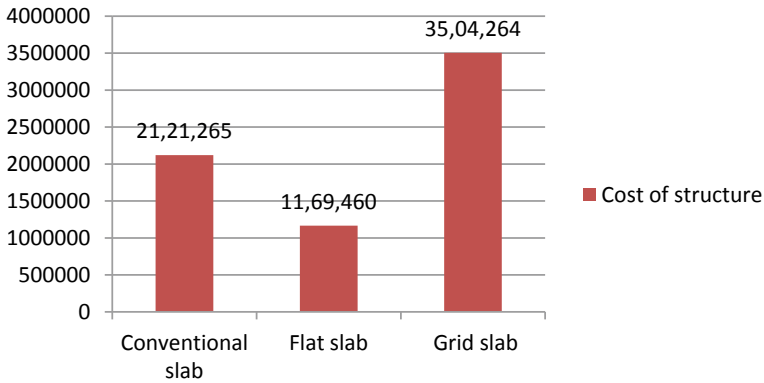


Fig. 4 Comparative study of cost of structure (Rs) in different slab structures

5.5 Cost of Structure

Required cost (Rs) for different slab structures is as shown in Fig. 4.

6 Conclusion

Analysis and design of different types of slab structures, bending moment, and displacement are obtained using STAAD Pro V8i software. The obtained results are compared and validated with manual calculations. The required area of reinforcement for the slab is obtained from results of shear forces and bending moment. Further as per the member sizes selected, quantity of concrete and quantity of steel have been obtained, and schedule of rates is used to find out the total cost of steel reinforcement and concrete. Maximum nodal displacement in x , y , z direction for grid/waffle slab structure is more as compared to other type of slab structure for given model. The quantity of steel and concrete required for the grid/waffle and conventional slab structure is more compare to flat slab. Costing of the flat slab structure is most economical for given span in present study as compared to the two way conventional slab structure and grid/waffle slab structure. According to above inferences in this study, flat slab of plate type structure is efficient as compared to other slab structures for given structure.

References

1. Shukla V, Singh P (2020) Comparative study between two-way slab, flat slab, grid slab and post tensioned slabs. *Int J Trend Res Dev* 07:292–297
2. Manvi A, Gouripur S, Sambrekar P et al (2015) Cost comparison between conventional and flat slab structures. *Int Res J Eng Technol (IRJET)* 02:1218–1223
3. Balhar L, Vyas JN (2019) Review paper on comparative analysis of flat slabs & conventional RC slabs with and without shear wall. *Int Res J Eng Technol (IRJET)* 06:77–81
4. Sathawane AA, Deotale RS (2012) Analysis and design of flat slab and grid slab and their cost comparison. *Int J Adv Technol Civ Eng* 01:203–207
5. Bhatia NK, Golait T (2017) Comparing the structural efficiencies of flat slabs, grid slabs & conventional slabs for square, hexagonal & octagonal plan geometries. *Int J Trend Res Dev* 04:696–700
6. Khan KM, Jeelani M (2018) Analysis and design of flat slabs in commercial building by using ETABS software. *Int Res J Eng Technol (IRJET)* 05:998–1002
7. Thu Htun PH, Phone N, Zeyar Win K (2018) Comparative study on analysis and design between flat slab and flat plate system for RC Building. *Int J Sci Eng Appl* 7:313–317. <https://doi.org/10.7753/ijsea0709.1013>
8. Yadav P, Khalotiya D (2019) Seismic performance of geometric vertical irregular flat slab multistoried building in different earthquake zone: a conceptual review. *Int Res J Eng Technol (IRJET)* 06:2638–2643
9. Nishanth CHL, Sai Swaroop Y, Jagarapu DC, Kumar Jogi P (2020) Analysis and design of commercial building with different slab arrangements using etabs. *Mater Today Proc* 33:700–704. <https://doi.org/10.1016/j.matpr.2020.05.823>
10. Nassar RR, Al-Qasem IA (2020) Comparative cost study for a residential building using different types of floor system. *Int J Eng Res Technol* 13:1983. <https://doi.org/10.37624/ijert/13.8.2020.1983-1991>

Model Order Reduction of MIMO Linear System Using Grey Wolf Optimization



Pranay Bhadauria and Nidhi Singh

Abstract Scientists and engineer are being encountered regularly with the workout, analysis and amalgam of real-life complications. The component of an actual framework can be broken down by the arrangement of differential conditions from which complex model of high order can be obtained in the state space structure or in transfer function form which are called frequency domain representation or time domain, respectively. Difficulties may be posed by a mathematical model of high order in its amalgam, analysis and recognition. Thus, a demand occurs for an organized method to develop a reduced model which preserves the main subjective properties of high-order framework like steadiness, dependability, good time and frequency response matching as in the original framework. Model reduction helps in simplifying the system, reduces computational efforts and makes the design of the controller numerically more efficient. This work is encouraged by nature-based algorithm for order reduction by grey wolf optimization. This algorithm mimes the ranking-based leadership and hunting conduct of grey wolves. The ranking-based leadership is simulated by employing four types of grey wolves such as alpha, beta, delta and omega. Grey wolf optimization technique is used for determining the denominator polynomial of the reduced model, while Pade approximation technique is used for finding the numerator polynomial. The approach is proposed for both single input single output (SISO) and multi-input multi-output (MIMO) systems. This technique assures the stable reduced models of stable systems. The technique is protracted to the issue of reducing a high-order multivariable system defined by its matrix transfer function. Some examples from the literature are taken for illustrating the feasibility of the method. ISE has been taken as target work for looking at the performance of the proposed strategy with other existing techniques in the writing.

P. Bhadauria (✉) · N. Singh

Department of Electrical Engineering, Gautam Buddha University, Greater Noida, Uttar Pradesh 201312, India

e-mail: pranayesp4u@gmail.com

N. Singh

e-mail: nidhi@gbu.ac.in

Keywords Stability · Grey wolf optimization · Transfer function · Pade approximation · Order reduction

1 Introduction

In the present scenario, highly complex environmental processes and technology of large dimension have brought large number of problems. When traditional techniques of modelling, analysis, computation, control and design fail to provide satisfactory response for a system having large dimensions, then it is said to be a large-scale system. Scientist and engineer are being encountered regularly with the workout, analysis and amalgam of real-life complications. Thus, a demand occurs for an efficient technique to acquire a lower-order model in state space or transfer function from which approximates completely the higher-order system such that the main qualitative properties like frequency response matching, reliability and stability as in the higher-order system are preserved in the lower-order system. In such studies, developing a ‘mathematical model’ is the first step and can be an alternate for the real issues. While modelling, simplicity and accuracy are two contrary aspects which prevail. On one hand, if a system model representing an actual system is oversimplified probably for computational capability, incorrect conclusion may be drawn from it. On the other hand, deeply exact model would add to a great deal of irrelevant problems. The viable benefit obtained from utilizing model order reduction is better comprehension of complex system, simplification in understanding and simulation of higher-order system. The MOR technique has been broadly utilized in field of control engineering, and some of the principle applications are power system stability, control system design, intelligent control, adaptive control, control system design, etc.

In this paper, hybrid of two dominant techniques for order reduction is utilized for deciding the numerator and denominator polynomial of reduced model. In this paper, Pade approximation is applied for deciding the numerator polynomial [1, 2] which may give unstable reduced order system even though the original system is stable [3] and grey wolf optimization method which is based on coursing nature of grey wolves to get denominator polynomial of the reduced model [4, 5]. The proposed technique assures the conservation of initial time moments and stability of the actual system in the lower-order system.

2 Problem Description

Consider a linear dynamic system given by the n th order transfer function

$$G(s) = \frac{N(s)}{D(s)} = \frac{p_{n-1}s^{n-1} + \dots + p_1s + p_0}{q_n s^n + \dots + q_1s + q_0} \quad (1)$$

The point of the work is to decide the obscure coefficients of r th request ($r < n$) reduced model without changing its substance and property which is given by the accompanying transfer function

$$G_r(s) = \frac{U_r(s)}{V_r(s)} = \frac{u_{r-1}s^{r-1} + \dots + u_1s + u_0}{v_rs^r + \dots + v_1s + v_0} \tag{2}$$

The linear dynamic transfer function of multiple input multiple output (MIMO) LTI system is given as below

$$[G(s)] = \frac{1}{D(s)} \begin{bmatrix} m_{11}(s) & m_{12}(s) & \dots & m_{1u}(s) \\ m_{21}(s) & m_{22}(s) & \dots & m_{2u}(s) \\ \vdots & \vdots & \vdots & \vdots \\ m_{v1}(s) & m_{v2}(s) & \dots & m_{vu}(s) \end{bmatrix} \tag{3}$$

$$= [g_{ij}(s)]_{v \times u} \tag{4}$$

where $i = 1, 2, 3 \dots v$; $j = 1, 2, 3 \dots u$ and v and u are the data sources and yields of unique framework individually. The $g_{ij}(s)$ can be composed as

$$g_{ij}(s) = \frac{m_{ij}(s)}{D(s)} \tag{5}$$

The point of this paper is to compute the reduced model of original framework so that the same model holds all the fundamental elements of the original framework. The transfer matrix of reduced model is given as

$$R_r(s) = \frac{1}{H_r(s)} \begin{bmatrix} t_{11}(s) & t_{12}(s) & \dots & t_{1b}(s) \\ t_{21}(s) & t_{22}(s) & \dots & t_{2b}(s) \\ \vdots & \vdots & \vdots & \vdots \\ t_{a1}(s) & t_{a2}(s) & \dots & t_{ab}(s) \end{bmatrix} \tag{6}$$

$$= [r_{ij}(s)]_{a \times b} \tag{7}$$

$i = 1, 2, 3 \dots a$; $j = 1, 2, 3 \dots b$.

Hence, $r_{ij}(s)$ can be expressed as

$$r_{ij}(s) = \frac{t_{ij}(s)}{H_r(s)} \tag{8}$$

3 Procedure of Proposed Technique

The proposed technique comprises the accompanying two stages.

Step 1: Grey wolf optimization technique is utilized for finding the denominator polynomial of r th order [4–7].

Grey wolf is mostly founded in Canada which is considered as apogee carnivore which follows a very strict community commanding chain. The ordering position in the grey wolves is given to alphas which can be male or a female. The alphas are the decision-makers of the group. The next position in the chain is given to beta which assists the alphas in taking decisions or other group action (Fig. 1).

The lowest position in the chain of grey wolves is given to omega. They are considered not so influential member in the group, but the whole group sees internal struggle and complications in case of losing the omega. There is one other category of grey wolf which is delta. Delta wolves are inferior to alphas and beta but superior to omega. Firstly, the grey wolves track, chase and reach the prey. Secondly, they surround and tease the prey and lastly raid the prey. As told earlier, grey wolves surround prey during the raid. The following equations suggest the mathematical model of surrounding action:

$$\vec{X} = \left| \vec{Y} \vec{S}_i(p) - \vec{S}(p) \right| \tag{9}$$

$$\vec{S}(p + 1) = \vec{S}_i(p) - \vec{Z} \cdot \vec{X} \tag{10}$$

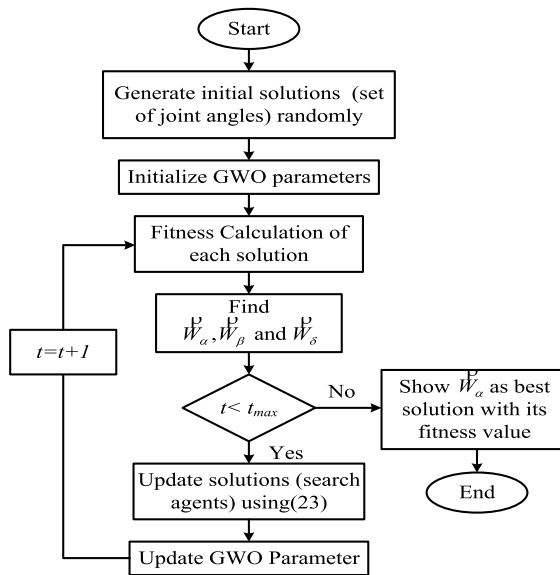


Fig. 1 Algorithm of GWO optimization process

where p illustrates the ongoing iteration. \vec{Z} and \vec{Y} are the coefficient vectors, \vec{S} illustrates the grey wolf position vector, and \vec{S}_i is the prey position vector. The \vec{Z} and \vec{Y} vectors are determined as follows:

$$\vec{Z} = 2\vec{b}.r_1 - \vec{b} \tag{11}$$

$$\vec{Y} = 2.r_2 \tag{12}$$

$$\vec{X}_\alpha = \left| \vec{Y}_1 \vec{S}_\alpha - \vec{S} \right| \tag{13}$$

$$\vec{X}_\beta = \left| \vec{Y}_2 \vec{S}_\beta - \vec{S} \right| \tag{14}$$

$$\vec{X}_\delta = \left| \vec{Y}_3 \vec{S}_\delta - \vec{S} \right| \tag{15}$$

Thus, using Eq. (10)

$$\vec{S}_1 = \vec{S}_\alpha - \vec{Z}_1 \cdot (\vec{X}_\alpha) \tag{16}$$

$$\vec{S}_2 = \vec{S}_\beta - \vec{Z}_2 \cdot (\vec{X}_\beta) \tag{17}$$

$$\vec{S}_3 = \vec{S}_\delta - \vec{Z}_3 \cdot (\vec{X}_\delta) \tag{18}$$

and finally

$$\vec{S}(p+1) = \frac{(\vec{S}_1 + \vec{S}_2 + \vec{S}_3)}{3} \tag{19}$$

Step 2: Pade approximation is utilized for finding the numerator polynomial of r th order reduced model [2, 8–10].

Power series expansion of the original r th order system about $s = 0$ is given as follows:

$$F(s) = \frac{\sum_{i=0}^{r-1} m_i s^i}{\sum_{i=0}^r n_i s^i} = k_0 + k_1 s + k_2 s^2 + \dots \tag{20}$$

The power series expansion coefficients are determined as follows:

$$k_0 = x_0 \tag{21}$$

$$k_i = \frac{1}{y_0} \left[x_i - \sum_{l=1}^i y_l k_{i-l} \right] \quad i > 0 \tag{22}$$

$$k_i = 0 \quad i > r - 1 \tag{23}$$

The reduced model of r th order is given as follows:

$$F_r(s) = \frac{N_r(s)}{D_r(s)} = \frac{\sum_{i=0}^{r-1} u_i s^i}{\sum_{i=0}^r v_i s^i} \tag{24}$$

Here $D_r(s)$ is known through grey wolf optimization technique.

For equation (18) representing $F_r(s)$ to be Pade approximants of Eq. (14) representing $F(s)$ reo, we have

$$\begin{aligned} u_0 &= v_0 k_0 \\ u_1 &= v_0 k_1 + v_1 k_0 \\ &\dots \\ &\dots \\ u_{r-1} &= v k_{r-1} + v_1 k_{r-2} + \dots + v_{r-1} k_1 + v_r k_0 \end{aligned} \tag{25}$$

By tackling the above r straight condition, the $u_k, l = 0$, can be determined.

4 Illustrative Examples

In order to analyse the suggested technique, one mathematical model has been taken from the writing. The existing techniques have been compared by the proposed method through minimizing the performance index, i.e. ISE, which is given by [11–13].

$$ISE = \int_0^\infty [\vartheta(t) - \vartheta_r(t)]^2 dt \tag{26}$$

Example 1: Examine a sixth-order MIMO system taken from [10–12]:

$$\begin{aligned} [G_6(s)] &= \frac{1}{D(s)} \begin{bmatrix} \frac{2(s+5)}{(s+1)(s+10)} & \frac{(s+4)}{(s+2)(s+5)} \\ \frac{(s+10)}{(s+1)(s+20)} & \frac{(s+6)}{(s+2)(s+3)} \end{bmatrix} \\ &= \frac{1}{D(s)} \begin{bmatrix} n_{11}(s) & n_{12}(s) \\ n_{21}(s) & n_{22}(s) \end{bmatrix} \end{aligned}$$

where

$$D(s) = 6000 + 13100s + 10060s^2 + 3491s^3 + 571s^4 + 41s^5 + s^6$$

$$n_{11}(s) = 6000 + 7700s + 3610s^2 + 762s^3 + 70s^4 + 2s^5$$

$$n_{12}(s) = 2400 + 4160s + 2182s^2 + 459s^3 + 38s^4 + s^5$$

$$n_{21}(s) = 3000 + 3700s + 1650s^2 + 331s^3 + 30s^4 + s^5$$

$$n_{22}(s) = 6000 + 9100s + 3660s^2 + 601s^3 + 42s^4 + s^5$$

The reduced second-order model can be taken in the form of

$$R_2(s) = \frac{1}{H_2(s)} \begin{bmatrix} t_{11}(s) & t_{12}(s) \\ t_{21}(s) & t_{22}(s) \end{bmatrix}$$

$$t_{11}(s) = u_0 + u_1s$$

$$u_0 = v_0k_0 = 2.8703$$

$$u_1 = v_0k_1 + v_1k_0 = 1.1837$$

$$t_{11}(s) = 2.8703 + 1.1837s$$

Similarly, we can find others

$$t_{12}(s) = 1.1481 + 0.94855s$$

$$t_{21}(s) = 1.43315 + 0.5194s$$

$$t_{22}(s) = 2.8703 + 1.68225s$$

The denominator $R_2(s)$ can be calculated using Eqs. (9)–(19) which comes as

$$H_2(s) = s^2 + 3.702s + 2.870295$$

The second-order model utilizing the proposed hybrid technique is obtained

$$[G_2(s)] = \frac{1}{s^2 + 3.702s + 2.870295} \begin{bmatrix} 1.1837s + 2.8703 & 0.94855s + 1.1481 \\ 0.5194s + 1.43315 & 1.68225s + 2.8703 \end{bmatrix}$$

5 Result Analysis

The step responses of the original order and lower-order systems are compared and shown in Fig. 2. Apparently, it can be analysed from the step responses that the reduced model obtained by the suggested method is much closer to the original model compared with some other existing methods. It can also be noticed through the frequency response characteristic as shown in Fig. 3. The qualitative analysis of the suggested method with other existing methods available in survey is given in

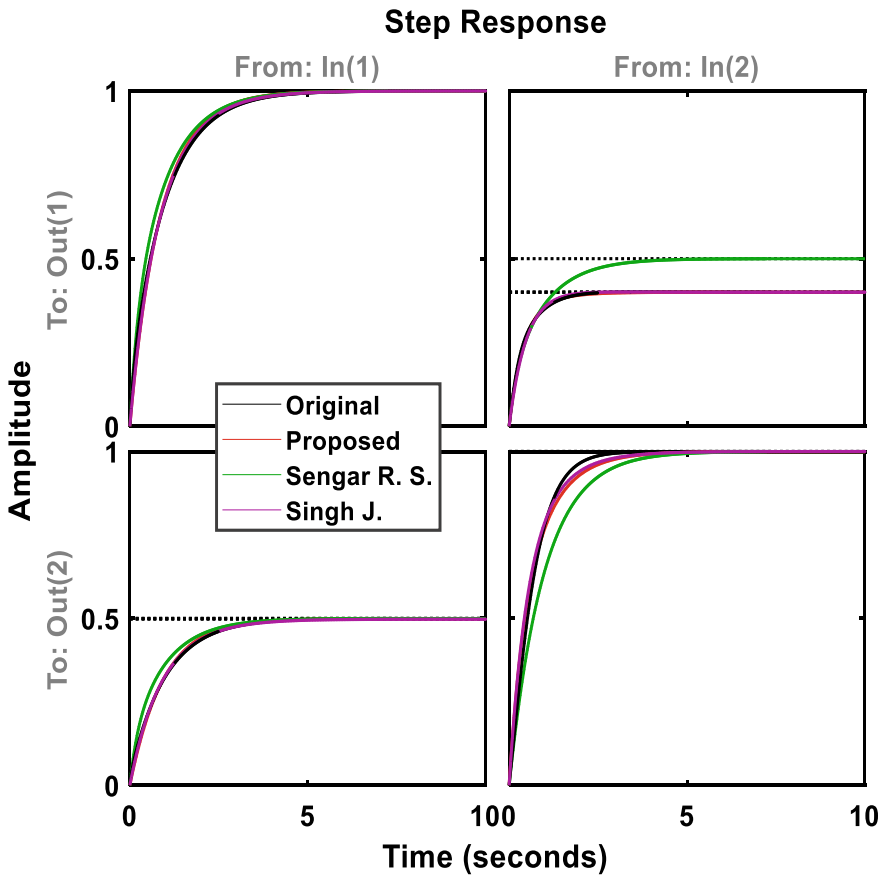


Fig. 2 Examination of original and reduced order models in terms of step response

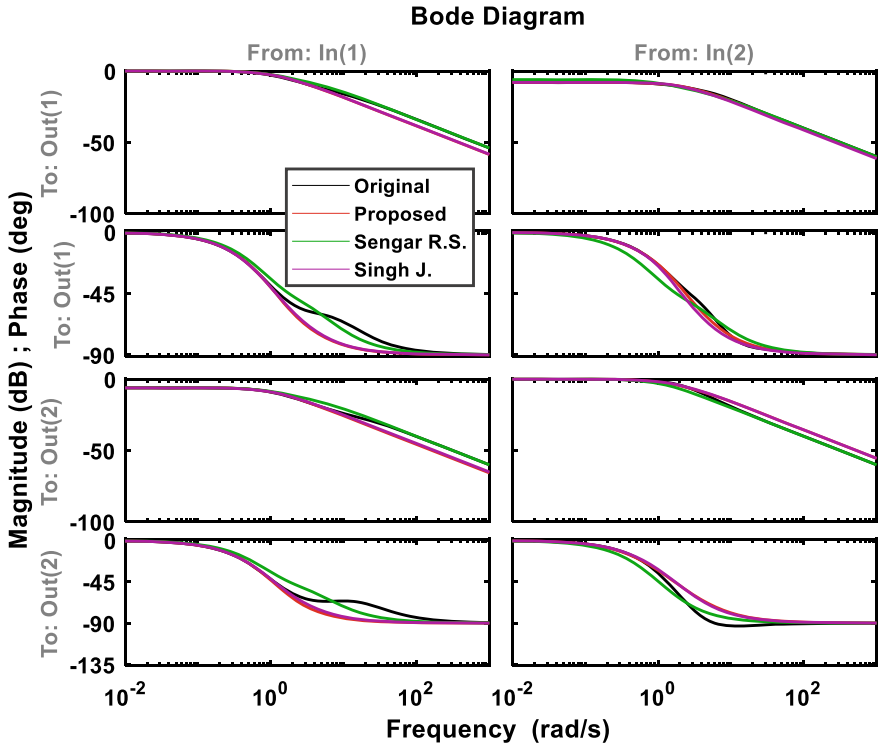


Fig. 3 Examination of original and reduced order models in terms of frequency response

Table 1. The proposed technique ensures the least value of ISE such that the reduced system obtained by the given technique is near to the original model.

Correlation of sixth-order model and second-order reduced model in terms of step response and frequency response has been displayed in Figs. 2 and 3. The ISE of the second-order reduced model has been compared with other existing techniques in Table 2.

It tends to be distinguished from Table 2 that the suggested strategy gives low worth of ISE when contrasted with the current procedures.

Table 1 Calculation parameters of GWO

Grey wolf optimization	Domain of search for \vec{Z}	$[-1000,1000]$
	Search boundaries for \vec{b}	$[-1,1]$
	Search boundaries for \vec{Y}	$[0,1000]$
	Search length	2
	Overall search particles	20
	Total iteration	100

Table 2 Examination of existing techniques with example 1 in terms of ISE

$r_{ij}(s) = \frac{t_{ij}(s)}{H_r(s)}$	ISE proposed technique	ISE Sengar et al. [12]	ISE Singh et al. [11]	ISE Parmar [2]	ISE Prasad [13]
$t_{11}(s)$	0.0012	0.0049	0.0008	0.03871	0.135505
$t_{12}(s)$	0.0003	0.0026	0.0012	0.02815	0.002446
$t_{21}(s)$	0.0000	1.9734	0.0002	0.00741	0.040013
$t_{22}(s)$	0.0042	0.0286	0.0039	0.14409	0.067897

6 Conclusions

A hybrid technique based on grey wolf optimization and Pade approximation has been recommended for order reduction of MIMO stable system. In this manuscript, coefficient of the denominator polynomial for reduced model is resolved by using grey wolf optimization. The numerator of the reduced model is acquired by utilizing Pade approximation. ISE has been taken as an objective function which is minimized while determining the numerator and denominator polynomial of lower-order system.

The performance of the proposed technique has also been tested by comparing the step and frequency responses of the existing methods with that of proposed method. The recommended technique is explained with the help of one example, and it has been noticed from Table 2 that this technique is superior than many other extant order reduction methods available in survey. This hybrid technique evades steady-state error and conserves model stability of the reduced model.

References

1. Singh N, Prasad R, Gupta HO (2007) Pade approximants for linear multivariable systems using stability equation method. In: National systems conference-2007. M.I.T, Manipal, Dec 14–15 (2007)
2. Pal J (1979) Stable reduced order Pade approximants using the Routh Hurwitz array. *Electron Lett* 15(8):225–226
3. Prajapati AK, Prasad R (2018) Reduced order modelling of LTI systems by using Routh approximation and factor division methods. *Circuit Syst Signal Process* 38(7):3340–3355
4. Mirjalili S, Mirjalili SM, Lewis A (2014) Grey wolf optimizer. *Adv Eng Softw* 69:46–61
5. Bhatnagar U, Gupta A (2017) Application of grey wolf optimization in order reduction of large scale LTI systems. In: 2017 4th IEEE Uttar Pradesh section international conference on electrical, computer and electronics (UPCON), Mathura, pp 686–691
6. Bhadauria P, Pal NS, Singh J (2019) Model order reduction using grey wolf optimization and factor division method. In: 2019 2nd International conference on power energy, environment and intelligent control (PEEIC). Greater Noida, India, pp 508–512. <https://doi.org/10.1109/PEEIC47157.2019.8976654>
7. Bhadauria P, Pal NS (2021) Model order reduction using grey wolf optimization and Pade approximation. In: 2021 Proceedings of International conference on scientific and natural computing. Greater Noida, India. <https://doi.org/10.1007/978-981-16-1528>
8. Shamash Y (1975) Linear system reduction using Pade approximation to allow retention of dominant modes. *Int J Control* 21(2):257–272

9. Shamash Y (1975) Linear system reduction by Pade approximation to allow retention of dominant modes. *Int J Control* 21:257–272
10. Wan B (1981) Linear model reduction using Mihailov criterion and Pade approximation technique. *Int J Control* 33(6):1073–1089
11. Singh J, Chatterjee K, Vishwakarma CB (2015) Model order reduction using Eigen algorithm. *Int J Eng Sci Technol* 7(3):17–23
12. Sengar RS, Chatterjee K, Singh J (2019) System approximation using modified inverse distance measure and modified Caueer continued fraction method. *IOP Conf Ser: Mater Sci Eng* 691:012006
13. Prajapati AK, Prasad R (2021) A novel order reduction method for linear dynamic systems and its application for designing of PID and lead/lag compensator. *Trans Inst Meas Control* 43(5):1226–1238

Smart Wheelchair for Specially Abled People



Prashant Verma and Kirti Pal

Abstract This paper is focused on the speech recognition technology. In recent years, it was not possible to control our machineries through the help of voice commands. As the home automation is very popular nowadays. In this method, all home appliances are controlled by android phone through voice command. Keeping this automation in mind a wheelchair is also automated here by android phone through voice command. This special feature is added in traditional wheelchair to make especially abled persons independent. In this project, a small model of voice-controlled wheelchair is designed for especially abled persons. The wheelchair can be easily controlled by speech recognition module. It is very helpful for elderly people also who cannot walk well due to aging effect. Here wheelchair is trained with forward, backward, left, right, and stop commands. These voice commands are given by user via android application which transfers to microcontroller through Bluetooth module. After receiving the command, wheelchair will respond by performing proper movement to the proper direction according to the received data.

Keywords Arduino · Android phone · DC motor · Bluetooth · Wheelchair · Voice recognition

1 Introduction

Even normal people prefer control of all appliances from one place through remote access. In this condition by using home automation, people can control all home appliances. The term home automation is well-explained in [1–3], and the home appliances are controlled by tablets, computers and mostly by an android smart phones with Internet connection [4, 5]. Home automation is also helpful for old-age and physically challenged peoples. In the same way, wheelchair of disabled people

P. Verma (✉) · K. Pal
Department of Electrical Engineering, School of Engineering, Gautam Buddha University,
Greater Noida, Uttar Pradesh, India
e-mail: toretto4900@gmail.com

© The Author(s), under exclusive license to Springer Nature Singapore Pte Ltd. 2022
V. Mahajan et al. (eds.), *Sustainable Technology and Advanced Computing*
in *Electrical Engineering*, Lecture Notes in Electrical Engineering 939,
https://doi.org/10.1007/978-981-19-4364-5_51

717

also needs automation. Due to unable to movability, the people don't get socialized with other person which leads to irritability, sickness and other mental problems.

Previous wheelchair needs human efforts to move from one place to another place. The force is provided either by any family member or by disabled person itself. The development of new technologies and their implementation at right place help many specially abled person a lot. Many researchers working in the directions of defining different types of disability [6]. In [7], author presented a survey on different types of wheelchair with their technology and function. The idea to reduce human efforts by using voice technology for movement of wheelchair is proposed by Aakash et al. [8], Simpson and Levine [9] and Aruna et al. [10]. Many researchers name as robotic and intelligent wheelchair [11–13].

Voice-controlled robots are also developed for human assistant in many fields [14, 15] and to detect any barrier, fire, smoke for physically challenged people [16]. In [17], different movements of wheelchair were explained by author are as: motion in forward direction, motion in backward direction, motion in right direction, motion in left direction, and function to stop. In the proposed model, these five movements are considered.

In this project, a small model to control wheelchair functions is presented by using android phone and voice recognition system with Bluetooth module and Arduino programming.

The main aim of the proposed model is to intend and apply an automatic wheelchair which is operated on the basis of voice command. It is based on Arduino Uno microcontroller with motor module, Bluetooth module, DC motor, and battery. This type of wheelchair is very useful for physically challenged and old-age persons.

2 Proposed Methodology

The block diagram of proposed model of smart wheelchair is shown in Fig. 1. Two DC motors are connected to two wheels to control the motion of wheelchair.

It also requires Wi-Fi connection to send the signal to connect android phone with Arduino. In this project, a Bluetooth module is used which helps the wheelchair to connect with smart phone by which the voice commands of the user can be received. Bluetooth module will transfer the voice signal to the Arduino. Arduino will operate according to the operation given to it. Here Arduino is programmed with five commands: right, left, forward, backward, and stop. Then, Arduino sends a signal to motor module to operate according to the receiving command. Two gear motors are attached to motor module with wheels fitted in it. For all these operation, 12 V battery is used.

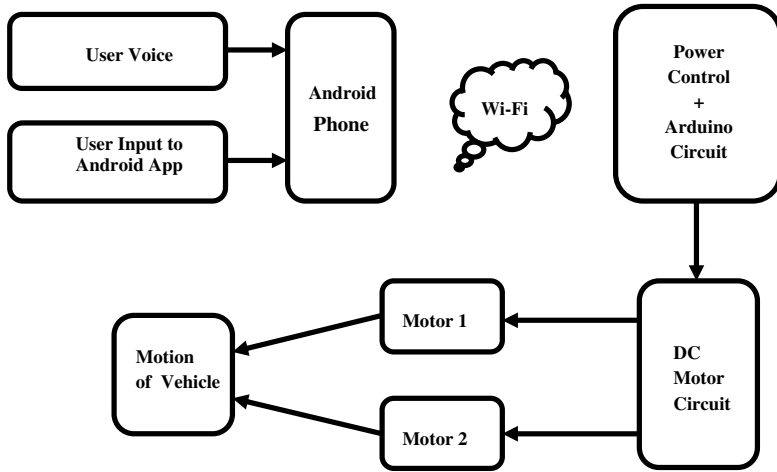


Fig. 1 Block diagram of proposed model

3 Component Description

This system consists of two parts, hardware equipment and software used in proposed model as given in Table 1.

Some of the important components are described below:

Arduino UNO: Arduino Uno is worked on principle of AVR microcontroller called Atmega328. The controller has 2 KB SRAM, 32 KB of flash memory, 1 KB of EEPROM. In Arduino Board, 14 digital with 6 analog pins are used for external connection of any kind of circuit. The pins are sampled by ON-chip ADC. The board requires only 5 V supply to turn on through USB port; however, it can be connected up to 12 V supply as per the requirement of the project (Fig. 2).

L293D Motor Module: This motor module is used to run two DC motors but with a condition that both must have same IC. With the help of this drive, we can control speed as well as direction of DC motor. There is an additional feature also available with this drive, automatic thermal shutdown (Fig. 3).

Table 1 Component detail

Type of component	List
Hardware	Arduino UNO, L 293D motor module, Bluetooth module HC-05, Gear motor with wheel, Battery(12 V), Chassis, Glue gun machine, Soldering iron
Software	Arduino IDE, android application—BT voice control for android, embedded C/C++, Java

Fig. 2 Arduino UNO board

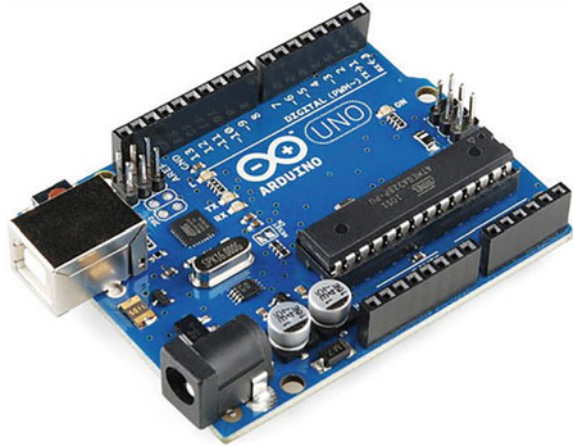
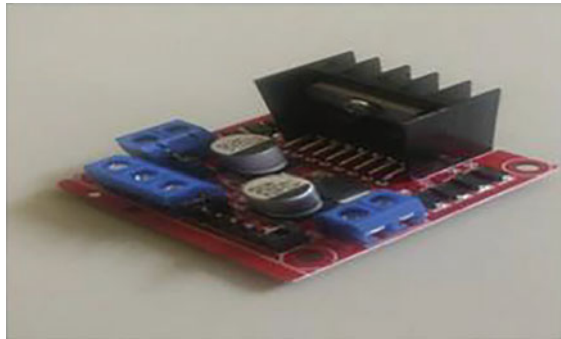


Fig. 3 L298D motor driver



Bluetooth Module HC-05: It is very easy-to-use Bluetooth system which is based on Serial Port Protocol (SPP) module which is specially made for transparent wireless serial connection setup. It communicates via serial communication which provides us a simple way to interface with PC (Fig. 4).

Fig. 4 HC05 Bluetooth module

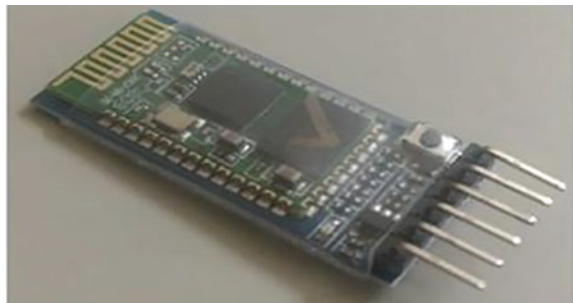


Fig. 5 Gear motor



Chassis: The internal framework of proposed car model is prepared first to support the other parts of car. This internal framework may be made up of metal or plastic and is known as chassis.

Gear Motor: Gear motor has the ability to generate high torque at low speed which can allow small motor to produce higher speed. It is a combination of speed reducer with a motor which function as a gearbox to reduce speed which will provide more torque (Fig. 5).

Wheels: To drive the car wheels are required. Wheels are made up of very hard durable plastic material with internal steel framework support. In our model, two wheels are used. Wheels are rotated as soon as they get torque by DC motor connected to each wheel. Figure 6 shows the two wheels used in proposed model. The instruction of type of movement that is forward, backward, right, and left is given through microcontroller to motor to move the wheel.

Circuit Diagram: Figure 7 shows the circuit diagram which is implemented in hardware, it consists of an Arduino Uno which is an open-source microcontroller, and it is easy to use in hardware. It consists of total 28 pins out of which 14 are digital pins and 6 are analog pins. A L293D motor module is also fitted after microcontroller. This module is a low-power module used for driving and controlling low-power DC and stepper motors. It can control drive of 4DC motors on/off or control drive of 2 DC motors with direction and speed control. The L293D IC pins 2, 5, 12, 13 are GND pins and 9,1,16 is connected with 5V power supply. But pin 8 of L293D is directly connected with 12 V power supply.

Fig. 6 Wheels



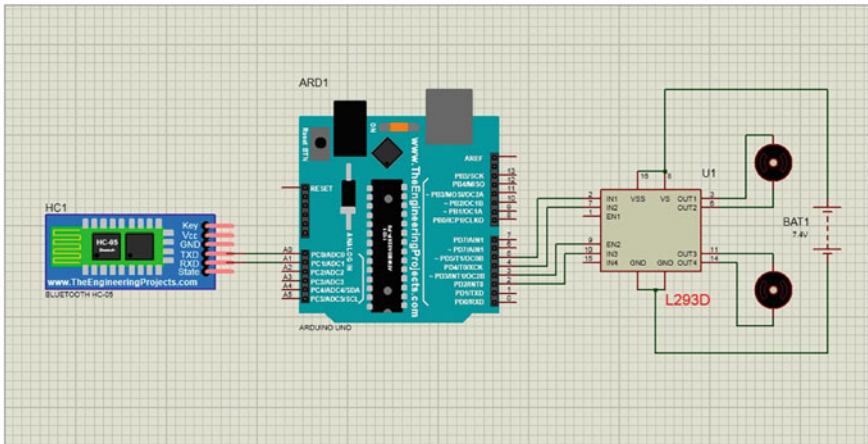


Fig. 7 Circuit diagram of proposed model

The Bluetooth module HC-05 is also connected in it which is very easy-to-use Bluetooth system and is based on Serial Port Protocol (SPP) module is specially designed for transparent wireless serial connection setup. The four components that are most useful in proposed model are Bluetooth module, Motor module, Arduino, and Battery. All the components are connected through jumper wire to each other.

4 Implementation of Proposed Model

The working of proposed model can be easily analyzed by the flowchart of Fig. 8. Firstly, it is checked that Bluetooth signal is ‘ON’ or not. If it is ‘OFF,’ then it must be switched ‘ON’. The system will start if 12 V supply is connected. As the battery is connected in the system, the red light on Bluetooth module starts blinking continuously.

When its blinking speed gets slower, it indicates that now android phone has been connected to our system. Make sure that all connections must be properly connected and codes are correct. After checking all the points, commands can be given directly through android phone and according to command wheelchair will work.

The proposed model system consists of voice recognition circuit, Arduino circuit, and controller circuit to control speed of DC motor. The voice recognition system is used to convert analog voice signal to digital signal. After conversion of signal, it is transferred to android phone. The speed of wheel movement that is DC motor speed is controlled by controller unit. The wheel movement will depend on amount of current that passes through DC motor and controller. When high current flow through motor wheel movement is fast, low current flow through motor wheel movement is slow.

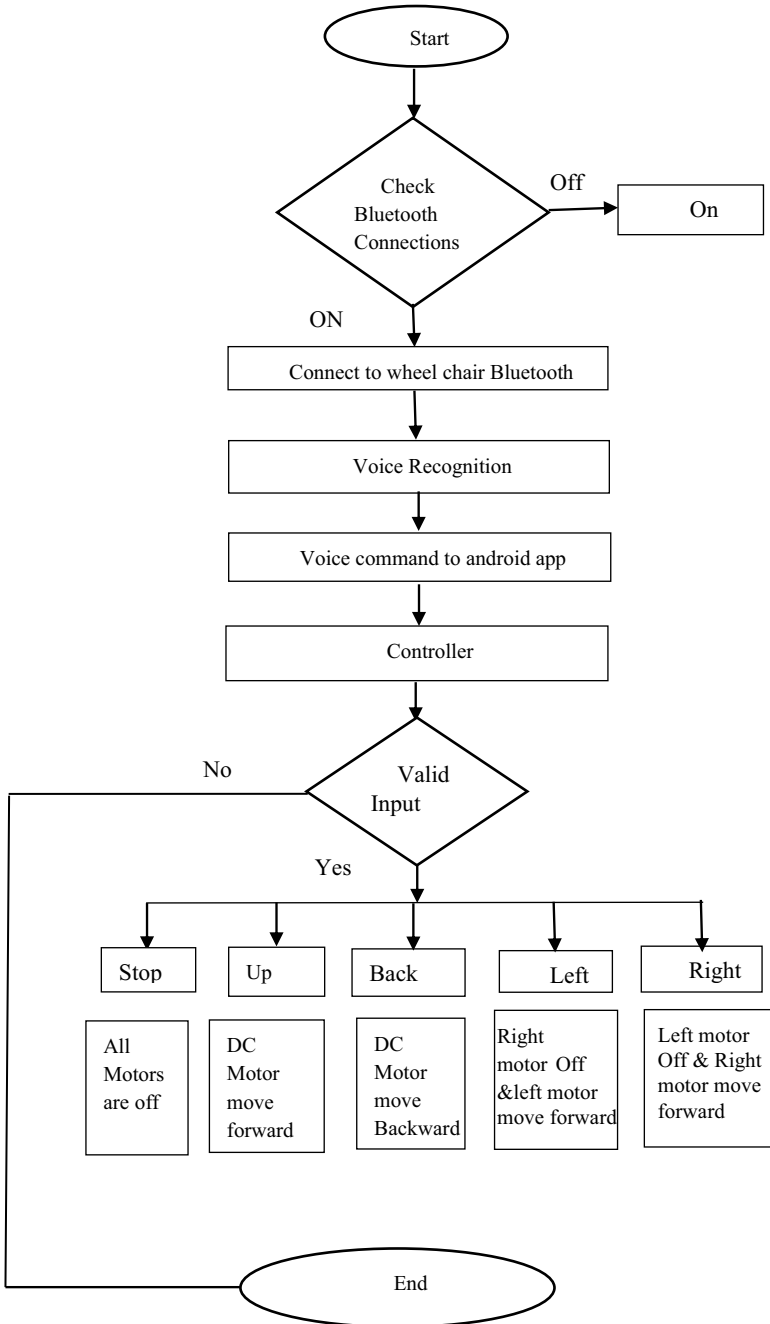


Fig. 8 Flowchart of proposed model

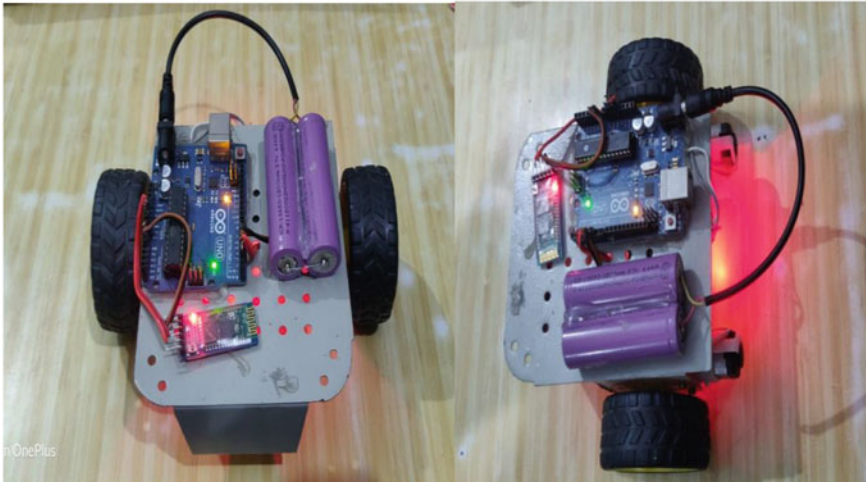


Fig. 9 Hardware model

The motors work differently for each and every command. In forward motion, both motors work in the same direction and in backward motion, motors work in the same ways but in reverse direction. In the same manner, for right and left movements, one of the motors will work and second one is in rest position and for stop, both motors stop working. All the motion directions are given to the Arduino controller through the Bluetooth application of android smart phone by user. The hardware model is shown in Fig. 9.

5 Conclusion

In this proposed model, a voice-controlled wheelchair is designed which works on the principle of voice recognition. The model is tested 50 times with voice commands for: right, left, upward, backward, and stop movement. It works efficiently. The speed of movement is also controlled by controller unit attached with DC motor. The voice recognition system is tested in single quite room, and also at public place in both cases, it works efficiently. The main advantage of proposed model is low cost, easy maintenance, and it works as a leg to the specially abled person. They can easily control their movement by own. They become independent. It is also very useful for old-age people.

References

1. Lobaccaro G et al (2016) A review of systems and technologies for smart homes and smart grids. *Energies* 9(5):348. <https://doi.org/10.3390/en9050348>
2. Bingol O et al (2014) (2014) Web-based smart home automation: PLC-controlled implementation. *Acta Polytechnica Hungarica* 11(3):51–63
3. ElShafee A, Hamed KA (2012) Design and implementation of a WIFI based home automation system, vol 68. *World Academy of Science Engineering and Technology*, pp 2177–2180
4. Sarwar M, Soomro T (2013) Impact of smartphone's on society. *Eur J Sci Res* 98
5. Fahim M (2012) Daily life activity tracking application for smart homes using android smart-phone. In: *Proceedings of the 2012 14th International conference on advanced communication technology (ICACT)*. IEEE, Pyeong Chang, South Korea, pp 241–245
6. Fehr L et al (2000) Adequacy of power wheel chair control interfaces for persons with severe disabilities: a clinical survey. *J Rehabil Res Dev* 37(3):353–360
7. Simpson RC (2005) Smart wheelchairs: a literature review. *J Rehabil Res Dev* 42:423–436
8. Aakash A et al (2014) Voice operated wheelchair. University of Pune. AISSMS Institute of Information Technology. Electronics and Communication Department, 4(4). ISSN: 2277-128X
9. Simpson RC, Levine SP (2002) Voice control of a power wheelchair. *IEEE Trans Neural Syst Rehabil Eng* 10(2):122–125
10. Aruna C et al (2014) Voice recognition and touch screen control based wheelchair for paraplegic persons. In: *IEEE International conference on green computing communication and electrical engineering*. India, pp 1–5
11. Kuo CH, Chen HHW (2006) Human-oriented design of autonomous navigation assisted robotic wheelchair for indoor environments. In: *IEEE International conference on mechatronics*, pp 230–235
12. Perkowski MA, Stanton K (1991) Robotics for the handicapped. In: *Northcon conference record*, pp 278–284
13. Cooper RA (2002) Intelligent control of power wheelchair. *IEEE Eng Med Biol Mag* 14:423–431
14. Bhanu Chandu M, Ganapathy K (2020) Voice controlled human assistance robot. In: *International conference on advanced computing & communication systems (ICACCS)*. ISBN: 978-1-7281-5197-7/20
15. John L et al (2020) Voice control human assistance robot. In: *National conference on technical advancements for social upliftment*. *Proceedings of the 2nd VNC*
16. Mahesh Reddy P et al (2020) Intuitive voice controlled robot for obstacle, smoke and fire detection for physically challenged people. In: *International conference on trends in electronics and informatics (ICOEI)*. ISBN: 978-1-7281-5518-0
17. Daerden F, Lefeber D (2001) The concept and design of pleated pneumatic artificial muscles. *Int J Fluid Power* 2(3):41–45

Integration of Plugged-in Electric Vehicles for Load Frequency Control in Two-Area System



Pratik Sanjay Kadge and Rajesh Joseph Abraham

Abstract In recent years, the penetration of large-scale renewable sources has potentially increased, which causes an imbalance in power systems due to the variable nature of generation. Battery energy storage has the potential to smoothen these variations and provide system-wide stability. Recent evolution in battery technology has made electric vehicles (EVs) a potential source to provide ancillary services to the grid. An optimum vehicle-to-grid (V2G) method has the potential to use electric vehicles for load frequency control as well as to meet EV owner demands. In this paper, an adaptive droop-based V2G control method is proposed to meet both load frequency control and EV owner demands. Three modes of operation are incorporated, i.e., idle, charging, and discharging considering EV owner's demand. For maintaining EV battery's state of charge (SOC), an idle mode is used to maintain battery SOC. If the EV owner wants to charge the battery up to a specific SOC level, a charging mode is used to charge the EV up to a specified level and to provide frequency regulation. If the EV owner has extra battery energy, discharging mode injects energy to the grid whenever an increase in system load is observed. Discharging mode switches to idle mode as soon as battery SOC is decreased up to specified SOC level. Simulations are carried out for a two-area power system considering real-time SOC and commute profile, and results have shown the effectiveness of the proposed method.

Keywords Two-area system · Primary frequency control · Plugged-in electric vehicles · Vehicle-to-grid · Adaptive droop control · State of charge · Commute profile

Nomenclature

B Frequency bias factor.
 E_i^F Total battery capacity of the i th EV (kWh).

P. S. Kadge (✉) · R. J. Abraham
Indian Institute of Space Science and Technology, Thiruvananthapuram 695547, India
e-mail: pratik.kadge65@gmail.com

© The Author(s), under exclusive license to Springer Nature Singapore Pte Ltd. 2022
V. Mahajan et al. (eds.), *Sustainable Technology and Advanced Computing in Electrical Engineering*, Lecture Notes in Electrical Engineering 939,
https://doi.org/10.1007/978-981-19-4364-5_52

727

ΔE_i	Change in energy of the i th EV battery (kWh).
Δf	Frequency deviation.
η_c	Efficiency while charging.
η_d	Efficiency while discharging.
$K_{i,k}^c$	Droop of the i th EV at time k while charging.
$K_{i,k}^d$	Droop of the i th EV at time k while discharging.
K_{\max}	Maximum droop of the EV.
P_{\max}	Maximum Power of the EVs battery (kW).
$P_{i,k}$	Vehicle to grid power of the i th EV at time k at the EV side (kW).
$P_{i,k}^p$	Vehicle to grid power of the i th EV at time k at the grid side (kW).
$P_i^s(k)$	Estimated power required for charging at the battery side of the i th EV.
P_i^c	Constant estimated charging power at the battery side of the i th EV.
ΔP_{tie}	Change of tie line power between areas A and B.
$\text{SOC}_{i,k}$	State of charge of the i th EV battery at time k .
$\text{SOC}_{i,\max}$	Maximum state of charge of the i th EV battery.
$\text{SOC}_{i,\min}$	Minimum state of charge of the i th EV battery.
SOC_i^{in}	Initial state of charge of the i th EV battery at plug-in time.
SOC_i^{e}	Expected state of charge of the i th EV battery at plug-out time.
T_i^s	Time required to achieve charging demand of the EV (s).
t_i^{in}	Plug-in time of the i th EV (h).
t_i^{out}	Plug-out time of the i th EV (h).
$T_{A,B}$	Torque coefficient between areas A and B (p.u./Hz)

1 Introduction

In recent years, the increase in emission of greenhouse gases, global warming, depletion of fossil fuels sources, has shifted the focus from conventional energy sources to renewable energy sources. Extensive integration of EVs and renewable energy sources will have implications on power systems because of the new type of load and variable generation. It provides new challenges and opportunities for the operation of a power system. EVs act as both controllable load and mobile storage devices. The bidirectional power transfer capabilities of EVs provide new applications for the optimal performance of power systems. Vehicle-to-grid (V2G) implementation allows the controlled exchange of power between vehicles and the grid. EVs can be used as both load and source due to their bidirectional property. Therefore, analysis of the ability of EVs to participate in ancillary services is important.

One of the major components affected due to load and generation imbalance is frequency. When demand exceeds generation, system frequency decreases to meet the extra load. EVs can act as a power source by injecting power into the grid when system frequency decreases. When generation is higher than demand (e.g., during off-peak hours or night time), system frequency increases. This additional energy can be utilized to charge EV batteries and restore system frequency to its original

value. As a greater number of EVs are being integrated into the power system, the effect of EVs on load pattern and ability of EVs to provide frequency control needs to be studied. A proper V2G control strategy is needed for the fulfillment of both EV customer demand and load frequency control when connected to the grid.

The general concept and idea of load frequency control using renewable sources and EVs are addressed in [1, 2]. The analysis of total V2G capacity considering aggregate model of EVs has been discussed in [3, 4]. Work on V2G-based load frequency control has been carried out in [5, 6]. In [6], the load frequency control signal is varied according to response speed and the controllable load without considering the charging demands of the EV owners since, the same SOC is assumed for all vehicles. The impacts of the variable renewable energy generation on primary frequency control (PFC) and SOC of the EV batteries was evaluated in [7] and [8]. In order to clamp down the frequency variations of a power grid, Autonomous distributed V2G control (ADC) was considered in [9, 10]. Partial V2G power was assigned in advance as a required charging power in [10]. The estimated charging time of the V2G control dependent on plug-in time was not considered in [9, 10]. Furthermore, daily driving pattern, parking time, commuter profile, and real-time battery SOC values are also not considered.

In this paper, the feasibility of plugged-in electric vehicles (PEV) to provide ancillary services and the effectiveness of adaptive droop-based V2G control strategy to fulfill power system, as well as EV owner's demand, is studied. For the same, variable load model, real-time SOC, commute profile, number of charging, discharging, and idle vehicles for a 24-hour scenario in two-area system are considered. An aggregate model of PEVs is incorporated in two-area systems and its effectiveness to provide primary frequency control is studied. Furthermore, an adaptive droop-based V2G control mechanism is presented for a set of PEVs under different conditions providing ancillary services to the grid, and its efficiency in PFC, considering EV owners' demands for a typical 24-hour weekday scenario, is demonstrated.

2 Two-Area System Under Consideration

2.1 Modeling of Two-Area System with PEV

The model system consists of a two-area (area 'A' and area 'B') interconnected power system, as shown in Fig. 1. Each area consists of thermal, hydro, and gas power generation with a combined capacity of 20,000 MW/area. Thermal, hydro, and gas systems are represented in Fig. 1 with the governor, turbine models. Frequency fluctuations from random load are simulated by a power system model. A real-time model of aggregate PEVs is included in area 'A' to incorporate the variations in energy of the battery during LFC. The system is modeled using MATLAB SIMULINK. Power system parameters are given below:

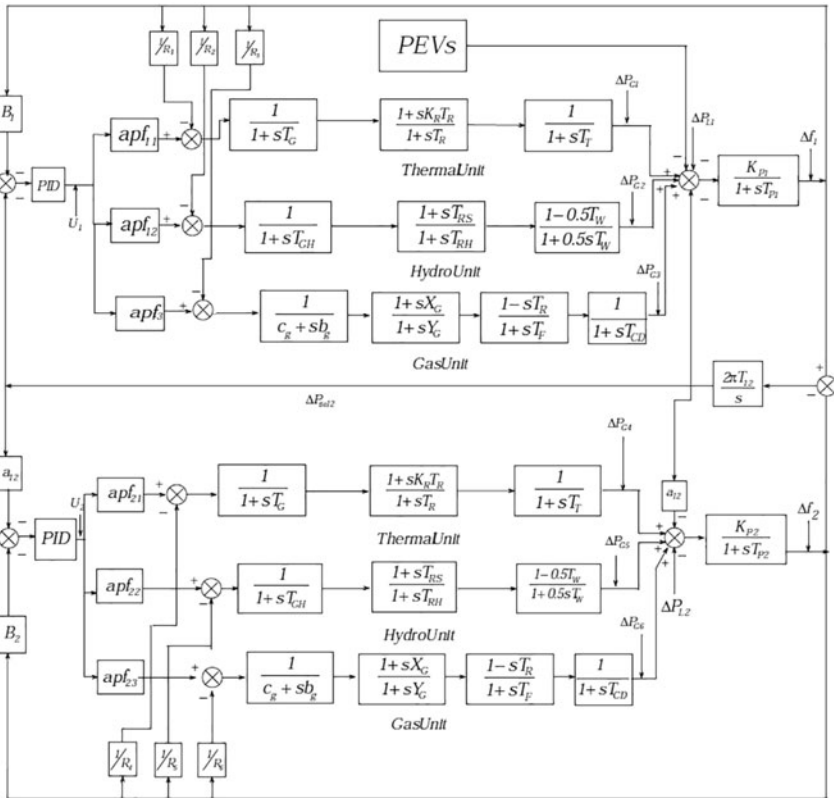


Fig. 1 Two-area system modeling

$T_G = 0.08$ s; $K_R = 0.3$; $T_R = 10$ s; $T_T = 0.3$ s; $apf_{thermal} = 0.4$; $T_{GH} = 0.2$ s; $T_{RS} = 5$ s; $T_{RH} = 28.75$ s; $T_W = 1$ s; $apf_{hydro} = 0.4$; $c_g = 1$; $b_g = 0.05$ s; $X_G = 0.6$; $Y_G = 1$ s; $T_{CR} = 0.01$ s; $T_F = 0.23$ s; $T_{CD} = 0.2$ s; $apf_{gas} = 0.2$; $H = 0.32$ p.u.s; $D = 0.04$ pu/Hz; $B = 1.29$ p.u./Hz; $R = 2.4$ Hz/p.u.; $T_{12} = 0.0433$ p.u./Hz.

Random load data [11] consisting of base and fringe components is used for the simulation. The base component has a large amplitude and varies slowly. The fringe component is a faster component with smaller amplitude variations. The random load data is generated with 100 MW base component and 15 MW fringe component. Both these components are multiplied with respective white noise with specifications mentioned in Table 1.

Table 1 Parameters for calculation of load fluctuation model

Component of load fluctuation	Load fluctuation (MW)	Noise power	Sampling interval	Number of seeds
Base	100	156	300	20,000
Fringe	15	156	30	10,000

2.2 Aggregate PEV Model

As mentioned in [12], an aggregate PEV model consisting of battery charger model with droop for primary load frequency control is shown in Fig. 2.

A dead band of 1 MHz is added to prevent frequent switching between charging and discharging of PEV battery due to small frequency variations. Saturation block is added for limiting the charging or discharging rate of battery due to large load variations. Power output from battery multiplied by number of vehicles gives aggregate power provided by all PEVs in their respective mode for load frequency control. V2G parameters are mentioned in Table 2.

3 Adaptive Droop-Based V2G Control

Change in the battery energy during charging or discharging can be given by

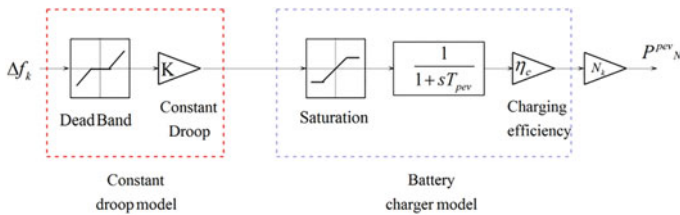


Fig. 2 Aggregate PEV model

Table 2 V2G parameters

Parameter	Value
Battery capacity (kWh)	32
Dead band of frequency (Hz)	[−0.001, 0.001]
Efficiency while charging or discharging	0.9/0.9
Maximum vehicle-to-grid power (kW)	7
Maximum V2G droop (kW/Hz)	120
Maximum/minimum SOC	0.95/0.10

$$\Delta E_i = \int_0^k P_i(k)dk \tag{1}$$

Battery SOC is expressed as the percentage of the rated capacity available in battery.

Change in SOC due to change in battery energy is given by

$$SOC_{i,k} = SOC_i^{in} + \frac{1}{E_i^\Gamma} \cdot \Delta E_i \tag{2}$$

Calculation of real-time SOC based on the above equations is modeled. Initial SOC is taken as an average of initial SOC's of vehicles in their respective modes, i.e., idle, charging, or discharging. At a point in time, an electric vehicle can be on a road or plugged into the grid whenever it is parked. When plugged into the grid, variable droop control [13] based on the following three modes are considered.

3.1 Idle Mode with Frequency Regulation

The EVs which are holding their SOC levels and as well as joining primary frequency control (PFC) are considered in idle mode. Depending upon frequency change, a frequency control loop with adaptive droop is designed for PFC as shown in Fig. 3. A saturation block with upper and lower limits is added as PEVs can both absorb or feed power to a grid. A dead band is added to prevent PEV batteries from rapidly switching between charging and discharging due to smaller and rapid frequency

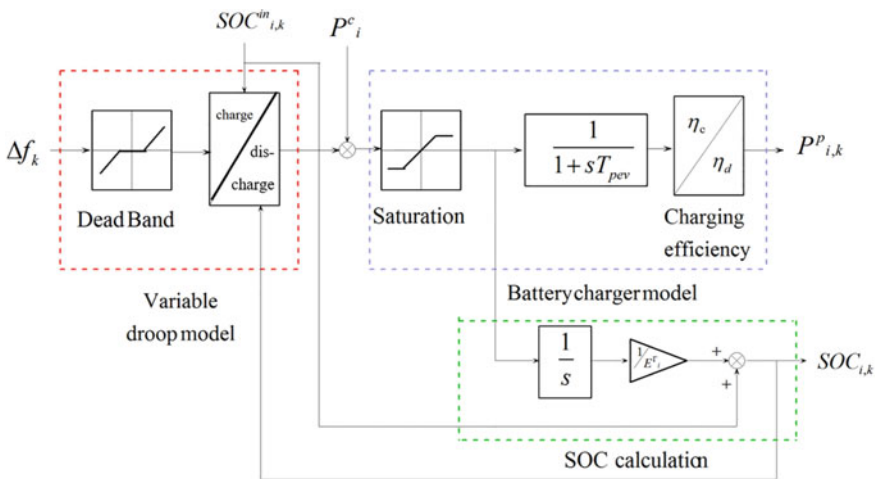


Fig. 3 V2G control block for PEVs in Idle mode

changes. EV will respond to those frequency changes which are outside the dead band. Depending upon increase or decrease in system frequency, idle mode is divided into two parts, and adaptive droop is used accordingly. Figure 3 shows the model designed for PEVs in idle mode.

Positive Frequency Deviation Whenever generation is greater than the demand, system frequency increases. In order to bring frequency to its scheduled value, this surplus generation is added as an extra charge to PEV batteries. Whenever real-time SOC of PEVs is greater than the SOC level at the beginning, droop is reduced to prevent the rise of the battery SOC, and smaller droop value is used to prevent further increase in battery SOC. If real-time SOC is lower than the SOC level at the start, higher droop value is used to charge batteries depending upon current SOC values. Adaptive droop is calculated as follows.

1. If $SOC_{i,k} \leq SOC_i^{\min}$ then,

$$K_{i,k}^c = K_{\max} \tag{3}$$

2. If $SOC_{i,k} \geq SOC_i^{\max}$ then,

$$K_{i,k}^c = 0 \tag{4}$$

3. If $SOC_i^{\min} < SOC_{i,k} \leq SOC_i^{\text{in}}$ then,

$$K_{i,k}^c = \frac{1}{2} K_{\max} \left(1 + \sqrt{\frac{SOC_{i,k} - SOC_i^{\text{in}}}{SOC_i^{\min} - SOC_i^{\text{in}}}} \right) \tag{5}$$

4. If $SOC_i^{\text{in}} < SOC_{i,k} \leq SOC_i^{\max}$ then,

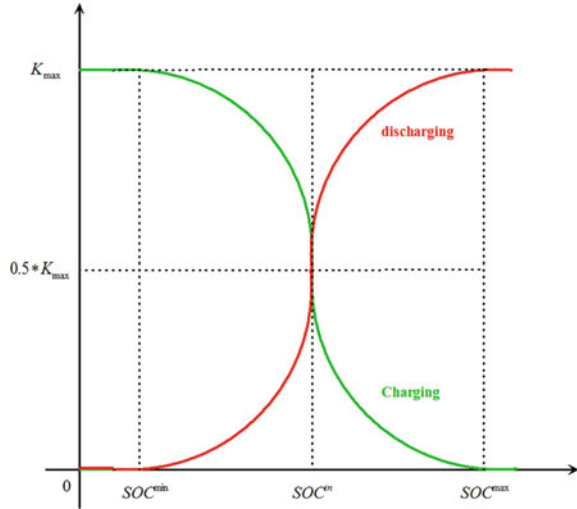
$$K_{i,k}^c = \frac{1}{2} K_{\max} \left(1 - \sqrt{\frac{SOC_{i,k} - SOC_i^{\text{in}}}{SOC_i^{\max} - SOC_i^{\text{in}}}} \right) \tag{6}$$

Negative Frequency Deviation When demand is higher than a generation, the frequency of the system decreases. Due to a decrease in frequency, power is injected from PEVs to the grid until frequency reaches its scheduled value. This causes the decrease in the SOC of the battery. Depending upon the real-time and initial SOC level of the battery, adaptive droop control is designed to sustain the initial battery SOC level. Adaptive droop prevents the decrease in battery SOC below its minimum value using SOC-dependent droop. Variation of adaptive discharging droop depending upon real-time SOC is explained below.

1. If $SOC_{i,k} \leq SOC_i^{\min}$ then,

$$K_{i,k}^d = 0 \tag{7}$$

Fig. 4 Droop variation with SOC



2. If $SOC_{i,k} \geq SOC_i^{max}$ then,

$$K_{i,k}^d = K_{max} \tag{8}$$

3. If $SOC_i^{min} < SOC_{i,k} \leq SOC_i^{in}$ then,

$$K_{i,k}^d = \frac{1}{2} K_{max} \left(1 - \sqrt{\frac{SOC_{i,k} - SOC_i^{in}}{SOC_i^{min} - SOC_i^{in}}} \right) \tag{9}$$

4. If $SOC_i^{in} < SOC_{i,k} \leq SOC_i^{max}$ then,

$$K_{i,k}^d = \frac{1}{2} K_{max} \left(1 + \sqrt{\frac{SOC_{i,k} - SOC_i^{in}}{SOC_i^{max} - SOC_i^{in}}} \right) \tag{10}$$

Figure 4 shows variation of charging and discharging droop based on SOC of PEVs.

3.2 Charging with Frequency Regulation

In this mode, the vehicle is connected to the grid, and the EV owner wants to charge the vehicle for his upcoming journey up to the specified SOC of battery within the stipulated time. EV owner specifies the final SOC of battery and expected time of charge. The vehicle will charge up to specified SOC and simultaneously participate in

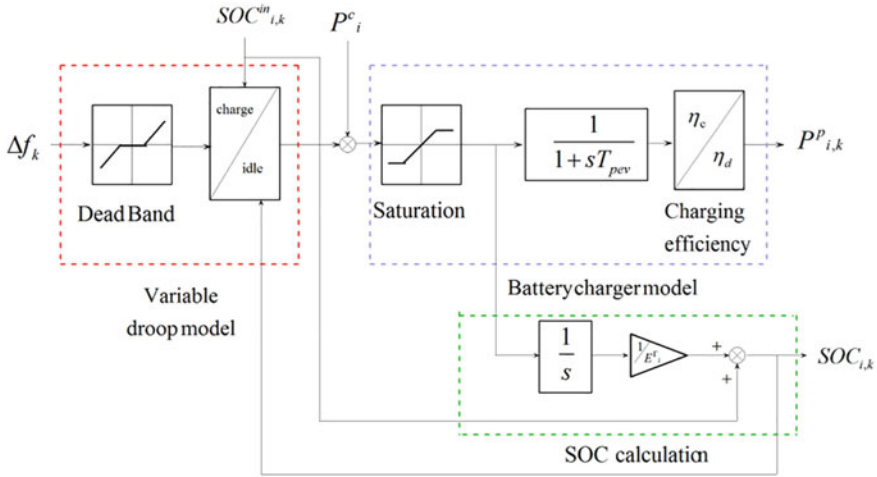


Fig. 5 EV V2G block for charging with frequency regulation

primary frequency control (PFC). When generation exceeds demand due to renewable energy sources or during night time when demand is less, surplus generated energy is used to charge EV batteries at cheaper rates. Estimated charging power based on the charging requirement for aggregate EVs is described as

$$P_{av}^c = E_i^\Gamma \cdot (SOC_{av}^e - SOC_{av}^{in}) / (t_{av}^{out} - t_{av}^{in}) \tag{11}$$

The frequency droop control loop is constructed with scheduled charging power and constant droop as shown in Fig. 5. Frequency deviations are suppressed by frequency droop control. When EVs are charged up to the expected SOC before the estimated time or the plug-out time, the charging mode will be switched to the idle mode for LFC, and battery SOC is maintained at the final SOC level as shown in Fig. 5. Switching mechanism is devised depending upon the final SOC level of EV after completion of charging.

3.3 Discharging with Frequency Regulation

EVs in this mode have surplus SOC than what is needed for the next trip. EV owners will be getting more incentives for providing PFC during peak hours when system frequency decreases due to additional load demand. Discharging EVs act as a source providing additional energy demand during the transient period of conventional generators. Frequency droop control loop with maximum constant droop is constructed as shown in Fig. 6. The expected SOC of the battery should be provided by the EV owner. EVs participate in PFC till SOC is decreased to holding SOC level

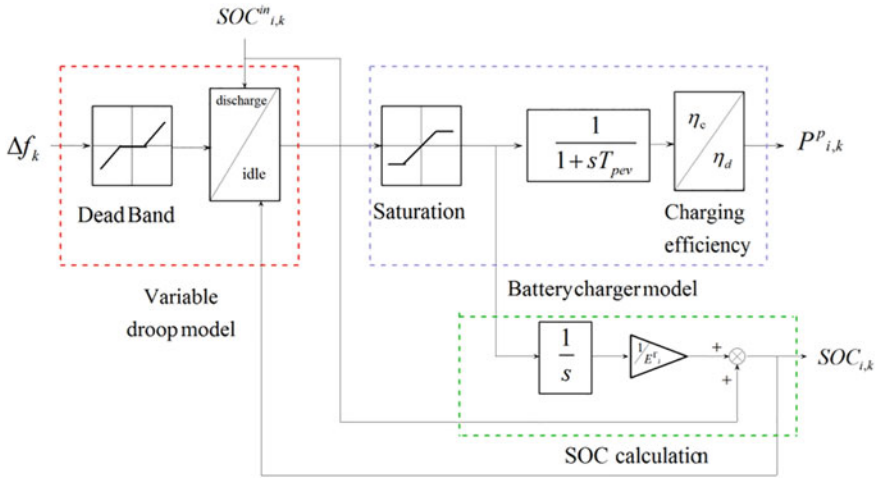


Fig. 6 EV V2G block for discharging with frequency regulation

of the battery. Once expected SOC is reached, EV will be switched from discharging mode to idle mode in which battery SOC is maintained around expected SOC while participating in load frequency control.

3.4 Commute Profile

The commute profile is derived in reference to the data of a survey completed in [14]. This profile depicts the round trip between home and offices during weekdays. In order to model the suitable commute pattern, response of commuters who travel between home and work is considered. The response of such 951 commuters is interpolated for 50,000 commuters. Total distance covered by the car is considered to build the profile as presented below.

Driving Distance During Weekdays As per the survey histogram, around 75% of the commuters complete less than 50 km per day, 15% drive average of 70 km per day, and 10% drive more than 100 km per day.

Parking Time of Vehicles Depending upon number of vehicles on the road as mentioned in [14], all vehicles are at home from 22:00 to 6:00, otherwise either they are on the road or parked at offices. Figure 7 depicts the parking time and number of parked vehicles. Based on 13 driving tests performed on an EV at ISR University of Coimbra, the average energy demand by an EV is assumed to be 150Wh/km.

Assuming storage capacity of EV around 32 kWh and 30% of the capacity as a reserve to inhibit the complete discharges and battery degradation, a typical battery capacity for an EV would be 22.4 kWh for everyday travel. Considering 150 Wh/km,

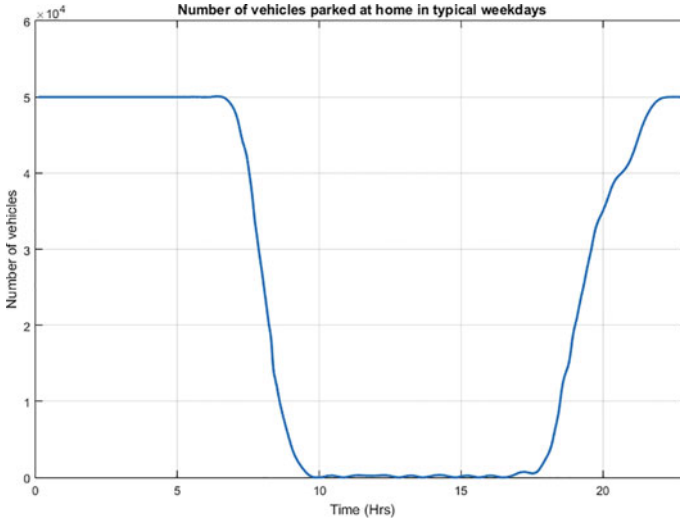


Fig. 7 Number of vehicles parked at home during typical weekday

with 22.4 kWh usable energy, EV can travel up to 150 km distance. But as mentioned, around only 10% of EVs travel more than 100 km, so we can safely assume that the EV owner does not need to charge EV when EV is away from home. We are assuming that whenever the vehicle is parked at home, it is acting in charging with frequency regulation mode. Hence, the profile of a number of charging a vehicle is the same as that of the number vehicles parked at home.

Discharging and Idle Vehicles Profile Vehicles that are not parked at home are considered to be either in discharging or idle mode. As mentioned in the above section, only about 10% of vehicles travel more than 100 km distance. Hence, 90% of vehicles, which are away from home (generally from 6:00 to 22:00) are considered to be in a discharging with frequency regulation mode and the remaining 10% to be in an idle mode participating in frequency control. Figure 8 denotes vehicle profile in both discharging and idle modes for a normal 24-h weekday.

3.5 Initial SOC Model Based on Distance Traveled

As mentioned in above section, assuming EV power consumption of 150 Wh/km, SOC levels are calculated for EVs. Following Table 3 denotes the initial SOC's depending upon average distance commuted throughout the day. These initial SOC values are used for the measurement of real-time battery SOC values.

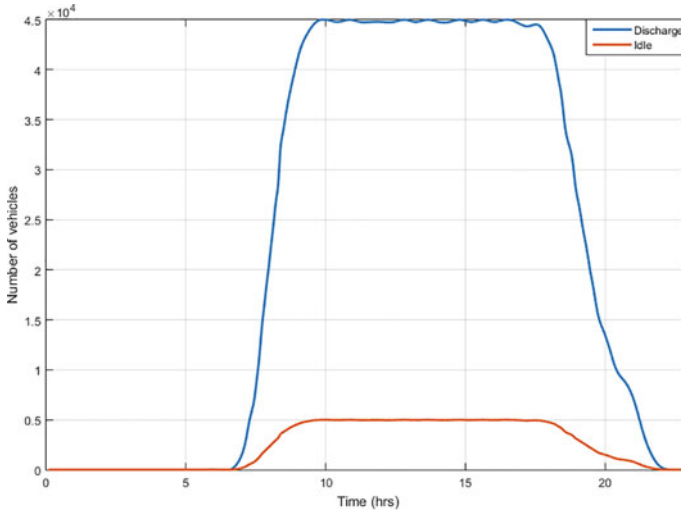


Fig. 8 Number of vehicles in discharging or idle mode

Table 3 Different initial SOC levels

Avg. distance traveled (km)	Leaving home	Reaching work	Leaving work	Reaching home
30	0.9	0.83	0.82	0.75
70	0.9	0.74	0.73	0.56
120	0.9	0.62	0.62	0.36

4 Results and Discussions

Simulations are carried out for a two-area power system, considering thermal, hydro, and gas generation units in both areas and PEVS integrated in Area-A.

4.1 Participation of PEVs in PFC

Simulation is carried out for a 5% step load increase in Area-A, with and without considering PEVs in Area-A. An aggregate model for 50,000 PEVs is integrated in Area-A. Results are compared for both the cases. Frequency undershoot improvement of 8% is observed compared to without PEV scenario.

From results in Fig. 9, it is evident that PEVs are able to suppress frequency deviations by injecting extra battery energy during transient time of conventional plants. Hence, participation PEVs during PFC is verified. Though PEVs are participating in PFC, SOC level of battery is not regulated. Adaptive droop control is used in order to regulate battery SOC.

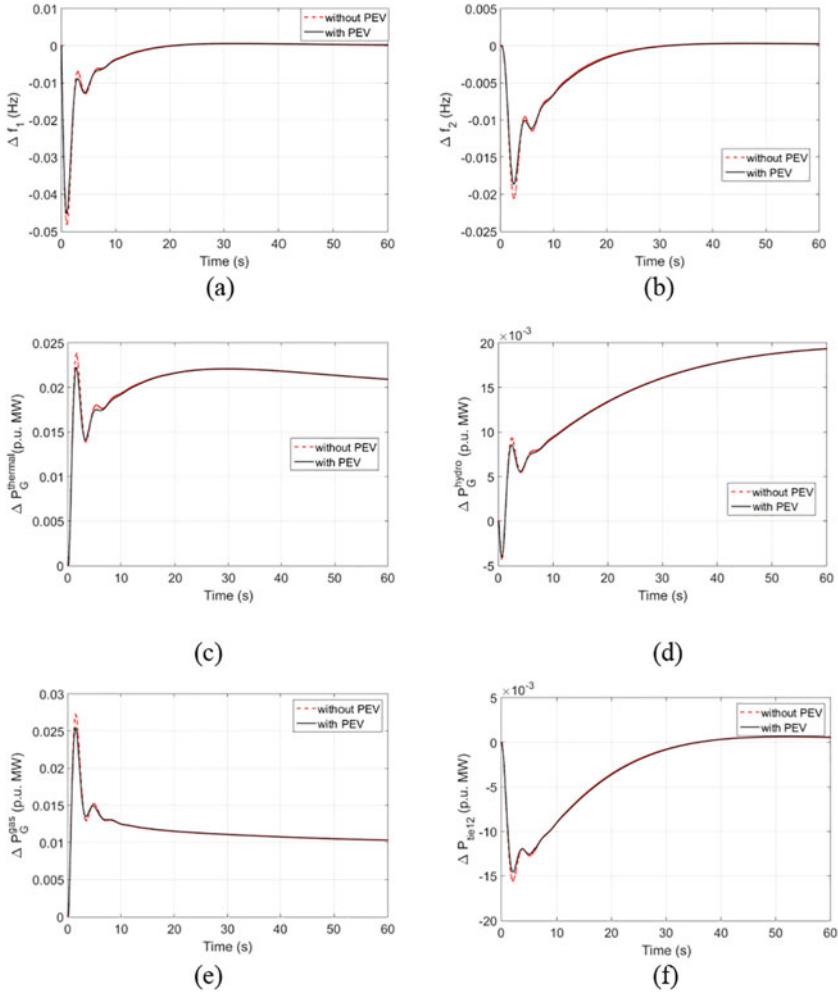


Fig. 9 **a** frequency deviation in Area-A, **b** frequency deviation in Area-B, **c** change in thermal power generation, **d** change in hydro power deviation, **e** change in gas power generation, and **f** change in tie line power deviation

4.2 Adaptive Droop Control

For a practical scenario, a typical 24-h weekday is considered. A 24-h load fluctuation curve is generated as shown in Fig. 10.

For V2G analysis, 50,000 PEVs operating in three different modes, i.e., charging, discharging, and idle mode, are integrated into Area-A. The number of PEVs varies in each mode depending upon the time of the day as per commute profile. Effectiveness of PEVs to suppress frequency deviations caused by load fluctuations and efficiency

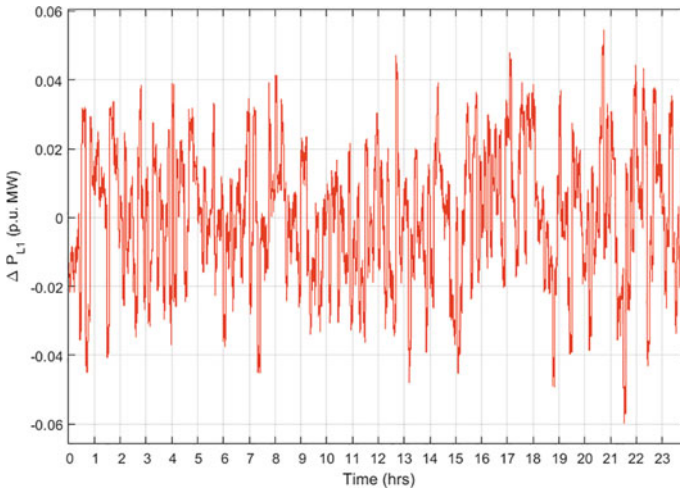


Fig. 10 Load fluctuation curve

of adaptive droop control to meet EV owners' demands are shown in Fig. 11 and the following sections, respectively.

Charging with Frequency Regulation As per the parking profile described in Fig. 7, all of the PEVs are at home from 22:00 to 06:00. The assumption is made that all PEVs parked at home are operating in charging mode. Figures 12 and 13 show real-time SOC levels of PEVs with different initial SOC levels and scheduled charging duration. PEVs switch to idle mode when scheduled SOC levels are reached.

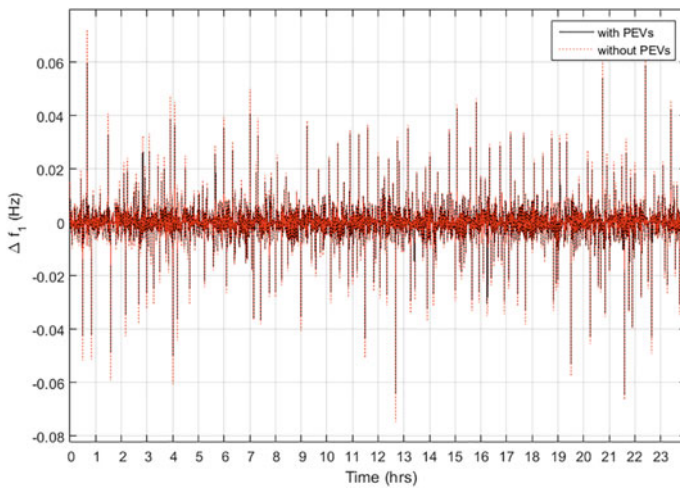


Fig. 11 Frequency deviation in area-A

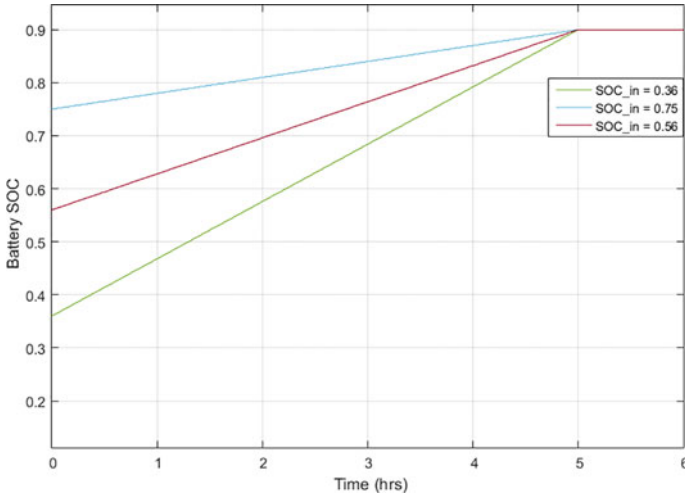


Fig. 12 Charging mode with different initial SOC and same charging times: real-time SOC

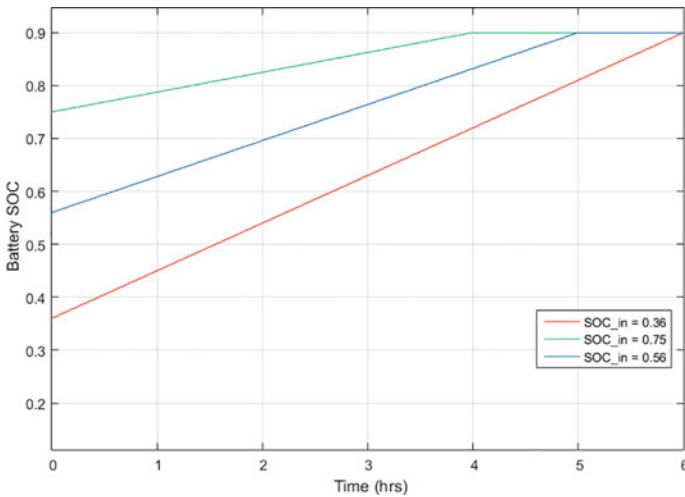


Fig. 13 Charging mode with different initial SOC and different charging times: real-time SOC

Variation in droop during charging and idle mode is shown in Fig. 14. Droop is constant till PEV is charging and starts varying when PEV enters idle mode. Variation in charging power of PEVs while participating in LFC is shown in Fig. 15.

Discharging Mode As mentioned in commute profile, 90% of total vehicles are in discharging mode from period of 07:00 to 22:00. SOC, variable droop, and V2G power of discharging vehicles are mentioned in Fig. 16, Fig. 17, and Fig. 18, respectively.

Fig. 14 Variation of charging droop

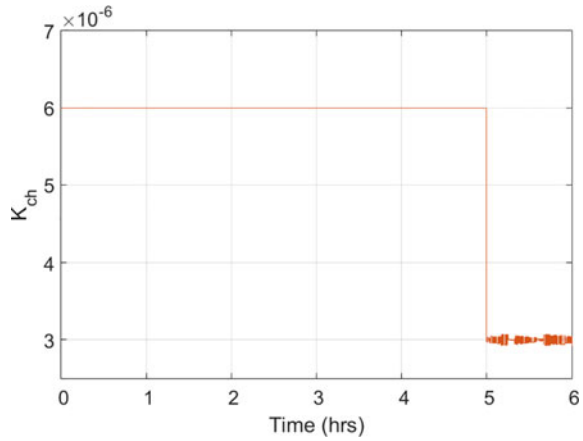
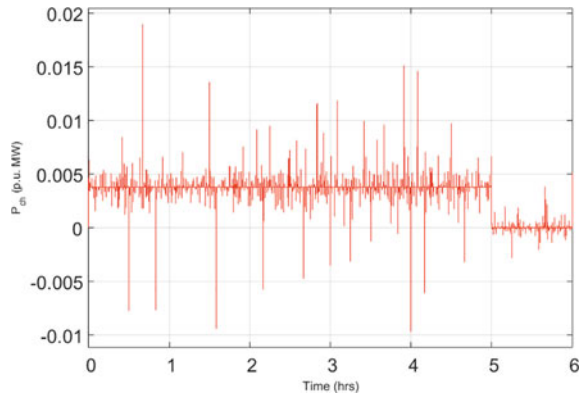


Fig. 15 V2G power of charging mode PEVs



Discharging droop continuously decreases as it approaches the scheduled value of holding SOC as shown in Fig. 17.

Discharging PEVs inject power to grid whenever system frequency decreases as shown in Fig. 18.

Idle Mode 10% of the total PEVs are in idle mode from the period of 07:00 to 22:00. SOC of idle mode PEVs varies around holding SOC value depending upon the increase or decrease in system frequency as shown in Fig. 19.

Droop of PEVs in idle mode, as shown in Fig. 20, varies around $0.5 * K_{max}$ as the variation of real-time SOC from holding SOC is small.

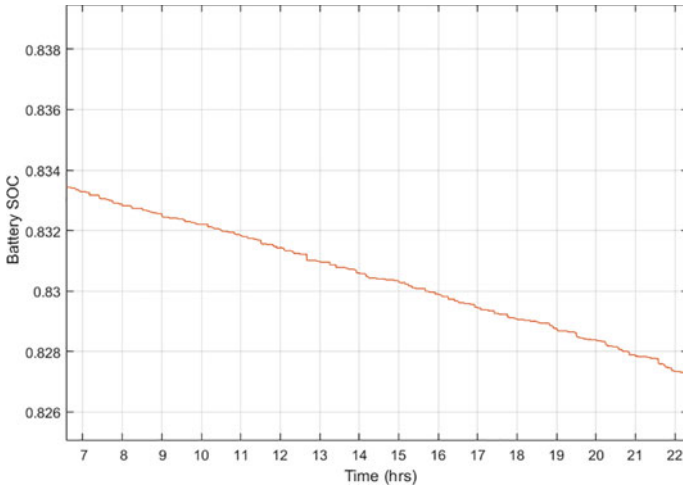


Fig. 16 Real-time SOC of discharging vehicles

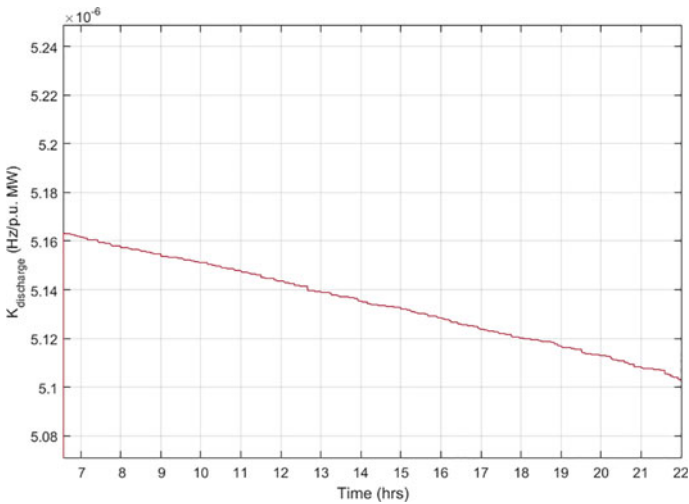


Fig. 17 Variation of discharging droop with time

5 Conclusion

Comparing the results of the scenario with PEVs and without PEVs in area-A, it is evident that PEVs can suppress frequency deviations and tie-line power deviations for the transient period, i.e., period of PFC. As PEVs are not used for secondary frequency control, settling time is not affected. For the proposed V2G method, results show that PEVs can charge, discharge, or hold their SOC limits as specified by the owner.

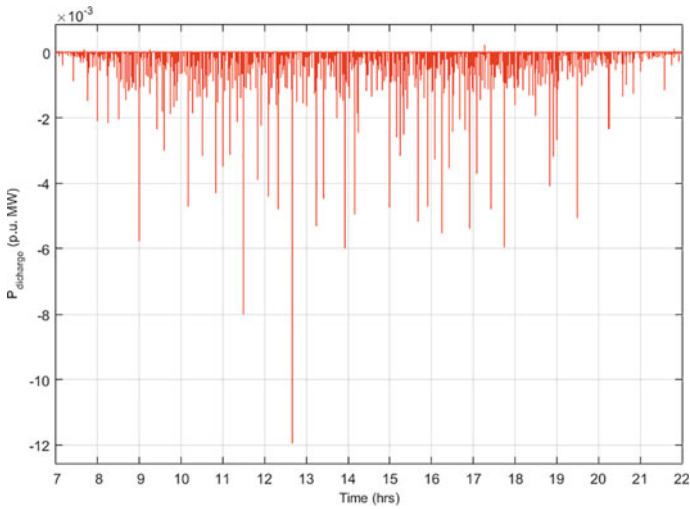


Fig. 18 V2G power of discharging mode PEVs

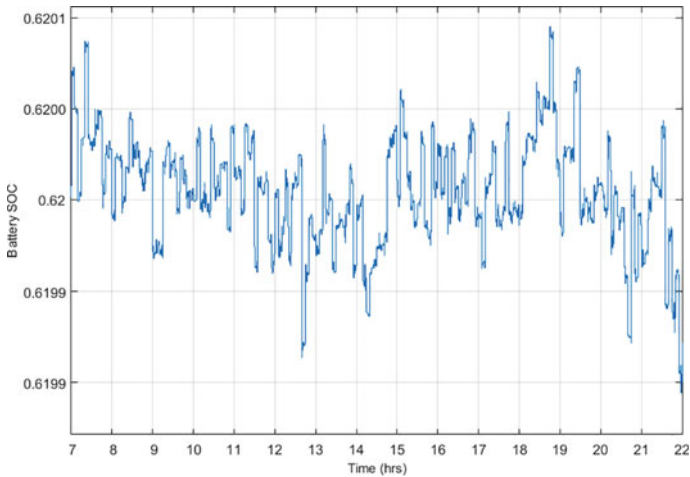


Fig. 19 Real-time SOC of idle mode PEVs

As shown in the results, PEVs in charging mode are able to charge up to specified SOC within the scheduled charging time and are able to participate in PFC. Once PEV is charged up to the specified SOC limit within the scheduled time and if EV is not plugged out, it switches from charging mode to idle mode to hold its final battery SOC level. During charging time, droop is held at constant maximum value. Real-time SOC and discharging droop decreases for discharging mode vehicles whenever an increase in load is observed. The battery is discharged up to the holding value of SOC. In idle mode PEVs, SOC is held at a specified value with small deviations

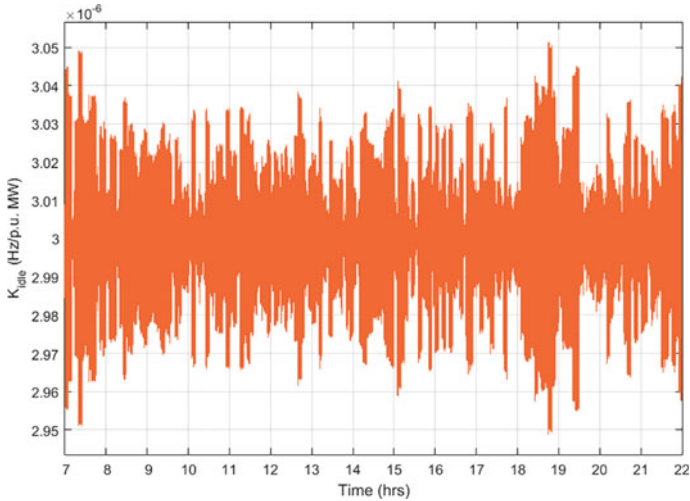


Fig. 20 Variable droop of idle mode PEVs

caused by load changes. Droop varies according to real-time battery SOC level. Results demonstrate the effectiveness of PEVs and adaptive droop control strategy to provide ancillary services to the grid as well as meeting EV owners' demands.

References

1. Datta A, Bhattacharjee K, Debbarma S, Kar B (2015) Load frequency control of a renewable energy sources based hybrid system. In: 2015 IEEE conference on systems, process and control (ICSPC), pp 34–38
2. Izadkhanst S, Garcia-Gonzalez P, Frías P, Bauer P (2017) Design of plug-in electric vehicle's frequency-droop controller for primary frequency control and performance assessment. *IEEE Trans Power Syst* 32(6):4241–4254
3. Yuan K, Song Y, Zhang Y, Huang Z, Sun C, Xing Z (2018) An energy storage capacity determination model of electric vehicle aggregator considering the real-time response state. In: 2018 IEEE International conference on energy internet (ICEI), pp 123–127
4. Zhang H, Hu Z, Xu Z, Song Y (2017) Evaluation of achievable vehicle-to-grid capacity using aggregate PEV model. *IEEE Trans Power Syst* 32(1):784–794
5. Falahati S, Taher SA, Shahidehpour M (2018) Grid secondary frequency control by optimized fuzzy control of electric vehicles. *IEEE Trans Smart Grid* 9(6):5613–5621
6. Masuta T, Yokoyama A (2012) Supplementary load frequency control by use of a number of both electric vehicles and heat pump water heaters. *IEEE Trans Smart Grid* 3(3):1253–1262
7. Rocha Almeida PM, Iria JP, Soares F, Lopes JAP (2017) Electric vehicles in automatic generation control for systems with large integration of renewables. In: 2017 IEEE power & energy society general meeting, pp 1–5
8. Almeida PR, Lopes JP, Soares F, Seca L (2011) Electric vehicles participating in frequency control: operating islanded systems with large penetration of renewable power sources. In: PowerTech, 2011 IEEE Trondheim. IEEE, pp 1–6

9. Chen C, Guo C, Man Z, Tong X (2016) Control strategy research on frequency regulation of power system considering electric vehicles. In: 2016 IEEE PES Asia-Pacific power and energy engineering conference (APPEEC), pp 2101–2105
10. Ota Y, Taniguchi H, Nakajima T, Liyanage KM, Baba J, Yokoyama A (2012) Autonomous distributed V2G (Vehicle-to-Grid) satisfying scheduled charging. *IEEE Trans Smart Grid* 3(1):559–564
11. Han H, Li Q, Lv Z, Yang X (2017) Energy storage frequency response control considering battery aging of electric vehicle. In: 2017 IEEE International conference on energy internet (ICEI), pp 72–76
12. Izadkhast S, Garcia-Gonzalez P, Frías P (2015) An aggregate model of plug-in electric vehicles for primary frequency control. *IEEE Trans Power Syst* 30(3):1475–1482
13. Liu H, Hu Z, Song Y, Lin J (2013) Decentralized vehicle-to-grid control for primary frequency regulation considering charging demands. *IEEE Trans Power Syst* 28(3):3480–3489
14. Melo NAC (2012) Potential of PEV to provide ancillary services in a smart grid context—the Portuguese case

Investigation on the Occurrence of Ferroresonance with the Variation of Degree of Transformer Core Saturation



Rajat Shubhra Pal  and Madhab Roy

Abstract Ferroresonance is a complex behavior of an electric network which if sustained, may be dangerous for power system equipment. Besides establishing mitigation techniques, researchers are also working on the prediction of ferroresonance occurrence in susceptible networks. The study requires appropriate mathematical model of transformer for computer simulations. A geometrical approach had been proposed by Rudenburg in the year 1950. But it was difficult to prove those proposals experimentally as ferroresonance may lead to complete destruction of the transformer and other equipment under test. Objective of this paper is to study on ferroresonance and observe the effect of variation of degree of saturation of transformer core materials on ferroresonance. For that, the transformer is approximated with its nonlinear dynamic model. With the help of that model, a Simulink block diagram has been developed in MATLAB. The Simulink model is examined under various circuit conditions, and a conclusion has been drawn that higher degree of saturation of the transformer core material increases the risk of ferroresonance to occur in the network.

Keywords Ferroresonance · Nonlinear model of transformer · Hysteresis model · Degree of saturation · Magnetizing curve

1 Introduction

The term ‘Ferroresonance’ was introduced for the first time in the literature in 1920 [1]. It refers to an oscillating behavior taking place in an electric network which contains a saturable inductance, a capacitor, a sinusoidal voltage source, and low or negligible losses. To extract maximum output, a transformer is normally designed to

R. S. Pal (✉)
Institute of Engineering & Management, Kolkata, India
e-mail: rajatshubhra.pal@iemcal.com

M. Roy
Jadavpur University, Kolkata, India

operate at the knee point of its core magnetizing curve. A slight variation in the circuit parameter may shift the operating point to the saturation region. Power networks are also comprised of a large number of capacitors like cables, series or shunt capacitor banks, voltage grading capacitors in circuit breakers. Those prepare environments under which ferroresonance can happen.

The main effect of ferroresonance is sustained overvoltage along with overcurrent which may be dangerous to the equipment in a power network [2]. The transformer voltages can increase up to 4–5 times over the normal ratings [3]. The large current during overcurrent can overheat the transformer windings and lead to insulation breakdown. Thus, prediction of the occurrence of ferroresonance is still relevant today.

In the year 1950, Rudenburg [4] proposed a graphical method, where the author discussed the effect on variation of different system parameters on the occurrence of ferroresonance. Hayashi [5] did more detailed work on it. After this, the researchers continue to improve the transformers model and study ferroresonance with the help of nonlinear mathematics [6].

Saturation of a transformer core depends on the core material used. Transformer core materials are selected depending on different design factors like core loss, efficiency, and cost. For example, the core losses in the amorphous alloy are several times lower than in grain-oriented silicon steel. Thus, the amorphous core is more efficient than the traditional one [7]. The degree of saturation of amorphous core is greater than the electrical steel [8]. This paper shows that the probability to occurrence of ferroresonance is higher for the core material having higher degree of saturation if other initial conditions match.

2 Rudenburg's Graphical Method

In his analysis [4], Rudenburg considers an electromotive force ' E ' of sinusoidal shape feeds a circuit consisting, as in Fig. 1, of a constant capacitance ' C ' in series with a coil ' L ', wound around a closed iron magnetic circuit (transformer at no load).

Fig. 1 Ferroresonance series circuit

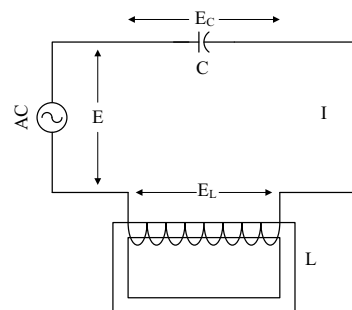
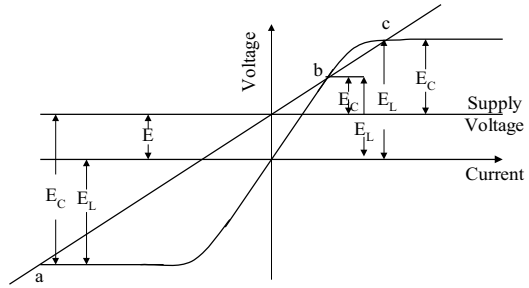


Fig. 2 Rudenberg's graphical method for coil and capacitor characteristics



As no-load condition is considered, the series resistance and leakage reactance of the circuit and the corresponding voltage drop can be neglected. So the voltage across the capacitance and the voltage across saturable inductance must balance each other.

$$E = E_L + E_C \tag{1}$$

The inductive voltage is proportional to the frequency and thus may be represented by

$$E_L = \omega f(I) \tag{2}$$

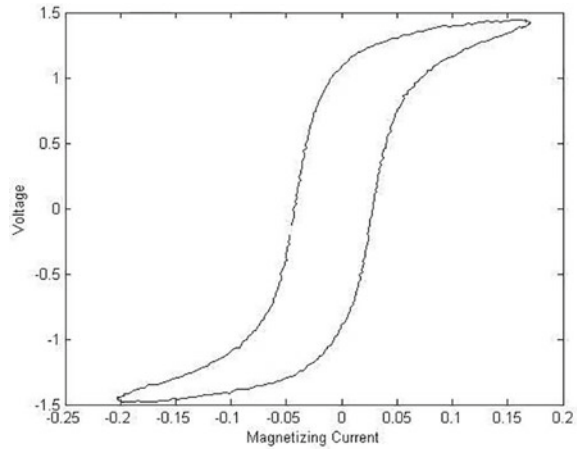
where $f(I)$ is a nonlinear function of current, which depends on the number of turns of the transformer winding, the dimensions, and magnetic characteristics of the iron core. The capacitor voltage is proportional to the current through it and inversely proportional to the product of frequency and capacitance. These relations give a simple graphical solution as shown in Fig. 2, where all the three voltages are plotted against the current.

The condenser line along with the supply voltage will intercept the inductor voltage line at three different points 'a', 'b', and 'c'. However, the points 'a' and 'b' indicate stable states of operation of the circuit, whereas point 'c' represents an unstable state. The point 'a' in the third quadrant represents stable state of operation of the circuit with large voltages (E_L and E_C) across the circuit elements. When an appropriate magnitude of any circuit parameter shifts the operating point in nonlinear region of magnetizing characteristics, the ferroresonance oscillations may occur if the other circuit conditions match.

3 Modeling of Nonlinear Characteristics of Transformer

The most critical part in this ferroresonance study is to find out an appropriate model of the transformer's core characteristics. To represent a practical transformer in simulation correctly, all of the parameters of the transformer are to be identified [9]. In most

Fig. 3 Hysteresis loop as obtained from experimental setup



of the simulation studies, the core losses are represented by a variable resistor. The saturation behavior of the transformer may be represented by a nonlinear inductor. The mathematical equation can be formed based on the transformer's B-H curve.

A special laboratory arrangement has been prepared [10], and from there, the data for hysteresis loop has been extracted (Fig. 3).

Rating of the single-phase transformers whose B-H loops were recorded as below:

Transformer: Single phase, 450 VA, 0–250–433 V/0–250–433 V/2 V, 50 Hz, major insulation 25 kV level.

Using the curve fitting tool the B-H loop is approximated with a nonlinear polynomial relation as below.

$$i_{\lambda} = a\lambda + b\lambda^n \quad (3)$$

Here λ = flux linkage, i_{λ} = magnetizing current of the transformer. The constants a and b are taken as 0.015 and 0.013, respectively. The power n is the degree of saturation of the magnetizing curve. Saturation is a state of a material where flux density B reaches its maximum possible value. At this stage, if field intensity is increased further, it will have no effect on the flux density. In the mathematical model, Eq. (3) n will define how quickly the transformer core will get saturated. Figure 4 shows the plot of (3) for $n = 7$.

Figure 5 shows the plot of (3) for different values of n . Here n is varied from 3 to 19 and the magnetizing curve for each plotted on the same graph to indicate how it changes with the variation in the degree of saturation. Higher the value of n , more quickly the core gets saturated.

Fig. 4 Simulated current versus flux linkage for $n = 7$

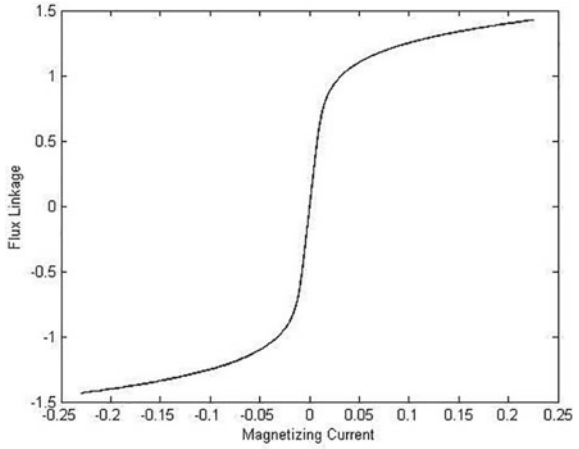
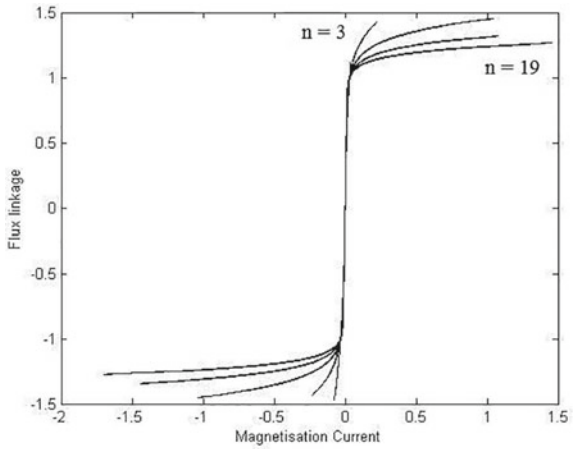


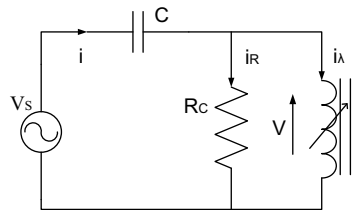
Fig. 5 Magnetizing curves for different n



4 Development of Ferroresonance Nonlinear Model

Figure 6 shows the circuit taken for ferroresonance analysis [11]. This consists of an alternating voltage source V_s , a capacitance C in series, a parallel resistance R_c

Fig. 6 Model circuit for ferroresonance study



representing core loss, and a saturable inductance. It is expected for the transformer to run at no or very low load conditions to observe ferroresonance. So series components of transformer's equivalent circuit are neglected.

The KVL equation for the circuit shown in Fig. 6 can be

$$V_s = V_C + V \quad (4)$$

Differentiating (4) with respect to time and rearranging one can obtain the following second-order nonlinear differential equation

$$\frac{d^2\lambda}{dt^2} = \frac{dV_s}{dt} - \frac{1}{C} \left(\frac{v}{R} \right) - \frac{1}{C} (a\lambda + b\lambda^n) \quad (5)$$

Equation (5) is nonlinear differential equation as the dependent variable λ contains a term with power n . Based on (5), a digital model is prepared. Validation of this model is shown in the paper [12], where authors compare the output of the digital simulation with Rudenburg's predictions.

5 Ferroresonance Results and Analysis

Occurrence of ferroresonance in a nonlinear circuit mainly depends on the value of circuit parameters, magnitude, and switching instant of supply voltage and initial conditions [11]. Ferroresonance and its dependency on degree of saturation have been studied and analyzed by simulation of (5). In this work, mainly time domain simulations of ferroresonance—voltage, current, and flux are presented.

With the increased value of the power n in (3), the degree of saturation of the magnetizing curve increases. Study has been made with different degree of saturation starting from $n = 1, 3, 5 \dots$ keeping input voltage and other parameter constant. Up to $n = 7$ system shows no ferroresonance. It can be observed from Fig. 7 which shows the high spike in transformer and capacitor voltage decay down after 2 or 3 cycles.

With $n = 9$, system suddenly jumps to sustained ferroresonance with increased per unit voltage and current as shown in Fig. 8. With further increase of the parameter n , system continues to show ferroresonance output if other parameters remain constant. Such variation of transformer and capacitor voltages along with the degree of transformer core saturation is shown in Fig. 9. A clear jump from non-ferroresonance state to ferroresonance state can be observed. Figure 9 also shows that the circuit behaves as an inductive circuit at normal condition and becomes capacitive under sustained ferroresonance. The study matches with Rudenburg's findings as described in Fig. 2.

Figure 10 shows the variation of magnetizing current with the degree of saturation. It can be observed from the simulation that at ferroresonance the magnetizing current can jump to almost 17–20 times of its base value.

These can be explained as follows. With small value of n , such as n_1 as shown in Fig. 11, there will be one stable operating point in the first quadrant which is

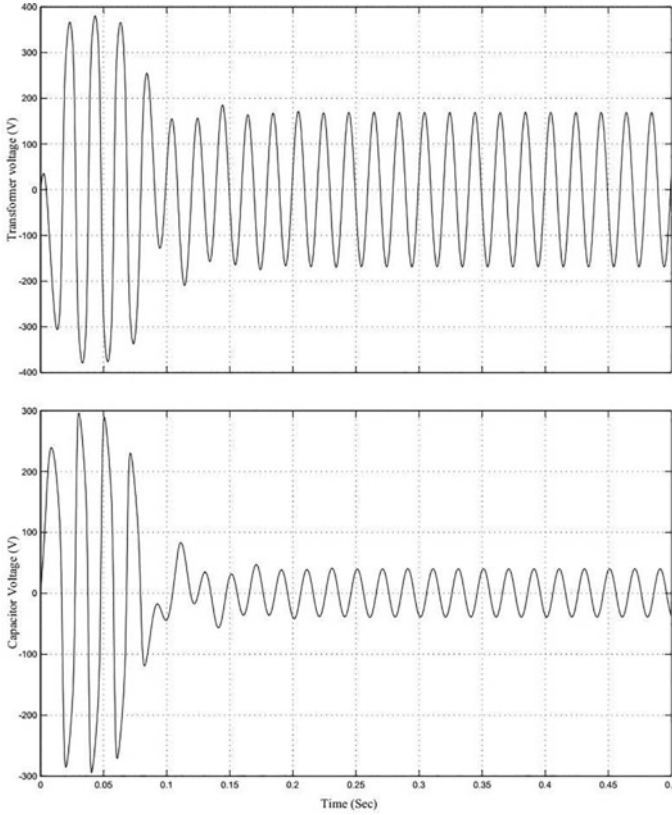


Fig. 7 Voltage across transformer (above) and voltage across capacitor (below) with $n = 7$

b_1 . But with a higher value of n , e.g., n_2 , no operating point is possible in quadrant 1. Whereas in quadrant 3, an operating point a_2 is possible which will produce a ferroresonance in the system as described by Rudenberg [4].

6 Conclusion

In this paper, the nonlinear dynamic model of the transformer is adopted to build up a ferroresonance circuit. Then from the second-order nonlinear differential equation, a Simulink model was build up in the MATLAB [13]. That model was examined under different degree of core saturation. Other circuit parameters like supply voltage, capacitance, frequency, and resistance have been kept constant. Variation of voltage across capacitor and voltage across transformer along with the magnetizing current is observed carefully. Observations show that increase of degree of saturation also

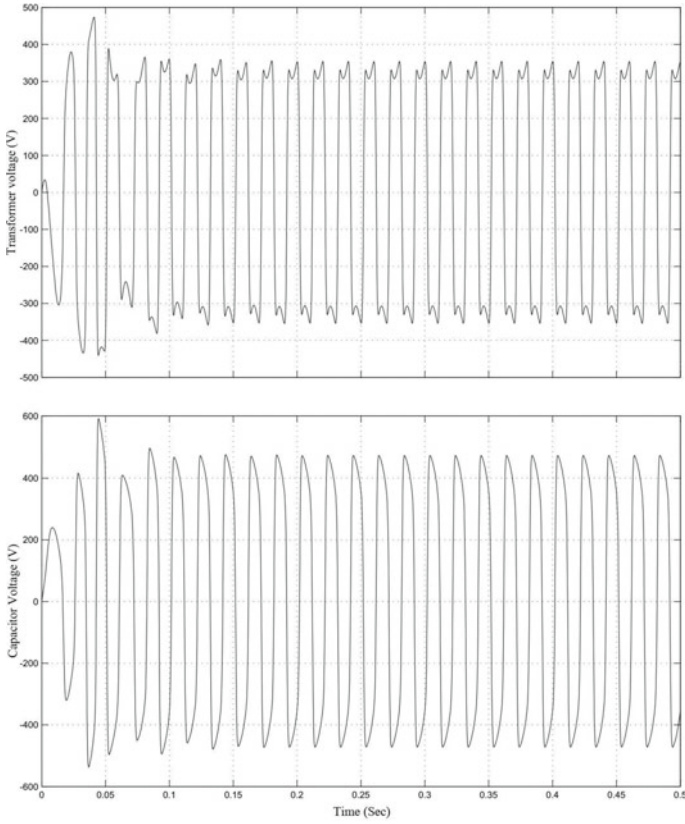


Fig. 8 Voltage across transformer (above) and voltage across capacitor (below) with $n = 9$

Fig. 9 Variation of p.u. voltages with degree of core saturation

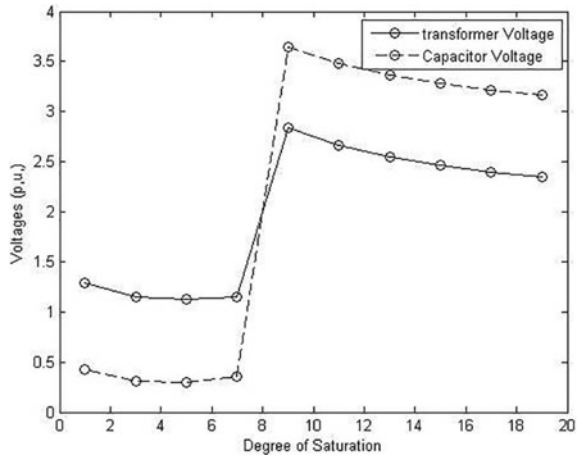


Fig. 10 Variation of p.u. transformer current with degree of core saturation

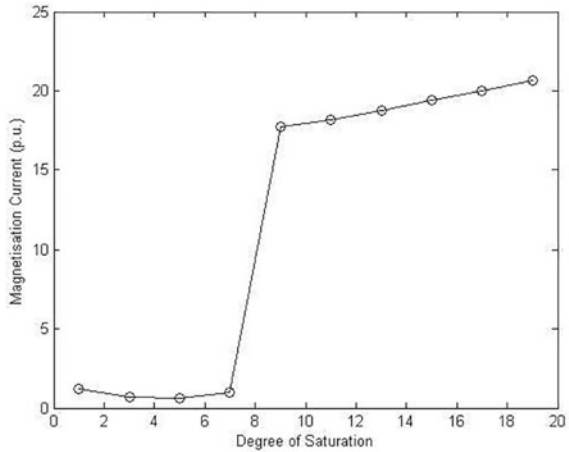
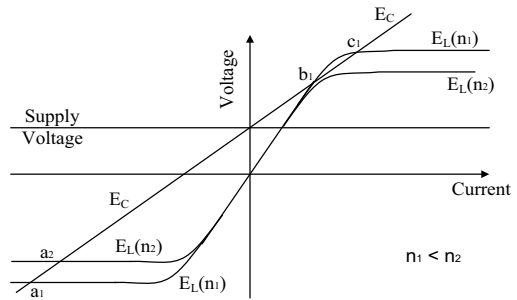


Fig. 11 Variation with different degree of core saturation



increases the probability of the occurrence of ferroresonance in the circuit. A comparison of the output result with Rudenburg’s methods [4] is also incorporated, and it has been seen that the experimental results are well-matched with the theoretical predictions.

References

1. Boucherot P (1920) Éxistence de Deux Régimes en Ferrorésonnance. Rev Gen de L’Élec 8(24):827–828
2. Tsao T-P, Ning C-C (2006) Analysis of ferroresonant overvoltages at Maanshan nuclear power station in Taiwan. IEEE Trans Power Delivery 21(2):1006–1012. <https://doi.org/10.1109/TPWRD.2005.860268>
3. Ray Crane D, Walsh GW (1988) Large mill power outages caused by potential transformer ferroresonance. IEEE Trans Ind Appl 24(4):635–640. <https://doi.org/10.1109/28.6115>
4. Rudenberg R (1950) Transient performance of electric power system. McGraw-Hill, New York, pp 642–656

5. Hayashi C (1985) *Nonlinear oscillations in physical systems*. Princeton University Press, Princeton-New Jersey
6. Slow Transient Task Force of the IEEE Working Group on Modeling and Analysis of System Transients Using Digital Programs (2000) Modeling and analysis guidelines for slow transients—part III: the study of ferroresonance. *IEEE Trans Power Delivery* 15(1):255–265
7. Chang H, Chun Y, Yeong HCh, Faa J, Chao M, Jau GL (2013) Effect of Magnetostriction on the core loss, noise, and vibration of fluxgate sensor composed of amorphous materials. *IEEE Trans Magn* 49(7). <https://doi.org/10.1109/TMAG.2013.2248702>
8. Njafi A, Iskender I (2015) Impacts of amorphous core to reduce the losses in distribution transformer based on time stepping finite element method. *Int J Tech Phys Probl Eng (IJTPE)* 7(3):53–57
9. Mork BA, Gonzalez F, Ishchenko D, Stuehm DL, Mitra J (2007) Hybrid transformer model for transient simulation—part 1: development and parameters. *IEEE Trans Power Del* 22(1):248–255. <https://doi.org/10.1109/PES.2007.385620>
10. Patel B, Das S, Roy CK, Roy M (2008) Simulation of ferroresonance with hysteresis model of transformer at no-load measured in laboratory In: *IEEE region 10 conference, TENCON 2008*. <https://doi.org/10.1109/TENCON.2008.4766386>
11. Roy M, Roy CK (2009) A study on ferroresonance with a varying initial conditions using a nonlinear model of transformer. In: *Proceedings of third international conference on power systems*, no. 213. India. <https://doi.org/10.1109/ICPWS.2009.5442728>
12. Pal RS, Roy M (2021) Study and verification of ferroresonance simulated with Rudenburg's method. In: *2021 Innovations in energy management and renewable resources (52042)*, pp 1–5. <https://doi.org/10.1109/IEMRE52042.2021.9386880>
13. MATLAB, MathWorks, Online: <https://in.mathworks.com/>

Application of Modified Artificial Bee Colony Algorithm for Optimization of Reactive Power



Rohini Mahadik, A. R. Thorat, and Iranna Korachagaon

Abstract Reactive power is beneficial to a power system's voltage stability. As a result, optimizing reactive power is required to enhance voltage profile. RPO also aids in the minimizing of active power losses while being compliant with all limitations. Honey bees' seeking behaviour is influenced by the ABC algorithm. Honeybee behaviour is used to a variety of RPO challenges. In this study, standard ABC is changed by using a weighted technique to improve exploitation capability. This updated ABC approach is used to solve the RPO problem as well as standard benchmark functions. For both regular ABC and MABC, the benchmark functions are tried with different dimensional sizes and the results are studied and compared. MABC is determined to be more successful than normal ABC for the majority of activities. To prove its effectiveness, the modified method is implemented on standard IEEE 30 and 57 test bus systems. Data from the literature is compared to the findings.

Keywords Optimization · Modified ABC algorithm · Weighted method · Benchmark functions · Reactive power optimization (RPO)

Nomenclature

ABC	Artificial Bee Colony
GABC	Global best guided artificial bee colony
MABC	Modified artificial bee colony
RPO	Reactive power optimization

R. Mahadik (✉) · A. R. Thorat
Electrical Department, Rajarambapu Institute of Technology, Uran Islampur, Maharashtra, India
e-mail: rohini mahadik1035@gmail.com

I. Korachagaon
Electrical Department, TCE, Gadag, Karnataka, India

1 Introduction

In power systems, reactive power is a crucial feature. Reactive power generation and distribution have a significant impact on the performance, efficiency and reliability of power systems [1]. The voltage in power system sags down when there isn't enough reactive power. This drop in voltage affects power delivered to load through transmission lines. Hence, reactive power is essential for improving voltage stability and to avoid voltage sag in power systems [2].

Optimization deals with the minimization of cost of production and maximization of efficiency of production. Reactive power optimization is essential for reduction in active power losses [3]. RPO helps in voltage profile improvement and for minimization of real power losses under various operating conditions.

There are different methods that can be used for RPO like artificial neural networks, Evolutionary programming,, Genetic Algorithm, Particle Swarm Optimization Algorithm and Artificial Bee Colony Algorithm [4]. As compared to other algorithms, ABC algorithm is simply effective in solving non-linear equation of reactive power. The ABC algorithm is more effective as compared to other algorithms. Also, ABC algorithm operates well in finding superior solutions of the objective functions. Hence, we have chosen ABC algorithm with modified method to study its exploitation capability for RPO problems. We are going to implement modified ABC with weighted method on benchmark functions. With the outcomes of benchmark functions, we will be able to understand the possibility of use of modified weighted method of ABC algorithm for reactive power optimization problems [4]. Further, this modified ABC approach is tested on IEEE 30 and 57 standard systems for RPO problems. Obtained outcomes of RPO problems with modified ABC are compared with existing results available in literature data.

The rest paper is organized as follows. In Sect. 2, information about ABC algorithm and its literature review is described. Section 3 gives description of modified ABC approach and process with flow chart. Section 4 describes mathematical expression of objective function for reactive power optimization problems with constraints. Section 5 includes experimental setup and results for the modified approach on benchmark functions. It includes simulation results of objective function of RPO problem on IEEE test bus system. The modified approach and its experimental results with comparison are concluded in Sect. 6.

2 Related Work

2.1 Artificial Bee Colony Algorithm

This is an optimization technique that stimulates finding behaviour of honeybees. The technique is implemented to various practical problems.

Employed bees, onlooker bees and scout bees are the three sorts of bees that exist. These three types worked together to find better solutions. The employed bee searches for food sources and informs onlooker bees. The onlooker bee continued to work on these selected food sources in order to locate better ones. Fitness values of sources determine the quality of food sources. The scout bee generates a new solution (food source) if limited iterations cannot give better fitness value of existing food source. This new solution generated by scout bee is used to update old solution.

Assume that $X_i = \{x_{i,1}, x_{i,2}, \dots, x_{i,D}\}$ is the i th solution where $i = 1, 2, 3, \dots, N$. A solution X_i is selected by each employed bee and search is conducted in the neighbourhood to find new solution V_i [4].

$$v_{i,j} = x_{i,j} + \emptyset_{i,j} \cdot (x_{i,j} - x_{k,j}) \tag{1}$$

where $j \in [1, D]$ is a dimensional index chosen randomly. X_k is an arbitrarily selected solution and $k \in [1, N]$. The weight $\emptyset_{i,j}$ is selected arbitrarily and value is between $[-1.0, 1.0]$.

We know that equation $\text{Min } f(x)$ is used by employed bees to find food sources. Further sharing of information of found food sources is done from employed bees to onlooker bees. Based on quality of found food sources, onlooker bees select some superior food sources for further search.

The selection method is as follows:

$$p_i = \frac{fit_i}{\sum_{i=1}^N fit_i} \tag{2}$$

where fit_i indicates fitness value of i th solution X_i . In standard ABC, the same equation $\text{Min } f(x)$ is used by the onlooker bees to find superior solution (food source).

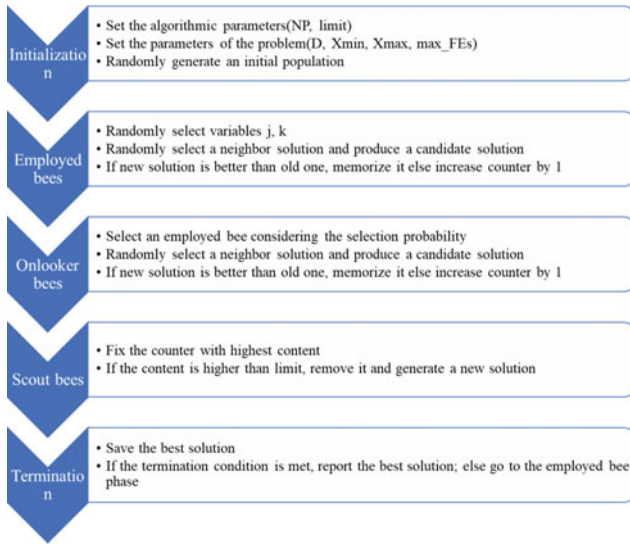
If limit iterations fail to improve the fitness value of an existing food source, the scout bee creates a new solution (food source). Scout bee generates a new solution that is utilized to update an existing one.

$$x_{i,j} = low_j + rand_j \cdot (up_j - low_j) \tag{3}$$

where $[low_j, up_j]$ is the frame of constraint and $rand_j$ is a randomly generated values between $[0, 1]$.

The standard ABC algorithm process is mentioned in following flowchart.

Flowchart 1. ABC Algorithm Process



2.2 Literature Review

Various benchmark functions and practical problems can be resolved using ABC algorithms. There were different types of algorithms proposed along with standard algorithm. The literature review of this work is summarized as follows.

Ozturk et al. [2] have proposed the ABC technique to obtain multi-objective RPO. IEEE 10 bus system is used for implementation of multi-objective RPO with ABC technique. In this paper, minimization of active power losses is achieved. Along with it, cost optimization and voltage quality are achieved. Ayan and Kılıc [5] have proposed ABC algorithm technique. It is implemented on standard IEEE 30 and 118-bus systems and further results are analyzed. They have discussed about why ABC algorithm is advantageous over other types of algorithm (like genetic algorithm and differential evolution). In this paper, ORPF supported ABC algorithm technique is discussed. It is implemented to reduce active power loss. The effectiveness and computing efficiency of the proposed technique for ORPF problems are verified and investigated. MATLAB software is used for result analysis.

Ettappan et al. [6], have proposed ABC algorithm technique with approach of optimal reactive power dispatch. This method is used for reduction in active power losses and voltage stability improvement. Simulations of standard IEEE 30 and 57 test bus are used for RPO problem study. Results obtained are compared with other methods.

Thorat A. R. [3] have proposed an approach of gbest-Guided ABC Algorithm for RPO problems. This algorithm is applied on IEEE test bus systems and comparative analysis of obtained results is done. Standard IEEE 30, 57 and 118 test bus systems

are used for analysis on MATLAB software. The analysis shows that gbest-Guided ABC is superior over standard ABC.

Cao et al. [4] have proposed a modified ABC to increase efficiency of GABC method. In this paper, they proposed a modified approach to increase exploitation capability. The modification is done at onlooker bee phase in search equation. Modified approach of ABC algorithm is implemented on different benchmark functions. The obtained results are compared with other algorithms.

Zhu and Kwong [7] mentioned gbest-Guided ABC algorithm in paper. It is implemented for numerical function optimization. The proposed gbest-guided method increases the exploitation capability. The method is implemented on benchmark functions with suitable parameters. Results show that GABC outperforms ABC algorithm. Li et al. [8] proposed hybrid differential evolution algorithm along with ABC algorithm. It is applied on reactive power optimization problems. Results of simulation show this method finds better solutions and having more convergence speed and same method is suitable for RPO problems.

3 Modified ABC Approach

Standard ABC possesses good exploration but it shows poor exploitation. Poor exploitation results in slow convergence speed. Hence, exploitation capability of ABC can be improved by using some different ABC variants. One of them is GABC—global best guided ABC— G_{best} is introduced in search equation and expected that G_{best} helps to find best solution.

In GABC, search equation is given by

$$v_{i,j} = x_{i,j} + \vartheta_{i,j} \cdot (x_{i,j} - x_{k,j}) + \varphi_{i,j} \cdot (G_{\text{best}} - x_{i,j}) \quad (4)$$

where G_{best} stands for the global best solution obtained using GABC algorithm. The weight $\vartheta_{i,j}$ is a selected randomly between $[0, C]$. We have chosen value of $C = 1.5$ [7] and it is a predefined value.

In G_{best} guided ABC algorithm, we are making use of Eq. (4) to find new solutions. The probability of each solution is derived by onlooker bees. These probabilities are used to make further searches and find better solutions. To find new solutions, same Eq. (4) is used by onlooker bees.

In standard ABC algorithm, the same equation has been used in employed and onlooker bee phase to find new solutions. As a result of it, employed bees possess good exploration capability and onlooker bees show lack of exploitation capability. Hence, we are choosing a modified version to study its exploitation capability for RPO problems. In modified approach, we are using two search phases: exploration and exploitation. This approach will help to improve exploration capability by employed bees. Onlooker bees help to improve exploitation using modified approach. To implement modified approach, we are making use of a new solution-finding equation with onlooker bees [4].

$$v_{i,j}^* = a_1 \cdot x_{i,j} + a_2 \cdot G_{\text{best},j} + a_3 \cdot (x_{k,j} - x_{i,j}) \quad (5)$$

where X_i stands for current solution, G_{best} denotes global best solution and X_k is arbitrarily generated solution for which ($i \neq k$). Weights w_1 , w_2 and w_3 are three random values and $a_1 + a_2 + a_3 = 1$. Firstly, we need to generate three values a_1 , a_2 and a_3 in the range $[0, 1]$. Then we use following Eqs. (6), (7) and (8) to generate new weights.

$$a_1 = \frac{w_1}{w_1 + w_2 + w_3} \quad (6)$$

$$a_2 = \frac{w_2}{w_1 + w_2 + w_3} \quad (7)$$

$$a_3 = \frac{w_3}{w_1 + w_2 + w_3} \quad (8)$$

In standard ABC algorithm, slow convergence speed can be obtained by change in one dimension of parent solutions. In this paper, the MR parameter is used in modified method which is useful for controlling the number of updating dimensions. For each food source solution, all dimensions j , ($j = 1, 2, \dots, D$) are checked. If $\text{rand}_j < \text{MR}$, then Eq. (5) is used to revise $v_{i,j}$. Then, new search equation is given by

$$v_{i,j} = \begin{cases} v_{i,j}^*, & \text{if } \text{rand}_j < \text{MR} \\ v_{i,j}, & \text{Otherwise} \end{cases} \quad (9)$$

where MR is an already defined parameter of probability, rand_j is a randomly generated value between $[0,1]$ for the j th dimension. The value $v_{i,j}^*$ is as mentioned in Eq. (5).

Step-wise process for modified ABC method is as follows [4].

Step 1. Make selection of N solutions randomly. Fitness values of N solutions are calculated. Then, put $\text{FEs} = N$ (no. of fitness evaluations and it is equal to no. of solutions generated).

Step 2. For every X_i solution, a latest solution V_i is derived by using Eq. (4). Calculate fitness value of V_i and further $\text{FEs} = \text{FEs} + 1$. Superior value between X_i and V_i is selected as new X_i . Following to this if $f(V_i) < f(X_i)$, then $\text{trial}_i = 0$; otherwise $\text{trial}_i = \text{trial}_i + 1$.

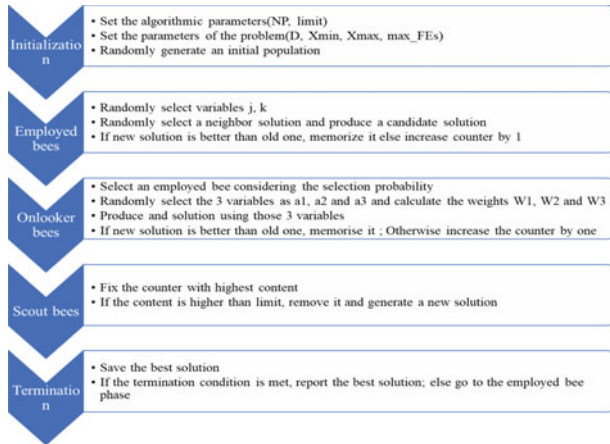
Step 3. Calculate the probability p_i consistent with Eq. (2). If X_i is chosen, then V_i is derived by Eq. (9). Fitness value of V_i is calculated and $\text{FEs} = \text{FEs} + 1$. Superior value between X_i and V_i is selected as new X_i . If $f(V_i) < f(X_i)$, then $\text{trial}_i = 0$; otherwise $\text{trial}_i = \text{trial}_i + 1$.

Step 4. Solution X_i is replaced by Eq. (4), if $\max(\text{trial}_i) > \text{limit}$.

Step 5. Fix $t = t + 1$. If $\text{FEs} < \max\text{FEs}$, then go to Step 2; else terminate algorithm.

We have summarized process for modified ABC algorithm in the flowchart as below.

Flowchart II. Modified ABC Algorithm Process



In comparison with standard ABC algorithm, modified ABC approach makes change in the search equation at onlooker bees phase. The weights a_1, a_2 and a_3 introduced in the modified method make helps to improve capability of standard ABC algorithm. So, in terms of computational time complexity, it is same for both MABC and ABC.

4 Mathematical Expression of Objective Function for RPO

4.1 Objective Function

Main aim of RPO is active power loss minimization. It is given by following Eq. (10). The control variables selected are as follows- capacity of reactive power compensation device, tap position of on-load tap changer and terminal voltage of the generator. PV bus reactive power output and PQ bus voltage are chosen as state variables.

$$\min F = \min \sum_{k=1}^n G_k(i, j) [u_i^2 + u_j^2 - 2u_i u_j \cos(\theta_i - \theta_j)] \quad (10)$$

where n stands for total no. of branches, $G_k(i, j)$ denotes conductance of branch k connecting bus i and j , θ_i and θ_j denote phase angles of bus i and j , voltages of bus i and j are denoted by u_i and u_j [8].

4.2 Equality Constraints

Equations (11) and (12) show power flow balance equations. Equation (11) is of active power and Eq. (12) is of active power and reactive power. The same equations are used as equality constraints in optimization problems.

$$P_i = u_i \sum_{j \in N_i} u_j (G_{ij} \cos \delta_{ij} + B_{ij} \sin \delta_{ij}) \quad (11)$$

$$Q_i = u_i \sum_{j \in N_i} u_j (G_{ij} \sin \delta_{ij} - B_{ij} \cos \delta_{ij}) \quad (12)$$

where u_i is voltage of bus i and u_j is voltage of bus j , P_i denote active power of bus i and Q_i denote reactive power of bus i . Conductance and susceptance of bus i and j are denoted by G_{ij} and B_{ij} , respectively. δ_{ij} denotes voltage phase angle difference between bus i and j . $i \in N$, N denotes the set of all buses in distribution system.

4.3 Inequality Constraints

The both state variable constraints (13) and control variable constraints (14) fall into inequality constraints.

$$\left. \begin{aligned} Q_{Gi \min} \leq Q_{Gi} \leq Q_{Gi \max} \\ U_{i \min} \leq U_i \leq U_{i \max} \end{aligned} \right\} \quad (13)$$

$$\left. \begin{aligned} U_{Gi \min} \leq U_{Gi} \leq U_{Gi \max} \\ T_{i \min} \leq T_i \leq T_{i \max} \\ Q_{Ci \min} \leq Q_{Ci} \leq Q_{Ci \max} \end{aligned} \right\} \quad (14)$$

where Q_{Gi} denotes reactive power output of generator bus G_i . U_i stands for voltage load bus i . The voltage of generator bus G_i is denoted by U_{Gi} and the ratio of on-load tap changer is denoted by T_i . Q_{Ci} stands for reactive power compensation capacity of reactive power device C_i .

5 Experimental Verification

This section includes two parts—(1) Experimental verification of MABC algorithm on standard benchmark functions. The outcomes are compared with standard ABC algorithm. (2) Modified method of ABC is implemented on standard IEEE 30 and 57 test bus systems to check its effectiveness. The outcomes are analyzed with data from

Table 1 Benchmark functions used in experiments

Benchmark functions		
Mathematical definition	Search scope	Opt
$f_1(x) = \sum_{i=1}^D x_i^2$	[-100, 100]	0
$f_2(x) = \sum_{i=1}^{D-1} 100(x_i^2 - x_{i+1}^2) + (x_i - 1)^2$	[-30, 30]	0
$f_3(x) = \sum_{i=1}^D (x_i^2 - 10\cos(2\pi x_i)) + 10$	[-5.12, 5.12]	0
$f_4(x) = \sum_{i=1}^D (\frac{x_i^2}{4000} - \prod_{i=1}^D \cos(\frac{x_i}{\sqrt{i}}) + 1)$	[-10,10]	0

existing literature. The comparative analysis of the outcomes reflects the effectiveness of MABC algorithm. The outcomes are tested in MATLAB software.

5.1 Experimental Setup

The performance of different optimization algorithms is checked by using various benchmark functions. We have to check performance of MABC algorithm with the help of four benchmark functions. Here four benchmark functions are selected for testing in experiments. Table 1 indicates the parameters used for benchmark functions such as their global optimum, mathematical definition, search scope [4]. The selected benchmark functions are minimization problems. We have tested all benchmark functions on both MABC and standard ABC algorithms in MATLAB software. The above-mentioned parameters are set to particular values for all benchmark functions and run both algorithms in MATLAB. The outcomes of algorithms are compared in respective sections.

Here, dimension D has been set to 10, 30 and 50, respectively. Algorithms are run with benchmark functions for each dimension and obtained best optimum solution. The obtained results on both algorithms (MABC and ABC) are compared.

To have better clarity in outcomes, we are using same parameters and values in both algorithms. The number of employed bees and onlooker bees is equal in this case, at 50. For every benchmark function, each algorithm is going for 30 trials. For ABC and MABC, the parameters N, limit and maxFEs values are as follows, respectively - 50, 100 and 1.5E + 05. As mentioned earlier, parameter C = 1.5 and MR to be fixed to 0.3 in MABC [4]. For each value of D, outcomes are mentioned in respective table. The superior outcome is mentioned in Bold in each table.

5.2 Outcomes for D = 10

With D = 10, both standard ABC and MABC algorithms are run on benchmark functions. Table 2 represents the outcomes obtained on the benchmark set for D = 10.

Table 2 Outcomes for $D = 10$

Functions	Standard ABC	Modified ABC
f_1	1.4189	0.924
f_2	2.4769	2.4977
f_3	1.1603	1.0458
f_4	3.7631	3.2357

Bold values indicate superior results obtained for particular function using mentioned algorithms

Table 3 Outcomes for $D = 30$

Functions	Standard ABC	Modified ABC
f_1	1.1223	0.5008
f_2	0.5008	6.0192
f_3	2.1115	0.3315
f_4	7.4462	0.0134

Bold values indicate superior results obtained for particular function using mentioned algorithms

We get to know that modified ABC method gives better solutions than standard ABC except for function f_2 . For function f_2 , modified ABC drops into local minima and find inferior solutions than standard ABC algorithm. It shows that the modified ABC strategy is not appropriate for this problem. For function f_3 , MABC outperforms on standard ABC and algorithm converge to global optimum. Modified ABC shows much superior functioning than ABC. Also, MABC shows much faster convergence speed than standard ABC.

5.3 Outcomes for $D = 30$

With $D = 30$, both standard ABC and MABC algorithms are run on benchmark functions. Table 3 gives outcomes obtained for $D = 30$. For function f_3 , MABC finds the overall minimum, but ABC falls into local minimum range. For function f_2 , ABC shows better solutions than MABC. It seems that modified approach may limit the search for this function. This also shows that MABC converges much faster than standard ABC on function f_1 .

5.4 Outcomes for $D = 50$

With $D = 50$, both standard ABC and MABC algorithms are run on benchmark functions. Table 4 shows the outcomes obtained when $D = 50$. With the increase in

Table 4 Outcomes for $D = 50$

Functions	Standard ABC	Modified ABC
f_1	2.3751	1.0644
f_2	3.7045	4.701
f_3	1.0419	0.9135
f_4	6.2676	6.0572

Bold values indicate superior results obtained for particular function using mentioned algorithms

Table 5 Limits of variables for IEEE-30 bus system

Variable	Upper limit	Lower limit
P_G (p.u)	0.50	2.00
V_G (p.u)	1.00	1.10
Q_C (MVAR)	0.00	0.05
T_i (p.u)	0.90	1.10

dimensions, the performance of the algorithms is severely affected. Related to ABC, MABC achieves superior solutions on benchmark functions. Like $D = 30$, ABC gives better results as compared to MABC for function f_2 . The convergence speed is more for MABC as compared to standard ABC.

5.5 Simulation Results in IEEE-30 Bus System

For simulation, we're using data from the IEEE-30 bus system, which we got from MATPOWER[3]. It includes six thermal generators, four transformer taps and nine reactive power compensators. Here, 283.4 MW is an active power load for 30-bus system whereas 126.2 MVAR is reactive power load[5]. The test system has total of 41 transmission lines. 100 MVA is selected as base MVA. Limit variables data for state variables and control variables are given in Table 5.

Figure 1 depicts the convergence characteristics of a 30-bus system. Here, it shows that MABC converges at 12th iteration. Obtained outcomes are compared with available literature data in Table 6. Total active power loss using MABC is obtained as 4.280 MW. When compared and analyzed the outcomes, it is observed that MABC outcome is good at tracking global optimum solutions.

5.6 Simulation Results in IEEE-57 Bus System

For simulation, we're using data from the IEEE-57 bus system, which we got from MATPOWER [3]. It includes six thermal generating units, three reactive power

Fig. 1 Convergence characteristics of IEEE-30 bus system

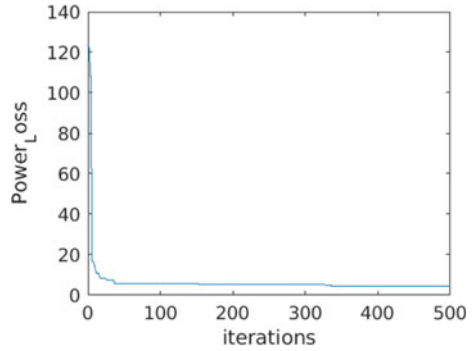


Table 6 Comparison table for IEEE-30 bus system

Algorithms	Power loss (MW)
MABC	4.280
SARGA [9]	4.574
GS [9]	5.101
PSO [10]	4.628
CLPSO [10]	4.561

compensators and seventeen transformer taps [6]. 100 MVA is selected as base MVA. Figure 2 shows convergence characteristics of test bus system. Here, MABC algorithm converges at 19th iteration. Total active power loss is reduced to 17.50 MW. Obtained outcomes are compared with available literature data in Table 7 [6].

Fig. 2 Convergence characteristics of IEEE-57 bus system

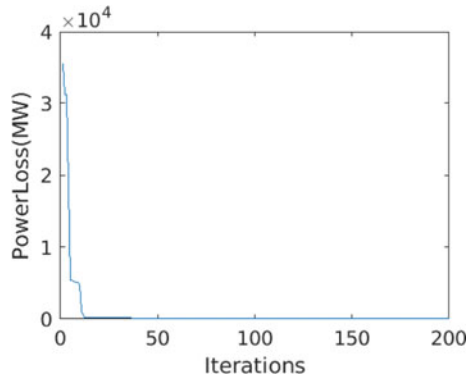


Table 7 Comparison table for IEEE-57 bus system

Algorithms	Power Loss (MW)
MABC	17.505
ABC [6]	24.102
CGA [6]	25.744
HAS [6]	24.501
CLPSO [6]	24.515

6 Conclusion

We worked on a modified approach to the ABC method and its implementation in this study. GABC has been enhanced by MABC. It aids in the enhancement of exploitation capabilities as well as the acceleration of convergence. This strategy can be used to tackle difficulties with reactive power optimization in power systems. Onlooker bees construct a weighted technique solution-finding equation for optimization purposes in a modified manner. ABC and MABC are tested using a set of benchmark functions. On both techniques, functions are examined with varied dimensions (10, 30 and 50). It compares the performance of the modified approach to the standard ABC method. On benchmark functions, MABC beats ordinary ABC, according to the results. Experimental studies support the use of MR in the MABC approach.

On IEEE 30 and 57 test bus systems, the modified ABC is used. We used MATLAB to run the system data from MATPOWER. The results of the test bus system demonstrate that MABC provides the best solution for the problem of reactive power optimization.

References

1. Saadat H (1999) Power system analysis, vol. 2. McGraw-Hill
2. Ozturk A, Cobanlı S, Erdogmus P, Tosun S (2010) Reactive power optimization with artificial bee colony algorithm. *Sci Res Essays* 5(19):2848–2857
3. Thorat AR (2019) A technique to optimize reactive power using Gbest guided artificial bee colony algorithm, pp 97–108
4. Cao Y, Lu Y, Pan X, Sun N (2018) An improved global best guided artificial bee colony algorithm for continuous optimization problems. *Cluster Comput* 1. <https://doi.org/10.1007/s10586-018-1817-8>
5. Ayan K, Kilic U (2012) Artificial bee colony algorithm solution for optimal reactive power flow. *Appl Soft Comput* 12:1477–1482. <https://doi.org/10.1016/j.asoc.2012.01.006>
6. Ettappan M, Vimala V, Ramesh S, Kesavan VT (2020) Microprocessors and Microsystems Optimal reactive power dispatch for real power loss minimization and voltage stability enhancement using Artificial Bee colony algorithm. *Microprocess Microsyst* 76:103085. <https://doi.org/10.1016/j.micpro.2020.103085>
7. Zhu G, Kwong S (2010) Gbest-guided artificial bee colony algorithm for numerical function optimization. *Appl Math Comput* 217(7):3166–3173. <https://doi.org/10.1016/j.amc.2010.08.049>

8. Li Y, Li X, Li Z (2017) Electric power components and systems reactive power optimization using hybrid CABC-reactive power optimization using hybrid CABC-DE algorithm. *Electr Power Compon Syst* 45(9):980–989. <https://doi.org/10.1080/15325008.2017.1311387>
9. Subbaraj P, Rajnarayanan PN (2009) Optimal reactive power dispatch using self-adaptive real coded genetic algorithm. *Electr Power Syst Res* 79(2):374–381
10. Mahadevan K, Kannan PS (2010) Comprehensive learning particle swarm optimization for reactive power dispatch. *Appl Soft Comput* 10(2):641–652

Levy Flight-Based Crow Search Algorithm for Optimum Protection Coordination in Combined Overhead/Cable Distribution System



Sagar Kudkelwar and Bam Bahadur Sinha

Abstract A flexible protection scheme is required to enhance the reliability of the distribution network. An adequate directional over current relay settings help to improve this reliability. This article focused to obtain the optimized relay settings to avoid the miss-coordination which leads to failure in the power supply. A novel Levy flight-based crow search algorithm (LFCSA) is introduced to obtain the TMS of directional over current relays in unique combined overhead line-underground cable system. The proposed Levy flight crow search algorithm results are contrasted with linear program method and found the improved operating time compared to the traditional method. The best part, LFCSA takes less population and iterations to give the optimum TMS with improved relay operating time.

Keywords Levy flight crow search algorithm · Time multiplier setting · Relay coordination

1 Introduction

An over current relay (OCR) performs the foremost operation in the distribution protection system. Its fine operation confirms the selectivity, sensitivity, and reliability of the network. As the system size increases, its protective system becomes complex. Therefore, the demand for required OCR's will increase. In such a situation, the coordination among the relays is a tedious task that cannot be solved traditionally. When the fault arises in the system, the nearest OCR will take over this fault. There may be many relays around the fault locations but the nearest relay will operate to this fault which is called the primary relay and the rest of the relays will act after

S. Kudkelwar (✉)

Electrical Engineering Department, G. H. Raisoni Institute of Engineering & Technology Nagpur, Nagpur 440028, India
e-mail: sagarkudkelwar100188@gmail.com

B. B. Sinha

Computer Science and Engineering, Indian Institute of Information Technology, Ranchi, Jharkhand 834010, India

the failure of the primary relay operation is called as backup relays. The time gap between the main relay and backup relay is termed as the selective time interval (STI) or coordination time interval (CTI) [1].

OCR provides main and backup protection in the power distribution network. Also, it can be used as backup protection in a sub-transmission line. The effective operation of OCR can be decided on its adequate relay settings. Inappropriate relay settings lead to the miss-coordination further it will disturb the system stability. OCR relay consists of Pickup current setting (PS) and Time Multiplier Setting (TMS). For a large distribution network, erecting a strong relay coordination system through its TMS and PS is the task of the optimization techniques. In mesh networks, traditional OCR coordinating approaches take a significant amount of computing time to identify the best relay settings. To attain the best possible relay settings and assure optimal relay coordination, a variety of optimization algorithms have been developed. The objective function can be set to reduce the overall relay operation time, which includes both the primary and backup relays. In early days, researchers such as Albrecht RE et al., Madani and Rijanto, Mahari A and Seyedi H, and Chung JL et al. used the analytical method, curve fitting method, trial and error method, and graph theory method, respectively [2–5]. All of these strategies are hampered by a large number of repetitions, as well as their time taking and gradual nature. The coordination difficulty becomes a linear issue when PSM is determined by a pre-calculated pickup current value and TMS is viewed as a variable. As a result, the author employs the linear programming (LP) technique to solve the optimal issue of relay coordination [6]. Consequently, by keeping fixed PSM, the simplex method can be used as linear program method to solve TMS. Various LP approaches have been proposed over time including active set method, interior point method simplex, and dual simplex [7–9]. Though LP is simple, it is possible to become locked in local optima. According to the literature, these problems are built with nonlinear equation to optimize pick up current value and TMS of directional OCR after attaining a solution through linear programming [10]. The researchers also presented an LP solution for the relay coordination problem in [11, 12].

A variety of optimization approaches were suggested in the last decades to solve the OCR setting problem. GA, ACO, and PSO algorithms are some of the most used optimization approaches [13–15]. TLBO [16], modified PSO [17], continuous GA [18], HAS [19], CSA [20], and HBA [21] have been proposed in addition to these approaches. Furthermore, the most recent meta-heuristic techniques in relay coordination problem were BSA [22], SOS [23], RTA [24], GWO [25], MVPA [26], and WCA [27]. However, the disadvantages of most of these strategies include the risk of becoming stuck in local minima, a slow convergence rate, the requirement for a large population, and increased computational time. As a result, there is still scope for progress in the search for an appropriate relay setting that might help reduce relay operating time.

This article proposed the novel Levy flight crow search algorithm (LFCSA) for the OCR coordination first time. The prime aim of this paper is to find out the best optimal TMS of OCR for the unique overhead-underground cable system. The suggested LFCSA results are compared with the dual simplex method (linear

program method) and found the improved performance over it. The design of the paper is follows as: Sect. 2 consists of the mathematical model of OCR coordination. The LFCSA’s theory and mathematical equations expressed in Sect. 3. Case study and results are discussed in Sect. 4. Conclusion of paper is given in Sect. 5.

2 Mathematical Formulation of OCR Coordination

Fig. 1 shows a simple radial distribution system. In a given system, relay R2 acts as main relay when fault name K occurs near bus B. But, in case R2 will fail to act to take fault K, relay R1 will comes in action that considered as second line of defense (backup relay). The backup relay system is always performed after a predefined interval that called as CTI. The operating time of R1 is can be obtained by summation of a time delay of 0.1 s. and R1’s overshoot time of R1 plus operating time of circuit breaker on bus B when R2’s operating time is set to 0.1 s.

The OCR coordination issue may be conceived as problem of optimization. The following is a mathematical representation of the operation time of all OC relays.

$$\text{Min. } z = \sum_{i=0}^N T_{ik} \tag{1}$$

Here, N is total relay numbers, z specifies the cost function of OCR coordination problem. T_{ik} is total relay operation time [27].

2.1 Constraints

The following are the various limitations for the OC relay coordination problem.

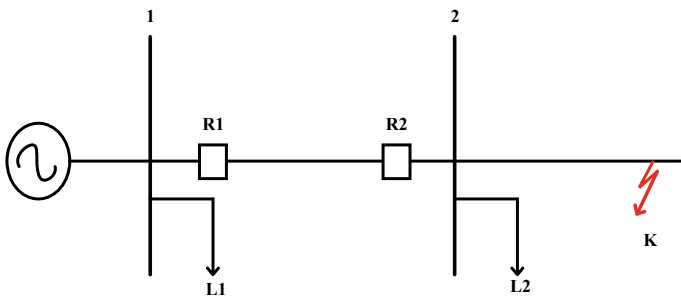


Fig. 1 Two bus radial distribution system

2.1.1 Constraints on Relay Operation Time

The distribution side load becomes unstable due to shifting load conditions. Small perturbations in the system are frequently caused by this variance. As a result, the relay should be aware of it at all times and anticipates a few cycles but not a long period to operate.

The following are the boundary conditions for relay operation time:

$$T_{ik \min} \leq T_{ik} \leq T_{ik \max} \quad (2)$$

Here, $T_{ik \min}$ and $T_{ik \max}$ are min/max ith relay operating time limit. The general bounds for $T_{ik \min} = 0.1$ s and $T_{ik \max} = 1.1$ s.

2.1.2 Constraints on TMS

The sensitive relay response is determined by the suitable TMS. TMS's restrictions can be expressed as follows:

$$\text{TMS}_{i \min} \leq \text{TMS} \leq \text{TMS}_{i \max} \quad (3)$$

Here, $\text{TMS}_{i \min}$ and $\text{TMS}_{i \max}$ are the bounds on TMS. TMS can be lies in the range of 0.015 to 1.1 [28]

2.1.3 Constraints on CTI

The coordination time interval constraints are mentioned in Eq. (4)

$$T_{b_{ik}} - T_{p_{jk}} \geq \text{CTI} \quad (4)$$

Here, $T_{p_{jk}}$ is operation time of P_R and $T_{b_{ik}}$ is operation time of B_R . CTI range can be varied from 0.1 s. to 0.6 s.

2.2 IDMT OCR Characteristics

Because of its exquisite properties, the IDMT relay in the OCR family is the most suitable OC relay. This can be demonstrated by using Eq. (5).

$$T_{\text{op}} = \frac{0.14 * \text{TMS}}{(\text{PSM})^{0.02} - 1} \quad (5)$$

Here, T_{op} is operating time of relay.

Although Eq. (5) is expressed in nonlinear form, PSM may be fixed by utilizing a predefined pickup current value, therefore, Eq. (5) may be reformed in linear form as

$$T_{op} = a_i * (TMS) \tag{6}$$

here $a_i = \frac{0.14}{(PSM)^{0.02}-1}$

with substitution of Eq. (6) in Eq. (1), objective function of relay coordination can be reformulated as [29]

$$\text{Min. } z = \sum_{i=1}^n a_{ik} * TMS \tag{7}$$

3 Levy Flight-Based Crow Search Algorithm (LFCSA)

3.1 Basic CSA

Askarzadeh was proposed the basic CSA [30]. The basic working principles of CSA are given below:

Crows live in flocks, each of which has a size of N .

Crow memories the location where they stores food, it may be expressed as $m^{iter}(i = i, 2, \dots, N)$.

Crows will track each other down to find and steal food from one another's hiding locations.

Crows are likely to hide their foodstuff from being stolen.

Considering flock living in a D-dimension matrix, each crow roams the area in search of good foodstuff. On every iteration $iter = 1, 2, \dots, itermax$, the present position of i th crow is located by a D-dimensional vector $x_i^{iter} = [x_{i,1}^{iter}, x_{i,2}^{iter}, \dots, x_{i,d}^{iter}]$. All hideout site upgrades during the converging process, and it compatible to the best place determined so far.

Suppose, at iteration $iter$, j th crow wishes to return its hiding place at m_j^{iter} , whereas i th crow decide to chase j th crow to steal its food supply. In this circumstance, one of two could thing happen:

State 1: j th crow is completely oblivious to the plunderer. Consequently, i th crow approaches j th crow hiding place. The i th crow new position is updated as follows

$$x_i^{iter+1} = x_i^{iter} + r_i \cdot fl_i^{iter}(m_j^{iter} - x_i^{iter}) \tag{8}$$

where r_i is randomly generated number $[0, 1]$ and fl_i^{iter} is the flight length of crow i at iteration $iter$.

State 2: The intention of a plunderer is noticed by crow j. As a result, to avoid getting pilfered, jth crow will defraud ith crow by moving to a random memory location inside the search space. As a result, the new crow i position is expressed by

$$x_i^{iter+1} = \text{a random position}$$

The new memory location of ith crow after iter is formulated as

$$x_i^{iter+1} = \begin{cases} x_i^{iter} + r_i \cdot fl_i^{iter} (m_j^{iter} - x_i^{iter}) & r_i \geq AP^{iter} \\ \text{a random position} & \text{otherwise} \end{cases} \tag{9}$$

where AP denotes awareness probability of ith crow at each iteration iter.

3.2 Levy Flight (LF)

The fact that crows in condition two of the basic CSA migrate at random affects speed of convergence and nearby search ability, as indicated by formula (9). In state 2, the random flight is replaced by LF to increase the optimization algorithm’s performance. LF is a non-Gaussian random process in that each step follows the Levy stable distribution, i.e., a standard power-law formula, $L(s) \sim |s|^{-1-\beta}$, where $0 < \beta < 2$ is an index. Equation (10) gives the simplified version of the Levy distribution [31]

$$L(s, \gamma, \mu) = \begin{cases} \sqrt{\frac{\gamma}{2\pi}} \exp\left[-\frac{\gamma}{2(s-\mu)}\right] \frac{1}{(s-\mu)^{3/2}} & 0 < \mu < s < \infty \\ 0 & s \leq 0 \end{cases} \tag{10}$$

Here, μ is a location variable and $\gamma > 0$ is a scale variable that control the distribution range.

Levy flight distribution function can be expressed in Fourier transform as

$$F(k) = \exp[-\alpha|k|^\beta], \quad 0 < \beta \leq 2 \tag{11}$$

Now, using LF, a new memory location of crow is determined by Eq. (12)

$$x^{iter+1} = x^{iter} + s \tag{12}$$

Here, s denotes the step length.

Equation (13) gives the nontrivial approach to generate step length s

$$s = \text{random}(\text{size}(D)) \otimes \text{Levy}(\beta) \sim 0.1 \frac{u}{|v|^{\frac{1}{\beta}}} \tag{13}$$

where v and u are taken from normal distribution. $u \sim N(0, \sigma_u^2)$, $v \sim N(0, \sigma_v^2)$. The product \otimes means entry wise multiplication. σ is given as

$$\begin{cases} \sigma_u \\ \sigma_v = 1 \end{cases} = \left\{ \frac{\Gamma(1+\beta)\sin(\frac{\pi\beta}{2})}{\Gamma[\frac{(1+\beta)}{2}]\beta \cdot 2^{(\beta-1)/2}} \right\}^{1/\beta} \tag{14}$$

Here, Γ is the standard gamma function.

At the end, the new memory of i th crow determined by LFCSA may be written as

$$x_i^{iter} = \begin{cases} x_i^{iter} + r_i \cdot fl_i^{iter} (m_j^{iter} - x_i^{iter}) r_i \geq AP^{iter} \\ x_i^{iter} + \text{random}(\text{size}(D)) \cdot \text{Levy}(\beta) \end{cases} \tag{15}$$

The pseudo code of proposed LFCSA is given below

```

1. Parameter definition:
    Folk dimension: N
    Awareness Probability: AP
    Max. Iteration: Imax
    Flight Length: fl
2. Initialization:
    Crow: Random positions; search space range
3. Replace the FE model's parameters with the positions of each crow.
4. Compute the value obtained using the following objective function and store the crow memories.
5. For i=1; I < Imax; i++
    For crowi:
        Choose Crowj to be followed randomly
        ri: Randomly generated
        if(ri > AP): (Crowi follows Crowj)
            Xiiter+1: Crowi new position
        Else: (Crowi follows Levy flight)
            Xiiter+1: Crowi new position
        If (Xiiter+1 is not in search space):
            Choose another crow to be followed and restart the process
        Else:
            Update Crow; memory after calculating the objective function
    
```

4 Case Study and Discussion

The suggested LFCSA have been developed in MATLAB to obtain the optimum TMS of OCR. To study the effectiveness of LFCSA, it is evaluated in a unique overhead-underground cable distribution network. The standard 13 bus radial distribution test feeder system is shown in Fig. 2. This test feeder comes with a number of unique characteristics. 4.16 kV is the operating voltage. The nodes are spaced by a reasonable distance and have a sufficient load. A combination of overhead and cable distribution system consists of 13 nodes connected by 10 overheads and 2 underground line sections. A 115/4.16 kV transformer (Δ -Y), a voltage regulator, and a 4.16/0.480 kV step down transformer (Y-Y) are interconnected in the feeder. The unbalanced load with phase changing configured is done between the nodes. Moreover, it is added with two distributed loads and eight unbalanced spot loads. This model is constructed and simulated in MATLAB without distributed load and VR.

Because single source generation causes fault current and load current to flow in unidirectional, directional OCRs are used in the protection strategy. The pure intention of this paper is to seek an optimum OCR setting to cables for a combined underground/overhead distribution network, therefore, outer factors such as renewable sources integration and topology change are not considered. The given test

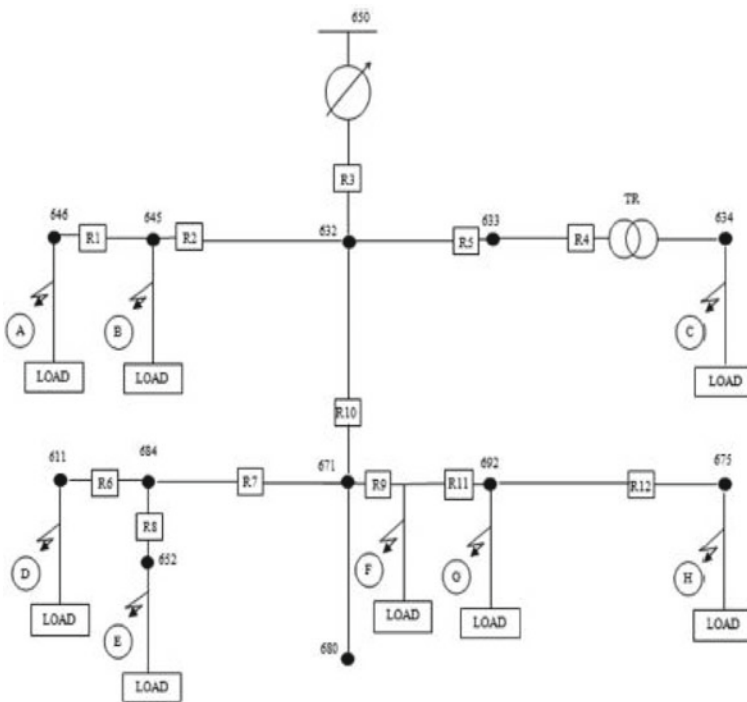


Fig. 2 Combined overhead-underground cable system

Table 1 Main/backup relay pairs

Fault location	Primary relay	Backup relay
B	R2	R3
C	R4	R5
A	R1	R2
D	R6	R7
F	R9	R10
G	R11	R10
H	R12	R11
E	R8	R7

Table 2 CTR and PS for all relay

Relay No	CTR (A)	PS (A)
1	100/1	1
2	200/1	1
3	600/1	1
4	300/1	1
5	300/1	1
6	100/1	1
7	300/1	1
8	100/1	1
9	400/1	1
10	1000/1	1
11	200/1	1
12	100/1	1

system consists of the 12 directional OCR. Relay pairs are tabulated in Table 1. The CT ratio and PS for 12 relay is provided in Table 2. The 3 Ø short circuit fault performed on each load and the obtained data of maximum load current are given in Table 3. As per Eq. (6), the linear objective function has been designed with six primary backup relay pair constraints. The optimized TMS value of relay for the given network with the proposed LFCSA is shown in Table 4.

Following steps are required to formulate the objective function:

- Step 1: Obtain the main/backup relay pairs.
 Table 1 shows the relay coordination pairs.
- Step 2: Define the max. (I_L) load current and (I_F) fault current for each load.
 The maximum load current value obtained from the simulated model of given test system in MATLAB. Later, short circuit analysis is done to get the maximum fault current. Table 2 shows the same data.
- Step 3: Determine the CT ratios and plug settings for all relay.

Table 3 Max fault current and load current

Relay Number	Max. fault current (A)	Max. load current (A)
1	3704	60
2	405	66
3	4184	316
4	9613	200
5	1109	23
6	51	75
7	2441	59
8	2448	48
9	3360	173
10	3374	365
11	2921	51
12	3101	57

Table 4 Comparison of the proposed LFCSA results with dual simplex method

TMS	Dual simplex method [32]	Proposed LFCSA
TMS5	0.0736	0.0256
TMS4	0.151	0.015
TMS3	0.0377	0.0377
TMS2	0.0403	0.0403
TMS1	0.1815	0.015
TMS6	0.1526	0.152
TMS7	0.0778	0.0736
TMS8	0.1526	0.0311
TMS9	0.0311	0.015
TMS10	0.053	0.073
TMS11	0.0158	0.0377
TMS12	0.1443	0.144
Total operating time (s)	0.4403	0.243
Total gain	0.1973	–

The linear cost function can be formed using the data given in Tables 2 and 3. Also, the coordination time interval can be formed using the primary/backup relay pair given in Table 1. TMS bounds lie in 0.015–1.1 (lower and upper bounds), respectively. The coordination time interval is set at 0.5 s. for all primary/backup relay pair constraints. A 50 number of crows (population) are considered along with the 100 iterations to run the code. For fair results, the proposed LFCSA runs 30 times. The optimized TMS for all twelve relay by LFCSA is given in Table 4.

Dual simplex method is a traditional mathematical linear program method. The total operating time obtained from dual simplex method is 0.4403 s. and when the same objective function is operated with the proposed LFCSA, it gives 0.243 s. The net time benefit obtained with the proposed LFCSA algorithm is 0.1973s. When this reduction in operating time is closely observed in a percentage scale, it is found a 45.45% reduction in total operating time. The small improvement in operating time greatly enhance the reliability of the protective scheme, and here it yielded the same. The best part of LFCSA, it gives the improved results with less controlling parameters such as it takes less population and a limited number of iterations to optimize the improved results.

5 Conclusion

The integrated cable/overhead lines pose a plethora of issues with the protection system due to the high capacitance and charging current buried cables. As, the charging current grows, the capacitance increases, and it could be as similar as a large portion of the load current. Minimum relay settings are limited as a result of this. Energization and de-energization of cable circuits also cause high current transients, which is approximately equals to fault current in the cable's exterior protection zone. The protective systems must capable to handle these transient currents in order to maintain their security and reliability. As a result, the protective techniques designed for overhead lines are fundamentally different from those established for underground cables [33]. Hence, the proposed LFCSA has efficiently handled a protection coordination problem for such a complex network with a directional over current relay. Adequate OCR coordination can be performed with the use of an optimum TMS-based protection scheme, which is required to avoid unplanned outages of the system's healthy parts. Besides, the proposed LFCSA outperformed the traditional dual simplex method with less effort.

References

1. Sarkar D, Kudkelwar S, Saha D (2019) Optimal coordination of overcurrent relay using crow search algorithm. *Smart Sci* 7(4):282–297
2. Albrecht RE, Nisja MJ, Feero WE, Rockefeller GD, Wagner CL (1964) Digital computer protective device co-ordination program I-general program description. *IEEE Trans Power Appar Syst* 83(4):402–410
3. Chung JL, Lu Y, Kao WS, Chou CJ (2008) Study of solving the coordination curve intersection of inverse-time overcurrent relays in subtransmission systems. *IEEE Trans Power Del* 23(4):1780–1788
4. Madani SM, Rijanto H (1998) Protection co-ordination: determination of the break point set. *IEE Proc Gener Transm Distrib* 145(6):717–721
5. Mahari A, Seyedi H (2013) An analytic approach for optimal coordination of overcurrent relays. *IET Gener Transm Distrib* 7:674–680

6. Urdaneta AJ, Perez LG, Gomez JF, Feijoo B, Gonzalez M (2001) Presolve analysis and interior point solutions of the linear programming coordination problem of directional overcurrent relays. *Int J Electr Power Energy Syst* 23(8):819–825
7. Bedekar PP, Bhide SR, Kale VS (2010) Optimum coordination of overcurrent relay timing using simplex method. *Electr Power Compon Syst* 38(10):1175–1193
8. Hussain MH, Rahim SRA, Musirin I (2013) Optimal overcurrent relay coordination: a review. *Procedia Eng* 53:332–336
9. Swathika OG, Das A, Gupta Y, Mukhopadhyay S, Hemamalini S (2017) Optimization of overcurrent relays in microgrid using interior point method and active set method. In: *Proceedings of the 5th international conference on frontiers in intelligent computing: theory and applications*. Springer, Singapore, pp 89–97
10. Bedekar PP, Bhide SR (2010) Optimum coordination of directional overcurrent relays using the hybrid GA-NLP approach. *IEEE Trans Power Delivery* 26(1):109–119
11. Amraee T (2012) Coordination of directional overcurrent relays using seeker algorithm. *IEEE Trans Power Del* 27(3):1415–1422
12. Birla D (2006) Maheshwari RP & Gupta HOA new nonlinear directional overcurrent relay coordination technique, and banes and boons of near-end faults based approach. *IEEE Trans Power Del* 21(3):1176–1182
13. Bedekar PP, Bhide SR, Kale VS (2009) Optimum coordination of overcurrent relays in distribution system using genetic algorithm. In: *Proceedings of the international conference on power system (ICPS)*. Kharagpur, India, pp 27
14. Asadi MR, Kouhsari SM (2009) Optimal overcurrent relays coordination using particle-swarm optimization algorithm. In: *2009 IEEE/PES power systems conference and exposition*, pp 1–7
15. Shih MY, Salazar CAC, Enríquez AC (2015) Adaptive directional overcurrent relay coordination using ant colony optimisation. *IET Gener Transm Distrib* 9(14):2040–2049
16. Kalage AA, Ghawghawe ND (2016) Optimum coordination of directional overcurrent relays using modified adaptive teaching learning based optimization algorithm. *Intell Ind Syst* 2(1):55–71
17. Zeineldin HH, El-Saadany EF, Salama MMA (2006) Optimal coordination of overcurrent relays using a modified particle swarm optimization. *Electr Power Syst Res* 76(11):988–995
18. Bedekar PP, Bhide SR (2011) Optimum coordination of overcurrent relay timing using continuous genetic algorithm. *Expert Syst Appl* 38(9):11286–11292
19. Barzegari M, Bathaee SMT, Alizadeh M (2010) Optimal coordination of directional overcurrent relays using harmony search algorithm. In: *2010 9th international conference on environment and electrical engineering*. IEEE, pp 321–324
20. Sinha BB, Dhanalakshmi R (2020) A recommender system based on a new similarity metric and upgraded crow search algorithm. *J Intell Fuzzy Syst* (Preprint) 1–16
21. Rashtchi V, Gholinezhad J, Farhang P (2010) Optimal coordination of overcurrent relays using Honey Bee Algorithm. In: *International congress on ultra modern telecommunications and control systems*. IEEE, pp 401–405
22. El-Hana Boucekara HR, Zellagui M, Abido MA (2016) Coordination of directional overcurrent relays using the backtracking search algorithm. *J Electr Syst* 12(2)
23. Saha D, Datta A, Das P (2016) Optimal coordination of directional overcurrent relays in power systems using symbiotic organism search optimisation technique. *IET Gener Trans Distrib* 10(11):2681–2688
24. Wadood A, Gholami Farkoush S, Khurshaid T, Kim CH, Yu J, Geem Z, Rhee SB (2018) An optimized protection coordination scheme for the optimal coordination of overcurrent relays using a nature-inspired root tree algorithm. *Appl Sci* 8(9):1664
25. Korashy A, Kamel S, Youssef AR, Jurado F (2018) Solving optimal coordination of direction overcurrent relays problem using grey wolf optimization (GWO) algorithm. In: *2018 twentieth international middle east power systems conference (MEPCON)*. IEEE, pp 621–625
26. Korashy A, Kamel S, Youssef AR, Jurado F (2019, February) Most valuable player algorithm for solving direction overcurrent relays coordination problem. In: *2019 international conference on innovative trends in computer engineering (ITCE)*. IEEE, pp 466–471

27. Kudkelwar S, Sarkar D (2019) Online implementation of time augmentation of over current relay coordination using water cycle algorithm. *SN Appl Sci* 1(12):1628
28. Kudkelwar S, Sarkar D (2020) An application of evaporation-rate-based water cycle algorithm for coordination of over-current relays in microgrid. *Sādhanā* 45(1):1–8
29. Sarkar D, Kudkelwar S (2021) Optimal over current relay coordination in Microgrid using a novel hybrid Water Cycle-Moth Flame algorithm. *Int J Syst Assu Eng Manag* 12(3):553–564
30. Askarzadeh A (2016) A novel metaheuristic method for solving constrained engineering optimization problems: crow search algorithm. *Comput Struct* 169:1–12
31. Wu H, Wu P, Xu K, Li F (2020) Finite element model updating using crow search algorithm with Levy flight. *Int J Numer Meth Eng* 121(13):2916–2928
32. Khond SV, Dhokane G (2019) A Optimum coordination of directional overcurrent relays for combined overhead/cable distribution system with linear programming technique. *Prot Control Mod Power Syst* 4(1):1–7
33. Tziouvaras DA, Needs J (2014, March) Protection of mixed overhead and underground cable lines. In: 12th IET international conference on developments in power system protection (DPSP 2014). IET, pp 1–6

Optimization of Graphene Oxide Layer Thickness of ZnO-Based Hybrid Solar Cell Using SCAPS 1D: A Comparative Study on ZnO/GO and ZnO/SiO₂ Hybrid Cells



Sakshi Tyagi, Pawan Kumar Singh, and Arun Kumar Tiwari

Abstract In this paper, simulative investigation of a fabricated ZnO/GO hybrid solar cell has been performed using SCAPS 1D software, and it is the one-dimensional solar cell capacitance simulator, widely used for analysis. We have investigated the repercussions of graphene oxide layer thickness on J_{sc} (current density), V_{oc} (open-circuit voltage), FF (fill factor), PCE (power conversion efficiency of the cell). A comparison was made between the simulated data and experimental data based on experimentation. It has been observed that V_{oc} and FF of simulation and experimental analysis show a good agreement. But J_{sc} is on a higher end for simulated results compared to experimental result, which is due to graphene layer thickness imperfection and absorption. Further, performance of ZnO/GO cell was compared to ZnO/SiO₂ cell and it was found that the efficiency of the two is nearly similar when evaluated at 32^o C under 1 Sun and AM 1.5. A limiting factor in using the high-efficiency Si homojunction solar cell is its high fabrication cost. Hence, here we try to replace GO with SiO₂ because of its simpler synthesis and involved fabrication processes. But the only backdrop is its lower efficiency, which can be improved by simulation analysis discussed in this work. This work presents the results which can improve the performance of graphene-based solar cells by simulation, increasing the efficiency, reducing the overall manufacturing cost and hence proves to be an asset to the society.

Keywords Synthesis · Simulation · SCAPS 1D

S. Tyagi (✉) · P. K. Singh

Department of Mechanical Engineering, Indian Institute of Technology (ISM), Dhanbad, Jharkhand 826004, India
e-mail: tyagi.sakshi615.hcst@gmail.com

A. K. Tiwari

Department of Mechanical Engineering, Institute of Engineering and Technology, Lucknow, Uttar Pradesh 226021, India

1 Introduction

The depletion of natural resources, considerable increase in energy demands and other environmental issues are the major reasons for many countries to prioritize the evolution of renewable energy resources. Nowadays, sustainable energy is one of the vital resolutions to encounter the energy demands of the upcoming era. It can be used as an eco-efficient substitute to fossil fuels and possesses a huge benefit of being clean, green and toxin-free. Solar energy is considered to be one of the best renewable energy sources that proved to be a marvellous substitute to fossil fuels because of its low cost, easy availability and environment-friendly nature. Nowadays, modelling and simulation of photovoltaic cells have achieved enormous heed in various areas. There has been the development of innovative methods for manufacturing and improving the efficiency of the solar cells. The next generation of solar cells involves development of hybrid cells, which are evolved by combination of inorganic and organic semiconductors which are certainly accessible in the nature and are harmless too. In this present scenario of pandemic, where the world is surviving hard, renewable energy sector has also suffered a steep reduction in manufacturing phase. Energy demands have soared high in the last few years, but the sector is facing unreliability to meet the demands with inappropriate resources, high manufacturing and fabrication price. Hence to maintain sustainable energy requirements, simulation of hybrid solar cells has emerged as an efficient substitute to the expensive PV cells. The presented work shows the simulation of ZnO/GO cell by implementing solar cell capacitance simulator (SCAPS 1D) software. ZnO has been used because of its ability of sustaining high temperatures and its large bandgaps. High absorption coefficient, abundant availability and acceptable sensitivity in UV region make it a useful candidate for application in thin-film solar cells. Graphene has also presented good results in solar cell applications. The discipline of hybrid devices has matured by adding of graphene layer in the device structure, hence making it more worthy. Current research has presented the use of graphene-based transparent electrodes for hybrid solar cells where graphene oxide/ZnO was used in the front contact on ITO [1]. Perovskite cells still have several drawbacks like UV and heat decomposition instability at moisture and ion electromigration. Graphene derivatives combat the following problems and prove to be a suitable candidate for inclusion in hybrid solar cell. Some authors have also discussed a reduced form of graphene oxide (r-GO)/CuSCN which acts as efficient bilayer hole transport layer (HTL) [2]. Numerous simulation analyses have already been performed on enhancing the stability and efficiency of nanotube and graphene contacted solar cells (CdTe, CIGS, CZTS, perovskites) [3, 4].

This research work aims to determine the possible chances of integrating zinc oxide along with graphene oxide layer in the proposed cell structure. The evidences obtained for such structures have been discussed here. SCAPS 1D software 3.3.08 version has been used as a platform for simulation of mentioned cell structure, and the results were compared to the experimental results. The synthesis and fabrication process of ZnO/GO hybrid cell along with device structure and simulation procedure are discussed. Effect of graphene oxide layer thickness on the various photovoltaic

parameters of cell is studied. Performance graphs of ZnO/GO and ZnO/SiO₂ solar cell are evaluated. Literature has not reported any research on the discussed pair of cells using the software SCAPS 1D. Further, this study is useful in modelling and simulation of hybrid solar devices which are useful in many solar polygeneration systems.

2 Experimental

2.1 Synthesis and Fabrication of ZnO/GO Cell

Synthesis of zinc oxide was done using ethanol, sodium hydroxide and zinc nitrate, purchased from Sigma-Aldrich. Nanoparticle synthesis was done using wet chemical technique. Aqueous ethanol solution of zinc nitrate (Zn(NO₃)₂·4H₂O) brought in use was 0.5 M. Then continuous stirring with the help of magnetic stirrer was performed over the solution. After an hour, zinc nitrate was dissolved. Similarly, 0.8 M aqueous ethanol suspension of potassium hydroxide (KOH) was composed and stirred for an hour maintaining a speed of 320–340 RPM [5]. On complete dissolving of zinc nitrate, 0.8 M KOH aqueous suspension was introduced drop by dropwise for 45 min. After mixing all the products, we set the seal onto the flask boundaries in order to permit the reaction to commence for 3 h. On completion of the reaction, the suspension was kept for overnight and then segregation is done [6]. The precipitate was separated from left over solution which was centrifuged for 15 min. Now washing of the precipitated NPs of ZnO with ethanol and deionized water and was performed three times to remove the by-products. Air drying at 60 °C in is performed for the precipitate. Now by desiccation, Zn(OH)₂ is entirely converted to ZnO, Fig. 1. SEM images of the ZnO NPs have been studied here for further investigation.

2.2 Synthesis of Graphene Oxide

Pure graphite particles with a purity of 99.8% and –325 mesh size were purchased from Hemadri Chemicals, Mumbai. The developments for processing of GO were done using modified Hummers' method. The measure of graphite particles and NaNO₃ used in the process was 5.5 g and 3.5 g, respectively. Now 12 ml H₃PO₄ and 108 ml H₂SO₄ were mixed to it, and the solution was kept under constant stirring for 15 min in an ice bath. The suspension temperature was kept below 50 °C, and then 15 g of KMnO₄ was slowly added to it. Then in an ice bath, the suspension was reacted for 2.5 h. Water was added continuously for 70 minutes to maintain a temperature of 98 °C. The solution volume was increased upto 500 ml by adding deionized water to it [7]. Then 15 ml of H₂O₂ was added after a gap of 15 mins. The product so obtained was centrifuged with 5% HCL and was dried at 60 °C, refer to Fig. 1.

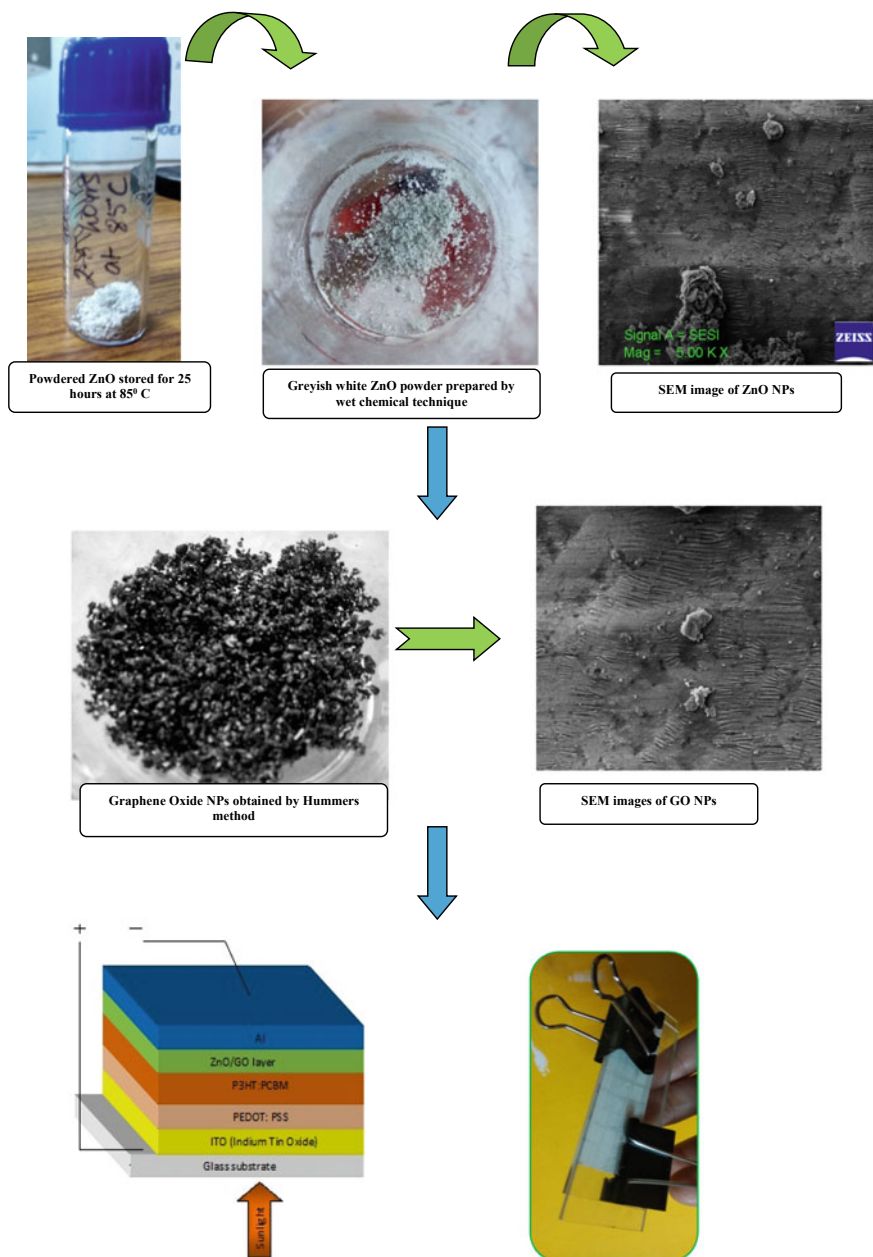


Fig. 1 Device structure of ZnO/GO hybrid solar cell and fabricated ZnO/GO cell

3 Device Structure and Simulation Method

SCAPS-1D software also known as solar cell capacitance simulator was developed at the Department of Electronics and Information Systems (EIS), University of Ghent, Belgium. Being single-dimensional simulation software, it is basically utilized for numerical analysis of solar cells [6, 8]. The present work reveals the numerical simulation performed on ZnO/GO hybrid solar cell using SCAPS-1D version 3.3.08 to analyse the performance of graphene oxide layer on the overall device performance. Also, photovoltaic parameters such as V_{oc} , J_{sc} , FF and power conversion efficiency were obtained from simulated results.

The schematic device structure of the ZnO/GO solar cell which has been adopted in this study is presented in Fig. 1. It comprises of transparent ITO glass substrate, where a layer of PEDOT:PSS of 5.0 eV work function is spread upon it for electron collection. ZnO/GO plays the role of electron transport layer and photoactive layer, respectively. P3HT:PCBM layer helps in photon electron conversion and is a good acceptor too. On the top, aluminium electrode is inserted. By this simulation, photovoltaic parameters (J_{sc} , V_{oc} , FF and PCE) of the ZnO/GO hybrid solar cell were obtained and then compared to the experimental results [6]. The selection of parameters was done used on the basis of the experimental and theoretical results; also, reasonable estimation has been performed, in Table 1. Here, for all the simulations, temperature of 27 °C, illumination values of 1000 W/m² and air mass of 1.5 G have been considered. Also, a precise comparison has been made between the PV characteristics of ZnO/GO and ZnO/SiO₂ cells.

4 Results and Discussion

4.1 Effect of Graphene Oxide Layer Thickness

The device structure of ZnO/GO hybrid solar cell illustrated in Fig. 1 was analysed in SCAPS 1D platform and the experimental results and literature helped in fetching the device parameters for the cells. The experimental results of the device have been presented in Table 1, and the device characteristics like short-circuit current density, power conversion efficiency, fill factor and open-circuit voltage have been reported here under 1.5 A and 1 sun [9]. However, simulation of the IV characteristics of the cell has been performed by placing appropriate values to the variables of the device layers. Furthermore, we have compared the PV characteristics like fill factor (FF), short-circuit current density (J_{sc}), open-circuit voltage (V_{oc}), PCE of ZnO/GO by experimental and simulation analysis. Also, comparison is drawn between characteristics of ZnO/GO and ZnO/SiO₂ cells. By incorporation of graphene layer in such devices, there is considerable reduction in ion electromigration from metallic electrode to ZnO layer along with improvement in the carrier collection at top electrode [10–12]. During actual operation, rise in the heat dissipation from the

Table 1 Extracted parameters of ZnO/GO solar cell

		Control parameters		Responses				
Data		Spectral power density (W m ⁻²)	Temperature (K)	Open-circuit voltage (V _{oc}) V	Current density (J _{sc}) (mA/cm ²)	Fill factor (%)	Power conversion efficiency (PCE) %	
Day 1	{	1	1006.6	305.6	0.69	6.89	56.62	8.96
		2	1005.7	305.1	0.62	7.24	56.94	9.12
		3	1005.5	305.7	0.74	6.77	56.87	8.42
		4	1008.2	306.4	0.72	6.49	56.22	8.64
		5	1006.4	304.3	0.71	6.58	56.87	9.07
		6	1009.6	302.4	0.68	7.17	54.12	8.45
		7	1007.1	305.6	0.69	7.24	52.91	8.66
		8	1005.6	306.4	0.68	7.13	51.78	8.52
		9	1004.5	304.7	0.64	7.51	54.76	8.49
		10	1006.4	306.4	0.63	7.11	53.85	9.12
		11	1008.6	302.5	0.69	6.66	54.72	8.46
		12	1007.8	304.8	0.72	6.85	55.74	8.62
		13	1005.8	306.9	0.68	6.94	56.92	8.44
		14	1006.4	303.4	0.64	6.96	56.84	8.38
		15	1005.1	305.9	0.72	7.24	52.19	8.52
		16	1006.2	303.2	0.69	7.24	51.27	8.46
		17	1009.6	306.6	0.63	7.17	54.71	8.39
		18	1007.4	306.4	0.72	6.28	56.78	9.08
		19	1008.6	302.8	0.65	6.44	57.83	9.07
		20	1007.5	301.7	0.68	6.84	56.87	9.12
		21	1006.2	301.2	0.66	6.11	56.22	9.08
		22	1009.7	308.9	0.65	6.47	56.87	9.12
		23	1008.1	306.8	0.64	6.82	54.12	9.12
		24	1005.5	307.2	0.72	7.17	52.91	9.04
		25	1008.3	309.3	0.78	7.24	51.78	8.56
		26	1009.2	304.6	0.72	7.13	54.76	8.97
		27	1006.7	301.2	0.74	7.51	53.85	8.67
		28	1007.4	307.5	0.68	7.11	54.72	8.29
		29	1005.4	307.4	0.65	6.66	55.74	8.38
		30	1006.8	309.8	0.64	6.85	56.92	8.52
		31	1005.9	304.7	0.68	7.17	56.84	8.46
		32	1006.2	306.7	0.68	7.24	52.19	8.39
		33	1006.3	307.9	0.64	7.24	51.27	9.08

(continued)

Table 1 (continued)

Data	Control parameters		Responses			
	Spectral power density (W m^{-2})	Temperature (K)	Open-circuit voltage (V_{oc}) V	Current density (J_{sc}) (mA/cm^2)	Fill factor (%)	Power conversion efficiency (PCE) %
34	1008.4	308.2	0.64	7.17	54.71	9.07
35	1009.8	307.7	0.62	6.28	56.78	9.12
36	1006.8	308.4	0.69	6.44	57.83	9.08
37	1008.6	305.5	0.72	6.84	56.62	9.12
38	1009.9	307.8	0.72	6.11	56.94	9.12
39	1007.6	304.6	0.64	6.47	56.87	9.04
40	1005.6	304.7	0.67	6.77	56.22	8.56
41	1006.7	307.7	0.64	6.49	56.87	8.97
42	1008.4	302.8	0.66	6.58	54.12	8.67
43	1007.6	304.8	0.64	7.17	52.91	8.29
44	1007.4	301.7	0.68	7.24	51.78	8.38
45	1008.2	305.4	0.65	7.13	54.76	8.52
46	1009.6	305.6	0.62	6.77	53.85	8.46
47	1007.8	307.8	0.67	6.49	54.72	8.39
48	1006.2	302.8	0.68	7.24	55.74	9.08
49	1005.4	301.2	0.62	7.24	56.92	9.07
50	1006.1	301.4	0.67	7.17	56.84	9.12
51	1006.7	302.5	0.72	6.28	52.19	9.08
52	1007.7	305.6	0.71	6.44	51.27	9.12
53	1007.8	302.7	0.72	6.84	54.71	9.12
54	1005.6	305.6	0.65	6.11	56.78	9.04
55	1006.1	307.2	0.70	6.47	57.83	8.56
56	1005.4	302.8	0.72	6.82	56.87	8.97
57	1006.7	307.2	0.71	7.24	56.22	8.67
58	1008.4	306.4	0.72	7.24	56.87	8.29
59	1009.4	304.7	0.71	7.17	54.12	8.38
60	1007.8	305.8	0.72	6.47	52.19	8.52
61	1008.8	304.7	0.69	6.77	51.27	8.46
62	1009.7	301.3	0.68	6.49	54.71	8.39
63	1007.8	304.6	0.72	6.58	56.78	9.08
64	1008.8	305.7	0.71	7.17	57.83	9.07
65	1007.5	302.8	0.72	7.24	56.87	9.12

(continued)

Table 1 (continued)

	Control parameters			Responses			
	Data	Spectral power density (W m^{-2})	Temperature (K)	Open-circuit voltage (V_{oc}) V	Current density (J_{sc}) (mA/cm^2)	Fill factor (%)	Power conversion efficiency (PCE) %
<div style="border: 1px solid black; padding: 5px; display: inline-block;">Day 16</div>	66	1006.7	308.5	0.71	7.13	56.22	9.12
	67	1005.9	304.9	0.70	6.77	56.87	9.04
	68	1005.8	302.9	0.71	6.49	52.19	8.56
	69	1005.9	309.2	0.72	7.24	51.27	8.97
	70	1006.8	304.9	0.72	6.28	54.71	8.67
	71	1009.2	304.8	0.72	6.44	54.76	8.29
	72	1005.2	308.4	0.68	6.84	53.85	8.38
	73	1006.4	301.4	0.68	6.11	54.72	8.52
	74	1008.2	303.5	0.66	6.47	55.74	8.46
	75	1007.8	308.4	0.68	6.82	56.92	8.39
	76	1006.2	309.7	0.66	7.17	56.84	9.08
	77	1008.8	302.7	0.69	7.24	52.19	9.07
	78	1006.7	302.9	0.66	7.13	51.27	9.12
	79	1009.5	304.9	0.71	7.51	54.71	9.12
	80	1008.9	308.7	0.72	7.11	56.78	9.04

graphene layer to the environment increases the thermal stability of cell; also, there is a reduction in the heat generated within the cell [13]. As suggested in several papers, graphene layer was considered as a planar structure. For this research, GO is considered as a planar layer with p type doping of up to 50 nm thickness.

4.2 Comparative Study on Experimental and Simulated Results for ZnO/GO Cell

The efficacy of solar cells is dependent on the extracted variables, i.e. short-circuit current density J_{sc} , the open-circuit voltage V_{oc} and the fill factor FF which eventually helps in deciding the power conversion efficiency of the device. The solar cell was positioned under the sun for 16 days for 7 hours daily. For each day, 5 readings were obtained, and the results were noted after every 150 min. The notable values of current are determined for the mentioned device on availability of solar energy. An ammeter and multimeter are used to measure the short-circuit current and voltage, respectively, for the solar cells. With reference to literature, these parameters are determined by examining an illuminated I–V characteristic curve for standard cells [6, 14, 15]. For

correct analysis of the I–V characteristics, it is important to execute the calculations under regular test environment with total irradiance equal to 1000 W/m^2 and 1.5 AM spectrum [16]. Temperature plays pivotal role in the determining the efficacy of a solar cell, which was estimated using thermometer. The mean value of temperature estimated for 16 days for the hybrid device was $33 \text{ }^\circ\text{C}$. Hence, depending on the mean value of estimated light intensity of 2612 lx for the cell, the results for spectral power density range from 1005.6 to 1009.4 W/m^2 for 16 days.

The simulated device metrics of the cell designed in SCAPS-1D have been plotted in Fig. 2. Comparable results were obtained by designing the cell and simulative analysis. Both V_{oc} and FF are comparable for the two modes of investigation. However, the simulated value of J_{sc} is on a higher end (12.46 mA/cm^2 vs. 7.24 mA/cm^2) than the pilot value. In SCAPS 1D, it is recommended to insert graphene planar layer of appropriate absorption coefficient. The experimental values are almost half of the simulated current–density. The higher value of current density could be due to the thickness of graphene oxide layer (50 nm).

The variables of simulated device have been presented here. Out of simulations, comparable metrics were investigated and few discrepancies were reported as the interface mismatch in the cell. Figure 2 represents the IV characteristic curve for ZnO/GO cell, where a comparable graphical analysis is made in between experimental (real) and simulated (identified) results. Also, graphene has been considered as a planar p type layer in SCAPS-1D simulation. Graphene has opto-electronics

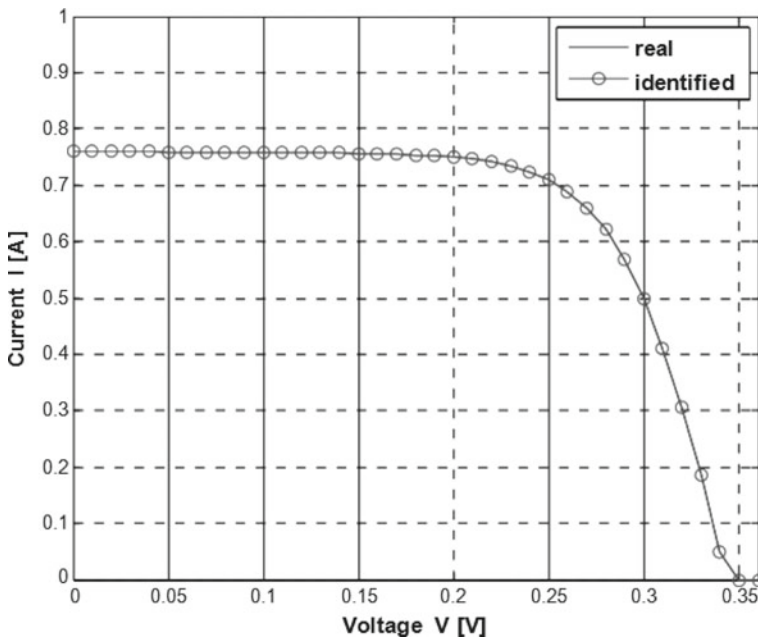


Fig. 2 IV characteristics curve of the ZnO/GO cell, designed in SCAPS-1D

properties which are similar to the p type doped thin metallic layer [16]. It is observed that by increase in graphene thickness, a significant change in the device parameters is noted. Figure 3a–d illustrates the variation of V_{oc} , J_{sc} , FF and PCE by increase in graphene oxide thickness. Also, Fig. 4a–d illustrates the variation of V_{oc} , J_{sc} , FF and PCE by increase in conventional silicon dioxide layer thickness. V_{oc} shows an increase in the beginning and then tends to be constant around 0.78 V for GO thickness (t_{GO}) >37 nm. The reason behind good interface and charge collection at the ZnO/GO layer could be due to the increased number of atomic orbitals of graphene layers [17, 18]. Also, match and interaction of the grid at the interactive boundary will enhance by increase in graphene atomic orbitals. Due to the more number of graphene atoms in the cell structure, there is high lateral resistance in the junction [19–21]. This resulted in sharp decline of fill factor for thickness lesser than 45 nm. When thickness exceeds the mark of 45 nm, FF shows a constant behaviour. In the beginning, J_{sc} has shown a slight odd pattern but then it started increasing for thickness >35 nm. It is expected since we have introduced graphene as a plane and smooth layer in the device framework [22]. Further, if the thickness of this layer is increased, it will increase the absorption rate. The efficiency has shown a decreasing pattern by increased t_{GO} values and gets saturated around 8.46 % for t_{GO} > 47 nm. The decrease in PCE generally follows the reduction in fill factor.

It is observed that for this cell structure, t_{gr} > 30 nm is optimum thickness value for V_{oc} and J_{sc} and t_{gr} > 45 nm is reported as optimal value for FF and PCE.

V_{oc} tends to increase upto a thickness of 34 nm and then becomes constant around 0.82 V for SiO_2 thickness from 30 to 42 nm. There is again an increase in voltage from thickness 45–52 nm. J_{sc} increases upto 50 nm and then comes around saturation point and follows a constant line for value of 15.52 mA/cm². Reduction in fill factor is recorded for thickness upto 45 nm. Then a constant curve is obtained for thickness of SiO_2 between 45 and 52 nm. A decreasing trend in the efficiency is noted around 9.46 % for SiO_2 thickness > 45 nm.

4.3 Performance Comparison of ZnO/GO and ZnO/SiO₂ Cell

To substantiate our work and for understanding the motive for using GO at the upper surface, we reproduced the different parameters like V_{oc} , J_{sc} , FF, PCE of the hybrid solar cell, where GO is replaced with silicon dioxide [23, 24]. The comparable simulation values state that graphene can be a suitable substitute for traditional silicon hole transporting layer in hybrid cells despite a moderately low PCE and fill factor values. It is also stated in many publications that a sensibly incapacitated graphene layer can efficiently work as back contact and hole conduction surface in hybrid solar devices [25–27]. By this comparable result, it is suggested that graphene can be a sensible contacting layer. We have determined good agreement between the experimental and simulation results for silicon dioxide hybrid cell where values of the fill factor, conversion efficiency and voltage are almost similar. Comparative

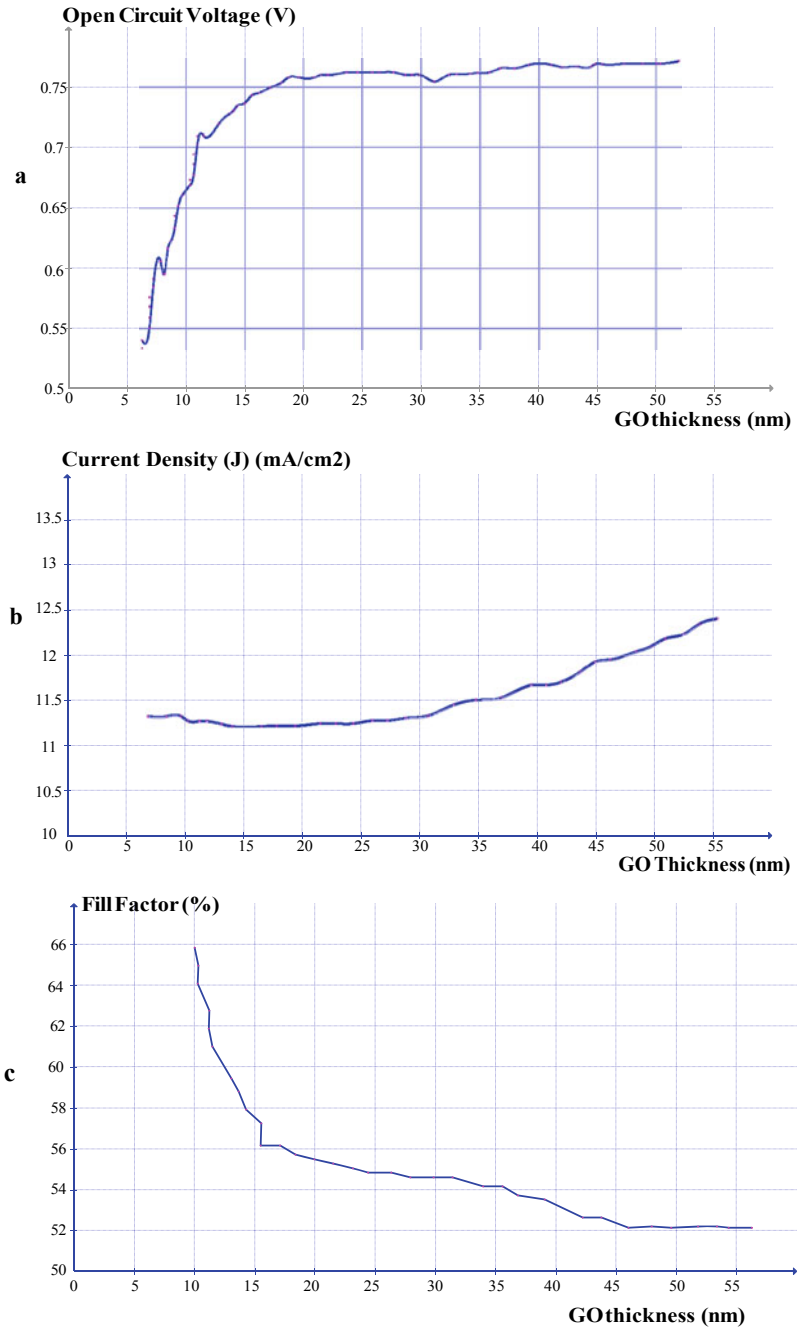


Fig. 3 a–d Influence of increased thickness of GO layer on VOC, JSC, FF, PCE of the hybrid solar device drawn in SCAPS-1D

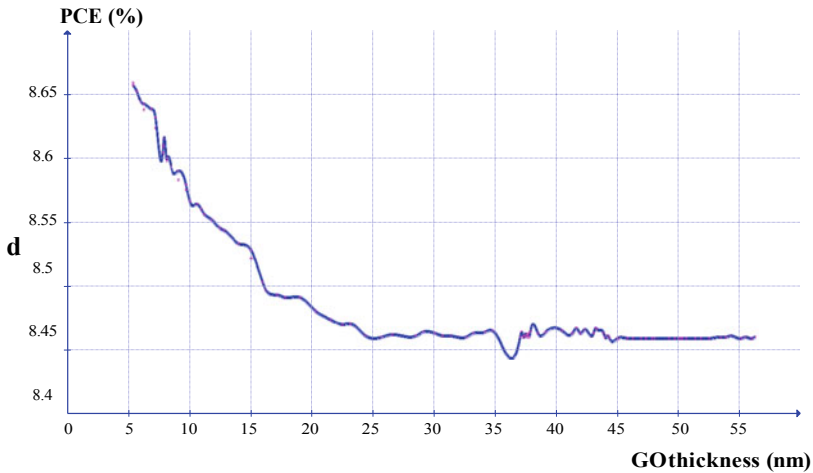


Fig. 3 (continued)

values of simulated and experimental results for both the device structures have been shown in Table 2.

Further, it is observed that on insertion of GO layer, there is increase in JSC in simulation results. It is certainly due to a better photo-absorption and thin thickness [28–30]. We believe that in SCAPS simulation there are no other mechanisms which can explain incorporation of the analytically fabricated cell which is due to multiple reflections from the interfaces and reflection at the back contact [31–33]. Hence, by this examination graphene oxide is again proved to be a promising material to replace SiO_2 for suitable architecture designing of hybrid solar cells.

5 Conclusion

In the present research, numerical simulations were performed for ZnO/GO and ZnO/ SiO_2 hybrid solar cell. The result of varied graphene oxide thickness on the photovoltaic parameters was closely studied. An experimental study has been made to determine the device variables of two hybrid solar cells and then the results were compared. We introduced the simulative investigation of the different features of graphene contacted ZnO hybrid solar devices where GO is attached on upper surface and it also acts as hole conducting layer. Similar procedure of comparison of simulated results has been applied and hence we were able to conclude that graphene can be a better candidate to replace the silicon layer in the hybrid cells. This investigation has efficiently resulted in comparable outcomes for current, voltage, fill factor and conversion efficiency. Conversion efficiency of 12.46 % was obtained which can easily be increased by parametric optimization of the cell, essential parameters

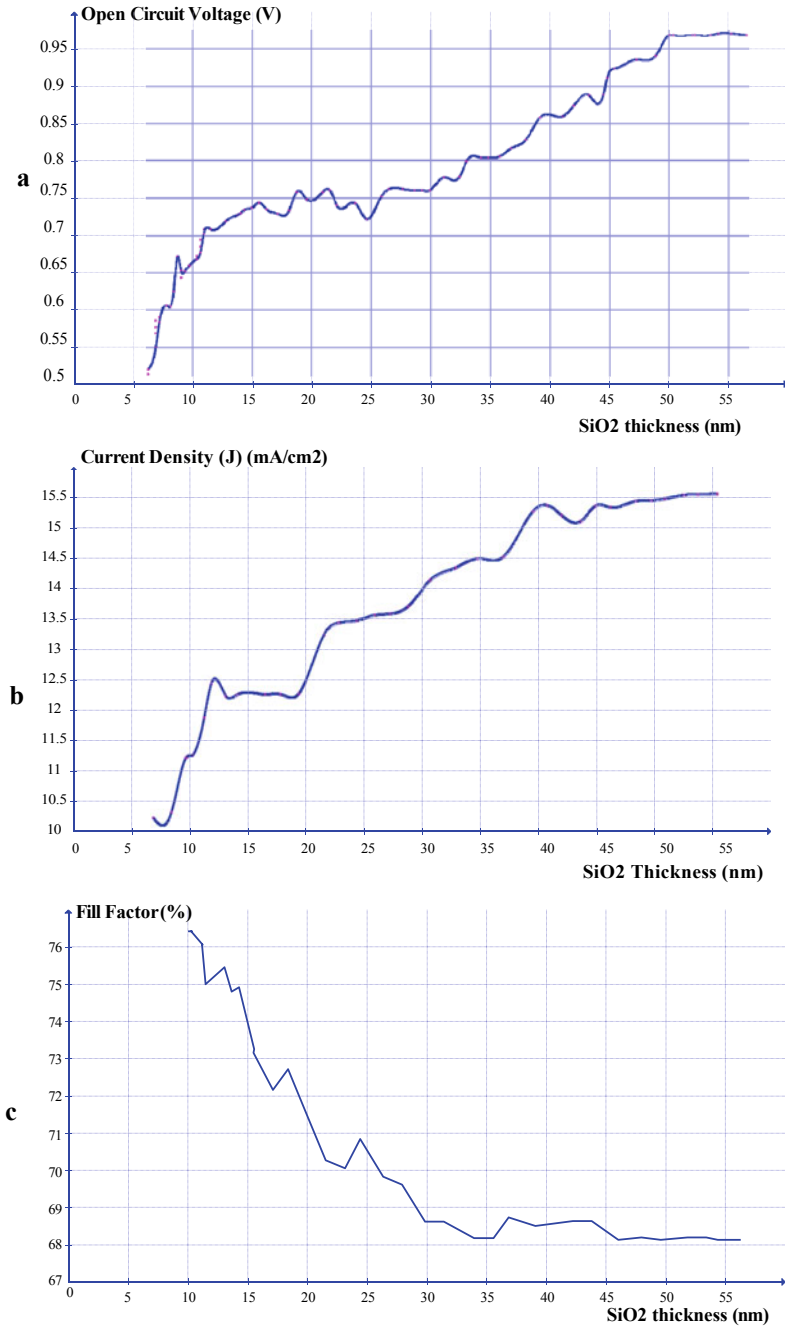


Fig. 4 a–d Influence of increased thickness of SiO₂ layer on V_{OC} , J_{SC} , FF, PCE of the hybrid solar device drawn in SCAPS-1D

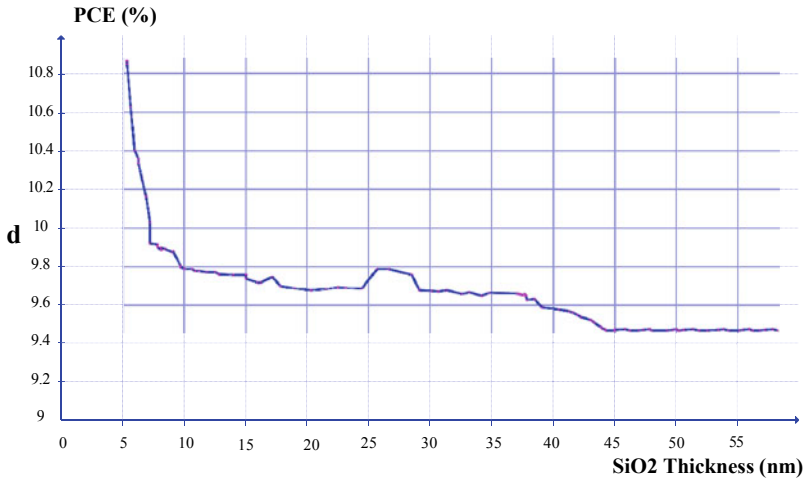


Fig. 4 (continued)

Table 2 Comparison of experimental and simulation analysis

Cell structure	V_{oc}	J_{sc}	FF	PCE
ZnO/SiO ₂ (experiment)	0.94	15.74	67.38	10.35
ZnO/SiO ₂ (simulation)	0.97	15.52	68.42	9.47
ZnO/GO (experiment)	0.72	7.24	56.94	9.12
ZnO/GO (simulation)	0.79	12.46	52.14	8.46

being doping density and gap of the GO layer. Graphene has been exhibited as a rational substitute for silicon traditional hole transporting layer. However, slightly lower value of fill factor of ZnO/GO can be easily optimized by suitable doping with metallic ions. Favourable thickness seems to be 30nm for which there is increase in Voc and Jsc. The optimum thickness value for FF and PC is 45 nm. It also appears that graphene oxide thickness shall produce lower values of fill factor for thicker layers. At last, comparisons were drawn in between experimental and simulated values for ZnO/GO and ZnO/SiO₂, respectively, and it can be summed up that GO can be efficiently replaced with SiO₂.

Performed work shows the evaluative features which can enhance the device performance of ZnO and GO nanostructured cells, and hence, the research also involves the designing and optimization of similar devices made of carbon nanotubes.

Acknowledgements The authors highly acknowledge and are thankful to Dr. Marc Burgelman at the University of Gent, Belgium for providing SCAPS to perform the simulation analysis.

Declaration of Competing Interest The authors proclaim that they have no known competing financial interests or personal relationships that could have appeared to influence the work reported in this paper.

References

1. Chen Y, Meng Q, Zhang L, Han C, Gao H, Zhang Y, Yan H (2019) SnO₂-based electron transporting layer materials for perovskite solar cells. A review of recent progress. *J Energy Chem* 35:144–167
2. Chowdhury TH, Akhtaruzzaman M, Kayesha M, Kaneko R (2018) Low temperature processed inverted planar perovskite solar cells by r-GO/CuSCN hole-transport bilayer with improved stability. *Sol Energy* 171:652–657
3. Milic JV, Arora N, Dar M (2018) Reduced graphene oxide as a stabilizing agent in perovskite solar cells. *Adv Mat Interfaces* 5:1800416
4. Kang AK, Zandi MH, Gorji NE (2019) Simulation analysis of graphene contacted perovskite solar cells using SCAPS- 1D. *Opt Quant Electron* 51:91
5. Abbasi HY, Habib A, Tanveer M (2017) Synthesis and characterization of nanostructures of ZnO and ZnO/graphene composites for the application in hybrid solar cells. *J Alloys Compd* 690:21–26
6. Tyagi S, Singh PK, Tiwari AK, Pain P (2021) Optimization and comparison of photovoltaic parameters of zinc oxide (ZnO)/graphene oxide (GO) and zinc oxide (ZnO)/carbon quantum dots (CQDs) hybrid solar cell using firefly algorithm for application in solar trigeneration system in commercial buildings. *Sustain Energy Technol Assess* 47:101357
7. Song J, Wang, X, Chang CT (2014) Preparation and characterization of graphene oxide. *J Nanomaterials* 2014
8. Fonash SJ (1997) A manual for AMPS-1D: a one-dimensional device simulation program for the analysis of microelectronic and photonic structures. The center for nanotechnology education and utilization, The Pennsylvania State University, University Park, PA 16802
9. Jhuma FA, Shaily MZ, Rashid MJ (2019) Towards high-efficiency CZTS solar cell through buffer layer Optimization. *Mat Ren Sust Energy* 8
10. Kuhn L, Gorji NE (2016) Review on the graphene/nanotube application in thin film solar cells. *Mat Letters* 171:323–326
11. Iqbal T, Haq Nawaz M, Sultan M, Tahir MB (2018) Novel graphene-based transparent electrodes for perovskite solar cells. *Int J of Energy Res* 42:1–9
12. Yang Y, Xiao J (2014) An all-carbon counter electrode for highly efficient hole- conductor-free organo-metal perovskite solar cells. *RSC Adv* 4:52825–52830
13. Yoo MJ, Park HB (2019) Effect of hydrogen peroxide on properties of graphene oxide in Hummers method. *Carbon* 141:515–522
14. Zhang Y, Gao Z, Song N, He J, Li X (2018) Graphene and its derivatives in lithium–sulfur batteries. *Mat Today Energy* 9:319–335
15. Ghosh S, Harish S, Ohtaki M, Saha BB (2020) Thermoelectric figure of merit enhancement in cement composites with graphene and transition metal oxides. *Mat Today Energy* 18:100492
16. Talam S, Karumuri SR, Gunnam N (2012) Synthesis characterization and spectroscopic properties of ZnO nanoparticles. *Int Sch Res Netw* 2012
17. Norton M, Gracia Amillo AM, Galleano R (2015) Comparison of solar spectral irradiance measurements using the average photon energy parameter. *Sol Energy* 120:337–344
18. Ansari ZA, Singh TJ, Islam SM, Singh S, Mahala P, Khan A, Singh KJ (2019) Photovoltaic solar cells based on graphene/gallium arsenide Schottky junction. *Optik Int J for Light and Electron Optics* 182:500–506
19. Wang C, Tang Y, Hu Y, Huang L (2015) Graphene/SrTiO₃ nanocomposites used as an effective electron-transporting layer for high performance perovskite solar cells. *RSC Adv* 5:52041–52047
20. Rao CNR, Subrahmanyam KS, Ramakrishna Matte HSS, Maitra U, Moses K, Govindaraj A (2011) Graphene: synthesis, functionalization and properties. *Int J of Modern Physics B* 25:4107–4143
21. Zhang Y, Pan C (2011) TiO₂/graphene composite from thermal reaction of graphene oxide and its photocatalytic activity in visible light. *J Mater Sci* 46:2622–2626

22. Marcano DC, Kosynkin DV, Berlin JM (2010) Improved synthesis of graphene oxide. *ACS Nano* 4:4806–4814
23. Guo S, Dong S (2011) Graphene nanosheet: synthesis, molecular engineering, thin film, hybrids, and energy and analytical applications. *Chem Soc Rev* 40:2644–2672
24. Cihui L, Bingce L, Xi FZ (2008) Electrical and deep levels characteristics of ZnO/Si heterostructure by MOCVD deposition. *Chi Phy B* 17:172292
25. Chabane L, Zebbar N, Trari M, Kechouane M (2017) Opto-capacitive study of n-ZnO/p-Si heterojunctions elaborated by reactive sputtering method, Solar cell applications. *Thin Solid Films* 636:419–424
26. Bingce L, Cihui L, Bo Y (2010) Grain boundary layer behavior in ZnO/Si heterostructure. *J Semicond* 31
27. Lee C, Shin M, Lim M, Seo JY, Lee JE, Lee HY, Kim BJ, Choi D (2011) Material properties of microcrystalline silicon for solar cell application. *Sol Energy Mater Solar Cells* 95:207–210
28. Huang CH, Chuang WJ (2015) Dependence of performance parameters of CdTe solar cells on semiconductor properties studied by using SCAPS-1D. *Vacuum* 118:32–37
29. Adewoyin AD, Olopade MA, Oyebola OO, Chendo MA (2019) Development of CZTGS/CZTS tandem thin film solar cell using SCAPS-1D. *Optik-Int J Light Electron Opt* 176:132–142
30. Anwar F, Mahub R, Satter SS, Ullah SM (2017) Effect of different HTM layers and electrical parameters on ZnO nanorod-based lead-free perovskite solar cell for high-efficiency performance. *Int J Photoenergy* 1–9
31. Mostefaoui M, Mayari H, Khelifi S, Bouraiou A, Dabou R (2015) Simulation of high efficiency CIGS solar cells with SCAPS-1D. *Softw Energy Procedia* 74:736–744
32. Minemoto T, Murat M (2014) Device modeling of perovskite solar cells based on structural similarity with thin film inorganic semiconductor solar cells. *J Appl Phys* 116
33. Lee DY, Na SI, Kim SS (2016) Graphene oxide/PEDOT:PSS composite hole transport layer for efficient and stable planar heterojunction perovskite solar cells. *Nanoscale* 8:1513–1522

An Algorithm for Estimation of Reference Current for a Shunt Active Power Filter with Active Compensation of DC Offset



Sangeeta L. Mahaddalkar and Vinayak N. Shet

Abstract Grid integration of distributed generation units (DG) and usage of nonlinear loads has increased drastically in recent years. However, it has also resulted in the injection of DC offset in the supply grid. Presence of DC component in the grid gives rise to incorrect estimation of reference quantity for mitigating devices such as dynamic voltage restorer and active power filter and also cause issues in grid synchronization due to the low-frequency oscillations in the estimated frequency and phase. This paper proposes an algorithm for accurate estimation of the reference current by compensating the DC offset. Performance of the algorithm is evaluated for control of a shunt active power filter. The control logic is designed for system-on-chip (SoC) technology due to advantages such as reduced size, reduced power consumption, reconfigurability and scalability. The designed controller utilizes less than 20% of the FPGA resources and requires only 0.225 W power.

Keywords DC offset compensation · Reference estimation · SoC · Shunt active power filter

1 Introduction

Integration of distributed generation (DG) Units has increased the complexity of grid network. As DG integration technology uses switching devices, it has also resulted in a variety of power quality (PQ) issues. Integration of a large wind turbine into a weaker grid introduces PQ issues during start and stop operations [1]. Issues such as voltage disturbances, harmonic injection and DC component injection are more frequently observed in today's grid network. Voltage disturbances such as sag and swell occur due to fault or sudden load switching while harmonic injection is

S. L. Mahaddalkar (✉) · V. N. Shet
Goa College of Engineering, Goa University, Goa, India
e-mail: sangeeta@gec.ac.in

V. N. Shet
e-mail: vns@gec.ac.in

caused by solid state drives and nonlinear loads. DC component is injected into grid network by grid connected solar PV inverters [2, 3], cycloconverters used for AC-to-AC frequency conversion [4], nonlinear loads such as LED lights [5] and also due to nonlinearities in data acquisition sensor. The power quality issues are further aggravated by usage of nonlinear loads. As per Bureau of Indian Standards (BIS), the PV system should limit the DC injection below 0.5% of the maximum rated output current of the inverter [6]. The ill effects of PQ disturbances include unwanted tripping of power supplies, thereby causing malfunctioning of sensitive biomedical healthcare equipment, reduction of transformer life due to overheating caused by harmonics [7], transformer core saturation [8], machine vibration, overheating of connected equipment, incorrect frequency and phase determination due to the presence of DC component in the PLL input. These PQ issues are mitigated using devices such as dynamic voltage restorer for voltage disturbances and active filters for harmonic cancellation. The control methodology typically involves sensing the grid voltage and current and accurately estimating the reference quantity for control of these mitigating devices. A phase locked loop (PLL) is used for determining the phase information from the angular frequency of the grid supply voltage. Synchronous reference frame phase locked loop (SRF PLL) is generally used as it has a simple structure with a PI controller. However, under distorted grid conditions, SRF PLL is not accurate for phase estimation [9]. PLL based on adaptive filter can extract the amplitude, frequency and phase under non-stationary conditions. However, presence of DC component in the sensed quantity results in low-frequency oscillations in the estimated frequency and phase [11, 12] and hence, the reference is not accurately estimated. Hence, the DC offset in the sensed signal should be compensated before applying the signal to PLL input which is used for estimating the reference signal for mitigating devices.

Various methods of DC offset compensation are reported in the literature. DC offset error compensation algorithm proposed in [13] estimates the second harmonic of the fundamental frequency in the current by using a second order generalized integrator (SOGI), along with its 90-degree phase shifted signal using an APF. An eighth order harmonic term is obtained from this signal and subsequently the DC component which is compensated using PI controller. Simulation model for DC offset compensation using a PI controller and an inverter is proposed in [14].

Hardware platforms such as microcontrollers and digital signal processors (DSP) are used for implementing the control algorithms. In a typical present day grid control, various parameters need to be controlled due to varied system dynamics. Complexity in control system design necessitates integrating the entire control task on a single chip. System-on-chip (SoC) technology is gaining popularity in spheres ranging from mobile computing to Internet of Things (IoT) due to advantages such as miniaturization, reduction in power consumption, reconfigurability and scalability. SoC FPGA is an integration of a processor and reconfigurable programmable logic on a single chip. The Zynq SoC FPGA family from Xilinx [16] comprises of ARM Cortex A9-based application processing unit and 28 nm programmable logic (PL) in a single device. The ARM Cortex core includes on-chip RAM and ROM, external memory interfaces and various peripheral interfaces. As the control system complexity and

size increase it becomes inherently necessary to incorporate the control on a single SoC hardware platform so that the system can be reconfigured easily by in system programming. Also, it should be possible to implement the entire control task on a single chip so that miniaturization and power optimization are achieved. This is possible by the use of SoC FPGA.

This paper proposes an algorithm for estimation of reference quantity for the shunt active power filter (SAPF) by compensating the DC offset and harmonics. Comparative evaluation of the reference estimator performance with and without the DC offset compensation algorithm is shown. The controller is targeted onto Zynq SoC XC7z020-1clg484 and resource, and power utilization of the SoC is evaluated. The paper is organized as follows. Section 2 discusses the design of the controller for a SAPF, Sect. 3 discusses the proposed algorithm for DC offset compensation, and Sect. 4 evaluates the performance of the proposed algorithm for a SAPF. Section 5 covers the Zynq FPGA implementation results in terms of the resource utilization and power requirement by the designed controller. The novelty is that the proposed control strategy is implemented as reconfigurable logic on SoC device. Currently SoC is state-of-the-art technology and so the controller can be incorporated in future smart mitigation devices.

2 SAPF Controller Design

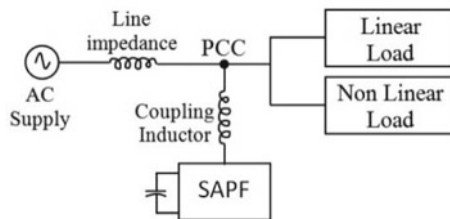
Shunt active power filter (SAPF) is used for compensating harmonics and reactive power in a distribution system. The SAPF is connected at the point of common coupling (PCC) through a coupling inductor as shown in Fig. 1.

Considering the supply voltage having an amplitude V_m , frequency f , angular frequency $\omega = 2\pi f$ and represented by

$$v(t) = V_m \sin(\omega t)$$

Using Fourier series expansion, the current drawn by a nonlinear load is expressed as

Fig. 1 Connection diagram of a SAPF



$$i_L(t) = \underbrace{i_{L1} \sin \omega t \cos \vartheta_1}_{\text{Active}} + \underbrace{i_{L1} \cos \omega t \sin \vartheta_1}_{\text{Reactive}} + \underbrace{\sum_{h=2}^{\infty} I_h \sin(h\omega t + \vartheta_h)}_{\text{Harmonic}} \quad (2)$$

where i_{L1} represents the amplitude of the fundamental component of the load current and ϑ_1 its phase. The instantaneous power drawn by the nonlinear load is expressed as

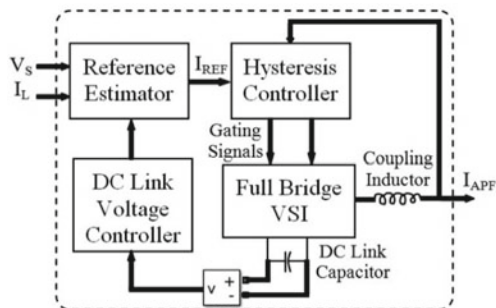
$$p_L(t) = \underbrace{V_m I_{L1} \sin^2 \omega t \cos \vartheta_1}_{\text{Active power}} + \underbrace{V_m I_{L1} \sin \omega t \cos \omega t \sin \vartheta_1}_{\text{Reactive power}} + \underbrace{V_m \sin \omega t \sum_{h=2}^n I_h \sin(h\omega t + \vartheta_h)}_{\text{Harmonic power}} \quad (3)$$

If the SAPF injects current supplying the reactive and harmonic components of the load power, then the supply has to provide only the real component of the load power. The supply current will hence be sinusoidal and in phase with the supply voltage. However, there is also some power loss in the switches of the current source inverter and DC link capacitor charge leakage. To account for this additional dc link voltage control loop is necessary. The subsystems of a SAPF are a reference current estimator, a PWM generator for generating the gating signals and a voltage source inverter. The block diagram of the control logic of the SAPF is shown in Fig. 2.

The frequency f and phase ϑ of the sensed source voltage V_s , along with the amplitude of the fundamental frequency component I_{L1} of the sensed load current I_L are tracked using the adaptive filter proposed in [10]. The load component of the compensating current is

$$I_{LC} = I_L - I_{L1} \sin \vartheta \quad (4)$$

Fig. 2 Control logic of SAPF



The DC link voltage controller estimates the loss component of the compensating current I_{LOSS} by regulating the drop in the DC link voltage using a PI controller. The reference current is given by

$$I_{REF} = I_{LC} + I_{LOSS} \tag{5}$$

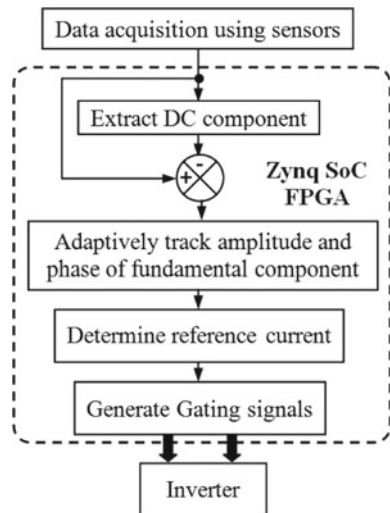
The hysteresis controller compares the error between the reference current and the filter output current with the hysteresis band and generates PWM signals for control of the SAPF. The SAPF control logic is implemented using Xilinx System Generator [15] blocksets.

3 Proposed Algorithm for Estimation of Reference Current by Compensating the DC Offset in the Sensed Signals

The controller designed in Sect. 2, however, does not account for the presence of DC offset in the grid voltage. With DC component, the reference estimation is not accurate due to slow varying oscillations in the estimated phase. Hence, the methodology as shown in the flowchart of Fig. 3 is used.

Let the supply voltage denoted by $V_{in}(t)$ comprise of a fundamental frequency component and disturbances which include DC component, harmonics and noise. Let load current be denoted by $I_L(t)$. These quantities are sensed using sensors and discretized using 12-bit ADC available in the Zynq SoC FPGA. The DC component of the voltage is extracted using DFT. The discrete Fourier transform (DFT) of a periodic discrete time series $x(n)$ is defined by

Fig. 3 Flowchart of proposed methodology for DC offset compensation



$$X(k) = \sum_{n=0}^{N-1} x(n)W_N^{kn}, k = 0, 1, 2, \dots, N-1 \quad (6)$$

where W_N is the twiddle factor and is defined as

$$W_N = e^{-j2\pi/N} \quad (7)$$

The first term in the DFT expression represented by (6) gives the DC component as

$$X(0) = \sum_{n=0}^{N-1} x(n) \quad (8)$$

The PLL input signal is thus derived as

$$V(t) = V_{in}(t) - e(t) - X(0) \quad (9)$$

where $e(t)$ denotes the noise and harmonic components. The fundamental component amplitude $V_m(t)$, frequency $\omega(t)$ and phase $\emptyset(t)$ are derived using the adaptive algorithm proposed by Ziarani [10] the dynamics of which are defined as

$$V_m(t) = \int k_1 e(t) \sin \phi(t) dt \quad (10)$$

$$\omega(t) = \omega_o + \int k_2 e(t) V_m(t) \cos \phi(t) dt \quad (11)$$

$$\emptyset(t) = \int [\omega(t) + k_2 k_3 e(t) V_m(t) \cos \phi(t)] dt \quad (12)$$

The load component of the reference signal is derived based on (4) from the derived amplitude I_m of the load current using another adaptive filter and using the phase information from (12). The reference current is derived using (5).

4 Performance Evaluation

The performance of the designed control strategy is evaluated by developing a simulation model of the SAPF based on Xilinx System Generator. The SAPF supplies a nonlinear rectifier load. The SAPF is switched on at 0.1 s. The performance is evaluated under healthy as well as distorted grid conditions. Different test cases for the input grid supply as specified below are used for performance evaluation.

Test Case 1: Pure sinusoidal input

$$V_{in1} = 230 \sin(100\pi t) \tag{13}$$

Test Case 2: Sine with constant DC offset alone

$$V_{in2} = 5 + 230 \sin(100\pi t) \tag{14}$$

Test Case 3: Sine with constant DC offset, third harmonic and fifth harmonic

$$V_{in3} = 10 + 230 \sin(100\pi t) + 45 \sin(300\pi t \angle - 25^\circ) + 34.5 \sin(500\pi t \angle 35^\circ) \tag{15}$$

Test Case 4: Sine with constant DC offset, third harmonic and third sub harmonic

$$V_{in4} = 10 + 230 \sin(100\pi t) + 46 \sin\left(\frac{100\pi}{3}t \angle - 20^\circ\right) + 23 \sin(300\pi t \angle - 32^\circ) \tag{16}$$

Test Case 5: Sine with exponentially decaying DC offset

$$V_{in5} = 230 \sin(100\pi t) + 100e^{-4t} \tag{17}$$

The estimated frequency of fundamental component of supply under healthy and polluted condition with DC offset is shown in Fig. 4. It is seen that after the initial PLL synchronization period, the frequency is correctly estimated under healthy conditions. However, in the presence of the DC component, low-frequency oscillations are observed in the estimated frequency. The frequency oscillates between 49.6 Hz and 50.4 Hz. These oscillations affect the estimation of reference quantity for the compensating devices.

The load current (I_L), current injected by the SAPF (I_{APF}) and the supply current (I_S) before and after the connection of the filter for Test case 3 are shown in Fig. 5.

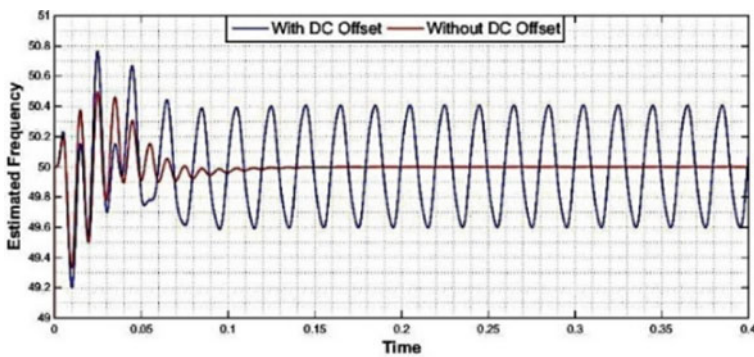


Fig. 4 Estimated frequency of fundamental component without and with DC offset in grid supply

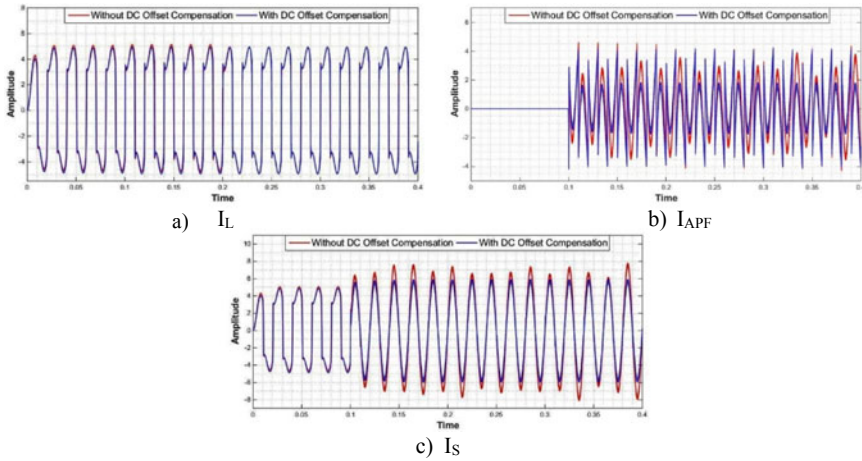


Fig. 5 Performance comparison for Test case 3

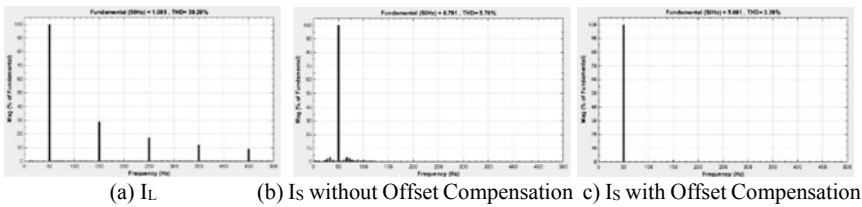


Fig. 6 FFT results

Fluctuations are observed in the supply current when DC component is present in the grid voltage. These fluctuations occur due to oscillations in the estimated frequency and phase. The THD content in various current components is determined using FFT, and results are shown in Fig. 6. The load current has a THD_i of 39.29%. For Case 2, the source current has a THD_i of 3.39% while for Case 3 the THD_i is 5.9%. The FFT results in Fig. 6b demonstrate that the presence of DC component in the grid voltage contributes to interharmonics in the low frequency range from DC to 150 Hz.

Test case 4 evaluates the performance corresponding to DC with subharmonic and harmonic content in grid voltage. The waveforms of I_L , I_{APF} and I_S before and after the connection of the filter for this case are shown in Fig. 7. It is observed that the proposed scheme effectively mitigates under subharmonic as well as harmonic and ensures pure sinusoidal source current.

Test case 5 considers presence of decaying DC component in the grid signal. The waveform of applied voltage is shown in Fig. 8a. The SAPF is switched ON at 0.1 s. The source current I_S before and after the connection of the filter is shown in Fig. 8b. The proposed scheme effectively mitigates decaying DC component also.

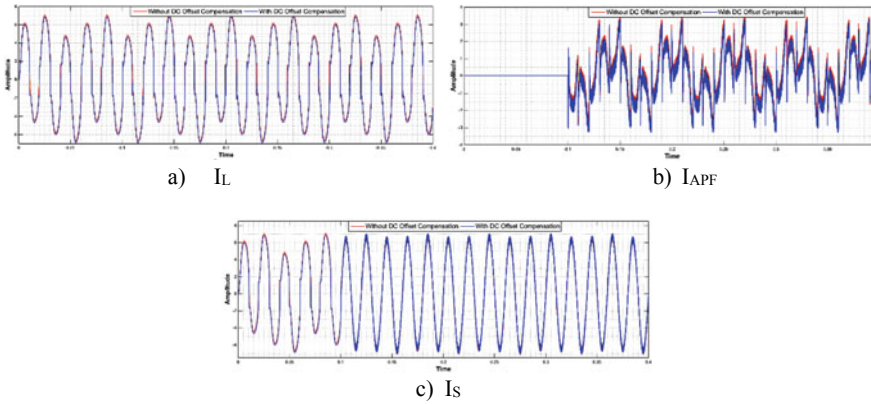


Fig. 7 Performance comparison for Test case 4

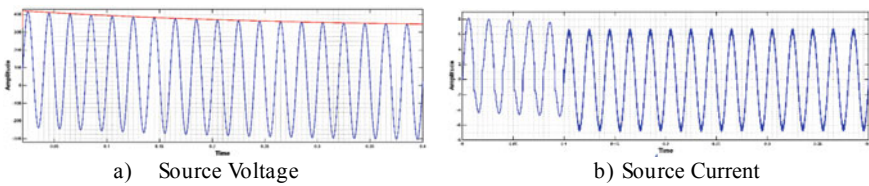


Fig. 8 Waveforms for Test case 5

5 FPGA Implementation

The controller for the SAPF is designed using System Generator. The binary file is generated using system generator token and targeted onto Zynq SoC FPGA XC7z1clg484. The top-level RTL schematic of the targeted design is shown in Fig. 9, while the detailed RTL schematic is shown in Fig. 10.

The FPGA resource utilization by the designed controller is shown in Table 1. The design utilizes 12% of slice LUT's, 1.39% of slice registers, 17.85% of memory and 6.36% of DSP blocks as shown in the chart in Fig. 11.

The power utilized by the design is evaluated using vector-based power analysis using Vivado tool and is shown in Fig. 12. Static power is the power requirement by the various power supply voltages for running the chip, while dynamic power is the power required by the designed controller. The total power requirement is 0.225 W. The device static power requirement is 54% of the total power requirement, while the dynamic power requirement is just 46%. Out of the total dynamic power requirement, 20% is required for signal switching, 35% is required by the slice LUT's and slice registers, 40% is required by the block RAM and 5% is required by the DSP blocks.

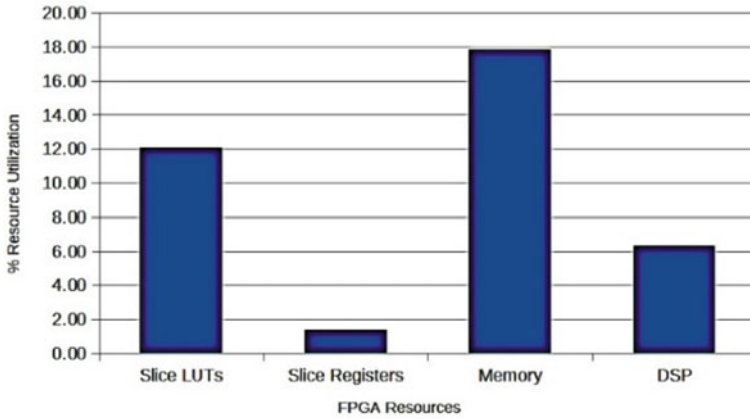


Fig. 11 Percentage of FPGA resources used by design

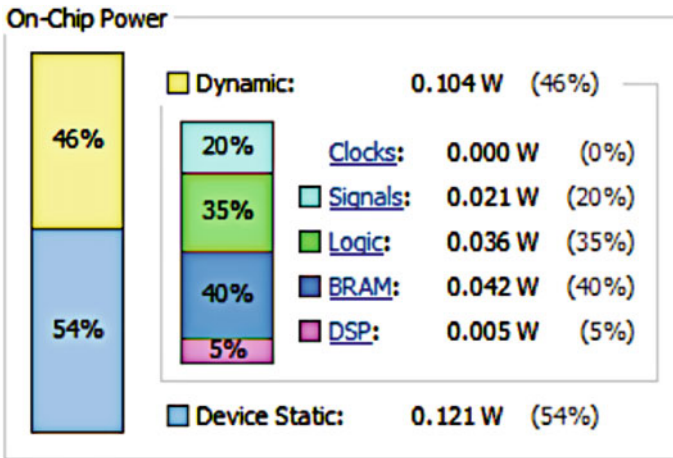


Fig. 12 Power utilization by design

presence of interharmonics in current drawn from source. The DC offset compensation algorithm is able to mitigate interharmonic components, sub harmonic components and decaying DC component, thereby reducing the THD content and hence improving the power quality. The controller is designed and targeted to Zynq SoC FPGA. The controller is optimized for resource and power requirements. The design occupies less than 20% of the FPGA resources and has a total power requirement of just 0.225 W. Results indicate the effectiveness of the proposed methodology under polluted conditions. Usage of reconfigurable logic SoC platform allows integration of other control algorithms on a single chip, thereby managing the entire control centrally and effectively.

References

1. Lucian ID, Mihail A, Dorin B (2013) Effects of distributed generation on electric power systems. In: Liviu M (ed) INTER-ENG 2013, The 7th international conference interdisciplinarity in engineering, Romania, October 2013, Procedia Technology, vol 12(2014). Elsevier, pp 681–686
2. Salas V, Alonso-Abella M, Olias E, Chenlo F, Barrado A (2007) DC current Injection into the network from PV inverters of <5kW for low-voltage small grid connected PV systems. *Solar Energy Mater Solar Cells* 91(9):801–806. <https://doi.org/10.1016/j.solmat.2006.12.016>
3. Salas V, Olias E., Alonso M, Chenlo F and Barrado A (2006) DC current injection into the network from PV grid inverters. In: IEEE 4th world conference on photovoltaic energy conversion, Waikoloa, HI, May 2006, IEEE, pp 2371–2374. <https://doi.org/10.1109/WCPEC.2006.279668>.
4. Gertmar L, Karlsson P, Samuelsson O (2005, September) On DC injection to AC grids from distributed generation. In: EPE 2005, European conference on power electronics and applications, Dresden, Germany. IEEE, pp 1–10. <https://doi.org/10.1109/EPE.2005.219420>
5. Mahaddalkar SL, Shet VN (2020) Real time monitoring of LED lighting loads—a study assessing power quality. In: ic-ETITE, international conference on emerging trends in information technology and engineering, Vellore, India, IEEE, pp 1–7. <https://doi.org/10.1109/ic-ETITE47903.2020.280>
6. Ministry of New and Renewable Energy (Standards & Quality Control Division) (2020) Draft standard on technical requirements for photovoltaic grid tie inverters to be connected to the utility grid in India, 21 April 2020. https://mnre.gov.in/img/documents/uploads/file_f-1587534563451.pdf. Assessed 12 Feb 2021
7. Singh R, Singh A (2010, September) Aging of distribution transformers due to harmonics. In: ICHQP, Proceedings of 14th international conference on harmonics and quality of power, Bergamo, Italy. IEEE, pp 1–8. E-ISBN: 978-1-42447245-1, <https://doi.org/10.1109/ICHQP.2010.5625347>
8. Macan M, Bahun I, Jakopović Z (2011, September) Output DC voltage elimination in PWM converters for railway applications. In: EDPE'11, 17th international conference on electrical drives and power electronics, Slovakia, pp 49–54
9. Golestan S, Guerrero JM, Vasquez JC (2017) Three-phase PLLs: a review of recent advances. *IEEE Trans Power Electron* 32(3):1894–1907. <https://doi.org/10.1109/TPEL.2016.2565642>
10. Ziarani AK, Blumenfeld IM, Konrad A (2002, August) Experimental verification of a novel method of extraction of nonstationary sinusoids. In: MWSCAS-2002, The 2002 45th midwest symposium on circuits and systems, vol 3, Tulsa, Oklahoma, pp I-455
11. Hwang SH, Liu L, Li H, Kim JM (2012) DC Offset error compensation for synchronous reference frame PLL in single-phase grid-connected converters. *IEEE Trans Power Electron* 27(8):3467–3471. <https://doi.org/10.1109/TPEL.2012.2190425>
12. Kherbachi A, Aissa C et al (2019) Enhanced structure of second-order generalized integrator frequency-locked loop suitable for DC-offset rejection in single-phase systems. *Electric Power Syst Res* 170:348–357. <https://doi.org/10.1016/j.epsr.2019.01.029>
13. Lee JS and Hwang SH (2018) DC Offset Error compensation algorithm for PR current control of a single-phase grid-tied inverter. *Energies* 11(9):2308, 1–13. <https://doi.org/10.3390/en11092308>
14. Omar A, Fouad M et al (2018, March) DC offset compensation technique for grid connected inverters. In: IREC 2018, the 9th international renewable energy congress, Hammamet, Tunisia, pp 1–7. <https://doi.org/10.1109/IREC.2018.8362473>
15. Xilinx (2009, December) System generator for DSP user guide, [Online]. Available https://www.xilinx.com/support/documentation/sw_manuals/xilinx11/sysgen_user.pdf. Assessed November 2020
16. Xilinx (2018, July) Zynq-7000 SoC data sheet: overview. [Online]. Available <https://www.xilinx.com/products/silicon-devices/soc/zynq7000.html>. Assessed December 2020

Optimal Design of Controllers for Brix Regulation in Sugar Industry



Sanjay Kumar Singh, Nitish Katal, Sanjay Kumar, and Neha Kumari

Abstract In the sugar industry, brix controller regulates the amount of dissolved sugar present in the solution and directly affects the quality of sugar being produced. Any deviations from the desired set-point will deteriorate the quality of sugar being produced and may indirectly impact the plant economy. The work emphasizes the optimal tuning of the PID controllers used for brix regulation in sugar plants. The plant dynamics are determined using system identification, and then optimal PID controller is synthesized using salp swarm algorithm. The efficacy of the designed controller has been compared against the PID controllers tuned using robust time response method and the optimal controllers obtained using genetic algorithm and simulated annealing. The obtained results have been compared, and it has been observed that the PID controllers tuned using salp swarm algorithm offer a good time and frequency domain behavior.

Keywords Salp swarm optimization · Brix regulation · Process control

1 Introduction

In sugar industry, efficient production of sugar demands precise and robust control of the various processes to provide steady production reliability. Brix regulation is one of the essential processes in the rodi-melter process in sugar manufacturing. In brix regulation systems, the PID controllers are generally used in a closed-loop along with a brix sensing device, i.e., conductivity-based device, for monitoring the amount of sugar content present in solution at a specific temperature. The simplicity

S. K. Singh (✉) · N. Kumari

Department of Electrical and Electronics, Amity University Rajasthan, Jaipur, India

e-mail: sksingh.eee@gmail.com

N. Katal

School of Electronics, Indian Institute of Information Technology, Una, H.P, India

S. Kumar

Electrical Engineering Department, UIET, Himachal Pradesh University, Shimla, H.P, India

and ease of tuning and implementation of PID controllers boost their application in the process control industry [1].

This paper proposes the design of an optimal controller for the brix regulation process in rodi-melter machines used in sugar industry. Initially, the PID controller is tuned using robust time response method, and to design optimal PID controllers, the optimal controller synthesis is expressed as an optimization problem and is solved using three nature-inspired algorithms, namely genetic algorithm, simulated annealing, and salp swarm algorithm (SSA) using time-domain performance objective of the minimization of the integral of the square of the error (ISE).

The results are compared, and it has been observed that the PID controllers obtained by nature-inspired algorithms offer better performance in both time and frequency domains, particularly the salp swarm optimization algorithm showed the best closed-loop time and frequency domain behavior.

2 Background

This section provides a brief background on the basics of the PID controllers and the nature-inspired algorithms used in this study.

2.1 PID Controller

PID controllers are widely used controllers in several processing plants and alone account a major share of the total controllers used in industries. They help in regulating the desired closed-loop characteristics of the processes, whether it is to regulate the pressure in a chamber or the control of motors, and many more, PID controllers are used extensively [2, 3]. Equation (1) gives the generalized equation of a PID controller. Figure 1 shows the schematic representation of a typical feedback control system with a PID controller.

$$K(s) = K_p + \frac{K_i}{s} + K_d \cdot s \quad (1)$$

where, K_p , K_i , and K_d are the tunable parameters.

2.2 Salp Swarm Algorithm

In 2017, Mirjalili et al. [4] proposed a nature-inspired stochastic algorithm inspired by the cooperative behaviors of salps, namely salp swarm algorithm (SSA). Salps use

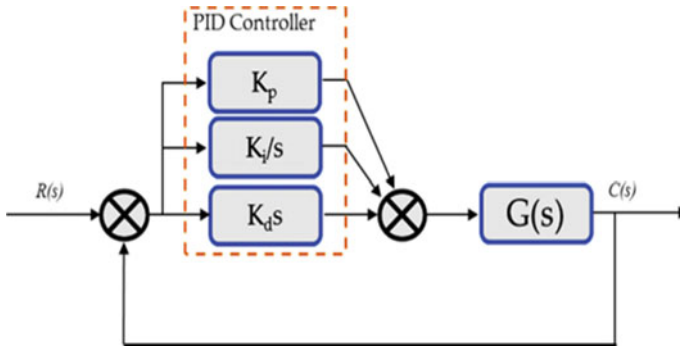


Fig. 1 Schematic representation of closed-loop control system with PID controller

swarm-based intelligence for navigation and for searching for food in the oceans. SSA randomly initializes the initial population and the algorithm operates in two phases, exploration and exploitation, to improve the solution iteratively. The exploration phase is also known as the diversification phase spans around the exploration of the various promising regions in the search space, and the exploitation phase focuses on the neighborhood to search for the best possible solution.

2.3 Genetic Algorithm

Genetic algorithm (GA) is an evolutionary algorithm proposed by Goldberg [5] and draws inspiration from Darwin's theory of natural evolution. In GA, initially, the individuals in the population are generated randomly followed by the application of the GA operators namely, selection, crossover, and mutation for generating subsequent generations. Initially, the selection operator, inspired by the process of natural selection, selects only the fittest individuals from the population. Then, in the crossover phase, the individuals selected in the first phase are selected randomly to participate in reproduction to generate a new population of individuals. Then the fitness or the cost of the new population is estimated. The mutation operator randomly changes the gene information of some of the offspring to maintain diversity and also to avoid premature convergence.

2.4 Simulated Annealing

Simulated annealing is a stochastic computational algorithm proposed by Kirkpatrick in 1983 [6]. Simulated annealing is inspired by the process of metallurgical annealing and is a blend of statistical mechanics and optimization. Annealing involves heating treatment of a material to the desired temperature followed by a controlled cool down.

This process improves the quality of the material by increasing the crystal size and reducing deformities.

In the simulated annealing algorithm, a new solution is generated randomly at each iteration and its cost is evaluated. If the random solutions lower or maximize the objective function based upon the nature of the optimization problem, it is accepted. The algorithm also reserves some solutions that are slightly different from the current best solution to prevent the algorithm from being trapped in non-optimal maxima or minima. As the search algorithm progresses, the temperature coefficient is reducing as the algorithm converges to a global best solution.

3 System Identification of Brix Regulation System

To produce quality sugar, the industrial setup consists of single-element control to regulate the brix level of sugar solution [7, 8]. The untreated sugar solution is first taken in the rodi-melter tank which is provided with a continuous stirrer, a brix sensor, and an inlet water supply with a control valve so that the dilution of the solution can be carried out so that the required brix level is maintained in the solution. For the control of the control valve, a Honeywell made PID controller and Brix Monitor has been installed in the factory facility, while the linear control valve and brix sensor have been supplied by M/s I&S Pvt. Ltd., Dehradun (Figs. 2 and 3).

System identification toolbox is used to approximate the equivalent first-order with time delay (FOTD) model of the system. $G(s)$ is the approximate FOTD transfer function of the rodi-melter system and is given by Eqs. (2) and (3) which gives the approximate FOTD model $H(s)$ for the brix sensor, which has been used in a feedback loop of the PID control loop.

$$G(s) = \frac{6.1}{19.496 \cdot s + 1} e^{-5.4s} \quad (2)$$

$$H(s) = \frac{0.0060752}{6.1785 \cdot s + 1} e^{-5.066s} \quad (3)$$

4 Optimal Controller Design

This section emphasizes on the design of the controllers using robust time response method and the optimal PID controller design using time-domain performances using nature-inspired algorithms.

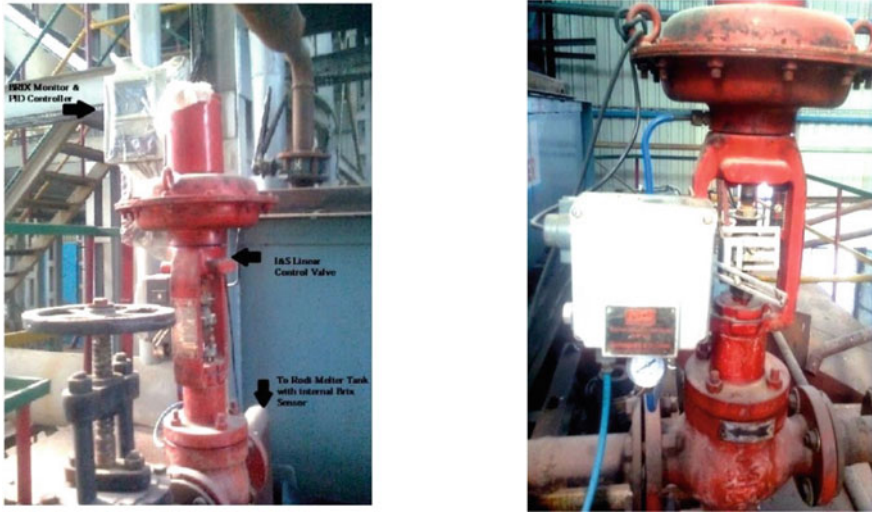


Fig. 2 Photograph of the brix controller set up at the plant

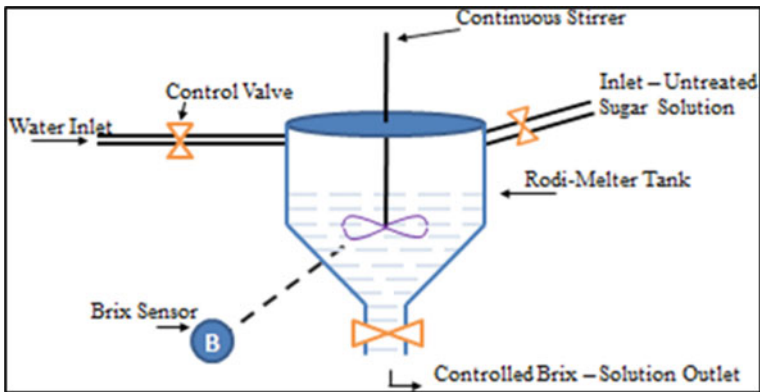


Fig. 3 Schematic representation of the process set up at the plant

4.1 Controller Synthesis Using Robust Time Response Method

Robust time response estimation is an automated tuning algorithm, used for tuning the controller parameters. It is a classical PID tuning method, and the cost of recursive least square of the control signal is reduced under the essence of disturbance to find the controller gains. The transfer function of the PID controller obtained using robust time response is given as:

$$K_{\text{RTR}}(s) = 9 + \frac{1}{s} + 10 \cdot s \quad (4)$$

4.2 Controller Synthesis Using Time-Domain Specifications

It has been observed that the response offered by the feedback control system with PID controller synthesized using robust time response method is oscillatory and slow, so the gains acquired using RTR method are not optimal. Therefore, controller gains need to be further tuned. In this work, nature-inspired algorithms have been used to tune the PID controllers by minimizing ISE given as $\mathbf{J}_{\text{ISE}} = \int_0^{\infty} [\mathbf{e}(\mathbf{t})]^2 \cdot d\mathbf{t}$, so that the designed controller offers a good time-domain response [5]. Nature-inspired algorithms, namely genetic algorithm, simulated annealing, and salp swarm optimization, have been used to obtain optimal compensator gains. The use of nature-inspired algorithms has been explored for designing QFT-based robust controllers for distillation columns [9], and in [7], design of optimal controllers has been considered for centrifugal machines used in sugar industries.

The optimal design process has been carried out in MATLAB. Firstly, the genetic algorithm with a population size of 150 and tournament-based selection has been used for design purposes. Equation (5) gives the PID controller gains obtained after the optimization process.

$$K_{\text{GA}}(s) = 24.91 + \frac{0.82}{s} + 121.71 \cdot s \quad (5)$$

Then, the simulated annealing algorithm has been used to find the optimal controller gains. An exponentially increasing temperature with Boltzmann annealing has been used in optimization. The controller obtained after optimization is given by the equation below, and Fig. 5 shows the closed-loop time-domain response of the compensated system.

$$K_{\text{SA}}(s) = 21.382 + \frac{0.992}{s} + 88.21 \cdot s \quad (6)$$

At last, salp swarm algorithm is used to find the optimal gains for the PID controller. The algorithm-specific parameters are set as follows, maximum iterations are set to 1000, the number of salps is taken as 150 with 50% of the population of salps acting as leaders and the other 50% as the followers. After the optimization, the controller obtained is given by Eq. (7).

$$K_{\text{SSA}}(s) = 26.521 + \frac{1.021}{s} + 132.5 \cdot s \quad (7)$$

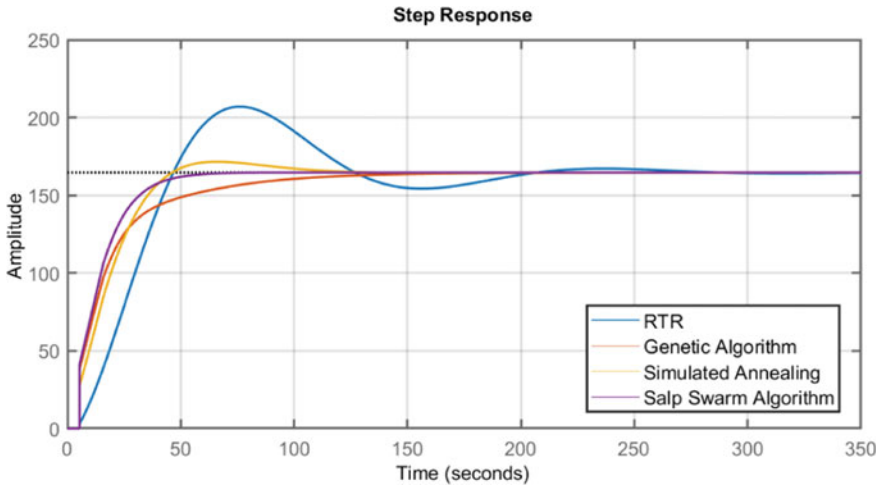


Fig. 4 Comparative step response of the compensated system

5 Results and Discussions

In this paper, optimal brix regulatory loop for the rodi-melter machine has been designed using GA, SA, and SSA by minimizing the ISE. The obtained controllers are compared with the controller obtained using the classical method of robust time response. The compared closed-loop time-domain response of the feedback control system with the controllers designed in Sect. 4 is shown in Fig. 4, and the Bode plot for the closed-loop frequency domain response is shown in Fig. 5. A comparative analysis of the various performance specifications is also illustrated in Table 1. From Figs. 4 and 5 and Table 1, it can be observed that the PID controller obtained.

It is observed that the PID controller incorporating the classical method of robust time response has an oscillatory closed-loop response with high overshoot percentage and poor settling time. The closed-loop time response offered by the PID controller tuned by the nature-inspired algorithms of GA, SA, and SSA offers a better response. Particularly, the PID controller tuned using SSA algorithm presents the minimum rise and settling times and also shows no overshoot. Thus, the PID controller synthesized using the SSA algorithm offers the best response when compared to the other controllers.

6 Conclusion

In this paper, the optimal tuning of the controllers used in brix regulation in rodi-melter process in sugar industry is done using three nature-inspired algorithms, namely GA, SA, and SSA. The work has been compared with the classical method

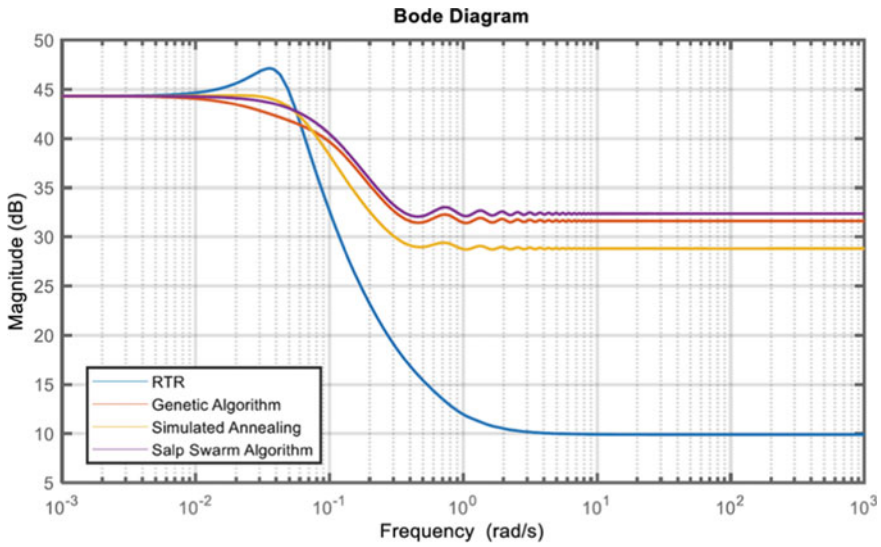


Fig. 5 Comparative frequency domain response of the compensated

Table 1 Compared time-domain performance

Algorithms	Overshoot percentage (%)	Rise time (s)	Settling time (s)
Robust time response	25.76	31.94	192.333
Genetic algorithm	0	43.37	107.138
Simulated annealing	4.23	29.14	94.605
Salp swarm optimization	0	25.12	48.016

of robust time response. The controllers obtained using SSA offer better-closed-loop time response as compared to other methods. The optimal design of controllers for brix regulation for rodi-melter processes in sugar industry can boost the quality of the sugar being produced and can also reduce the plant downtimes and thus boost the plant economy.

References

1. Åström KJ, Hagglund T (1995) PID controllers: theory, design and tuning, NC, USA, Research Triangle Park, Instrument Society of America
2. Åström KJ, Albertos P, Quevedo J (2001) PID control. Control Eng Pract 9:159–1161.J

3. Bequette BW (2003) Process control: modeling, design, simulation. Prentice Hall Professional
4. Mirjalili S, Gandomi AH, Mirjalili SZ, Saremi S, Faris H, Mirjalili SM (2017) Salp swarm algorithm: a bio-inspired optimizer for engineering design problems. *Adv Eng Softw* 114:163–191
5. Krishnakumar K, Goldberg DE (1992) Control system optimization using genetic algorithms. *J Guidance Control Dyn* 15(3):735–740
6. Kickpatrick S, Gelatt CD, Vecchi MP (1983) Optimization by simulated annealing. *Science* 220(4508):671–680
7. Singh SK, Boolchandani D, Modani SG, Katal N (2014) Multiobjective optimization of PID controller for temperature control in centrifugal machines using genetic algorithm. *Res J Appl Sci Eng Technol* 7(9):1794–1802
8. Sunori SK, Juneja PK, Chaturvedi M, Mittal J (2017) Dead time compensation in sugar crystallization process. In: *Proceeding of international conference on intelligent communication, control and devices*. Springer, Singapore, pp 375–381
9. Katal N, Narayan S (2021) Automated synthesis of multivariate QFT controller and pre-filter for a distillation column with multiple time delays. *J Process Control* 99:79–106

DNN Machine Translation for Indian Languages



Shashi Pal Singh, Ajai Kumar, Lenali Singh, and Tanya Angra

Abstract For developing and using various features provided by the internet by all the sections of the society, it is important to make the technology accessible irrespective of the language. So, the translation between the languages becomes important criterion. Previously, the machine translation has been used to translate between different languages, which eased the communication between people from different linguistic backgrounds. But in the last couple of years, the advancement and enhancement of Deep Neural Network (DNN) allowed us to rewrite our approach for machine translation completely. This paper discusses the process and the methodology to build the Machine translation system using Deep Neural Network (DNN) for translation between different Indian languages, using the combination of two ideas, i.e., Recurrent Neural Networks and Encoding.

Keywords RNN · Deep neural networks · Sequence to sequence · Machine translation · Natural language processing

1 Introduction

The method of translation using probability gives, quite surprisingly, better results than rule-based or any other systems as designed by linguistics. In SMT, each and every word in the input sentence is translated by finding all the ways humans have translated the same word in the training data. Then, every possible grouping of

S. P. Singh (✉) · A. Kumar · L. Singh
Center for Development of Advanced Computing, AAIG, Pune, India
e-mail: shashis@cdac.in

A. Kumar
e-mail: ajai@cdac.in

L. Singh
e-mail: lenali@cdac.in

T. Angra
Banasthali Vidyapith, Banasthali, Rajasthan, India

these words is considered to make a bunch of most possible sentences. Probability plays an important role here. Out of this bunch of possible sentences, it helps to get the best out of it. This approach obviously sounds better than the rule-based one but it requires the human efforts in case of building a multi-step model. Wouldn't it sound amazing if the whole machine translation system acts as a black box that learns how to translate by itself— just by looking at training data?

Yes, this thing does happen because of the presence of neural network-based sequence-to-sequence learning. This seq2seq learning model is essentially an encoder-decoder model, in which the sentence is fed into the encoder (RNN), one word at a time, and the result is obtained after proper processing of all the words will be the values that signify the entire sentence. The decoder (RNN) takes these values and applies the similar logic in reverse so as to decode the original sentence, in another language.

In this paper, our whole attention is on building this seq2seq model that will translate Hindi sentences to Punjabi sentences. We took parallel corpora of around 30 K sentences for training our basic model and the results are evaluated. To improve our results further, we incorporated attention, copy net mechanism, and bidirectional RNN modules into our model.

2 Literature Survey

2.1 *Machine Learning*

Machine learning is ability to automatically learn and improve from experience without being explicitly programmed. This means there is no need of writing a specific program for a specific task, instead, some observations or data is provided, at which the system looks on, finds out the patterns, and in this way, builds a program for itself for that specific task.

The tasks such as classification of images, clustering the data based on some observations, prediction of any real-value based on the inputs provided, etc. all are performed with the help of deep learning. Deep learning models can achieve state-of-the-art accuracy, sometimes even exceeding human-level performance. Models are trained by using a large set of labeled/unlabeled data and neural network architectures that contain many layers. In this paper, the complete focus is on labeled data.

2.2 *Deep Neural Networks*

These are the neural network architectures that are used by most of the deep learning models. Traditional neural networks contain only 2–3 hidden layers, while deep networks can have as many as 150 (Fig. 1).

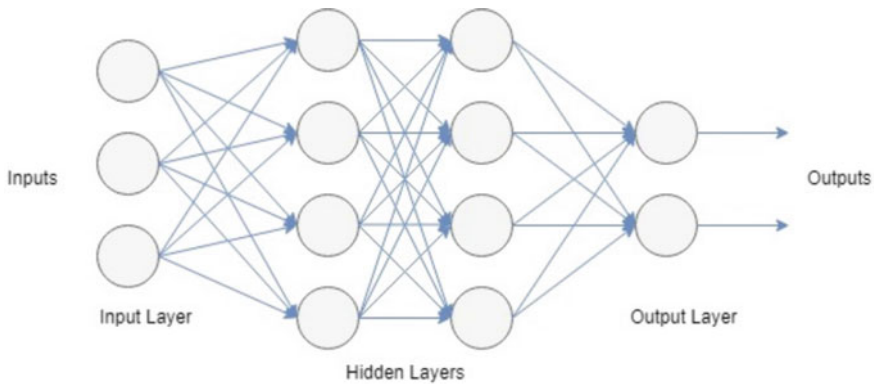


Fig. 1 A deep neural network

There are two phases of deep learning. One is training, where both input and the desired output are given to the model so that it can learn the patterns, and the other is an inference, where only source data is available and the model predicts the output. While training, a feedback loop is introduced in the model to improve quality of the model on the basis of error showing. The weights are adjusted to minimize the error and optimize the model. During inference, the feedback loop is removed and the trained model gives the prediction.

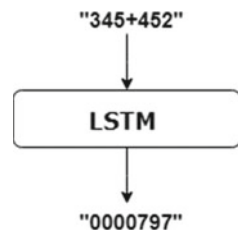
2.3 Sequence to Sequence

This is a supervised learning algorithm that is based upon the sequence of tokens or words or segments (for example, text, and audio) and the output generated is another sequence of tokens. One of the major applications of this algorithm is Machine Translation which is being discussed throughout this paper.

The implementation of this model is based upon the length of input and output sequences (Fig. 2).

Here, in this case (adding strings of digits), it is possible to generate target [...] given input [...t]. But, in general cases (e.g., Machine Translation), input sequences and output sequences have different lengths and the entire input sequence is necessary in order to start generating the target sequence.

Fig. 2 Sequence to sequence [1]



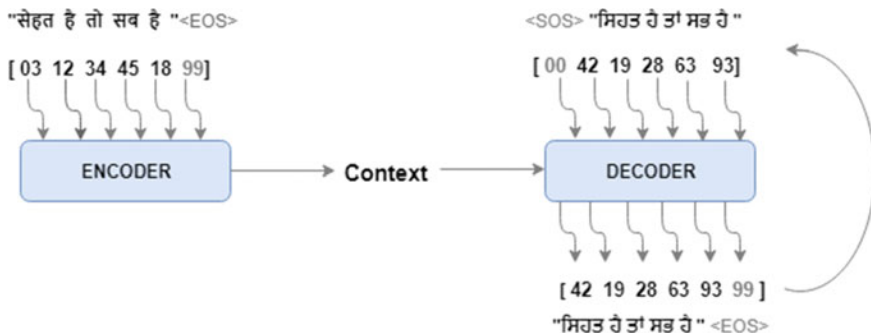


Fig. 3 Encoder and decoder

To implement the model by considering this aspect, two RNNs are required that are connected end-to-end. The first one is commonly known as encoder and the other one is known as decoder (Fig. 3).

2.4 The Encoder

The output is discarded and the hidden state is used as an input along with the next input word. In this fashion, at the end of the sentence, the hidden state captures the context of the sentence and is used in the decoding step (Fig. 4).

2.5 The Decoder

At every step of decoding, the decoder is given an input token and a hidden state. The early input token is the start-of-sequence <SOS> token, and the primary hidden state is the context vector (Fig. 5).

Fig. 4 Encoder

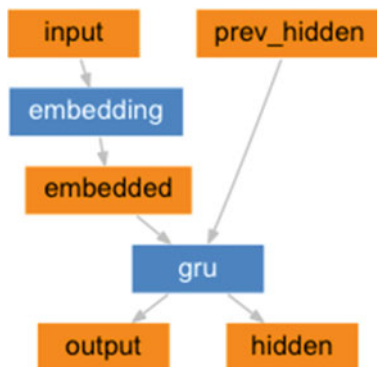
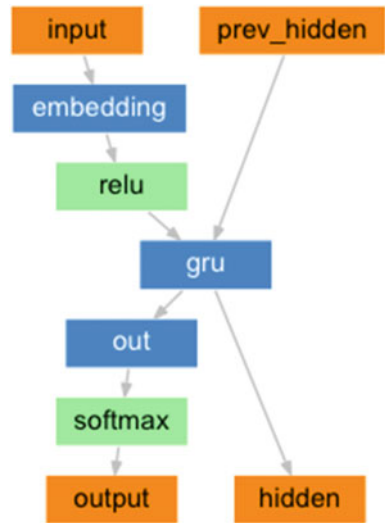


Fig. 5 Decoder



The working of decoder is slightly different in the two modes: Training and Inference (Fig. 6).

In the inference process, the output at the current time step becomes the input in the next time step. This means that the decoder must have dynamic embedding capability in the inference model. But, to make the embeddings dynamically, the embedding parameters should be present that are created by the decoder in the

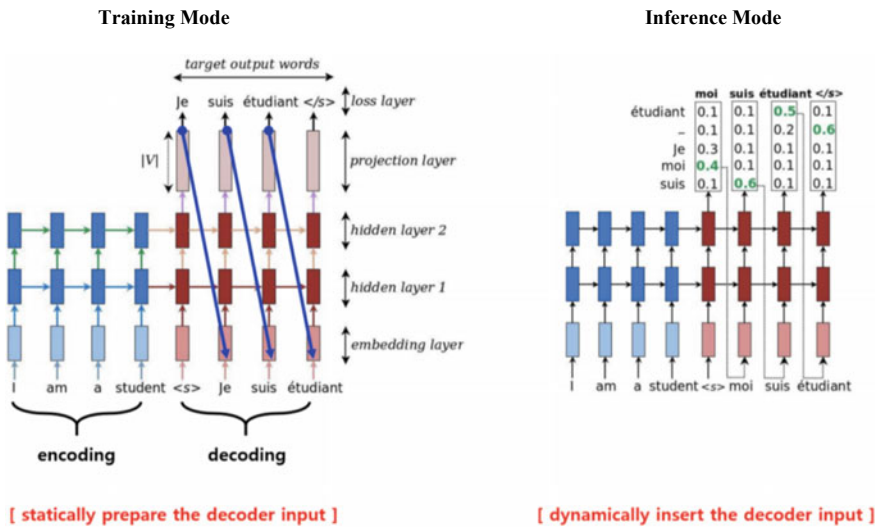


Fig. 6 Training and inference modes

training mode. To create these parameters, the input (i.e., a sequence of words) on the decoding side must be right-shifted to one-time step by prefixing a start marker to it.

2.6 *Projection Layer*

The projection layer is responsible for mapping the top hidden states of the decoder to a continuous vector space. From the mapped vector, the corresponding word can be known. Whereas this vector form is used as an input for predicting the next vector, the corresponding word form is used for generating the translated sequence.

2.7 *Attention*

This approach works fine for short sentences. But, if the size of the sentence is too long, then this is not enough to capture the entire meaning and will surely lead to information loss, etc. Attention is the mechanism that plays a role here. It allows machine learning module to look the information the original sentence holds, then generate the correct word according to input word it works on and the context.

It further means that the translation is not done only by using the last hidden state of the encoder, rather by using the context vector along with it. This process allows the decoder to capture somewhat global information which is very necessary in case of long sentences.

2.8 *Copy Net*

It is quite possible that the embeddings generated in the decoder at the time of inference don't correspond to any word present in the vocabulary, created by using training data. In that case, these embeddings are represented by <unk> marker marking them as unknown.

It would be better to replace these <unk> tags by something relatable. Here, copy net mechanism plays a role. It allows us to find out the corresponding source word for which the target word is defined to be unknown. Then, it depends upon us whether to replace these <unk> tags by the related source words or by the resultant words that come after transliterating the related source words into the target language.

For example:

Source: ਤੁਹੱ ਂਗੁਲੋਫੁੰਡਯਿਨ ਅਖਬਾਰ ਕਹਾ ਜਾਤਾ ਖਾ |

Predicted: ਉਹਨਾਂ ਨੂੰ <unk> ਅਖਬਾਰ ਕਹਿਾ ਜਾਂਦਾ ਸੀ |

Reference: ਉਹਨਾਂ ਨੂੰ ਏਗਲੋ - ਇੰਡੀਅਨ ਅਖਬਾਰ ਕਹਿਾ ਜਾਂਦਾ ਸੀ |

3 Methodology

We have taken a parallel aligned corpus consisting of 30,000 Hindi and Punjabi sentences for the training purpose.

3.1 Pre-processing

Our first task is pre-processing these input sentences which includes cleaning followed by vocabulary construction.

The cleaning of the text is done by normalizing the case into lower case, removing punctuation from each word, removing non-printable characters, and at last, tokenizing the text by white space. The tokenized text is further used to construct the vocabulary. Two types of vocabulary tables are needed. One is word to id and the other is id to word.

In word to id, unique ids are assigned to each word in the text.

For example:

Sentence I: “पत्रकार व्यवसाय में जबरदस्त प्रतियोगिता है।”

Sentence II: “हॉट्टी में खेल संबंधी पत्रिकाएं निकलीं।”

Then word to id table is formed up in the following way (Table 1).

And so on. The starting ids are reserved for special tags like <EOS>, <UNK >, etc. Similarly for the Punjabi text.

In id to word, the words are mapped to ids. This is basically used in the inference process.

3.2 Embeddings

Embeddings are generated for each and every word in the source and target corpus. It is nothing but a simple conversion of the words into numbers so that computation can be done on them.

Table 1 Id table

ID	Word	ID	Word
0	<EOS>	7	प्रतियोगिता
1	<UNK>	8	है
2	<SOS>	9	हॉट्टी
3	पत्रकार	10	खेल
4	व्यवसाय	11	संबंधी
5	में	12	पत्रिकाएं
6	जबरदस्त	13	निकलीं

Embeddings are created in the form of matrix shape is (batch size, max words in a sequence, embedding size). Here, batch size is no of sentences considered at a time for the training purpose and embedding size is the size of a vector represented by a word.

Let's continue our example:

Assume batch size is 2 and embedding size is 10.

Then, the resultant embedding matrix will be of shape (2 * 6 * 10) and represented by the following fig:

“पत्रकार” “व्यवसाय” “मे” “जबरदस्त” “प्रतियोगिता” “है”.
 [[[- - - - -], [- - - - -], [- - - - -], [- - - - -], [- - - - -]
 - - -], [- - - - -]],
 [[- - - - -], [- - - - -], [- - - - -], [- - - - -], [- - - - -]
 - - -], [- - - - -]].
 “हृदि” “मे” “खेल” “संबंधी” “पत्रिकाएं” “नकिली”.
 Here, “-” “represents a random floating value.

3.3 Training

The source embedding and target embedding are fed into the encoder and decoder, respectively and the model is trained until we get good embedding parameters that are required in inference mode.

The construction of the model depends upon the following parameters (Table 2).

The adjustment of these parameters depends upon the amount and nature of our corpus data.

Finally, when the training is over, the model is saved.

3.4 Inference

In inference, source sentence is our only input, so the first task is to pre-process it and generate embeddings. Then, the saved model is restored and embeddings are fed into the encoder. The thought vector is computed in the similar way, as in

Table 2 Hyperparameters

Parameter	Meaning
Epochs	A cycle consists of forward pass and backward pass
Batch size	No of sentences taken at a time for training
RNN size	No of cells in RNN
Number of layers	No of hidden layers in deep neural network
Encoding-embedding-size	Size of source word vector
Decoding embedding size	Size of target word vector
Learning-rate	The rate at which the network abandons old features for new ones
Dropout rate	The fraction of the features that are being zeroed out

training mode, and is used for initializing the decoder. We are using a simple Beam Search decoder in inference mode.

Let's take Xs as an input sentence for translation, XR as a reference sentence, and k as the beam size.

Xs: "भारतीय पत्रकारिता का आरंभ कलकत्ता से माना जाता है ।" $k = 3$.

XR: "ਭਾਰਤੀ ਪਤਰਕਾਰੀ ਦਾ ਆਰੰਭ ਕਲਕੱਤਾ ਤੋਂ ਮੰਨਿਆ ਜਾਂਦਾ ਹੈ ।"

Assume "v" as the thought vector corresponds to the source sentence Xs.

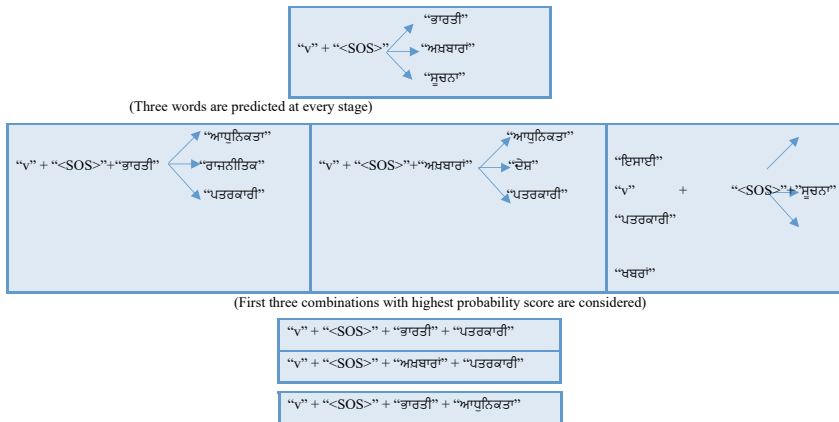
The decoder LSTM is initialized with v.

For the initial prediction step, predict $y_{T2}(1)$, $y_{T2}(2)$, and $y_{T2}(3)$ by conditioning the prediction on $y_{T1} = \langle s \rangle$ and v.

For subsequent time steps, while $y_{T1} \neq \langle e \rangle$, predict $y_{Tm+1}(1)$, $y_{Tm+1}(2)$, and $y_{Tm+1}(3)$ by conditioning the prediction on.

{ $(y_{Tm}(1), y_{Tm-1}, \dots, \langle s \rangle)$, $(y_{Tm}(2), y_{Tm-1}, \dots, \langle s \rangle)$ and $(y_{Tm}(3), y_{Tm-1}, \dots, \langle s \rangle)$ } and v.

As per this algorithm, the reference sentence XR is predicted on the word basis as follows:



4 Testing

We can calculate or define the accuracy percentage of the machine translation system with the formula:

$$A = \frac{N_S}{N_T} \times 100$$

where NS is the number of sentences for which the system has done perfect translation and NT is the total number of test sentences.

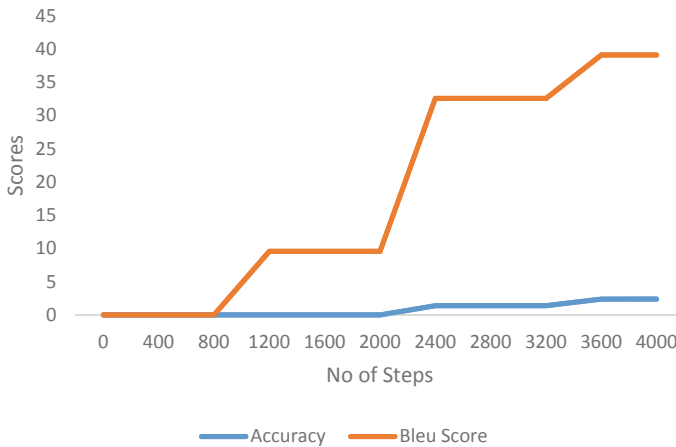


Fig. 7 Bleu score [1]

As accuracy deals with the perfect translation which is obviously rare to see. So, we are also considering the BLEU score for the evaluation purpose.

We take the geometric mean of altered precision scores of the test corpus/test data and then multiply the outcome by an exponential brevity penalty factor. BP is added with the aim that a high-scoring candidate translation must now match the reference translations in length, in word choice, and in word order.

$$BP = \begin{cases} 1 & \text{if } c > r \\ e^{(1 - r/c)} & \text{if } c \leq r \end{cases}$$

Here, c be the measurement of the candidate translation and r be the actual reference corpus length.

We took around 1000 sentences for the testing purpose. And the results are summarized in Fig. 7.

The no of steps is basically used in calculating the no of epochs. One epoch is equal to 563 steps.

5 Conclusion and Future Work

We proposed sequence-to-sequence model for the machine translation and shed light on the modules like attention, bidirectional RNN, etc. that are easily incorporated into the framework for achieving a remarkable performance.

For future work, we will extend this idea to the task where the training parameters are optimized by the network itself depending upon the results. This approach will make NMT- a complete black box for the user.

References

1. Chollet F, Ceator of Keras. Author of Deep Learning with Python. Opinions are my own. <https://blog.keras.io/a-ten-minute-introduction-to-sequence-to-sequence-learning-in-keras.html>
2. Wu Y, Schuster M, Chen Z, Le QV, Norouzi M (2016) Google's neural machine translation system: bridging the gap between human and machine translation. arXiv:1609.08144v2 [cs.CL]. 8 Oct 2016
3. Luong M-T, Pham H, Manning CD (2015) Effective approaches to attention-based neural machine translation
4. Gu J, Lu Z, Li H, Li VOK (2016) Incorporating copying mechanism in sequence-to-sequence learning. arXiv:1603.06393v3 [cs.CL]. 8 June 2016
5. Luong M-T (2016) Neural machine translation: a dissertation
6. Neubig G (2017) Neural machine translation and sequence-to-sequence models: a tutorial. arXiv:1703.01619v1 [cs.CL]. 5 Mar 2017
7. Papineni K, Roukos S, Ward T, Zhu W-J (2002) BLEU: a method for automatic evaluation of machine translation
8. <https://www.tensorflow.org/>
9. <https://medium.com/mlreview/understanding-lstm-and-its-diagrams-37e2f46f1714>
10. <https://cv-tricks.com/tensorflow-tutorial/save-restore-tensorflow-models-quick-complete-tutorial/>
11. <https://machinelearningmastery.com/beam-search-decoder-natural-language-processing/>
12. <https://medium.com/@ageitgey/machine-learning-is-fun-part-5-language-translation-with-deep-learning-and-the-magic-of-sequences-2ace0acca0aa>

Cyber Security for Smart Grid: Vulnerabilities, Attacks, and Solution



Shreyash More, Suraj Hajari, Mahshooq Abdul Majeed,
Neeraj Kumar Singh, and Vasundhara Mahajan

Abstract The smart grid (SG) is an emerging technology. To overcome the limitations of traditional power grid systems, it is an optimistic alternative. Smart grid includes green energy resources and enhances the reliability of power generation, transmission, as well as distribution. This transformation involves a bidirectional communication network that monitors the power flow and stores the data at each level. Moreover, as numerous information data and communication devices are involved in the smart grid, it is a prime target for cyber attacks. Targeting the smart grid can lead to disclosure of private data, supply chain failures, and it can also lead to blackouts. Therefore, cyber security becomes a major concern of all power companies around the world. This paper talks about the basic overview of SG, its security objectives, followed by the existing vulnerabilities in the SG network, attack types, some major attacks on the power grid, and highlight some recent solutions.

Keywords Smart grid (SG) · Vulnerabilities · Cyber security · Smart grid security

1 Introduction

The SG is an electrical network, which can smartly combine the action of all the components that are connected to the system. In SG, power flow is bidirectional, which means utility to consumer and consumer to the utility if a surplus is available at the consumer's end [1]. According to the National Institute of Standards and Technology (NIST), SG is described as an integration of traditional grid and Information and Communication Technology (ICT) [2]. NIST described the SG as follows:

S. More · S. Hajari · M. A. Majeed · N. K. Singh · V. Mahajan (✉)
Department of Electrical Engineering, SVNIT, Surat, India
e-mail: vmahajan@eed.svnit.ac.in

S. More
e-mail: p20ps019@eed.svnit.ac.in

S. Hajari
e-mail: p20ps020@eed.svnit.ac.in

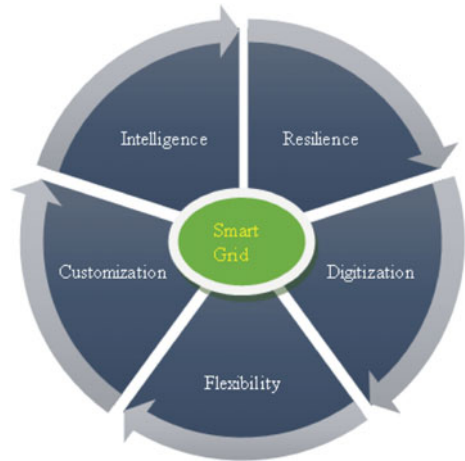
- Provide reliable and quality power.
- Increased capacity and enhanced efficiency.
- Strengthen resiliency to disturbance and self-healing in nature.
- Self-operating and automated maintenance.
- Use renewable energy sources effectively and utilize distributed energy sources.
- Reduced oil consumption.
- Adapt plug-in electric vehicles.
- Minimize requirements of backup.
- Increase consumer choice.
- Decreased greenhouse gas emissions.

SG technology enriches the traditional power grid with enhanced capabilities, which introduces more complexity and vulnerabilities to several attacks [3–7]. The attacker targets these vulnerabilities and gets access to the system. This compromises the integrity and confidentiality of system data and, as a result, makes the system unreachable.

SG is an emerging technology; hence, very less data is available related to security ruptures. Hence, identifying security threats to the system is a very complex and tough job. Also, relatively less practical knowledge about cyber attacks and their influence on the network is available. Cyber security professionals are trying to learn the concept and develop algorithms and devices to protect the network and for mitigation of attacks [77–80]. However, physical safety and attacks are well known to the persons and workers of the grid deployment. Any natural accidents like earthquakes or hurricanes that affect the grid physically are very random, but cyber attacks are not. Cyber attacks depend on the attackers, their motives, interests, and capabilities. Apart from this, the above-mentioned aspects change with time. This makes cyber security a huge challenge that becomes very necessary to be solved.

This paper presents a survey that shows the vulnerabilities present in the SG, attacks that might happen, and highlights some of the existing solutions to overcome them. The remaining paper is categorized as given. Section 2 presents the features of the SG followed by the conceptual model based on NIST and key subsystems of the SG. Section 3 explains the security objectives as well as the requirements for a SG. Section 4 describes the core vulnerabilities of the SG system in detail. Section 5 highlights the possible threats to the SG system and its categories. Section 6 discusses the major attacks that happened on the power grid. Section 7 points out the human factor in the SG. Section 8 discusses the solutions that overcome the challenges of the SG security system. Section 9 concludes this paper.

Fig. 1 Smart grid’s features



2 Smart Grid Technology

2.1 Smart Grid’s Features

The SG provides some advantages over the traditional grid, given as increasing grid resilience, intelligence, digitization, customization, and flexibility [9] as shown in Fig. 1. Resilience specifies the capability of a given system to resist unexpected events and recover rapidly thereafter [8]. Intelligence means inheritance to intelligent technology. Digitization indicates the digital platform that makes the system faster and reliable too. Customization indicates that the system needs to be client-tailored. And the last is flexibility, which means the SG needs to be adaptable, compatible as well as expandable. Nowadays, grid resilience has become an essential feature, especially when power interruption can greatly impact financially. As SG involved the renewable energy resources and energy storage system, it assures reliable power supply by providing corrective capabilities when a failure occurs.

2.2 Smart Grid Model

NIST classifies the SG into seven domains, given as generation, transmission system, distribution network, electricity market, provider, customer, and operations [10]. All these seven domains involve players and applications. The player includes devices, programs, and systems, whereas applications are functions accomplished by the player in the above given domain [11]. Figure 2 shows the conceptual SG model.

Generation Domain: In a bulk generation domain, players are the generators. Generation is the first step in order to deliver electricity to end users. Energy resources

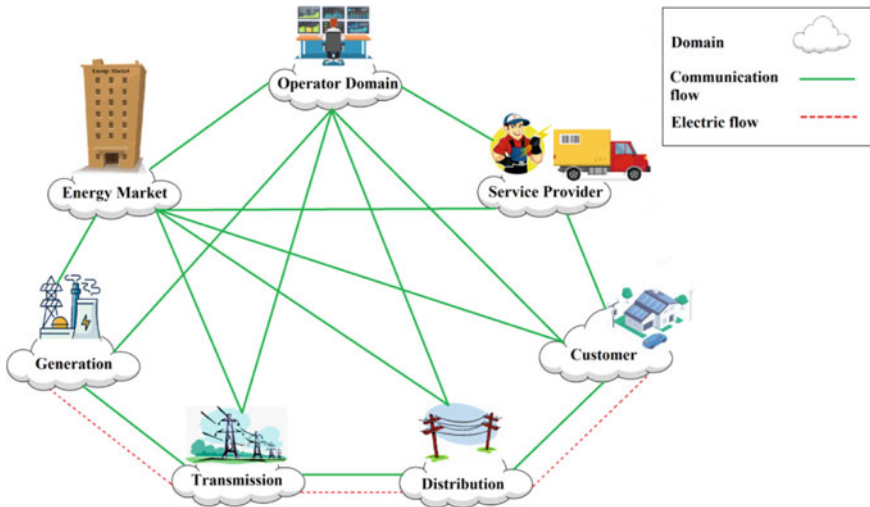


Fig. 2 Conceptual model of SG based on NIST

like coal, water, solar radiation, wind, and nuclear fission are used to generate electricity.

Transmission Domain: In the transmission domain, the generated energy is transmitted over a long distance from the generation to the distribution domain. For control and monitoring the transmission domain, SCADA is used.

Distribution Domain: In the distribution domain, actors are the distributors of electricity. This domain contains different structures like radial, parallel, ring, etc. Energy storage and generation can also integrate with this domain. The domain is electrically connected to the transmission domain and has communication flow with the market, transmission, customer, and operator domains.

Market Domain: In this domain, the players in the electricity market are service operators and end users. The market domain maintains the balance between electricity demand and supply. In order to fulfill the demand, the market domain communicates with the bulk generation domain.

Service Provider Domain: The organization is the main actor in the service provider domain which provides services to both utilities and consumers. The services managed by the organization include billing, use of energy, and customer accounts. This domain interacts with the operator domain for system control and situational awareness. It also communicates with the market and customers to grow smart services, like allowing interaction between both, power generation at consumer premises, etc.

Customer Domain: The end user is the main player in this domain. These are categorized as: residential, commercial, and industrial. In addition to consuming power, SG gives provision to this domain to generate power (by using solar PV, EV, etc.), store it (batteries, etc.) and also control the usage.

Operator Domain: In the operator domain, actors are managers who control the electricity flow between the domains. The objective of the domain is to maintain efficiency as well as optimal operation in transmission and distribution. It also applies energy management system (EMS) in the transmission system, whereas in distribution it uses distribution management system (DMS).

2.3 Key Subsystem in Smart Grid

Advanced Metering Infrastructure (AMI): AMI is a system that combines several technologies which measures, collects, and analyzes the energy use. It enables bidirectional communication between utility and users. It has three parts: a smart meter, an AMI head end, and a communication network [50]. Smart meters are integrated meters which consist of memory and microprocessors that are used to monitor and collect energy use as well as communicate data in real time to the utility's AMI head end. The AMI head-end is the server of AMI which contains the meter data management system (MDMS) [12]. Many communication protocols like Zigbee and Z-wave [50] are used for communication between MDMS and smart meters.

Supervisory Control and Data Acquisition (SCADA): It is a system that monitors, regulates, and measures the electrical power grid. The SCADA system contains three components: The RTU, i.e., remote terminal units, a central master terminal unit (MTU) and the human-machine interface (HMI) system [13]. RTU is used to interface field devices with the SCADA system. RTU is governed by the MTU system. The HMI is a graphical interface for the operators present at the SCADA system.

Plug-in Hybrid Electric Vehicle (PHEV): PHEVs offer the ability to minimize emissions, transportation costs, and dependency on fossil fuels. In addition to this, it can also provide support to distributed energy resources (DER) in SG [14]. During the peak periods, PHEVs can be used to supply the grid, and in off-peak periods they can be charged, thus it improves the reliability and efficiency of the grid.

3 Smart Grid Security Objectives and Requirements

In SG, there is mainly the exchange of operational data and information data. The operational data is instantaneous voltage (V) and current (I) values, relay status, circuit breaker status, fault location, transformer tap changer, and capacitor banks [15]. Information data includes consumer's information and emails, power consumption bills, etc. [15–17]. A high level of security is needed for operational data to secure SG against vulnerable attacks which compromise reliable supply.

3.1 The Security Objectives of Smart Grid

Availability: Availability is one of the most important objectives of the SG. It guarantees reliable and punctual entry to data. The power delivery could be affected by the loss of availability. The attacks which target availability are considered Denial of Service attacks (DoS). A DoS attack makes resources unavailable due to which legitimate users may be unable to access the data. For example, if availability is compromised, then information flow in the network will be interrupted and control over the system will not be possible. So, the security of the communication channel is necessary.

Integrity: It refers to the detection or prevention of modification of system information by an unauthorized person. Due to loss of integrity, illegitimate users can modify the sensor values, which may affect the power management. For example, attackers purposely modify the original information in the SG communication system, which results in wrong system decisions. The protection of customer's data and operational network data is needed.

Confidentiality: It refers to protecting personal privacy and safety from unauthorized access. If not, then data can be compromised. For example, smart meters are full of user data and they can be used as a tool by the attacker for future attacks. Hence, the protection of the smart meter data is also very important.

3.2 The Security Requirements of Smart Grid

Authentication: Verifying the true identities of communicating parties. It is very important to authenticate humans and machines. Due to any weakness in it, it may lead the attacker to gain access to information. For example, the implementation of strong authentication is needed such that only authenticated persons are able to communicate.

Authorization: Issuing permission and allowing access to the system, there are large numbers of devices and users in SG that need authorization of appropriate governance for resources as well as information. If the defense mechanism for authorization is weak, then the attacker will get easy access control to plan an attack on the system.

Non-Repudiation: It promises that tasks done by the user cannot be denied later. If integrity is compromised, then it will affect non-repudiation too. It is most important regarding regulatory requirements. The violation of it will have legal and commercial consequences.

4 Security Challenges and Vulnerable Links in the Smart Grid System

As stated earlier, SG is a fusion of the traditional grid and ICT. It improves the capabilities of the conventional network. It also adds complexity to the power network, making it vulnerable. It might make a passage for attackers to attack the network. As a result, compromise the data and broke the security objectives of SG, i.e., confidentiality and integrity. The next paragraphs highlight vulnerable links in the SG [22–27].

In a smart grid, ICT acts as a central nervous system. Generation, transmission, and distribution are the sectors of the grid, and data associated with them is foremost important. Besides, while considering the end user, ensuring customer's privacy is an important aspect, and it should be well preserved and protected. There are many challenges regarding customer's information privacy as all data is collected by smart meters in the SG. If hackers get access to the meters, then it will be available to the hacker. This data includes information about the time of availability of consumers at home. Also, it is possible to extract information about daily activities like at what time they are sleeping or which household gadgets they use. Criminals can utilize this information to commit crimes, and marketers can also utilize data for marketing. Hence, it is very important to secure both transfer and storage process to avoid leakage [27].

SG comprises abundant devices which monitor the power supply and network conditions [28]. Smart meters and AMI communication infrastructure are the best suitable example. Managing these multiple devices is an intricate task. Hence, the attacker will get wide area access points to attack.

The interconnection between the ICT and distribution domains extends the security threats. For example, smart meters are installed inside the consumer's premises, buildings, etc. These meters not have any direct control over the operators. Hence, they might interfere as it has already happened with old electromechanical meters. Additionally, once the attacker gets an entry in the smart meter, they may get access to the AMI network and use it as a medium to send malware [29]. Protection of such devices located at faraway is again a major task.

The IT components present in a grid have a limited life, hence their up-gradation is needed. If they continue to work in the older version, then it acts as the weakest point for the attack, and it also introduces connection issues [22].

There are different teams working in different domains of SG, incompatibility and any miscommunication among them will give the wrong command. And, it might act as a vulnerable point in the system [21].

SG has a very intricate infrastructure, and it needs to collaborate with more and more stakeholders to get a better result out of it. There are a huge number of actors involved: consumers, power producers, retailers, EV-related businesses, etc. The coordination between all these stakeholders along with each of its own organizational processes, priorities, requirements, and standards, is very difficult. The authorized person might attack the system and will be difficult to identify. Many of the standards

used in SG were never made by considering the security threats. These standards are currently used for the control and communication of all three domains of the grid, i.e., generation, transmission, and distribution. They might be helpless against cyber attacks such as denial of service (DoS), spoofing, etc. However, new standards are now developed for the application of SG, and these are designed by considering security principles like cryptography, encryption, etc. But, controlling cryptographic material for a large number of devices is a tough task.

The supply chain is the most vulnerable area of the SG. The supply chain present in the SG consists of many embedded software, control systems, sensors, microchips, SCADA systems, operating systems, etc. The supply chain might be invaded at some steps by the attacker. The attacker changes the electronic circuitry of the devices or could substitute a dummy part. They could add logic bombs, malware, etc. All these backdoors could be used by enemy states or terrorists to execute their plans. They might use the logic bombs to cause terrible harm. So, the supply chain security, well-regulated manufacturing process of electronic devices used in the chain is very important. Table 1 summaries common challenges on smart grid.

5 Possible Threats and Their Categories

The attacker first identifies the vulnerabilities, which could be anyone from the previous section or any other, and plans the attack against the network for its own intentions. The attackers could be categorized based on their intentions of the attack and listed in Sect. 5.1 [30], Further, Sect. 5.2 highlights some of the attacks that can be performed on the smart grid system by attackers. The attacker follows the steps given in Sect. 5.3 to execute the plan of any attack.

5.1 Types of Attackers

Non-malicious hackers: These attackers consider the security network as a puzzle and try to break the system with their technical skills.

Customers: As SG is a very beneficial technology, many customers are accepting it. As a result, SG connectivity increased. But, the system does not know the intentions of a user, so some might not be trustworthy. Some users will not adhere to the agreement and policies. Users may try to compromise the smart meter to reduce the bill amount by interfering with the meter reading.

Subversive Hackers: These types of attackers are subversive in nature. They target the power grid, try to interrupt the supply, and so the entire area can suffer from blackouts. They could break the system and get access to crucial information. Terrorists, bombers, arsonists, etc., can be considered under this category.

Employee: A person who is unhappy with the service provider or with the customers, or may be an untrained employee.

Table 1 Common challenges on smart grid

Challenge	Asset/target	Effects	Measures
Privacy [18]	Data and information, generation, transmission, distribution related data, customer data-consumption pattern, sleeping time, appliances used, billing information	Misuse of data, for ex- by terrorists for destruction, by criminals to commit crimes, by marketers for marketing and etc.	Privacy impact assessment (PIA), Encryption-Decryption for data flow, authentication, digital certificate, etc. [20]
Increased access point [19]	Electronic devices including smart meters, AMI, monitoring and control devices, data and information	Attacker can use it for blackouts, supply interruption, damage the grid, etc.	Cloud computing security, routine service, in depth strategies of security system, etc. [20]
Physical security [20]	Remotely installed devices like smart meters, etc.	Financial loss, data and information can be compromised and attacker can get control over the grid and etc.	Strong authorization, protect access credentials, etc. [20]
Frequent updating of component [21]	IT components	Acting as a weakest point and can be attacked easily, etc.	Routine up-gradation [21]
Dissimilarity among teams [21]	Communication links	Wrong decisions, incorrect command or action, etc.	Effective and efficient communication standards, etc. [21]
Stakeholders [20]	Data and information control mechanisms	Data misuse, reliability compromised, etc.	Strong authentication and authorization, etc. [20]
Communication protocols [20]	Communication links	Service unavailable, etc.	Cryptography for end to end encryption– decryption and authentication, efficient and effective implementation of keys, certificates needed for the cryptography, etc. [20]
Supply chain [20]	SCADA system, operating system, control system, microchips, electronic devices, etc.	Blackouts, operation, control and monitoring system compromised, serious physical damages to the grids, etc.	Well controlled and duly regulated design, manufacturing, components assembly and administration of electrical components, etc. [20]

Competitor: These types of attackers are also called rivals. They try to target the grid for their personal profit, or they trying to end the competition in the market.

5.2 *Types of Attacks*

Using Malware: Malware is malicious software designed with the main intention to harm the services. An attacker can use malware to gain access and collect critical data. It could also be used for data modification or for eradicating sensitive information [31].

Illegal Access: It is also called an unauthorized access. It can manipulate systems settings and operations.

Replay: In order to create an unauthorized effect, an intruder may send an identical message or false message multiple times. This may create an unnecessary burden on the receiver. This burden may cause communication to falloff.

Denial of Service attack: This type of attack is used by the attacker to make the system unavailable for the users [32].

Traffic Analysis: In this type of attack, the attacker attacks the system to get an idea about the routing structure and to analyze the traffic in the network. In such attacks, an attacker may gain sensitive data like energy usage, smart grid structure, price, etc.

5.3 *Attack Formats*

Firstly, the attacker identifies the target; in this case, it is smart grid. Then he/she follows the below steps,

Reconnaissance: The term refers to the practice of gathering and collecting information about the target. It is also continuously used by cyber security experts to find out cyber threats and to prevent them. In this step, the system confidentiality can be compromised.

Scanning: In this step, attacker tries to find out the weakest link in the system or the vulnerability of the system. It can compromise the confidentiality of the system.

Exploitation: Here, attacker executes his plan of action and tries to get full control of the system and compromise the data. Confidentiality, integrity, and availability will be compromised during this step.

Future Access: After execution of the attack, the attacker installs an undetectable and cloaked program that could be used in the future for the attack. In this confidentiality, integrity, and availability can be compromised.

Table 2 shows the comparison between some of the most general types of attack and illustrates their respective effects on the smart meter and related economical impact [33]. The availability attacks are the most serious because they have the most detrimental impact on smart meters, and the remaining three types of attacks have

Table 2 Types of attacks and their impacts

Attack	Objective violation	Smart meter systems delay	Financial impact	Smart meter communication blockade duration	Counter measure
DoS	Availability	Mild	Moderate	Extreme	Strong authorization, trolling techniques, honey-pot models
Radio frequency jamming	Availability	Extreme	Mild	Extreme	Use anti-jamming technologies
Replay attacks	Availability	Extreme	Mild	Extreme	Time stamping
False data injection attack (FDIA)	Integrity	Extreme	Mild	Mild	Use encryption-decryption techniques
Unauthorized access	Confidentiality	Extreme	Mild	Mild	Use virus or spyware protection programs, protect password and login credentials

serious economical effects. The availability attack class, replay attacks, and radio frequency jamming, having severe financial impacts and smart meter communication blockade. However, DoS is also a good choice of weapon for producing a delay in smart meters [33].

6 Major Cyber Attacks on the Power Grid

Table 3 shows, some major cyber attacks against power utilities and the grid over the past decade [35–47]. Note that there have been numerous attacks, either not detected or not announced in the public domain for security reasons. For example, in 2012 there were nearly 200 cyber attacks detected and nearly half of these attacks targeted a power grid. Now attacks on the power grid are becoming more frequent. According to ESET security researchers, Industroyer malware was used to attack Kiev in December 2016 to be the biggest threat to industrial control systems [43]. Malware such as Industroyer is very dangerous as it permits attackers to carry out huge industrial sabotage as well as it allows them access to control power utility networks. As a result, they can control the commands given to the equipment like switches, circuit breakers, and relays, and interrupt the electricity flow at anytime and cause blackouts [46].

Table 3 Major cyber attacks on the power grid

Year	Cyber attack	Cause	Discussion
Jan. 2003	Nuclear power plant was infected with MS SQL worm in Ohio	Entry of malicious code through a secondary pathway into the control network	On 25 January 2003, Davis Besse nuclear power plant's private computer network was infected by 'slammer' Microsoft SQL worm. As a result, network site overloaded by traffic, which makes safety and monitoring system not accessible and temporary failure of process computer [35]
Feb. 2011	Brazilian power plant management system	By an infected machine	The power plant was contaminated by the worm called "Conficker". It affects the management system of the plant make it stop. And hence unable to displace data [36]
June 2011	Petrobras, Brazilian energy company website hacked	It is a DDoS attack, multiple infected computers targeted the website with useless requests and make them out of action	Based on anarchic intentions, LulzSec, a hacking group, attacks the website of the biggest energy producer of Latin America, Petrobras. The attack has made total shutdown of the site [37]
2012	Power utility of German	DoS attack with a botnet involves thousands of requests was sent to a server each second to make a system inoperable	German power utility specialized in renewable energy was hit by a DoS attack and make its Internet communications systems offline [38]
2013–14	Attack against 1000 + energy companies from 84 countries	Hackers had infected the websites with malicious software, which were visited by the targeted individuals often. The targeted individuals visited the site and unknowingly downloaded the software	Dragonfly, a hacker group, used a Havex, a type of Trojan, and take control over the 1000+ energy firms from 84 countries which include Germany, Spain, US, etc. Their target maybe industrial sabotage [39, 40]

(continued)

Table 3 (continued)

Year	Cyber attack	Cause	Discussion
Dec. 2015	Against Ukrainian regional power companies	The hackers sent an email to employees, attached with malware, which allows them to get login credentials and shut down substations	Hacker team, sandworm, by using black energy malware took control over the control actions of many regional power stations of Ukraine, around 225 k people suffered from blackouts [41, 42]
Dec. 2016	Attack on the capital of Ukraine	Industroyer malware, designed for power grid attack	The attacker cut the power supply for 1/5th of Kiev, the capital of Ukraine for one hour. This attack is considered to have been a large-scale test [43]
2017	Electricity distribution board, West Bengal, India	Ransomware	WannaCry ransomware infected around 4 billing departments of West Bengal, India, that cater to around 800 k houses. As a result, electricity bill payment operations were interrupted for the day. The attacker asked for the ransom to restore the system [44]
2017	Petrochemical power plant, Saudi Arabia	Computer system compromised	The power plant was hit by a cyber strike. The strike was planned to destroy the data and make the plant offline. According to the expert the attack was designed for sabotage and an explosion trigger [45]
2017	Attack many western energy companies	Phishing mails, Trojanized software, etc.	Dragonfly 2.0, a Russian hacking group, attacked many western energy firms, enter into networks of around 20 + firms, also get operation control in the US and Turkey, and also aimed to sabotage operational systems at energy facilities [46]

(continued)

Table 3 (continued)

Year	Cyber attack	Cause	Discussion
2019	Power grid cyber attack in western US	Distributed Denial of Service (DDoS) attack	Communication lines between the power control center and power generation sites interrupted resulted in communication loss and system and firewall of the system were restarting and again becomes offline [47]

7 Human Factor in Cyber Security

The human factor is considered by many security experts as the weakest link in cyber security. It is because many individuals are easily trapped in phishing and equivalent attacks. These attacks are utilized to get access credentials of the system. This has earlier happened in Ukraine. The hackers had sent emails to the concerned individuals. The malware carrying links were attached to the emails. After opening the links, hackers obtained the credentials which allowed them to get access to the systems control and operations parameters. It caused a power cut in regional distribution utilities [41]. The security method named ‘multifactor authentication’ is one of the methods which mainly concentrates on the human factor. The method needs two or more than two credentials, i.e., biometric, password, or security key to verify the identity of an individual who is trying to access the network, and this is all needed prior to access [49]. On that account, the combination of all, something you know, something you have, and something unique you have, like a password, token, and biometrics, makes you a recognized user for that network.

8 Solution to Smart Grid Security

8.1 Three Phase Strategy

The author in [6] suggested that security can only be achieved by combining many strategies into a worldwide plan, rather than by relying on a single solution. They also propose a cyber security strategy consisting of three phases, given as, pre-attack, under attack, and post-attack, as shown in Fig. 3.

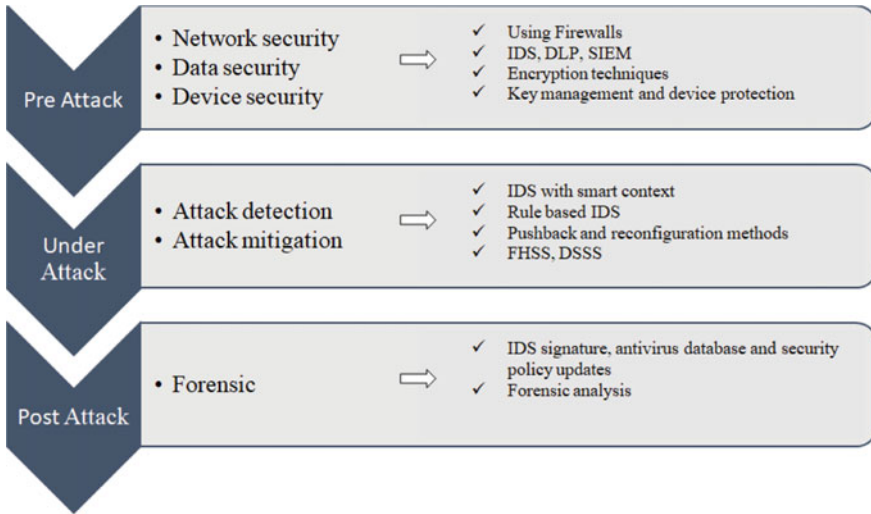


Fig. 3 Smart grid security solutions

8.1.1 Pre-attack

In the first stage, before the attack, it is recommended to use various solutions (like network, data, and device security, etc.) to improve the security of SG and be ready for any possible attack. Security countermeasures are generally classified into three main categories as given below,

Network security: The network is a very important part of the smart grid. The security of the network is necessary and if it is not, then the whole system becomes vulnerable. It is suggested to use a firewall additionally with the other examining and monitoring techniques to secure SG [8]. Based on some policies and rules, the firewall is designed to permit or decline network connections. But, more advanced or unknown attacks can break the firewall. Therefore, technologies like security information and event management systems (SIEM), intrusion detection system (IDS), and data loss prevention (DLP) should be used along with firewalls. SIEM is a system that collects and compiles information from all devices that are present in a network [50]. This gathered data will then be processed and analyzed by the central server, so it can identify any threats or destructive activity in the network [8]. To detect any malicious activity in the network, an IDS system is used. To prevent any data theft or loss of information, a DLP system is used [51].

Data security: To protect users’ data, secure communication, and authenticate users, cryptography methods and algorithms are used to encrypt the data [56–58]. There are two types of encryption, namely: symmetric key encryption and asymmetric key encryption. Symmetric key encryption requires lower computing capabilities regardless of key size. However, asymmetric key encryption requires more computing capabilities for long key size (better security).

Authentication is an important identification process in SG to terminate an attack that targets data integrity. Certain requirements have to be met for authentication, like tolerance to faults and attacks, high efficiency, and multicast support. Multicast has many applications in SG, which include monitoring, protection, generation, and distribution. For example, if an IED monitoring the feeder senses any abnormality like high current or high voltage, then it will issue a trip command to CB. Under such conditions, unicasting the same time-crucial tripping signal to every circuit breaker will inescapably lead to a huge delay and may damage the power equipment. To avoid this, multicasting is the most systematic method to multicast time-crucial signals to all correlated breakers belonging to the corresponding multicast category. Multicast authentication can be done through secret information asymmetry, time asymmetry, or hybrid asymmetry [59].

Key management plays an important role in encryption and authentication in order to safeguard the SG. Public key infrastructure (PKI) is a technology that attaches public keys to individual users' identities through a certificate authority (CA). Before starting any communication, the PKI mechanism ensures security by cross-checking the real identity of the user by getting a certificate from a certificate authority (CA). There are four steps that are utilized in symmetric key management, namely: generation of key, distribution of key, key storage, and key update. The benefit of it over public key infrastructure is its speed and effectiveness for a large amount of data.

Device Security: In the secure supply chain of SG, the protection of devices is the third critical component. In order to assure the security of end devices in SG, various security technologies are recommended, like data loss prevention, antivirus, and intrusion detection systems [8]. These tools perform checks on all components of SG to verify that the configuration of each device is up-to-date, particularly current configuration files and device firmware. Since SG components are extremely interconnected, any deficiency in a device can put the whole system at risk.

8.1.2 Under Attack

Generally, there are two tasks in this step: detection and mitigation of the attack. For example, denial of service (DoS) is the most frequent attack in SG. The main goal of this attack is to make the system not work as expected. DoS attacks must be detected in the SG to take proper countermeasures. Some recent DoS identification methods are [53]:

Using signal strength: In this method, wireless devices are used to detect signal strength. By measuring the strength of a signal, a device can decide if it is under a jamming attack or it is receiving legitimate data. In a jamming attack, the attacker chooses to send a continuously amplified signal to jam the channel or send a noise-like signal. A detector must detect these types of signals [54].

Using measurement of sensing time: Carrier sense multiple access (CSMA) is a commonly used multiple access technique. In this case, by sensing the channel, the transmitter confirms that it is free before sending the data. The sensing time will be large in the case of a jamming attack, and the channel will not be free. Each time

before transmitting the data transmitter records the sensing time. If sensing time is larger than the threshold value, then the transmitter will reveal it as a DoS attack [55].

Detection using transmission failure: This method keeps the record of transmission failure. A jamming attack can cause failure in data transmission or can corrupt the transmitted packets. It is declared as a jamming attack if the count of failures crosses the threshold value [55].

Using signature: Attack signatures are generally built using known attack patterns. Some doubtful actions are compared with signature, and if it matches, then it is considered as a DoS attack [53].

After confirming the DoS attack, the smart grid should take proper measures as soon as possible to minimize the outage period and to safeguard nodes. In the SG, countermeasures to mitigate DoS attacks are generally implemented in two layers: physical and network layer. The mitigation methods for the network layer are given below [60].

Pushback: After confirming the attack, properties of the attack like the pattern or IP address are sent back to the upstream router, and then all the traffic that matches the attack properties is blocked by the router [53].

Rate limiting: Once the detector determines that a certain user is executing the DoS attack, the router will limit the user's data rate. Thus, the effectiveness of the attack is reduced. One drawback of this method is the high false detection rate. Under such instances, if the user is legitimate, then they can make a complaint to increase the data speed.

Reconfiguration: This is accomplished by modifying the network's topology to make available more resources to the victim or isolate an attack. Since reconfiguration is costlier, it is rarely used.

Filtering: A suspicious packet's source IP is checked through the detector's blacklist by the router. If a match is found, packets are quickly filtered to create a path for legitimate packets to pass.

Cleaning center: Basically, it is a combination of reconfiguration and filtering. Once the attack has been confirmed on a node, the traffic is redirected to the "cleaning center". It is a node present in the network which is capable of filtering suspicious packets [54].

Physical layer mitigation: Frequency jamming is the usual form of DoS attack at the physical layer level. Some algorithms used to mitigate such attacks are: Direct sequence spread spectrum (DSSS), frequency hopping spread spectrum (FHSS), and chirp spread spectrum (CSS).

8.1.3 Post Attack

The post-attack phase is critical when the attack is not detected. After the attack, it is necessary to identify the entities affected or compromised in the attack. After that, the anti-virus database, IDS signature, and security policies need to be updated by learning from the attack, so that the SG will be able to withstand similar upcoming

attacks. Forensic analysis is the main methodology used after the attack. SG forensic collects, analyzes, and intercepts the data to recognize the entities involved in the incident. Forensic studies can also be used to identify and resolve physical and network vulnerabilities in SG to predict potential attacks. Additionally, SG forensic studies play a crucial role in the inspection of cybercrimes like cyber terrorism, hacking, and digital spying, violating users' privacy, viruses, modifying SG data, state property, and secret [52].

8.2 *Blockchain Technology*

Blockchain is the technology in which each block contains the data, timestamp, index, hash, and previous hash [61]. These blocks form a chain in which newly generated blocks are continuously added at regular intervals [62]. In recent years, researchers have been trying to integrate blockchain technology into the security of the smart grid [63]. The features like decentralization, scalability, immutability, resiliency, smart contracts, transparency, and auditability, etc. make it a hopeful alternative to ensure the security and privacy of the smart grid [62]. There are mainly three types of blockchain variants being studied: public, consortium, and private blockchain. As a large number of nodes are present in the public blockchain, it is not possible to interfere with the public blockchain [64]. And practically, in the case of private and consortium blockchain, the nodes are authorized and well protected [65].

The author in [66] discussed cyber security technologies like firewalls with an intrusion detection system for network security, IDS for device security, and authentication and encryption for data security. But due to the real-time performance and continuous functioning requirements of the smart communication network, these techniques are hardly integrated into the network [67]. In SG, the communication network is centralized which makes it more prone to single-point failure [68]. To overcome this, blockchain provides peer-to-peer (P2P) data transfer and decentralized replication of data storage on multiple devices, which avoids single-point failure and ensures high availability [69]. In a blockchain-based smart grid system due to features like distributed data validation, verification, and storage, the data is immutable [63]. Hence, data confidentiality, integrity, and availability of the smart grid can be protected. Further, accountability/non-repudiation attacks are nearly impossible in blockchain-based smart grids, due to the high auditability of technology. The authentication and authorization level of blockchain-based AMI is increased because of asymmetric cryptography. This can secure the electricity data integrity and privacy of customers [70]. Data integrity attacks like FDIA, consumption data tampering, altering power trading transactions, customer's data compromised, get access to IEDs control, etc. [71] are major threats to the smart grid. Many papers like [8, 50, 72] give firewall-based methods as countermeasures against these attacks. However, due to the low computational power of ICT devices, these techniques are slow and vulnerable to cyber attacks [73]. The blockchain has been proven to be an efficient and

best alternative to FDIA [74]. Further, to ensure the immutability of data, protection of cyber attacks against data collection and transfer, researchers in [69, 74–76] introduced some solutions. The article [63] discussed blockchain-based platforms, services, and applications for the cyber security of the smart grid and concluded that it is a propitious solution for the cyber security of the smart grid.

9 Conclusion

SG is a new and growing technology. The advanced features of the SG will give plentiful advantages to the customers. However, the system has to face some huge challenges, so security is a big concern. Currently, the implementation of security cautions against the cyber attacks in SG is very trending among industrialists, researchers as well as government firms. The paper introduced the SG concepts, point out core vulnerabilities, discussed the types of attacks, types of attackers and their intentions, tabular analysis of some major cyber attacks in the last two decades, and reviewed existing security solutions and integration of blockchain in SG. Blockchain comes out as a promising solution for the cyber security of the SG.

Smart grid has a complex network; hence, spotting all the possible sensitive areas is necessary to secure them from the attacks. In order to have a better future and popularity for the smart grid, it should be free from the security gaps and drawbacks. The SG has to be future resistance, which means, if there will be any attacks in the future, then it should be able to get through it. The SG is now in the earlier stage, so it is easier to implement things now instead of running without considering the security problems. The paper concludes brief conceptual understanding of the security of SG, necessity, and objectives.

It is now critical to raise cyber security awareness among SG's human interface platform. If the SG system is totally secure but the peoples are not aware of the security concept, threats, and how it works, then the security system is of no use. For example, Dec 2015 attack against Ukraine companies [41, 42], 2017 attack on western countries [46], are due to less awareness of cyber security.

The SG's total prevention is not realistic. Instead, it should be ready for the attacks, able to detect them quickly and be prepared as possible to respond.

References

1. Wang W, Lu Z (2016) Cyber security in the smart grid: survey and challenges. *Comput Netw* 57(7):1344–1371
2. Gopstein A, Nguyen C, O'Fallon C, Hastings N, and Wollman D (2021) NIST framework and roadmap for smart grid interoperability standards, release 4.0. Department of Commerce. National Institute of Standards and Technology
3. Farhangi H (2010) The path of the smart grid. *IEEE Power Energy Mag* 8(1):18–28. [Online]. Available <http://ieeexplore.ieee.org/document/5357331/>

4. Konstantinou C, Mohanty SP (2020) Cybersecurity for the smart grid. *Computer* 53(5):10–12. <https://doi.org/10.1109/MC.2020.2975901>
5. Faquir D et al (2021) Cybersecurity in smart grids, challenges and solutions. *AIMS Electron Electr Eng* 5(1):24–37
6. Liang X, Gao K, Zheng X, Zhao T (2013), A study on cyber security of smart grid on public networks. *IEEE Green Technol*
7. Essaaidi M et al (2015) An overview of smart grid cyber-security state of the art study. In: 3rd international renewable and sustainable energy conference (IRSEC), pp 1–7
8. Knapp ED, Samani R (2013) Applied cyber security and the smart grid: implementing security controls into the modern power infrastructure. Syngress, Elsevier Amsterdam
9. Li F, Qiao W, Sun H et al (2010) Smart transmission grid: vision and framework. *IEEE Trans Smart Grid* 1(2):168–177. (Article ID 5535240)
10. Panda DK, Das S (2021) Smart grid architecture model for control, optimization and data analytics of future power networks with more renewable energy. *J Cleaner Prod* 301:126877
11. N. Framework, Roadmap for smart grid interoperability standards, release 2.0. NIST Special Publication, 1108
12. Ghosal A, Conti M (2019) Key management systems for smart grid advanced metering infrastructure: a survey. In: *IEEE communications surveys and tutorials*, vol 21, no 3, pp 2831–2848, thirdquarter 2019. <https://doi.org/10.1109/COMST.2019.2907650>
13. Pliatsios D, Sarianniadis P, Lagkas T, Sarianniadis AG (2020) A survey on SCADA systems: secure protocols, incidents, threats and tactics. *IEEE Commun Surv Tutor* 22(3):1942–1976. <https://doi.org/10.1109/COMST.2020.2987688> (thirdquarter 2020)
14. Bilal M, Rizwan M (2020) Electric vehicles in a smart grid: a comprehensive survey on optimal location of charging station. *IET Smart Grid* 3(3):267–279
15. Naidua H, Thanushkodib K (2010) Recent trends in SCADA power distribution automation systems. *J Sci Ind Res* 45(3):205–218
16. Liu Y (2012) Wireless sensor network applications in smart grid: recent trends and challenges. *Int J Distrib Sens Netw* 492819-1–492819-8
17. Panel SGI (2010) Guidelines for smart grid cyber security: vol. 1, smart grid cyber security strategy, architecture, and high-level requirements, and vol. 2, privacy and the smart grid, National Institute of Standards and Technology (NIST). Interagency Rep, vol 7628
18. Khurana H, Hadley M, Ning L, Frincke DA (2010) Smart grid security issues. *IEEE Secur Priv* 7(I):81–85
19. Line MB, Tondel IA, Jaatun MG (2011) Cyber security challenges in smart grids. In: Presented at the 2nd IEEE PES international conference and exhibition, innovative smart grid technologies (ISGT Europe), Manchester
20. European Network and Information Security Agency (ENISA). Smart Grid Security, Annex II. Security aspects of the smart grid [online]. Available <https://bit.ly/3xU3xnv>
21. Yadav SA, Kumar SR, Sharma S, Singh A (2016) A review of possibilities and solutions of cyber attacks in smart grids. In: 2016 international conference on innovation and challenges in cyber security (ICICCS-INBUSH), pp 60–63. <https://doi.org/10.1109/ICICCS.2016.7542359>
22. Clements S, Kirkham H (2010) Cyber-security considerations for the smart grid. *IEEE Power and Energy Society General Meeting* 2010:1–5
23. Ericsson GN (2010) Cyber security and power system communication—essential parts of a smart grid infrastructure. *IEEE Trans Power Del* 25:1501–1507
24. Mo Y, Kim T-J, Brancik K, Dickinson D, Lee H, Perrig A, Sinopoli B (2012) Cyber-physical security of a smart grid infrastructure. *Proc IEEE* 100(1):195–209
25. Baig ZA, Amoudi A-R An analysis of smart grid attacks and countermeasures. *J Commun* 8(8):473–479
26. Ustun TS, Hussain SMS (2019) A review of cybersecurity issues in smartgrid communication networks. In: 2019 international conference on power electronics, control and automation (ICPECA). IEEE
27. Lisovich MA, Mulligan DK, Wicker SB (2010) Inferring personal information from demand-response systems. *IEEE Secur Priv* 11–20

28. Chang YH (2010) Cyber security of a smart grid: vulnerability assessment. s.l. <http://www.ece.nus.edu.sg/stfpage/elejp/FYP/CYH09.pdf>
29. McDaniel P, McLaughlin S (2009) Security and privacy challenges in the smart grid. *IEEE Secur Priv* 7(3):75–77
30. Flick T, Morehouse J (2010) *Securing the smart grid: next generation power grid security*. Syngress, Elsevier
31. Li X, Liang X, Lu R, Shen X, Lin X, Zhu H (2012) Securing smart grid: cyber attacks, countermeasures, and challenges. *IEEE Commun Mag* 50(8):38–45
32. Huseinović A et al (2020) A survey of denial-of-service attacks and solutions in the smart grid. *IEEE Access* 8:177,447–177,470
33. Tellbach D, Li Y-F (2018) Cyber-attacks on smart meters in household nanogrid: modeling, simulation and analysis. *Energies* 11(2):316
34. Engebretson P (2013) *The basics of hacking and penetration testing: ethical hacking and penetration testing made easy*. Elsevier
35. Poulsen K (2006) Slammer worm crashed Ohio nuke plant net. *The Register*, 20 Aug 2003 [online]. Available https://www.theregister.com/2003/08/20/slammer_worm_crash-ed_ohio_nuke/
36. McMillan R (2011) A power plant hack that anybody could use. *COMPUTERWORLD*, 5 Aug 2011 [online]. Available <https://www.computerworld.com/article/2509910/a-power-plant-hack-that-anybody-could-use.html?page=2>
37. Rapoza K, Lulzsec attacks Brazil Gov, Petrobras. *Forbes* 22 June 2011 [online]. Available <https://www.forbes.com/sites/kenrapoza/2011/06/22/lulzsec-attacks-brazil-gov-petrobras/?sh=7e4f0dc71cab>
38. Neslen A (2012) European renewable power grid rocked by cyber-attack. *EURACTIV*, 10 Dec 2012 [online]. Available <https://www.euractiv.com/section/energy/news/european-renewable-power-grid-rocked-by-cyber-attack/>
39. Finkle J (2014) U.S. Government asks firms to check networks after. ‘Energetic Bear’ attacks. *Reuters*, 2 July 2014 [online] Available <https://reut.rs/3xSvTyy>
40. Symantec (2014) Dragonfly: cyberespionage attacks against energy suppliers. Symantec Security Response Version 1.21, 7 July 2014 [online] Available https://docs.broadcom.com/doc/dragonfly_threat_against_western_energy_suppliers
41. Schwartz MJ (2016) More phishing attacks target Ukraine energy sector. *Information Security Media Group*, 22 Jan 2016 [online]. Available <https://www.bankinfosecurity.com/phishing-attacks-again-target-ukraine-energy-sector-a-8822>
42. Zetter K (2017) The ukrainian power grid was hacked again. *Motherboard*, 10 Jan 2017 [online]. Available <https://www.vice.com/en/article/bmvkn4/ukrainian-power-station-hacking-december-2016-report>
43. Cherepanov A (2017) Industroyer: biggest malware threat to critical infrastructure since Stuxnet. *ESET*, 12 June 2017 [online]. Available www.eset.com/int/industroyer
44. Correspondent HT (2017) WannaCry ransomware attack hits computers in West Bengal and Kerala. *Hindustan Times*, 15 May 2017 [online]. Available <https://bit.ly/2VVR70D>
45. Perlroth N, Krauss C (2018) A cyber attack in Saudi Arabia failed to cause carnage, but the next attempt could be deadly. *Independent* [online]. Available https://www.independent.co.uk/news/long_reads/cyber-warfare-saudi-arabia-petrochemical-security-america-a8258636.html
46. Greenberg A (2017) Hackers gain direct access to US power grid controls. *Wired* [online]. Available <https://www.wired.com/story/hackers-gain-switch-flipping-access-to-us-power-systems/>
47. Kass DH (2019) DOE: cyber event hit power grid in three U.S. States, No Outage Reported, *MSSP Alert*, 7 May 2019 [online]. Available <https://www.msspalert.com/cybersecurity-news/cyberattacks-us-energy-grid/>
48. Greenberg A (2017) Hackers gain direct access to US power grid controls. *Wired* [online]. Available www.wired.com/story/hackersgain-switch-flipping-access-to-us-power-systems
49. TechTarget (2018) Network, Multifactor Authentication [online]. Available <https://searchsecurity.techtarget.com/definition/multifactorauthentication-MFA>

50. Faisal MA, Aung Z, Williams JR, Sanchez A (2015) Data-stream based intrusion detection system for advanced metering infrastructure in smart grid: a feasibility study. *IEEE Syst J* 9(1):31–44
51. Zhang Y, Wang L, Sun W, Green RC II, Alam M (2011) Distributed intrusion detection system in a multi-layer network architecture of smart grids. *IEEE Trans Smart Grid* 2(4):796–808
52. Erol-Kantarci M, Mouftah HT (2013) Smart grid forensic science: applications, challenges, and open issues. *IEEE Commun Mag* 51(1):68–74
53. Abliz M (2011, March) Internet denial of service attacks and defense mechanisms. Department of Computer Science, University of Pittsburgh, Pittsburgh, PA, USA, Tech. Rep. TR-11-178 [Online]. Available <https://people.cs.pitt.edu/mehmud/docs/abli11-TR-11-178.pdf>
54. Lin D (2013, April 2013) Network intrusion detection and mitigation against denial of service attack. WPE-U Report, University of Pennsylvania
55. Xu W, Trappe W, Zhang Y, Wood T (2005) The feasibility of launching and detecting jamming attacks in wireless networks. In: Presented at the 6th ACM international symposium on mobile ad hoc networking and computing
56. Peng T, Leckie C, Ramamohanarao K (2007) Survey of network-based defense mechanisms countering the DoS and DDoS problems. *ACM Comput Surv* 39(1):3
57. Zargar ST, Joshi J, Tipper D (2013) A survey of defense mechanisms against distributed denial of service (DDoS) flooding attacks. *IEEE Commun Surv Tutor* 15(4):2046–2069
58. Masdari M, Jalali M (2016) A survey and taxonomy of DoS attacks in cloud computing. *Secur Commun Netw* 9(16): 3724–3751. [Online]. Available <https://onlinelibrary.wiley.com/doi/abs/https://doi.org/10.1002/sec.1539>
59. Challal Y, Bettahar H, Bouabdallah A (2004) A taxonomy of multicast data origin authentication: issues and solutions. *IEEE Commun Surv Tutor* 34–57
60. Molsa J (2005) Mitigating denial of service attacks: a tutorial. *J Comput Secur* 13(6):807–837
61. Tufail S, Parvez I, Batool S, Sarwat A (2021) A survey on cybersecurity challenges, detection and mitigation techniques for the smart grid. *Energies* 14:5894
62. Mollah MB, Zhao J, Niyato D, Zhang X (2021) Blockchain for future smart grid: a comprehensive survey. *IEEE Internet of Things J* 8(1)
63. Zhaung P, Zamir T, Liang H (2021) Blockchain for cybersecurity in smart grid: a comprehensive survey. *IEEE Trans Ind Inf* 17(1)
64. Wang W et al (2019) A survey on consensus mechanisms and mining strategy management in blockchain networks. *IEEE Access* 7:22328–22370
65. Hamida EB, Brousmiche KL, Levard H, Thea E (2017, July) Blockchain for enterprise: overview, opportunities and challenges. In: Proceedings of ICWMC, pp 83–88
66. Mrabet ZE, Kaabouch N, Ghazi HE, ElGhazi H (2018) Cybersecurity in smart grid: survey and challenges. *Comput Electr Eng* 67(1):469–482
67. Yan Y, Qian Y, Sharif H, Tipper D (2012) A survey on cyber security for smart grid communications. *IEEE Commun Surv Tutor* 14(4):998–1010
68. Bani-Ahmed A, Rashidi M, Nasiri A, Hosseini H (2019) Reliability analysis of a decentralized microgrid control architecture. *IEEE Trans Smart Grid* 10(4):3910–3918
69. Winter TMGL (2018) The advantages and challenges of the blockchain for smart grids. MS thesis, TU Delft University of Technology, Delft, Netherlands
70. Lazaroiu GC (2018) Blockchain and smart metering towards sustainable prosumers. In: Proceedings of IEEE international symposium on power electronics, electrical drives, automation and motion, pp 550–555
71. Hao J, Piechocki RJ, Kaleshi D, Chin WH, Fan Z (2015) Sparse malicious false data injection attacks and defense mechanisms in smart grids. *IEEE Trans Ind Informat* 11(5):1198–1209
72. Grammatikis PR, Sarigiannidis P, Liatifs T (2018, October) An overview of the firewall systems in the smart grid paradigm. In: 2018, GIIS, pp 1–4
73. Tan S, Song W, Member S, Stewart M, Yang J, Tong L (2018) Online data integrity attacks against real-time electrical market in smart grid. *IEEE Trans Smart Grid* 9(1):313–322
74. Kurtm MN, Yilmaz Y, Wang X (2019) Secure distributed dynamic state estimation in wide-area smart grids. *CoRR* 1(1):1902–1918

75. Wang S, Ouyang L, Yuan Y, Ni X, Han X, Wang F (2019) Blockchain enabled smart contracts: architecture, applications, and future trends. *IEEE Trans Syst Man Cybern Syst* 49(11):2266–2277
76. Wang S, Taha AF, Wang J (2018) Blockchain assisted crowdsourced energy systems. In: *Proceedings of IEEE power energy society general meeting*, pp. 167–172
77. Singh NK, Mahajan V (2019) Smart grid: cyber attack identification and recovery approach. In: *2019 2nd international conference on innovations in electronics, signal processing and communication (IESC)*, 2019, pp 1–5. <https://doi.org/10.1109/IESPC.2019.8902401>
78. Abdul Majeed M, Kumar Singh N, Tak L, Mahajan V (2021) Detection of stealthy cyber intrusion in smart electric grid using advanced state estimation. In: *2021 11th international conference on cloud computing, data science & engineering (Confluence)*, pp 660–665. <https://doi.org/10.1109/Confluence51648.2021.9377067>
79. Singh NK, Mahajan V (2021) End-user privacy protection scheme from cyber intrusion in smart grid advanced metering infrastructure. *Int J Crit Infrastruct Prot* 100410
80. Gupta PK, Singh NK, Mahajan V (2020) Monitoring of cyber intrusion in wireless smart grid network using weight reduction technique. In: *2020 international conference on electrical and electronics engineering (ICE3)*, pp 136–139. <https://doi.org/10.1109/ICE348803.2020.9122981>

Descriptive and Comparative Analysis of YouTube Trending Videos



Janki Chandiwala, Sarvesh Agrawal, and Shrushti Agarwal

Abstract YouTube is one of the largest and most popular video-sharing websites, including user-generated material. Since its launch in early 2005, YouTube has grown to become one of the fastest-growing websites, with traffic ranking second among all websites. Content creators can use websites such as YouTube to share their knowledge, ideas, and intriguing material with their viewers. As of 2021, the video-sharing network has 2.3 billion members globally. YouTube maintains a list of popular videos that is updated regularly. We give an exhaustive data analysis of YouTube's most popular videos in this study. User features such as title, video categories, tags are used in the analysis. Trending videos from two nations, India and the USA, will be evaluated and compared, with a total of 62,689 and 67,591 videos and 16 attributes in our dataset. Pandas, NumPy, NLTK, Image AI, and matplotlib are used to create bar graphs, heatmaps, word clouds, boxplots, and other visualizations.

Keywords YouTube · Trending videos · Analysis · API · NLP · India · The USA

1 Introduction

As a new killer application, networked video-sharing has exploded on the Internet. YouTube is one of the largest and most popular video-sharing websites, including user-generated material. YouTube has been one of the fastest-growing websites since its launch in early 2005, and according to Alexa, it ranks second in traffic among all websites on the Internet [1]. YouTube, which is owned by Google, has over a billion users and billions of views. According to the most recent YouTube data, there are

J. Chandiwala · S. Agrawal · S. Agarwal (✉)
Narsee Monjee Institute of Management Studies, Mumbai, India
e-mail: shrushti.agarwal02@nmims.edu.in

J. Chandiwala
e-mail: janki.chandiwala18@nmims.edu.in

S. Agrawal
e-mail: sarvesh.agrawal04@nmims.edu.in

2.3 billion subscribers on the video-sharing platform globally as of 2021. They are, without a question, altering popular culture and how people use the Internet. YouTube is not only available but also localized (YouTube, 2021) in over 100 countries [2]. This means that the platform adjusts to the various languages spoken in the various markets it serves. Given this, and the fact that users post 72 h (about 3 days) of video every minute, YouTube is the perfect venue for brand engagement or advertising, yet capturing viewers' attention is incredibly challenging and competitive [3].

YouTube maintains a list of popular videos that is updated regularly. Analyzing these popular videos can help content creators have a better understanding of how to increase their channel's popularity and brand. YouTube offers a trending feature that displays content that has the potential to become popular in a brief period. Viewers can keep up with what is going on YouTube and around the world by using the trending feature. Trending's goal is to bring videos to the attention of a large number of viewers. When YouTube declares a video as trending, it is usually not popular (yet), but it has the potential to become popular (eventually). Some videos, for example, are labeled as trending despite having only a few hundred views. In a different light, YouTube's trending videos attempt to highlight growing patterns within various audience communities [4].

We present an in-depth measuring study of YouTube video data in this report. We also look at several new elements that have not been looked at in past measurement studies, such as video growth trends and lifespan. This paper intends to aid in the discovery of video trends and the extraction of crucial characteristics that may be used to boost the growth of YouTube channels. We ran the study on a total of 62,689 and 67,591 trending videos in India and the USA from August 2020 until July 2021, respectively.

The remainder of the paper is structured as follows. Section 2 provides a high-level overview of our dataset. Section 3 describes the tools we used for this Exploratory Data Analysis (EDA) and the preprocessing performed upon the dataset. The statistics of YouTube videos and the conclusions drawn are analyzed in Sect. 4. Section 5 of the paper focuses on the related work that was performed in the past to analyze YouTube videos. Finally, Sect. 6 concludes the paper and notes some future directions.

2 Dataset

The YouTube API was used to get the data for this study. In this study, hot videos from India and the USA will be evaluated and compared, with a total of 62,689 and 67,591 videos, respectively.

As a result, we have 1,30,280 trending videos to examine. The same video could be on YouTube's trending list for several days. As a result, not all the 1,30,280 videos are unique. There are 17,778 unique videos among the 62,689 popular videos for India and 11,305 unique videos among the 67,591 trending videos for the USA, bringing the total number of unique videos to 29,083. To put it another way, from August 2020 to July 2021, 29,083 videos appeared on the hot list. Some may have

Table 1 Dataset description

Column name	Description	Data type
video_id	A distinct value for the video on YouTube	object
title	Title of the video posted by the publisher	object
publishedAt	Date and time of video publishing	object
channelId	Channel id of the publisher	object
channelTitle	Channel name that published the video	object
categoryId	ID of the category chosen by the publisher	int64
trending_date	The day that this video was trending	object
tags	Tags included by the publisher in the description	object
view_count	The number of people who have watched the video	int64
likes	The number of people who have liked the video	int64
dislikes	The number of dislikes for the video	int64
comment_count	The number of comments left on the video	int64
thumbnail_link	Download link for the video’s thumbnail	object
comments_disabled	Whether or not the comments have been disabled by the publisher	bool
ratings_disabled	If the publisher has disabled, the ratings or not	bool
description	The description entered by the publisher to describe the videos	object

been on the list for ten days, some for twenty, and so on. In the dataset, there are 16 columns. The columns of the dataset are listed in Table 1 for your convenience.

The same video could be trending for several days. Thus, it implies that we could find another data record for the same video ID, but with a different “trending date” and possibly a changed number of views, comments, likes, etc. (because those numbers will most probably rise from one day to the next).

3 Methodology

The dataset is not in the most appealing state for analysis, and the initial portion comprises of data cleaning and manipulation with Pandas. We will analyze and visualize the data in the second phase to get significant insights.

3.1 Preprocessing

Before beginning the analysis, the dataset was preprocessed using a variety of methodologies. Four columns were removed from the 16 listed above because they

were unnecessary for our analysis: `video_id`, `thumbnail_link`, `ratings_disabled`, and `comments_disabled`. The YouTube API was used to link column `categoryId` to its associated category name. The textual data preprocessing approaches that were used are explored in more detail.

3.1.1 Uppercase to Lowercase

Some titles, tags, and descriptions contain all capital letters, whereas some are a mixture of capital and lowercase letters. The `string.lower()` function converts all uppercase and mixed-case characters in a string into lowercase characters and returns it [5]. Next, we remove all the punctuation marks so that we have cleaner textual data. We use regex-based replacement for this purpose.

3.1.2 Expanding Contractions

Contracted words (also known as contractions) are short words formed by combining two words [6]. There are primarily two reasons, while dealing with contractions makes sense in NLP. For starters, a computer does not understand that contractions are abbreviations for a series of words. As a result, a computer considers `hasn't` and `has not to be` two distinct concepts and fails to understand that these two phrases have the same meaning. Second, contractions increase the dimensionality of the document term matrix. This increase in dimensionality raises the cost of computation. As a result, we evaluated the data from all trending videos and replaced contractions with their expansions. For example, the words `"didn't"` and `"can't"` were substituted with `"did not"` and `"cannot"`, respectively.

3.1.3 Tokenization

Tokenization is the process of replacing data with unique identification symbols that maintain all the material's vital information without risking its integrity and security. It has a significant influence on the text. Unstructured data and natural language text are broken down into chunks of information that can be regarded as separate elements using a tokenizer. The token occurrences in a document can be utilized to create a vector that represents the document. An unstructured string (text document) is instantly transformed into a numerical data structure appropriate for machine learning. They can also be directly triggered by a computer to perform beneficial actions and responses [7].

3.1.4 Stopwords

Stopwords are a set of extensively used words that can be found in any language, not only English. Stopwords are significant because they allow us to concentrate on the keywords by removing the words that are frequently used in a language [8].

When stopwords are eliminated from a dataset, its size decreases, so does the time required to train the model. After stopwords are deleted, there are only usable tokens left, therefore performance increases. As a result, it has the potential to improve classification accuracy. Stopwords are being removed from search engines like Google to allow for faster and more appropriate data retrieval from databases [9].

3.1.5 N-gram

An N-gram model determines the word which is most likely to follow a sequence of $N-1$ words given in the sequence. It is a probabilistic model that has been trained on a text corpus. It can be used in a variety of NLP applications such as search auto-correct and autocomplete, chatbots, and language translation. An N-gram model is constructed by calculating the frequency with which word sequences occur in corpus text and then predicting the probability. An N-gram model is a subset of a language model (LM), which is concerned with determining the probability distribution over word sequences [10].

Consider the following two sentences: “There was heavy snow” and “There was heavy snowfall”. Because the first sentence sounds better, an N-gram model will tell you that “heavy snow” occurs considerably more frequently in the training corpus than “heavy snowfall”. Thus, the first statement is more likely and will be chosen by the model. A unigram is a model that depends solely on how frequently a word occurs without considering prior words. Bigram refers to a model that uses only the prior word to predict the current word. If the two preceding words are taken into account, the model is a trigram.

3.2 EDA

Statistics of trending section videos are used to conduct the analysis for this paper. This method entails acquiring all data related to trending videos, such as the number of views for each trending video, the time it took for the video to be in the trending area, the number of likes, comments, and descriptions for that video, and so on.

3.2.1 Most Trending Video Category

YouTube organizes videos into distinct categories. Entertainment, music, gaming, comedy, sports, etc. are examples. The above bar charts compare the number of

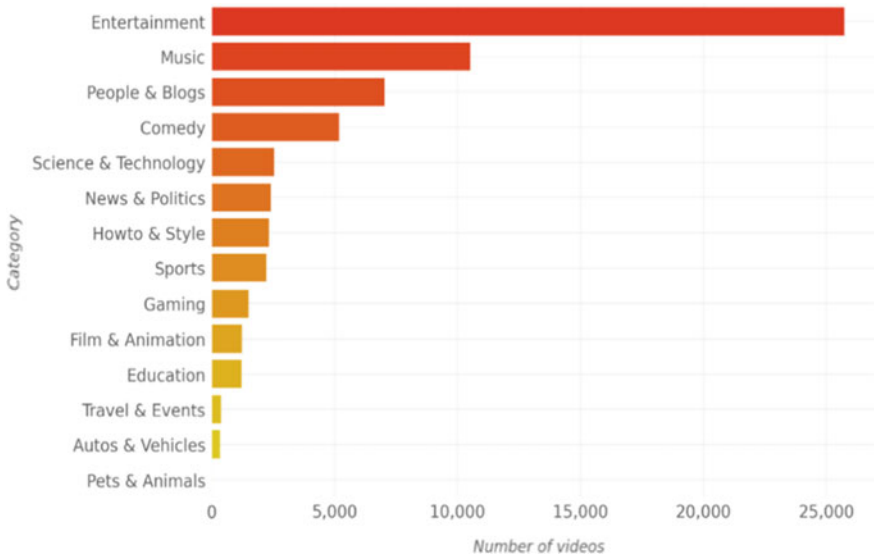


Fig. 1 Most trending video categories in India

trending videos in each category in India and the USA. The y-axis indicates the category, and x-axis indicates the number of trending videos.

With 25,740 trending videos (shown in Fig. 1), 41% of 2020–2021 trending videos in India and 13,796 trending videos (shown in Fig. 2), 20.41% of 2020–2021 trending videos in the USA, entertainment is the most popular category in both nations.

The music category is ranked second in terms of most trending videos, and the figures are close.

The “people and blogs” category is ranked third in India (shown in Fig. 1), but fifth in the USA. While the gaming category is ranked third in the USA (shown in Fig. 1), it is ranked ninth in India.

“Autos and vehicles”, “Travel and Events”, “Pets and Animals”, and “Education” constitute the categories which have least number of trending videos in both the countries. This may imply that there is untapped potential in these categories.

Thus, after analyzing the watching preferences of users in both countries, it can be inferred that the videos belonging to the entertainment and music category are the most trending.

This implies that there is a large positive correlation between both the countries based on the categories which have the greatest number of trending videos (Figs. 3 and 4).

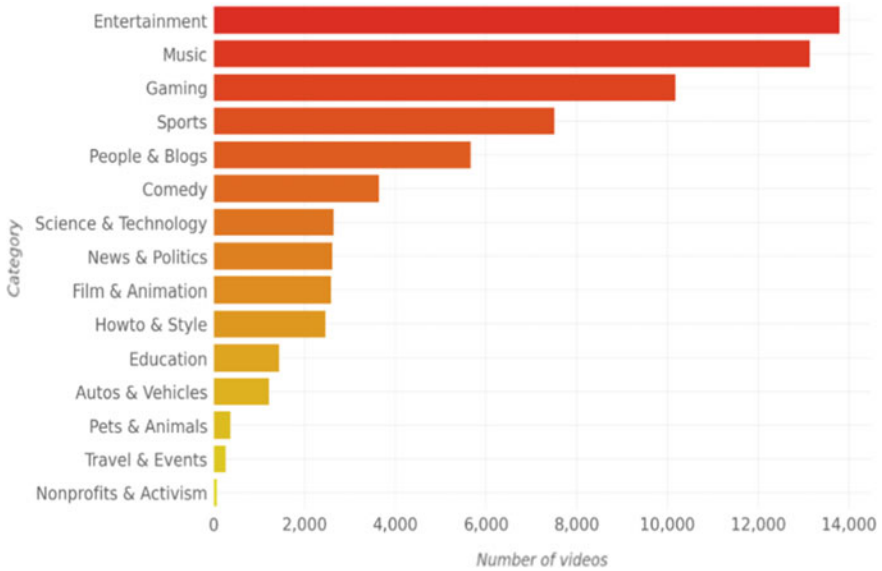


Fig. 2 Most trending video categories in the USA

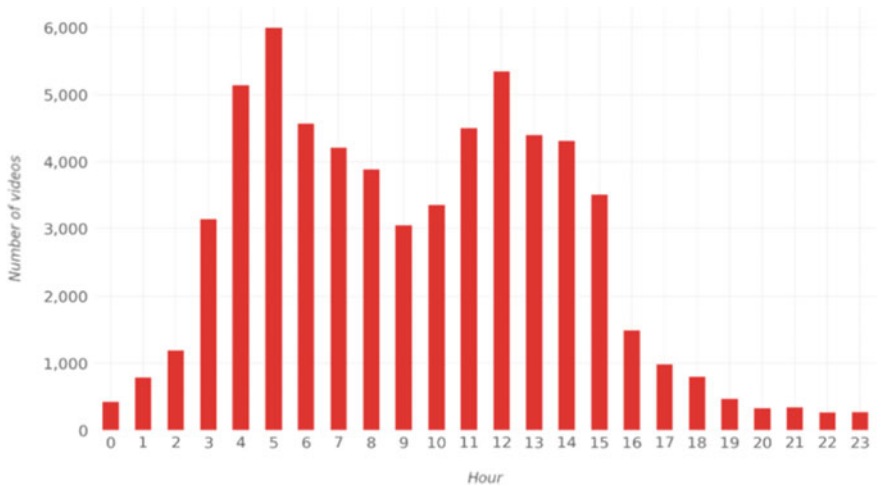


Fig. 3 Upload time of most trending videos in India

3.2.2 Upload Time and Day of Most Trending Videos

The graphs above show the number of trending videos published at each hour of the day, beginning from 0 which indicates 12 a.m. and ending with 23 which depicts 11 p.m.

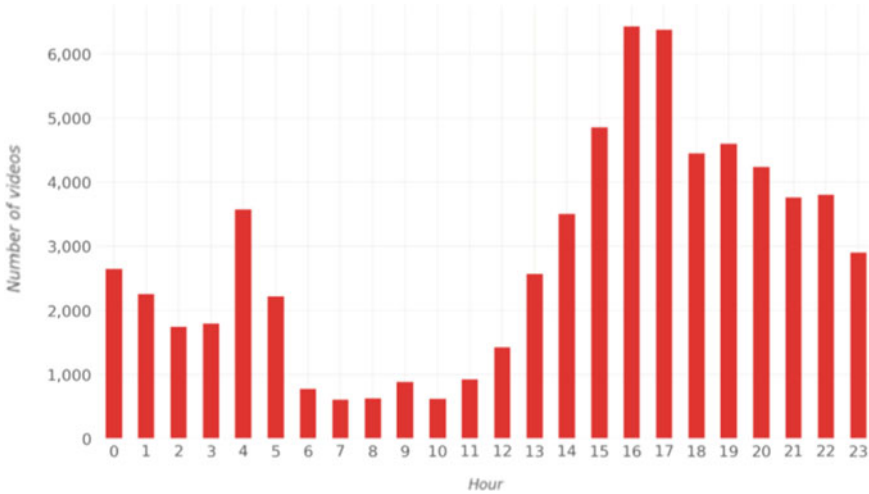


Fig. 4 Upload time of most trending videos in the USA

According to the graph (shown in Fig. 5), the top hours for releasing trending videos in India were 5 a.m. and 12 p.m. While on the other hand, peak hours for releasing trending videos in the USA were in-between 16 and 18 (i.e., starting from 4 p.m. to 6 p.m.); when converted to Washington time, we learn that the peak hours were 12 p.m. and 2 p.m.

The graphs above (shown in Fig. 6) depict how many trending videos were posted on a day in a week, arranged by descending video count. We can notice that there

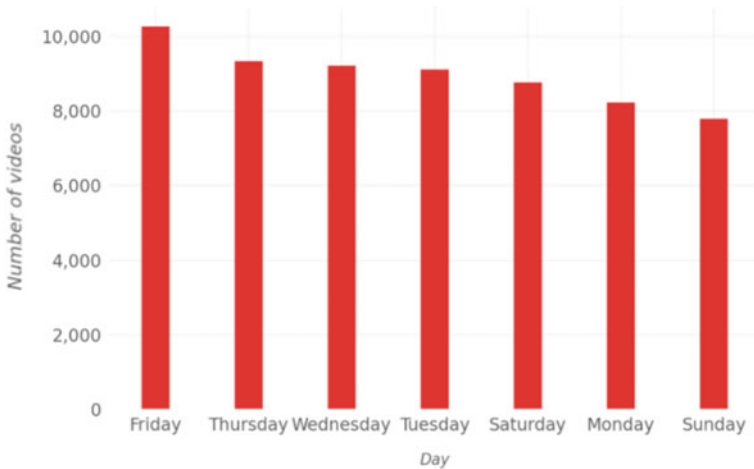


Fig. 5 Upload day of most trending videos in India

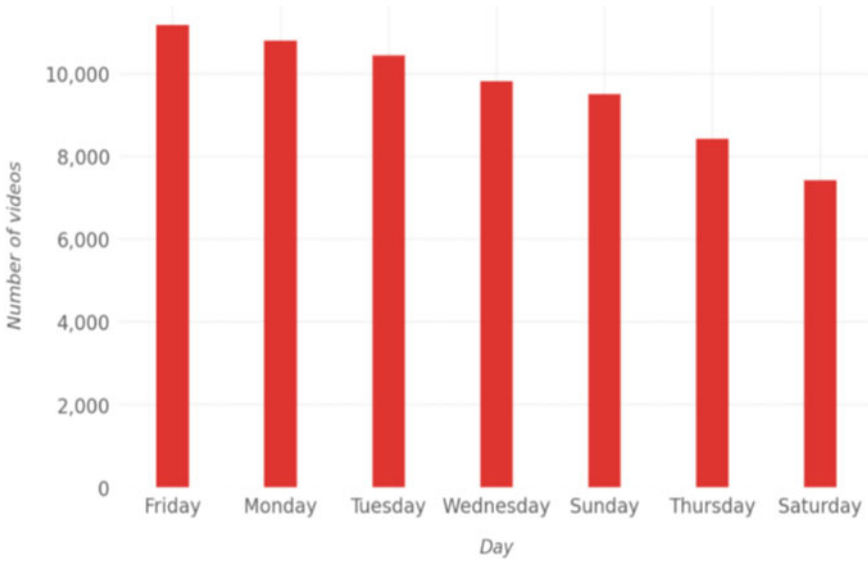


Fig. 6 Upload day of most trending videos in the USA

were comparatively more prevalent videos on Friday compared to other days of the week.

Thus, it can be concluded that Friday, 12 p.m. is the time when the highest numbers of trending videos were published.

3.2.3 Title Length of Trending Videos

Each video’s title is a crucial component. They provide users with a description of the video before they decide whether or not to watch it. As a result, video title is one of the principal variables in video success. Thus, it can be implied that the video title is crucial in influencing video click-through rate (CTR).

For India, we can observe (shown in Fig. 7) that the majority of trending videos have titles that are between 51 and 93 characters long. Seventy characters are the average length of a title. The title’s maximum length is 100 which happens to be the maximum title length, and the minimum length is two characters.

On the other hand, the USA have titles that are between 36 and 64 characters long (shown in Fig. 8). The maximum title length limit is 100, and the minimum title length is three characters. The average length of a title is 51 characters long.

We can see that the length of titles in India is greater than USA. This large disparity may be due to the fact that many titles have Hinglish (Hindi pronounced using English literals) titles in India, making them longer. Since that gives a complete meaning and more information to the user, it makes sense that trending videos have longer title length in India.

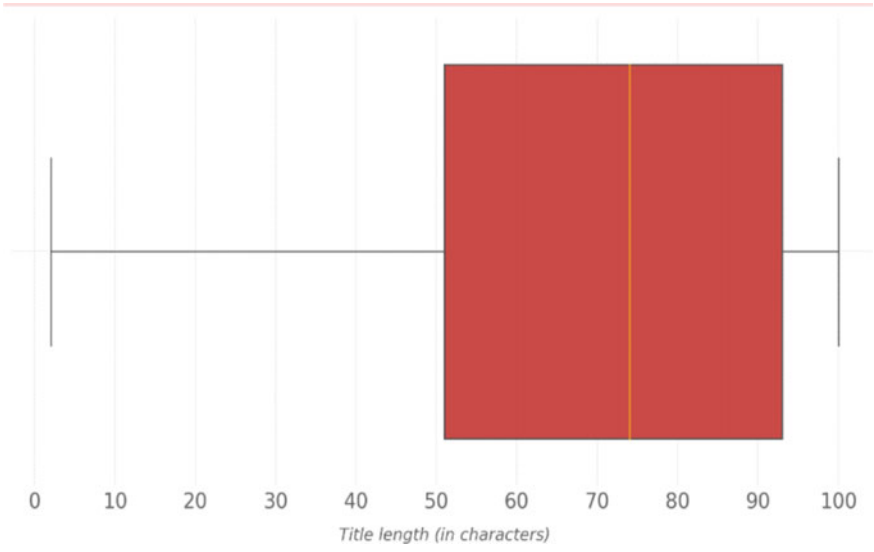


Fig. 7 Title length of most trending videos in India

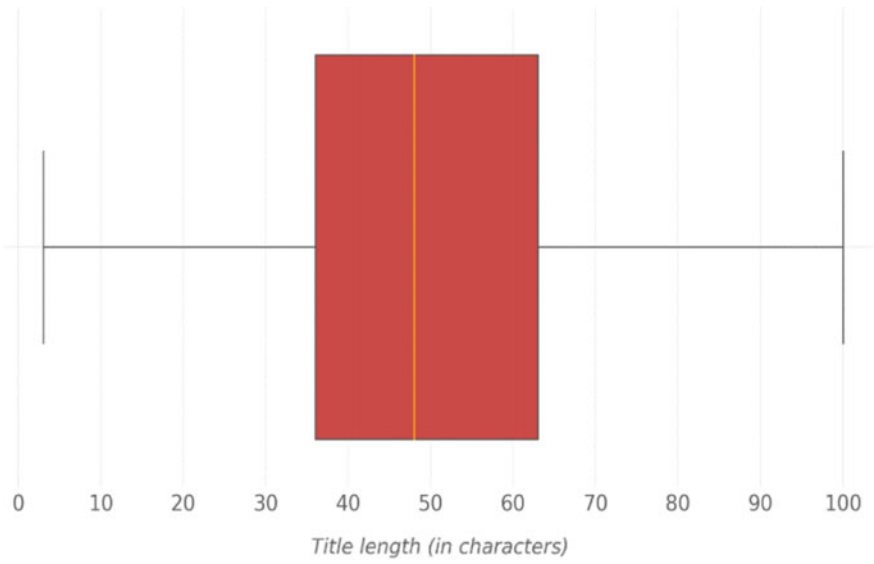


Fig. 8 Title length of most trending videos in the USA

Whereas in the USA, words like “official”, “music”, “video”, “vs”, and “new” are the most frequently added words in the title.

We can relate these words to the most trending video category in both the countries. Words like “official” and “video” are most frequently occurring in the titles of both countries and are written in the same large typeface.

- 2-gram

When 2-grams from all the titles of the trending video are extracted, we see that each 2-gram’s words is connected by a “-”. “Punjabi songs”, “latest Punjabi”, and “official video” are the most commonly used 2-gram words in trending videos in India (shown in Fig. 10). These can be mapped to the most trending video categories of India, i.e., entertainment and music.

On the other hand, 2-gram words like “official video”, “music video”, “official music”, and “among us” are the top ones for the USA (shown in Fig. 11). Like before, these can be mapped to the most trending video categories of the USA, i.e., entertainment, music, and gaming.

```
[(('punjabi', 'songs'), 2094),
 (('latest', 'punjabi'), 2026),
 (('official', 'video'), 2009),
 (('ਐ', 'ਐ'), 1550),
 (('new', 'punjabi'), 1374),
 (('mehta', 'ka'), 1335),
 (('ka', 'ooltah'), 1335),
 (('ooltah', 'chashmah'), 1328),
 (('taarak', 'mehta'), 1322),
 (('punjabi', 'song'), 1308),
 (('त', 'रक'), 1195),
 (('रक', 'म'), 1189),
 (('म', 'हत'), 1189),
 (('web', 'series'), 1129),
 (('songs', '2021'), 1096),
 (('tv', 'serial'), 1047),
 (('song', '2020'), 1044),
 (('chashmah', 'त'), 1013),
 (('song', '2021'), 1003),
 (('S', 'S'), 947),
 (('music', 'video'), 929),
 (('official', 'trailer'), 917),
 (('songs', '2020'), 855),
 (('full', 'video'), 840),
 (('क', 'य'), 826)]

[[('official', 'video'), 3340),
 (('music', 'video'), 2848),
 (('official', 'music'), 2656),
 (('among', 'us'), 1254),
 (('official', 'trailer'), 907),
 (('video', 'oficial'), 904),
 (('in', 'the'), 774),
 (('official', 'audio'), 727),
 (('of', 'the'), 697),
 (('to', 'the'), 677),
 (('reacts', 'to'), 622),
 (('how', 'to'), 534),
 (('game', 'highlights'), 515),
 (('friday', 'night'), 511),
 (('on', 'the'), 489),
 (('minecraft', 'but'), 482),
 (('full', 'game'), 475),
 (('from', 'the'), 463),
 (('lyric', 'video'), 437),
 (('video', 'ft'), 392),
 (('at', 'the'), 387),
 (('in', 'a'), 368),
 (('highlights', 'nfl'), 353),
 (('nfl', '2020'), 353),
 (('for', 'the'), 352)]
```

Fig. 11 Most common 2-gram words occurring in title of trending videos in India (left) and in the USA (right)

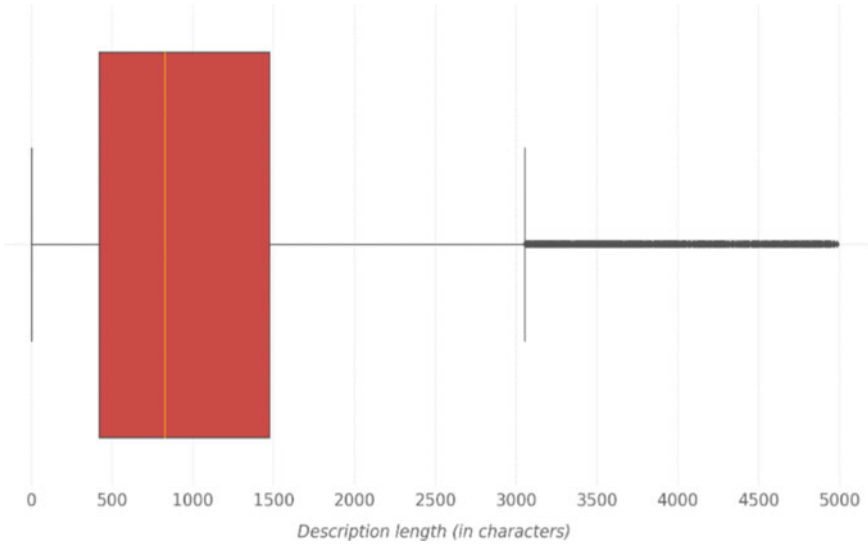


Fig. 12 Description length of trending videos in India

3.2.5 Description Length of Trending Videos

A description for a YouTube video can be up to 5000 characters long. For India and the USA, the average description length is 1083 (shown in Fig. 12) and 1031 (shown in Fig. 13) characters, respectively. We can see that the minimum, maximum, and mean lengths for both countries are reasonably close to each other. The most common description length for trending YouTube videos is 400–1400 characters, which is understandable.

3.2.6 Number of Tags Used in Trending Videos

When you post a video to YouTube, you have the option of adding tags to it. On the video page, tags are not visible. Tags are only marginally useful in assisting people in finding your video. The distribution of the number of tags is depicted in violin plots below.

It can be observed that the majority of trending videos in India have 10–25 tags. The maximum and the minimum number of tags a trending video has, are 75 and 1, respectively, (shown in Fig. 14).

It can be seen that the majority of trending videos in the USA have between 6 and 26 tags. While the maximum number of tags a trending video has, is 74, the minimum number of tags is 1 (shown in Fig. 15).

As a result, adding 10–25 tags to your video may increase your video’s chances of getting popular.

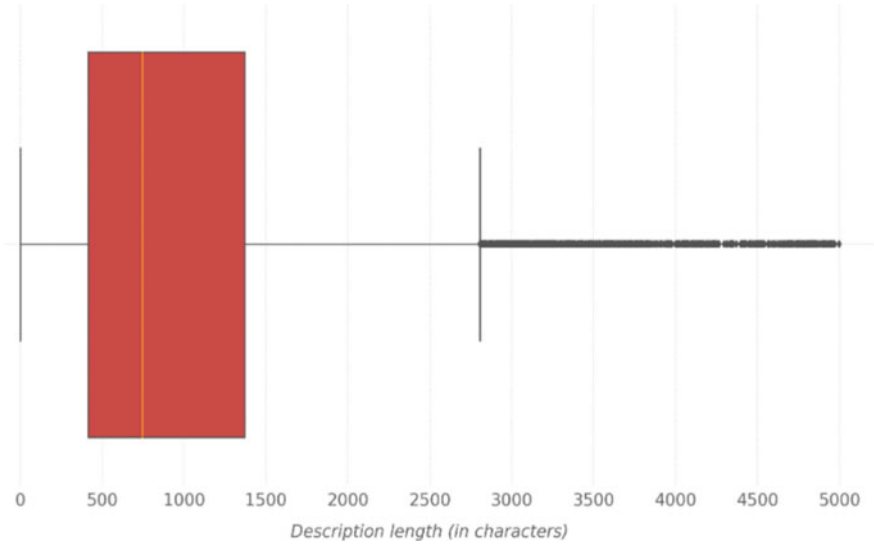


Fig. 13 Description length of trending videos in the USA

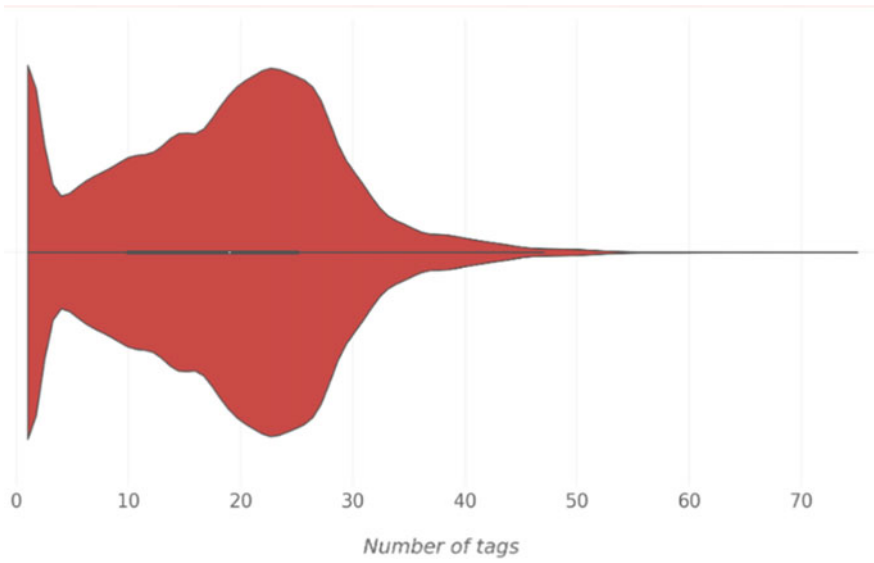


Fig. 14 Number of tags used in trending videos in India

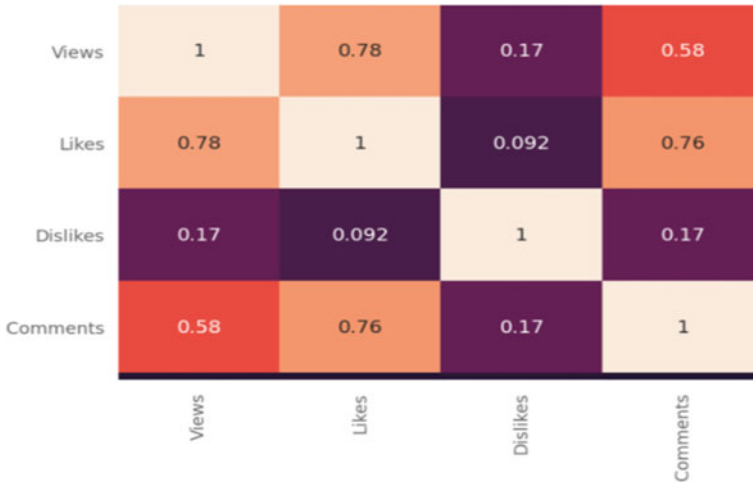


Fig. 18 Correlation of the factors used to compare trending videos in India

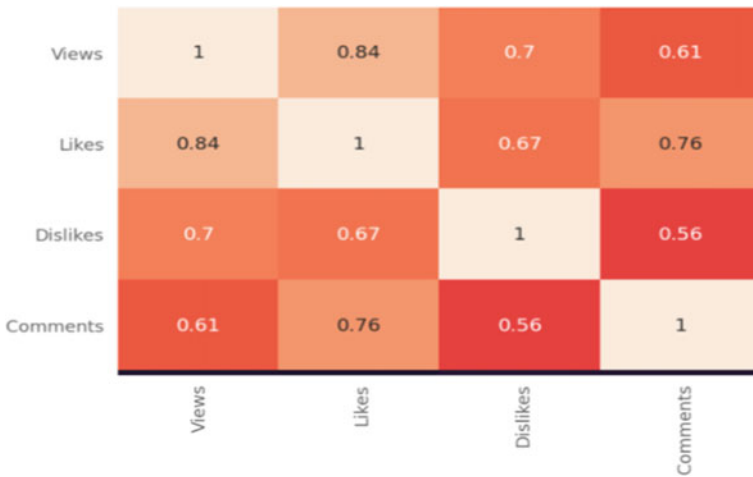


Fig. 19 Correlation of factors used to compare trending videos in the USA

4 Conclusion

We presented our findings in this work, for measuring, assessing, and comparing trending videos on YouTube—the most popular Internet short video-sharing site, for two countries: India and the USA. The factors taken into account for this purpose are titles, categories, time of publishing, appropriate tagging, and the length of description, among others. Understanding these statistics can help individual YouTubers, content creators, businesses, movie makers, and others make the most effective

choices. As a result, a thorough analysis of the characteristics of over 20,000 most recent and distinct YouTube videos is given. We conducted a comprehensive data-driven study and determined the best strategies that a publisher should follow to maximize the likelihood of their video included in the trending videos list.

References

1. Cheng X, Dale C, Liu J (2008) Statistics and social network of youtube videos. IEEE Int Work Qual Serv IWQoS 229–238. <https://doi.org/10.1109/IWQoS.2008.3>
2. Mohsin M (2021) 10 Youtube stats every marketer should know in 2021 [infographic]. <https://www.oberlo.in/blog/youtube-statistics> Accessed 16 Jul 2021
3. Ward C (2021) Social media marketing for venues: a complete guide. <https://business.getonbloc.com/social-media-marketing-for-venues> Accessed 16 Jul 2021
4. Barjasteh I, Liu Y, Radha H (2014) Trending videos: measurement and analysis
5. Rai A (2021) Python string lower method. <https://www.geeksforgeeks.org/python-string-lower> Accessed 16 Jul 2021
6. Lukei (2019) Dealing with contractions in NLP. https://medium.com/@lukei_3514/dealing-with-contractions-in-nlp-d6174300876b. Accessed 17 Jul 2021
7. Webster J, Kit C (1992) Tokenization as the initial phase in NLP. Adv Mater 4:116. <https://doi.org/10.3115/992424.992434>
8. Ganesan K (2021) What are Stop Words? <https://kavita-ganesan.com/what-are-stop-words/#.YPztCegzZPZ>. Accessed 17 Jul 2021
9. Singh S (2019) NLP essentials: removing stopwords and performing text normalization using NLTK and spaCy in Python. <https://www.analyticsvidhya.com/blog/2019/08/how-to-remove-stopwords-text-normalization-nltk-spacy-gensim-python/>. Accessed 17 Jul 2021
10. Devopedia (2021) N-gram model. <https://devopedia.org/n-gram-model>. Accessed 19 Jul 2021

Phase Frequency Detector Using CNTFET



Shubham Tomar and Rutu Parekh

Abstract A conventional phase frequency detector (PFD) at nanoscale using standard CNTFET model is implemented. At supply voltage of 800 mV, CNTFET-based PFD has a dead zone of 1.5 ps which is 66.67% less as compared to conventional CMOS, the maximum operating frequency of 12.5 GHz which is 6.4% more than conventional CMOS, and lower power consumption up to 2.475 μ W which is 7.38% less as compared to conventional CMOS design. This paper focuses on PFD and CNTFET, i.e., at nanodimensions where conventional CMOS design suffers from many short channel effects, CNTFET-based designs give admirable characteristics. All the designs and simulations are performed in Cadence Virtuoso.

Keywords Phase frequency detector · Phase-locked loop · Carbon nanotube field-effect transistor · Simulation

1 Introduction

A phase-locked loop (PLL) is a wide area of applications such as receivers, wireless communication systems, and digital circuits. The main purpose of PLL is to synchronize the output oscillator signal with the reference signal to achieve a lock condition. Basic PLL comprises of four blocks, i.e., phase detector (PD) or phase frequency detector (PFD), charge pump (CP), low pass filter (LPF), and voltage control oscillator (VCO) along with negative feedback from the output of VCO to PFD as shown in Fig. 2 [1]. This paper focuses on implementing the conventional phase frequency detector (PFD), and an article by Kim et al. [2] said that at lower technological nodes, typical Si CMOS suffers from many issues like MOSFET scaling, small geometry effects, and short channel effects like drain-induced barrier lowering (DIBL), impact ionization, velocity saturation, hot carrier injection, and surface scattering [3], so to overcome these effects, emerging devices in nanoelectronics are preferred. Some of

S. Tomar (✉) · R. Parekh
VLSI and Embedded Systems Group, Dhirubhai Ambani Institute of Information and Communication Technology, Gandhinagar, Gujarat 382007, India
e-mail: tomar.shubham4j@gmail.com

© The Author(s), under exclusive license to Springer Nature Singapore Pte Ltd. 2022
V. Mahajan et al. (eds.), *Sustainable Technology and Advanced Computing in Electrical Engineering*, Lecture Notes in Electrical Engineering 939,
https://doi.org/10.1007/978-981-19-4364-5_62

them are nanowire transistors, carbon nanotubes field-effect transistors (CNTFETs), graphene nanoribbon (GNR), single-electron transistors (SET), quantum cellular automata (QCA), and so on.

Detecting phase difference had been used in wide area such as speed control of the motor, radar and telecommunication systems, demodulators, phase-locked loops. The main concept of PFD is comparing the two signals in terms of both phase and frequency and produces an error signal. However, there is a problem of a dead zone in PFD which can be minimized using different PFD topologies. In the dead zone, the phase error is not identified by PFD leading to introduce a jitter in PLL. Many articles and journal are there which show alternate methodologies to reduce dead zone in PFD; one of them is a work by Abolhasani et al. [4] which shows that two alternative circuits to implement PFD reduce dead zone in PFD significantly by using a differential amplifier. The notable advantages over conventional CMOS PFD include wider operating frequency, decreased power consumption, and reduced dead zone.

In this paper, we are focusing on CNTFETs-based PFD; a paper by Sinha et al. [5] said that as compared to MOSFET, CNTFETs have high channel mobility and improved gate capacitances against gate voltage, also CNTFET gate capacitance decreases with a decrease in oxide thickness at the nanometer scale. This decrease can be observed at a gate voltage of 0.5 V and above which tends to decrease in propagation delay and leakage current as compared to MOSFET [6]. Also, the effect of an increase in temperature on the threshold voltage of CNTFET is very small as compared to MOSFET [7].

2 CNTFET Working and Simulation Setup

According to Moore's law, the number of transistors in a dense integrated circuit doubles every eighteen months. And as stated earlier due to continuous scaling of MOSFET, short channel effects are seen predominantly to avoid such circumstances; many alternative technologies are evolved like SET, CNT, QCA, GNA out of which CNTs are promising as these are exploited to have low-resistance high-strength interconnections and highly scalable CNTFETs [8]. In this paper, CNTFET used is referred from Stanford University Virtual-Source Carbon Nanotube Field-Effect Transistor Version 1.0.1 [9]. Fig. 1 represents the model of CNTFET.

The Stanford Virtual-Source Carbon Nanotube Field-Effect Transistor (VS-CNFET) is a model that captures dimensional scaling properties and includes parasitic resistance (CNT-metal contact and doped extensions), parasitic capacitance (metal-to-metal coupling capacitance and metal-CNT fringe capacitance), and tunneling leakage currents (direct source-to-drain tunneling and gate-to-drain junction band-to-band tunneling) (Fig. 2).

In this paper, CNTFET is modeled at channel length of 16 nm as per current scenario and advancement in microelectronics short channel devices.

Parameters involved in CNTFET used in designing of PFD are shown in Table 1,

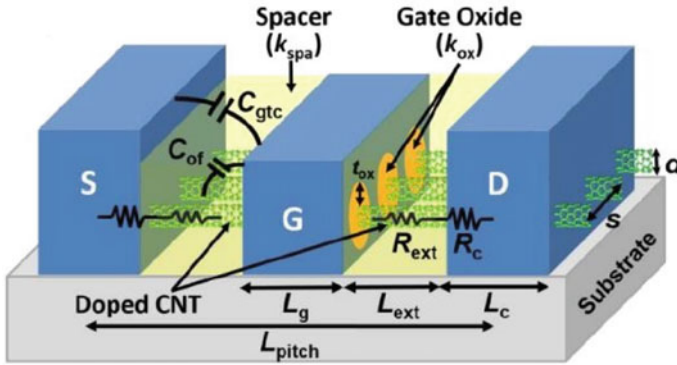


Fig. 1 CNTFET model [9]

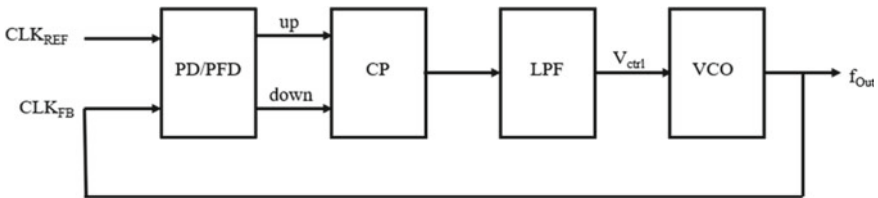


Fig. 2 Basic PLL system

3 Phase Frequency Detector

The PFD detects the phase and frequency between the two input waveforms. Traditional PFD shown in Fig. 3 uses two D-FFs whose input is kept always at high potential, and the reference signal is provided at the clock input of one D-FF, i.e., CLKREF and VCO output are feedback to another D-FF which serves as input clock to it, i.e., CLKFB. An AND gate is provided at the output of both D-FFs to generate a reset signal and set the output of both the D-FFs to zero.

3.1 Design and Working

In the circuit diagram of conventional PFD using CNTFET shown in Fig. 4, the PMOS and NMOS of conventional PFD are replaced by p-type CNTFET and n-type CNTFET, respectively [15]. The PFD generates two outputs UP and DOWN. The UP signal is generated when the rising edge of CLKREF is leading the rising edge of CLKFB, and the DOWN signal is generated when the rising edge of CLKFB is leading the rising edge of CLKREF [10]. When the UP signal is generated (high) as shown in Fig. 5a, this signifies that the reference signal is leading the VCO output,

Table 1 Parameters of CNTFET used in the design

Input	Range	Value	CNTFET	
			<i>n</i> -type	<i>p</i> -type
Type	−1 or 1	1	1	−1
<i>s</i>	[2.5e−9:inf)	10 nm	1e−06	1e−06
<i>W</i>	[s:inf)	1 μm	20e−09	40e−09
<i>L_g</i>	[5e−9:100e−9]	11.7 nm	16e−09	16e−09
<i>L_c</i>	[1e-9:inf)	12.9 nm	1.1e−08	1.1e−08
<i>L_{ext}</i>	(0:inf)	3.2 nm	3e−09	3e−09
<i>d</i>	[1e−9:2e−9]	1.2 nm	1.2e−09	1.2e−09
<i>t_{ox}</i>	[1e−9:10e−9]	3 nm	3e−09	3e−09
<i>k_{ox}</i>	[4:25]	23	23	23
<i>k_{cnt}</i>	1	1	1	1
<i>k_{sub}</i>	[1:kox)	3.9	3.9	3.9
<i>k_{spa}</i>	[1:16)	7.5	3.9	3.9
<i>H_g</i>	[0:inf)	20 nm	1.5e−08	1.5e−08
<i>E_{f_{sd}}</i>	[−0.1:0.5]	0.258	0.258	0.258
<i>V_{fb}</i>	[−1:1]	0.015	0	0
<i>G_{eo_mod}</i>	1 or 2 or 3	1	1	1
<i>RC_{mod}</i>	0 or 1 or 2	1	0	0
<i>R_{s0}</i>	[0:inf)	3300	3300	3300
<i>SDT_{mod}</i>	0 or 1 or 2	1	1	1
<i>BTBT_{mod}</i>	0 or 1	1	1	1
Temp	25	25	25	25

so to match the reference signal and feedback signal, VCO input must be tuned such that it generates a high-frequency output signal. This process continues till both the signal match and PLL enters into lock condition. Similarly, when the DOWN signal is generated (high) as shown in Fig. 5b, this signifies that VCO output leads the reference signal, so VCO must be tuned such that it generates a low output frequency till it matches with reference signal [11].

The corresponding pulse width of UP and DOWN signal on Figs. 5a and b, respectively, is proportional to the phase difference between the reference signal and VCO output. Suppose if the pulse of the reference signal and VCO output is not equal but the reference signal is leading the VCO output, then UP continues to generate pulses with unequal pulse width, while DOWN remains in a low state as shown in Fig. 5c [12].

Now when both the input of D-FF’s becomes high then UP and DOWN become zero because of AND gate which provides a reset signal to both the D-FF’s. So, PFD can only operate in three states and is hence also termed as a 3-state phase detector. The state diagram corresponding to PFD is shown in Fig. 6 [13].

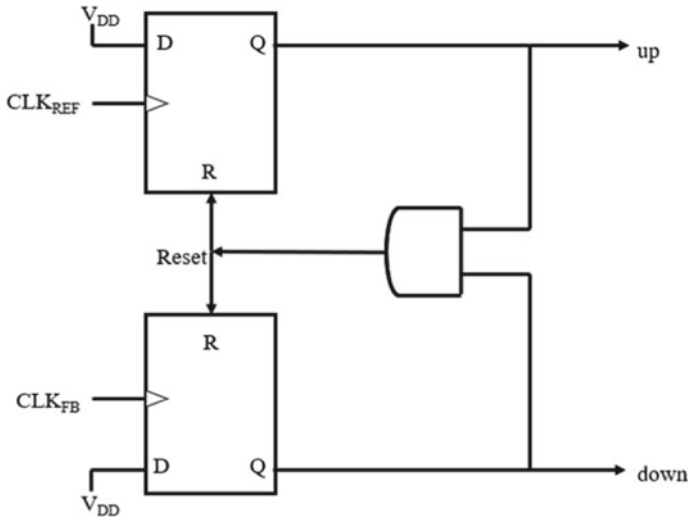


Fig. 3 Basis PFD implementation

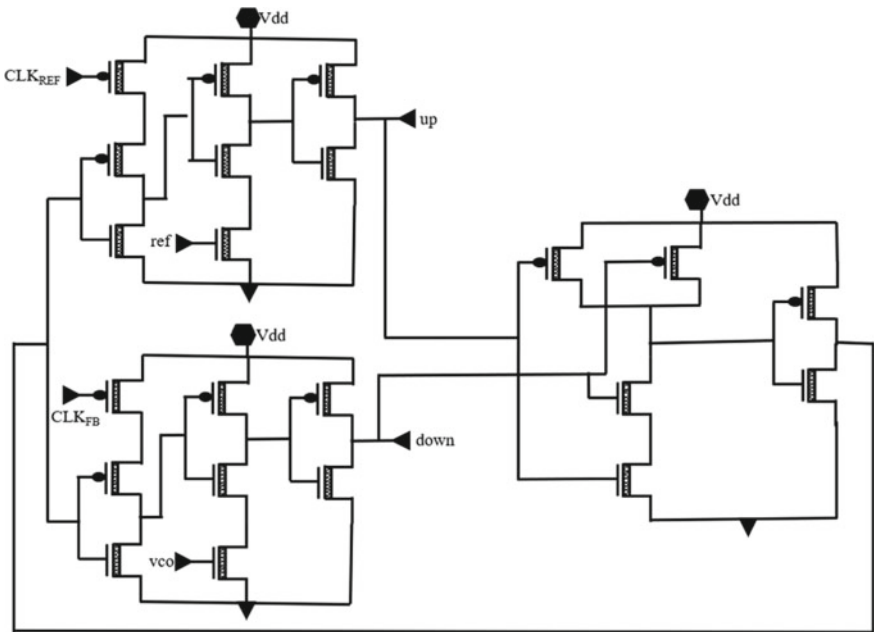


Fig. 4 Conventional PFD using CNTFET

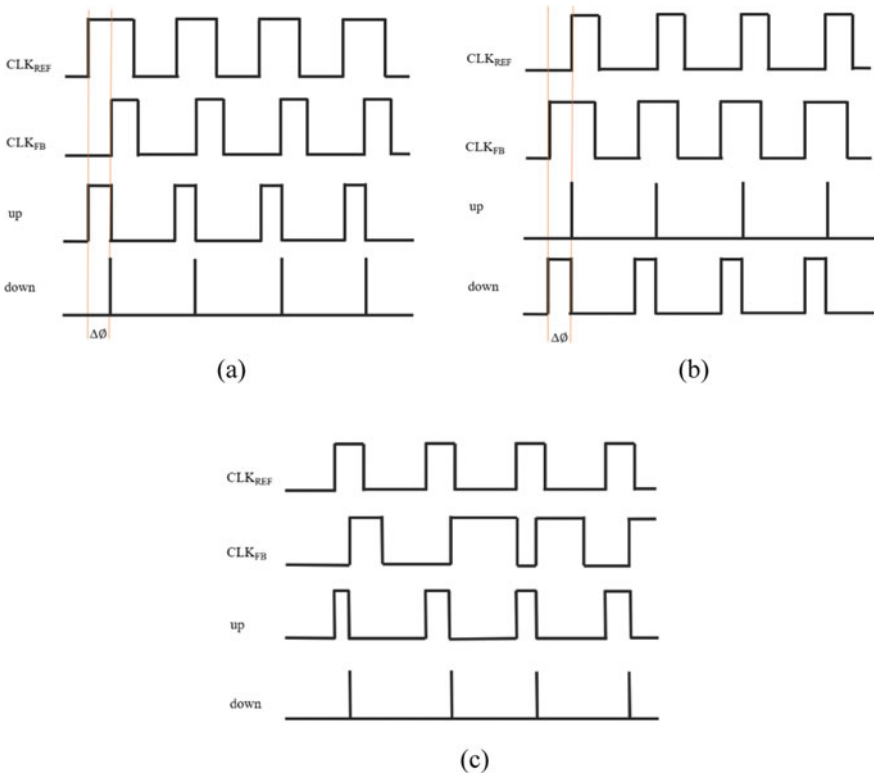


Fig. 5 **a** When reference signal leads VCO output, **b** When VCO output leads reference signal, and **c** When reference signal leads VCO output, but both have a different pulse width

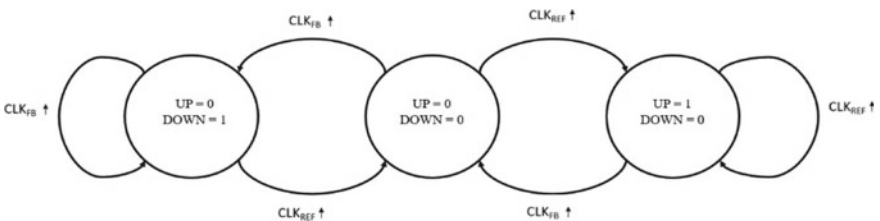


Fig. 6 State diagram of PFD

3.2 Dead Zone in PFD

The dead zone in PFD occurs when the loop does not respond to small phase errors between input signals of PFD. This problem occurs because of the delay time of both the D-FFs and time taken by ANG gate to reset D-FFs, i.e., as shown in Fig. 7 when the two input signals are close to each other such that there is a very small phase

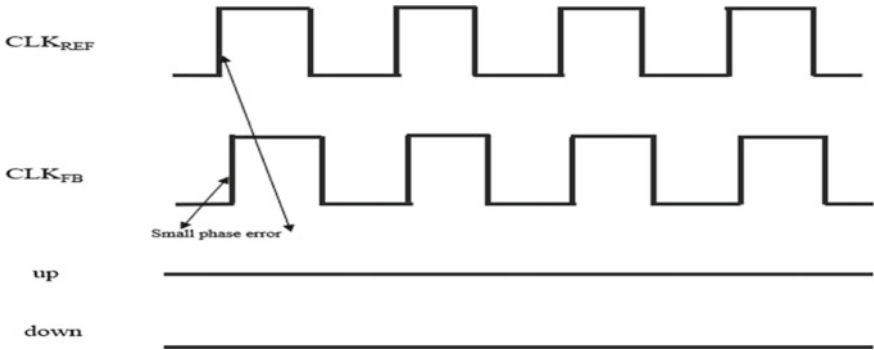


Fig. 7 Dead zone

error between both the signals, then because of delay and reset time of D-FFs and AND gate, respectively, the output signal UP and DOWN will not be able to charge, and hence, no output is generated. When the dead zone occurs, the output signal of PFD will not be proportional to this error [14].

There are many solutions to this problem like the use of tristate PFD which uses three delay elements between AND gate and reset path of D-FFs, but this solution comes with another problem of reference spurs which affects the output of PLL. Other solutions include the removal of reset path and provide new techniques to implement PFD, and since reset path is removed, speed of PFD also increased.

4 Simulation and Analysis

The simulation result shows the different scenarios of when PFD operates in different conditions as discussed earlier when CLK_{REF} leads CLK_{FB} as shown in Fig. 8,

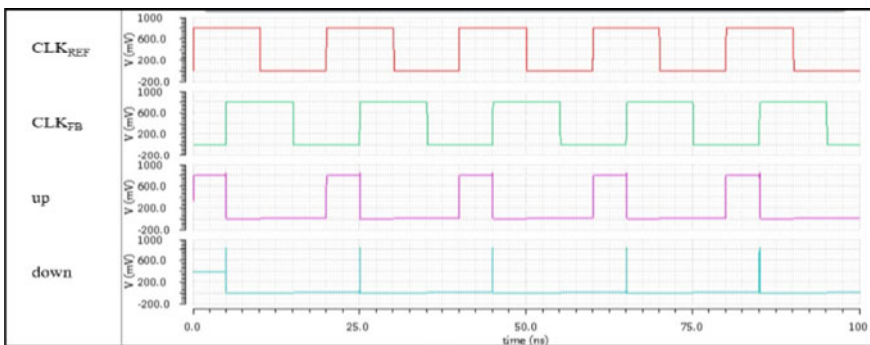


Fig. 8 Reference signal leads VCO output

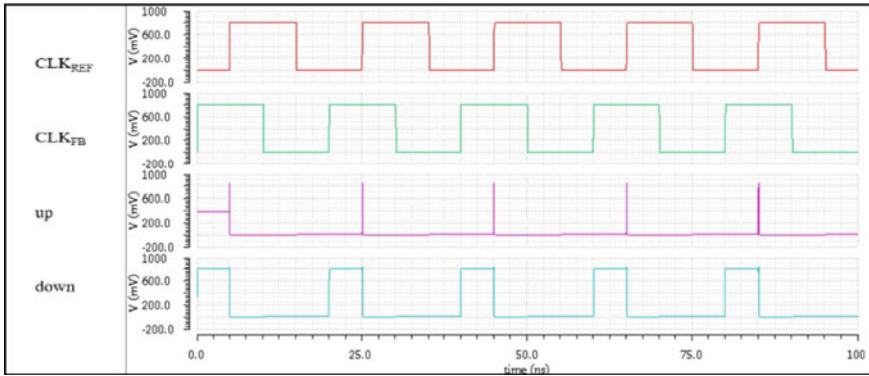


Fig. 9 Reference signal lags VCO output

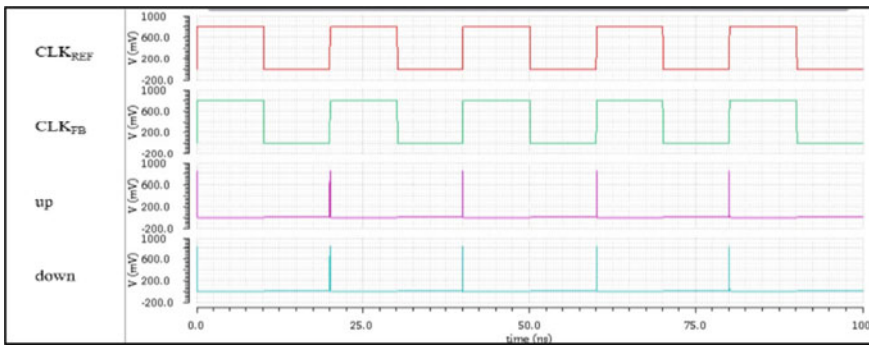


Fig. 10 Reference signal in phase with VCO output

then for PLL to achieve lock condition, VCO output must be tuned such that output frequency of VCO is increased.

Likewise, when CLK_{REF} lags CLK_{FB} as shown in Fig. 9, in this scenario to operate PLL in lock condition, VCO output frequency must be decreased so that there is no phase difference between both the input signals. Now, when CLK_{REF} is in phase with CLK_{FB} as shown in Fig. 10, i.e., there is no phase difference between both the signal, hence in this condition, PLL operates under lock condition.

4.1 Analysis

This section of the paper deals particularly with temperature analysis, determining the maximum operating frequency and dead zone of the PFD as these are the important parameter for application point of view.

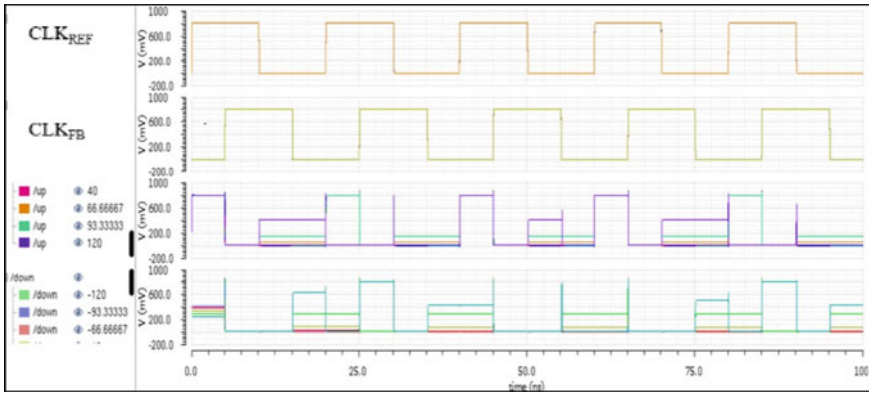


Fig. 11 Parametric analysis of PFD in temperature ranges from -120 to 120 °C

4.2 Temperature Analysis

Parametric analysis is done to analyze temperature effects on CNTFET-based PFD. The temperature ranges from -120 to 120 °C, and transient analysis is shown in Fig. 11. This indicates that CNTFET can withstand temperature from -120 °C to approximately 60 – 70 °C with negligible variation in output which is considerable, but the output will suffer from heavy penalty as shown if we further increase temperature [13].

4.3 Maximum Operating Frequency

Maximum operating frequency is defined by the short period conveying function characteristics with correct phase-detection information united with the same frequency and 90° phase difference on the input signals, as shown in Fig. 12; the PFD will work significantly up to 12.5 GHz [16, 17].

4.4 Dead Zone

As discussed earlier, dead zone in PFD is defined as the minimum phase difference which cannot be detected by the PFD which is 1.5 ps in CNTFET-based PFD as shown in Fig. 13 [13, 15, 18].

Table 2 shows some references that were taken for comparison with this work.

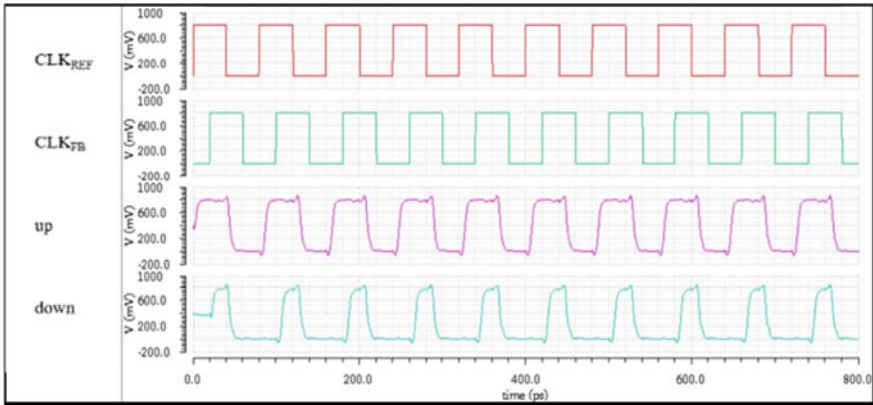


Fig. 12 Maximum operating frequency of 12.5 GHz

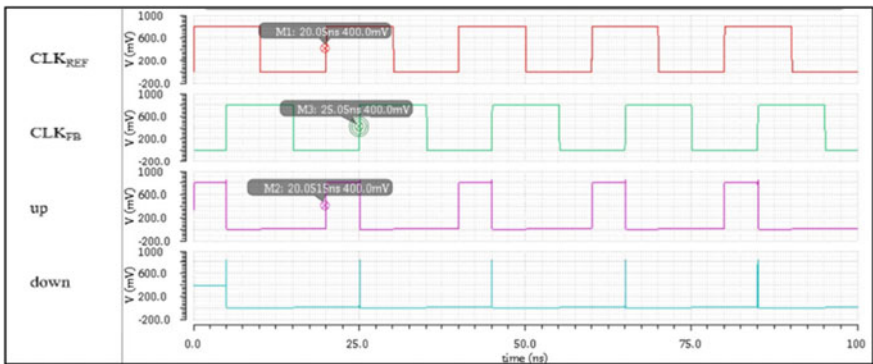


Fig. 13 Dead zone

5 Conclusion

CNTFET-based PFD design shows better output response in comparison to conventional CMOS-based design as shown in Table 2; CNTFET-based PFD gives maximum operating frequency up to 12.5 GHz, also power consumption reduces significantly which is up to 2.475 μ W, and a dead zone is approximate up to 1.5 ps with reset path available. This shows that CNTFET is very effective over conventional CMOS; since in this paper, conventional PFD is implemented using CNTFET; now when upgraded design of PFD is implemented using CNTFET, it gives much better response as compared to CMOS technology.

Table 2 Comparison to previous works

References	Tech.	Supply (V)	Maximum freq.	Average power consumption (μW)	Dead zone (ps)
Abolhasani et al. [4]	0.18 μm (CMOS)	1.8	1 GHz	107	40
Rashmi et al. [13]	0.18 μm (CMOS)	1.8	5 GHz	8	20
Ghaderi et al. [19]	CNTFET	0.9	12.5 GHz	24.5	1
Conventional PFD	0.18 μm (CMOS)	1.8	800 MHz	33.5	76.7
Halwai et al. [20]	16 nm (CMOS)	1	–	2.93	2.83
This work	16 nm (CNTFET)	0.8	12.5 GHz	2.475	1.5

References

- Rajole A (2013) Online case study on phase frequency detector. *Int J Sci Res (IJSP)*, ISSN:2319–7064
- Kim YB (2010) Challenges for nanoscale MOSFETs and emerging nanoelectronics. *Trans Electr Electron Mater* 11(3):93–105
- Sinha SK, Kumar K, Chaudhury S (2013) CNTFET: the emerging post-CMOS device. *Int Conf Sig Process Commun (ICSC)*. IEEE
- Abolhasani A, Mousazadeh M, Khoei A (2020) A high-speed, power efficient, dead- zone-less phase frequency detector with differential structure. *Microelectron J* 97:104719
- Sinha SK, Chaudhury S (2014) Advantage of CNTFET characteristics over MOSFET to reduce leakage power. In: 2014 2nd international conference on devices, circuits and systems (ICDCS), pp 1–5 IEEE
- Sinha SK, Chaudhury S (2013) Impact of oxide thickness on gate capacitance—a comprehensive analysis on MOSFET, nanowire FET, and CNTFET devices. *IEEE Trans Nanotechnol*:958–64
- Sinha SK, Chaudhury S (2014) Comparative study of leakage power in CNTFET over MOSFET device. *J Semiconductors* 35(11):114002
- Dang T, Anghel L, Leveugle R (2006) Cntfet basics and simulation. *Int Confe Des Test Integr Syst Nanoscale Technol*, 2006. DTIS 2006. IEEE
- <https://nano.stanford.edu/stanford-cnfet-model>
- Nishath SY, Revathi S (2016) Design of an efficient phase frequency detector for a digital phase locked loop. *Int J Eng Res* 5(04)
- Ayat M, Babaei B, Atani RE, Mirzakuchaki S, Zamanlooy B (2010) Design of A 100MHz–1.66 GHz, 0.13 μm CMOS phase locked loop. In: 2010 international conference on electronic devices, systems and applications. IEEE, pp 154–158
- Solanke S (2009) Design and analysis of novel charge pump architecture for phase locked loop. Diss.
- Rashmi SB, Yellampalli SS (2012) Design of phase frequency detector and charge pump for high frequency pll. *Int J Soft Comput Eng* 2:88–92
- Al Sabbagh MZ (2007) 0.18 μm phase/frequency detector and charge pump design for digital video broadcasting for handheld’s phase-locked-loop systems. Diss. The Ohio State University

15. Ravisaheb HB, Nagpara BH (2017) Design and implementation of phase frequency detector using different logic gates in 45nm CMOS process technology
16. Zhang L et al (2018) An improved fast acquisition phase frequency detector for high speed phase-locked loops. AIP Conf Proc 1955(1). AIP Publishing LLC
17. Mohammadi MS, Sadughi S, Razaghian F (2021) Low-power high-speed phase frequency detector based on carbon nano-tube field effect transistors. Analog Integr Circ Sig Process:1–3
18. <https://ietresearch.onlinelibrary.wiley.com/doi/full/https://doi.org/10.1049/iet-cds.2019.0135>
19. Ghaderi N, Alidadi-Shamsabadi M (2017) A novel ultra high speed and low power phase detector using carbon nanotube field effect transistors. In: 2017 10th international conference on electrical and electronics engineering (ELECO). Bursa, pp 467–471
20. Halwai AKS et al (2020) Estimation of power and delay of CMOS phase detector and phase-frequency detector using nano dimensional MOS transistor. In: 2020 IEEE VLSI device circuit system (VLSI DCS). IEEE

RTL to GDSII: Fully Digital Indirect Time of Flight SoC



Het Suthar, Shubham Tomar, and Rutu Parekh

Abstract Time of Flight (ToF) technologies have become a significant part of this era with the developments in the fields of augmented reality and 3D imaging. The indirect ToF (iToF) method uses the phase difference between an emitted and received light using a time to digital converter (TDC) to calculate the distance. It is very useful in short-distance depth measurement for applications such as FaceID, autonomous driving cars. In this paper, we design and implement a high-precision indirect Time of Flight (iToF) SoC based on a single-photon avalanche diode (SPAD), consisting of a coincidence detection circuit, two 12-bit counter TDCs, and output buffer memory. Open-source EDA tools such as Yosys, Graywolf, OpenTimer, Qrouter, Magic, and IRSim are used to synthesize the design at 180 nm and 45 nm technology nodes. It is observed that the circuit at 45 nm can work at 984 MHz clock frequency, which is sufficient for imaging applications usually requiring 30–120 fps. The circuit area is 558.34 μm^2 and consumes a total power of 423.31 μW at 180 nm and 19.03 μW at 45 nm.

Keywords Time of Flight · Physical design · Open-source EDA · Synthesis · Placement · Routing

1 Introduction

Recent developments in the areas of augmented reality [1], autonomous driving systems [2], and authentication systems such as FaceID have drawn significant attention toward optical non-contact Time of Flight (ToF)-based ranging techniques. ToF method is used for measuring the distance between a sensor and an object, based on the time taken by a light signal (photons) to travel to the target and back to the sensor.

H. Suthar · S. Tomar (✉) · R. Parekh

VLSI and Embedded Systems Research Group, Dhirubhai Ambani Institute of Information and Communication Technology, Gandhinagar, Gujarat 382007, India
e-mail: tomar.shubham4j@gmail.com

H. Suthar

e-mail: 201911042@daiict.ac.in

This technology is considered as the key technology for machine vision, autonomous driving, robotics, surveillance, consumer electronics, or bio-metrics [3, 4]. ToF techniques provide a significant advantage as compared with traditional methods such as stereocameras in terms of system size, resolution, and power consumption. One of the widely known ToF methods is light detection and ranging (LiDAR) [5]; it is being used in many fully autonomous self-driving cars out on the street [2].

There are two types of ToF techniques [6], one that directly obtains depth information from the time delay between the emitted and reflected lights or the second method which obtains depth information indirectly from the phase difference between emitted and reflected lights. The methods are known as the direct Time of Flight (dToF) and indirect Time of Flight (iToF), respectively. The dToF is generally used in LiDAR applications that require a range of a few hundred meters and a strong background light condition [2, 4]. It uses an on-chip time to digital converter (TDC) to measure the depth information based on the arrival time of the incident photons, whereas iToF is appropriate in indoor environments for authentication and human-computer interactions within a few meters range [4].

Single-photon avalanche diode (SPAD)-based sensors have been widely used in ToF applications [2, 3, 7, 8]. SPADs are reverse biased p-n junction diodes that operate in Gieger mode. The incidence of a single photon on the SPAD can produce an avalanche breakdown, which can be converted into a pulse waveform using a quenching circuit [7, 8]. These can be used in both dToF and iToF measurements. The iToF systems are better in terms of accuracy and time resolution as compared to dToF.

Various implementations of SPAD-based ToF sensors have been done previously. In [9], a 64×64 pixel array is designed at 180 nm technology, and a time-gated SPAD array is used to reduce the power consumption. A similar SPAD array for the unmanned vehicle was designed in [10] at 130 nm node operating at 30fps. A 64×64 SPAD array with 16-bit TDC was designed in [11] at 150 nm node, and the circuit was able to operate at a maximum frame rate of 17.9 kfps. Flash LiDAR with 1782 TDCs was designed in [12] at 180 nm.

In this work, a fully digital CMOS iToF circuit at 180 nm as well as 45 nm is implemented, based on the design of SPADs discussed in [8]. To the best of our knowledge, such work has not been done previously. The block diagram of the circuit for a single iToF pixel is shown in Fig. 1. Here, the digital circuit is marked with dotted lines, and this is the circuit that is designed in the proposed work. Designing digital CMOS circuits generally starts with an RTL description in HDL languages such as Verilog or VHDL. Then, the RTL design is processed through different stages of transformation and analysis to get a final file known as GDSII. It contains the layout geometry and layers information which can be used to fabricate the CMOS chip.

To perform RTL to GDSII, various electronic design automation (EDA) tools and library files are required. In this paper, we are using open-source EDA tools [13] such as Yosys for performing logical synthesis, OpenTimer for performing timing analysis, Graywolf and Qrouter for placement and routing, and Magic for the physical layout and generating the GDSII file [14].

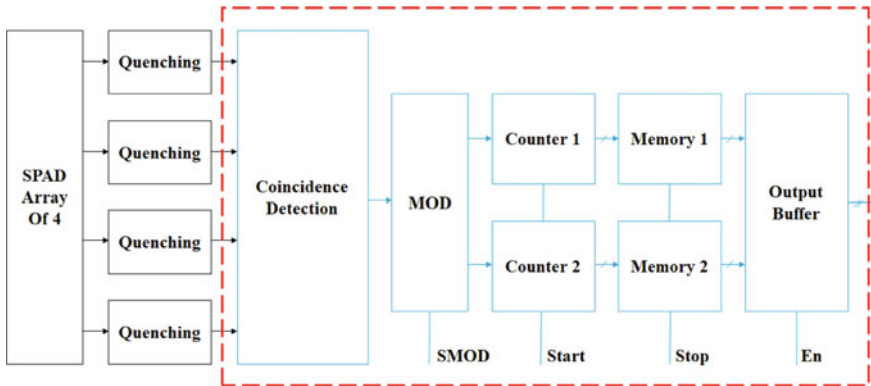


Fig. 1 iToF block diagram

The remainder of this paper is organized as follows. In Sect. 2, we shortly explain the working of the digital iToF circuit and its timing diagram. In Sect. 3, we discuss the front end of the RTL to GDSII flow, i.e., RTL design, logic synthesis, and static timing analysis (STA) and the back end of the flow, which includes floor planning, place and route, physical layout, LVS, and GDSII. We show our results and discuss its performance parameters in Sect. 4, before concluding this paper in Sect. 5.

2 Working of iToF Circuit

The iToF method emits a light pulse and then measures the phase difference between emitted and received lights to calculate the distance traveled. The working of the digital circuit used in this work is shown by a timing diagram in Fig. 2. We use external control signals, viz., Start, Stop, SMOD, and En to capture, read, and reset the iToF data. A pulse of light is emitted, when reflected from a surface, it will be detected as multiple pulses by the SPAD array, and for simplicity, it is shown as a single pulse named ‘Reflect’. TDC is used to count the duration of reflected light. It consists of two 12-bit counters, where the signal SMOD will control which counter

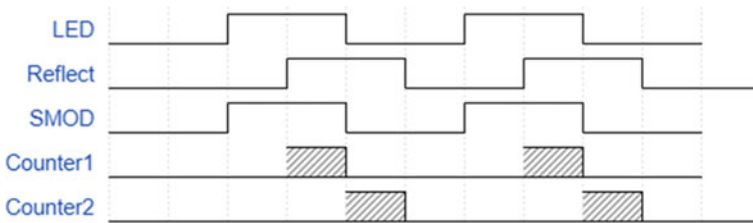


Fig. 2 iToF timing diagram

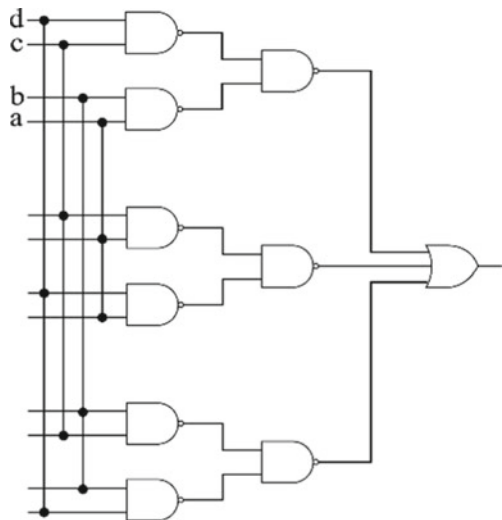
will count the time of received photon pulses. As can be seen from Fig. 2, when SMOD is equal to one, Counter1 is enabled, otherwise Counter2 is enabled. At the end of each cycle, the values of Counter1 and Counter2 are stored in a memory as shown in Fig. 1.

Start signal is used to reset the counters to zeros, Stop signal is used to store the value from counters to registers before starting the next cycle, En signal allows to readout the values of memory any time before the next cycle finishes, and this allows high speed operation of the circuit. The main performance metrics of this circuit are its speed of operation and accuracy. And both of these parameters depend on the operating speed of the counter and effectiveness of the coincidence detection circuit, respectively. In this work, we implement the digital circuit at RTL level, and verify that the circuit will work at required operating speed and then using EDA tools, create the GDSII tape-out for a single SPAD pixel.

2.1 Coincidence Detection Circuit

The coincidence detection circuit helps in avoiding false triggering the TDC circuit. A pulse is only considered valid if two or more than two quenching circuits have detected it. As shown in Fig. 3, the circuit consists of ‘and or invert’ (AOI) type of logic circuit which can be easily synthesized using standard cells available in library files.

Fig. 3 Coincidence detection circuit [8]

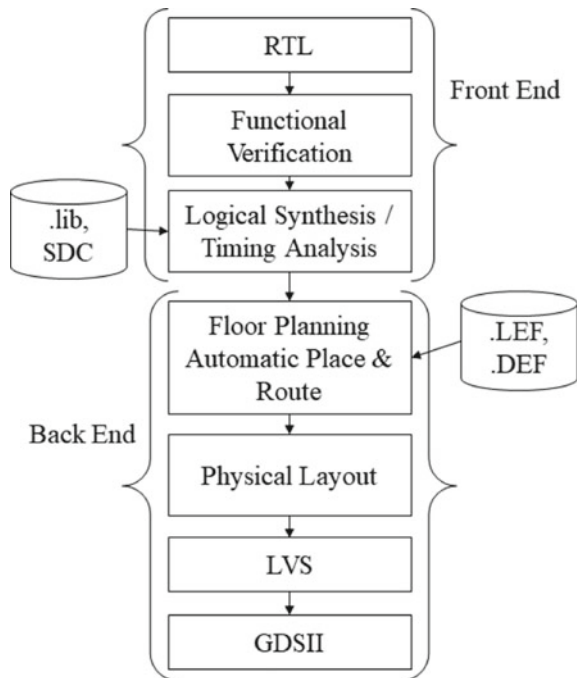


3 Physical Design Flow

Various tools are available for designing a CMOS digital circuit, the ultimate goal of these tools and digital design in general is to obtain minimum path delay (i.e., high speed of operation), minimum power dissipation and minimum area, and all the steps performed in a digital design flow are aimed to achieve either of the previously mentioned constraints.

A CMOS digital design starts with behavioral description at RTL level, and at this stage, only the functionality of the design is verified as no other information regarding timing delays, routing, or interconnects is available at this level. Once the RTL is verified to be functional, the RTL is synthesized to a gate-level netlist (GLN), since the GLN is synthesized from a standard cell library, it contains timing information about the delays of different cells being used. Hence at this stage static timing analysis (STA) can be used to identify the critical timing paths, this information can in turn be used to perform logic optimization. Post logic optimization STA can be re-run to check for other critical paths. In order to verify that the design works at a specified clock frequency, a constraint can also be provided to the tool to check any paths that do not meet the timing requirements. The steps discussed till now are generally known as front end of the design flow as shown in Fig. 4. Once the GLN is said to meet the timing constraints, physical implementation (back end) of the digital design begins.

Fig. 4 VLSI design flow



Here, the logic cells are placed in a floorplan, routing is done to connect the cells by metal routes, and clock tree synthesis (CTS) is performed to distribute the clock signal. The RC parasitic of these metal layers adds to the path delays, and hence, design needs to be optimized in order to meet the timing constraints. The length of these metal layers and approximate RC parasitic based on the fan-outs of a cell can be obtained by wire load model. STA is performed at multiple levels of the flow in order to obtain the critical path and optimize the metal routes for minimum delay. Before finalizing the routing of metal layers, an estimate length of routes is used to determine RC parasitic, and this phase is called global route. These estimate RC values and wire lengths are then used to perform the final route. Further, the placement and metal layer information can be used to generate the layout and finally the masks in GDSII format to fabricate the CMOS digital chip.

4 Results and Discussion

The physical design flow consists of mainly two parts as shown in Fig. 4, namely front end and back end [15]. Front end usually deals with logical synthesis and timing verification of the circuit, which outputs a gate-level netlist which is then used to perform the physical synthesis in back end flow, where the standard cells are replaced with their layouts and processes such as routing, clock tree synthesis are performed. The detailed steps involved, tools used, and the obtained results are discussed in this section.

4.1 Front End

Front end of the physical design flow deals with RTL description, functional verification, logical synthesis, and STA. The RTL description is a program written in HDL, and its functionality is verified by providing different set of inputs. But, functional verification does not verify if the design will work correctly at designated clock frequency when parameters such as gate delays, setup, and hold times will be introduced. The functional verification of RTL description is performed using Xilinx ISE design suite, and the output waveforms are shown in Fig. 5. As it can be observed, the TDC starts counting every time more than 2 SPAD signals are high, and the SMOD signal controls which counter will be enabled. Start signal is used to reset the counters back to zero, whereas Stop signal will store the value from counters to a buffer, and to read the value of counters, En signal is used. In order to get the timing information, first the RTL description has to be converted to a gate-level netlist which consists of standard cells.

Standard cells are defined in a library file obtained from the foundry (also known as liberty file) [16], and it contains information such as the input and output pins, timing delay, area, and the functionality of the standard cells such as AND, OR, AOI,

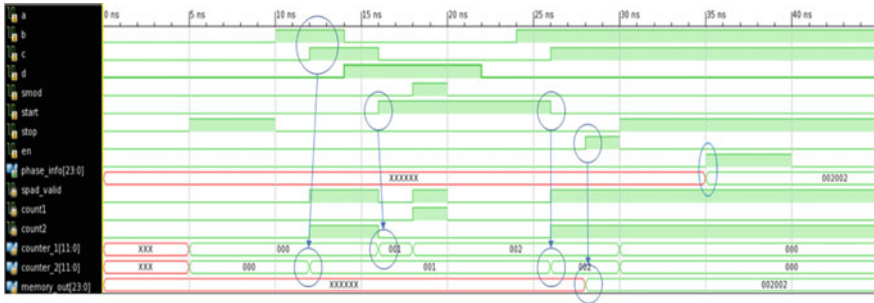


Fig. 5 Simulation waveform at RTL level

Table 1 Logical synthesis table

Technology node (nm)	Maximum freq. (MHz)	Maximum delay (ps)	TDC area (μm^2)	Power dissipation (μW)
180	719	1389	4972.96	447.09
45	1020	980	495.55	11.26

D Flip Flop. The gate-level netlist is called a synthesized netlist, which is then used to verify that the design meets required timing constraints.

STA is a method used to verify if the design meets the timing constraints, it uses the delay information available from liberty file, calculates the path delays from the gate-level netlist, and verifies it against the provided timing constraint file. The results obtained post logical synthesis are shown in Table 1. The design was synthesized using 180 nm and 45 nm standard cell libraries, and each input clock to the design was constrained to have a positive edge every 5 ns, and according to the timing reports, the design is meeting all constraints. And the maximum operating frequency of the design is obtained to be approximately 700 MHz.

4.2 Back End

Once the gate-level netlist is verified to meet the timing constraints, it is passed on in order to create a basic skeleton for the final GDSII file. It uses the gate-level netlist to determine what kind of cells are used in the design. Then from a library exchange format (LEF) file, information such as which metal layers are to be used, location of pins, and the area occupied by each cell is obtained, and a floorplan is created, and later, the cells are placed. The floorplan and placement process add some extra cells known as physical only cells other than the ones used in the logical synthesis.

One example is addition of fill cells to the design. It is observed that a total of 197 standard cells was used in the design, and additional 104 fill cells were added to ensure structural and functional integrity of the design when fabricated. These fill

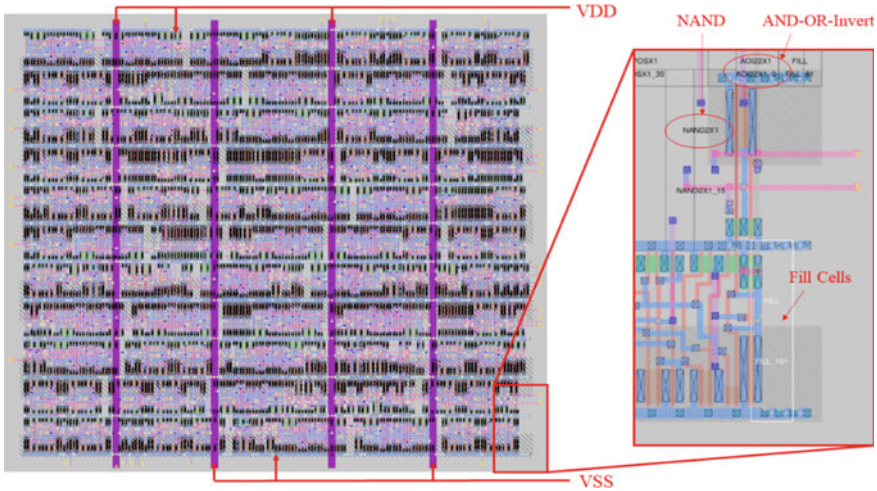


Fig. 6 Circuit layout at 180 nm

cells can be identified from the layout, and a zoomed area is shown in Fig. 6. Followed by placement, routing and post routing STA are performed in order to verify that the design still meets the timing constraints considering the RC delays included from the routing paths. Results obtained post routing are shown in Table 2. And Fig. 6 shows the complete layout of the digital iToF system on chip. The complete design post layout is also verified for functionality using IRSim, and the results are shown in Fig. 7. Comparison of previous works is done with this work in Table 2, and it can be observed that our work consumes less power as compared to other works and less area except [12].

Table 2 Post routing results and comparison with other works

Reference	Technology node (nm)	Maximum freq. (MHz)	Maximum delay (ps)	TDC area (μm^2)	Power dissipation (μW)
This work	180	686	1456	6014.35	423.31
This work	45	984	1016	558.34	19.03
Xie et al. [10]	130	–	–	110028	–
Zhang et al. [12]	180	–	–	4200	2000

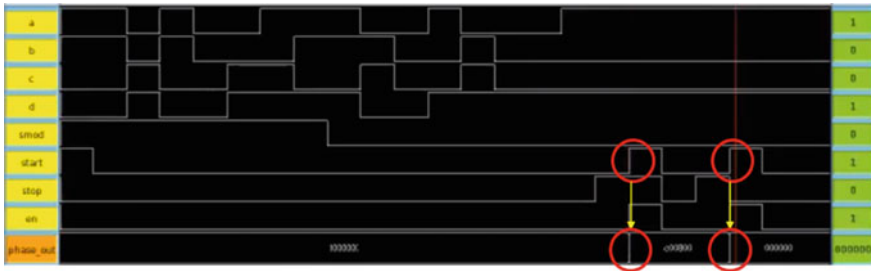


Fig. 7 Post layout simulation waveform

5 Conclusion

In this work, we implemented a design of indirect Time of Flight digital circuit, which is being widely used in various applications such as AR, autonomous driving, FaceID. The circuit is capable of operating at maximum speed of approximately 984 MHz which is more than sufficient for imaging purposes that usually work in the range of 30–120 frames per second (fps). Complete RTL to GDSII flow is carried out on 180 nm and 45 nm using open-source tools such as Yosys, OpenSTA, Graywolf, Qrouter, Magic Layout, IRSim. The physical verification shows that functionality of the circuit post layout is still maintained with the logical description. The circuit is capable of operating at a power dissipation of 19.03 μ W occupying an area of 558.34 μ m². The design synthesized at 45 nm node occupies 90.7% less area, consumes 96.9% less power, and can operate $1.38 \times$ faster as compared to 180 nm.

References

1. Maier-Hein L, Franz AM, Fangerau M, Schmidt M, Seitel A, Mersmann S, Meinzer HP (2011) Towards mobile augmented reality for on-patient visualization of medical images. In: Bildverarbeitung für die Medizin 2011. Springer, Berlin, Heidelberg, pp 389–393
2. Fersch T, Weigel R, Koelpin A (2017) A CDMA modulation technique for automotive time-of-flight LiDAR systems. *IEEE Sens J* 17(11):3507–3516
3. Süß A, Rochus V, Rosmeulen M, Rottenberg X (2016) Benchmarking time-of-flight based depth measurement techniques. *Smart Photonic Optoelectron Integr Circ XVIII*
4. Lee S, Park D, Lee S, Choi J, Kim S (2019) Design of a time-of-flight sensor with standard pinned-photodiode devices toward 100-mhz modulation frequency. *IEEE Access* 7:130451–130459
5. Ackerman E (2016) Lidar that will make self-driving cars affordable [News]. *IEEE Spectr* 53(10):14–14
6. St.com (2020). https://www.st.com/content/dam/technology-tour-2017/session-1_track-4_time-of-flight-technology.pdf. Accessed 16 Oct 2020
7. Beer M, Schrey OM, Hosticka BJ, Kozozinski R (2017) Modelling of SPAD-based time-of-flight measurement techniques. In: 2017 European conference on circuit theory and design (ECCTD). IEEE, pp 1–4

8. Chen X, Cai L, Xu Y, Ou J, Liao J (2020) A 180nm CMOS fully digital Indirect Time-of-Flight SOC based on SPAD. In: 2020 IEEE 5th information technology and mechatronics engineering conference (ITOEC). IEEE, pp 523–526
9. Vornicu I, Carmona-Galán R, Rodríguez-Vázquez Á (2015) A SPAD-based 3D imager with in-pixel TDC for 145ps-accuracy ToF measurement. In: Image Sens Imaging Syst 9403:94030I. Int Soc Opt Photonics
10. Xie G, Xu Y, Lian D, Zhang Z, Zhang J (2017) Single-photon avalanche diode array with column-level time-to-digital converter for unmanned vehicle. In: 2017 IEEE 2nd international conference on opto-electronic information processing (ICOIP). IEEE, pp 49–54
11. Perenzoni M, Perenzoni D, Stoppa D (2016) A 64 \times 64-Pixels Digital Silicon Photomultiplier Direct TOF Sensor With 100-MPhotons/s/pixel Background Rejection and Imaging/Altimeter Mode With 0.14% Precision Up To 6 km for Spacecraft Navigation and Landing. IEEE J Solid State Circ:151–60
12. Zhang C, Lindner S, Antolovic I, Mata Pavia J, Wolf M, Charbon E (2019) A 30-frames/s, 252 \times 144 SPAD Flash LiDAR With 1728 Dual Clock 48.8-ps TDCs, and Pixel-Wise Integrated Histogramming. IEEE J Solid State Circ 54(4):1137–1151
13. “Open Circuit Design”, Opencircuitdesign.com, 2020. <http://opencircuitdesign.com/>. Accessed 16 Oct 2020
14. Ghosh KP, Ghosh AK (2018) Technology mediated tutorial on RISC-V CPU core implementation and sign-off using revolutionary EDA management system (EMS)—VSDFLOW. In: 2018 China semiconductor technology international conference (CSTIC). Shanghai, pp 1–3
15. Kang S, Leblebici Y, Kim C (2015) CMOS digital integrated circuits. McGraw Hill, New York
16. Bhasker J, Chadha R (2011) Static timing analysis for nanometer designs. Springer, New York

MOODY: A Natural Language Processing-Based Chatbot for Mental Health Care



Shubhangi Thakur, Dhruv Rastogi, and Leena Singh

Abstract A chatbot is a software that establishes a human–machine interaction by using natural language processing (NLP) and natural language understanding (NLU). One of the essential tasks in machine learning and artificial intelligence is the mechanism through which conversation between a bot and a human is built and modelled. On the other hand, mental health issues have emerged up as one of the most rising diseases affecting millions around the world and are still one of the most untreated ones. People suffering from mental health disorders and issues have to live with it every single day, and the cases rose prominently during the COVID-19 pandemic. In this paper, a machine learning and natural language processing-based chatbot has been implemented to hold conversations with the purpose of mental healthcare assistance. It has been named MOODY; an intelligent conversational agent built with Dialogflow integration on NLP, NLU and its sentiment analysis feature. Dialogflow’s architecture has been taken from the end-to-end neural network machine translation domain. There are plenty of variations and features that have been introduced resulting in remarkably enhancing the conversational capabilities of chatbots. MOODY’s dependency, quick response generation and privacy provide a unique opportunity to assist those in need of adequate information and resources at one place.

Keywords MOODY · Natural language processing · Machine learning · Sentiment analysis · Natural language understanding · Dialogflow

S. Thakur · D. Rastogi · L. Singh (✉)
Amity School of Engineering and Technology, Amity University, Noida, UP 201301, India
e-mail: leenasafya@gmail.com

S. Thakur
e-mail: shubhangi.thakur1@s.amity.edu

D. Rastogi
e-mail: dhruv.rastogi1@s.amity.edu

1 Introduction

Technological progress is an essential engine of economic development. “General technology”, as the economists have labelled it, is the most important of these era-defining innovations, which includes steam engine, internal combustion engine and electric power in the eighteenth, nineteenth and the twentieth centuries. Artificial intelligence (AI) is the most important general technology of the twenty-first century, with machine learning being the most influential theme within AI.

Since the coronavirus pandemic threw global health care into a whirlwind, and lifestyles were forced to be changed drastically, mental health diseases have been on the rise because of the lack of physical social interaction and increasing number of COVID-19-related deaths around us. Almost everything we submerged ourselves in on a daily basis, be it schools, universities or workplaces, have been forced to be closed, and humans as beings that thrive on comfort and familiarity have been thrown into a lifestyle behind closed doors. This has had detrimental effects on the mental health of people.

Globally, an estimated 264 million people suffer from anxiety and depression, according to a recent World Health Organization (WHO) report [1]. The organisation also reported back in 2019 that around 7.5% Indians suffer from a mental disorder of some kind and that number reached 20% in the year 2020 alone. The escalation can be cited as one of the consequences of the recent global pandemic, but the pattern established points directly towards the rates increasing over the coming months.

If there is one thing that has increased with the decrease in physical interaction, it is the interaction on social media. The definition of social has been in the changing module ever since the rise of the social media applications, but what truly cemented it has been these applications taking their rightful place during the pandemic. In order to curb the increasing rate of cases of people being infected due to the coronavirus pandemic, physical distancing and isolation measures have been implemented. With an end goal to meet this order whilst attempting to keep up with the state of affairs, different kinds of human conduct (e.g. shopping, getting the hang of, working, meeting and engaging) moved from offline to online, bringing about an acceleration in emergence digital technologies amongst ordinary people along with the beneficiary propensity to utilise these gadgets and their expanding solace with one.

Having a conversation with a machine is not a far-fetched idea anymore. It is being done on a daily basis in the tech field, but what most individuals do not realise is that the seamless integration of smart electronic devices in our lives over the past two decades has almost happened without the realisation of the general public. Today, people would much rather prefer to keep their mental health-related queries and conversations private, whilst simultaneously getting over the stigma that is around mental health disorders, the situations leading unto it, and its consequences on one’s life if it goes untreated.

The mental health therapy bot implemented in this paper is the bridge between the stigma around mental disorders and the increasing rate of the online presence

including people's adaptability of the human-machine interactions and its integration in our daily lives.

2 Literature Review

In this section, we discuss the empirical examples of applications of healthcare assistance and the implications of developing chatbots for mental health. It is muddled how exact an emotional wellness application can be with following dispositions or making ideas with the moderately low degree of interest in this space (contrasted with different spaces of medical care, like pharma or clinical diagnostics) and the low degree of goal in getting clients. However, it is a field which is still growing with various bots like SERMO [2], which is rooted in regulating emotions and ERIN [3], which uses Internet of Things to develop a chatbot for mental health resources. Both of these provide resources without an adequate sentiment analysis, but their analysis and implementation establish a growing market. Designing and framework generation of certain bots have either properties of acting like a mediator [4], to assist human chat operators of mental healthcare services [5] or use sentiment to generate a fixed reply [6], and reviews of various applications ranging from studies about automation in the treatment and diagnosis of mental health issues to current trends of chatbots and their accessibility. These reviews show results such as potential for conversational agents in psychiatric use was reported to be high across all studies [7], majority of chatbots were rule based and implemented in stand-alone software [8], and chatbots focused mainly on depression and autism [9], or generally accessed the usability of introducing a machine element in a vulnerable aspect like mental health [10]. Applications like Woebot [11] is a bot that screens the dispositions of clients and gives a scene where clients can communicate their contemplations and feelings through restorative discussions; Pacifica [12] is an application that can assist with tending to tension issues dependent on cognitive behavioural therapy; Wysa [13] is an AI-based "genuinely astute" bot that professes to assist clients with managing their sentiments and considerations through a variety of devices and strategies, and Moodkit [14] is an arrangement of utilisation that assists clients with lightening side effects of psychological maladjustment.

These applications explored new dimensions into helping patients suffering from mental health issues are too specific in their diagnosis or treatment methods to be able to provide real help to those that either have not been properly diagnosed or do not have the means to recognise the initial symptoms so that their treatment is indeed correct and does not essentially hurt the issue more.

3 Objective

In this paper, a chatbot that holds conversations with users about mental health themes has been implemented, which has become one of the world's most common illnesses with various intents ranging from advice, self-assessment and information like toolkits. It is deeply rooted in natural language understanding (NLU), natural language processing (NLP) and sentiment analysis using Dialogflow.

4 Methodology

Methodological approach is more qualitative than quantitative by interviewing several people and building a ten-people focus group and using participation observation to build real conversations for the chatbot. The diverse focus group is involved in the planning phase to form a base of the flow of entities in terms of options and intents, ranging from the usability of resources provided and the ease of the conversation. The questions range from basic accessibility of human-machine interactions, name of the chatbot, flow of conversation, tone of replies, small talk, default fallback answers and the quality of resources. Attributes such as feasibility, connectivity and ease of formation have been provided by the focus group.

5 Design and Implementation

5.1 Proposed System

In this paper, MOODY, the NLP-based chatbot being proposed is being presented as a therapy bot, which can go about as a conversational specialist that can offer advice, suggest helpful toolkits, help with self-assessment for various kinds of mental disorders and offer legitimate medical resources. MOODY leverages artificial intelligence into the healthcare space, specifically that of mental health to help further develop an understanding of insight and decision-making in response generation of the machine. It will also simultaneously help erase the stigma around seeking help for psychological issues and helping those in dire need of professional help. A mental health chatbot like MOODY is structurally designed to learn with every query it gets due to the machine learning algorithm, whilst the NLP aspect comes into play in the various options, and it offers a user over the discourse of the conversation. Users can choose from various options such as to talk and take advice from MOODY in terms of toolkits; using sentiment analysis plays a role here. By analysing each user response, the algorithm produces a query score using the sentiment analysis feature of Dialogflow which in turn helps the chatbot answer a user's question with an adequate reply; especially considering the mindset of a user could vary in terms

of their mental status and vulnerability. The toolkits in the advice section provide users with easy-to-follow instructions to curb certain symptoms in the healthiest way possible, which greatly helps those who either do not have the means to get properly treated or cannot afford it. The online psychologist sessions provide the user with an option to get in touch with professionals if they feel the need to extend beyond a human therapy bot, which is necessary in order to decrease the distance between a potential patient and their diagnosis and subsequent treatment. Simulation parameters for the chatbot were getting identification of users initially, recognising their need, analysing their requirements amongst the options provided by MOODY and sticking to the vibrant menu that the chatbot provides. The navigation in the chatbot is extremely easy and accessible.

The “About MOODY” choice plays an important role as well, since a chatbot is really just a machine and a human user clearly knows it. Bridging the gap from a conversation held between a human psychologist and a client to a conversation held between an automatic chatbot and a client is both hard but not unachievable. Users need to feel like they know MOODY but can never guess its response; hence, a lot of time has been put into building MOODY’s personality so that it is able to hold small talk whilst simultaneously being very easy and accessible to use as shown in Fig. 1.

5.2 *Implementation*

The following ordered phases have been followed in the implementation and integration of the chatbot as shown in Fig. 2 and expanded upon as follows.

Planning. The themes of the chatbot are mental health issues and disorders directed towards providing an accessible and easy to navigate route towards imitating a conversation between a psychologist and a client. The machine aspect provides the veil of privacy, whilst the accessibility aspect provides an escape from the stigma around seeking help for mental disorders.

Content Acquisition. The required resources detailing toolkits, self-assessments and medical resources have been acquired from various legitimate mental health organisations, whilst simultaneous research into its content and use has been undertaken by the focus group and then later questioned to everyone that has been involved in the training phase of the model.

Dialogflow Integration. Whilst most of these “smart” platforms are in early stages of growth and development, one service primed to provide value today is Google Cloud Platform’s Dialogflow, which is the integrating platform that essentially brought the chatbot together. The GCP Dialogflow platform enables users to build interactive and engaging text or voice-based conversational interfaces such as chatbots, using natural language processing (NLP) powered by Google’s AI.

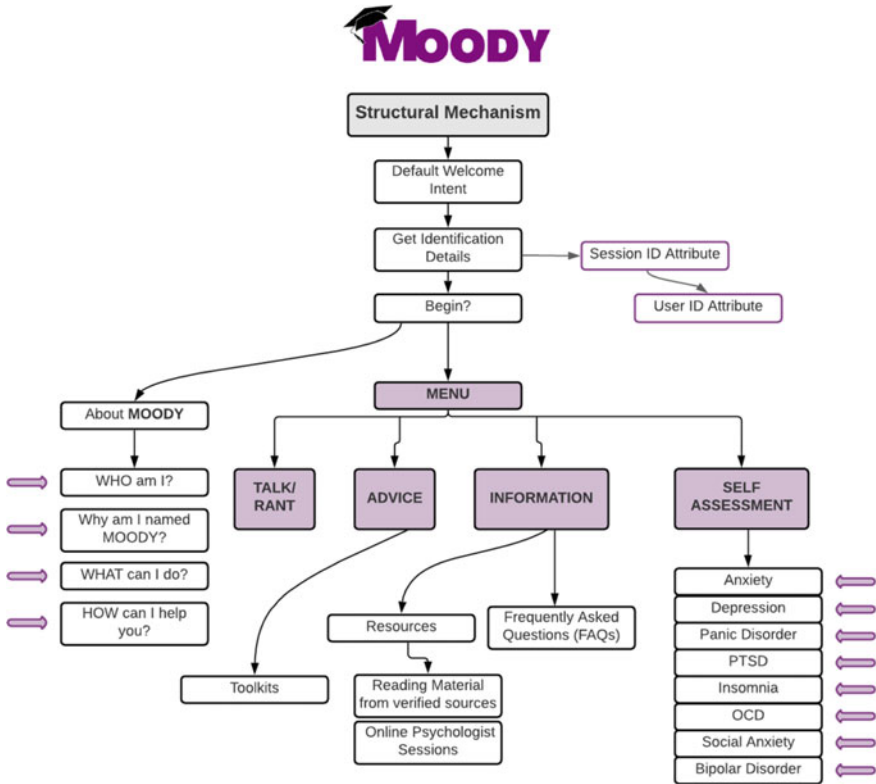


Fig. 1 Internal structural mechanism of the chatbot

Build a Prototype. Dialogflow helped integrate the different intents and entities to form the basic flow of conversation, whilst knowledge bases built on frequently asked questions and small talk were being developed simultaneously.

Test the Prototype. The training of the model and generation of query score for the sentiment analysis is conducted during this phase. Feedbacks have been taken from the people who helped train the machine, and simultaneous developments have been made to the chatbot.

Launch the Version. The model is named MOODY and has been launched to be able to integrate it externally.

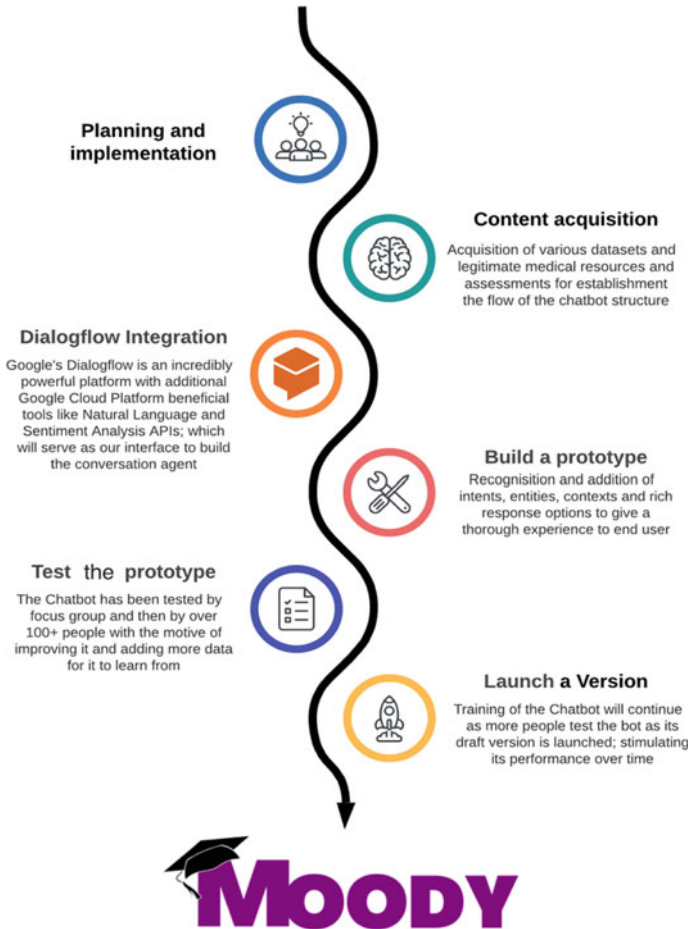


Fig. 2 Implementation and integration of the chatbot

6 Result

The chatbot is launched to be active for use. MOODY creates a unique virtual environment for a patient seeking help whilst simultaneously creating an opportunity in the mental healthcare sector. Several past chatbots have been launched and worked upon for years in this particular field, but most fail to either comply with basic demands of a patient or have simplified access. MOODY does both with the inclusion of the element of sentiment analysis added which generates a query score for every user response. Human-centric computing in terms of machine-human interactions with the inclusion of social and behavioural sciences as evaluation methods along with psychology is the basic ideology. A feedback survey was conducted during the training phase of the chatbot which was tried out by over 100 people and yielded

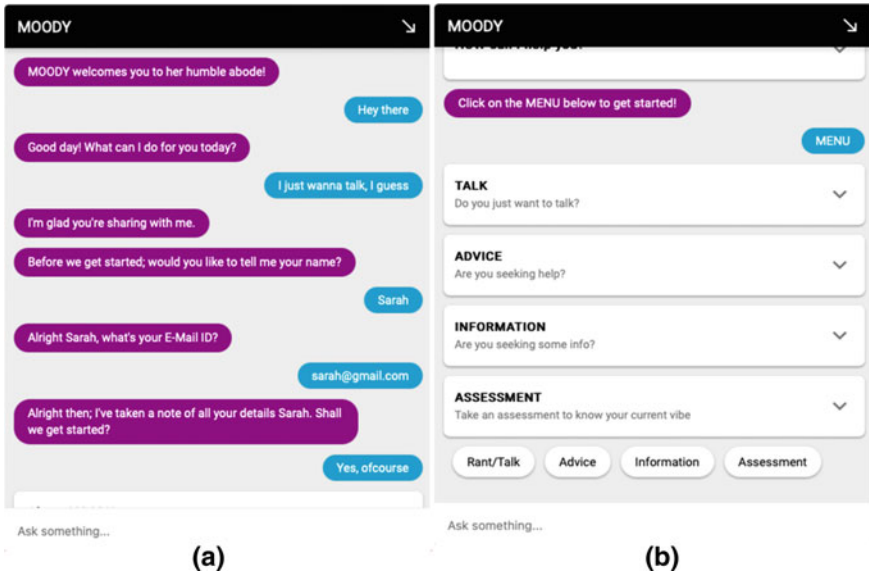


Fig. 3 a MOODY’s interactive interface. b MOODY’s menu option

generally positive results for the display interface, interactive quality, information handling and overall therapy. With its highly engaging interface as shown in Fig. 3a and inculcating choices as shown in Fig. 3b, the user feels very much in control of his choices and feels like he has a say over the flow of the conversation. Essentially, it is important to acknowledge that a therapy chatbot like MOODY cannot be rule based because after a time period, its replies will repeat, and the conversation will turn stagnant. It is also important to recognise the vulnerable mental space a user could potentially be in whilst they seek to use a chatbot providing mental healthcare advice or therapy; hence, eradicating elements that appear visibly robotic or automatic is equally vigilant so as to create an environment that appears comforting, familiar and trustworthy.

Further, as more signs of acceptance of such applications in the medical sector are embraced by centres, clinics or other well-being and clinical organisations, the true potential of adaptability, accessibility and wellness will be measured. A chatbot like MOODY further decreases that distance by eliminating the need to use several different resources for the kind of easy information that it provides at one place effectively as shown in Fig. 4a, b.

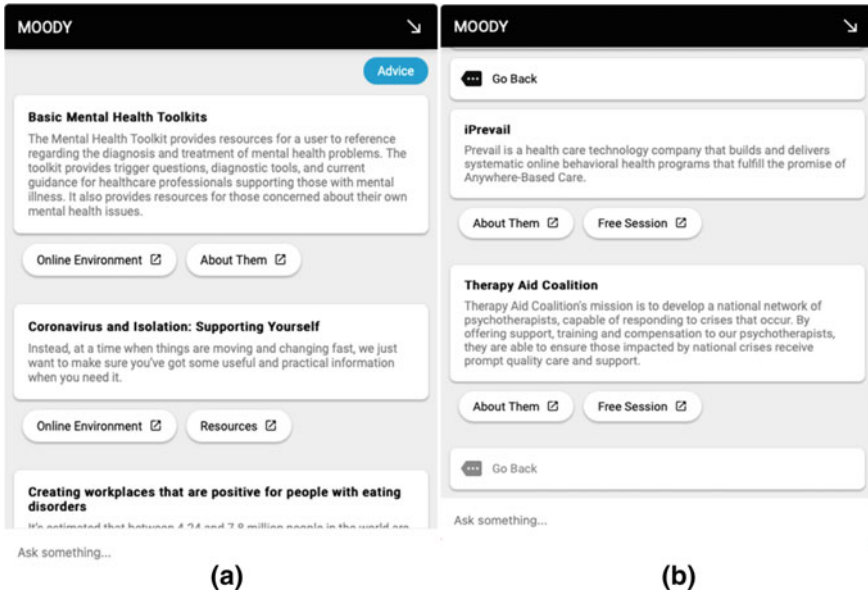


Fig. 4 a MOODY’s advice toolkits. b MOODY’s information option

7 Conclusion

The scope of the integration of artificial intelligence with the healthcare sector is huge and directly proportional to the increasing rates of people adopting elements of automation in their daily lives. Applications that address psychological well-being messes are genuinely new, yet as the WHO and the developing number of clients recommend, there is a requirement for emotional wellness customer applications. With the wide utilisation of cell phones and web networks, these mysterious and private applications have become available in helping a huge number of patients. In any case, various main points of interest encompass emotional wellness chatbots. For one, the disgrace of emotional wellness issues is hard to scatter and keeps on nagging conditions and societies in which patients live. This is banishing them from venturing forward to look for treatment. An application like MOODY helps bridge that gap whilst recognising the stigma around such issues and the vulnerability of seeking help. Its usefulness to users at initial phases of feeling down or those that just feel amiss is huge because of the bot’s ability to provide every resource such a user would need like basic information about symptoms, legitimate organisations to book professional sessions with, easy-to-follow toolkits or self-assessments. It is able to create a unique opportunity to help those seeking it.

In the future, MOODY has the scope to be truly revolutionary in terms of its integrity as more legitimate resources get added to it, and improve its properties in order to truly help a user talk about their emotions. Involvement of psychologists will provide significant advancement in further developing real change in this sector.

References

1. Depression WHO (2020) <https://www.who.int/news-room/fact-sheets/detail/depression>
2. Denecke K, Vaaheesan S, Arulnathan A (2020) A mental health chatbot for regulating emotions (SERMO)—concept and usability test. *IEEE Trans Emerg Top Comput* 14(8):1–1
3. Persons B, Jain P, Chagnon C, Djamasi S (2021) Designing the empathetic research IoT network (ERIN) chatbot for mental health resources, vol 12783. *Lecture Notes in Computer Science*. Springer, Cham
4. Lee YC, Yamashita N, Huang Y (2020) Designing a Chatbot as a mediator for promoting deep self-disclosure to a real mental health professional. *Proc ACM Hum-Comput Interact* 4(CSCW1), Article No. 031:1–27
5. Madeira T, Bernardino H, Souza J, Gomide H, Machado N, Silva B, Pacelli A (2020) A framework to assist chat operators of mental healthcare services. In: *Proceedings of second workshop for NLP open source software (NLP-OSS)*, pp 1–7
6. Bloom A, Thorsen S (2013) A sentiment-based chat bot. *KTH Computer Science and Communication*, pp 1–24
7. Vaidyam AN, Wisniewski H, Halamka JD, Kashavan MS, Torous JB (2019) Chatbots and conversational agents in mental health: a review of the psychiatric landscape. *Can J Psychiatry* 64(7):456–464
8. Abd-Alrazaq AA, Rababeh A, Alajlani M, Bewick BM, Househ M (2020) Effectiveness and safety of using chatbots to improve mental health: systematic review and meta-analysis. *J Med Internet Res* 22(7):e16021
9. Abd-Alrazaq AA, Alajlani M, Alalwan AA, Bewick BM, Gardner P, Househ M (2019) An overview of the features of chatbots in mental health: a scoping review. *Int J Med Informatics* 132:103978
10. Cameron G et al (2019) Assessing the usability of a chatbot for mental health care. In: Bodrunova S et al (eds) *Internet science workshops*, vol 11551. *Lecture notes in computer science*. Springer, Cham, pp 121–132
11. Relational agent for mental health. Woebot Health. <https://woebothealth.com/> (2021)
12. A place to feel better, wherever you go. Sanvello (n.d.). <https://www.thinkpacific.com/>
13. Everyday mental health. Wysa (n.d.). <https://www.wysa.io/> (2020)
14. Thriveport (n.d.). <http://www.thriveport.com/products/moodkit/> (2021)

Predictive Shift of Vehicles by Recent Market Trends



Rajgor Siddhi Bharatkumar, Shubh Patel, Shambhavi Chakrabarti,
and Siddharth Joshi

Abstract The harmful effects of pollutants released by cars that run on conventional fuels have prompted scientists all around the world to change to more environmentally friendly energy sources. It should come as no surprise that, to assure a sustainable future, the world must limit the use of non-renewable energy sources in vehicle usage. The world has started to look into electric cars with hydrogen fuel cell and electric cars with battery. As they are still new and developing technologies, much of it still is at its infancy. In this paper, we are comparing hydrogen cars to gasoline and electric cars in various locations of the world, considering factors like fuel supply and storage, driving range, and social acceptance. This review paper intends to provide comparisons between internal combustion (IC) engine vehicles, electric vehicles (EVs), and fuel cell electric vehicles (FCEVs) based on numerous factors and present technologies. The goal is to provide a thorough understanding of where the transportation sector is going and where it is right now.

Keywords Energy · Internal combustion engine · Hydrogen fuel cell electric vehicle · Electric vehicle · Hydrogen fuel cell · Sustainability · Renewable source · Fuel availability · Electric vehicle battery pack · Fossil fuel · Fuel cell · Energy density · Emission · Hydrogen energy

Abbreviations

FCEV	Fuel cell electric vehicles
EV	Electric vehicles
IC	Internal combustion
BEV	Battery electric vehicle
ESS	Energy storage system
UHC	Unburned hydrocarbons

R. S. Bharatkumar · S. Patel · S. Chakrabarti · S. Joshi (✉)
Department of Electrical Engineering, Pandit Deendayal Engineering University, Gandhinagar, India
e-mail: siddharth.joshi@sot.pdpu.ac.in

TWC	Three-way catalyst
SI	Spark ignition
PM	Particulate matter
DOC	Diesel oxidation catalyst
DPF	Diesel particulate filters
GHG	Greenhouse gas emission
HEV	Hybrid electric vehicles
PHEV	Plug in hybrid electric vehicles
TTW	Tank-to-wheel
WTT	Well-to-tank
RES	Renewable energy source
WTW	Wheel to wheel
HFC	Hydrogen fuel cell
WTP	Wheel to pump
PTW	Pump to wheel
SMR	Steam methane reforming
HFCEV	Hydrogen fuel cell electric vehicle
FCHV	Fuel cell hybrid vehicle
PEM	Polymer electrolyte membrane
PEMFC	Polymer electrolyte membrane fuel cell
DOE	Department of energy

1 Introduction

Energy influences a nation's economy, infrastructure, commerce, and standards of living. The world is currently going through a huge shift in the energy sector, and this is being taken into caution, and countries all over the world are reflecting upon the energy crisis that has ascended upon the world. The research investigated the power crisis and explored reform solutions in the world's major areas, comprising the sub-Saharan African, Asian and Pacific countries, Latin America, and Central Asia. It also expands to major parts of Europe and the Caribbean as well as parts of South Asia [1]. On reading the results, it can be seen that the impact of greenhouse gas emissions on energy consumption would be the worst, perhaps causing unforeseen changes in the global climate. Hence, it is the need of the hour for policymakers to bring in a change to adapt hydrogen fuel cell vehicle (HFCV) or electric vehicle (EV), which has core source of energy is renewable and does not emit harmful gases.

In past years increase in demand for electric vehicles is noted, which certainly comes with its challenges [2]. It is evident that unless we provide clean sources to produce energy, we may not experience the desired positive environmental impact from electric vehicles. Pollution may be mitigated in cities or vehicle-heavy areas, but if power is obtained from non-renewable sources, it just shifts the pollution elsewhere and does not ebb away [3].

An EV is a brief shape for electric-powered vehicles, EVs are automobiles that run on electricity, both partly or entirely. The automobile makes use of a big fraction battery percentage (70–80%) to strengthen the electrical motor, and all EVs have an electric-powered motor rather than an inner combustion engine. Both heavy-duty and low-duty motors are to be had commercially, even though the EV fee is expensive, however, the cash may be stored thru gasoline savings, federal tax, kingdom incentives. Generally, the using situations rely upon lots of factors such as but not limited to, the particularly severe outdoor temperature, that tends to lessen the performance due to the fact greater strength is needed to cool/warm the cabin. High using pace additionally impacts is due to the improved drag. Rapid acceleration additionally reduces the range. Hauling heavy masses or using up sizeable inclines additionally reduces range. This paper reviews the recent scenario of the transportation industry and the shortcoming of conventional internal combustion to the renewable and non-pollution source of energy like hydrogen fuel cell or battery storage vehicle.

2 Fuel Availability

2.1 Number of Charging Stations in India

It is safe to say that we have plenty of gas stations all over the world; there will not be a time when someone is stuck somewhere, and there is not a gas station within a few miles' radius, therefore fuel availability in the case of petrol is now abundant. However, facts and predictions show petrol and diesel which are non-renewable resources that will soon deplete. Given the quick rise in crude oil and petrol costs, the assumption of non-renewable resources will be depleted soon, and there is a need to begin exploring alternatives and take numerous steps toward it.

The biggest number of charging stations in India are in Delhi, with 94, followed by Hyderabad with 50, Jaipur with 49, Chandigarh with 48, Bengaluru with 45, and Ranchi with 29. There are 343 charging stations in all, with 1 in Lucknow, 17 in Goa, and 10 in Agra [4].

2.2 The Number of Electric Vehicle Stations in Different Countries

According to Department of Energy, around 41400 electric vehicle charging stations are functioning in United States, there are fewer than 5000 fast chargers. According to GasBuddy, there are about 136,400 gas stations in the United States [5]. China flaunts the most electric vehicles on the planet, with around 1.8 million in all-out that counts 30.1 battery electric vehicles per 1000 individuals (2018 numbers), concerning just 1.26 in China. Japan, a pioneer in hybrid and battery innovation industrialization, has

gained the most headway in this field, and today has the biggest armada of crossover vehicles on the planet. In 2019, 77% of French individuals plan to buy an electric or hybrid vehicle as their next vehicle [6]. Electric charging stations just are not available everywhere, but thanks to government backing, this is rapidly changing. Various technologies for electric vehicle charging stations are adapting all over the world, and this rapid growth will ensure a far brighter future. Electricity is produced in a variety of ways, some of which are renewable and others that are not. Many countries produce electricity on a large scale using renewable resources such as solar, wind, and hydro-energy, so it is safe to assume that electric charging stations are a good investment, and that fuel availability will increase significantly. Japan has the most hydrogen fuel stations of any country on the planet. There were 134 functioning hydrogen refueling stations in the country as of March 2021. Given that Japanese automakers Toyota and Honda are among only three automobile manufacturers in the world supplying hydrogen cars to the public, Japan's position as the major provider of hydrogen automotive fuel is expected. Hydrogen stations available in California are 48, the total number of hydrogen stations around the world is vanishingly small, so to conclude that the fuel availability of H₂ cars is currently low. California has plenty of hydrogen stations, so to buy the car and use it locally, will be fine, but for long trips, there needs to be an alternative source like a battery backup or hydrogen refueling van on highways.

3 Fuel Refilling

Typical “fast-fill” fuel stations, such as those found at public and big private stations, require about the same amount of time to fill as a gasoline car, about 3–5 min. Charging an electric vehicle might take anywhere from 25 min to 12 h. The capacity of the battery and the charging station's power flow speed both plays a role in this. A typical electric vehicle can charge at a rate of 7 kW (60 kWh battery) takes 8 h to charge from zero to a fully charged battery. Refilling a hydrogen tank takes roughly three to five minutes, similar to gas refueling. More than 46 hydrogen refueling stations are presently operational in California, with many more in the works [7].

4 Environmental Factors

At present, 99.80% of transportation is driven by filtered crude oil like combustion engines (ICEs), and 95% of transportation vitality is obtained from petroleum-based fuels. As technology advances, numerous alternatives such as lithium-ion battery vehicles (BEVs) and other energy sources such as hydrogen, natural gas, and biofuels have begun to emerge. This had a direct effect on the environment as we have been observing over the years. Here are the trends of all three types of vehicles and their impact on the environment via various studies.

Energy storage systems (ESSs) with a large storage capacity, power density, and compact size are needed for best possible energy storage applications in EVs. Furthermore, in the development and selection of ESSs for EV powering, zero-carbon footprint, insignificant self-draining charge, limited substance corrosion owing to a molecular reaction, prolonged life cycle, high-level efficiency, and minimal maintenance are demonstrated [8].

Upon taking a look at 2018 statistics, the % share of global transport energy demand across all modes of transportation was 44% of consumer sector light-duty vehicles, 7% of buses and 2–3 wheelers, and rail, aviation of 10%, the heavy-duty road of 26%, marine transport of 8%, and rail and pipeline of 5% [9].

Since the 1970s, gasoline engines have been outfitted along with emissions-controlling catalysts [10]. These were primarily created in response to pollution, they aimed at the removal of CO and unburned hydrocarbons (UHC) from exhausts, which was prevalent in the United States at the time. The three-way catalyst (TWC) was established in the 1980s to reduce NO_x emissions. The TWC is still the leading balance for all gaseous engine local pollutants at the moment and it has substantial storage capability for NO_x as well as CO. Though gasoline vehicles have shown some control and regulation over their pollution, other pollutants such as NH₃ and N₂O are not currently regulated, the latter here being a highly potent greenhouse gas and significantly contributing to greenhouse gas emission. The most significant smokeless local pollutant generated by spark ignition (SI) engines is particulate matter (PM). All of that is primarily composed of solid as well as liquid phase particles and is caused mostly by inhomogeneity in the composition of the fuel–air during combustion [11]. The diesel oxidation catalyst (DOC), like the TWC in gasoline engines, has demonstrated effectiveness in eradicating UHC and carbon monoxide from diesel exhaust.

However, there is still research going on toward the NO_x of diesel engines and like gasoline vehicles, diesel engines emit PM. Modern diesel automobiles are embedded with diesel particulate filters (DPF) which have elevated percolation efficiency (~99%) but they need to be revived sporadically but because of significant utilization of fuel requirements for them to attain the soaring temperatures required for renewal leads them to a penalty on CO₂ emissions [8].

It can be concluded that, though there has been significant improvement in conventional automobiles, there requires to be a change toward more environmentally friendly vehicles. There has been a shift toward hybridization of vehicles and electrification, but they bring new challenges. Electric Vehicles have been regarded as more ecologically, sustainable-technology that can aid in the reduction of air pollution and global GHG emissions.

All these cars have varying degrees of electrification, as well as advantages and shortcomings as compared to regular internal combustion engine vehicles (ICE), because hybrid electric vehicles are entirely reliant based on petroleum-based fuels, they might be considered as energy efficient form of an ICE vehicle. Future interest is being shown in rechargeable EVs (PHEV and BEV), notably zero-emission cars (BEV and FCV) [13]. Battery costs were lowered by around 74% between 2009 and

2016. Simultaneously, energy density has been increased by 4 times [12]. Furthermore, battery price declines are conceivable as battery capacity grows, production capacity grows, and battery chemistries change. Further, battery cost reductions are conceivable as battery capacity grows, production capacity grows, and battery chemistries change. Electric vehicles have proved to have various benefits and the final goal to reduce GHG emission by the transportation sector can be potentially achieved by this technology. To compare conventional automobile emissions to those of electric cars, the complete energy supply chain must be examined, including tank-to-wheel (TTW) emissions from gasoline usage in the car, well-to-tank (WTT) emissions from energy generation and delivery (fossil fuel, electricity, or hydrogen) method is used [8]. There are various levels of CO₂ levels emitted depending on the source used to produce electricity. It is observed that when 884 g CO₂ per kWh is emitted, the coal power plants have an average efficiency of 39%. This estimate for natural gas is 421 g CO₂ per kWh, assuming a 47% natural gas plant efficiency. A one-third mix of wind, hydropower, and PV is anticipated for RES energy generation [14]. According to this statistic, using 100% coal-generated energy results in greater CO₂ emissions than using typical fossil fuel-driven automobiles. When compared to gasoline ICE cars, using 100% natural gas for power generation results in a 40% savings. Nevertheless, as the percentage of renewable energy sources (RES) in the energy mix increases, the amount of CO₂ reductions from BEVs grows. Both fuel cell cars and battery electric vehicles have much lower total wheel-to-wheel (WTW) emissions than traditional automobiles when using hydrogen or electricity supplied by RES [13].

The other most common merging technology in the automobile sector is the HFCV. The concept of fuel cells has been a mode of prime discussion in recent years. During the 2008 Beijing Olympics, 20 Shanghai-Volkswagen fuel cell passenger vehicles served as public cars, while three Beiqi Foton Motor Co., Ltd. and Tsinghua University fuel cell buses functioned as municipal buses [15]. Hydrogen emits no hazardous pollutants, which stands as a noteworthy advantages of fuel cells, and its calorific value is three times that of petroleum [16]. Because hydrogen cannot be found naturally, it must be harvested from various energy sources; it is now largely produced from non-renewable energy sources by steam reforming of natural gas [14].

In terms of pollution, as compared to gasoline or traditional combustion engine vehicles, HFCEVs have a significantly higher energy conversion efficiency and emit no tailpipe air pollution emissions.

To study the greenhouse gas pollution associated with HFCs, we must look at the WTW assessment. This can further be broken down into two primary stages such as wheel to pump (WTP) and the pump to wheel (PTW). The WTP stage includes fuel generation from a central source and distribution into the vehicle's fuel storage structure. Fuel consumption during vehicle operation is included in the PTW stage. When the results of the WTP and PTW investigations are combined, the WTW energy usage and emissions during the fuel cycle are derived [17].

The investigations examine the well-to-wheel energy and outflows profiles of a light-obligation traditional IC motor (Mazda 3) with a comparable HFCEV (Toyota Mirai) using two elective FE assessment strategies the EPA-detailed FE and in this

way the 5-cycle testing strategy. This examination likewise portrays the profundity of WTW energy utilization and HFCEV outflows to the wellspring of power utilized for H₂ pressure or liquefaction. SMR-based H₂ conveyed through charge tube trailers (SMR G.H₂), SMR-based L.H₂ conveyed utilizing cryogenic-fluid big haulers (SMR L.H₂), solar-oriented electrolysis-assembled H₂ conveyed through propellant cylinder trailers, sun-based electrolysis-based L.H₂ conveyed through cryogenic-fluid big haulers (Solar L.H₂), and sun-powered electrolysis-based L.H₂ conveyed utilizing cryogenic-fluid big haulers (S (Solar L.H₂)). An HFCEV gets the conveyed H₂ (i.e., Toyota Mirai).

The WTW discoveries show that an HFCEV, in any event, when controlled by an H₂ fossil-based creation route (through SMR of flammable gas), utilizes 5–33% less fossil fuel energy and emanates 15–45% less GHG than a gas standard ICEV. The category of force utilized for H₂ pressure or liquefaction has an impact on the WTW outcomes. The SMR L.H₂ course is the direst outcome imaginable for an HFCEV, accepting a U.S. normal force matrix age blend for H₂ liquefaction. Nonetheless, when contrasted with a gas regular ICEV, this methodology lessens GHG discharges by 15%.

It tends to be inferred that the ecological effect of hydrogen fuel energy components is subject to how Hydrogen is favorable to reduce. Hydrogen is dominantly being created by flammable gas, although it has the capability of being delivered by different techniques. Sustainable power is currently somewhat low in the hydrogen age. Be that as it may, this may be changed later on, given the proceeding with ecological issues and expanded utilization of RES in power generation [13].

5 Social Structure and Acceptance

As we have established in the previous parts of this article, that the transportation sector requires a huge shift in the vehicle that is currently being used. In [18], we see a case study where data were collected on customers' decided preferences for vehicles using their view research survey. Four main types of automobiles were considered (gasoline, diesel, hybrid, and electric) along with four fuel types utilized to create energy for electric vehicles according to the mix.

It was seen that given the rising public interest in safe and environmentally friendly energy, the power sources utilized to create electricity might influence consumer attitudes regarding electricity, and hence, this factor was considered in the study. It was also observed that customers were willing to pay \$10000-\$17000 lesser on the median for BEVs than gasoline vehicles, and this is probably because of the drawbacks associated with BEVs. While concluding the study, it was seen that regardless of the anticipated power generating mix alternatives, electric cars were not favored above any other class of vehicle. However, we discovered that there are substantial variations in vehicle choice for BEVs dependent on the energy-generating mix. To summarize, in the findings, it appears that an environmentally friendly renewable-orientated approach can both increase BEV uptake and enhance their environmental

performance in terms of GHG emissions. However, the story is not as black and white as it seems, and in [19], we can see that the environmental benefits were not a strong factor on their own.

However, being at a nascent level has still shown low levels of reluctance through various studies and surveys. In a survey organized in Northern California, participants were given a brief exposure to a model Mercedes-Benz A-Class “F-cell” FCV. The study had one hundred and eighty two drivers conduct a test drive and they had conducted a before and after survey. As a result of the survey, above 90% of participants believed that a driving range of an FCV of 480 km would be satisfactory [20].

The research participants identified several barriers to FCV adoption, the most significant of which were lack of recharging infrastructure and repository of hydrogen that is derived primarily from fossil fuels. The inability of FCVs to be charged at home, the cost of the cars, and safety concerns was the other three major impediments [21].

In addition, a survey of London taxi drivers was conducted to determine their propensity to drive emission-free hydrogen fuel cell taxis. The survey observed that while the mainstream guarantees dependable services of (89%) supported environmentally beneficial technology, their desire to embrace FCVs was largely driven by financial reasons. The prospective inclination to adopt was heavily influenced by the possibility of lower overall operating expenses for the cab in comparison to choices [22].

After a month of test driving in which subjects were instructed to use the fuel cell hybrid vehicle (FCHV) as a substitute for their vehicles and they were properly trained to refuel with hydrogen, a follow up second survey was conducted in which drivers were asked to reflect on their driving and fueling experiences, as well as their perceptions of the FCHV-adv test cars’ safety and performance. The overall mileage for the vehicle fleet throughout the test drive period amounts to an average of more than 1400 miles per driver. There are 54 drivers in all. The performance of their fuel cell vehicle (FCV) “exceeded” or “greatly exceeded” their expectations, according to 80% of research participants. 85% of study respondents thought hydrogen fueling was “pretty or very clear.” 75% were comfortable with having to spend up to \$40000 on a new FCV with the condition that refueling infrastructure was not a major stumbling block. Because of the significant statistical increase in FCV attitudes as a result of vehicle experience, regulators should give drivers experiential opportunities like ride-to-drive events and opportunities to experience FCVs through car sharing businesses [23].

6 Fuel Storage and Efficiency

From the previous sections, it is quite evident that hydrogen fuel cells and EVs have proven to be of greater advantage in various aspects and have proven to be a reliable

alternative to the ICE engine vehicles, but despite all this, they do have their drawbacks. ESS is becoming vital in power quality and maintenance market to boost the usage of renewable energy, minimize CO₂ emissions, and convey the principle of modern grid technology. Consumers may support during power outages caused by natural disasters, as well as decrease electricity costs to meet power demands, by storing energy at a low cost during off-peak hours [24]. According to the usage of energy in a certain form, the categorization of ESS systems is defined. ESS is characterized as mechanical, electro, chemical, electrical, thermal, hybrid, and chemical [25]. The life cycle of an ESS is determined by the materials used in its construction as well as its level of safety. The quantity of energy transmitted through the energy which is stored in an ESS is referred to as efficiency.

For fruitful energy storage applications in EVs, ESSs must have a high-energy density, high-power density, and compact size. Furthermore, zero emissions, trivial self-discharge, minimal material corrosion due to a chemical reaction, long cycle life, elevated efficiencies, and low maintenances are demonstrated for manufacturing and selecting ESSs for EV powering. With an energy-power combination, the ESS must respond rapidly to climbing while being steady at a normal pace. The current state of ESS development is enough for EV energy storage and power. Furthermore, it decreases the need for oil, CO₂ emissions, and GHG emissions. With technology advancements and advancements in specific applications, ESSs continue to grow. However, challenges such as raw material support and disposal, energy management, power electronics interface, size, safety precautions, and cost continue to plague these applications. These present ESS problems are the major impediments to improved R&D efforts for the improvement of energy storage in EV functions (Figs. 1 and 2) [25]

The fuel cells are subject to several parameters, including but not limited to the type, size, temperature, and pressure of fuel cell gas. A fuel cell provides around 1 V or less electricity, hardly enough even for the most basic applications. Individual fuel cells are connected in sequence to form a stack to maximize the quantity of electricity generated. However, there are several varieties of fuel cells, which are distinguished largely by the type of electrolyte utilized. The electrolyte regulates the type of chemical processes that occur in the fuel cell, the temperature range at which it operates, and other parameters that define its most appropriate uses. Polymer electron membrane or proton exchange membrane are the ones most used in transportation. PEM has shown to have an efficiency of around 50–60% electric [26].

In June 2013, ACAL Energy Ltd claimed PEM hydrogen fuel cell had achieved a durability test of over 10,000 h for a third-party automotive sector, without noticeable deteriorating signs. Under such test conditions, hydrogen fuel cell durability is the finest light-weight diesel engines at 10000 h or 300,000 driven miles. This endurance considerably exceeds the current 2017 US Department of Energy (DOE) objective for the industry regarding automobiles powered by fuel cells, which is 5000 h, or 150,000 road miles, with an estimated deterioration tolerance of 10%.

As many of the hydrogen fuel cell Vehicles are still at the emerging stage, it is difficult to know the exact rates of efficiencies, and a lot of work is yet to be conducted in the respective field. To meet the full energy requirements, fuel cell

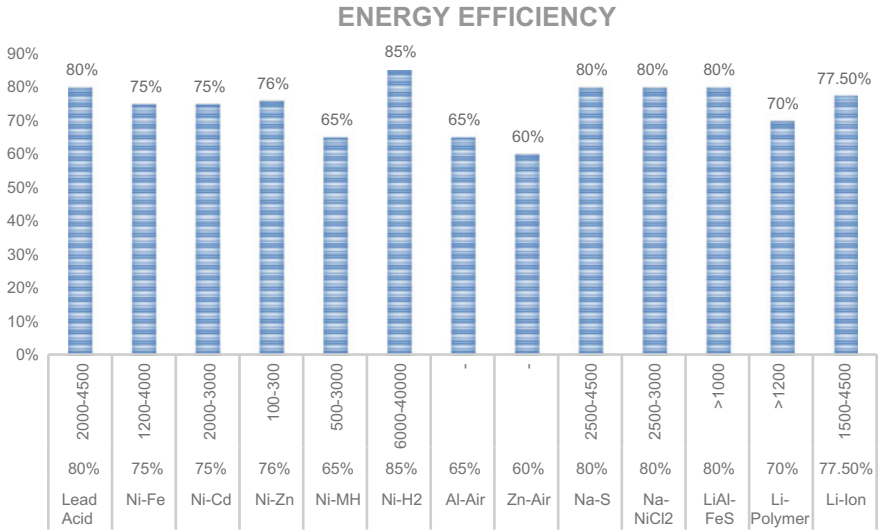


Fig. 1 Battery cell efficiency [25]

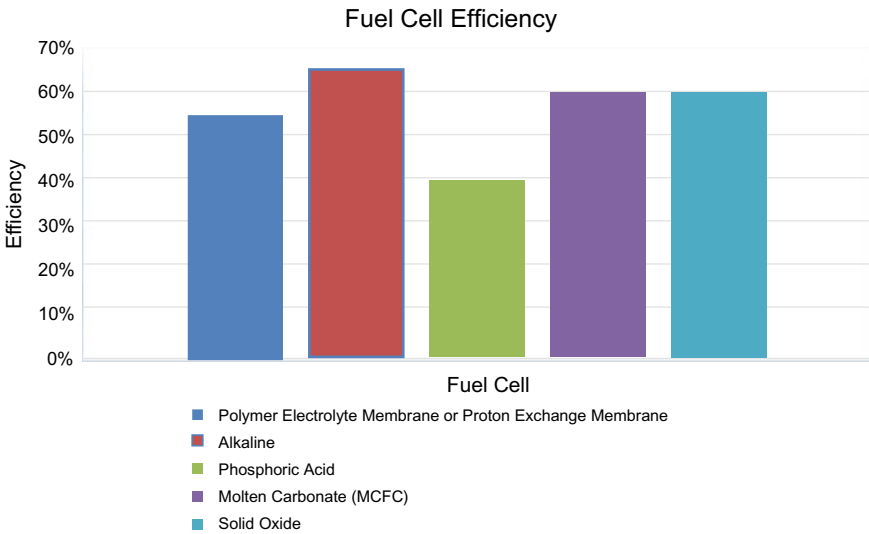


Fig. 2 Fuel cell efficiency [26]

researchers must solve fundamental issues relating to the expense of high fuel cell automobiles, limited durability, hydrogen fuel refuel infra- structure, and hydrogen storage (FCVs) [27].

7 Driving Range

As the main anxiety of consumers is a range, how much anyone can drive a vehicle after refueling of gasoline or recharging a battery or hydrogen tank; so as of now IC engines overtake at the nominal price but emits hazardous gases to take measure to replace ICs into a renewable and non-polluting energy source. As Tesla offers a range of more than 400 miles in one charge but it is not cost-effective in the Indian transportation market and adding more battery capacity into vehicle increase the weight, heating effect in battery, and component failure risk due to high-power transmission while fast charging, whereas FCEV generates electricity itself in the vehicle and provide power to motor and controller. The energy density of hydrogen is also less so it can be store at pressure in compact carbon fiber material storage tank to have a high range.

The power output of hydrogen fuel cells is calculated by the driving power balance equation of automobiles.

$$P_{fc} = \frac{1}{\eta} \left(\frac{Gfu^{\max}}{3600} + \frac{C_dAU_{\max}}{76140} \right)^3 \tag{1}$$

Toyota Mirai miles per full hydrogen tank ranged from the low 50 s to the upper 60 s rpm, with a low of 238.3 miles and a high of 310.3 miles. HFC outweigh BEV in five major parameters as mention:

- (i) It weighed less
- (ii) Less space in vehicle
- (iii) Greenhouse gas emissions are ameliorated
- (iv) Well-wheels energy requirements were also less
- (v) It required less time to be refueled than an EV battery [28].

To understand figuratively, assume FCEV and BEV of the same range of 300miles, the FCEV will be 1280 kg while BEV being 2270 kg [29] (Table 1).

8 Energy Density of Fuel Types

8.1 Polymer Electrolyte Membrane Fuel Cell

As electrolyzer breaks the bond of hydrogen as proton and oxygen’s into electron; membrane of FC only allows proton to pass through it; negatively charged electron travels through an external circuit and provides power to an electric motor.

The operating temperature of PEMFC is less than 120 °C with tank-wheel efficiency of 60% with a motor efficiency of 93% and rectifier up to 97% in the operating hour of 3000 h. The energy density of the fuel cell is 2.0 kW/kg with electric motor output of 5.0 kW/kg. The weight of the 130 kW drive drain is 152 kg which includes

Table 1 Summary of FCV and EV attribute [29]

	Range: 300 miles			Range: 200 miles		
	Fuel cell vehicle	Battery vehicle	Ratio BEV/FCEV	Fuel cell vehicle	Battery vehicle	Ratio BEV/FCEV
Weight of vehicle (kg)	1281	2260	1.76	1250	1766	1.41
Storage volume (L)	102	565	5.53	80	310	3.80
	300	550	1.83	220	305	1.38
Greenhouse gas (g/mile)	240	540	2.25	230	450	1.95
Incremental cost (\$)	3650	19,600	5.36	2840	10,210	3.59
Natural gas required (MBTU)	0.89	1.14	1.28	0.50	0.63	1.26
	0.80	1.76	2.2	0.55	0.93	1.69

fuel cell-65 kg, air compressor-10 kg, hydrogen storage tank-47 kg, supercapacitor-4 kg, and electric motor of 26 kg. The cost of an electric motor, fuel cell, and hydrogen storage will be around Rs. 5589/kWh generation [30].

8.2 Li-Ion Battery Electric Vehicle

In BEV energy storage is a form of electricity only in battery, it loses less energy in conversion form as PEMFC does; as the battery is directly charged through a plug-in charger there is no loss in fuel conversion efficiency.

Efficiency from tank-wheel is 95% at an operating temperature less than 90 °C, electric motor is 93% efficient, and rectifier is 97% for the operating hour of 7900 h.

The energy density of batteries is 0.25 kWh/kg, and electric motors of 5 kW/kg are efficiently working. The drive train of 130 kW is 326 kg which includes components like battery-300 kg, electric motor-26 kg which is double than PEMFC. Presently, batteries and electric motors cost Rs. 35543/kW [30].

9 Combustion Engine

In engine, as there are more moving parts compared to PEMFC and BEV and fuel, conversion from gasoline to mechanical rotation by combustion of fuel reduces the efficiency of IC engine vehicle. Though the energy density of gasoline is high, it unable to give the desired output, and the main reason to shift from IC to BEV and FCV is the emission of GHG like NO_x and CO_x gases.

Statistically, tank-wheel efficiency of combustion engine is 45% only with operating hours of 10000 h. The energy density of gasoline is 12kWh/kg and compressed hydrogen of 1.59kWh/kg. Drive train of 130 kW weight around 193 kg which includes component like combustion engine—87 kg, transmission—40 kg, electric motor—15 kg, air compressor—47 kg, and supercapacitor weight 4 kg [30].

10 Durability Performance and Progress

As of 2018, the educational demonstration projects of NREL have analyzed the data over 230 different models of cars from the 6 original equipment manufacturers. This car has accumulated data for almost 7 million miles driven with over 83000 h of fuel cell stack operation time.

The output efficiency of the fuel cell stack has 22% Eff with the operation of 564 8 h. For 2500 h, all stacks have not operated past 10% voltage degradation. The DOE's MYRD&D 2020 goal for hydrogen fuel cell power systems for transport applications is 65% peak efficiency at 25% rated power.

The high expense of FCVs is mostly due to the usage of expensive chemical catalysts and other components in the fuel cell "stack." Platinum being a prime example fuel cells, as of current times, that are made now cost roughly \$280/kW at modest numbers of 20 k units per year, according to a US DOE estimate. Additionally, their cost would sink to \$53/kW if they were manufactured at value (500 k units). The US DOE similarly predicted a cost of roughly \$40/kW in 2020, with a final aim of \$30/kW [31].

11 Conclusion

Battery electric vehicles (BEVs), such as Tesla, are the electric cars with which we are all too acquainted today. They utilize electricity stored in a battery to operate an electric motor. A hydrogen fuel cell electric vehicle (FCEV), such as Toyota's Mirai, creates electricity by combining hydrogen and oxygen in a fuel cell, which is then used to power the vehicle's electric motor. People are not buying BEVs for a variety of reasons, including the fact that they take too long to charge, have a short-range before requiring recharging, and are significantly more expensive than comparable gas-powered vehicles. Hydrogen vehicles have an advantage over battery electric vehicles when it comes to recharging. The three fuel cell vehicles on the market currently have a range of 312 miles (Toyota Mirai), 360 miles (Honda Clarity), and 380 miles (Hyundai Nexo). Most electric vehicles have a range of fewer than 250 miles, and while certain Tesla models have a range of more than 300 miles, they are generally out of reach for the average car customer. Because of its range and refueling times, fuel cell vehicles, according to 75% of automotive executives, will be the breakthrough for electric mobility. Today's fuel cell vehicles have a

suggested retail price of roughly \$60000, which is \$15000 more than any entry-level BEV. The issue with hydrogen fuel cells stems from a lack of infrastructure. In the United States, California has the most hydrogen stations, with little over 40 hydrogen stations available to fuel cell owners. To become the game-changer that auto executives anticipate they will be, FCEVs will require a large network of hydrogen stations. To increase the miles per charge, battery with high-energy density is required. A high-energy density battery will increase the car's weight. A larger battery is required to extend the range. Infrastructure is the only thing holding FCEVs back, and if hydrogen stations become more common, EVs may lose much of the zero-emissions market. The advantage of petrol automobiles is that refueling stations are plentiful, and many of them provide excellent mileage. In petrol cars, an IC engine is featured, which uses gasoline to create combustion and enough pressure and temperature power to drive the pistons. An electric vehicle's power source is a battery pack that is converted to three-phase AC by an inverter. As a result, an induction motor is substantially lighter than an IC engine and produces significantly more power and torque. Both the IC engine and the induction motor require cooling, and both must reject waste heat produced in order to maintain a fixed temperature. In comparison with an IC engine, an induction motor produces substantially less waste heat. The ease with which an automobile with an IC engine may be refueled is the most significant benefit. A gas automobile can be refueled in 5 min or less, however, it takes at least an hour to charge an electric car at this time. Another important benefit of gasoline automobiles over electric cars is their high-energy density, the battery's low-energy density results in a significant weight penalty for the electric vehicle. The battery pack also has significant heat-generating issues: dismantling an electric car's battery pack reveals a assortment of lithium-ion cells that you might use in your daily life. Electric car battery packs have their own set of benefits. Another significant distinction is that in an IC engine automobile, a sophisticated exhaust after treatment is required to maintain emissions and noise below legal limits. When the power dynamics of these two technologies are compared, electric automobiles come out on top. As a result, the speed of an electric car can be regulated immediately from the motor. As a result, an electric car does not require a spore variable transmission. An electric automobile can produce a lot of torque right away, whereas a car with an internal combustion engine will struggle at low RPM. To get the engine to the optimal RPM range at the start, a DC motor is required. Furthermore, an electric motor's torque and power can be regulated instantly, but an IC engine's response is slow. When we look at which vehicle is most cost-effective, we can say that an electric car is significantly more costly than a typical gasoline vehicle. According to a calculation based on current gasoline and power pricing, gasoline vehicles are one-third less expensive than electric vehicles. Electric cars are also less expensive to maintain than cars with internal combustion engines. It is a well-established fact that electric vehicles are significantly safer than internal combustion engines. With internal combustion engine technology nearly saturated and the rapid development of electric cars underway, electric automobiles have an advantage over IC engine cars as the case of the future.

References

1. Qureshi MI, Rasli AM, Zaman K (2016) Energy crisis, greenhouse gas emissions and sectoral growth reforms: repairing the fabricated mosaic. *J Clean Prod* 112:3657–3666. <https://doi.org/10.1016/j.jclepro.2015.08.017>
2. Aswani G, Bhadoria VS, Singh J (2018) Electric vehicles in India: opportunities and challenges. In: 2018 international conference on automation and computational engineering (ICACE). <https://doi.org/10.1109/icace.2018.8687043>
3. Nichols BG, Kockelman KM, Reiter M (2015) Air quality impacts of electric vehicle adoption in Texas. *Transp Res Part D: Transp Environ* 34:208–218. <https://doi.org/10.1016/j.trd.2014.10.016>
4. <https://www.autocarindia.com/car-news/india-gets-350-new-ev-charging-stations-installed-under-fame-ii-scheme-421495>
5. <https://www.energy.gov/>
6. <https://easyelectriclife.groupe.renault.com/en/outlook/lifestyle/electric-implantation/>
7. <https://www.nytimes.com/interactive/2021/03/10/climate/electric-vehicle-fleet-turnover.html>
8. Leach F, Kalghatgi G, Stone R, Miles P (2020) The scope for improving the efficiency and environmental impact of internal combustion engines. *Transp Eng*, 100005. <https://doi.org/10.1016/j.treng.2020.100005>
9. The United States Energy Information Administration International Energy Outlook (2019). Available at: <https://www.eia.gov/outlooks/ieo/pdf/ieo2019.pdf>
10. Stone R (2012) Introduction to internal combustion engines, 4th edn. Palgrave Macmillan, London
11. Eastwood P (2008) Particulate emissions from vehicles. Wiley
12. International Energy Agency, OECD/IEA (2017)
13. Ajanovic A, Haas R (2019) Economic and environmental prospects for battery electric and fuel cell vehicles: a review. *Fuel Cells*. <https://doi.org/10.1002/fuce.201800171>
14. Ajanovic A, Haas R (2015) Driving with the sun: why environmentally benign electric vehicles must plugin at renewables. *Sol Energy* 121:169–180. <https://doi.org/10.1016/j.solener.2015.07.041>
15. Dixon RK, Wang X, Wang MQ et al (2011) Development and demonstration of fuel cell vehicles and supporting infrastructure in China. *Mitig Adapt Strateg Glob Change* 16:775–789. <https://doi.org/10.1007/s11027-011-9293-y>
16. Manoharan Y, Hosseini SE, Butler B, Alzahrani H, Senior BTF, Ashuri T, Krohn J (2019) Hydrogen fuel cell vehicles; current status and future prospect. *Appl Sci* 9(11):2296. <https://doi.org/10.3390/app9112296>
17. Liu X, Reddi K, Elgowainy A, Lohse-Busch H, Wang M, Rustagi N (2019) Comparison of well-to-wheels energy use and emissions of a hydrogen fuel cell electric vehicle relative to a conventional gasoline-powered internal combustion engine vehicle. *Int J Hydrogen Energy*. <https://doi.org/10.1016/j.ijhydene.2019.10.19>
18. Choi H, Shin J, Woo J (2018) Effect of electricity generation mix on battery electric vehicle adoption and its environmental impact. *Energy Policy* 121:13–24. <https://doi.org/10.1016/j.enpol.2018.06.013>
19. Chung J-B, Kim E-S (2018) Public perception of energy transition in Korea: Nuclear power, climate change, and party preference. *Energy Policy* 116:137–144. <https://doi.org/10.1016/j.enpol.2018.02.007>
20. Martin E, Shaheen SA, Lipman TE, Lidicker JR (2009) Behavioral response to hydrogen fuel cell vehicles and refueling: results of California drive clinics. *Int J Hydrogen Energy* 34(20):8670–8680. <https://doi.org/10.1016/j.ijhydene.2009.07.09>
21. Hardman S, Shiu E, Steinberger-Wilckens R, Turrentine T (2017) Barriers to the adoption of fuel cell vehicles: a qualitative investigation into early adopters attitudes. *Transp Res Part A: Policy Pract* 95:166–182. <https://doi.org/10.1016/j.tra.2016.11.012>

22. Mourato S, Saynor B, Hart D (2004) Greening London's black cabs: a study of driver's preferences for fuel cell taxis. *Energy Policy* 32(5):685–695. [https://doi.org/10.1016/s0301-4215\(02\)00335-x](https://doi.org/10.1016/s0301-4215(02)00335-x)
23. Lipman TE, Elke M, Lidicker J (2018) Hydrogen fuel cell electric vehicle performance and user-response assessment: results of an extended driver study. *Int J Hydrogen Energy* 43(27):12442–12454. <https://doi.org/10.1016/j.ijhydene.2018.04.17>
24. Hannan MA, Hoque MM, Mohamed A, Ayob A (2017) Review of energy storage systems for electric vehicle applications: issues and challenges. *Renew Sustain Energy Rev* 69:771–789. <https://doi.org/10.1016/j.rser.2016.11.171>
25. Electrical Energy Storage (2011) White paper. The International Electrotechnical Commission (IEC), Switzerland, Geneva
26. https://www.californiahydrogen.org/wp-content/uploads/files/doe_fuelcell_factsheet.pdf
27. Alaswad A, Baroutaji A, Achour H, Carton J, Al Makky A, Olabi AG (2016) Developments in fuel cell technologies in the transport sector. *Int J Hydrogen Energy* 41(37):16499–16508. <https://doi.org/10.1016/j.ijhydene.2016.03.16>
28. <https://evannex.com/blogs/news/how-does-a-toyota-mirai-fuel-cell-car-compare-to-a-bev-in-the-real-world>
29. Fuel cell and battery electric vehicles compared by C. E. (Sandy) Thomas, Ph.D., President H2Gen Innovations, Inc. Alexandria, Virgin
30. Handwerker M, Wellnitz J, Marzbani H, Comparison of hydrogen powertrains with the battery powered electric vehicle and investigation of small-scale local hydrogen production using renewable energy 2
31. <https://www.businessinsider.in/?r=US&IR=T>

Energy Management of Grid Connected Renewable Sources with Energy Storage Unit for an EV Charging Station



Sohankumar Prajapati and Sanjay R. Vyas

Abstract The electrical vehicles selling increase in last few years due to availability of charging facility. The charging station located on highways defines public EV charging station plays an important role to fast charge of electrical vehicles. In this paper, grid-tied PV and energy storage unit base charging station design by considering different modes of operation. The MPPT base boost converter is used to extract maximum power from the PV. The charging–discharging of energy storage battery design by the buck–boost converter. Five EVs battery parameters are considered to calculate real-time EV load. For the uninterrupted charging of EVs, whenever PV and energy storage power are not available or the available power does not meet load demand throughout the day, the deficient power is taken from the grid. The optimal energy flow between PV, ESU, grid, and EVs is obtained by a PI-based current control strategy. The different operating modes of power flow among sources and EV load are designed, and the same is formulated and validated in MATLAB/Simulink.

Keywords RES Base EV C.S · Energy management of EV C.S · PV-ESU C.S

1 Introduction

When the use of electric vehicles (EVs) rises in future, parallel to that charging infrastructure on the highway will increase and it will increase stress on the existing grid. In this mind scenario, if charging stations are powered by local power generation sources, the problem can be solved. Solar PV power installation and equipment prices have dropped dramatically in India in recent years, making it one of the most cost-effective energy sources. The optimal utilization of energy among connected sources is very important for EV charging stations to maximize profit as well as to make it

S. Prajapati (✉)
Kadi Serva Vishwavidhalaya, Gandhinagar, Gujarat, India
e-mail: sgp.gec@gmail.com

S. R. Vyas
L.D.R.P Institute of Technology and Research, Gandhinagar, Gujarat, India
e-mail: srvyas_ee@ldrp.ac.in

© The Author(s), under exclusive license to Springer Nature Singapore Pte Ltd. 2022
V. Mahajan et al. (eds.), *Sustainable Technology and Advanced Computing*
in *Electrical Engineering*, Lecture Notes in Electrical Engineering 939,
https://doi.org/10.1007/978-981-19-4364-5_66

925

Table 1 EV battery parameter and load demand

EV NO	Capacity of battery (KWh)	Initial SOC (%)	Required SOC (%)	Plugged time (h)	EV load demand (KW)
1	1	20	95	1.40	0.53
2	2	30	95	1.40	0.92
3	3	50	95	1.40	0.96
4	2	80	95	1.40	0.214
Total					2.62 KW

Capacity of battery (KWh): It is a capacity of battery of EV

Initial SOC (%): It is a state of charge of EV battery when it comes to charging station

Final SOC (%): It is state of charge of EV after being fully charged

Plugged time is time required to fully charged from initial SOC

EV load demand is the amount of the load on charging station when all the EVs are connected to it

environmental concern. The PV cost nowadays decreased due to global competition so it is beneficial to mount it on the roof of the charging station to utilize maximum energy and reduce grid stress during peak intervals. The energy storage unit cost is high but as a backup, it is necessary to tie up with the system. In this paper, the dummy load is considered to compensate for surplus power from PV. For the calculation of real-time EV load demand, the four Indian companies' EV battery parameters and initial to final SOC are considered and are given in Table 1.

1.1 Literature Review

The work done by many researcher in similar objectives is mention here as part of literature survey. The work presented by Karki on design PV, BESS, and grid base fast C.S topology implemented for the grid stress reduction which occur due to fast charging of EVs [1]. In their work, idea implemented by modeling EV loads profiles and prioritizing the sources. The droop regulation method is implemented for the effective load sharing among different sources. The overall system was tested by algorithm run in MATLAB/Simulink. In other existing work approach on design, a control strategy of PV-powered smart charging station for PHEV to reduce grid burden on peak hours by Goli [2] was presented work on power flow management by considering irradiation and PV power base DC link voltage sensing and according to direction of power flow of various modes designed. The another researcher Hassoune, Khafallah presented work on title power management strategies of electric vehicle charging station based grid-tied PV-battery system, he designed power predictive model for forecast EVs power demand and to enhance the charging station performance. The PV array with battery storage implemented to avoid an extra burden on the grid during peak hours. PV array with storage battery supported by the grid increased the reliability and flexibility of the system [3]. Hassoune et al. represent their work on control strategies of a smart topology of EVs charging station based

grid-tied RES-battery. In their work, 6 h data of generation of RES and considered EV load pattern, a power flow management technique designed. PI control technique implemented to regulate the margin error between the charging current and its reference which followed by pulse width modulation (PWM) technique [4].

2 Model of EV Charging Station

The proposed energy management system developed for highway located EV public charging station. The system is designed for five EVs charge at 3 KW charging port (Fig. 1).

The 6 kW capacity of PV with 24 solar modules of each 250 Wp connected in parallel. To extract maximum power from solar due to variable weather condition, MPPT with P&O algorithm considered [4]. Boost converter uses to boost the PV voltage as required to DC link, and PI controller uses to regulated DC link voltage. On the energy storage unit side, buck-boost converter uses for charging–discharging

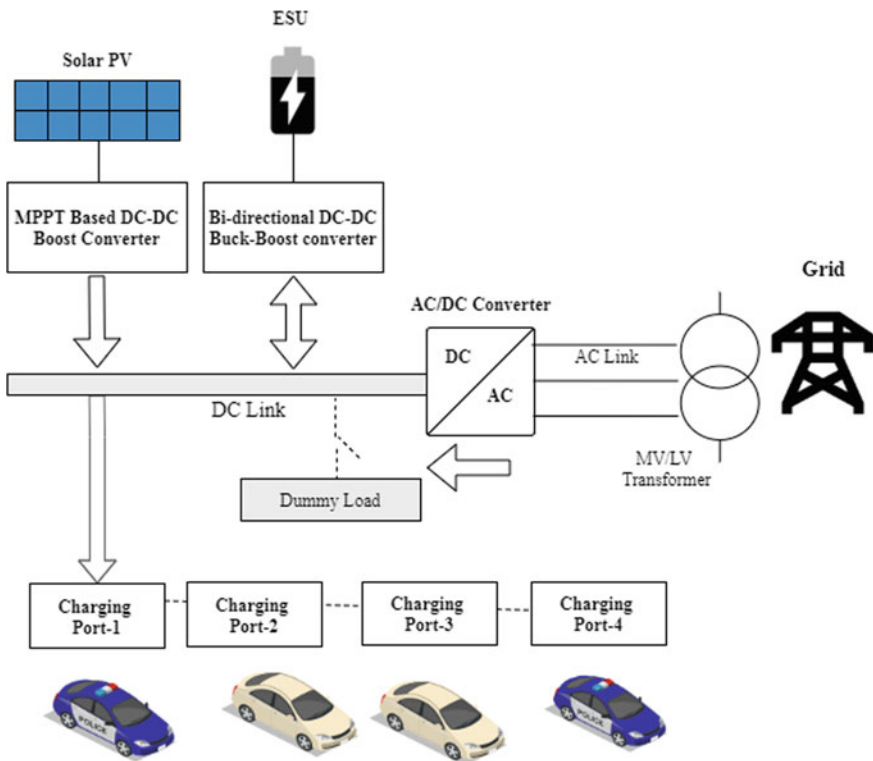


Fig. 1 PV, ESU, and grid-powered EV charging station

of energy storage unit batteries [5]. During charging mode, buck mode is activated and on discharging boost mode activated. The grid rectification mode considered to provide uninterrupted power to the charging station during maximum EV load and intermittent power from PV.

2.1 EV Load Demand Calculation

Mainly three parameters are considered for the modeling of EV Load demand

- (1) Rated battery capacity (KWh)
- (2) Initial SOC (%) and final SOC (%)
- (3) Plug in time (Hrs).

In this proposed EV charging model, it is assumed that the required final SOC of the EV batteries is 95% of its rated capacity. The initial SOC of all four EVs considered as 20%, 30%, 50%, and 80%. Calculation of the required power demand of EV at charging station is referred based on work in [6].

$$P_{EVi} = \frac{(SOC_{Required} - SOC_{Initial})}{P_{TEVi}} \quad (1)$$

where P_{EVi} is load demand of i th EV.

P_{TEVi} is plug time in which EVs connected for charging.

Table 1 shows the battery parameters for four electric vehicles.

2.2 Solar PV Power Calculation

Considered PV plant capacity for MATLAB/Simulink: 6 kW.

PV module rating: 250 Wp.

No. of modules in parallel: 24.

$$\begin{aligned} \text{Power from PV array} &= \text{Plant capacity} \times \text{operating factor} \\ &= 6 \times 0.75 \\ &= 4.5 \text{ KW} \end{aligned}$$

The operating factor is used to estimate the actual output from a PV module.

In above equation, operating factor is taken 0.75, because due to temperature and dust, the module output power is 60 to 80% lower than rated output power. Hence, it considered 75% in this proposed work.

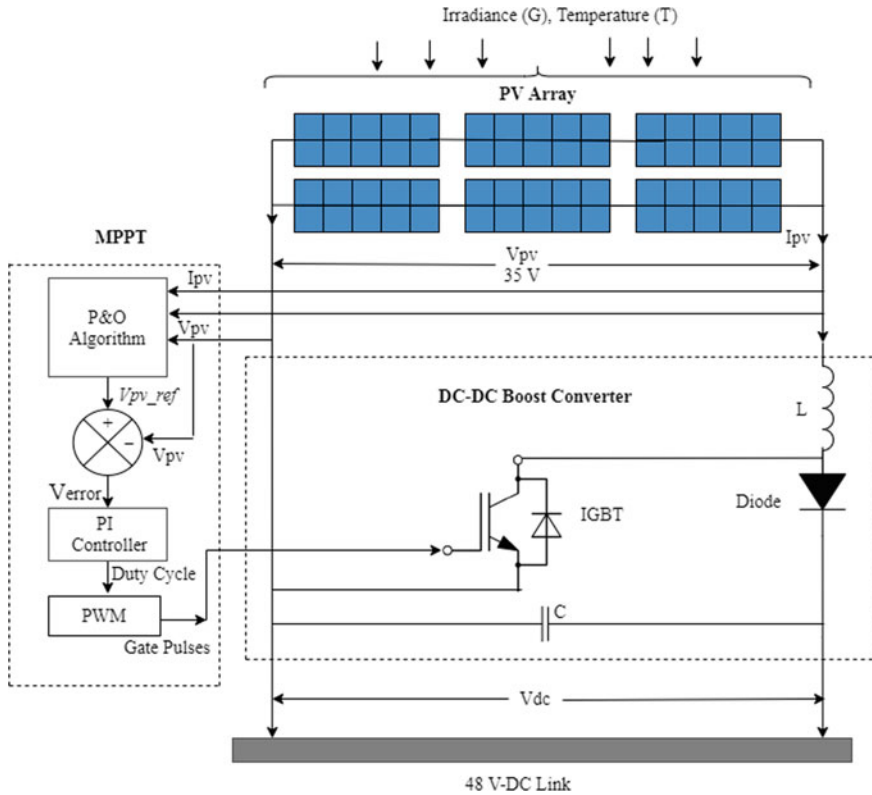


Fig. 2 Solar PV array, MPPT, and boost converter

Boost Converter

The boost converter raises the voltage from the PV array’s 37.3 V to 48 V, which is the required voltage for the common DC link (Fig. 2).

The capacity of solar PV decided according to 2.6 KW load demand of EVs through the day and energy storage unit charging–discharging scenario. Maximum power obtained by MPPT from perturb and observe (P&O) algorithm under variable weather conditions [7]. The DC link voltage kept constant by using PI controller. DC link voltage is 48 V, and V_{mp} of 250 Wp PV modules is 37.3 V so no buck operation required, so it is considered only boost converter.

2.3 ESU Power Calculation

The energy storage unit is one of the backup source to charge the EVs during PV power in not available at night time. In this work, for MATLAB simulation 8.4 kW

capacities of energy storage unit considered which having 24 V, 350 Ah. The ESU initial and final SOC considered as 20% and 95%, respectively.

The charging–discharging of the ESU is done by a PI Control bidirectional DC-DC converter where it charges in buck mode and discharges in boost mode [8].

The energy storage system (ESU) will be charged whenever there is excess solar electricity, and then discharged at night to provide power for the EVs. On buck mode, the duty ratio of the converter given in;

$$P_{ESU} = P_{PV} - P_{EV}$$

$$P_{ESU} = V_{ESU} \times I_{ESU}$$

$$\therefore I_{ESU} = \frac{P_{PV} - P_{EV}}{V_{ESU}} \tag{2}$$

$$I_{Charging} = \frac{P_{PV} - P_{EV}}{V_{DC_Link}} \tag{3}$$

$$D_{buck} = \frac{I_{Charging}}{I_{ESU}} \tag{4}$$

On the other hand, the ESU discharges to deliver power for charging all of the EVs in the electrical vehicle charging station on boost mode. Dboost is the duty ratio for bidirectional converters.

Delivered Power by ESU, $P_{ESU} = P_{EV} - P_{PV}$

$$P_{ESU} = V_{ESU} \times I_{ESU}$$

$$\therefore I_{ESU} = \frac{P_{EV} - P_{PV}}{V_{ESU}} \tag{5}$$

$$I_{Discharging} = \frac{P_{EV} - P_{PV}}{V_{DC_Link}} \tag{6}$$

$$D_{boost} = 1 - \frac{I_{Discharging}}{I_{ESU}} \tag{7}$$

2.4 Grid Power

The grid power of 230 V, AC is acknowledged for MATLAB/Simulink. A step-down transformer is considered for additional power requirements, and finally, from the rectifier, it converts to 48 V DC for the common DC link. The voltage stability of the grid can be reduced by incorporating the voltage regulating device such as DVR in the grid.

2.5 Operating Modes of Power Flow

Mode 1: PV2EV, PV_{Surp.}2ESU

Condition: $P_{PV} > EV_{Load}$ and $SOC_{ESU} < SOC_{ESUmax}$

If the solar PV's delivered power is greater than all of the plugged EVs' load, in this scenario, EVs are charged solely by solar power. Meanwhile, if ESU's current SOC is under its maximum SOC, it will be charged with surplus power from solar PV.

Mode 2: ESU2EV, Grid_{def.}2 eV

Condition: $P_{PV} = 0$ and $SOC_{ESU} > SOC_{ESUmin}$

When PV power is zero at night time, ESU delivered energy to charge EVs by maintaining the set initial SOC of battery.

Mode 3: PV2EV, Grid_{def.}2 eV

Condition: $P_{PV} < EV_{Load}$

If the solar PV's delivered power is less than all of the plugged EVs' load due to bad weather conditions, in this case, EVs charged from PV as well as deficit power taken from the grid via common DC link.

Mode 4: ESU2EV, Grid_{def.}2 eV

Condition: $P_{PV} = 0$ and $SOC_{ESU} < SOC_{ESUmin}$

Similar to the previous scenario, if PV is not available at night or due to inclement weather, and ESU SOC is less than its initial, the needed power for charging the electric vehicles will be taken from the grid via the DC link.

Mode 5: PV2EV, PV_{Surp.}2Dum-load

Condition: $P_{PV} > EV_{Load}$ and $SOC_{ESU} = SOC_{ESUmax}$

If the solar PV's delivered power is greater than all of the plugged EVs' load, in this case, EVs are charged solely by solar power. Meanwhile, it is considered that SOC of ESU is at maximum level and surplus PV power delivered to dummy load for power balance.

3 Simulation Results and Discussion

The MATLAB modeling and simulation of grid-tied PV and ESU are mention in Fig. 3.

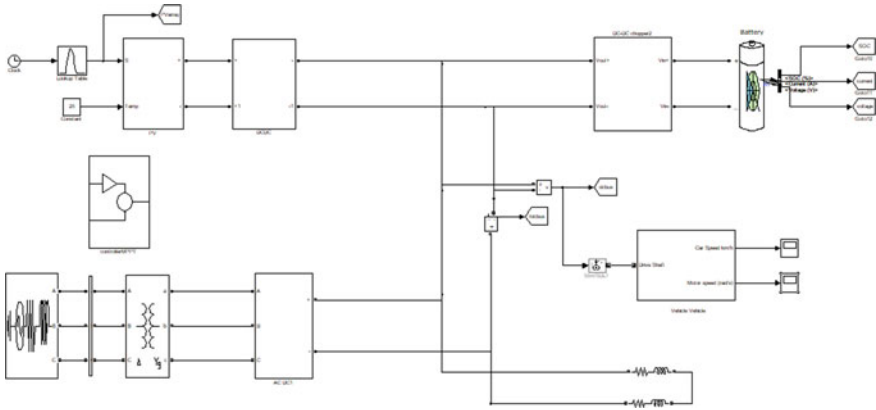


Fig. 3 MATLAB simulation model of grid-tied PV and ESU

The 6 KW solar PV system is designed, a MPPT extract maximum power of 4.5 KW under inconsistent weather condition. The P&O MPPT algorithm considered to extract maximum power from solar PV array.

The duty cycle set by the MPPT algorithm is given to the boost converter for output DC voltage regulation. The boost converter converts 37.3 V V_{oc} of solar PV to 48 V (Figs. 4 and 5).

There is a buck-boost dual converter topology also developed by PI controlling for charging and discharging control for a battery storage unit.

The EV charging rate is controlled through a proposed bidirectional DC-to-DC converter. The regulating supply is helpful for EV charging stations. With the help of the proposed system, EVs can be charged through a charging station, and the energy cost is also very optimal due to the use of RES. (Figs. 6, 7, and 8).

The result shows that DC link voltage (48 V) remains constant by PI controller during EV charging operations.

Figure 9 depicts the charging station's continuous operation throughout the day. The five operating modes as per defined conditions presented here in simulation results. In mode-1, during 9:00 a.m. to 15:30 p.m., average available PV power is 3.7 KW, the EV load is 2.6 KW, on that scenario, all the EVS charge by solar PV

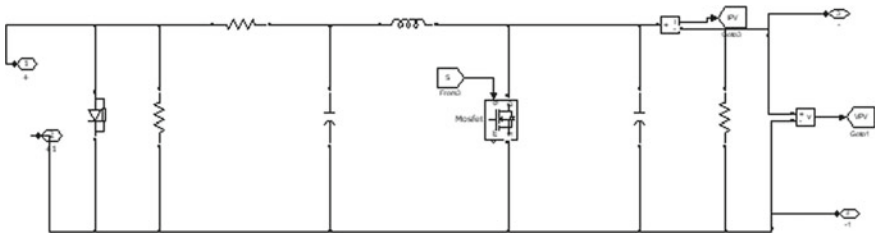


Fig. 4 MATLAB simulation model of DC-DC boost converter

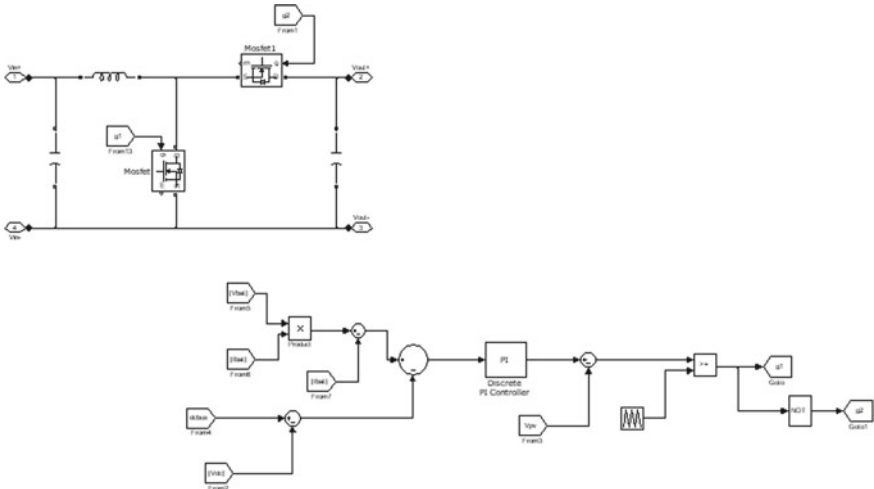


Fig. 5 MATLAB simulation of DC-DC bidirectional converter with PI controller

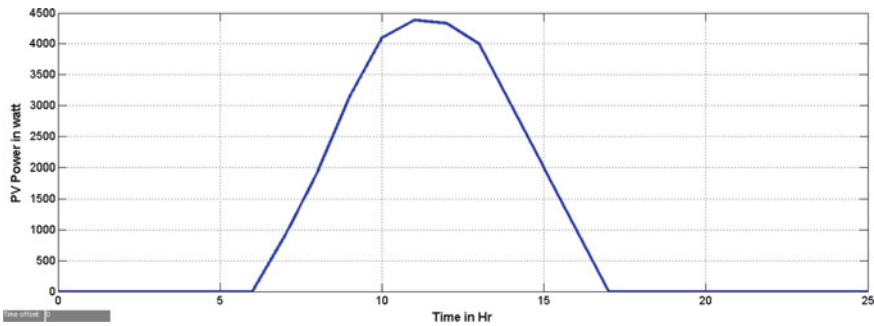


Fig. 6 Maximum power extracted from the PV array

power and surplus PV power is transferred to charge ESU. In mode-2, during 0–3 h. and 18.30 p.m. to 12 a.m. time slot, PV power is zero. On that scenario to charge the EVs, power taken from ESU and deficit power taken from the grid. In mode-3, during 6:00 a.m. to 8:30 a.m. at morning time and 17.30 p.m. to 18:30 p.m. at evening time, the available PV power is less that EV load, in this scenario, EVs charged mainly from AC grid by rectification process. In mode-4, during 3:00 a.m. (early morning) to 6:30 a.m. at morning time, to charge the EVs, necessary power taken from the grid only via the DC link. In mode-5, during 16:00 p.m. to 17:00 p.m., the available PV power and ESU power are higher than EV load, so on that scenario, surplus PV power is delivered to dummy load for power balance.

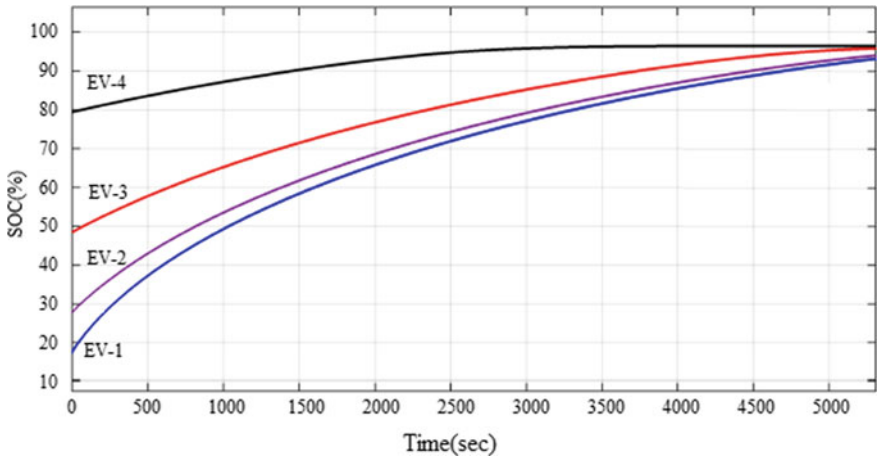


Fig. 7 EV charging SOC

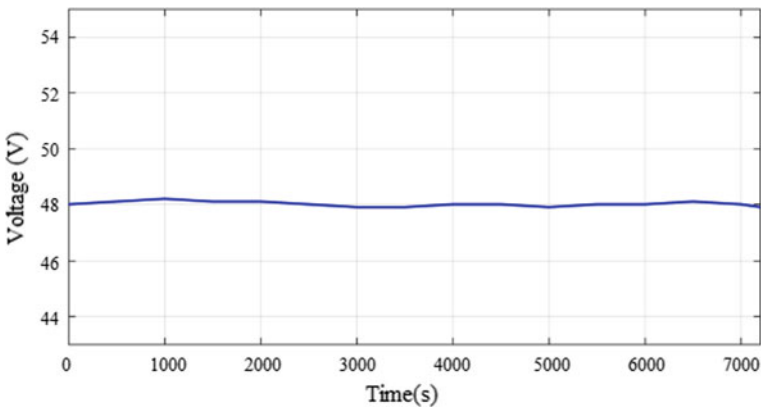


Fig. 8 DC link voltage

4 Conclusion

In this paper, proposed power flow management system of solar PV, battery energy storage unit, and grid connected electric vehicle charging station has been presented. The electrical vehicle charging at charging station throughout the day is developed in MATLAB Simulink by considering five different operational modes on the basis of available power scenario of the sources. The results indicate that the proposed power flow management technique meets the charging requirements of all EVs connected at C.S throughout the day. The desired power is obtained using PI current control and voltage control by keeping the DC link voltage constant at the charging station. From the MATLAB Simulink result of five operating modes, it is observed

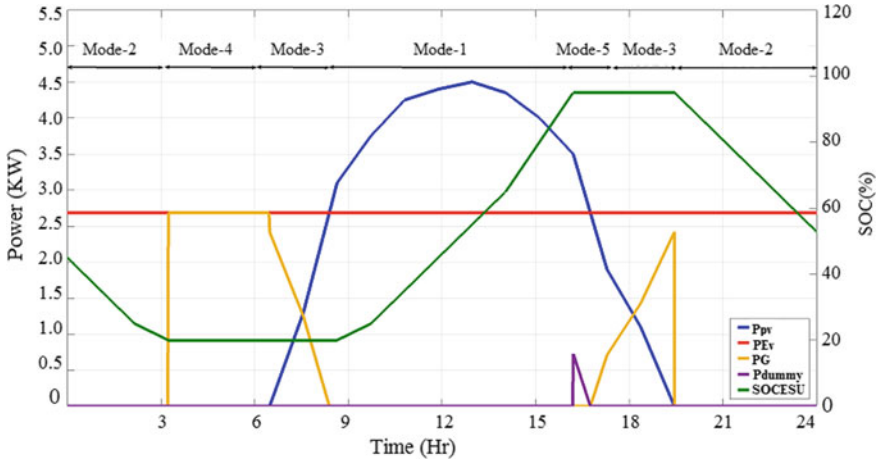


Fig. 9 Operating modes

that proposed system reduces the significant stress on grid during peak intervals. The proposed system can be adopted for high-power rating and a large number of EV capacity charging stations located on highways for fast charging of EVs. For further work, wind power generation sources can be added to solar, ESU, and grid to enhance renewable energy power availability and to reduce stress on the grid and to increase charging station profit. Also, V2G can be implemented for EVs charged at the workplace or parking lot to serve the peak needs of the grid.

References

1. Karki M, Kunwar DR, Sharma B, Paudel S (2019) Power flow management among PV, BESS and grid for EV charging. *Tech J* 1(1):102–112
2. Goli P, Shireen W (2014) PV powered smart charging station for PHEVs. *J Renew Energy* 66:280–287
3. Hassoune A, Khafallah M (2018) Power management strategies of electric vehicle charging station based grid tied PV-battery system. *Int J Renew Energy Res* 8(2)
4. Hassoune A, Khafallah M, Mesbahi A, Benaouinate L, Bouragba T (2018) Control strategies of a smart topology of EVs charging station based grid-tied RES-battery. *Int Rev Electr Eng.* <https://doi.org/10.15866/iree.v13i5.15520>
5. Azad ML, Das S, Sadhu PK (2017) P&O algorithm based MPPT technique for solar PV system under different weather conditions. In: *IEEE international conference on circuit, power and computing technologies (ICCPCT)*. <https://doi.org/10.1109/ICCPCT.2017.8074225>
6. Zhang Y, Cai L (2017) Dynamic charging scheduling for EV parking lots with photovoltaic power system. In: *2017 IEEE 86th vehicular technology conference (VTC-Fall)*, pp 1–2
7. Chandra Mouli GR, Bauer P, Zeman M (2016) System design for a solar powered electric vehicle charging station for workplaces. *Appl Energy* 168:434–443
8. Akshya S, Ravindran A, Srinidhi AS, Panda S, Kumar AG (2017) Grid integration for electric vehicle and photovoltaic panel for a smart home. In: *2017 international conference on circuit, power and computing technologies (ICCPCT)*

Design and Techno-Economic Analysis of Electric Vehicle Charging Station for a Railway Metro Station Parking Area



Sumit Kumar Verma , Sombir Kundu , and Sukhbir Singh 

Abstract This paper investigates the possibility of an electric vehicle (EV) charging station at the parking space of a railway metro station in New Delhi, India. As the solar potential in this part of the world is very high, thereby solar power system is integrated with the grid to meet power requirement for the EVs parked at the railway metro station parking area as well as the other auxiliary load. Three different cases are examined in this paper only grid mode, PV-Grid mode and PV-Grid-Battery mode. All the three cases are compared with each other with respect to cost of energy (COE), net present cost (NPS), electrical output of different components of system and pollutants emitted. Hybrid optimization model for electric renewables (HOMER) software is used for simulation purpose and verification of the results. From the simulation results, PV-Grid system found to be most feasible solution amongst all and grid only mode is least suitable.

Keywords Renewable energy resources · Net present cost · Cost of energy · Hybrid energy system · Battery energy storage

1 Introduction

Future smart grids are anticipated to see two main trends in energy usage:

1. Photovoltaic (PV) systems for large-scale decentralized renewable energy generation.
2. The rise of battery-operated electric cars (EV) for the method of transportation of the future.

S. K. Verma (✉) · S. Kundu · S. Singh
School of Engineering and Technology, Haryana, Bahadurgarh, India
e-mail: sumitkumarverma17@gmail.com

S. Kundu
e-mail: sskundu46@gmail.com

S. Singh
e-mail: sss.singh149@gmail.com

To begin with, solar energy being available to most of the population as compared to other renewable sources as the cost of PV panels has decreased [1]. With their enormous surface area on flat rooftops, parking lots at railway metro stations, industries and commercial complexes in India have a significant potential for solar energy. This potential is now mostly untapped. Second, as compared to fuel cars, EVs offer a carbon free, energy-efficient and silent mode of transportation. Due to the waste of oil and the environmental effect of its usage, on-road quantity of EVs is anticipated to grow rapidly in the coming years. This results in coordination between the efforts of reducing urban pollution and greenhouse gases. Underdeveloped charging infrastructure is one of the most pressing issues in the growth of EVs. PV integration with grid and PV characteristics are considered from [21] and [22]

At present, the transportation sector is going through three revolutions, i.e. autonomous driving, shared mobility and electrification [2]. So, when planning for the charging infrastructure for the electric vehicles, it is crucial to take into account the synergies and potential interactions amongst these three emerging revolutions. With the increase in the adoption of electric vehicles, a new emerging significant electrical load is introduced to the power grid, which will require changes in the infrastructure [3]. The transfer of electrical energy is done only via the distribution grid, which limits the energy that is flowing in the transmission lines [4]. The large-scale reconstruction of the distributions grid to meet the EV's charging requirement is difficult.

According to the study [5, 6], 29% of the greenhouse gases were released from transportation sector, while 28% were released from electric sector in the US. If we take a detail look into the transportation sector, it is seen that big portion of this amount (59%) comes from light-duty vehicles and 70.19% of this is due to the passenger vehicles. From 1990 to 2017, the CO₂ emission caused by passenger vehicles was increased by 20.5% and keep increasing with the growing population. In another study [7, 8], it is revealed that 30% of the EU's total CO₂ emission comes from the transportation and 60.7% of this is due to the passenger vehicles. Although the CO₂ emission is likely to reduce due to the increasing utilization of renewable energy sources, CO₂ emission in transportation sector keeps increasing. This shows that conventional vehicles should be replaced with more environment friendly types such as hydrogen and electric cars.

India is fortunate to have the capability to capture solar energy, so much that it collects almost 5000 trillion kWh of energy per year, with nearly all parts receiving 4–7 kWh/m²/day [2]. In India, electricity from solar energy can be created on large scale. This electricity can increase grid's capacity and can be distributed easily.

The effect of charging station load on grid has been studied by many writers. They discuss several techniques for levelling the load curve. Xu et al. [3] proposed coordinated charging approach to enhance the impacts of charging station on the electric load and EV station profitability. Zhang and Qian [4] proposed a technique for charging electric vehicles at night. Cao et al. [5] suggested an intelligent charging technique for electric vehicles w.r.t time-of-use pricing which reduces network load during peak times. Fazelpour et al. [6] devised a two-phase method to combine intelligent car parks with plug-in hybrid electric vehicle. The programme, for starters,

optimizes the magnitude and quantity of green energy mechanisms as they go through the system. This optimizes the EV charging attributes. This enhances network's quality and efficiency.

Some studies address the issue of where these EV stations should be built and even how big they should be, but they make assumptions regarding demand and operation. To place fast-charging stations in a town, Sadeghi-Barzani et al. [7] utilized a mixed integer nonlinear optimization method, taking into account construction and electrification expenses, electric vehicle power losses and distribution network loss as goals. The model covered the quantity of electric vehicle entering charging station, although it does not consider the station's occupancy time. To minimize power losses and voltage variations in the network, Wang et al. [8] modelled a multi-purpose electric vehicle charging station. They looked at a set demand and did not think about how the billing process worked. To locate the EV station, Sungwoo and Kwasinski [9] utilized geographical and temporal models of EV charging demand. They utilized a queueing theory and a fluid dynamic traffic model. Xiang et al. [10] created a model to help decide where charging stations should be placed and how big they should be. Above-mentioned studies considered load on electrical network but did not consider other types of power resources.

Most of the literature available focusses on the mathematical modelling of the EV charging station and its impact on grid. But, very less emphasis is given on the economic aspect of this, and there is scope for comparative analysis of different configurations power system. Following are the main aims of this paper:

1. Developing an electrical charging system for EVs that is reliable and steady.
2. Ensuring proper power management between hybrid/renewable sources and electric vehicles.
3. Comparing different configurations, viz. only Grid, PV-Grid and PV-Grid-Battery in terms of harmful pollutants emitted, NPC and COE.

2 EV Charging Through PV Source in Parking Area

The Type 2 Mennekes plug is the most used plug-in India for equipment charging. At the level 2 charging power level [39], 1-Ø and 3-Ø charging is possible. But, Chademo and combined charging standard (CCS) DC charging methods might gain popularity due to below factors:

1. By their very nature, both electric vehicles and photovoltaic panels are DC.
2. EV charging may be done in a dynamic mode, in which the charging power varies over time.
3. Vehicle-to-grid (V2G) protocol is facilitated by DC charging.

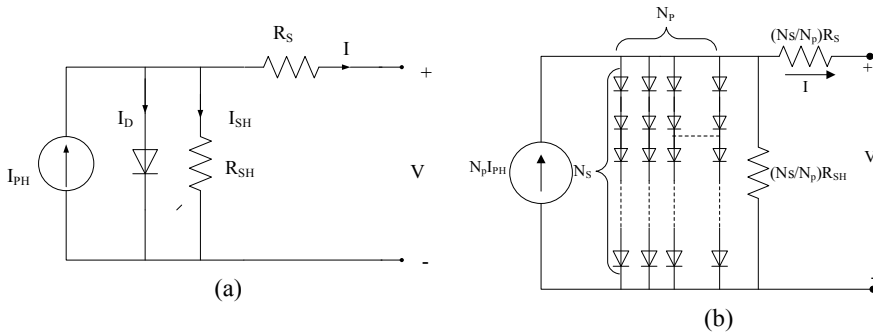


Fig. 1 Diagram of **a** solar cell and **b** solar panel

3 Modelling of Different Components of the Proposed System

3.1 PV System

A photovoltaic panel is the basic technology for converting light energy into green energy. When multiple solar cells are linked in series and parallel, a PV panel is created which generates electricity. An individual PV cell can be thought of as an electrical circuit element. It consists of a diode, a photocurrent generator and two resistors, one in series and the other in parallel. A single-diode solar cell model is then created from this combination.

The solar cell diagram is shown in Fig. 1a, where series and parallel resistances of solar cell are given by R_{sh} and R_s , generally the values of R_{sh} and R_s are enormous and minuscule, respectively. In the corresponding circuit, the currents I_D , I_{SH} , I and I_{PH} represent the diode current, current through shunt resistance, output current of cell and photocurrent of cell, respectively. A schematic representation of a PV module is shown in Fig. 1b. Table 1 [represents the different specifications of a photovoltaic module].

3.2 Battery Energy Storage System (BESS)

Currently, electro-chemical batteries remain most preferred and widely used ESS because of its broad availability. Various kinds of electrical batteries (e.g. Li-ion, Ni–Cd, NaS, lead acid and Ni-MH) are accessible from which plumbing batteries are mostly preferred for various applications because of their less price, recyclability and security. Batteries are connected in series or parallel to generate voltage and current as per the requirement. In general, the size of battery energy storage system in ampere

Table 1 Photovoltaic module’s specifications

Parameters	Value
V_{OC}	47.5 V
I_{SC}	9.64 A
Operating temperature	47°C
Temperature co-efficient	-0.5%/°C
Ground reflection	20%
Derating factor	80%
Efficiency	17%
Life time	25 years
Capital cost	50,000 ₹/kW
Replacement cost	50,000 ₹/kW
O&M cost	100 ₹/kW/year
MPPT system	Horizontal axis continuous adjustment
Parameters	Value

Table 2 Specification details of BESS [28–30]

Parameters	Value
Nominal voltage	12 V
Nominal capacity	3.12 kWh
Maximum capacity	260 Ah
DoD	60%
Roundtrip efficiency	85%
Capital cost	₹25,000
Replacement cost	₹20,000
O&M cost	₹250/year
Life time	10 years
Parameters	Value

hour (CAh) and watt hour (CWh) is vital in determining system’s dependability. Battery energy storage system specification details are shown in Table 2.

4 Input Data and Control Strategy

4.1 Availability of Solar Energy

The data is considered as per the NASA’s surface meteorology and solar energy data for checking the solar energy availability at required location. The solar energy is in

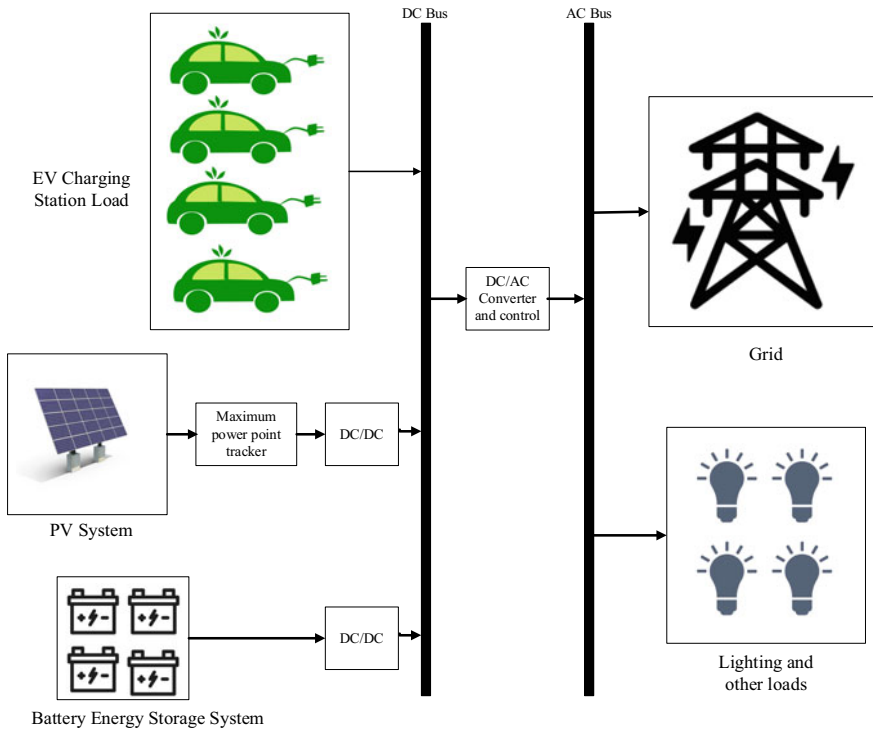


Fig. 2 Proposed system configuration

ample quantity at the required area with monthly average solar radiation amounts to 5.02 kWh/m²/day and average clearness index of 0.58 (Fig. 2).

4.2 Load Profile

Mainly, two types of loads are considered in this work:

- EVs charging station load
- Lighting and other load of the Metro Station.

In the parking area of the metro station, there is space of 20 EVs, and these can be charged simultaneously. The average size of the battery of the EV is assumed to be 40 kWh. The charging station is equipped with level-2 chargers of 10 kW [19] capacity that can fully charge the EV battery in four hours. The peak load of the charging station is 200 kW and with 0.6 load factor average energy consumption is 2640 kWh. The lighting load and other load consist of LED flood lights installed in the compound of the metro station, consumption related to UPS, and equipment

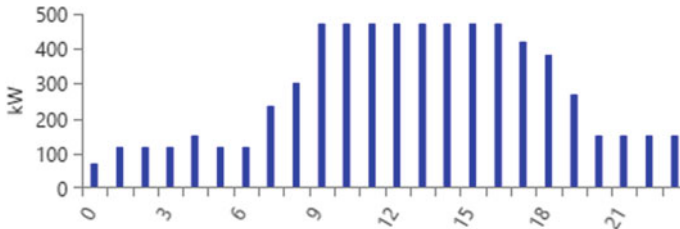


Fig. 3 Day-to-day load profile

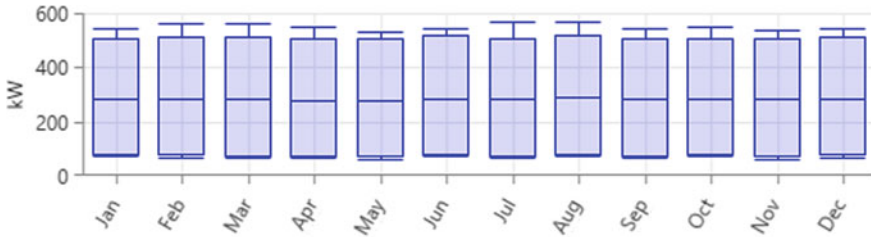


Fig. 4 Monthly load profile

for maintenance and cleaning work inside the metro station premises. This total load accounts to be around 122 kW peak with load factor of 0.3. This accounts 878.5 kWh of average daily energy consumption. The total daily average energy consumption is around 3518 kWh for both EV charging station and other types of electric load of the metro station and commutative load factor of 0.55. Figure 3 depicts the day-to-day load profile, and Fig. 4 depicts the monthly load profile of the system.

4.3 Grid

Grid supply is taken to fulfil the metro station’s power requirement. The average cost of electricity bought from DISCOM is ₹7/kWh [20] and sell back to grid at average price of ₹3.5/kWh. Although the continuity of supply from the grid is assured, the grid electricity is mainly from conventional energy resources, and for integration of RERs to the system not only the green energy will be available but also the cost of energy will be less as compared to the conventional energy resources-based electricity generation system.

4.4 Control Strategy

The cycle charging (CC) approach is a dispatch technique in which a generator operates at full output power whenever it needs to supply the primary load. Generator system cost includes permanent costs like running cost and maintainability cost.

For analysing the electric vehicle charging pattern, following assumptions are established for the first two elements.

- It is expected that EVs arrive at PBES in the same pattern as small motor vehicles purchasing petrol at a petrol station.
- Considering the growth in charging station size, the charging period of electric vehicles is influenced by a number of random variables, thus we assume that the charging time is distributed according to a Gaussian distribution.
- Even if all of the charging stations were full, the waiting EVs would not pick another.
- The technology of the chargers should determine the rating of each charger.

EV charging techniques currently include AC charging, DC charging and wireless charging, amongst others. These technologies are appropriate for a variety of situations. Where automobiles are to be charged for longer durations, AC charging technology is preferred. For charging stations that are for public use and are on inter-city highways, DC charging technology is used. Wireless charging method provides better cost savings and convenience as compared to above mentioned technologies. Also, the future potential of this technology is very promising.

Though, having great cost benefits, still wireless charging is not widely used because of its setup costs and technological advancements. The simulation procedure is then depicted in Fig. 5 and explained as follows.

5 Simulation Results and Discussion

In this work, a comparison is carried out between different combinations, viz. PV-Grid-BESS, PV-Grid and only Grid.

5.1 Only Grid

As the name suggests, only grid is the source of electricity for the total load which is to be served. Only grid-based power system for satisfying electric power demand of EVs charging station in parking of metro station along with its lighting and auxiliary load. In New Delhi, the commercial unit price of electricity is around ₹7/kWh. The net present cost of this configuration is ₹133 million.

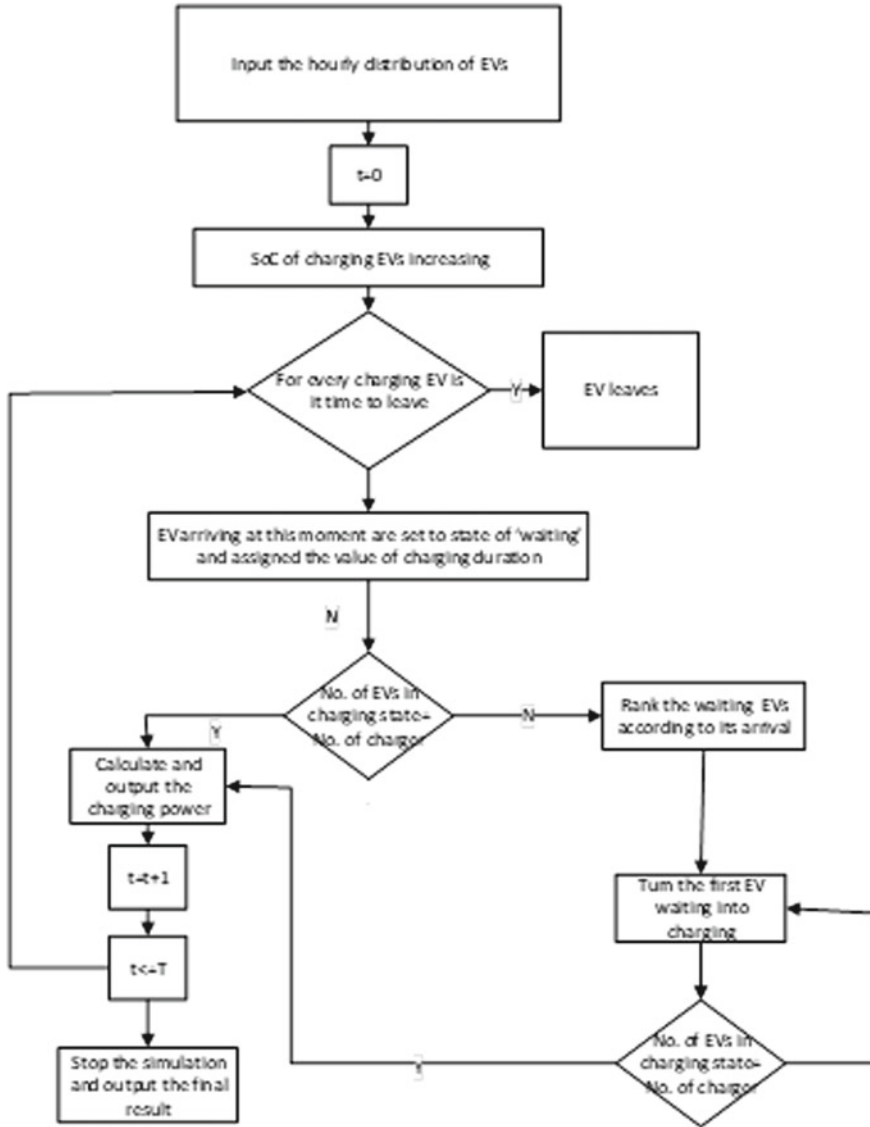
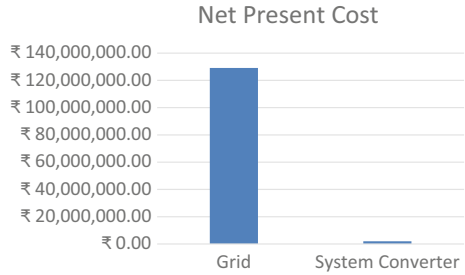


Fig. 5 Cycle charging control strategy

Major portion of the system cost accounts for the O&M cost, i.e. payment to the DISCOM for consumption of electricity. The remaining portion of the cost goes to the converter system cost, i.e. capital cost, replacement cost and salvage value. The COE for this case is ₹7.9/kWh for the period of 25 years. Figure 6 shows the cost summary of this case, where it can be clearly seen that major portion of the cost is related to grid and some system converter accounts the remaining cost.

Fig. 6 Graph for grid only case



As the grid is the only source of power, there is 0% RERs share. Figure 7 shows electricity consumption across the year. Electricity purchased per year is 1,426,734 kWh. Table 3 depicted the quantity and type of harmful pollutants emitted in case when the grid is the only source of electricity. In this case, there is small capacity shortage (9 kWhr/year) also occurs due to maintenance work on the grid network.

However, the capital cost in this case is zero because no initial investment is required for the infrastructure by the consumer, but O&M cost is on higher side in the electricity bills to be paid to DICOM (Table 4).

5.2 PV-Grid

In this case, PV system is also integrated to the grid. As only 7000 m² rooftop area is available and usable area for PV installation is 500 m², thus the total installation of PV is only 500 kW as per the area availability. The NPC of the system decrease at a good amount, i.e. ₹85 million and COE also reduces up to ₹4.59/kWh. The net energy bought from the network reduces as electricity is now also available from the PV system. Figure 7 shows the cost summary of PV-Grid case. From the figure, it can be observed that O&M charges from the grid reduces to ₹85.6 million from ₹129 million (Tables 5 and 6).

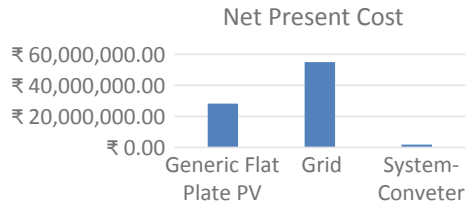
Table 3 Cost summary for grid only case

Component	Capital cost	Replacement cost	O&M cost	Fuel cost	Salvage	Total
Grid	₹0.00	₹0.00	₹12,91,08,932.65	₹0.00	₹0.00	₹12,91,08,932.65
System converter	₹14,92,968.75	₹6,33,427.57	₹0.00	₹0.00	₹1,19,217.46	₹20,07,178.86
System	₹14,92,968.75	₹6,33,427.57	₹12,91,08,932.65	₹0.00	₹1,19,217.46	₹13,11,16,111.51

Table 4 Pollutants emitted in grid only case

Quantity	Value	Units
Carbon dioxide	901,696	Kg/yr
Carbon monoxide	0	Kg/yr
Unburned carbons	0	Kg/yr
Particulate matter	0	Kg/yr
Sulphur dioxide	3909	Kg/yr
Nitrogen oxides	1912	Kg/yr

Fig. 7 Graph for PV-grid case



Of the total consumption, 45.2% of the electricity is purchased from the grid and PV panels generates accounts 54.2%. The outage due to maintenance of grid network now covered by PV-Battery combination and in this case net power outage occurs. The amount of pollutants emitted in this case is significantly lower as compared to previous case as shown in Table 4 (Table 7).

5.3 PV-Grid-Battery

In PV-Grid-Battery case, the COE of this system was reduced significantly and found to be ₹4.62/kWh. The NPC of the system is also reduced to ₹85.6 million. Figure 8 shows the cost summary of PV-Grid-Battery case. This reduction in COE and NPC is mainly due to electricity purchased from the grid decreases significantly on yearly basis and generation from the PV system increased significantly. The surplus power supplied back to grid is also a factor for reduced COE and NPC in this case. Also, the pollutants emitted reduces significantly in this case (Table 6) because dependency on grid is reduced which is the main source of pollutants. The power outage is 0 kWh in Grid-PV-BESS case as the maintenance and faults mainly occurs on grid network and in this case the grid dependency is very low. The power outage is 0 kWh in PV-Grid-BESS case (Tables 8, 9 and 10).

Table 5 Cost summary for PV-Grid case

Component	Capital cost	Replacement cost	O&M cost	Fuel cost	Salvage	Total
Generic flat plate PV	₹2,50,00,000.00	₹0.00	₹32,31,879.14	₹0.00	₹0.00	₹2,82,31,879.14
Grid	₹0.00	₹0.00	₹5,49,53,296.50	₹0.00	₹0.00	₹5,49,53,296.50
System converter	₹13,50,781.55	₹5,73,101.13	₹0.00	₹0.00	₹1,07,863.42	₹18,16,019.26
System	₹2,63,50,781.55	₹5,73,101.13	₹5,81,85,175.64	₹0.00	₹1,07,863.42	₹8,50,01,194.90

Table 6 Electricity purchased/sold from/to the grid across the year

Month	Energy purchased (kWh)	Energy sold (kWh)	Net energy purchased (kWh)	Peak demand (kW)	Energy charges
Jan	62,936.692022	14,359.824417	48,576.867605	278.909574	₹390,297.46
Feb	51,977.786890	13,417.870262	38,559.916629	265.019401	₹316,881.96
Mar	55,160.281627	15,915.893140	39,244.388487	262.261352	₹330,416.35
Apr	49,766.915978	14,097.734231	35,669.181747	249.245082	₹299,026.34
May	51,692.433290	12,028.802909	39,663.630381	260.225193	₹319,746.22
Jun	52,130.509006	9058.052882	43,072.456124	273.925686	₹333,210.38
Jul	61,414.537634	7047.012646	54,367.524988	284.545299	₹405,237.22
Aug	63,859.380739	7875.840399	55,983.540339	270.758101	₹419,450.22
Sep	56,475.003706	14,455.741592	42,019.262114	253.754691	₹344,729.93
Oct	52,133.717591	15,276.145016	36,857.572575	244.888857	₹311,469.52
Nov	58,653.316902	14,839.827911	43,813.488991	281.875786	₹358,633.82
Dec	65,971.665337	11,435.146784	54,536.518553	281.296860	₹421,778.64
Annual	682,172.240721	149,807.892188	532,364.348533	284.545299	₹4,250,878.06

Table 7 Pollutants emitted in PV-Grid case

Quantity	Value	Units
Carbon dioxide	43,133	Kg/yr
Carbon monoxide	0	Kg/yr
Unburned carbons	0	Kg/yr
Particulate matter	0	Kg/yr
Sulphur dioxide	1869	Kg/yr
Nitrogen oxides	914	Kg/yr

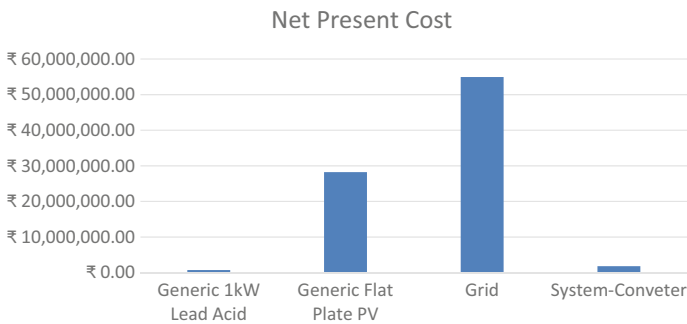


Fig. 8 Graph for PV-Grid-BESS Case

Table 8 Cost summary for PV-Grid-BESS case

Component	Capital cost	Replacement cost	O&M cost	Fuel cost	Salvage	Total
Generic 1 kW lead acid	₹3,75,000.00	₹2,65,031.29	₹48,478.19	₹0.00	₹35,933.68	₹7,24,443.16
Generic flat Plate PV	₹2,50,00,000.00	₹0.00	₹32,31,879.14	₹0.00	₹0.00	₹2,82,31,879.14
Grid	₹0.00	₹0.00	₹5,49,53,296.50	₹0.00	₹0.00	₹5,49,53,296.50
System converter	₹13,44,856.77	₹5,70,587.53	₹0.00	₹0.00	₹1,07,390.33	₹18,08,053.97
System	₹2,67,19,856.77	₹8,35,618.82	₹5,82,33,653.83	₹0.00	₹1,43,324.01	₹8,56,45,805.41

Table 9 Electricity purchased/sold from/to the grid across the year

Month	Energy purchased (kWh)	Energy sold (kWh)	Net energy purchased (kWh)	Peak demand (kW)	Energy charges
Jan	62,936.692022	14,359.824417	48,576.867605	278.909574	₹390,297.46
Feb	51,977.786890	13,417.870262	38,559.916629	265.019401	₹316,881.96
Mar	55,160.281627	15,915.893140	39,244.388487	262.261352	₹330,416.35
Apr	49,766.915978	14,097.734231	35,669.181747	249.245082	₹299,026.34
May	51,692.433290	12,028.802909	39,663.630381	260.225193	₹319,746.22
Jun	52,130.509006	9058.052882	43,072.456124	273.925686	₹333,210.38
Jul	61,414.537634	7047.012646	54,367.524988	284.545299	₹405,237.22
Aug	63,859.380739	7875.840399	55,983.540339	270.758101	₹419,450.22
Sep	56,475.003706	14,455.741592	42,019.262114	253.754691	₹344,729.93
Oct	52,133.717591	15,276.145016	36,857.572575	244.888857	₹311,469.52
Nov	58,653.316902	14,839.827911	43,813.488991	281.875786	₹358,633.82
Dec	65,971.665337	11,435.146784	54,536.518553	281.296860	₹421,778.64
Annual	682,172.240721	149,807.892188	532,364.348533	284.545299	₹4,250,878.06

Table 10 Pollutants emitted in PV-Grid-Battery case

Quantity	Value	Units
Carbon dioxide	43,133	kg/yr
Carbon monoxide	0	kg/yr
Unburned carbons	0	kg/yr
Particulate matter	0	kg/yr
Sulphur dioxide	1869	kg/yr
Nitrogen oxides	914	kg/yr

6 Conclusions

PV energy and electric vehicles are critical components in reducing CO₂ emissions and fossil fuel usage. Despite the fact that electric vehicles are more cost-effective and ecologically benign than gasoline cars, their adoption is limited for a variety of reasons. Lack of planning in electric vehicle’s charging and efficient design of charging facilities are the most evident of those reasons. If the charging facility and underground metro station rely exclusively on the central grid to fulfil the load requirement, the distribution system will be overburdened, which is undesirable. This would put a lot of strain on the main grid, which could happen during peak demand hours, resulting in higher operational costs and more greenhouse gas emissions. In this context, creating a specialized charging station in parking of a metro station can reduce reliance on the main grid while also allowing for more efficient load scheduling for electric vehicles and underground metro station. In this thesis, a

comparison is made between three cases, viz. only grid, PV-Grid-BESS and PV-Grid is made for a case study of a metro station. The load of the metro station consists of a charging station of EVs and other auxiliary load like lighting load, UPS load, etc. From the simulation, it is found that grid only mode has highest COE i.e. ₹7.9/kWh and highest NPC ₹133 million. In PV-Grid-BESS case, the COE is ₹4.62/kWh, and NPC is ₹85.6 million. In the third system, i.e. PV-Grid system, the COE and NPC is least, i.e. 4.59/kWh and ₹85 million. The pollutants emitted from the system is highest in case of grid only case, and least in PV-Grid case.

From the above discussion, it is concluded that PV-Grid system is best suited for fulfilling the electricity demand of lighting load for a underground metro station. In the coming years, with the technological advancements, the cost of PV system and other power electronics converter system will decrease and fossil fuel-based electricity generation cost will increase. So, it is suggested that PV-Grid based configuration is best suited for the particular case study.

References

1. Photovoltaic (PV) pricing trends: historical, recent, and near-term projections. National Renewable Energy Laboratory (2021)
2. Ghosh A (2020) Possibilities and challenges for the inclusion of the electric vehicle (EV) to reduce the carbon footprint in the transport sector: a review. *Energies* 13:2602
3. Green RC, Wang L, Alam M (2011) The impact of plug-in hybrid electric vehicles on distribution networks: a review and outlook. *Renew Sustain Energy Rev* 15:544–553
4. Zhang C, Huang Q, Tian J, Chen L, Cao Y, Zhang R (2011) Smart grid facing the new challenge: the management of electric vehicle charging loads. *Energy Procedia* 12:98–103
5. CO, Carbon Dioxide, and Nitrous Oxide N₂O. “Fast facts.” *Transportation* 6, no. 7,000 (2017): 8–000
6. US EPA (2020) Fast facts on transportation greenhouse gas emissions | US EPA. [online] Available at: <https://www.epa.gov/greenvehicles/fast-facts-transportation-greenhouse-gas-emissions>. Accessed 12 Sept 2021
7. Rau A, Bongardt S, Schmid GD (2010) Facts and figures on transport. Technical report, GTZ Transport Policy Advisory Service
8. Transport and Environment, CO₂ emissions from cars: the facts report, April 2019
9. Ministry of Transport and Highways India 2021. <https://morth.nic.in/>. Accessed on 15 Aug 2021
10. Chandra Mouli GR, Bauer P, Wijekoon T, Panosyan A, Barthlein E-M (2016) Design of a power-electronic-assisted OLTC for grid voltage regulation. *IEEE Trans Power Delivery* 30:1086–1095
11. Xu Z, Hu Z, Song Y, Luo Z, Zhan K, Wu J (2012) Coordinated charging strategy for PEVs charging stations. In: 2012 IEEE power and energy society general meeting, San Diego, CA, pp 1–8. <https://doi.org/10.1109/PESGM.2012.6345045>
12. Zhang P, Qian K (2012) A methodology for optimization of power systems demand due to electric vehicle charging load. *IEEE Trans Power Syst* 27(3):1628–1636
13. Cao Y, Tang S, Li C, Zhang P, Tan Y, Zhang Z et al (2012) An optimized EV charging model considering TOU price and SOC curve. *IEEE Trans Smart Grid* 3(1):388–393. <https://doi.org/10.1109/TSG.2011.2159630>
14. Farivar F, Majid V, Omid R, Rosen MA (2014) Intelligent optimization to integrate a plug-in hybrid electric vehicle smart parking lot with renewable energy resources and enhance

- grid characteristics. *Energy Convers Manage* 77:250–261. <https://doi.org/10.1016/j.enconman.2013.09.006>.
15. Sadeghi-Barzani P, Rajabi-Ghahnavieh A, Kazemi Karegar H (2014) Optimal fast charging station placing and sizing. *Appl Energy* 125:289–299
 16. Wang G, Xu Z, Wen F, Wong KP (2013) Traffic-constrained multiobjective planning of electric-vehicle charging stations. *IEEE Trans Power Deliv* 28:2363–2372
 17. Bae S, Kwasinski A (2012) Spatial and temporal model of electric vehicle charging demand. *IEEE Trans Power Syst* 3(1)
 18. Xiang Y, Liu J, Li R, Li F, Gu C, Tang S (2016) Economic planning of electric vehicle charging stations considering traffic constraints and load profile templates. *Appl Energy* 178:647–559. <https://doi.org/10.1016/j.apenergy.2016.06.021>
 19. NITI Aayog, RMI India, Rocky Mountain Institute, Electric Vehicle Charging Infrastructure, a Guide For DISCOM Readiness; May 2020
 20. Electricity Tariff Schedule For FY 2020–21—BRPL, BYPL, TPDDL & NDMC
 21. Sombir S, Singh M (2020) Voltage and frequency control of self excited induction generator integrated with PV system, pp 4306–4311
 22. Kundu S, Singh M, Giri AK (2021) Design and control of a standalone wind–solar system with SEIG feeding linear/nonlinear loads, pp 317–327

IoT-Assisted Framework for Efficient Healthcare Monitoring and Alert Unit for a Patient



Suneeta S. Raykar and Vinayak N. Shet

Abstract The remote healthcare monitoring framework is the fusion of hardware units using wearable sensor nodes, cloud storage, and mobile communication. In the countries like India, the availability of medical facilities is not uniform across all places. There is a need for increasing the effectiveness of the medical system, thus accelerating the medical services. Internet of Things (IoT)-assisted healthcare system helps in the diagnosis of disease at an early stage and saves the patients from critical events. The knowledge of understanding the vital parameters of any individual and taking adequate care of health is becoming essential. Connecting people with expertise in the field of medicine with the acquaintance of electronic gadgets is the primary objective of the proposed paper. The proposed framework demonstrated that the aids of I-connect (Internet of Things) with machine learning model increased the efficiency of the medical sector. Monitoring of vital parameters of patients remotely by the specialists will help to seek advice and alert the patient with notification. Outcomes of the proposed IoT-enabled health care prove better returns compared to the traditional healthcare system in place.

Keywords Health care · Internet of Things · Wearable sensor nodes · Mobile application

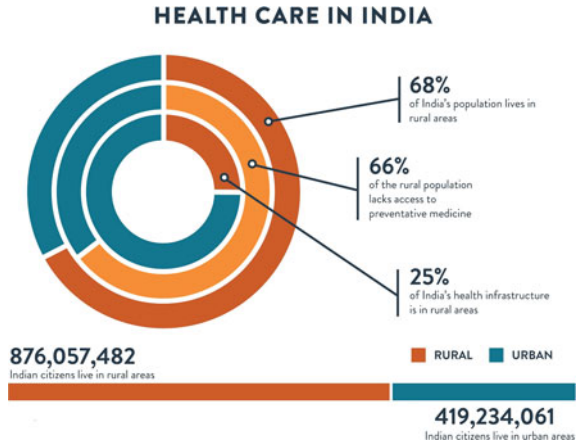
1 Introduction

According to the World Health Organization, health care embraces all the goods and services designed to promote health, including “preventive, curative, and palliative interventions, whether directed to individuals or populations” [1]. Indian healthcare situation gives a spectrum of complementary scenarios. When we visualize this

S. S. Raykar (✉) · V. N. Shet
Department of Electrical and Electronics Goa College of Engineering, Goa University, Goa, India
e-mail: suneeta@gec.ac.in

V. N. Shet
e-mail: vns@gec.ac.in

Fig. 1 Rural versus urban healthcare system



spectrum in terms of facility, services, and availability; it is observed that on one side of the band, the extravagant structures are delivering high-tech medicare to the well-heeled, on the other side, there is the very scanty availability of the medical facility to the most of remote parts of rural India. With the rapid pace of change currently being witnessed, this spectrum is likely to widen further, presenting even more complexity in the future [2].

The present statistical study on the population and medical facility available in India is illustrated using the chart shown in Fig. 1. India is populated densely with limited medical infrastructure as compared to urban India. 66% rural population lacks access to preventative medicine, only 25% of the medical infrastructure is available to the rural population. The healthcare services and systems in India are still developing and have challenges of workforce shortages, absenteeism, poor infrastructure, and quality of care [3]. The main reason for poor health in rural regions of India is probably due to the following reasons [4].

- (1) Poor knowledge in understanding early detection of symptoms and taking preventative care.
- (2) Barrier in reaching the medical center/physician, testing laboratory due to transportation difficulty, cost in treatment, and spending a long time in getting appointments with doctors.
- (3) Low priority or negligence of health due to poverty and due to nonavailability of continuous accessibility of service. People have no sufficient time for proper health management due to a heavy workload or poor financial status.

In general, the poorer areas of northern and central India have lower densities of health workers compared to the southern states [5]. These challenges need some solution to improving the healthcare system. The practice of wearable sensors benefits in improving the standard of healthcare amenities. Continuous advances in the semiconductor technology industry have led to sensors and microcontrollers that are smaller in size, faster in operation, low in power consumption, and affordable

in cost. Furthermore, patients who do not monitor the vital parameters regularly nor report to the doctor will discover health catastrophes. Statistical reports reveal that many people lose their lives every month due to insufficient knowledge about the health parameters.

The traditional hospital centric and doctor centered health management model appear to be incapable of adequately dealing with the increasing number of patients and diseases [6]. In this regard, the proposed hardware aims toward finding the solution to the problem faced by the people. Providing low-cost internet-enabled hardware to an individual helps in monitoring all the vital parameters of the human health condition. These parameters can be digitally transmitted and stored in the cloud. The doctor/physician can read the parameters using a smartphone or computer. The parameters will be shared or reported by the registered patient to the doctor using a suitable application. A patient can get advice and virtual consultation through this platform.

2 Traditional Health care versus IoT Assisted Health care

In the traditional healthcare system, data collected from the patient is analyzed traditionally, hence they are not helpful in the early prediction of complex health conditions. Data generated using IoT-assisted health care is used in the prediction and early detection of disease. Self-monitoring of parameters is possible in IoT-assisted health care thereby it helps to get remote monitoring of the health status from medical experts. During an ongoing pandemic situation, it helps to check regular monitoring of vital parameters of an elderly patient by staying at home. IoT-assisted health care supports the patient-centric system.

Quick diagnosis of disease and subsequently future health condition can be analyzed with the help of data analytic. Cloud-based storage help to analyze structured and unstructured data generated in the healthcare system. Data gathering in traditional health care is limited to the time that patients spend in a clinic or hospital, with modern health care, it can be extended to collect data from wearable sensor nodes as per the requirements. Consequently, it affords to know how symptoms fluctuate over a period and in the context of different activities.

2.1 Existing IoT Assisted Healthcare Applications

As the health consciousness is increased among the people, the medical healthcare industry has become the emerging area of research and realized the need for a smart and interactive healthcare system that will provide more cost-effective and efficient treatment [7]. Demographic aging is changing the demands on healthcare services, and older people are increasingly self-managing their long-term conditions with the increased use of mobile phones and technologies [8]. Thereby smart

healthcare system in a secure manner is gaining more interest among physicians and patients. Table 1 gives the various solution to smart health care proposed by various researchers, and the challenges in the research findings is tabulated. The real-time sensor-based monitoring of health parameters and reporting to the physician for further investigation is considered in this work. The threshold data of the vital parameters is considered in understanding sensor anomaly detection at the hardware unit.

This research paper also explores the impact of IoT technology and machine learning algorithm in the development of smart health care. Internet of Things (IoT) and machine learning components in the proposed design make the system smarter.

3 Design of IoT-Assisted Healthcare System

The proposed model has four blocks:

Acquire data: The data is captured using sensor nodes from the human body. Digital sensors are selected to reduce the time required for the transmission. Temperature sensor, heart rate sensor, and oxygen saturation sensor are selected in the proposed unit.

Gateway node: Data collected from the sensor node is transmitted to the gateway or a microcontroller unit equipped with a communication module. Sensor anomaly detection algorithm developed in this work helps to detect malfunctioning of sensor unit. Only valid information from the sensor is transferred to the cloud. The microcontroller unit selected in this work is integrated with a Wi-Fi module to transfer the data to the chosen cloud unit.

Cloud storage: The information from the sensor is transferred to the cloud storage. The sensor data from the cloud is further accessed remotely using a designed mobile application. The patient information is securely stored in the database.

Prediction model with Mobile Application: Prediction model in early detection of the disease along with user-friendly interface is developed to virtually monitor the health-related signals of a person. The framework is the fusion of four main units, sensors, a control unit or gateway, cloud storage, and a prediction model with mobile application. Mobile application is developed by considering the requirement of patients and doctors. The block diagram of the proposed model is represented in Fig. 2. The selection and configuration of each block are described in the following sections.

3.1 Selection of Wearable Sensor Nodes

Wearable sensors, being progressively more comfortable and less obtrusive, are appropriate for monitoring vital parameters of a human body without interrupting their daily activities [19]. The sensors can measure several physiological

Table 1 Comparative research challenges and contribution of IoT-based healthcare system

No	Title of the paper	Contribution	Challenges
1	An intelligent real-time IoT-based system for monitoring ICU patients [9]	Helps in monitoring ICU patient accurately	Accuracy in the data needs an improvement
2	Smart health: A novel paradigm to control the chikungunya virus [10]	Real-time monitor and feedback system	A compulsion to implement data security
3	A reliable IoT system for personal healthcare devices [11]	Assisted in knowing health parameters	Only a specific fault algorithm is implemented
4	Delivering home health care through a cloud-based smart home environment [12]	Convenience for old and disabled people	Alert message is not included
5	Simultaneously aided diagnosis model for outpatient department via healthcare big data analytics [13]	Machine learning-based healthcare delivery	Simulation studies should be replaced using sensors
6	Wearable IoT sensor-based healthcare system for identifying and controlling chikungunya virus [14]	Quick alert notification and efficient system	High power consumption needs to be addressed
7	Cloud-centric IoT-based disease diagnosis healthcare framework [15]	Sensors are used to collect real-time feedback	Lacks security issues
8	Technological improvement in modern healthcare applications using the Internet of Things (IoT) [16]	Safety, security, and timely treatment factors	Urge for real-time implementation
9	An Internet of Things (IoT) network system for connected safety and health monitoring applications [17]	Monitoring of environment/workers health	Verification of security algorithm
10	Novel AI-Enabled Framework to Diagnose Coronavirus COVID-19 Using Smartphone Embedded Sensors [18]	Low-cost solution using mobile sensor	Issues in reliability of the mobile sensor

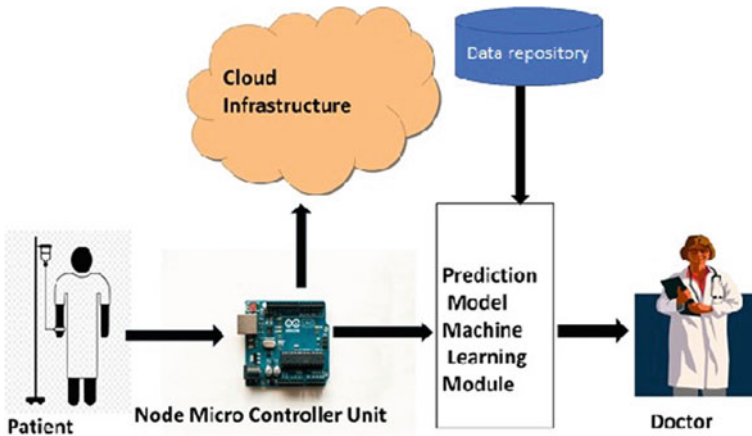


Fig. 2 Proposed IoT-assisted healthcare model

signals/parameters of an individual by placing them at different locations of the body. The advancement in low-power, compact wearable (sensors, actuators, antennas, and smart textiles), inexpensive computing, and storage devices coupled with modern communication technologies paves the way for low-cost, unobtrusive, and long-term health monitoring systems. The selected sensors are the body temperature sensor, heartbeat sensor, and oxygen saturation sensor. More sensors can be interfaced with the gateway node based on the requirement of the patient. The projected model demonstrated using only three sensors for measurement and reporting purposes. The proposed system is designed using low-cost digital sensors are tabulated in Table 2.

MAX30205: Is a digital IC, used to measure human body temperature. I2C port is used to interface the sensor to the microcontroller. The readings obtained from digital sensors are more precise in monitoring human body temperature. The sensor readings are calibrated to obtain the actual value by comparing with standard equipment used for measuring. The accuracy of the body temperature measured using MAX 30205 is found more accurate as compared to sensors used in the earlier design (LM 35 and DS 18B20).

MAX 30102: Heart beat can be measured based on optical power variation as light is scattered or absorbed during its path through the blood as the heartbeat changes. The sensor works on the principle of photoplethysmography (PPG) which is a non-invasive method of measuring the variation in blood volume in tissues using a light source and a detector [20].

Table 2 Selection of sensor nodes

Sensor	Functionality
Max 30102	Heart beat sensor
Max 30205	Body temperature
Max 30105	Oxygen saturation

MAX 30105: Pulse oximeter is used as a non-invasive measurement of oxygen saturation. Based on the recorded data, medical intervention is made, and an alarm system alerts the patients if the oxygen saturation reaches a critical level. MAX 30102 sensor can be also used in the measurement of oxygen saturation level. The hardware unit is configured using only MAX 30102 sensor: The sensor used in the proposed hardware may malfunction due to physical damage or environmental interference or blocked due to shortage of power supply. The proposed Algorithm 1 is implemented at the gateway node,

Algorithm 1 Processing sensor data

Input: Sensor input values

Output: Sensor data uploading to cloud storage

Result: Accept or rejection of data and generation of alert message

Start:

Step 1: Read the sensor value from the configured port used for interfacing for each received data d_i for an interval T

Step 2: Compare the sensor reading d_i with the lookup table values stored as reference values according to vital parameters

Step 3: if $d_i < \text{threshold}$ or $d_i > K * \text{threshold}$ assume a chosen value of $K > 1$. reject the sensor reading and go to step 1
else

continue

Step 4: If reading d_i is greater than $K * \text{threshold}$ ($0 < K < 1$) generate alarm signal

Step 5: Delay of t (5) seconds to obtain the stabilized reading, and then transfer the data to the cloud storage

Step 6: End

3.2 Selection of the Gateway Node

Various microcontroller (MCU) performance was observed by interfacing sensors. Based on the requirement of interfacing ports on the gateway node, power consumption, and communication port available on the MCU, a few microcontrollers such as Arduino Uno, ESP 8266, Raspberry Pi, Bolt, MSP 430, and ESP 32 MCU are compared. ESP 32 microcontroller is selected to build the final prototype due to its processing speed, ports, power rating, and its size. The hardware unit used in the proposed system is having the following specifications.

Microcontroller ESP 32, consisting of 1 W speaker, Type C USB connector, Grove (I2C connector), TF Carder, Ip5306 (I2C), Microphone, and display section (LCD panel). A chargeable battery of 3.7 V, 110 mAh. The weight of the unit is 200 g, size of the unit is 55 mm × 55 mm × 17 mm in dimension. The sensor readings are collected at the gateway node are represented in Fig. 3. The recorded data of a patient on the LCD panel is heart rate (HR) 97 beats per minute, oxygen saturation level (SpO2) 97%, and body temperature 98.39 °F. The delay of 5 s is configured in the gateway node to obtain stabilized values of all the sensors. If the sensor values exceed the

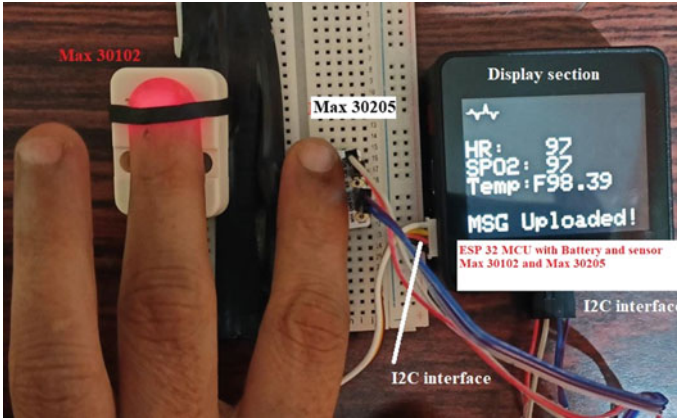
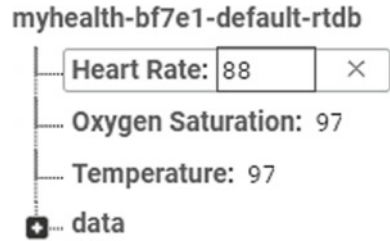


Fig. 3 Sensors attached to the hardware unit

Fig. 4 Sensor data recorded in the Firebase cloud



threshold value (based on patient health condition and previous history), an alarm will trigger at the hardware unit. This will also send a message to the caretaker. Under the normal conditions, sensor data will be uploaded to the cloud storage, and an appropriate message gets displayed on the hardware unit. This ensures the user will understand the information is communicated to the cloud server for seeking further assistance.

Collected data from the sensor is transferred to the cloud storage using patient ID and credentials. Various cloud platforms like Firebase, ThingSpeak, Ubidots, and IBM Bluemix features were compared while selecting the cloud services. The hardware unit transfers the sensor data to the Firebase cloud structure is represented in Fig. 4. The figure represents the patient ID and various field values stored.

3.3 Mobile Application Interface for Health care

The mobile application is created to fulfill the basic needs of the patient and doctor. Input and feedback are collected from various users through google forms. The

service of the developed application is available only to the registered user to safeguard the patient data from unauthorized access. Mobile application (app) is developed to know the patient parameter measured using the hardware unit attached to the human body. We have developed a mobile app using a freeware service provided by the Thunkable app. Thunkable is a cross-platform app builder that means all apps built on this platform work for both Android and iOS devices [21]. The application demonstrated the use of remote accessing health parameters. Mobile application is verified to collect the sensor data is depicted in Fig. 5. The display option in the mobile app collects the sensor data of the registered patient. It can be further viewed by the doctor by using a registered app and knowing the patient’s email ID.

In addition to the regular monitoring and cautioning of the patient, a prediction model is developed to support the doctor in the analysis of the disease. The prediction model is created to understand the patient’s health parameters in an effectual way.

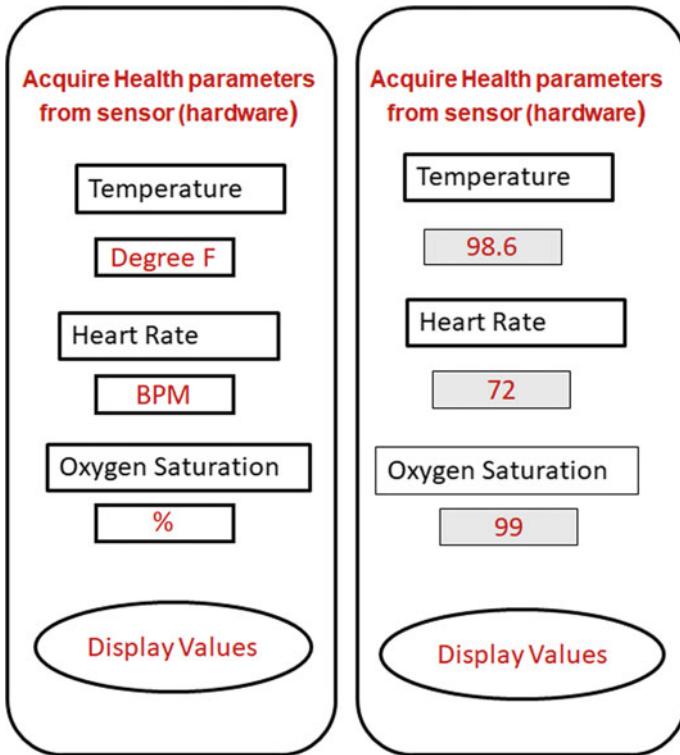


Fig. 5 Mobile app to display sensor data from Firebase cloud

4 Prediction Model Using Machine Learning

The methodology used in the prediction of a particular disease is proposed using an algorithm. In the proposed model, heart disease dataset is used to construct the prediction model. The prediction model is trained using a machine learning algorithm by selecting appropriate attributes from the given dataset. Outcome of the model is to predict the chances of whether the patient is having heart disease or not. The prediction model can able to receive data entered by the user or data from cloud storage. The input parameters are entered based on the patient database to obtain the result. Selection of data source: Kaggle heart disease dataset is used in training and testing of the prediction model [22]. Dataset attributes are represented in Table 3.

The proposed Algorithm 2 is used in the development of the prediction model.

Algorithm 2 Proposed prediction algorithm

Input: Dataset D [RXC]

Output: Confusion matrix of machine learning algorithm

Result: Prediction output in terms of Yes or No

Start:

Step 1: Apply various feature selection algorithms and for each method calculate performance of the selected machine learning algorithm

Step 2: Save the reduced dataset as D1 with extracted feature, partition the data as 80% train and 20% test data. Select the best machine learning algorithm for training

Step 3: Train the selected machine learning algorithm to predict the outcome

Step 4: Test the algorithm with 20% dataset

Step 5: Verify the results and save

Step 6: Measure the performance of machine learning with new data collected, Display the results using the user interface application

Stop

Table 3 Attributes of heart disease dataset

Attributes	Description
Age	Age in years
Sex	(Male is (0) or female is (1))
cp	(chest pain) expressed as 0,1,2
restbp	(blood pressure) systolic blood pressure
fbs	(blood sugar) fasting blood sugar
restecg	(rest ECG) ECG waveform
thalach	(maximum heart rate) heart rate
exang	(angina pain) pain due to exercise
oldpeak	(ECG information) slope of ST segment
Slope	(ECG information)
ca	(Colored by fluoroscopy)
thal	Stress information
Target	Presence of disease (1) absence(0)

Table 4 Comparison of accuracy of machine learning algorithms

Algorithm	Accuracy (%)
Logistic regression	85.00
Naive Bayes	83.00
Support vector machine	85.00
K's-nearest neighbor	78.69
Random forest	90.16

Dataset considered in this work is retrieved from the Cleveland Clinic Foundation. It consists of 303 records; it has 165 instances with heart disease and 138 instances with normal cases. Dataset D is clustered using cross-validation method and partitioned into train dataset and test dataset. Dataset is preprocessed to remove noisy data. Dimension reduction techniques are used to obtain most important input attributes from the selected dataset.

The algorithm is tested on five different machine learning algorithm to select the most appropriate algorithm. The comparison of random forest with the other four machine learning algorithms selected are LR logistic regression, Naive Bayes (NB), support vector machine (SVM), and K's-nearest neighbor (KNN). The machine learning algorithm using a random forest is selected to know the prediction of getting chances of heart disease to a person. Table 4 represents machine learning prediction accuracy achieved using five different algorithms.

4.1 Mobile Application for the Prediction Model

The mobile application is developed to verify the results of the prediction model. A trained prediction model assists the doctor in knowing the health status of a patient. The screenshot of the developed application is represented in Fig. 6. The prediction model designed will work as back end service to the mobile application. Random forest algorithm is used in user-friendly application. The developed mobile application assists in determining whether the patient will suffer from heart disease or not. Patient health attributes are personally entered in the designed mobile application to know the prediction status. This model helps the physician to understand the patient data in a more significant manner. The data fed to the application is collected from the user database. The application accepts the most important eight attributes from the dataset. They are patient sex, chest pain type, maximum heart rate, exercise due to angina, ECG wave oldpeak, ECG ST slope (up, down, normal) of the ECG, major vessels colored by fluoroscopy, and stress test details (thal). The feeding of the attributes in the prediction application determines the detection of a person has heart disease or not.

Fig. 6 Prediction of heart disease using mobile app

The screenshot displays a mobile application interface for heart disease prediction. At the top, there is a red-bordered header labeled "IoT healthcare". Below it is a white box with the title "Heart Disease Prediction". The interface contains several input fields, each with a label and a numerical value: "Sex male 0, female 1" with value "1"; "Chest pain" with value "0"; "Maximum heart rate" with value "78"; "Angina pain" with value "1"; "Old peak: ECG wave" with value "2"; "ECG ST segment" with value "1"; "CA No of major vessels" with value "2"; and "Thal" with value "1". At the bottom, there is a blue-bordered button labeled "Predict Result".

4.2 Feedback Collected from Physicians

The developed mobile applications, hardware unit in smart health care, and the results were demonstrated to the physicians to collect their feedback. The feedback collected from the several doctors regarding the developed mobile application and hardware unit in collecting data is summarized with the recommendation below.

- (1) Safety of the hardware unit: It is necessary to protect the hardware unit from water damage and be weatherproof. The unit should be mobile and light in weight with less obstruction. As the designed unit is having these features,

it will help the community to wear the gadget without affecting their daily activities.

- (2) Security regarding patient data: The application developed should be accessible only to an authorized person. The authentication and confidentiality of the data should be focused on as the highest priority. Since the designed application permits login with email, it can be safely used.
- (3) Accuracy of the model: Results produced should be near accurate. The model should help to get early warning signals and educate the people. As the results produced in the hardware unit are found near accurate it can be used to understand the vital parameters. Any critical situation is maneuvered with physical consultation with the doctor.
- (4) Warning messages: Providing an alarm and beep at the hardware unit provides the patient to get physical assistance from the doctor as soon as possible. These features in the developed prototype evade the emergency or crucial condition to occur and save the people's life.

5 Results and Discussion

The cost of the hardware unit used in measuring health parameters and sending alert messages is comparatively low cost with satisfactory accuracy. The single unit costs \$50 and further if the unit is ordered for mass production, it will reduce the cost of the unit. Each of the sensor costs used in developing the model is approximately calculated as \$10 and gateway node ESP 32 with a waterproof case and port expansion feature to interface more sensors is calculated as \$40. The mobile application in connection with the prediction model is an added advantage to the doctor for a quick decision and early detection of disease. The prediction model is developed using the random forest algorithm gave prediction accuracy score for new test data is 90.16% with eight most important parameters. Thirteen input parameters from the Kaggle dataset are reduced to eight utmost important parameters Prediction model can be reconfigured for prediction of any new disease using an unsupervised machine learning method. Designed application is economically affordable to people as compared to the commercial applications available in the market. Comparison of the developed unit with the existing applications is summarized.

- (1) Wearable fitness trackers measures heartbeat, calories they help in educating people, whereas the proposed model consists of multiple features in alerting and warning the patient.
- (2) Sleep monitoring band monitor sleep patterns posture helps to track only specific patterns in the diagnosis of disease. The proposed model can be expanded to include more features.
- (3) Smart contact lenses used in early detection of diabetes cost of the devices are expensive. The proposed unit is at low cost, so it is affordable and configurable to accommodate further changes.

- (4) Smart bandages sensors that measure the wound's temperature and pH are limited to specific diseases and have low assistance from the physician.
- (5) Smart pills stomach-related information tracker. It requires careful attention from the physician. The designed unit sensor is easy to use as compared to the ingestible sensor units.

The merits of using the developed hardware unit are low cost, compact size, expansion ports for interface more sensors, less obstruction unit, and the person can wear while working without affecting their daily schedule. The solution proposed is having an intelligence component using machine learning which assists in the prediction of any chronic diseases at an early stage.

6 Conclusion

The hardware unit proposed in this work successfully collected the sensor data and saved it in the cloud storage. During the critical event, it generated a warning signal at the hardware unit. Also, a prediction model designed using machine learning assisted to produce quick decisions at the doctor's end. Such a full-fledged mobile application will benefit society by availing remote assistance of the doctors. Designed application is economically affordable to people as compared to the commercial applications available in the market.

The feedback collected from the doctor regarding the mobile application and hardware unit developed in this work was implemented and tested. Results are near accurate and security of patient data is maintained. The hardware unit is having a chargeable battery and is easy to carry along with the patient and weatherproof. The proposed hardware unit with mobile applications in health care produced acceptable results. Developed mobile applications permit the doctor in managing patient data analysis and virtual monitoring. Doctors can provide advice or communicate with the patient about the treatment without difficulty.

References

1. Dorland WAN (1925) Dorland's illustrated medical dictionary. WB Saunders
2. Pang Z (2013) Technologies and architectures of the internet-of-things (IoT) for health and well-being. Ph.D. diss., KTH Royal Institute of Technology
3. Health Management Information System, Government of India. Highlights: <https://nrhm-mis.nic.in/Pages/RHS2019.aspx?RootFolder>
4. Kasthuri A (2018) Challenges to healthcare in India—the five A's. *Indian Assoc Prev Soc Med* 43(3):141
5. Rao KD (2014) Situation analysis of the health workforce in India. Human Resources Background Paper 1
6. Willard-Grace R, DeVore D, Chen EH, Hessler D, Bodenheimer T, Thom DH (2013) The effectiveness of medical assistant health coaching for low-income patients with uncontrolled

- diabetes, hypertension, and hyperlipidemia: protocol for a randomized controlled trial and baseline characteristics of the study population. *BMC Family Pract* 14(1):1–10
7. Tian S, Yang W, Grange JML, Wang P, Huang W, Ye Z (2019) Smart healthcare: making medical care more intelligent. *Glob Health J* 3(3):62–65
 8. Uddin MS, Alam JB, Banu S (2017) Real time patient monitoring system based on Internet of Things. In: 2017 4th international conference on advances in electrical engineering (ICAEE). IEEE, pp 516–521
 9. Prajapati B, Parikh S, Patel J (2017) An intelligent real time IOT based system (IRTBS) for monitoring ICU patient. In: International conference on information and communication technology for intelligent systems. Springer, Cham, pp 390–396
 10. Rani S, Ahmed SH, Shah SC (2018) Smart health: a novel paradigm to control the chikungunya virus. *IEEE Internet Things J* 6(2):1306–1311
 11. Woo MW, Lee J, Park K (2018) A reliable IoT system for personal healthcare devices. *Future Gener Comput Syst* 78:626–640
 12. Pham M, Mengistu Y, Do H, Sheng W (2018) Delivering home healthcare through a cloud-based smart home environment (CoSHE) *Future Gener Comput Syst* 81:129–140
 13. Hu Y, Duan K, Zhang Y, Hossain MS, Mizanur Rahman SM, Alelaiwi A (2018) Simultaneously aided diagnosis model for outpatient departments via healthcare big data analytics. *Multimed Tools Appl* 77(3):3729–3743
 14. Sood SK, Mahajan I (2017) Wearable IoT sensor based healthcare system for identifying and controlling chikungunya virus. *Comput Ind* 91:33–44
 15. Verma P, Sood SK (2018) Cloud-centric IoT based disease diagnosis healthcare framework. *J Parallel Distrib Comput* 116:27–38
 16. Rath M, Pattanayak B (2019) Technological improvement in modern health care applications using Internet of Things (IoT) and proposal of novel health care approach. *Int J Hum Rights Healthcare*
 17. Wu F, Wu T, Yuce MR (2019) An internet-of-things (IoT) network system for connected safety and health monitoring applications. *Sensors* 19(1):21
 18. Maghded HS, Ghafoor KZ, Sadiq AS, Curran K, Rawat DB, Rabie K (2020) A novel AI-enabled framework to diagnose coronavirus COVID-19 using smartphone embedded sensors: design study. In: 2020 IEEE 21st international conference on information reuse and integration for data science (IRI). IEEE, pp 180–187
 19. Dias D, Cunha JPS (2018) Wearable health devices—vital sign monitoring, systems and technologies. *Sensors* 18(8):2414
 20. Rhee S (2000) Design and analysis of artifact-resistive finger photoplethysmographic sensors for vital sign monitoring. Ph.D. diss., Massachusetts Institute of Technology
 21. ThinkableX Cross Platform. <https://community.thinkable.com/thinkable-cross>
 22. UCI machine learning repository: heart disease dataset (2018). <http://archive.ics.uci.edu/ml/datasets/heartdisease>

Comprehensive Survey on Recent Trends in Optimization Methods and Different Facts Controllers-Based Power Quality Improvement System



A. V. Sunil Kumar, Prakash, Shivakumara R. S. Aradhya, and G. Swetha

Abstract Power consumption has risen dramatically in the last two decades, yet power generation and transmission have been severely hampered due to limited resources and environmental restrictions. Some transmission lines are essentially charged, and system stability becomes a limiting issue in energy transmission. A range of steady-state control problems has been addressed by flexible AC transmission system (FACTS) controllers. A FACTS is a system made up of static equipment used to transmit electrical energy via AC lines. Since the 1970s, FACTS devices have been utilized to create and improve the dynamic performance of modern power systems. This paper examines different techniques and tactics for coordinating control across FACTS controllers in multi-machine power systems in depth. The authors are certain that academics will find this survey study to identify important references in FACTS controller coordination.

Keywords Flexible alternating current transmission system · Power transfer limiting · Unified power flow controller · Optimization methods

1 Introduction

Electric utility planners have a significant problem in fulfilling rising load demand while maintaining good dependability and investing little in new transmission systems. The cost of laying more parallel lines and procuring the appropriate right of ways and boosting system operating voltages may be prohibitive due to economic and other factors.

The need for electrical energy is continuously increasing. Given the restricted availability of transmission corridors, optimal transmission line usage has become a

A. V. Sunil Kumar (✉) · Prakash · S. R. S. Aradhya
Department of EEE, Acharya Institute of Technology, Bangalore, India
e-mail: sunilkumarav@acharya.ac.in

G. Swetha
Department of EEE, Saptagiri College of Engineering, Bangalore, India

severe necessity for energy systems. With the growing need for bulk power transmission to expanding load centers through constrained right of ways, the necessity to use transmission infrastructure as efficiently as possible is becoming more apparent. The development of modern transmission lines, in particular, is required to keep up with the rising power plant capacity and energy demand.

Finding the adequate right of ways is especially difficult in developed nations, and obtaining the requisite clearance takes time, especially owing to environmental concerns. Due to these restrictions, making better use of existing electricity cables has become a major task. This problem may be seen from two perspectives. First and foremost, long-distance high-voltage transmission lines must enhance their transient and steady-state stability. Long transmission lines have a restricted power transfer capability, both in terms of steady-state and transient stability.

Another consideration is the flexibility that an energy deregulation market needs. Innovative characteristics are required for power systems operating to ensure that energy supply contracts can be honored in a deregulated market.

1.1 Flexible A.C Transmission Systems

Basic transmission issues that have resulted in ineffective transmission and other assets have prompted power system experts to reconsider traditional compensating approaches in favor of power electronics-based technologies. The flexible AC transmission system (FACTS) technology was created to address issues in power networks caused by rising demand and supply of electricity and restrictions on transmission line development owing to required right of ways. The main objectives of FACTS technology are

- i. To improve transmission systems' power transfer capacity.
- ii. Maintaining power flow over defined pathways.

According to the first aim, power flow in a particular line should be raised to the thermal limit by pushing the required current through the series line impedance. FACTS technology allows transmission lines to be operated at their thermal limitations, resulting in greater electricity. This motivation does not imply that the lines are typically loaded to their thermal limits (the transmission losses would be intolerable). Even yet, if serious system contingencies were to arise, this alternative would be accessible. However, the standard power transfer through transmission lines is projected to rise dramatically by employing FACTS controllers instead of huge steady-state margins to provide the requisite rotational and voltage stability. This article provides a detailed overview of how FACTS controllers may enhance power quality.

2 Literature Survey

Voltage stability, FACTS devices, and intelligent methods have all received much attention in the literature. The first study on voltage stability concepts and techniques and FACTS devices clarifies the fundamentals of FACTS device operations. Following that, modeling, analysis, and control are examined, culminating in the most recent application testing.

2.1 Survey on Optimal Location

Vijayapriya et al. [1] presented optimal placement for a FACTS device to increase system stability, optimize system load capacity, and decrease network losses. Power system analysis toolbox (PSAT) was used to perform small signal stability and time-domain analysis. UPFC was built to reduce losses, increase load capacity, and preserve stability in a line connected to the most critical buses.

Minguez et al. [2] looked at where SVCs should be placed in a transmission network to maximize its loading margin. For determining the actual SVC placement, this issue began as a nonlinear programming problem with binary decisions as variables. Contingencies were examined in a multi-scenario framework. To determine the best number, position, and settings for a range of UPFC devices, Shaheen et al. [3] employed evolutionary optimization methods, such as particle swarm optimization (PSO) and genetic algorithm (GA).

Saravanan et al. [4] presented the PSO technique for determining the optimal location of TCSC, SVC, and UPFC devices. By using this method, system load ability is increased and also cost is decreased. The buses' temperature and voltage limit have been used as constraints for the optimum location.

Samimi et al. [5] presented a particularly sensitive strategy for the transmission system to improve the power load capacities of TCSC and UPFC. The efficacy of the suggested technique was evaluated and shown on the IEEE 5 bus and IEEE 14 bus systems. Santiago-Luna and Cedeno-Maldonado [6] developed a strategy based on the evolutionary algorithm and evolution strategies to place the FACTS controllers in a power system to maximize load capacity. All key optimization factors were the sorts of FACTS devices utilized where they were positioned and set. The results suggest that using a variety of FACTS devices simultaneously is the most effective way to increase system load capacity using the IEEE 30 bus system.

In three-phase imbalanced distribution networks, Sarker et al. [7] have introduced cuckoo optimization algorithm (COA). UPQC's efficiency is tested by minimizing load disturbance in test systems during the fault, reducing the percentage of overall harmonic distortion and the individual harmonics, reducing true power losses, and reducing voltage imbalance and cost savings under ordinary operating circumstances.

Singh et al. [8] provided simulated experiments to conduct by correct positioning of FACTS devices ideally verified by traditional technique, with the results being

compared to the evolutionary method. A comparison is conducted between traditional and evolutionary computation techniques to authenticate performance, and the findings demonstrate that the projected approach is more beneficial.

Piatek et al. [9] evaluated existing techniques for the optimal positioning of metering stations in distribution networks. For a comprehensive analysis and comparison testing, three approaches were used. It has been discovered that the approaches can be used, although their effectiveness varies greatly depending on the topology of the test grid. Because the approaches rely on state estimates, their effectiveness is solely dependent on observability analysis.

The swarm moth-flame optimization (SMFO) was utilized to solve a Tan et al. [10] objective function that included integrated power losses, voltage profile, and pollution emission. The performance of SMFO was validated using simulation with IEEE 33 bus configuration.

Karunarathne et al. [11] suggest an area where distributed generators (DGs) may be optimally integrated into an active network distribution (AND) that contains multiple soft opening points (SOPs) which depends on the DG size and the DG integration node's impedance.

2.2 Survey on Nonlinear Programming

Nonlinear programming (NLP) is a problem-solving approach that uses nonlinear objectives and constraints to solve issues. Equation and inequality formulations may be used as restrictions, and the inequality can be defined as being both above and below bounded. The solutions applied to the OPF issues were the sequential uncomprising minimization method (SUMT), a big multiplier based on the modular idea enhanced for core nonlinear optimization systems. This class was solved utilizing quadratic programming and network flow programming approach together. Each area's tie-line security and transfer restrictions are taken into account. In addition, a multi-area examination of a purchasing and selling contract is offered. Four linked electricity networks were used to test this approach, and it is both possible and efficient.

Daryani et al. [12] proposed to overcome the optimal power flow issues using adaptive group search optimization (AGSO). Many elements of the OPF problem are studied in this work to create an acceptable multi-target model. The system's overall operation cost, emission, and safety index are the first, second, and third targets. Transmission losses and other equality and inequality restrictions are also addressed to build an exact scenario model such as the actual operating ranges of generator units and power flow equations. Furthermore, this research proposes an adaptable form of traditional group search optimization (GSO) to pinpoint GSO's convergence feature. To verify the efficiency and correctness of the suggested technique for managing nonlinear and non-convex problems, simulation testing on sample benchmarks and 30 bus and 57 bus IEEE standards is utilized. Extensive simulation studies have proved the accuracy of this technique.

Jordehi [13] used thyristor-controlled phase-shifting transformers (TCPSTs) and thyristor-controlled series compensators-based FACTS device to reduce the power losses. The most popular ways to coping with FACTS part problems are metaheuristics. The imperialistic competitive algorithm (ICA) is a well-known optimization approach used to tackle complicated optimization issues in various sectors. The results of using ICA for the FACTS portion issue show that it reduces voltage deviations better than other methods.

Dalman et al. [14] dealt multi-objective nonlinear programming problems using interactive fuzzy goal programming (FGP) with interval type 2 fuzzy numbers (IT2-FNs) method. This IT2-FNs method gives a good result against all power quality issues.

In the presence of renewable energy sources (RES) and fluctuating loads, Chamanbaz et al. [15] examined some approaches to handle the optimal power flow (OPF) issue. The inclusion of renewable energy sources and fluctuating demands is inherent in today's power networks. Their existence creates considerable uncertainty in the grid that must be considered when sending regulated (conventional) generators. Alternatively, network restrictions are virtually definitely breached resulting in line tripping or even cascading failures.

Multi-Population Modified Jaya (MPMJ) nonlinear optimization technique based on optimal power flow solution is considered by Padma et al. [16]. This algorithm, developed from the Jaya algorithm, includes multi-population-based population diversity control for early convergence and optimal values. Use the OPF solution of the UPFC's instrument to calculate the total generator fuel cost, active power reduction, voltage deviation purpose function, and voltage stability indicator increase using the standard IEEE 57 bus test system.

2.3 Survey on Quadratic Programming

The objective function is a quadratic programming (QP) which is quadratic, and the constraints are linearized. To deal with OPF (loss, voltage economic dispatch) issues, several QP methods (about 15%) have been used. In real-world online OPF issues, quasi-Newton and sensitivity-based techniques have been used.

Suresh et al. [17] offered reactive power optimization, which took a wide range of practical restrictions into account. A sequential quadratic programming method was used to formulate and solve the reactive power optimization problem. A simulation test on a 3 bus and 6 bus system was conducted to assess the method's usefulness.

Fortenbacher et al. [18] introduced new approaches to convert nonlinear optimal AC issues into tractable LP/QP-based OPF planning and operational power system problems. Four OPF techniques are shown in this article, each of which loosens the absolute power loss functions as linear constraints.

The technique for hybrid sequential quadratic programming (SQP) has been presented by Angalaeswari et al. [19]. In the form of an active method set, this approach minimizes actual power loss while meeting power equations and voltage

levels inside radial distribution systems (RDS) to establish optimal distribution generation (DG) location and ratings. To obtain the optimum answer, SQP employs an active set approach for sequence-level quadratic programming.

Arteaga et al. [20] developed the approach of hurricane optimization to specify the optimum delivery in the master phase of the DG system. The power balancing limitations of non-convexities issues are rectified using a sequential power control approach. This paper's main contribution was an unadulterated algorithmic OPF for DC networks.

Dao et al. [21] suggested a home energy management system (HEMS) to fulfill home energy demands while increasing profits. Intensive quadratic programming optimizations for each HEMS are also used to smooth the sales and procurement profiles while keeping the utility proportion of the decline in the home profit. It helps to flatten the trading power curve, resulting in a drop in fair profit for families. According to a calculation, peak power demand at the transformer at the substation would be reduced by 44%, and each residence would only get 10% of the maximum possible home prof.

2.4 Survey on Linear Programming

Linear programming (LP) is used to solve constraint and objective function problems with non-negative variables. About a quarter of the publications evaluated employed LP-based techniques to address OPF issues. The improved simplex approach is the most widely utilized methodology. The simplex method is well known for its success in addressing LP problems. The objective functions are linearized to allow an LP solution, such as voltage, loss, and economic dispatch.

Harini et al. [22] have linearized the difficult nonlinear security-constrained optimal power flow problem (SCOPF). The goal functions are partially linearized, and linear sensitivity factors are used to build the constraints. The addition of power router control in the post-contingency period formalizes the typical SCOPF. To assess the actual flow in lines, DC flow studies are done. As a result, power router control is utilized in this study to save even more money, and it is compared to the standard SCOPF approach.

Lom et al. [23] introduced the sequential linear programming (SLP) formulation approach to handling reactive power optimization problems. The fundamental goal is to reduce transmission losses as much as possible. A secondary feasibility improvement target is utilized when the initial base case contains overvoltages, yielding a more feasible solution than the loss minimization objective.

The wind-driven optimization (WDO) method was established by Senthilkumar et al. [24] to overcome the OPF issue in power systems. The best optimization approach based on atmospherical motion is the WDO algorithm, a global optimization method inspired by nature. An IEEE 30 bus system WDO has been effectively and successfully implemented by minimizing generation fuel cost as an objective function.

Naderi et al. [25] gave an in-depth look at the most recent applications of heuristic-based optimization methods to tackle various variations of the OPF issue. In addition, a thorough examination of the different methodologies from diverse perspectives is provided. The examination of about 50 publications is the most noteworthy element of this study that adds substantial value to its thoroughness.

Karimulla et al. [26] suggested strategies for solving multi-target power flow functions, including production costs, losses, power plant emissions, and voltage stabilization. The IEEE Standard 30 bus system was evaluated using four different multi-objective functions. The enhanced sine cosine algorithm (ESCA) obtained a good convergence rate compared with GA and PSO strategies.

2.5 Survey on Optimizing Flexible AC Transmission System Controllers

Sahu et al. [27] examined the issue of static voltage stability and voltage collapse. The main inspiration of the work is the incidence of a multi-voltage crash in the last few decades throughout the world. A new voltage stability index has been developed to estimate load bus loading of the distance between operational and collapse points. Other tensile stability indices are compared to the suggested index for static tensile instability assessment.

The symbiotic organisms search (SOS) system for FACT devices was presented in Prasad and Muharjee [28]. SOS is the most up-to-date, parameter-independent evolutionary algorithm. This addresses the issue of optimal power flow in fact-based power systems. A thyristor-controlled array capacitor and a thyristor-controlled phase shift are used to evaluate the effectiveness of the emergency algorithm at fixed positions.

Niknam et al. [29] developed the multi-target optimal power flow (OPF) issue improved particulate swarm optimization (IPSO) approach. The multi-target OPF presented covers costs, losses, voltage stability, and emission effects. The optimal compromise choice in the Pareto set provided by this algorithm is utilized with a furious decision-based technique. This research also contains an IPSO that employs messy queues and self-adaptive principles to change the PSO's parameters to enhance solution quality, particularly to avoid the system becoming caught in optimal local circumstances. A new mutation is also used to improve the suggested algorithm's search capabilities.

In addition to total fuel cost and total emissions, the updated teaching-learning optimization techniques employed by Shabanpour-Haghighi et al. [30] have solved the multiple objective optimum flow problems. These techniques enable the algorithm to scan for optimum solutions while maintaining a rapid rate of convergence. Furthermore, a smooth clustering technique and intelligent population selection for the following iteration are given to avoid an overly huge repository. The performance of this technique is evaluated using IEEE 30 bus and 57 bus systems, with results that

are comparable to those published. It was demonstrated that the suggested method outperforms alternative options.

Including just tap-change transformers does not considerably enhance voltage stability, according to Patel et al. [31]. Voltage levels and critical voltages but not the maximum voltages associated with these critical voltages are impacted. As such, a tap-changing transformer at the load terminals can perhaps help to maintain tensile stability. If a static VAR compensator with variable control gains is provided, the maximum load power can be increased several times higher than its original quantity. Controller increases and reference voltages interact with the off-nominal tap transformer ratio to maintain constant load node voltage in all load situations.

To design a fast and accurate heuristic optimization technique for the sized shunt condensers in radial distribution systems, Sirjani and Bade [32] utilized the global harmony search algorithm (GHS), incorporating mutual coupling and load imbalance and harmonic effects. The reverse/further power stream and harmonic radial power flow techniques were developed to evaluate power loss.

Dwivedi et al. [33] suggested an optimization-based method to filter design that decreases power consumption during filter execution while minimizing passband and stopband ripples. The trade-off is between passband ripple, stopband ripple, and power consumption avoid using traditional single-objective optimization methods. Consequently, the filter design task has been reframed by employing the modified version of the multi-target artificial bee colony technique.

The optimal reactive power dispatch is defined by Mukherjee and Mukherjee [34] as a method of reducing active power transmission losses and introducing voltage fluctuations by regulating various control variables that fulfill specified balances and disparity criteria. The suggested Chaotic Krill Herd (CKHA) algorithm was designed and tested satisfactorily inside the IEEE 30 bus test control framework. For the power framework patterns under investigation, there are two types of FACTS controllers. In the end, the novel CKHA approach is replicated in various important control models, including IEEE 57 buses and IEEE 118 bus test control frameworks.

Sai Ram and Kota [35] projected a novel approach for updating FACTS devices in power transmission networks to preserve voltage constancy. The suggested algorithm is a feasible method for locating and sizing FACTS controllers in the best possible position. In the suggested improvement, the PSO method maximizes gravitational consistency and improves the GSA's searching performance.

According to Mahdad and Srairi [36], developing a flexible and dependable power framework arranging approach under basic conditions is critical for experts and industry to reduce the likelihood of power outages. The primary goal of this proposed arranging approach is to maintain an acceptable power framework by preventing power outages caused by a hazy view of defects in generating units or critical transmission links. The fundamental phase of this functional technique is shown in this paper, which employs gray wolf optimizer in conjunction with a pattern search algorithm to address the security smart grid power system management problem in basic settings. The suggested method's reachability and efficacy are determined using the IEEE 30 bus test framework. The findings are encouraging, demonstrating that the proposed procedure may assure system security in everyday settings.

The voltage profile on a power framework's load buses, according to Subramanian et al. [37], is a crucial element in maintaining the framework's security and keeping a safe distance from voltage collapse. Therefore, the voltage profile (VP) should be monitored and regulated on load transporters. Another method has been added to this article to better distribute FACTS devices in appropriate locations and enhance their parameters. The method was compared to PSO and GA algorithms using IEEE standard 14, 30, and 57 bus frameworks. The results are appropriate, indicating the method's applicability and components.

Gupta and Sharma [38] introduced a non-traditional optimization technique with genetic algorithm-based FACTS devices to control the function of line flow, maintain desired bus voltage, and reduce the power loss. The main goals are to enhance static safety margins and stability in voltage while reducing losses. FACTS controllers are also strategically managed by putting them in areas where line failures occur. For simulation, MATLAB code was created. SVC and TCSC-based two FACTS devices are built in a steady state to test the IEEE 30 bus system under various loading circumstances. The findings demonstrate that the propounding algorithm is effective in determining the best location for power system stability.

Rashtchi and Pirooz [39] utilized the imperialist competitive algorithm (ICA) to figure out where the static compensator (STATCOM) should be in power systems and how big it should be. The technique gives the optimal number and STATCOM size of the bus, a two-dimensional array, to decrease all deviations of bus voltage from their nominal value. IEEE 5, 14 and 30 bus testing systems are used for simulations. In several instances, ICA has been contrasted with the famous PSO algorithm. The findings show that this electric network is one of the most sensitive methods for determining the proper stabilizer position.

Arul and Chellaswamy [40] presented cuckoo search algorithm (CSA) to increase the IPFC in multiline transmission. It significantly decreases the congestion of the transmission line. Subtracting a line use factor (SLUF) and CSA-based optimum tuning will enhance IPFC placement. CSA improves the multifunctional function and finds the best position for reduced congestion in the transmission line. The performance of the CSA was comparable under different loading situations with two other optimization techniques: PSO and differential development algorithm (DEA). The results show that CSA exceeds the two other methods.

Vijay Kumar and Srikanth [41] introduced a hybrid algorithm (the firefly algorithm (FA) and cuckoo search (CS)) to improve the power system stability. These algorithms enhanced searchability, decreased impressibility, and made the procedure easier. The FA technique is used to optimize the highest power loss line as the ideal placement for the UPFC. Using the CS method, the damaged location parameters and dynamic stability restrictions are restored.

Zeinhom [42] considered the UPFC for a genuine 380 kV 400 km double circuit line linking Saudi Arabia's central and western networks. The GA method is used to establish the UPFC's optimum size and assignment in the real system. In addition, UPFC assesses the impact of the existing protection system and offers different options. To frame the problem and identify the best UPFC settings and locations, MATLAB/Simulink is utilized. The simulation's findings are shown and analyzed,

and recommendations are made to enhance the interconnection system's voltage and stability margin.

Amirtham and Uma [43] recommend discovering the unified power flow controller in light of the real power execution record (severity list) in the power system network. The two-voltage source (power infusion) model is used to improve the UPFC's performance in regulating active power, reactive power, and voltage profile. The particle swarm optimization (PSO) method was employed in this study to minimize fuel consumption with and without a unified power controller. The IEEE 30 bus system has been used to approve and correlate the logic for the recommended techniques and simulations. The proper placement of the unified power flow controller might enhance the power framework's exhibitions substantially.

Sekhar et al. [44] projected that by constructing the power injection representation of UPFC as indicated by the regular algorithm, they would improve the voltage profile and reduce losses in electrical systems. The study also discusses the best placement and size for a UPFC and the optimization techniques GA-PSO and DA-PSO, which were suggested to determine the device's best setup and dimensions. The stated optimization was the optimum method for selecting the ideal UPFC device configuration, improving the voltage profile, and lowering transmission line power system losses. On IEEE 57 test frameworks, this hybrid GA-PSO and DA-PSO has a lot of experience.

Pilla et al. [45] introduced teaching–learning-based optimization (TLBO) tuned, PID two-area hydro-thermic generator controller for automatic generation control (AGC). This approach considers physical constraints such as transit delay (TD), generation rate constraint (GRC), and governor dead band (GDB) nonlinearities.

A fractional evolving method using FACTS devices was presented by Muhammade et al. [46] to achieve reactive power planning objectives. In the conventional bus test system of IEEE 30, IEEE 57, and IEEE 118, fractional-order Darwinian particle swarm optimization (FODPSO). Static VAR compensator (SVC) offers shunt compensation, whereas thyristor-driven series compensator (TCSC) provides series compensation.

2.6 Control Stability of FACTS

The control stability of the FACTS model is shown in Fig. 1. The optimization control method is seen as the most efficient way to solve single-transform optimum power flow problems. Static VAR compensator (SVC), thyristor-controlled series compensator (TCSC), and thyristor-controlled phase-shifting transformer (TCPST) are the best shunt-connected devices in FACTS family. Bus voltage can be controlled by injecting reactive power into the system. FACTS need equipment that can take on an essential job for side management and, in this way, control the transmission line congestion.

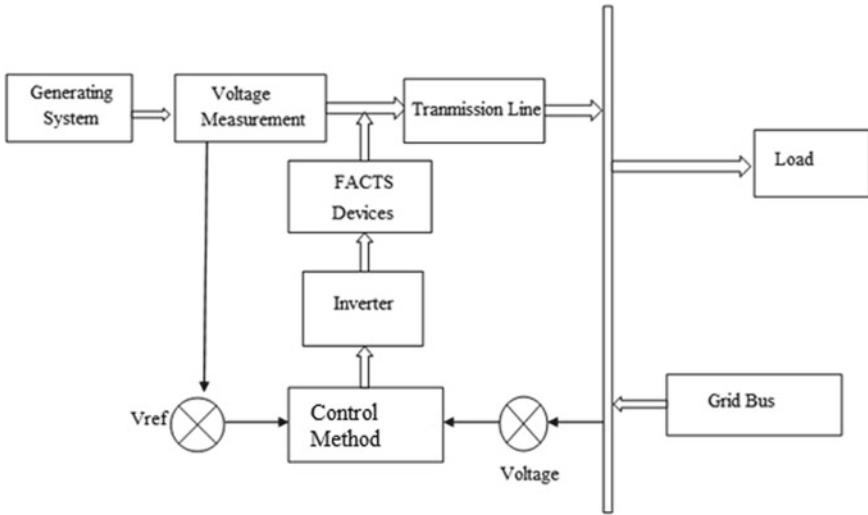


Fig. 1 Control stability analysis of FACTS

2.7 Performance Evaluation

Based on this literature survey, GA, PSO, and selective PSO methods give good results. The performance analysis of this methods is discussed for this section.

Table 1 discusses the line loss analysis of different optimization methods with different FACTS control devices.

Table 2 discusses the settling time analysis of different optimization methods with different FACTS control devices.

Table 1 Line losses analysis

Control technique	Line losses PSO (%)	Line losses SPSO (%)	Line loss GA (%)
SVC	5.3	6.1	6.5
TCSC	4.5	5.7	5.1
TCPST	2.5	3.3	2.9

Table 2 Settling time analysis

Control technique	Settling time PSO (s)	Settling time SPSO (s)	Settling time GA (s)
SVC	11.5	9.56	8.36
TCSC	9.6	8.64	7.62
TCPST	8.2	7.9	6.98

3 Conclusion

In the literature, several approaches have been examined. Considering one objective as a target and the others as a constraint is one approach for reducing a multi-objective issue to a single-objective problem. Another option is to combine all objective functions into a single one. The following techniques have several flaws, such as restricting the number of options accessible and requiring previous selection of weights for each objective function. Apart from the flaws mentioned above, the most serious flaw in these techniques is their inability to identify a single solution to a multi-objective issue.

The real power, voltage magnitude, and angle, which are maintained by altering the above parameters, are the fundamental determinants of the framework's voltage stability. Furthermore, the FACTS controller's location and size may be seen as a multi-objective issue with several destinations and needs. The control variables, y and v , do not affect the minimum objective function, equal to zero. The inequality restriction R is based on the control variables y and v which are less than or equal to zero. Under identical conditions, the actual power generated in bus n is the same as the real power generated by the n th generator and the real power generated by the n th load bus.

The injecting reactive power into the n bus is the n th generator reactive power and n th load bus reactivation power. The lowest real power flow is below or equal to the n th bus's maximum real power flow limitation in terms of inequality. The lowest reactive power flow must be equal or less than the n th bus's maximum reactive power flow restrictions. The minimum voltage magnitude must be less than or equal to the n th bus's maximum voltage magnitude restrictions. The following findings are drawn from the examination of existing mechanisms:

- i. In FACTS devices, the essential criticalness is optimizing and keeping up the voltage stability in the power transmission frameworks.
- ii. Power flow controllers are generally changing from mechanical to electrical cases. In the past, reactors were associated with power lines by mechanical switches, and nowadays, they are changed to power electronic-based switching devices.
- iii. Even though shunt and series capacitors and reactors can change the voltage profile and power flow pattern, they are one moment as FACTS components.
- iv. The power flow research resolves bus voltages, active power, reactive power, and power loss.
- v. The equality and inequality restrictions are used to determine where and how big the FACTS devices should be. These various characteristics determine different outcomes on the target work.
- vi. Finding the best position and size for FACTS devices is challenging when using several systems.

To overcome these issues, effective techniques must be developed.

In the future, some of them are considered and overcome by proposing effective techniques. Hence, the objectives can be formulated as follows:

- i. To design optimal localization and sizing of FACTS devices with the aid of predictive cross-difference progression optimization (PCDPO)
- ii. To develop optimal localization and sizing of FACTS devices with the substantial transformative optimization (STO) method.

References

1. Vijayarpiya P, Kowsalya M (2010) Increasing the loadability and minimizing the losses using UPFC. *Int J Eng Sci Technol* 2(12):7343–7349
2. Mínguez R, Milano F, Zarate-Miano R, Conejo A (2007) Optimal network placement of SVC devices. *IEEE Tran Power Syst* 22(4):1851–1860
3. Shaheen H, Rashed GI, Cheng SJ (2008) Optimal location and parameters setting of UPFC based on GA and PSO for enhancing power system security under single contingencies. In: 2008 IEEE power and energy society general meeting—conversion and delivery of electrical energy in the 21st century
4. Saravanan M, Slochanal SMR, Venkatesh P, Prince Stephen Abraham J (2007) Application of particle swarm optimization technique for optimal location of FACTS devices considering cost of installation and system load ability. *Electric Power Syst Res* 77(4):276–283
5. Samimi A, Naderi P (2011) A new method for optimal placement of TCSC based on sensitivity analysis for congestion management. *Smart Grid Renew Energy* 3(1):10–16
6. Santiago-Luna M, Cedeno-Maldonado JR (2006) Optimal placement of FACTS controllers in power systems via evolution strategies. In 2006 IEEE/PES Transmission and Distribution Conference and Exposition: Lat Am, pp. 1–6. <https://doi.org/10.1109/TDCLA.2006.311461>
7. Sarker J, Goswami SK (2016) Optimal location of unified power quality conditioner in distribution system for power quality improvement. *Int J Electr Power Energy Syst* 83:309–324
8. Singh M, Gupta S (2019) Optimal placement of facts devices in power system for power quality improvement. *Int J Recent Technol Eng (IJRTE)* 7(6)
9. Piatek K, Firlit A, Chmielowiec K, Dutka M, Barcentewicz S, Hanzelka Z (2021) Optimal selection of metering points for power quality measurements in distribution system. *Energies* 14:1–18
10. Tan Z, Zeng M, Sun L (2021) Optimal placement and sizing of distributed generators based on swarm moth flame optimization. *Front Energy Res* 9:1–8
11. Karunarathne E, Pasupuleti J, Ekanayake J, Almeida D (2021) The optimal placement and sizing of distributed generation in an active distribution network with several soft open points. *Energies* 14
12. Daryani N, Hagh MT, Teimourzadeh S (2015) “Adaptive group search optimization algorithm for multi-objective optimal power flow problem,” *Appl Soft Comput*, 38:1012–1024
13. Jordehi AR (2016) Optimal allocation of FACTS devices for static security enhancement in power systems via imperialistic competitive algorithm (ICA). *Appl Soft Comput*, 48, <https://doi.org/10.1016/j.asoc.2016.07.014>
14. Dalman H, Bayram M (2017) Interactive fuzzy goal programming based on Taylor series to solve multiobjective nonlinear programming problems with interval type-2 fuzzy numbers. *IEEE Trans Fuzzy Syst* 26(4):2434–2449
15. Chamanbaz M, Dabbene F, Lagoa C (1999) Algorithms for optimal AC power flow in the presence of renewable sources. In: *Wiley Encyclopedia of electrical and electronics engineering*. <https://doi.org/10.1002/047134608X.W8403>
16. Padma K, Maru Y (2021) Comparative analysis of a performance of metaheuristic algorithms in solving optimal power flow problems with UPFC Device in the transmission system. *Int J Recent Technol Eng* 9(5):316–326

17. Suresh V, Varadarajan M (2015) Reactive power optimization by using sequential quadratic programming. *Int J Eng Res Technol* 3(4)
18. Fortenbacher P, Demiray T (2019) Linear/quadratic programming-based optimal power flow using linear power flow and absolute loss approximations. *Int J Electr Power Energy Syst* 107:68–689
19. Angalaeswari S, Sanjeevikumar P, Kamaraj J, Leonowicz Z (2021) Hybrid PIPSO-SQP algorithm for real power loss minimization in radial distribution systems with optimal placement of distributed generation. *Sustainability* 12(14):1–21
20. Arteaga J, Montoya O, Grisales-Noreña L (2020) Solution of the optimal power flow problem in direct current grids applying the hurricane optimization algorithm. *J Phys Conf Ser*
21. Dao T, Ishii H, Takenobu Y, Yoshizawa S, Hayashi Y (2020) Intensive quadratic programming approach for home energy management systems with power utility requirements. *Int J Electr Power Energy Syst* 115
22. Harini D, Ramesh Babu M, Kumar CV (2020) LP based solution for security constrained optimal power flow including power routers. *WSEAS Trans Power Syst* 15
23. Lomi A, Krismanto A, Wartana I, Sarkar D (2020) A numerically robust sequential linear programming algorithm for reactive power optimization. *E3S Web of Conferences*, vol 188
24. Senthilkumara R (2021) Solution for optimal power flow problem using WDO algorithm. *Turk J Comput Math Educ (TURCOMAT)* 12:889–895
25. Naderi E, Narimani H, Pourakbari-Kasmaei M, Cerna FV, Marzband M, Lehtonen M (2021) State-of-the-art of optimal active and reactive power flow: a comprehensive review from various standpoints. *Processes* 9(8)
26. Karimulla S, Ravi K (2021) Solving multi objective power flow problem using enhanced sine cosine algorithm. *Ain Shams Eng J*
27. Sahu SK, Reddy S, Jayaram Kumar SV (2012) New voltage stability index (NVSI) for voltage stability analysis in power system. *Int J Electr Electron* 2(4):13–20
28. Prasad D, Mukherjee (2016) A novel symbiotic organisms search algorithm for optimal power flow of power system with FACTS devices. *Eng Sci Technol Int J* 9(1):79–89
29. Niknam T, Narimani MR, Aghaei J, Azizipanah-Abarghooee R (2012) Improved particle swarm optimization for multi-objective optimal power flow considering the cost, loss, emission and voltage stability index. *Inst Eng Technol* 6(6):515–527
30. Shabanpour-Haghighi A, Seifi AR, Niknam T (2014) A modified teaching–learning based optimization for multi-objective optimal power flow problem. *J Energy Convers Manage* 77:597–607
31. Dipesh Patel A, Nirav Patani P, Kumar P (2013) Analysis of the effect of tap changing transformer on performance of SVC. *Int J Emerg Technol Adv Eng* 3:217–224
32. Sirjani R, Bade MG (2015) A global harmony search algorithm for finding optimal capacitor location and size in distribution networks. *J Central South Univ* 22:1748–1761
33. Dwivedi AK, Ghosh S, Narendra Londhe D (2016) Low power FIR filter design using modified multi-objective artificial bee colony algorithm. *J Eng Appl Artif Intell* 55:58–69
34. Mukherjee A, Mukherjee V (2016) Chaotic krill herd algorithm for optimal reactive power dispatch considering FACTS devices. *J Appl Soft Comput* 44:163–190
35. Inkollu SR, Kota VR (2016) Optimal setting of FACTS devices for voltage stability improvement using PSO adaptive GSA hybrid algorithm. *Eng Sci Technol Int J* 19(3):1166–1176
36. Mahdad B, Srairi K (2015) Blackout risk prevention in a smart grid based flexible optimal strategy using Grey Wolf-pattern search algorithms. *J Energy Convers Manage* 98:411–429
37. Subramanian A, Jaisiva S, Swathana R, Neelan S (2015) Optimal allocation of facts device for voltage profile enhancement. *Int J Enhanced Res Sci Technol Eng* 4:187–193
38. Gupta A, Sharma PR (2014) Application of GA for optimal location of FACTS devices for steady state voltage stability enhancement of power system. *Int J Intell Syst Appl* 03:69–75
39. Rashtchi V, Pirooz A (2015) Application of imperialist competitive algorithm for optimal location and sizing of static compensator considering voltage profile. *Universal J Electr Electron Eng* 3(2):39–48

40. Arul S, Chellaswamy (2016) Optimal location of IPFC for improving power system performance using cuckoo search algorithm. *IOSR J Electr Electron Eng* 11(4):33–43
41. Vijay Kumar B, Srikanth NV (2017) A hybrid approach for optimal location and capacity of UPFC to improve the dynamic stability of the power system. *Appl Soft Comput* 52:974–986
42. Zeinhom AN (2016) Optimal sizing and allocation of unified power flow controller (UPFC) for enhancement of Saudi Arabian interconnected grid using genetic algorithm (GA). In: *Proceedings of Saudi Arabia smart grid (SASG)*, pp 1–6
43. Steffy Amirtham J, Uma V (2016) Optimal location of unified power flow controller enhancing system security. In: *Proceedings of second international conference on science technology engineering and management*, pp 326–331
44. Hema Sekhar H, Lakshmi Devi A (2017) Optimal location of advanced model of UPFC device for analyzing the performance of transmission system: a hybrid DA-PSO approach. *Int J Control Theory Appl* 10(22):217–232
45. Pilla R, Azar AT, Gorripotu T (2019) Impact of flexible AC transmission system devices on automatic generation control with a metaheuristic based fuzzy PID controller. *Energies* 12(1)
46. Muhammad Y, Akhtar R, Khan R (2021) Design of fractional evolutionary processing for reactive power planning with FACTS devices. *Sci Rep* 11(593)

Speed Control of Brushless DC Motor by Using Particle Swarm Optimization Algorithm



Suraj R. Kamde and Meghraj S. Morey

Abstract Over the years, the applications of variable speed drive system have been increases very vast in the field of automobile industries and many more household applications. The non-polluted electronics are implemented in order to use for energy consumption of various devices. This leads to the evolution of brushless DC motor. BLDC motor provides the dominancy over the conventional DC motor with respect to high torque-to-weight ratio, more torque per watt, and many more. This paper represents the speed control of BLDC motor using particle swarm optimization algorithm. The PSO algorithm is used to tune PI controller in order to get fast convergence to optimum values. Compared with traditional Ziegler–Nichol’s method, PSO algorithm provides an improved time response performance with lower overshoot and effective speed control. The model is implemented in MATLAB Simulink, and simulation results are presented.

Keywords BLDC motor · PI controller · Particle swarm optimization · MATLAB · Simulink

1 Introduction

The brushed DC motor or the conventional DC motor is invented by the German inventor Ernst Werner von Siemens, in the year 1856 [1]. The disadvantage of a dc motor includes the need of a separate dc source for excitation of the field winding, which increases the size of the motor, and the need for frequent brush maintenance, which results in a physical increase in cost. To overcome this problem, a brushless DC motor, or a DC motor with a permanent magnet, was invented by A. H. Hoffman in 1962 [2]. A brushless DC motor has similar characteristics to a DC motor, except the brush and commutator assembly. Instead of wire-wound field poles, a permanent magnet provides air gap flux in this motor. Permanent magnet synchronous motor with trapezoidal back emf is another name for BLDC motor [3]. This motor has

S. R. Kamde (✉) · M. S. Morey
Government College of Engineering, Aurangabad, Aurangabad, India
e-mail: surajkamde55@gmail.com

© The Author(s), under exclusive license to Springer Nature Singapore Pte Ltd. 2022
V. Mahajan et al. (eds.), *Sustainable Technology and Advanced Computing in Electrical Engineering*, Lecture Notes in Electrical Engineering 939,
https://doi.org/10.1007/978-981-19-4364-5_70

987

high torque-to-speed ratio and a wide range of speed, and it is notable for its low acoustic noise, low maintenance due to the absence of a brush and commutator, and high torque-to-weight ratio due to the use of a permanent magnet [4]. Because of low rotor inertia, the position control is quick and efficient. When compared to conventional DC motors, it operates at a very high speed with good performance and has a long life. BLDC motor has a wide range of applications such as steel rolling mills, electric vehicles, electric trains, chemical mining, automotive ventilation, air conditioning, and robotics [5]. The speed control of BLDC motors is the focus of this paper. Speed control techniques include traditional control, intelligent control [fuzzy logic controller, artificial neural network, evolutionary algorithm], and hybrid control. A proportional integral controller is a traditional control technology with the simplest structure that provides acceptable responsiveness in both transient and steady-state situations. It reduces the error between the reference and actual signals. The PI controller is a hybrid of a proportional and an integral controller, each of which performs a different control function.

- (I) Proportional controller: It improves the system's DC gain and delivers current SP-PV error values $e(t)$.
- (II) Integral controller: It reduces steady-state error by looking for the most recent values of SP-PV error and integrating them over time.

There are several techniques for tuning a PI controller, including trial and error, Routh array, and Cohen-Loon technique, but the most efficient and first method is Ziegler-Nichol's method which is used in this paper. John G Ziegler and Nathaniel B Nichols developed the Z-N method in 1942. This method is used to determine the system open-loop transfer function, which is determined by two parameters delay time (T_d) and time constant (T_i). The controller gain K_p , K_i , is calculated using T_d and T_i . Although this method is based on time response and experience, it still has an excessive overshoot in time response and a longer settling time [6]. The acceleration of BLDC motor is such an important parameter of the system; the Z-N method is quite difficult to design because the slope of the PI controller response is considered. The main objective of this paper is to improve the time response characteristics and has a defined algorithm rather than a conventional Z-N method [7]. The main motive behind this project work is to get the efficient control over the variation in speed of the motor by considering the nonlinearity of the BLDC motor; the "Particle Swarm Optimization" technique is introduced for the speed control of the BLDC motor. It is a searching technique by using a population of particles corresponding to individuals. It is used to obtain the best values of the PI controller to minimize the overshoot and rise time of the system. This method is more efficient and fast for solving nonlinear large-scale optimization problems. It is used to explore the search space of a given particle to optimize a particular objective function [4].

2 BLDC Machine Modeling

The working principle of brushless DC motor is similar to that of conventional DC motor but different in construction. It is a self-rotating synchronous machine with a rotor is a permanent magnet, and the stator is similar to the induction motor. Brushes and commutator are absent in BLDC motor instead of it, electronically commutated system is used. The model of this motor consists of two major elements electrical and mechanical which are placed in stator and rotor, respectively [8]. This motor commutates electronically and generates trapezoidal back emf with the help of Hall Effect position sensors and an inverter circuit as shown in Figs. 9 and 15. These sensors detect the rotor magnetic pole position and provide correct switching information for the logical switching circuit as shown in Fig. 19. The rotor magnetic pole positions signal is converted to an electric signal and the stator winding switch to the winding current control system switches. The BLDC motor can operate in a variety of modes (phases) although the most common is a three-phase system. This offers a high efficiency along with greater control accuracy, which is especially useful for controlling stator current (Fig. 1).

According to the concept of stator winding excitation, the inverter circuit energizes two windings at the same time; therefore, the motor input voltage is defined as the terminal voltage between two windings, with a magnitude equal to the supply voltage.

This condition is expressed in below equations.

$$V_{ab} = R(i_a - i_b) + L \frac{d(i_a - i_b)}{dt} + (e_a - e_b) \tag{1}$$

$$V_{bc} = R(i_b - i_c) + L \frac{d(i_b - i_c)}{dt} + (e_b - e_c) \tag{2}$$

$$V_{ca} = R(i_c - i_a) + L \frac{d(i_c - i_a)}{dt} + (e_c - e_a) \tag{3}$$

where

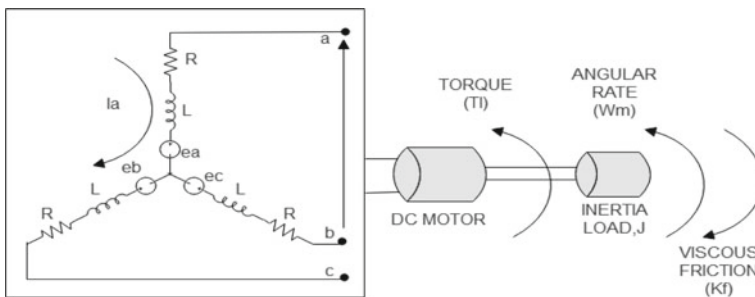


Fig. 1 Schematic diagram of BLDC motor

L = Per phase inductance of stator winding (Henry)

R = Per phase resistance of stator winding (Ohms)

V_a, V_b, V_c = Phase voltages of stator winding

I_a, I_b, I_c = Phase currents of stator winding

e_a, e_b, e_c = Per phase back emf of stator winding.

The matrix form representation of voltage equations:

$$\begin{bmatrix} V_a \\ V_b \\ V_c \end{bmatrix} = \begin{bmatrix} R + \rho L & 0 & 0 \\ 0 & R + \rho L & 0 \\ 0 & 0 & R + \rho L \end{bmatrix} \begin{bmatrix} i_a \\ i_b \\ i_c \end{bmatrix} + \begin{bmatrix} e_a \\ e_b \\ e_c \end{bmatrix} \tag{4}$$

The emf equations for each phase are written as,

$$e_a = k_e \cdot w_m \cdot f(\theta) \tag{5}$$

$$e_b = k_e \cdot w_m \cdot f\left(\theta - \frac{2\pi}{3}\right) \tag{6}$$

$$e_c = k_e \cdot w_m \cdot f\left(\theta + \frac{2\pi}{3}\right) \tag{7}$$

The mechanical component of BLDC motor is expressed as,

$$T_{em} = k_f w_m + J \frac{dw_m}{dt} + T_l \tag{8}$$

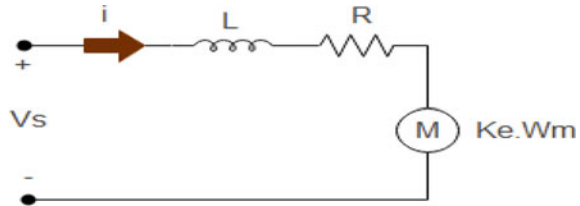
where

- T_{em} = Electromotive torque
- k_e = Back emf constant [v/rad/s]
- k_f = Viscous friction constant
- θ = Electrical rotor angle
- w_m = Angular speed of the motor
- B = Viscous friction
- J = Moment of inertia
- T_l = Load torque
- $\rho = \frac{d_i}{d}$
- k_t = Torque constant.

2.1 Transfer Function of BLDC Motor

One of the most significant aspects of control theory is the transfer function. It is based on mathematical modeling and applicable in automatic control fields. The stator

Fig. 2 Equivalent circuit of BLDC motor



winding is energized sequentially in order to rotate the motor, and there is not any physical contact between the stator and rotor windings [7]. Because the mechanisms of back emf and electromagnetic torque for each phase winding conduction are identical to those of a conventional DC motor, the same analysis may be used.

From Fig. 1, it refers that phase a and phase b are in a conduction mode and expressed as,

$$\frac{di_a}{dt} = -\frac{di_b}{dt} = \frac{di}{dt} \tag{9}$$

Assuming the system in a steady-state condition, e_a and e_b are same in magnitude but opposite in direction. Hence, Eq. 1 can be rewritten as,

$$V_{ab} = 2Ri + 2L\frac{di}{dt} + (e_a - e_b) \tag{10}$$

From Fig. 2,

$$V_s = Ri + L\frac{di}{dt} + k_e w_m \tag{11}$$

$$k_t i - T_l = J\frac{dw_m}{dt} + k_f w_m \tag{12}$$

Assume $T_l = 0$,

$$i = \frac{J}{k_t} \frac{dw_m}{dt} + \frac{k_f}{k_t} w_m \tag{13}$$

Substitute Eq. (12) in Eq. (11)

$$V_s = R\left(\frac{J}{k_t} \frac{dw_m}{dt} + \frac{k_f}{k_t} w_m\right) + L\frac{d}{dt}\left(\frac{J}{k_t} \frac{dw_m}{dt} + \frac{k_f}{k_t} w_m\right) + k_e w_m \tag{14}$$

$$V_s = \frac{LJd^2w_m}{dt^2} + \frac{RJ + w_m}{k_t} \frac{dw_m}{dt} + \frac{Rw_m + k_e k_t}{k_t} w_m \tag{15}$$

Applying Laplace transform to Eq. 15, we get,

Table 1 Parameter of BLDC motor

Rating	Symbol	Units	Value
Nominal voltage	V	V	12.0
Nominal speed	w_m	RPM	2860
Nominal current	I	A	2.14
Nominal power	P	W	250
Nominal torque	T	Nm	5.9
Armature resistance	R	Ohms (Ω)	1.20
Inductance	L	mH	0.56
Torque constant	k_t	mNm/A	25.5
Rotor inertia	J	gcm ²	92.5
Electrical torque	k_e	V s/rad	1.54
No. of phase			3

$$G(s) = \frac{k_t}{s^2 J L + s k_f L + S R J + k_f R + k_e k_t} \tag{16}$$

By considering the following assumptions,

1. The friction constant is considered to be very small; hence, k_f tends to zero.
2. $R J \gg k_f L$
3. $k_e k_t \gg R k_f$ (Table 1).

The modified transfer function is written as,

$$G(s) = \frac{k_t}{s^2 J L + S R J + k_e k_t} \tag{17}$$

The final transfer function becomes,

$$G(s) = \frac{13.1061}{2.660 \times 10^{-6} \cdot s^2 + 0.01710s + 1} \tag{18}$$

3 PI Controller Tunning

The proportional integral (PI) controller is work on the principle of control loop feedback mechanism. It can detect the error between measured value and intended value and send the appropriate correction to keep the process running smoothly. The PI-type control algorithm is essentially a simple mathematical equation-based controller that is used to obtain the controlled variables.

The PI controller is represented in Fig. 3, shows that E_n is the speed error between the reference speed N_r and the actual speed N of controller, and K_p and K_i are the

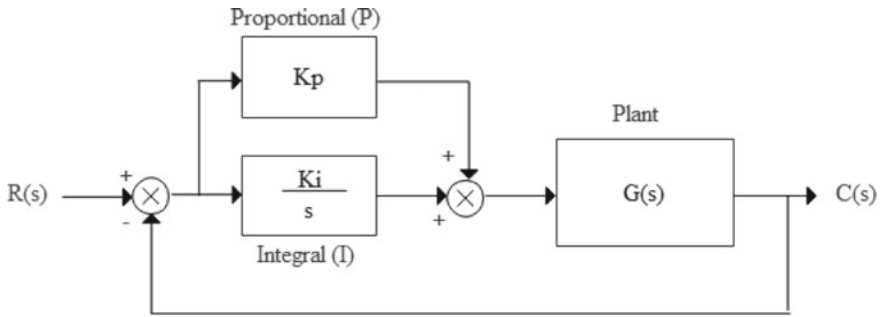


Fig. 3 Block diagram of PI controller

proportional and integral gain. The equation of PI controller is given as,

$$P_{out} = K_p e(t) + K_i \int e(t) \tag{19}$$

The gain K_p is used by the proportional controller to generate an output which is proportional to the current error value. When the proportional gain is high, the system becomes unstable. Integral action is required in order to stabilize the system function. This integral mode is used to collect steady-state error produced by proportional action while also producing a sluggish response. The derivative controller responds to the rate of variation in error; however, noise will form due to this action [9]. As a result, this paper refers only proportional integral (PI) controller to control the speed of a BLDC motor as defined by Eq. (19).

3.1 Ziegler–Nichols Method for PI Controller Gain

The feedback system of PI controller which is tuned with Z-N step response method is very well known for its rejection in disturbances. The compensated system response to a step signal has a high percent overshoot, and the control signal is often high, which may lead the actuator to saturation.

According to Z-N method, the parameter is setting in four steps.

- I. Determine the step response of the system.
- II. Draw the tangent to the response curve.
- III. Obtain the value of L and T shown in Fig. 4.
- IV. Set the value of K_p, T_i, T_d as shown in Table 2.

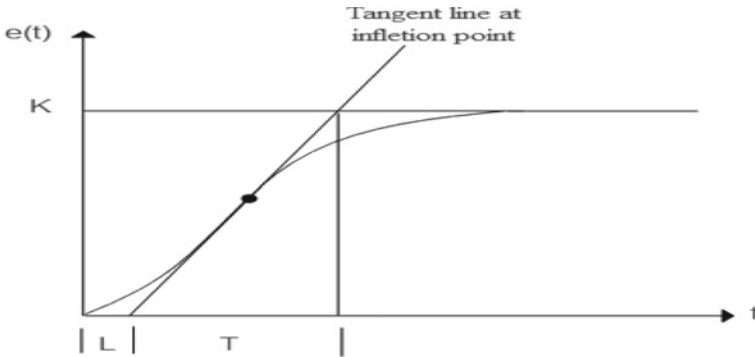


Fig. 4 Step input response curve

Table 2 Determination of controller gain using Z-N method

Type of controller	K_p	T_i	T_d
P	$\frac{T}{L}$	∞	0
PI	$0.9 \frac{T}{L}$	$\frac{L}{0.3}$	0
PID	$1.2 \frac{T}{L}$	$2L$	$0.5L$

3.2 PSO Algorithm for PI Controller Gain

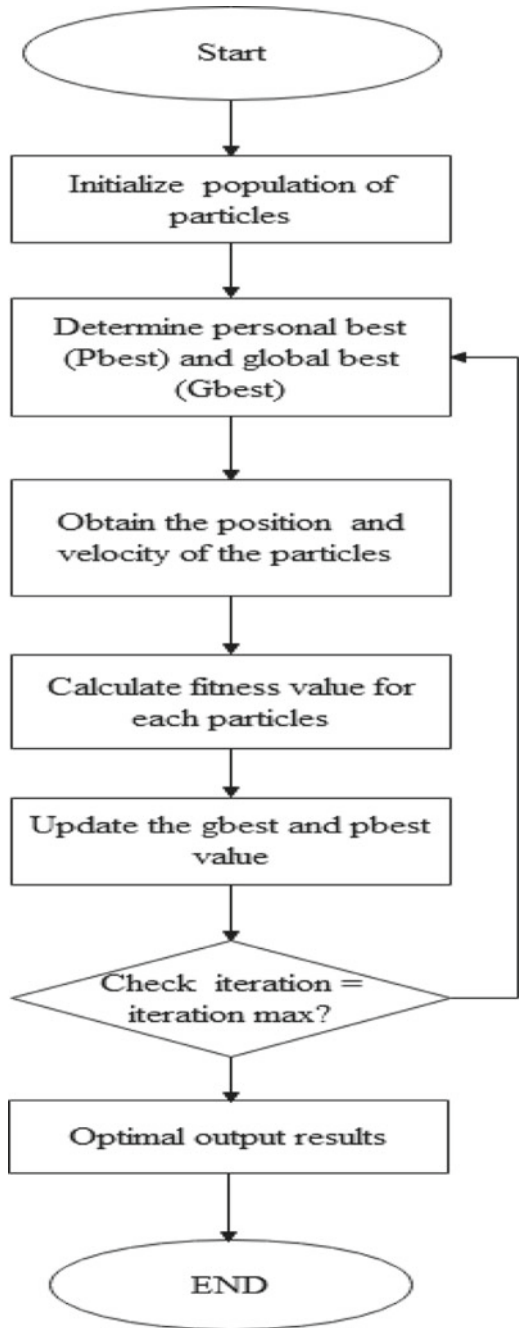
The particle swarm optimization (PSO) algorithm is a form of stochastic optimization technique proposed in this paper to tune the PI controller parameters. Eberhart and Kennedy introduced the PSO method in 1995. This method is inspired by the social behavior of flocking birds, is simple to implement, and does not require any gradient information about the system’s response [4].

A PI controllers are widely employed in a variety of sectors. This controller reduces the plant sensitivity to perturbations. Different strategies of optimization techniques are available for tuning purpose. Among them, the PSO technique is one of most effective and simple to implement.

In this technique, the number of particles is randomly initialized to fly in multi-dimensional search space and update its velocity and position, so it can reach near to the optimal solution region. The fitness function of the particle is analyzed to determine the best position. For every iteration, the position is updated depend on experience of particle as well as other particles. The movements are guided by local best position termed as (P_{best}), and overall swarm best position is known as (G_{best}) in a search space [5]. The steps for designing the algorithm are discussed in the flowchart (Fig. 5),

Initially, the algorithm of PSO determines with a random position and random velocities. Each particle in the swarm flies toward the searching space and remember its best position and deliver all other particle by the best position and adjust its own

Fig. 5 Flowchart of PSO algorithm



position and velocity as well [8]. It also monitors the horizontal behavior of particles. The expression for updating velocity and position is given in Eq. (20) and (21).

The velocity of particle is calculated by the formula given below,

$$V_{id}^{t+1} = wV_{id}^t + c_1\text{ran}_1(P_{\text{best id}}^t - X_{id}^t) + c_2\text{ran}_2(G_{\text{best id}}^t - X_{id}^t) \tag{20}$$

The position of each particle is to be updated by the given formula,

$$X_{id}^{t+1} = X_{id}^t + V_{id}^{t+1} \tag{21}$$

where

- V_{id}^t = Current velocity of id particle at iteration t
- V_{id}^{t+1} = Updated velocity
- X_{id}^t = Current position of id particle at iteration t
- X_{id}^{t+1} = Updated position
- w = Inertia weight.

The PSO implementation procedure can be illustrated using the algorithm described in Fig. 5. The optimization procedure is as follows: Initialize the searching point $X_{id}(0)$ and velocities $V_{id}(0)$ generates randomly with in the specified range. The current searching point is set to pbest for each particle. The best-evaluated value of pbest is set to gbest, and the particle number with the best value is stored. The objective function value is calculated for each particle. If the value is better than the current pbest, then the pbest value is replaced by the current value. In the second step, if the best value of the pbest is better than the gbest, the current gbest is replaced with the best value of pbest, and the particle with the best value is preserved. The third step demonstrates the modification of each searching point when the current searching point of each agent changes using the first and second steps, it is necessary to check the exit condition; if the current iteration number reaches the predetermined maximum iteration number, the agent must exit. Otherwise, proceed to the second step. The limit condition is applied to the PI parameter gain which can diverge the controller [7, 8].

The parameter used for implementation in PSO algorithms for this paper is mentioned in Table 3.

Table 3 Parameter of PSO algorithm

Parameter	Value
No. of particles	20
No. of iteration	80
Cognitive factor (c1)	2.050
Exploration factor (c2)	2.050

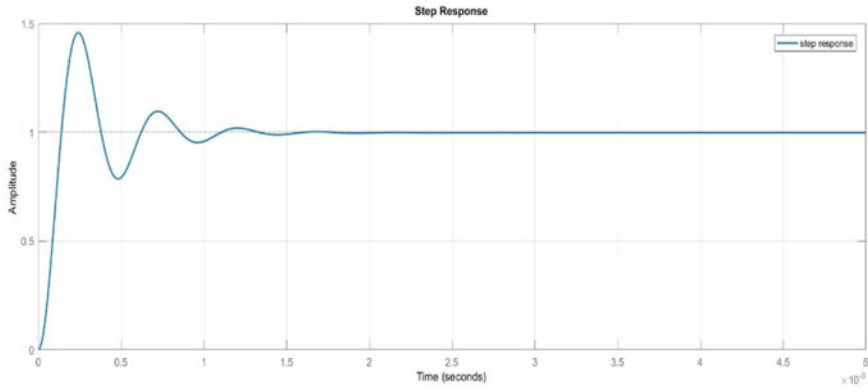


Fig. 7 Closed-loop step response of system

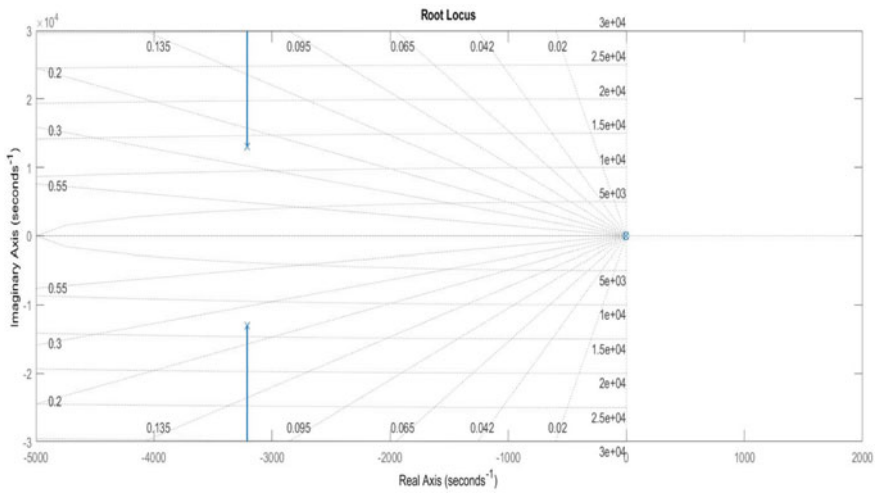


Fig. 8 Root locus of the system

Table 4 PI controller parameter and performance index

Parameters	Value
K_p	8.563
K_i	621.70
Rise time (s)	9.e-05
Settling time (s)	0.00105
Overshoot (%)	46.0

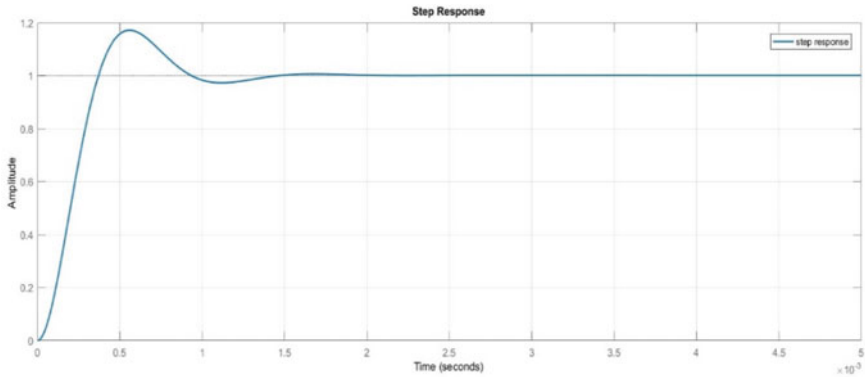


Fig. 9 Closed-loop step response of system

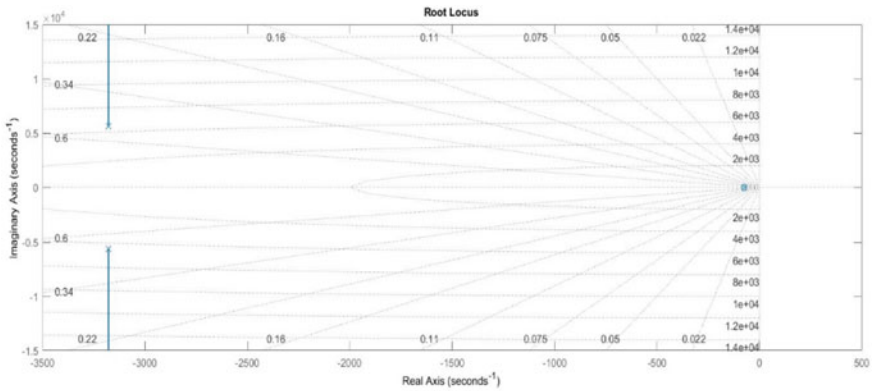


Fig. 10 Root locus of the system

As observed in Fig. 10, both the poles of the second-order system are located on the left half of the s-plane. Hence, the BLDC motor system is stable (Figs. 11 and 12; Table 5).

Case 1: For 40 iteration, $K_p = 38.085$ and $K_i = 213.562$.

Three-dimensional path followed by particles to get the optimum value of PI controller is represented in Fig. 12. For 40 iteration, the initial value of $K_p = 29.22$ and $K_i = 189.12$, and final value in $K_p = 38.085$ and $K_i = 213.5621$.

Speed-time waveform for 40 Iteration is plotted in Fig. 13. Whose maximum amplitude is 2860 RPM, and at a specific interval of time, it changes its direction due to the Hall sensor effect which changes the polarity of phases of BLDC motor (Figs. 14, 15, and 16).

Case 2: For 80 Iteration, $K_p = 36.678$ and $K_i = 183.809$.

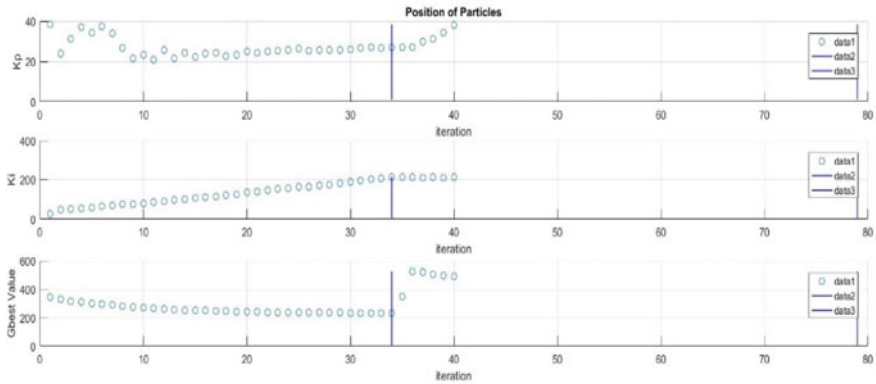


Fig. 11 Position of particles

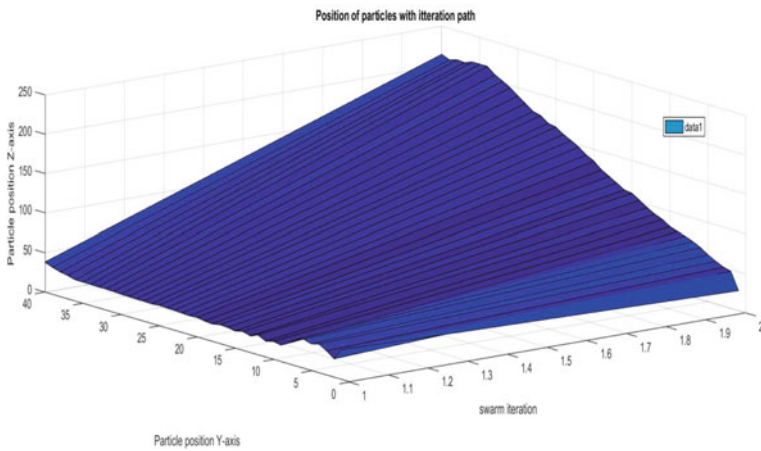


Fig. 12 Three-dimensional path of particles

Table 5 PI controller parameter and performance index

Parameter	Value
Rise time (s)	2.51e-4
Settling time (s)	0.00124
Overshoot (%)	17.2

Three-dimensional path followed by particles to get the optimum value of PI controller represents in Fig. 12. For 80 iteration, the initial value of $K_p = 32.56$ and $K_i = 179.12$, and final value in $K_p = 36.678$ and $K_i = 183.809$ (Figs. 17 and 18).

Speed-time waveform for 80 Iteration is plotted in Fig. 19. Whose maximum amplitude is 2860 RPM, and at a specific interval of time, it changes its direction

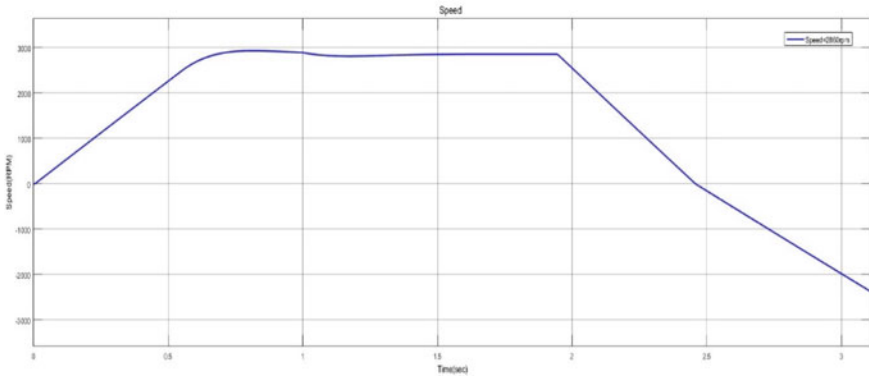


Fig. 13 Speed waveform of motor

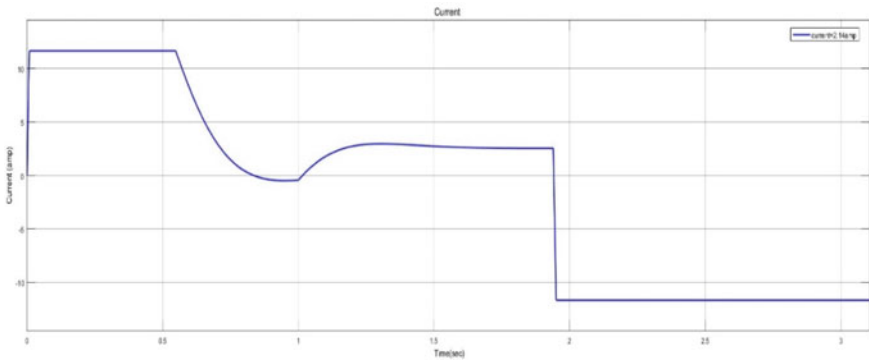


Fig. 14 Voltage waveform of motor

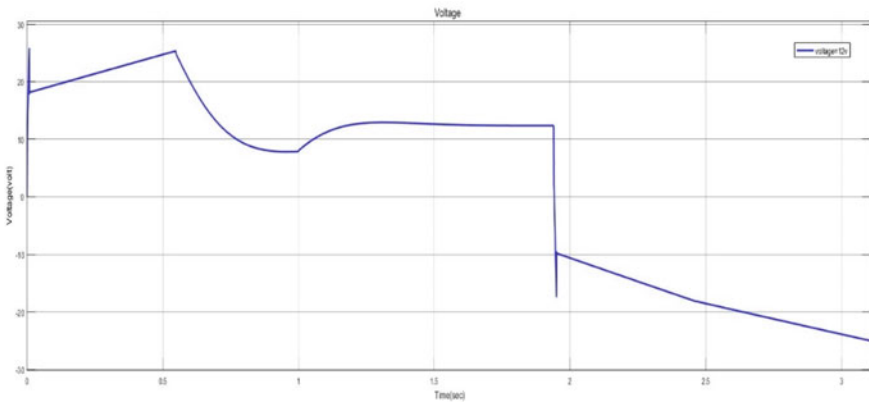


Fig. 15 Current waveform of motor

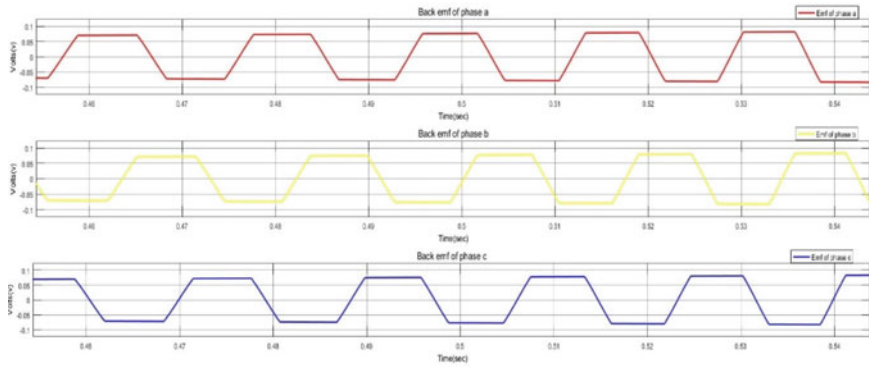


Fig. 16 Three-phase back emf of BLDC motor

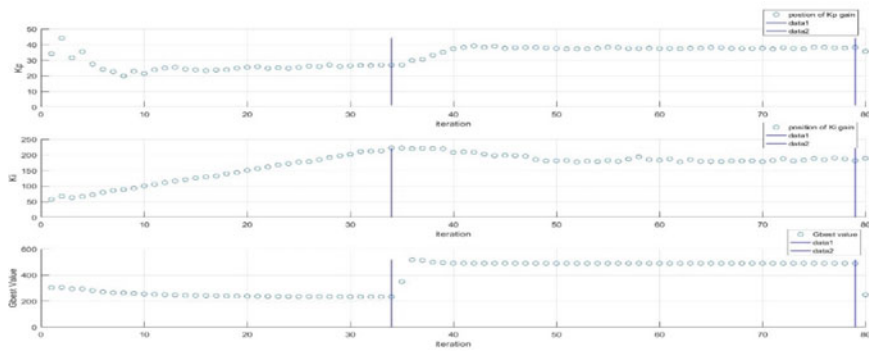


Fig. 17 Position of particles

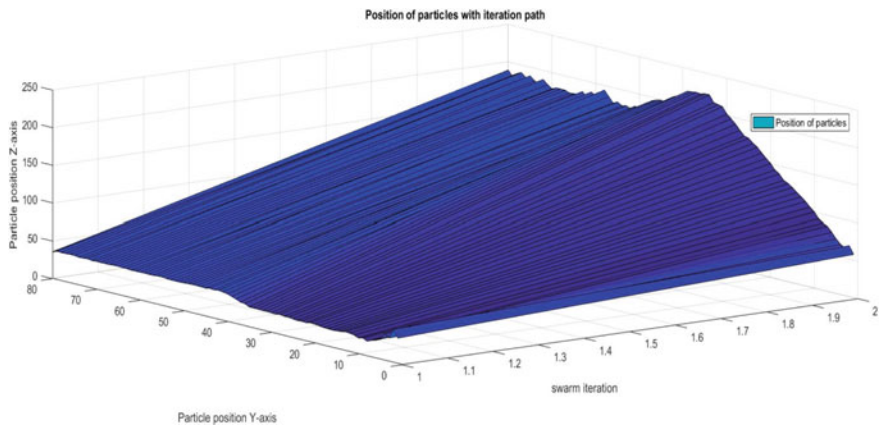


Fig. 18 Three-dimensional path of particles

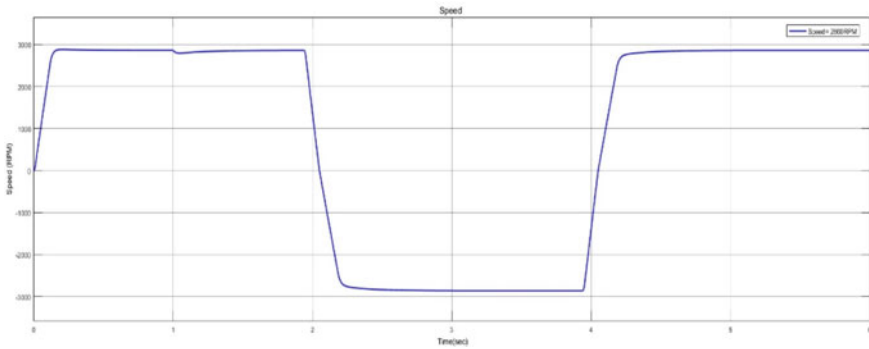


Fig. 19 Speed waveform of motor

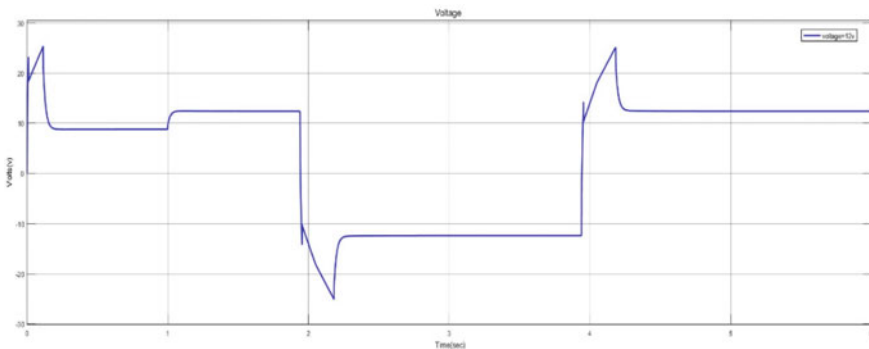


Fig. 20 Voltage waveform of motor

due to the Hall sensor effect which change the polarity of phases of BLDC motor. As the number of iteration increases, the optimum results are obtained.

The output voltage waveform of BLDC motor is as shown in Fig. 20. In which, the output voltage amplitude is settled to 12.0 V. The polarity of voltage changes due to Hall sensor effect.

Figure 21 shows the output current waveform of BLDC motor with the magnitude of 2.14 A.

The three-phase back emf waveform of BLDC motor is shown in Fig. 22. Each phase having a displacement of 120° (Fig. 23).

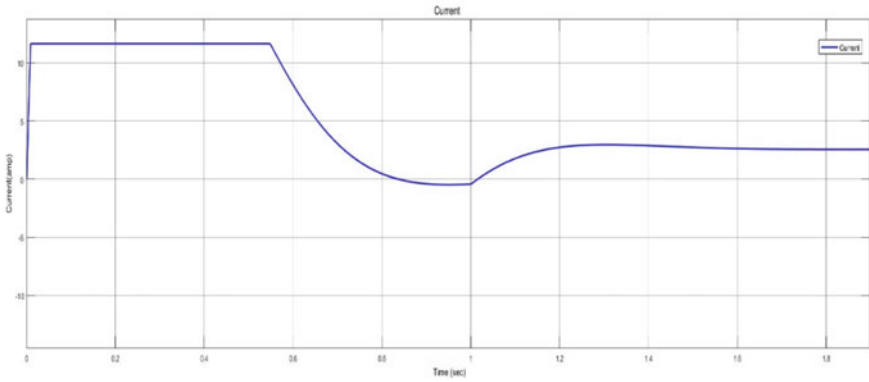


Fig. 21 Current waveform of motor

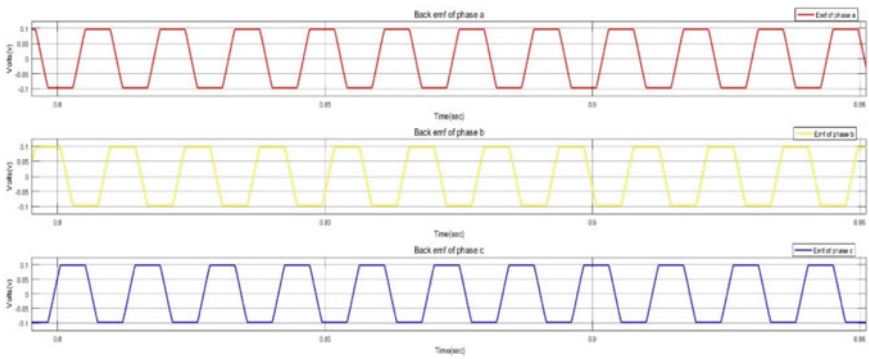


Fig. 22 Three phase back emf of BLDC motor

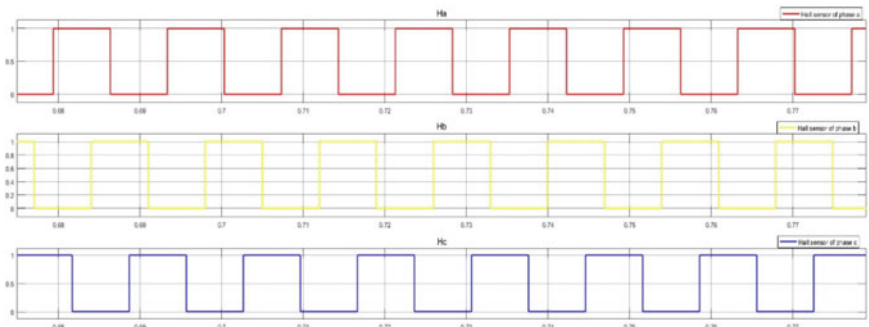


Fig. 23 Hall sensor waveform of motor

6 Conclusion

This paper shows particle swarm optimization algorithm-based closed-loop speed control of BLDC motor. The main objective of this paper is to develop a simple and efficient algorithm to control the speed and drive the motor at maximum efficiency. The comparison between conventional Ziegler–Nichols method and PSO algorithm is based on parameters like maximum overshoot, rise time, and settling time. By closely observing the results, the PI controller tuned with PSO algorithm has improvement in the time response with faster settling time and lower overshoot. To optimize PI controller, PSO algorithm generates new value of K_p and K_i for every iteration. The PSO algorithm can be adopted for lots of industrial applications to reduce the error, overshoot, torque ripples, and provides more stability to the system with smooth speed response.

References

1. Jha AKV, Verma VK, Prince P, Priyadarshini B, Ranjan RK (2018) PSO based design of current CCI-PID controller for the speed control of BLDC motor. In: International conference on power system, Chennai, pp 245–248, February 2018
2. Kennedy J, Eberhart R (1995) Particle swarm optimization. In: Proceedings of IEEE international conference on neural networks, vol IV, Perth, Australia, pp 1942–1948
3. Nasri M, Nezamabadi-Pour H, Maghfoori M (2007) A PSO based optimum design of PID controller for a linear brushless DC motor. *Int J Electr Comput Energetic Electronic Commun Eng* 1(2):171–175
4. Rajasekhar A, Chaitanya V, Das S (2011) Fractional-order PIK DI controller design using a modified artificial bee colony algorithm. *Swarm, evolutionary, and memetic computing*. Springer, Berlin, pp 670–678
5. Mustafa DM, Youssef KH, Elarabawy IF (2018) Hybrid particle swarm optimization and gravitational search algorithm for BLDC motor speed control. In: Twentieth international Middle East power system conference (MEPCON), Egypt
6. Kumar R, Chakravarthi CV, Anuradha S, Puroshatham Prakash B, Rama Krishna D (2018) Advanced speed control strategies of PMBLDC motor in simulation environment. *J Sci Technol (JST)* 3(3):13–23
7. Ridwan M, Raiwan DC, Suryoatmojo H (2017) Particle swarm optimization based BLDC motor speed controller with response speed consideration. In: International seminar in intelligent technology
8. Durgadevi S, Sundari KT, Raaghavi D, Akshaya RS (2019) Comparative study of controller optimisation for CSTR using particle swarm optimization technique. In: Fifth international conference on electrical energy systems (ICEES), Chennai, pp 1–6, February 2019
9. Ayam M, Liqaa SM, Raof TH (2016) Speed control for separately excited DC motor with PID controller, GA and PSO. *Int J Sci Res (IJRSR)* 7(7):12673–12678

A New Approach to Analysis of Disturbances in Generation-Deficit Regions Interfaced with a Large Grid



Suresh Varwandkar and Vijay L. Sonavane

Abstract In this paper, we analyze recent disturbances in the generation-deficit Mumbai distribution network which imports almost the same amount of power that it generates. A new I^2 -analysis is used which has several advantages. In this approach, the alternating sinusoidal current waveform is squared and converted into positive pulses averaged over a cycle, which mimic *particles*, and which constitute power displacement in the power network. Magnitudes of pulses are used in lieu of phasor vectors to determine electrical quantities such as line-flows and voltages from the accumulated magnitudes in the circuit elements. The procedure for computation takes an entirely different route and is suitable for analyzing disturbances in the context of the systems mentioned above. The example includes a recent blackout in the Mumbai region.

Keywords Disturbance analysis · Outage at the slack bus · Load flow

1 Introduction

Blackout has been a topic of high interest among researchers in power systems. Many blackout studies usually appear as diagnostic reports which reconstruct the scenario [1, 2]. Reports are not generally aimed at mathematical analysis and many conclusions are based on engineering wisdom of cause and effects. These post-event investigations rely on measurement data for conclusion and recommendations for future planning and operation. Some papers discuss modeling and philosophical issues [3] and some others analyze network's topological features [4]. IEEE task force [5] reviews methods of analyzing cascading failures but it does not include effects of frequency on line-flows and voltages. Few studies, if any, are available that

S. Varwandkar (✉)
Veermata Jijabai Technological Institute, Mumbai, India
e-mail: varwandkar@gmail.com

V. L. Sonavane
MERC, Mumbai, India

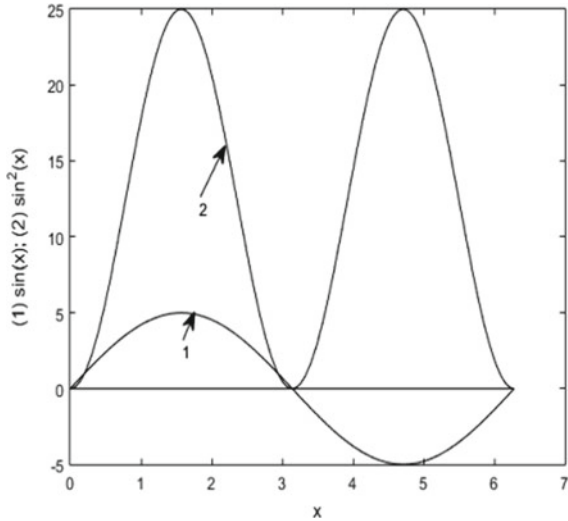
provide analytical assessment of line-flows, voltages and, dynamic conditions that vary violently during blackouts using a case study. Also, blackouts in generation-deficit regions are of special significance as the deficit conditions may be a man-made creation—the market forces. Nevertheless, guidelines must be derived for future planning and secure operation of the system. Mumbai region in India has *available* generation capacity of about 1350 MW and a load of about 2600 MW. Approximately, 1200–1300 MW is imported from the 400 kV main grid. Some local generation in Mumbai is generally not in operation due to commercial considerations. Such systems create special need for disturbance studies. For example, recent blackout in the Mumbai region arose from the depletion and subsequent discontinuance of the imported power which comes from the 400 kV network considered as *source*. The disturbance is thus at the *source*. In conventional analysis, such a source is usually designated as slack bus. The disturbance on the source side, however becomes difficult to investigate since the slack bus is not a part of power-mismatch equations of the load flow! The higher the deficit, the more difficult it is to specify guess voltages to conduct the load flow. Convergence is a very real issue under these circumstances. No *direct* solution is available in literature (except [6]) to obtain line-flows and voltages. Equations are set up in terms of $PQV \delta$ variables which are then solved iteratively using a mismatch convergence criterion, namely the Gauss–Siedel, Newton Raphson, etc. Analysis in this paper is based on transformation of current waves to pulses. We draw clues from the well-established theory of wave-particle duality in physics and translate the load flow formulation in the framework of the *power* particles instead of the sinusoidal waves of voltages and angles. The trick is to square the waveform so that it turns into positive pulses. The available power at any instant is thus converted into positive current pulses. Obvious advantage of this lies in the scalar nature of pulses which can easily deal with superposition of powers (scalars). The renewables sources injecting real power into the system become easy to analyze. Analysis of the recent blackout in Mumbai on October 12, 2020 establishes superiority of the method over other methods which defy application.

2 I^2 Versus \bar{I}

Current is usually treated as a phasor-vector that represents an alternating sinusoidal variable in power system analysis. If the waveform is squared, the alternating wave turns into positive pulses.

This is a qualitative change in the variable in that the negative sign for instantaneous current values disappears. Non-negativity is a characteristic feature of particles which have mass and occupies volume, both greater than zero. “Derivative” operation like those on sinusoidal waveforms cannot be performed on pulses. Pulses can however be directly *summed* as scalars, whereas adding two sinusoids require phase angles. Figure 1 is only a mathematical view—an interpretation. The observed physical phenomenon remains unchanged. Measure of I^2 is the average magnitude of its integral over a time period of the waveform. Net—the sum of—magnitude of the

Fig. 1 Sinusoid and its square



pulses coming from all sources constitutes power in an element from which voltages across it can be computed. For short duration after a large disturbance, Q can be assumed constant (constant flux linkage). Frequency can then be assessed by using an RL representation (instead of RX) by separating frequency in the reactance terms. I^2 -analysis thus makes it possible to evaluate voltages and frequency in the system.

3 Analysis

Consider a single source looking into the driving point impedance offered by the power network. Turbine power P is then equal to $I^2 R$, which immediately gives the magnitude of the current-square. Following expression can be derived for power in every circuit element e in the network [6].

$$p_{ei} = (\xi_{ei} \xi_{ei}^* y_e^*) I_{ii}^2 \tag{1}$$

- p_{ei} power in circuit element
- R_{ii} $\text{Re}(Z_{ii})$; Z is Z -bus
- $\xi_{ei} = (A^T Z)_{ei}$ A is node-element incidence matrix
- y_e admittance of element e
- I_{ii}^2 magnitude of pulses of generator i .

Net pulses (due to all generators) in the element have a magnitude,

$$p_e = \sum_{i=1}^{ng} \xi_{ei} \xi_{ei}^* y_e^* I_{ii}^2 \tag{2}$$

3.1 How to find I_{ii}^2

I_{ii}^2 represents current pulses from only one—the i th generator. Therefore, the transmission and load impedance network are considered with only the i th generator to begin with. Driving point impedance at the i th bus is given by the diagonal of the Z-bus, $R_{ii} + jX_{ii}$. For the turbine power of generator, P_i , the power balance gives,

$$I_{ii}^2 = \frac{P_i}{R_{ii}} \quad (3)$$

Equation (2) can now be readily used to find the net magnitude of power in the element. According to the voltage-drop Pythagorean for a circuit element e ,

$$v_e^2 = i_e^2 r_e^2 + i_e^2 x_e^2 \quad (4)$$

Substituting $p_e = i_e^2 r_e$ and $q_e = i_e^2 x_e = \frac{x_e}{r_e} p_e$,

$$v_e^2 = p_e r_e \left(1 + \frac{x_e^2}{r_e^2} \right) \quad (5)$$

Voltage across an impedance is determined from (5).

With the assumption that Q remains constant before and after the disturbance (at least for a short time), we use $P = I^2 R$ and $Q = I^2 \omega L$ to estimate frequency.

$$\omega = \frac{QR}{PL} \quad (6)$$

In fact, dynamic equations can be cast in terms of frequency and its time trajectory be obtained [7].

Algorithm

1. Convert all power injections into I -squares using (3)
2. Compute p_e from Eq. (2)
3. Compute voltages with (5)
4. Apply procedure of [7] to obtain frequency trajectory.

4 Illustrative Examples

4.1 Example 1

A practical example of the blackout in Mumbai on October 12, 2020 is considered. Details of 220 kV lines can be found in [8]. Multiple parallel lines have

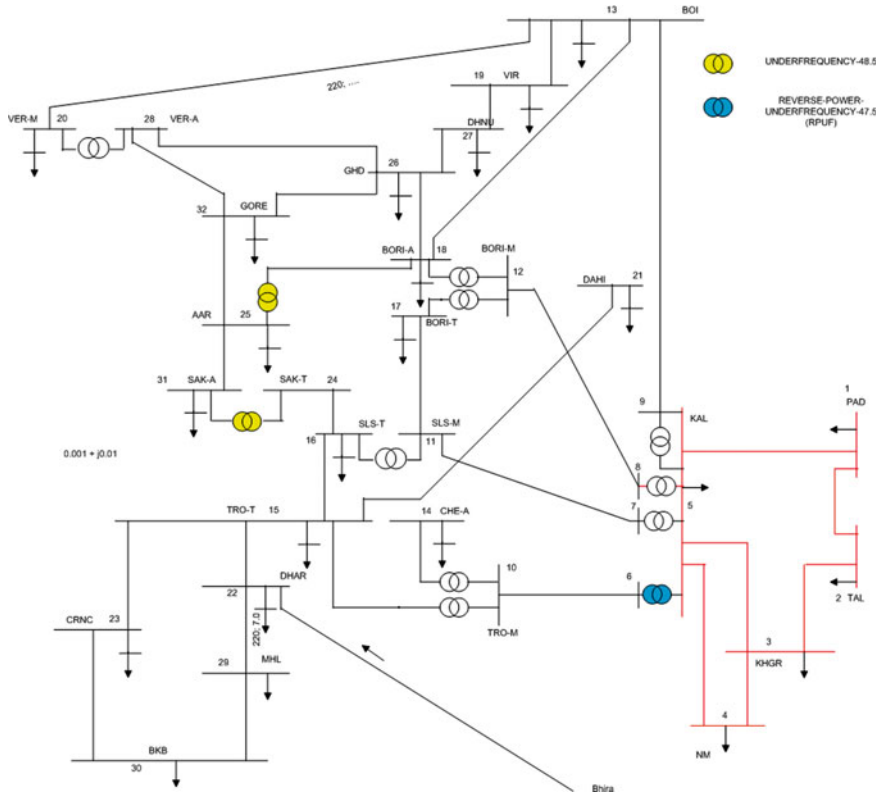


Fig. 2 Mumbai network

been shown by a single line in Fig. 2. Loads in the region belong to four distribution companies: Tata Power (TATA); BEST (included in TATA), Adani Electricity Mumbai Limited (AEML) and Maharashtra State Electricity Distribution Company Limited (MSEDCL) Electrical networks of the companies however do not recognize the ownership of loads. Entire network is an impedance field which draws power according to the design requirements.

Load impedances can be calculated from $Z = 1/(P - jQ)$ (standard specifications, i.e., PQ data of loads are used). All downstream loads are clubbed together at a bus connected by a relatively high impedance distribution/feeder connected to the 220 kV network. Network shown in Fig. 2 is a fair representation for the blackout study. Actual circuit parameters are proprietary data and not available to the authors. Hence, reasonable values are assumed for analysis. For 400/220 kV lines, assumed resistances and impedances range from 0.0004 to 0.0016 (resistances) and 0.001 to 0.004 (reactances), respectively. Cables are assigned higher resistances and relatively lower reactances. All voltage level till the last mile to loads are clubbed together and a representative distributor/feeder impedance used between 220 kV network and the load buses. Parameter values are representative. Detailed data would occupy space.

Those used in this analysis can be provided by the authors on request. Conclusions about voltages obtained under disturbed conditions can be relied upon. Generator and load data are specified in Tables 1 and 2.

Table 1 Load and generation data

220/400 kV bus	LV Load bus	Load MW	Load MVAR	Generation (220 kV)
1	33	5	0	1023 (Padghe)
2	34	5	0	387 (Talegaon)
3	35	200	50	0
4	36	387	18	0
5	37	5	0	0
6	38	5	0	0
7	39	5	0	0
8	40	5	0	0
9	41	5	0	0
10	42	5	0	0
11	43	5	0	0
12	44	5	0	0
13	45	5	0	0
14	46	5	0	0
15	47	88	10	864 (Trombay + Hydro)
16	48	80	10	0
17	49	90	10	0
18	50	130	20	0
19	51	30	0	0
20	52	5	0	0
21	53	110	10	0
22	54	90	10	0
23	55	310	70	0
24	56	300	50	0
25	57	87	10	0
26	58	75	10	0
27	59	115	10	485 (Dahanu)
28	60	115	10	0
29	61	280	30	0
30	62	185	20	0
31	63	200	70	0
32	64	170	60	0

Table 2 Load-bus voltages: Base case and after event 1 and event 2

Bus	33	34	35	36	37	38	39	40
Base	1.0843	1.0717	0.9136	0.9434	1.0593	1.0573	1.0568	1.0568
Event 1	1.2065	1.0773	0.9035	0.9324	1.0445	1.0427	1.0421	1.0421
Event 2	0.7300	0.7295	0.6287	0.6503	0.7341	0.736	0.7338	0.7336
Bus	41	42	43	44	45	46	47	48
Base	1.0582	1.0531	1.0504	1.0502	1.0555	1.0531	0.9974	0.9981
Event 1	1.0435	1.0389	1.0359	1.0358	1.041	1.0389	0.9841	0.9844
Event 2	0.7349	0.7418	0.7329	0.7324	0.7373	0.7418	0.7057	0.6978
Bus	49	50	51	52	53	54	55	56
Base	0.9942	0.9628	1.0458	1.0464	0.9809	0.9898	0.8321	0.8430
Event 1	0.9805	0.9496	1.0317	1.032	0.9679	0.9766	0.8210	0.8314
Event 2	0.6935	0.6726	0.7359	0.7316	0.6941	0.7003	0.5887	0.5891
Bus	57	58	59	60	61	62	63	64
Base	0.9915	1.003	0.9934	0.9769	0.8687	0.9251	0.8783	0.9036
Event 1	0.9779	0.9893	0.9802	0.9635	0.8571	0.9128	0.8662	0.8912
Event 2	0.6927	0.7029	0.7037	0.6831	0.6147	0.6546	0.6137	0.6317

In case of underfrequency (48.5 Hz), the interconnecting transformers between Saki-A and Saki-T, and that between Aarey and Borivli-M enable separation of Tata and AEML networks. The ICT-T at Kalwa has an RPUF (reverse power under-frequency relay) which operates at 47.9 Hz. Settings of the frequency relays are changeable. Following events are considered [9].

1. Base case
2. Disconnection of 400 kV Padghe Ck-II (line 1–5)
3. Disconnection of 400 kV *source* at Padghe (1023 MW) and 387 MW at Talegaon
4. ICT between SAK-T and SAK-A (UF) and ICT between Aarey-A and Borivli (UF) operate simultaneously.

The method mentioned above gave following results for load voltages.

4.2 Peculiarities of Events 3 and 4

Events 3 and 4 cause major upheavals in the system and pose difficulty in conduct of the conventional power flow analysis. Frequency departs substantially from nominal during these events and that invalidates the basic power flow equations. I-square analysis comes in handy under the circumstances. Using the method of [2], the system frequency is seen to follow a time trajectory shown in Fig. 3.

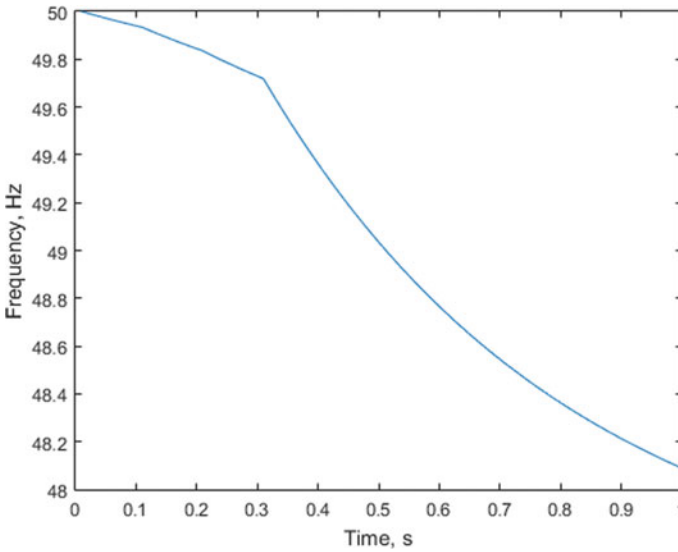


Fig. 3 System frequency

5 Conclusion

Small power systems interfaced with large grids offer interesting opportunity for system studies. Not all studies can be performed with conventional methods. A new approach is presented which can determine system voltages under all frequency conditions. A recent blackout in the generation-deficit Mumbai region is analyzed in detail to illustrate application of the method. Unfortunately, there are no case studies available to compare our results of line-flows and voltages, under varying frequency conditions. Outages are separated in time to be able to visualize the system behavior. In practice, the time interval between outages will be much smaller and the time-axis in the frequency plot will be a fraction of, say, 0.2 to 0.5. Line-flows can be plotted if desired.

Acknowledgements Exchanges with Shri Vasant Pande, Dr. K. Rajamani, Prof. B. G. Fernandes and Shri Girish Jawale were helpful in preparation of this paper. The authors are much thankful to them for sharing practical insights and providing information.

References

1. 1996 System Disturbances: North American Electric Reliability Council, August 2002, Review of selected 1996 Electric System Disturbances in North America, [Online, accessed October 2021], 1996_Disturbance_Report_Final.doc (nerc.com)
2. U.S.–Canada Power System Outage Task Force, Final report on the August 14, 2003 blackout in the United States and Canada: causes and recommendations. Canada: April, 2004. [Online, accessed October 2021]. <http://www.nerc.com>
3. Dobson I, Carreras BA, Lynch VE, Newman DE (2004) Complex system analysis of series of blackouts: cascading failures, criticality and self-organization. In: Bulk power system dynamics and control—VI, 22–27 Aug 2004, Cortine d' Ampezzo, Italy
4. Soltan S, Mazauric D, Zussmann G (2017) Analysis of failures in power grids. *IEEE Trans Control Netw Syst* 4(2):288–300
5. IEEE PES CAMS Task Force on understanding, prediction, mitigation and restoration of cascading failures, Initial review of methods for cascading failure analysis in electric power transmission systems. In: IEEE Power engineering society general meeting, Pittsburgh, USA, July 2008
6. Varwandkar S (2019) Realification of power flow. *IEEE Trans Power Syst* 34(3):2433–2440
7. Varwandkar SD, Hariharan MV (2017) Frequency excursions in complex power systems—a modular approach. In: Int'l conference on power systems (ICPS2017), 21–23 Dec 2017, Pune
8. Maharashtra Electricity Regulatory Commission. Transmission License No. 1 of 2014 (Second Amendment) Available: www.merc.gov.in
9. Maharashtra Electricity Regulatory Commission. Case No. 202 of 2020: Suo Motu Proceeding in the matter of Grid Failure in the Mumbai Metropolitan Region on 12 October 2020 at 10.02 Hrs.: Available: www.merc.gov.in

Human Activity Recognition Using 1-Dimensional CNN and Comparison with LSTM



Suryakant Kumar Kashyap, Parikshit Narendra Mahalle,
and Gitanjali Rahul Shinde

Abstract The practice of recognizing different forms of human activities is known as human activity recognition (HAR). We are using two deep learning architectures LSTM and CNN for recognizing activities using smartphones sensors data and then, comparing them with each other because they are best suited for time series data which is generated from sensors. Our proposed architecture, a lightweight CNN model, achieved an accuracy of 96.06%, outperforming more complex and cumbersome algorithms like fast and robust deep convolutional neural network structure (FR-DCNN) and residual LSTM (Res-LSTM). Further, we compared our model to the LSTM model, in terms of accuracy, time taken for training, f1-scores of each activity, precision, recall values, and resources consumed. Our CNN architecture performed better than the LSTM architecture in all the mentioned terms. Hence, it is concluded that for real-world applications, CNN models should be adopted for this purpose.

Keywords Human activity recognition · Convolutional neural network · Long short-term memory · Deep learning

1 Introduction

Human activity recognition (HAR) has always been a popular issue since support vector machines (SVMs) were the state-of-the-art models in machine learning. It

S. K. Kashyap (✉)

Computer Engineering, Smt. Kashibai Navale College of Engineering, Savitribai Phule Pune University, Pune, India
e-mail: suryakantk94@gmail.com

P. N. Mahalle

Department of Artificial Intelligence and Data Science, Vishwakarma Institute of Information Technology, Pune, India

G. R. Shinde

Department of Computer Engineering, Vishwakarma Institute of Information Technology, Pune, India

has maintained its appeal to this day, and it now has even more uses. Human activity prediction is the process of recognizing certain behaviors obtained from the sensors data which are obtained from smartwatches and smartphones. Healthcare, fitness, human–computer interfaces, ambient-assisted living (AAL), and surveillance systems are some of the most well-known uses. In healthcare, it is used to track any abnormal activity in the patient’s routine activities which gives doctors an early sign of a potential disease which helps in the proper treatment of the disease. Ambient-assisted living is a subset of ambient intelligence. It is used for eldercare to assist them so that they can leave independently in their advanced years and remain socially connected to their community. More specifically, fall detection is the primary concern of AAL where it can detect falls and transfer all the details of the event to their nearest hospitals and caretakers. Sensors have become an important aspect of people’s lives today. It has been present in smartphones and now, smartwatches like the Apple watch contain different types of microsensors like heart sensors, accelerometers, and gyro meters which keep track record of all the vital elements of the human body like heart rate and sleep time. Smartwatches are also capable of fall detection and have now become popular among people. For fitness, people use it for tracking daily calories burned, step counts, and total sleeping time. And after COVID-19, the use of sensors has increased even more for tracking SPO₂ levels and pulse rate as a simple and early detector for COVID-19. Further, there has been a significant boom in the number of users of devices like smartwatches that use sensors to assist humans in their daily lives.

As a result, there has been a growing demand for more and more strong deep learning models that are both accurate and fast. We demonstrate two models, such as Conv1D and LSTM, and compare them in terms of F1-scores, accuracy, and training duration in this paper. For this, we are using the UCI-HAR dataset, which contains six basic activities of everyday living. In particular, we employ a one-dimensional CNN that beats the LSTM, a type of RNN, with respect to F1-scores and accuracy.

There are 8 sections in this paper in total. Section 1 introduces to the topic of this paper with its significant application in today’s world and the paper’s purpose. Section 2 discusses the previous work that has been done prior on this topic. Section 3 discusses the research gap present in the literature. Section 4 describes the dataset and its features. Section 5 talks about the proposed work, the methodology we adopted, and the model architectures. Section 6 discusses, compares, and analyzes in detail the results we obtained. Section 7 is the conclusion that can be elicited from all the work done in this research paper and future work that can be done further in this field. Last section is the references section which enlists all the references taken from different research papers.

2 Literature Review

Very first machine learning models on this dataset were proposed by Girija et al. [1], in which the Naïve Bayes classifier had 79% accuracy, random forests had 96.3%

accuracy, K-means clustering algorithm had only 60% accuracy, and IBK classifier was the best among them with more than 90% accuracy. In paper [2], we can see 89% accuracy achieved using the MCHF-SVM model. All of these are the baseline models.

Since the advent of deep learning, its techniques are applied in this field too like CNN. Maximum precision of 93.31% for 3 convolutional layers and kernel size of 32 was achieved by Cruciani et al. [3]. They utilized a 1D-CNN with varying numbers of convolutional layers and a different number of kernel sizes. With a modest pooling size, Ronao CA et al. constructed a deep convolutional network (ConvNets) [4]. It obtained an accuracy of 94.79% on the test dataset. They showed how different learning rates affect accuracy.

A more complicated version of CNNs was also applied and tested on the UCI-HAR dataset. In the paper [5], Mohammed et al. demonstrated that they achieved an accuracy of 95.4% using a one-dimensional convolutional network with random search (RS-1D-CNN). They used random search for hyperparameters tuning and applied global pooling layer (GAP) for dimensionality reduction to achieve maximum accuracy. They also used the batch normalization (BN) technique to speed up the convergence.

The combination of CNNs with LSTMs has also been implemented to improve accuracy. In paper [6], K. Xia et al. describe a model which combines LSTM with CNN. Their LSTM-CNN architecture was shown to have a 95.78% accuracy. The three models suggested in the study [7] are residual LSTM (Res-LSTM), LSTM, and residual bidirectional LSTM (Res-Bidir-LSTM), with an accuracy of 91.6%, 90.8%, and 93.6%, respectively. They have concentrated mostly on the utilization of residual networks. A fast and robust deep CNN structure was proposed in the paper [8], which achieved an accuracy of 95.2%. A detailed comparison table of accuracies is shown in the later parts of this document of different models.

3 Gap Analysis

Human activity recognition has always kept the attention of the machine learning community due to its applications. There are a lot of papers concerning this area of study using different datasets based on human activity recognition like UCI-HAR, OPPORTUNITY, PAMAP2, and WISDM. We are using the UCI-HAR dataset in this paper which is described below. Almost all current deep learning models are demonstrated on this dataset, including ANNs, self-organizing maps (SOMs) [9], CNNs, autoencoders [10], recurrent neural networks (RNNs) [11], LSTMs, Boltzmann machines [12], and gated recurrent units (GRUs) [13]. To the best of our knowledge, it has not been proved which of the above-mentioned techniques are better and more suited for human activity recognition in general. Which should a practitioner gain in a real-world application such that it is both precise and lightweight? In other words, a crucial comparison of different strategies for HAR is missing. The goal of this research is to fill in some of the gaps that have been explained and to show how

Table 1 Activities and their corresponding labels are shown in the table

Label	Activities
0	Laying
1	Sitting
2	Standing
3	Walking
4	Walking downstairs
5	Walking upstairs

powerful a simple 1D CNN model can be when compared to LSTM. The performance of a simple 1D CNN is provided in this study, and its performance is examined with LSTM in terms of performance, training time, and efficiency.

4 Dataset and Features

The dataset we are working on is “human activity recognition using smartphones”. It is available on the machine learning repository from UCI [14]. It contains six activities labeled as shown in Table 1.

The dataset was developed using data from studies conducted with a group of 30 volunteers ranging in age from 19 to 48 years old. These six tasks were completed by each participant while wearing a Samsung Galaxy S-II smartphone around their waist. They recorded 3-axial linear acceleration and 3-axial angular velocity at a constant rate of 50 Hz using the device’s inbuilt accelerometer and gyroscope. The collected dataset was randomly partitioned into two sets, with 70% of the volunteers being chosen to provide training data and 30% being chosen to generate test data. The dataset consists of 561 feature vectors making it a highly multidimensional dataset. It contains a total of 10,299 records out of which 2947 records are in the test set, and 7352 records are in the training set. It contains 3 motion activities (walking, walking downstairs, walking upstairs, and 3 rest activities (laying, sitting, standing). We performed exploratory data analysis (EDA) of the data to extract useful information from the data. The dataset is almost balanced as can be visualized in the chart in Fig. 1. It was generated using Matplotlib and Seaborn libraries.

5 Proposed Work

5.1 Data Preprocessing

The data were pre-processed before feeding it to the convolutional neural network. We split the dataset into two sets in training and test set in the ratio of 80% to

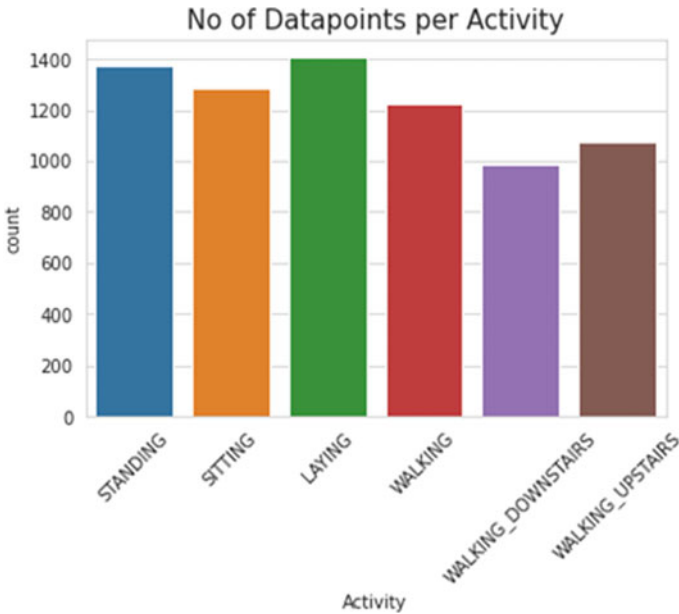
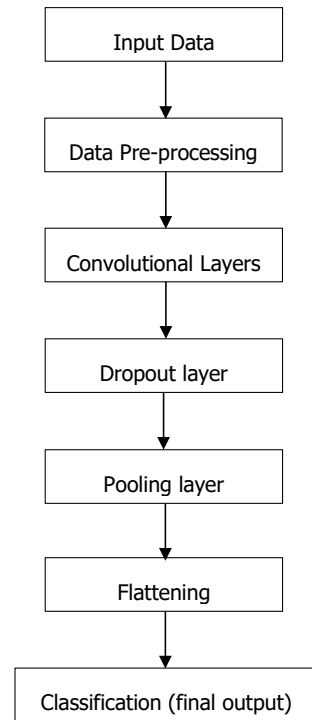


Fig. 1 Chart shows the number of records per activity

20%, respectively. We further bifurcated both training and test set into two sets with one containing all the input features and the other containing the output labels corresponding to them. Then, we encoded the train and test output labels column, so that each of the six activities got numerical values from 0 to 5. We then one hot encoded the data into dummy variables as neural network algorithms cannot directly work on categorical data. We reshaped the train and test input features dataset such that it is compatible with our architecture. Data augmentation was not done as there was no need.

5.2 Methodology

The data obtained from the sensors like accelerometer and gyro meter are time series data. The models best suited for time series data for extracting features and classification are CNNs and LSTMs. Hence, we are training two deep learning models such as LSTM and CNN (Conv1D) to predict 6 different categories of activities trained on 561 features. Both models learn from the temporal dependencies between outputs. The main distinction between the two models is that LSTMs can learn long-term dependencies and predict the next output from the context of prior output information by remembering the relevant information and forgetting the irrelevant. We tried different optimizers like Adam, Adamax, and Adadelta and different model

Fig. 2 Flowchart

structures with a varying number of hidden layers and dropout layers with dropout percent from 10 to 90% for both models, of which these models came to be the best for 1D CNN and LSTM which are described in next sub-section model architecture. A flowchart showing data transfer from one step to another is shown in Fig. 2.

The complexity of a neural model is defined by the number of trainable parameters present in a neural network. Trainable parameters depend on weight biases, the number of neurons, and their connections, i.e., if the convolution layers will be more, more complex the model will become. As our proposed model includes only 2 convolutional layers, trainable parameters for our proposed model are less compared to other algorithms which use a lot greater number of these layers. Further, by adding the dropout layer, we have reduced parameters even more. The high accuracy achieved by the model on the dataset in a smaller number of epochs and time makes it efficient. Thus, our model is lightweight as well as efficient.

5.3 Model Architecture

LSTM Model: We are using stacked LSTM with two LSTM layers and one dropout layer because two layers are reasonably enough for extracting complex features from

the dataset. A dropout layer is added after the first layer to prevent overfitting, and the second LSTM layer is added to extract the more complicated features, followed by a dense layer using an activation function Softmax. Finally, we used Adam as the optimizer out of others as it showed better accuracy than others as Adam, AdaDelta, and RMSProp have similar algorithms. The basic model architecture is shown below:

$$\text{Lstm_layer1} \rightarrow \text{Dropout_layer} \rightarrow \text{Lstm_layer2} \rightarrow \text{Dense_layer}$$

In Fig. 3, the architecture of the LSTM model is shown with input and output parameters.

Conv1D model (our proposed model): We are using a 1-dimensional convolutional neural network (Conv1D) with 2 convolutional layers, followed by a dropout layer to reduce overfitting to the data and to reduce parameters. We are using filters of size 64 and kernel size of 3 which slides in only one direction. The activation function used is rectified linear unit (ReLU). The max-pooling layer, which calculates the maximum value for each section of the feature map covered by the filter and flattening layer, is then followed by two dense layers and a max-pooling layer. The classification layer is the final dense layer. There are no optimization methods, such as random search or Bayesian optimization [15], used, and no dimensionality reduction is done, as in [5]. The basic model architecture of the proposed model is shown below:

$$\text{Conv1D_layer1} \rightarrow \text{Conv1D_layer2} \rightarrow \text{Dropout_layer} \rightarrow \text{Maxpooling1D} \\ \rightarrow \text{Flatten_layer} \rightarrow \text{Dense_layer1} \rightarrow \text{Dense_layer2}$$

Fig. 3 LSTM model architecture

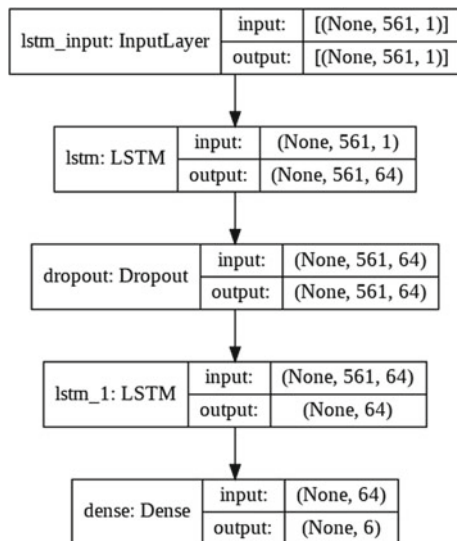
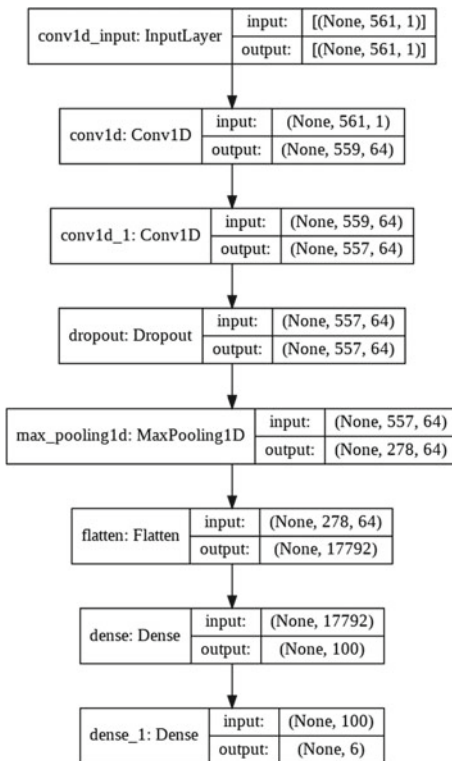


Fig. 4 Our proposed Conv1D model architecture with all input and output parameters and convolutional layers



In Fig. 4, the detailed architecture of the Conv1D model is shown with input and output parameters.

6 Results and Discussion

Conv1D model achieved a test accuracy of 96.06% with the proposed architecture described in Fig. 2. It is greater than 95.4% which was achieved in the paper [5]. They have used random search with 1D-CNN, applied batch normalization (BN), and dimensionality reduction. The precision the proposed model has achieved is 96% which is greater than 93.31%, as demonstrated in the paper [3], by 3%. They have used 3 convolutional layers. The accuracy is also greater than some cutting-edge models like Res-LSTM, LSTM, Res-Bidir-LSTM, and fast and robust deep CNN structure (FR-DCNN) as described in papers [7] and [8], respectively. A detailed comparison of accuracies can be seen in Table 4.

For the best accuracy, both models were trained with different hyperparameter settings. The best results we got are listed below. The accuracy of the Conv1D model was 99.18% on the training set, and the accuracy was 95.88% on the validation

set. The LSTM model, on the other hand, achieved an accuracy of 92.91% on the training set and an accuracy of 89.20% on the validation set. In Conv1D, we received an F1-score ranging from 93 to 100% for each activity, while in LSTM, we received an F1-score ranging from 83 to 97%. LSTM's test accuracy was 87.54%. As a result, it can be concluded that CNNs outperform LSTMs in terms of accuracy. CNN architecture obtained the greatest accuracy in only 17 epochs, whereas LSTM took 150 epochs. Therefore, it is concluded that CNNs require far fewer training epochs than LSTMs.

We also used Google Colab to train both of our models, using the same Python 3 Google Compute Engine backend and no GPU or TPU. Google Colab is a Google application for researchers. On the Google server in the browser, we can run several types of Python codes. Conv1D was substantially faster than the LSTM model, and it took much less time to train and validate than the LSTM model. As a result, it can be stated that CNNs train faster than LSTMs. When comparing Conv1D to LSTM, it was also observed that the Conv1D consumed far fewer resources. Due to the LSTM's complicated structure, the LSTM model demanded more compute engine power than the CNN one. Tables 2 and 3 show the classification report generated by the LSTM model and the proposed CNN model, respectively. It mentions the average accuracy, precision, recall, and F1-score values corresponding to every 6 activities.

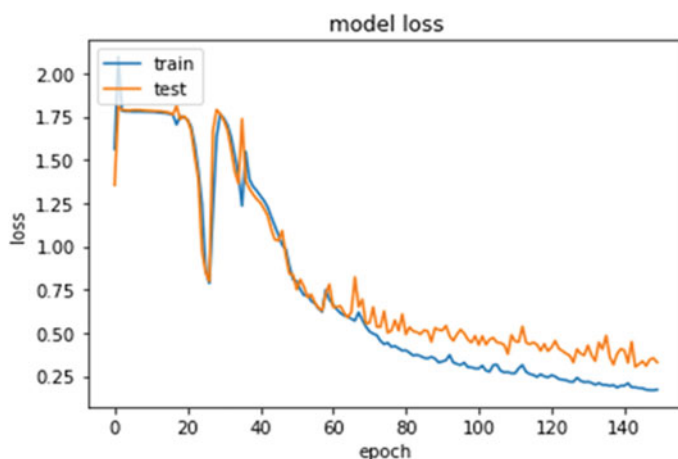
Figures 5 and 6 show model loss graphs generated by the LSTM and Conv1D model, respectively, on both train and test sets in both figures. Figures 7 and 8 display the confusion matrix generated for the LSTM and Conv1D model, respectively. In Table 4, a comparison of accuracies achieved by different approaches of LSTM and CNN is listed.

Table 2 Classification report for LSTM

Activity	Precision	Recall	F1-score	Support
Laying	1.00	0.95	0.97	537
Sitting	0.84	0.82	0.83	491
Standing	0.84	0.85	0.85	532
Walking	0.92	0.88	0.90	496
W. downstairs	0.93	0.78	0.85	420
W. upstairs	0.76	0.95	0.84	471
Accuracy			0.88	2947
Macro avg.	0.88	0.87	0.87	2947
Weighted avg.	0.88	0.88	0.88	2947

Table 3 Classification report for Conv1D (CNN)

Activity	Precision	Recall	F1-score	Support
Laying	1.00	1.00	1.00	537
Sitting	0.95	0.91	0.93	491
Standing	0.92	0.97	0.94	532
Walking	0.95	0.99	0.97	496
W. downstairs	0.98	0.93	0.96	420
W. upstairs	0.95	0.96	0.95	471
Accuracy			0.96	2947
Macro avg.	0.96	0.96	0.96	2947
Weighted avg.	0.96	0.96	0.96	2947

**Fig. 5** Model loss graph for LSTM model

7 Conclusion and Future Work

We have presented a lightweight one-dimensional CNN model (Conv1D), in this paper. The novelty of the model is its simpleness and effectiveness when compared to other complicated algorithms, i.e., without applying any dimensionality reduction or batch normalization techniques, it performed comparably to some state-of-the-art architectures in this field such as LSTM-CNN architecture and DeepConvLSTM as represented in Table 4. Our lightweight model achieved an accuracy of 96.06% on the test dataset. It is compared in the tabular form above with other models. It also performs better than Res-LSTM, LSTM, Res-Bidir-LSTM proposed in paper [7] and FR-DCNN proposed in paper [8]. For Conv1D, the greatest F1-score was 100% for laying activity, and the lowest was 93% for sitting. Additionally, we compared the Conv1D model to the LSTM model. We demonstrated in the experiments that the

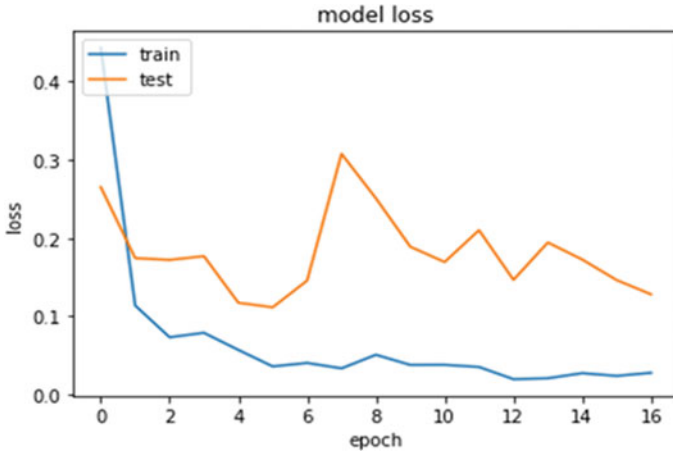


Fig. 6 Model loss graph for Conv1D model

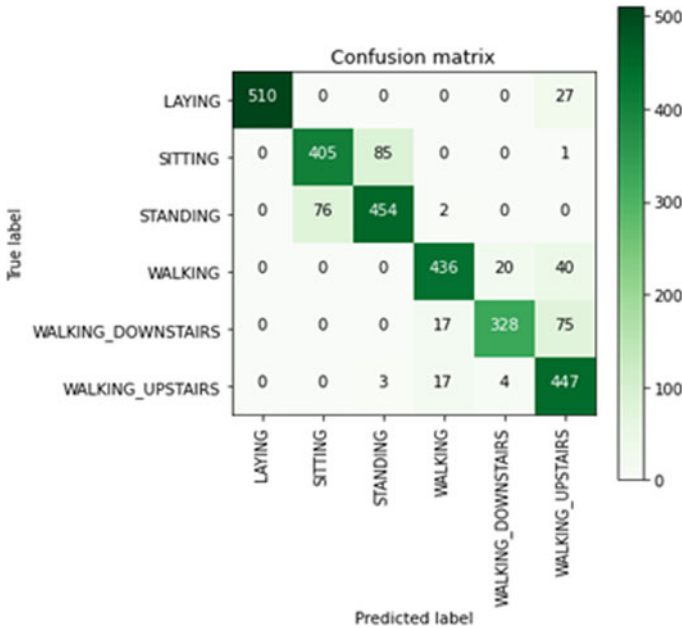


Fig. 7 Confusion matrix for LSTM model

suggested Conv1D (CNN) architecture outperforms LSTM by 8% in accuracy. It can be concluded that the models based on CNN perform better than the models based on LSTM. After comparing the CNN architecture to the LSTM architecture used in the paper, we recommend that practitioners use CNN instead of LSTM in real-world

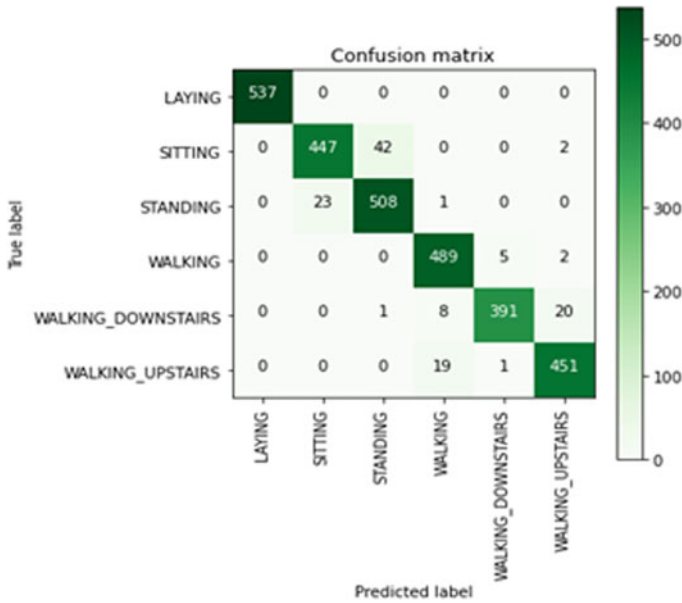


Fig. 8 Confusion matrix for Conv1D model

Table 4 Comparison of accuracy achieved in different LSTM and CNN approaches

References	Method/model used	Best accuracy (%)
[4]	Deep CNN (ConvNets)	94.79
[16]	CNN	95.31
[8]	FR-DCNN	95.2
[7]	Res-LSTM	91.6
	LSTM	90.8
	Res-Bidir-LSTM	93.6
[17]	Deep ConvLSTM	95.8
[6]	LSTM-CNN architecture	95.78
[3]	1D CNN with 3 layers	93.31 (precision)
[5]	RS-1D-CNN	95.4
Proposed model	Conv1D	96.06

applications because it is easier to train, takes less time, and uses less compute engine power, as analyzed in detail above, leading to lower battery consumption.

Even after so much progress, and usage of multiple algorithms for forecasting human activity more correctly and precisely, as we mentioned in Sect. 2, there is still more need for improvement. By merging deep learning approaches in future studies, accuracy can be raised and loss can be reduced even more, and more robust models can be made.

Contributions Methodology—S.K.K.; Conceptualization—S.K.K.; Experiment—S.K.K.; Resources—S.K.K.; Dataset Curation—S.K.K., and P.N.M.; Dataset Analysis—S.K.K.; Writing—Original Draft Preparation—S.K.K.; Writing—Review and Editing—P.N.M., G.R.S., and S.K.K.; Project Administration—P.N.M, G.R.S.; Supervision—P.N.M., G.R.S.

References

1. Anguita D, Ghio A, Oneto L, Parra X, Reyes-Ortiz JL (2012) Human activity recognition on smartphones using a multiclass hardware-friendly support vector machine. In: International workshop on ambient assisted living. Springer, Berlin, Heidelberg, pp 216–223
2. Anguita D, Ghio A, Oneto L, Parra X, Reyes-Ortiz JL (2012) Human activity recognition on smartphones using a multiclass hardware-friendly support vector machine. In: International workshop on ambient assisted living. Springer, Berlin, Heidelberg, pp 216–223. Haslam E (1993) Shikimic acid metabolism and metabolites. Wiley, New York
3. Cruciani F, Vafeiadis A, Nugent C, Cleland I, McCullagh P, Votis K, Hamzaoui R (2019) Comparing CNN and human crafted features for human activity recognition. In: 2019 IEEE SmartWorld, Ubiquitous intelligence & computing, advanced & trusted computing, scalable computing & communications, cloud & Big Data computing, Internet of people and smart city innovation (SmartWorld/SCALCOM/UIC/ATC/CBDCom/IOP/SCI). IEEE, pp 960–967
4. Ronao CA, Cho SB (2016) Human activity recognition with smartphone sensors using deep learning neural networks. *Expert Syst Appl* 59:235–244
5. Ragab MG, Abdulkadir SJ, Aziz N (2020) Random search one dimensional CNN for human activity recognition. In: 2020 International conference on computational intelligence (ICCI). IEEE, pp 86–91
6. Xia K, Huang J, Wang H (2020) LSTM-CNN architecture for human activity recognition. *IEEE Access* 8:56855–56866
7. Zhao Y, Yang R, Chevalier G, Xu X, Zhang Z (2018) Deep residual bidir-LSTM for human activity recognition using wearable sensors. *Math Prob Eng*
8. Qi W, Su H, Yang C, Ferrigno G, De Momi E, Aliverti A (2019) A fast and robust deep convolutional neural networks for complex human activity recognition using smartphone. *Sensors* 19(17):3731
9. Parisi GI (2020) Human action recognition and assessment via deep neural network self-organization. In: *Modelling human motion*. Springer, Cham, pp 187–211
10. Garcia KD, de Sá, CR, Poel M, Carvalho T, Mendes-Moreira J, Cardoso JM, Kok JN (2021) An ensemble of autonomous auto-encoders for human activity recognition. *Neurocomputing* 439:271–280
11. Mekruksavanich S, Jitpattanakul A (2021) Lstm networks using smartphone data for sensor-based human activity recognition in smart homes. *Sensors* 21(5):1636
12. Sedighi H (2020) Classification of human activity recognition using smartphones. *arXiv preprint arXiv:2001.09740*
13. Dua N, Singh SN, Semwal VB (2021) Multi-input CNN-GRU based human activity recognition using wearable sensors. *Computing*, 1–18
14. Anguita D, Ghio A, Oneto L, Parra X, Reyes-Ortiz JL (2013) A public domain dataset for human activity recognition using smartphones. In *Esann*, vol 3, p 3
15. Mekruksavanich S, Jitpattanakul A (2021) Biometric user identification based on human activity recognition using wearable sensors: an experiment using deep learning models. *Electronics* 10(3):308

16. Ignatov A (2018) Real-time human activity recognition from accelerometer data using convolutional neural networks. *Appl Soft Comput* 62:915–922
17. Ordóñez FJ, Roggen D (2016) Deep convolutional and LSTM recurrent neural networks for multimodal wearable activity recognition. *Sensors* 16(1):115

Optimal VA Loading of UPQC Using Rao-1 Algorithm



Swati Gade  and Rahul Agrawal 

Abstract In a modern power system, a unified power quality conditioner (UPQC) is considered an effective and promising mitigating equipment for all types of power quality (PQ) problems. Use of variable phase angle control (PAC) technique for controlling UPQC results in increased utilization of both PECs most efficiently making the system more attractive economically. In this research work, the Rao-1 algorithm along with variable PAC is implemented to find the optimal loading of UPQC. The outcomes obtained from Rao-1 are compared with the JAYA optimization to show the dominance and competence of the Rao-1 over JAYA. This research work will help in developing instantaneous control techniques based on optimization techniques.

Keywords Power electronic converter · Rao algorithm · UPQC

Abbreviations and Symbols

APF	Active power filter
PAC	Phase angle control
PEC	Power electronic converter
PEC1	Series PEC
PEC2	Shunt PEC
PF	Power factor
PQ	Power quality
PSO	Particle swarm optimization
UPQC	Unified power quality conditioner
UPQC-P	Active power control of UPQC
UPQC-Q	Reactive power control of UPQC
UPQC-S	Simultaneous active reactive power control of UPQC

S. Gade (✉) · R. Agrawal

Electrical Engineering Department, Sandip University, Nashik 422213, India

e-mail: swatiagade@gmail.com

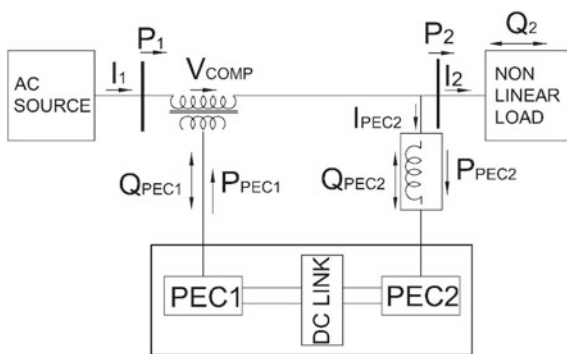
UPQC- VA_{min}	Minimum VA loading UPQC
V_{comp}	Series voltage injected by DVR, volts
V_1, I_1	Rated source voltage and current
V_2, I_2	Rated load voltage and current

1 Introduction

The use of nonlinear load in modern power systems introduces several power quality (PQ) issues such as voltage dip, voltage swell, harmonics, excessive neutral current, unbalance, and reactive power compensation. Interruption of the critical load which results in poor power factor (PF) of the system and huge financial loss are the major consequences of these PQ issues [1, 2]. Maintaining the PQ of the supply to specified standards is necessary to improve the system’s performance and reliability [3, 4]. In a modern power system, a unified power quality conditioner (UPQC) is considered the utmost powerful and efficient mitigating device to mitigate all these PQ issues. In 1998, Fujita and Akagi proposed UPQC which belongs to the APF family [5]. As illustrated in Fig. 1, UPQC is made up of two back-to-back connected power electronics converters (PEC) via common DC-Link. PEC1 which is connected in series between source and load end is responsible to mitigate voltage-related PQ issues. On the other hand, to compensate load reactive power and current-related PQ issues PEC2 is utilized. It is connected at the point of common coupling in parallel with the load. As UPQC is utilized in a distribution system for voltage and current-related PQ problem mitigation simultaneously, it is categorized as a custom power device [6].

From the literature of UPQC, it is found that UPQC is more popular among researchers due to its feature of simultaneous series and shunt compensation. In recent years, researchers are trying to utilize UPQC in various applications along with its performance improvement. Based on the method of compensation, it is categorized as active power control (UPQC-P), reactive power control (UPQC-Q), minimum volt

Fig. 1 Block diagram of UPQC



ampere (UPQC- VA_{\min}), and simultaneous active reactive power control (UPQC-S) [6]. In the case of active power control, only active power is required for compensation as the compensating voltage is added in phase with the supply current. Similarly, in the case of reactive power control, only reactive power is delivered by PEC1 as the compensating voltage is added in quadrature with source current [7]. For compensation by UPQC- VA_{\min} and UPQC-S method, both active power and reactive power are required as the compensating voltage is added at a some specific angle with the supply current [8–10]. This results in increased utilization of UPQC as PEC1 is used for compensation of a small fraction of load reactive power. To reduce the VA burden on PEC2 and hence the overall UPQC system, the researcher had tried to use PEC1 for load reactive power compensation using the phase angle control (PAC) technique [11]. Compared to conventional control techniques, PAC-based techniques offer advantages such as load reactive power compensation by PEC1 [12].

With the offline optimization approach, a suitable optimum angle at which compensating voltage is to be injected is pre-calculated. A 2-D look-up table is figured and is utilized to control PEC1 [10]. In Siva Kumar et al. [13], the effect of total harmonic distortion on load voltage and source current, as well as system parameters like load PF, load current, and voltage dip, was considered as design variables while formulating the optimization problem. The particle swarm optimization (PSO) method is implemented to find the optimal value of power angle δ between the load and the supply voltage. Compensating voltage has to be injected so that this optimum angle is maintained to keep the VA loading of UPQC minimum. However, its effect on VA loadings of both PECs along with series transformer is not considered.

An algorithm for designing UPQC for an optimal rating of both PECs was proposed by Ambati and Khadkikar [14]. The relation between the VA loadings of both UPQC PECs, the amount of voltage dip, swell, and angle has been determined using mathematical modeling. The fixed optimum angle δ at which the utilization of UPQC will be maximum is determined for the worst voltage dip and voltage swell conditions. On the other hand, optimal design of UPQC based on variable PAC is proposed by Ye et al. [15]. Based on this technique for the worst operating condition such as voltage dip and swell, a two-level control technique is implemented to determine the optimal ratings of both the PECs of UPQC with improved utilization of overall UPQC. Furthermore, for various compensating operations, this control technique is used to decrease the projected online VA loadings of UPQC. The maximum series injected voltage causes the series transformer's VA rating to increase. The ratings of the PECs and the series transformer, on the other hand, will have an effect on each other [16].

The literature suggests that power angle δ is controlled for optimization of VA loading of UPQC. However, the power rating limits of all the components of the UPQC such as both PECs and the series transformer are not taken into account while determining this optimal angle. Teaching learning-based optimization technique is implemented to determine optimal utilization of both PECs for various operating environments such as voltage dip and voltage swell [17]. Optimal utilization of UPQC during steady state using the JAYA algorithm is presented in Gade and Agrawal [18].

From the literature, it has been noted that optimization of VA loading has received little attention thus far. There is no all-encompassing approach for optimizing UPQC loading for all operating conditions. The main aim of this work is determination of the optimal VA loading of an individual component of UPQC such as PEC1 and PEC2 under any operating condition. An optimization technique named as Rao-1 algorithm is used to determine this optimal value of the angle δ corresponding to the operating condition. The results are compared with the JAYA algorithm.

It has been found that many researchers used numerous advanced optimization techniques to solve engineering optimization problems. For improved performance of these algorithms, it is required proper tuning of common control parameters along with algorithm-specific parameters of the algorithms [19]. Improper tuning of algorithm-specific parameters results in increased computing effort and poor algorithm performance. Algorithm-specific parameter-less techniques such as the JAYA algorithm [20, 21] and Rao algorithm [22] are used to solve the problem of tuning algorithm-specific parameters. These methods simply require population size and the number of generations, etc. The main contributions of the present research paper are as follows:

1. Examine the VA loading of a UPQC for various operating conditions such as voltage dip and steady state using the Rao-1 algorithm
2. Analyzing various optimization techniques such as JAYA and Rao-1 algorithm to determine the optimal value of angle δ and K
3. Implementation of various optimization techniques such as JAYA and Rao-1 algorithm to minimize VA loading of UPQC
4. Compare the results of the proposed algorithm using the Rao-1 algorithm with the results of the JAYA optimization technique.

The remaining paper covers the following sections: The problem statement is illustrated in Sect. 2. A brief explanation of the JAYA and Rao-1 optimization techniques is presented in Sect. 3. Section 4 covers the implementation of the Rao-1 algorithm for optimal VA loading. Results and discussions are covered in Sect. 5. The paper is concluded with concluding remarks and future scope in Sect. 6.

2 Problem Formulation

Phasor diagram illustrating the operation of UPQC-VA_{min} is shown in Fig. 2. For maintaining the proper power angle δ between load and supply voltages, PEC1 has to add compensating voltage V_{comp} at an angle γ . Likewise, during operation, there will be phase difference of power angle δ between load current I_2 and resulting load current I'_2 which results in the constant load current with constant power factor angle φ .

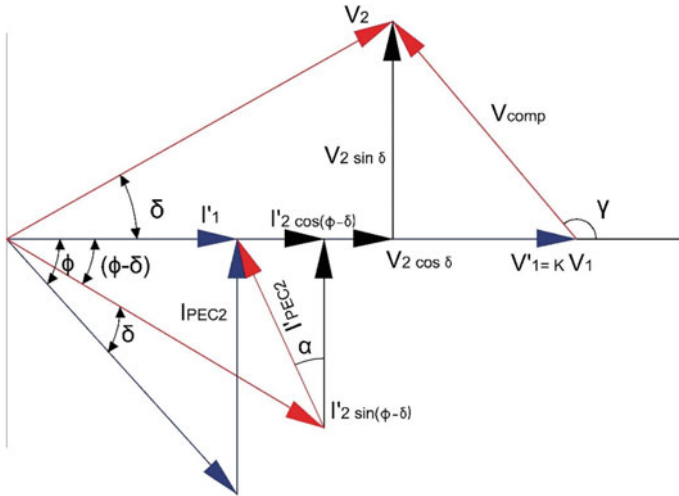


Fig. 2 Phasor diagram of UPQC-VA_{min}

2.1 Mathematical Modeling of UPQC-VA_{min}

The mathematical model used in this research work is taken from Ambati and Khadkikar [14]. For maintaining load voltage V_2 , constant series voltage V_{comp} is added at an angle γ with instantaneous source voltage V_1 . During steady state, PEC2 provides the entire load reactive power for maintaining unity PF at the source. On the other hand, PEC2 supplies active power needed for PEC1 during dip/swell as well as the load reactive power.

Injected voltage by PEC1,

$$V_{Comp}(\delta, K) = \sqrt{(V_2 \cos \delta - K V_1)^2 + (V_2 \sin \delta)^2} \tag{1}$$

where V_1 and V_2 are the sources and load voltage in volts, respectively.

Power delivered by PEC1,

$$S_{PEC1}(\delta, K) = \sqrt{(P_{PEC1}(\delta, K))^2 + (Q_{PEC1}(\delta, K))^2} \tag{2}$$

where S_{PEC1} is the VA loading in kVA, P_{PEC1} (kW) is the active power delivered, and Q_{PEC1} (kVar) is the reactive power delivered by the PEC1.

Power delivered by the series transformer,

$$S_{trans}(\delta, K) = \max_{K=K_{min}}^{K=K_{max}} [V_{Comp}] \times \frac{I_1}{K_{min}} \tag{3}$$

where S_{trans} is the VA loading of series transformer in kVA, K_{min} is the worst voltage dip, and k_{max} is the worst voltage swell condition. I_1 is the source current in Amp.

Power delivered by the PEC2,

$$S_{\text{PEC2}}(\delta, K) = \sqrt{(P_{\text{PEC2}}(\delta, K))^2 + (Q_{\text{PEC2}}(\delta, K))^2} \quad (4)$$

where S_{PEC2} is the VA loading in kVA of the PEC2; P_{PEC2} (kW) and Q_{PEC2} (kVAr) are the active and reactive power delivered by PEC2, respectively.

VA loading of the UPQC, as a function of δ at any operating condition,

$$S_{\text{UPQC}}(\delta, K) = S_{\text{PEC1}} + S_{\text{PEC2}} \quad (5)$$

where S_{UPQC} is the VA loading in kVA of the UPQC.

2.2 Objective Function and Constraints

The foremost objective of this research work is finding the optimal value of δ for the corresponding operating condition for which the VA loading of UPQC will be minimum. The objective function is framed as follows:

$$\text{Min } S_{\text{UPQC}}(\delta, K) = S_{\text{PEC1}} + S_{\text{PEC2}} \quad (6)$$

Subjected to inequality constraints,

$$S_{\text{PEC1}} \leq \text{kVA rating of PEC1} \quad (7)$$

$$S_{\text{PEC2}} \leq \text{kVA rating of PEC2} \quad (8)$$

$$V_{\text{Comp}} \leq \text{max of } V_{\text{Comp}} \quad (9)$$

The maximum value of V_{comp} is calculated from Eq. (1) by putting $K = K_{\text{max}}$ and $\delta = 45^\circ$.

This optimization problem is subjected to the following design variable limit constraints,

$$0^\circ \leq \delta \leq 45^\circ \quad (10)$$

$$0.6 \leq K \leq 1.4 \quad (11)$$

3 Optimization Techniques

Optimization is a branch of mathematics that aims to determine the best value for a physical system that is constrained in a certain manner. Traditional optimization approaches are limited by their long calculation times and lack of accuracy. Many powerful intelligent optimization algorithms have been developed in recent years to overcome these challenges.

3.1 JAYA Algorithm

R. Venkata Rao proposed the ‘JAYA’ algorithm, a swarm intelligence-based heuristic method for addressing constrained and unconstrained optimization problems, in 2016. A solution advances closer to the best solution with each iteration of the JAYA algorithm, while it travels away from the worst. As a result, the search process has been successfully accelerated and extended [23]. The initial population is stochastically updated as follows:

$$x_{jk}^{i+1} = x_{jk}^i + r_{1j}^i \{x_{j\text{best}}^i - |x_{jk}^i|\} - r_{2j}^i \{x_{j\text{worst}}^i - |x_{jk}^i|\} \tag{12}$$

where $x_{j\text{best}}^i$ is the best solution and $x_{j\text{worst}}^i$ is the worst solutions among the current population. i, j , and k are the index of iteration, variable, and candidate solution. r_{1j}^i, r_{2j}^i are random numbers and act as scaling factors for ensuring the good diversification.

3.2 Rao-1 Algorithm

In 2020, metaphor-less heuristic search method named as Rao-1 algorithm was proposed by Rao [22]. In the Rao-1 algorithm, equation for the solution update is simple, with only addition and multiplication operations being included.

Moreover, the Rao-1 has no algorithm-specific parameters and is thus suitable for determining the optimal VA loading of UPQC [24]. In the Rao-1 algorithm, the population is updated as follows:

$$x_{jk}^{i+1} = x_{jk}^i + r_j^i (x_{j\text{best}}^i - x_{j\text{worst}}^i) \tag{13}$$

r_j^i is consistently scattered random number in the range of [0, 1]. It is utilized as a scaling factor and guarantees appropriate diversity during the search process. Figure 3 shows the pseudocode for the Rao-1 algorithm.

4 Implementation of Rao-1 Algorithm for Optimal VA Loading of UPQC

In this research work, UPQC is connected to serve for maintaining supply side PF to unity PF and 40% compensating capacity for mitigation of voltage dip and voltage swell. Authors have tried to find the optimal angle δ for corresponding operating conditions by using the Rao-1 algorithm. Objective function of the optimization problem is framed using the mathematical model presented in Sect. 2. Figure 3 shows the pseudocode of Rao-1 algorithm is implemented as per pseudocode given in Fig. 3. The system parameters used are given in Table 1, and algorithm parameters used are given in Table 2.

The step-by-step procedure of implementation of the Rao-1 algorithm for optimal VA loading is given as follows. Figure 4 shows the flowchart of the same.

- Step 1: Enter the system parameters $P_2, Q_2, V_1,$ and V_2 as per Table 1.
- Step 2: Initialize algorithm as per Table 2.
- Step 3: Initialize design variables, power angle $\delta,$ and operating condition $K.$
- Step 4: Estimate various parameters of UPQC such as $V_{comp}, S_{PEC1}, S_{PEC2},$ and S_{trans} from the mathematical model presented in Sect. 2 for without optimization and with TLBO and JAYA optimization techniques.
- Step 5: Generate an initial population $x_{j\ k}^i$ and calculate the objective function $f_{j\ k}^i$ for each design variable.
- Step 6: Determine the best $x_{j\ best}^i$ and worst $x_{j\ worst}^i$ solution from the initial population.
- Step 7: Modify the initial population of the j th variable as per Eq. (13).

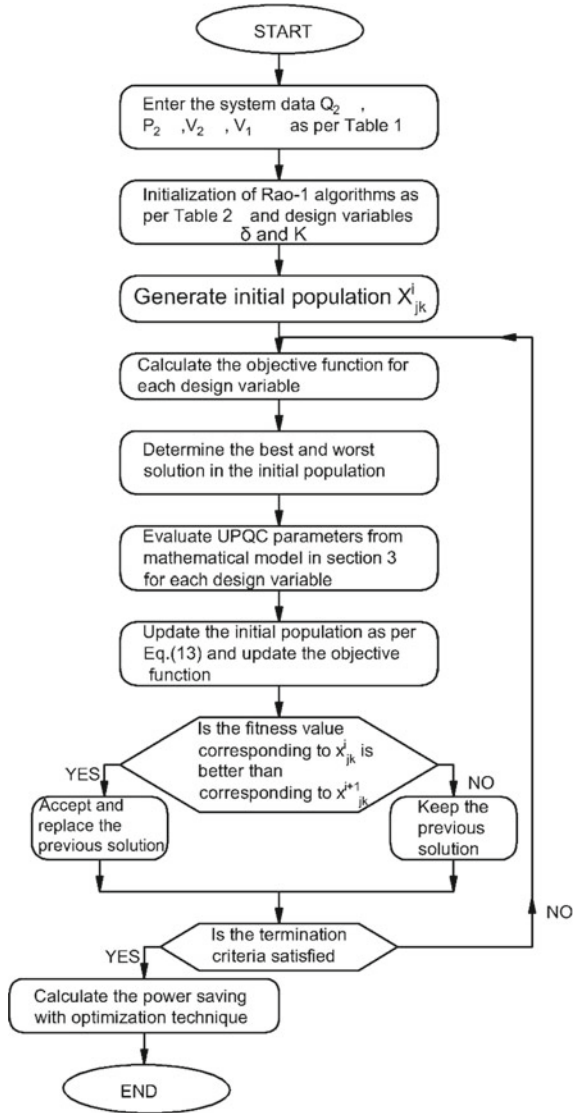
Table 1 System parameters

Parameter	Quantity
Load	10 kW + 10 kVAr
Source voltage (V_1)	400 V
Load voltage (V_2)	400 V
Per phase VA rating of PEC1	2490 VA
Per phase VA rating of PEC2	2907 VA
Voltage dip condition	0.6–0.9 pu
Steady-state condition	0.9–1.1 pu

Table 2 Algorithm parameters of Rao-1 algorithm

Parameter	Value
Design variables (D)	2
Population size (N)	50
Iterations (i)	50
Random number (r)	[0,1]

Fig. 4 Flowchart: Implementation of Rao-1 algorithm for optimal VA loading of UPQC



Step 8: Check the boundary limits.

Step 9: Calculate the updated objective function f_{jk}^{i+1} for corresponding to x_{jk}^{i+1} .

Step 10: Update the solutions as per the equation below,

$$\text{if } f_{jk}^{i+1} \leq f_{jk}^i \tag{14}$$

Table 3 UPQC parameters without optimization

K	UPQC approach	Per phase VA loading (VA)			V_{comp} (volt)	Power angle (δ)
		PEC1	PEC2	UPQC		
K = 0.6	UPQC-P	2223	4007	6230	93	0
	UPQC-VA _{min}	3577	1048	4625	148	38
K = 1	UPQC-P	0	3334	3334	0	0
	UPQC-VA _{min}	0	3333	3333	0	0

$$\text{then } \begin{cases} x_{jk}^i = x_{jk}^{i+1} \\ f_{jk}^i = f_{jk}^{i+1} \end{cases} \quad (15)$$

Step 11: Terminate the algorithm as per termination criteria and display the optimal solution.

5 Results and Discussions

In the MATLAB environment, the proposed optimization algorithms are written. The algorithms are tested using a balanced and harmonic-free system. Tables 1 and 2 list the system's parameters as well as optimization algorithms. The parameters for the system were obtained from Ref. [14].

5.1 VA Loading Analysis of UPQC Without Optimization

Loading of UPQC without optimization approaches is given in Table 3. From the results, it is clear that VA loading of the UPQC-VA_{min} approach is reduced considerably compared to UPQC-P. However, VA loading of PEC1 is increased during voltage dip conditions. On the other hand, PEC1 remains ideal during steady state and entire load reactive power is supplied by PEC2 only which results in an increased burden on PEC2.

5.2 VA Loading Analysis of UPQC with Optimization

Table 4 presents the VA loading of UPQC during voltage dip and steady state with optimization approaches. From the output results, it is observed that with the Rao-1 algorithm the optimum value of power angle δ is minimum compared to the JAYA algorithm. For the small value of angle, compensating voltage and hence the burden

Table 4 UPQC parameters with optimization techniques

	Voltage dip		Steady state	
	JAYA	Rao-1	JAYA	Rao-1
K	0.854	0.9	0.9	0.944
Power angle (δ)	30.8	25.8	18.83	19.290
Vcomp (volts)	118.25	100.5	75	76.293
<i>VA loading (VA)</i>				
PEC1	1998.2	1612	1208	1166.664
PEC2	1335.3	1721.4	2145	2166.669
Series transformer	2239.1	1958.58	1324	1290.418
UPQC	3333.549	3333.334	3353	3333.333

on series transformer reduces. The detailed analysis of VA loading of UPQC with optimization for voltage dip and steady state is given in the following subsection.

Voltage dip: To create voltage dip condition in the simulation, design variable K is varied from 0.6 to 0.9 pu. Output results show that with optimization loading of both PECs reduced considerably. Figure 5 shows the VA loading of both PECs and series transformers. In the case of the Rao-1 algorithm for compensation, reactive power is utilized which results in a reduction in the active power burden on PEC2. To maintain the unity PF at source side, load reactive power is supplied by PEC2 in case of UPQC-P and PEC1 in case of UPQC- V_{min} approaches. However, with optimization approaches load reactive power is shared by PEC1 (60% with JAYA algorithm and 48% with Rao-1 algorithm) and PEC2 (40% with JAYA algorithm and 52% with Rao-1 algorithm). From the output results, it is found that with optimization both PECs are loaded in their maximum efficiency region which results in increased efficiency of the overall UPQC, making it more attractive economically. Figure 6

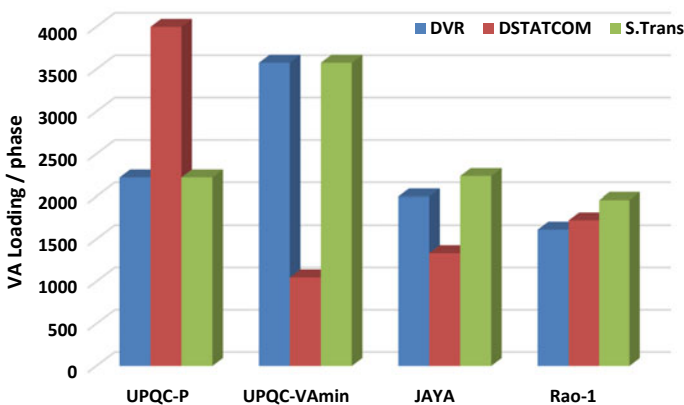


Fig. 5 Loading of PECs and series transformer during voltage dip

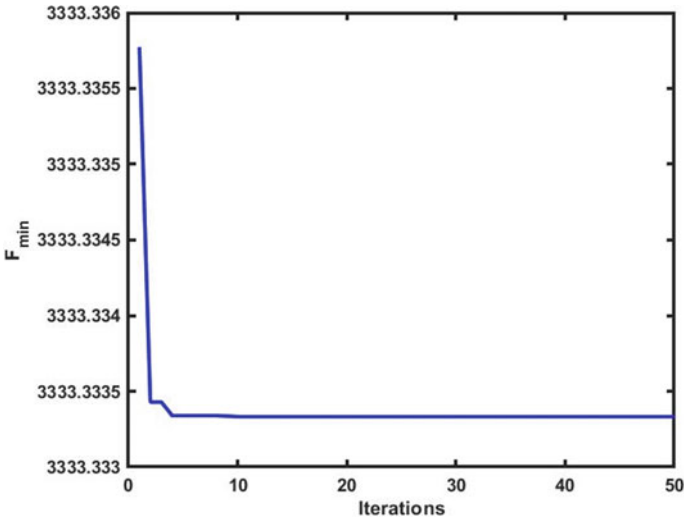


Fig. 6 Convergence characteristics of Rao-1 algorithm during voltage dip

shows the conversion characteristics of the Rao-1 algorithm. From Fig. 6, it is clear that the Rao-1 algorithm converges in five iterations. The statistical analysis of the optimization algorithm is presented in Table 5. The robustness of the Rao-1 algorithm and its ability to discover the optimum solution in every run is confirmed by the value of standard deviation (SD) which is minimum (0.107517) compared to the JAYA algorithm.

Steady state: By varying design variable K from 0.9 to 1.1 pu, steady-state condition is created. Figure 7 shows the VA loading of both PECs and series transformers during a steady state. To maintain the unity PF at source side, load reactive power is supplied by PEC2 in case of without optimization approaches. However, output results show that with optimization both PECs are utilized for load reactive power compensation which enhances the effective utilization of UPQC. With optimization approaches, around 35% load reactive power is shared by PEC1 and the remaining

Table 5 Statistical analysis of optimization algorithms

	Voltage dip		Steady state	
	JAYA	Rao-1	JAYA	Rao-1
Mini	3333.549	3333.334	3353	3333.333
Mean	3334.168	3334.838	3117	3333.335
Best	3333.549	3333.334	3353	3333.340
Worst	4023.568	3335.879	3498	3333.343
SD	0.111372	0.107517	18.53	0.00838

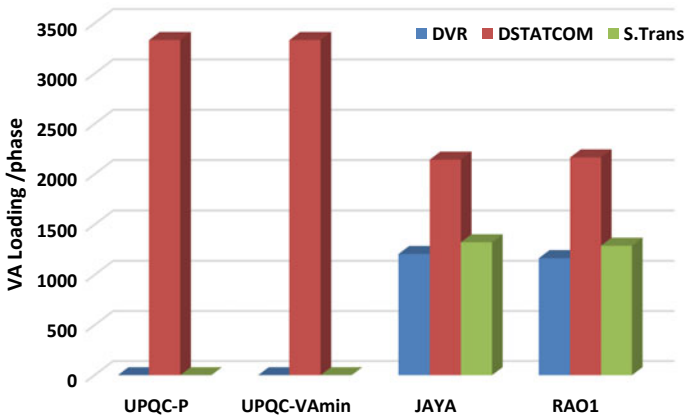


Fig. 7 VA loading of both PECs and series transformer during steady state

is shared by PEC2. Figure 8 shows the convergence characteristics of the Rao-1 algorithm during a steady state. From Fig. 8, it is clear that the Rao-1 algorithm converges in five iterations. The statistical analysis of the optimization algorithm is presented in Table 5. The robustness of the Rao-1 algorithm and its ability to discover the optimum solution in every run is confirmed by the value of SD (0.00838) compared to the JAYA algorithm.

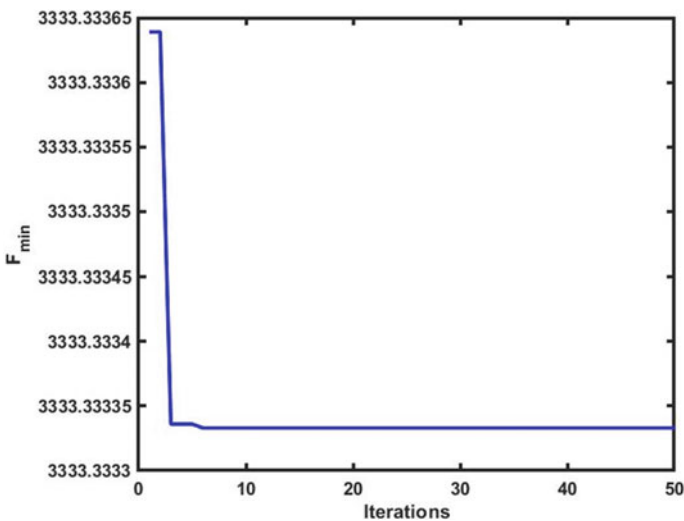


Fig. 8 Convergence characteristics of Rao-1 algorithm during steady state

6 Conclusion

This paper presents a unique algorithm using Rao-1 optimization to determine the optimal values of δ and K for optimal VA loading of UPQC. In view of evaluating the capability of this proposed UPQC-VA_{min} with Rao-1, its performance is compared with the JAYA algorithm. From the output results obtained, it is found that the Rao-1 algorithm converges faster to the global optimal value than the JAYA algorithm. The proposed technique is easy to implement than other approaches. In the proposed algorithm, the compensation is based on the variable PAC method and this algorithm does not require any algorithm-specific parameters. The increased use of both PECs reduces power loss and reduces the UPQC system's manufacturing cost. This makes the UPQC more appealing as a cost-effective and efficient solution for eliminating the PQ problem and integrating renewable energy sources into the main grid. As a conclusion, this paper will contribute to the development of a UPQC control strategy based on optimal instantaneous VA loading in order to increase UPQC efficiency and VA loading.

References

1. Dugan RC, McGranaghan MF, Beaty HW (1996) Electric power system quality. McGraw-Hill, New York
2. Bollen MHJ (2000) Understanding power quality problems: voltage sags and interruptions, ser. IEEE Press Power Eng. IEEE, Piscataway, NJ
3. Singh B, Chandra A, Haddad KA (2015) Power quality problems and mitigation techniques. Wiley
4. Ghosh A, Ledwich G (2002) Power quality enhancement using custom power devices. Kluwer, Norwell, MA
5. Fujita H, Akagi H (1996) New trends in active filters for improving power quality. In: International conference on power electronics, drives and energy systems for industrial growth, vol 1, pp 417–425
6. Khadkikar V (2012) enhancing electric power quality using UPQC: a comprehensive overview. IEEE Trans Power Electron 27(5):2284–2297
7. Lee WC, Lee DM, Lee TK (2010) New control scheme for a unified power-quality compensator-q with minimum active power injection. IEEE Trans Power Delivery 25(2):1068–1076
8. Khadkikar V, Chandra A (2011) UPQC-s: a novel concept of simultaneous voltage sag/swell and load reactive power compensations utilizing series inverter of UPQC. IEEE Trans Power Electron 26(9):2414–2425
9. Kolhatkar YY, Errabelli RR, Das SP (2005) A sliding mode controller based optimum UPQC with minimum VA loading. In: IEEE Power engineering society general meeting, vol 1, 2005, pp 871–875
10. Kolhatkar YY, Das SP (2007) Experimental investigation of a single-phase UPQC with minimum VA loading. IEEE Trans Power Delivery 22(1):373–380
11. Khadkikar V (2013) Fixed and variable power angle control methods for unified power quality conditioner: operation, control and impact assessment on shunt and series inverter kva loadings. Power Electron, IET 6:1299–1307
12. Fagundes SM, Cardoso FL, Stangler EV, Neves FAS, Mezaroba M (2021) A detailed power flow analysis of the dual unified power quality conditioner (iUPQC) using power angle control (PAC). Electr Power Syst Res 192(1):106933

13. Siva Kumar G, Kalyan Kumar B, Mahesh Kumar M (2010) Optimal VA loading of UPQC during mitigation of unbalanced voltage sags with phase jumps in three-phase four-wire distribution system. In: 2010 International conference on power system technology, pp 1–8
14. Ambati BB, Khadkikar V (2014) Optimal sizing of UPQC considering VA loading and maximum utilization of power-electronic converters. *IEEE Trans Power Deliv* 29(3):1490–1498
15. Ye J, Gooi HB, Wu F (2018) Optimal design and control implementation of UPQC based on variable phase angle control method. *IEEE Trans Ind Inf* 14(7):3109–3123
16. Ye J, Gooi HB, Zhang X, Wang B, Manandhar U (2019) Two-level algorithm for UPQC considering power electronic converters and transformers. In Conference proceedings—IEEE applied power electronics conference and exposition—APEC, vol 2019-March, pp 3461–3467
17. Patil D, Antonov S, Gade S, Agrawal R (2021) Optimal utilization of UPQC at different operating condition using TLBO. In 56th International scientific conference on information, communication and energy systems and technologies (ICEST), pp 197–200
18. Gade S, Agrawal R (2021) Optimal utilization of UPQC during steady state using evolutionary optimization techniques. In 2021 International conference on intelligent technologies (CONIT), pp 1–7
19. Gotmare A et al (2017) Swarm and evolutionary computing algorithms for system identification and filter design: a comprehensive review. *Swarm Evol Comput* 32:68–84
20. Venkata Rao R (2016) Jaya: a simple and new optimization algorithm for solving constrained and unconstrained optimization problems. *Int J Industrial Eng Comput* 7:19–34
21. Rao RV (2018) *Jaya: an advanced optimization algorithm and its engineering applications*. Springer International Publishing, Switzerland
22. Rao RV (2020) Rao algorithms: three metaphor-less simple algorithms for solving optimization problems. *Int J Ind Eng Comput* 11(1):107–130
23. Rao RV, Waghmare GG (2017) A new optimization algorithm for solving complex constrained design optimization problems. *Eng Optim*. <https://doi.org/10.1080/0305215X.2016.1164855>
24. Wang L, Wang Z, Liang H, Huang C (2020) Parameter estimation of photovoltaic cell model with Rao-1 algorithm. *Optik (Stuttg)* 210:163846

Effective Stabilization of the Retaining Wall with Inclusion of Geo-Cell: A Review and Critique of Research



Sweta Soni 

Abstract Nowadays, the usage of concrete in civil engineering is remarkably increased, and the resources required for concrete-like cement, which was emitting about two-third of polluting gases like CO₂ and other greenhouse gases. Concrete panels and reinforcement are used to support the backfill construction of the retaining wall; however, the installation time is relatively high. Geo-Cell can be used significantly in the retaining wall to overcome these issues. It can reduce the 70% of concrete consumption in retaining walls which can affect the carbon footprints. Geo-Cell is a system having cellular confinement, which is composed of High-density Polyethylene (HDPE). The geometric configuration of Geo-Cell is a 3-D honeycombed shape. Besides, the installation is easy, and the accessibility is high without any specialized equipment and human resources. Most probably used to control erosion and soil stabilization on a flat and steep slope as it is anti-ageing, acid, and alkali resistant. This method holds its versatility in terms of Economy, durability, and stiffness, especially in soft soils; lateral spreading is prevented. The other parameters include its lightweight assembly compared to conventional concrete panels, low environmental impact, non-corrosive, non-toxic in nature, and to avail free drainage through the soil with the help of perforations. This paper shows the review over stability analysis with the Geo-Cell through the Limit Equilibrium method. The flexibility of Geo-Cell can provide positive results for the betterment of retaining the wall against the differential settlement.

Keywords Geo-Cell · Confinement · Soil stabilization · Economy · Low environmental impact

S. Soni (✉)

Water Resource Engineering, Shantilal Shah Engineering College, Bhavnagar, India
e-mail: ssoni0760@gmail.com

© The Author(s), under exclusive license to Springer Nature Singapore Pte Ltd. 2022
V. Mahajan et al. (eds.), *Sustainable Technology and Advanced Computing in Electrical Engineering*, Lecture Notes in Electrical Engineering 939,
https://doi.org/10.1007/978-981-19-4364-5_74

1047

1 Introduction

Subbase soil has a significant consequence of design, construction, structural members' stability, and the high efficiency of the retaining wall. Geo-Cell is a three-dimensional honeycombed cellular structure that forms a system that is confined in nature when it is filled with soil, which is compacted. Geo-Cell comprises a series of interconnected cells filled with granular soil, which helps for the drainage purpose as well as for confinement, which produces a thick mattress. Since the soil is confined within the cell, its compressive strength increases much like confining stress in a Triaxial soil test apparatus enhances the soil sample's compressive strength. Material is ultrasonically strip welded together in series form. The strip of Geo-Cell was expanded to form the typically textured and perforated walls of the flexible three-dimensional cellular patterns having stiffness. A Presto company is the original inventor of Geo-Cell, having 3-dimensional technology and working with the U.S. Army Corps of engineers [1]. There are various applications of Geo-Cell in the civil industry as follow.

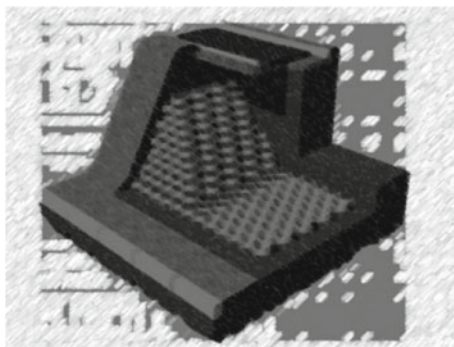
1.1 Abrasion Control

Mainly, on non-vegetated soil slopes or in the semi-arid region, soil erosion occurs where the intensity of rainfalls is high. Two mechanics are used for causing soil erosion: (i) Due to the impact of rain; particles are detached. (ii) Due to surface water flow, particles start a movement. As in slope protection, prevention is crucial due to the high-velocity runoff, which causes downslope movement. Geo-Cell is filled to avoid mass sliding of a layer on the surface and decrease the undermining of slope due to the scouring effect. Geo-Cell panels, which are expanded hydraulically, are connected through the process like extrusion of material. These connections help prevent excess water from the cell, and that water is used as the weight to the whole structure and undermining the slopes.

1.2 Ground Stabilization

Geo-Cell serves as a load spreader when a load is imposed upon the system. Furthermore, in many instances, it is possible to use locally available inexpensive aggregate in a multitude of stabilization projects such as road, access lanes, runway, parking plot, railroad, track bedding, bedding for sewer and water pipes generally in stabilization end-use, the aggregate layer spread the load imposed upon it, thus reducing the pressure exerted on the Sub-grade below a critical value.

Fig. 1 Geo-Cell confinement the retaining wall. Source Dhane [2]



1.3 The Retaining Wall

To stabilize a very steep slope, the retaining walls are constructed. Geo-Cell serves as both the fascia surface and reinforcing elements, as shown in Fig. 1. Geo-Cell is also used for the proper drainage throughout the retaining wall. Some of the Geo-Cell outer surfaces are vegetated—forgiving, pleasing and environmentally compatible look. An additional benefit is that the outer cell can be vegetated. Hence, the adequate thickness of the retaining wall can be increased by expanding the Geo-Cell panels. Geo-Cell Retaining Structure adjusts its shape and grade of soil through flexible forms acting as an expansion joint. As it figured out that, it requires approx.—three days for the installation process.

1.4 Slopes and Canal Protection

Geo-Cell assures the long term stability of slopes by having its lateral confinement structure and its anchoring techniques using aggregates, concrete, or vegetated topsoil on the front surface of it. The Downslope movement of the Geo-Cell wall and other impacts of raindrops, channelling, and shear stress due to hydraulic forces was prevented by properly enhancing the drainage, frictional forces, and iteration of cell soil–plant in Geo-Cell structure. Application of slopes and channels includes cut and fill with gradients with its stability, embankments of rails and road pavements, the stability of pipelines, protection work of channels, and other coastline structures. The slope's stability near the channel or river bank is low due to water flow, and these water flows impact the hydraulic shear stresses against the surface of the soil through the scouring effect, so foe that material having bearing capacity against water impact was taken into consideration. For that problem, Geo-Cells are used for the channel lining because Geo-Cell is three-dimensional, which helps to confine its infilled material in channels with low flow. Due to hydraulic shear stresses, the

soil material present in the cell wall has a greater depth containing infield material, which was held in its location.

1.5 Reservoir

Membrane linear protection creates stable soil, berms, and slopes for non-slip safety and durable impoundment of liquid and waste. To prevent the cracks and the flow of velocity, Geo-Cell composite with the concrete is used as a flexible slab to indulge the minor movements of Sub-grade soils.

2 Properties of Geo-Cell

Nowadays, Geo-Cell is made of new polymer structures characterized by low-temperature flexibility similar to high-density polythene [3]. Geo-Cell has a three-dimensional structure made of polyethene fibres and added to different infilled materials like sand, soil, aggregate, and concrete to resist the weakness of soil sub-grade and the downslope movement of the soil. Polyethene is used to make strips for the Presto Geoweb section having a density of 58.4–60.2 lb/ft³ under ASTM D1505 or D792 [4, 5]. Geo-Cell is already a confined 3-D structure which has high tensile strength as shown in Fig. 2 strong adhesion force, and friction force having by adjacent layers and between network and stones and become a wall structure to resist earth pressure by combining both the Geo-Cell and sand or gravels as shown in Fig. 3. As an Earth pressure acting on the wall, which brings some flexural and shear deformation so that it reduces lateral earth pressure on the wall and improve the bearing capacity of a structure as results observed. The properties of Geo-Cell are analysed by using finite element software MARC. As the environmental apprehension increases, simultaneously usage of the synthetic material also increases because of its material property. There were specified geosynthetic products developed primarily to improve the soil's strength to resist the erosion effects; thus, it has a different size and shape according to its compositions and usages.

Fig. 2 Section of Geo-Cell

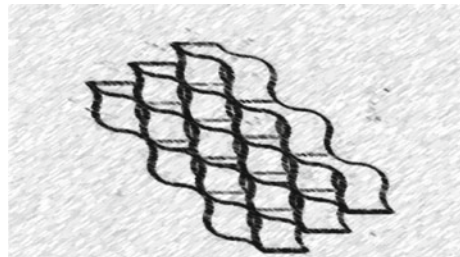
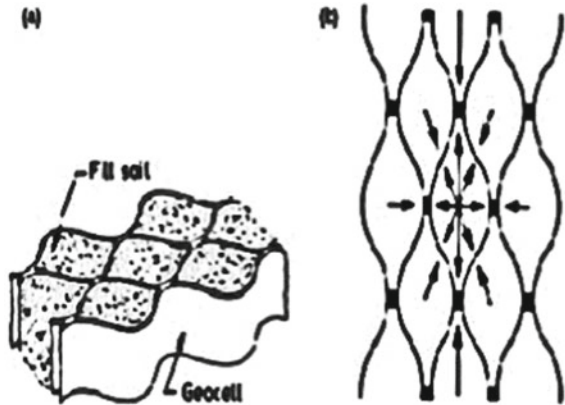


Fig. 3 Confinement of soil in Geo-Cell



2.1 Deformation Properties

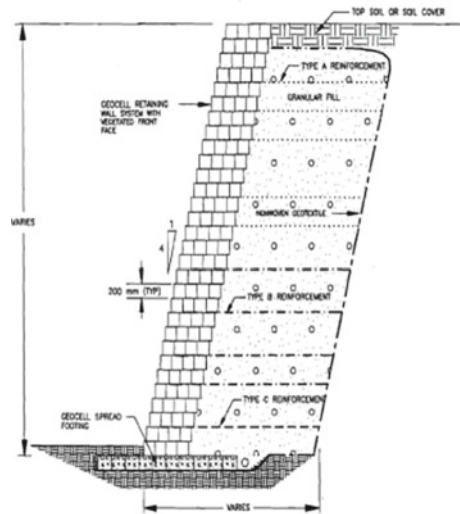
Displacement occurs non-linearly at the back of the wall, and the centre of wall displacement is more than the end of the walls. The slope of the curve alters less when the applied external load is small, so rotation of the rigid body is significant deformation. When the external load on the back of the wall increase, the change of curve slope increases.

As the external load is small on fill behind the wall, the slope should be 0–4 m move on the upper part of the wall, showing wall rotation in the clockwise direction. When the load is more significant than 400 kPa, the displacement is more on the top of the wall than on the toe of the wall, which shows clockwise rotation and converts to counterclockwise rotation gradually with increasing external load. As the external load increase, the position of maximum displacement moves up [6].

Displacement properties depend on the back of the wall with having different widths, the distance between reinforced layer and foundation modules as the foundation modulus increase the displacement decrease and degree of flexure of wall increase simultaneously. As the foundation of modulus has little impact on earth pressure as compared to the external load.

When the reinforced layers move apart from fill through increasing the external load simultaneously, horizontal displacement increases, between the joints of the Geo-Cell layer and wall, displacement is maximum. Meanwhile, in the direction of the Geo-Cell layer, horizontal displacement decreases gradually, as shown in Fig. 4. When the minor load is applied to the Geo-Cell wall, the top layer of the Geo-Cell wall moves towards the fill, which was beyond the wall, and; at other positions, the layer of cell moves away from packing. Due to pressure, deformation in the Geo-Cell membrane occurs, and this deformation of the membrane mobilizes the stress by this pressure to take place in soil confinement. This pressure increase confinement pressure, so due to this resistance against the deformation of the Geo-Cell membrane increase and can resist more load. To resist the deformation, the interlocking of

Fig. 4 Horizontal displacement of the retaining wall



Geo-Cell and frictional resistance between soil and Geo-Cell are also contributing [7].

2.2 Mechanical Properties

In Geo-Cell, resistivity is directly proportional to the mechanism, which affects together to the Geo-Cell for its development and increases the bearing capacity of the soil. There are three effects in the Geo-Cell to increase the bearing capacity of the soil as the effects are developed on the loading condition.

An effects due to confinement structure: Geo-Cell increases its confining stress whilst applying the load, and its stiffness property is also increased due to the presence of infilled material. Hence, due to confinement structure, Horizontal stress in Geo-Cell can dissipate the loads and resist the load, which was applied by its strength and deformability. Confinement of Geo-Cell effects depends on the friction between the material, which is filled in walls and pockets of Geo-Cell. The development of confinement is improved by its load magnitude, infilled material in Geo-Cell, and Geo-Cell pockets' dimensions.

An effect due to stress dissipation: It dissipates the stresses acting on the Geo-Cell with the help of its three-dimensional structure, which has the Geo-Cell pockets which interconnect with each other in series. Infilled material in Geo-Cell, which expands to resist the bending, compression, tension, and shear stresses due to its stiffness property. Due to the dispersion effect, the load is carried by the soil in the foundation, which has a large surface in which load to its lower level of stresses.

An effect due to membrane: In geosynthetic material, the concave shape is formed in tension due to foundation, displacement in a vertical direction under mattresses of Geo-Cell. This phenomenon is called a membrane effect. Bearing capacity is improved by its stiffness and its lateral anchoring due to exerting upward force by its reinforced material having a concavely curved portion that can resist the applied load, which acts as the tension membrane. And although it helps to reduce the pressure exerted on the sub-grade. For the mobilization of anchorage, it requires minimum friction between soil and the reinforcement. Therefore, it requires massive displacement of sub-grade and high stiffness properties. It considers that for the mechanism development only, two effects are taken into consideration, i.e. a product due to confinement and an effect due to dissipation of stresses.

3 Methodology

There is various method to find the soil's stability, but here limit equilibrium analysis was used for calculating the stability of the soil. Limit equilibrium analysis of Geo-Cell reinforced the retaining wall widely used and accurate amongst other methods for engineers. Limit equilibrium analysis is the oldest method used method for slope stability analysis in geotechnical engineering practises. Failure in soil mass is divided into various vertical slices. In limit equilibrium analysis, there are three conditions where been taken into consideration are,

Equilibrium forces in Vertical direction.

Equilibrium forces in Horizontal direction.

Equilibrium about the moment of soil stability.

The effectiveness and scope of limit equilibrium analysis were discussed by Duncan (1996). This method has the drawback of not considering the deformation or failure of the slope, which is progressive. The peak strength of soil was considered at the location of the critical failure surface for the limit equilibrium approach.

Unfortunately, in the soil, the slope's failure is progressive in nature, and strain softening along the failure surface is inevitable if the soil is dense enough and shear strain inadequately high. Mobilized internal friction angle different location is different due to along the failure surface, a shear strain of soil is additional at a different location.

Mobilized internal friction is small when sliding deformation is increased. Mobilizes internal friction depending on the soil and location, which exhibits strain softening. As mobilized strength is smaller than peak strength and soil having different locations only reaches the peak strength. Zhang and Yang discussed this. If peak strength was adopted in the stability analysis, the Factor of safety (FOS) was calculated using the Limit equilibrium method.

The strength of Geo-Cell reinforced soil was investigated, and shows that using Geo-Cell in the retaining wall improves the strength and stiffness of sandy soil. The friction angle is not changed in Geo-Cell unreinforced confinement soil. So, it

assumes that the angle of friction is the same in Geo-Cell soil, and apparent cohesion is considered for Geo-Cell reinforced soil.

Bathurst, Karpurapu, and Rajagopal give the empirical formula to estimate the apparent cohesion

$$c_r = \frac{\Delta\sigma_3}{2} \tan \left[\frac{\Pi}{4} + \frac{\phi}{2} \right] \tag{1}$$

where

ϕ = Internal friction angle of soil.

$\Delta\sigma_3$ = Increase confining stress provided by Geo-Cell.

$$\Delta\sigma_3 = \frac{2M\varepsilon_C}{D} \frac{1}{1 - \varepsilon_C} \tag{2}$$

$$\varepsilon_C = \frac{1 - \sqrt{1 - \varepsilon_a}}{1 - \varepsilon_a} \tag{3}$$

ε_a = Axial strain of Geo-Cell reinforced soil at failure.

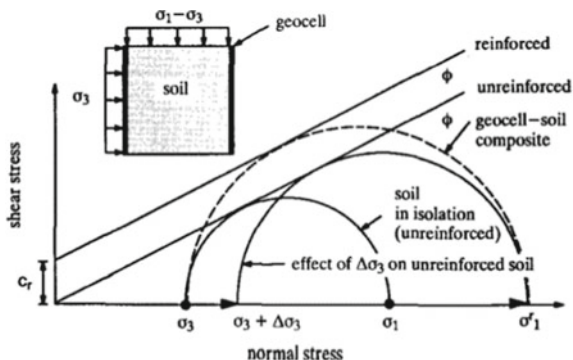
ε_C = Corresponding circumferential strain relationship between ε_c and ε_a .

M = Secant Modulus of cell membrane corresponding to an axial strain equal circumferential strain ε_c (KN/m).

D = Diameter of cell pocket at axial strain ε_a (m).

Based on the above analysis, we can conclude that using limit equilibrium analysis, the slope stability approach is proper for stability analysis of the retaining wall using reinforced Geo-Cell, and apparent cohesion is also determined by this method. By using peak strength, a critical failure surface can be examined by using a limit equilibrium. Then onwards, if peak strength is adopted along the failure surface, then the Factor of safety is overappraisal because of having different locations. In some locations, the value of the mobilized internal friction angle is comparatively than the peak strength of that location in the soil. As for calculation, if residual strength is

Fig. 5 Mohr-Circle of Geo-Cell and soil for calculating cohesion



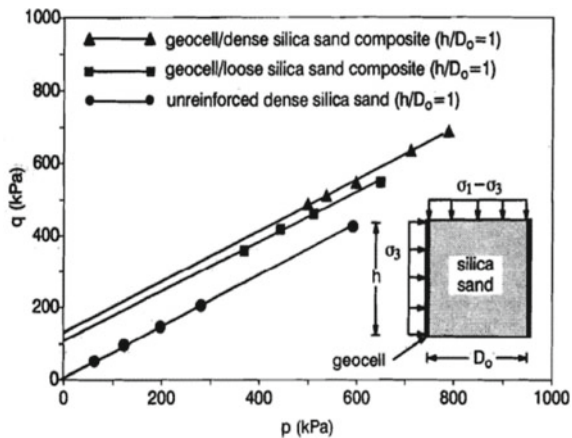
taken for the failure surface and the Factor of safety is probably underestimates the author’s responsibility to obtain all necessary approvals from the author’s employer before submitting the paper.

4 Review of Literatures’

The three-dimensional cellular confinement of HDPE Geo-Cell usually is used for erosion control, channel and landfill protections, Earth retention by providing structural reinforcement and the soil stability of the flat and steep slopes. Hindered amine light stabilizer (HALS) is used for ultra-violet stabilization and distributed homogeneously throughout the material [4]. Using the Geo-Cell structural strength of the soil is increased by maintaining soil compaction [8] and making the flexible structure and easy and speedy construction [9]. The concept of Geo-Cell confinement was developed by the U.S. Army corps of Engineers in service. Around 100 flexible Geo-Cell, the retaining wall structures are constructed in North America [10]. Geo-Cell flexible retaining walls are built by stacking 3-D Geo-Cell layers filled with confined soils or gravels on each layer and built under any slope condition [6]. The author observed and described the properties of Geo-Cell unreinforced granular soil by using a triaxial test shown in Fig. 6 and researched the structural behaviour of Geo-Cell flexible retaining walls by triaxial test, centrifuge test, and finite element calculation, respectively [10].

When Geo-Cell and soil mix their own geotechnical and mechanical properties, these mixtures cause lateral stresses on perimeter cell walls and pressure. By using Geo-Cell confinement, it creates 3-D zones that decrease the lateral movement of soil particles. Geo-Cell filled with sand confinement results in durable reinforcement, which maintains soil compaction and high lateral stress and resistance on the cell interface [11].

Fig. 6 Triaxial test sample.
Source Song et al. [10]



For the retention of Earth, Geo-Cells are widely in use whenever the construction work is interpreted. As each layer is sounded in structural parameters, providing excess for all purposes like for workers and equipment. It can also be used where structures are bulky in design and to increase the load capacity. Tendon-Anchoring systems offer structural supports to the Geo-Cell layers and, although it protects the integrity of liners [1]. PRS is an exclusive developer and manufacturer of PRS. neoweb Geo-Cell for soil stabilization [11].

In this, R. J Bathurst describes the use of polymeric Geo-Cell confinement system used for the steepened slope and to form the facia of geosynthetic reinforced soil resting wall structure. Discusses about two case studies illustrate the concept and number of designs and issues regarding this construction type [10].

Using Geo-Cell in the retaining wall, it was observed that after one year of construction, 400 mm settlement was recorded by a survey of having 11 m height high embankment crest for achieving design grades, facia was simply extended by adding additional lifts of Geo-Cell materials [10]. Stability may be improved by either lengthening the Geo-Cell layer or reinforcing the upper zone of the backfill [12]. The location and combination of geosynthetic reinforcement were determined by stability analysis and using the concept of limit equilibrium in soil geosynthetic and assumed as coulomb type soil [10].

In the gravity wall, the structure was formed between the Geo-Cell layer and the reinforcement layer by confining the soil, extending beyond the facia. By using a pattern of alternating layering length because to minimize the volume of polymeric reinforcement and also to ensure that this reinforced zone should act as monolithic mass (gravity structure) [10]. As result shows, whilst constructing the retaining wall, the earth pressure at the base is more as compared to calculate by the numerical analysis method. And though after construction, pressure at base level of retaining wall is slightly decrease due to heavy construction machineries [13].

By using Geo-Cell in a steeped slope, it confines the soil, which is infilled in Geo-Cell so that there is the prevention of ravelling and sloughing. Also, soil penetrates Geo-Cell facing into the wall, which increases the resistance to shear failure of soil structure and also provides formwork for placement and compaction of the retained soil. It considers 200 mm wide strips of high-density polyethylene ultrasonically welded together to give an open-cell construction having a cell diameter of 200 mm. The standard expanded length of Geo-Cell is 6 m. However, the author in paper, short width is used to minimize the wastage due to trimming of the site [10]. As result shows, whilst constructing the retaining wall, the earth pressure at the base is more as compared by calculating through the numerical analysis method. Even so, after construction, pressure at base level of retaining wall is slightly decrease due to heavy construction machineries [13, 14]

By stability analysis, the dimension of the Geo-Cell layer is comprised performing active earth pressure theory. Bathurst has assumed that horizontal earth pressure is developed behind the wall due to an active coulomb wedge extending from the heat of each layer through backfill containing soil material and that friction generated at the interface between Geo-Cell resist to sliding effect [10]. A drum shape distribution of earth pressure is showed between the inner side of retaining wall and middle of the

retaining wall, when the wall is in the stable condition. Besides, linear distribution was eventuate at the outer side of the Retaining wall [13]

The friction angle is found from the resist to direct shear box for calculating horizontal stability. To resist the retaining wall's overturning, which is related to the toe of Geo-Cell of each layer. Bathurst has given a minimum factor of safety of 1.5 against sliding, and a minimum factor of safety of 2 against overturning width of Geo-Cell is dependent on the manufacturing companies, i.e. Presto [14]. As limestone is used as the infill material in reinforced Geo-Cell, assuming peak friction angle as 40° but as sand, sand is economical and has 35° as peak friction angle. For backfill, the same sand is used to ensure that the backslope has free drainage and is easy to compact with having a co-efficient of uniformity $C_u = 2.8$. The experimental analysis on the different infill material was showed by Hasthi Venkateswarlu. And that of increment in resonant frequency by 62%, 53%, 48%, and 42%, respectively, by using aggregate, slag, sand, and silty sand as an infill material in the Geo-Cell retaining wall. For the higher isolation performance, steel slag (Industrial waste) is used as infill material rather than other natural aggregate in the Geo-Cell reinforced bed [15].

The modes of failure of the Geo-Cell-reinforced retaining wall differ from a rigid retaining wall [16]. Centrifuge model tests to carry out the performance of Geo-Cell reinforce the retaining wall whilst limiting equilibrium under various conditions [16]. To determine the displacement vector of soil and Geo-Cell reinforced soil, and digital image analysis is used, which were used to find failure and G-level at limit equilibrium. By this result, it was found that reducing the span between welded spots of Geo-Cell, increase the stiffness of the Geo-Cell membrane and adds geogrid to Geo-Cell walls. It is described that two-tiered Geo-Cell the retaining wall performed better than single tiered ones at having equal heights [16]. Sixteen centrifuge model tests are conducted of Geo-Cell reinforced retaining wall under the complex condition and to validate the limit equilibrium method for stability analysis of this type of wall. An Elastic Membrane model test is used for the composite structure to estimate the additional apparent cohesion [14]. Digital image analysis is used to analyse the displacement fields of reinforced and unreinforced soils and reconstruct the failure surface of walls. The result from the centrifuge test is an increased acceleration of which may modify the soil behaviour and is considered an inherent limitation of the testing method, which should further be validated but large scale or field test [6]. Reinforced base is compared with the base of unreinforced Geo-Cell then it has been proven that Geo-Cell having reinforced has to provide more lateral and vertical confinement and affects the tension membrane and wider the stress distribution [3]. For the application of typical base reinforcement, a Specimen of reinforced Geo-Cell is used for the testing with the addition of a height-to-diameter ratio of unity that shows the dimension of the reinforced system. And meanwhile, this shows stiffness effect and strength increase imparted to the soil by enhancing the confinement effect [14]. As the interaction between the wall and reinforced layer, is very important by using finite element software, MARC, and evaluation of the stress distribution of Geo-Cell retaining wall [6]. Finite element strength reduction tactic was used for the numerical analyses by finite element package ABAQUS of the Geo-Cell reinforced

retaining wall on the various failure modes. ABAQUS software is also used for the strength reduction technique where, field variable was defined by the Factor of Safety and mobilized strength parameters vary with a field variable [17]. To measure the lateral pressure of Geo-Cell, a field testing method is used. The deformation of this wall depends on various parameters (a) width of walls, (b) distance between adjacent reinforced layers, and (c) foundation modulus. Stress level is affected by the width of the wall and external load on the behind the wall increases, horizontal displacement of reinforced increase. For the analysis of the horizontal displacement of the reinforced retaining wall with inclusion of the Geo-Cell under the earthquake condition, was calculated by FLAC 3-D non-linear finite difference method which manifest better restraint towards the horizontal displacement and also by increasing the length of Geo-Cell and change the spacing of the Geo-Cell [18]. The horizontal stress of tied reinforced layers develop in three phases bending and stretching stages, which increase external load.

Bending stage: When the external load is small, horizontal stress is converted into tensile stress. Due to the bending of tied Geo-Cell emerges at the centre of tied Geo-Cell as reinforced layer maximum tensile stress occurs but not includes the joint of layers and walls.

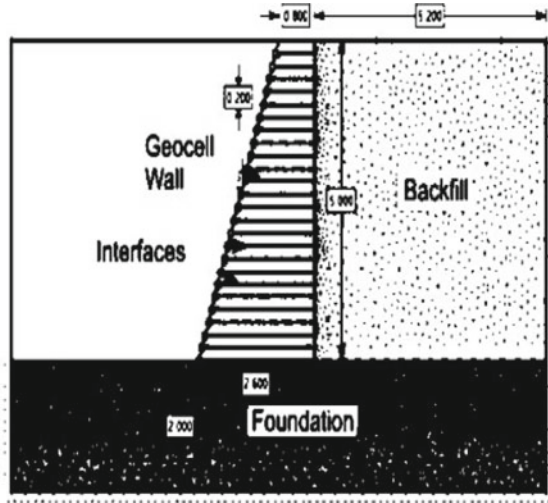
Stretching bending stages: At two points, horizontal stress was induced at the joint of layers, and the wall is at the centre of layers. Due to horizontal displacement, stretching ting is at the point of a joint between tied Geo-Cell and wall; and at the centre, bending is caused.

Stretching stage: “first fast and second slow” tensile stress caused by stretching remains in dominant positions.

The height of the retaining wall should be kept limited due to a higher bearing capacity of foundation with low adaptability to deformation, which is difficult to restore from diseases [6]. Moreover, for the bearing capacity in foundation, the requirements of the Geo-Cell flexible retaining wall is not up-to-the-mark. Whilst increasing the filling height, the base earth pressure also increase which tends to non-linear distribution [16]. The FEM method and numerical analysis are compared with experimental data [12]. In Reinforced soil contained with apparent cohesion, the Numerical Model test is carried by Mohr–Coulomb for soil shown in Fig. 5, which shows the development in reduced scale Geo-Cells respecting similitude relationship. Total of four tests to measure the strong performance of the Geo-Cell (a) junction test under shear, (b) the junction peel strength test, and (c) junction split strength test. This test is based on ASTM D4595 and ASTM D5035 Standard, using a local velocity of 50 mm/min [12].

PLAXIS 3-D version 2013.01 is a geotechnical programme that offers flexible and operable geometry, simulation of staged construction, and reliable package and making proper solutions for geotechnical design and analysis as shown in Fig. 7 [19]. Using PLAXIS, the output shows such as the deflection, strain, Factor of safety is known for analysed problems. The tilt sensor was used to measure deflection, and an inclinometer was used to measure horizontal displacement, and this method applies to the relocation project of Yan’an airport [16]. Shaking table test is used for the seismic response of Geo-Cell subjected to ground shaking condition of different acceleration

Fig. 7 Configuration of numerical model of Geo-Cell the retaining wall. *Source* Tanyu et al. [19]



or shaking frequency increased, acceleration amplification, and displacement also increases. Differential settlement of crest is an issue if infill material inside the Geo-Cell is other than backfill material [20]. The thickness of the wall should be optimized based on Earthquake design parameters, allowable deformation, and its amplification. Under seismic excitation, crest settlement was more than the horizontal deformation of the wall [20].

5 Conclusion

In Geo-Cell, the retaining wall shows an unprecedented structural capacity, showing its ability to withstand a high surcharge before failure. This material is eco-friendly for soil stabilization on any soil type and quickly gets attached to the natural environment. Geo-Cell reduces the carbon footprints as compared to cement materials. Easily withstand geotechnical construction activities due to its 3-D shape structure. Wall of Geo-Cell allows infill to interlock with the cell walls as it reduces the downslope sliding forces in a saturated condition, which results in a more stable system. The Geo-Cell reinforced retaining wall stability is to be analysed by the limit equilibrium method, which provides that the apparent cohesion of Geo-Cell reinforced soil is accurately estimated and assumes that the shape of the critical failure surface is accurate. The similitude condition of Geo-Cell is achieved through its apparent strength and apparent strength crucial factor for determining the stability of the Geo-Cell reinforced structure.

Eliminating rutting prevents the lateral movement of infill for confinement; lower quality fill material can also be used without any specialized equipment and skilled labours; it can be installed easily and quickly. Drainage is freely by infill material

Fig. 8 Vegetation on Geo-Cell



as soil with the help of perforation. Increasing Geo-Cell fascia thickness will not result in a proportional decrease in deformations and acceleration amplifications. The confining cell structure bestows cohesion to infill material to increase its shear strength and stiffness. And this shows passive resistance of adjacent and high frictional interaction between infill soil and Geo-Cell retaining walls. With the help of reinforcement, the deformation and settlement of the wall are reduced because of more frictional resistance between the reinforcement interfaces. Moreover, the soil was mobilized when the surcharged load was increased. Hence it had been proven that Geo-Cell the retaining wall is to be adaptable in an environment in terms of its benefit–cost ratio, less pollution occurring, its round confinement materials, and can tolerate differential settlement. As the vegetation can also be grown on the front surface of the Geo-Cell retaining wall for erosion control and environmental sustainability, as shown in Fig. 8, which reduces the carbon footprint, and can reuse the site won materials as compared to the concrete retaining wall.

References

1. AR. USA Erez (1978) (12) United States Patent 2(12)
2. Dhane GDA (2014) Geo-Cell: an emerging technique of soil reinforcement in civil engineering field. *IOSR J Mech Civ Eng*, 2278-1684
3. Soil stabilization (1987) *Dev Geotech Eng* 41(C):251–283
4. Xie Y, Yang X (2009) Characteristics of a new-type Geo-Cell flexible the retaining wall. *J Mater Civ Eng* 21(4):171–175
5. <https://2y2qpw2op3o93ygu164frm9z-wpengine.netdna-ssl.com/wp-content/uploads/2016/07/Presto-Geosystems-All-Products-Catalog.pdf>
6. Lepcha KH, Agnihotri AK, Priyadarshee A, Yadav M (2014) Application of Tire chips in the reinforcement of soil: a review. *J Civ Eng Environ Technol Print* 1(5), 2349-8404

7. Bathurst RJ (1992) Recent case histories of flexible Geo-Cell the retaining walls in North America. In: International symposium on recent case histories of permanent geosynthetic-reinforced soil the retaining walls, no. November, pp 3–20
8. H. Geo-Cell (1980) Benefits of HDPE Geo-Cell cellular confinement
9. IGS UK & University of Manchester
10. Pincus HJ, Bathurst RJ, Karpurapu R (1993) Large-scale triaxial compression testing of Geo-Cell-reinforced granular soils. *Geotech Test* 16(3):296
11. Chen RH, Chiu YM (2008) Model tests of Geo-Cell retaining structures. *Geotext Geomembr* 26(1):56–70
12. Gomez D, Caicedo B, Estrada N (2014) Physical and numerical modeling of a Geo-Cell gravity the retaining wall. In: 10th International conference on geosynthetics, ICG 2014, no. January 2014
13. Wang J-Q, Ye B, Zhang L-L, Li L (2018) Large-scale model analysis on bearing characteristics of Geocell-reinforced Earth retaining wall under cyclic dynamic load. In: Proceedings of GeoShanghai 2018 international conference: ground improvement and geosynthetics, pp 455–462
14. Song F, Hu H, Xie Y (2018) Centrifuge tests of Geo-Cell-reinforced the retaining walls at limit equilibrium. *J Geotech Geoenviron Eng* 144(3):04018005
15. Venkateswarlu HHA (2020) Effect of infill materials on vibration isolation efficacy of geocell-reinforced soil beds. *Can Geotech J* 57(9):1304–1319
16. Teja VR (2015) Numerical analysis of Geo-Cell reinforced Earth the retaining wall
17. Song F, Liu H, Ma L, Hu H (2018) Numerical analysis of geocell-reinforced retaining wall failure modes. *Geotext Geomembr* 46(3):284–296
18. Zhu Y, Tan K, Hong Y, Tan T, Song M, Wang Y (2021) Deformation of the Geocell flexible reinforced retaining wall under earthquake. *Adv Civ Eng* 2021:1–11
19. Tanyu BF, Aydilek AH, Lau AW, Edil TB, Benson CH (2013) Laboratory evaluation of Geo-Cell-reinforced gravel subbase over poor sub-grades. *Geosynthetics Int* 202:47–61
20. Madhavi Latha GGS (2016) Seismic response of Geo-Cell the retaining walls through shaking table tests. *Int J Geosynthetics Gr Eng* 2(1):1–15

Swarm Intelligence-Based Tuning of Hybrid Controller for Control of Neutron Density in Nonlinear Pressurized Water Reactor



Swetha R. Kumar and D. Jayaprasanth

Abstract Nuclear energy has zero-emission and can generate power as a baseload station to meet demand in this energy crisis. To enhance the safety and control in power generation, artificial intelligence shall be utilized. This study aims design a healthy control system for regulating the neutron density in the highly nonlinear pressurized water reactor (PWR) core. The conventional way of controlling reactor power or the neutron density is by using a proportional-integral-derivative controller. But the internal variables of the reactor core are not considered in the PID controller. The proposed methodology implements hybrid state feedback and PID controller for neutron density regulation where the controller parameters are tuned optimally via swarm intelligence like particle swarm optimization and ant colony optimization. Swarm intelligence uses metaheuristic algorithms for resolving optimization problems and obtains optimal controller gains. This hybrid controller gives robust performance in the occurrence of disturbances on internal variables.

Keywords Pressurized water reactor · Linear quadratic regulator · Particle swarm optimization · Ant colony optimization · Hybrid controller · Swarm intelligence

1 Introduction

Nuclear reactors serve 10% of the world's energy usage approximately, and above 55 nuclear power plants are built at present globally. Due to the radiation hazards seen after Chernobyl and Fukushima events, it is essential to critically monitor the neutron density in the nuclear reactor and control it within limits. With considerable advancements in computational speed and electronics becoming cost effective,

S. R. Kumar (✉) · D. Jayaprasanth
Department of Instrumentation and Control Systems Engineering, PSG College of Technology,
Coimbatore, Tamil Nadu, India
e-mail: srk.ice@psgtech.ac.in

D. Jayaprasanth
e-mail: djp.ice@psgtech.ac.in

artificial intelligence has made implausible growth in recent times [1]. Thus, meta-heuristic algorithms of AI can be used to tune the controller parameters for critical reactor control.

Accordingly, several optimization algorithms have been implemented on the pressurized water reactor (PWR) model in the literature. In [2], the PID controller gains are optimized using particle swarm optimization (PSO) algorithm to control power in a pressurized water reactor; whereas in [3], genetic algorithm [4] is implemented for the same purpose of controlling reactor power.

Few literatures suggest utilizing a two-point kinetic model of nonlinear PWR rather than a point kinetic model [5–7]. Consequently, load following of NPP is achieved by the PID controller, which are tuned by a real-coded GA or PSO with decision variables that include performance indices like the “integral square error (ISE)” or the “integral of time-weighted absolute error (ITAE)” as an objective function. The demerit of conventional PID controller design is that the controller parameter depends only on the difference between output variable and reference variable. The internal variables or the state variables of the system are not reflected in controller design.

Further, hybrid control strategies [8, 9] for a PWR by integrating “linear quadratic integrator (LQI), linear quadratic Gaussian (LQG), and loop transfer recovery (LTR)” approaches are also proposed. In these hybrid control strategies, a linearized version of PWR is attained from nonlinear PWR model by linearizing around an equilibrium point. Though the above optimal controllers achieve finest disturbance rejection, their performance in load following scenarios might not be satisfactory. Several other control approaches like fractional order PID, fuzzy controller [10], sliding mode control are also designed for nonlinear PWR [7, 11, 12]. Such advanced control structures lack usage in real-time.

Thus, the work proposes a hybrid control structure [13] which is a combination of PID and LQR whose gains are tuned optimally using particle swarm optimization [14] and ant colony optimization [15–18]. The proposed objective function for the swarm intelligence algorithms will minimize both error and control efforts. Linear quadratic regulator is proposed in state feedback because it achieves optimal regulatory performance eliminating disturbances affecting the process. These disturbances could be changes in coolant average temperature, fuel temperature, xenon concentrations, or iodine concentrations.

The layout of this paper is as follows: Sect. 2 presents the nonlinear mathematical model of pressurized water reactor (PWR) core of 9th order. The steady-state power is 3000 MW. Section 2 also covers the details of swarm intelligence techniques used and proposed control methodology. In Sect. 3, the details the parameters obtained for controllers are briefed, and simulation results are studied. Subsequently, in Sect. 4, the conclusions are summarized.

2 Materials and Method

2.1 Nuclear Reactor Model

The reactor power model is devised based on the point kinetic equations with three groups of delayed neutrons c_{ri} , $i = 1, 2, 3$; and the reactivity feedback that is caused by changes in the fuel and coolant temperatures and xenon and iodine concentrations [10, 19]. This SISO model has 9 state variables. The equations of a pressurized water nuclear reactor core are as follows.

The three group delayed neutrons-based point kinetic equations are

$$\frac{dn_r}{dt} = \frac{\rho_t - \beta}{\Lambda} n_r + \sum_{i=1}^3 \frac{\beta_i}{\Lambda} c_{ri} \tag{1}$$

$$\frac{dc_{ri}}{dt} = \lambda_i n_r - \lambda_i c_{ri}, i = 1, 2, 3 \tag{2}$$

Xenon and iodine are considered as neutron poisons. Their concentrations are specified as

$$\frac{dX}{dt} = (\gamma_X \Sigma_f - \sigma_X X) \frac{P_0}{G \Sigma_{ff} V} n_r - \lambda_X X + \lambda_I I \tag{3}$$

$$\frac{dI}{dt} = \gamma_I \Sigma_f \frac{P_0}{G \Sigma_{ff} V} n_r - \lambda_I I \tag{4}$$

The reactor’s thermal–hydraulic model is given by

$$\frac{dT_f}{dt} = \frac{f_f P_0}{\mu_f} n_r - \frac{\Omega}{\mu_f} T_f + \frac{\Omega}{2\mu_f} T_{in} + \frac{\Omega}{2\mu_f} T_{out} \tag{5}$$

$$\frac{dT_c}{dt} = \frac{(1 - f_f) P_0}{\mu_c} n_r - \frac{(2M + \Omega)}{2\mu_c} T_{out} + \frac{(2M - \Omega)}{2\mu_c} T_{in} \tag{6}$$

The reactivity changes due to variations in speed of control rod and the total reactivity are

$$\frac{d\rho_{rod}}{dt} = G_r Z_r \tag{7}$$

$$\begin{aligned} \rho_t &= \rho_{rod} + \rho_T + \rho_X \\ &= \rho_{rod} + \alpha_f (T_f - T_{f0}) + \alpha_c (T_c - T_{c0}) - \frac{\sigma_X}{v \Sigma_f} (X - X_0) \end{aligned} \tag{8}$$

Also μ_c , M , Ω , α_f , and α_c are related to initial equilibrium neutron density (n_{r0}). The dependence is shown via the Eqs. (9)–(13)

$$\mu_c = \left(\frac{160}{9}\right)n_{r0} + 54.022 \quad (9)$$

$$M = 28n_{r0} + 74 \quad (10)$$

$$\Omega = \left(\frac{5}{3}\right)n_{r0} + 4.93333 \quad (11)$$

$$\alpha_f = (n_{r0} - 4.24) \times 10^{-5} \quad (12)$$

$$\alpha_c = (-4n_{r0} - 17.3) \times 10^{-5} \quad (13)$$

The reactor power is expressed as

$$p_t = p_0 n_r(t) \quad (14)$$

The reactor model's parameters and the values are shown in Tables 1 and 2, respectively [2, 3, 20].

2.2 Hybrid Control

The proposed methodology of hybrid control scheme is as shown in Fig. 1. The combination of PID and LQR offers several advantages as a PID controller aids in load following scenarios, LQR controller ensures optimal rejection of disturbances to guarantee stable output power. Moreover, as PID parameters are tuned using metaheuristic algorithm with LQR objective function, abrupt movements of control rods are minimized making it feasible for real-time implementation.

PID Control

Because of simple structure, PID controllers are widely used as real-time controllers in most industries. Figure 1 depicts a closed-loop control system with the equations shown below:

$$C(s) = K_P + \frac{1}{s}K_I + \frac{s}{1 + \tau s}K_D \quad (15)$$

K_P , K_I , $K_D \in \mathbb{R}$ are the respective proportional, integral, and derivative gains. The control input,

Table 1 Parameters in PWR model

P_0	Full core power, MW
n_r	Normalized neutron density (relative to neutron density at rated power P_0)
c_{ri}	i th group normalized precursor density (relative to density at rated power)
X	Xenon concentration, cm^{-3}
I	Iodine concentration, cm^{-3}
T_f	Fuel average temperature, $^{\circ}\text{C}$
T_{f0}	Fuel average temperature at the initial condition, $^{\circ}\text{C}$
T_c	Coolant average temperature, $^{\circ}\text{C}$
T_{c0}	Coolant average temperature at the initial condition, $^{\circ}\text{C}$
T_{in}	Coolant inlet temperature, $^{\circ}\text{C}$
T_{out}	Coolant outlet temperature, $^{\circ}\text{C}$
ρ_t	Total reactivity, δ K/K
ρ_{rod}	Reactivity due to control rod movement, δ K/K
ρ_T	Temperature reactivity feedback, δ K/K
ρ_x	Xenon reactivity feedback, δ K/K
Z_r	Control rod speed, fraction of core, length/s
G_r	Control rod total reactivity, δ K/K
β	Effective delayed neutron fraction
β_i	i th group effective delayed neutron fraction
α_c	Coolant temperature coefficient, $(\delta \text{ K/K})/^{\circ}\text{C}$
α_f	Fuel temperature coefficient, $(\delta \text{ K/K})/^{\circ}\text{C}$
Λ	Neutron generation time, s
λ_i	i th delayed neutron group decay constant, s^{-1}
γ_X	Xenon yield per fission
λ_X	Xenon decay constant, s^{-1}
γ_I	Iodine yield per fission
λ_I	Iodine decay constant, s^{-1}
Σ_f	Macroscopic thermal neutron fission cross-section, cm^{-1}
ν	Average number of neutrons produced per fission of ^{235}U
σ_X	Microscopic thermal neutron absorption cross-section of xenon, cm^{-2}
G	Useful thermal energy liberated per fission of ^{235}U , MW-s
V	Core volume, cm^3
f_f	Fraction of reactor power deposited in the fuel
μ_f	Fuel total heat capacity, $\text{MW}\cdot\text{s}/^{\circ}\text{C}$
μ_c	Coolant total heat capacity, $\text{MW}\cdot\text{s}/^{\circ}\text{C}$
M	Mass flow rate time heat capacity of water, $\text{MW}/^{\circ}\text{C}$
Ω	Coefficient of heat transfer between fuel and coolant, $\text{MW}/^{\circ}\text{C}$

Table 2 Values of parameters used in reactor model

Thermal power	3000 MW	β	0.0065
Core height	400 cm	β_1	0.00021
Core radius	200 cm	β_2	0.00225
σ_X	$3.5 \times 10^{-18} \text{ cm}^2$	β_3	0.00404
Σ_f	0.3358 s^{-1}	λ_1	0.0124 s^{-1}
G	$3.2 \times 10^{-11} \text{ MW}$	λ_2	0.0369 s^{-1}
γ_X	0.003	λ_3	0.632 s^{-1}
γ_I	0.059	G_r	$14.5 \times 10^{-3} \text{ } \delta\text{K/K}$
λ_X	$2.1 \times 10^{-5} \text{ s}^{-1}$	T_{in}	$290 \text{ } ^\circ\text{C}$
λ_1	$2.9 \times 10^{-5} \text{ s}^{-1}$	μ_f	$26.3 \text{ MW-s/}^\circ\text{C}$
Λ	10^{-4} s	f_f	0.92

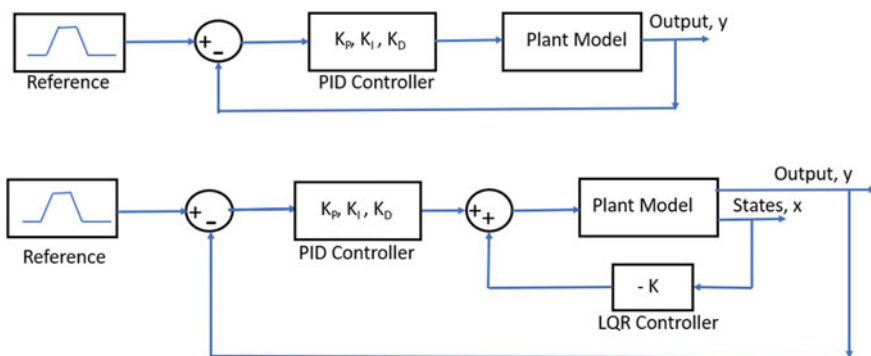


Fig. 1 Conventional PID control and proposed hybrid control structure

$$u(t) = K_p e(t) + K_I \int_0^t e(\tau) d\tau + K_D \frac{d}{dt} e(t) \tag{16}$$

$$e = r - y; \tag{17}$$

where r is desired signal, e is error and, u and y are the plant input signal and output signal, respectively.

Conventional tuning methods, like Ziegler-Nichols (ZN) relay feedback, process reaction curve, continuous cycling, and pole placement, are available for tuning PID gains [21]. Nevertheless, almost all of these methodologies have been proposed for linear time invariant (LTI) systems, which necessitate comprehensive knowledge about the system and its frequency response. As a result, several metaheuristic optimization methods are used to tune PID controllers of nonlinear systems.

LQR Control

LQR is an optimal regulator that is used in the construction of a state feedback controller for a linear time variant or invariant processes which, as shown, helps to minimize a cost function in Eq. (18) [22].

$$J(K) = \frac{1}{2} \int_0^{\infty} (x' Q x + u' R u) dt \tag{18}$$

This cost function has scaling matrices Q, R which fine-tunes the weights of the state vector $x(t)$ as well as system input $u(t)$, respectively, to ensure all state variables and control inputs gets equal weightage. Q is a positive semi-definite symmetric state weighted matrix, and R is a positive symmetric control weighted matrix.

The optimal LQR controller is given as

$$u(t) = -R^{-1} B' P x(t) \tag{19}$$

where P denotes the algebraic Riccati equation solution.

$$" PA + A' P + Q - P B R^{-1} B' P = 0" \tag{20}$$

Thus, the LQR controller gain is $K = R^{-1} B' P(t)$.

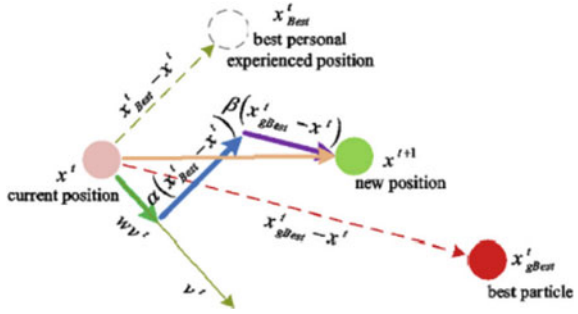
To ensure stability of the system in the presence of uncontrollable but stabilizable state variables, Q matrix is assumed as $Q = C' C$ or $Q = w C' C$ where w is a scalar [23].

Since PID controller is implemented widely and is best suited for trajectory tracking applicatory but the control effort depends only on the output variable, neutron density. On a contrary, the LQR controller is a fully state feedback controller and constructed with the prime motive of regulation of all state variables.

2.3 Swarm Intelligence

Swarm intelligence is done as an effort to develop techniques or distributed problem-solving tools motivated by the cohesive nature of the social insect territories or other animal communities. Self-organization and labour separation are special swarm intelligent behaviour. It identifies the best controller gains for optimal performance which is quantified in units of integral square error, absolute error, and absolute control value. Integral absolute control (IAC) is a unique performance measure introduced

Fig. 2 Particles movement pattern [2]



as equal importance should be given to control signals as output signals to ensure smooth control during actual implementation.

Particle Swarm Optimization

Particle swarm optimization simulates the behavioural patterns of swarming birds or schooling fish. Each particle/bird has its own position and velocity. These particles adjust their velocities to alter their position in order to seek meal, avoid danger, or identify best possible environmental parameters. Furthermore, each particle remembers the best location that it has identified. Each particle conveys this information about the best location to the other particles. The velocity of such particles is then updated based on the particle’s or the group’s flying experience as shown in Fig. 2.

The PSO algorithm is built as follows [11, 14, 17, 22]:

1. “Initialization of particle position $x^k(0)$, $k = 1, 2, \dots, \text{max_swarm}$ ”
2. “Initialization of particle velocity $v^k(0)$, $k = 1, 2, \dots, \text{max_swarm}$ ”
3. “Fix a local best particle $p^k = x^k(0)$, $k = 1, 2, \dots, \text{max_swarm}$ ”
4. “Fix a global best particle $g = \text{argmin}(f(p^k)$, $k = 1, 2, \dots, \text{max_swarm}$)”
5. “Update particle along time t .

for $t = 0 : \text{max_}t$
 for $k = 1 : \text{max_swarm}$
 Calculate the particle velocity $v^k(t + 1)$

$$v^k(t + 1) = wv^k(t) + c_1r_1(p^k - x^k(t)) + c_2r_2(g - x^k(t))$$

Update the particle position $x^t(t + 1)$

$$x^k(t + 1) = x^k(t) + v^k(t + 1)$$

Calculate the fitness of particle $f(x^k(t + 1))$
 Update local best particle $p_{ij}^{k'}$

$$p^k = \arg \min_x (f(x^k(0)), f(x^k(1)), \dots, f(x^k(t)), f(x^k(t + 1)))$$

End
 Update global best particle g_y

$$g = \arg \min_p (f(p^k), k = 1, 2, \dots, \text{max5warm})$$

End”

Ant Colony Optimization

Ant colony optimization is a probability-based technique in which the optimal route in a plot is sought observing the behaviour of ants looking to find a path between their colony and a food source. The ants find the best route to any distanced food source. Refer to Fig. 3 to understand the mechanisms behind this. First, an ant leaves the hives in looking for food and finds it in a particular location; the leftover ants will follow the pheromones left by the first ant. If there are different routes to the same source, the pheromones on the quickest route will last longer than the pheromones from the other paths, causing the quickest route more rewarding for new ants emerging from the nest. The pheromone intensity on that path will rise, whilst the pheromone intensity on the longest path will drop.

The ACO algorithm can be built as described in the following [15, 17, 22]:

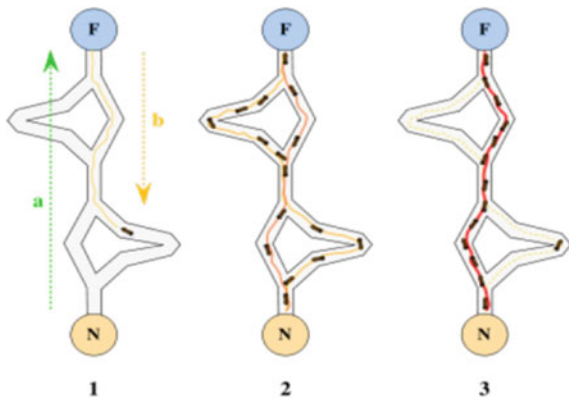
1. “Set the number of ants N and the pheromone decay factor ρ ”.
2. “Generate maximum populations feasible solutions, and determine the probability and fitness equation”

$$\text{fitness}_k = \frac{1}{(f(X^s)+1)}, k = 1, 2, \dots, \text{mpop}$$

$$p(X^k) = \frac{\text{fitness}_k}{\sum_{k=1}^{\text{mpop}} \text{fitness}_k}, k = 1, 2, \dots, \text{mpop}$$

3. “Compute cumulative probability range C'' ”.
4. “Generate random variable $r_s \sim U(0, 1)s = 1, 2, \dots, N''$ ”.
5. “Find selected variable $X^k, k \in \{1, 2, \dots, \text{max pop}\}$ and for every ant s ”.

Fig. 3 Ant’s behaviour



6. "Calculate objective function $f(X^k)$ for every ant s ".
7. "Choose minimum fitness function $f_{\text{best}} = \min(f(X^k), k \in \{1, 2, \dots, \text{max pop}\})$, and count N_{best} , the number of f_{best} "
8. "Set constant Q and calculate $\sum \Delta\tau(X^k), k = 1, 2, \dots, \text{max pop}$ "

$$\sum \Delta\tau(X^k) = \begin{cases} N_{\text{best}} \cdot \frac{Q}{f_{\text{best}}}, & \text{if } X^k \text{ is the best variable} \\ 0, & \text{otherwise} \end{cases}$$

9. "Update the pheromone"

$$\tau_k = (1 - \rho)\tau_k + \sum \Delta\tau(X^k), k = 1, 2, \dots, \text{mpop}$$

10. "Update the pheromone probability"

$$p(X^z) = \frac{\tau_k}{\sum \tau_k}, k = 1, 2, \dots, \text{mpop}$$

11. "Repeat step 3–10 until all ants choose the best path consisting pheromone and process converges".

Both the PSO and ACO algorithm are data clustering algorithms that show swarm behaviour. However, the ACO is more suitable for problems where origin and destination are predefined and precise. On the other hand, PSO is a clustering algorithm for multiobjective, dynamic optimization and constraint handling. Thus, ACO gives improved solutions to problems that needs crisps results and PSO for problems that are fuzzy is nature. Here, the optimization problem is finding PID parameters: K_P, K_I, K_D that minimize the sum of integral square error and integral absolute control as objective function (fitness function).

3 Results and Discussion

The nonlinear model of PWR was created in the MATLAB Simulink environment. The 9th order system has one input and one output with 9 state variables. Since the system is highly unstable, mild control rod speed is given as input, and corresponding rise in neutron density is plotted in Fig. 4. The neutron density spikes rapidly with slight increase in the order of 0.01 in control rod speed.

The steady-state values are calculated from the system Eqs. (1)–(14) and are listed in Table 3. These are set as initial conditions of states.

Initially, a closed-loop control system is built with conventional PID controller tuned using relay feedback approach as in Fig. 5. A relay input is given to the nonlinear PWR and continuous oscillations in n_t obtained.

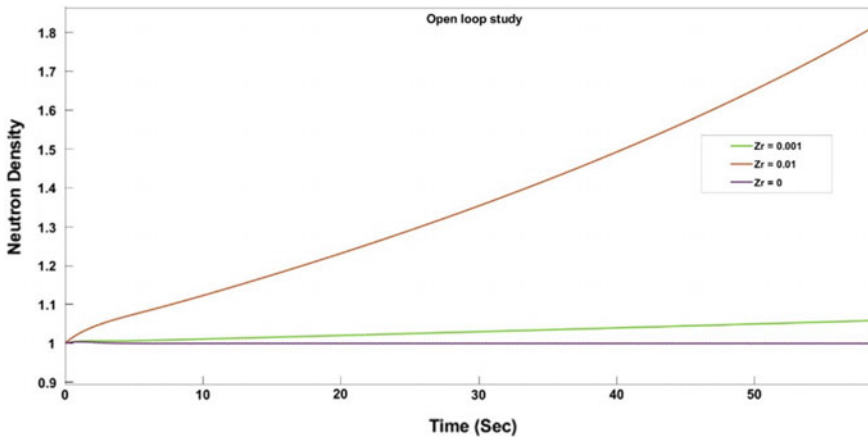


Fig. 4 Variations in neutron density for different Zr

Table 3 Steady-state values of variables for $Z_r = 0$

State variable	Steady-state values
Normalized neutron density, n_r	1
Normalized 1st group precursor density, c_{r1}	0.999
Normalized 2nd group precursor density, c_{r2}	0.999
Normalized 3rd group precursor density, c_{r3}	0.999
Xenon concentration, X	$5.5 \times 10^{10} \text{ cm}^{-3}$
Iodine concentration, I	$3.79 \times 10^{10} \text{ cm}^{-3}$
U-235 fuel average temperature, T_f	723.8 °C
Coolant average temperature, T_c	319.5 °C
Reactivity owing to control rod movement, ρ_{rod}	0

This PID–ZN is to be compared with PID controllers tuned with metaheuristic algorithms like PSO and ACO. The number of particles employed in the PSO method is 50, with a maximum iteration of 200. The number of ants in the ACO algorithm is 30, and the maximum iteration is 100. Both the metaheuristic algorithms use the sum of integral square error and integral absolute control as objective function. The PID controller parameters are listed in Table 4.

The performance of the designed PID–ACO, PID–PSO, and PID–ZN controllers is studied under load following conditions of PWR. For the first 100 s, a nominal neutron density of 1 is used as the set point. The desired value is then increased to 1.1, then decreased to 0.9, and finally returned to nominal load. The responses are seen under these load conditions. Figure 6 depicts the overall and zoomed closed

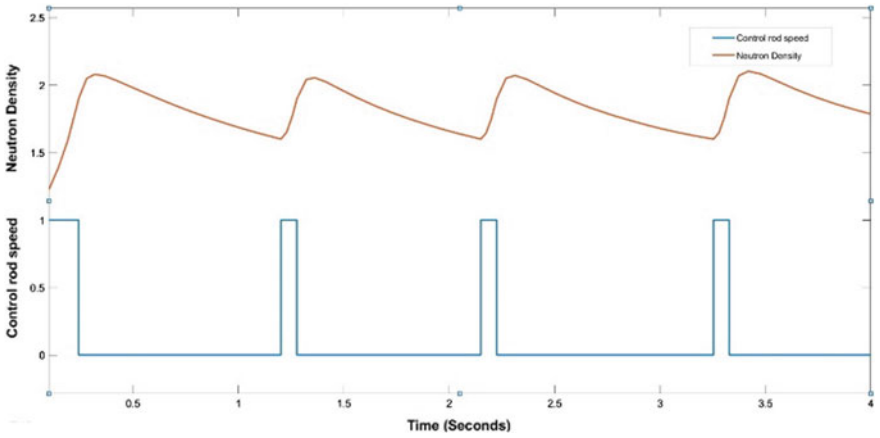


Fig. 5 Relay feedback tuning

Table 4 PID controller parameters

	Proportional term	Integral term	Derivative term
PID-ZN	1.6641	6.6564	0.104
PID-PSO	4.98	3.2369	0.0475
PID-ACO	4.7498	9.6101	0

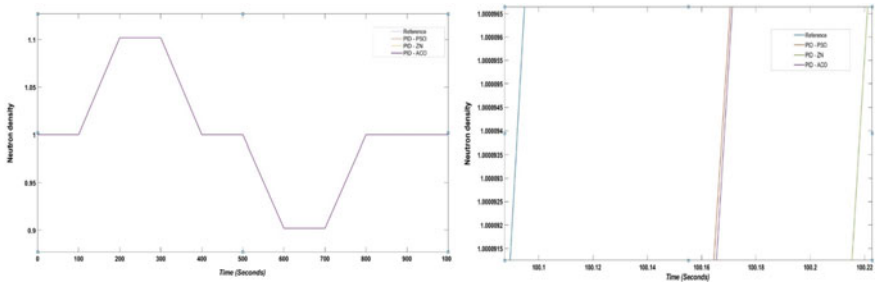


Fig. 6 Relative neutron density with tuned PID controllers

loop response of nonlinear PWR with PID controller. It proves the PSO and ACO tuned PID controller’s ability in efficient tracking. The error plot of neutron density is shown in Fig. 8. Further, the plot of control rod speed Z_r as in Fig. 7 shows the noisy PID-ZN response. The three groups of delayed neutron precursors when a PID-ACO is implemented are depicted by Fig. 9. The delayed neutron precursors, Cr_i , are the vital internal variables of the nuclear reactor as the neutron density relies directly on reactivity and delayed neutron precursors concentration as in Eq. (1). The figure shows that Cr_i also varies in a controlled manner to support load following condition.

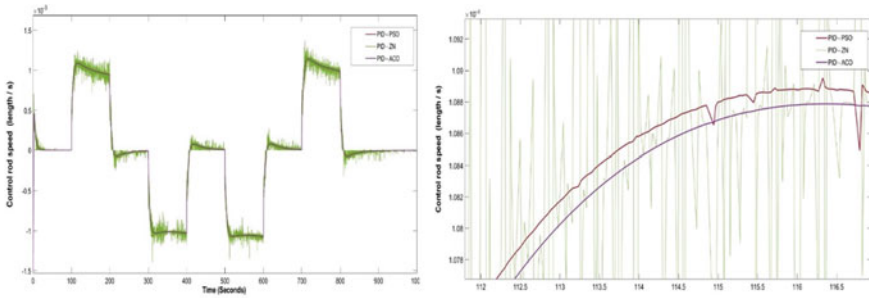


Fig. 7 Control input Z_r

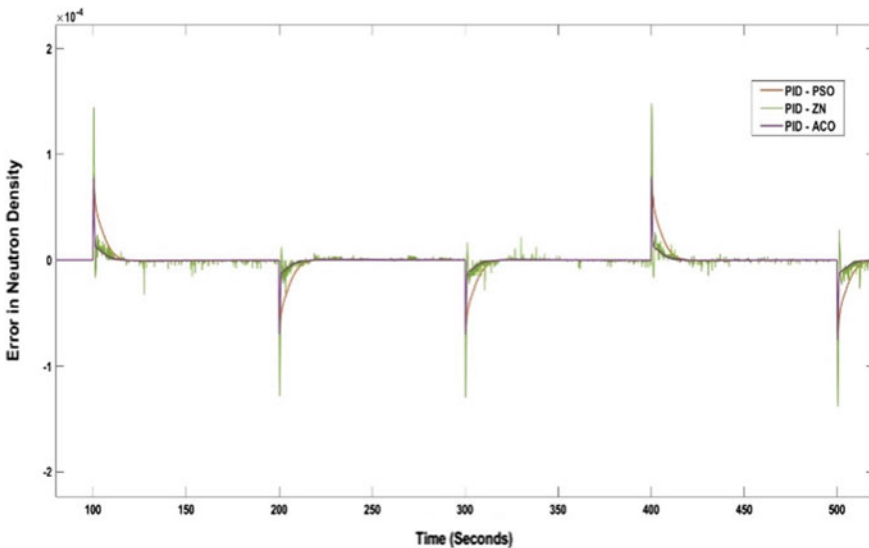


Fig. 8 Error in n_r

Table 5 lists the various quantitative performance measures like “integral square error” (ISE), “integral absolute error” (IAE), and “integral absolute control” (IAC). IAC is proposed in this work in order to provide equal weightage to speed of response and control efforts. It is clearly depicted that PID–ACO outperforms the other controller parameters.

The main drawback of PID controller is the internal variables are not considered for controller design. To overcome this, a hybrid controller is designed as a combination of LQR-PID. When a disturbance affects other state variables, the hybrid controller provides optimum control. Linear quadratic regulator is designed for linearized model of PWR. The linearized model is built around the operating point as shown in Table 3. The linear model is

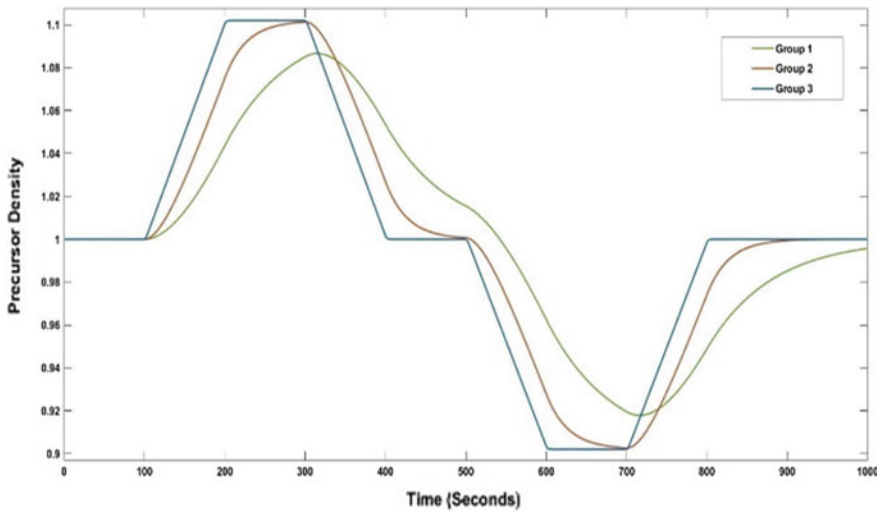


Fig. 9 Delay neutron precursors

Table 5 Quantitative performance measures

	PID-ZN	PID-PSO	PID-ACO
ISE	4.096e-6	1.9630e-7	0.9261e-7
IAE	0.02303	0.003445	0.00134
IAC	0.6298	0.4296	0.4295

$$\dot{x} = Ax + Bu \tag{21}$$

$$y = Cx + Du \tag{22}$$

A

$$= \begin{bmatrix} 0 & 0 & 0 & 0 & 0 & 0 & 0 & 0 & 0; \\ 10,000 & -65 & 2.1 & 22.5 & 40.4 & 4.1e-14 & 0 & -0.324 & -2.13; \\ 0 & 0.0124 & -0.0124 & 0 & 0 & 0 & 0 & 0 & 0; \\ 0 & 0.0369 & 0 & -0.0369 & 0 & 0 & 0 & 0 & 0; \\ 0 & 0.632 & 0 & 0 & -0.632 & 0 & 0 & 0 & 0; \\ 0 & 55,947.3 & 0 & 0 & 0 & 2.1e-05 & 2.9e-05 & 0 & 0; \\ 0 & 1,100,000 & 0 & 0 & 0 & 0 & -2.90e-05 & 0 & 0; \\ 0 & 78.5180 & 0 & 0 & 0 & 0 & 0 & -0.251 & 0; \\ 0 & 1.5729 & 0 & 0 & 0 & 0 & 0 & 0.092 & -1.466 \end{bmatrix}$$

$$B = [0.0145; 0; 0; 0; 0; 0; 0; 0; 0];$$

$$C = [0 \ 1 \ 0 \ 0 \ 0 \ 0 \ 0 \ 0 \ 0]$$

$$D = 0$$

Table 6 LQR controller gains

LQR parameters	LQR controller gains
$Q = C'C; R = 1$	[143.5657 0.0149 0.0300 0.3175 0.4531 -0.0000 -0.0000 -0.0049 -0.0185]
$Q = 10C'C; R = 1$	[458.0730 0.1521 0.0960 1.0250 1.6928 -0.0000 -0.0000 -0.0154 -0.0801]
$Q = C'C; R = 0.1$	[458.0730 0.1521 0.0960 1.0250 1.6928 -0.0000 -0.0000 -0.0154 -0.0801]
$Q = 10C'C; R = 0.1$	[1335.9465 1.2939 0.2803 3.0001 5.2272 -0.0000 -0.0000 -0.0439 -0.2644]

The LQR controller gains obtained for the various Q, R values are listed in Table 6. It can be seen that the controller gains increase when more weightage is given to Q and vice versa. In this work, equal weightage is applied to both Q and R .

A disturbance of $\pm 5^\circ\text{C}$ is applied on coolant temperature at every 200 secs, and $\pm 100^\circ\text{cm}^{-3}$ is applied on iodine concentration at every 300 secs to test the efficacy of hybrid controller designed. Figure 10 shows the response of neutron density, and Fig. 11 gives the control rod speed applied by hybrid controller. Oscillations are found in PID-ACO response nearer to the zone of disturbances whereas Hybrid-ACO has a smooth response. The improved tracking and control of the hybrid controller is perceived.

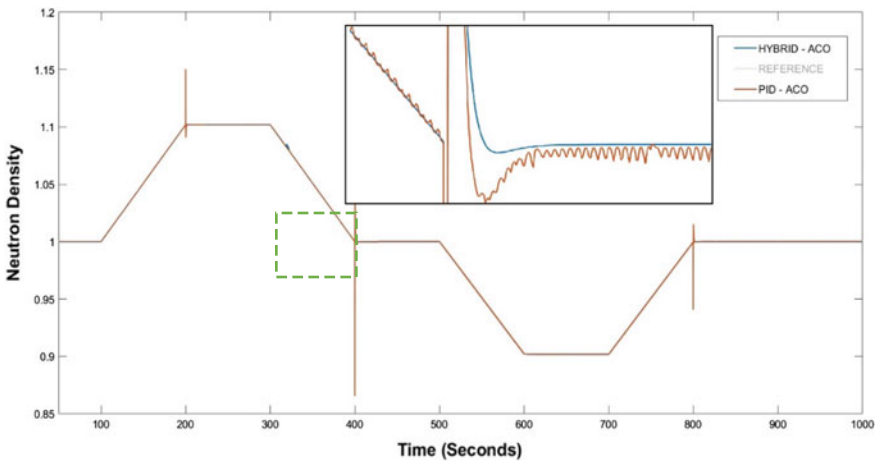


Fig. 10 n_t response with disturbance

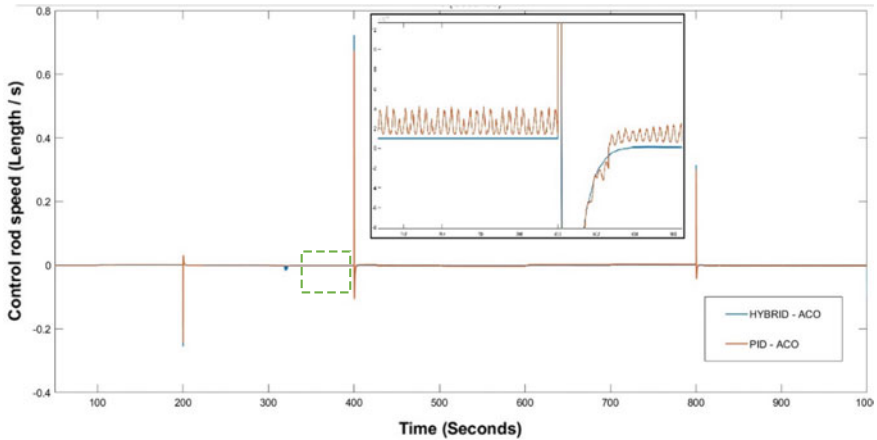


Fig. 11 z_r response with disturbance

4 Conclusion

In this work, a hybrid controller which is a combination of LQR and PID is applied for controlling a neutron density in a pressurized water reactor. The controller parameters are optimally tuned with PSO and ACO algorithms with the optimization objective that minimizes error and control efforts. Swarm intelligence-based tuning of PID controller determines optimal K_P , K_I , and K_D as compared with conventional tuning methods. The designed hybrid-ACO control structure outperforms PID-ACO control structure in the presence of disturbances in the state variables. The simulation results show excellent tracking with optimal control efforts.

Conflict of Interest The authors announce that there is no conflict of interest.

Declaration of Interest The authors affirm that there is no declaration of interest.

References

1. Suman S (2021) Artificial intelligence in nuclear industry: Chimera or solution? J Clean Prod 278:124022. <https://doi.org/10.1016/j.jclepro.2020.124022>
2. Mousakazemi SMH, Ayoobian N, Ansarifar GR (2018) Control of the pressurized water nuclear reactors power using optimized proportional–integral–derivative controller with particle swarm optimization algorithm. Nucl Eng Technol 50(6):877–885. <https://doi.org/10.1016/j.net.2018.04.016>
3. Mousakazemi SMH, Ayoobian N, Ansarifar GR (2018) Control of the reactor core power in PWR using optimized PID controller with the real-coded GA. Ann Nucl Energy 118:107–121. <https://doi.org/10.1016/j.anucene.2018.03.038>

4. Swetha R Kumar (2017) Vectorized quadrant model simulation and spatial control of advanced heavy water reactor. *WSEAS Trans Syst Control* 12:73 – 81, E-ISSN: 2224–2856
5. Mousakazemi SMH (2019) Control of a PWR nuclear reactor core power using scheduled PID controller with GA, based on two-point kinetics model and adaptive disturbance rejection system. *Ann Nucl Energy* 129:487–502. <https://doi.org/10.1016/j.anucene.2019.02.019>
6. Mousakazemi SMH (2021) Control of a pressurized light-water nuclear reactor two-point kinetics model with the performance index-oriented PSO. *Nucl Eng Technol*. <https://doi.org/10.1016/j.net.2021.02.018>
7. Mousakazemi SMH, Ayoobian N (2019) Robust tuned PID controller with PSO based on two-point kinetic model and adaptive disturbance rejection for a PWR-type reactor. *Prog Nucl Energy* 111:183–194. <https://doi.org/10.1016/j.pnucene.2018.11.003>
8. Vajpayee V, Becerra V, Bausch N, Deng J, Shimjith SR, Arul AJ (2021) LQG/LTR based robust control technique for a pressurized water nuclear power plant. *Ann Nucl Energy* 154:108105. <https://doi.org/10.1016/j.anucene.2020.108105>
9. Li G (2014) Modeling and LQG/LTR control for power and axial power difference of load-follow PWR core. *Ann Nucl Energy* 68:193–203. <https://doi.org/10.1016/j.anucene.2014.01.022>
10. Ramaswamy P, Riese M, Edwards RM, Lee KY (1993) Two approaches for automating the tuning process of fuzzy logic controllers [PWR application]. In: *Decision and control. 1993, Proceedings 32nd IEEE conference, IEEE, 1993*, pp 1753–1758
11. Zameer A, Muneeb M, Mirza SM, Raja MAZ (2020) Fractional-order particle swarm based multi-objective PWR core loading pattern optimization. *Ann Nucl Energy* 135:106982. <https://doi.org/10.1016/j.anucene.2019.106982>
12. Yadav DK, Gupta A, Munshi P (2020) Design of NDI-SMC based robust hybrid nonlinear controller for load following operation in pressurized water reactor. *Nucl Eng Des* 363:110604. <https://doi.org/10.1016/j.nucengdes.2020.110604>
13. Calgan H, Demirtas M (2021) A robust LQR-FOPID controller design for output voltage regulation of stand-alone self-excited induction generator. *Electr Power Syst Res* 196:107175. <https://doi.org/10.1016/j.epsr.2021.107175>
14. Noordin A, Mohd Basri MA, Mohamed Z, Zainal Abidin AF (2017) Modelling and PSO fine-tuned PID control of quadrotor UAV. *Int J Adv Sci, Eng Inf Technol* 7(4):1367. <https://doi.org/10.18517/ijaseit.7.4.3141>
15. Mughees A, Mohsin SA (2020) Design and control of magnetic levitation system by optimizing fractional order PID controller using ant colony optimization algorithm. *IEEE Access* 8:116704–116723. <https://doi.org/10.1109/ACCESS.2020.3004025>
16. Karami M, Tavakolpour-Saleh AR, Norouzi A (2020) Optimal nonlinear PID control of a micro-robot equipped with vibratory actuator using ant colony algorithm: simulation and experiment. *J Intell Robot Syst* 99(3–4):773–796. <https://doi.org/10.1007/s10846-020-01165-5>
17. Herlambang T, Rahmalia D, Yulianto T (2019) Particle swarm optimization (PSO) and ant colony optimization (ACO) for optimizing PID parameters on autonomous underwater vehicle (AUV) control system. *J Phys: Conf Ser* 1211:012039. <https://doi.org/10.1088/1742-6596/1211/1/012039>
18. Rahman M, Ong ZC, Chong WT, Julai S, Ng XW (2019) Wind turbine tower modeling and vibration control under different types of loads using ant colony optimized PID controller. *Arab J Sci Eng* 44(2):707–720. <https://doi.org/10.1007/s13369-018-3190-6>
19. Hetrick D (1993) *Dynamics of nuclear reactors*. American Nuclear Society
20. Mousakazemi SMH (2021) Comparison of the error-integral performance indexes in a GA-tuned PID controlling system of a PWR-type nuclear reactor point-kinetics model. *Prog Nucl Energy* 132:103604. <https://doi.org/10.1016/j.pnucene.2020.103604>
21. Åström KJ, Hägglund T (1995) *PID controllers: theory, design, and tuning*
22. Herlambang T, Rahmalia D, Yulianto T (2019) Particle swarm optimization (PSO) and ant colony optimization (ACO) for optimizing PID parameters on autonomous underwater vehicle (AUV) control system. *J Phys: Conf Ser*
23. Naidu DS (2002) *Optimal control systems*. CRC Press

False Data Injection Attack Detection Using Machine Learning in Smart Grid: Approaches, Datasets, and Comparative Study



Tania Gupta, Richa Bhatia, and Richa Sharma

Abstract Aging power sectors and rising demand from industrial and retail consumers are the key motivation for policymakers to establish a path map to the next phase of the traditional grid called as the smart grid (SG). In SG, the potential cost of surveillance would be minimized, but the possibility of cyber threats may be raised simultaneously. Many machine learning (ML)-based methods for detecting cyber threats have been established in recent years. In this article, a detailed survey of ML technique developments for threat detection has been given. The article starts by presenting a short description of the architecture of SG. To provide a detailed summary of current research and define future research issues, this paper performs a study of attacker perception. In addition, kinds of false data attacks and data protection standards have been introduced. The most recent detection techniques based upon machine learning are then summed up by categorizing them in three critical identification situations: non-technical casualties, load forecasting, and state estimation. The vulnerabilities of existing ML detection approaches with new testing problems and future directions have finally been addressed.

Keywords Cybersecurity · Machine learning · Attack · Smart grid

T. Gupta (✉)

Department of Electronics & Communication, Affiliated to GGSIPU, NSUT East Campus (Formerly AAICTR), New Delhi, Delhi, India
e-mail: taniagupta2409@gmail.com

Department of Electronics & Communication, ABES Engineering College, Ghaziabad, India

R. Bhatia

Department of Electronics & Communication, NSUT East Campus (Formerly AAICTR), New Delhi, Delhi, India

R. Sharma

Department of Electronics & Communication, Malaviya National Institute of Technology Jaipur, Jaipur, India

1 Introduction

The stocks of FOSSIL fuel are finite, and the established oil reserves are estimated to be depleted by 2050 [1]. Renewable energies, such as solar and wind energy, will be a solution to energy shortages and a sustainable climate. In terms of energy-saving and reducing carbon emissions, smart and efficient energy use will also be effective. Smart grid (SG) technology is an efficient way of integrating different renewable energy sources into the current energy infrastructure and making smart energy a reality [2]. SG is an adaptive electricity distribution system combined with modern information and communications technology. To improve the sustainability and accuracy of energy usage, specialized software segments such as Advanced Distribution Management (ADM) and Advanced Metering Infrastructure (AMI) are introduced [3]. SG has received increasing interest from companies, governments, and academia with its potential developments in recent years. The SG market is expected to expand, as a recent market study shows ☆23.8 billion in 2018 to ☆61.3 billion in 2023 [4]. However, the large implementation of SG systems has been disrupted by various security issues. False data attacks are described as a serious hazard. By compromising the SG sensors' measurements, an intruder can target the SG systems while bypassing conventional security measures. An attacker will introduce false readings into the state calculation process, resulting in a serious incident [5, 6]. Therefore, considerable attention has been drawn to defend against such attacks, and in the last decade, different detection methods have been established. Machine learning (ML) techniques are increasingly accepted as an appropriate method to efficiently detect such attacks because of their ability to scale massive structures at low computational costs [7, 8].

Several similar articles in the literature deal with the ML approach for intrusion detection systems. Authors categorize the studies based on the following parameters, as seen in Table 1:

- Machine learning approaches (ML): It demonstrates whether machine learning approaches for attack detection systems were considered in the article.
- Evaluation of machine learning approaches (EML): It shows whether the systematic research approaches machine learning for a false data injection attack.

Table 1 Related studies on cybersecurity attack detection

Paper	Year	ML	EML	Dataset	FDA
Den et al. [9]	2016	×	×	×	✓
Hossain et al. [13]	2019	✓	✓	×	×
Elmrabet et al. [11]	2018	×	×	×	×
Wang et al. [12]	2018	✓	×	×	✓
Kumar et al. [14]	2019	×	×	×	✓
Tan et al. [10]	2017	×	×	×	✓

- Datasets used by attack detection: It indicates whether the study focused on the datasets used for attack detection.
- False data attack (FDA): It shows whether the study considers the false data attack.

In [9], the influence of information control on state estimation (SE) was examined, and existing methods to false data injection (FDI) assaults were checked. The author investigated SG data security issues such as data creation, data processing, and data storage. Furthermore, author summed up few data-driven methods for security investigation in [10]. In [11], Z. Elmrbet et al. examine security standards, detailing many major cyber risks, and suggest a cybersecurity system to detect and guard against such threats. It should be noted that no survey includes an overall analysis of the use of ML, especially in the field of false data identification study. While investigating the taxonomy of risks, vulnerability analysis, safety standards, and vulnerability against steps, most recent studies discuss SG security concerns. In reality, several ML-based techniques have been created in the last few years with substantial contributions. Nonetheless, the new survey articles, though, either research a few data analytical literature or focus exclusively on one particular application. In order to address these gaps, a systematic survey to present the new developments in SG data protection methods focused on ML has been carried out. In specific, the analysis of false data attacks has been discussed with regard to three important SG applications: identification of state estimation (SE), non-technical losses (NTL), and load forecasting (LF). Furthermore, paper also shows the different possible challenges and future paths. A systematic and detailed survey of new studies would help track the latest advances in the field, which will be the key inspiration for this paper. However, in many surveys on SG security problems, no investigation has been identified, which was conducted specifically for false data injection attacks using detection techniques based on ML. Our survey is going to try to fill this gap. The main contributions are summarized in the following:

- An exhaustive analysis of the technology of the smart grid.
- It contains a quick summary of safety issues caused by falsified data attacks in SG. The terminology and the effects of the assault and data security criteria are described.
- The perception of the attackers, the aim, and the consequences of the FDI attack shall be examined in such a way as to summarize the process of invasion against physical networks, communication of the SG, and their effect on the comprehensive cyber-physical SG services.
- A comprehensive nomenclature of machine learning defensive systems against malicious data injection attacks, incorporating the NTL for state estimation, metering infrastructure, and load forecasting.
- Security flaws of current detection methods based on machine learning, mainly the problem of inefficiency against conflicting attacks and issues of privacy outflow, are examined. Few complex and difficult ways are listed in the paper, along with early countermeasures.

The rest of the paper has the following structure. Section 2 summarizes the SG framework. In Sect. 3, we describe several false injection attacks and their consequences on the power grid activity. Section 4 provides a comprehensive analysis of ML-based approaches for detecting false data attacks. Finally, Sect. 5 offers a conclusion on emerging research issues that need to be addressed further.

2 Analysis of Smart Grid Architecture

An analysis of the SG with energy details has been carried out in this section. Thus, beginning from the analysis of SG architecture has been discussed. According to the National Institute of Standards and Technology (NIST) [15], in the smart grid there are seven domains: bulk production, transmission, distribution, markets, utility providers, consumers, and operations. Based on these domains, two primary architectures are Supervisory Control and Data Acquisition networks (SCADA) and Advanced Metering Infrastructure (AMI).

2.1 *Advanced Metering Infrastructure*

For electrical, gas, and water usage, AMI is necessary to gather, monitor, and assess data. This enables the user-utility two-way communication. It includes three components: the headend system, the data concentrator, and the smart meter [16]. AMI also encourages data collection, such as market price assessment and control and device tracking. It is in charge of collecting, monitoring, and evaluating energy consumption data from various smart meters and delivering this data to the data concentrator unit, which is connected to the smart meter, and ultimately to the utility end. As a result, it is responsible of the two-way information flow. It allows for smart meter remote control, data collecting and transfer for applications, and decision-making for invoicing, pricing, and other tasks. As a sophisticated system, AMI is vulnerable to a variety of security concerns, including data theft, energy theft, unlawful monetary gain, and other criminal acts. Figure 1 shows how data is stored, distributed, and processed to better illustrate the AMI hierarchy.

2.2 *Supervisory Control and Data Acquisition Networks*

SCADA is a system that monitors, records, and controls data from the power grid. It is usually found in large-scale environments. It comprises three components: human-machine interface (HMI), master terminal device (MTU), and remote terminal unit (RTU). SCADA usually can gather data in real time across the system. The information could be analogs, position information, or other operational limits. SCADA

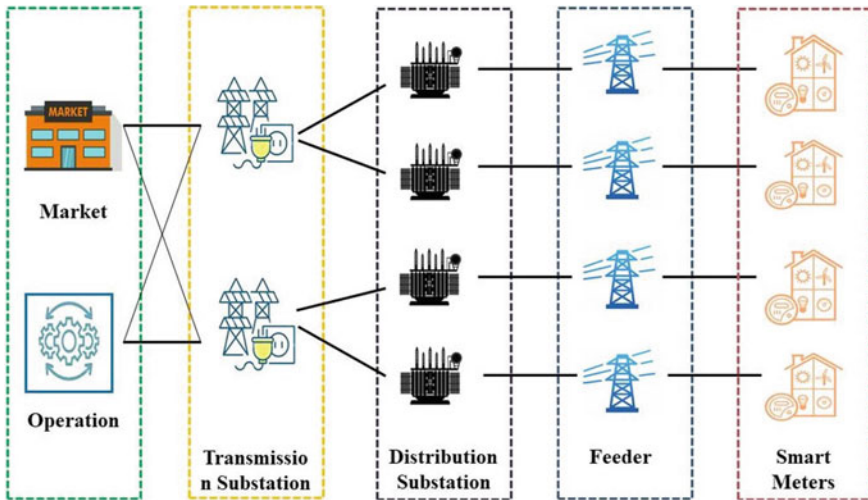


Fig. 1 The centralized structure of advanced metering infrastructure

may perform safety analysis with the collected data, such as reactive power dispatch. RTU consists of three components: the first for data collection, the second to be used to execute the instructions coming from MTU, and the third to be used for communication. The MTU is important for RTU regulation. The HMI is a graphical framework for the device operator of SCADA [17].

3 False Data Attack

The SG contains a variety of terminal devices, as an example PLCs, RTUs, and the like. The availability of these end devices permits power systems to work properly, even when they are operated remotely. However, these devices are vulnerable to false data attacks. When a disparity between the energy delivered by the utility and the energy indicated by smart meters is found, fraud detection is activated. This section contains, the leading false data attack has been introduced. False data attacks are defined in three main groups, which are FDI attacks and replay attacks.

FDI aims to corrupt some measurements to affect state estimation. For example, adversaries may decrease the power consumption to imbalance energy systems. The real-world situation could be that incorrect signal information is transmitted after manipulating sensor or RTU data. There are two main aspects to initiate a successful attack. The first is that adversaries will access and extract the configuration data from the existing energy grid. Thus, data stored in physically secured environments can be utilized. Secondly, the adversaries will attempt their uttermost without being caught to exploit the data. As a result, FDI assaults represent a substantial risk to energy networks and are hard to detect in real time.

A replay attack transfers the stealthy data several times to end devices within a time frame. To launch the replay attack, it is required to hack the PMUs. The attackers have been tracking the data for a while. The attackers can then try to replicate the same details so that the central authority will be misled. Replay attacks are challenging to detect because of limitations in cryptography operations in real time. The additional risk in replay attacks is that a hacker does not need technical expertise to decode a message after being captured from the network. By simply resending the entire thing, the attack could be successful. These attacks would therefore cause a lack of genuine data within the central authority and hence would disrupt routing services.

4 False Data Attack Detection Using Machine Learning-Based Methods: An Overview

ML strategies offer an effective way to evaluate and then make the best choices to operate the grid, allowing the smart grid to work as expected. The term machine learning (ML) refers to a system’s ability to learn and make decisions based on available data. It consists of several algorithms, which evaluate the given data by providing instructions for making data-driven predictions. ML features include predictive usage, price, fault prediction, power generation, adaptive management, scale, and prediction of network invaders during the data breach.

In this section, ML techniques for false data attack have been discussed. In the smart grid, ML can also be applied to numerous security applications. The ML techniques for detecting non-technical losses (NTL), FDI in SE, and FDI in LF have been studied. Figure 2 shows the summary of ML methods used to detect FDI in different applications. The widely used dataset is the Customer Behavior Trial which can be obtained from Irish Social Science Archive (ISSA). These trails were set up

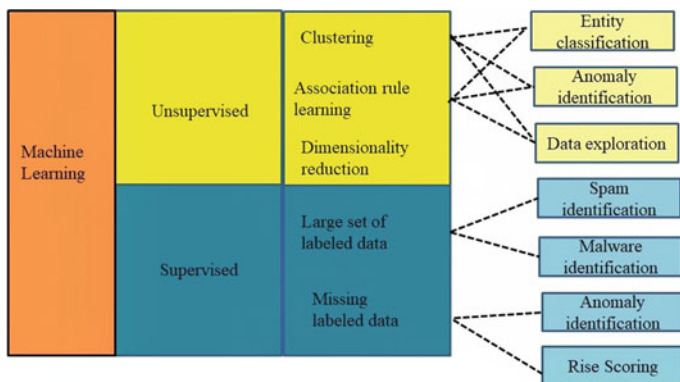


Fig. 2 Summary of ML techniques used for detecting FDI in different application

Table 2 Summary of public available datasets

Name	Duration	Frequency	Number of customers (min)
UMass Smart [27]	2014–2016	114	Every 1
Low Carbon London [28]	2013/1-2013/12	5567	Every 30
Customer Behavior Trials [29]	2009–2011	6445	Every 30
UCI [30]	2011–2014	370	Every 15

to see how smart meter technology affected the behavior of different categories of customers when it came to power use.

A challenge for the conduction of smart meter data analytics analysis, attack detection and its implementation is the dataset. Many power providers are reluctant to disclose their smart meter data to the public due to many concerns, such as privacy and protection. Nevertheless, over the past few years, many semi-anonymized or anonymized household-level datasets have been made publicly available. Based on the smart meter dataset, various experiments have been performed. In Table 2, several public load datasets are summarized.

4.1 Detection of NTL

Detection of NTL seems to be a great concern to power providers, as NTL is responsible for a large proportion of cumulative revenue losses related to anomalies or fraud. It is possible to divide the simple ML-based NTL algorithms into two categories: supervised and unsupervised. In [18], hybrid strategy based on SVM, power grid optimization, and voltage sensitivity analysis was proposed. Other supervised machine learning algorithms that have been researched include artificial neural networks, k-nearest neighbors (KNN), and regression-based algorithms [4, 19, 20].

Although supervised approaches can enable use of smart meter data that is readily available at a moderate cost, there are several drawbacks that influence both the detection rate and the false-positive rate. The main issue is that they necessitate labeled datasets, which are tough to come by in real. A consumption pattern for each customer has been created by picking some attributes then applied fuzzy K-means clustering in [21] (Table 3).

4.2 Detection of FDI on State Estimation

FDI attacks have been a significant threat to the SE mechanism and for the power system. It is more conceivable that by changing multiple SG measurements, attackers will ensure that the control centers keep making incorrect decisions. There are various supervised algorithms used in SE to detect FDI, such as [22, 23]. Recent work in [23]

Table 3 An overview of various machine learning techniques for detecting false data in smart grids

References	Year	Approach	ML algorithm	Type
[4]	2016	Classification	SVM-based	Non-technical loss
[18]	2019	Classification	SVM-based	Non-technical loss
[19]	2016	Regression	PARX	Non-technical loss
[20]	2018	Clustering	CFSFDP	Non-technical loss
[21]	2011	Clustering	K-means	Non-technical loss
[23]	2016	Classification	KNN and SVM	State estimation
[23]	2019	Classification	KNN and SVM	State estimation
[31]	2018	Regression	Neural network	Load forecasting
[26]	2019	Classification	Naive Bayes	Load forecasting

analyzed the efficacy of many traditional supervised ML algorithms and numerous selection techniques of heuristic features. By comparison, the authors concluded that in FDI identification, KNN and SVM algorithms could achieve greater precision than ANN. The anomaly detection approach for PMU data has recently been studied in several studies. As it is quite difficult to obtain the actual labels over PMU's rapid data, unsupervised learning model has been presented as a detector [25].

4.3 Detection of FDI on Load Forecasting

The LF method, which plays a fundamental role in SG, has been commonly utilized by utilities and operators. Recent developments in ML methods have greatly increased the accuracy of forecasting. According to [31], an effective LF model is not inherently resistant to hostile attacks. In cite 24, an unique ML-based detection method named MLAD was suggested for identifying LF data assaults. The suggested approach can be used to approximate the actual event and parameter details of a single attack. Considering that the load data's invariant structures and nonlinear characteristics cannot be well derived from deep ML models.

5 Conclusion and Future Scope

A detailed evaluation of several ML-based approaches for malicious data attack detection in NTL, state estimation, and load forecasting has been done in this article. The new advances in this field have been outlined and discussed. Different open datasets available have also been summarized. Although attack detection has received extensive attention, still there are lots of open research challenges as follows: The

majority of the time current machine learning-based activities concentrate largely on enhancing detection efficiency but neglect these algorithms' security and robustness.

- The majority of existing ML-based initiatives are primarily focused on increasing detection efficiency, but they overlook the algorithms' safety and strength. But again, real-world implementation of certain ML-based detection techniques is problematic.
- Sending all energy data to a single point for analysis or detection is relatively inadequate due to efficiency and delay constraints in commercial processes. As a result, there has been a lot of interest in a new detection method that increases distributed protection while enabling source data to remain on edge devices.
- Existing ML methods, particularly for energy data processing, present considerable challenges in real-world SG applications. When public databases and labeled samples are scarce, guaranteeing the correctness of a trained model is a significant challenge.

Cybersecurity in SG is already an emerging and exciting field of study. The analysis given in this paper will provide a full image and in-depth perspectives into this field for readers.

References

1. Sharma S, Niazi KR, Verma K, Rawat T (2020) Coordination of different DGs, BESS and demand response for multi-objective optimization of distribution network with special reference to Indian power sector. *Int J Electr Power Energy Syst* 121:106074
2. Sridhar S, Hahn A, Govindarasu M (2011) Cyber-physical system security for the electric power grid. *Proc IEEE* 100(1):210–224
3. Yang X et al (2016) Toward a Gaussian-mixture model-based detection scheme against data integrity attacks in the smart grid. *IEEE Internet of Things J* 4(1):147–161
4. Jokar P, Arianpoo N, Leung VCM (2015) Electricity theft detection in AMI using customers' consumption patterns. *IEEE Trans Smart Grid* 7(1):216–226
5. Nizar AH, Dong ZY, Wang Y (2008) Power utility nontechnical loss analysis with extreme learning machine method. *IEEE Trans Power Syst* 23(3):946–955
6. Pancholi S, Joshi AM (2020) Advanced energy Kernel-based feature extraction scheme for improved EMG-PR-based prosthesis control against force variation. *IEEE Trans Cybern*
7. Hossain E et al (2019) Application of big data and machine learning in smart grid, and associated security concerns: a review. *IEEE Access* 7:13960–13988
8. Sharma S, Niazi KR, Verma K, Rawat T (2020).A bi-level optimization framework for investment planning of distributed generation resources in coordination with demand response. *Energy Sources, Part A: Recovery, Utilization, and Environmental Effects* 1–18
9. Deng R, Xiao G, Lu R, Liang H, Vasilakos AV (2016) False data injection on state estimation in power systems—Attacks, impacts, and defense: a survey. *IEEE Trans Ind Inf* 13(2):411–423
10. Tan S, De D, Song W-Z, Yang J, Das SK (2017) Survey of security advances in smart grid: a data driven approach. *IEEE Commun Surv Tutor* 19(1):397–422
11. El Mrabet Z, Kaabouch N, El Ghazi H, El Ghazi H (2018) Cyber-security in smart grid: survey and challenges. *Comput Electr Eng* 67:469–482
12. Wang Q, Tai W, Tang Y, Ni M (2019) Review of the false data injection attack against the cyber-physical power system. *IET Cyber-Phys Syst: Theory Appl* 4(2):101–107

13. Hossain, Eklas, Imtiaj Khan, Fuad Un-Noor, Sarder Shazali Sikander, and Md Samiul Haque Sunny. "Application of big data and machine learning in smart grid, and associated security concerns: A review." *IEEE Access* 7 (2019): 13960–13988.
14. Kumar P, Lin Y, Bai G, Pavard A, Dong JS, Martin A (2019) Smart grid metering networks: a survey on security, privacy and open research issues. *IEEE Commun Surv Tutor* 21(3):2886–2927
15. Framework N (2012) Roadmap for smart grid interoperability standards, Release 2.0 (2012), NIST Special Publication, vol 1108
16. Faisal MA, Aung Z, Williams JR, Sanchez A (2014) Data-stream-based intrusion detection system for advanced metering infrastructure in smart grid: a feasibility study. *IEEE Syst J* 9(1):31–44
17. Choi D, Lee S, Won D, Kim S (2009) Efficient secure group communications for SCADA. *IEEE Trans Power Deliv* 25(2):714–722
18. Messinis GM, Rigas AE, Hatziaargyriou ND (2019) A hybrid method for non-technical loss detection in smart distribution grids. *IEEE Trans Smart Grid* 10(6):6080–6091
19. Liu X, Nielsen PS (2016) Regression-based online anomaly detection for smart grid data. arXiv preprint [arXiv:1606.05781](https://arxiv.org/abs/1606.05781)
20. Zheng Z, Yang Y, Niu X, Dai H-N, Zhou Y (2017) Wide and deep convolutional neural networks for electricity-theft detection to secure smart grids. *IEEE Trans Industr Inf* 14(4):1606–1615
21. Angelos EWS, Saavedra OR, Carmona Cort'es OA, de Souza AN (2011) Detection and identification of abnormalities in customer consumptions in power distribution systems. *IEEE Trans Power Deliv* 26(4):2436–2442
22. Ozay M, Esnaola I, Tunay Yarman Vural F, Kulkarni SR, Vincent Poor H (2015) Machine learning methods for attack detection in the smart grid. *IEEE Trans Neural Netw Learn Syst* 27(8):1773–1786
23. Yan J, Tang B, He H (2016) Detection of false data attacks in smart grid with supervised learning. In: 2016 International joint conference on neural networks (IJCNN). IEEE, pp 1395–1402
24. Sakhnini J, Karimipour H, Dehghantanha A (2019) Smart grid cyber attacks detection using supervised learning and heuristic feature selection. In: 2019 IEEE 7th international conference on smart energy grid engineering (SEGE). IEEE, pp 108–112
25. Zhou M, Wang Y, Srivastava AK, Wu Y, Banerjee P (2018) Ensemble-based algorithm for synchrophasor data anomaly detection. *IEEE Trans Smart Grid* 10(3):2979–2988
26. Liang Y, He D, Chen D (2019) Poisoning attack on load forecasting. In: 2019 IEEE innovative smart grid technologies-Asia (ISGT Asia). IEEE, pp 1230–1235
27. Cui M, Wang J, Yue M (2019) Machine learning-based anomaly detection for load forecasting under cyberattacks. *IEEE Trans Smart Grid* 10(5):5724–5734
28. Umass Smart Dataset (2017). [Online]. Available: <http://traces.cs.umass.edu/index.php/Smart/Smart>
29. Schofield JR et al (2016) Low Carbon London Project: data from the dynamic time-of-use electricity pricing trial. Accessed: Aug 8, 2017. [Online]. Available: <https://discover.ukdataservice.ac.uk/catalogue?sn=7857>, <https://doi.org/10.5255/UKDA-SN-7857-2>
30. Irish Social Science Data Archive (2012) Commission for energy regulation (CER) smart metering project. [Online]. Available: <http://www.ucd.ie/issda/data/commissionforenergyregulationcer/>
31. Lichman M (2013) UCI machine learning repository. [Online]. Available: <http://archive.ics.uci.edu/ml>
32. Luo J, Hong T, Fang S-C (2018) Benchmarking robustness of load forecasting models under data integrity attacks. *Int J Forecast* 34(1):89–104

A Protection Approach for Power System Fault Categorization



Tarachand Yadav, Shoyab Ali, and Gaurav Kapoor

Abstract This paper introduces a protection approach for power system fault categorization. Making use of 3- Φ currents of primary side bus, the protection system absolutely identifies faults in power system. Wavelet has been utilized to split the time domain information from the frequency domain information to identify faults effectively. The protection system has been widely evaluated under a range of active situations. Simulation results completed by MATLAB prove the aptitude and effectiveness of the protection system in identifying power system faults.

Keywords Power system · Fault identification · Wavelet analysis

1 Introduction

Protection systems are designed and employed to avoid the destruction caused by the unwanted faulty situations in power systems. A protection system must have a perfect fault identification potential in order to activate appropriately. In wind transmission network system, power swing identification using synchro-phasor method is suggested in [1]. For HVDC system, long short-term memory (LSTM) method is introduced in [2]. Stockwell with neural network can be validated to locate faults in a multi-bus system [3]. In [4], a complicated method was suggested; however, a variety of tools were used in the method. In [5], a backup-assisted method is presented for fault identification with high impedance. Convolutional neural network with LSTM can be authenticated to locate faults in [6]. Wavelet along with the neural network can achieve better functioning as suggested in [7]. In [8], a transfer function method is accomplished with a frequency domain method. In [9], a capsule network along with sparse filtering is employed. In [10], a distance relaying method is suggested.

T. Yadav · S. Ali

Department of Electrical Engineering, Vedant College of Engineering and Technology, Bundi, India

G. Kapoor (✉)

Department of Electrical Engineering, Modi Institute of Technology, Kota, India
e-mail: gaurav.kapoor019@gmail.com

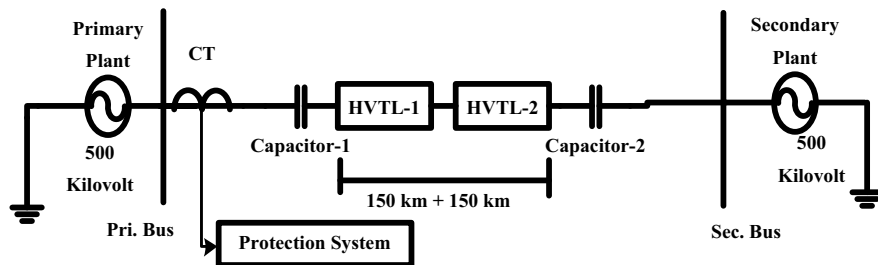


Fig. 1 Illustrated model

A protection system is suggested in this paper for power system fault identification. The suggested system is designed using wavelet.

The power system selected is illustrated in Sect. 2. The flowchart of the protection system is presented in Sect. 3. Simulation results are provided in Sect. 4. Section 5 gives the conclusion.

2 Power System

Figure 1 displays the system on which the protection system has been tested. The primary and secondary plants (500 kV each) are connected through 300 km high-voltage transmission lines (HVTLs). The 3- Φ currents measured at the primary bus are entered as input to the protection system as illustrated in Fig. 1. The protection system is tested for unlike situations of faults.

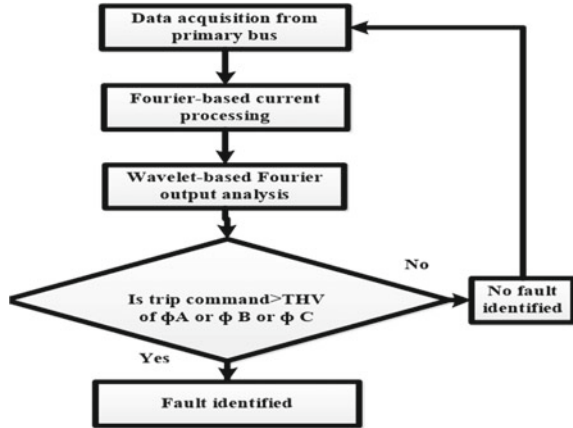
3 Flowchart for Power System Fault Identification

The flowchart for power system fault identification is shown in Fig. 2. The data acquisition from the primary bus is continuously monitored. The fault is identified in HVTL using wavelet-based Fourier output analysis. Equation 1 given below suggests the low-pass (H_p) type wavelet filter, and Eq. 2 suggests the high-pass (G_p) type filter. Here, p is the particular order of a filter.

$$H_p(z) = \sum_{k=0}^p \binom{p}{k} z^{-k} \cdot \sum_{k=1}^p m_{k-1} (-1)^{k-1} z^{-k+1}, \tag{1}$$

$$G_p(z) = \sum_{k=0}^p \binom{p}{k} - 1^k z^{-k} \cdot \sum_{k=1}^p m_{p-k} z^{-k+1}, \tag{2}$$

Fig. 2 Flowchart for power system fault identification



4 Simulation Effects

Functioning of the system under unlike situations is described in this section.

4.1 Functioning During High Impedance Fault

Functioning of the method during a high impedance fault is illustrated in Fig. 3. The functioning during AC fault created with FI 50 Ω, FIT 0.15 s and the corresponding trip commands of Φ-A and Φ-C sent by the protection system is presented in Fig. 3. In this case, the initiation time of trip command is 0.185 s. The tripping time is 0.185–0.15 = 0.035 s which is 35 ms.

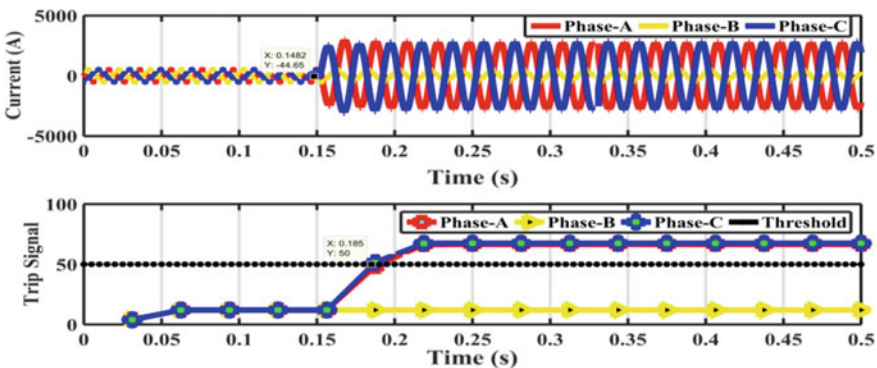


Fig. 3 Functioning through AC fault: FI = 50 Ω and FIT = 0.15 s

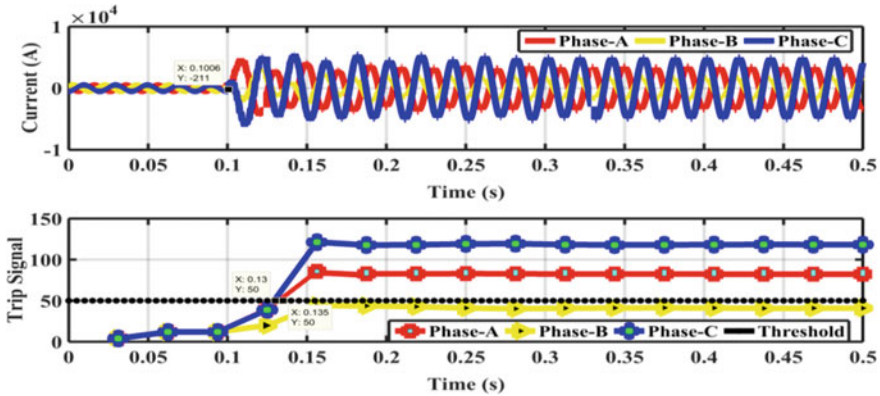


Fig. 4 Functioning through CG fault at 155 km and AG fault at 145 km with FIT 0.1 s

4.2 Functioning During Multiposition Fault

A multiposition fault CG created at 155 km, AG created at 145 km with FIT 0.1 s and the resultant trip commands of Φ -C and Φ -A sent by the protection system are illustrated in Fig. 4. In this case, the initiation time of trip command of Φ -C is 0.13 s and that of Φ -A is 0.135 s. The tripping time of Φ -C is $0.13 - 0.1 = 0.03$ s which is 30 ms and that of Φ -A is $0.135 - 0.1 = 0.035$ s which is 35 ms.

4.3 Functioning Through Unlike System Voltage and Frequency

Figure 5 explains the functioning of protection system through AB fault at FIT 0.05 s, system voltage 510 kV and system frequency 51.5 Hz. The resulting trip commands of Φ -A and Φ -B sent by the protection system are illustrated in Fig. 5. In this case, the initiation time of trip command of Φ -A and Φ -B is 0.07 s. The tripping time is $0.07 - 0.05 = 0.02$ s which is 20 ms.

4.4 Functioning Through Unlike Short Circuit Limit

Figure 6 explicates the operation of protection system through AB fault at FIT 0.25 s, SCL 75 GVA. The resulting trip commands of Φ -A and Φ -B sent by the protection system are illustrated in Fig. 6. In this case, the initiation time of trip command of Φ -A and Φ -B is 0.26 s. The tripping time is $0.26 - 0.25 = 0.01$ s which is 10 ms.

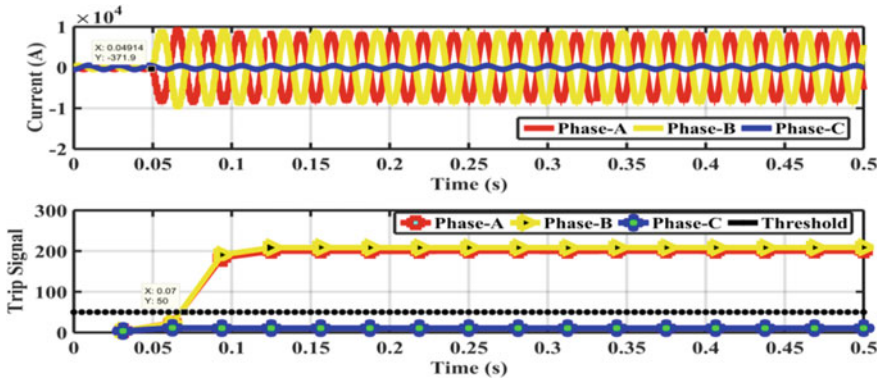


Fig. 5 Functioning through AB fault with FIT 0.05 s, SV 510 kV and SF 51.5 Hz

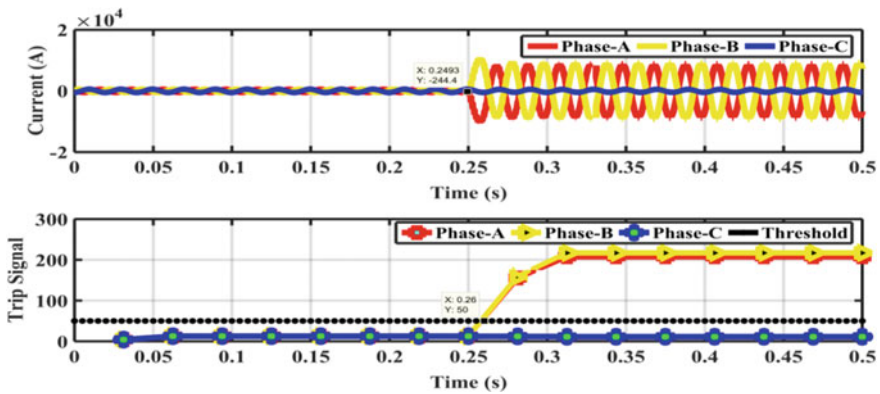


Fig. 6 Functioning through AB fault with FIT 0.25 s and SCL 75 GVA

4.5 Functioning Through Capacitive Load Operation

The procedure of protection system through AG fault with FIT 0.35 s and capacitive load 70 MVAR connected at 0.25 s is depicted in Fig. 7. The resulting trip command of Φ -A sent by the protection system is displayed in Fig. 7. In this case the initiation time of trip command of Φ -A is 0.365 s. The tripping time is $0.365 - 0.35 = 0.015$ s which is 15 ms.

5 Conclusion

A protection system for fault identification in power system has been presented in this paper. The system can identify various types of faults under any situation. Many

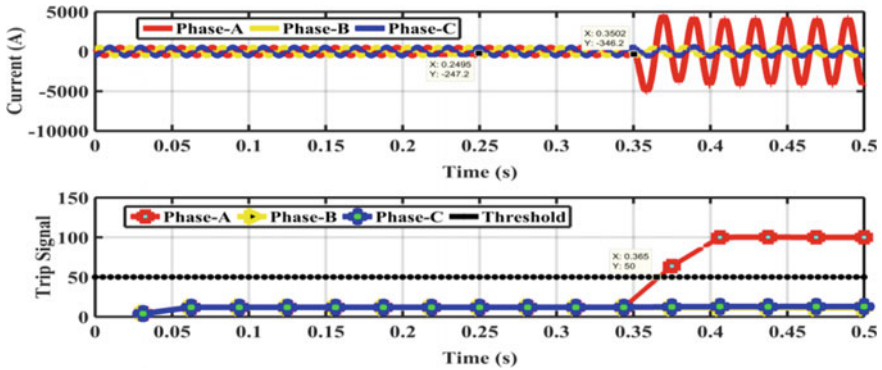


Fig. 7 Functioning through AG fault with FIT 0.35 s, capacitive load 70 MVar connected at 0.25 s

simulations were operated in unlike circumstances using MATLAB. The results indicated the supremacy of the presented system in every instance. The fault identification accuracy attained is 100%, considering high impedance fault, multiposition fault, unlike system voltage and frequency, unlike short circuit limit, and capacitive load operation. As future work, the case of differential protection system can be suggested.

References

1. Juttu TR, Bhalja BR, Andreev M, Malik OP (2021) Synchrophasor assisted power swing detection scheme for wind integrated transmission network. *IEEE Trans Power Deliv*
2. Swetapadma A, Chakrabarti S, Abdelaziz AY, Alhelou HH (2021) A novel relaying scheme using long short term memory for bipolar high voltage direct current transmission lines. *IEEE Access* 9:119894–119906
3. Arranz R, Paredes Á, Rodríguez A, Muñoz F (2021) Fault location in transmission system based on transient recovery voltage using Stockwell transform and artificial neural networks. *Electric Power Syst Res* 201
4. Hassani H, Razavi-Far R, Saif M, Zarei J, Blaabjerg F (2021) Intelligent decision support and fusion models for fault detection and location in power grids. *IEEE Trans Emerg Top Comput Intell*
5. Vlahinić S, Franković D, Juriša B, Zbunjak Z (2021) back up protection scheme for high impedance faults detection in transmission systems based on synchrophasor measurements. *IEEE Trans Smart Grid* 12(2):1736–1746
6. Moradzadeh A, Teimourzadeh H, Mohammadi-Ivatloo B, Pourhossein K (2022) Hybrid CNN-LSTM approaches for identification of type and locations of transmission line faults. *Int J Electr Power Energy Syst* 135
7. Rathore B, Mahela OP, Khan B, Padmanaban S (2021) Protection scheme using Wavelet-Alienation-Neural technique for UPFC compensated transmission line. *IEEE Access* 9:13737–13753
8. Teimourzadeh H, Moradzadeh A, Shoaran M, Mohammadi-Ivatloo B, Razzaghi R (2021) High impedance single-phase faults diagnosis in transmission lines via deep reinforcement learning of transfer functions. *IEEE Access* 9:15796–15809

9. Fahim SR, Sarker SK, Muyeen SM, Das SK, Kamwa I (2021) A deep learning based intelligent approach in detection and classification of transmission line faults. *Int J Electr Power Energy Syst* 133
10. Mohamed AAR, Sharaf HM, Ibrahim DK (2021) Enhancing distance protection of long transmission lines compensated with TCSC and connected with wind power. *IEEE Access* 9:46717–46730

Analysis and Simulation of Various Parameters of Mixed CNT Bundle for Interconnect Applications



Tirth Patel, Nishtha Diwanji, Michika Gayari, Himadri Patel, Kinjal Patel, and Rutu Parekh

Abstract This paper studies and investigates how carbon nano-tube (CNT) bundle serves as future interconnect technology. Interconnects are the main body connecting elements of the integrated circuits (IC). The material that the interconnect is made from is important for its performance. CNTs exhibit excellent properties in terms of electrical, mechanical as well as thermal strength. Its high thermal conductivity and large current carrying capacity makes it an ideal candidate to replace copper interconnects. CNTs can be categorized as single-walled CNT (SWCNT) and Multi-walled CNT (MWCNT). Mixed carbon nanotube bundle has both SWCNTs and MWCNTs. In this paper, different properties of mixed CNT bundle have been analyzed, and effects have been observed by varying the physical properties and dimensions of the bundle. Here, CNT interconnect analyzer (CNIA) tool is used to perform the analysis and simulation. Changes in bundle conductance, bundle inductance, bundle capacitance, bundle propagation delay, drift velocity will be studied by simulating its performance at different values. When bundle width was increased from 2000 to 10,000 nm, bundle conductance increased by almost 433%. Temperature variation was also performed which led us to the conclusion that on increasing temperature by 400 K, bundle conductance increased $8 \Omega^{-1}$, drift velocity increases by 17.64%, propagation delay decreased by 20%. When bundle length was increased from 20 to 100 μm , inductance and capacitance also increased by 500 and 450%.

Keywords Bundle conductance · Bundle inductance · Bundle capacitance · Bundle propagation · Delay drift velocity

T. Patel (✉) · N. Diwanji · M. Gayari · H. Patel · K. Patel · R. Parekh
VLSI and Embedded Systems Group, Dhirubhai Ambani Institute of Information and
Communication Technology, Gandhinagar, Gujarat 382421, India
e-mail: pateltirth2710@gmail.com

R. Parekh
e-mail: rutu_parekh@daiict.ac.in

© The Author(s), under exclusive license to Springer Nature Singapore Pte Ltd. 2022
V. Mahajan et al. (eds.), *Sustainable Technology and Advanced Computing*
in *Electrical Engineering*, Lecture Notes in Electrical Engineering 939,
https://doi.org/10.1007/978-981-19-4364-5_78

1099

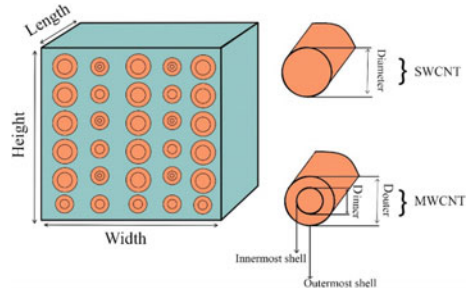
1 Introduction

For proper functioning and reliability of an IC, interconnect needs to have proper design and layout. Interconnects are classified as local, intermediate, or global interconnects depending on the signal propagation distance it is able to support. For decades, the material used for creating interconnects has been debatable in the manufacturing industry. Aluminum interconnects were the industry standard before getting replaced by copper which conducts electricity better than aluminum [1]. Currently, copper interconnects are utilized in ICs to decrease propagation delays and power consumption. Since copper is a finer conductor than aluminum, ICs using copper for their interconnects have narrow dimensions, lower resistivity, and utilize less energy to pass electricity within them. Together, these effects lead to ICs with better performance [2].

Almost two decades ago, there was a realization that even copper can't attain requirements of today's interconnects. An alternative material to replace Cu is being considered by researchers because of certain reasons. Cu interconnects have seen quick increase in resistivity due to improved scattering phenomenon and extensive interconnects. Also, rapid increase in copper resistivity was observed due to Joule heating. Lastly, standard scaling of silicon VLSI faces a crucial barrier of power dissipation per unit area associated with higher interconnects [3].

Many materials were used as interconnect such as copper, aluminum, and graphene. As copper faces challenges, there is a potential candidate for replacement to copper called CNTs. It is a fine conductor and has thousand times the tensile strength of steel; its thermal conductivity is as proficient as the purest diamond, and electrical conductivity is higher than copper, but with the capability to carry much higher currents, they appear to be ideal materials for ICs compared to Cu [4]. CNTs are cylindrical tubes made up of carbon atoms with diameter ideally measured in nanometers. CNTs may be metallic or semiconducting which relies on their chirality [5]. CNTs have exceptional reliability as compared with Cu due to Cu's electromigration concerns at high temperature [6]. Studies show two types of CNTs, single-walled CNT (SWCNT), and multi-walled CNT (MWCNT). SWCNT is the single folding of a thick-layer graphene sheet. MWCNT can be examined as a collection of concentric SWCNT with different diameters. MWCNT is multiple rolled layers or concentric tubes of graphene. Figure 1 shows a mixed CNT bundle which is a combination of both SWCNTs and MWCNTs [7, 8].

CNT was studied intensively, and attempt was made to achieve high density, directional growth, and well-aligned carbon nanotubes by Todri-Saniel et al. Also, CNT composite materials were investigated for the potential replacement of global copper interconnects. CNTs present energy efficient, high bandwidth, and high-performance circuit systems [9]. Major efforts were made in designing and fabrication of CNTs. But, some of the problems remained unsolved such as large interconnect resistance, high deposition temperature, and imperfect growth quality [5]. There is constant demand for the higher speed and constant density of future IC technology since there is increase in resistivity of aluminum and copper. Thus, CNT is possible interconnect

Fig. 1 Mixed CNT bundle

to be used [3]. CNTs are mechanically stable and flexible. Current carrying capacity is much higher than copper, and they are reliable due to much higher resistance to electromigration and have very low Joule heating effect [10]. When power dissipation and delay of SWCNT was compared with Cu interconnect at different technology for intermediate and global interconnects, it was found that SWCNT has better power handling and faster than Cu [11]. At intermediate and global level, copper and SWCNT have equal delay at low temperature, but copper interconnects perform faster at higher temperature [12]. MWCNT and SWCNT change its performance according to the change in temperature. By rising temperature, MWCNT performance was much better in all aspects than SWCNT. Thus, MWCNT is the suitable candidate for VLSI interconnects [13]. An investigation was done between mixed carbon nanotube and SWCNT and MWCNT. It was found that it outperforms in lesser propagation delay and low power dissipation. Thus, mixed carbon nanotube is good candidate for VLSI interconnects [4]. In intermediate interconnects, SWCNT can outperform Cu interconnects, and its performance can be increased by further increasing the bundle length and technology scaling. In the case of global interconnects, the improvement is weakened [14]. A comparative analysis of stability and timing was done between SWCNT and MWCNT bundle. It was analyzed that MWCNT has lesser propagation delay and was more stable. Thus, MWCNT is potentially strong for interconnects [15].

Through this paper, different properties like conductance, inductance, capacitance, propagation delay, drift velocity, thermal conductance of CNTs using CNIA tool have been studied and analyzed, how it can be the future of interconnect technology, and has been compared with the existing interconnect material, i.e., copper. CNIA tool takes into account the different parameters associated with CNT bundle by varying with the width, height, length of the bundle along with density, diameter, and temperature.

2 CNT Bundle Interconnect and Simulation Framework

CNT bundle is mixture of SWCNT and MWCNT. CNT bundle has its own dimensions such as height, width, and length. Different parameters and different simulation

lead to various results giving a brief idea about the working of bundle. SWCNT has a single shell of a fixed diameter, while MWCNT has multiple shells with D_{inner} to D_{outer} ($D_{\text{outer}} > D_{\text{inner}}$). Diameter-dependent parameters will also be studied and discussed further.

3 Carbon Nanotube Interconnect Analyzer (CNIA)

CNIA estimates the conductance and inductance of CNT bundles for interconnect applications. The analysis is based on bundle structure which is dependent on mixture of MWCNT and SWCNT [7, 8]. Different input parameters are bundle's geometry which includes width, height, and length; process parameters include density, average diameter, standard deviation of diameter, ratio of inner to outer diameter, prospect of metallic CNTs; CNT parameters include carbon-carbon spacing, shell spacing, tight binding energy, and ambient parameter includes temperature. Changing these input parameters leads us to varying output parameters like tube count, bundle conductance, MWCNT conductance, bundle inductance, bundle capacitance, bundle thermal conductance, MWCNT thermal conductance, bundle propagation delay, drift velocity, total number of electrical conduction channel of the bundle, number of electrical conduction channel of MWCNT, total number of thermal conduction channel of the bundle, and number of thermal conduction channel of MWCNT. Table 1 shows the input parameters used in the tool. Out of all the input parameters, those which were varied in values and plotted are (a) Bundle width (b) Bundle height (c) Bundle length (d) Temperature.

Table 1 Parameters used in the study

Input parameters	Values
Bundle width	2000–10,000 nm
Bundle height	2000–10,000 nm
Bundle length	20–100 μm
Temperature	100–500 K
Density	1e12
Average diameter	4.2 nm
Dinner/Douter	0.5
C–C spacing	1.42 Å
Tight binding energy	3 eV

3.1 Bundle Conductance

In a mixed CNT bundle, we have two categories of CNTs: SWCNTs and MWCNTs. Conductance of both these types is determined by the number of shells present in bundle and conducting channels per shell. An SWCNT involves a single shell, and the quantity of shells inside MWCNT is determined by the formula [7]:

$$N_{\text{shell}} = 1 + \frac{D_{\text{outer}} - D_{\text{inner}}}{2\delta} \tag{1}$$

where D_{outer} equals to maximum shell diameter and D_{inner} stands for the minimum shell diameters, and $\delta = 0.34 \text{ nm}$ is what we call Van der Waals distance. Approximate total of channels inside each shell is found out using the formula [16]:

$$N_{\text{channel/shell}} = \begin{cases} (ad_i + b) \cdot p_m, & d < 6 \text{ nm} \\ 2p_m, & d > 6 \text{ nm} \end{cases} \tag{2}$$

where $a = 0.1836 \text{ (nm)}^{-1}$, $b = 1.275$, p_m (probability of metallic tubes in bundle) is taken as $1/3$. d_i (diameter of each shell) $= D_{\text{inner}} + i \times (2\delta)$, in which i stands for the i th shell from 0 to $N_{\text{shell}} - 1$. It is known that conductance and resistance are reciprocals, and channel resistance for each shell is given as [9]:

$$R_{\text{shell}}(d_i, l) = \frac{R_o}{N_{\text{channel/shell}}}, \quad l > \lambda \tag{3}$$

where d_i stands for diameter of an individual shell, λ stands for mean free path (MFP), l equals to length of the tube, and R_o is the ohmic resistance. MFP can be related to diameter of the bundle using $\lambda = 0.9d_i \text{ }\mu\text{m/nm}$. Therefore, when length of the tube is more than MFP, ohmic resistance increases leading to decrease in conductance.

3.2 MWCNT Conductance

In an MWCNT, there are multiple number of shells. The number of shells is determined by D_{outer} , which can be found using Eq. (1). Each shell has its own d_i , λ , and $N_{\text{channel/shell}}$, which can be derived from D_{outer} using Eq. (2). Therefore, the combined conductance of an MWCNT can be calculated using the formula below [7]:

$$G_{\text{MWCNT}}(D_{\text{outer}}, l) = \sum_{N_{\text{shell}}} G_{\text{shell}}(d_i, l)$$

$$= \sum_{d_i=D_{\text{inner}}}^{D_{\text{outer}}} G_{\text{shell}}(d_i, l) \quad (4)$$

MWCNT and CNT bundles have similar behavior, and hence, MWCNT conductance also decreases with the increase in the length of the tube which is observed in the results in Fig. 3b. Increasing temperature also leads to increase in number of channels per shell which further contributes in increasing conductivity.

3.3 Bundle Inductance

The inductance of CNT has two components (L), kinetic inductance (L_k) and magnetic inductance (L_e). Kinetic inductance refers to electron's kinetic energy, present in the length of the nanotube. It mostly depends upon the how many SWCNTs are there in a bundle. The magnetic field inside the tubes, or in between the tubes, determines the magnetic inductance [17]. The total value of inductance is calculated by the sum of the kinetic and the magnetic components.

$$L = L_k + L_e \quad (5)$$

where L is the total inductance, L_k is the kinetic inductance, and L_e is the magnetic inductance. Magnetic inductance has small value; therefore, it is neglected. Kinetic inductance of SWCNT (L_k) can be expressed as:

$$L_k = \frac{h}{2e^2} \quad (6)$$

where v_f represents fermi velocity, which is approximately equal to 8×10^5 m/s. From this equation, the value of L_k is approximately equal to 16 nH/ μm . The SWCNT's kinetic energy and that of each shell of MWCNT are similar because MWCNT consists of more than one shells of SWCNT. Let's say there are x number of propagating channels associated with SWCNT. Hence, the effective kinetic conductance is L_k/x [3]. The bundle's kinetic inductance is as follows:

$$L_{kb} = L_k/xn_{\text{SWCNT}} \quad (7)$$

where L_k is the kinetic inductance of each SWCNT and n_{SWCNT} represents the number of SWCNTs that the bundle contains. As in [3], the effective kinetic inductance of a bundle of SWCNT and MWCNT, $L_{k\text{-ESC}}$ is as follows:

$$L_{k\text{-ESC}} = \frac{L_{k_0}}{2n_{\text{SWCNT}}} \quad (8)$$

where $L_{k_0} = h / (2e^2 v_f)$.

The main factors determining the inductance of the bundle are density of the tube, metallic tube ratio, D_{in}/D_{out} r , tube distribution, and geometry of the bundle. In this paper, values of bundle inductance have observed by varying the dimensions of the bundle as well as bundle temperature. The bundle inductance and the number of conduction channels are inversely proportional to each other. It is observed in Figs. 2b, 3c, 4b, and 5b that with the increase in bundle width, length and height, the bundle inductance also increases. The number of channels increases with increase in width and height. By increasing the bundle temperature, number of conducting channels increase, thereby decreasing the bundle inductance.

3.4 Bundle Capacitance

The capacitance of a SWCNT emerges from the electrostatic capacitance (C_E) which is calculated by Eq. (9) and the quantum capacitance (C_Q) [18]. The quantum capacitance is the variation of electrical charge with reference to the variation of the electrochemical potential. It records the quantum electrostatic energy preserved in the nanotube when it transmits current.

$$C_E = \frac{2\pi\epsilon}{\ln \frac{y}{d}} \tag{9}$$

Considering a CNT of diameter d is situated distance y away from the ground plane [18]. The quantum capacitance of a single CNT is given by Eq. (10):

$$C_Q = \frac{2 * 2e^2}{h v_f} \tag{10}$$

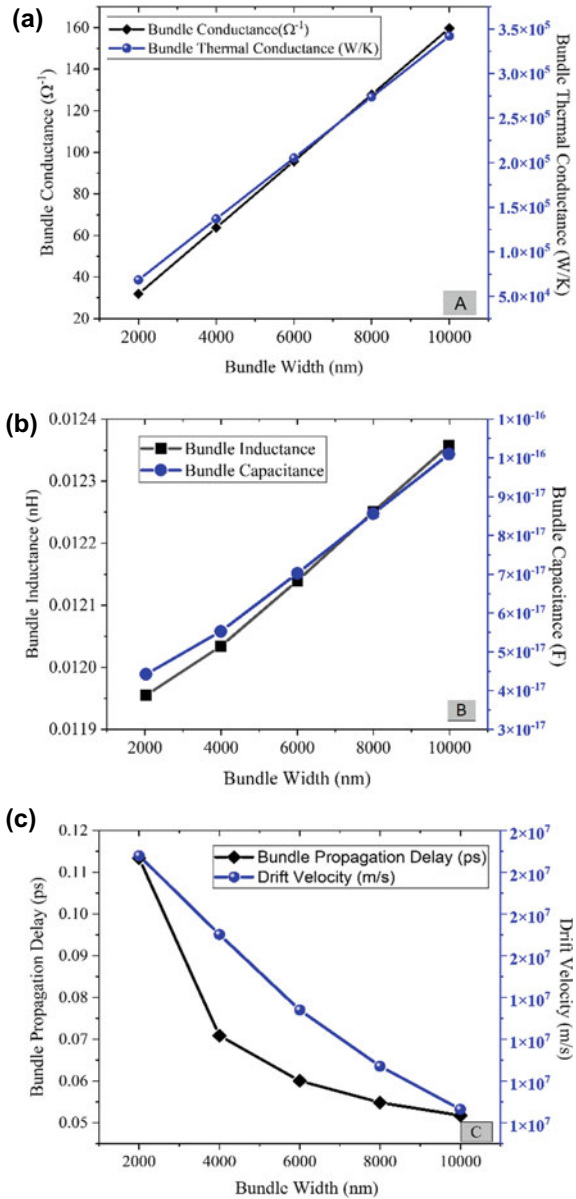
Here, h is Planck’s constant, $h = 6.63 \times 10^{-34}$ Js. When bundle CNT conducts current, it is assumed that each CNT carrying current is held at the same potential. Considering methods and steps of [19, 20], the electrostatic capacitance of a bundle CNT is given by Eq. (11) and quantum capacitance by Eq. (12). The total capacitance of the CNT bundle is given by Eq. (13).

$$C_E^{bundle} = 2C_E + \frac{n_w - 2}{2} C_E + \frac{3(n_H - 2)}{5} C_E \tag{11}$$

$$C_Q^{bundle} = C_Q * n_{CNT} \tag{12}$$

$$\frac{1}{C_{bundle}} = \frac{1}{C_E^{bundle}} + \frac{1}{C_Q^{bundle}} \tag{13}$$

Fig. 2 **a** Variation of bundle conductance and bundle thermal conductance with respect to bundle width, **b** variation of bundle inductance and bundle capacitance with respect to bundle width, **c** variation of bundle propagation delay and drift velocity with respect to bundle width



When the tool was simulated with different values of bundle length, it was observed that bundle capacitance was changing.

Fig. 3 **a** Variation of bundle conductance and bundle thermal conductance with respect to bundle length, **b** variation of MWCNT conductance and MWCNT thermal conductance with respect to bundle length, **c** Variation of bundle capacitance with respect to bundle length, **d** variation of bundle propagation delay with respect to bundle length, **e** variation of bundle inductance with respect to bundle length

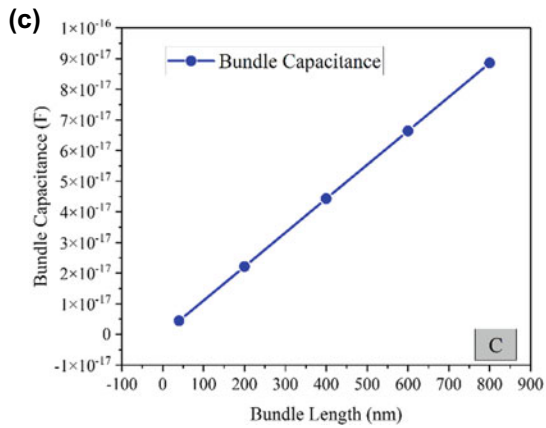
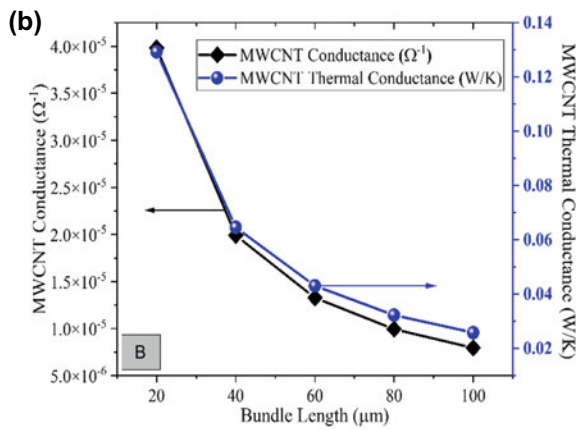
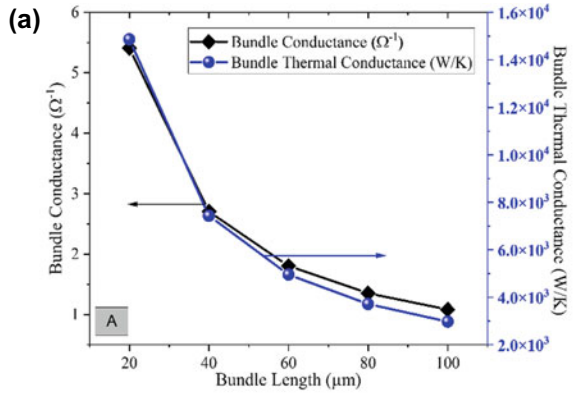
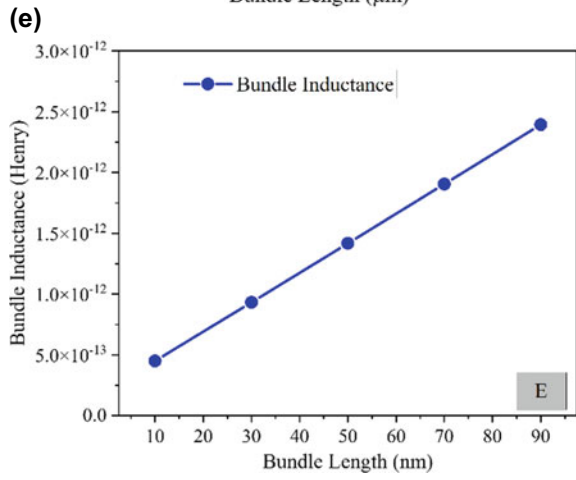
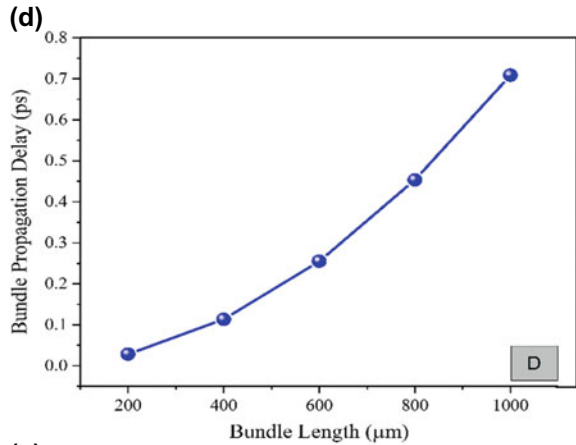


Fig. 3 (continued)



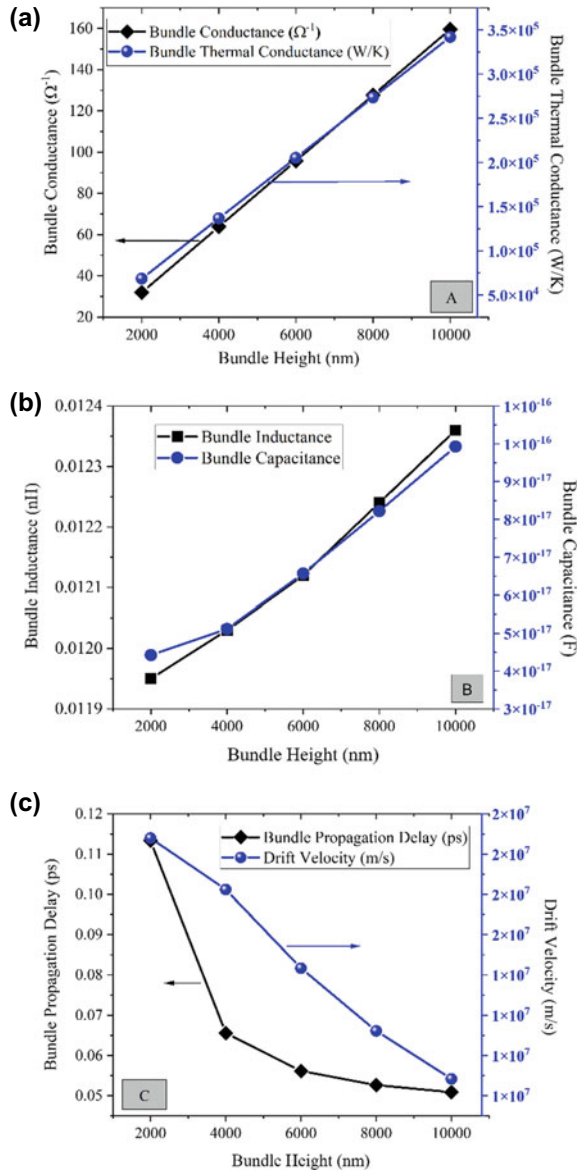
3.5 MWCNT Thermal Conductance

A MWCNT consists of many shells. The length L and the diameter of the shell d_i are the factors determining the thermal conductance of each shell. The bundle's thermal conductance is calculated by following formula:

$$K_{\text{bundle}} = \sum_{D_{\text{outer}}} N_{\text{tube}} K_{\text{tube}} \tag{14}$$

where K_{tube} and N_{tube} are functions of D_{outer} . K_{tube} represents the total value of thermal conductance of CNT, and N_{tube} follows a normal Gaussian distribution, where $\sigma_{D_{\text{outer}}}$ is the standard deviation.

Fig. 4 a Variation of bundle conductance and bundle thermal conductance with respect to bundle height, **b** variation of bundle inductance and bundle capacitance with respect to bundle height, **c** variation of bundle propagation delay and drift velocity with respect to bundle height



$$K_{\text{tube}} = \sum_{N_{\text{sh}}} K_{\text{sh}} \tag{15}$$

$$N_{\text{tube}} = \left(\frac{N_{\text{bundle}}}{\sqrt{2\pi}\sigma_{D_{\text{outer}}}} \right) \exp \left[-\frac{1}{2} \left(\frac{D_{\text{outer}} - \overline{D_{\text{outer}}}}{\sigma_{D_{\text{outer}}}} \right)^2 \right] \tag{16}$$

Fig. 5 **a** Variation of bundle conductance and MWCNT conductance with respect to bundle temperature, **b** variation of bundle inductance with respect to bundle temperature, **c** variation of bundle propagation delay and drift velocity with respect to bundle temperature, **d** variation of bundle capacitance with respect to bundle temperature

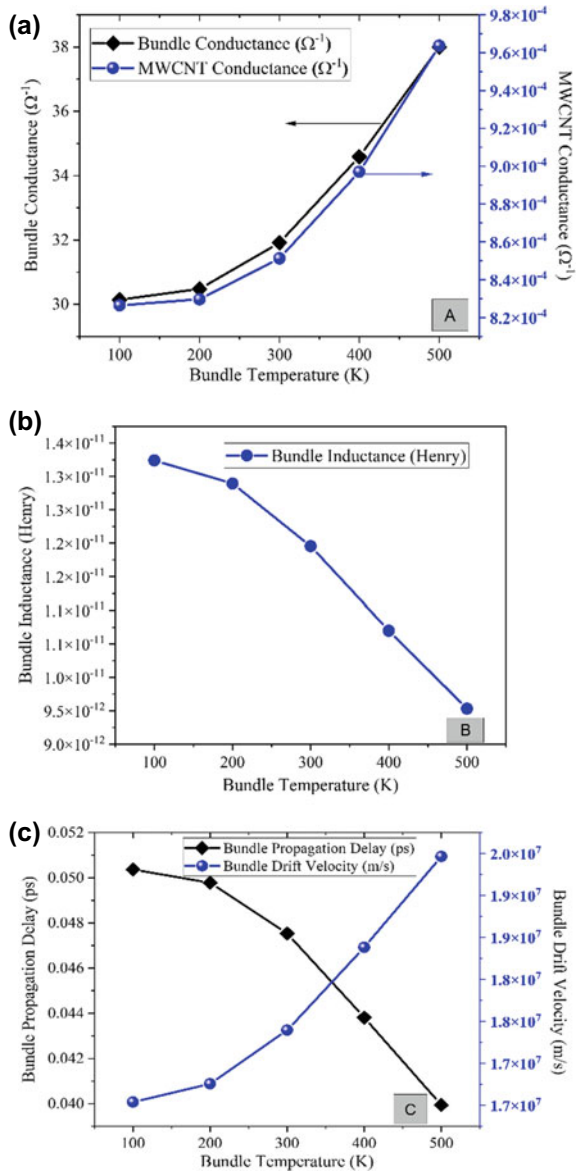
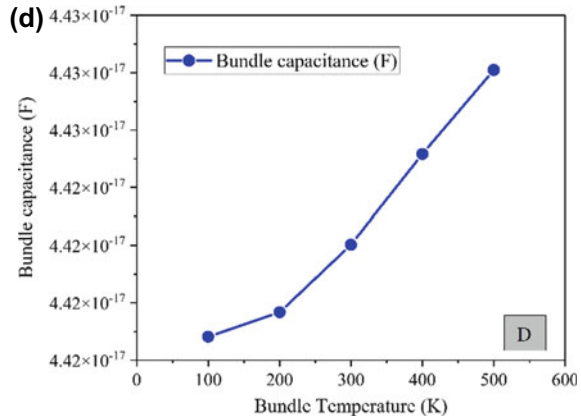


Fig. 5 (continued)



where N_{bundle} represents the amount of CNTs contained in the bundle. This is determined from cross-section area as well as density [21]. In this paper, thermal conductivity has been analyzed based on various factors such as length, height, temperature and width.

3.6 Bundle Thermal Conductance

Thermal conductivity of a material is its ability to conduct heat. It is the amount of thermal energy, flowing per unit time through a unit area, having 1° temperature gradient, per unit distance. The thermal conductivity of nanotubes is large; it is anticipated that thermal conductivity at room temperature is >200 W/mK which is approximately 6600 W/mK (the highest) [19, 20]. The thermal conductivity consists of two things, electronic conductivity and phononic conductivity. As the bundle size increases, electronic conductivity increases. Because electronic conductivity is directly proportional to thermal conductivity, the thermal conductivity will increase with more SWNTs in the bundle as shown in Fig. 2a.

3.7 Bundle Propagation Delay

Propagation delay is determined by the time taken by a signal to reach its destination. Thus, it is directly proportional to the bundle length, also observed in Fig. 3d. Some researchers proved that delay considerably decreases for MWCNTs as compared to mix CNT bundle and bundled SWCNT [22]. MWCNT has a minor impact on propagation delay as compared to SWCNT and mixed CNT bundle. Studies show that interconnects which are created from mixed bundles of CNTs show lesser values of resistance across intermediate and global lengths, and because of this reason, they

are able to substitute copper in terms of delay. Structures formed from metallic SWCNTs and greater diameter MWCNTs attain the highest conductivity with the shortest delay [8]. Bundle propagation delay is inversely proportional to bundle height and bundle width as delay depends on the amount of CNTs present in the bundle, so there is an increase in the conducting channels resulting in smooth movement of electrons in CNTs.

3.8 Drift Velocity

The drift velocity is the velocity with which a carrier, i.e., electron or hole, propagates while encountering collisions through the length of the device [23]. The high-speed CNTs, having very high mobilities, are in demand for most of the applications of nanoelectronics. The super mobility of CNTs is due to low scattering probability. A high electric field is encountered for high mobility, which may result in the electrons to move closer to saturation. The important factors that determine drift velocity are band structure, temperature, and degeneracy level. In this paper, the change in drift velocity by varying the bundle geometry as well as bundle temperature has been analyzed. Drift velocity is inversely proportional to area [24].

4 Results

Various simulations were made by varying different parameters like width, height, temperature, and length. By changing the values, different observations were taken and have been demonstrated using the graphs below.

4.1 Varying Bundle Width

Different results were analyzed and recorded of different parameters of the mixed CNT bundle by varying the width of the bundle as in Fig. 2.

In Fig. 2a, by increasing width, a greater number of CNTs can be accommodated leading to greater conductance. In Fig. 2b, by increasing the width, great increase in inductance and capacitance was found. Bundle capacitance almost increased by 122%. In Fig. 2c, drift velocity is inversely proportional to width. Thus, by increasing 8000 nm, the drift velocity approximately decreases by 56.52%. A study done to compare CNT bundle with copper interconnects was done in [25], where it was seen that conductance of CNT bundle increases with width, and similar result was observed in CNIA tool.

4.2 Varying Bundle Length

Different results were analyzed and recorded of different parameters of the mixed CNT bundle by varying the length of the bundle as in Fig. 3.

In Fig. 3a, by increasing the bundle length, conductance decreases by 77%, while thermal conductance decreases by 80% with increase in length from 20 to 100 μm . In Fig. 3b, by increasing the bundle length, MWCNT conductance decreased by 87.5%, while MWCNT thermal conductance decreased by 75%. In Fig. 3c, when length is increased from 20 to 100 μm , both bundle inductance and capacitance follow similar trends. Inductance increases by 500%, while capacitance increases by 450%. In Fig. 3d, by increasing the length, the distance to be traveled will increase. Thus, it will lead to increase in delay.

A comparison was made with previous results of bundle length and propagation delay. Results were found in the exact same trend. Increasing length increased the propagation delay which verifies our results [23]. The relation between the capacitance and length can be validated and verified from work done by Subhash et al. In Fig. 3c, it was observed that with increase in length of bundle, capacitance also increases. The value at length 200 nm and 400 nm obtained in simulation is 2.21×10^{-17} F and 4.428×10^{-17} F, respectively, which is verified using the previous work. In Fig. 3e, the same relation between inductance and length was also verified using the same work. The values obtained at 30 nm and 50 nm are 0.932×10^{-12} H and 1.418×10^{-12} H, respectively. The same values and results were obtained in previous work [19]. A study done to analyze different parameters of mixed CNT bundle for interconnect applications was done in [26], where it was seen that inductance, capacitance, and propagation delay of CNT bundle increases with length; similar result was shown by our CNIA tool, which can be observed in the following graphs.

4.3 Varying Bundle Height

Different results were analyzed and recorded of different parameters of the mixed CNT bundle by varying the height of the bundle as in Fig. 4.

In Fig. 4a, by increasing the height, a greater number of CNTs can be accommodated leading to increase in conductance. In Fig. 4c, by increasing the bundle height, a greater number of CNTs can be accommodated, thus, leading to better conductivity. Thus, bundle propagation delay decreases as it is inversely proportional with bundle height. Drift velocity decreases by 52.17% by increasing 8000 nm height which clearly indicates the inverse relation.

4.4 Varying Bundle Temperature

Different results were analyzed and recorded of different parameters of the mixed CNT bundle by varying the temperature of the bundle as in Fig. 5.

In Fig. 5a, by increasing temperature, the number of channels per shell increases. Thus, it leads to better conductivity. Conductance increased by $8 \Omega^{-1}$ by increasing 400 K temperature. In Fig. 5b, by increasing temperature from 100 to 500 K, the bundle inductance decreases by 30.76%. In Fig. 5c, by increasing temperature, electrons gain kinetic energy thus making the current flow faster. This change leads to decrease in propagation delay and an increase in drift velocity. By increasing 400 K temperature, delay decreased by 20%, and the drift velocity increased by 17.647%.

5 Conclusion

The whole paper basically analyzes mixed CNT bundle and its properties. The stimulation was done, and various parameters were examined such as conductance, inductance, capacitance, thermal conductance, propagation delay, and drift velocity of mixed CNT bundle. The results obtained on changing input parameters like width, height, length, and temperature, befitting results were obtained which can change the future of interconnect technology. When bundle width was increased from 2 to 10 μm , bundle conductance, bundle thermal conductance, bundle capacitance, and inductance showed an increase of almost 433%, 366%, 122%, and 3.34%, respectively. In case of changing bundle height, same behavior was observed as of varying bundle width. Upon increasing length from 20 to 100 μm , electrical and thermal conductivity of mixed bundle decreased by 77% and 80%, respectively. Also, MWCNT conductance and thermal conductance decreased by 87.5% and 75%, while inductance and capacitance increased by 500% and 450%, respectively. When temperature was increased by 100–500 K, bundle conductance increased by $8 \Omega^{-1}$; drift velocity increased by 17.64%; propagation delay decreased by 20%. Since the properties showed variation with respect to input parameters, a huge number of implementations are possible if CNT are used as an interconnect. Thus, CNT can be used as a potential candidate for future interconnects.

References

1. Turkane SM, Kureshi AK (2017) Emerging interconnects: a state-of-the-art review and emerging solutions. *Int J Electron* 104(7):1107–1119
2. Valencia D (2018) Modeling electronic transport in metal interconnects (doctoral dissertation, Purdue University)
3. Kaushik BK, Majumder MK (2015) Carbon nanotube-based VLSI interconnects: analysis and design. Springer India, New Delhi, pp 1–14

4. Kumar MG, Agrawal Y, Chandel R (2016) Carbon nanotube interconnects—a promising solution for VLSI circuits. *IETE J Educ* 57(2):46–64
5. Todri-Saniai A, Dijon J, Maffucci A (2017) Carbon nanotubes for interconnects. Springer, Berlin, Germany
6. Im S, Srivastava N, Banerjee K, Goodson KE (2005) Scaling analysis of multilevel interconnect temperatures for high-performance ICs. *IEEE Trans Electron Devices* 52(12):2710–2719
7. Haruehanroengra S, Wang W (2007) Analyzing conductance of mixed carbon-nanotube bundles for interconnect applications. *IEEE Electron Device Lett* 28(8):756–759
8. Shang L, Liu M, Tanachutiwat S, Wang W (2008) Diameter-dependent thermal conductance models of carbon nanotubes. *International Journal of Nanoparticles* 1(2):85–95
9. Todri-Saniai A, Ramos R, Okuno H, Dijon J, Dhavamani A, Widlicenus M, Teo K (2007) A survey of carbon nanotube interconnects for energy efficient integrated circuits. *IEEE Circuits Syst Mag* 17(2):47–62
10. Jiang D, Chalmers TH (2015) Carbon nanotube based interconnect material for electronic applications. Sweden
11. Gopalan AS (2015) Performance comparison of single-walled carbon nanotube bundle interconnects and copper interconnects with respect to propagation delay and power dissipation. Diss. Texas A&M University-Kingsville
12. Alizadeh A, Sarvari R (2015) Temperature-dependent comparison between delay of CNT and copper interconnects. *IEEE Trans Very Large Scale Integr (VLSI) Syst* 24(2):803–807
13. Singh K, Raj B (2015) Temperature-dependent modeling and performance evaluation of multi-walled CNT and single-walled CNT as global interconnects. *J Electron Mater* 44(12):4825–4835
14. Lu Q, Zhu Z, Yang Y, Ding R (2016) Analysis of propagation delay and repeater insertion in single-walled carbon nanotube bundle interconnects. *Microelectron J* 54:85–92
15. Kumar MG, Chandel R, Agrawal Y (2015) Timing and stability analysis of carbon nanotube interconnects. In: 2015 IEEE International symposium on nano electronic and information systems, pp 308–313
16. Alam T, Dhiman R, Chandel R (2011) Resistive analysis of mixed carbon nanotube bundle interconnect and its comparison with copper interconnect. In *Proceedings of the international conference & workshop on emerging trends in technology*, pp 1157–1160
17. Zhao S, Pan Z (2018) Inductive peaking technology for bandwidth enhancement in carbon nanotube bundle interconnect. *Phys Status Solidi (A)* 215(5):1700459
18. Alam T, Dhiman R, Chandel R, Solanki D (2011) Mixed carbon nanotube bundle: capacitance analysis and comparison with copper interconnect. In: 2011 International conference on emerging trends in electrical and computer technology. IEEE, pp 697–701
19. Subash S, Chowdhury MH (2009) Mixed carbon nanotube bundles for interconnect applications. *Int J Electron* 96(6):657–671
20. Banerjee K, Srivastava N (2006) Are carbon nanotubes the future of VLSI interconnections? In: *Proceedings of the 43rd annual design automation conference*, pp 809–814
21. Hone J, Llaguno MC, Biercuk MJ, Johnson AT, Batlogg B, Benes Z, Fischer JE (2002) Thermal properties of carbon nanotubes and nanotube-based materials. *Appl Phys A* 74(3):339–343
22. Berber S, Kwon YK, Tománek D (2002) Unusually high thermal conductivity of carbon nanotubes. *Phys Rev Lett* 84(20):4613
23. Das PK, Majumder MK, Kaushik BK, Dasgupta S (2012) Analysis of propagation delay in mixed carbon nanotube bundle as global VLSI interconnects. In 2012 Asia Pacific conference on postgraduate research in microelectronics and electronics, IEEE, pp 118–121
24. Dhillon G, Sandha KS (2021) Mixed CNT bundles as VLSI interconnects for nanoscale technology nodes. *J Comput Electron* 20(1):248–258
25. Dehghani S (2020) Numerical study of long channel carbon nanotube based transistors by considering variation in CNT diameter. *J Nano Res* 61:78–87
26. Chowdhury R Non-dependence of drift velocity of electron on length of carbon nanotubes, dependence on quantum state and expression of current density. *Int J New Technol Res* 2(7)

Reliability Evaluation in Physical Power Systems and Communication Network for Protection Failures



Trisha Parekh, Bansi R. Kanzariya, Kartavi Patel, Mithilesh G. Solanki, Neeraj Kumar Singh, Atul Kumar Yadav, Mahshooq Abdul Majeed, Lalit Tak, and Vasundhara Mahajan

Abstract At progressive stages of modern power system and development of modern society, there are various factors that influence the reliability of entire power system. Physical power system and Communication network are two imperative ingredients of modern power system which invite researchers to build the idea of feasible, resilient and reliable system. As plenty amount of research has been done on some aspects, this research paper gives a reliability prediction analysis using Monte Carlo Simulation method for physical power system. It offers a probabilistic approach which is typically faster and more accurate. Another approach via node analysis has been explained in the methodology part for the communication network. At the last, this paper also provides a case study on communication network through node analysis. It contains miscellaneous configurations to demonstrate the effect of failure rate and number of nodes on the system. An approach is exerted on the system for enumeration purpose. Further, the output from the introduced method has been accomplished successfully.

Keywords Power system reliability · Probability · Distribution systems · Weibull distribution · Communication network · Graph theory · Node

1 Introduction

For the past time, in power system quantitative analysis has been used which is based on probability theory and significant growth has been achieved in the modeling and calculation of the reliability of power systems [1–3]. As reliability evaluations are probabilistic, the reliability indices are evaluated on the basis of the failure rate and time interruption of the equipment. Moreover, reliability of protection systems has

T. Parekh · B. R. Kanzariya · K. Patel · M. G. Solanki
Electrical Engineering Department, Pandit Deendayal Energy University, Gandhinagar, India

N. K. Singh · A. K. Yadav · M. A. Majeed · L. Tak · V. Mahajan (✉)
Electrical Engineering Department, Sardar Vallabhbhai National Institute of Technology, Surat, India
e-mail: vasu.daygood@gmail.com

arisen as an essential topic, because safety failures have a crucial influence on power system reliability [4]. The idea of the “unreadiness probability” [5] was incorporated into a unique concept for examination of protection system dependability. In order to offer an adequate reliability analysis of protection system failures, other reliability indices, like “abnormal unavailability” and “protective system unavailability,” [6–8] were created. In addition to that researchers have continually attempted to determine the impacts of failure protection on power systems, include protection of failure in power system analysis and improve reliability of power systems assessment in light of protection failures [9–13]. Despite this effort, however, the reliability analysis technique incorporating defects has not yet been sufficiently extensive. The protection systems are still considered to be not that much reliable in typical composite reliability analysis, i.e., the failure of the current carrying component leads the removal of the component and that if the power can be shipped again to cover all loads, it is assumed that the system condition has no load. The removal of the transmission line, even if the protective mechanisms are working properly, might cause cascade failures due to post fault overload or difficulties in transient stability, but these factors cannot be taken into consideration for the normal study of reliability of the composite power system. Therefore, in the power system as illustrated in Fig. 1 only few strategies are available to decrease the likelihood of failure.

The probabilistic approach is more realistic in which a risk index allows for the comparison of different operations. When modes and probabilities of protection failures are added, complex interactions between the current carrying components occur to make complicated changes both in component and in system conditions [14]. More than the faulty one isolated, there is a limited likelihood. It is intuitively apparent that when numerous failures occur due to protection system failures, the chance of cascades due to post fault events is larger than if only one component

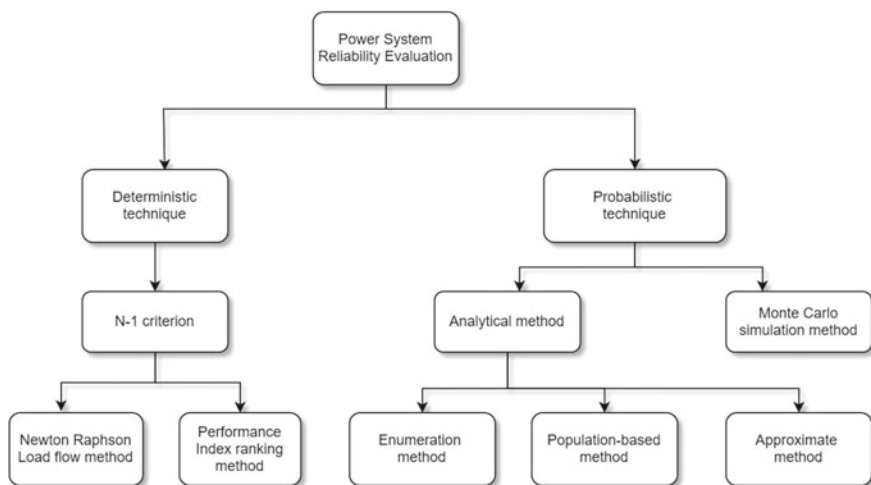


Fig. 1 Power system reliability evaluation methods

has been taken for granted on failure. For that a model-based reliability evaluation using linear programming technique has been introduced in recent steps [15]. The findings of fake power flows were analytically stated to explain the upstream and upstream connection with the nodes and then reliability indices. A quick application was investigated in order to take the reliability indices of a distribution network design problem using the reliability evaluation model. Later in [16], an algebraic method substituted the model-based linear programming approach and algebraic equations of upstream to downstream expressed the reliability indices recursively. Successful use of these approaches urges us to replace the model-based method in reliability evaluation with the simulation-based method for computer efficiency improvement and easy integration into operational and planned optimization models. The reliability study of composite production and transmission systems is more practicable using this three-stage multi-stage model [17]. However, we are aware that even for a single component the number of states is so huge that the application of this model straight away in the reliability of the power system is in fact restricted. In reliability analysis, which include system protection from failures, the notion of the “power unit zone” was therefore proposed [18].

As moving toward the evolution of modern, feasible and resilience smart grid, reliability techniques of modernization of smart grid infrastructure seek a lot of attention from the researchers and engineers. It consists of power system components and communication components. Wherever communication components take into consideration with power system it becomes unavoidable to include cyber security as paramount aspect. The combination of two such systems communication and physical power system is widely famous as cyber physical power system. These three networks are co-related. Thus, the study and research work on cyber physical power system are obligatory for healthy power system. The paper [19] introduces the structural analysis of CPPS. The strong understanding of cyber-attacks and vulnerabilities would be helpful to maintain continuity of the power system. Hence, [20] presents cyber physical threats. The cyber network is interconnected to communication and physical power system, failure in cyber network may impact remaining components of the system. As a result, it is essential to discover those parameters or causes which can affect continuous and stable operation of power system. Therefore, the perception of dependency of one appropriate component’s operation on other existing components in the system which is also known as cyber interdependency is explained in [21]. Further, the effect of additional interdependence on reliability is described in [22]. Bagen and Billinton [23] elaborates paths in which information and communication network failure cause a loss of control over a power system’s operation. Agalgaonkar and Hammerstrom [24] finds probability of ICT network security-based mis-operation with the help of Markov model. Cyber power reliability modeling is demonstrated in [25]. Cyber physical reliability analysis and implementation part are revealed in [26]. Li et al. [27] accesses complex network theory to analyze structure of power communication network. Furthermore, paper [28] expounds an analytical approach based on Complex Network Theory (CNT) for assessing the Smart Grid failure risk owing to failure of communication network, which is linked to latency and ICT network dependability.

In the power system, there are several types of networks, in which mesh constructed distribution network design has gain the popularity nowadays to gain improvement in reliability [29, 30], whether it functions radially or not. A network structure made of mesh has redundant lines that are arranged as backups in the case of a failure on the main line for the purpose of redirecting power and therefore functions better than radial network and more dependable. Accordingly, a reliability measurement technique is necessary not only for assessing current but also designing networks [31] for mesh constructed distribution networks. Distribution network reliability is clearly enhanced via the use of optimum re-configuration of the post fault network [32]. Literature [33] has provided a framework for resolving the problem of reconfiguration of distribution systems with the goal of improving reliability. Increasing the number of new lines in transmission system grids can also help to enhance dependability [34]. The appealing increase in the reliability and application of automation systems have made it more important to use the reliability evaluation model to take account of network reconfiguration.

The flow of this research paper is organized as follows: In the methodology part, two techniques have been explained for physical power system and communication network. Section 3 is the case study section where some system has been studied through node analysis. Results of case study have put in the Sect. 4. At the end, Sect. 5 concludes the conclusion of this research paper.

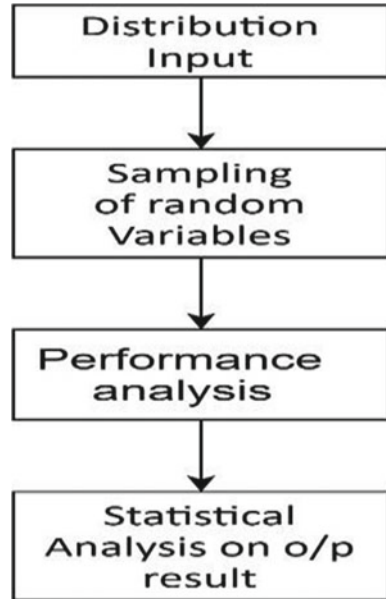
2 Reliability Prediction Using Monte Carlo Simulation

Monte Carlo Simulation has become an important part of analysis and modeling for system reliability. Adequate implementation of the instrument calls for a grasp of its basic concepts. Any component failure in the power system will have a number of consequences for security performance. A number of points have been presented [35] that may help to improve the system's dependability. In Monte Carlo analysis, the focus is on application in estimation of reliability assessment in the power system [36]. There are two basic approaches for Monte Carlo Simulation:

1. sequential simulation
2. random sampling.

The sequence simulation is performed using the random number and probability distributions of random parameters indicating component status durations to generate an event sequence. In random samples, states are chosen on the basis of probability distributions and random numbers of the component states. In addition, two techniques are available in order to represent the time in the simulation of a sequence: (1) a set interval approach, also known as synchronous timing, and (2) the next event or asynchronous timing method. Time is advanced in fixed-length increments and the system status is updated with the fixed—interval technique. In the following method of events, the time for the following event is progressed. Combinations of the timing controls can probably be utilized in practical implementations. The sampling

Fig. 2 Generalized steps of Monte Carlo Simulation



approach is typically faster than the sequence procedure, but suited for separate component failures and repairs (Fig. 2).

Monte Carlo Simulations employ failure and repair statistical distributions of the individual units to represent the behavior of the system over time when used to the reliability analysis. The findings of the simulation may be utilized to decide more precisely on the dependability of the system. A measurement parameter, “percentage of difference α ” is used to measure the accurateness of prediction method is used. It calculates the difference between the Monte Carlo point estimate and the exact reliability value. The accuracy between the exact value and the Monte Carlo point is estimated using Monte Carlo method [37].

$$\alpha = \frac{|\text{Estimated value} - \text{Exact value}| * 100}{\text{Exact value}} \tag{1}$$

The percentage of difference for broadcast reliability is found to be less than 0.210%. The predictions obtained through Monte Carlo method are nearly accurate comparing it with the results obtained through analytical methods, making this method ideal for estimating the reliability of ICT components in a power system. In a deterministic approach, the basic premise of Monte Carlo Simulation is that if we let the simulation to develop randomly, an impartial, representative set of sampling will take place from a vast ocean. It is a time-consuming process, thus a more organized method for assigning contingencies is needed with the deterministic approach.

2.1 Probabilistic Approach

Monte Carlo Predictability Simulations depend on how well the model mimics reality and the no. many values of system performance will be created depending on the anticipated distribution model utilizing random variables. Repeated system performance calculations are conducted using (simulated) randomly generated values based on probability distributions which represent each element in the model. The simulations are performed several times to table the resulting behavior information. The model includes the construction of a collection of predefined variables as input and then simulations and the analysis of combined results in all simulations on several occasions. This probabilistic risk assessment incorporates random aspects, in which we are likely to achieve different outcomes each time we make the model [38, 39].

In real-life data, conventional distributions often do not follow, strength and stress differ because various factors and mathematical solutions may not be viable. It might be Weibull, lognormal or else. Taking the example of a wind turbine, the weight on the blades will change substantially depending on the wind speed. The blades' strength also depends on the cabling of the resin, strengthening, etc. Thus, using Monte Carlo Simulation, reliability of the system can be predicted.

For example, a unit has got a mean strength of 65 kg per mm² and standard deviation of 5 kg per mm². The unit is exposed to a stress that follows Weibull distribution with a scale parameter of 20 kg per mm² and a shape parameter of 1.5. So, using Similar software in excel, probability of failure can be determined. Using Similar menu with input variables define name as 'strength' in normal distribution, mean and standard deviation value is to be chosen. Similarly, we choose Weibull distribution and use input variables define name as 'stress' putting alpha value as 1.5 and beta value as 20. We define margin as "strength–stress" and will select this scale as output parameter. Simulating it for 10000 iterations, based on the result the software helps to find out, in how many cases the value of margin has become negative. The negative value will mean stress is more than strength in those cases. Based on the number of cases where it has shown negative margin, Reliability or Probability of Failure can be estimated. As an output, Histogram of the difference that is of the margin is obtained running 10000 simulations is obtained.

3 Reliability of Communication Network via Graph Theory

This section contemplates the reliability of communication network as node and covers the effect of total number of nodes on the reliability of network. Here, number linked with each edge is edge weight W_e , and the number affiliated with each vertex is vertex weight W_v , which stands for the latency or delay that occurs at each communication channel and node, respectively. The illustration of n communication network as node can be shown in the Fig. 3. It consists of n nodes where the value of nodes can be given as 1, 2, ..., n . A sec, b sec, ..., n sec represents the latency or delay between

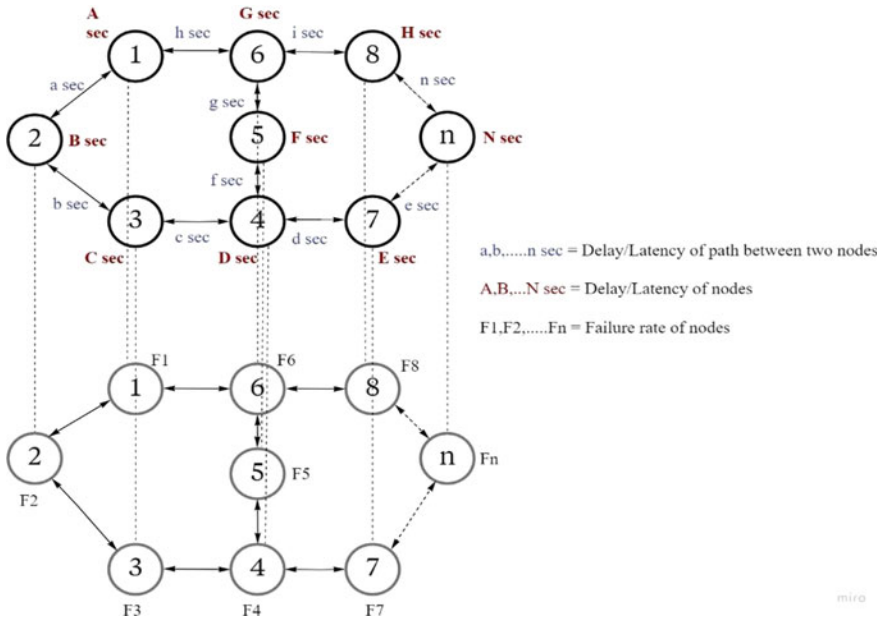


Fig. 3 Generalized configuration of the communication network

paths. While A sec, B sec, ..., N sec stand for the delay or latency of respective nodes. Whereas, F1, F2, ..., Fn are the failure rates of nodes. By discerning source node and target node, the total number of possible paths between sources to target node can be specified. For instance, if source node is 1 node and target node is n node then, the forward path can be given as 1-2-3-4-7.... -(n-1)-n and backward path n-(n-1)-....7-4- 3-2- 1. Comprehension of the forward and backward paths delineates the bidirectional nature of the communication network. As it is known that communication network is sensor connected network.

Thus, by finding total number of possible paths for the given system the system reliability index of the system can be found. According to the Fig. 4, necessary steps are adhered to compute system reliability index of the referred system. During this entire procedure, there are some assumptions which conjectured such as,

- The control center node has a processing time of 1 s.
- The data collection time and command execution time of RTUs both are 1 s.
- As remaining nodes manage signal instantaneously the routing strategies and their total latencies are given in Table 1.

Below formulas are used for theoretical evaluation of desirable parameters.

$$R = \prod_{n=1}^N P_n = \prod_{n=1}^N 1 - Q_k \tag{2}$$

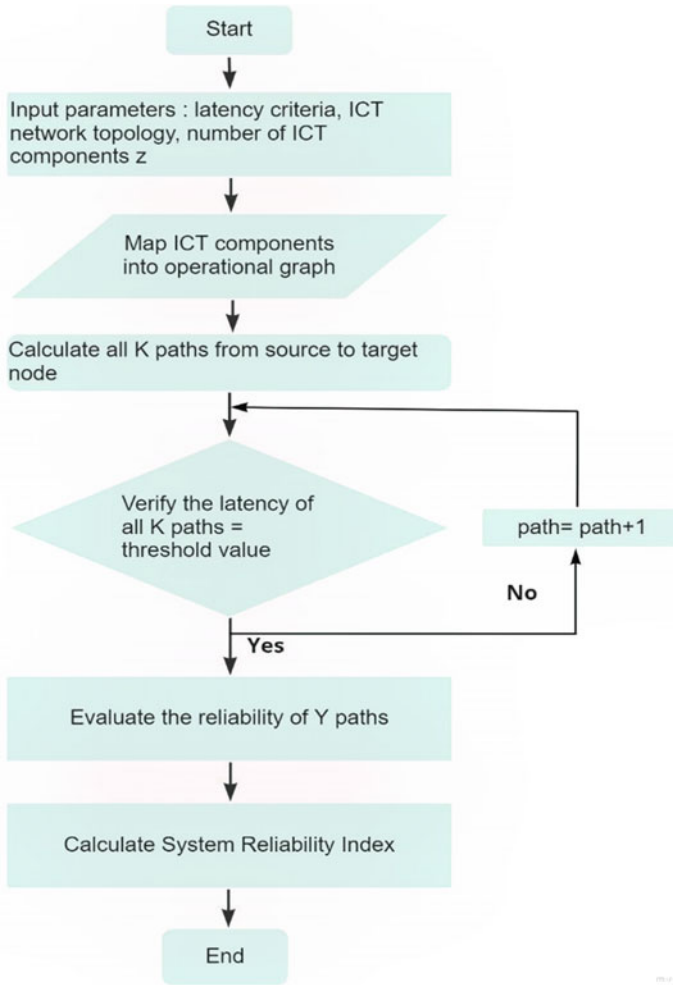


Fig. 4 Flow chart to enumerate system reliability index of the network

Table 1 The data of failure rates which considered for calculation

Different failure rate for specific node	Different failure rate for every node	Same failure rate for every node
$F1 = 0.17$	$F1 = 0.1, F2 = 0.75, F3 = 0.25$	$F1 = F2 = F3 = F4 = F5 = F6 = F7 = F8 = 0.125$
$F2 = F3 = F4 = F5 = F6 = 0.1$	$F4 = 0.175, F5 = 0.85$	
$F7 = 0.2, F8 = 0.75$	$F6 = 0.2, F7 = 0.45, F8 = 0.5$	

$$SRI = \frac{1}{N(N - 1)} \sum_{z=1}^Y \frac{1}{\ln(rh_j)} \tag{3}$$

where

N = number of ICT components in the system

Y = number of operational paths that meet the threshold condition $r(h_j) =$ path that satisfies the threshold condition, $h \neq j$

The procedure to acquire system reliability index of the system can be described as below:

- Step 1: The values of latency criteria, ICT network topology and number of ICT components will be input quantities to the system.
- Step 2: ICT components will map into operation graph to discover total attainable operational paths.
- Step 3: Calculate all possible K paths from source node (e.g., node 4) to target node (e.g., node 1).
- Step 4: Verify the latency of all K paths = $t\theta$. It will check the latency of path is equal to or greater than the latency criteria or not. If it is then, the reliability of this path will enumerate. If it is not then, it will check for another path. For every case, the threshold value of the power system control action is chosen as 1 second. In the case study section, the paths which have latencies equal or greater than 1 second are highlighted in Table 2.
- Step 5: According to the formula (2), it will calculate the reliability of Y paths which satisfies the latency criteria condition.
- Step 6: Utilizing Eq. (3), it will calculate system reliability index from Y paths.

Further, to calculate system reliability advancement worth and system reliability deteriorate worth parameters the value of failure rate for node in particular network is taken zero and one for instance, respectively. Same procedure will continue with other nodes of networks. With the help of following formulas this paper experiments to estimate range of parameters to explore more options.

$$C_{SRAW(i)}^{GR} = \frac{SRI(0_i) - SRI}{SRI} \tag{4}$$

$$C_{SRDW(i)}^{GR} = \frac{SRI(1_i) - SRI}{SRI} \tag{5}$$

Table 2 Operational paths of exemplar network

No.	Forward path	Backward path	Latency (s)
1	4-1	1-4	0.5
2	4-5-1	1-5-4	1.3
3	4-5-6-7-1	1-7-6-5-4	1.7
4	4-3-2-1	1-2-3-4	1.15
5	4-1	1-5-4	0.9
6	4-1	1-7-6-5-4	1.1
7	4-1	1-2-3-4	0.825
8	4-5-1	1-4	0.9
9	4-5-1	1-7-6-5-4	1.5
10	4-5-1	1-2-3-4	1.225
11	4-5-6-7-1	1-4	1.1
12	4-5-6-7-1	1-5-4	1.5
13	4-5-6-7-1	1-2-3-4	1.425
14	4-3-2-1	1-4	0.825
15	4-3-2-1	1-5-4	1.225
16	4-3-2-1	1-7-6-5-4	1.425

4 Case Study

This case study deliberates of four cases to compute and contrast system reliability index and other parameters such as system reliability advancement worth and system reliability deterioration worth. It yields the outcomes from three conditions such as different failure rate for particular nodes, distinct failure rate for every node and identical failure rate for every node for four different cases of networks. However, Researchers can explore more complexity for practicing in real world scenario. Figure 5 elucidates the operation graph and reliability graph for seven nodes. The node 1 is selected as control center node. While source node is chosen as node 4. The target node can be denoted as Remote Terminal Unit (RTU) node and source node as control center node. In this research paper, the values of delay or latency of source node and target node are taken into account to uncover total number of paths from source to target node. The latency or delay of remaining nodes is not counted for the latency enumeration of paths.

Table 1 contains the data set which is utilized for this case study. Valuable parameter such as failure rate for these four dissimilar node systems can be referred from this table.

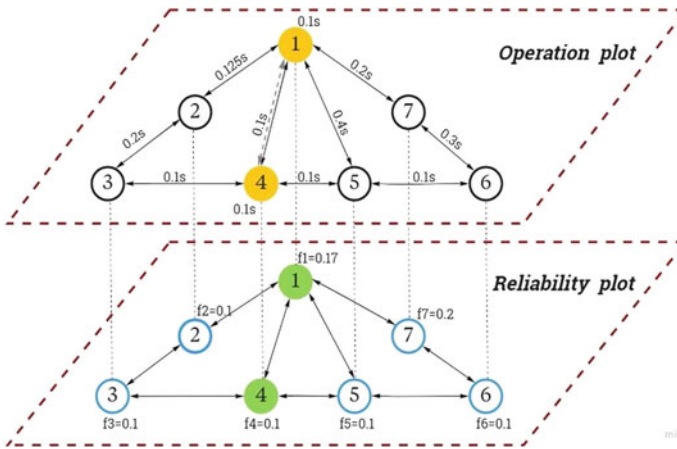


Fig. 5 Exemplification of operation plot and reliability plot via graph theory

5 Results

Using Monte Carlo Simulation to predict the reliability, keeping probability less than zero and performing 10000 iterations, a histogram of the margin is obtained (Fig. 6). The probability of failure comes out to be 0.4%. Thus, 0.996 reliability is predicted per load cycle. As number of iterations are increased more accurate value is predicted.

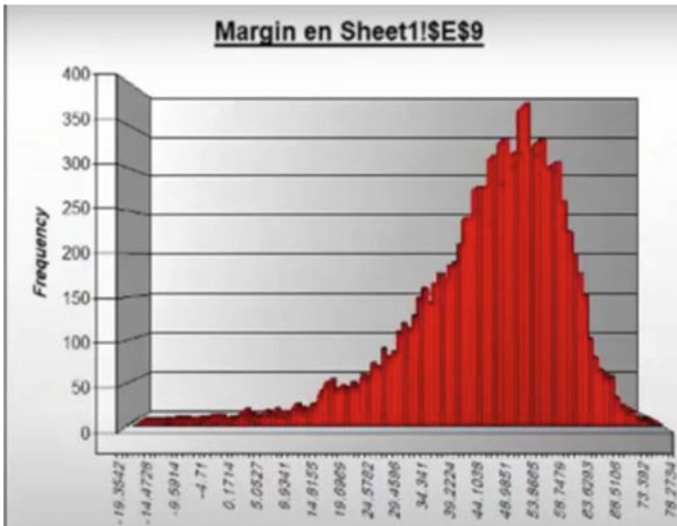


Fig. 6 Histogram of the margin obtained with the probability of less than 0

Table 3 Calculated system reliability index for each case

<i>Different failure rate for particular nodes</i>	
Cases	System reliability index
When no. of nodes = 8	0.543
When no. of nodes = 7	1.069
When no. of nodes = 6	1.66
When no. of nodes = 5	0.90179
<i>Different failure rate for every node</i>	
Cases	System Reliability Index
When no. of nodes = 8	0.247
When no. of nodes = 7	0.361
When no. of nodes = 6	0.527
When no. of nodes = 5	0.193
<i>Analogous failure rate for every node</i>	
Cases	System Reliability Index
When no. of nodes = 8	0.695
When no. of nodes = 7	1.0876
When no. of nodes = 6	1.62
When no. of nodes = 5	0.745

In the calculation of reliability of communication network via graph theory, Table 1 indicates the total number of possible operational paths from source to target node or vice-versa and their respective latencies for seven node networks. The highlighted paths are those paths, which pursue the latency criteria condition. By tracing mentioned steps, the system reliability index for every case can be attained. Equation (2) is beneficial to evaluate system reliability index.

As mentioned in the Table 3, system reliability index is calculated for four cases. When the value of failure rate is different for specific nodes, the SRI is evaluated accordingly. For 8 node system, 7 node system, 6 node system and 5 node system, it is obtained 0.543, 1.069, 1.66 and 0.90179, respectively. Whereas distinct failure is considered for every node then it comes 0.247 for node 8 system, 0.361 for node 7 system, 0.527 for 6 node system and 0.193 for 5 node system. If the failure rate is similar for every node in the system, then the value of SRI is received 0.695 for 8 node system, 1.0876 for 7 node system, 1.62 for 6 node and 0.745 for 5 node system.

Complying Eqs. (4) and (5) the advancement and deteriorate worth of the systems have been found. Tables 4, 5 and 6 exhibit the values of C_{SRAW}^{GR} for C_{SRDW}^{GR} and for all four diverse cases.

Here, C_{SRAW}^{GR} (1) and C_{SRDW}^{GR} (1) are the values of system reliability advancement worth and deterioration worth with respect to node 8. While C_{SRAW}^{GR} (2) and C_{SRDW}^{GR} (2) are for node 7. The values of C_{SRAW}^{GR} (3), C_{SRDW}^{GR} (3) and C_{SRAW}^{GR} (4), C_{SRDW}^{GR} (4) are co-related to node 6 and node 5. Table 4 indicates the values of C_{SRAW}^{GR} and C_{SRDW}^{GR} considering all three conditions for four varied node systems. From the Table 4, it

Table 4 System reliability advancement and deteriorate worth for different failure rate for selected nodes

Node no	1	2	3	4	5	6	7	8
$C_{SRAW}^{GR}(1)$	73.84%	10.50%	10.50%	28.91%	10.49%	4.97%	12.33%	38.12%
$C_{SRAW}^{GR}(2)$	81.01%	7.11%	7.11%	31.89%	16.37%	4.30%	11.04%	-
$C_{SRAW}^{GR}(3)$	84.22%	6.44%	6.44%	33.73%	19.28%	8.55%	-	-
$C_{SRAW}^{GR}(4)$	75.43%	11.71%	11.71%	31.85%	20.21%	-	-	-
$C_{SRDW}^{GR}(1)$	100.00%	39.23%	39.23%	100.00%	37.38%	28.18%	28.18%	11.60%
$C_{SRDW}^{GR}(2)$	100%	26.52%	26.52%	100%	51.10%	24.51%	24.51%	-
$C_{SRDW}^{GR}(3)$	100%	23.92%	23.92%	100%	62.29%	31.93%	-	-
$C_{SRDW}^{GR}(4)$	100%	44.11%	44.11%	100%	55.86%	-	-	-

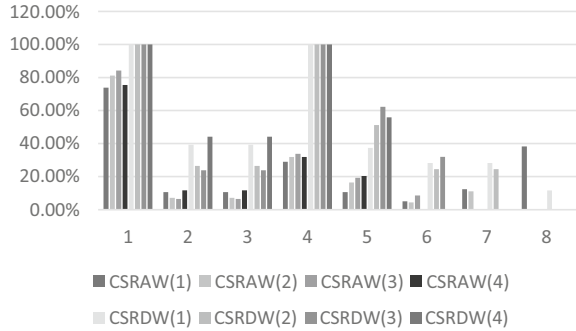
Table 5 System reliability advancement and deteriorate worth for different failure rate for every node

Node no	1	2	3	4	5	6	7	8
$C_{SRAW}^{GR}(1)$	28.74%	79.76%	31.58%	93.12%	53.04%	1.21%	3.64%	4.86%
$C_{SRAW}^{GR}(2)$	26.87%	47.37%	3.32%	85.87%	144.30%	1.38%	4.16%	-
$C_{SRAW}^{GR}(3)$	26.19%	45.54%	3.23%	83.11%	186.50%	2.09%	-	-
$C_{SRAW}^{GR}(4)$	5.18%	124.40%	8.81%	9.84%	300.52%	-	-	-
$C_{SRDW}^{GR}(1)$	100%	21.86%	21.86%	100%	29.55%	14.57%	14.57%	14.97%
$C_{SRDW}^{GR}(2)$	100%	20.22%	20.22%	100%	35.73%	17.73%	17.73%	-
$C_{SRDW}^{GR}(3)$	100%	19.35%	19.35%	100%	38.33%	21.06%	-	-
$C_{SRDW}^{GR}(4)$	100%	52.79%	52.79%	100%	47.67%	-	-	-

Table 6 System reliability advancement and deteriorate worth for same failure rate for every node

Node no	1	2	3	4	5	6	7	8
$C_{SRAW}^{GR}(1)$	43.89%	9.35%	9.35%	43.89%	25.18%	6.48%	6.48%	9.35%
$C_{SRAW}^{GR}(2)$	47.57%	8.22%	8.22%	47.57%	22.29%	6.66%	6.66%	-
$C_{SRAW}^{GR}(3)$	48.77%	7.43%	7.43%	48.77%	25.93%	9.88%	-	-
$C_{SRAW}^{GR}(4)$	67.79%	33.96%	33.96%	67.79%	50.74%	-	-	-
$C_{SRDW}^{GR}(1)$	100%	9.76%	9.76%	100%	52.52%	23.74%	23.74%	29.49%
$C_{SRDW}^{GR}(2)$	100%	24.60%	24.60%	100%	58.99%	26.26%	26.26%	-
$C_{SRDW}^{GR}(3)$	100%	22.84%	22.84%	100%	61.48%	30.68%	-	-
$C_{SRDW}^{GR}(4)$	100%	33.02%	33.02%	100%	49.79%	-	-	-

Fig. 7 Results of $C_{SR\Delta W}^{GR}$ and C_{SRDW}^{GR} for different failure rate for selected node



can be seen that for target node advancement worth is comparatively higher than other nodes. While in deterioration worth, the value of source node as well as target node is also higher than others. Whereas the values of node 2 and 3 are equal for every calculation. There is no other similarities or pattern received among remaining nodes of the networks. Figure 7 evinces the graphical relationship between nodes of sundries networks.

Table 5 presents values of every node for condition 2. It is noticed that the values for this condition do not follow any pattern as there is abnormalities among all values of nodes. Figure 8 discloses distinctiveness of networks. Table 6 reveals the values of advancement and deterioration worth for indistinguishable failure rate. As it can remark that the values of source node and target node are superior and alike than rest of nodes. It is expressed that the values of node 2 and 3, node 6 and 7 are analogous to each other. Figure 9 shows the visual presentation of data for analogous condition.

From Tables 4, 5, 6 and Figs. 7, 8 and 9 some observations are taken for analysis purpose which can be described as below:

- From Table 6, it can be observed that for similar failure rate of every node condition, as moving toward high number of nodes the value of $C_{SR\Delta W}^{GR}$ decreases. This statement is veritable for source node as well as target node. Therefore, it is desirable to not have more numbers of nodes in the real system so that the system reliability advancement worth can be lied under or around desirable value of the system. As a result, reliability of system can also be maintained.

Fig. 8 Results of $C_{SR\Delta W}^{GR}$ and C_{SRDW}^{GR} for different failure rate for every node

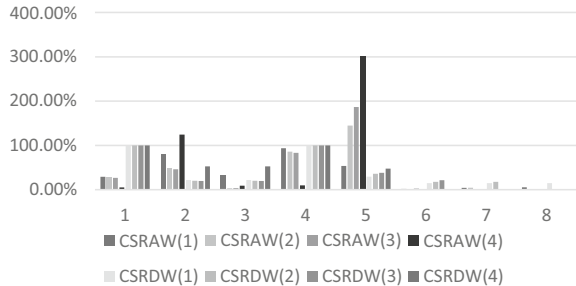
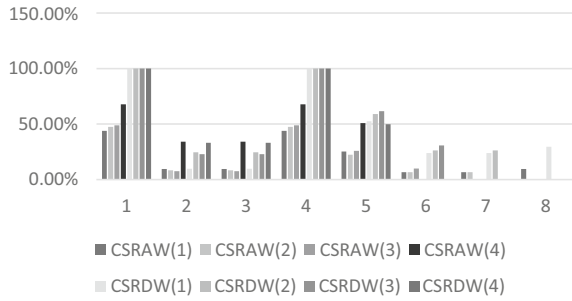


Fig. 9 Results of C_{SRAW}^{GR} and C_{SRDW}^{GR} for akin failure rate for every node



- From the Tables 4, 5 and 6, the values of C_{SRAW}^{GR} seven node system is compared to eight node system for all three conditions then it can state that the value of source node, target node and node 5 are decreased while for remaining nodes the value of C_{SRAW}^{GR} is increased as shown in the Table 3 for condition 1. The values of node 2 and 3 are identical as node 2, 3, 4, 5 and 6 have akin value of failure rate. Thus, it can add that the advancement or deterioration worth does not only depend upon failure rate, but also depends upon latencies of respective path which is chosen. While the values of all nodes are almost raised, if failure rate for every node is not analogous. Whereas in similar failure rate, the value of majority nodes is decreased.
- Referring Tables 4, 5 and 6, by comparing five node system to six node system then for condition 1 and 2 the value of source and target node is increased. While for condition 3, all nodes have lower values.
- Deterioration worth of source and target node in all three conditions is identical.

Therefore, from the above observations which compare a node system to its higher number of node system, it can be said that there is no specific pattern for these cases as some of advancement worth is enhanced and some are not. Researching on this area, it is found that the pattern of C_{SRAW}^{GR} and C_{SRDW}^{GR} of one certain node system does not depend upon on another node system. As every node system has distinct value of failure rate and it is independent from other node systems. If it has same value of failure rate then the first observation can be delivered to it. In that case also even if every node in system has similar value of failure rate, advancement and deterioration worth are not analogous. It describes that the results of advancement and deterioration worth depend upon failure rate and latency of respective path. Same discussion can be applied for deterioration worth also.

6 Conclusion

In this paper, to evaluate reliability of a system, two different approaches have been discussed. One is used for the study on reliability prediction using Monte Carlo Simulation method. This method can be used to describe various types of observed

failures of components and phenomena where there is range of values for various inputs. Various factors affect the reliability and through this method probability of failure can be predicted accurately increasing the number of iterations. While for communication network an approach which is clarified in the form of flow chart has been beneficial to calculate reliability index of the system. Moreover, the case study on communication network contributes salient role to discover the behavior of node systems. This case study can be utilized to evaluate the reliability and elaborate the effect of failure rate of each ICT components on the system with the help of given systems. It concludes that there is no specific change of pattern found in the system. Dissimilar patterns for all three cases have obtained. As cases which studied in the research paper are distinctive from each other for the values of failure rates. Thus, it mainly depends upon failure rate of every node in the system and number of nodes associated to the system. Therefore, with the help of these two approaches reliability in physical power systems and communication network can be estimated. As the Monte Carlo Simulation is advantageous in physical power system where more iterations need to be done such as wind turbines and elevators. Whereas the node analysis approach and the case study integrate the notion of more reliable communication system.

References

1. Billinton R, Allan RN (1996) Reliability evaluation of power systems, 2nd edn. Plenum, New York
2. Singh C, Billinton R (1977) System reliability modeling and evaluation. London, U.K., Hutchinson Educational
3. Endrenyi J (1979) Reliability modeling in electric power systems. Wiley, New York
4. Anderson PM (1999) Power system protection—part iv: “reliability of protection systems.” McGraw-Hill/IEEE Press, New York
5. Singh C, Patton AD (1980) Protection system reliability modeling: Unreadiness probability and mean duration of undetected faults. *IEEE Trans Reliab R-29(4)*:339–340
6. Anderson PM, Agarwal SK (1992) An improved model for protective-system reliability. *IEEE Trans Reliab* 41(3):422–426
7. Kumm JJ, Hou D, Schweitzer EO (1995) Predicting the optimum routine test interval for protective relays. *IEEE Trans Power Del* 10(2):659–665
8. Anderson PM, Chintaluri GM, Magbuhat SM, Ghajar RF (1997) An improved reliability model for redundant protective systems—Markov models. *IEEE Trans Power Syst* 12(2):573–578
9. Yang F, Meliopoulos APS, Cokkinides GJ, Dam QB (2006) Effectsof protection system hidden failures on bulk power system reliability. In: Proceedings 2006 IEEE 38th North American power symposium, pp 517–523
10. Yu X, Singh C (2002) Power system reliability analysis considering protection failures. In: Proceedings 2002 IEEE power engineering society summer meeting, vol 2, pp 963–968
11. Bozchalui MC, Sanaye-Pasand M, Fotuhi-Firuzabad M (2005) Composite system reliability evaluation incorporating protection system failures. In: Proceedings 2005 IEEE Canadian conference electrical and computer engineering, pp 486–489
12. Wang H, Thorp JS (2000) Enhancing reliability of power protection systems economically in the post-restructuring era. In Proceedings 2000 IEEE 32nd North American Power Symposium
13. Singh C, Patton AD (1980) Models and concepts for power system reliability evaluation including protection-system failures. *Int J Elect Power Energy Syst* 2(4):161–168

14. Pei Z, Meng K, Dong Z Probabilistic vs Deterministic Power System Stability and Reliability Assessment”, *Emerging Techniques in Power System Analysis*, pp 117–145
15. Muñoz-Delgado G, Contreras J, Arroyo JM (2018) Reliability assessment for distribution optimization models: a non-simulation based linear programming approach. *IEEE Trans Smart Grid* 9(4):3048–3059
16. Tabares A, Munoz-Delgado G, Franco JF, Arroyo JM, Contreras J (2019) An enhanced algebraic approach for the analytical reliability assessment of distribution systems. In: *IEEE transactions on power systems*. Early Access
17. Billinton R, Tatla J (1983) Composite generation and transmission system adequacy evaluation including protection system failure modes. *IEEE Trans Power App Syst PAS-102(6)*:1823–1830
18. Jiang K, Singh C (2009) The concept of power unit zone in power system reliability evaluation including protection system failures. In: *Proceedings 2009 IEEE power and energy soc. power systems conference and exposition*, pp 1–10
19. Gulati R, Dugan JB (1997) A modular approach for analyzing static and dynamic fault trees. *IEEE*
20. Falahati B, Kargarian A, Fu Y (2013) Impacts of information and communication failures on optimal power system operation. *IEEE*
21. Sanghvi A (1982) Strategic planning for power system reliability and vulnerability: an optimization model for resource planning under uncertainty. *IEEE*
22. Zhu W, Panteli M, Milanović JV (2018) Reliability and vulnerability assessment of interconnected ICT and power networks using complex network theory. *IEEE*
23. Bagen, Billinton R (2005) Impacts of energy storage on power system reliability performance. *IEEE*, pp 494–497
24. Agalgaonkar YP, Hammerstrom DJ (2017) Evaluation of smart grid technologies employed for system reliability improvement: Pacific northwest smart grid demonstration experience. *IEEE Power Energy Technol Syst J*
25. Aravinthan V, Balachandran T, Ben-Idris M, Fei W, Kapourchali MH, Hettiarachchige-Don A, Jiang JN, Lei H, Liu CC, Mitra J, Ni M, Papic M, Parvania M, Saphary M, Singh C, Srivastava A, Stefanov A, Sun H, Tindemann S Reliability modeling considerations for emerging cyber-physical power systems. *IEEE*
26. Davis KR, Davis CM, Zonouz SA, Bobba RB, Berthier R, Garcia L, Sauer PW A cyber-physical modeling and assessment framework for power grid infrastructures. *IEEE*
27. Li Q, Cao Z, Tanveer M, Pandey HM, Wang C An effective reliability evaluation method for power communication network based on community structure. *IEEE*
28. Zhu W, Han M, Milanović JV, Crossley P Methodology for reliability assessment of smart grid considering risk of failure of communication architecture. *IEEE*
29. Islam FR, Prakash K, Mamun KA, Lallu A, Pota HR (2017) Aromatic network: a novel structure for power distribution system. *IEEE Access* 5:25236–25257
30. Sampath Kumar D, Srinivasan D, Sharma A, Reindl T (2018) Adaptive directional overcurrent relaying scheme for meshed distribution networks. *IET Gener Trans Distribut* 12(13):3212–3220
31. Tian Y, Benidris M, Sulaeman S, Elsaiah S, Mitra J (2016) Optimal feeder reconfiguration and distributed generation placement for reliability improvement. In: *2016 international conference on probabilistic methods applied to power systems (PMAPS)*, Beijing, pp 1–7
32. López JC, Lavorato M, Rider MJ (2016) Optimal reconfiguration of electrical distribution systems considering reliability indices improvement. *Int J Electr Power Energy Syst* 78:837–845
33. Elsaiah S, Benidris M, Tian Y, Mitra J (2018) A comprehensive analysis of reliability-oriented optimal distribution system reconfiguration. In: *2018 IEEE industry applications society annual meeting (IAS)*, Portland, OR, pp 1–9
34. Yadav AK, Mahajan V (2019) Reliability improvement of power system network with optimal transmission switching. In: *2019 IEEE 1st international conference on energy, systems and information processing (ICESIP)*, pp 1–6

35. Yadav A, Mudgal S, Mahajan V (2020) Monte Carlo simulation application in composite power system reliability analysis
36. Singh C, Mitra J Monte Carlo simulation for reliability analysis of emergency and standby power systems. IEEE
37. Gunawan I (2013) Reliability prediction of distributed systems using Monte Carlo method. *Int J Reliab Safety* 7(3)
38. Yadav AK, Mahajan V (2019) Transmission Line Switching For Loss Reduction And Reliability Improvement. *Int Conf Inf Commun Technol (ICOIACT) 2019*:794–799
39. Yadav AK, Mudgal S, Mahajan V Transmission switching based available transfer capability assessment to make system network reliable, pp 27–32

Metallographic Image Analysis for Quality Assurance of Metals: A Review



Tushar Shirsat and Vinayak Bairagi

Abstract Metallographic analysis is crucial in the study of metallic materials because it provides information about properties (yield strength, tensile strength, elongation), which has a direct impact on material. An ultramicroscope is a valuable tool in particle characterization due to its direct measurement of particle size and morphology. An ultramicroscope, i.e., microscope with resolutions greater than 100x, has an illumination system that allows viewing of tiny particles. The basic aim of the research work is to develop ultramicroscopy-based metallographic image analysis for quality assurance of metals quantifying microstructural characteristics of metals such as aluminum, cast iron, and steel alloy. Literature survey observes that image processing is widely used in the metallographic microstructure analysis. Morphological and counter-based image processing techniques are applied, and grain size is calculated. There is major need to progress the efficiency of analysis to great extent.

Keywords Metallography · Grain size · Microscopic image

1 Introduction

The metal industry is divided into two categories: ferrous and non-ferrous metals. Iron ore is a central component of ferrous metals, and steel is the most common ferrous metal. Aluminum, zinc, and lead, as well as tin and nickel, are non-ferrous metals. Nowadays, measurement methods are focusing on the interaction of application handling and computer science, which has resulted in a broad range of applications. In metallography, image processing has evolved into a tool for procedures that involve full reproducibility and repeatability. Image analysis is particularly useful in the microstructure analysis of metals to get grain boundaries, grain size, and size distribution, among other things [1–3].

T. Shirsat (✉) · V. Bairagi
Department of E&Tc AISSMS IOIT, University of Pune, Pune, India
e-mail: rtushar.shirsat@gmail.com

Metallographic analysis is important in the study of metallic materials because it provides data associated with the properties such as yield strength, tensile strength, and elongation. These characteristics have effects on material properties [2].

Many users involved in the study of raw steel or finished steel products need quality assurance. The majority of users are from foreign public and private organizations such as International Organization for Standardization (ISO), American Society for Testing and Materials (ASTM); defense agencies, car manufacturers, and private individuals. It is essential to meet authorized standards by finding accuracy of analysis of all possible values of the specified parameters for getting quality assurance. USA defines quality assurance as “all those expected or systematic measures required to provide sufficient trust that an item or facility will perform satisfactorily in operation,” according to ASTM. Quality assurance is a continuous assessment of the quality management program’s suitability and utility.

To ensure a cleaner, defect-free finished product, manufacturers assess the cleanliness and integrity of metallic components and liquids. As a result, cleanliness analysis using a microscope is a significant workflow phase in modern manufacturing processes, especially for gearboxes, turbines, and engines, which are assembled using various components from different suppliers. The characteristics of the material with fitting tolerances determine the final product’s quality, durability, and life cycle. A defect in a single component may cause the entire end product to fail. Particle size and grain size are the most significant physical properties of particulate samples. Particle size calculation is a common practice in many industries, and also, it is frequently a crucial parameter in the production of many products [2].

Since it is the most direct measurement of particle size and morphology, the microscope is an effective tool in particle characterization [4]. For calculating particle size and shape, a manual microscopic technique is tedious and subjective. Automated microscopy measures the size and shape of a large enough number of particles, ensuring statistical confidence in the final result.

The microstructure influences many essential macroscopic properties of metallic materials. The microstructure has a direct relationship with critical mechanical properties such as tensile strength, elongation, thermal and electrical properties. The relationship knowledge among the microstructure and macroscopic properties is important in the production and manufacturing of the materials, and it can be done quickly with ultramicroscopic imaging analysis [2, 3]. An ultramicroscope, i.e., microscope with resolutions greater than 100x, has an illumination system that allows viewing of tiny particles, when a particle’s diameter is less than or equals to the wavelength of visible light (around 500 nm).

It is essential to analyze microstructural properties of metal for better control of product quality and understanding of product, ingredients, and processes. It can be used to improve product performance, optimize the efficiency of manufacturing processes, troubleshoot manufacturing and supply issues, which leads to increase in output or improve yield and make the manufacturer to stay ahead of the competition.

Microstructural analysis includes the different types of analysis [4–6] as discussed below:

- Inclusion size, porosity, and flake estimation analysis
- Grain size detection
- Particle analysis.

1.1 Inclusion, Porosity, Crack, and Flake estimation analysis

Compound materials found within steel during the production process are known as inclusions. Accurate results can be obtained by separating and rating inclusions and shape analysis. Updated modules can also correctly artifacts like scratches on the samples by artificial intelligence. They come from different chemical sources and give steel different mechanical properties. Steel properties such as formability, hardness, machinability, and corrosion resistance are all affected by inclusions. The higher the standard steel, the less or less serious the inclusions are. As a result, quality management requires analysis and recording of non-metallic and metallic inclusions.

The substrate, chemical, mechanical, and metallurgical properties of various kinds of steels are classified, evaluated, and defined using ASTM standards. These steel standards assist metallurgical laboratories, refineries, product manufacturers, and other end-users of steel for properly processing of the steel and its variants for ensuring the quality [7].

1.2 Grain Analysis

Grain analysis is important for quality control in metal and alloy samples. The internal borders of most metals, referred as “grain boundaries,” are crystalline in nature. The atoms within each growing grain of a metal or alloy are lined up in a particular pattern dependent on the crystal structure of the sample. It is well known that as the grain size of the sample decreases, the mechanical properties improve to achieve the desired grain size, alloy composition, and processing must be carefully managed. After metallographic sample preparation, the size and distribution of grains in a given alloy are analyzed to determine the sample’s integrity and quality. The grain size and distribution are studied to determine the component’s ability to withstand extreme conditions. Aerospace product manufacturers must examine grain size and delivery patterns, as well as adhere to stringent internal quality-control procedures. The ASTM grain size number n , which ranges from 1 to 10, is used to describe the grain size of metals. A larger number indicates smaller grains [7] as shown in Figs. 1, 2 and 3.

Total number of grains in 1 sq. area with 100x magnification will be calculated using Eq. 1.

$$N = 2n - 1 \tag{1}$$

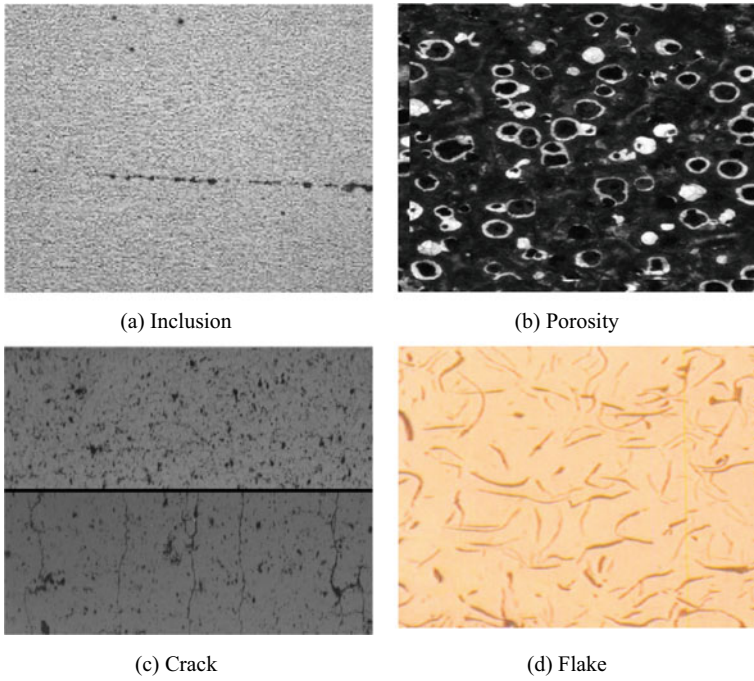
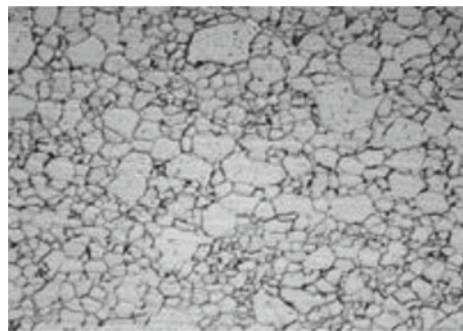


Fig. 1 Images of the **a** Inclusion **b** Porosity **c** Crack **d** Flake

Fig. 2 : Grain image with 100x magnification in steel



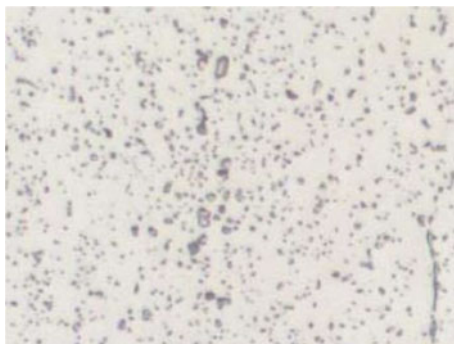
where N is total number of grains in 1 sq. area in at 100x magnification.

n is grain size number.

To expose the grain structure, a specimen must be correctly prepared and photographed with the 100x magnification.

For example, at 100x, a steel with $N = 6$ has 32 grains on average in a 1 sq. in. area.

Fig. 3 Image of aluminum at 100x magnification



1.3 Particle Analysis

Most significant physical property of particulate sample is particle size. Industries carry out the measurement of particle size distributions as one of the most critical parameters. Metal manufacturing business success depends upon the quality of the product that can be measured using particle size, count, shape distributions, and effect of these parameters on products. Particle area percentage, size, diameter, and aspect ratio of the black particles are need to be analyzed for all images to find quality of product [3, 5].

2 Literature Survey

Traditional grain size determination methods depend heavily on manual processes, making them time-consuming and error-prone. For automated quantitative metallographic analysis and determination of grain size, digital image processing and pattern recognition methods are essential tools [2, 3, 5, 8]. The automatic method increases processing speed, allowing users to analyze a large number of images in a short amount of time. To find the fractures in steel, Dutta et al. [9] have presented an automated characterization of images based on texture and fractal analysis. To find the grain boundaries, Coster et al. [10] have used automated image processing by using top-hat transformation for the analysis of the morphological parameters of the microstructure during the sintering of ceria. For detecting the grain boundary of steel alloys, Dengiz et al. [11] applied a neural network and fuzzy logic algorithms. Many researchers have looked at a material's grain size as a significant parameter for determining mechanical properties including strain, ductility, and stress resistance. Colás [12] used stainless steel and low alloy steel to investigate the relation between grain size and thermal treatments.

David M. Rubin et al. [13] have developed an autocorrelation algorithm for grain size detection. Through a bed of cross-sectional image, the autocorrelation value between the pixels is used to calculate average grain size of sediment on the bed,

grain size distribution of bed sediment, and grain size vertical profile. The developed method is 100 times faster but less sensitive than traditional method.

For a range of optical microscopy images of aluminum alloy Al 99.5 percent (ENAW1050A) samples with different grain size values, Lucijano Berus et al. [14] have suggested a novel method for automated edge detection and concatenation. This method gives higher automatization, lower processing times, and an automatic edge retrieval procedure.

Bairagi et al. [15] have discussed various methods (average method, maxima, wavelet transform) used for image fusions and fused three images together having standard size of 640×480 pixels. Image fusion improves the quality of image and helps to determine the edge structure.

Campbell et al. [16] have developed new methods for quantifying microstructural features automatically. Separate microstructural features (grains and alpha lath colonies) are isolated using digital image processing algorithms. The picture is segmented into regions that reflect grains and colonies. Due to this, morphological features (grain size, volume fraction of globular alpha grains, and alpha colony size) can be determined with a significant increase in speed and repeatability.

Peregrina-Barreto et al. [2] used image processing to automatically determine grain size in microstructures. Many automated techniques are documented in ASTM standards, but with the major disadvantage of digital image quality. The research focuses on a novel methodology that uses efficient image processing techniques to allow a clear description of the grain and boundary regions for the detection of accurate automatic grain size.

Qinghai Bai [17] presents a particle swarm optimization method and proposed an optimization algorithm, using swarm intelligence. The algorithm is beneficial because of its simplicity of implementation and needs only a few particles to be tuned. The PSO theory is also explained, with the benefits, and drawbacks of the said method. PSO and research situation have been improved, and potential research problems have been identified.

A literature review concludes that image processing is commonly used in metallographic microstructure analysis. The efficiency of research must be greatly improved. When images have low contrast and poorly defined borders, identifying grain boundaries is difficult. Many new image processing algorithms have been implemented, resulting in significant changes in grain size determination, as seen in Table 1, but there are still some flaws that need to be addressed. The most common issue is that the universality of current methods is very poor due to the differences in the characteristics of different alloys' metallographic images. There are number of techniques for measurement of particle shape and size such as laser diffraction particle sizing, dynamic light scattering, and automatic image analysis with microscope. Among this, automatic image analysis with microscope is most effective and reduced cost technique [4, 7]. As a result, metallography is used in product durability, materials development, incoming inspection, production and manufacturing control, and failure analysis. Rain boundaries low contrast and bad defined in the images boundaries are becoming more complex and required highly qualified expert to identify. Researchers are facing many challenges such as acquiring the microscopic images

Table 1 Summary of literature survey showing the aim, methodology, conclusion, and limitation of the given research

Authors	Aim of Paper	Methodology	Conclusion	Limitation
Dutta et al. [9]	Detection of the presence of fractures in steel	An automated image classification system focused on texture and fractal analysis	Long-run emphasis shows good correlation between eight descriptors	Systematic variation of image texture properties is observed with strain rate
Coster et al. [10]	The morphological parameters of the microstructure during ceria sintering were investigated	To obtain the grain boundaries, a top-hat transformation is used	Can control the migration of CeO ₂ grain boundaries and can limit grain growth	
Dengiz et al. [11]	Detection of steel alloy grain boundaries	A neural network and fuzzy logic algorithms		Boundary is not continuous and smooth often
Colas [12]	The relationship between grain size and thermal treatments is being investigated	Microstructure: electrolytic etchant Average grain size: mean line intercept technique	The fractal dimension of the microstructure increases when grain size reduces	
David M. Rubin [13]	Grain size detection	Autocorrelation algorithm for image of sediments	100 times faster for sampling surficial sediments	Less sensitive than traditional method
Lucijano Berus et al. [14]	Grain Size detection in Single-Phase Material	Image processing: Local Laplacian, Gaussian smoothing, gradient, and Zhang's thinning algorithm are used to link the edges	As compared to manual optical microscopy, it produces higher-resolution images, has a higher level of automation, and takes less time to process	Small sample size: 20 images

(continued)

with required magnification and high resolution. Metal has variable microstructure and hence grain boundary reconstruction, and it becomes extremely difficult with normal image analysis process. Further, processing of the image requires good filtering algorithms, edge rounding correction, intelligent algorithm for particle analysis. Currently, new image processing algorithms lacking in getting accurate results to get precise grain size determination (Table 2).

Table 1 (continued)

Authors	Aim of Paper	Methodology	Conclusion	Limitation
Campbell et al. [16]	Automatic quantification of microstructural features	Individual microstructural features, such as grains and alpha lath colonies, are isolated using digital image processing algorithms	drastic increase in speed and repeatability	
Peregrina-Barreto et al. [2]	Automatic grain size determination in microstructures	Image processing: a new technique that allows for a precise automatic grain size determination by clearly defining the grain and boundary regions	For an accurate automatic grain size determination, the grain and boundary regions must be clearly defined	
Qinghai bai [17]	Analysis of particle swarm optimization method	An idea of the principle of PSO is presented	Only a few particles were to be fine-tuned It is very easy to complete, and it only requires a few parameters, so it's fully developed	PSO is still at the initial stage of research

Table 2 Basic grain size calculation

Name of metal alloys	ASTM standards value	n (Grains size number)	AVG (average grain diameter)	Mean result values compared [1]
Al5052	8.45	9.07	0.01077 mm	7.02

3 Methodology

The basic aim of the research work is to develop ultramicroscopy-based metallographic image analysis for quality assurance of metals quantifying microstructural characteristics of metals such as aluminum, cast iron, steel alloy, titanium, copper, and brass. Ultramicroscopic images of metals will be taken with optical microscope at various magnification levels, i.e., at 100x, 200x, 400x, 1000x with optical magnification for further analysis. Figure 4 shows the block diagram of the proposed research work (Fig. 5).

Any ordinary picture can be processed using automatic grain boundary reconstruction analysis. It necessitates filtering with various algorithms, such as cleaning

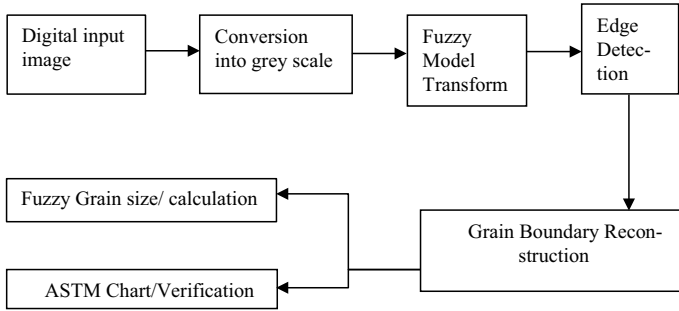


Fig. 4 Block diagram of the proposed research for finding grain size

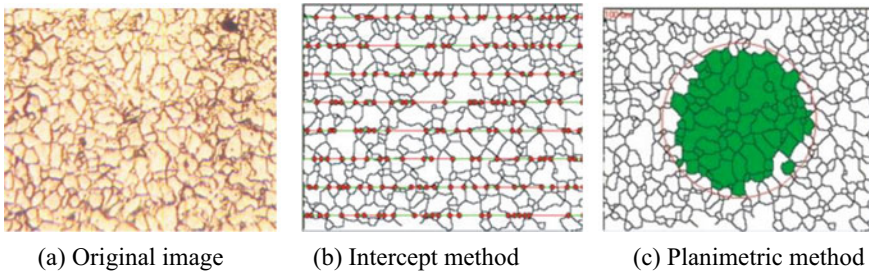


Fig. 5 Original image, intercept method, and planimetric method results

the image, automatically replacing the broken grain boundaries, and preparing the image for further automated analysis.

The digital image is given to the system as input which converted into gray scale; further, the fuzzy logic is used, and image gets converted into gray values of pixels. The degree of membership function is calculated using fuzzy logic and describes the fuzziness, and it is possible by using degree of membership function. It is a curve which defines the values in between 0–1, as over this range the pixel values vary. Again, fuzzy logic is used to detect whether pixels are on edge or not. The fuzzy logic follows fuzzifiers and de-fuzzifiers, and from this, the fuzzy values are stored into fuzzy database. Fuzzy logic is easy to detect only edges and corners. But still some noise is present in the image. With the help of canny operator, the output can sharpen and removes noise and consistent output is obtained. The type of the metal is detected automatically.

Grayscale conversion: Based on the gray level difference as many phases can be identified and measured to its fine perfection based on thresholding gray levels adjusted with fuzzy logic. Image enhancement functions for grayscale images can be easily added to any form of image to improve contrast and highlighting.

Fuzzy model: Improvement in analysis method can be possible based on multi-scale fuzzy logic-based; planimetry method; and comparison method. Also, results can be obtained in the form of grain size distribution, individual grain area, its

perimeter, L/D ratio, mean linear intercept length, average grain size, largest grain size in microns, etc., measurements in advance.

Edge detection: Individual particles in the field of view can be marked, separated as per their sizes. Distribution curve can be plotted based on shape and sizing. It will be useful for improving results of Particle Count and Phase analysis (ASTM standard).

Grain size estimation (as per ASTM standard): Histograms can be generated for exact distributed information collection and analysis can be done with the percentage of material composition original image, processed image, inclusion, porosity, crack, and flake estimation analysis (ASTM standard). Accurate results can be obtained by separating and rating inclusions and shape analysis. Updated modules can also correctly artifacts like porosity, inclusions, and scratches on the samples by artificial intelligence.

Measurement of non-spherical particle's size such as needle-shaped crystals or cracks where only particle size does not provide distinction identification and enumeration of agglomerates, oversized particles, or contaminant particles.

4 Results

Magnification calculation:

$$M = (\text{Print width})/(\text{Real width}) \quad (1)$$

(ASTM) ASTM grain size number:

$$N = 2((n - 1)) \quad (2)$$

where

N = No. of grains presented in the image.

n = Grain size no.

Average grain size diameter (AGD):

$$\text{AGD} = (\text{Total True length})/(\text{Grain intercepted}) \quad (3)$$

$$\text{Total True length} = (\text{Length of lines})/M \quad (4)$$

where

M = Magnification.

when number of grain increases the grain, size increases.

Accuracy:

$$\text{Accuracy} = (\text{Corrected output})/(\text{Total size}) \tag{5}$$

Sample calculations of grain size analysis are given below:

Consider the given size of Image M×N is 165 × 124.

Magnification = Print width/Real width. = 165 mm/0.215 mm = 768.

Number of grains in image = Whole grain + 0.5 (Partial grains).

Number of grains in image = 108 + 0.5 (32) = 140.

True Area = Width/Magnification × Height/Magnification.

$$= 165/768 \times 124/768.$$

$$= 0.0351\text{mm}^2.$$

ASTM gain size number.

Number of grains in 1 inch square = 2ⁿ (Grain number – 1).

As 1 inch square = 0.0645 mm² for 100 × as per ASTM.

Grain size number = Number of grains in 1 inch square X (0.0645 mm²/True Area).

Grain size number = 140 X (0.0645/0.0351) = 257.26.

log (257.26) = (n-1) *log (2).

n = 9.07ASTM grain size number:

Grain diameter average = True length Total / grains got intercepted.

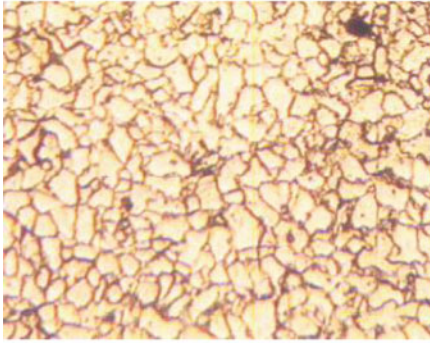
True length total = Lines Length /magnification = 2 (124)/768 = 0.323 mm.

Average grain diameter = 0.323/ (16 + 14) = 0.01077 mm.

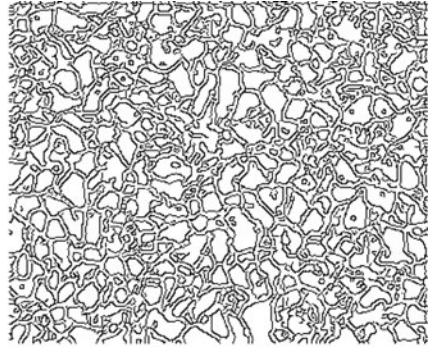
Original input image is enhanced and boundary reconstructed using fuzzy classification models as Fig. 6. Grain count measured using planimetric or intercept methods [ASTM standard] and grain size estimated based on number of grains in region.

5 Conclusion

The application of proposed research is in metal industry because the packing density of metal depends on the size and shape of the grains. Literature is reviewed, and researchers are facing many challenges such as acquiring the microscopic images with required magnification, and high resolution and concludes that there is a need of good filtering algorithms, edge rounding correction, intelligent algorithm for particle analysis. In the said research, methodology is proposed with new image processing techniques. The digital image is converted into grayscale image as input to the second part of system. After preprocessing of the image, grain boundaries and grain size are extracted using fuzzy logic. Noise presence is observed in the image due to the presence of defect in the image while performing metallographic classes. Edge rounding correction gets completely defocused image at higher resolutions with edge boundary correction. Generation of perfect image for edge analysis is complex at higher magnification, i.e., at 100x. The physical properties of the constituent particles also dictate the behavior of particulate materials. From a manufacturing



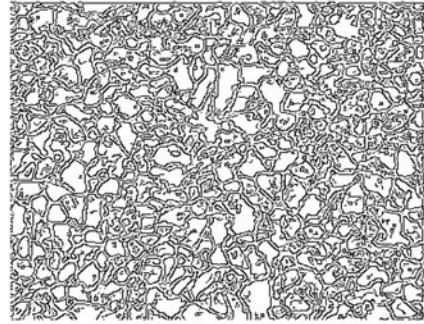
(a) Original Image



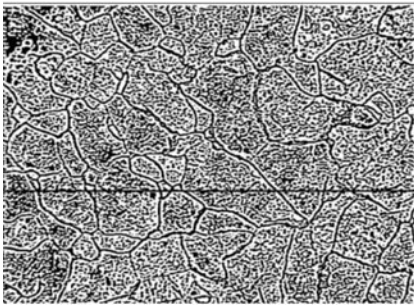
(b)Cannybased



(c) TanTriggs based



(d) Hough based



(e) Morphological based



(f) Contour based

Fig. 6 Original and processed image **a** Original **b** Canny-based **c** Tan–Triggs-based **d** Hough-based **e** Morphological-based **f** Contour-based

and development perspective, this can have an effect on a broad variety of material properties.

References

1. Zhang L, Xu Z, Wei S, Ren X, Wang M (2016) Grain size automatic determination for 7050 Al alloy based on a fuzzy logic method. *Rare Metal Mater Eng* 45(3):0548–0554
2. Peregrina-Barreto H, Terol-Villalobos IR, Rangel-Magdaleno JJ, Herrera-Navarro AM, Morales-Hernández LA, Manríquez-Guerrero F (2013) Automatic grain size determination in microstructures using image processing. *SciVerse Sci Direct Measure* 46:249–258
3. Zhang W, Zhou C, Bao X (2015) Investigation on digital media image processing algorithm based on asynchronous and inertia adaptive particle swarm optimization. *Int J Signal Process* 8(2):65–76
4. <http://www.olympus-ims.com/>
5. Wang L, Zhang L, Yan Y, Huang X (2014) Imaging based size measurement of fine particles from industrial stack. *IEEE-ICSP Proceeding*
6. Allegro S, Chanel C, Jacot J (1996) Particle size analysis under a microscope
7. <https://www.astm.org/Standards>
8. Anovitz LM, Cole DR (2015) Characterization and analysis of porosity and pore structures. *Rev Mineral Geochem, Mineral Soc Am* 80:61–164
9. Dutta S, Das A, Barat K, Roy H (2012) Automatic characterization of fracture surfaces of AISI 304LN stainless steel using image texture analysis. *Measurement* 45(5):1140–1150
10. Coster M, Arnould A, Chermant JL, Chermant L, Chartier T (2004) The use of image analysis for sintering investigations the example of CeO₂ doped with TiO₂. *J Eur Ceram Soc* 25(15):3427–3435
11. Dengiz O, Smith AE, Nettleship I (2005) Grain boundary detection in microstructure images using computational intelligence. *Comput Ind* 56(8–9):854–866
12. Colás R (2001) On the variation of grain size and fractal dimension in an austenitic stainless steel. *Mater Charact* 46(5):353–358
13. Rubin DM (2004) A simple autocorrelation algorithm for determining grain size from digital images of sediment. *J Sediment Res* 74(1):160–165
14. Berus L et al (2020) Determination of the grain size in single-phase materials by edge detection and concatenation. *Metals* 10(10):1381
15. Bairagi VK, Ekbote Shrutika A, Bhosale Akshada R (2017) *Metallographic Image Fusion* 5(6):347–351
16. Campbell A et al (2018) New methods for automatic quantification of microstructural features using digital image processing. *Mater Design* 141:395–406
17. Bai Q (2010) Analysis of particle swarm optimization algorithm. *Comput Inf Sci* 3(1)

‘Smart Construction Safety Helmet’: a Construction Safety Tool Embedded with Health Monitoring and Salary Deduction Function



Vikas Suresh and Raju Narwade

Abstract Accidents on-site are most commonly the result of carelessness or a lack of adequate safety procedures and facilities, inflicting serious injury to workers and, in some circumstances, culminating in death due to a lack of real-time monitoring of accidents on-site. Although personal protective equipment (PPE) plays an important role in reducing such occurrences, traditional PPEs cannot give warning signs in risky situations, necessitating the integration of smart technologies with current PPE. Thus, the proposed paper is concerned with the integration of a standard safety helmet with various sensors such as an infrared sensor, a DS18B20 temperature sensor, a sound sensor, an MQ-3 gas sensor and an MQ-135 smoke sensor, all of which are used to detect distinct parameters of working labourers such as drowsiness, body temperature, sound, gas leakage and smoke concentration. The Arduino nano, which is connected to a Bluetooth module, syncs the data acquired from each sensor and wirelessly sends it to the manager’s or supervisor’s mobile screens through Bluetooth. The smart helmet has also been programmed to generate and maintain the wearer’s pay records. Based on the severity of the hazard, the manager or supervisor can then take necessary action. The results of the studies and testing on this smart construction safety helmet have shown that it is quite useful in protecting personnel from the different hazards stated in the previous claim. Additional research on this helmet might be very useful in enhancing its efficiency.

Keywords Safety · Construction helmet · Bluetooth · Arduino · Management · Sensor

V. Suresh (✉)

Department of Civil Engineering, Pillai HOC College of Engineering and Technology, Affiliated to University of Mumbai, Rasayani, Khalapur, Raigad, Maharashtra, India
e-mail: vikassuresh@mes.ac.in

R. Narwade

Department of Civil Engineering, Pillai HOC College of Engineering and Technology, Affiliated to University of Mumbai, Rasayani, Khalapur, Raigad, Maharashtra, India
e-mail: marwade@mes.ac.in

1 Introduction

The smart construction helmet is a piece of personal protective equipment (PPE) that has been intended to reduce on-site accident rates [1, 2] by shielding users (workers) from physical impacts (such as brain injuries) and limiting employees' direct exposure to any given hazard [3, 4]. The incorporation of standard PPE kit parts such as safe jackets, gloves, shoes and goggles [5] can improve the efficiency of smart construction helmets [6]. Accidents are prevalent in industries such as warehouses, ports and construction sites; hence, the efficiency of smart construction helmets is a crucial mechanism for maintaining the wearer's (workers') safety and health [7], especially on building sites. Most construction firms have mandated the wearing of helmets by employees whenever they enter the working premises.

From 2011 to 2016, the Department of Occupational Safety and Health data revealed an average of 37.85–51.50 percent of 1116 incidents resulting in permanent/non-permanent impairment or causing death [8]. Concerning a report, accidents at construction sites of Malaysia resulted in many deaths. Despite the Malaysian government's efforts to eliminate these accidents, there was a static increase in the rate of accidents from 21.72% to 30.30% from 2013 to 2016, with 40% of these accidents occurring as a result of failing to wear PPE properly and failing to follow safety protocols. According to India: British Safety Council, around 48,000 individuals die in industrial accidents in India each year. Even the Indian government has adopted numerous steps, yet it seems to be somewhat ineffective.

According to many writers and experts, a lack of safety training and health concerns has resulted in a lack of safety awareness, which has resulted in a rise in workplace accidents resulting in significant injuries and, in some cases, death [9]. Because of the indisputable effects of management difficulties, employment circumstances and the industry's unique nature, there is a constant stock of workplace accidents [10]. Because most experienced employees are already used to their work, they think that safety helmets are unnecessary. Meanwhile, rookie employees favour this helmet because they feel helmets are important since they protect them from accidents. This can be addressed by mandating employees to wear safety helmets or by increasing worker understanding. The limitations of current safety helmets might be the source of recurrent industrial accidents. Existing safety helmets have the passive advantage of merely reducing the severity of accidents. However, it would be ideal if helmets could provide warning signals in the event of a hazard, allowing the user or relevant authorities to be alerted or take required actions before the situation escalates (an indicator of an impending disaster). Aside from that, workers are drowsy and take many naps in between the ongoing construction work, which can lead to a huge disaster or result in an accident and as a result of such factors, the project is delayed and the project manager must deal with such uncertainties and take quick actions to resist the project's delaying.

Despite the limitations of conventional safety helmets, as described above, the safety helmet design has been re-engineered with the addition of several hazard detection sensors to develop a smart construction safety helmet that looks to be promising.

The capacity to recognize and respond to stimuli is referred to as 'smart.' Through automation and intelligent manufacturing, highly customized smart construction safety helmets with sensors are feasible. Indeed, it has recently been proposed that future PPE be outfitted with sensors that provide wearer/concerned authority alarm signals. In the present effort, an existing safety helmet will be improved by adding different sensors and an Arduino mini. These sensors work together to provide better security by sending alerting and warning messages to the supervisor's screen/smartphone for future or ongoing hazards experienced by the user. This smart safety helmet will be critical for construction workers who are at high risk of injury owing to sleepiness, body temperature and increased amounts of sound, smoke and alcohol intake. More importantly, this smart helmet will offer the construction manager a real-time report on diverse workers (or respective authorities). The construction manager will be responsible for the wearer's (labourers' or employees') physiological parameters as well as the surrounding dangerous parameters that they experience while working on building sites. If any worker's data is frightening, the management will take the appropriate action straight away based on real-time data. Thus, under these settings, the smart safety helmet looks to be more effective than the traditional design in informing managers about employees' physical and surrounding situations.

The development of an improved version of a smart safety helmet is in keeping with the fourth industrial revolution (IR4.0) goal of incorporating current technologies into the industry. Furthermore, its design addresses SDG 8 (decent work and economic growth) and SDG 9 (environmental sustainability) (industry, innovation and infrastructure). This article will go over the design details, prototype photo, input from target responders and future modifications depending on the input obtained.

Aside from all of this, several researchers have produced numerous helmet modifications in recent years. Von attempted to evaluate the possibility of recording the electrocardiogram (ECG), respiration and EEG from the lead locations by integrating numerous electrodes into a standard helmet [11]. Jorge and his colleagues developed an ontology-based framework to manage healthcare routine recommendations for chronic disease patients [12]. Many researchers have suggested the use of various sensors separately, but no one has yet integrated all of these sensors into a unit that is revolutionary in design.

2 Materials

The smart construction helmet is seen in Fig. 1 and the materials utilized to make it are depicted in Table 1. The smart helmet is made up of three parts: the smart helmet itself (integrated with different sensors and Arduino), the Bluetooth module and the receiving screen (i.e. the manager's phone or laptop screen). All of these supplies are mentioned in Table 1 and are easily purchased from a hardware shop, either online or locally. The smart helmet system is made up of numerous electrical components, including an Arduino nano, an MQ-135 smoke sensor, an MQ-3 gas

Fig. 1 Smart construction safety helmet



sensor, an HC-05 Bluetooth sensor, a sound sensor, an IR module, jumping wires, connectors, a 9 V battery, a buzzer, and a DS18B20 temperature sensor. The entire smart kit is minimal in weight, causing no additional load or discomfort to the wearer. It should be noted that the various sensors are mounted in various positions on the helmet to get efficient results and the position of various sensors and other electrical parts is detailed in Table 1. The entire cost of producing such a smart helmet was 1500 Indian rupees (in the present year 2021).

3 Objectives

The objectives of this smart construction helmet are as follows:

1. To strictly adhere to the safety protocols and prevent laziness and alcoholism when operating on-site.
2. To limit the exploitation of construction workers' lives, health and safety.
3. To monitor and manage the health and safety of construction workers.
4. To test the efficiency of this smart helmet against the conventional smart helmet.
5. To establish an economical approach for the manufacturing of smart construction helmets with multifunctional features
6. Raising awareness among construction workers about this life-saving, technologically sophisticated smart construction helmet.
7. Using colour coding in excel sheets to actively indicate potentially hazardous situations.
8. The face shield helps the user prevent harmful particles from entering the wearer's eyes.

Table 1 Materials used in smart construction safety helmet

Sr No	Name of item	Price in Indian rupees (As per year 2021)	Weight	Location w.r.t helmet/wearer
1	Sound sensor	Single-Rs 70 Bulk-Rs 50	0.007 kg	At the left side of the frontal top of the helmet
2	MQ-135-Smoke sensor	Single-Rs 200 Bulk-Rs 100	0.011 kg	At the right side of the frontal top of the helmet
3	DS18B20 Temperature sensor	Single-Rs 70 Bulk-Rs 50	0.0227 kg	At the frontal side of the helmet’s inner sweatband
4	IR module	Single-Rs 50 Bulk-Rs 30	0.05 kg	Placed at the inner side of the faceshield at the eye level.
5	HC-05-Bluetooth module	Single-Rs 320 Bulk-Rs 280	0.05 kg	On the outer right side of the helmets lower back
6	Arduino nano	Single-Rs 250 Bulk-Rs 120	0.007 kg	In the outer middle part of the helmets lower back
7	MQ-3-Gas sensor	Single-Rs 150 Bulk-Rs 100	0.09 kg	Placed at the inner side of the face shield at the mouth level.
8	Battery	Single-Rs 30 Bulk-Rs 15	0.037 kg	Below the Arduino and in the middle of the helmet’s lower back
9	Helmet with face shield	Single-Rs 300 Bulk-Rs 150	0.50 kg	On the head of the wearer and face shield covers the entire face
10	Jumping wires	Single-Rs2/per wire Bulk-Re 1/per wire	0.001 kg	Between every sensor
11	Buzzer	Single-Rs. 12 Bulk-Rs. 6	0.0016 kg	In the outer right most corner of the helmet

9. The removal of this helmet during working hours immediately deducts the wearer’s salary for failing to follow safety measures and stamps his/her attendance as sleeping.
10. The buzzer also warns the user of any potential working risks, such as toxic fumes, high temperatures, or loud noises.

4 Problem Statement

- (a) Not all construction managers or concerned authorities care about safety measures in the construction sector and they also do not always follow safety protocols.

- (b) There is a lack of technological awareness among construction workers in a developing country like India.
- (c) Workers are exploited in many areas of our country.
- (d) Most construction projects are delayed due to a lack of real-time monitoring of workers because they tend to be drowsy, alcoholic, or lazy.
- (e) There is a lack of awareness about safety measures among fresher Civil engineers and managers.

5 Methodology

Incidents most commonly occur on-site owing to heedlessness or insufficient safety procedures and facilities, causing significant damage to workers and occasionally leading to death [13] due to a lack of real-time monitoring of accidents on-site. So, to reduce the likelihood of accidents, this smart construction safety helmet was designed to monitor the factors that cause accidents and automatically assist construction managers in managing workers who avoid safety procedures. In addition to these characteristics, it contains an alerting system in the form of alerting sound from buzzer that will notify the user of an ongoing or impending threat, perhaps saving their life.

When a labourer or worker puts on the smart helmet, data of various parameters and risks, such as drowsiness, temperature, sound, gas leakage and smoke concentration, are generated by their distinct sensing sensors, such as infrared sensor, DS18B20 Temperature sensor, Sound sensor, MQ-3 Gas sensor and MQ-135 Smoke sensor and this unsynchronized and jumbled data is transferred on to the Arduino nano via circuit system (refer Fig. 2). The Arduino nano serves as the primary processing unit in the

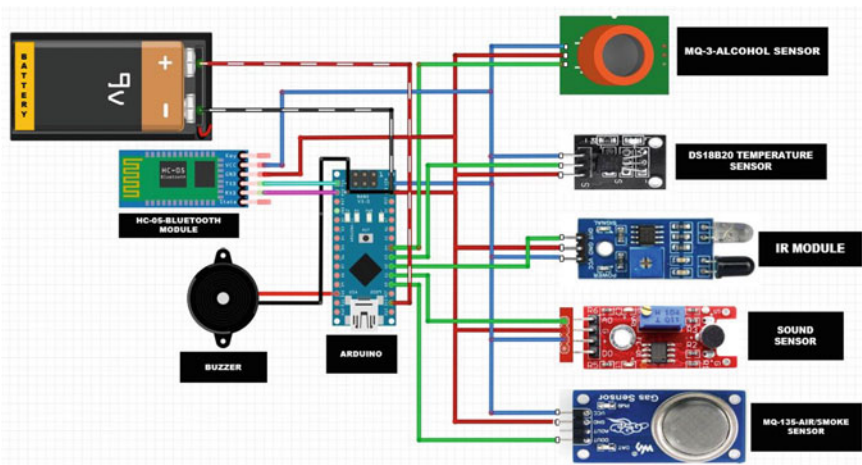


Fig. 2 Smart construction helmet circuit diagram

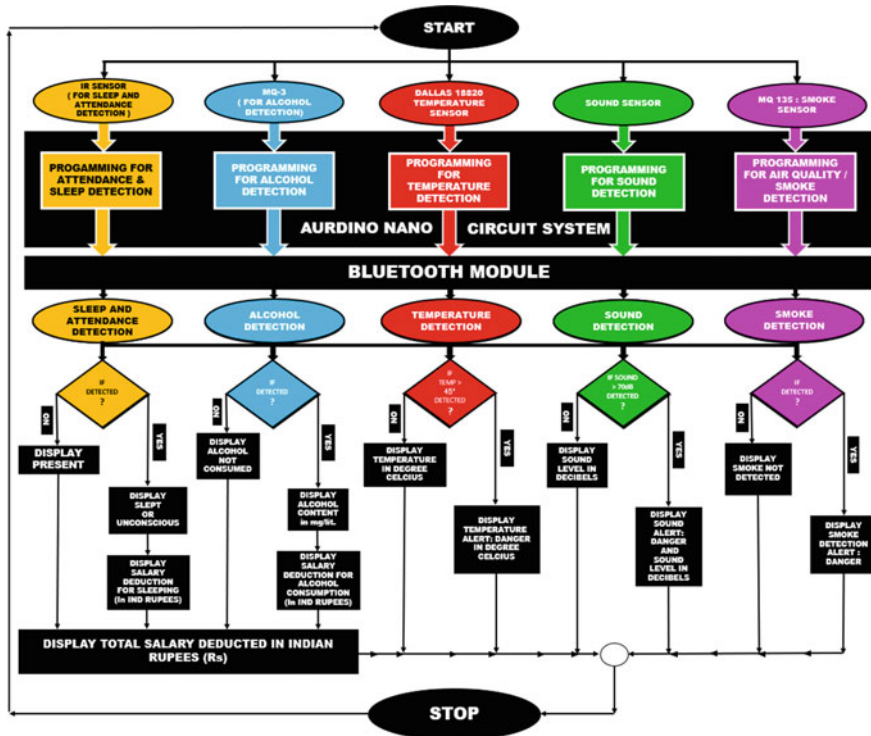


Fig. 3 Working methodology of Arduino

smart helmet system (Fig. 3). It gathers data from all sensors and generates warning signals depending on the coding that has previously been put into its programme by managers and coders (see Fig. 4). It produces warning and alerting messages [14] by analyzing data from its sensors. Data is provided clearly and helpfully so that the supervisor may evaluate the data generated by each worker. Based on the data, Arduino can determine if there is an alerting event, which leads Arduino to generate an alarming message informing the manager/supervisor of the likelihood of danger to the wearer. All of this data is wirelessly [15] transferred to a manager's or supervisor's smartphone [16] and computer screen within a 10-m Bluetooth range.

To receive data on the phone, the Arduino Bluetooth controller app for Android is utilized. The supervisor or manager must install this application on his or her smart Android phone to get data from the wearer (see Fig. 5) However, for real-time data to be assembled on computers (see Fig. 6), excel must be used in conjunction with PLX-DAQ, a free online tool. Furthermore, the manager should pre-set the excel settings bar to give colours based on his / her requirements in the excel sheets. Figure 6 depicts that red colour signifies danger, green colours represent a safe working environment and blue colours represent income. When a supervisor gets worrisome data on his or her phone or laptop screen, he or she can take the necessary steps to mitigate the

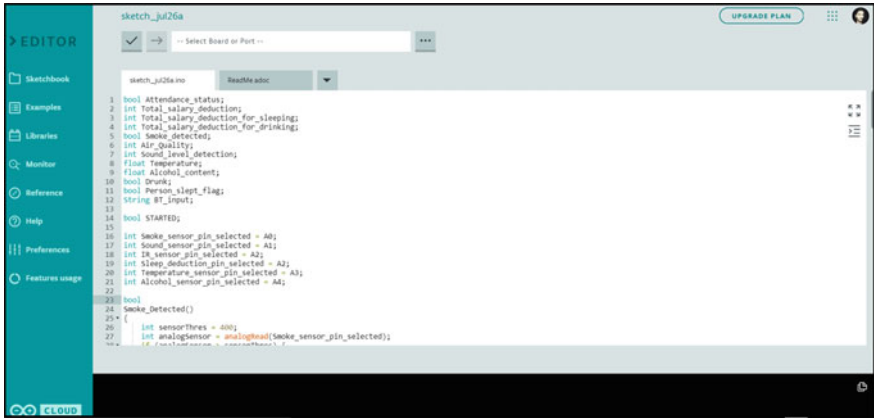


Fig. 4 Coding in Arduino software for smart construction safety helmet



Fig. 5 Mobile interface

hazard. The colour-coded spreadsheet on a laptop is a helpful tool for supervisors to monitor real-time data and the highlighted danger signals give rapid access for managers and supervisors to differentiate data.

In addition to monitoring the dangerous circumstances around the wearer, the Arduino code deducts the user’s income if he or she is determined to be sleepy or intoxicated at work. If the wearer is assessed as drowsy or intoxicated, their income will be reduced instantly from their overall pay. Every second, the code produces the

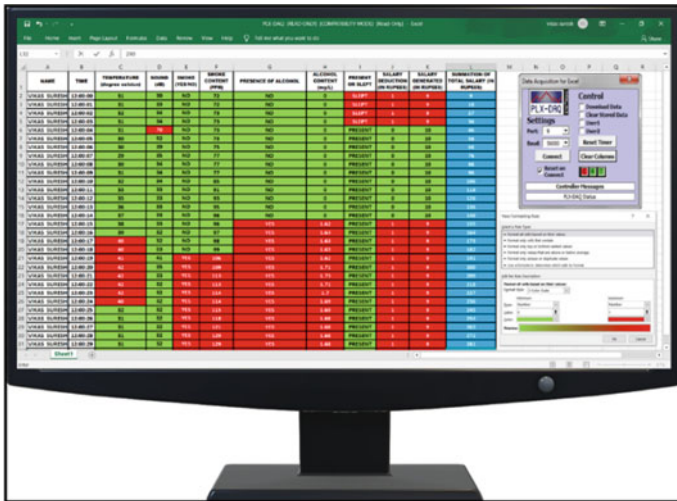


Fig. 6 Laptop interface presenting colour-coded excel sheet

wearer’s salary. A portable battery backed by the complete system [17] can keep it running for 3 hours. Figure 7 depicts the whole smart helmet design approach.

When a harmful scenario arises near the user, the buzzer linked to the helmet’s Arduino functions as a warning agent and the buzzer alerts the wearer of any ongoing or impending hazards that may occur (through alerting/buzzing sound), such as smoke concentration, body temperature, or sound conditions.

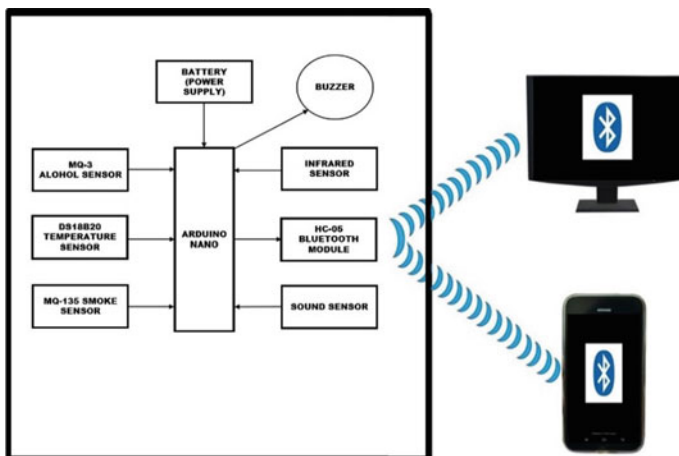


Fig. 7 Block diagram of smart construction safety helmet system

6 Result

6.1 Outcomes from the Perspectives of Respondents and Project Managers

Surveys, quality assurance, market research and product testing are all well-known ways of assessing the viability of a freshly created product. To accomplish this, a total of 100 respondents were recruited from various construction sites, with the bulk of them being construction managers, engineers, workers and some inexperienced freshers. They were all shown the prototype smart helmet and allowed to watch its operation during an on-the-spot demonstration.

Table 2 outlines the respondents' characteristics (such as job experience, gender and age). It's worth mentioning that approximately 70% of respondents had prior employment experience in the engineering industry. Respondents were asked to fill out a questionnaire in order to provide feedback. The questionnaire's five questions are as follows:

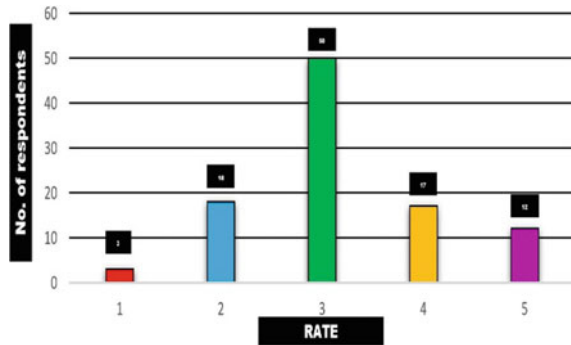
- (Q1) Do you believe that a construction safety helmet that detects 'danger' may give more protection than a standard safety helmet?
- (Q2) How do you think this smart helmet design is? (In terms of design environmental friendliness, practicability, efficiency, low weight and usability).
- (Q3) What, in your opinion, is/are the smart helmet's strength(s)?
- (Q4) What, in your opinion, is/are the smart helmet's weakness(es)?
- (Q5) If you work on a construction site, how inclined are you to purchase and utilize this smart helmet?

According to 85% of responders, this smart safety construction helmet, which is fitted with different hazard detecting systems, provides better workplace protection than standard safety helmets. Meanwhile, just 15% of respondents disagreed with this assertion, showing that the majority of them are unable to keep up with technological progress and prefer to use old-school safety measures. This discovery indicates that the current generation realizes the need for enhanced smart safety equipment that may provide a user with an instantaneous warning signal when it identifies a potential hazard. This type of smart gear is required for the safety of those working on the job site.

Table 2 Characteristics of respondents

Gender	Count	Age range (in years old)			Total working experience	
		20–29.9	30–39.9	40–50	Yes	No
Male	76	45	23	8	55	26
Female	24	17	4	3	17	7
Total	100					

Fig. 8 Number of respondents versus rate given by respondents



Respondents were asked to rate their chances of purchasing and utilizing the smart safety helmet during the questioning session. According to the graphical Fig. 8, about 12 people voted for Rate 5 (very likely), 17 people voted for Rate 4 (likely), 50 people voted for Rate 3 (neutral), 18 people voted for Rate 2 (unlikely) and just three people voted for Rate 1. (Very unlikely). Overall, respondents offered neutral feedback, with a mean rating of 3.17. Nonetheless, while being aware of the need for smart construction helmets, more than half of the respondents were undecided about acquiring and utilizing this smart helmet gear. As mentioned in Q4 of the survey, such outcomes might be ascribed to the restrictions of the current prototype. When this gear is made waterproof and has a longer detection range, the mean rating scale is predicted to move higher.

Following that, respondents were asked to assess the design of the smart safety helmets. The evaluations were classified into four categories: Rate 1 (poor), Rate 2 (moderate), Rate 3 (good) and Rate 4 (excellent) (excellent). As shown in Table 4, the majority of respondents rated the design’s simplicity, environmental friendliness, lightweight and ease of use as acceptable to excellent. These four criteria earned a mean rating of higher than 3, with the exception of the practicability of smart helmets, which received a mean rating of 2. The majority of smart helmets now on the market have weight issues that will limit employees’ willingness to utilize these helmets. Even though the current design of this smart helmet presented in this paper is relatively basic, due to the inclusion of many sensors, it appears quite substantial, but it is not. These sensors add negligible weight to the overall weight of the helmet and will not influence worker compliance with the usage of these helmets. When the wearer is in good health and the working circumstances are favourable, the wearer can choose to turn on or off the entire circuit by removing the battery. Aside from that, the design’s effectiveness received a good grade. Aside from that, the helmet was rated as somewhat practicable. Despite the fact that this helmet was accurate, a few respondents were dissatisfied with the generated results; hence, further input from respondents was gathered by asking them to offer their opinion on the merits and weaknesses of this smart construction helmet.

Table 3 highlights the respondents’ perspectives on the advantages and disadvantages of the current prototype version of the smart safety helmet. Respondents

Table 3 Strength and weakness of smart construction safety helmet

Strength	Weakness
It can help in avoiding accidents even in dark places	Water or sweat might affect the electronic system
Ease of use and easy to install	The range of the Bluetooth sensor is less than 10 m
Alerts the wearer through a buzzer attached to the helmet during a hazard and provides information and warning signals to the supervisor about the wearer	It is not environmentally friendly as it is not using solar batteries
It increases the productivity of the workers	The sound produced by the buzzer is not audible enough if the working environment is noisy
It is employed as an accident detection system, attendance tracking system, safety and health monitoring and alerting message system [18]	It is way much more expensive than conventional safety helmets
All the parts are easily available in the hardware store	Scrambling of wires can cause problems
Robust and lightweight	Overheating of circuits along with sensors can cause problems
It's quite accurate	Heavy usage of battery
It also aids in the management of the widespread of false whispers about any worksite event involving a worker since it gives accurate and real-time data that can be stored in excel for a long time and examined by relevant authorities if there is any doubt about these false rumours	There can be technical glitches as all sensors are working at the same time

agreed that the concept is sturdy, innovative and easy to implement. More importantly, while the wearer is working in a hazardous environment, this smart safety helmet can reduce accidents. When the user is very focused on his or her job, the buzzing sound may alert him or her. Nonetheless, respondents felt that the current design had certain flaws. One of the most frequently expressed concerns is that the current prototype version can only be monitored from a short distance, i.e. Bluetooth range distance (5–10 m) and that it cannot be used during the rainy season because it is not waterproof and contains electronic circuits that can be damaged by water or cause the smart helmet to malfunction. As a consequence, the average rating for effectiveness was near to excellent (Table 4). One of the respondents suggested that by using IoT, the detection range of this smart helmet be increased to at least 50 m. Meanwhile, a tiny percentage of respondents voiced concern about the cost. Meanwhile, a few respondents expressed concerns about the expense of this smart safety helmet, which is expected to be more expensive than a standard safety helmet.

Table 4 Rating on various parameters of smart construction helmet

Criteria	Mean rating	Rate 1 (Poor)	Rate 2 (Moderate)	Rate 3 (Good)	Rate 4 (Excellent)
Design simplicity	3.41	3	14	22	61
Lightweight	3.57	2	8	21	69
Environment Friendliness	3.04	4	18	48	30
Practicability	2.04	28	46	20	6
Ease of use	3.48	5	10	17	68
Effectiveness	3.43	4	9	27	60

6.2 Results for Finding Values of Performance Metrics

6.2.1 Performance Metrics

Performance metrics are being used to assess a company’s behaviour, operations and overall performance. These should take the form of data that evaluates the needed data within a range, causing a foundation to promote overall business objectives. Measuring performance via metrics is critical for determining how staff are doing and if objectives are being fulfilled.

While building this smart construction project, many learning algorithms were proposed and finally, a notable algorithm was chosen from which Arduino code was constructed to make the smart helmet work efficiently. It is frequently useful to evaluate an algorithm’s effectiveness. In many circumstances, such evaluation is relative, i.e. determining which of numerous different algorithms is best suited to a particular application. People even wind up inventing metrics that are tailored to the application. This research article will deal with some of the most popular metrics in a problem categorization setting.

The following are the most often used performance measures for categorization problems.

1. Accuracy
2. Recall
3. Precision
4. F1-score
5. Error Rate

Moreover, many more are there, but these are the most prominent performance measures for categorization problems and all these measures will also be calculated further in this paper for various conditions that will be applied to the working of smart construction helmets. If the values of all these smart helmet measurements are not accurately computed, the product may fail during production due to poor accuracy.

Accuracy, Precision, Recall, F1-score and Error rate values were determined using this prototype. It has been calibrated and tested in a variety of scenarios. The preceding measures will now be briefly outlined one by one.

Accuracy

Accuracy is defined as the simple ratio of correctly categorized points to total points.

$$\text{Accuracy} = (TP + TN) \div (TP + TN + FP + FN) \quad (1)$$

Here, TP—True Positive, FN—False Negative, FP—False Positive, TN—True Negative.

If the detection meets the expectation, we consider the circumstance to be a true positive or negative. If our test case was meant to be an accident and our detection, i.e. smart construction helmet, successfully identified it as such, it is reported as a true positive. Similarly, if our objective was not to cause an accident and the system fails to record one, it is a true negative.

Precision

Precision is defined as the ratio of accurate True occurrences to total True instances provided by the detection system.

$$\text{Precision} = TP \div (TP + FP) \quad (2)$$

Here, TP—True Positive, FP—False Positive.

Recall

The percent of True occurrences recorded by the detecting system is referred to as Recall.

$$\text{Recall} = TP \div (TP + FN) \quad (3)$$

Here, TP—True Positive, FN—False Negative.

F1 Score

The harmonic mean of accuracy and Recall is used to get the *F1* score.

$$F1 \text{ score} = [2 * \text{Precision} * \text{Recall}] \div [\text{Precision} + \text{Recall}] \quad (4)$$

Table 5 Evaluation of performance metrics for Sound sensor

TP	FP	TN	FN	Accuracy	Recall	Error rate	Precision	F1-score
5	0	5	0	1	1	0	1	1

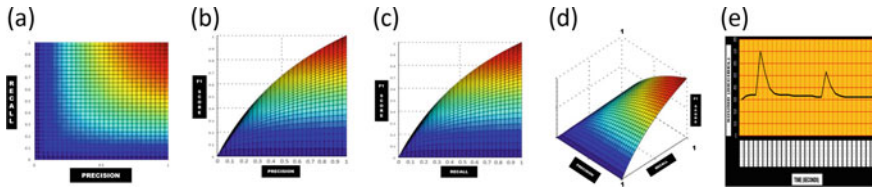


Fig. 9 Graphical depiction of several aspects of sound sensor performance metrics like **a** Recall versus Precision, **b** F1-score versus Precision, **c** F1-score versus Recall and **d** Precision versus Recall versus F1-score, **e** Experimental results on sound (decibel) versus time (seconds)

Here, TP—True Positive, FP—False Positive, FN—False Negative.

Error Rate

The error rate is derived by dividing the total number of inaccurate predictions by the total number of observations in the dataset.

$$\text{Error rate} = (1 - \text{Accuracy}) \tag{5}$$

6.2.2 Test Results of Various Sensors for Measuring Performance Metrics Values

From a pool of 100 responses, ten were picked at random. Hazardous and accidental scenarios and non-hazardous settings were created to verify the smart helmet’s sensor’s total accuracy. The results of situations-based trials and the F1 score for each sensor were computed using these ten respondents and the findings are jotted down in the following sections.

Performance Metrics Results of Sound Sensor

Sound sensor detects sound intensity, i.e. if the sound intensity is greater than 70 dB then it will generate warning data. Table 5 displays the performance metric values derived from the actual and generated sound sensor readings. Figure 9 depicts a graphical representation of the sound sensor’s experimental and performance metrics data.

Table 6 Evaluation of performance metrics for MQ-135-air/smoke sensor

TP	FP	TN	FN	Accuracy	Recall	Error rate	Precision	F1-score
3	0	5	2	0.8	0.6	0.2	1	0.75

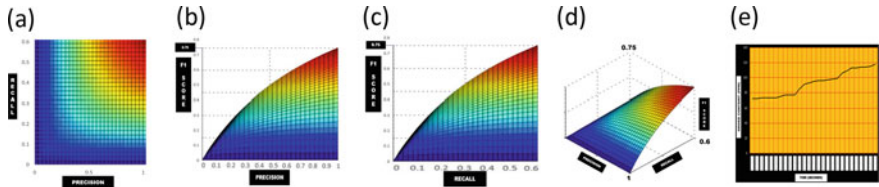


Fig. 10 Graphical depiction of several aspects of MQ-135 Smoke sensor performance metrics like **a** Recall versus Precision, **b** F1-score versus Precision, **c** F1-score versus Recall and **d** Precision versus Recall versus F1-score, **e** Experimental results on smoke concentration (PPM) versus time (seconds)

Table 7 Evaluation of performance metrics for temperature sensor

TP	FP	TN	FN	Accuracy	Recall	Error rate	Precision	F1-score
5	0	5	0	1	1	0	1	1

Performance Metrics Results of MQ-135-Air/Smoke Sensor

Smoke sensor detects and produces warning data if the smoke concentration around the wearer is greater than 100 ppm. Table 6 displays the performance metric values derived from the actual and generated smoke sensor readings. Figure 10 depicts a graphical representation of the MQ-135-Air/Smoke sensor’s experimental and performance metrics data.

Performance Metrics Results of DS18B20 Temperature Sensor

Temperature sensor detects the body temperature of the wearer and generates warning data if the body temperature of the wearer is greater than 40 °C or less than 33 °C. Table 7 displays the performance metric values derived from the actual and generated temperature sensor readings. Figure 11 depicts a graphical representation of the Temperature sensor’s experimental and performance metrics data.

Performance Metrics Results of MQ-3-Gas Sensor

This sensor will detect and generate warning data if any traces of alcoholic matter are consumed by the wearer. Along with that salary of the wearer will be deducted if found guilty of consuming any alcoholic substance during working hours on-site.

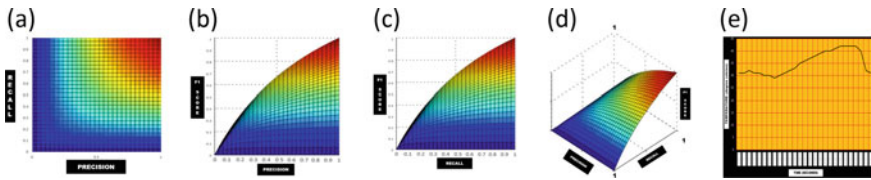


Fig. 11 Graphical depiction of several aspects of DS18B20 Temperature sensor like **a** Recall versus Precision, **b** F1-score versus Precision, **c** F1-score versus Recall and **d** Precision versus Recall versus F1-score, **e** Experimental results on body temperature (Celsius) versus time (seconds)

Table 8 Evaluation of performance metrics for MQ-3-gas/alcohol sensor

TP	FP	TN	FN	Accuracy	Recall	Error rate	Precision	F1-Score
3	0	5	2	0.8	0.6	0.2	1	0.75

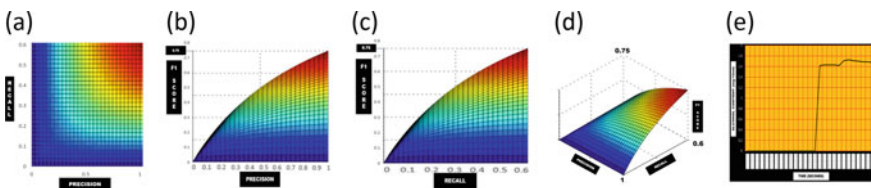


Fig. 12 Graphical depiction of several aspects of MQ-3 Gas sensor like **a** Recall versus Precision, **b** F1-score versus Precision, **c** F1-score versus Recall and **d** Precision versus Recall versus F1-score, **e** Experimental results on alcohol content(mg/L) versus time (seconds)

Table 9 Evaluation of performance metrics for IR sensor

TP	FP	TN	FN	Accuracy	Recall	Error rate	Precision	F1-score
5	0	5	0	1	1	0	1	1

Table 8 displays the performance metric values derived from the actual and generated gas sensor readings. Figure 12 depicts a graphical representation of the MQ-3-Gas sensor experimental and performance metrics data.

Performance Metrics Results of IR Module

IR Module detects the eye-blinking nature of the wearer. If eyes are closed then warning data is generated and along with that salary of the wearer will be deducted. Table 9 displays the performance metric values derived from the actual and generated IR sensor readings. Figure 13 depicts a graphical representation of the IR sensor's experimental and performance metrics data.

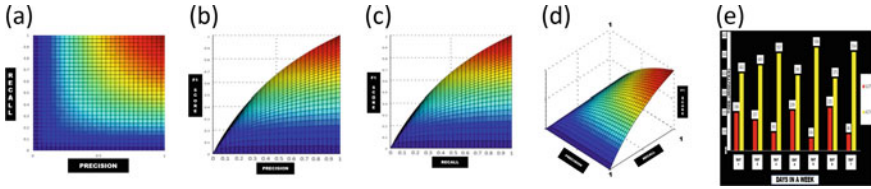


Fig. 13 Graphical depiction of several aspects of IR module like **a** Recall versus Precision, **b** F1-score versus Precision, **c** F1-score versus Recall and **d** Precision versus Recall versus F1-score, **e** Experimental results on slept time(minutes) and active time(minutes) in a week

7 Conclusion

The Arduino nano was successfully integrated with the safety helmet, along with several sensors, throughout this study to generate a modified version. This system is very efficient since these sensors when combined with Arduino, provide a multitude of additional functions that increase safety by wirelessly transferring real-time data from the sensors to the construction manager's mobile device through Bluetooth. Management (managers and supervisors) can send out warning signs to decontaminate live dangerous situations. Case studies have demonstrated the usefulness and precision of several sensors, including their ability to alert users of alcohol intake [19], smoke, noise, drowsiness and body temperature. Aside from these features, the helmet serves as a protective barrier, reducing the danger of brain injury associated with the wearer's employment. Furthermore, the helmet's face shield protects the wearer from dust particles. The smart helmet is used to generate and manage data [20, 21] on salary deductions made as part of the Arduino coding. Aside from all of this, the real-time buzzer alerting mechanism on the smart helmet itself is crucial. Taking into account the findings described above as well as the intelligent features included in this smart construction helmet, it may be thought of as accident detection, monitoring, and alerting/warning system developed for real-time health monitoring [22–24]. As a result, integrating smart automation with traditional safety helmets [25] enables high accuracy outcomes in terms of real-time safety and monitoring. This newly designed smart safety helmet benefits employees by serving as an accident warning and detection system and it benefits managers by acting as money management and monitoring system. This study gathered input from target respondents on the smart safety helmet's design, functionality and practicability. Based on their suggestions, further enhancements were suggested. Furthermore, researchers are highly encouraged to widen the scope of this study to broaden the knowledge base and further examine the feasibility of smart safety helmet adoption.

References

1. Jesudoss A, Vybhavi R, Anusha B (2019) Design of smart helmet for accident avoidance. In: Proceedings 2019 IEEE international conference of communication signal processing, ICCSP 2019, pp 774–778
2. Uniyal M, Rawat H, Srivastava M, Srivastava VK (2018) IOT based smart helmet system with data log system. In: Proceedings IEEE 2018 international conference on advances in computing, communication control and networking, ICACCCN 2018, pp 28–31
3. Prasad SR, YVSSSV PR (2013) Study on validation of wholesaler selection of personal protective equipment to improve safety performance in a construction organization in India. *Int J Manag Value Supply Chain* 4(2):17–24
4. Balkhyour MA, Ahmad I, Rehan M (2019) Assessment of personal protective equipment use and occupational exposures in small industries in Jeddah: health implications for workers. *Saudi J Biol Sci* 26(4):653–659
5. Baszczyński K (2018) Effects of falling weight impact on industrial safety helmets used in conjunction with eye and face protection devices. *Int J Occup Saf Ergon* 24(2):171–180
6. Rajendran SD, Wahab SN, Yeap SP (2020) Design of a smart safety vest incorporated with metal detector kits for enhanced personal protection. *Saf Health Work* 11(4):537–542
7. Lombardi DA, Verma SK, Brennan MJ, Perry MJ (2009) Factors influencing worker use of personal protective eyewear. *Accid Anal Prev* 41(4):755–762
8. Barro-Torres S, Fernández-Caramés TM, Pérez-Iglesias HJ, Escudero CJ (2012) Real-time personal protective equipment monitoring system. *Comput Commun* 36(1):42–50
9. Nataraja N, Mamatha KS, Keshavamurthy, Shivashankar (2018) Smart helmet. In: 2018 3rd IEEE international conference on recent trends electronics information communication technology. RTEICT 2018—Proceedings, pp 2338–2341
10. Izudi J, Ninsiima V, Alege JB (2017) Use of personal protective equipment among building construction workers in Kampala, Uganda. *J Environ Public Health* 2017
11. Von Rosenberg W, Chanwimalueang T, Goverdovsky V, Looney D, Sharp D, Mandic DP (2016) Smart helmet: wearable multichannel ECG and EEG. *IEEE J. Trans Eng Heal Med* 4(February):1–11
12. Gómez J, Oviedo B, Zhuma E (2016) Patient monitoring system based on internet of things. *Procedia Comput Sci* 83(Ant):90–97
13. Jayasree V, Kumari MN (2020) IOT based smart helmet for construction workers. In: 2020 7th international conference on smart structures and systems. ICSSS 2020, pp 1–5
14. Ahuja P, Bhavsar K (2018) Microcontroller based smart helmet using GSM GPRS. In: Proc. 2nd international conference on trends in electronics and informatics, ICOEI 2018, no. Icoei, pp 175–180
15. Hazarika P (2017) Implementation of smart safety helmet for coal mine workers. In: 1st IEEE international conference on power electronics, intelligent control and energy systems. ICPEICES 2016, pp 1–3
16. Mahmud MS, Wang H, Esfar-E-Alam AM, Fang H (2017) A wireless health monitoring system using mobile phone accessories. *IEEE Internet Things J* 4(6):2009–2018
17. Muthiah M, Aswin Natesh V, Sathindran RK (2017) Smart helmets for automatic control of headlamps. In: 2015 international conference on smart sensors and systems. IC-SSS 2015, pp 2–5
18. Divyasudha N, Arulmozhivarman P, Rajkumar ER (2019) Analysis of smart helmets and designing an IoT based smart helmet: a cost effective solution for riders. Proc. 1st international conference on innovations in information and communication technology ICICT 2019, pp 1–4
19. Shrivaya K, Mandapati Y, Keerthi D, Harika K, Senapati RK (2019) Smart helmet for safe driving. In: E3S Web Conference vol 87(January)
20. Shabina S (2014) Smart helmet using rf and wsn technology for underground mines safety. In: Proceedings 2014 international conference on intelligent computing applications. ICICA 2014, pp 305–309

21. Ahmed SU, Uddin R, Affan M (2020) Intelligent gadget for accident prevention: smart helmet. In: 2020 international conference on computing and information technology. ICCIT 2020, pp 31–34
22. Punit Gupta I PKD, Agrawal D, Chhabra J (2016) IoT based smart healthcare kit Punit. In: I2016 international conference on computational techniques in information and communication technologies Proceedings, March 11–March 13, 2016, New Delhi, India, IEEE, pp 1–6
23. Khoi NM, Saguna S, Mitra K, Ahlund C (2015) IReHMo: an efficient IoT-based remote health monitoring system for smart regions BT. In: 2015 17th international conference on e-health networking, application and services, pp 563–568
24. Wan J et al (2018) Wearable IoT enabled real-time health monitoring system. *Eurasip J Wirel Commun Netw* 1:2018
25. Savaridass MP, Ikram N, Deepika R, Aarnika R (2021) Development of smart health monitoring system using Internet of Things. *Mater. Today Proc.* 45:986–989

Analysis of Quadratic Boost Converter with PV and BESS Using SMC



Vinay Kumar Naguboina and Satish Kumar Gudey

Abstract In this paper, a PV-based standalone system with battery energy storage system using a Quadratic Boost Converter is presented. A constant voltage at the output is obtained using SMC mechanism. A conventional Sliding Mode Controller with linear sliding surface is chosen to generate firing pulses to Quadratic Boost converter. This paper highlights the advantage of Quadratic Boost Converter over the conventional Boost Converter for low-power applications. The output voltage of the conventional boost converter is less compared to Quadratic Boost Converter which has a high voltage gain. A Quadratic Boost converter is used to step up the input source voltage of 50 V to 240 V. The Quadratic Boost converter is operated in parallel with the energy storage system battery. The role of this battery is to share the power along with PV panel during the need of the hour. The simulations are performed in PSCAD v4.5 version and its corresponding outputs are analyzed.

Keywords Sliding mode controller (SMC) · Boost converter (BC) · Quadratic boost converter (QBC)

1 Introduction

The demand for electricity is increasing exponentially day by day. The fossil fuels are getting depleted. This made the researchers to shift their focus on the generation of electricity by using the renewable energy resources. There are different renewable energy resources like solar, wind are available in abundant quantity in India. As per the statics of solar radiation data available it is smart to choose the solar energy as a resource to generate the electrical energy in India.

V. K. Naguboina (✉)

Department of Electrical and Electronics Engineering, Vignan's Institute of Information and Technology(A), Visakhapatnam, India
e-mail: naguboina.vinay@gmail.com

S. K. Gudey

Department of Electrical and Electronics Engineering, Gayatri Vidya Parishad College of Engineering (Autonomous), Visakhapatnam, India

The output from the PV panel is a variable DC. Most of appliances require AC power supply but there are few loads that will operate for DC power supply. To feed these DC loads with an AC power supply a rectifier is needed. This DC power can be directly fed to DC loads and batteries. Thus by providing the DC power supply to the DC loads the need for additional converter can be eliminated [1].

As the per-unit cost of power production by using fossil fuels has been increasing day by day, people's interest to utilize power generation from PV panels is also increasing adversely. As the density of solar power is very less, large space is required to generate the power by using solar. A group of PV panels placed in certain area is called as solar farm. Generally, these solar farms are installed in dry lands. These dry lands are located far away from the consumers. Hence it is not advisable to transmit the power at low DC voltage and high DC currents. This will reduce the overall efficiency of the system as the losses are very high. To reduce these power losses the voltage levels have to be increased drastically so the current levels will decrease concurrently.

2 Conventional Boost Converter Circuit with SMC

Boost converter is a DC-DC converter that is mainly used to step up the dc voltage. The relation between the output voltage and input voltage is

$$V_0 = \frac{V_{\text{input}}}{1 - D} \quad (1)$$

Conventional boost converter is preferred in many of the practical solar applications in order to step up the DC voltage to the desired and to maintain the voltage constant. The output voltage of the PV panel is a fluctuating voltage depending upon the change in solar radiation. This output voltage cannot be supplied to the electrical loads directly. A DC-DC converter is needed in order to maintain this voltage as constant. The circuit topology of a conventional boost converter fed with a solar panel is as shown in Fig. 1 and Table 1.

The controller has to be designed by comparing the reference voltage with actual voltage. The reference voltage value will be chosen as per the load specifications. If the load is designed to operate at 220 V then the reference voltage value should be chosen as 220 V. The functionality of the controller is to adjust the duty ratio of the controller dynamically in such a way to maintain the voltage at the load as constant (Fig. 2).

The output voltage from the PV panel is around 50 V. This 50 V is given as an input to the conventional boost converter, which is boosted up to a maximum voltage magnitude of 120 V in this work.

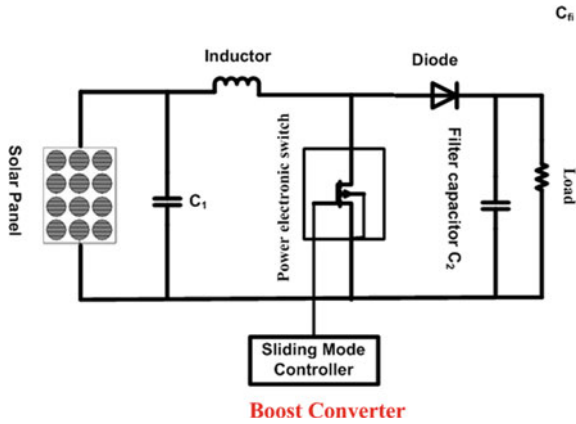


Fig. 1 Conventional boost converter with SMC

Table 1 System parameters of boost converter

Symbol	Parameters	Value
V_g	Input voltage	50 V
L_I	Inductor	0.383 mH
C_I	Capacitor	100 μ F
R_L	Load resistance	23 Ω

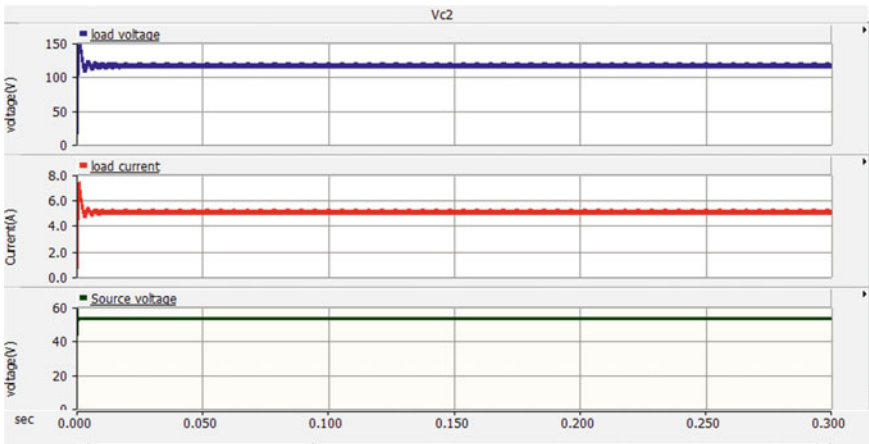


Fig. 2 Load voltage, load current, Source Voltage

3 Quadratic Boost Converter

In this paper, the functionality of the conventional boost converter is analyzed with variable input. It is found that output voltage can be stepped up to some extent. This made the researchers to search for the converter which will drastically increase the voltage at the output [2].

Quadratic boost converter (QBC) is found to be effective in increasing the low input voltage to a high output voltage, i.e. it has an effective voltage gain. In majority of low voltage PV applications, this QBC is preferred. Also nowadays the usage of DC microgrids is increasing day by day. To transmit the power at low voltage and high current the resultant power losses will increase. So in order to reduce these power losses a converter that will step up the low input voltage, high input current to high output voltage and low output current a high gain DC to DC converter is required.

Figure 3 shows the circuit diagram of a QBC with solar PV array as input. It consists of two inductors, two capacitors and three diodes in its configuration. It is a higher-order circuit and the complexity lies in making it stable using a suitable control algorithm.

The operation of boost converter can be analyzed in two modes. In mode 1 operation the switch S is in ON condition. The inductors L_1 and L_2 are in charging condition. The inductors will charge through the diode D_2 , Diodes D_1 and D_0 will be in off condition. The steady-state equations governing the system operation in mode 1 are given by (2–5) (Fig. 4).

$$\frac{di_{L1}}{dt} = \frac{V_g}{L_1} \tag{2}$$

$$\frac{di_{L2}}{dt} = \frac{V_{c1}}{L_2} \tag{3}$$

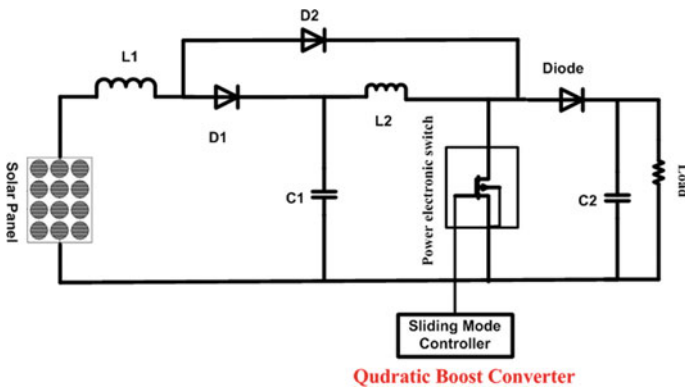


Fig. 3 Quadratic boost converter with SMC [1]

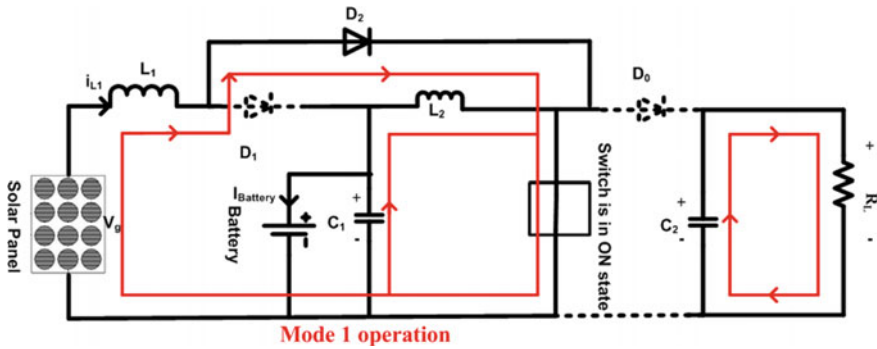


Fig. 4 Mode 1 operation of Quadratic Boost Converter when the switch is in ON state [1]

$$\frac{dv_{c1}}{dt} = \frac{i_{L2}}{C_1} - \frac{I_{battery}}{C_1} \tag{4}$$

$$\frac{dv_{c2}}{dt} = \frac{V_{c2}}{R_o C_2} \tag{5}$$

When the switch (*S*) is in ON state the state-space equations obtained are as(6).

$$\begin{bmatrix} \dot{i}_{L1} \\ \dot{i}_{L2} \\ \dot{V}_{C1} \\ \dot{V}_{C2} \end{bmatrix} = \begin{bmatrix} 0 & 0 & 0 & 0 \\ 0 & 0 & \frac{1}{L_2} & 0 \\ 0 & \frac{1}{C_1} & 0 & 0 \\ 0 & 0 & 0 & \frac{1}{R_o C_2} \end{bmatrix} \begin{bmatrix} i_{L1} \\ i_{L2} \\ V_{C1} \\ V_{C2} \end{bmatrix} + \begin{bmatrix} \frac{1}{L_1} & 0 \\ 0 & 0 \\ 0 & -\frac{1}{c_1} \\ 0 & 0 \end{bmatrix} \begin{bmatrix} v_g \\ I_{battery} \\ 0 \\ 0 \end{bmatrix} \tag{6}$$

In the mode 2 operation, the triggering pulse to switch is removed. Now the inductors which are in charged state will try to find a path to discharge. As the inductor will not allow the sudden changes in current inductor will interchange its positive and negative terminals [3]. This will make the diodes *D*₁ and *D*₀ to get forward biased (Fig. 5).

The relation between the Input voltage and Output voltage in the QBC is given in Eq. (7).

$$V_0 = \frac{V_{input}}{(1 - D)^2} \tag{7}$$

When the switch is in off state the state-space equations obtained are as shown in equation.

$$\frac{di_{L1}}{dt} = \frac{V_g - V_{C1}}{L_1} \tag{8}$$

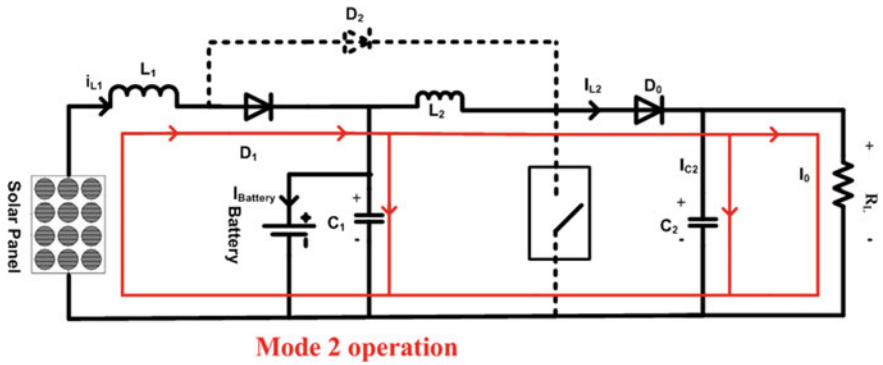


Fig. 5 Mode 2 operation of quadratic boost converter when the switch is in OFF state [1]

$$\frac{di_{L2}}{dt} = \frac{V_{C1} - V_{C2}}{L_2} \tag{9}$$

$$\frac{dV_{C1}}{dt} = \frac{-i_{L1}}{C_1} + \frac{i_{L2}}{C_1} - \frac{I_{battery}}{C_1} \tag{10}$$

$$\frac{dV_{C2}}{dt} = \frac{-i_{L2}}{C_2} - \frac{V_{C2}}{R_0 C_2} \tag{11}$$

$$\begin{bmatrix} \dot{i}_{L1} \\ \dot{i}_{L2} \\ \dot{V}_{C1} \\ \dot{V}_{C2} \end{bmatrix} = \begin{bmatrix} 0 & 0 & \frac{-1}{L_1} & 0 \\ 0 & 0 & \frac{1}{L_2} & \frac{-1}{L_2} \\ -\frac{1}{C_1} & \frac{1}{C_1} & 0 & 0 \\ 0 & \frac{1}{C_2} & 0 & -\frac{1}{R_0 C_2} \end{bmatrix} \begin{bmatrix} i_{L1} \\ i_{L2} \\ V_{C1} \\ V_{C2} \end{bmatrix} + \begin{bmatrix} \frac{1}{L_1} & 0 \\ 0 & 0 \\ 0 & \frac{1}{C_1} \\ 0 & 0 \end{bmatrix} \begin{bmatrix} v_g \\ I_{battery} \\ 0 \\ 0 \end{bmatrix} \tag{12}$$

Figure 6 indicates the comparison waveforms of load voltage, load current and source voltage. The output voltage from the PV panel is found to be 50 V. The output

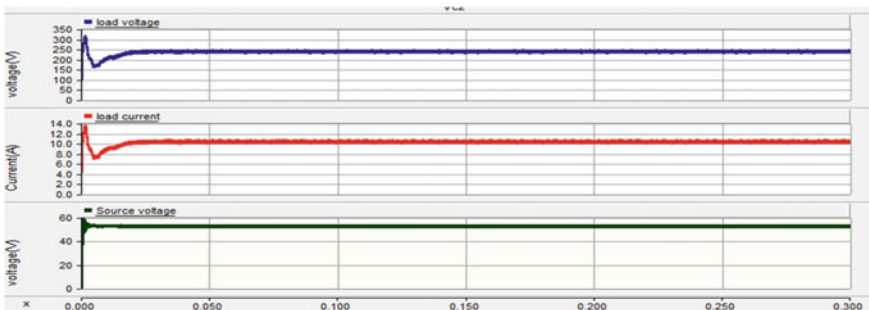


Fig. 6 Quadratic boost converter load voltage, load current and Source voltage

is fed to QBC the output voltage is raised up to 240 V. There is a large amount of improvement in the output voltage after QBC.

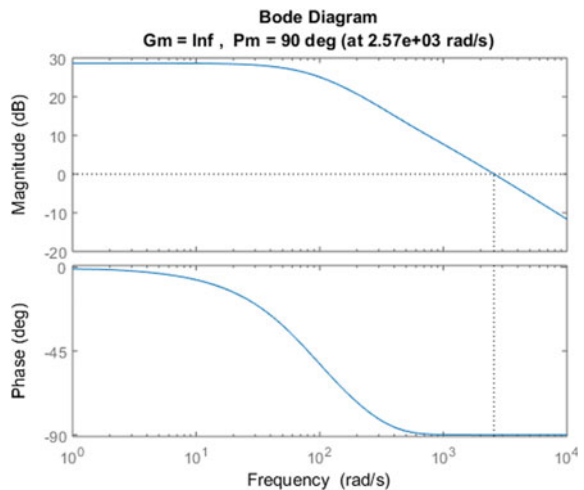
4 Mathematical Modelling of Quadratic Boost Converter Using State Feedback Approach

The average state-space model was obtained by solving the above two Eqs. (6) and (12). In this model to generate the switching pulses to the QBC a controller should be designed. The controller can be designed by choosing any one of the state variables as a control variable [4, 5]. Before selecting the control variable the stability margins of the system should be analyzed. For that purpose, the frequency response characteristics for the four control variables is analyzed. The output matrix is chosen as $C = (i_{L1}, i_{L2}, V_{C1}, V_{C2})$.

Case I: Considering i_{L1} as control variable (Fig. 7).

$$\begin{aligned} \begin{bmatrix} \dot{i}_{L1} \\ \dot{i}_{L2} \\ \dot{V}_{C1} \\ \dot{V}_{C2} \end{bmatrix} &= \begin{bmatrix} 0 & 0 & \frac{-(1-D)}{L_1} & 0 \\ 0 & 0 & \frac{1}{L_2} & -\frac{(1-D)}{L_2} \\ \frac{(1-D)}{C_1} & -\frac{1}{C_1} & 0 & 0 \\ 0 & \frac{(1-D)}{C_2} & 0 & -\frac{1}{R_0 C_2} \end{bmatrix} \begin{bmatrix} i_{L1} \\ i_{L2} \\ V_{C1} \\ V_{C2} \end{bmatrix} \\ &+ \begin{bmatrix} \frac{1}{L_1} & 0 \\ 0 & 0 \\ 0 & -\frac{1}{c_1} \\ 0 & 0 \end{bmatrix} \begin{bmatrix} v_g \\ I_{battery} \\ 0 \\ 0 \end{bmatrix} \end{aligned} \tag{13}$$

Fig. 7 Frequency response plot of the system for (14)



The transfer function obtained is given by (14)

$$\frac{2611s^3 + 1.135e06s^2 - 5.889e08s - 4.268e11}{s^4 + 434.8s^3 - 3.3e05s^2 - 2.089e08s - 1.571e10} \tag{14}$$

Case 2: Considering V_{C2} as control variable (Fig. 8).

The transfer function obtained is given by (15)

$$\frac{-3.926e11}{s^4 + 434.8s^3 - 3.3e05s^2 - 2.089e08s - 1.571e10} \tag{15}$$

Case 3: Considering i_{L1} as control variable (Fig. 9).

The transfer function obtained is given by (16)

$$\frac{0.5222s^2 + 227s + 7.853e04}{s^4 + 434.8s^3 - 3.3e05s^2 - 2.089e08s - 1.571e10} \tag{16}$$

Case 4: Considering V_{C2} as control variable (Fig. 10).

The transfer function obtained is given by (17)

$$\frac{-751.9 s}{s^4 + 434.8s^3 - 3.3e05s^2 - 2.089e08s - 1.571e10} \tag{17}$$

It was found that the stability margins of all the control variables in the system are good. Hence it can be concluded that any of the four-state variables available can be chosen as a control variable. In this paper, the control algorithm is designed

Fig. 8 Frequency response plot of the system (15)

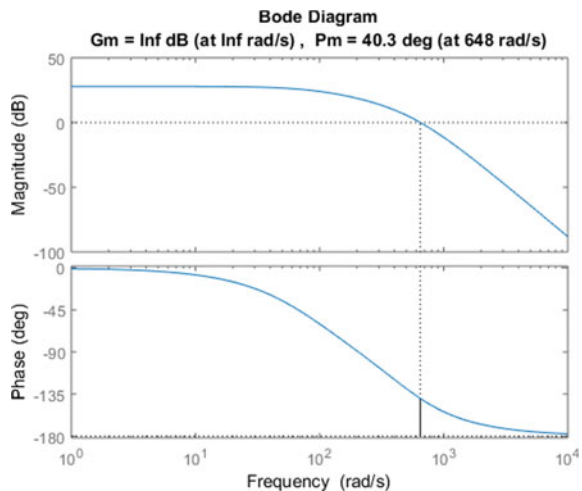


Fig. 9 Frequency response plot of the system for (16)

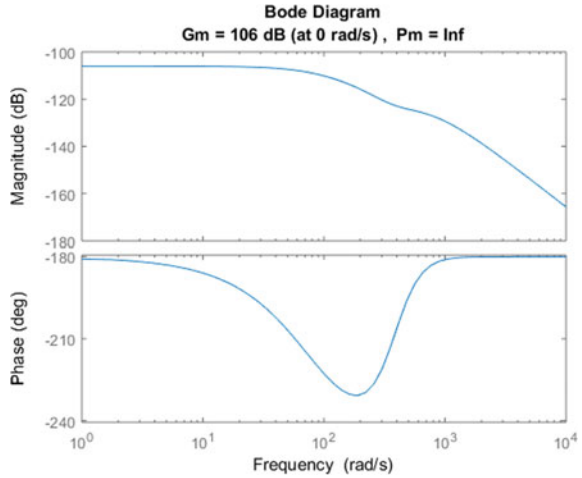
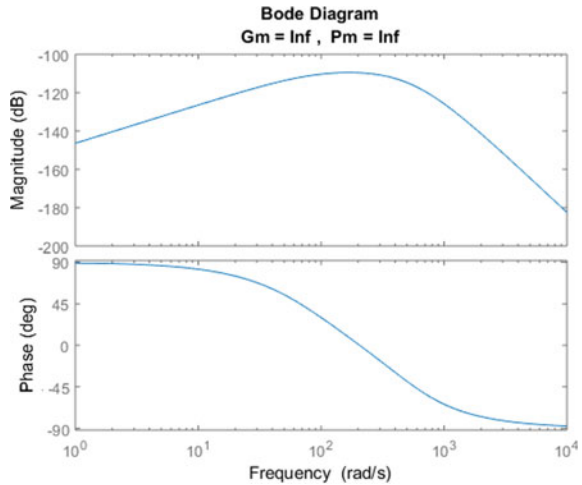


Fig. 10 Frequency response of the system



by choosing I_{L1} as a state variable along with the output voltage V_{c2} for obtaining a stable system [6, 7]. Two sensors are much required for a closed-loop operation of the circuit.

5 Quadratic Boost Converter with Bess

In this proposed work a QBC is designed which is operated in parallel with a battery. The reliability of the standalone system is quite low. The main reason is the output of the solar will not be constant. It will vary frequently with the change in solar

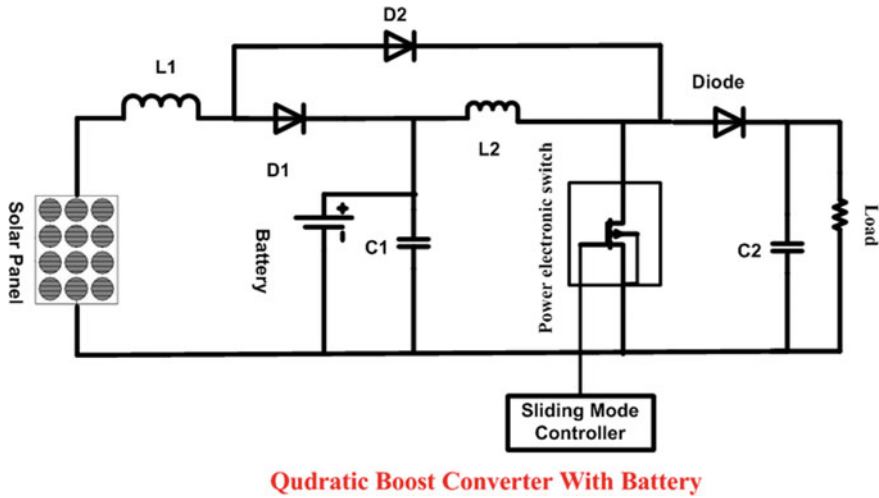


Fig. 11 QBC with energy storage system [1]

insolation [8]. Now to improve the reliability of the system a DC voltage source battery is added. Here battery serves two purposes.

- (i) Battery will be in charging state whenever there is an excess power.

$$P_{input} = P_{Load} + P_{battery} \tag{18}$$

- (ii) It will remain in discharging state whenever the PV panel cannot supply the demand requirements of load (Fig. 11).

$$P_{input} + P_{battery} = P_{Load} \tag{19}$$

The state of charge (SOC) of battery is also an important factor that has to be considered in order to increase the lifetime of a battery. Overcharging and over-discharging will reduce the life span of a battery. So a charge controller has to be placed to limit the charging and discharging limits of a battery. To improve the life span of a battery, the battery has to be operated in between the fixed limits like 20% to 90%, 30% to 80%, etc. There are certain cases where the battery gets fully charged but there is an excess power occurring from the solar. In that case, few additional loads have to be turned on to consume the additional power, i.e. $P_{input} = P_{Load}$. Also, dump loads has to be turned on to consume the excess power. These dump loads are nothing but the resistive loads which will absorb the electrical power and convert it into heat energy [9]. These dump loads will be turned on instantly whenever the battery gets fully charged. In this paper, the solar panel is designed to deliver a DC power of 3.5 kW. In this simulation, the designed system is evaluated under normal STC conditions. During the normal operating conditions, the irradiation and

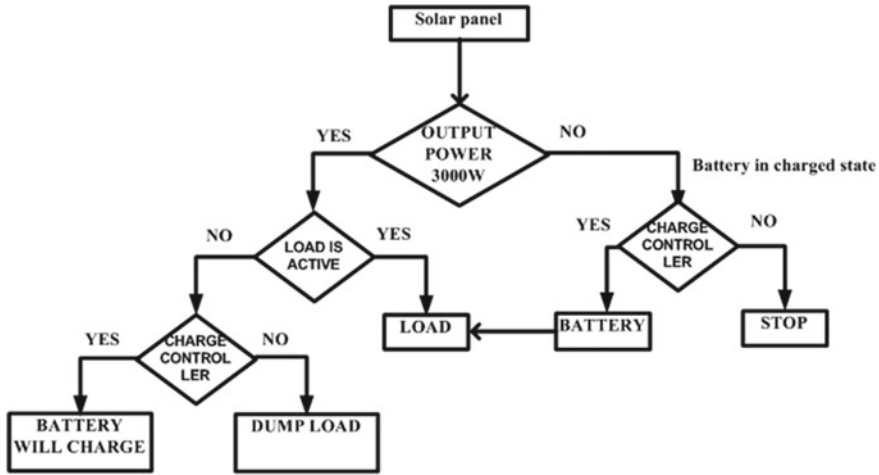


Fig. 12 Flowchart representation of the operating system

temperature will remain constant. The output power is supplied to loads. There is an excess power of 1000 W which is supplied to the battery. The initial charging state of the battery is low and hence the battery will continue to charge until it gets fully charged [10]. The entire working of this QBC fed with PV panel in various cases is explained by using the flowchart as shown in Fig. 12.

6 Non-Linear Sliding Mode Controller for QBC with BESS

Sliding mode controller (SMC) is one of the non-linear controllers used extensively for its robustness and insensitivity toward parameter changes [11, 12]. This controller mainly consists of designing a linear sliding surface to bring the state variables under consideration nearer to the sliding surface with less settling time [13, 14]. Once error signal reaches nearer to sliding surface the signal is forced to stay near the sliding surface. Here in this work, the sliding surface is designed with inductor current i_{L1} and voltage across the capacitor V_{c2} as shown in (20). It requires the generation of inductor current reference through a PI controller as shown in (21). The voltage reference is the desired DC voltage of 240 V (Figs. 13, 14 and 15 and Table 2) [2].

$$S = k_1(i_{L1ref} - i_{L1}) + k_2(v_{c2ref} - v_{c2}) \tag{20}$$

$$i_{L1ref} = (k_p + k_i/s)(v_{c2ref} - v_{c2}) \tag{21}$$

From the simulation results, it is clear that PV panel is delivering an output power of 3500 W. In this total power, 2500 W is consumed by the electrical load. Remaining

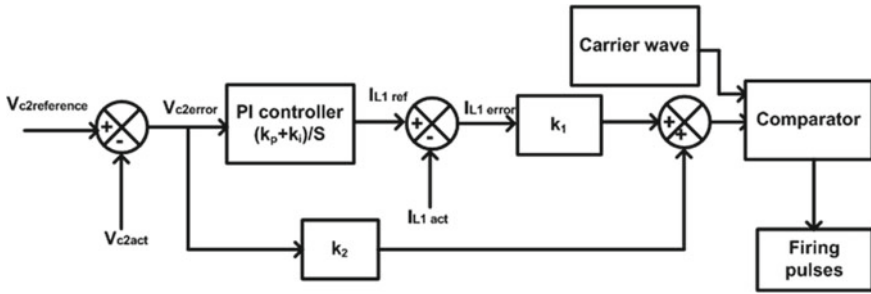


Fig. 13 Sliding mode controller for the QBC [2]

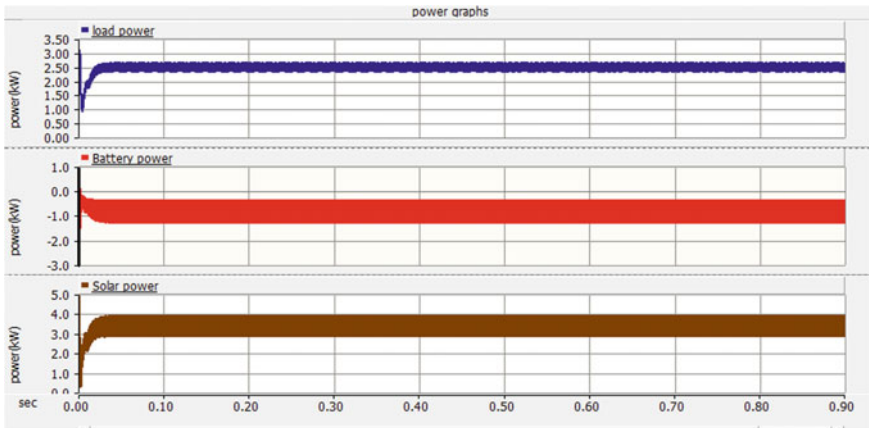


Fig. 14 Simulation waveform of PV panel power, Battery power and power consumed by the load

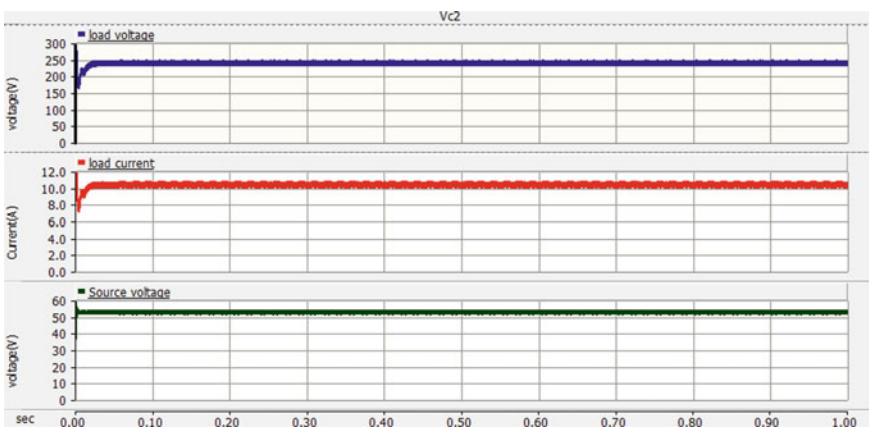


Fig. 15 Simulation waveforms of load voltage, load current and source voltage

Table 2 System parameters of quadratic boost converter [1]

Parameters	Value
Input solar power	
Case 1	3500 W
Case 2	2400 W
Battery power	7Ah
Input voltage	50 V
Capacitor C ₁	100μF
Capacitor C ₂	100 μF
Inductor L ₁	0.383mH
Inductor L ₂	2.66mH
Load resistance	23Ω

excess power is supplied to the battery. Battery was initially in fully drained state. Hence this power is used to charge the battery. Also in the simulation results, it is identified that the power at the battery is in negative which indicates charging state of battery (Fig. 16).

The voltage tracking of reference voltage and actual voltage is plotted through simulation. It was identified that a steady-state error of 2% difference is present in between the reference values and actual values. In the second case, the solar irradiation and temperature is reduced. This will concurrently reduce the output power of the solar panel. In this case, it is observed that the battery is compensating the deficient power (Figs. 17, 18 and 19).

In this case, the solar irradiation is reduced to 700 W/m² from its nominal value of 1000 W/m². The temperature is also reduced from 25 °C to 20 °C. Thus with the change in solar insolation the output power from the PV panel is reduced to 2.3 kW which is not sufficient to feed the electrical load connected to QBC. In this case, the deficient power is supplied by battery. The reference load current value is found out to be 10.41 A and the current ripple in the load current is observed to be 4%. Thus from the results, it is evident that the power required by the load is shared by the two

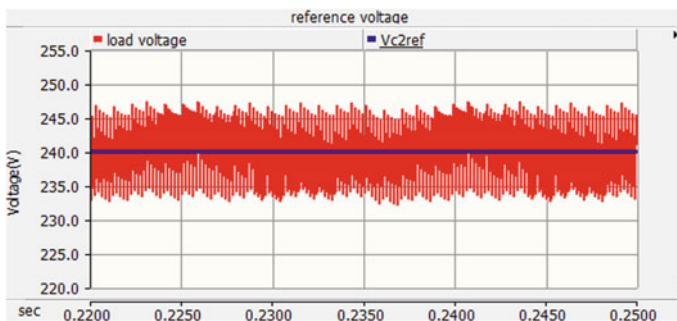


Fig. 16 Voltage tracking of reference voltage and load voltage

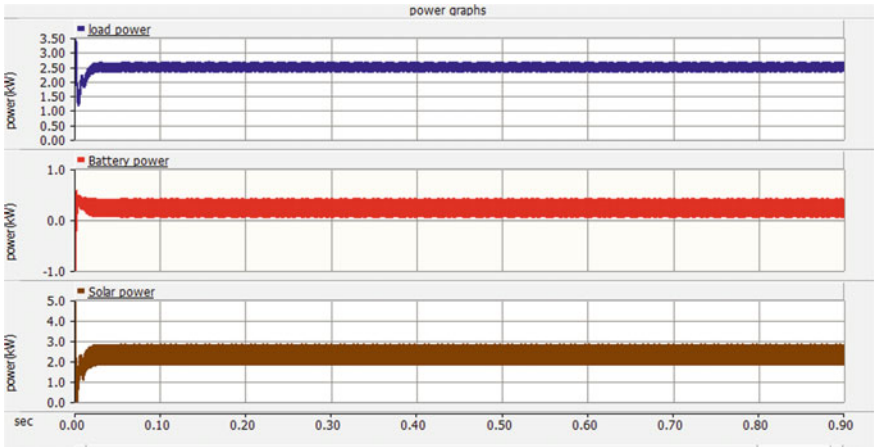


Fig. 17 Simulation waveforms of PV panel power, battery power and power consumed by the load

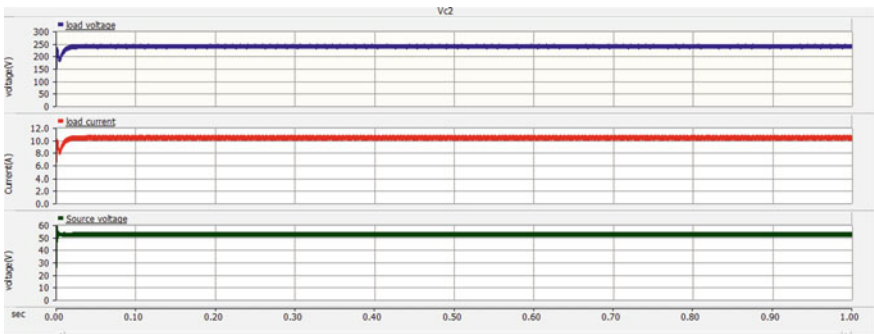


Fig. 18 Simulation waveforms of load voltage, load current and source voltage

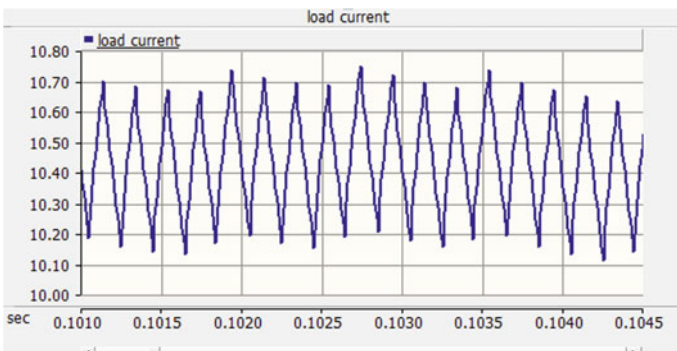


Fig. 19 Current tracking of load current

sources. Solar power is given outmost priority in supplying power to the electrical load. If solar power is not sufficient to meet the load requirements then the battery will supply that deficient power. In the simulation solar power is reduced by reducing the irradiation and temperature of the PV panel and desired results are obtained.

7 Conclusions

The paper presents the analysis of QBC with battery energy storage system. Mathematical model of the QBC is developed and the stability of the system is done using state feedback approach through frequency response plots. A comparison with the conventional boost converter is also presented. Sliding Mode Control is used to derive the switching signals to the IGBT switches used in the QBC. The inductor current references are generated with the voltage across the capacitors using a PI controller. Battery and Solar power as sources of power to QBC, different cases are presented. During the normal operating condition, the PV will supply the entire power to the DC load. Due to any change in climatic conditions if the output power of PV panel gets reduced then battery is supplying that deficient power. The results obtained show effective sharing of power by solar and battery during changes in temperature and irradiance. QBC having more voltage gain than the conventional boost converter and can be used with Solar and Battery is realized.

References

1. Amudhavalli D, Mohanty N (2020) Quadratic boost converter with integrated energy storage using pi controller for low power photovoltaic applications. *J Control Eng Appl Inf* 22(3):50–61
2. Naguboina VK, Gudey SK (2018) A compensation strategy using THSeAF in a distribution system based on smc for source side and load side control. In: *IEEE International conference on computing, power and communication technologies*. 27th and 28th September, Galgotias University, pp 433–438
3. Park S, Choi S (2010) Soft-switched CCM boost converters with high voltage gain for high-power applications. *IEEE Trans Power Electron* 25(5):1211–1216
4. VJ S, G, K, MP (2020) Interleaved quadratic boost DC–DC converter with high voltage gain capability. *Electric Eng* 102(2):651–662
5. Javadi A, Hamadi A, Al-Haddad K (2015) Three-phase power quality device for weak systems based on SRF and p-q theory controller. In: *IECON 2015—41st annual conference of the IEEE industrial electronics society*, pp 000345–000350. <https://doi.org/10.1109/IECON.2015.7392123>
6. Javadi A, Hamadi A, Woodward L, Al-Haddad K (2016) Experimental investigation on a hybrid series active power compensator to improve power quality of typical households. *IEEE Trans Industr Electron* 63(8):4849–4859. <https://doi.org/10.1109/TIE.2016.2546848>
7. Rashid MH (2011) *Power electronic converters handbook*. 3rd edn. Elsevier, Chapter-41, pp 1215–1216
8. Gupta R, Ghosh A, Joshi A (2011) Performance comparison of VSC based shunt and series compensators for load voltage control of a distribution systems. *IEE Trans Power Delivery* 26(1):268–278

9. Zhao Q, Tao F, Lee FC (2003) High-efficiency, high step-up dc–dc converters. *IEEE Trans Power Electron* 18(1):65–73
10. Naguboina VK, Gudey SK (2018) Enhanced exponential reaching law SMC for analyzing PQ issues in a distribution system using ThSeAF. In: Indian council international conference (INDICON)—15–18th December, IIT Madras, p 2018
11. Ban M, Yu J, Shahidehpour M et al (2019) Optimal sizing of PV and battery-based energy storage in an offgrid nan grid supplying batteries to a battery swapping station. *J Mod Power Syst Clean Energy* 7:309–320
12. Leyva-Ramos J, Ortiz-Lopez MG, Diaz-Saldierna LH, Morales-Saldana JA (2009) Switching regulator using a quadratic boost converter for wide DC conversion ratios. *IET Power Electron* 2(5):605–613
13. Yang P, Xu J, Zhou G, Zhang S (2012) A new quadratic boost converter with high voltage step-up ratio and reduced voltage stress. In: Proceedings of the 7th international power electronics and motion control conference, pp 1164–1168. <https://doi.org/10.1109/IPEMC.2012.6258989>
14. Yang HZ, Liu J (2009) Research on maximum power point tracking control based on the low power photovoltaic grid-connected inverter. In: IEEE power electronics and motion control conference, p 2165. <https://doi.org/10.1109/IPEMC.2009.5157760>

Thickness Control of Anti-Reflection Coatings Using TiO₂/SiO₂ Multilayer Films for Silicon Solar Cells



M. Vishwas

Abstract Application of titanium dioxide (TiO₂) and silicon dioxide (SiO₂) thin films prepared by the sol-gel process were studied for anti-reflection coating on silicon and glass substrates. The films were produced by spin-coating process using titanium tetra isopropoxide (TTIP) as the precursor material for TiO₂ and tetraethylorthosilicate (TEOS) as a precursor for SiO₂. The film thickness was controlled by adjusting the spinning speed and time to reduce the reflectance of the film on silicon wafer. The crystallinity, morphology and microstructure of the films were analyzed by x-ray diffraction (XRD) and scanning electron microscopy (SEM). Single, double and triple-layer TiO₂/SiO₂ stack coatings were fabricated on silicon wafer. The reflectance was reduced to 3% for three-layer film. Single and two-layer coatings were fabricated on glass substrates. The transmittance increased to ~97% for two-layer film measured in the visible region.

Keywords Anti-reflection coatings · TiO₂ · SiO₂ · XRD · SEM

1 Introduction

Titanium dioxide (TiO₂) is a trendy metal oxide nanomaterial with a large band gap used as high adsorbents and photo-electrodes [1, 2]. TiO₂ has an excellent photocatalytic property for the oxidative decomposition of some organic compounds [3, 4]. TiO₂ nanostructures attracted researchers due to their unique properties and potential applications in catalysis [5, 6]. Perkas et al. [7] reported the insertion of Au nanoparticles into titania by sonochemical reduction of gold ions. Sol-gel method is the cost-effective technique to deposit films at room temperature (RT) [8, 9]. There are many advantages and a few disadvantages of the films prepared by the sol-gel method. The preparation of TiO₂ and its applications are reported previously [10–13]. The research on anti-reflection coating (ARC) used for silicon solar cells has been continued both theoretically and experimentally from the last decade. Silicon

M. Vishwas (✉)

Department of Physics, Nrupathunga University, Nrupathunga road, Bengaluru 560001, India
e-mail: vishwasm46@yahoo.com

nitride (SiN), TiO_2 and silicon dioxide (SiO_2) are the excellent ARC materials with very good optical and electrical properties. Their combination will provide excellent optical reflection losses for photovoltaic applications [14, 15]. In this work, the efforts are made to fabricate ARC on glass and silicon substrates by controlling the film thickness of TiO_2 and SiO_2 .

2 Experimental Procedure

TiO_2 thin films were prepared by the sol-gel spin-coating technique using titanium tetra isopropoxide (TTIP) as the precursor and absolute ethanol as a solvent. TTIP, ethanol and concentrated HCl were taken in the volume ratios of 1:12:0.3, respectively. The solutions were stirred continuously for 30 min using a magnetic stirrer. The resultant sol obtained was kept in an air-tight beaker for 24 h to form colloidal gel of TiO_2 . SiO_2 gel was also prepared by the same process. Tetraethylorthosilicate (TEOS) was used as precursor of SiO_2 , ethanol as solvent and concentrated HCl as a catalyst. TEOS, ethanol and HCl were taken in the volume ratios 1:12:0.5, respectively. The resultant sol was stirred for 30 min and kept at rest for 24 h to obtain SiO_2 gel. Then two drops of TiO_2 and SiO_2 gel were taken on pre-cleaned (with RCA cleaning procedure) glass and silicon substrates and spin-coated alternately with a speed of 2000 to 3000 rpm with variable spinning duration to control the film thickness. $\text{TiO}_2/\text{SiO}_2$ multilayer films of anti-reflection coatings (ARC) were fabricated on glass and silicon substrates by making multiple trials of different thicknesses of films. Flow chart for the preparation of ARC is shown in Fig. 1. After the deposition of each layer, the film was dried at 80°C for 5 min in a furnace. The films were characterized

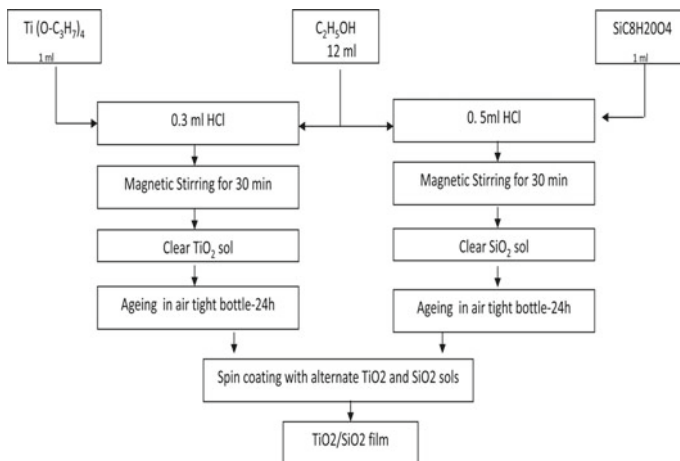


Fig. 1 Flow chart for the preparation of $\text{TiO}_2/\text{SiO}_2$ films

with reflectance and transmittance measurements using UV-VIS-NIR spectrophotometer (Ocean optics, USA). The film thickness was in the range 130-250 nm as measured by envelope method [16]. The refractive indices of the films deposited on silicon were measured using spectroscopic ellipsometer. The microstructure of the films was studied using SEM images.

3 Results and Discussions

Figure 2 shows the XRD spectra of $\text{TiO}_2/\text{SiO}_2$ film deposited on silicon substrate. It is clear from the figure that, both TiO_2 and SiO_2 films are amorphous as the diffraction peaks are not observed. The glancing angle is varied from 20 to 70 degrees. The diffraction peaks are the characteristics of crystallinity of the material. The x-rays of Cu-K α radiation are used for these studies. Amorphous materials do not scatter the x-rays. Only in crystalline materials, diffraction take place.

Figure 3 shows the SEM images of TiO_2 and SiO_2 films deposited on silicon substrates at RT. It is clear from the figure that, these films are featureless and amorphous. It is also observed in the figure that, SiO_2 film is more densely packed and compact compared to TiO_2 film. TiO_2 film converts from amorphous to polycrystalline anatase phase after annealing at 300 °C and higher temperatures [17]. At very high temperatures, TiO_2 exhibits rutile phase, which is not a stable phase and hence the anatase phase is the most stable phase. Here, amorphous materials are

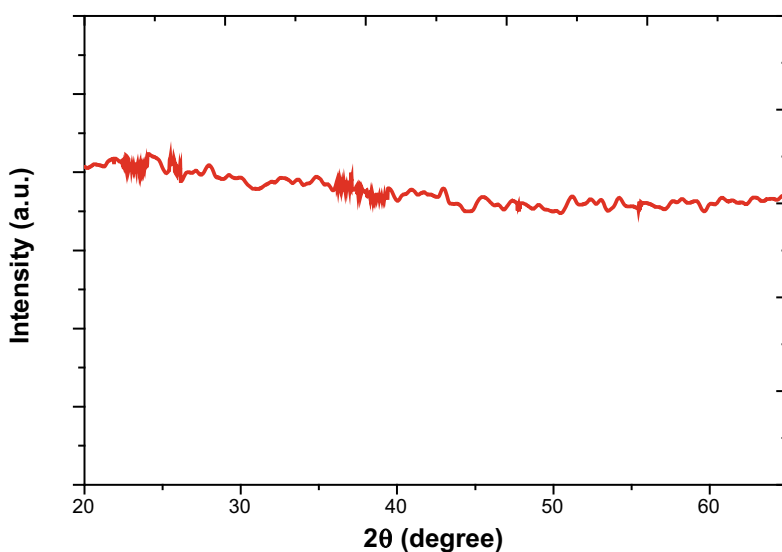


Fig. 2 XRD spectra of $\text{TiO}_2/\text{SiO}_2$ film deposited on silicon substrate at RT

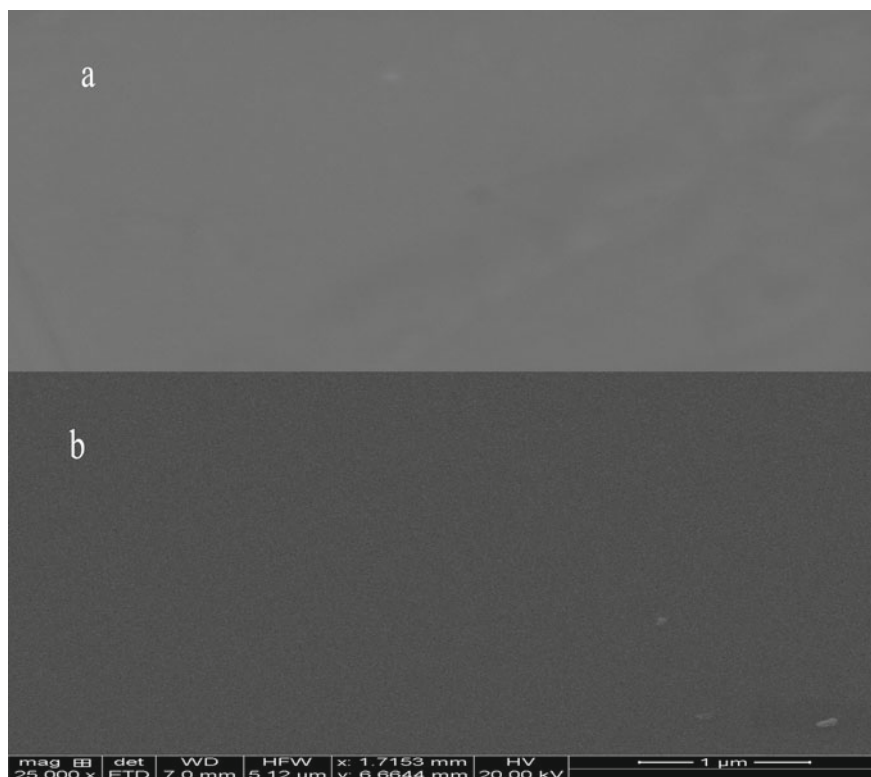


Fig. 3 SEM images of **a** TiO₂ film **b** SiO₂ film prepared on silicon substrate at RT

used for the anti-reflection coating applications. SiO₂ thin films are more uniform and transparent, with very low refractive index compared to TiO₂ thin films.

The refractive indices of the films are measured from the reflectance spectra and spectroscopic ellipsometry. The refractive indices of TiO₂ and SiO₂ films are 2.346 and 1.563, respectively measured at 550 nm.

Alternate layers of TiO₂ and SiO₂ films are deposited on glass and silicon substrates. Three-layer TiO₂/SiO₂ coating is fabricated on silicon substrate with film thickness as TiO₂(136 nm)/SiO₂(163)/TiO₂(187)/SiO₂(204)/TiO₂(232)/SiO₂(251). The average reflectance has been reduced from 38% (for one layer TiO₂/SiO₂) to 6% for two-layer TiO₂/SiO₂ and 3% for three-layer TiO₂/SiO₂ coatings in the wavelength range 500-750 nm as shown in Fig. 4. This is due to the fact that when the light undergoes reflections at multi layers, if the thickness of the film is equal to one-fourth of the wavelength of light, then reflected rays from different layers undergo destructive interference and the intensity of reflected light becomes virtually zero. In this work, it was not possible to get good ARC for one layer TiO₂/SiO₂.

One layer and two-layer ARC of TiO₂/SiO₂ film were fabricated on glass substrates with film thickness TiO₂(147 nm)/SiO₂(181)/TiO₂(203)/SiO₂(239). The

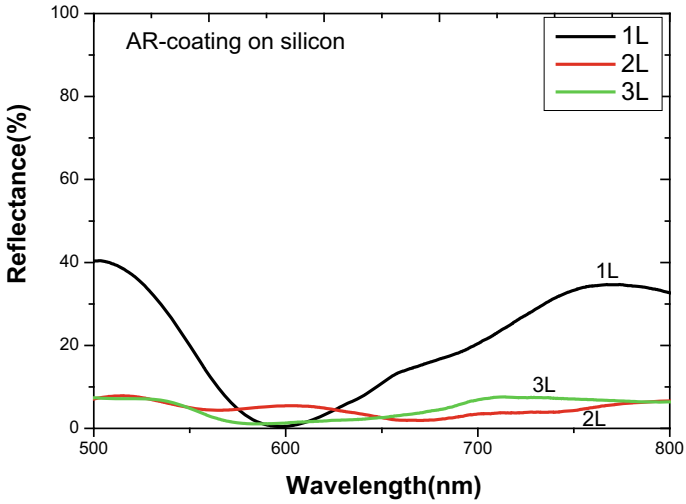


Fig.4 Reflectance spectra of single, double and triple-layer $\text{TiO}_2/\text{SiO}_2$ film anti-reflection coatings on silicon substrates

optical transmittance has been increased from 90% (for one layer $\text{TiO}_2/\text{SiO}_2$) to ~97% for two-layer $\text{TiO}_2/\text{SiO}_2$ coatings in the wavelength range 450–550 nm as shown in Fig. 5.

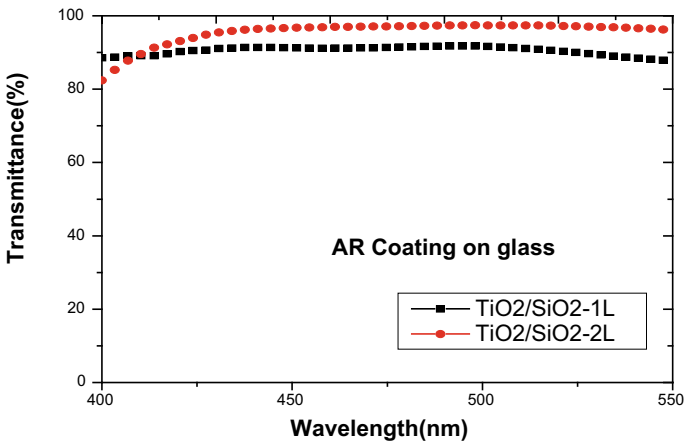


Fig.5 Transmittance spectra of single and double-layer $\text{TiO}_2/\text{SiO}_2$ film (ARC) on glass substrate

4 Conclusion

TiO₂/SiO₂ films of cost-effective ARC were fabricated successfully on glass and silicon substrates by controlling the film thickness by the sol-gel method. Three-layer ARC on silicon exhibited very low reflectance in the visible region. This can be used for silicon solar cell applications.

Acknowledgements The author is thankful to Dr. K. Narasimha Rao, Chief Research Scientist (Retd.), Department of Instrumentation and Applied Physics, Indian Institute of Science, Bangalore, for their support and encouragement. The author is also grateful to DST-FIST programme, Central Instrumentation Centre (CIC), Nrupathunga University, Bangalore for utilizing the facilities.

References

1. Sonawane RS, Kale BB, Dongare MK (2004) Preparation and photo-catalytic activity of Fe-TiO₂ thin films prepared by sol-gel dip coating. *Mat Chem Phys* 85:52–57
2. Yu JC, Wang XC, Fu XZ (2004) Pore-wall chemistry and photocatalytic activity of mesoporous titania molecular sieve films. *Chem Mater* 16:1523–1530
3. Temerov F, Haapanen J, Mäkelä JM, Saarinen JJ (2021) Photocatalytic Activity of Multicomponent TiO₂/SiO₂ nanoparticles. *Inorganics* 9(21):1–12
4. Hashimoto K, Irie H, Fujishima A (2005) TiO₂ photocatalysis: a historical overview and future prospects. *Jap J Appl Phys* 44(12):8269–8285
5. Bagheri S, Julkapli NM, Hamid SBA (2014) Titanium dioxide as a catalyst support in heterogeneous catalysis. *Sci World J* ID-727496, 1–21
6. Magalhães P, Andrade L, Nunes OC, Mendes A (2017) Titanium dioxide photocatalysis: fundamentals and application on photoinactivation. *Rev Adv Mat Sci* 51:91–121
7. Perkas N, Pol VG, Gedanken A (2006) Gold-induced crystallization of SiO₂ and TiO₂ powders. *Cryst Growth Des* 6:293–296
8. Vishwas M. Rao, K. N., Phani, A.R., Arjuna Gowda, K.V.: Sol-gel synthesis and optical characterization of nano-crystalline ZnTiO₃ thin films. *J Opt.* **41** (1) 60–64 (2012).
9. Vishwas, M., Rao, K. N., Phani, A.R., Arjuna Gowda, K.V., Chakradhar, R.P.S.: Spectroscopic and electrical properties of SiO₂ films prepared by simple and cost effective sol-gel process. *Spectrochimica Acta Part A.* **78**, 695–699 (2011).
10. Vishwas M, Rao KN, Neelapriya D, Raichur AM, Chakradhar RPS, Venkateswarulu K (2014) Effect of TiO₂ nano-particles on optical, electrical and mechanical properties of poly (vinyl alcohol) films. *Proc Mat Sci* 5:847–854
11. Vishwas, M. Sharma, S. K., Rao, K. N., Mohan, S., Arjuna Gowda, K.V., Chakradhar, R.P.S.: Sol-gel synthesis, characterization and optical properties of TiO₂ thin films deposited on ITO/glass substrates. *Mod. Phys. Lett. B.* **24**, 807–816 (2010).
12. Vishwas, M., Rao, K. N., Chakradhar, R.P.S., Raichur, A. M. : Effect of film thickness and annealing on optical properties of TiO₂ thin films and electrical characterization of MOS capacitors, *J Mat. Sci.: Mat. Electron.* **25**, 4495–4500 (2014).
13. Ali, Z., Raj, B., Vishwas, M., Athhar, M. A.: Synthesis, Characterization and Antimicrobial Activity of Ce Doped TiO₂ Nanoparticles. *Int. J Cur. Microbio. & Appl. Sci.* **5**(4), 705–712 (2016).
14. Sahuane N, Zerga A (2014) Optimization of antireflection multilayer for industrial crystalline silicon solar cells. *Energy Procedia* 44:118–125
15. Richards BS (2004) Comparison of TiO₂ and other dielectric coatings for buried-contact solar cells: a review. *Progress Photo Res Appl* 12(4):253–281

16. Swanepoel R (1983) Determination of the thickness and optical constants of amorphous silicon. *J Phy E: Sci Instr* 16:1214
17. Vishwas, M., Sharma, S. K., Rao, K. N., Mohan, S., Arjuna Gowda, K.V., Chakradhar, R.P.S.: Influence of surfactant and annealing temperature on optical properties of sol-gel derived nano-crystalline TiO₂ thin films. *Spectrochim. Acta Part A*.**75**, 1073–1077 (2010).

Implementation of Optocoupler Test Fixture in Incoming Quality Control



S. G. Yashaswini and Rashmi

Abstract The optocoupler is an electronic component that transmits an electrical signal between isolated circuits using light. Its high failure causes in most of the cases the breakdown of the whole equipment. To overcome this, we need to implement one optocoupler test fixture in this work, the process and electrical characteristics of this component is studied and a special attention to the most significant parameters. The hardware design of optocoupler test fixture is used for automated testing of optocoupler. Test fixture is a customized tool specially made to hold the device under test. It is automated test equipment (ATE) that is used to verify quality specifications, reliability and functionality of the component. This test provides information on performance of optocoupler in advance to avoid reloading due to defective PCB assembly. This fixture will test all voltage conditions, current conditions and current transfer ratios. The description of the test fixture, test plan and its implementation and results are presented and discussed.

Keywords Automated test equipment · Test fixture · Current transfer ratio

1 Introduction

Hardware design of test fixture is used for automated testing of optocoupler. Automated Test Equipment is a customized fixture made for testing of the component. When designing a test fixture that will be susceptible to lightning strikes, power supply spikes and voltage surges, there is a need to protect and also an electrical type of control is adopted with the help of all electrical ratings to design the test fixture that is used to test the optocoupler sample. Different types of accelerated endurance

S. G. Yashaswini · Rashmi (✉)

Department of Electrical and Electronics Engineering, Siddaganga Institute of Technology,
Tumakuru, Karnataka, India

e-mail: rash_mysore@sit.ac.in

S. G. Yashaswini

e-mail: yashaswini.govindaraju@gmail.com

test under high temperature, high current and other types are applied to some batches of optocoupler samples to determine the best fault signature of the components [1].

In this paper, Optocoupler test fixture is designed and implemented for Industrial applications. In Industry, quality is the basic thing therefore any component before giving to the production line it should be tested in incoming quality control. Optocoupler test fixture is used in the incoming quality control for verifying the quality of the component before giving to the production line [2].

Implementation of optocoupler test fixture which is interesting by design and implementation. The proposed automated optocoupler test fixture design is to overcome the existing manual testing of optocoupler with related test plan to demonstrate the optocoupler test fixture.

All the data from the test fixture will be forwarded to LCD display. Embedded C is used to programme the PIC16F886 microcontroller with the help of mikroC PRO for PIC software to display the output condition in the hexadecimal display which will indicate the voltage, current and current transfer ratio (CTR) ratings. The purpose of testing is to determine which part of optocoupler is not functioning and also recognize fault in the component in advance to avoid defective PCB assembly at production line, to avoid field failure and collect data from the defective samples for analysis purposes [1, 2].

2 Methodology

2.1 Circuit Diagram of Test Fixture of Optocoupler

The Proposed Test Fixture of Optocoupler comprises of Current Regulator, Voltage Regulator, Relay, zero insertion force socket, Capacitor, Resistor, Transistor, SPDT, SPST Switches and Connectors as appeared in Fig. 1.

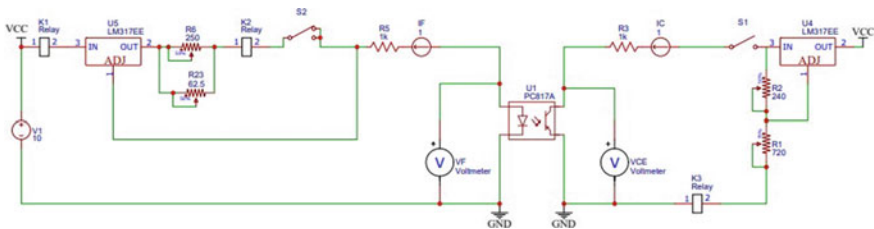


Fig.1 Schematic of the proposed optocoupler test fixture

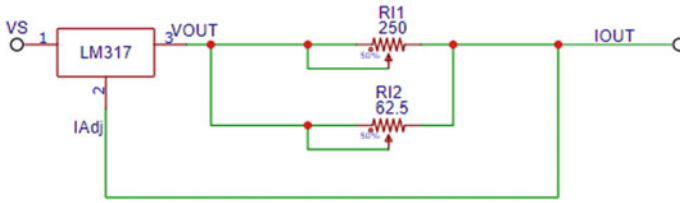


Fig. 2 Circuit diagram of Adjustable Current Regulator

2.2 Current Regulator

LM317 Adjustable Current Regulator is shown in Fig. 2. It is so difficult to vary the current and voltage at a same time in a circuit. So two regulators are used in test fixture design. LM317 Current Regulator is used in the input side. It usually involves variation in the resistance to achieve the required current [3]. The formula to calculate value of variable resistance R11 and R12 is

$$\begin{aligned}
 I_{out} &= 1.25/R11 & I_{out} &= 1.25/R12 \\
 R11 &= 1.25/5mA & R12 &= 1.25/20mA \\
 R11 &= 250\Omega & R12 &= 62.5\Omega
 \end{aligned}
 \tag{1}$$

Adjust R11 is 250 Ω and R12 is 62.5 Ω by using regulator to maintain the constant current.

2.3 Voltage Regulator

LM317 Adjustable Voltage Regulator is shown in Fig. 3. It is used in the output side. By varying the resistance or current to achieve the required voltage. Being the

Fig. 3 Circuit diagram of adjustable voltage regulator

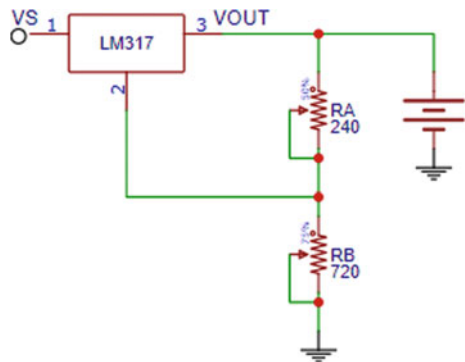




Fig.4 Front and back view of LCD display panel

variable resistance RA is 240Ω. To calculate RB will yield an output of 5V. The output voltage is shown in the below equation [3, 4]

$$\begin{aligned}
 V_{out} &= 1.25\left(1 + \frac{RA}{RB}\right) \\
 5V &= 1.25\left(1 + \frac{RB}{240}\right) \\
 RB &= 720 \Omega
 \end{aligned}
 \tag{2}$$

Set RA is 240 Ω and RB is 720 Ω resistances by using the regulators to maintain constant voltage.

2.4 LCD Display

Liquid crystal Display is a Flat panel display technology. It is connected to the test fixture. Embedded C is used to programme the PIC16F886 microcontroller. Programming is done with the help of MikroC Pro for PIC software to display the output condition in the display (Fig. 4).

2.5 Pic Kit 3 Programmer

Pic kit 3 is a programmer used for software and hardware development of microchip pic microcontroller. The input is from PC and then pic kit 3 programmer is connected to the LCD Display. It is used to feed the program in it and display the output condition in the display (Fig. 5 and Table 1).

- Current Transfer Ratio is the ratio of collector current (Ic) at the output side to the forward current (If) passes through the light-emitting diode at the input side. It is calculated by using the below formula:

Fig. 5 Pic kit 3 programmer

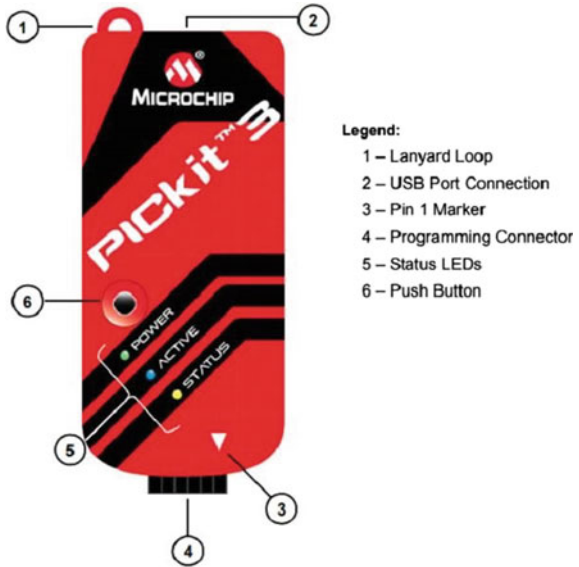


Table 1 Electrical characteristics of Optocoupler

Parameter	Min	Type	Max	Units	Test Conditions
Forward voltage (V_f)	-	1.2	1.4	V	$I_F = 20 \text{ mA}$
Reverse Current (I_r)	-	-	10	μA	$V_R = 4 \text{ V}$
Terminal Capacitance	-	30	250	pF	$V = 0, f = 1 \text{ kHz}$
Collector Current	2.5	-	30	mA	$I_F = 5 \text{ mA}, V_{ce} = 5 \text{ V}$
Collector dark Current (I_{ceo})	-	-	100	nA	$V_{CE} = 20 \text{ V}$
Collector-emitter saturation voltage ($V_{ce(sat)}$)	-	0.1	0.2	V	$I_C = 1 \text{ mA}, I_F = 20 \text{ mA}$
Collector-Emitter Breakdown voltage (BV_{ceo})	70	-	-	V	$I_C = 0.1 \text{ mA}$
Emitter-Collector Breakdown voltage (BV_{eco})	6	-	-	V	$I_E = 10 \text{ mA}$
Collector-emitter saturation voltage	-	0.1	0.2	V	$I_C = 1 \text{ mA}, I_F = 20 \text{ mA}$
Floating Capacitance	-	0.6	1.0	pF	$V = 0, f = 1 \text{ MHz}$
Cut-off Frequency	-	80	-	kHz	$V_{cc} = 5\text{v}, I_c = 2 \text{ mA}$
Current transfer ratio (CTR)	50	-	600	%	$I_C/I_F * 100$

$$\text{CTR} = \frac{\text{IC}}{\text{IF}} * 100 \quad (3)$$

Based on the above theory and electrical characteristics of the Optocoupler [5], the automated test fixture is designed. Insert the optocoupler in Zip socket, Switch on the power supply set 12v dc supply, set forward current (IF) using current regulator, noted down forward voltage (VF), collector-emitter voltage (V_{ce}), Current transfer ratio (CTR) in the LCD display. It will display the VF , IF and CTR and also it will display optocoupler sample is 'Pass' or 'Fail'. Embedded C is used to program the PIC16F886 microcontroller. Programming is done with the help of mikroC pro for PIC software to display the output condition in the LCD display. PC is connected to PIC kit 3 programmer is used to store the program then it will load to the hardware testing jig. Testing jig is connected to the LCD display according to the inbuilt program it will display the results. As studied earlier, if any one condition is not valid the optocoupler sample is 'NOT OK' it will display the 'FAIL' and if all the condition is valid the optocoupler sample is 'OK' then it will display 'PASS' in the output screen [1, 1].

2.6 Hardware Designing of Test Fixture

The automated test fixture designing is done with the help of embedded C language to program the microcontroller using mikroC pro software the data is fed in the pic kit 3 through the connectors it is connected to the LCD to display the output conditions.

By pressing the ON button, the working of the system started and the test fixture gets initialized. As per the coding, the microcontroller will check all conditions step by step if any one condition will fail further testing is stopped. All the condition is displayed in the LCD display.

Figure 6 shows the indication of the output condition in the LCD display. When the working of the system is started. Test fixture is initialized with help of microcontroller it will display the initializing command 'Press Start Switch to Begin' in the screen.

Figure 7 shows the after initializing command by pressing the start switch in the LCD display after 100ms delay it will indicate the 'Testing' started in the display.

Figure 8 indicates Voltage conditions, Current conditions and Current transfer ratio (CTR) output ratings of the Optocoupler in the LCD display.

If all the conditions are 'ok' as per the electrical characteristics of the optocoupler then it will indicate all the conditions forward voltage, collector current and current transfer ratio and also the pass in the lcd display. If any one condition is failed further testing is stopped and also indicates fail in the display [8, 8].

For a Good Optocoupler—It will display Forward Voltage (VF)—(1.1 to 1.4V), Collector Current (IC)—30mA(max), Current Transfer Ratio (CTR)—(50 to 600%).

For a BAD Optocoupler—It will display Forward Voltage (VF) lesser than 1.1V more than 1.4V, Collector Current shows less than 30mA, Current Transfer Ratio (CTR) shows the lesser than 50% more than 600%.

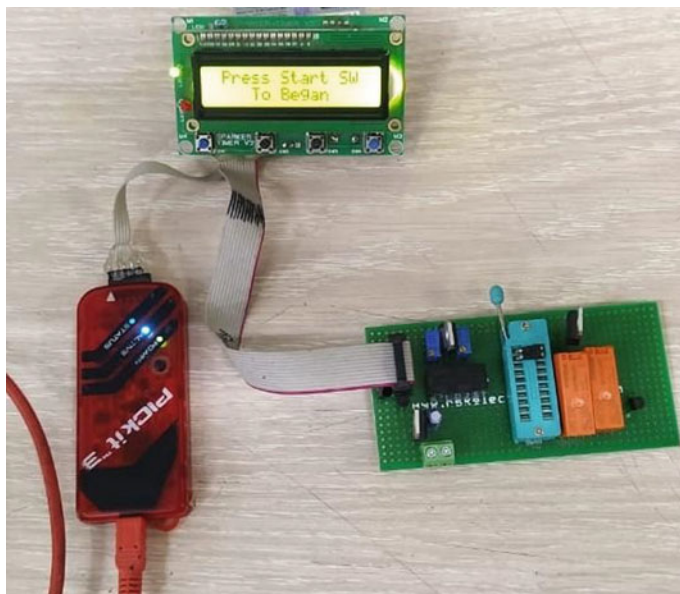


Fig. 6 Front panel of the output display indicates initializing command

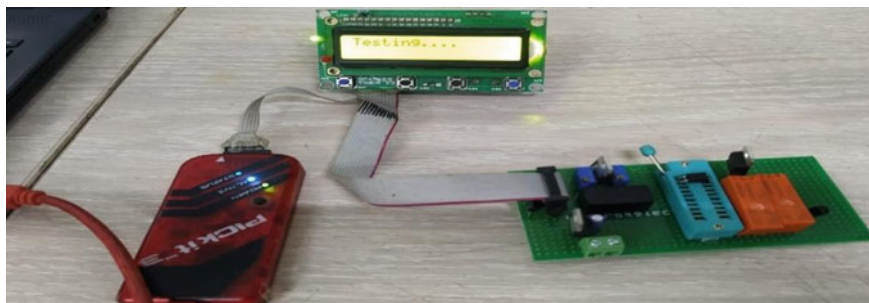


Fig. 7 Front panel of the output display indicates testing after 100 ms delay

2.7 Flow Chart

See Fig. 9.

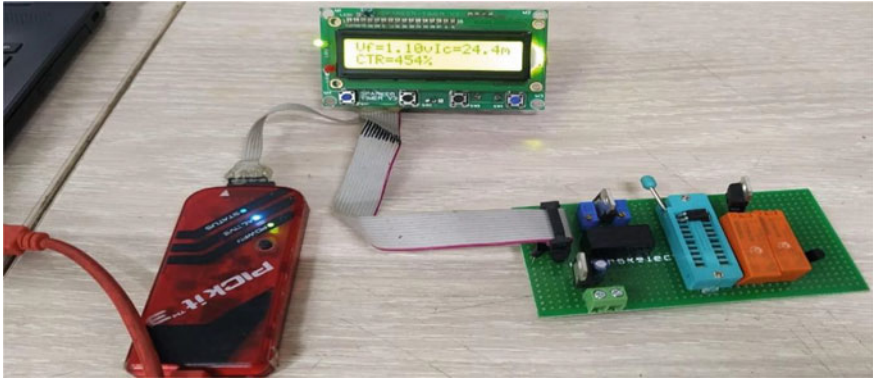
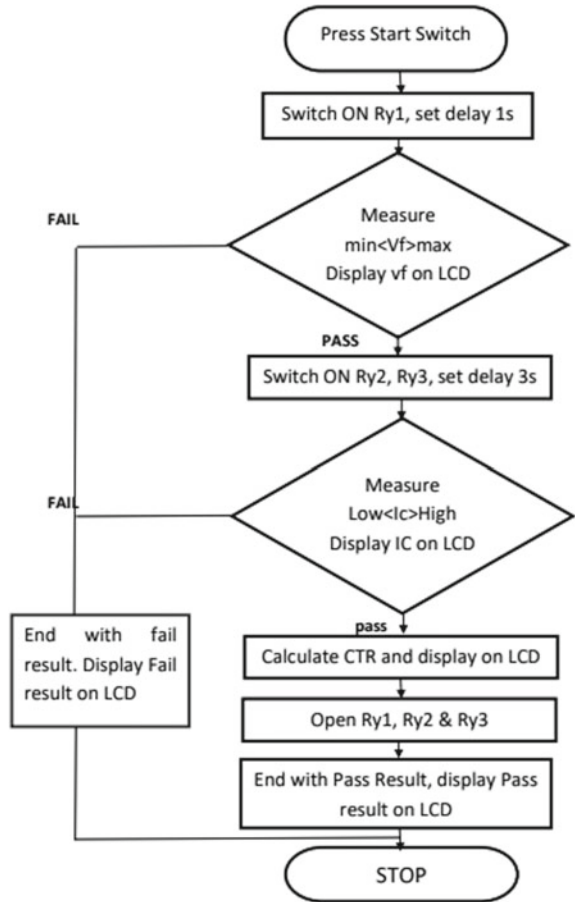


Fig. 8 Output display indicates Forward Voltage, Collector Current, CTR

Fig. 9 Flow chart of optocoupler test fixture



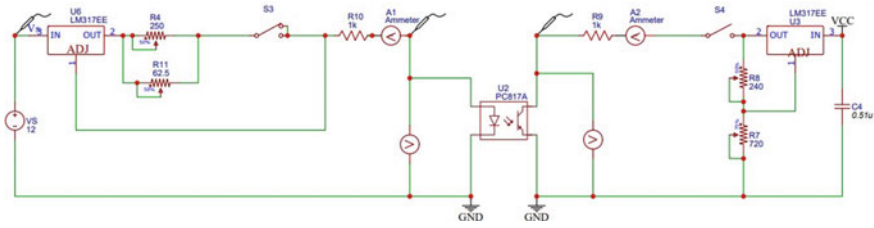


Fig. 10 Simulated circuit configuration of test fixture of optocoupler

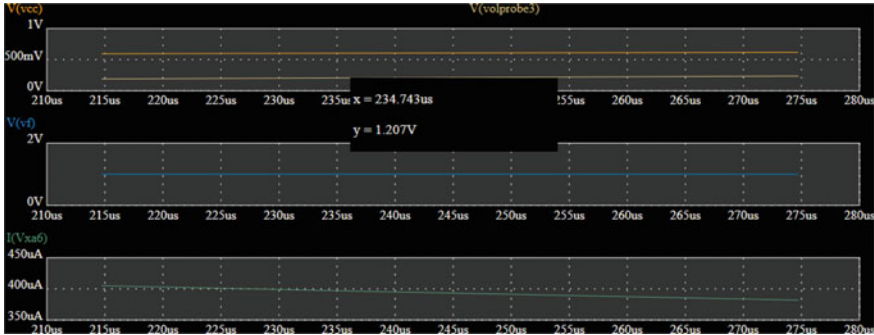


Fig. 11 Simulated waveform of input voltage, forward voltage and current

3 Simulation Results

Simulation of Optocoupler test fixture diagram is carried out in Electrical Design Software. It helps to identify whether the signal flow is correct or not. Simulated waveforms of input voltage, Forward voltage and Current as shown in Figs. 10 and 11.

4 Conclusion

Automated testing of optocoupler is more accurate, faster, more efficient and eliminates human error compared with manual testing. The implementation of new optocoupler test fixture design in incoming quality control process in order to measure the quality specifications of the component and also to avoid component failures in production line [11]. Automated testing is executed in a planned manner offers greater benefits and also worth it. Embedded C is used to programme the PIC16F886 microcontroller with the help of mikroC pro for PIC software to display the output condition and also shows the test results are obtained as Pass or Fail. Moreover, the automated testing of optocoupler test fixture is efficient and interesting as tests are demonstrated in less time and economical.

References

1. Verma S, Wagdarikar NM Automated test jig for refrigerator PCB performance” 2016 “International conference on automatic control and dynamic optimization techniques (ICACDOT). In: International Institute of Information Technology (I²IT), Pune
2. Andria G, Di Nisio A, Scarano VL, Bregoli M, Franceschi M, Tavernini N (2014) Accelerated life tests of a new opto-coupler aerospace application. In: 2014 IEEE 978–1–4799–2069–3/14© 2014
3. Napolitano P, Kelliher K Design of voltage regulators for automotive applications: a sensitivity-driven approach. In: IEEE 2017 28th Irish signals and systems conference (ISSC)—Killarney, Co Kerry, Ireland 2017 28th Irish Signals
4. P. Napolitano, K. Kelliher, B. Al Mukhtar, D. Carey, and O. Cregg, “An effective methodology for robust design of monolithic voltage regulators,” 2016 IEEE International Conf. on Electronics, Circuits and Systems (ICECS), pp. 197–200, 2016.
5. Ben Hadj Slama J, Helali H, Lahyami A, Louati K, Venet P, Rojat G (2007) Optocouplers ageing process: study and modeling. In: International conference on Electrical Engineering Design and Technologies, Hammamet Tunisia
6. Damle R, Sujatha R, Kumar D Electron beam induced degradation in electrical characteristics of Optocoupler. 1530–4388© 2020 IEEE
7. Xialiang L, Pengchao X, Yanqiu L, Bo M, Hongwei Z, Lei L (2019) Study on radiation mechanism and test for CTR of optocoupler. 5(32):543–548
8. Panov Y, Jovanovic MM (2005) Small- signal analysis and control design of isolated power supplies with optocoupler feedback. IEEE Trans Power Electron 20(4)
9. Zhicheng S, Xiaolin WYZ, Rong Y (2015) Evaluation of radiation performance of optocouplers used in LEO spacecrafts. Spacecraft Environ Eng 5(32):543–548
10. Shi Z, Lu Y, Chen Y, Feng J The real-time fault diagnosis of optocoupler inswitching mode power supply. In: 2014 international conference on reliability, maintainability and safety (ICRMS)
11. Thaduri A, Verma AK, Vinod G, Gopalan R (2011) Reliability prediction of optocouplers for the safety of digital instrumentation. In: IEEE international conference on quality and reliability, pp 491–495

Energy Resource Planning for a Rural Microgrid: A Sensitivity Analysis



Yuvraj Praveen Soni  and E. Fernandez

Abstract In this paper, we present the sensitivity analysis of an optimal renewable energy resource allocation for a rural microgrid using four renewable energy resources—solar PV energy, micro-hydro energy, wind energy, and biomass energy. Three issues are considered that can have an impact on the sensitivity, namely cost of energy due to each energy resource, the changes in the demand for energy, and the efficiency of the conversion devices used with each energy resource. The sensitivity is determined as the value of the influencing parameter at which the solution of the optimization becomes infeasible. For the analysis, using a linear programming (LP) optimization model, data used have been drawn from a reported study on a rural hilly village cluster in Ranikhet district of Uttarakhand state (India). The sensitivity analysis shows that each control parameter shows different levels of sensitivity to change in regard to the four renewable energy resources providing energy for the microgrid.

Keywords Energy resource planning · Linear programming · Sensitivity analysis · Rural microgrid

1 Introduction

Resource allocation has always been a great challenge and area of interest for rural energy planners. In developing countries like India, the access to electrical energy for rural areas, in general, has been seen as a major challenge. Conventional grid supply runs through coal, or oil-based plants are either too expensive, or it is not feasible to reach remote areas due to geographical challenges. To promote clean energy and green energy, it is advisable [1] to utilize renewable energy that are abundantly presents, and combination can be made through different sources so as to accommodate reliable power with optimum operation cost. Area where grid connection is not feasible may acquire for renewable energy sources which are integrated

Y. P. Soni (✉) · E. Fernandez
Indian Institute of Technology Roorkee, Roorkee, India
e-mail: Yuvraj.soni21092@gmail.com

© The Author(s), under exclusive license to Springer Nature Singapore Pte Ltd. 2022
V. Mahajan et al. (eds.), *Sustainable Technology and Advanced Computing in Electrical Engineering*, Lecture Notes in Electrical Engineering 939,
https://doi.org/10.1007/978-981-19-4364-5_85

1203

and installed locally to generate and supply power to local consumers. However, if available and required, grid can be connected for an external support. Renewable energy resources such as solar, micro-hydro, wind, biomass, and biogas, which are environmentally friendly and clean sources of energy [2], can be profitably tapped for an integrated power delivery system to the rural microgrid.

Least cost optimization of the supply of integrated rural energy system resources for meeting the energy demands of the villages is an important policy exercise that ensures economic benefits. With this in view, several studies have evolved optimization models for study of rural energy resource allocation systems.

Many of these use a linearized objective function for minimum cost of energy supply to the system. Joshi et al. [3] applied linear programming (LP) to develop a model for energy resource allocation in a typical Indian rural scenario. In another paper, Joshi et al. developed LP optimization models for energy resource planning in villages of Nepal [4]. Das [5] proposed multi-objective linear programming for energy policy referring to renewable sources in Tamilnadu, India. Similar algorithm is implemented by Raja et al., [6] for energy planning for sustainable agriculture development in the Madurai District, Tamilnadu, India.

LP optimization model developed by Kanniappan and Ramachandra [7] to assess the land area for agriculture and cultivation to meet the food requirement through biomass optimal location. Proposed model contains human labor, animal and tractor power as per the identified region of Tamilnadu area in India. Devdas [8] presents optimum resource allocation in rural area of Kanyakumari District in Tamilnadu, India, with use of LP algorithm. Objective function defined is to increase the revenue of the rural system with optimum resource allocation with energy and non-energy relevant constraints. Parikh [9] discusses general LP model used to indicate supply-demand model to capture energy and agricultural interaction.

Thus, we see that LP has been a popularly used optimization tool for energy planning. However, in the recent years, there has been a spate of literature reporting the use of nonlinear algorithms for use in optimizing energy management [10–14].

A fuzzy-based multi-objective analysis for the energy allocation for household cooking in Uttar Pradesh, India, was presented by Agrawal and Singh [10]. The results focused on the economic, environmental, and technical concerns. Chauhan and Saini [11] applied the discrete harmony search technique for energy planning for remote areas of Uttarakhand state (India). Genetic algorithms (GAs) were tried for energy planning studies by some researchers [12–14]. Sharafi and El Mekawy [15] applied the particle swarm optimization (PSO) algorithm for hybrid energy system planning.

Thus, we see that in general, optimization algorithms have been widely used in energy planning studies. Studies that deal with the sensitivity analysis of optimization algorithms are, however, rare. This paper therefore attempts a study in this direction. For simplicity, we have used a LP model pertaining to the energy resource allocation problem in a rural microgrid supplied by various energy resources.

2 Energy Allocation Problem

An LP optimization model has been used which incorporates available renewable energy sources for power generation to have electricity as an end product. The generated power is mainly supplied to different rural activities such as for agricultural uses, domestic and small-scale industrial sectors. Considered linear model is shown below—

$$\text{Minimize } C_{\text{total}} = \sum C_{ij} * R_{ij} \tag{1}$$

$$\text{Subject to } \sum R_{ij} = D_j \tag{2}$$

$$\sum \frac{R_{ij}}{\eta_{ij}} \leq S_{ij} \tag{3}$$

$$R_{ij} \geq 0 \tag{4}$$

where

C_{Total} = Total cost of energy (Rs in INR).

C_{ij} = Energy cost per unit for i th resource for j th end use (Rs/kWh).

R_{ij} = Optimal value of i th resource for j th end use (kWh).

D_{ij} = Total energy available for j th end use (kWh),

S_{ij} = Availability of the i th resource in the area for j th end use (kWh).

η_{ij} = Conversion efficiency for the i th resource for j th end use.

To conduct the analysis, we need to use practical field data. As a working basis, this data were drawn largely from [16] with minor modifications for other data used in the model formulation. Typical practical efficiencies for the energy resource conversion have been used.

The resources used for the model are as follows: solar photovoltaic resources (SPVs), wind energy resources (WESs), micro-hydro power (MHP), and biogas energy (BES) for biomass gasified generators. Details of the available potential in respect of these resources are given in Tables 1 and 2 pertaining to efficiency

Table 1 Available potential, efficiency, and cost of energy resources in the area [16]

S. No.	Available type of generation	Maximum capacity (kWh/yr)	Efficiency	Cost (Rs/kWh)
1	Micro-hydro power (MHP)	293,040	0.80	1.96
2	Solar photovoltaic power (SPV)	12,859	0.13	3.0
3	Wind energy (WES)	8890	0.47	3.48
4	Biomass energy (BES)	198,556	0.30	3.1

Table 2 Effective considered cost of operation for various generation options

S. No.	Type of energy activity	Average energy demand (kWh/year)
1	Domestic	157,130
2	Rural industries	18,815
3	Agriculture	177,779
4	Community activities	5276
Total		359,000

of conversion, energy demand for various activities, and effective cost of energy obtained from each type of generation.

3 The Sensitivity Analysis

The energy allocation model used shows that there are three factors that control the optimized outputs. These are as follows: (a) Cost of the energy resource/kWh C_{ij} (b) The resource availability of each source of energy for the supplied area S_{ij} and (c) The efficiency of the conversion of the system used η_{ij} . The object of the analysis is to understand how each of these factors, if changed, will affect the overall optimized cost of total supplied energy. These changes in the control variables are carried out one at a time keeping the other system parameters or energy resources magnitudes fixed. The changes are introduced from +1% to +50%. The sensitivity of each of the control variable can then be observed for each energy resource used in the model.

4 Results and Discussions

Tables 3, 4, and 5 show the changes in the optimal cost for variation of the three control variables from +1% to +50%. Table 3 shows how changes in C_{ij} will affect the magnitude of Z (Total optimal cost of supplied energy).

Table 3 Effect of changes of C_{ij} on total optimal cost of energy supplied

S. No.	% Change in C_{ij} (%)	% Change in total optimal cost Z			
		MHP	SPV	WES	BES
1	+1	0.5425	0.0059	0.0309	0.4361
2	+2	1.0851	0.0118	0.0309	0.8721
3	+5	2.7127	0.0296	0.0773	2.1805
4	+10	5.4254	0.059	0.1546	4.361
5	+20	10.8508	0.1125	0.3092	8.722
6	+30	16.2763	0.1570	0.4638	13.083
7	+50	27.1272	0.2460	0.7730	21.746

Table 4 Effect of changes of S_{ij} on total optimal cost of energy supplied

S. No	% Change in S_{ij} (%)	% Change in total optimal cost Z			
		MHP	SPV	WES	BES
1	+ 1	-0.4207	-0.00095	0	-0.0534
2	+ 2	-0.7999	-0.0019	0	-0.1069
3	+ 5	-1.7466	-0.0047	0	-0.1688
4	+ 10	-3.324	-0.0095	0	-0.1688
5	+ 20	-6.480	-0.019	0	-0.1688
6	+ 30	-9.636	-0.0285	0	-0.1688
7	+ 50	-15.947	-0.047	0	-0.1688

In Table 3, we see that for an increase from + 1% to + 50%, the largest changes in magnitude of Z are largest for MHP and least for SPV. In fact, for SPV and WES, the changes in Z are less than 1% even at + 50% changes in C_{ij} . The relative ordering of the sensitivity changes for C_{ij} for the different energy resources follows the descending order: **MHP > BES >> WES > SPV**.

This observation leads to the conclusion that in an optimal resource allocation scenario, relative impacts of SPV and WES on Z are not as significant as those for BES and MHP. Table 4 shows how changes in resource availability S_{ij} affect the magnitude of Z.

Table 4 shows that in case of three energy resources, namely MHP, SPV and BES, there is a successive fall in the magnitude of Z. (i.e., negative change) It is maximum in case of MHP by as much at -16% approximately and least for SPV with - 0.05% approximately. BES also shows an insignificant change, which is maintained constant maximum of approx. -0.17%. WES shows zero change for the entire range of variation. The increase in Z can also be interpreted as a greater consumption of a particular energy resource vis-a-vis' others. Thus, it becomes clear that increases in the resource availability of BES, SPV, and WES may not yield as much effect on Z as MHP. The greater availability of MHP resource and its relatively lower cost/unit steers the optimal solution accordingly. The relative ordering of the sensitivity changes for S_{ij} for the different energy resources follows the descending order: **MHP > > BES > SPV > WES**.

Table 5 shows how changes in efficiency of conversion (η_{ij}) affect the magnitude of Z.

Table 5 shows that of the four energy resources, only, WES has an increasing impact on Z. The others show a negative impact, i.e., Z is reduced. The greatest impact is observed in the case of MHP (-16% approx.) and the least in the case of SPV (-0.05% approx.). BES appears to indicate an unchanging (but very low) change of -0.17% approximately. Thus, in regard to efficiency improvements, it is more beneficial to improve efficiency of MHP subsystem in comparison to the other energy resource sub-systems.

Table 5 Effect of changes of η_{ij} on total optimal cost of energy supplied

S. No.	% Change in η_{ij} (%)	% Change in total optimal cost Z			
		MHP	SPV	WES	BES
1	+ 1	-0.4207	-0.0009	0.0155	-0.053
2	+ 2	-0.7999	-0.0019	0.0155	-0.1069
3	+ 5	-1.7466	-0.0047	0.0155	-0.1688
4	+ 10	-3.324	-0.0095	0.3092	-0.1688
5	+ 20	-6.480	-0.0189	0.3092	-0.1688
6	+ 30	-9.630	-0.0284	0.4638	-0.1688
7	+ 50	-15.94	-0.0473	0.7730	-0.1688

The relative ordering of the sensitivity changes for S_{ij} for the different energy resources follows the descending order: **MHP >> BES >> SPV >> WES**.

5 Conclusion

In conclusion, the paper presents a sensitivity analysis for energy resource allocation of a rural microgrid supplied by four energy resources, i.e., MHP, SPV, WES, and BES. From the results of the analysis, it is observed that it would be preferable to direct further attention to the MHP sub-system in comparison to the other energy resources sub-systems, as it can provide the most profitable benefits in relation to cost objective function “Z.”

References

1. Kumar A, Singh AR, Deng Y, He X, Kumar P, Bansal RC (2019) Integrated assessment of a sustainable microgrid for a remote village in hilly region. *Energy Convers Manag* 180:442–472
2. Kanase-Patil AB, Saini RP, Sharma MP (2007) Development of integrated renewable energy systems for electrification of rural remote areas. All India Seminar on ‘Energy, Environment Economics’. Rourkela, 3–4
3. Joshi B, Bhatti TS, Bansal NK (1992) Decentralized energy planning model for a typical village in India. *Energy* 17(9):869–876
4. Joshi B, Bhatti TS, Bansal NK, Rijal K, Grover PD (1991) Decentralized energy planning model for optimum resource allocation with a case study of the domestic sector of rurals in Nepal. *Int J Energy Res* 15:71–78
5. Das TK (1987) Multi-objective linear programming approach to renewable energy policy analysis. *Energy Manag Convers* 55–121
6. Raja R, Sooriamoorthi CE, Kannappan P, Ramachandran T (1997) Energy planning and optimization model for rural development—a case of sustainable agriculture. *Energy Res* 21:527–548
7. Kannappan P, Ramachandran T (1998) Optimisation model for energy generation from agricultural residue. *Energy Res* 22:1121–1132

8. Devdas V (2001) Planning for rural energy system: Part I". *Renew Sustain Energy Rev* 5:203–226
9. Parikh J (1985) Modeling energy and agriculture interactions: a rural energy systems model. *Energy* 10(7):793–804
10. Agrawal RK, Singh SP (2001) Energy allocations for cooking in UP households (India): fuzzy multi-objective analysis. *Energy Manag Convers* 42:2139–2154
11. Chauhan A, Saini RP (2016) Discrete harmony search based size optimization of integrated renewable energy system for remote rural areas of Uttarakhand state in India. *Renew Energy* 94:587–604
12. Vergara PP, Torquato R, Silva LCP (2015) Towards a real-time energy management system for a microgrid using a multi-objective genetic algorithm. *IEEE PES General Meet* 1–55
13. Husmann H, Tantau H (2001) Integrated optimization of energy supply systems in horticulture using genetic algorithms. *Comput Electron Agric* 31(1):47–59
14. Arabali A, Ghofrani M, Fadali MS, Baghzouz Y (2013) Genetic-algorithm-based optimization approach for energy management. *IEEE Trans Power Delivery* 28(1):162–170
15. Sharafi M, El Mekkawy TY (2014) Multi-objective optimal design of hybrid renewable energy systems using PSO-simulation based approach. *Renew Energy* 68:67–79
16. Kanase-Patil AB, Saini RP, Sharma MP (2010) Integrated renewable energy systems for off grid rural electrification of remote area. *Renew Energy* 35:1342–1349

Optimized Renewable Energy Resource Planning for a Rural Microgrid with Linear and Nonlinear Algorithms



Yuvraj Praveen Soni , E. Fernandez, Md. Mustafa Kamal, and Imtiaz Ashraf

Abstract In this paper we present an optimal renewable energy resource allocation for a rural microgrid using four renewable energy resources—solar PV energy, micro-hydro energy, wind energy and biomass energy. A linear optimization algorithm [Linear Programming (LP)] is contrasted with a nonlinear optimization [Genetic Algorithm (GA)] to examine the relative effectiveness of each approach. It is seen that the nonlinear approach yields better optimized estimates. Data for the analysis has been drawn from a reported study on rural hilly village in Uttarakhand state, India.

Keywords Energy resource planning · Linear programming · Nonlinear programming · Genetic algorithm (GA) · Rural microgrid

1 Introduction

Being rapid utilization of fossil fuels which are almost at the verge to get into the category of extinction, it is required to look for an alternate source of energy for power generation. Renewable energy sources are abundantly available and can also be harnessed for power generation. However, proper planning and utilization is the main key which also helps overall growth of the country. These renewable energies such as solar photo-voltaic system [SPV], micro-hydro plant [MHP], wind energy system [WES], biomass [BES] and biogas are climate friendly and clean source of energy [1]. It would be very great if a country mainly developing country like India can have access to this resources for the electrification purposes. Grid power which operates through majorly coal plants are sometimes not feasible to reach to the rural community due to complex geographical location or even if it gets into that location

Y. P. Soni (✉) · E. Fernandez
Indian Institute of Technology Roorkee, Roorkee, India
e-mail: yuvraj.soni21092@gmail.com

Md. M. Kamal · I. Ashraf
Zakir Hussain College of Engineering and Technology, Aligarh Muslim University, Aligarh, India

it may be costly to have for core rural people. To have sustainable and economical power, it is a need to make proper planning for hybridization of renewable energy sources [2]. Even a combination of renewable energy sources can be installed in a rural area which can supply reliable power as grid supplies or even it can get connected to conventional grid for power support.

Xubin Wang et al., [3], Yongle Zheng et al., [4] and Habib Ur Rahman Habib et al., [5] discusses the planning of rural microgrid concerning energy policies, transformation, geographical characteristics to calculate the optimum point for economical and sustainable operation. G. Muñoz-Delgado [6] utilizes non-simulated-based linear programming model to evaluate the reliability of the system. Patil [7] have considered energy index ratio (EIR) and expected energy not supplied (EENS) for remote area planning and solved through LINGO and HOMER software.

Joshi [8] utilizes linear programming considering domestic and irrigation sectors to minimize cost function for a typical village in India. It was suggested that uses of bio gas with reduced rate might results into a decent combination for power generation and supply. A similar work is discussed by Zhen [9] for minimization of energy cost through linear model optimization. An advancement to the technique is proposed by Rijal [10] which used linear regression model to forecast energy requirement at different scenarios by rural community and so to operate the generation to minimize cost.

Energy resource allocation for a rural area has been always a great challenge and area of interest among rural energy planners. Most of the reported work in the literature makes use of optimization algorithms, of which the most widely used is the Linear Programming (LP) approach. However, some research investigations have suggested the possibility of obtaining improved optimization results when the linear form used in the case of LP is solved using nonlinear algorithms.

In this paper an attempt has been made to investigate with respect to the LP algorithm, the Genetic Algorithm a nonlinear algorithm to solve the energy allocation problem for a rural microgrid. Taking the case of reported data of a rural hilly village from Uttarakhand State in Northern India, the two algorithms are compared for relative effectiveness.

2 Structure of the Proposed Microgrid

The microgrid being considered here is a microgrid proposed for a rural hilly area in the state of Uttarakhand (India). Proposed system is a general and common layout which is opted by most of the literature's [11–13]. The shown structure is consisting of AC and DC buses which can facilitate the loads based on its type to be connected from AC or DC bus. Both the bus is interlinked with appropriate power converter which further improves its reliability as compared other proposed system which have unconnected AC/DC bus structure [14].

In proposed layout four renewable energy resources have been identified for harvesting energy to meet local load requirements. There are: solar PV, wind, biomass

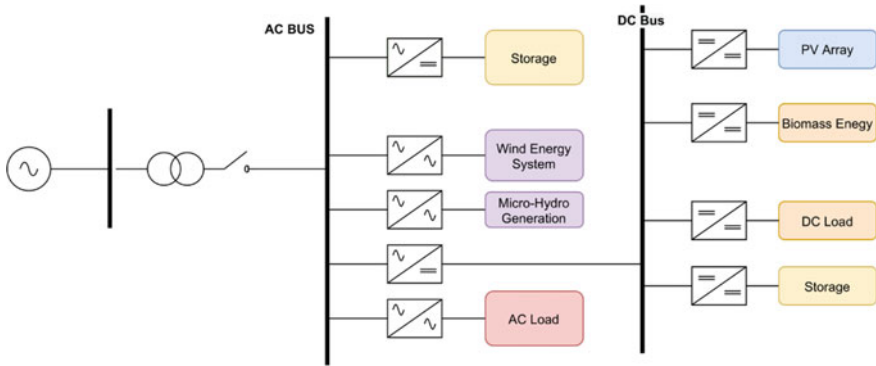


Fig. 1 Basic layout of the proposed microgrid scheme

resources and small hydro potential. AC/DC and DC/DC converters are employed to power two separate microgrid buses- AC and DC. AC and DC loads are present with energy storage available at each bus. AC motor loads (M) are directly connected to the AC bus. Figure 1 shows the schematic layout of this system. Both isolated as well as grid connected operation is possible.

Power generation from renewable energy cannot be accurately forecasted due to intermittent nature which depends upon the surrounding climate and geographical topology. Some resources may have great potential in summer while other may have in different seasons. Considering this facts a proper combination of these resources are necessary for planning so as to make operation cost to be optimum. The village considered in this study lies in hill ranges where grid electrification may not be an suitable solution due to extra burden and charges involved due to geographical limitation. Due to the limitation, isolated microgrid is the viable option that can be installed at the area to have an access to power.

3 Optimization Using Linear Programming and Genetic Algorithm

Linear Programming (LP) has been a popular choice of a simple optimization algorithm expressed as a linear objective function. In the literature a number of energy resource planning studies have been reported that make use of LP [7–10]. It is felt worthwhile to examine if nonlinear algorithms can yield better objective function estimates, when used with linear objective functions. In order to test this hypothesis, we need to apply a nonlinear algorithm to a linear objective function. In this paper, we try to see the outcome using a single nonlinear algorithm. In the literature there are several such nonlinear algorithms [15–18]. However, here we have applied only one algorithm—the Genetic Algorithm (GA) to examine the hypothesis [19–22].

The basic GA algorithm is explained as follows:

1. Generate the initial population strings of possible solutions
2. Evolve a fitness function and test the initial population possible solutions.
3. Filter out the favorable possible solutions.
4. Magnify the possible feasible solutions as a new population to be further tested.
5. Subject the new population to processes like mutation and cross over to avoid the local minima trap.
6. Test proposed solution again with fitness function.
7. If acceptable solution is obtained based on the convergence limits set, print solution and end.
8. If not, redo step 3–7.
9. Select the best solution based on the convergence limits set (Fig. 2).

4 The Microgrid Energy Resource Planning Model

The energy resources used for the model are: SPV, WES, MHP and BES for biomass gasified generators. To examine the hypothesis, we make use of the data reported in literature [23] for a rural hilly village in Uttarakhand State (India). For structuring the linear objective function, the data presented in literature [23] was therefore used to arrive at a cost minimization objective function Z that would yield the least cost of the operation. This objective function [23] is given as:

$$\text{Minimize } Z = 1.50 \text{ HP} + 15.27 \text{ SPV} + 3.50 \text{ WES} + 3.10 \text{ BES} \quad (1)$$

$$\text{Subject to : } \text{MHP} + \text{SPV} + \text{WES} + \text{BES} = D \quad (2)$$

$$\text{MHP}/0.90 \leq 128, 166 \text{ kWh} \cdot \text{m}^2 \cdot \text{yr}^{-1} \quad (3)$$

$$\text{SPV}/0.90 \leq 22, 363 \text{ kWh} \cdot \text{m}^2 \cdot \text{yr}^{-1} \quad (4)$$

$$\text{WES}/0.80 \leq 15, 251 \text{ kWh} \cdot \text{m}^2 \cdot \text{yr}^{-1} \quad (5)$$

$$\text{BES}/0.90 \leq 641, 385 \text{ kWh} \cdot \text{m}^2 \cdot \text{yr}^{-1} \quad (6)$$

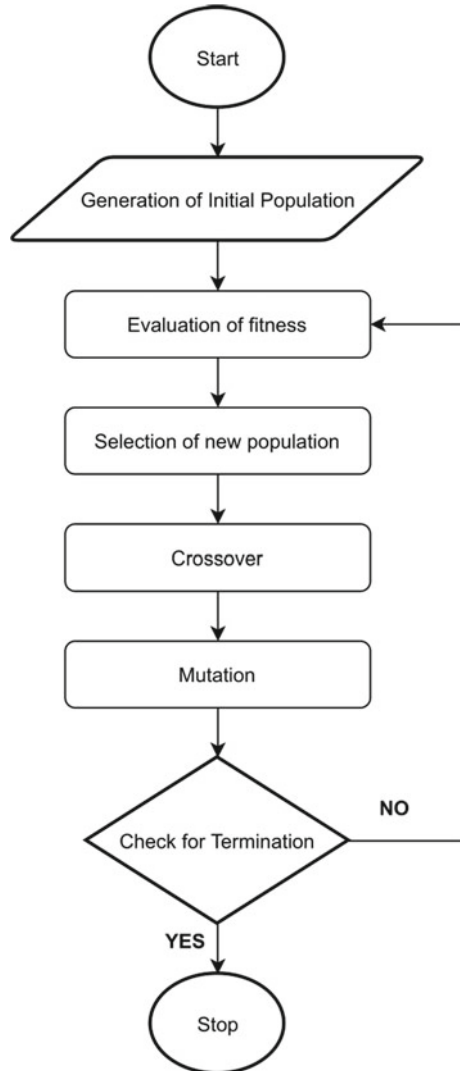
$$\text{MHP, SPV, WES, BES} \geq 0 \quad (7)$$

Where

$D = 686,800 \text{ kWh/yr}$ or 687 MWh/yr .

$\text{MHP} = \text{Energy Contribution from micro-hydro power plant.}$

Fig. 2 Flow chart of genetic algorithm



SPV = Energy Contribution from the solar power plant,
 BES = Energy Contribution from biogas gasifier electricity generation,
 WES = Energy Contribution from wind energy power plant.

Due to non-regular availability of renewable energy inputs, introduced a factor called Effective Power Delivery Factor (EDPF) to give an estimation of the reduced power available with respect to the designed output capacity. This factor is defined as the ratio of power obtained per season (year) to the maximum power theoretically possible per season.

$$EPDF = \frac{\text{Power obtained per season}}{\text{maximum power possible per season}} \tag{8}$$

Introduction of EPDF factor gives rise to different sub-models, which may be investigated by an optimization algorithm.

5 Results and Discussion

It is clear that in each case of EPDF, the estimates using GA are much better than those using LP. Table 2 shows the relative distribution allocation of the energy resources (Table 1).

Table 2 shows that although the objective function (Total cost of energy, as indicated in Table 1) is much lower for GA than for LP, yet the relative distribution/allocation of the energy resources follows no specific pattern, although, in most cases the allocation of a resource using GA is lower than the corresponding values using LP. The manner in which each algorithm operates to generate the least cost results in widely different allocations of resources.

From Table 1 it is noted that with EPDF reduction GA tends to give more improved results. As when EPDF = 1, GA provides 0.6% improved results whereas for EPDF

Table 1 Total cost of energy by different algorithms

S. No.	EPDF	Linear Programming (LP) [19] in Rs	Genetic algorithm(GA) in Rs
1	1.00	2,134,710	2,121,732
2	0.75	4,176,533	1,601,264
3	0.50	1,613,229	1,061,798
4	0.35	1,438,320	743,045
5	0.25	1,321,715	530,881

Table 2 Performance for active load increases in individual buses

EPDF	SOLAR PV (kWh)		WES (kWh)		MHP (kWh)		BES (kWh)	
	LP	GA	LP	GA	LP	GA	LP	GA
0.25	5037	3049.84	3050	3576.82	542,826	28,836.98	135,886	136,236.34
0.35	7051	4269.61	4270	4991.95	485,237	40,370.73	190,241	190,747.70
0.5	10,073	6014.08	6100	7159.38	398,853	57,673.34	271,773	272,553.18
0.75	183,391	9149.16	9151	11,429.04	86,599	86,435.51	407,660	408,086.28
1	15,588	12,191	12,201	14,160.45	115,465	115,347.88	543,546	545,100.65

= 0.25, GA gives 60% more improved result as compared to linear programming algorithm. With an EPDF = 0.25, GA reduces the cost involved by 60%.

6 Conclusion

In this paper, planning of rural microgrid is discussed considering and comparing linear and nonlinear algorithms for cost minimization. It is observed that nonlinear algorithm provides more suited results in comparison to linear programming. Both the algorithms result to different allocation of each energy resources however it is worth to mention that for a planner final resource allocation may not be of any disconcertment when it leads to optimum operation cost with satisfying all operating constraints. Thus a conclusion can be drawn that nonlinear algorithm mainly focusing on GA gives more improved results as compared to LP. Although in this study a single case is considered, further work can aim to compare it with other novel algorithms that are being developed to solve more complex problems and can be tried and tested before generalizing the trend. Also, as an extension to this study other nonlinear algorithms like PSO, Ant colony optimization, etc. maybe tried to see if the trends observed here can be safely generalized.

References

1. Kanase-Patil AB, Saini RP, Sharma MP (2007) Development of integrated renewable energy systems for electrification of rural remote areas. All India Seminar on 'Energy, Environment Economics', NIT Rourkela, 3–4
2. Kumar A, Singh AR, Deng Y, He X, Kumar P, Bansal RC (2019) Integrated assessment of a sustainable microgrid for a remote village in hilly region. *Energy Convers Manag* 180:442–472
3. Wang X, Li P, Zhang J, Zheng Y, Li H, Hu W (2021) Optimal planning and operation of typical rural integrated energy systems based on five-level energy hub. In: *Proceedings of 2021 3rd Asia energy and electrical engineering symposium (AEEES)*, 1108–1117
4. Zheng Y, Xiang Y, Hu W, Li H, Wang Y, Xu L (2020) Optimal rural integrated energy system configuration against the background of the rural energy transformation strategy. In: *Proceedings of 2020 15th IEEE conference on industrial electronics and applications (ICIEA)*, 516–521
5. Habib HUR et al (2021) Optimal planning and EMS design of PV based standalone rural microgrids. *IEEE Access* 9:32908–32930
6. Muñoz-Delgado G, Contreras J, Arroyo JM (2018) Reliability assessment for distribution optimization models: A non-simulation-based linear programming approach. *IEEE Trans Smart Grid*. 9(4):3048–3059
7. Kanase-Patil AB, Saini RP, Sharma MP (2010) Integrated renewable energy systems for off grid rural electrification of remote area. *Renew Energy* 35:1342–1349
8. Joshi B, Bhatti TS, Bansal NK (1992) Decentralized energy planning model for a typical village in India. *Energy* 17(9):869–876
9. Zhen F (1993) A model of the energy-supply and demand system at the village level. *Energy* 18(4):365–369

10. Rijal K, Bansal NK, Grover PD (1990) Rural household energy demand modeling. *Energy Econ* 279–88
11. Jayachandran M, Ravi G (2017) Design and optimization of hybrid micro-grid system. *Energy Procedia* 117:95–103
12. Liu Z, Miao S, Wang W, Sun D (2021) Comprehensive control scheme for an interlinking converter in a hybrid AC/DC microgrid. *CSEE J Power Energy Syst* 7(4):719–729
13. Fu Q, Nasiri A, Solanki A, Bani-Ahmed A, Weber L, Bhavaraju V (2015) Microgrids: architectures, controls, protection, and demonstration. *Electric Power Components Syst* 43(12):1453–1465
14. Alanazi A, Lotfi H, Khodaei A (2017) Coordinated AC/DC microgrid optimal scheduling. In: 2017 North American power symposium (NAPS), pp 1--6
15. Bernal-Agustin JL, Dufo-Lopez R (2009) Efficient Design of hybrid renewable energy using evolutionary algorithms. *Energy Convers Manage* 50(3):479–489
16. Hakimi SM, Moghaddas-Tafreshi SM (2009) Optimal sizing of a stand-alone hybrid power system via particle swarm optimization for Kahnouj area in south-east of Iran. *Renewable Energy* 34(7):1855–1862
17. Chauhan A, Saini RP (2016) Discrete harmony search based size optimization of Integrated Renewable Energy System for remote rural areas of Uttarakhand state in India". *Renew Energy* 94:587–604
18. Suganthi ST, Devaraj D, Hosimin Thilagar S (2015) An improved differential evolution algorithm for congestion management considering voltage stability. *Indian J Sci Technol* 8(24):1–9
19. Mayer MJ, Gróf G (2020) Techno-economic optimization of grid-connected, ground-mounted photovoltaic power plants by genetic algorithm based on a comprehensive mathematical model. *Sol Energy* 202:210–226
20. Arabali A, Ghofrani M, Fadali MS, Baghzouz Y (2013) Genetic-algorithm-based optimization approach for energy management. *IEEE Trans Power Delivery* 28(1):162–170
21. Vergara PP, Torquato R, Silva LCP (2015) Towards a real-time energy management system for a microgrid using a multi-objective genetic algorithm. In: 2015 IEEE power and energy society general meeting, pp 9–13
22. Husmann H, Tantau H (2001) Integrated optimization of energy supply systems in horticulture using genetic algorithms. *Comput Electron Agric* 31:47–59
23. Akella AK, Sharma MP, Saini RP (2007) Optimum utilization of renewable energy sources in a remote area. *Renew Sustain Energy Rev* 11(5):894–908